Proceedings Book

International Conference on Engineering Sciences

November 11-12, 2022 / Baku

Azerbaijan Technical University

International Conference on Engineering Sciences

November 11-12, 2022 / Azerbaijan Technical University / Baku

PROCEEDINGS BOOK

EDITORS
Prof. Dr. Vilayat Valiyev
Assoc. Prof. Dr. Derya Çini Şimşek

by
IKSAD PUBLISHING HOUSE®

All rights of this book belong IKSAD Publishing House
Authors are responsible both ethically and jurisdically
IKSAD Publications – 2022©
Issued: 20.12.2022

ISBN: 978-625-6955-08-0

CONFERENCE ID

CONFERENCE TITLE
International Conference on Engineering Sciences

DATE and PLACE
November 11-12, 2022 / Azerbaijan Technical University / Baku

PARTICIPATION
Keynote & Invited

ORGANIZATION
Azerbaijan Technical University, Azerbaijan
IKSAD-Institute of Economic Development and Social Research, Türkiye

PARTICIPANTS COUNTRY
Azerbaijan, Türkiye, North Macedonia, Colombia, India, Nigeria, Iraq, Bulgaria, Pakistan, Algeria, Portugal, UK, China, Brazil, Tunisia, Austria, France

PRESENTATION
Oral presentation

EVALUATION PROCESS
All applications have undergone a double-blind peer review process

Number Of Accepted Papers-**80**
Number Of Rejected Papers-**13**
The number of abstracts from foreign countries-**43**
The number of abstracts from Türkiye-**37**

Organazing Board

Prof. Vilayat Valiyev
Rector of Azerbaijan Technical University
Head of Conference

Prof. Nurali Yusifbeyli – Azerbaijan Technical University, Vice-Rector
Prof. Subhan Namazov – Azerbaijan Technical University, Vice-Rector
Assoc. prof. Ph.D. Kamran Rasulov – Azerbaijan Technical University, Vice-Rector
Assoc. prof. Ph.D. Rashad Aliyev – Azerbaijan Technical University, Vice-Rector
Assoc. prof. Ph.D. Rashad Kazimov – Azerbaijan Technical University, Vice-Rector
Ph.D. Fariz Mammadov - Azerbaijan Technical University, Rector's Adviser on International Relations
Assoc. prof. Ph.D. Arastun Mammadov - Azerbaijan Technical University, Head of the Education Department
Prof. Yusuf Sonmez - Azerbaijan Technical University, Director of the Institute of Higher Education
Assoc. prof. Allahverdi Sharifov - Azerbaijan Technical University, Dean of the Faculty of Transport and Logistics
Assoc. prof. Huseyngulu Guliyev - Azerbaijan Technical University, Dean of the Faculty of Energy and Automation
Assoc. prof. Nizami Poladov - Azerbaijan Technical University, Dean of the Faculty of Metallurgy and Materials Science
Assoc. prof. Malik Garayev - Azerbaijan Technical University, Dean of the Faculty of Mechanical Engineering and Robotics
Assoc. prof. Taleh Shirinov - Azerbaijan Technical University, Dean of the Faculty of Information and Telecommunication Technologies
Assoc. prof. Fargana Musayeva - Azerbaijan Technical University, Dean of the Faculty of Economics and Management
Assoc. prof. Elchin Rzayev - Azerbaijan Technical University, Dean of the Faculty of Special Techniques and Technology
Safa Bagirov - Azerbaijan Technical University, Deputy Head of Media and Communication Department
Ali Khalilov - Azerbaijan Technical University, Head of Information and Communication Technologies Department
Sevinj Isgandarov - Azerbaijan Technical University, Press Secretary

Scientific Board

Prof. Eldar Gocayev, Azerbaijan Technical University, Natural and fundamental sciences
Prof. Alakbar Huseynov, Azerbaijan Technical University, Special equipment and technology
Prof. Diego Alejandro Penagos Vásquez - Instituto Tecnológico Metropolitano, Medellín, Colombia
Prof. Dr. Brahim Lejdel - University of El-Oued, Algeria.
Prof. Fakhreddin Yusubov, Azerbaijan Technical University, Chemical technology
Prof. Isa Khalilov, Azerbaijan Technical University, Mechanical engineering and robotics
Prof. Dr. Kamil Bostan - İstanbul Aydın University, Türkiye
Prof. Dr. Muhammad Ovais Omer -
Prof. Nadir Aghayev, Azerbaijan Technical University, modern methods and application of computer modeling of engineering and technical systems
Prof. Nizami Yusubov, Azerbaijan Technical University, Mechanical engineering technology
Prof. Dr. Osman Yazicioglu - İstanbul Ticaret University, Türkiye
Prof. Rasim Bashirov, Azerbaijan Technical University, Special purpose materials and tools
Prof. Rufat Guliyev, Azerbaijan Technical University, International trade, logistics and marketing
Prof. Vagif Gasimov, Azerbaijan Technical University, Information technologies and cyber security
Prof. Vagif Maharramov, Azerbaijan Technical University, Radioelectronic and aerospace systems
Prof. Valeh Bakhshali, Azerbaijan Technical University, Mechanics
Assoc. prof. Agil Babayev, Azerbaijan Technical University, Metallurgy and materials technology
Assoc. prof. Arzu Suleymanov, Azerbaijan Technical University, Socio-economic development trends
Assoc. prof. Habib Mirzayev, Azerbaijan Technical University, Humanities
Assoc. prof. Hikmet Aliyev, Azerbaijan Technical University, Electrical Engineering
Assoc. prof. Gasim Manafov, Azerbaijan Technical University, Transport and logistics
Assoc. prof. Mehman Hasanov, Azerbaijan Technical University, Telecommunications and radio engineering
Assoc. prof. Ramiz Kalbiyev, Azerbaijan Technical University, Green energy technologies
Assoc. Prof. Murat Eyvaz - Gebze Technical University, Türkiye
Assoc. Prof. Ezgi Topçu - Atatürk University, Türkiye
Assoc. Prof. Kader Dağcı Kıranşan - Atatürk University, Türkiye
Assoc. Prof. Özkan Açışlı - Atatürk University, Türkiye
Assoc. prof. Razim Bayramov, Azerbaijan Technical University, Transport and logistics
Assoc. prof. Sabina Almammadova, Azerbaijan Technical University, Foreign languages
Assoc. prof. Vahid Farhadov, Azerbaijan Technical University, Automation and control
Assist. Prof. Meenakshi Mat - Avinashilingam Institute for Home Science and Higher Education for Women, India
Assist. Prof. Murat Kıranşan - Gümüşhane University, Türkiye
Assist. Prof. Rupesh G. Mahajan - Dr. D. Y. Patil Institute of Technology, India
Assist. Prof. Hüseyin Çağan KILINÇ - İstanbul Esenyurt University, Türkiye
Assist. Prof. Y. M. Ahire - P.V.G's College of Engineering, India
Dr. Eugene Sviyazheninov - Russian Academy of Sciences, Russia

PHOTO GALLERY






Azərbaycan
TEXNİKİ
Universiteti
Şuşa
2022


Azərbaycan
TEXNİKİ
Universiteti



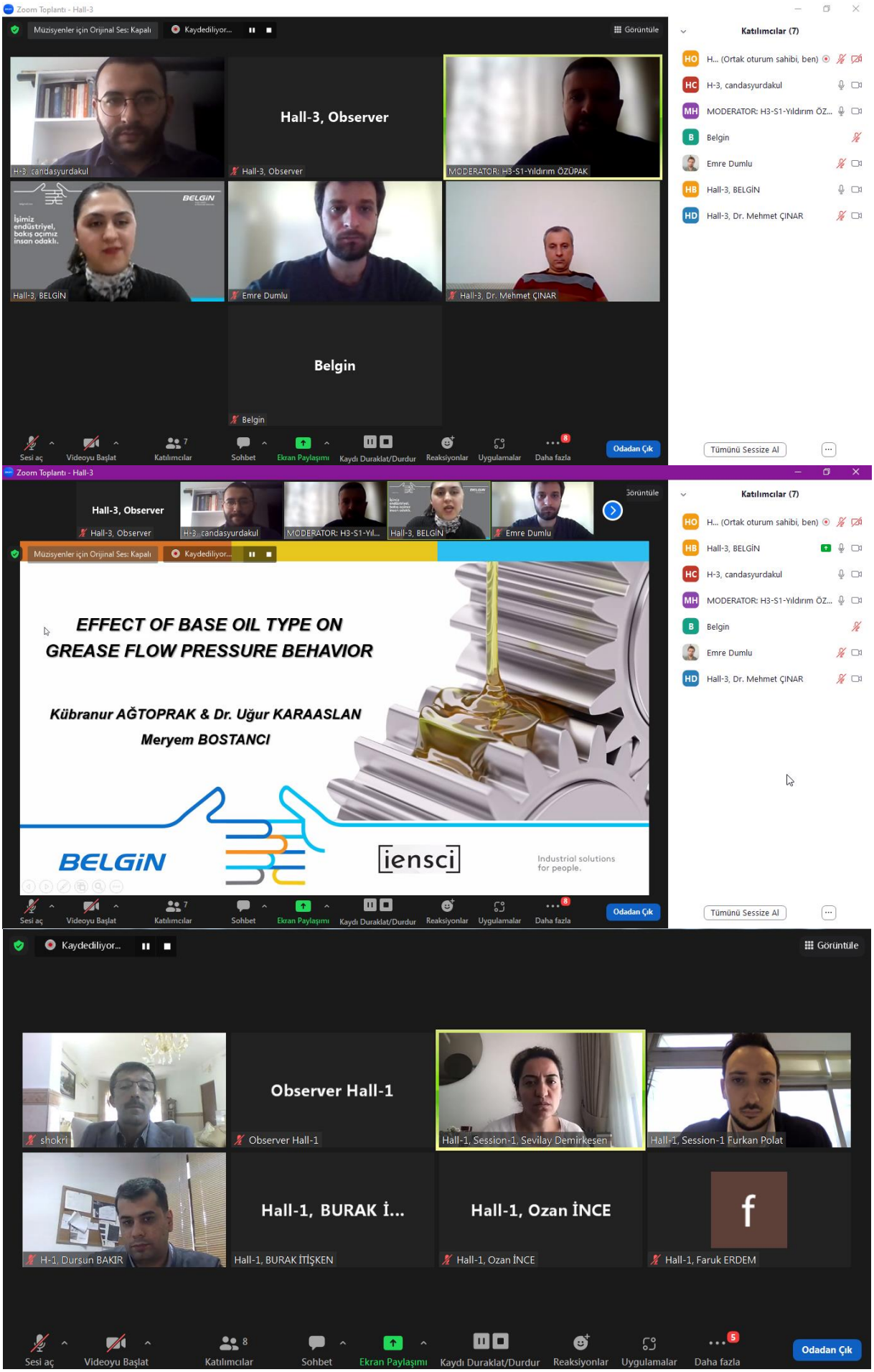

Azerbaijan

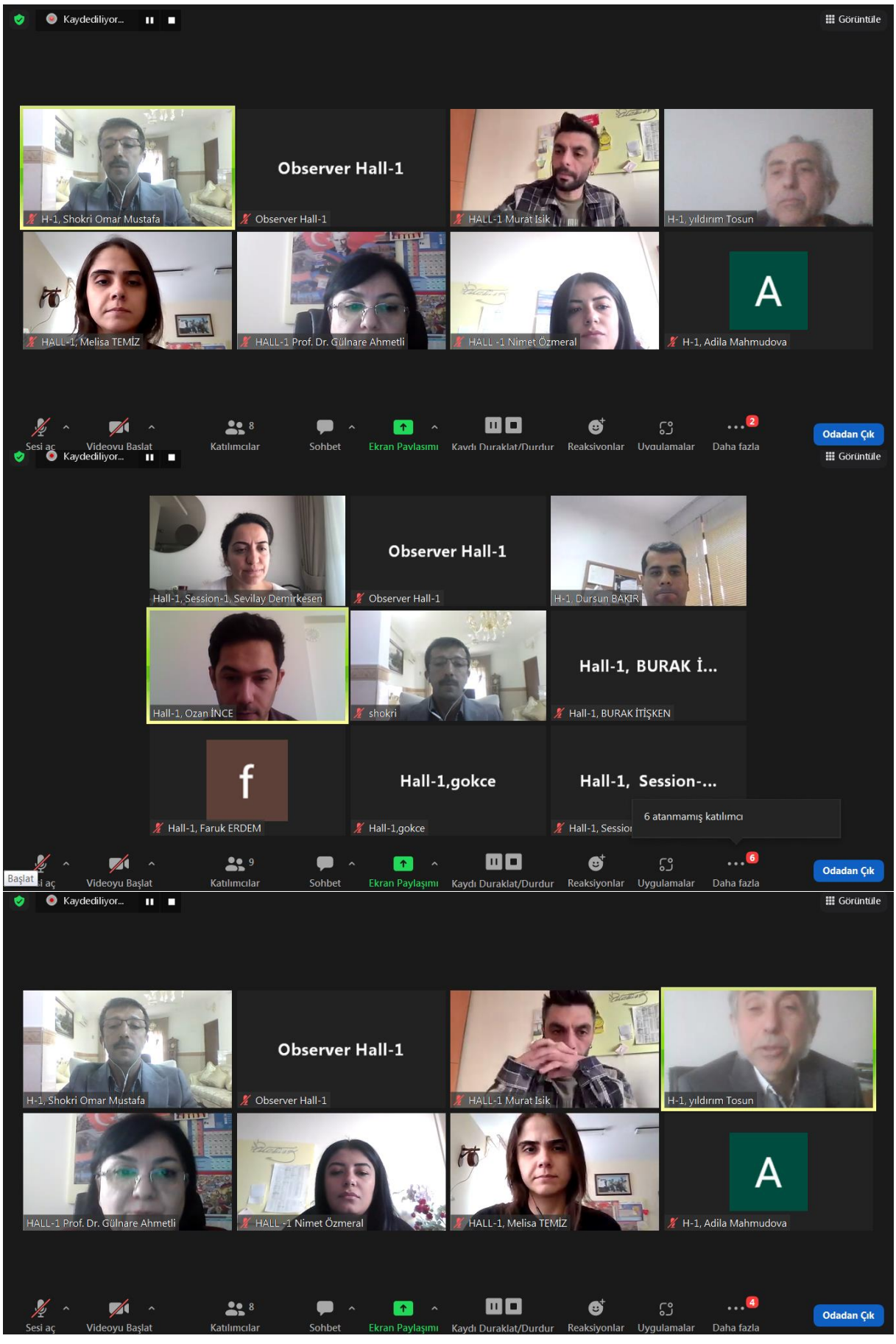



İQTİSADİ İNKİŞAF VƏ
SOSİAL TƏDQİQAT
İNSTİTUTU
www.ikaad.org.tr




ИКСАД
ИНСТИТУТ ЭКОНОМИЧЕСКОГО РАЗВИТИЯ И СОЦИАЛЬНЫХ ИССЛЕДОВАНИЙ
www.iksad.org.tr


Zoom Toplantı - Hall-3
Müzisyenler için Orijinal Ses: Kapalı
Kaydediliyor...
Görüntüle
Hall-3, Observer
MODERATOR: H3-S1-Yıldırım ÖZÜPAK
Hall-3, BELGİN
Emre Dumlu
Hall-3, Dr. Mehmet ÇINAR
Belgin
Katılımcılar (7)
Sesi aç
Videoyu Başlat
Katılımcılar
Sohbet
Ekran Paylaşımı
Kaydı Duraklat/Durdur
Reaksiyonlar
Uygulamalar
Daha fazla
Odadan Çık
Tümünü Sessize Al
EFFECT OF BASE OIL TYPE ON
GREASE FLOW PRESSURE BEHAVIOR
Kübranur AĞTOPRAK & Dr. Uğur KARAASLAN
Meryem BOSTANCI
BELGİN
[iensci]
Industrial solutions
for people.
Observer Hall-1
shokri
Hall-1, Session-1, Sevilay Demirkesen
Hall-1, Session-1 Furkan Polat
Hall-1, BURAK İ...
Hall-1, Ozan İNCE
H-1, Dursun BAKIR
Hall-1, BURAK İTİŞKEN
Hall-1, Faruk ERDEM


Kaydediliyor...
Görüntüle
H-1, Shokri Omar Mustafa
Observer Hall-1
HALL-1 Murat Isik
H-1, yıldırım Tosun
HALL-1, Melisa TEMİZ
HALL-1 Prof. Dr. Gülnare Ahmetli
HALL -1 Nimet Özmeral
A
H-1, Adila Mahmudova
Sesi aç
Videoyu Başlat
Katılımcılar
Sohbet
Ekran Paylaşımı
Kaydı Duraklat/Durdur
Reaksiyonlar
Uygulamalar
Daha fazla
Odadan Çık
Hall-1, Session-1, Sevilay Demirkesen
Observer Hall-1
H-1, Dursun BAKIR
Hall-1, Ozan İNCE
shokri
Hall-1, BURAK İ...
Hall-1, BURAK İTİŞKEN
Hall-1, Faruk ERDEM
Hall-1,gokce
Hall-1, Session-...
6 atanmamış katılımcı
Başlat

International Conference on Engineering Sciences

November 11-12, 2022 / Baku
Azerbaijan Technical University

Conference Programme

Meeting ID: 874 8834 1420
Passcode: 111222

Important, Please Read Carefully (Online Presentations)

- To be able to attend a meeting online, login via https://zoom.us/join site, enter ID "Meeting ID or Personal Link Name" and solidify the session.
- The Zoom application is free and no need to create an account.
- The Zoom application can be used without registration.
- The application works on tablets, phones and PCs.
- The participant must be connected to the session 5 minutes before the presentation time.
- All congress participants can connect live and listen to all sessions.
- Moderator is responsible for the presentation and scientific discussion (question-answer) section of the session.

Points to Take into Consideration - TECHNICAL INFORMATION (Online Presentations)

- Make sure your computer has a microphone and is working.
- You should be able to use screen sharing feature in Zoom.
- Attendance certificates will be sent to you as pdf at the end of the congress.
- Requests such as change of place and time will not be taken into consideration in the congress program.

***

Before you login to Zoom please indicate your hall number, name and surname

exp. Hall-1, Ethem KILIÇ

Meeting ID: 874 8834 1420

Passcode: 111222

Participant Countries: Azerbaijan, Türkiye, North Macedonia, Colombia, India, Nigeria, Iraq, Bulgaria, Pakistan, Algeria, Portugal, UK, China, Brazil, Tunisia, Austria, France

-Opening Ceremony-

Date: **11.11.2022**
Baku Local Time: **10:30-11:00**
Ankara Local Time: **09:30-10:00**
Place: **Azerbaijan Technical University**

FACE TO FACE & ONLINE
Zoom Meeting ID: 874 8834 1420
Zoom Passcode: 111222

***

Prof. Vilayat Valiyev
Rector of Azerbaijan Technical University
HEAD OF CONFERENCE

***

Dr. Mustafa Latif EMEK
President of IKSAD Institute

FACE TO FACE PRESENTATIONS

11.11.2022 / Hall-1, Session-1

BAKU LOCAL TIME	ANKARA LOCAL TIME
11 ^{00} : 13 ^{00}	10 ^{00} : 12 ^{00}

HEAD OF SESSION: Prof. Dr. Abdullah SOFIYEV

AUTHORS	AFFILIATION	TOPIC TITLE
Prof. Dr. Abdullah SOFIYEV	Istanbul Commerce University, Türkiye	STABILITY BEHAVIOUR OF NANOCOMPOSITE CYLINDRICAL SHELLS UNDER LATERAL PRESSURE IN DIFFERENT ENVIRONMENTS
Elekberov Allahverdi	Azerbaijan Technical University, Azerbaijan	STRUCTURAL SYNTHESIS OF ROBOT FINGERS
Kerimov Savalan Ismailova Shabnam Hajiyeva Firangiz	Azerbaijan Technical University, Azerbaijan	KINETOSTATICS OF THE MECHANISM OF THE PLANING MACHINE
Nadir Atayev	Azerbaijan Technical University, Azerbaijan	STUDY OF PROTOTYPE NANO SATELLITE SUBSYSTEMS BASED ON RADIO AND OPTICAL COMMUNICATION TECHNOLOGIES
Savalan Karimov Samaya Bagirova İlaha Rahimova	Azerbaijan Technical University, Azerbaijan	KINEMATIC ANALYSIS OF THE MECHANISM OF THE PLANING MACHINE
Shahin Mehdiyev	Selcuk University, Türkiye	DESIGN AND STRUCTURAL ANALYSIS OF 120 MM GUN BARREL BY FINITE ELEMENT METHOD
Farid Bayramov Amirasan Manafov	Azerbaijan Technical University, Azerbaijan	INSECT ROBOTS
Nijat Bakırlı	Azerbaijan Technical University, Azerbaijan	DURABILITY CALCULATION OF SHELL COMPONENTS OF THE 120-mm TRAINING MORTAR AMMUNITION

FACE TO FACE PRESENTATIONS

11.11.2022 / Hall-2, Session-1

BAKU LOCAL TIME	ANKARA LOCAL TIME
11 ^{00} : 13 ^{00}	10 ^{00} : 12 ^{00}

HEAD OF SESSION: Assoc. Prof. Natavan Namazova

AUTHORS	AFFILIATION	TOPIC TITLE
Prof. Dr. Habip DAYİOGLU Prof. Dr. Nigar MERDAN Doç. Dr. Irmak BAYBURTLU Dr. Öğr. Üyesi Sema Hatun TÜRKER	Istanbul Commerce University, Türkiye	INVESTIGATION OF DYEING PROPERTIES AND VISUAL VALUES IN TERMS OF COLOUR OF WOOL FABRICKS IN DIFFERENT FABRIC STRUCTURES DYED WITH NATURAL DYE OBTAINED FROM RED ROBIN PHOTINIA LEAVES
Sevinj Javadova Samira Jafarova Vusala Majidzade Akif Aliyev	Ministry of Science and Education Republic of Azerbaijan Institute of Catalysis and Inorganic Chemistry named after M. Nagiyev, Azerbaijan	OPTIMAL MODE FOR OBTAINING Bi_2Se_3 THIN FILMS BY ELECTROCHEMICAL METHOD
Natavan Babayeva Sayyada Suleymanova Lala Azimova	Azerbaijan Technical University, Azerbaijan	DIE STEELS, EXPLOITATION CONDITIONS AND DEMANDS THEM
R.M. Sadigov I.R. Nuriev A.M. Nazarov M.S. Sadigov	Azerbaijan Technical University, Azerbaijan Institute of Physics, Ministry of Science and Education, Azerbaijan	RESEARCH OF THE SURFACE STRUCTURE OF $Pb_{1-x}Eu_xTe$ EPITAXIAL FILMS
Aytaj Farzaliyeva Marziyya Aghayeva Sayyada Suleymanova	Azerbaijan Technical University, Azerbaijan	ADDITIVE MANUFACTURING TECHNOLOGIES
Coshgun Yahyayev	Azerbaijan National Academy of Sciences. Azerbaijan	IN MECHANICS OF DEFORMABLE SOLIDS PRIMARY PLASTIC ON PANEL DURING POWER UP DEVELOPMENT OF DEFORMATIONS

FACE TO FACE PRESENTATIONS

11.11.2022 / Hall-1, Session-2

BAKU LOCAL TIME	ANKARA LOCAL TIME
14 ^{00} : 16 ^{00}	13 ^{00} : 15 ^{00}

HEAD OF SESSION: Assoc. Prof. Natavan Namazova

AUTHORS	AFFILIATION	TOPIC TITLE
Murad JAHANGIROV Aziz SULEYMANOV	Azerbaijan Technical University, Azerbaijan	KEY ARCHITECTURAL CHANGES IN 5G NETWORK AND THEIR EFFECTS ON END USER SERVICES
Füzuli Saleh	Special Communication And Information Security State Service, Azerbaijan	SERVER-SIDE REQUEST FORGERY (SSRF)
Ibrahimov Bayram Tagiyev Ali	Azerbaijan Technical University, Azerbaijan	RESEARCH AND ANALYSIS METHODS FOR CALCULATION OF THE EFFICIENCY MULTISERVICE TELECOMMUNICATION NETWORKS ON THE BASIS ARCHITECTURAL CONCEPT NGN AND FN
Aliev Eldar Ismailova Shabnam	Azerbaijan Technical University, Azerbaijan	MATHEMATICAL MODELING OF THE ROUGH SURFACE OF THE PRINTING FORM
Aysel Talıflı Eldar Gojaev	Sumgait State University, Azerbaijan Azerbaijan Technical University, Azerbaijan	ELECTROPHYSICAL PROPERTIES OF THE BINARY COMPOUND In_2Se_3
Eldar Gojaev Sevinj Osmanova Naghi Gasimov	Azerbaijan State Oil and Industry University, Azerbaijan Azerbaijan Technical University, Azerbaijan	SPECTRA OF RAMAN SCATTERING OF LIGHT IN A III B VI TYPE COMPOUNDS
Alasgarova Durdana Eldar Gojayev Kamal Gulmammadov Gafarova Dilara	Sumgayit State University, Azerbaijan Azerbaijan Technical University, Azerbaijan Azerbaijan University of Architecture and Construction, Azerbaijan	INFLUENCE OF $BiSe_3Te_6$ SEMICONDUCTOR COMPOUND MECHANICAL AND ELECTRICAL STRENGTH OF LOW-DENSITY POLYETHYLENE.
İftikhar Chalabi	Azerbaijan Technical University, Azerbaijan	RELIABILITY ANALYSIS OF THE HOUSING-COVER CONNECTIONS OF GEAR REDUCERS

FACE TO FACE PRESENTATIONS

11.11.2022 / Hall-2, Session-2

BAKU LOCAL TIME	ANKARA LOCAL TIME
14 ^{00} : 16 ^{00}	13 ^{00} : 15 ^{00}

HEAD OF SESSION: Prof. Dr. Ekrem TUŞAT

AUTHORS	AFFILIATION	TOPIC TITLE
Shahin Charkasov	Azerbaijan Technical University, Azerbaijan	FORTITUDE OF THE OPTIMUM HEIGHT OF THE MAIN BEAM OF A BRIDGE CRANE
Prof. Dr. Ekrem TUŞAT Prof. Dr. Tayfun ÇAY	Konya Technical University, Türkiye	A STUDY ON THE TECHNICAL EVALUATION OF URBAN TRANSFORMATION PROJECTS
Prof. Dr. Fariz MİKAİLSOY Dr. Erhan ERDEL Prof. Dr. Fatih ER	Iğdır University, Türkiye Selçuk University, Türkiye	DETERMINING THE INITIAL RATE OF ENZYME REACTION. APPLICATION OF CATALASE ENZYME IN SOIL
Reşat MİKAİL Prof. Dr. Elman HAZAR Prof. Dr. Fariz MİKAİLSOY	Iğdır University, Türkiye	DETERMINATION OF SOIL THERMAL DIFFUSIVITY BASED ON DAILY MEASUREMENTS OF TEMPERATURE THE SURFACE AND AT DIFFERENT DEPTHS OF THE SOIL
Assoc. Prof. Dr. Natig H. Pasha Leman Safarova	Azerbaijan Technical University, Azerbaijan	APPLICATION POSSIBILITIES OF NANOTECHNOLOGY IN WASTEWATER TREATMENT
Valeh Bakhshali Konul Huseynzade	Azerbaijan Technical University, Azerbaijan	THERMODYNAMICAL ANALYSIS of the GAS STREAM in the COMPRESSOR STATIONS

ONLINE PRESENTATIONS

11.11.2022 / Hall-1, Session-1

BAKU LOCAL TIME	ANKARA LOCAL TIME
11 ^{00} : 13 ^{00}	10 ^{00} : 12 ^{00}

HEAD OF SESSION: Assoc. Prof. Dr. Sevilay Demirkesen

AUTHORS	AFFILIATION	TOPIC TITLE
Res. Assist. Dursun BAKIR Assist. Prof. Dr. Sedat SAVAŞ	Fırat University, Türkiye	INVESTIGATION OF THE BEHAVIOR OF SEMI-STATICALLY SUPPORTED REINFORCED CONCRETE SLABS UNDER CONTACT BLAST LOAD
Res. Assist. Dursun BAKIR Assist. Prof. Dr. Sedat SAVAŞ	Fırat University, Türkiye	INVESTIGATION OF THE EFFECT OF BASALT FIBER REINFORCEMENT BARS ON CONCRETE STRENGTH
Res. Assist. Dursun BAKIR Hasan ÜSTÜNDAĞ Assist. Prof. Dr. Sedat SAVAŞ	Fırat University, Türkiye	EXPERIMENTAL AND NUMERICAL INVESTIGATION OF THE RESISTANCE OF RECTANGULAR CORE HOLLOW PLATES AGAINST CONTACT EXPLOSION
Ozan İNCE Prof. Dr. Mehmet ÜLKER	Firat University, Türkiye	OPTIMUM DESIGN OF STEEL-CONCRETE COMPOSITE BOX GIRDER BRIDGES WITH HARMONY SEARCH ALGORITHM
Faruk ERDEM Prof. Dr. Alper BÜYÜKKARAGÖZ	Gazi Unıversıty, Türkiye	NUMERICAL ANALYSIS OF REINFORCED CONCRETE BEAMS WITH VARIABLE OPENING RATIO
Burak ITISKEN Prof. Dr. Alper BÜYÜKKARAGÖZ	Gazi University, Türkiye	STRENGTHENING OF REINFORCED CONCRETE COLUMNS AGAINST SHEAR WITH STEEL PLATES BY FINITE ELEMENT METHOD
Furkan Polat Sevilay Demirkesen	Gebze Technical University, Türkiye	RESEARCHING THE SYNERGY BETWEEN LEAN CONSTRUCTION AND BUILDING INFORMATION MODELING (BIM)

ONLINE PRESENTATIONS

11.11.2022 / Hall-2, Session-1

BAKU LOCAL TIME	ANKARA LOCAL TIME
11 ^{00} : 13 ^{00}	10 ^{00} : 12 ^{00}

HEAD OF SESSION: Assoc. Prof. Dr. Derya Çini Şimşek

AUTHORS	AFFILIATION	TOPIC TITLE
Assoc. Prof. Dr. Derya Çini Şimşek	Başkent University, Türkiye	ENGINEERING EDUCATION IN TURKEY FROM THE LAST PERIOD OF THE OTTOMAN STATE TO THE FIRST YEARS OF THE REPUBLIC
Assoc. Prof. Dr. Derya Çini Şimşek	Başkent University, Türkiye	THE HISTORY OF THE TRANSITION FROM MADRASA TO ENGINEERING IN THE OTTOMAN PERIOD
Cansu BOZKURT Prof. Dr. Mahmut FIRAT	Ardahan University, Türkiye Inonu University, Türkiye	ANALYSIS OF COST EFFECTS FOR NON-REVENUE WATER COMPONENTS IN WATER UTILITIES WITH PERFORMANCE INDICATORS
Cansu BOZKURT Prof. Dr. Mahmut FIRAT	Ardahan University, Türkiye Inonu University, Türkiye	MONITORING THE PERFORMANCE OF DISTRICT METERED AREA ACTIVITIES FOR SUSTANIABLE MANAGEMENT OF WATER LOSSES
Bora AKSAR Ali Ikbal TUTAR Vesile Hatun AKANSEL Ferit CAKIR	Isik University, Türkiye Gebze Technical University, Türkiye Mugla Sitki Kocman University, Türkiye	STRUCTURAL PERFORMANCE EVALUATION OF THE HISTORICAL EMIR SALTUK TOMB
Assist. Prof. Dr. Adem AHISKALI Aydın ARSLAN	Kastamonu University, Türkiye	TRAFFIC ACCIDENTS AT LAND POINTS IMPORTANCE OF TRAFFIC SAFETY SYSTEM "GÖKÇEBEY INTERCHANGE EXAMPLE"
Shehu, M. Ogaji, A. N. Abdulrahman H. S. Haruna, A. M. Adamu, H. N. Mahmud, M. B.	Federal University of Technology, Nigeria	A COMPARATIVE ANALYSIS OF TRAVEL TIME, SPEED AND DELAY OF DIFFERENT VEHICLES IN MINNA, NIGER STATE, NIGERIA

ONLINE PRESENTATIONS

11.11.2022 / Hall-3, Session-1

BAKU LOCAL TIME	ANKARA LOCAL TIME
11 ^{00} : 13 ^{00}	10 ^{00} : 12 ^{00}

HEAD OF SESSION: Yildirim Özüpak

AUTHORS	AFFILIATION	TOPIC TITLE
Dr. Yildirim Özüpak Dr. Mehmet Çinar	Dicle University, Türkiye Bitlis Eren University, Türkiye	INVESTIGATION OF THE EFFECTS OF ROTOR SLOTS STRUCTURE ON MOTOR PARAMETERS IN INDUCTION MOTORS
Dr. Yildirim Özüpak Dr. Mehmet Çinar	Dicle University, Türkiye Bitlis Eren University, Türkiye	ANALYSIS OF A MOTOR USED IN ELECTRIC VEHICLES USING FEM BASED ANSYS-RMXPRT-MAXWELL
Muhsin KILIÇ Candaş YURDAKUL	Bursa Uludag University, Türkiye	INVESTIGATION OF THE HEATING PROCESS OF THE AMBULANCE CABIN AIR
Kübranur AĞTOPRAK Dr. Uğur KARAASLAN	Belgin Oil R&D Center, Türkiye	EFFECT OF BASE OIL TYPE ON GREASE FLOW PRESSURE BEHAVIOR
Meryem BOSTANCI Dr. Uğur KARAASLAN	Belgin Oil R&D Center, Türkiye	INVESTIGATION OF HIGH TEMPERATURE PERFORMANCE OF DIFFERENT TYPES OF VISCOSITY INDEX IMPROVER POLYMERS WITH HTHS AND TGA
Prof. Dr. Mehmet Sukru Guney Emre Dumlu Merve Okan Prof. Dr. Birol Kaya	Izmir University of Economics, Türkiye Dokuz Eylul University, Türkiye	EXPERIMENTAL STUDY OF THE EVOLUTION OF THE BREACH AND THE DISCHARGE THROUGH THE BREACH RESULTING FROM PIPING DUE TO SEEPAGE AT THE EARTH-FILL DAM WITH CLAY CORE

ONLINE PRESENTATIONS

11.11.2022 / Hall-4, Session-1

BAKU LOCAL TIME	ANKARA LOCAL TIME
11 ^{00} : 13 ^{00}	10 ^{00} : 12 ^{00}

HEAD OF SESSION: Prof. Diego Penagos-Vásquez

AUTHORS	AFFILIATION	TOPIC TITLE
Prof. Diego Penagos-Vásquez Prof. Diana Ivonne González-Arango Prof. Oscar Darío Monsalve-Cifuentes	Instituto Tecnológico Metropolitano, Colombia	TYPE 1 ENERGY AUDIT APPLIED TO A SCHOOL LIGHTING SYSTEM BASED ON THE ISO 50002 STANDARD
Assist. Prof. B. Rohini Assist. Prof. R. Bala Murali Krishna	G Pulla Reddy Engineering College (Autonomous), India University College of Engineering, India	EXPERIMENTAL STUDY ON BRICKS USING PAPERWASTE
Babak Emdadi Ahmed Asimov	Khazar University, Azerbaijan	QUANTUM DOTS SYNTHESIS AND APPLICATION IN SOLAR CELLS
Moses Adeolu AGOI Oluwakemi Racheal OSHINOWO	Lagos State University of Education, Nigeria	THE EFFICACY OF IOT (INTERNET OF THINGS) AND DIGITAL RESOURCES AMONG STUDENTS: IMPLICATION ON EDUCATIONAL MANAGEMENT
Harikrishna Jivvaji B.S. Anuradha	Sree Chaitanya deemed to be University, India	ANTIMICROBIAL ACTIVITY OF CERTAIN CYANOBACTERIA ON PATHOGENIC BACTERIA
FH-Prof. Dr. Felix HIMMELSTOSS	University of Applied Sciences Technikum Wien, Austria	THREE DC/DC CONVERTERS WITH CONTINUOUS INPUT AND OUTPUT CURRENT FOR LED APPLICATIONS
Sowmiya N Brindha M Vigneswar R	Saranathan College of Engineering, India Bannari Amman Institute of Technology, India	ATMOSPHERIC OXYGEN ANALYSER
Giselle Francine Brito Muniz Kenedy Marconi Geraldo dos Santos	Federal Institute of Education, Brazil	ELECTRIC TRANSFORMER: PRINCIPLE OF OPERATION THROUGH ELECTROMAGNETISM

ONLINE PRESENTATIONS

11.11.2022 / Hall-1, Session-2

BAKU LOCAL TIME	ANKARA LOCAL TIME
14 ^{00} : 16 ^{00}	13 ^{00} : 15 ^{00}

HEAD OF SESSION: Prof. Dr. Gulnare Ahmetli

AUTHORS	AFFILIATION	TOPIC TITLE
Shokri Omar Mustafa MUSTAFA Prof. Dr. Muzaffer Mustafa HARLIOĞLU Dr. Mehmet Nuri ÇAKMAK	Firat University, Türkiye Nutritionist and President of Fish Resources Association in Iraq	EFFECT OF DIETARY ZINC ON THE GROWTH OF JUVENILES COMMON CARP *(CYPRINUS CARPIO)*
Salisu Nuhu	Hussaini Adamu Federal Polytechnic. Nigeria	FACTORIAL ANALYSIS OF QUICKLIME PRODUCTION FROM EGGSHELL
Melisa Temiz Nimet Ozmeral Suheyla Kocaman Alaaddin Cerit Gulnare Ahmetli	Konya Technical University, Türkiye	NEW APPROACH STUDY FOR THE EVALUATION OF EPDM RUBBER WASTE
Murat Işık Gulnare Ahmetli	Konya Technical University, Türkiye	COMPARATIVE STUDY ON EPOXY-BASED NANOCOMPOSITES
Nimet Ozmeral Merve Turkben Suheyla Kocaman Ulku Soydal Gulnare Ahmetli	Konya Technical University, Türkiye	EVALUATION OF RUBBER WASTES IN COMPOSITES
Adila Mahmudova	Azerbaijan State Pedagogical University, Azerbaijan	SYNTHESIS OF 1,2-NONANEDIOL PHENOXY ETHERS
Dr. Y. I. Tosun	Şırnak University, Türkiye	MOLTEN CAUSTIC SALT ELECTROLYSIS OF FERROUS Ti/Mn WASTE BY MICROWAVE RADIATED BATH
Dr. Y. I. Tosun	Şırnak University, Türkiye	MICRO JET GRINDING OF WASTE SLAG, SOOT CARBON OF WASTE TYRE, WASTE SOOT OF COAL BOILERS BY MICROWAVE RADIATION
Leman Mesiyava Ümmühan Özdemir Özmen Ayla Balaban Gündüzalp Ebru Aktan	Azerbaijan Technical University, Azerbaijan Gazi University, Türkiye	ECO-FRIENDLY SULFONYLHYDRAZONE SYNTHESIS WITH POTENTIAL BIOACTIVITIES AND THEORETICAL CALCULATIONS

ONLINE PRESENTATIONS

11.11.2022 / Hall-2, Session-2

BAKU LOCAL TIME	ANKARA LOCAL TIME
14 ^{00} : 16 ^{00}	13 ^{00} : 15 ^{00}

HEAD OF SESSION: Assist. Prof. Dr. Melda PATAN ALPER

AUTHORS	AFFILIATION	TOPIC TITLE
Mehriban MAMMADOVA	Institute of Mathematics and Mechanics of NAS of Azerbaijan, Azerbaijan	THE SOLUTION OF THE PROBLEM OF CYCLE LOADING OF HEREDITARY ELASTICO-PLASTIC BALL AT PULSATING INTERNAL PRESSURE
Prof. Dr. Nuray GÜZELER Dr. Dilek SAY İrem Döndü BAKIR	Cukurova University, Türkiye	PLANT BASED MILKS AND THEIR USE IN THE DAIRY INDUSTRY
Assist. Prof. Dr. Melda PATAN ALPER	Yeditepe University, Türkiye	SYNTHESIS AND CHARACTERIZATION of WATER SOLUBLE of CdTe QUANTUM DOTS
Dr. Esra BALCI Prof. Dr. Cengiz TATAR Assoc. Prof. Fethi DAĞDELEN	Firat University, Türkiye	ANALYSIS OF THERMAL AND CORROSION BEHAVIOR OF Ti-44Ni-6Cd SHAPE MEMORY ALLOYS

ONLINE PRESENTATIONS

11.11.2022 / Hall-3, Session-2

BAKU LOCAL TIME	ANKARA LOCAL TIME
14 ^{00} : 16 ^{00}	13 ^{00} : 15 ^{00}

HEAD OF SESSION: Assist. Prof. Dr. Metin SALİHMUHSİN

AUTHORS	AFFILIATION	TOPIC TITLE
İsa AVCI Bahadır Furkan KINACI	Karabuk University, Türkiye	CHALLENGES AND OPPORTUNITIES OF BLOCKCHAIN IN ELECTRIC VEHICLES
İsa AVCI Bahadır Furkan KINACI	Karabuk University, Türkiye	INVESTIGATION OF E-SECURITY STANDARDS USED IN INTELLIGENT TRANSPORTATION SYSTEMS
Ahamadi Abdallah IDRISSE Assoc. Prof. Dr. Oktay YILDIZ Prof. Dr. Ugur BAYSAL	Gazi University, Türkiye Hacettepe University, Türkiye	A LIGHTWEIGHT DEEP LEARNING MODEL FOR THE CLASSIFICATION OF A LIMITED LUNG SOUND DATASET
Leyla ZEYNALLI-HUSEYNZADE	Baku Engineering University, Azerbaijan	ADVANCEMENT OF CHATBOT TECHNOLOGY IN CUSTOMER SERVICE
Leyla ZEYNALLI-HUSEYNZADE	Baku Engineering University, Azerbaijan	DIGITAL TRANSFORMATION METRICS
Buğra Kaan Türkmenoğlu Assoc. Prof. Oktay Yıldız	Gazi University, Türkiye	REDUCING TICKET RESOLUTION TIME THROUGH SUGGESTION IN THE HELP DESK SYSTEM
Assist. Prof. Dr. Metin SALİHMUHSİN	Kahramanmaraş Sütçü İmam University, Türkiye	SMALL SIGNAL ANALYSIS OF A FLYBACK CONVERTER USING STATE SPACE AVERAGING METHOD
Bahdişen Gezer Mustafa Atalan Can Gezer Rahşen gezer	Uşak University, Türkiye Sofia Technical University, Bulgaria	OBTAINING BORON OXIDE (B_2O_3) DOCUMENTED TUNGSTEN OXIDE (WO3) THIN FILM BY RADIO FREQUENCY (RF) MAGNETRON BREAKING METHOD AND INVESTIGATION OF THEIR STRUCTURAL PROPERTIES

ONLINE PRESENTATIONS

11.11.2022 / Hall-4, Session-2

BAKU LOCAL TIME	ANKARA LOCAL TIME
14 ^{00} : 16 ^{00}	13 ^{00} : 15 ^{00}

HEAD OF SESSION: Abdul Jabbar

AUTHORS	AFFILIATION	TOPIC TITLE
Yahaya Abdullahi Ibrahim Dr. Danladi Bello Al'amin	Ahmadu Bello University, Nigeria	HYDROLOGICAL MODELLING OF GURARA WATERSHED UNDER THE IMPACT OF LAND-USE AND CLIMATE CHANGE
Saeed Nawaz Naveed Ahmad Khan Muhammad Yasir Khan	National University of Sciences and Technology, Pakistan HITEC University, Pakistan Government College of technology, Pakistan	EXPERIMENTAL ANALYSIS OF CIRCULAR, RECTANGULAR AND SQUARE NOTCHES ON THE STRENGTH OF COMPOSITE MATERIALS
Abdessamed ATOUI Prof. Dr. Abderrezak BEZAZI Prof. Dr. Salah GUENFOUD Prof. Dr. Abilo SILVA Prof. Dr. P.N.B. REIS Prof. Dr. Fabrizio SCARPA	8 Mai 1945 Guelma University, Algeria University of Beira Interior, Portugal University of Coimbra, Portugal Bristol Composites Institute, UK	PHYSICAL-CHEMICAL AND MECHANICAL PROPERTIES OF AMPELODESMOS MAURITANICUS NATURAL FIBERES
Abdul Jabbar	Zhejiang University, China	IMAGE-TO-IMAGE TRANSLATION BASED FACE PHOTO DE-MESHING USING WASSERSTEIN GANs
Dr. Nasser BOUHEMAME Prof. Dr. Abderrezak BEZAZI Dr. Hocine KHELIFA Prof. Dr. Kamal Eddinne AIADI Prof. Dr. Gilberto García DEL PINO Prof. Dr. P.N.B. REIS Prof. Dr. Fabrizio SCARPA	Kasdi Merbah Ouargla Unversity, Algeria 8 Mai 1945 Guelma University, Algeria Larbi Tebessi Tebassa University, Algeria Kasdi Merbah Ouargla Unversity, Algeria State University of Amazonas-UEA, Brazil University of Coimbra, Portugal Bristol Composites Institute, UK	PHYSICO-CHEMICAL AND THERMAL ANALYSIS OF WASHINGTONIA PALM LEAFLET FIBERS
Nasraoui Hajaji Afef Ammari youssef	University of Carthage, Tunisia	CITRIC ACID IS A CRUCIAL COMPOUND PLAYING AN ALLEVIATION ROLE OF SALT-INDUCED OXIDATIVE STRESS IN MORINGA OLEIFERA

CONTENT

CONFERENCE ID	**I**
SCIENTIFIC & REVIEW COMMITTEE	**II**
PHOTO GALLERY	**III**
PROGRAM	**IV**
CONTENT	**V**

Author	Title	No
Abdullah SOFIYEV	STABILITY BEHAVIOUR OF NANOCOMPOSITE CYLINDRICAL SHELLS UNDER LATERAL PRESSURE IN DIFFERENT ENVIRONMENTS	1
Elekberov Allahverdi	STRUCTURAL SYNTHESIS OF ROBOT FINGERS	7
Kerimov Savalan **Ismailova Shabnam** **Hajiyeva Firangiz**	KINETOSTATICS OF THE MECHANISM OF THE PLANING MACHINE	13
Nadir Atayev	STUDY OF PROTOTYPE NANO SATELLITE SUBSYSTEMS BASED ON RADIO AND OPTICAL COMMUNICATION TECHNOLOGIES	18
Shahin Mehdiyev	DESIGN AND STRUCTURAL ANALYSIS OF 120 MM GUN BARREL BY FINITE ELEMENT METHOD	28
Farid Bayramov **Amirasan Manafov**	INSECT ROBOTS	30
Nijat Bakırlı	DURABILITY CALCULATION OF SHELL COMPONENTS OF THE 120-mm TRAINING MORTAR AMMUNITION	35
Sevinj Javadova **Samira Jafarova** **Vusala Majidzade** **Akif Aliyev**	OPTIMAL MODE FOR OBTAINING Bi_2Se_3 THIN FILMS BY ELECTROCHEMICAL METHOD	44
Natavan Babayeva **Sayyada Suleymanova** **Lala Azimova**	DIE STEELS, EXPLOITATION CONDITIONS AND DEMANDS THEM	45
R.M. Sadigov **I.R. Nuriev** **A.M. Nazarov** **M.S. Sadigov**	RESEARCH OF THE SURFACE STRUCTURE OF $Pb_{1-x}Eu_xTe$ EPITAXIAL FILMS	49
Aytaj Farzaliyeva **Marziyya Aghayeva** **Sayyada Suleymanova**	ADDITIVE MANUFACTURING TECHNOLOGIES	52
Coshgun Yahyayev	IN MECHANICS OF DEFORMABLE SOLIDS PRIMARY PLASTIC ON PANEL DURING POWER UP DEVELOPMENT OF DEFORMATIONS	57
Murad JAHANGIROV **Aziz SULEYMANOV**	KEY ARCHITECTURAL CHANGES IN 5G NETWORK AND THEIR EFFECTS ON END USER SERVICES	59
Füzuli Saleh	SERVER-SIDE REQUEST FORGERY (SSRF)	67
Ibrahimov Bayram **Tagiyev Ali**	RESEARCH AND ANALYSIS METHODS FOR CALCULATION OF THE EFFICIENCY MULTISERVICE TELECOMMUNICATION NETWORKS ON THE BASIS ARCHITECTURAL CONCEPT NGN AND FN	68
Aliev Eldar **Ismailova Shabnam**	MATHEMATICAL MODELING OF THE ROUGH SURFACE OF THE PRINTING FORM	76

Aysel Talıflı **Eldar Gojaev**	ELECTROPHYSICAL PROPERTIES OF THE BINARY COMPOUND In_2Se_3	86
Eldar Gojaev **Sevinj Osmanova** **Naghi Gasimov**	SPECTRA OF RAMAN SCATTERING OF LIGHT IN A III B VI TYPE COMPOUNDS	89
İftikhar Chalabi	RELIABILITY ANALYSIS OF THE HOUSING-COVER CONNECTIONS OF GEAR REDUCERS	95
Shahin Charkasov	FORTITUDE OF THE OPTIMUM HEIGHT OF THE MAIN BEAM OF A BRIDGE CRANE	102
Ekrem TUŞAT **Tayfun ÇAY**	A STUDY ON THE TECHNICAL EVALUATION OF URBAN TRANSFORMATION PROJECTS	107
Fariz MİKAİLSOY **Erhan ERDEL** **Fatih ER**	DETERMINING THE INITIAL RATE OF ENZYME REACTION. APPLICATION OF CATALASE ENZYME IN SOIL	108
Reşat MİKAİL **Elman HAZAR** **Fariz MİKAİLSOY**	DETERMINATION OF SOIL THERMAL DIFFUSIVITY BASED ON DAILY MEASUREMENTS OF TEMPERATURE THE SURFACE AND AT DIFFERENT DEPTHS OF THE SOIL	117
Natig H. Pasha **Leman Safarova**	APPLICATION POSSIBILITIES OF NANOTECHNOLOGY IN WASTEWATER TREATMENT	138
Valeh Bakhshali **Konul Huseynzade**	THERMODYNAMICAL ANALYSIS of the GAS STREAM in the COMPRESSOR STATIONS	141
Dursun BAKIR **Sedat SAVAŞ**	INVESTIGATION OF THE BEHAVIOR OF SEMI-STATICALLY SUPPORTED REINFORCED CONCRETE SLABS UNDER CONTACT BLAST LOAD	146
Dursun BAKIR **Sedat SAVAŞ**	INVESTIGATION OF THE EFFECT OF BASALT FIBER REINFORCEMENT BARS ON CONCRETE STRENGTH	157
Dursun BAKIR **Hasan ÜSTÜNDAĞ** **Sedat SAVAŞ**	EXPERIMENTAL AND NUMERICAL INVESTIGATION OF THE RESISTANCE OF RECTANGULAR CORE HOLLOW PLATES AGAINST CONTACT EXPLOSION	162
Ozan İNCE **Mehmet ÜLKER**	OPTIMUM DESIGN OF STEEL-CONCRETE COMPOSITE BOX GIRDER BRIDGES WITH HARMONY SEARCH ALGORITHM	171
Faruk ERDEM **Alper BÜYÜKKARAGÖZ**	NUMERICAL ANALYSIS OF REINFORCED CONCRETE BEAMS WITH VARIABLE OPENING RATIO	175
Burak ITISKEN **Alper BÜYÜKKARAGÖZ**	STRENGTHENING OF REINFORCED CONCRETE COLUMNS AGAINST SHEAR WITH STEEL PLATES BY FINITE ELEMENT METHOD	184
Furkan Polat **Sevilay Demirkesen**	RESEARCHING THE SYNERGY BETWEEN LEAN CONSTRUCTION AND BUILDING INFORMATION MODELING (BIM)	209
Derya Çini Şimşek	ENGINEERING EDUCATION IN TURKEY FROM THE LAST PERIOD OF THE OTTOMAN STATE TO THE FIRST YEARS OF THE REPUBLIC	216
Derya Çini Şimşek	THE HISTORY OF THE TRANSITION FROM MADRASA TO ENGINEERING IN THE OTTOMAN PERIOD	218
Cansu BOZKURT **Mahmut FIRAT**	ANALYSIS OF COST EFFECTS FOR NON-REVENUE WATER COMPONENTS IN WATER UTILITIES WITH PERFORMANCE INDICATORS	220
Cansu BOZKURT **Mahmut FIRAT**	MONITORING THE PERFORMANCE OF DISTRICT METERED AREA ACTIVITIES FOR SUSTANIABLE MANAGEMENT OF WATER LOSSES	227
Bora AKSAR **Ali Ikbal TUTAR** **Vesile Hatun AKANSEL** **Ferit CAKIR**	STRUCTURAL PERFORMANCE EVALUATION OF THE HISTORICAL EMIR SALTUK TOMB	235
Adem AHISKALI **Aydın ARSLAN**	TRAFFIC ACCIDENTS AT LAND POINTS IMPORTANCE OF TRAFFIC SAFETY SYSTEM "GÖKÇEBEY INTERCHANGE EXAMPLE"	248
Shehu, M. **Ogaji, A. N.** **Abdulrahman H. S.**	A COMPARATIVE ANALYSIS OF TRAVEL TIME, SPEED AND DELAY OF DIFFERENT VEHICLES IN MINNA, NIGER STATE, NIGERIA	250

Haruna, A. M. **Adamu, H. N.** **Mahmud, M. B.**		
Yildirim Özüpak **Mehmet Çinar**	INVESTIGATION OF THE EFFECTS OF ROTOR SLOTS STRUCTURE ON MOTOR PARAMETERS IN INDUCTION MOTORS	251
Yildirim Özüpak **Mehmet Çinar**	ANALYSIS OF A MOTOR USED IN ELECTRIC VEHICLES USING FEM BASED ANSYS-RMXPRT-MAXWELL	260
Muhsin KILIÇ **Candaş YURDAKUL**	INVESTIGATION OF THE HEATING PROCESS OF THE AMBULANCE CABIN AIR	267
Kübranur AĞTOPRAK **Uğur KARAASLAN**	EFFECT OF BASE OIL TYPE ON GREASE FLOW PRESSURE BEHAVIOR	277
Meryem BOSTANCI **Uğur KARAASLAN**	INVESTIGATION OF HIGH TEMPERATURE PERFORMANCE OF DIFFERENT TYPES OF VISCOSITY INDEX IMPROVER POLYMERS WITH HTHS AND TGA	287
Mehmet Sukru Guney **Emre Dumlu** **Merve Okan** **Birol Kaya**	EXPERIMENTAL STUDY OF THE EVOLUTION OF THE BREACH AND THE DISCHARGE THROUGH THE BREACH RESULTING FROM PIPING DUE TO SEEPAGE AT THE EARTH-FILL DAM WITH CLAY CORE	298
Diego Penagos-Vásquez **Diana Ivonne González-Arango** **Oscar Darío Monsalve-Cifuentes**	TYPE 1 ENERGY AUDIT APPLIED TO A SCHOOL LIGHTING SYSTEM BASED ON THE ISO 50002 STANDARD	308
B. Rohini **R. Bala Murali Krishna**	EXPERIMENTAL STUDY ON BRICKS USING PAPERWASTE	309
Babak Emdadi **Ahmed Asimov**	QUANTUM DOTS SYNTHESIS AND APPLICATION IN SOLAR CELLS	320
Moses Adeolu AGOI **Oluwakemi Racheal OSHINOWO**	THE EFFICACY OF IOT (INTERNET OF THINGS) AND DIGITAL RESOURCES AMONG STUDENTS: IMPLICATION ON EDUCATIONAL MANAGEMENT	329
Harikrishna Jivvaji **B.S. Anuradha**	ANTIMICROBIAL ACTIVITY OF CERTAIN CYANOBACTERIA ON PATHOGENIC BACTERIA	334
Felix HIMMELSTOSS	THREE DC/DC CONVERTERS WITH CONTINUOUS INPUT AND OUTPUT CURRENT FOR LED APPLICATIONS	335
Sowmiya N **Brindha M** **Vigneswar R**	ATMOSPHERIC OXYGEN ANALYSER	348
Giselle Francine Brito Muniz **Kenedy Marconi Geraldo dos Santos**	ELECTRIC TRANSFORMER: PRINCIPLE OF OPERATION THROUGH ELECTROMAGNETISM	349
Shokri Omar Mustafa MUSTAFA **Prof. Dr. Muzaffer Mustafa HARLIOĞLU** **Mehmet Nuri ÇAKMAK**	EFFECT OF DIETARY ZINC ON THE GROWTH OF JUVENILES COMMON CARP *(CYPRINUS CARPIO)*	359
Salisu Nuhu	FACTORIAL ANALYSIS OF QUICKLIME PRODUCTION FROM EGGSHELL	369
Melisa Temiz **Nimet Ozmeral** **Suheyla Kocaman** **Alaaddin Cerit** **Gulnare Ahmetli**	NEW APPROACH STUDY FOR THE EVALUATION OF EPDM RUBBER WASTE	370
Murat Işık **Gulnare Ahmetli**	COMPARATIVE STUDY ON EPOXY-BASED NANOCOMPOSITES	371
Nimet Ozmeral **Merve Turkben** **Suheyla Kocaman** **Ulku Soydal** **Gulnare Ahmetli**	EVALUATION OF RUBBER WASTES IN COMPOSITES	372
Adila Mahmudova	SYNTHESIS OF 1,2-NONANEDIOL PHENOXY ETHERS	373

Y. I. Tosun	MOLTEN CAUSTIC SALT ELECTROLYSIS OF FERROUS Ti/Mn WASTE BY MICROWAVE RADIATED BATH	375
Y. I. Tosun	MICRO JET GRINDING OF WASTE SLAG, SOOT CARBON OF WASTE TYRE, WASTE SOOT OF COAL BOILERS BY MICROWAVE RADIATION	376
Leman Mesiyava **Ümmühan Özdemir Özmen** **Ayla Balaban Gündüzalp** **Ebru Aktan**	ECO-FRIENDLY SULFONYLHYDRAZONE SYNTHESIS WITH POTENTIAL BIOACTIVITIES AND THEORETICAL CALCULATIONS	377
Mehriban MAMMADOVA	THE SOLUTION OF THE PROBLEM OF CYCLE LOADING OF HEREDITARY ELASTICO-PLASTIC BALL AT PULSATING INTERNAL PRESSURE	386
Nuray GÜZELER **Dilek SAY** **İrem Döndü BAKIR**	PLANT BASED MILKS AND THEIR USE IN THE DAIRY INDUSTRY	393
Melda PATAN ALPER	SYNTHESIS AND CHARACTERIZATION of WATER SOLUBLE of CdTe QUANTUM DOTS	401
Esra BALCI **Cengiz TATAR** **Assoc. Prof. Fethi DAĞDELEN**	ANALYSIS OF THERMAL AND CORROSION BEHAVIOR OF Ti-44Ni-6Cd SHAPE MEMORY ALLOYS	408
İsa AVCI **Bahadır Furkan KINACI**	CHALLENGES AND OPPORTUNITIES OF BLOCKCHAIN IN ELECTRIC VEHICLES	418
İsa AVCI **Bahadır Furkan KINACI**	INVESTIGATION OF E-SECURITY STANDARDS USED IN INTELLIGENT TRANSPORTATION SYSTEMS	426
Ahamadi Abdallah IDRISSE **Oktay YILDIZ** **Ugur BAYSAL**	A LIGHTWEIGHT DEEP LEARNING MODEL FOR THE CLASSIFICATION OF A LIMITED LUNG SOUND DATASET	432
Leyla ZEYNALLI-HUSEYNZADE	ADVANCEMENT OF CHATBOT TECHNOLOGY IN CUSTOMER SERVICE	438
Leyla ZEYNALLI-HUSEYNZADE	DIGITAL TRANSFORMATION METRICS	442
Buğra Kaan Türkmenoğlu **Oktay Yıldız**	REDUCING TICKET RESOLUTION TIME THROUGH SUGGESTION IN THE HELP DESK SYSTEM	446
Metin SALİHMUHSİN	SMALL SIGNAL ANALYSIS OF A FLYBACK CONVERTER USING STATE SPACE AVERAGING METHOD	452
Bahdişen Gezer **Mustafa Atalan** **Can Gezer** **Rahşen Gezer**	OBTAINING BORON OXIDE (B_2O_3) DOCUMENTED TUNGSTEN OXIDE (WO3) THIN FILM BY RADIO FREQUENCY (RF) MAGNETRON BREAKING METHOD AND INVESTIGATION OF THEIR STRUCTURAL PROPERTIES	459
Yahaya Abdullahi Ibrahim **Dr. Danladi Bello Al'amin**	HYDROLOGICAL MODELLING OF GURARA WATERSHED UNDER THE IMPACT OF LAND-USE AND CLIMATE CHANGE	461
Saeed Nawaz **Naveed Ahmad Khan** **Muhammad Yasir Khan**	EXPERIMENTAL ANALYSIS OF CIRCULAR, RECTANGULAR AND SQUARE NOTCHES ON THE STRENGTH OF COMPOSITE MATERIALS	483
Abdessamed ATOUI **Abderrezak BEZAZI** **Salah GUENFOUD** **Abilo SILVA** **P.N.B. REIS** **Fabrizio SCARPA**	PHYSICAL-CHEMICAL AND MECHANICAL PROPERTIES OF AMPELODESMOS MAURITANICUS NATURAL FIBERES	493
Abdul Jabbar	IMAGE-TO-IMAGE TRANSLATION BASED FACE PHOTO DE-MESHING USING WASSERSTEIN GANs	494
Nasser BOUHEMAME **Abderrezak BEZAZI** **Hocine KHELIFA** **Kamal Eddinne AIADI** **Gilberto García DEL PINO** **P.N.B. REIS** **Fabrizio SCARPA**	PHYSICO-CHEMICAL AND THERMAL ANALYSIS OF WASHINGTONIA PALM LEAFLET FIBERS	495

Nasraoui Hajaji Afef **Ammari youssef**	CITRIC ACID IS A CRUCIAL COMPOUND PLAYING AN ALLEVIATION ROLE OF SALT-INDUCED OXIDATIVE STRESS IN MORINGA OLEIFERA	496
Alasgarova Durdana **Eldar Gojayev** **Kamal Gulmammadov** **Gafarova Dilara**	INFLUENCE OF $BiSb_3Te_6$ SEMICONDUCTOR COMPOUND MECHANICAL AND ELECTRICAL STRENGTH OF LOW-DENSITY POLYETHYLENE	497
Savalan KARIMOV **Samaya BAGIROVA** **İlaha RAHIMOVA**	KINEMATIC ANALYSIS OF THE MECHANISM OF THE PLANING MACHINE	501
Habip DAYİOGLU **Nigar MERDAN** **Irmak BAYBURTLU** **Sema Hatun TÜRKER**	INVESTIGATION OF DYEING PROPERTIES AND VISUAL VALUES IN TERMS OF COLOUR OF WOOL FABRICKS IN DIFFERENT FABRIC STRUCTURES DYED WITH NATURAL DYE OBTAINED FROM RED ROBIN PHOTINIA LEAVES	506

STABILITY BEHAVIOUR OF NANOCOMPOSITE CYLINDRICAL SHELLS UNDER LATERAL PRESSURE IN ELASTIC AND THERMAL ENVIRONMENTS

Sofiyev AH

Istanbul Ticaret University, Beyoglu 34445 /Istanbul, Turkey

Abstract

By modeling the micro and macro mechanical properties of nanocomposite cylindrical shells, constitutive relations and basic equations on the Winkler elastic foundation in the thermal environment are derived. The stability problem of nanocomposite cylindrical shells on Winkler elastic foundation and in thermal environments is solved and an analytical expression for the critical lateral pressure within classical shell theory is obtained. Using the obtained formulas, the effects of CNT patterns on the critical lateral pressure are analyzed in detail, taking into account the effects of the Winkler soil and the thermal environment.

Keywords: Stability, nanocomposites, shell, elastic foundation, thermal environments, critical pressure

Introduction

Since the discovery of carbon nanotubes (CNTs) [1], there has been great interest among researchers in finding potential applications of CNTs as reinforcing materials for polymeric composites [2-4]. Although single-walled carbon nanotubes have a structure that is a hundred times more durable than steel, their density is one-sixth that of steel. This feature draws attention especially in structural reinforcement. Carbon nanotubes attract attention with their thermal properties as well as their interesting mechanical properties. There are some studies on the stability behavior of unconstrained nanocomposite structural elements with extraordinary properties [5, 6]. Contemporary technology enables the use of carbon nanotube reinforced structural elements in different environments such as elastic and thermal environments [7, 8]. In recent years, some studies have been carried out on the buckling of nanocomposite shells on elastic soil [9-12]. In general, these studies do not take into account the thermal effect. When modeling the structural elements containing carbon nanotubes, reliable results cannot be obtained without examining the effects of functional graded reinforcement, thermal environment and elastic foundations together on critical parameters. These applications lead researchers to examine the stability behavior of structural elements composed of nanocomposites in these environments. In this paper, the solution of the stability problem of nanocomposite shells resting on Winkler soil and in thermal environment under the lateral pressure is presented.

2. Statement of the problem

The CNT-reinforced cylindrical shell with length L, radius R and thickness h, presented in Figure 1, resting on Winkler base, is under the effect of lateral compressive load and the Oxyz coordinate system is selected on its middle surface. Coordinate axes are oriented as in Figure 1. The Winkler elastic foundation is mathematically modeled as follows [9]:

$$K(w) = kw \tag{1}$$

where k is the Winkler elastic foundation coefficients.

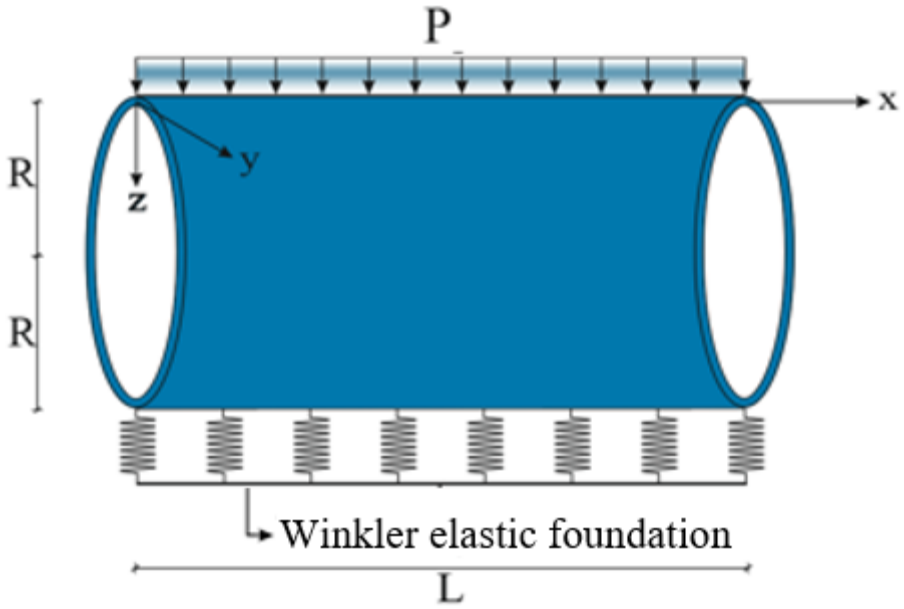


Figure 1. CNT reinforced cylindrical shell resting on Winkler elastic foundation under lateral pressure

In this study, the effective material properties, such as Young's modulus and Poisson's ratio of nanocomposite cylindrical shells are expressed as follows [6-8, 10-12]:

$$E_{11}(Z)=\eta_1 V_{cnt}(Z)E_{11}^{cnt}+V^m E^m,\quad \frac{\eta_2}{E_{22}(Z)}=\frac{V_{cnt}(Z)}{E_{22}^{cnt}}+\frac{V^m}{E^m},$$

$$\frac{\eta_3}{G_{12}(Z)}=\frac{V_{cnt}(Z)}{G_{12}^{cnt}}+\frac{V^m}{G^m},\quad \nu_{12}=V_{cnt}^{*}\nu_{12}^{cnt}+V^m\nu^m,\quad Z=\frac{z}{h},\ V^{cnt}+V^m=1 \tag{2}$$

where, V is the volume fraction, superscript "cnt" and "m" represent the corresponding property for CNTs and matrix, respectively, the efficiency parameters are indicated by $\eta_i(i=1,2,3)$. The Young and shear moduli of the matrix and CNTs are indicated by E^m, E_{11}^{cnt}, E_{22}^{cnt}, and G_{12}^{cnt}, respectively. Here ν_{12} is the Poisson's ratio.

It is assumed that the thermal expansion coefficients, as well as the material properties, vary with temperature (T) and location [7]:

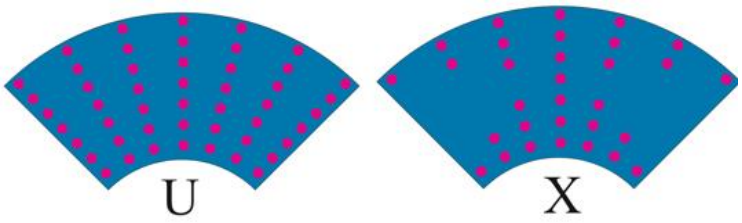
$$\alpha_{11}(Z)=\frac{\alpha_{11}^{cnt}V_{cnt}(Z)E_{11}^{cnt}+V^m E^m\alpha^m}{V_{cnt}(Z)E_{11}^{cnt}+V^m E^m},\quad \alpha_{22}(Z)=(1+\nu_{12}^{cnt})\alpha_{22}^{cnt}V_{cnt}(Z)+(1+\nu^m)V^m\alpha^m-\nu_{12}\alpha_{11}(Z) \tag{3}$$

where α_{11}^{cnt}, α_{22}^{cnt} and α^m are thermal expansion coefficients of CNT and matrix, respectively.

The volume fraction of CNTs changes as a linear function depending on the dimensionless thickness coordinate (Z) of the cylindrical shell [7,8, 10].

$$V^{cnt} = \begin{cases} U & for \quad V_{cnt}^{*} \\ \\ X & for \quad 4|Z|V_{cnt}^{*} \end{cases} \tag{4}$$

While the first line of the Eq. (2) shows that the CNT distribution is the uniform (U), the other distribution is in the form of linear function and is represented by the symbol X. Based on Eq. (2), the patterns formed by the CNT distribution throughout the thickness of the cylindrical shell are illustrated in Fig. 2.



(a) **(b)**

Figure 2. (a) Uniform and **(b)** X-shape CNT distribution throughout the thickness of the cylindrical shell

In the presence of temperature field, the basic relationships of nanocomposite cylindrical shells are constructed in the scope of classical shell theory as follows [6-8]:

$$\begin{bmatrix} \sigma_{11} \\ \sigma_{22} \\ \sigma_{12} \end{bmatrix} = \begin{bmatrix} K_{11}(Z) & K_{12}(Z) & 0 \\ K_{21}(Z) & K_{22}(Z) & 0 \\ 0 & 0 & K_{66}(Z) \end{bmatrix} \begin{bmatrix} \varepsilon_{11} \\ \varepsilon_{22} \\ \gamma_{12} \end{bmatrix} + \begin{bmatrix} \sigma_{1T} \\ \sigma_{2T} \\ 0 \end{bmatrix} \tag{5}$$

where $[\sigma]$ and $[\varepsilon]$ indicate stress and strain tensors, respectively, and $K_{ij}(i,j=1,2,6)$ are described as:

$$K_{11}(Z) = \frac{E_{11}(Z)}{1-\nu_{12}\nu_{21}}, K_{12}(\overline{z}) = \frac{\nu_{21}E_{11}(Z)}{1-\nu_{12}\nu_{21}}, K_{21}(Z) = \frac{\nu_{12}E_{22}(Z)}{1-\nu_{12}\nu_{21}},$$
$$K_{22}(Z) = \frac{E_{22}(Z)}{1-\nu_{12}\nu_{21}}, K_{66}(Z) = G_{12}(Z) \tag{6}$$

in which σ_{1T} and σ_{2T} are defined by

$$\sigma_{1T} = -\frac{E_{11}(Z)\alpha_{11}(Z)T(Z)}{1-\nu_{12}\nu_{21}}, \sigma_{2T} = -\frac{E_{22}(Z)\alpha_{22}(Z)T(Z)}{1-\nu_{12}\nu_{21}} \tag{7}$$

3. Basic equations and solution method

Using the above mentioned basic relations, the fundamental linear differential equations for nanocomposite cylindrical shell and resting on the Winkler elastic foundation and in thermal environments under the lateral pressure take the following form:

$$\begin{aligned} L_{11}(F)+L_{12}(w)+kw&=0\\ L_{21}(F)+L_{22}(w)&=0 \end{aligned} \tag{8}$$

where F is the Airy stress function and $L_{ij}(i,\ j=1,2)$ are linear differential operators.

Since the nanocomposite cylindrical shell is subject to simply supported boundary conditions, the approximation functions are sought as follows:

$$w = A\sin(\alpha x)\sin(\beta y),\ \ F = B\sin(\alpha x)\sin(\beta y) \tag{9}$$

where A and B are the unknown amplitude, $\alpha = m\pi / L,\ \beta = n / R$, in which m denotes the half wave number in the axial direction, and n is the circumferential wave number.

Substituting the expression (9) in the set of equations (8) and applying the Galerkin procedure, the following expression is obtained for the nondimensional critical lateral pressure (NCLP) of the nanocomposite cylindrical shell on the Winkler elastic foundation in the thermal environment:

$$\bar{P}_{cr}^{L} = \frac{U_{2wp}\times U_4 + U_3 \times U_5}{U_4 R\beta^2 E^m} \tag{10}$$

where $U_i(i=1,2,...,5)$ are parameters that depend on nanocomposite cylindrical shell characteristics, soil coefficient and temperature.

5. Numerical computations

The thermomechanical properties of poly methyl methacrylate (PMMA) and CNT at room temperature, that is, for T=300 K, are obtained [7]:

$$\begin{aligned}
&E^m = (3.52-0.0034T) = 2.5\,\text{GPa},\ \alpha^m = 45(1+0.0005\Delta T)\times 10^{-6} = 45\times 10^{-6}/\text{K},\ \ \nu^m = 0.34,\\
&E_{11}^{cnt} = (6.18387 - 2.86\times 10^{(-3)}\times T + 4.22867\times 10^{(-6)}\times T^2 - 2.2724\times 10^{(-9)}\times T^3) = 5.6451\,\text{TPa}\\
&E_{22}^{cnt} = (7.75348 - 3.58\times 10^{(-3)}\times T + 5.30057\times 10^{(-6)}\times T^2 - 2.84868\times 10^{(-9)}\times T^3) = 7.0796\,\text{TPa}\\
&G_{12}^{cnt} = (1.80126 + 0.77845\times 10^{(-3)}\times T - 1.1279\times 10^{(-6)}\times T^2 + 4.93484\times 10^{(-10)}\times T^3) = 1.9466\,\text{TPa}\\
&\alpha_{11}^{cnt} = (-1.12148 + 2.289\times 10^{(-2)}\times T - 2.88155\times 10^{(-5)}\times T^2 + 1.13253\times 10^{(-8)}\times T^3)\times 10^{(-6)}\\
&\qquad = 3.4579\times 10^{(-6)}/\text{K}\\
&\alpha_{22}^{cnt} = (5.43874 - 9.95498\times 10^{(-4)}\times T + 3.13525\times 10^{(-7)}\times T^2 - 3.56332\times 10^{(-12)}\times T^3)\times 10^{(-6)}\\
&\qquad = 5.1682\times 10^{(-6)}/\text{K}
\end{aligned}$$

The efficiency parameters are given in Table 1 [7]:

Table 1. Typical properties of CNT/matrix efficiency parameters based on the volume fraction of CNTs

V_{cnt}^{*}	η_1	η_2	η_3
0.12	0.137	1.022	0.715
0.17	0.142	1.626	1.138
0.28	0.141	1.585	1.109

The geometrical characteristics of CNTs are: $l_{cnt} = 9.26\,\text{nm},\ a_{cnt} = 0.68\ \text{nm},\ h_{cnt} = 0.067\text{nm}$, $\nu_{12}^{cnt} = 0.175$ [7].

The distribution of nondimensional critical lateral pressure (NCLP= values of the cylindrical shell reinforced with carbon nanotubes on the Winkler foundation, depending on the various soil stiffnesses (*k*), and U and X reinforcement profiles are presented in Table 2. The following data are used: *L*/*R* =1, *R*/*h*=20; *h*=0.002m, V_{cnt}^{*} =0.28. As seen in Table 2, the values of the nondimensional critical lateral pressure increase when the Kw increases, and those decrease when the temperature increases. While the X pattern effects on the NCLP decrease continuously when Kw increases, the X pattern effect changes as a parabola when the temperature increases. When the temperature increases, the influence of the Winkler foundation on the NCLP shows differences. For example, in uniform patterned cylindrical shells, when k=4×10^8 (N/m^3) and T=300 T, the effect of the ground on the NCLP is 3%, and when T=700 K, this effect decreases to 2.84%. In X-patterned shells, those effects are 2.21% when T=300 K, and increase to 2.44 when T=700. When the heat and Winkler foundation increase together, the effect of the X pattern on the NCLP decreases compared to the U pattern, but it remains prominent. For example, for T =300 K, when k =0, the effect of X pattern on NCLP value is 35.74%, and when k =4×10^8 (N/m^3), the effect is 34.69%. For T =700 K, when k =0, the effect of X pattern on NCLP value is 36.02%, when k=4×10^8 (N/m^3), the effect is 35.49%.

Table 2. Variation of NCLP of nanocomposite cylindrical shells against the *k* for different *T*

	T=300(K)		*T*=500(K)		*T*=700(K)	
k (N/m^3)	U	X	U	X	U	X
0	0.333(8)	0.452(8)	0.275(9)	0.373(9)	0.211(10)	0.287(10)
1×10^8	0.336(8)	0.455(8)	0.277(9)	0.375(9)	0.212(10)	0.289 (1,0)
2×10^8	0.338(8)	0.457(8)	0.279(9)	0.377(9)	0.214(10)	0.290(10)
3×10^8	0.341(8)	0.460(8)	0.281(9)	0.379(9)	0.216(10)	0.292(10)
4×10^8	0.343(8)	0.462(8)	0.283(9)	0.381(9)	0.217(10)	0.294(10)

Conclusions

In this study, the stability problem of nanocomposite cylindrical shells subjected to lateral pressure in thermal environment and on Winkler elastic foundation is discussed. After deriving the fundamental equations, an analytical expression is obtained for the critical lateral pressure of the nanocomposite cylindrical shell on the Winkler elastic foundation and in thermal environments within the classical shell theory. By using the obtained formulas, the effects of CNT patterns on the critical lateral pressure and analyzes are carried out, taking into account the effects of Winkler soil and thermal environment.

Acknowledgements

This study is supported by Istanbul Ticaret University.

References

1. Iijima S. Helical microtubules of graphitic carbon, Nature **1999**, 354, 56–58,
2. Coleman JN, Khan U, Blau WJ, Gun'ko YKç Small but strong: A review of the mechanical properties of carbon nanotube-polymer composites, Carbon N. Y. **2006**, 44, 1624–1652.
3. Rafiee R, Moghadam RM. On the modeling of carbon nanotubes: A critical review, Composites B **2014**, 56, 435–449.
4. Fantuzzi N, Bacciocchi, M, Agnelli J, Benedetti D. Three-phase homogenization procedure for woven fabric composites reinforced by carbon nanotubes in thermal environment. Compos. Struct. **2020**, 254,112840.
5. Zhang XH. Carbon nanotube/polyetheretherketone nanocomposites: mechanical, thermal, and electrical properties. J. Compos. Mater. **2021**, 55(15),2115-2132.
6. Hieu PT, Tung HV. Thermal and thermomechanical buckling of shear deformable FG-CNTRC cylindrical shells and toroidal shell segments with tangentially restrained edges. Arch. Appl. Mech. **2020**, 90(7), 1529-1546.
7. Shen HS. Thermal buckling and postbuckling behavior of functionally graded carbon nanotube-reinforced composite cylindrical shells. Compos. Part B-Eng. **2012**, 43 (3),1030-1038.
8. Avey M., Fantuzi N, Sofiyev AH. Mathematical modeling and analytical solution of thermoelastic stability problem of functionally graded nanocomposite cylinders within different theories. Mathematics **2022**, 10, 1081.
9. Kerr D. Elastic and viscoelastic foundation models. J. Appl. Mech. **1964**, 31,491–498.
10. Sofiyev AH, Mammadov Z, Dimitri R, Tornabene F. Vibration analysis of shear deformable carbon nanotubes-based functionally graded conical shells resting on elastic foundations. Math. Meth. Appl. Sci. **2020**, 1-15, DOI: 10.1002/mma.6674
11. Sofiyev AH, Pirmamedov IT, Kuruoglu N. Influence of elastic foundations and carbon nanotube reinforcement on the hydrostatic buckling pressure of truncated conical shells. Appl. Math. Mech. (Eng. Edit.) **2020**, 41(7), 1011-1026.
12. Sofiyev AH, Kuruoglu N. Buckling analysis of shear deformable composite conical shells reinforced by CNTs subjected to combined loading on the two-parameter elastic foundation. Defence Techn. **2022**, 18(2), 205-218.
13. Volmir AS. Stability of Elastic Systems. English Translation: Foreign Tech. Division, Air Force Systems Command. Wright-Patterson Air Force Base, Ohio, AD628508, Moscow, Nauka: 1967.

STRUCTURAL SYNTHESIS OF ROBOT FINGERS

Elekberov Allahverdi

Department of "Mechatronics and Machine Design" Azerbaijan Technical University, AZ 1073, Azerbaijan, Baku, 25 G.Javid Ave.,

Abstract

The mechatronic design of robotic hands is a very complex task, which involves different aspects of mechanics, actuation, and control. In most of cases inspiration is taken by the human hand, which is able to grasp and manipulate objects with different sizes and shapes, but its functionality and versatility are very difficult to mimic. Human hand strength and dexterity involve a complex geometry of cantilevered joints, ligaments, and musculotendinous elements that must be analyzed as a coordinated entity. Furthermore, actuation redundancy of muscles generates forces across joints and tissues, perception ability and intricate mechanics complicate its dynamic and functional analyses. By considering these factors it is evident that the design of highly adaptable, sensor-based robotic hands is still a quite challenge objective giving in a number of cases devices that are still confined to the research laboratory.

This work is devoted to the structural synthesis of mechanical fingers of a robot arm using manipulators of sequential structure and Watt mechanisms. On the basis of structural synthesis, manipulators of sequential structure and two-circuit Watt mechanisms are presented, which reproduce the presented angular displacements. Metacarpal - phalangeal (PF), Mid–interphalangeal (MF) and Distal – interphalangeal (DF) joints of the fingers of the robot hand. The paper also presents two-stage manipulators of sequential structure and single-loop articulated, rocker and slide mechanisms to achieve Metacarpophalangeal (PF) and Distal – interphalangeal (DF) joints of the robot thumb. The classification of the structural synthesis of robot fingers is based on the methods of using graph theory, new formulas of structural synthesis and the development of structures between them. New approaches and formulations on the design of robot fingers are illustrated by various examples.

Keywords: manipulator, Watt mechanism, structural graph, structural shapes, mechanical finger.

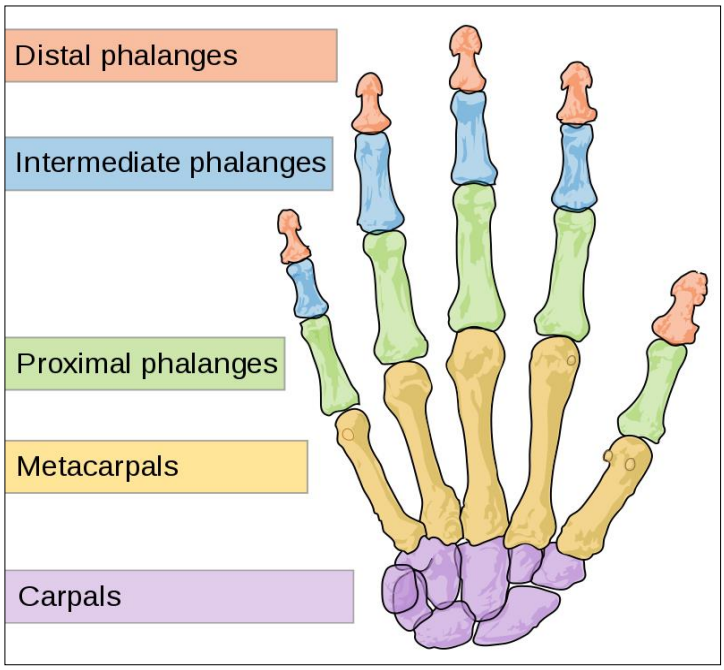
1. Introduction.

The development of the science of mechanisms and machines allows today to develop new areas of robotics - micromechanisms, mechatronics, etc. The new theory should contribute to the development of scientific directions with subsequent use in practice. One of the most important stages of designing a robotic mechanical system is solving the problem of structural synthesis of manipulators. An inefficient system of mechanisms leads to heavy loads on kinematic pairs. Therefore, the correct determination of the structure of manipulators with different values of the mobility of independent closed loops can be carried out only with the help of the development of the structural synthesis theorem of manipulators.

Mechatronic design of robotic arms is a very complex task that includes various aspects of mechanics, actuation and control. In most cases, these aspects are taken over by the human hand, which is capable of capturing and manipulating objects of various sizes and shapes, but its functionality and versatility are very difficult to imitate. The strength and dexterity of human hands include the complex geometry of cantilever joints, ligaments and musculoskeletal elements, which must be analyzed as a coherent object. In addition, the redundancy of muscle activation generates forces in the joints and tissues, the ability of perception and complex mechanics complicate its dynamic and functional analysis. Taking into account these factors, it becomes obvious that the development of robotic manipulators with a high degree of adaptation based on sensors is still quite a difficult task, since in some cases devices that are still limited to the research laboratory are used. Many implementations of hand-held robots can be found in the literature.

The selection of leading designs reported here is limited in scope in terms of mechanical architecture rather than control or monitoring circuits. To copy the structure of a human hand, in order to capture and execute a

technological process, Watt's six-link mechanisms are used. Angular displacements of the joints of human fingers proximal (PP), middle (MP) and distal (DP) phalanx are considered as rotational kinematic pairs connected by means of links, which are used to solve the problem of synthesis of mechanisms of the fingers of the hand [1-3]. A phalanx is named according to whether it is proximal, middle, or distal and its associated finger or toe. The proximal phalanges are those that are closest to the hand or foot. In the hand, the prominent, knobby ends of the phalanges are known as knuckles. The proximal phalanges join with the metacarpals of the hand or meta- tarsals of the foot at the metacarpo phalan- geal joint or metatarsophalangeal joint. The intermediate phalanx is not only intermediate in location, but usually also in size. The thumb large toe do not and possess a middle phalanx.



In works [4-5], families of six-link mechanisms are presented on the basis of two groups of six-link mechanisms. The problem of identification of assembly configurations of flat two-circuit mechanisms with limited hinges, links and an area of limiting their movement were considered in [6]. The Watt mechanism has two linearly independent closed circuits with one degree of freedom, i.e. four double-joint and two three-joint links, which form the structure of a two-circuit six-link mechanism, similar to the structure of the fingers of a robot's hand [7-8]. It is known that there are analytical methods for the synthesis of six-step Uatta1 mechanisms using the theory of approximation of functions, as well as optimization synthesis of mechanisms. In the works [9-11], the friction and efficiency of the transmission of the opening and capture of the positions of the mechanical fingers of the robot are considered, and in the studies [12-13], the problems of the synthesis of the mechanical fingers of the robot are solved, where the prescribed finger movements were considered as input data and the design parameters of the parameter under consideration were determined. In [14-16], a matrix approach was adopted to describe a mathematical model for the synthesis of guiding six-fold mechanisms for generating given points of curves. Based on the analysis of published works on the design of Watt's six-branched mechanisms as mechanical fingers of a robot, it becomes clear that more attention is devoted to the tasks of analysis than to the problems of structural and kinematic synthesis. It should be noted that during the synthesis of the robot's mechanical fingers, the linear parameters of the fingers were determined, while it would be appropriate to also determine the angular parameters of the PP, MP and DP hinges.

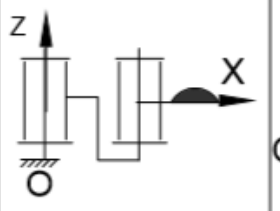
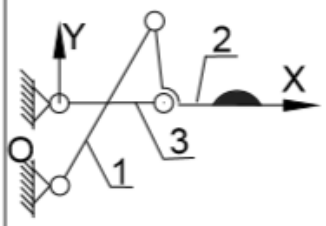
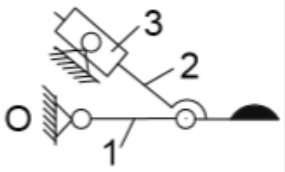
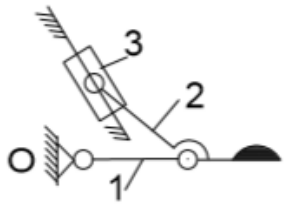
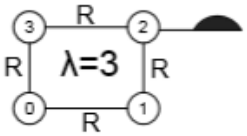
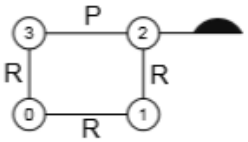
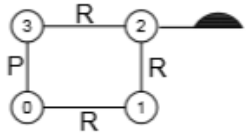
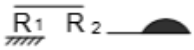
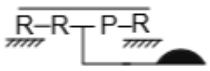
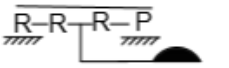
2.Structural analysis of the robot's mechanical fingers

Mechanical fingers of robots, as a rule, are manipulators of a sequential structure (Table1. 1,1 (1,2)) or closed single-circuit and double-circuit (Table1. 1,2), (Table2. 2,3) kinematic chains made of solid bodies (links) connected to each other by single-stage hinges.Table 1.1 illustrates mechanical fingers of a sequential structure with three drives (M=3) and two drives (M=2), for a thumb with mutually parallel axes of rotational pairs. The graphs of the finger manipulator represent circles with links connected by rotational kinematic pairs (Table1. (1,1) and Table2.(2,2)) and (Table1. (2,4) and Table2.(2,1)). Like the human finger, the mechanical finger has local, middle and distal phalanges (PF, SF, DF) and is able to reach the position of the outstretched arm and grip (Table 1. (1 and 4)). It is important that the Watt1 finger mechanism be structurally synthesized using the specified angles of rotation of the finger joint because the "data transmission glove" (a device for tracking the movement of fingers is put on the hand) typically measures the angles of rotation PP, MP, DP. For a four - ringer 0 -1-2-5-0 (Table 1,1(2)) the angle of rotation of the hinge A is the angle of rotation of the AB link relative to the O pillar and the rotation of the

hinge B is the angle of rotation of the BC link relative to the AB link.

On the other hand,for four-links nick 1-2-3-4 the angle of rotation of the hinge With is the angle of rotation of link 3 relative to link 2.

Table 1. The structure of the mechanisms of the robot's fingers

	Manipulator of the thumb	Mechanism of the thumb		
		Articulated	Rocker	Slider
	M=2 Σf_i=2 λ=3	M=1	L=1 λ=3	$\Sigma_i f$ =4
	1	2	3	4
1				
2				
3				

The task of structural analysis of the robot's mechanical fingers is:

* Analysis of structural schemes of serial manipulators and mechanisms with linearly independent contours of mechanical fingers of the robot hand.

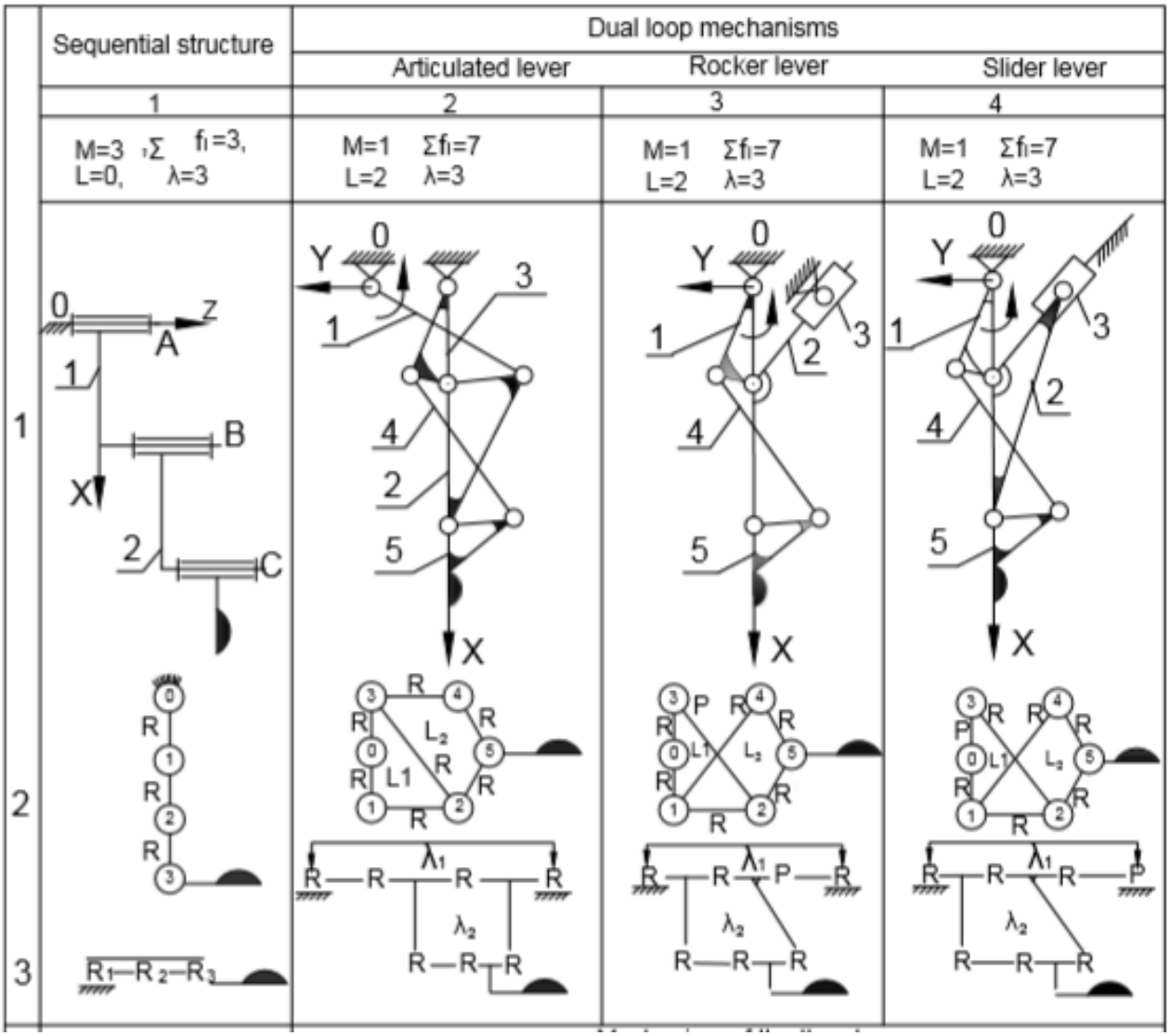
* Determination of the parameters of redundant connections (d) and the mobility of the connecting rod of closed-loop (λ) mechanisms.

* Analysis of the construction of kinematic finger schemes based on graph theory.

* Construction of structural formulas for the analysis of mechanical systems.

* Construction of a coordinate system and the corresponding kinematic parameters of mechanical models of robot fingers.

Table 2. The structure of the mechanism of the thumb



3. Structural synthesis of robot fingers.

Consider the kinematic chains of the robot's fingers, consisting of closed circuits, taking one of the links stationary - we get a mechanism. We introduce the concepts of structural synthesis formulas, which are the basis of the structural classification of mechanisms:

- The motion of an independent closed loop is determined by the maximum number of motion of the connecting coopler in contour $\{\lambda\}_1^6$
- Redundant connections imposed on independent loops by a special arrangement

of links and axes of kinematic pairs $\{d_i\}_0^5$, i.e. $\lambda_i+d_i=6$. $\{\lambda_i$ i.e. $i=0\ldots..6\}$

The number of independent contours of the mechanism (formula of R. I. Alizadeh) has the form

$l=j_b-B-c_b$, where B is the number of platforms; c_b - is the number of branches between platforms; j_b - the total number of joints on the mobile platforms.

- $\sum_{i=1}^{j} f_i$ - sum of degrees of freedom of the kinematic chain of the mechanism ;
- M - is the number of drivers of the mechanism.

The structural formula with a constant value of the mobility for the linearly closed loops of the mechanism will take the following form:

$$M = \sum_{i=1}^{j} f_i - \lambda L + q - j_r$$

where: q –redundant linear connections; j_p –is number of passiv DoF in kinematic pairs.

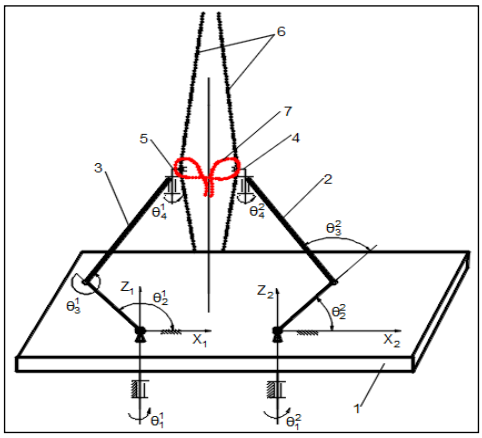
The structural formula with a variable value of the motion of the linearly closed loops of the mechanism is represented as:

$$M = \sum_{i=1}^{j} f_i - \sum_{k=1}^{L} \lambda_k + q - j_r$$

The structural formula of the manipulators of the sequential structure will be written as $M = \Sigma f_i$, and parallel structure $M = \sum_{i=1}^{j} f_i - \lambda L$ with constant parameter λ, and with variable parameter λ in the form $M = \sum_{i=1}^{j} f_i - \sum_{k=1}^{L} \lambda_k$. The values of the structural parameters of the Watt mechanisms and the robot finger manipulators are presented in Table 2.

4.The use of mechanical robot fingers in looping

In this case, we replace the flat mechanisms with spatial mechanisms - a robot manipulator. In this case, the replaced new looper will have four degrees of freedom (RRRR). The created manipulator simulates the work of a carpet weaver's hand. By implementing this mechanism, the looping process will be more accurate and faster (Fig.1). The figure shows two manipulators of a sequential structure operating in parallel, installed on the platform.



The principle of operation of the manipulators is as follows:

the right manipulator, having made a turn at an angle of θ_1, with the help of a grab, takes and pulls a colored thread from a colored thread store, and the left manipulator catches the second end of the colored thread, while automatically using scissors, the colored thread is cut to the desired length. The introduction of this manipulator replaces the work of several mechanisms. The manipulators will be equipped with servomotors controlled by a special program. A mathematical model of this process based on the final stage of development. The platforms of the looping mechanisms and the drive mechanisms will be structurally improved and reliable.

Drawing. 1. Manipulator-looper

1 - platform, 2, 3 - manipulators, 4, 5 - grippers, 6 – main (warp) threads, 7 – loop

Literature

[1]. R.Vinet, U.Lozach, N.Beaudry and G.Drowin, Design methodology for a multifunctional hand prosthesis hand, Proceeding of the 2nd International Symposium of Robotics and Automation.Monterrey,N.I.Mexico,2008.

[2]. N.E.Rodriguez, G.Carbone and M.Ceccarelli, Optimal design of driving mechanism in a 1-DOF anthropomorphic finger. Mechanism and Machine Theory 41 (2006) 897-911.

[3]. N.Dechev,W.I.Cleghorn and S.Naumann, Thumb design of an experimental prosthesis hand.Procceding of the 2nd International Symposium of Robotics and Automation,Monterrey,N.I.Mexico,2008.

[4]. J.E.Baker, A curious and family of overconstrained six bars.Journal of Mechanical Design 127, pp.602-606,2005.

[5]. J.I.Baker, On generating a class of foldable six-bar spatial linkages, Journal of Mechanical Design 128,pp.374-383,2006.

[6]. D.E.Foster and R.J.Cipra, Assembly configurations of planar multi-loop mechanisms with kinematic limitations, Journal of Mechanical Design 128, pp.747-751,2006.

[7]. G.A.Bekey, R.Tomovic and I.Zeljokovic, Control architecture for the Belgrade/USC hand, Dextrous Robot Hands, Springer-Verlag, New York,2008.

[8]. J.K.Salisbury and J.J.Craig, Artculated hands: forse control and kinematic issue, International Journal of Robotic Research 1, pp.4-17, 1982.

[9]. Sanibrian, R.I.Improved GRG method for the optimal synthesis of linkages in function generation problems. Mech. and Mach. Theory, 46(10). Pp.1350-1375, 2011.

[10]. N.E.N.Rodriguez,G.Carbone and M.Ceccarelli, Optimal design of driving mechanism in a 1-DOF anthropomorphic finger, Mechanism and Machine Theory,41, pp.879-911,2006.

[11]. J.Zhang,G.Guo and W.A.Gruver, Optimal design of a six-bar linkage for an anthropomorphic three-jointed finger mechanism, Proceeding of the ASME Mechanisms Conference,Phoenix,Arizona,1992.

[12]. Q.Shen,K.Russel,W.Lee and R.S.Sodhi, On mechanical finger design for expanded prescribed grasping poses,Journal of Advanced Mechanical Design Systems and Manifacturing 2, pp.903-914,2008.

[13]. Q.Shen,K.Russel,W.Lee and R.S.Sodhi, On motion generation of Watt 1 mechanisms for mechanical finger design, Transactions of the Canadian Sosiety for Mechanical Engineering 32, pp.411-421,2008.

[14]. H.S.Kim,S.Hamid and A.H.Soni,Synthesis of six-link mechanisms for path point generation, Journal of Mechanisms 6,pp.447-461,1971.

[15]. C.H.Sah and C.W.Radcliffe, Kinematics and Mechanis. Design,John Willy and Sens,New York,1978.

[16]. Johm Q.Shen,Kelvin Russel and Raj S.Sodhi, On the function generation of Watt1 mechanisms for finger design. Proceeding of the International Symposium of Mechanism and Machine Science (2010), pp.382-388.

KINETOSTATICS OF THE MECHANISM OF THE PLANING MACHINE

Karimo Savalan Khanlar

Doc. Azerbaijan Technical University, Faculty of Mechatronics and Robotics, Department of Mechatronics and Machine Design, Baku, Azerbaijan, ORCID NO: 0000-0001-7711-6683

Hajieva Firangiz Shukur

Doc. Azerbaijan Technical University, Faculty of Mechatronics and Robotics, Department of Mechatronics and Machine Design, Baku, Azerbaijan, ORCID NO: 0000-0001-9579-5966

Ismailova Shabnam Vidadi

Phd. Azerbaijan Technical University, Faculty of Mechatronics and Robotics, Department of Mechatronics and Machine Design, Baku, Azerbaijan, ORCİD NO: 0000-0001-6063-0096

Abstract

The article deals with the kinetostatics of a lever mechanism that moves the chisel head of a straightening machine tool, which is widely used in the machining of flat parts in mechanical engineering. In kinetostatic analysis, by adding inertial forces resulting from the unequal motion of the links to the forces acting on the parts of the mechanism, the dynamic unbalanced system is considered as balanced, and the dynamic problems are solved using the balance equations of statics.

For the kinetostatic analysis of the mechanism, its kinematic scheme, the law of motion of the input dam, the dimensions of the inertia of its dams, masses, moments of inertia, the center of mass, and the positive resistance force acting on the chisel are known.

In the article, the acceleration plan of the third-class flat-link mechanism, which moves the chisel head of the planing machine, is established. The built-in plan of momentum allows to find the inertial forces and moments of inertia forces of the dams.

The goal of performing a kinetostatic analysis of mechanisms is to find the reaction forces that occur in kinematic pairs and the balancing force acting on the entry point.

Since the Assyr groups are a statically resolved system, they break the mechanisms into Assyr groups when unknown forces are found.

Since the flat motion mechanism that moves the cutting head is a third-class mechanism, a special point, i.e., the Assyr point, was used to determine the reaction forces generated in the kinematic pairs of the Assyr group of the third class. Using the graphoanalytical method, the reaction forces generated in the kinematic pairs and the balancing force affecting the entry point were found.

Key words: Planing mechanism, kinetostatic analysis, Assyr point, graphoanalytical method.

Introduction

A flat link mechanism is used to drive the chisel head of the straightening machine. This mechanism is a third-class pulley mechanism. The kinematic scheme of the mechanism is shown in figure 1. The mechanism is a 6-dam mechanism. It consists of a fixed frame, 3 kulis and 5 slider. The mechanism includes 3 forward and 4 single-action kinematic pairs. The structural analysis of this single-degree-of-freedom mechanism shows that it is a third-class flat-link mechanism.

In kinetostatics of mechanisms, the type I problem of dynamics is solved. When the lawof motion of the mechanism and the external forces acting on the points are known, the unknown forces are found (Kəngərli, 2021).

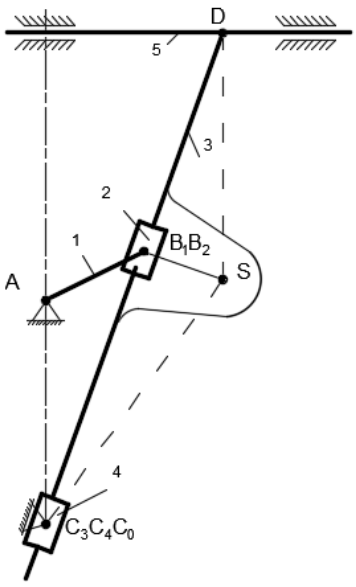


Figure 1. The kinematic schem of the mechanism

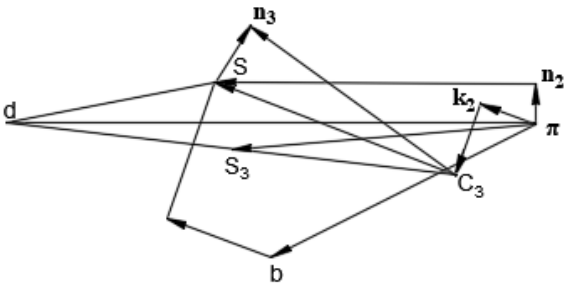


Figure 2. Acceleration plan of the mechanism.

In the kinetostatic analysis, by adding the inertial forces arising from the irregular (impulsive) movement of the joints to the composition of the forces acting on the points of the mechanism, a system that is not in dynamic equilibrium is viewed as a system in equilibrium, a dynamic system is viewed as a system in equilibrium, and a dynamic system is solved by means of equilibrium equations of statics (Kərimov and Həsənov, 2012).

In order to perform a kinetostatic analysis, the law of motion of the input point of the mechanism, the inertia measurements of its points: masses, moments of inertia, the center of mass of the points, and the balance or driving force acting on the mechanism must be given. Ab entrance dam, 2 and 4 kulis stones are not taken into account because the weights are relatively small. $m_1 = m_2 = m_4 = 0$ is assumed (Kəngərli, Əliyev and Kərimov, 2005). The mass m_3 of the 3 pulleys, the moment of inertia J_{s3} and the mass of the chisel head m_5 are given. The center of mass of those points is known. $F_{x.m}$ which affects the chisel of the machine. It is known for its good resistance. In order to carry out kinetostatic analysis, we need to add the load forces of the dams to the composition of the known forces. For this purpose, inertia forces and moments of inertia forces of the points of the mechanism should be determined. For this purpose, in the considered situation, the acceleration plan of the mechanism should be established. In order to build the acceleration plan of the mechanism, its kinematic scheme, the law of motion of the input point $-\omega_1$, the angular velocity are given. In order to find the accelerations of the points and dams of the mechanism, its velocities plan must first be established in that situation . Since the mechanism is a flat-linkage mechanism, the vector equations of the plane-parallel motion must be formulated to establish its plan of momentum. Since the considered planing mechanism of the alignment machine is a third-class mechanism, since the number of components in the vector equation for the momentum of points is more than 2, those equations cannot be solved either graphically or analytically. A special point, that is, the Assyr point, is used to solve the problems of speeds and accelerations of the mechanism. The momentum plan of the mechanism is shown in figure 2. Since the masses of the first, second and fourth points are not taken into account, their inertial forces are assumed to be zero. The inertia force of the third point will be ($\bar{F}_{э3} = -m_3 \cdot \bar{a}_{s3}$ moment of inertia (Стрелков, 1975).

$M_{э3} = -J_{s3} \cdot \varepsilon_3$ – acceleration of the center of mass of the third point, ε_3 – angular acceleration of that point. The inertia force of the cutting head - the fifth point will be $\bar{F}_{э3} = -m_5 \cdot \bar{a}_D$.

Since structural groups (Assyr groups) are statically resolved systems, the mechanism is divided into structural groups. The considered kulis mechanism is composed of third-class Assyr groups and first-class mechanism

composed of one 2nd, 3rd, 4th and 5th point. The Assyr group is shown in figure 3 and the first class mechanism is shown in figure 5.

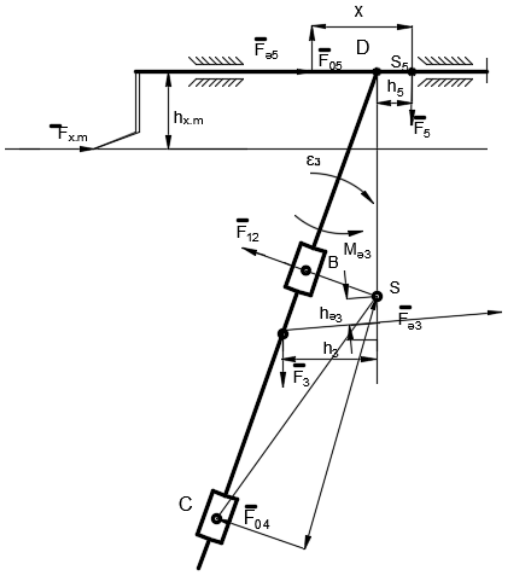


Figure 3. Assyr group

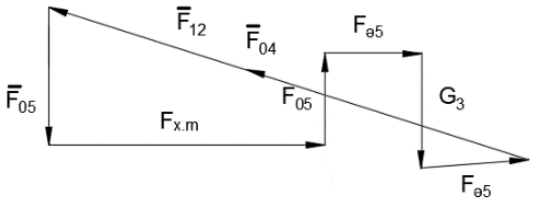


Figure 4. Forces plan of the mechanism.

We apply the corresponding reaction forces to the kinematic pairs of the Assyr group separated from the mechanism. Three kinematic pairs are separated from the mechanism, since the third class Assyr group separated from the mechanism is the third arrangement. 1) The reaction force $\bar{F}_{21}$ generated in the rotation kinematic couple separated from the 1 elbow of the 2 kulis stone will be perpendicular to the CD backend block. Because the weight of the 2-kulis stone is not taken into account. 4 - $\bar{F}_{04}$ formed by the separation of the kulis stone from the support will be directed perpendicular to the CD kulis dam in the direction of the reaction force. The direction of the reaction force $\bar{F}_{05}$ of the support to the 5 - slider separated from the support will be perpendicular to the movement direction of the slider. The point of application of that reaction force will be fixed at x. The goal of kinetostatics is to find these unknown reaction forces and the balancer $\bar{F}_t$ acting on the input point and the reaction force $\bar{F}_{01}$ exerted by the support on the input point. The directions of reaction forces $\bar{F}_{21}$, $\bar{F}_{04}$ və $\bar{F}_{05}$ affecting the structural group are known. Since these reaction forces are generated in forward kinematic pairs, they are oriented in the direction normal to the forward direction. Their values should be found from the balance equations of statics. If there are two unknowns in the vector equations written for the equilibrium of a flat kinematic series, since that equation can be written in the form of two scalar equations, from those equations $|\bar{F}_{21}|$, $|\bar{F}_{04}|$, $|\bar{F}_{06}|$ three unknowns cannot be found. This is because the structural group under consideration is a tertiary group. Therefore, a special point - the Assyr point - is used to solve the problem. As the Assyr point, the intersection point S of the perpendicular drawn to the directions of the relative drifts of the 2 kulis stones and the chisel head - the slider (figure 3) was taken.

The solution of the problem is considered by graphoanalytical method. First, the balance of the chisel head - point 5 is considered. The moment equation is written considering the point D of the forces acting on that point.

$$\sum_{i=1}^{n} M_D = F_{x.m.} \cdot h_{x.m.} + F_5 \cdot h_5 \cdot x = 0$$

From here

$$F_{05} \cdot x = F_{x.m.} \cdot h_{x.m.} + F_5 \cdot h_5 \,. \qquad (1)$$

After that, the moment equation is written considering the point S of the forces acting on the structural group.

$$\sum M_S = -F_{05} \cdot x + F_5 \cdot h_5 - F_{x.m.}(SD - h_{x.m.}) - F_{ə_3} \cdot h_{ə_3} +$$

$$+M_{ə_3} \cdot \frac{1}{\mu_l} + F_3 \cdot h_3 - F_{04} \cdot h_{04} = 0\,. \quad (2)$$

Considering (1) in (2).

$$-F_{x.m.} \cdot h_{x.m.} - F_5 \cdot h_5 + F_5 \cdot h_5 - F_{x.m.}(SD - h_{x.m.}) - F_{ə_3} \cdot h_{ə_3} +$$

$$+M_{ə_3} \cdot \frac{1}{\mu_l} + F_3 \cdot h_3 - F_{04} \cdot h_{04} = 0\,. \quad (4)$$

From here

$$F_{04} = \frac{1}{h_{04}}\left[-F_{x.m.} \cdot h_{x.m.} - F_{x.m.}(SD - h_{x.m.}) + F_{ə_3} \cdot h_{ə_3} + M_{ə_3} \cdot \frac{1}{\mu_l} + F_3 \cdot h_3\right] \quad (5)$$

Here, μ_l is the scale of the plan of stiuations, F_3=$m_3 g$ is the gravity force of the flat motion.

After finding the reaction force $\bar{F}_{04}$ shown by the support to the curtain stone from the equation (4), the reaction forces $\bar{F}_{21}$ and $\bar{F}_{05}$ are found by constructing a polygon of forces. Because of this

$$\overline{F_{05}}+\overline{F_{x.m.}} + \overline{F_{05}}+\overline{F_{ə_5}}+\overline{F_3}+ \overline{F_{ə_3}}+ \overline{F_{04}} +\overline{F_{12}} =0 \quad (6)$$

It can be seen from the vector equation (5) that when constructing the polygon of forces ($\bar{F}_{05}$), the construction starts with the direction of one of the unknown forces, and the known forces are marked one after the other with a certain scale. The polygon of forces is closed by marking the direction of the second unknown $\bar{F}_{12}$) to the construction. The modules of forces ($\bar{F}_{05}$ and $\bar{F}_{12}$ are found by multiplying straight line segments taken from the polygon of forces on the brain of the plane of forces (Fig. 4). The reaction force $\bar{F}_{35} = -\bar{F}_{53}$ generated in the single-motion kinematic pair formed by the 3rd kulis dam and 5 slider is found from the condition that the geometric sum of the forces acting on the 3rd or 5th block is equal to "0".

$$\begin{cases} \bar{F}_{x.m} + \bar{F}_{ə5} + \bar{F}_{05} + \bar{F}_5 + \bar{F}_{53} = 0 \\ \bar{F}_{04} + \bar{F}_3 + \bar{F}_{ə3} + \bar{F}_{21} + \bar{F}_{35} = 0 \end{cases} \quad (7)$$

$\bar{F}_{35} = -\bar{F}_{53}$ reaction forces are found from the constructed force polygon (Figure 4). After that, the force analysis of the conditional first-class mechanism formed by the AB access point and the support is considered (Figure 5). The reaction force ($\bar{F}_{21}$) that the second point acts on the first point will be $\overline{F}_{21} = -\bar{F}_{12}$.

Since the degree of freedom of the considered conditional first-class mechanism is equal to 1 the system is a statically non-solvable system. If we take into account the balancing force acting on this system, under the influence of that force, the system becomes a statically soluble system. Let's assume that $\bar{F}_t$ – balancing force acts on the point B of the input point AB in the direction perpendicular to that point. In this case, three forces act on this flat system in equilibrium: $\bar{F}_t$, $\bar{F}_{21}$ və $\bar{F}_{01}$. $\bar{F}_{01}$ is the reaction force of the support on the first member at point A. For the balance of three forces located on a plane, a triangle of forces is established under the condition that their line of action meets at one point (Figure 5). The forces $\bar{F}_{01}$ and $\bar{F}_t$ are found:

$$\overline{F_{01}} + \overline{F_{21}} + \bar{F}_t=0. \quad (7)$$

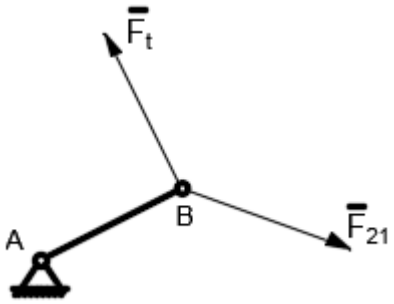


Figure 5. Entry dam

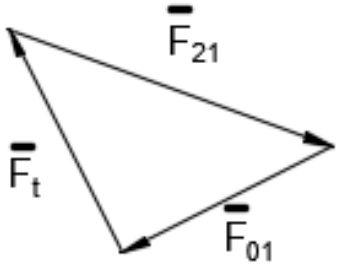


Figure 6. Force plan of the entry dam.

Conclusions

1. In order to solve the kinetostatic analysis of the mechanism, the acceleration plan of the third-class flat pulley mechanism, which moves the chisel head of the straightening machine in the considered position, is constructed.
2. The moment of inertia of the mechanism's points was found with the help of the plan of impulses.
3. The mechanism was divided into a statically resolved system, the reaction forces generated in the kinematic pairs and the balancing force acting on the input point were found using the balance equations of statics.

Literature:

1. Kəngərli A.M. Maşın və mexanizmlər nəzəriyyəsi, Dərslik, Bakı, 2004.
2. Kərimov S.X. və b. Maşın və mexanizmlər nəzəriyyəsi kursu. Dərs vəsaiti, Bakı, NPM “Təhsil”, 2012, 350s.
3. Xəlilov Ə.M. Tətbiqi mexanika. Bakı, Dərslik, “Təhsil”, 2008.527s.
4. Н. И. Левитский. Теория механизмов и машин, М, «Наука», 1990.
5. Əliyev Ş.N., Məmmədov F.H., Kəngərli L.A. Maşın və mexanizmlər nəzəriyyəsi. Layihələndirmə. Dərs vəsaiti. Bakı, “Təhsil” NPM, 2010, 286 s.
6. Kəngərli A.M., Əliyev Ş.N., Kərimov S.X. Maşın və mexanizmlər nəzəriyyəsi kurs layihəsi. Dərslik. Bakı, “Təhsil” NPM, 2005, 428 s.

STUDY OF PROTOTYPE NANO SATELLITE SUBSYSTEMS BASED ON RADIO AND OPTICAL COMMUNICATION TECHNOLOGIES

Nadir ATAYEV ARZU

P.h.D student, Azerbaijan Technical University, Telecommunication technology, Department of radiotechnics and telecommunication, Azerbaijan, Baku, ORCID NO: 0000-0002-5335-1053

ABSTRACT

In terms of availability and technical functionality, CubeSat platforms are already widely used in high-speed and high-volume data exchange missions. However, there are difficulties in achieving this with the current radio (RCT) communication method. So, optical or laser communication (OCT), has some major advantages over the RCT, such as: High information value; Better signal-to-noise ratio; Overall lower energy demand; Considering the fact that it is difficult to cross and block narrow light rays, it can be effectively shielded and can be effective for future technological development for quantum communication systems. However, due to the coherent and monochromatic, the process of directing it to the terrestrial reception antenna becomes difficult. This mainly leads to an increase in the accuracy of the position determination and control (PDC) subsystems in CubeSat platforms, thus increasing the parameters of the platform such as mass, size and electrical power. Given conceptual CubeSat platform mainly consists of a few sub-systems, 1) Structure of the laser beam control and transponder-based payload: Three-axis point (X, Y, Z) laser-head transmitting beam source and receiving photodetectors; 2) Data exchange, control and active transponder: Transceiver subsystems incorporating one or more radio frequency parameters are widely used for RCT data exchange; 3) Structure of power output, power supply and controller: For the autonomous supply of the whole platform with the necessary electric power; 4) Structure of microcontroller-based on-board computer and position determination: 5) A central MCU-based on-board computer for data processing and management of all subsystems. Along the subject, the algorithmic structures of the control programs of the four main subsystems, which is the second part of the initial conceptual model developed by combining the advantages of RCT and OCT technologies, which is considered effective in solving PDC difficulties on CubeSat platforms with OC technology, were developed.

Keywords: CubeSat, Nano Satellite, Radio Communication Technology (RCT), Optical Communication Technology (OCT)

INTRODUCTION

Looking at the statistics of satellite platforms launched over the past decade, we see that Nano Satellite space systems are in high demand compared to other small and mostly large satellite platforms. Briefly, when saying Nano Satellite platforms, these include any satellites from 1kg to 10kg and 1U (Unit) 10x10x11cm. CubeSat satellites are the most representative of their group (NASA, 2017).

The following main factors can be attributed to the attractive design factors of CubeSat platforms:

- Compared with other satellite platforms, costs such as ordering, transporting, designing, and launching internal components are very low;
- Possibility to easily launching CubeSats mainly into low Earth orbit (LEO), the possibility of operating off-the-shelf components of the subsystem (COTS) instead of very expensive components that are resistant to specific sources of obstacles in the space environment;
- Low degree of complexity due uniform-based standardized (S) structure, etc.

In terms of availability and technical functionality, the CubeSat platforms, which are mainly used in low Earth orbit, are already widely used in high-speed and large-scale data exchange missions. However, with the current conventional radio frequency (RF) communication method, this is difficult to achieve. Optical or laser

communication (OC), RF overcomes the mentioned disadvantages due to: a) high data cost, b) ultra-low channel-to-channel interference, c) better signal-to-noise ratio, d) overall lower power consumption, e) the possibility of effective protection, taking into account attention to the difficulty of crossing and blocking narrow light beams, and f) the effectiveness for the future technological development of quantum communication systems.

One of the widely used applications of optical communication technology is to send large amounts of data received from geostationary (GEO) surveillance satellites to the ground segment (GS) with low earth orbit (LEO) OC CubeSat satellites using a data repeater/transponder. In addition, it is possible to provide a large volume and directed data flow through the OC CubeSat platforms, organized according to the radial-nodal principle around low Earth orbit, similar to terrestrial wired communication networks (NASA, 2017).

An example of this can be seen in the same output of strong communication directions in two different directions with space segment RF and OC technologies described in Table 1.

Table 1. Output parameters for both TF and OC technologies

Contact example	Data volume	Frequency bands		
		Optic	Ka frequency band	Millimeter frequency band
GEO-LEO	2.5 Gb/s			
Antenna diameter		10.2 sm	2.2 m	1.9 m
Weight		65.3 kq	152.8 kq	131.9 kq
Power		93.8 W	213.9 W	184.7 W
LEO-LEO	2.5 Gb/s			
Antenna diameter		3.6 sm	0.8 m	0.7 m
Power		23.0 kq	55.6 kq	48.6 kq
Power		33.1W	77.8 W	68.1 W

Along with the advantages of CubeSat platforms with OC technology mentioned in Table 1 and above, there are some disadvantages. The beam generated by the OC is difficult to direct to a ground receiving antenna due to the fact that the beam generated by the OC is coherent and monochromatic, as well as microradial, in other words, the radiation coverage area is based on a wavelength of ~1600nm. This mainly leads to an increase in the accuracy of the position/environment (MMI) subsystems in CubeSat platforms, thereby increasing platform parameters such as mass, size and electrical power.

This difference between the wavelengths in these technologies leads to the following features (Desire, Daria, Shreya, 2020):

- **High output frequency range:** It is well known that as the frequency of the data carrier increases, the output of the system increases. In radio frequency communication, the bandwidth of the radiation can be no more than 20% of the carrier frequency. In FSO communication, this value can even rise to 100 THz when the carrier frequency is 1% ($\approx 10^{16} Hz$);

$$C = \frac{1}{\log(2) E_\lambda} * \left(\frac{P_{req}^2}{\frac{P_{req}}{\log(PPM)} + \frac{2P_n}{PPM-1} + \frac{P_{req}^2 * PPM * T_s}{\log(PPM) * E_\lambda}} \right) \quad (1)$$

- **Low power and mass consumption:** Considering the aperture diameter of the optical beam and the wavelength λ / D_R, it becomes clear that as one increases, the value of the other decreases inversely. And in these FSO systems, the intensity of the signal directed to the receiving side determines the reception of the receiving power with maximum efficiency:

$$\frac{\text{Gain}_{(\text{optical})}}{\text{Gain}_{(\text{RF})}} \approx \frac{4\pi/\theta^2_{\text{div}(\text{FSO})}}{4\pi/\theta^2_{\text{div}(\text{RF})}} \quad (2)$$

- **High shielding:** FSO communications cannot be detected by a spectrum analyzer or RF meter, unlike RF. The main reason for this is that it has a very narrow beam. At the same time, On-Off Keying (OOK) is widely used in FSO systems.

$$p_{tx}(t) = \sum 2P_{tx} b_n * \text{rect}\left(\frac{t - nT_b}{T_b}\right) \quad (3)$$

MATERIALS AND METHODS

First consideration is the algorithmic structures of the control programs of the four main subsystems of the original conceptual model, which is considered effective in solving the difficulties arising on the CubeSat platforms MMI with OC technology, hybrid, in other words, combining the advantages of RF and OC technologies (Hemani and Georges, 2017).

1) The structure of the laser beam control subsystem and the transponder payload.

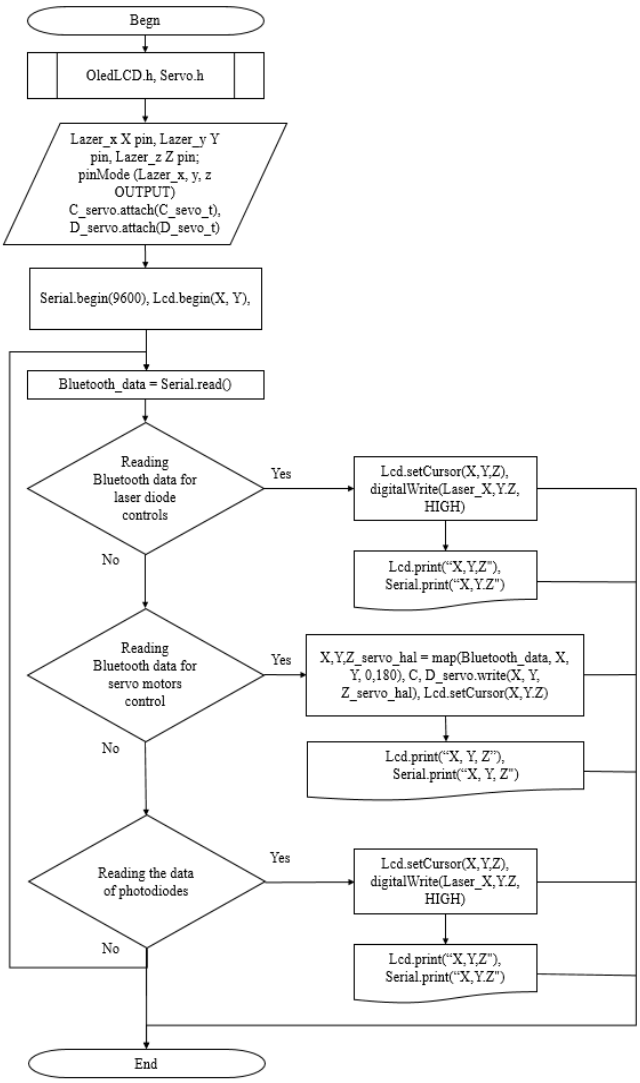


Figure 1. The algorithm of laser beam control and transponder payload subsystem.

One of the two modulation principles of CubeSat platforms with OR technology is based on on-off keying (OOK), controlling a constantly produced stream of photons with a discrete signal generator connected to it, where "1" data bit is an optical pulse, 0-bit data is not an optical pulse. The modulation of another pulse per minute (PPM) is defined as $M = 2^n$, and n is calculated as the number of bits in one symbol, and the symbol duration T_s is divided by the number L in the time interval.

The calculation of the budget for connecting the OC system is one of the main stages and is calculated according to the following expression (Christian, Maxim, Ryan, 2016):

$$P_r = P_t \tau_t G_t L_{fs} G_r \tau_r \tau_{rp} \tag{4}$$

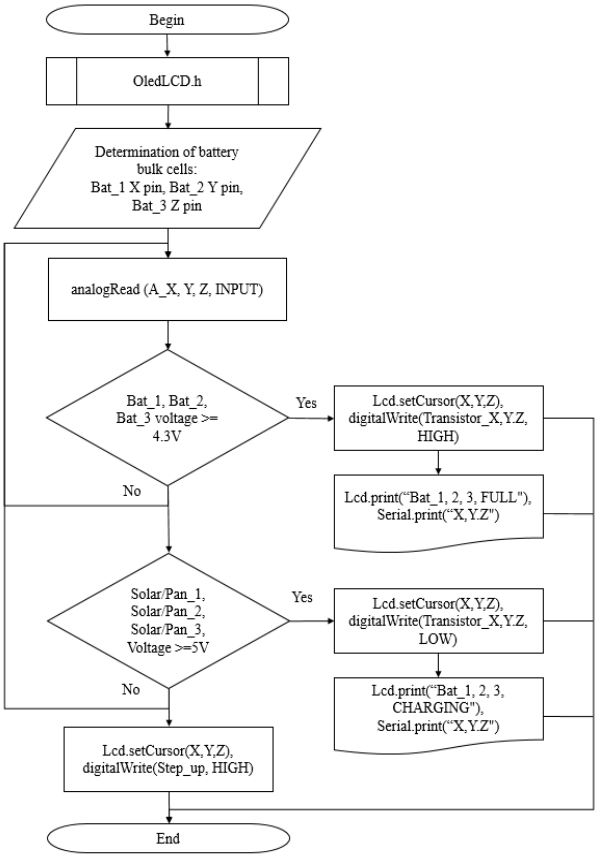


Figure 2. The algorithm of power harvesting, power, supply, and controller.

Here $P_r(W)$ is the received optical power, $P_t(W)$ is the delivered optical power, τ_t is the optical loss in the transmitter, G_t is the transmit gain, L_{fs} is the free space loss, and G_r is the antenna receive gain, τ_r is the receive optical loss, and τ_{rp} is the receiver loss (Morio, 2010).

$$G_t = \frac{16}{\theta_{div}^2} \tag{5}$$

$$L_{fs} = \left(\frac{\lambda}{4\pi z}\right)^2 \tag{6}$$

$$G_r = \left(\frac{2\pi R_x}{\lambda}\right)^2 \tag{7}$$

The algorithm of the laser beam controller and transponder for the OC, shown in Figure 1, first includes the necessary software libraries; the physical interfaces of various control components to the microcontroller (MCU) are defined; the data is read in serial communication and the appropriate control of laser diode servo motors and microactuators is started to provide data emission and control of the X, Y and Z axes of the system.

In another part, in order to provide full duplex optical communication between the CubeSat platform and GS, the OOK laser beam incident on it is processed, modulated by laser diodes of the X, Y and Z axes and sent back to the GS. This developed sub-system will have the following advantages (Mehman, Nadir B., Nadir A. and Vali, 2021):

- Compact lens assembly, depending on the number of beam sources, with laser light sources located together or separately on the 360^0 rotating head;
- Multiple increased switching time of optical signals arriving at the translucent mirror platform through two high-precision microactuators;
- Possibility of constant monitoring of the operation of the switchgear through the electronic control and measuring system built into the device and effective diagnostics of the problems that have arisen.

2) Structure of electrical output, power supply, and controller.

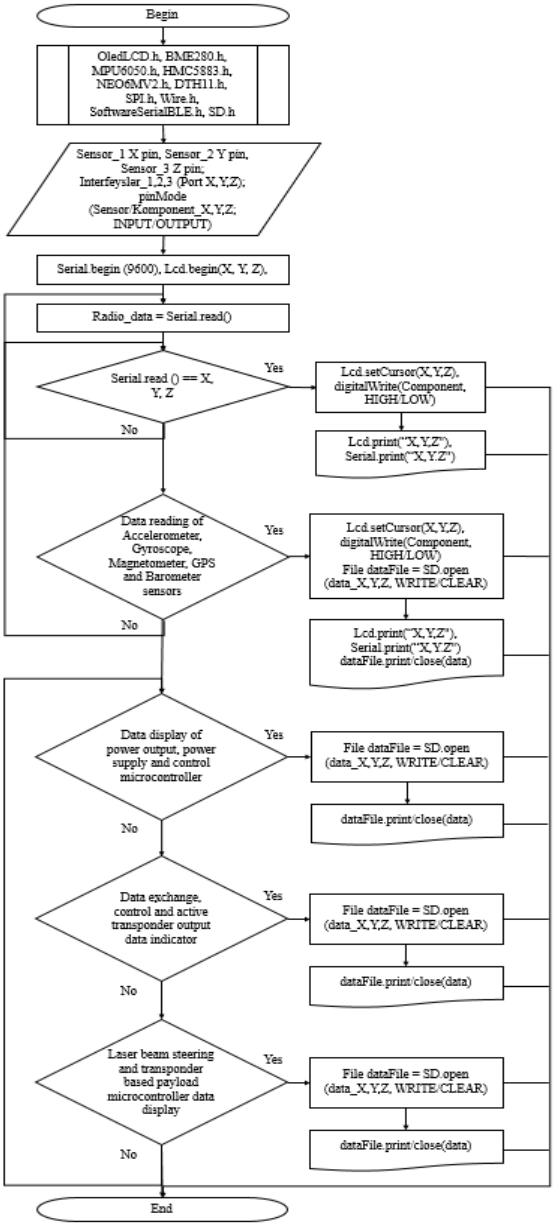


Figure 3. The algorithm of microcontroller-based on-board computer and position/environment determination system.

In Figure 2, the software algorithm of the subsystem that provides power to all systems of the CubeSat platform first includes the necessary software libraries; the connected battery pack is configured to connect to the appropriate physical interface, determined by the MCU; battery and solar panel voltage values are continuously read and processes such as battery charging, and voltage increase/decrease are performed accordingly, and the data is displayed on serial and LCD screens for monitoring through the central MCU (Alberto and Ramon, 2020).

3) The structure of the onboard computer based on the microcontroller and the algorithms for working with the position/environment detection system.

In Figure 3, the software algorithm, which includes an MCU-based central on-board computer for data processing and control of all subsystems of the CubeSat platform, and another auxiliary MCU for position/environment, first add a set of libraries for the corresponding software structure; the input/output physical interfaces of the required sensors/components are defined; starting to read data from the auxiliary RF module connected to the serial port, the important ones are displayed on the LCD screen; the necessary data is collected from the MEMS sensor modules of the position/environment part, and the process of sending GS via RF and writing to the on-board SD card takes place.

In the original CubeSat concept platform, the positioning/environment subsystem performs only high-precision self-positioning by means of a 9-axis accelerometer, gyroscope, magnetometer, GPS, and barometer, capable of accurately and reliably transmitting YS of the discussed laser pulses with less technical requirements. The before mentioned 1, 2, and 3 as well as the SDR-based active RF transporter control MCU transmits the data collected by the onboard computers 3 MCUs through the "SoftwareSerial" interface, displaying the data on the corresponding serial outputs (Joshi, Patil and Shimpi, 2017).

4) Communication, management, and active transponder structure.

Transceiver subsystems, including one or more radio frequency parameters, are widely used for the exchange of RF data on various satellite platforms. However, these systems cannot change their parameters with software alone if necessary. Software-Regulatory Radio (SDR) platforms with low power consumption (1-10 W), support for wide bandwidth (50-8 GHz), a wide range of sampling rates (32-56 MHz), and most importantly, the traditional physical components of the RF as part of the systems (mixer, modem, codec, filter, etc.) are controlled by software from the FPGA controller, and their small size (0.3-1U) allows them to be widely used in various satellites, mainly CubeSat platforms. Application of SDR-based RF technology in the CubeSat platform conceptual model being developed, the need for communication in a subsystem in addition to OC, simultaneous high processing of RF and OC systems data when necessary, and automatic tuning of RF-based GS mobile stations to the required frequency band, weak and strong, will allow active relaying of signals (Dirk, Florian, Christopher, 2012).

One widely used modulation technique in RR technology on SDR-based CubeSat platforms is "binary code-based phase modulation" (BPSK) by transmitting "0" and "1" bit symbols with different carrier signal phases shifted by 1800 from each other. each other, as a result of which the unit time bit of the transmitter block is determined by the following correspondence.

$$S(t) = A\cos(2\pi f_c t) \text{ – for 1 bit} \quad (3)$$

$$S(t) = A\cos(2\pi f_c t + \pi) \text{ – for 0 bit} \quad (4)$$

Here $t - 0 \leq t \leq T$, and f_c is the carrier frequency.

In fig. 2b, the algorithm of the SDR-based RF has been integrated in addition to the OC technology on the CubeSat platform, first the low frequency is generated by the RF; information is modulated by a complex converter and a high-frequency signal F(x) to prepare for transmission; The information is extracted from the output SMA antenna part of the SDR; The useful information signal at the input of the SMA antenna of the receiver of the SDR part is separated from the carrier; In addition to the mentioned sequential processes of the algorithm, the USB interface and the computer with the YS software ensure the continuity of the process, the presentation of the relevant telemetry data in numerical and graphical form on the interface, and also ensure that information is recorded in the required file format during the process.

FINDINGS and DISCUSSION

The CubeSat satellite in low orbit at an altitude of approximately 1000 km has a total rotation period of T = 90 minutes. To reduce this value, one way is to increase the number of satellites in orbit. Communication between satellites in this type of infrastructure and between themselves and the ground segment (GS) can be provided by the aforementioned RF or FSO technologies (Zlata and Vladimir, 2017).

A simple parametric comparison table for inter-satellite data (Tx/uplink) and (Rx/downlink) using FSO and RF communication methodologies can be shown as follows in Table 2.

The results in the table gives a good result compared to RF systems considering the center frequency f = 5.8 GHz.

Table 2. The center frequency parameters comparasion between RF and OC technologies

	Optik ISL	**RF ISL**
Transmitter system power, W	1 W	1 W
Receiver system power, dBm	74x74 mrad: -40	a) -88 b) -75 c) -67
Sensitivity value of the receiver, dBm	PIN: -52 APD: -65	-102

As can be seen from figures 5, the 2U CubeSat platform consists of two 1U electromechanical parts connected in series with each other. These include: 1 - 2U mechanical housing subsystem with active and passive organization, 2 - active repeater and data exchange subsystem, 3 - location and situation determination subsystem, 4 - microcontroller-based on-board computer subsystem, 5 - power generation, power and control subsystem, 6, 7 - optical transponder with laser guidance in two planes, 8, 9 - 3D optical switch with laser beam guidance in two planes, 10 - solar panels.

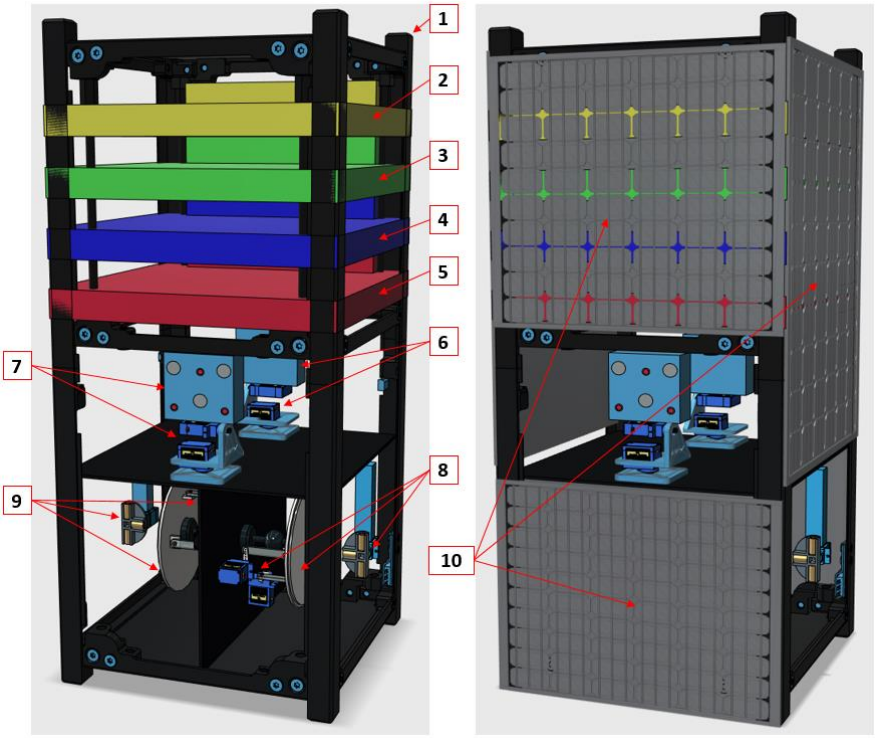


Figure 5. A simplified view of the prototype model of the 2U CubeSat platform.

On fig. 6 is a functional block diagram of the subsystems of the previously introduced 2U CubeSat platform. Briefly, the circuit can be divided into two subsystems (1U and 2U), and the corresponding workflows can be noted as follows:

a) Subsystem of a mechanical body with active and passive structure parts.

It provides a reliable structure of the system within a single enclosure, protecting it from external sources of interference, as well as determining the internal temperature indicators of the platform with thermistors and ensuring the stability of the heating wires.

b) Active transponder and data exchange subsystem.

As an important communication subsystem of the CubeSat platform, the desktop is equipped with a remote module for establishing bluetooth, long-range radio communication and conducting the necessary tests. In addition, due to the platform's active radio transponder functionality, the integration of a programmable radio (SDR) device is planned.

c) Subsystem for determining location and environment.

To determine the position of the platform in a free environment, gyroscope, magnetometer and accelerometer sensors were used, and a GPS module and photodetectors were used to determine the coordinates of the geographical position.

d) On-board computer subsystem based on a microcontroller.

It performs the function of central control with an external interface/connection terminal with functions such as reading the data packets provided by all subsystems and executing the corresponding autonomous and controlled commands.

e) Power generation, power, and control subsystem.

"10) Solar panels" from the second type of solar electroconverting panels for the autonomous supply of the entire platform with the necessary electricity, a lithium-ion battery as a regular source of

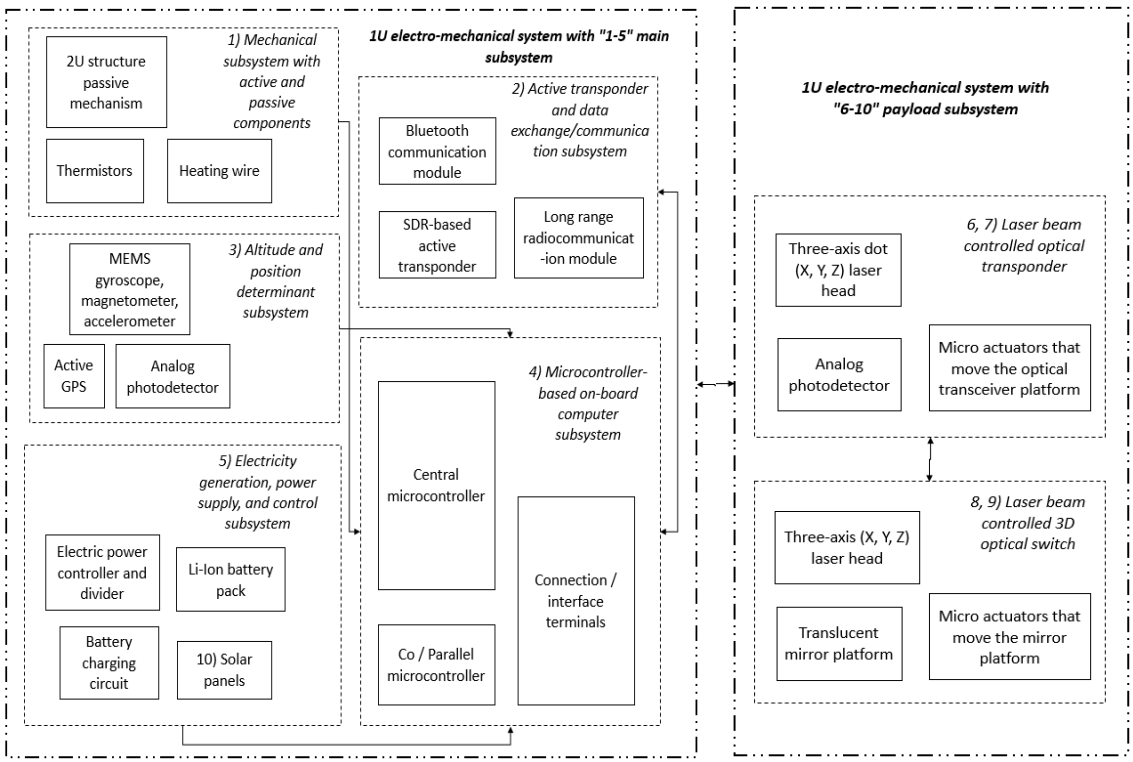


Figure 6. Electro-mechanical structural diagram of the 2U CubeSat platform.

energy, a control and separation circuit for electrical energy in these two parts, as well as charging batteries for desktop tests consists of a loop.

6,7) Optical transponder controlled by a laser beam.

Unlike addition to the active radio transponder, this optical transponder subsystem consists of a three-axis point (X, Y, Z) laser head, a transmit beam source, and receiving photodetector components capable of establishing full duplex optical communication with the GS described earlier.

8, 9) 3D optical switch controlled by a laser beam.

This subsystem, as the most important subsystem of the CubeSat platform, combines a new applied direction of previous scientific and practical research (a three-dimensional optical switch of a new generation).

These points will pay off on the developed CubeSat platform, allowing to effective exchange of volumetric and high-speed optical data of two or more satellites at the level of inter-satellite communication between satellite constellations (Laser, 2022).

CONCLUSION and RECOMMENDATIONS

Within the framework of the topic under study, four subsystems of the CubeSat satellite platform of a new generation, which includes the advantages of existing communication technologies RF and OC of the NanoSat satellite system, as well as the laser beam control subsystem, transponder, and SDR based on an active RF repeater based on a three-dimensional optically switchable operating room, which is the subject of a previous study, theoretically and aspects of operating room technology improvement have been taken into account by an algorithmic study of important processes and application of the entire system.

Based on the layout of the nanosatellite prototype equipped with the described functionality, when developing and launching the final flying nanosatellite (CubeSat) into Low Earth Orbit (LEO, 1000 km-2000 km), it can be used in the following areas:

- Ensuring volumetric and fast full-optical information exchange between a constellation of nanosatellites located in the same orbit and IS;
- Ensuring the relaying of information from a low-power GS by acting as an active relay of the orbital nanosatellite.

REFERENCES

Alberto Carrasco-Casado and Ramon Mata-Calvo (2020). Free-space optical links for space communication networks. – Japan. – 66 p.

Desire Muhireab, Daria Stepanovaac, Shreya Santraad, Prerna Baranwalae, Marco Romeroaf, Rushanka Amrutkarag, Sébastien Bonnartah , Devanshu Jhaai, Aaron Zuchermanak (2020). – IAC. – 14 p.

Dirk Giggenbach, Florian Moll, Christopher Schmidt,Christian Fuchs, and Amita Shrestha (2012).Optical onoff keying data links for low Earth orbit downlink applications.–33 p.

Hemani Kaushal and Georges Kaddoum (2017). Optical Communication in Space: Challenges and Mitigation Techniques. – India. – 41 p.

Morio Toyoshima (2010). Trends in satellite communications and the role of optical free-space communications. – Japan. – 12 p.

M. P. Joshi, Prof. Dr. S. A. Patil, Prof. D. C. Shimpi (2017). Design and Implementation of BPSK Audio Transmiter & Receiver Using SDR. – India. – 5 p.

Mehman Huseyn Hasanov, Nadir Bafadin Agayev, Nadir Arzu Atayev, Vali Muxtar Fataliyev (2021). A NEW GENERATION OF CONTROLLED OPTIC SWITCH.–TOM15.– 5 s.

Zlata Gibalina, Vladimir Fadeev. OPTICAL INTER-SATELLITE LINK IN COMPARISON WITH RF CASE IN CUBESAT SYSTEM. Kazan National Research Technical University named after A.N.Tupolev, 10 Karl Marx Str., Kazan 420111, Russia. September 22, 2017.

Christian Haughwout, Maxim Khatsenko, Ryan Kingsbury, Jonathan Twichell, Kathleen Riesing, Hyosang Yoon, Caleb Ziegler, Kerri Cahoy, "Nanosatellite optical downlink experiment: design, simulation, and prototyping," Opt. Eng. 55(11), 111610 (2016).

NASA, CubeSat 101 Basic Concepts and Processes for First-Time CubeSat Developers. California Polytechnic State University, October 2017.

Laser communication in space.

Available at: https://en.wikipedia.org/wiki/Laser_communication_in_space [Accessed November, 2022]

120 MM TOP NAMLUSUNUN TASARIMI VE SONLU ELEMANLAR YÖNTEMİYLE YAPISAL ANALİZİ

Şahin MEHDİYEV[1]

[1]*Selçuk Üniversitesi, Teknoloji Fakültesi, Savunma Teknolojileri Anabilimdalı, Konya, Türkiye.*
[1]*ORCID ID: https://orcid.org/0000-0001-6900-4411*

Özet

Günümüzde savunma teknolojileri alanı önemli ölçüde gelişmekte ve uluslararası düzeyde pek çok araştırma yapılmaktadır. Bu nedenle ülkemizin ve dünyanın bu alanda birçok yeni araştırmaya ihtiyacı vardır. Bu ihtiyacı karşılamak için yapılması gereken birçok uygulamadan biri olan bu çalışma, belirli bir sayısal hesaplamalar ile bir top namlusunun optimal bir tasarımının oluşturulmasını mümkün kılmaktadır. Ayrıca silah tasarımının en önemli parçası namludur. Analizde atış esnasında namludaki en fazla gerilmenin olduğu noktalara etki eden gerilmelerin matematiksel modeli çıkarılmışdır. Burada model çözümlenerek analiz edilmiş ve gerilim dağılımındaki kritik noktalar belirlenmişdir. Bu yüksek gerilim değerlerine uygun olarak namlunun et kalınlığı ve güvenlik faktörü dikkate alınarak optimize edilmiştir. Bu basınç değerlerinin modele doğru bir şekilde aktarılabilmesi için basınçlar değerlendirilmiş ve gerçek patlama olayını temsil edecek bir sistem oluşturulmuştur. Normal sevk barutlarının kullanıldığı atışlardan elde edilen anlık namlu iç basınç değerleri kullanılmışdır.Toplam deformasyon değerleri zamana bağlı olarak yapılan analizler neticesinde elde edilmiştir. Matematiksel hesaplamalar sonuçu çıkan değerlerle sonlu elemanlar yöntemi sonuçu çıkan değerler karşılaştırılmışdır Çalışma, patlama anında oluşan şok dalgaları ve mermi çekirdeği ile namlu arasında bulunan sürtünme kuvveti hariç tutularak sınırlandırıldı.Araştırmanın amacı top namlusunun tasarımında kullanılan denklemleri ve sabitleri daha basit hale getirmekdir. Bu araştırmada elde etdiğimiz matematiksel modellerden çıkan değerlerle sonlu elemanlar yöntemiyle bulduğumuz değerler kıyaslanmıştır. Optimal boyutları elde etmek için silahı tasarlamak ve ardından sistemi analiz etmek zorunlu bir adımdır. Namlunun katı modeli bir 3D tasarım programı olan Solidworks'de yapılmış ve yapısal analizi AnsysWorkbench sonlu elemanlar paketinde yapılmıştır.

Anahtar Kelimeler: Namlu, Matematiksel Model, Sonlu Elemanlar Yöntemi ,Ansys.

DESIGN AND STRUCTURAL ANALYSIS OF 120 MM GUN BARREL BY FINITE ELEMENT METHOD

Abstract

Today, the field of defense technologies is developing significantly and much research is being carried out at the international level. For this reason, our country and the world need much new research in this field. This study, one of the many applications to meet this need, makes it possible to create an optimal design of a gun barrel with certain numerical calculations. In addition, the most important part of the weapon design is the barrel. In the analysis, the mathematical model of the stresses acting on the points where the maximum stress is present in the barrel during the shooting is derived. Here, the model is analyzed and critical points in the stress distribution are determined. B these high stress values, it has been optimized considering the wall thickness of the barrel and the safety factor. In order to transfer these pressure values to the model correctly, the pressures were evaluated and a system was created to represent the real explosion event. Instant barrel internal pressure values obtained from shots using normal propellant gunpowder were used. Total deformation values were obtained as a result of time-dependent analyzes. The values obtained from the mathematical calculations were compared with the values obtained from the finite element method. The study was limited by excluding the shock waves that occurred during the explosion and the friction force between the bullet and the barrel. The aim of the research is to simplify the equations and constants used in the design of the cannon barrel. In this study, the values obtained from the mathematical models and the values obtained by the finite element method were compared. It is a mandatory step to design the weapon and then analyze the system to

achieve optimal dimensions. The solid model of the barrel was made in Solidworks, a 3D design program, and its structural analysis was done in the AnsysWorkbench finite element package.

Keywords: Barrel, Mathematical Model, Finite Element Method ,Ansys.

INSECT ROBOTS

Farid Bayramov

Azerbaijan Technical University, Electrotechnica, Baki, Azerbaijan, 0000-0001-7784-4381

Amirasan Manafov

Azerbaijan Technical University, Electrotechnica, Baki, Azerbaijan

Abstract

This article is about insect robots. Their tasks in the modern era are discussed here. It is very important where and for what purposes they are used. They are used for intelligence and information gathering. Besides, their most important feature is that they are very small. That is why these devices can perform tasks that humans cannot do. they can. In this article, the perfection of the electronic part of these robots is discussed in detail. Although they are very small, they get the information accurately and correctly and can transmit it reliably to the user. In addition, the disadvantages of these robots are also reflected in this article. Since these devices are very small, electronic the brain is not quite enough. In other words, in normal robots, it is possible to perform more tasks because the electronic brain is large. It provides information on where, when and why these devices are used. The pros and cons of the device are discussed. In addition, this article discusses in detail what parts insect robots are made of and what functions these parts perform. This article discusses the future applications of insect robots in detail. They are currently in the development stage. That is, they are not widely used by humans. Only are used in several fields. But insect robots will be widely used in all fields of production in the near future.

Keywords: Insect robots,Wings, Electronics, Weight, speed

Scientists develop insect-sized robots that flap their wings to fly Inspired by bees and other flying insects, the technology means conventional motors and gears are no longer needed to fly the devices and could lead to smaller, lighter and more effective micro flying robots.Inspired by bees and other flying insects, the technology means conventional motors and gears are no longer needed to fly the devices.It could lead to smaller, lighter and more effective micro flying robots, which could be used for environmental measuring, search and rescue, and in dangerous surroundings such as collapsed buildings.Known as micro air vehicles, the robots are better than other drones at manoeuvring in tight spaces and resisting air turbulence.Until now, similar machines have used motors, gears and other complicated systems to achieve the up-and-down motion of the wings, which added complexity, weight and other unwanted effects.Jonathan Rossiter, professor of robotics at the University of Bristol, led the team that successfully demonstrated an artificial muscle system, called the Liquid-amplified Zipping Actuator (Laza)."Laza is an important step toward autonomous, flying robots that could be as small as insects and perform environmentally critical tasks such as plant pollination and exciting emerging roles such as finding people in collapsed buildings."In the study, researchers showed how their cost-effective and easy to construct system provided enough power to fly a robot across a room at 18 body lengths per second, which was more than insect muscle of the same weight.

Micromechanical **Flying Insect** (**MFI**) is a miniature UAV (unmanned aerial vehicle) composed of a metal body, two wings, and a control system. Launched in 1998, it is currently being researched at University of California,Berkeley. The MFI is among a group of UAVs that vary in size and function. The MFI is proving to be a practical approach for specific situations. The Office of Naval Defense Advanced Research Project Agency are funding the project. The Pentagon hopes to use the robots as covert "flies on the wall" in military operations.

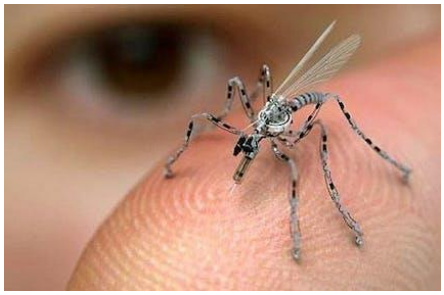


Figure 1.

There are a variety of UAVs that perform different operations. The MFI is of greatest potential use to the United States Military. There are currently various UAVs in this field that perform tasks such as gaining battlefield intelligence or being a decoy for potential missiles. In respect to gaining battlefield intelligence there are many drones in use by the military to execute different missions The US Military is constantly upgrading to stealthier UAVs that can perform more missions while remaining virtually undetected. Essential qualifications for a military grade UAV include:

1. Size
2. Noise level
3. Versatility

This is what makes the MFI a great candidate for the military. It takes the functions of larger UAVs and crunches it down into a miniature undetectable device. It virtually eliminates size and noise level and increases versatility beyond the capabilities of current UAVs. The actual "crunching" of these capabilities into the MFI raises the problem of creating a supple frame and a pair of wings with an autonomous computer to control them.

problem is the initial input of visual data that is to be computed. There is a substantial degree of noise in the data obtained through the "eyes", when this is passed through the system to the wings it produces an inaccurate output therefore not achieving the initial action correctly.

Structure and materials

The initial prototypes of the MFI weighed 100 milligrams and had wingspans of 2 centimeters. They were structured stainless steel beams and polymer flexures as joints. This created a weight-to-lift ratio that led to an issue with achieving flight. The beams and joints were then changed to lighter materials that perform better. The beams were converted from stainless steel to honey-carbon fiber beams, while the joints were changed to silicon, mimicking typical micromechanical structures. These raw materials used cost around 10 cents to construct.

Functions and mobility

The overall functionality of the MFI is broken up into smaller components that cohesively work with one another to sustain a stable and particular flight pattern. These components are:

1. Power supply – a battery pack rechargeable through solar panels on the exterior body
2. Sensory system – a group consisting of two eyes and multiple temperature, wind, and speed sensors
3. Locomotive and control – the wings connected to respective actuators
4. Communication – the internal network of algorithms and sensory signals

These units work together to take a specific task, such as "fly forward", as an input and signals are sent through to both wings to produce a calibrated output to perform the task. This is a more in depth view of the flow of operations; the initial visual system analyzes the location in three-dimensional space, through computing the displacement between objects and itself.

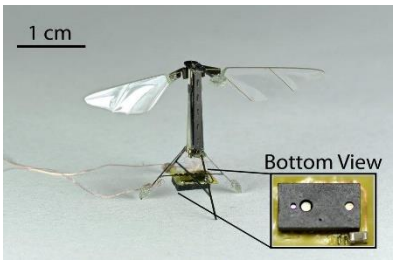


Figure 2.

The fly is then chosen to execute a task, i.e. "find an object" or "explore". Unlike other UAVs, the MFI has to have an autonomous computer system because it is too small to be controlled by a remote, so it must be able to sustain itself. Once the action has been chosen the signal moves on to the inertial system to then distribute the specific functions, in respect to the action, to the wings. The wings then use a number of sensors to deliver the most accurate wing thrusts to fulfill the action.

Problems and complications

There are problems pertaining to this system that have arisen during the development of the MFI, and this has demanded further research. The first problem is the initial input of visual data that is to be computed. There is a substantial degree of noise in the data obtained through the "eyes", when this is passed through the system to the wings it produces an inaccurate output therefore not achieving the initial action correctly.

Another problem is the "hovering" method of the MFI. Essentially the MFI has to be in equilibrium in three-dimensional space while producing a wing thrust that will sustain the desired altitude. The issue with this concept is the inadequate research on the flight patterns of flies, furthermore creating an algorithm to perform such patterns.

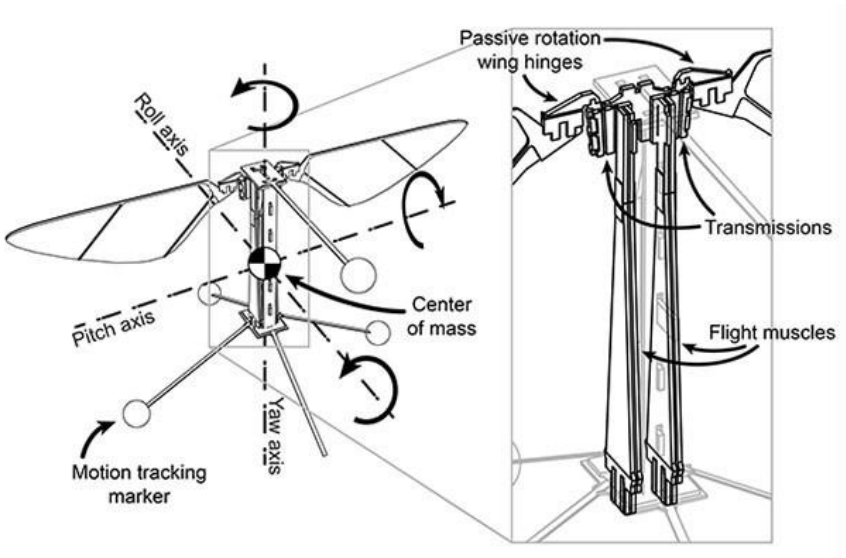


Figure 3.

Schematic diagrams and photographs of the two robotic designs used in this work. (a) This figure illustrates the mechanical design of the RoboBee. (b) A flexure transmission converts the approximately linear motion generated by a bimorph piezoelectric actuator, δ, into a flapping angle, ϕ. (c) Photograph of a RoboBee

prototype. Four retroreflective 5-mg markers for motion tracking are attached. A U.S. penny indicates the scale. (d) This figure illustrates the mechanical design of Bee + . (e) A zoomed-in view of the flapping mechanisms. Two pairs of unimorph actuators drive four wings to flap independently through four transmissions. (f) A photograph of a Bee + prototype. This robot has a mass of 95 mg and a wingspan of 33 mm. Protective spars and legs are installed on the top and bottom of the robot for crash-protection and landing during flight experiments. Four 5-mg retroreflective markers for motion tracking are attached as well. A U.S. penny indicates the scale.

We discuss the problem of designing and implementing controllers for insect-scale flapping-wing micro air vehicles (FWMAVs), from a unifying perspective and employing two different experimental platforms; namely, a Harvard RoboBee-like two-winged robot and the four-winged USC Bee +. Through experiments, we demonstrate that a method that employs quaternion coordinates for attitude control, developed to control quadrotors, can be applied to drive both robotic insects considered in this work. The proposed notion that a generic strategy can be used to control several types of artificial insects with some common characteristics was preliminarily tested and validated using a set of experiments, which include position-and attitude-controlled flights. We believe that the presented results are interesting and valuable from both the research and educational perspectives.A small robot with wings like an insect can fly and generate more power than a similarly sized animal in nature.

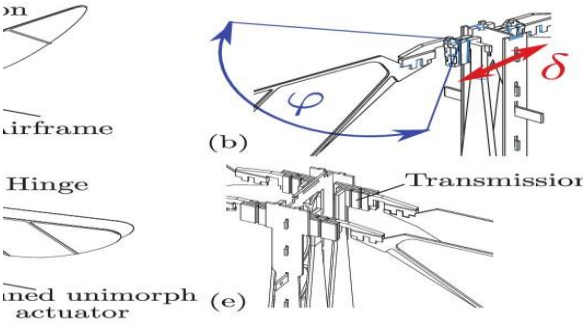


Figure 4.

Most flying robots, whether they use wings or propellers , have motors and gears and transmission systems to connect the components, but these can weigh the robot down and fail.

Now, Tim Helps at the University of Bristol, UK, and his colleagues have designed a small robot that uses an electric field – and a droplet of oil that increases the strength of the field – to flap the wings directly, avoiding the need for a motor or a transmission system. Helps and his team tested the mechanism for a million wing flaps and found it had a steady power output that was slightly better than that of an insect muscle of the same weight.

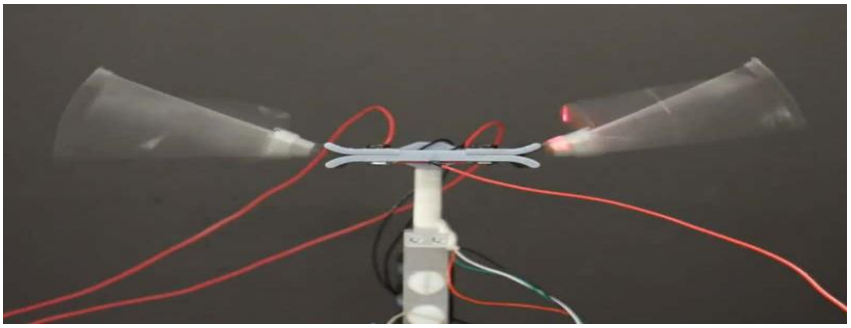


Figure 5.

Thee winged robot lacks on-board electronics or controls and flew while attached to a nylon string, so was largely a proof of concept. For use in real-world situations, miniature electronics would need to be incorporated without adding too much weight, so that the robot could generate enough power to take off.

But the wing mechanism could still be a useful component of future flying microrobots, Raphael Zuffery at the Swiss Federal Institute of Technology in Lausanne. “It’s one of those core building blocks that you need in any flying vehicle. Any kind of technology… that allows us to build new types of flying robots is going to be something that has a strong impact.”

Biography

1. Pdf of “SKY NEWS” 2 February ,2022

2. Pdf of “New Scientist “ 26 June,2019

DURABILITY CALCULATION OF SHELL COMPONENTS OF THE 120-mm TRAINING MORTAR AMMUNITION

Nijat Bakirli

Azerbaijan Technical University, Special technique and technology, Higher Education Institute, Baku, Azerbaijan, ORCID ID: https://orcid.org/0000-0002-9812-9915

Abstract

In this paper is presented the shell components 120-mm training mortar ammunition. These components are constructed and added to the shell of a 120- mm high explosive mortar round. Inertial forces are next in importance to the strength of the training shell. They occur in shell and in shell details as a result of the acceleration they receive as they move under the influence of the system forces generated by the pressure of the exhaust gases. Since the shell does not rotate, the main inertial force will be the axial force that arises from the accelerated gradual movement of the training shell. When fired as a result of maximum gunpowder pressure, which causes the movement of the training shell and its own masses of smoke charge, an inertial force is raised which generates tensile stresses in the body of the smoke cartridge. The largest tangential stresses that have arisen in the smoke cartridge during a shot have been calculated in order to prevent the self-ignition of the charge. During the shot, stresses occur not only in the mortar cannon barrel and training shell but also in the shell smoke charge. In the strength calculations, the critical state of the shell and shell parts is determined, which is characterized by the highest values of stresses and deformations. The time at which the critical state is reached is determined and the magnitude of the stresses and deformations that occur is calculated. These stresses are generated by the inertial forces in the movement of the smoke cartridge in which the smoke charge is placed, and if they exceed the magnitude of the permissible firing stresses, they may cause premature chemical reaction of combustion or detonation. Therefore, it is necessary to perform calculations with high accuracy. Now let's look at the strength calculation of the shell parts of the 120-mm mortar ammunition.

Keywords: ammunition, mortar system, firmness calculation, training mortar shell.

Introduction

The mortar crew's training exercises are crucial to developing and upholding each serviceman's high level of professional proficiency and work ethics. The essential field conditions, such as distinct locations far from towns and the position of military formations, equipped with facilities and extra troops to assure firing and security of the firing range, are needed for field combat shooting with a 120-mm mortar. A variety of 120-mm training mortar ammunition was developed in order to best prepare mortar crews given that the trajectory of the mortar shell flight and at a very close range preserves its shape. In that the initial training of mortarcrews, consisting of recruits, helps to more quickly psychologically overcome theeffects of mortar shot on the one hand, while reducing the financial cost of ammunition, transporting the crews and 120-mm mortar system to the firing multiple necessary human resources and logistic resources for conducting firing. There are also problems with wear out of mortar barrel and storing large amounts of ammunition.

Forces acting on the training shell at a shot

Forces are applied to the shell body and the shell body details during the phenomenon of shot (from the moment the shell is resting in the lower position of the mortar tube, with the subsequent accelerating motion in the barrel until the effect of the powder gases): the exhaust powder gas pressure; the mass of the shell; the reaction of the cannon tube wall; and the friction between the mortar shell and mortar cannon tube [5].

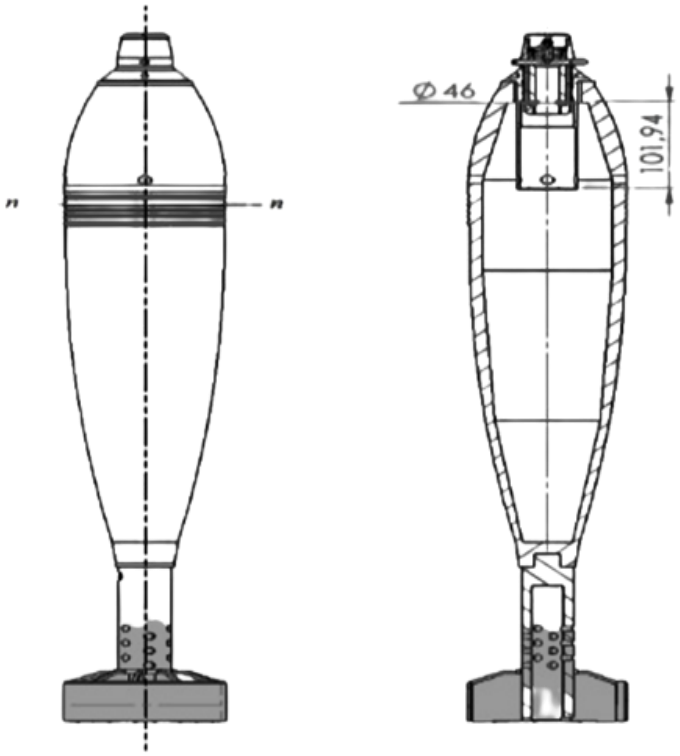


Figure 1: 120-mm training mortar ammunition

The loading circumstances heavily influence the exhaust powder gas pressure, which places the largest force on the shell body. Since the training mortar shell is made from the shell of a 120-mm high explosive mortar round, one of the elements of the loading condition (1) [3, 4], namely the capacity of the loading chamber, will be equal to that of the high explosive mortar round.

$$\Delta = \frac{m}{W_0} \quad (1)$$

where m – mass of the shell, kg; W_0 – charging chamber volume, m^2.

The absence of the bursting high explosive charge causes the second parameter of the training shell mass to differ slightly as the high explosive shell is employed, but the difference is balanced by the addition of new shell components like a smoke cartridge with a burst imitation charge and a new fuse. Due to the training shell's much shorter range of fire, the third parameter, the mass of the combat charge, is smaller than that of the high explosive round. Additionally, it significantly affects how much powder gases form and grow over time in the mortar charging chamber. It is obvious that under these loading conditions, the maximum pressure of powder gases at a shot will occasionally be significantly lower than it would be when firing high explosive rounds. Since a high explosive shell is used for training and the maximum pressure of the charge chamber's powder gases during a shot is significantly lower than that of a high explosive shell firing, it follows that when firing a training shell, the stresses and deformations in the shell will also be significantly lower than the allowed ones. Consequently, only the newly designed details need to be computed rather than the training shell's strength, which is no longer necessary.

It is obvious that under these loading conditions, the maximum pressure of powder gases at a shot will occasionally be significantly lower than it would be when firing high explosive rounds. Since a high explosive shell is used for training and the maximum pressure of the charge chamber's powder gases during a shot is significantly lower than that of a high explosive shell firing, it follows that when firing a training shell, the stresses and deformations in the shell will also be significantly lower than the allowed ones. Consequently, only the newly designed details need to be computed rather than the training shell's strength, which is no longer necessary. Using Newton's second law, the equation of motion in function of time "t" has the following form, given that the propellant's energy is solely used for the training shell's gradual movement in the mortar cannon

barrel.

$$m\frac{dv}{dt} = PS \quad (2)$$

where V – shell speed, m/s; P – pressure of the powder gases in in the shell rear space, N/m^2; S – cross-sectional area of mortar cannon barrel, m^2

or

$$a_{ts} = \frac{dv}{dt} = \frac{1}{4}P\pi D^2\frac{g}{m} \quad (3)$$

where g – acceleration of gravity, m/s^2; D –caliber of training shell, m.

It follows from (3) that the acceleration of the training shell in mortar cannon barrel isdetermined by the expression

$$a_{ts} = \frac{dv}{dt} = \frac{1}{4}P\pi D^2\frac{g}{m} \quad (4)$$

According to the second principle of mechanics, the axial inertial force in section nn (Fig. 1) of the training shell is then represented by the equation.

$$F_{ts} = \frac{m_s}{g}\frac{dv}{dt} \quad (5)$$

where m_s –weight of part of training shellabove cross section n-n, kg.

After replacement with (4) in (5) final

$$F_{ts} = \frac{1}{4}P\pi D^2\frac{m_s}{m} \quad (6)$$

The ratio of the external forces (F_{ts}) acting on the training shell to the mass forces, or the ratio of the training shell's acceleration to the acceleration of the weight force, is known as the load factor [13, 14], and it is used to help explain the physical process.

$$n = P\pi D^2\frac{1}{4m} \quad (7)$$

The load factor is obviously influenced by the training shell's weight, caliber, and the pressure of the powder gases. The magnitude of the pressure of the powder gases will determine how much n because the final two values in this situation are constant. As a result, the design pressure of powder gases, which is larger than the maximum, must be considered while developing training shell details. Equation (2) will then be used to find the maximum axial force of inertia in section n-n in line with expression (7).

$$F_n = nm_s \quad (8)$$

Again, because the training shell is made of a high explosive shell and has a lower firing load, the impact of inertial forces will only be taken into account for the newly designed parts.

The critical state of the shell and its component pieces, which is defined by the highest values of stresses and deformations, is identified in the strength calculations. Calculations are made to identify the critical state's onset time as well as the size of the resulting stresses and deformations.

Body details at a shot and the training shell's stress and strain condition

The training shell starts to move down the mortar barrel when a shot is fired as a result of the pressure produced by the expelled powder gases, while its body is under mechanical stress. Depending on where it is in the barrel, the stressed state of the shell body can be conditionally assumed to go through three stages. The largest stresses and deformations in the shell walls occur before the centering thickening and the details therein during the first stage, which is when the propellant charge is ignited and the maximum pressure of the powder gases is reached.

The following stage starts when the pressure in the shell's rear space reaches its peak and stops when the tube's snout is traversed by the centring thickening. The last phase of the strained condition also includes the instant when the thickening at the center passes through the muzzle section and the end of the powder gas' influence on the flying out shell.

Major stresses often occur in the matching normal and conical portions as well as bending stresses in the training shell body and shell details. The fundamental load is determined by the axial inertial forces while designing shell features, and the formula for determining the axial stresses in the normal section is as follows: [1]

$$\sigma_{ts} = \frac{F_n}{S} \tag{9}$$

Creating a smoke cartridge for the practice gun

When the pressure of the powder gases reaches its highest levels, the inertial force acts to cause a smoke cartridge to load to its full capacity. Therefore, the greatest value of the axial inertial force that can be obtained at a shot must be considered while building a smoke cartridge.

When fired as a result of maximum gunpowder pressure, which causes the movement of the training shell and its own masses of smoke cartridge and smoke charge, an inertial force is created which induces tensile strains in the body of the smoke cartridge. We assume that the smoke cartridge's body was constructed using the same cylindrical wall thickness as specified in the technical specifications. In this instance, section n-n will be where the critical stresses and strains occur, as shown in fig. 2. At addition to the hazardous section n-n, the tensile stress can also compromise the smoking cartridge's structural integrity in the region close to the bottom, where four holes have been drilled into the cup's cylindrical wall.

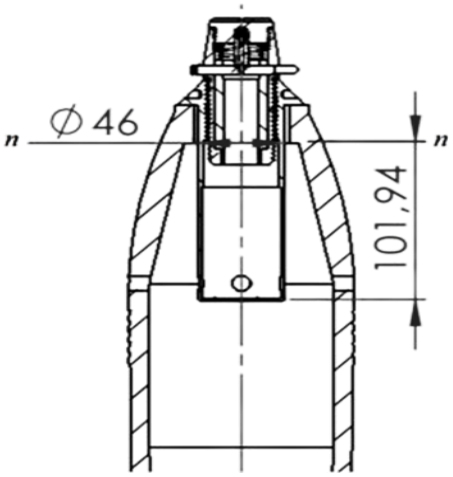


Figure 2: Axial inertial force for smoke cartridge

According to item 2 and fig. 2 axial inertial force for smoke cartridge in section n-n will be of the form

$$F_{cn} = n(m_{sn} + J) \tag{10}$$

where m_{sn} – weight of part of smoke cartridge above cross section n-n, kg; J – weight of part of smoke charge, kg.

Substituting in (10) the expression (7) for the axial force we have finite

$$F_{sn} = P\pi D^2 \frac{(m_{sn}+J)}{4m} \tag{11}$$

The cross-sectional area along the line n-n

$$S_{sn} = \frac{1}{4}\pi(D_n{}^2 - d_n{}^2) \quad (12)$$

where D_n – outer diameter of the smokecartridge in section n-n, mm; d_n – inside diameter of the smoke cartridge in section n-n, mm.

It follows from formula (9) that the tensile stress values will be determined by

$$\sigma_{tsn} = \frac{F_{sn}}{S_{sn}} \quad (13)$$

After replacing in (13) with (11) and (12) for tensile stress, we obtain the equation

$$\sigma_{tsn} = P\frac{D^2}{(D_n{}^2 - d_n{}^2)}\frac{(m_{sn}+J)}{m} \quad (14)$$

The strength condition is

$$\sigma_{tsn} \leq [\sigma] = \frac{\sigma_y}{k} \quad (15)$$

where $[\sigma]$ – allowable stress of the steel, MPa; σ_y – yield strength of the steel of which the smoke cartridge is made, MPa; k – safety factor.

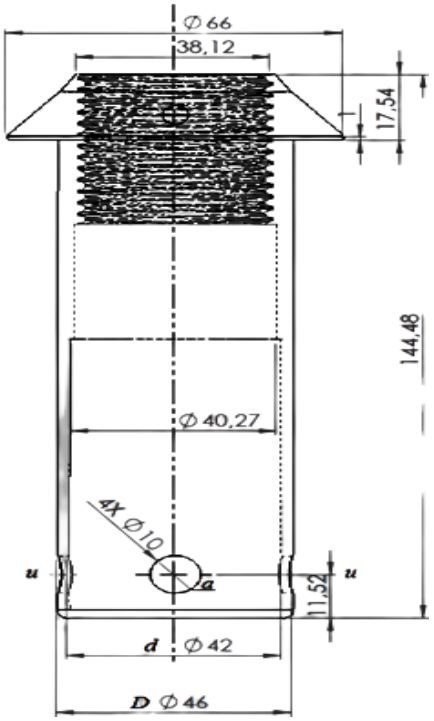


Figure 3: Smoke cartridge

The four apertures in the cross section u-u (fig. 3) reduce the cylindrical wall's bearing capacity, necessitating a calculation of the strength. Since the weight of the smoke charge below the line u-u is not significant enough to change the inertial force's magnitude, it can be disregarded. In this instance, the equation in this section will be used to determine the inertial force.

$$F_{su} = P\pi D^2 \frac{m_{su}}{4m} \quad (16)$$

where m_{su} –weight of part of smoke charge below cross section u-u, kg. The cross-sectional area along the line uu according to fig. 3 is determined by the formula

$$S_{su} = \frac{1}{4}\pi(D_u{}^2 - d_u{}^2) - 2(D_u - d_u)a \quad (17)$$

where D_u– outer diameter of the smoke cartridge in section u-u, mm; d_u – inside diameter of the smoke cartridge in section u-u, mm; a – diameter of openings in the section u-u, mm. Analogous to the above calculation the tensile stress is determined by the expression

$$\sigma_{tsu} = \frac{F_{su}}{S_{su}} \quad (18)$$

After substituting in (18) for tensile stress, we obtain the equation

$$\sigma_{tsu} = P\frac{D^2 m_{su}}{(D_u - d_u)[(D_u - d_u) - \frac{8a}{\pi}]} \quad (19)$$

The strength condition is

$$\sigma_{tsu} \leq [\sigma_{su}] = \frac{\sigma_y}{k} \quad (20)$$

where [σ] - allowable stress of the stell, MPa. The design calculations for the smoke cartridge were made using the following baseline data: P=34MPa; D=120mm; m=16,2kg; m_s=0,570kg; m_{sn}=0,210 kg; m_{su}=0,060 kg; d_n=40,27mm; D_n=D_u=46mm; d_u=42mm; a=10 mm. After the calculation the σ_{tsn} and σ_{tsu} and substitution in (15), (20) with the resulting numerical values we obtain the following result

$$\sigma_{tsu} \leq [\sigma] \quad \text{and} \quad \sigma_{tsu} \leq [\sigma_{su}]$$

It implies that the designed shell parts won't be damaged at a shot and will serve their intended purpose because the calculated maximum stresses in the shell details (the smoke cartridge and in the portion near the bottom) are smaller than the permissible ones. The calculations of strength were successful.

During a shot, the power of the practice shell charge

Stresses are put on the mortar cannon barrel, practice shell, and shell smoke charge during the shot. If these stresses are greater than those allowed during firing, they may result in an early chemical reaction such as combustion or detonation. These stresses are produced by the inertial forces in the movement of the smoke cartridge in which the smoke charge is placed. Similar to the smoke cartridge strength study, the smoke charge axis is under the largest load in this case, necessitating the use of the axial inertial force in the calculations. Based on the logic in Section 2.1, it can be inferred that axial stresses in smoke charge appear as a result of the axial inertial force that develops during the movement of the training shell and may be computed by the equation (14). Given that the smoke charge is thick and cylinder-shaped geometrically, it may be inferred that the section near the bottom of the smoke cartridge experiences the highest axial stresses.

$$\sigma_{tssc} = P\frac{D^2}{d_b{}^2}\frac{m_{sc}}{m} \quad (21)$$

where d_b – diameter of the bottom of the smoke cartridge, mm; m_{sc} – weight of smoke charge, kg. The strength condition of the charge is of the form

$$\sigma_{tssc} \leq [\sigma_{sc}] \quad (22)$$

where $[\sigma_{sc}]$ - allowable stress of the smoke charge, MPa. The design calculations for the smoke charge were made using the following baseline data: m_{sc}=0,012kg; d_b=42mm. The composition of the charge is of black powder for which $[\sigma_{sc}]$=15MPaThe calculation reveals that the inequality (22) is satisfied, demonstrating that the charge in the training shell's smoke cartridge won't be lost. [2]

References

[1] Petrov N., V. Dimitrov, Forecasting the Technical Resource of the Mechanical and Civil Building Structure, International Journal of Civil Engineering and Technology (IJCIET), (3), ISSN Print: 0976-6308 /ISSN Online: 0976-6316, pp. 173–181, 2016.

[2] Krasimir G., Strength calculatıon of shell components of the 120-mm multıple use short-range traınıng mortar ammunıtıon, International conference KNOWLEDGE-BASED ORGANIZATION 26 (3):120-125, June 2020

[3] Donald E. Carlucci and Sidney S. Jacobson, Theory and Design of Guns and Ammunition, CRC Press, Boca Raton-London-New York, Taylor & Francis Group, 2014, Page 111-126.

[4] Kuprianov V., Левин D. and Селиванов V., Osnovi proektirovania boeprpasov, Moskva, Izd. MGTU N. E. Bauman, 2019, Page 44-50, 71-90.

[5] Stanag 4110. Definition of pressure terms and their interrelationship for use in the design and proof of cannons or mortars and ammunitions. North Atlantic Treaty Organization, Standardization Agreement.

OPTIMAL MODE FOR OBTAINING Bi_2Se_3 THIN FILMS BY ELECTROCHEMICAL METHOD

Sevinj Javadova[1]

[1]*Ministry of Science and Education Republic of Azerbaijan Institute of Catalysis and Inorganic Chemistry named after M. Nagiyev, Baku, Azerbaijan, ORCID ID: https://orcid.org/ 0000-0001-7974-6072*

Samira Jafarova[2]

[2]*Ministry of Science and Education Republic of Azerbaijan Institute of Catalysis and Inorganic Chemistry named after M. Nagiyev, Baku, Azerbaijan*

Vusala Majidzade[3]

[3]*Ministry of Science and Education Republic of Azerbaijan Institute of Catalysis and Inorganic Chemistry named after M. Nagiyev, Baku, Azerbaijan, ORCID ID: https://orcid.org/ 0000-0001-5639-3104*

Akif Aliyev[4]

[4]*Ministry of Science and Education Republic of Azerbaijan Institute of Catalysis and Inorganic Chemistry named after M. Nagiyev, Baku, Azerbaijan, ORCID ID: https://orcid.org/ 0000-0003-0560-5263*

Abstract

Bismuth Selenide (Bi_2Se_3), is a 3-dimensional (3D) Topological Insulator. Before its discovery as a topological insulator, Bi_2Se_3 was well known as the binary thermoelectric material. As a novel idea, Bi_2Se_3 rectangular nanosheets with thicknesses of 200–500 nm were used in lithium-ion batteries to improve efficiency [1]. The method of preparation of functional materials is essential as different methods give rise to different structures and morphologies with diverse research and applications. In among various methods - electrochemical deposition is relatively simple and very economical. Its use does not require expensive equipment (including a vacuum unit) and excludes high-temperature annealing operations. In addition, the method is very environmentally friendly, has high selectivity, and makes it possible to conduct deposition on substrate electrodes of complex shapes and large sizes.

In this present work, in the galvanostatic mode, we studied the effect of various factors (concentrations of starting components, temperature, current density, electrolysis time) on the composition of the deposited Bi_2Se_3 films to determine the optimum qualitative composition of the electrolyte and the best electrolysis conditions at the preset deposition potential. The experiments were performed on a Ni electrode. The results show that, with an increase in the current density and H_2SeO_3 concentration, the bismuth content of the thin films decreases. As the electrolyte temperature, $Bi(NO_3)_3 \cdot 5H_2O$ concentration, and electrolysis time are increased, the bismuth content of the thin films increases. The optimum electrolyte composition and electrochemical deposition conditions for obtaining thin Bi_2Se_3 films of the composition close to stoichiometric were determined.

Keywords: Bi_2Se_3 thin films, electrochemical deposition, thermoelectric properties, semiconductors.

References

[1]. Z. Ali, C. Cao, J. Li, Y. Wang, T. Cao, M. Tanveer, M. Tahir, F. Idrees, F.K. Butt. Effect of synthesis technique on electrochemical performance of bismuth selenide, J. Power Sources 2013, 229, p. 216–222.

DIE STEELS, EXPLOITATION CONDITIONS AND DEMANDS THEM

Natavan Babayeva

Azerbaijan Technical University, Faculty:Metallurgy and material science. Department: Metallurgy and material technologies. City: Baku, Country :Azerbaijan, Orcid İD : https://orcid.org/0000-0002-2330-7924

Sayyada Suleymanova

Azerbaijan Technical University, Faculty: Metallurgy and material science. Department: Metallurgy and material technologies (Candidate of technical sciences, docent) City: Baku, Country: Azerbaijan, Orcid İD: https://orcid.org/0000-0002-1335-9245

Lala Azimova

University: Azerbaijan Technical University, Faculty:Metallurgy and material science. Department: Metallurgy and material technologies (Senior Lecturer) City: Baku, Country: Azerbaijan, Orcid İD: https://orcid.org/0000-0003-4976-4426

Abstract

The main types of cold working tools are designed for

a) cutting, b) punching, c) drawing, d) extrusion, e) molding, e) convexity

The most common in this group of stamping tools are punching tools.Die hardness penetration and hardenability is very are important when choosing a die steel due to the large size of the die block.The wear resistance of dies can be improved by cutting surfaces with annular grooves with anti-wear coating.Sometimes for coating using non-traditional methods and special equipment are used. For example, the use of "Chromtik" and "Carbochrome".

The systems have tripled the life of die tooling. Steels with high hardness and wear resistance, as well as impact strength (if the tool is dynamically loaded) are mainly used

for cold forming dies.At present, some countries producing steel for heavy-duty

stamps, there is a tendency to reduce the content of tungsten due to alloying with molybdenum and vanadium.Therefore, Cr-Mo-V steels are mainly used for making dies and

accessories for them. Temperature and content of most alloying elements determined by the properties that are necessary for successful operation of various tools.

Keywords: Tools, cutting surfaces, equipment, high hardness, resistance, impact strength, alloying elements.

Entry

The main types of cold-working tools are died for a) parting, b) blanking, c) drawing, d) extruding, e) forming, f) bul ging.

The more spread ones in this group of die tools are blanking tools. While blanking the punch and die block are strongly loaded as they share died material to thickness range from several decimal portions of millimeteres to 10 mm along the closed boundary. While blanking the punch and die block are triaxially loaded. [1,1]

The great compressibility on the edge leads to the dulling, while tension force leads to flaking. Besides, this loading has cyclic and alternating character that leads to the die material fatigue.

Die block is most loaded. While vibrating of press punch slide there are additional loading, which primarily destroy the punch. Periphery of die block cutting edge is axially stressed, the value of which depends on properties of punched material.The friction of processed material upon the die elements as well as that of punch upon the die block also takes place that leads to wear of tool.

Due to friction the temperature of die cutting edges may be more than 300°C. Thus, the tool life depends on conditions of its exploitation, i.e. structure and properties of processed material, rize of clearance, deformational rate etc. For example, works demonstrates that as the deformation rate and billet's thickness

increase, the temperature of cutting edges achieve 500°C that leads to the softening and wear of die. As the "material-die" friction coefficient reduces, for example, by means of lubrication or coating of died materials, the die life is significantly increased. [1,2]

Die hardness penetration and hardenability are very important at die steel selection because of die block's great sizes.

Thus, the steels used for manufacturing of blanking dies is to be wear resistant, hardness, high resistance to the dynamic loading. Tools life also depends on such die steel properties as strength, resistance to fatigue rapture, elasticity etc. Oxidation resistance, machinability, grindability, size preserving at heat treatment are also very important at steel selection for dies and die accessory. The most detailed data about the exploitation conditions of blanking die and demands to them are reflected in works.

Wear resistance of dies can be increased by means of covering cutting surfaces with antiwear coating. In the whole range of strengthening technologies ~30% refers to the thermochemical treatment (TCT). TCT is conducted by means of the most contemporary technical and scientific achievements, such as glow discharge, plasma , laser , ionic implamation , electronic radiation, high-frequency current , vacuum equipment etc. Work demonstrates that carbide and boride coating allow to reach the hardness of 21000 MPa on X12M steel surface at hardness middle of 5900 MPa (60 HRCE). Sometimes for coating made the nontraditional methods and special equipment are used. For example, using of "Khromtik" and "Karbochrom"systems increased the tool life of die accessory as much as thrice.Combined thermochemical treatment with hardening in fluidised bed also is very widespread . Such technology is integrated in industry of the USA and Canada at 5-8% . The work suggests coating applying while cooling of steels after austenitization in hot medium. Boron and copper applying on X12M steel in fluidised bed is also very perspective. Black copper oxide adding leads to increasing of borated layer thickness and reduces the brittleness of intermetallide zone. [1,3]

Such methods of surface strengthening as ionic nitriding , ion-plasmous coating with titanium nitride, ionization , electric hydroimpulsive strengthening. Die wear resistance is increased by laser treatment of the surface, The thermochemical treatment is also conducted by means of laser on "Kvant 15" setting . The alloyed surface is covered with C, Cr and B allowed to increase the wear resistance as much as 2.5 times . Sometimes laser treatment is combined with heat treatment. Thus, the combining of heat and laser treatment of surface increases the microhardness of surface as much as 1.5-1.8 times.

The properties of die steels can be increased by means of thermocycling , a special heat pretreatment , modified thermomechanical treatment , as well as vacuum thermotechnology . It is necessary to mention that all methods of increasing the tool life listed above are not widely used in the world because they demand special expensive equipment and materials, lead to the great power imputs, increase the prices of products and do not provide stability of steel properties.

The increasing of steel mechanical and technological properties, providing the high die life can be achieved by the following methods:

1) Optimization of chemical composition of known steels or development of new ones by means of additional alloying and microalloying.

2) Development of new technological processes of heat treatment of known steels for achieving structural state, providing the maximal possible properties of material and, therefore, the maximal die life . The combination of these methods is widely used. For instance, it was successfully performed in work , when the new methods of heat treatment were developed for standard steels and new steel grades were suggested for new methods of heat treatment. The results of that work allowed to achieve the high complex of wide-class steel properties.

Cr-Mo-V steels are widely used for die making of cold and hot deformation. [1,4]

Steels with high hardness and wear resistance as well as toughness are (if the tool is dynamically loaded) primarily used for cold deformation dies. In such steels vanadium is used in small quantities (up to 0.5-0.6%) for grain fining at austenitization. If the die needs to be highly hard and wear resistant, and not very highly ductile then the steels with chromium and vanadium such as 85Х6НФТ, Х6Ф4М (ЭП770), Х6Ф5М, 6ХМ2ФС are chiefly used. Steels of analogous compound are used abroad: in the UK - 5CC, in the USA - Concord V. These steels contain 1-2%C, about 6%Cr, 4-5%V and about 1%Mo. Their ductility is as high as

that of high-speed steels. But high temper provides the noticeable inclusion volume fraction of carbides (20-25%) that adds the high hardness and wear resistance to steels. Chromium noticeably increases hardness penetration, which is necessary for big size tool and also forms the great amount of M2C3 and M23C6 carbides. Molybdenum, according to Y.A.Geller [5] promotes the increasing of M23C6 carbides amount that is positively influences on mechanical properties. Vanadium, forming the highly dispersed VC carbide particles and noticeably increases the wear resistance (see below "High-speed steels"). The venerable place refers to the steels with high containing of vanadium, the main carbide phase of which is VC carbide such as Х3Ф12 [5] and American Ottawa 60 . These steels are highly strength and wear resistant but as their properties have not been studied yet, they are not widely used in the industry. Y.A.Geller , for example, recommends using Х3Ф12 steels for die blocks of highly hard powders pressing.

All the high vanadium steels mentioned above are badly machined and ground. That is the only disadvantage, which does not allow to have a venerable place in die making. But these difficulties can be escaped of grinding is made by abrasive, made of cubic boron nitride or diamonds .Thus, in steels for dies of cold deformation the vanadium alloying is applied for increasing of wear resistance (due to formation of VC carbide) as well as for fine grain. But vanadium alloying is especially effective if the dies during operation are heated much, are not impact loaded and primarily tensed or compressed. In that case such steels as 4Х2В5ФМ, 4Х3ВФ2М2, 4Х3ВМФ, 3Х3М3Ф, 4Х5МФ1С are used . In abroad for these purposes the analogue materials are used: in the UK - CV9, CVM4, Cyclone 56, in the USA – Forge Wear I . The complex of high mechanical and heat resistant properties in these steels is achieved due to the complex alloying by carbide formers: chromium, molybdenum, tungsten and vanadium, which forms a lot of M23C6, M6C, VC carbides. Vanadium except forming its own carbide, also dissolves in chro- mium carbides and add the increased stability against coagulation. Besides, vanadium increases martensite stability against tempering and reinforces the precipitation hardening effect.

The influence of molybdenum, according to Y.A.Geller , in these steels is concluded in increasing of M6C carbide amount that noticeably increases steels heat resistance. Tungsten acts the same way, but a little weaker.

Currently some countries producing steel for heavy-loaded dies tend to tungsten reducing due to alloying by molybdenum and vanadium.

Thus, Cr-Mo-V steels are primarily used for dies and die accessories. Temper and most alloying elements content is determined by properties, which are necessary for successful exploitation of various tools.

Some economically alloyed ЭП971, ЭК15 steels, which do not contain tungsten and molybdenum and can successfully substitute standard steels have been developed by Special Constrac tional Bureau of Physical Metallurgy with Experimental Plant "Krystal", Table 26 reflects the mechanical properties of ЭК15 steel after oil quenching at 1060-1080°C and tempering at 180. 200°C (the properties of Х12М are mentioned for comparison).

Figure 1 Mechanical properties of Х12М and ЭК15 Steels.

Melt №	Steel grade	Hardness HRS_E ,after tempering	Toughness MJoule/m^2	Bending strength, MPa	Amount of retained austenite, %
1.	ЭК15	62-63	0.5-0.7	2400-2800	8-12
2.	Х12М	60-61	0.4-0.6	1800-2200	15-20

According to data ЭК15 steel is more hardness, strength and impact strength than those of standard Х12М steel that is positive point for wear resistance of steels.

Die comparison tool life testing of Х12М and ЭК15 steels was conducted on "Dzerzhinets" enterprise . There the blanking of 0.3-0.5 mm thick details made of 49К2Ф and

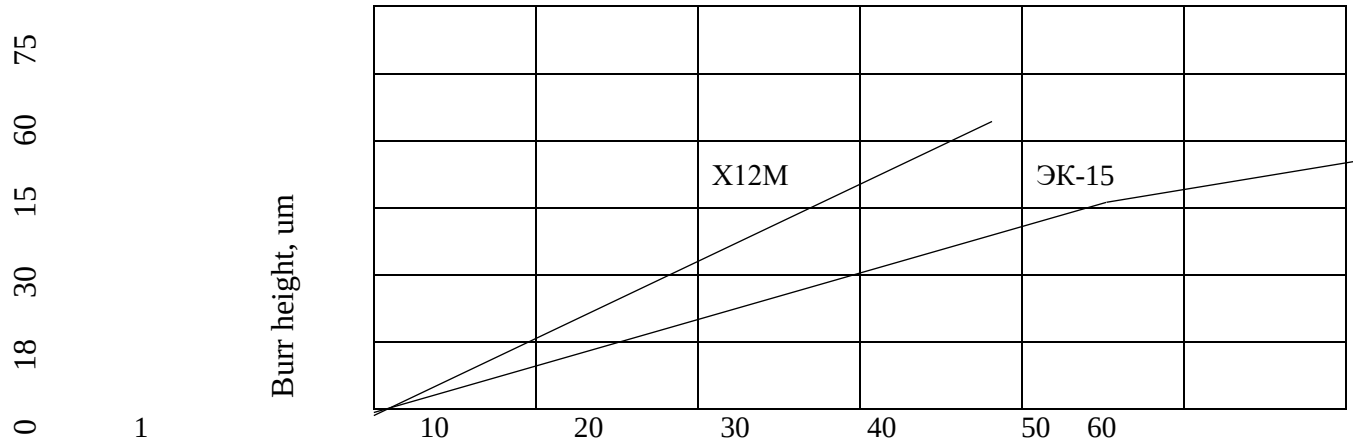
49К2ФА alloys is made along with dies of working details made of Х12М and Х12Ф1 steels. Due to the high hardness of blanked materials (HRCE 35…40), the die life is not sufficient.

The aim of that work was the determination of the die life influence X12M, X12Ф1 steels substitution on ЭК15 steel. The heat treatment of die working details was conducted in

the hardening workshop of the enterprise. The hardness after treatment was HRCE 59-60 for punches, and 62-63 for die blocks.

Tool life was assessed by the number of blanked details before regrinding, i.e. generating of accepted level of 0.06 mm burr stability.

Figure 2 demonstrates the dependence of burr height on the number on die details. The intensity of wear-out of working details made of ЭК15 steels is much lesser than those of X12M.[1,5] The dependence of burr height on the number of die details



Testing results

Testing results of industrial series of dies showed that ЭК15 steel can be successfully applied on blanking die with increasing tool life as much as twice. [1,6]

Literature

1] Suleymanov,N.M. New Directions in Development and Strengthening of Steels-Baku, 2002, 385 pages

2]https://studbooks.net/2538022/tovarovedenie/shtampovye_stali_deformirovaniya_goryachem_sostoyanii_poluteplostoykie_teplostoykie

3] https://www.totalmateria.com/page.aspx?ID=CheckArticle&site=kts&NM=8

4] http://aliansmetall.ru/shtampovie-staly

5]https://studbooks.net/2557194/tovarovedenie/trebovaniya_predyavlyaemye_stali_shtampov_goryachego_deformirovaniya

6] http://repo.ssau.ru/bitstream/Metodicheskie-ukazaniya/Termoobrabotka-i-stoikost-shtampovyh-stalei-Elektronnyi-resurs-Metod-ukazaniya-k-lab-rabotam-pdf

RESEARCH OF THE SURFACE STRUCTURE OF $Pb_{1-x}Eu_xTe$ EPITAXIAL FILMS

Rafiq Mikail SADIGOV

Ass. Prof. Azerbaijan Technical University, Department of Engineering Physics and Electronics, Baku, Azerbaijan

Hidayat Rahim NURIEV

Prof. Dr. Institute of Physics, Ministry of Science and Education, Laboratory of epitaxial layers and structures, Baku, Azerbaijan

Afin Mahammad NAZAROV

Ass. Prof. Institute of Physics, Ministry of Science and Education, Laboratory of epitaxial layers and structures, Baku, Azerbaijan

Mahammad Sadig SADIGOV

Ass. Prof. Institute of Physics, Ministry of Science and Education, Laboratory of epitaxial layers and structures, Baku, Azerbaijan

SUMMARY

In this work, was carried out an electron microscopic research of the surface of epitaxial $Pb_{1-x}Eu_xTe$ (x=0.01) films grown by condensation of molecular beam in a vacuum of 10^{-4} Pa on (111) BaF_2 substrates using an additional compensating source of Te vapor during growth. On the electron microscope images of films obtained at substrate temperatures T_s=573-623 K and condensation rates ϑ_k=8÷9 Å/s was observed black clusters, the number of which increases with a decrease in the condensation rate and increase in the substrate temperature. The use of additional compensating tellurium source, made it possible to obtain structurally perfect $Pb_{1-x}Eu_xTe$ films with a clean, smooth surface and with specified electrical parameters.

Keywords: solid solutions, rare earth elements, black clusters

INTRODUCTION

In recent years, semimagnetic semiconductor materials of the type of A^4B^6 (PbS, PbSe and PbTe) have been widely used and are in the focus of attention of researchers. These materials are characterized by a narrow band gap (Eg~0.1 eV). Optoelectronic devices created on the base of these materials can be controlled by a magnetic field.

It is well known that the lattice parameters of PbTe based solid solution depend on the impurity concentration [1-6]. The use of rare earth elements in this kind of solid solutions leads to greatly increasing the band gap and reducing the refractive index. Since the $Pb_{1-x}Eu_xTe$ ($0\leq x\leq 1$) solid solution is based on the binary compounds PbTe and EuTe, all its properties are somehow close to the properties of these compounds. It is natural to assume, and this is confirmed experimentally, that solid solutions with Eu content close to zero have properties very similar to those of PbTe. Since under normal conditions the PbTe and EuTe compounds have the same type of structure (NaCl) and symmetry (Oh5 - Fm3m) theirs solid solution retains them at any Eu content ($0\leq x\leq 1$). They have a face-centered cubic crystal lattice with a very close lattice parameter a_{PbTe}=0.6462 nm, a_{EuTe}=0.6595 nm. There are two atoms in the bases; one atom (Te) is located in the corner (0,0,0) and another atom (Pb) in the center (1/2, 1/2, 1/2) of the unit cell. Each atom in it is surrounded by six atoms of another element, so each atom is octahedrally coordinated by six nearest neighbors of the other type. PbTe crystals are highly brittle and can easily be cleaved along the (100) plane. When a PbTe compound is formed, it is energetically more favorable for two electrons from a partially filled lead 6p orbital to go to the tellurium 5p orbital, filling it completely. Therefore, the PbTe compound has a predominantly ionic type of chemical bond [7-9] and, under normal conditions and at any Eu content, the $Pb_{1-x}Eu_xTe$ ($0\leq x\leq 1$) solid solution retains its structure. The practical application of these semiconductors in IR photoelectronics has great prospects for their epitaxial films due to the fact that epitaxial films are becoming increasingly important in modern electronic technology. Microelectronic devices are created in a thin near-surface layer of a crystal; therefore, the rapid development of the technology for growing structurally perfect epitaxial films requires, along with a detailed study of the features of their growth, also the study of the surface structure. In this regard,

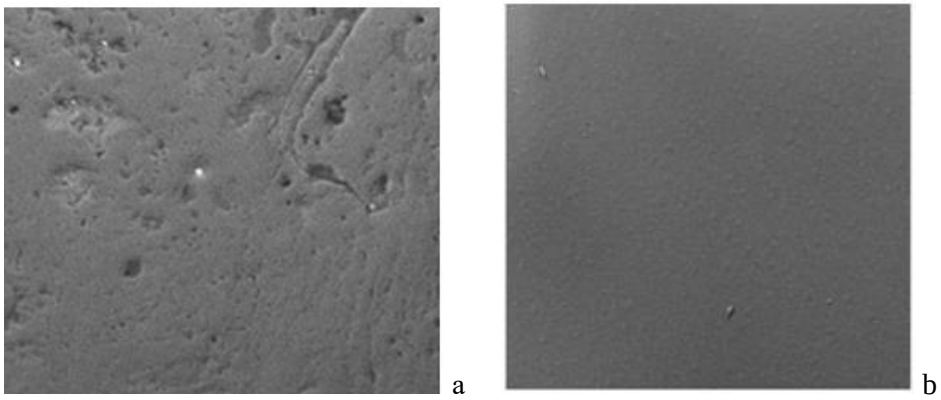
it is necessary to develop a technology for obtaining structurally perfect epitaxial films with a smooth clean surface and specified electrical parameters.

METHODOLOGY AND RESULTS

In this paper are presented the results of an electron microscopic study of the surface structure of $Pb_{1-x}Eu_xTe$ (x=0.01) epitaxial films grown by condensation of molecular beam in a vacuum of 10^{-4} Pa onto freshly cleaved (111) surface of BaF_2 substrates. As a source material for deposition was used the powder of $Pb_{1-x}Eu_xTe$ (x=0.01) solid solutions synthesized in evacuated and sealed quarts ampoule at 1050°C. It is known that the properties of an epitaxial film are largely determined by the parameters of the substrate. In particular, it is desirable to have the maximum possible coincidence of the lattice parameters and thermal expansion coefficients of the substrate and the epitaxial film. In our case, there are satisfactory correlations between these parameters. On the other hand, this substrate is dielectric, the main advantage of which is the possibility of electrical decoupling of individual functional elements in creating multi-element devices.

It should be noted that, now in addition to X-ray diffraction methods, electron microscopy is also successfully used to study the structure of the surface of bulk crystals and epitaxial films. The surface morphology and structure of obtained epitaxial films were studied by a Bruker XRD D8 Advance X-ray unit using filtered CuK_α radiation and scanning electron microscopy (JEOL JSM-7600F Fiels Emission Scanning Electron Microscope (SEM)). Measurements of the main electrical characteristics of the $Pb_{1-x}Eu_xTe$ solid solution (x=0.01) epitaxial layers: the type of conductivity, mobility and concentration of charge carriers were carried out by the Hall effect method [9] at temperatures of 77 K.

$Pb_{1-x}Eu_xTe$ epitaxial films were obtained on freshly cleaved (111) surface of BaF_2 at substrate temperatures T_p=573-623 K and condensation rate of ϑ_k=8÷9 Å/sec. Under these conditions, $Pb_{1-x}Eu_xTe$ epitaxial films are grown in the direction of (111).



a b

Fig.1. Electron microscope images of surfaces of $Pb_{1-x}Eu_xTe$ epitaxial films on BaF_2 substrate: a) without Te compensation, b) with Te compensation.

On the electron microscopic images of films obtained under the above described conditions was observed the black spots indicating the presence of inclusions of the second phase, the number of which increases with a decrease in the condensation rate and an increase in the substrate temperature (Fig.1a). According to [2], these spots are metal oxides (PbO) formed as a result of oxygen capture during growth. Oxygen capture occurs on the surface of the film with an excess of lead, which diffuses from the volume through the interstices. Excess lead is formed as a result of partial decomposition of the evaporated material during deposition due to the volatilization of the volatile component of chalcogen (in this case, Te). To create various photosensitive epitaxial structures, it is necessary to obtain films with a clean, smooth surface without any inclusions of second phase. For this purpose, an additional compensating Te source was used during film growth. The use of Te source led to the production of $Pb_{1-x}Eu_xTe$ films with a clean smooth surface without inclusions of the second phase (Fig.1b).

CONCLUSIONS

It has been established that by adjusting the temperature of the compensating Te source, it is possible to obtain structurally perfect $Pb_{1-x}Eu_xTe$ films with given electrophysical parameters: n,p(77K)= $0,5\div3\cdot10^{18}$ см$^{-3}$; $\mu_{77k}=1.5\div2\cdot10^4$ cm^2/V· sec.

REFERENCES

1. Abrikosov N.H., Shelimova L.E. Semiconductor materials based on $A^{IV}B^{VI}$ connections. M:Nauka, 1975. 196 p. (Russian)
2. Nuriev I.R., Farzaliev S.S., Sadigov R.M. Growth of epitaxial films Pb_{1-x} Mn_xTe (Ga) on single crystals $PbTe_{1-x}Se_x$ // Surface. 2004. No. 2. P. 110-112. (Russian)
3. Freik D.M., Shperun V.M., Solonichnyy Ya.V., Brodin I.I. Synthesis and growth of PbTe and PbSe films // Crystallography. 1979. V. 24. No. 3. P. 636-640. (Russian)
4. Ravich Yu.I., Efimova B.A., Smirnov I.A. Methods for studying semiconductors as applied to lead chalcogenides PbTe, PbSe and PbS. M:Nauka, 1968. 383 p. (Russian)
5. Zasavitskyi I. И. Injection lasers based on narrow-angle semiconductors and their application // Zarubezhnaya radioelektronika. 1974. No. 10. P. 74-119. (Russian)
6. Volkov B. A., Pankratov O. A., Sazanov A. B. Zonal structure of solid solutions based on compounds A^4B^6 // PTS. 1984. V. 26. No. 2. P. 430. (Russian)
7. Wachter P. Europium Chalcogenides: EuO, EuS, EuSe and EuTe // Handbook on the Physics and Chemistry of Rare Eath // Ed. Gschneider K.A., Eyring L. R. North-Holland, Amsterdam: Elsevier, 1979. V. 2. P. 507-574.
8. Golubkov A.V., Goncharova E.V., Zhuze V.I., Loginov G.M., Sergeeva V.M., Smirnov I.A. Physical properties of chalcogenides of rare earth elements. Leningrad:Nauka, 1973. 238 p. (Russian)
9. Kuchis E.V. Galvanomagnetic effects and methods of their research. Moscow:Radio and communication, 1990. 174 p. (Russian)

ADDITIVE MANUFACTURING TECHNOLOGIES

Aytaj Farzaliyeva[1]

[1]*Azerbaijan Technical University, Metallurgy and materials science, Higher Education Institute, Baku, Azerbaijan, ORCID ID: https://orcid.org/0000-0001-6200-2624*

Marziyya Aghayeva[2]

[2]*Azerbaijan Technical University, Metallurgy and materials science, Higher Education İnstitute, Baku, Azerbaijan, ORCID ID: https://orcid.org/0000-0002-6384-2518*

Sayyada Suleymanova[3]

[3]*Azerbaijan Technical University, Metallurgy and materials science, Department of metallurgy and materials science, Baku, Azerbaijan, ORCID ID: https://orcid.org/0000-0002-1335-9245*

ABSTRACT

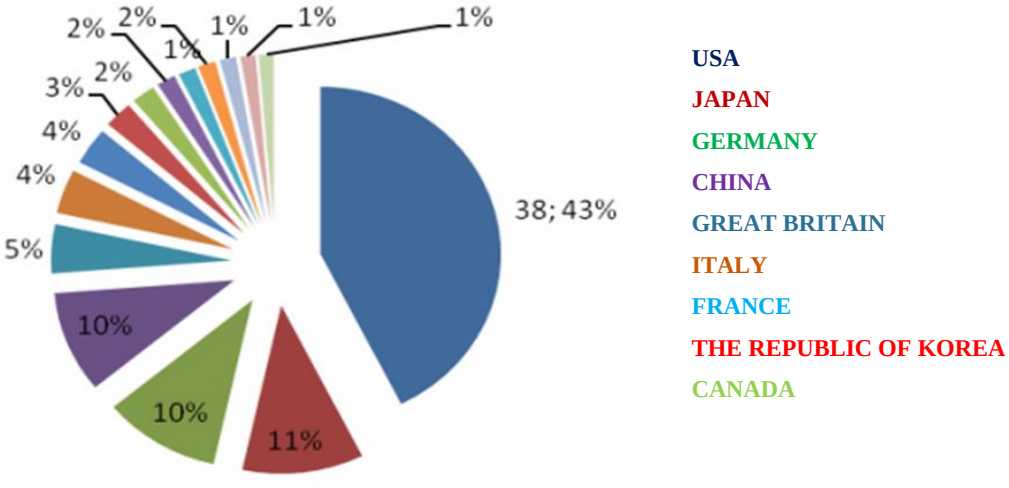
Additive manufacturing technologies have grown rapidly in the past decade and have become a technology with significant advantages compared to conventional manufacturing. With modern technologies emerging in manufacturing processes, companies need to adapt to these technologies to remain competitive. Additive manufacturing is one of the future technologies that will make significant changes in the manufacturing process. As new materials and techniques are discovered, additive manufacturing technologies develop and become more cost-effective and sustainable technologies. The widespread use of this technology in industrial areas has speeded up development and helped to improve product quality. However, in order to ensure the development and continuity of this technology, it is necessary to reduce production costs, increase quality, and speed up production processes. These processes also create competition and speed up technology development. A literature review was conducted to understand current AM processes, their applications in different manufacturing areas, and their impact on business strategies, operations, and the product lifecycle. Areas where additive manufacturing technologies are mainly applied can be grouped into aerospace, biomedicine, smart technologies, and other industrial applications. The fact that they are popular areas of research also speeds up the development of additive manufacturing technologies. In this review, the additive manufacturing technologies of the past to the present, the pros and cons of these technologies, the aspects to be developed and the industrial applications are examined and explained. From the study, it was concluded that AM technologies are still in their maturation state and have many uncertainties that need to be overcome. The main obstacles are implementation costs, limited materials, and protection of intellectual property. When looking at studies of additive manufacturing technologies and industrial applications, the technology has a wide range of uses. With the use of additive manufacturing technologies, previously encountered in prototypes and special applications in automotive, biomedical, and smart technologies, it is seen that they have begun to take place more in people's daily lives Furthermore, methods for assessing sustainability, such as life-cycle assessment and low-cost models and standards, are presented from various studies. The AM is beneficial for environmental and economic sustainability, with very little research on social sustainability

Keywords: additive manufacturing, 3D printing, digital technologies.

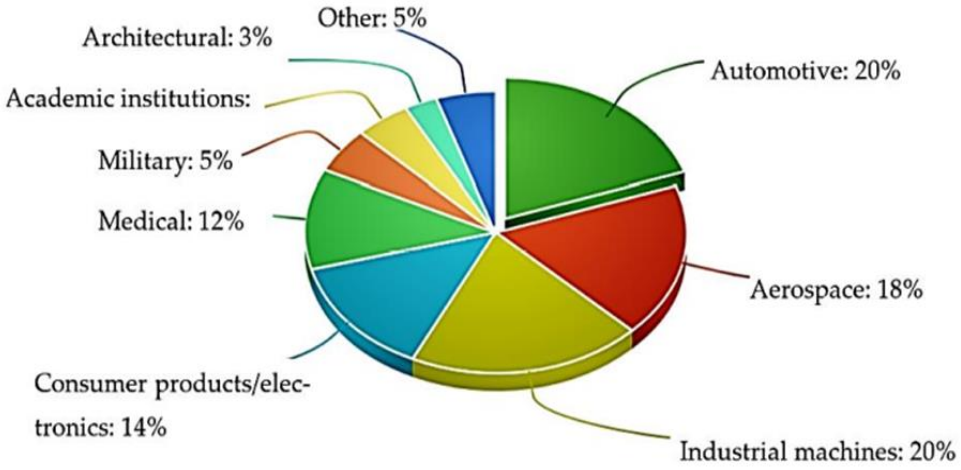
INTRODUCTION

The age of scientific discoveries brings many innovations that are associated with different branches of activity. Therefore, in the modern world, enterprises need to quickly respond to changes in the external environment and take measures to remain competitive in the market. An important role here is played by the understanding by managers of the need to introduce innovations in the production process. The increase in technology and its availability pose a challenge for managers to choose the most efficient mode of production. The emergence and development of additive technologies have attracted the attention of both foreign and domestic companies. In foreign practice, these technologies are widely used in various industries. The US is well ahead of other countries in additive manufacturing.

The diagram below shows the share of additive manufacturing in the leading countries in the world. (Fig. 1).



3D printing is actively used in the aerospace, automotive, oil and gas industries, shipbuilding, medicine, jewelry, and many other industries. (Fig. 2).



The main technologies used in the creation of products on additive installations:

• SLM (Selective Laser Melting), which uses a ytterbium laser to selectively melt metal powder in accordance with mathematical CAD models;

Layer-by-layer deposition is accomplished using the FDM (Fused Deposition Modeling) technique, which uses plastic thread or granules;

• SLA (Laser Stereolithography), a form of laser stereolithography that uses a laser to cure liquid materials layer by layer;

• DLP (Digital Light Processing), a technique for 3D printing employing stereolithography and digital LED projectors;

• LCD (Liquid Crystal Display), another form of photopolymer printing in which an LED UV matrix illuminates a photopolymer resin through an LCD screen mask;

• SLS (Selective Laser Sintering), which involves selective laser sintering of powdered material particles using laser beams until a real item is created from a supplied CAD model;

• MJP (MultiJet Printing) – multi-jet modeling utilizing photopolymer or wax; • Binder Jetting – layer-by-layer bonding of a composite powder (sand, polymer, metal, etc.);

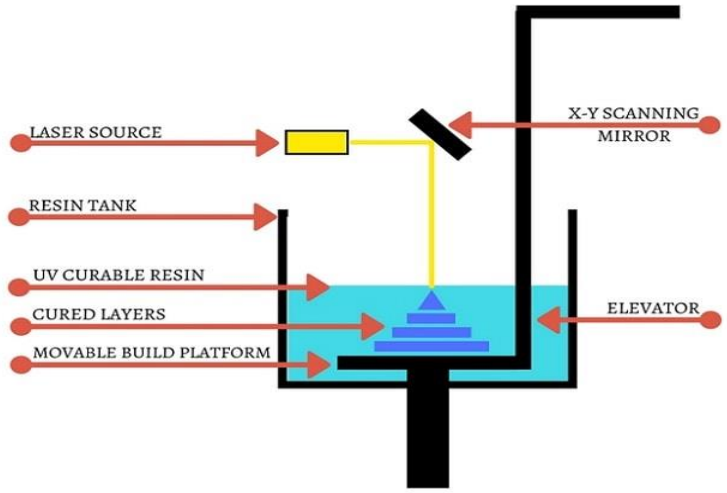
• CJP (ColorJet Printing): full-color 3D printing technology is produced by adhering a unique gypsum-based powder.

The first commercial 3D printer was based on stereolithography

(Steriolithography Apparatus, SLA), developed by Charles Hull in 1984.

A stereolithographic printer has a body that is immersed in a tank of liquid photopolymer. It stands out noticeably at the depth of the generated layer. The laser passes through the calculated surface of the cultured section of the object, resulting in a thin layer of photopolymer that hardens. The structure is then described below, with another thin tissue layer formed over the hardened dense layer. liquid polymer, and the laser again outlines the next layer on the surface of the mirror. Layer for a dense foundation described in a deep tank, until the object is completely built in liquid photopolymer

The stereolithography printer is one of the most precise pieces of 3D printing equipment: the thickness of the generated layer is 0.06 mm, and the accuracy in the Z-direction is 0.025 mm. (Fig. 3).



Advantages:

– creation of an object using a single procedure;

- the possibility of manufacturing an object that cannot be manufactured in any other way;

– construction of an object of any complexity with minimal time spent on

process preparation (no need to develop a technological process);

- construction of an object, the elements of which consist of different materials;

2) disadvantages:

– expensive consumables;

- low accuracy with fast printing;

– relatively low strength of models;

- the need in some cases for subsequent surface treatment.

Bioprinting is a new branch of medicine, formed during the rapid development of additive technologies. From science fiction to scientific fact, 3D-printed organs are making their way into the world of medicine. At first, the idea of 3D printing organs for on-demand transplants sounds like something out of a movie. However, machines that promise to regenerate living human tissue, replace vital organs, and quickly heal open wounds are much closer to reality than you might imagine.

3D-printed organs are already being used as training aids for would-be surgeons to fine-tune their skills before entering real emergencies. 3D-printed bone replacements have also been successfully transplanted, but living tissue is the next big step for this groundbreaking technology. Like any other 3D printing, layers are stacked on top of each other, but instead of PLA or ABS, living cells suspended in a gel are used to "create" living tissue. The cells then grow to form and develop into tissue, bone, and even entire organs. The promise of what this technology can do for humanity is great. There is a worldwide shortage of organ donors, and 3D bioprinting can solve this problem. Dying people can get a 3D-printed organ made from their own cells instead of waiting in long lines. Such a futuristic dream is still far from reality, but university labs and private companies have already taken the first careful steps using 3D printing technology to create tiny organ fragments.

Nowadays, scientists all over the planet are hard at work developing multifunctional printers that can print workable organs suitable for human transplants. It is curious that even today, prototype bioprinters are capable of printing bone and cartilage implants as well as complex biological food products that include well-known proteins, fats, carbohydrates, and vitamins. Additive technologies can be attributed to external benefits that increase the value of the product for potential consumers. This is confirmed by the use case of these technologies for the production of consumer goods by Nike. At the end of 2015 the company began producing sneakers using 3D printing. The main advantage is that you can make shoes individually for each person, taking into account the features of not only the foot, but also the design. To create sneakers, you just need to download the developed model to the computer.

In addition, the company's future plans include the idea that the consumer himself will be able to print sneakers at home, if he has a 3D printer, after customizing the design of the chosen models on the company's website. To date, Nike customers can also choose the design of sneakers and order on manufacturer's website. After manufacturing using additive technologies, the shoes will be delivered to the consumer.

With the help of 3D printing, Nike creates a huge competition for other manufacturers, as in today's world many people strive for individuality, and this manufacturer provides this opportunity. Nike also outperforms competitors who make shoes using traditional manufacturing, due to high quality and costs, which are reduced when using additive technologies.

Considering the use of additive manufacturing in the automotive industry, it should be said that the number of manufacturers that use these technologies in the manufacture of parts is increasing. However, Local Motors has developed the world's first Strati car, which was almost entirely 3D printed. The advantages of this car model over others that are made using traditional production are time to create and profitability. The company plans to put the "Strati" into small-scale production, as this model aroused interest among consumers.

As for the Ford Motor Company, the company also uses additive technologies in the production of cars. The company is testing a 3D printer for mass production of automotive components, in addition, Ford management notes, that additive manufacturing is a more cost-effective and efficient way to make parts, and also opens up broader frontiers for designers than traditional manufacturing methods.

CONCLUSIONS

In a more understandable language, additive technologies are understood as 3D printing. The process of creating a product is controlled by a computer, in whose memory there is a three-dimensional model of the future part, cut into thin layers and sections.

In the modern world, enterprises need to quickly navigate in a constantly changing environment in order to maintain their competitiveness, so company management should pursue an innovative policy, as well as improve production processes. Additive technologies are a tool that allows in a short time produce a unique product. The development and use of these technologies in the future will be an integral part in various industries.

RESOURCES

1. L. Jyothuish Kumar, Pulak M.Pandey, David Ian Wimpenny - 3D printing and additive manufacturing technologies. p.155

2. Клюев С.В., Клюев А.В. Исследование физико-механических свойств композиционных вяжущих // Успехи современной науки. 2015. № 1. С. 21 – 24..

3. Revilla-León M., Özcan M. Additive manufacturing technologies used for 3D metal printing in dentistry. Current Oral Health Reports. 2017. vol. 4. no. 3. pp. 201-208..

4. Денис Кузнецов. Adidas и Nike будут печатать обувь на 3D-принтере в присутствии клиента принтере [Электронный ресурс] URL: https://rg.ru/2015/10/12/shoes-site.html 5. 5.Petar Kocovic, 2017. History of Additive Manufacturing

6. Jopson, Barney. "New stamping ground for Nike and Adidas as 3D shoes kick off." *Financial Times.* June 9, 2013. Jopson, Barney. "New stamping ground for Nike and Adidas as 3D shoes kick off." *Financial Times.* June 9, 2013.

7. NIKE, Inc. Form 10-K, 2018.

8. Additive manufacturing and 3D printing. Available at: https://blog.iqb.ru/additive-manufacturing-basics/.

9.М.А. Зленко, А.А. Попович, И.Н. Мутылина. Аддитивные технологии в машиностроении. СПБ. : Издательство политехнического университета, 2013, 222 с.

10. Леонид Попов. Компания Ford испытала 3D-печать на массовых моделях [Электронный ресурс] URL: https://www.drive.ru/news/ford/559aa26d95a656a0bc000050.html

11. Эзра Даер, Первый автомобиль, напечатанный на 3D-принтере [Электронный ресурс] URL: http://www.popmech.ru/technologies/53426-avto-iz-printera/

12. Wohlers Report 2014 – 3D Printing and Additive Manufacturing State of the Industry, Annual Worldwide Progress Report, Wohlers Associates, 2014.

13. Баева Л.С. Современные технологии аддитивного изготовления объектов / Л.С. Баева, А.А. Маринин // Вестник Мурманского гос. технич. ун-та. стр.7

14. 10. Strati the world's first 3d-printed electric car [Электронный ресурс] URL: https://localmotors.com/strati/

15. Панков, Д.Э. Лазерная стереолитография (SLA): технология 3D-печати, стр.20

16. Brian Evans. Practical 3D Printers — The Science and Art of 3D printing, p.15

DEFORMASİYA OLUNAN BƏRK CİSİM MEXANİKASINDA GÜC YÜKLƏNMƏSİ ZAMANI PANELDƏ İLKİN PLASTİK DEFORMASİYALARIN İNKİŞAFI

Yahyayev Coşqun

Bakı şəhəri, Azərbaycan Milli Elmlər Akademiyası Rəyasət Heyəti aparatı İşlər idarəsinin baş mütəxəssisi

Xülasə

Bərk cisim mexanikasında ən vacib məsələlərdən biri dağılma materiallarının müqavimətinin qiymətləndirilməsinin optimal usüllarının işlənib hazırlanması və tətbiq edilməsidir. Hal-hazırda texnologiyanın müxtəlif sahələrində yüksəkdavamiyyətli materiallardan və iriqabaritli konstruksiyalardan, qurğulardan geniş istifadə edilməsi ilə bağlı bərk cisimlərdə çatların yayılması nəzəriyyəsi geniş yayılmışdır.

Məqalədə iki amilin qarşılıqlı təsiri problemlərinin - panelin biristiqamətli kompozit materialdan hazırlanmış sərtlik qabırğaları ilə möhkəmləndirilməsi və onun konturuna çıxan bir sıra dairəvi dəliklər və çatlarla zəifləməsinin tədqiqi üsullarından bəhs edilir .

Dairəvi dəliklərin dövri sistemi və hər dəliyin yaxınlığında absis oxu seqmentləri boyunca iki çat ilə zəifləmiş sonsuz izotropik elastik pərçimlənmiş panel nəzərdən keçirilir. Dəliklərin konturları və çatların sahilləri kənar qüclərdən azaddır. Plitəyə metal kompozit materialdan hazırlanmış köndələn sərtlik qabırğaları pərçim edilmişdir. Hesablama sxemində pərçim edilmiş möhkəmləndirici qabırğaların təsiri pərçimlərin yerləşmə nöqtələrində tətbiq olunan cəmlənmiş güclərlə əvəz olunmuşdur. Konsentrasiya edilmiş qüvvələrin qiymətləri problemin həndəsi və fiziki parametrlərindən asılı olaraq tapılmışdır. Gərginlik intensivliyi əmsalları və son hədd yükləmələri problemin həndəsi və fiziki parametrlərindən asılı olaraq hesablanmışdır. Bəzi müəyyən edilmiş şərtlərdə çatın inkişafının sabit bir mərhələsinin olduğu göstərilmişdir.

Sərtlik qabırğaları ilə gücləndirilmiş plitədəki dairəvi dəliklərin konturundan çıxan ilkin plastik deformasiyaların (embrional çatların) inkişafı öyrənilir. Plitənin materialı Tresca-Saint-Venant şərtini təmin edən elastik-mükəmməl-plastikdir. Plastik deformasiyaların dəliyin konturundan çıxan bəzi sürüşmə xətləri boyunca cəmləşdiyi qəbul edilir. Həddşərtlərini təmin etməklə, problemin həlli sinqulyar inteqral tənliyinə gətirir. Sonra problemin sinqulyar tənliyi onun Fredholm tənliyinə gətirilməsinin ara mərhələsi olmadan cəbri tənliklər sisteminə gətirir. Alınan sistem Gauss üsulu ilə n-nin (n – intervalın bölünməsi üzrə Çebışev qovşaqlarının sayıdır) fərqli dəyərləri üçün əsas element seçimi ilə həll edilirdi. Cəmlənmiş güclərin qiymətləri problemin həndəsi və fiziki parametrlərindən asılı olaraq tapılmışdır. Plastiklik zolaqlarının uzunluğunun tətbiq olunan yükləmədən, problemin həndəsi parametrlərindən və materialın axıcılıq həddindən asılılıqları tapılmışdır.

Yerli dağılma şərtindən (KPT- meyarları) istifadə etməklə, dağıdıcı kənar yüklələmənin müəyyən edilməsi üçün nisbət əldə edilmişdir.

Açar sözlər: deformasiya, panel, plitə, kompozit material, konsentrasiya

IN MECHANICS OF DEFORMABLE SOLIDS PRIMARY PLASTIC ON PANEL DURING POWER UP DEVELOPMENT OF DEFORMATIONS

Abstract

One of the most important issues in solid mechanics is the development and application of optimal methods for estimating the resistance of dispersion materials. Currently, the theory of propagation of cracks in solid bodies is widespread due to the wide use of high-strength materials and large-sized structures and devices in various fields of technology.

The article discusses the methods of studying the problems of the interaction of two factors - strengthening the panel with stiffening ribs made of unidirectional composite material and weakening it with a number of circular holes and cracks protruding from its contour.

An infinite isotropic elastic riveted panel weakened by a periodic system of circular holes and two cracks along the abscissa axis segments near each hole is considered. The contours of the holes and the edges of the cracks are free from external forces. Transverse stiffness ribs made of metal composite material are riveted to the plate. In the calculation scheme, the effect of riveted reinforcing ribs is replaced by the concentrated forces applied at the points of location of the rivets. The values of the concentrated forces are found depending on the geometrical and physical parameters of the problem. Stress intensity factors and ultimate loadings were calculated depending on the geometrical and physical parameters of the problem. It has been shown that there is a stable phase of crack development under certain specified conditions.

The development of initial plastic deformations (embryonic cracks) emerging from the contour of circular holes in a plate reinforced with stiffness ribs is studied. The material of the plate is elastic-perfect-plastic satisfying the Tresca-Saint-Venant condition. It is assumed that the plastic deformations are concentrated along some slip lines emanating from the contour of the hole. By satisfying the boundary conditions, the solution of the problem leads to a singular integral equation. Then the singular equation of the problem is brought to a system of algebraic equations without the intermediate step of bringing it to the Fredholm equation. The resulting system was solved by the Gaussian method with the selection of principal elements for different values of n (n is the number of Chebyshev nodes in the division of the interval). The values of concentrated forces are found depending on the geometrical and physical parameters of the problem. The dependences of the length of the plasticity bands on the applied load, the geometrical parameters of the problem and the yield point of the material were found.

Using the local dissipation condition (KPT-criteria), a ratio was obtained to determine the destructive edge loading.

Keywords: deformation, panel, plate, composite material, concentration

KEY ARCHITECTURAL CHANGES IN 5G NETWORK AND THEIR EFFECTS ON END USER SERVICES

Murad JAHANGIROV

Azerbaijan Technical University, Faculty of Information and Telecommunication Technologies, Department of Radio Engineering and Telecommunications, Baku, Azerbaijan, https://orcid.org/0000-0000-0000-0000

Aziz SULEYMANOV

Azerbaijan Technical University, Faculty of Information and Telecommunication Technologies, Department of Radio Engineering and Telecommunications, Baku, Azerbaijan, https://orcid.org/0000-0002-0708-2059

ABSTRACT

In mid 2010s, in order to meet new set of data connectivity requirements 3GPP, international authority organization responsible for standards and specifications for mobile networks started development of new, fifth generation mobile networks. Mentioned business requirements were mostly related to capacity and quality enhancements i.e., massive machine communication, high reliability, low round trip time, etc. To satisfy these demands 5G network model introduced some conceptual architectural changes compared to previous technologies.

This study provides detailed analysis of 3 key changes in Core Network architecture and their effects on end user serviceability.

1. Implementation of Cloud native Functions instead of bare metal based Network Elements led to simplified architecture, faster development and deployment process by adopting open source as well as industry standard best practices and cost effective deployments, including over public cloud providers.
2. Control and User Plane Separation (CUPS) model is a key feature to provide some critical 5G services, especially URLLC and some eMBB cases. To provide high throughput services with low delay UPF shall be placed at a location as close to end user as possible, sometimes even at Radio sites next to gNb.
3. Transition to Service Based Architecture enabled utilization of unified application layer protocol HTTPv2 over secure transmission TLS, seamless subscriber migration between AMF functions without service interruption and connection to 3rd party systems via APIs.

Keywords: 5G architecture, Cloud native, CUPS, Service Based Architecture, Core Network

1. Introduction

Mobile telecommunication networks generally referred as 1G technologies started in 1980s with the introduction of analog wireless phones. They were the pioneers of civil mobile communication. In 1990s started the 2G technology era by development of regional standards, i.e. GSM specifications by ETSI and CDMA by ANSI. They were first digital telecom networks initially designed to deliver voice connectivity and by totally demilitarization of Internet technology in mid-1990s this was also adopted at a later specification (GPRS/EDGE). Afterwards, followed the 3G technology which was focused on enhancement of voice quality, introduction of video call service and improvement of mobile internet quality. Main objective during 4G network design was improvement of data connectivity throughput.

And, all these developments and technological enhancements were capable of covering requirements of their respective time periods. However, in mid 2010s new set of requirements emerged for mobile networks. These requirements are categorized into 3 main groups:

- Enhanced Mobile Broadband (eMBB)
- Ultra Reliable and Low Latency Communication (URLLC)
- Massive Machine Type Communication (mMTC)

None of previous technologies had sufficient capabilities to satisfy these demands. Thus, specifications for new, fifth generation of mobile network technologies were developed and published by related international standardization organization, 3GPP.

5G network model introduced some technological enhancements, i.e., common Core Network for 3GPP and non-3GPP access, network slicing, beam forming, end-to-end flow based QoS enforcement, common DB layer, stateless DB, edge computing, Cloud native Functions, Control and User Plane Separation (CUPS), Service Based Architecture, etc [4 - 6].

This study provides detailed analysis for the most important architectural changes and their effects on end user serviceability.

1. Cloud native Functions
2. Control and User Plane Separation (CUPS)
3. Service Based Architecture

2. From Bare-Metal to Cloud Native

Network elements used in traditional telecommunication systems i.e. Base Station Controller (BSC), Radio Network Controller (RNC), Mobile Switching Server (MSS), Multimedia Gateway (MGW), Serving GPRS Support Node (SGSN), Gateway GPRS Support Node (GGSN), Mobility Management Entity (MME), Serving Gateway (SGW), Packet Gateway (PGW), etc. were initially designed on bare metal based platforms.

Any of these network elements consists of many functional hardware (HW) blocks depending on the functions and features supported by the Network Element (NE). Operation and Maintenance Unit, Signaling Processing Unit, VLR Unit, Charging Unit, Statistics Unit, Interface Unit, Database Unit, etc. are some of the components of Core Network (CN) elements like MSS or SGSN. Each functional HW block in turn is split into several modules, cards or units. Generally, these modules are equipped with custom built CPU processors rather than utilizing x86 or other common CPU models available in the market. Each of these CPUs are designed to carry out very specific functions.

In terms of software there is no human friendly Operating System running on these systems, like Windows or Linux based OS. Most of the operations are processed at hardware level. On top of it each functional block of the system has its own specific software component.

Figure 1 illustrates Nokia DX 200 MSC Server with several functional blocks[9].



Figure 1: Nokia DX 200 MSC Server

As all the CPUs and SW components running on it are custom designed based on their respective functionality this approach has a very big advantage in terms of performance. However, it bears following issues as well:

- System is very rigid, there is very little or no flexibility
- For each new feature or functionality new CPU or chipset customization may be required
- Development of new HW may take long time and it affects product readiness schedule
- Cost associated with it
- Operational complexity for the maintenance personnel
- As these modules aren't mutually replaceable the operator needs to keep spare part for each unit type separately

At earlier stages of telecom industry when the networks were relatively simple, composed of just several network elements these aspects were acceptable and manageable.

However, in time these drawbacks became real challenges. By introduction of new NEs operator networks became much more complex, business units demanded faster time-to-market products and due to increase in CAPEX / OPEX expenditures operating costs increased significantly. Thus, a necessity emerged for a new conceptual approach in network design. Target architecture shall have:

- Possibility to deploy on standard x86 based IT COTS HW
- Use well known OS (i.e. Linux) as common platform
- Much faster development and deployment
- Flexible and automated management and automation

To fulfill all these requirements "Virtualization" concept was introduced as an interim solution. Figure 2 illustrates architectural concept introduced by ETSI for Network Function Virtualization [8].

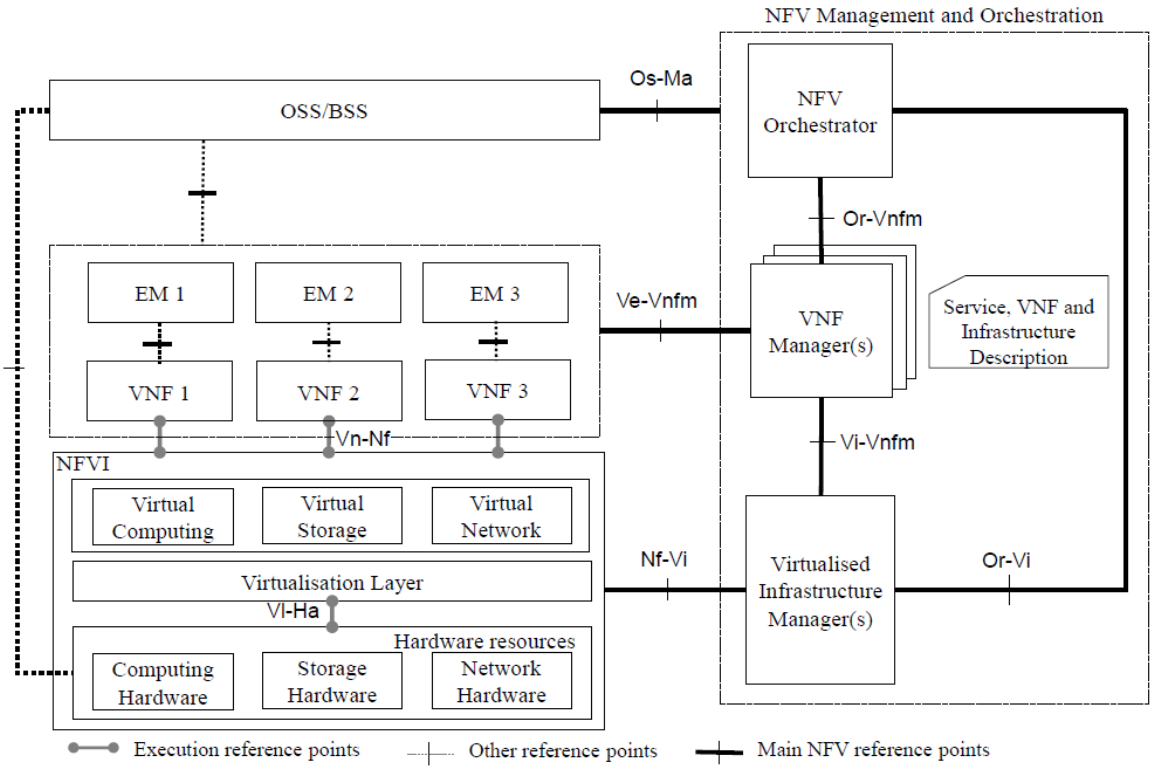


Figure 2: ETSI NFV reference architectural framework

As seen from the picture main purpose of this architecture is to deploy all network elements on top of common HW. To control HW resource utilization by Virtual Network Functions (VNFs) a new Virtualization Layer (Hypervisor) was introduced. Main function of the Hypervisor is to dedicate HW resources (Compute, Storage and Network) to certain VNFs and manage them throughout the lifecycle of that VNF.

In reality, none of the existing network elements were re-designed from scratch in order to fit this reference framework. Instead, they were just converted into VNFs by keeping general high-level architecture untouched. Thus, functional blocks of the NEs converted into Virtual Machines (VMs) with similar functionality. Each VNF is composed of several VMs depending on the capacity and the functionalities of the VNF. VNFM (VNF Manager) is introduced for all lifecycle management activities of the VNFs.

Real world deployments of this concept started with EPC and IMS and afterwards spread to other systems as well. Nowadays, most of the network elements have the virtual version and can be deployed as VNF. During last 5 years there was a major shift towards VNF model all over the world. However, this model has also some drawbacks, like:

- Additional Hypervisor layer utilizes up to 10% of system resources and creates point of failure
- Most of the time compatibility issues between different vendor HW, hypervisor and VNFs
- Not flexible as expected
- Because all functional units of NE are transferred as is without serious optimization complexity of the systems are kept as well

One of the main deficiencies of virtualization is performance issue. Virtual platforms sometimes really struggle to fulfill infrastructure requirements of NE, especially for user plane traffic forwarding capabilities. As described in CUPS chapter of this document user plane traffic demands high throughput capacity which was covered by custom built chipsets and NIC cards. However, standard virtualization platforms, like Open Stack running on COTS HW isn't capable to provide it by default. Virtual switch embedded into the system doesn't have such a capability. Some workaround solutions, like SR-IOV and DPDK are implemented for this issue.

In order to solve all listed issues and problems associated with them “Cloud native” architecture model was selected for 5G technology from the beginning. Main characteristics of this model are:

- Fully compatible with any available COTS HW
- No Hypervisor layer
- Running only on Host OS unlike NFV model where there are both Host OS and Guest OS
- Everything is an Application
- Container (i.e. Dockers) based architecture is adopted
- Open source management and orchestration systems (i.e. Kubermetes) to be used

Basically, during transition to 5G, network architecture is re-designed from scratch. Figure 3 illustrates 5G network topology [4].

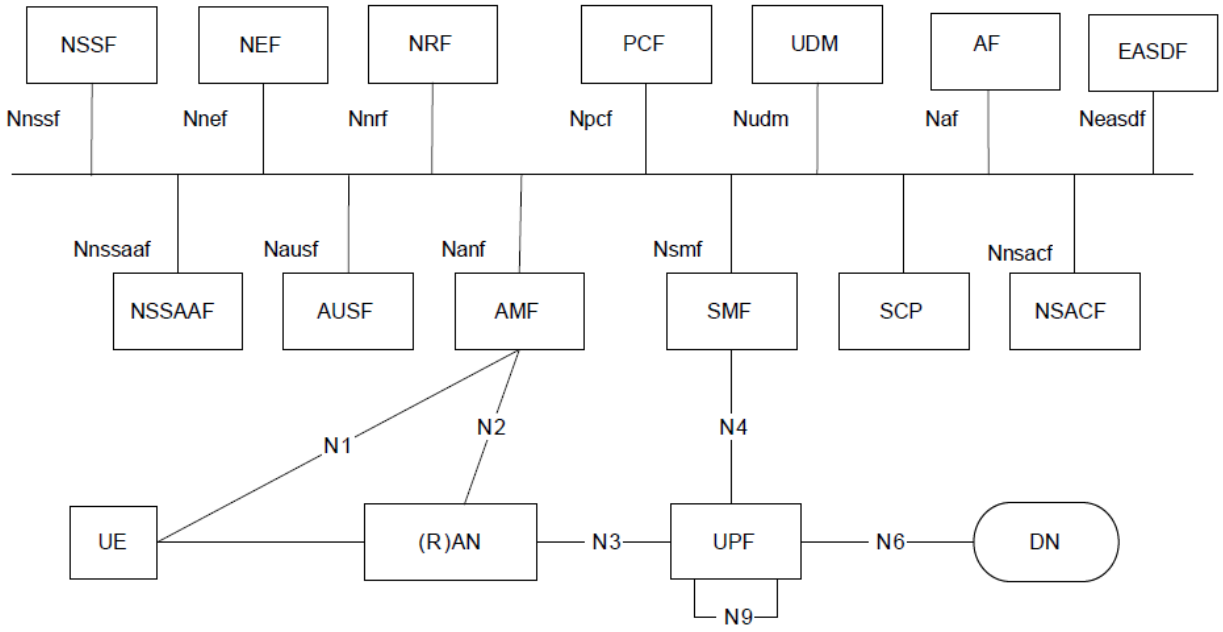


Figure 3: 5G system architecture

"Network element" concept is dismissed. Instead, NEs are split into smaller Functions and all Functions are running as applications directly on Host OS. For example, 4G network is composed of 4-5 mandatory Network Elements whereas 5G network consists of approximately 15 Functions. This approach provides better flexibility for deployment, scalability and resiliency. Industry best practice solutions, like Docker containerization and Kubernetes based orchestration are adopted which provides significant improvement in development and deployment schedule.

Based on target network design these Functions can be independently located at any cloud environment, even in the public clouds. In fact, there are many ongoing and successfully completed test cases where some of the functions are deployed over public clouds.

3. Control and User Plane Separation (CUPS)

In telecommunication systems there are two types of traffic:

a) Control Plane (CP) – Control plane represents the signaling traffic required to enable subscribers to use any kind of service. Network registration/deregistration (attach/detach), call establishment, location update, data session establishment, etc. procedures can be listed as examples for Control Plane traffic.

b) User Plane (UP) – User plane represents real traffic generated by end user subscribers, like voice transferred during call or data traffic while users use internet.

These traffic types have different, or we may say totally opposite requirements from underlying systems in terms of processing capacity, interface throughput and connectivity delay.

Due to nature of signaling procedures control plane traffic demands high processing power, whereas low interface throughput capacity is enough to carry this type of traffic. And it's not sensitive in terms of message delays, end users will not feel the difference of 1 second delay during call setup.

In contrast, user plane traffic is very sensitive for packet delays, especially for the real-time applications. If the voice packets delay for more than 150-200 ms the receiving party will start to feel the discomfort. Doesn't matter whether it's ordinary voice call or VoIP effect will be similar. User plane traffic requires much more

interface throughput capacity however, as it is just relayed from A party to B party without any processing it doesn't demand much CPU power.

Considering all these dependencies it's logical to deploy powerful systems designated for control plane handling in central data centers and distribute smaller capacity user plane systems throughout the network to the locations near to the end users. However, in traditional network technologies like 2G, 3G and 4G both CP and UP traffic were generally handled by same network elements (i.e. MSC for 2G voice, SGSN/GGSN for 2G/3G data and SGW/PGW for 4G data traffic) [1 - 2].

Although first official introduction of CUPS architecture and usage as a term in 3GPP specifications took place at Release 14 in 2017, by which SGW and PGW were separated into their constituent User Plane and Control Plane functions [3] this concept was first implemented much earlier in voice core (Circuit Switched network) during transition to 3G technology. MSC, which was the voice core network element responsible for both CP and UP processing was divided into MSS and MGW. MSS is designated to handle all control plane tasks, whereas MGW is responsible for voice traffic relaying.

As stated above, at a later stage of 4G EPC standardization (Release 14) this architectural change was adopted for SGW and PGW network elements as well. SGW was split into SGW-C and SGW-U, whereas PGW was split into PGW-C and PGW-U. As the names imply SGW-C and PGW-C are responsible for CP processing; SGW-U and PGW-U are responsible for UP traffic forwarding. New, Sxa and Sxb interfaces were introduced for interconnection of these new elements.

Figure 4 illustrates initial 4G network architecture without CUPS and Figure 5 illustrates Release 14 and onwards 4G network architecture including CUPS model [3].

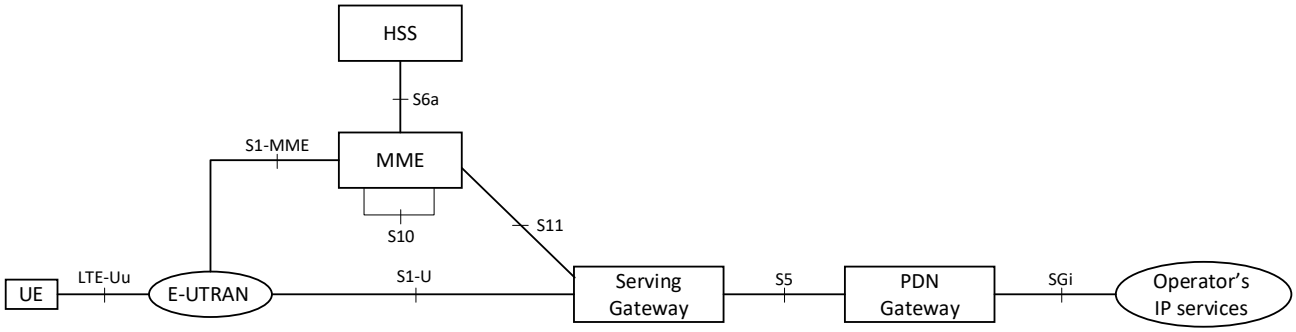


Figure 4: Initial 4G system architecture

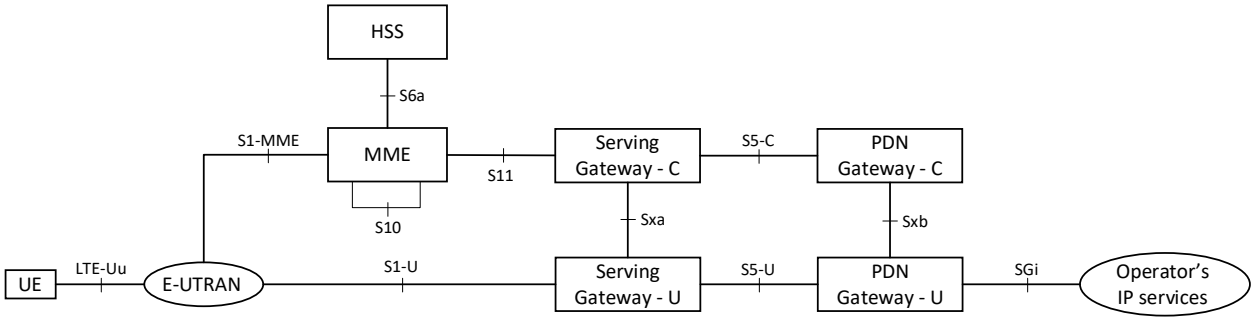


Figure 5: 4G system architecture with CUPS

For 3G and 4G technologies separation of Control Plane and User Plane traffic processing was rather by adoption or transformation of certain network elements. And, sometimes, these changes are not always implemented in real networks due to several reasons.

However, some specific requirements for 5G networks like very high traffic forwarding capacity in certain area and low round trip time made it mandatory to place user plane forwarding functions near to the end users as much as possible. To fulfill these requirements, it's assumed that UPFs will be located at regional data centers, edge data centers or even at Radio sites next to gNb. Thus, CUPS architecture was planned to be implemented as a default model for 5G networks and it was included into specification since the initial release. Figure 3 illustrates 5G network topology.

As indicated in 3GPP specifications Access Management Function (AMF) and Session Management Function (SMF) functions are purely responsible for Control Plane traffic processing and in real Communication Service Provider (CSP) networks these functions are located at central data centers (DCs). Whereas User Plane Function (UPF) is the function responsible for User Plane traffic handling and its location mostly depends on applications and traffic type to be handled [4].

4. Transition from point-to-point links to Service Based Architecture

Core Network architecture of 2G, 3G and 4G technologies are composed of point-to-point links between Network Elements, as illustrated in Figure 4 and Figure 5 as an example for 4G topology. These are proprietary interfaces with fixed characteristics and specific protocol stacks. Below listed are main drawbacks of this architecture:

a) Various application layer protocols are used for these interconnections, like Mobile Application Part (MAP), ISDN User Part (ISUP), GPRS Tunnelling Protocol (GTP), Diameter, SGSAp, etc [1, 2, 7]. Transport layer protocols varied very much as well. MTP3-User Adaptation Layer (M3UA), Stream Control Transmission Protocol (SCTP), Signalling Connection Control Part (SCCP), Transaction Capabilities Application Part (TCAP), TCP and UDP are some examples for transport layer protocols used in Core network. Such a concept results in design and operational complexity.

b) Subscriber migration challenges between Core Network NEs (MSSs, SGSNs, MMEs, etc.). Subscriber data is stored within NE in stateful mode thus, it's nearly impossible to migrate subscribers from one Core network element to another without service interruption. Generally, it's performed by forcefully detaching user from current NE and re-attaching to target NE. User is losing all ongoing services during this process, e.g. calls are dropped, data sessions are interrupted.

c) There is no interaction with outside of Core Network infrastructure. Only pre-integrated connections are supported. There is no flexibility for 3rd party system integrations.

To overcome these problems Service Based Architecture is adopted at 5G technology. Service based principles are applied within Core Network only between the Control plane Functions. User plane traffic forwarding function UPF still uses point-to-pint connections [4]. This architecture addressed listed challenges with following solutions.

a) To unify and simplify complexity common application layer protocol is selected and security is enhanced by applying encryption. HTTPv2 over TLS is selected as a well-known best practice application layer protocol. This facilitated 3rd party system connections as well.

b) Common DB layer is introduced where Functions save all subscriber stateful data. This enabled seamless migration of subscribers between AMF functions without service interruption.

c) Function discovery mechanism is introduced through Network Resource Function (NRF). All the Functions register themselves into NRF during startup indicating the list of supported features. And, they are dynamically discovered by other Functions when required. APIs registered in service registry (NRF) as well. APIs may be discovered and used by 3rd party applications outside 5G Core Network. Connection control is done through 3rd party system authorization process.

5. Conclusion

Architectural changes during transition to 5G technology introduced some major enhancements for Communication Service Providers (CSP), manufacturers end users (subscribers). 3 key changes are analyzed in this study with following conclusions:

1. Adoption of Cloud native topology provides some major enhancements which are critical for both network management and end user serviceability.
    - Simplified architecture and less vertical integration components
    - Less maintenance and spare part costs
    - More open source and industry standard best practices, i.e. Linux OS, Dockers containers, Kubernetes orchestration, etc. are accommodated
    - Functions can be independently located at any cloud environment which provides better flexibility for deployment, scalability and resiliency. It also improves end user service quality
    - Faster development and deployment schedule shortens new service introduction to end users
    - Cost effective deployments, including over public cloud providers decreased service fees for end users.
2. Control and User Plane Separation (CUPS) model is a key feature to provide some critical 5G services, especially URLLC and some eMBB cases. To provide high throughput services with low delay UPF shall be placed at a location as close to end user as possible, sometimes even at Radio sites next to gNb.

    CUPS architecture also plays a significant role in Core network design. CP functions AMF and SMF are generally located at central data centers. Whereas UPF responsible for user plane traffic handling and its location mostly depends on applications and traffic type to be handled.
3. Transition to Service Based Architecture resulted in some major improvements, like:
    - Unified application layer protocol HTTPv2 over secure transmission TLS
    - Common DB architecture to optimize resources and enable seamless subscriber migration between AMF functions without service interruption
    - Interconnection to 3rd party systems via APIs

References

[1] 3GPP TS 23.060: General Packet Radio Service (GPRS); Service description; Stage 2

[2] 3GPP TS 23.401 – General Packet Radio Service (GPRS) enhancements for Evolved Universal Terrestrial Radio Access Network (E-UTRAN) access

[3] 3GPP TS 23.214 – Architecture enhancements for control and user plane separation of EPC nodes

[4] 3GPP TS 23.501 – System Architecture for the 5G System; Stage 2.

[5] 3GPP TS 23.502 – Procedures for the 5G System; Stage 2.

[6] 3GPP TS 23.503 – Policy and Charging Control Framework for the 5G System; Stage 2.

[7] 3GPP TS 29.002 – Mobile Application Part (MAP) specification

[8] ETSI GS NFV 002 – Network Functions Virtualisation (NFV); Architectural Framework

[9] Nokia DX200 MSC Server Operation and Administration guide

SERVER-SIDE REQUEST FORGERY (SSRF)

Füzuli Saleh

Special Communication And Information Security State Service, Baku, Azerbaijan, Full Stack Web Developer, ORCID: https://orcid.org/0000-0001-6488-865X

Abstract

We will talk about server side request forgery, which is one of the top 10 most dangerous web applications in Owasp (The Open Web Application Security Project). As web applications evolve, so does the reach of their development, and more attention needs to be paid to securing web applications. In the early days of web applications, a web server and a database containing application data were sufficient to run these applications. Nowadays, many web applications can receive data from external services or applications. Currently, if security measures are not taken into account in this type of application, SSRF (Server Side Request Forgery) gaps can be created. In this case, an attacker can send requests to other applications or local services used by the application using the application name.

The article also discusses how an attacker in an SSRF loophole can change parameters and manipulate requests in hyperlinks that a web application sends to other resources. When a web application needs to receive data from an external source, such as when downloading an image from another website, etc. In some cases, the attacker who sent the request can achieve their malicious intent by changing the entire request or the domain part. For example, a server might link to a web application on that server https://numune.com/rss.php?url=xaricitetbiq.com/rss/ as a hyperlink to get RSS feeds from another server. If an attacker can change the url parameter in the hyperlink to localhost, he can get information about the server hosting the web application. Or it can access other servers or applications for which the web server has privileges.

The study includes materials describing SSRF vulnerabilities and how to deal with them. In a web application where SSRF vulnerabilities are found, the following operations are also possible in most cases.

- Gaining access to web services that depend on the vulnerable server.
- Inability to bypass IP verification
- Bypass systems that identify users
- Do not scan server ports
- Access to local files and internal services available on the server
- Access to sensitive information secretly used by the web application.

Key words: Security, web, owasp, ssrf

RESEARCH AND ANALYSIS METHODS FOR CALCULATION OF THE EFFICIENCY MULTISERVICE TELECOMMUNICATION NETWORKS ON THE BASIS ARCHITECTURAL CONCEPT NGN AND FN

Ibrahimov Bayram

Azerbaijan Technical University, Baku, Azerbaijan, https://orcid.org/0000-0002-5364-1181

Tagiyev Ali

Azerbaijan Technical University, Baku, Azerbaijan, https://orcid.org/0000-0002-7685-3452

Abstract

Qualitative and quantitative performance indicators multiservice telecommunication networks built in accordance with the architectural concept of NGN (Next Generation Network) and FN (Future Network) based on the technology building distributed communication networks are analyzed. Important directions for the development multiservice networks NGN and FN based on innovative technologies in the digital economy are studied. It should be noted that the future FN networks, as well as NGN (Next Generation Network) networks, are based on the principle "Many multimedia services - one network", using promising innovative technologies. In multiservice telecommunications networks, the transmitted useful and service traffic have a special structure, that is, the traffic has self-similarity properties. Given the importance of the system criterion for building multiservice telecommunication networks of the next and future generation using hardware and software systems based on SDN (Software Defined Networking), NFV (Network Functions Virtualization), ATM (Asynchronous Transfer Mode), MPLS (Multiprotocol Label Switching), IMS (Internet Protocol Multimedia Subsystem), 4G LTE (Long Term Evolution) and 5G New Radio (5G NR), you should pay attention to their performance. In addition, it is necessary to pay special attention to their ability and efficiency using various resources in the provision multimedia services and functioning in the transmission and processing of self-similar traffic. In multiservice communications networks, the proposed next and future generation technologies are designed to integrate all mobile and fixed networks to provide high capacity packet-switched communications networks, allowing a number new core, value-added and intelligent services with new cloud computing structures such as fog computing and edge computing, and big data technologies. At the same time, URLLC (Ultra-Reliable Low Latency Communication) is an important direction in the development telecommunication network technologies, which are created in order to achieve the lowest possible latency indicators while maintaining high reliability packet stream transmission. Based on the study, a new approach is proposed to construct a method for calculating the efficiency multiservice telecommunication networks, taking into account the self-similarity property transmitted useful and service traffic. On the basis of the calculation method, analytical expressions are obtained for estimating indicators channel and network resources, throughput and probabilistic-temporal characteristics of a communication network, reliability hardware and software complexes of a communication system in the provision of multimedia services. Based on the analysis indicators, the calculation method, current problems are identified, recommendations are developed to improve the efficiency using the IntServ and DiffServ architectures for multiservice telecommunication networks.

Keywords: Telecommunication network, software defined networking, IMS, model network,

INTRODUCTION

According to the principles building networks of the next NGN and the future generation FN, as a technological basis for building the transport layer of multiservice communication networks, it is supposed to use telecommunication technologies based on packet switching, which should provide the necessary level quality of service [1, 2, 3, 4].

At present, packet switching is an efficient way to jointly transmit voice and data over a single channel using SDN, IMS, and NFV technologies [2, 5, 6, 7]. In packet-switched networks, speech packets are usually transmitted synchronously, which makes it possible to restore the speech signal with a fairly good QoS (Quality

of Service). Here, for speech synchronization, various recovery algorithms based on timestamps are proposed in the implementation MPLS [8, 9, 10].

It is worth noting that the procedure for synchronizing speech packets, which is necessary for restoring speech in the receiver, is essentially passive in nature, and its implementation is rather complicated. Until recently, this method of restoring speech was mainly studied [2, 8, 9].

In MTN, on the contrary, the synchronous transmission packet streams can be considered as an active process. Therefore, from the point of view of implementation, it is more preferable. To synchronize speech packets in the MTN, the delay time in it must be fixed.

However, with multiple voice sources on the same common channel, the asynchronous nature of the ATM packet-switched network does not allow for a constant delay interval through voice priority service alone. For this reason, for synchronous transmission in a packet switched network, it is necessary to use the basic frame format adopted in the time multiplexing model. For the proposed frame structure, the delay interval during the transmission each speech packet will be equal to or a multiple of one-the interval between the moments generation of speech packets [10, 11, 12, 13, 14, 15].

Considering the above, this paper considers the problem studying methods for calculating the efficiency MTS based on the architectural concept NGN and FN.

DESCRIPTION OF THE SYSTEM FOR THE JOINT TRANSMISSION VOICE SIGNALS AND DATA

Based on the study [2, 6], it was found that within the framework of the development NGN and FN as a public communication network, the following tasks are solved: a smooth transition to a single transport technology for carrying heterogeneous traffic (Data, Speech, Video), providing new opportunities in the field development multimedia services, building a simple and efficient unified communication network for all types of applications and the active development new additional and intelligent types of services.

In Fig.1. shows a block diagram of the functioning model used to describe the process system multiplexing in the joint transmission voice packets and data packets.

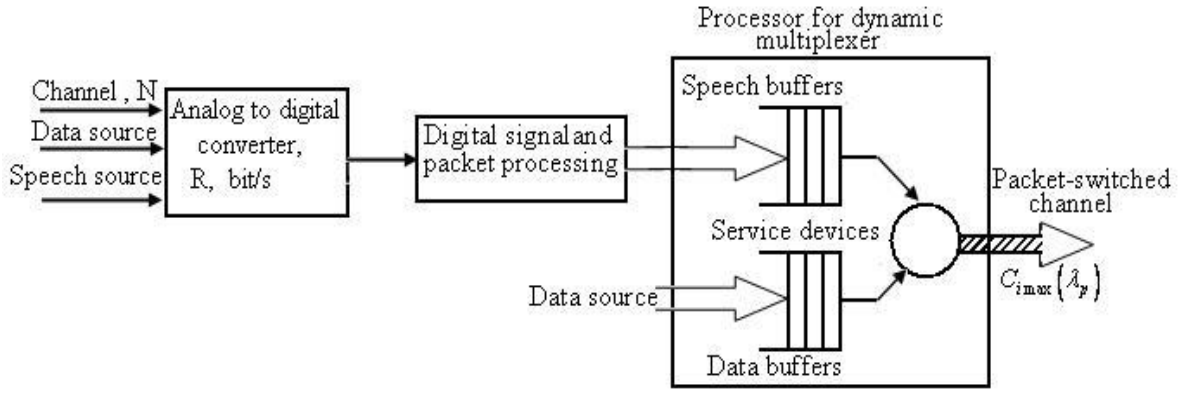


Figure1. Block diagram of the functioning of the model used to describe the process multiplexing speech signals and data

In the process of packetizing speech signals, packets are generated periodically during the active phase of speech sources [16]. To synchronize speech packets in the network, we will use their sequence numbers and the time interval between the appearance of packets at the input to the receiver. In order to derive an estimate of the interval between the moments of generation of packets and the period of activity speech sources from the received packet streams, we will use the frame structure of the same duration as the interval between the

moments of generation of speech packets. In this case, the synchronization of the latter can be carried out without additional headers, such as time markers.

In this system N , speech sources generate, during their activity, fixed-length packets every second T , with each stream packets being served synchronously at the start of the frame on a first-come, first-served basis.

Based on the timing of the speech signal in analog-to-digital converters, the transmission time of voice traffic using hardware-software packet processing complexes is determined by the expression [8]:

$$T_{nn} = \frac{L_n - r_k}{K_k \cdot V_{APK}} \quad , \tag{1}$$

where $K_k -$ the number of information elements of the code; $r_k -$ number of check digits; $L_n -$ length of the transmitted packet; $V_{APK} -$ speed of operation of hardware-software packages processing complexes.

Expressions (1) largely determine the throughput of the dynamic multiplexer and the quality of voice transmission QoS. At the same time, the throughput hardware-software complexes for processing voice traffic packets with acceptable losses of the *i*-th traffic $P_{i.n.\text{adm.}}$ is defined as:

$$\tilde{N}_{p..\max}(P_{i.n} \le P_{i.n.adm.}) = Arg \max_i \left\lfloor C_{i.\max}(\lambda_p) \cdot K_{i.\tilde{n}\alpha} \right\rfloor, \qquad i = \overline{1,n} \ , \tag{2}$$

where $C_{i.\max}(\lambda_p)$ - the maximum throughput of the system with the speed λ_p when transmitting voice traffic.

From the block diagram functioning of the model used to describe the process multiplexing the system when transmitting packets of speech signals, it can be seen that the throughput of the communication channel is equal to the throughput of the packets M of speech signals, i.e.

$$C^p_{\max}(\lambda_\partial) = R(\lambda_\partial) \cdot M \ , \quad bit/s, \tag{3}$$

where $R(\lambda_p) -$ information rate transmission of packets speech signals with intensity λ_p, bit/s.

Figure 2 shows the time diagram of the interval between the moments packet generation and the period activity of speech sources during the transmission of speech signals and data.

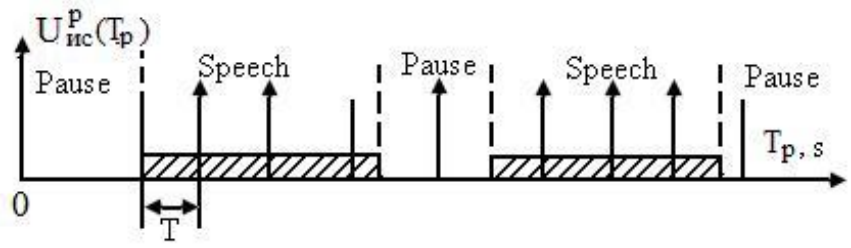


Figure 2. Timing diagrams of the interval between the moments packet generation

From the timing diagram of the interval between the moments of packet generation and the period of activity of speech sources during the transmission of speech signals, it follows that the speech signal consists sets time intervals speech t_{ap} and pause t_{kn}, which is defined as follows:

$$T_p = t_{ap} + t_{kn}, \tag{4}$$

From figure 2 it can be seen that the speech message contains "0" (speech pause) and "1" (active speech) states $U_{\grave{e}\tilde{n}}^{\eth}(\grave{O}_{\eth})$ and consists of the time active speech t_a dialogue and pause t_n:

$$U_{uc1}^{p}(T_p) = \sum_{p=1}^{h} t_{ap} + \sum_{k=1}^{e} t_{\text{кп}}, \quad \text{p} = \overline{1,h}, \ \text{k} = \overline{1,e}. \tag{5}$$

From (4) and (5) it follows that the processing of speech messages is accompanied by a large redundancy caused by speech pauses.

To eliminate redundancy and increase the efficiency of hardware-software complexes for processing voice traffic packets, various differential algorithms and speech signal interpolation algorithms can be used.

Figure 3 shows the timing diagram of the interval of the period activity speech sources during the transmission speech signals and data packets.

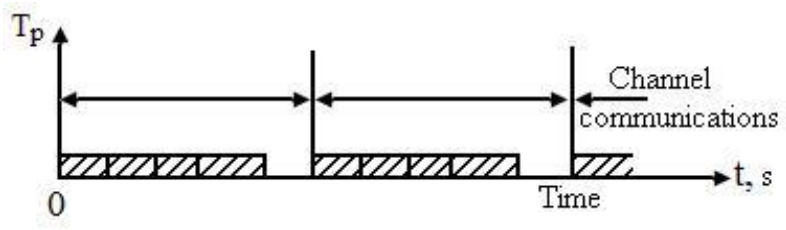


Figure 3. Timing diagram interval of the period activity of speech sources

It can be seen from the timing diagram that the synchronization of a packetized voice signal in a packet-switched MTN, while simultaneously transmitting voice and data signals, provides an efficient multiplexing scheme that uses a synchronous frame format.

Let's assume that there are two separate buffers for voice and data, and that voice signals have a higher priority in packet processing. Packets that do not fit in the frame are stored in the buffer for service during the next frame.

Therefore, buffered packets require an additional latency multiple of the frame duration. These discrete delay characteristics of speech packets make it possible to avoid processing the temporal information contained in them when reproducing a speech signal [2, 7].

In this case, as far as data packets are concerned, they are transmitted in the remaining frame time after the speech packets have been served. If the remaining frame time is not long enough for the data packet, then it is stored in a buffer for transmission in the next frame.

As a result, synchronization of voice packets is achieved at the cost of reducing the frame utilization factor. Thus, the results of the study show that the proposed circuit has discrete characteristics delay time and allows you to easily restore the speech signal in the MTN.

ESTIMATION PROBABILISTIC-TEMPORAL CHARACTERISTICS FRAME TRANSMISSION SYSTEMS

The study showed [2, 4, 9] that for the analysis and evaluation of the average frame transmission delay time, an important indicator is the capacity of the buffer drives of speech packets $N_{\delta n}^{v}$ and data packets $N_{\delta n}^{d}$. In order to explore the proposed frame structure, we assume that the sizes of the buffers speech packets and data packets at the beginning of the *i*-th frame, respectively, are equal $N_{\delta n}^{v}(q_n^{v})$ to and $N_{\delta n}^{d}(q_n^{d})$.

Taking into account the parameters of the dynamic multiplexer, the capacity of the buffer storage for the transmission of packets of speech signals is determined as follows:

$$N^{v}_{бн}(q^{v}_{n+1}) = (q^{v}_{n} - M)^{+} + a^{v}_{n} \quad , \quad q^{v}_{n} \geq M \tag{6}$$

Similarly, the buffer storage capacity when transmitting data packets is determined by the following expression:

$$N^{d}_{бн}(q^{d}_{n+1}) = (q^{d}_{n} - v^{d}_{n})^{+} + a^{d}_{n}, \qquad q^{d}_{n} \geq v^{d}_{n} \qquad , \tag{7}$$

where a^{v}_{n} and a^{d}_{n} - mean, respectively, the number packets of speech signals and data received in the system during the n-th frame; M and v^{d}_{n} - respectively, the maximum number speech and data packets served during the n-th frame.

Using (6) and (7), after some algebraic transformations, it can be shown that the generating functions moments for the sizes speech packet $Q^{v}(z)$ buffers are represented in the stationary state of the next generation networks NGN and FN, respectively, by the values [4, 6]:

$$Q^{v}(z) = \frac{\sum_{k=0}^{M-1} P[q^{v}_{n} = k] - z^{-M} \sum_{k=0}^{M-1} P[q^{v}_{n} = k] \cdot z^{k}}{1 - z^{-M} \cdot G^{v}_{a}(z)} \cdot G^{v}_{a}(z) \quad , \tag{8}$$

where M - the number of multiplexed speech channels.

Therefore, for the capacity of buffer data packets in the form generating functions moments $Q^{d}(z)$, which characterizes the stationary state of the system for transmitting heterogeneous traffic and is determined by the following expression [4, 6, 9]:

$$Q^{v}(z) = \frac{\sum_{k=0}^{M-1} P[q^{v}_{n} = k] - z^{-M} \sum_{k=0}^{M-1} P[q^{v}_{n} = k] z^{k}}{1 - z^{-M} G^{v}_{a}(z)} G^{v}_{a}(z) \quad , \tag{9}$$

where $G^{v}_{a}(z)$, $G^{d}_{a}(z)$ и $V^{d}(z)$ - generating functions moments random variables a^{v}_{n}, a^{d}_{n} and v^{d}_{n} respectively, and $P[*]$ - denotes the probability density function.

Now that the initial speech and data model has been determined, queuing statistics can be obtained from (8) and (9). In (8) $G^{v}_{a}(z)$ can be found using the Markov chain model for active speech sources [2, 4, 9].

Assuming that the execution of the speech packet queuing algorithms is stationary and that the data sources are distributed exponentially with an average value $1/\mu$, we get:

$$V^{d}(z) = \sum_{k=0}^{M-1} \exp\left[-\mu\left(1 - \frac{k}{M}\right) \cdot T(1-z) \right] P[q^{v}_{n} = k] + \sum_{k=M}^{\infty} P[q^{v}_{n} = k] \tag{10}$$

As a result, you can determine the average latency for voice and data packets $E[D^{v}]$ and $E[D^{d}]$ as follows:

$$E[D^{v}] = \sum_{k=1}^{\infty} [[\frac{k}{M} + 1]] \cdot T \cdot P[q^{v}_{n} = k] \, , \tag{11}$$

Similarly, taking into account the peculiarity packet flow queuing, the average waiting times for data packets $E[D^{d}]$ are defined as follows:

$$E[D^{v}] = \sum_{k=1}^{\infty} [[\frac{k}{\ell} + 1]] \cdot T \cdot P[q^{d}_{n} = k] \cdot P[q^{v}_{n} = l], \tag{12}$$

where $[[.]]$ - the maximum integer less than the value in parentheses.

Based on the calculation methods, the obtained analytical expressions (10), (11) and (12) allow estimating the probabilistic-temporal characteristics of MTC networks and is an indicator of the system efficiency and QoS traffic quality of service.

ANALYSIS GRAPHIC DEPENDENCE AND DISCUSSION OF THE RESULTS

Let us assume that the interval between the moments generation speech packets, or the frame duration, is 10 *ms*, that the intervals sound and silence for speech sources are distributed according to an exponential law, and their averages are 1.2 and 1.8 s, respectively [8, 14]. We also assume that the sources digital information are distributed exponentially with the same averages as for speech packets. We will not consider here constant delays due to the processing and distribution of speech packets, that is, we will accept that $T_{ad}^{r} = 0$ and $T_{ad}^{pr.} = 0$

Figure 4 shows the complementary cumulative delay distributions voice packets for a different number of input voice channels N and a fixed number output voice communication M channels.

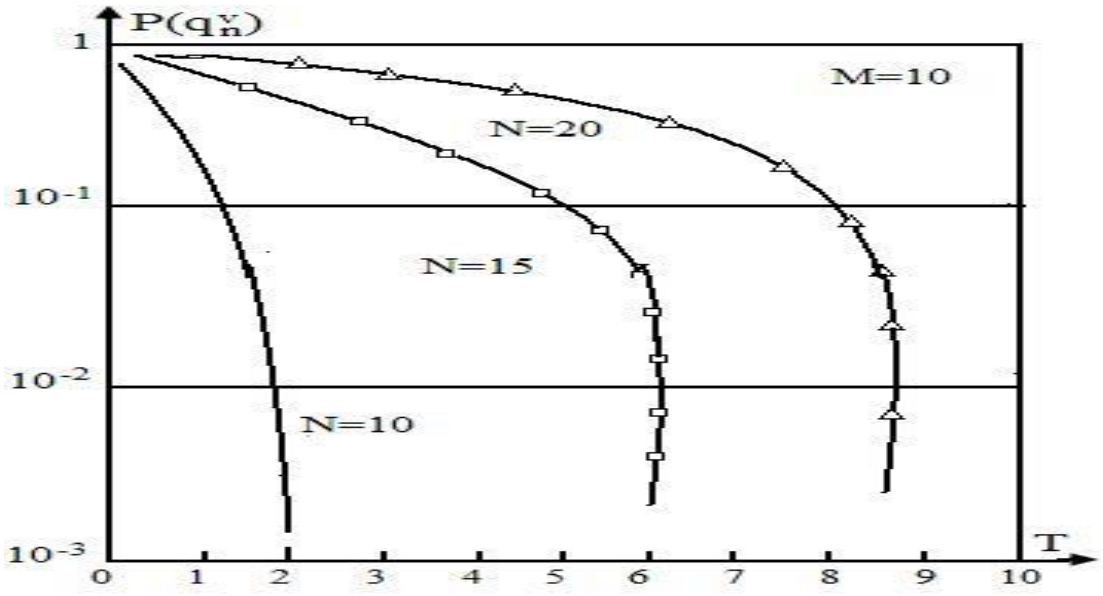


Figure 4. Graphical dependences of the distribution delay of voice packets for a different number channels

Note that in this graph, the delay of the speech packet occurs at times that are multiples of the frame duration. It can be seen that with the multiplexing coefficient

$$(N / M) = (15/10) \geq 1$$

a network voice receiver receives approximately 99.8% of voice packets in a period equal to two times the interval between voice packet generation times.

Therefore, if the output bandwidth is 10 voice channels and it is necessary to multiplex at least 15 input voice channels, then the network receiver of voice signals will be able to reproduce these signals with satisfactory quality and a delay equal to two intervals between the moments of generation of speech packets.

Figure 5 shows a graphical dependence of the average delay time of data packets on the variable bandwidth utilization factor for a different number input speech channels, where $M = 5$.

It can be seen from the family graphic dependencies that as the intensity of data transmission decreases, the packet delay interval approaches its minimum value - the duration of one frame. In addition, in this figure, the delay interval is normalized to the average service time of a data packet.

Therefore, it can be seen that the numerical results are in good agreement with the simulation results of the system obtained on the type model $M/M/1$ and $M/D/1$ with the same load activity. When the packet utilization rate is low, the delay is greater than in the system $M/M/1$ or $M/D/1$.

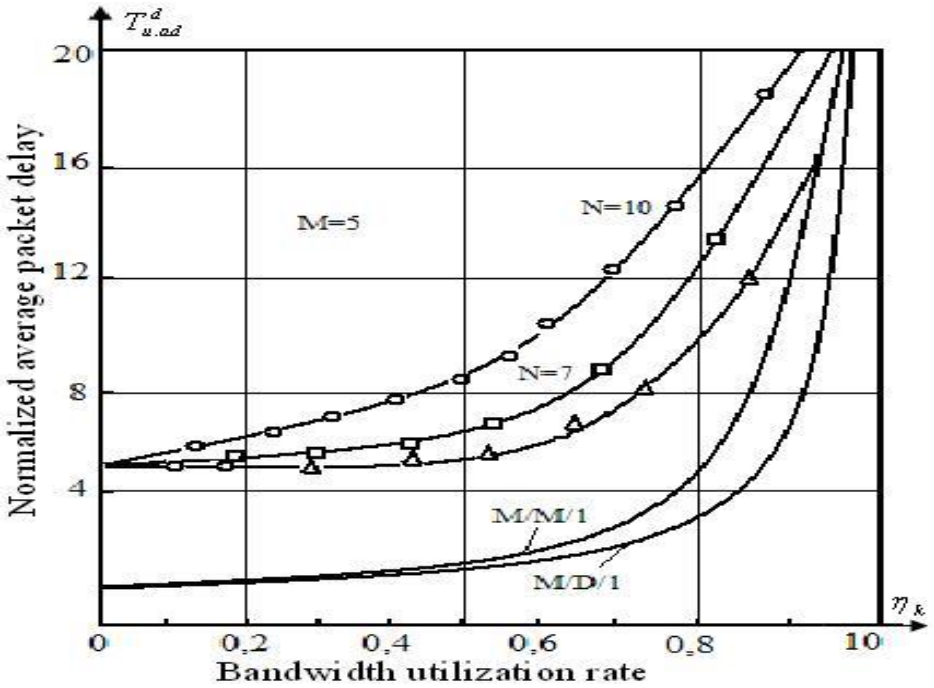


Figure5. The dependence of the average packet delay time on the bandwidth utilization factor for a different number input speech channels at $M = 5$

CONCLUSIONS

As a result of the study, the effectiveness of the functioning MTN was analyzed using the concept NGN and FN based on the technology building distributed communication networks. Developed and investigated methods for calculating the efficiency MTN, using the generating functions of the moments random variables.

A frame structure for multiplexing is proposed, which makes it possible to transmit voice messages synchronously without loss and clipping information. This scheme can also provide different rates in the speech channels as the sizes of the speech packets change. Such a synchronous frame structure can be easily used in more complex services with different bit rates without a significant reduction in the utilization of the communication channel.

On the basis of the calculation method, analytical expressions are obtained for estimating the probabilistic-temporal characteristics MTN based on the technology for constructing distributed communication networks in the joint transmission speech signal packets and data packets.

LITERATURE

1. Friis H. T. A note on a simple transmission formula.Proceedings of the IRE, 1946, vol. 34(5), pp. 254–256. doi:10.1109/JRPROC.19 46.234568.

2. Ibrahimov B. G., Hasanov M. H., Tagiyev A.D. Research of the quality of functioning fiber-optical transmission systems on the basis modern technologies// The Proceedings International Scientific Conference

«2022 Systems of Signals Generating and Processing in the Field of on Board Communications», IEEE Conference # 53456, (15-17 March), Moscow, 2022. – pp.1-5. DOI: 10.1109/IEEECONF53456.2022.9744281.

3. Nain P., Towsley D., Liu B., and Liu Z. Properties of random direction models. IEEE 24th Annual Joint Conference of the IEEE Computer and Communications Societies, 2005, vol. 3, pp. 1897–1907. doi:10.1109/INFCOM.200 5.1498468.

4. Vishnevsky VM Theoretical foundations of designing computer networks. Moscow.: Technosphere, 2003. – 512 p.

5. J.N.Daigle and J.D.Langford. Models for analysis of packet voice communications systems// IEEE J.Selected areas Communications. vol. SAC-4, no.6, Sept.1986.- pp.221-234.

6. Ibrahimov B. G., Ismaylov Z. A., Orujova M. Y. and Mammadov I. M. About One Problem of Control Network and Channel Resources in Communication Networks During Processing Useful and Service Message Signals. 2022 Wave Electronics and its Application in Information and Telecommunication Systems (WECONF), IEEE Explore Conference # 51803, 2022, pp. 1- 4,

doi: 10.1109/WECONF55058.2022.9803316.

7. Shelukhin O.I. (2018). Modeling of information systems. Textbook for universities. M .: Hot line – Telecom. - 516 p.

8. Ibrahimov B.G. Research and estimation characteristics of terminal equipment a link multiservice communication networks //Automatic Control and Computer Sciences. 2010. USA. Vol. 44, No.6, pp.360-364.

9. Ershov V.A., Kuznetsov N.A. Multiservice telecommunication networks. - M .: Publishing house of MSTU im. N.E. Bauman. 2003. - 432p.

10. Ibrahimov B.G., Hashimov E.Q., Hasanov A.H., Talıbov A.M. Research and analysis indicators fiber-optic communication lines using spectral technologies//Advanced Information Systems. 2022. Vol. 6, No. 1. pp.61-64. doi: https://doi.org/10.20998/2522-9052.2022.1.10.

11. Islamov I.J., Hunbataliyev E.Z., Zulfugarli A.E. (2021) Numerical Simulation Characteristics of Propagation Symmetric Waves in Microwave Circular Shielded Waveguide With a Radially Inhomogeneous Dielectric Filling, Cambridge University Press: International Journal of Microwave and Wireless Technologies, 9, 1-7.

12. Senderov S.M., Yusifbayli N.A., Rabchuk V.I., Huseynov A.M., Nasibov V.Kh., Vorobev S.V., Guliyev G.B., Smirnova E.M. Geopolitical Features of Energy Security in the Caspian Regions of Russia and Azerbaijan// Geopolitics of Energy, Volume 41, Issue 1, January 2019, Canadian Energy Research Institute, Calgary, Alberta, Canada, p. 5-9.

13. Lee H.H.and Un C.K. A study of on-off characteristics of conversational speech // IEEE Trans Communications., vol.COM-34, no.6, June 1986. - pp.356-368.

14. Michalopoulos D. S., Viering I., and Du L. User-plane multiconnectivity aspects in 5G // 23-rd International Conference on Telecommunications, May. 2016, pp. 1–5.

15.Efrosinin D. Sztrik J. Optimal Control of a Two-Server Heterogeneous Queuing System with Breakdowns and Constant Retrials // Communications in Computer and Information Sciences. 2016. Vol. 638. P. 57-72.

16. Ibrhimov B.G., Namazov M. B. Humbatov, R.T, Guliyev M.N. Investigation and analysis of immunity characteristics receiving discrete messages// Proceedings of the 8-th International Conference on Control and Optimization with Industrial Applications. Vol. II. 2022. - pp.237 – 239.

MATHEMATICAL MODELING OF THE ROUGH SURFACE OF THE PRINTING FORM

Aliev Eldar Abbas

Doc. Azerbaijan Technical University, Faculty of Mechatronics and Robotics, Department of Mechatronics and Machine Design, Baku, Azerbaijan, ORCİD NO: 0000-0002-6409-1293

Ismailova Shabnam Vidadi

Phd. Azerbaijan Technical University, Faculty of Mechatronics and Robotics, Department of Mechatronics and Machine Design, Baku, Azerbaijan, ORCİD NO: 0000-0001-6063-0096

ABSTRACT

It has been established that the deckle deformation depends on the surface roughness of the printing plate. To further study the influence of the surface roughness of the printing plate on the actual deckle contact area in the printing zone, a method has been developed for determining the profile of the rough surface of the offset printing plate. For this purpose, the issue of mathematical modeling of the surface profile of an offset printing plate is considered. An algorithm for obtaining a normally distributed value was adopted. A random arbitrary function for describing the surface profile is decomposed into a Fourier series. The question of approximate calculation of Fourier series coefficients to obtain an analytical expression of the surface profile is considered. The values of the roughness parameters of the printing plate surface, which provide elastic saturated contact of the deckle and, consequently, high quality of the prints, were established.

A review of studies on contact problems and roughness measurement is conducted, their advantages and disadvantages are discussed. Theoretical and experimental relations are given. The data obtained showed good convergence of the above modeling approach. The research results confirm the legitimacy of this approach. The developed method allows you to set the surface profile function, based on the normal distribution law, using a finite number of harmonics with a zero initial phase. This approach allows, with the help of the developed software, to analytically calculate the main parameters of surface roughness, as well as to ensure relative simplicity of calculations, significantly reduce the time and improve the accuracy of the calculation. The results of the studies show that for discrete contact of the surfaces of the printing plate and the deckle, the roughness of the surface of the form is one of the main factors of conjugation.

Key words: printing plate, surface profile, roughness function, Fourier series.

Introduction:

To obtain high-quality prints in the offset printing process, it is required to provide the necessary technological pressure, which creates a deformation of the elastic label in the printed contact area (Тюрин, 1980). Therefore, it is necessary to analyze and calculate the real contact area for a better understanding of friction, wear, lubrication, thermal conductivity, as well as the transfer of the ink layer from the printing plate to the deckle and from the deckle to paper (Wang, Xing and Zhao, 2014). The resulting deformations and the actual contact area depend on the properties of the deckle material and the surface roughness of the printing plate. It is known that the mutual contact of parts occurs along the peaks and projections of the roughness, which is deformed under the action of an external load (Демкин и Измайлов, 2010). With an increase in the load, the surfaces of the bodies approach each other, and the protrusions of a more rigid body are introduced into the material of a softer one (Торская, 2012). In this case, both elastic and plastic deformation of the contacting protrusions are observed, and new microroughnesses come into contact. A plurality of contact areas located at different levels are formed, on which real contact is made.

Based on the above, it can be concluded that when studying a printed pair, it is necessary to take into account the roughness of the surface of the printed form. This, in turn, will allow obtaining more accurate values of technological, design and operational parameters of the printing process.

In our case, the interacting bodies are inhomogeneous, and their surfaces are rough.

Analysis of Literature Data and Statement of Problems.

It is known that the surfaces of real bodies have deviations from their nominal shape. The measured diameters of the elastic and rigid cylinders also include the height of microroughnesses that affect the deckle deformation. Therefore, to improve the accuracy of calculating the contact characteristics in a discrete model of a rough surface, it is necessary to take into account the real distribution of microroughness sizes (Огар, Горохов и Кожевников, 2007).

In most cases, the contact of metal rough surfaces is elastoplastic (Огар, Горохов и Елсуков, 2017). In this case, it is possible to introduce irregularities into a less hard surface or to flatten the irregularities with a harder surface.

For this purpose, the forces that have arisen in the printed contact zone are determined, taking into account the surface roughness of the printing plate (Халилов, Алиев и Гусейнзаде, 2015; Халилов, Алиев и Гусейнзаде, 2015). The dimensions of the contact strip for flat printing are also established, taking into account the roughness of the surface of the printing plate (Алиев и Халилов, 2015). The mechanics of a printed pair by a friction powered has been investigated (Khalilov, Aliyev and Huseynzade, 2020). The relative gear ratio, total force in zone of printed contact, relative movement of blanket cylinder and plate cylinder are determined taking into account roughness of surface of printing plate. However, the calculation does not take into account the model of the rough surface profile of the printing plate.

In various areas of industry, surface roughness is controlled by various methods that allow you to display and measure the three-dimensional surface topography with varying accuracy (Favaro, 2004). A sampling method is proposed for measuring the roughness of the surface of a circular plane. According to the mathematical conclusion and modeling analysis, this method has good sampling results, so it can be widely used to measure the roughness of the surface of a circular plane плоскости (Meng, Wan, Wu, Shen, and Song, 2014). The theoretically obtained correlation between the roughness parameters Ra and Rq is presented. To measure these parameters, the optical reflection method is proposed (Mironchenko, 2009). An alternative method for measuring roughness is proposed using a two-dimensional profile extracted from the image of the edge of the surface of the workpiece (Shahabi and Ratnam, 2010).

Surface roughness is characterized by uncertainties that are necessary for an accurate measurement of the result, since the quality of the surface is characterized by the obtained roughness measurements. For this purpose, the determination and analysis of the measurement uncertainty of 2D roughness parameters on surfaces prepared by various processing methods are described (Farkas and Drégelyi-Kiss, 2018).

The considered methods for evaluating surface roughness indicators cannot be applied to offset printing plates due to the impossibility of ensuring the required measurement accuracy, they also have a high complexity of the process and the estimates obtained in this way are not always adequate. An objective assessment of the indicators characterizing the roughness of the shape surface is impossible without a mathematical model of the profile of the surface under study.

One of the most significant factors complicating the mathematical description of the roughness of a printing plate is its irregularity, which manifests itself due to the peculiarities of the methods of shaping surfaces in the process of manufacturing printing plates.

During electrochemical processing of offset plates, when voltage is applied to the electrodes, the anode blank material begins to dissolve. The dissolution occurs mainly on the protrusions of the microroughness of the surface, due to the higher current density at the tops. As a result of selective dissolution, i.e. dissolution of protrusions, smoothing of microroughnesses of the processed surface occurs.

Purpose and objectives of the study.

The aim of the work is to develop a mathematical model of the profile of the surface under study for an objective assessment of indicators characterizing the roughness of the mold surface. To achieve the goal, the following tasks were set:

- development of an algorithm for describing the surface profile;
- definition of a function that describes the surface profile;

- determination of the analytical expression of the surface profile.

Algorithm for describing the surface profile.

The relief profile of technical surfaces can be described by some function F(x), which will be called the roughness function in what follows. This function can be represented as the sum of the systematic component $f_0(x)$, determined by the average values of the controlled factors of the processing process, and the random component f_C (x), caused by random variations of the same and all other process factors (Sadykov and Yakovlev, 2003). Therefore, the surface profile equation can be represented as follows:

$$F(x) = f_0(x) + f_c(x) \qquad (1)$$

The selection of the systematic component $f_0(x)$ of the roughness function is justified by the very physical essence of the technological process. In the simplest case, this component can be constant, but in the general case it depends on time and on the corresponding spatial coordinates. The relief variation characterizing the random component $f_c(x)$ of the roughness function should be considered as variations in the values of parameters and profiles on a single part or relief parameters in a certain technological operation, as well as in details performed on specific technological equipment.

Thus, in mathematical modeling of surface roughness, a random component plays a significant role, the presence of which creates additional difficulties in the modeling process.

As is known, the random variable X is described by integral $F(x)$ and differential $f(x)$ distribution functions. Knowing one of these functions, it is possible to predict the behavior of a random variable in time.

Both functions are linked,

$$F(x) = \int_{\infty}^{x} f(x)dx \quad \text{и} \quad f(x) = F'(x)$$

It is known that the integral function F(x) satisfies the following conditions:

1. $\lim_{x\to-\infty} F(x) = 0,$

2. $\lim_{x\to+\infty} F(x) = 1,$

3. $F(x) -$ is a non-decreasing function.

According to the definition of an integral function, it has the following form:

$$F(x) = P(X < x) \qquad (2)$$

Obviously, with an increase in the current value of X, this probability will tend to unity. The function $F(x)$ is a monotonically increasing function.

It follows from equality (2) that,

$$P(x_1 < X < x_2) = P(x_1 < x_2)$$

If we accept that the random variable r=F(x) and find the distribution function of this variable $F_r(r)$, then we have:

$$F_r(r) = P(R < r) = P[F(X) < F(x)] = P(X < x) = F(x) = r$$

Where $R = F_r(r) - F(x)$.

According to this expression, the probability of hitting a random variable in the interval $0 - r$ is equal to the length of this interval, and this is a sign of hitting that this distribution is uniform.

As a result, we obtain an algorithm for forming a continuous value X according to a given distribution law. Since it is necessary to perform the transformation

$$X_i = F^{-1}(r_i)$$

where ri is a uniformly distributed random number, $F-1$ is a function inverse to the distribution of a random variable X.

Thus, it is possible to model numbers with a given distribution law, for example, normal. The distribution density and distribution function of this law has the form:

$$F(x) = \frac{1}{\sigma_x\sqrt{2\pi}} \cdot \int_{-\infty}^{\infty} e^{-(x-m_x)^2/(2\sigma_x^2)} dx$$

Where m_x and σ_x are, respectively, the mathematical expectation and the standard deviation of a normal random variable.

However, the direct use of the expression $F(x)$ for calculating a random variable distributed according to the normal law requires a relatively large amount of computer time, since it is associated with a numerical solution of an integral that cannot be analytically calculated. There are tabulated values of the integral for the normalized quantity $f(x) = e^{-\frac{(x-m_x)^2}{\sigma_x^2}}$, by which, having written in a table in the computer's memory, one can find random variables distributed according to the normal law.

At present, in practice, for this law, a method based on the central limit theorem of probabilities is used. According to this theorem, as a result of summing a certain number of independent random variables, the first two moments of the distribution yield a random variable approximately distributed according to the normal law.

The accepted algorithm for obtaining a normally distributed value X is as follows:

1. N random uniformly distributed values ri are drawn (usually $N \geq 12$);
2. We find the sum of these quantities $S = \sum_{i=1}^{N} r_i$, the mathematical expectation of which is equal to $m = \sum_{i=1}^{N} r_i P_i = 0{,}5N$ (since the mathematical expectation of a random quantity uniformly distributed along the length l of the interval is equal to l/2), the variance $D = \sum_{i=1}^{N} (r_i - m)^2 / N = 1$, and the standard deviation $\sigma = \sqrt{D} = 1$.
3. The value is normalized

   $S_H = (S - m)\sigma = S - 0{,}5N;$
4. The value of the random variable X, distributed according to the normal law, is found, based on the inverse normalized value:

   $$X = \sigma_x S + m \quad or \quad x_i = \sigma_i \left(\sum_{i=1}^{N} r_i + 0{,}5N \right) + m_x$$
5. In the work, both uniformly distributed random numbers and normally distributed ones were modeled in accordance with the above algorithm.

The following algorithm is based on the developed model for constructing the surface relief. Since the surface profile can in principle be described by a random function of an arbitrary form, it can be expanded into a Fourier series. In practice, when choosing the type of model, one should, first of all, proceed from the concept of the essence of the physical processes that determine the formation of surface roughness. This suggests that the surface profile of the offset printing plate, formed during electrochemical processing, is the implementation of a random function.

Function describing the surface profile.

The function describing the surface profile can be represented as the corresponding expansions into harmonic components using the Fourier series.

Each function f(x) absolutely integrable on the interval $[-\pi, \pi]$, describing the surface topography with high accuracy, can be associated with the Fourier series.

$$f(x) = \frac{a_0}{2} + \sum_{k=1}^{\infty} (a_k coskx + b_k sinkx) \qquad (3)$$

which is the expansion of a periodic function in terms of frequencies. In formula (3), a0 is the average value of the function $f(x)$. For this function, the constant coefficient a0 can be obtained by integrating both parts of formula (3) in the range from $-\pi$ to π, i.e.:

$$\int_{-\pi}^{\pi} f(x)dx = \int_{-\pi}^{\pi} \left[a_0 + \sum_{k=1}^{\infty} (a_k coskx + b_k sinkx) \right] dx \qquad (4)$$

When integrating this expression, you can get:

$$\int_{-\pi}^{\pi} f(x)dx = a_0 \int_{-\pi}^{\pi} dx + \sum_{k=1}^{\infty} \left(a_k \int_{-\pi}^{\pi} \cos kx + b_k \int_{-\pi}^{\pi} \sin kx dx \right) \qquad (5)$$

The first component on the right is $\pi \cdot a_0$, and the rest are zero. Thus, the constant coefficient of the Fourier series will be equal.

$$a_0 = \frac{1}{\pi} \int_{-\pi}^{\pi} f(x)dx \qquad (6)$$

The coefficient a_k can be obtained by multiplying the expression (4) by $\cos kx$, where k is some positive number, and integrating over the interval from $-\pi$ to π, similarly to the previous one.

Thus, the coefficient a_k can be obtained from the expression.

$$a_k = \frac{1}{\pi} \int_{-\pi}^{\pi} f(x) coskx dx \text{, where } k = 0, 1, 2, \ldots \qquad (7)$$

To calculate the bk coefficient, we multiply expression (4) by sinkx, then taking into account the above.

$$b_k = \frac{1}{\pi} \int_{-\pi}^{\pi} f(x) sinkx dx \quad \text{where } k = 0,1,2, \ldots. \qquad (8)$$

For the piecewise-smooth function given on the segment [-l, l], with the help of linear substitution, the corresponding formulas are obtained:

$$f(x) = \frac{a_0}{2} + \sum_{k=1}^{\infty}\left(a_k cos\frac{k\pi x}{l} + b_k sin\frac{k\pi x}{l}\right) \quad (9)$$

$$a_0 = \frac{1}{l}\int_{-l}^{l} f(x)dx, \quad (10)$$

$$a_k = \frac{1}{l}\int_{-l}^{l} f(x)cos\frac{k\pi x}{l}\,dx, \qquad k = 1,2,\ldots\ldots \quad (11)$$

$$b_k = \frac{1}{l}\int_{-l}^{l} f(x)sin\frac{k\pi x}{l}\,dx, \qquad k = 1,2,\ldots\ldots \quad (12)$$

Analytical expression of the surface profile.

To obtain an analytical expression for the surface profile, consider the question of the approximate calculation of the coefficients of the Fourier series, i.e., practical harmonic analysis.

In most cases encountered in practice, the function f(x) is set either in the form of a table or in the form of a curve that is drawn by some device. In these cases, the Fourier coefficients are calculated using approximate integration methods.

We consider the interval $-1 \le x \le 1$ of length 2l. This can be achieved by choosing the appropriate scale along the Axis axis. We divide the interval [-l, l] into n equal parts with points $-1 = x_0, x_1, x_2, \ldots . x_n = 1$. Then the step of division will be equal to $\Delta x = 21/n$.

We denote the values of the function f(x) at the points $x_0, x_1, x_2, \ldots x_n$ by $z_0, z_1, z_2, \ldots . z_n$, respectively. These values are determined either from a table or from a graph of a given function by measuring the corresponding ordinates. Using the formula of right rectangles, we obtain formulas for finding the Fourier coefficients for the profile function depending on a specific section y=yi:

$$a_0(y) = \frac{2}{n}\sum_{i=1}^{n} z_i(y); \quad a_k(y) = \frac{2}{n}\sum_{i=1}^{n} z_i(y)cos\frac{k\pi x_i}{l}; \quad b_k(y) = \frac{2}{n}\sum_{i=1}^{n} z_i(y)sin\frac{k\pi x_i}{l} \quad (13)$$

The decomposition accuracy is estimated using the standard deviation of the partial sum of the series.

$$\sigma(n) = \sqrt{\int_{0}^{2l}(f(x) - S_n(x)^2)dx}, \quad (14)$$

where Sn(x) is the partial sum of the Fourier series, which is calculated by the formula.

$$S_n(x) = \frac{a_0}{2} + \left[\sum_{k=1}^{n}\left(a_k cos\frac{k\pi x}{l} + b_k sin\frac{k\pi x}{l}\right)\right], \quad k = 1,2,\ldots\ldots, n \quad (15)$$

To obtain an analytical expression of the profile of the surface of the printing plate in the section y=yi, we continue in an odd way the periodic function of the profile, given on the segment [0;l], for the interval [-l,0).

Let's imagine the function obtained on the segment [-l, l], and hence this function on the segment [0;l], in the form of a Fourier polynomial in sines with any given degree of accuracy:

$$S_n(x,y) = \sum_{k=1}^{n} b_k sin\frac{k\pi x}{l} \qquad (16)$$

The coefficient b_k in (16) is calculated by the formula

$$b_k(y) = \frac{2}{l}\int_0^L z(x,y)sin\frac{k\pi x}{l}dx\,, \qquad (17)$$

$z(x,y) = f(x),|_{y=c}$ is a function of the profile with a fixed value of y; l is the length of the sample.

Let us find expressions for calculating the main parameters of surface roughness, based on the obtained surface profile equation.

For calculate

$$R_a = \frac{1}{l}\int_0^l |z|dx = \frac{1}{l}\int_0^l |S_n|dx \qquad (18)$$

The average value of the absolute value of the profile deviation Y within the base length l, we approximately calculate the value of the coefficient using the formula of average rectangles.

$$b_k = \frac{2}{l}\sum_{j=0}^{n-1}\left(hf\left(\frac{x_j + x_{j+1}}{2}\right)sink\pi\frac{\left(\frac{x_j + x_{j+1}}{2}\right)}{l}\right) \qquad (19)$$

We get the expression

$$R_a = \frac{1}{l}\int_0^l \left|\sum_{k=1}^{n}\sum_{j=0}^{n_i-1}\left(hf\left(\frac{x_j + x_{j+1}}{2}\right)sink\pi\frac{\left(\frac{x_j + x_{j+1}}{2}\right)}{l}\right)sin\frac{k\pi x}{l}\right|dx\,, \qquad (20)$$

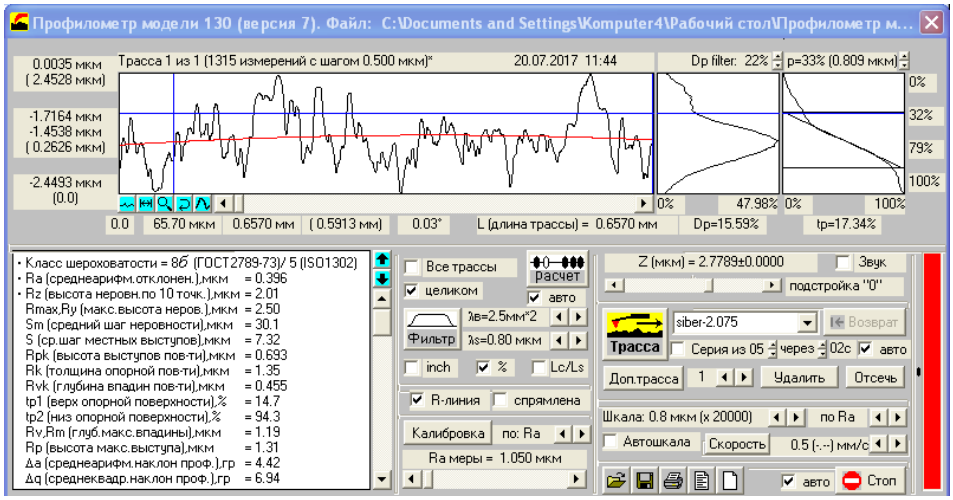
where n_1 by the formula of middle rectangles, while calculating the Fourier coefficients b_k, the segment [0; l] is the number of partitions, h −step of divisions.

To calculate R_z, it is enough to select 5 maximum and 5 minimum values from a series of "z" values and use the formula.

$$R_z = \frac{1}{5}\left(\sum_{i=1}^{5} z_{imax} - \sum_{i=1}^{5} z_{imin}\right). \qquad (21)$$

Discussion of research results.

For the analytical representation of the surface profile and the evaluation of the roughness parameters of the printing plate, software and algorithms have been developed using the Visual basic language. The data used by the software are the coordinates of the surface profile of the printing plate, established by the profilogram taken by the profilometer mod 130. Figure 1 shows the profilogram using the LUXEL VX 9600 Fujifilm printing plate as an example.



Pic. 1. Profilogram of the surface of the printing plate

The standard Chart component is used for plotting graphs. Figure 2 presents a graph based on initial data (fig. 2, profile 1) and a graph based on analytical calculation (fig. 2, profile 1).

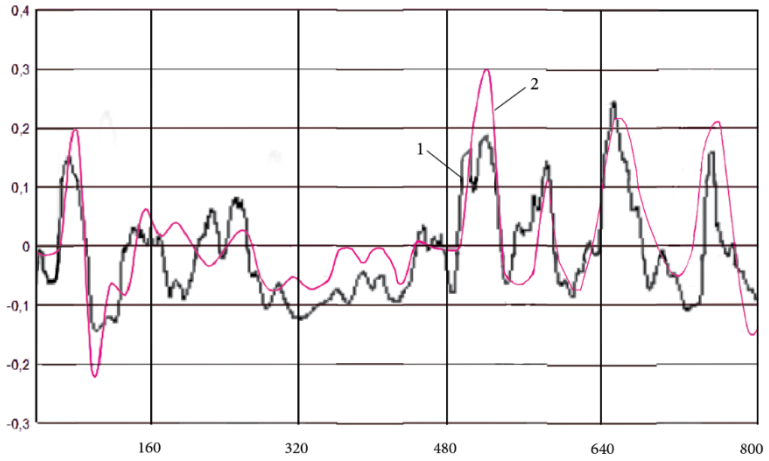


Fig. 2. The initial graph of the surface profile

The developed approach allows to determine the surface profile function based on the normal distribution law using a finite number of harmonics with a zero initial phase, which allows analytical calculation of the main parameters of the surface roughness using the developed software, as well as the relative simplicity of the calculations, reflecting the practical value of the work. allows to significantly reduce the time and increase the accuracy of the calculation.

Table 1 presents examples that illustrate the compliance with the experimental data of the results of calculating the roughness indices performed according to the developed model. The relative deviations of the calculated values of the roughness parameters from the average experimental values for each sample are given. The average relative deviation of Ra, Rz, Rmax is 0.152, 0.368, 0.151, respectively.

It has been verified that the model is adequate according to the Fisher criterion with a confidence level of 0.95.

Table 1. Roughness parameters

Sample name (printing form)	Experimental values of roughness, mkm			Roughness parameters, by model mkm			Standard deviation %			Dispersion		
	R_a	R_z	R_{max}	R_a	R_z	R_{max}	R_a	R_z	R_{max}	R_a	R_z	R_{max}
LUXEL VX 9600 Fujifilm	0,101	0,559	0,884	0,117	0,586	0,929	4,52	4,57	5,36	0,00205	0,00209	0,00288
XM – P ZAC Fujifilm	0,224	1,184	1,661	0,231	1,236	1,652	7,09	5,98	8,11	0,00503	0,00357	0,00658
LH – PLE ZAC Fujifilm	0,372	1,598	2,532	0,383	1,640	2,518	5,22	5,08	5,98	0,00272	0,00258	0,00358

Conclusions

1. The developed algorithm allows you to determine the function that describes the profile of the rough surface of the printing plate;
2. Based on a certain function that describes the surface profile of the printing plate, an analytical expression has been developed that illustrates the surface profile without profilometric measurement
3. The developed analytical expression of the surface profile and the software allow calculating the main parameters of the surface roughness, which correspond to the experimental data.

Literature:

1. Торская Е.В. Моделирование фрикционного взаимодействия шероховатого индентора и двухслойного упругого полупространства //Физическая мезомеханика, 2012, Т.15, № 2, С. 31-36.
2. Огар П.М., Горохв Д.Б., Кожевников А.С. Контактные задачи в герметологии неподвижных соединений. Братск: Изд-во БрГУ, 2007.242 с.
3. Огар П.М., Горохв Д.Б., Елсуков В.К. Критерии появления пластических деформаций при контактировании шероховатых поверхностей в соединении технологического оборудования //Системы Методы Технологии. 2017, № 3 (35) С. 32-39.
4. Огар П.М., Елсуков В.К., Угрюмова Е.В. Относительная площадь контакта при внедрении и сплющивании сферических неровностей шероховатых поверхностей // Системы Методы Технологии. 2018. №1 (37) с.12-17.
5. Тюрин А.А. Печатные машины, автоматы. Москва. Книга, 1980. 416 с.
6. Халилов И.А., Алиев Э.А., Гусейнзаде Э.М. Влияние шероховатости поверхности печатной формы на силы трения в контактной зоне. //АзТУ. Научные труды. Том 1, № 4, Баку, 2015. С. 33-36.
7. Халилов И.А., Алиев Э.А., Гусейнзаде Э.М. Влияние шероховатости поверхности ротационной печатной формы на силы образованные в печатной контактной зоне. //АзТУ. Машиноведение. Международный научно-технический журнал. Том 4, № 1, Баку, 2015. С. 38-41.
8. Алиев Э.А., Халилов И.А. Влияние шероховатости поверхности печатной формы на размеры контактной полосы при плоском печатном процессе. //АзТУ. Научные труды. Том 1, № 3, Баку, 2015. С. 108-110.
9. Khalilov I.A., Aliyev E.A., Huseynzade E.M. The effect of surface roughness of a printing plate on the mechanics of a friction printing pair. // SYLWAN, Vol. 164, 2020, p.13-32.
10. Favaro P. Scene and motion reconstruction defocused and motion-blured images via anisotropic diffusion / Favaro, M. Burger and S. Soatto // In Proc. 8th European Conference on Computer Vision (ECCV´04), Prague, May 2004. – P. 257-269.

11. Садыков С.С., Яковлев А.В. Математическая модель шероховатой поверхности, Формирование и исследование // Заводская лаборатория. -2003. -№. 9.С. 52-53.

12. Kai Meng, Yongjian Wan, Fan Wu, Lijun Shen, Weihong Song, "A sampling method to measure surface roughness of circular flat," Proc. SPIE 9282, 7th International Symposium on Advanced Optical Manufacturing and Testing Technologies: Optical Test and Measurement Technology and Equipment, 92820J (18 September 2014); doi: 10.1117/12.2073329

13. Mironchenko, V.I. Correlation of roughness parameters R_a and R_q with an optical method of measuring them. *Meas Tech* **52**, 354–359 (2009). https://doi.org/10.1007/s11018-009-9289-0

14. Shahabi, H.H., Ratnam, M.M. Noncontact roughness measurement of turned parts using machine vision. *Int J Adv Manuf Technol* 46, 275–284 (2010). https://doi.org/ 10.1007/s00170-009-2101-0

15. Farkas G., Drégelyi-Kiss Á. Measurement uncertainty of surface roughness measurement. XXIII International Conference on Manufacturing (Manufacturing 2018). IOP Conf. Series: Materials Science and Engineering 448 (2018) 012020 doi:10.1088/1757-899X/448/1/012020

16. Jia Chun Wang, Bo Qiang Xing, Teng Zhao. Finite Element Analysis (FEA), Fractal Characterization, Real Contact Area, Rough-Smooth (2014) Surface Contact. Key Engineering Materials (Volumes 579-580). P. 517-522. DOI: https:// doi.org /10.4028/ www.scientific. net/KEM.579-580.517

17. Демкин Н. Б., Измайлов В. В. (2010). Зависимость эксплуатационных свойств фрикционного контакта от микрогеометрии контактирующих поверхностей. Трение и износ. т.31, № 1, с. 68—77.

ELECTROPHYSICAL PROPERTIES OF THE BINARY COMPOUND In_2Se_3

Aysel Talıflı

Sumgait State University, Faculty of Physics and Electroenergetics, Department of Solid State and Semiconductor Physics, Sumgait, Azerbaijan, ORCID NO: 0000-0003-1201-7742

Eldar Gojaev

Azerbaijan Techinal University, Faculty of Energy and Automation, Department of engineering physics and electronics, Baku, Azerbaijan, ORCID NO: 0000-0003-1864-6515

ABSTRACT

In the presented work, In_2Se_3 compounds were obtained, In-99.99% were used as starting materials: Se-OSCH 6-05, single crystals were grown by Bridgeman-Stogbarger methods, X-ray phase analysis was performed, X-ray images were obtained on a URS-50 diffractometer and on a filtered K-radiation λ=1.54178 Å, voltage $25 \cdot 10^3$V, current $15 \cdot 10^{-3}$ A, measuring range 1 m/s. Time constant 11, slit width S,: S_2: $S_3 \div -0.5$; 1; $4.25 \cdot 10^{-3}$, brush rotation speed 0.15 K/s and it was found that this phase crystallizes in a hexagonal syngony with lattice parameters a=4025 Å, c=28762 Å. Studies of the temperature dependence of the specific electrical conductivity, the Hall coefficient and the thermo- e.m.f. determined the concentration of free carriers, the Hall mobility and the width of the forbidden zone by the high temperature slopes of the specific electrical conductivity and the Hall coefficient, the Hall mobility of carriers. It is established that In_2Se_3 is a characteristic semiconductor compound with a band gap of 0.9 eV.

Keywords: Hall coefficient, electrical conductivity, In_2Se_3 binary compound, thermal-e.m.f. coefficient.

INTRODUCTION

Diagrams of the In-Se system state were constructed by methods of physicochemical and X-ray phase analysis and it was revealed that nanosystems form compounds InSe, In_2Se, In_2Se_3 and intermediates In_6Se_7, In_4Se_3, In_2Se_2. Of these compounds, InSe, In_2Se_3 melt congruently, other compounds identified in the In-Se system melt incongruently. Among these compounds, In_2Se_3 attracts special attention. This compound refers to compounds of type $A^{III}B^{VI}$. The In_2Se_3 compound decomposes easily under the action of acids in a humid environment, gradually oxidizing. This compound has a defective structure. This is due to the fact that metal atoms are occupied under the lattices. Along with these studies of the structure and properties, it was revealed that the results obtained by different authors practically do not agree. In the literature there are structural data on the presence of several – α, β, γ, δ - type of syngony of these phases. The physical characteristics of the In_2Se_3 compound obtained by different authors also differ significantly. Thus, values of 0.97-1.25eV were obtained for the band gap width, 2.35 eV were obtained at room temperature for the band gap width, this compound has a p-type of conductivity, the resistivity varies within $10\text{-}10^3$ Om •cm. In_2Se_3 single crystals in the range of 400-800 nm have a high optical absorption coefficient, and are widely used in various fields of photoelectronics.

Thus, due to the fact that the literature data on the study of physical properties differ significantly, we experimentally investigated the temperature dependences of the specific electrical conductivity, Hall coefficient and thermo-e.m.f. In_2Se_3 and determined their physical parameters of this phase.

EXPERIMENTAL METHODOLOGY

The In_2Se_3 compound was synthesized by melting the initial components taken by stoichiometry. In and Se with a frequency of 99.9998% were used for synthesis [3]. Synthesis of this compound was carried out in pumped and sealed quartz ampoules. In the synthesis of the stoichiometric composition of the In_2Se_3 compound, the following regime was adhered to. The temperature of the heater containing quartz ampoules with the substance was increased at a rate of 100K/hour to a temperature of 1000K, where it was held for two

to three hours, and then the temperature was raised to a temperature of 1200K with an additional holding for another two hours, after which the ampoule was cooled at a rate of 2K /h to room temperature. For the purpose of final homogenization, the ingots obtained were subjected to prolonged annealing (110-120 hours). The obtained crystals were subjected to X-ray phase analysis. Radiographic studies of the In_2Se_3 compound were carried out on a DRONE-3M (CuKa radiation λ=1.54178Å) with a low temperature prefix.Decoding of the In_2Se_3 X-ray showed that this phase crystallizes in a hexagonal syngony with lattice parameters a=4025 Å, c=28762 Å.

The experiments were performed using a MiniFlex 600 X-ray diffractometer from RIGAKU (X-ray patterns) and a JSM 6610-LV scanning electron microscope from JEOL (stoichiometry).

The samples were examined on a MiniFex 60 XRD (Rigaku) X-ray diffractometer. mode - 40 kV, 15 mA. The research interval is 2 θ, 5-60 degrees. The study of radiographs was carried out with reference to the PDF-2 database (2011).

The results of stoichiometric analysis showed that the compound In_2Se_3 contains the following results:

Element	**Weight**	**Nuclear**
Se	48.64	57.94
In	51.36	42.06

RESULTS AND THEIR DISCUSSION

The temperature dependence of the electrical conductivity and the Hall coefficient in the direction along the layers for In_2Se_3 in the temperature range 300-1000 K is shown in fig. 1. All the studied samples in the entire measured temperature range have a p-type of conductivity. In the In_2Se_3 crystal, the change in the temperature dependence of the Hall mobility of current carriers at high temperatures follows the law $\mu \sim T^{-3/2}$, which testifies to the main role of carrier scattering on longitudinal acoustic phonons (fig. 2b). As can be seen from fig. 2a coefficient of thermo- emf in In_2Se_3, with an increase in temperature, it first increases in the temperature range of 300-450K, reaches a maximum, and with a further increase in temperature, the area of intrinsic conductivity for In_2Se_3 decreases according to the measurement of thermo-emf. Just as the electrical conductivity begins at 450K, i.e. for In_2Se_3, there is no complex character of the change in thermo-emf from temperature, typical for materials with a multi-valley energy spectrum and with a significant difference in the mobility of electrons and holes.

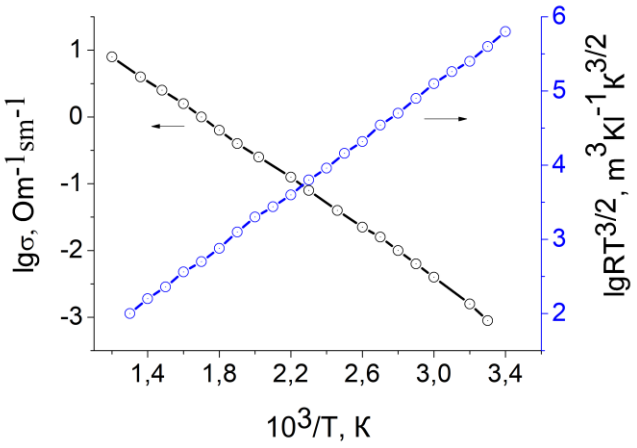


Fig.1 Temperature dependences of electrical conductivity (a) and Hall coefficient (b) of binary compound In_2Se_3

A similar dependence is also observed for the Hall coefficient. The temperature dependences of the electrical conductivity and the Hall coefficient are in good agreement. The band gap determined from the slope of the dependencies $lg\sigma=f(10^3/T)$ and $lgRT^{3/2}=f(10^3/T)$ is 0.9 eV and 0.89 eV. These values of the width of the

forbidden zone are in good agreement with each other and the signs calculated by us from the zone structure, respectively [1]. In Fig. 2 and the temperature dependence of the coefficient of thermo-e.m.f. is given, which is typical for compounds of type $A^{III}B^{III}C_2^{VI}$ increases at low temperatures, and decreases at high temperatures. This indicates the complexity of the zone structure of this phase, which is confirmed when calculating the zone structure In_2Se_3. In fact, in the work [2] it was found that in the energy range -15÷-10 eV, the lowest valence bands owe their origin to the 4s states of Se. Another group of zones about -5 eV are formed from the s-states of indium atoms and from the p-states of Se atoms. Finally, in the energy range of -4÷0 eV, the uppermost group is formed mainly from the p-states of Se atoms and partly from the p-states of indium atoms. The minimum of the conduction band is formed mainly from the s-states of indium and from the p-states of selenium atoms. In fig. 2b shows the dependence of the Hall mobility of current carriers, from which it follows that the change in the Hall mobility occurs according to the law $T^{-3/2}$, indicating the scattering of carriers on longitudinal acoustic phonons.

CONCLUSIONS

Studies of the electrical properties of the binary compound In_2Se_3 revealed that this phase is a typical p–type semiconductor.

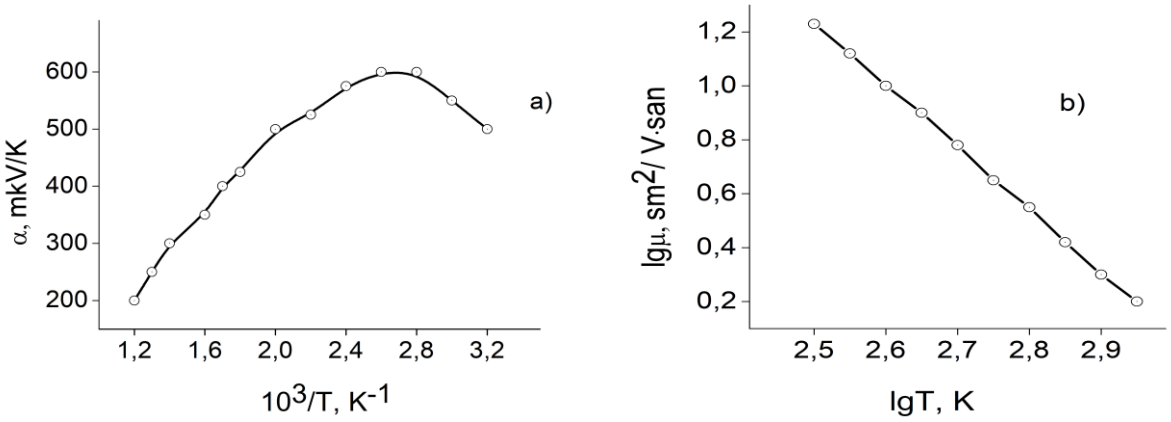


Fig.2. Temperature dependences of the thermo-e.m.f. coefficient (a) and the Hall mobility (b) of the In_2Se_3 compound

1. E.M. Qocayev, Z.A. Cahangirli, A.F.Garibli , S.A. Nabiyeva, Electronic spectrum of α- In_2Se_3 compound and nature of the chemical bonds, Journal of Baku Engineering University Physics 2020. Volume 4, Number 2, pg. 82-85
2. T. Zhai, X. Fang, M. Liao, X. Xu, L. Li, B. Liu, Y. Koide, Y. Ma, Y. Yao, Y. Bando. Fabrication of hihg-quality In_2Se_3 nanowire arrays toward hihg-performance visible-light potodetectors. ACS, Nano,Volume4, Iusse 3 2010,Pages 1596-1602
3. И.В. Боднарь, Г.А. Ильчук, Р.Ю. Петрусь, В.Ю. Рудь, Ю.В. Рудь, М. Сергинов Электрические свойства монокристаллов In_2Se_3 и фоточувствительность барьеров Шоттки Al/In_2Se_3, Физика и техника полупроводников, 2009, том 43, вып. 9

SPECTRA OF RAMAN SCATTERING OF LIGHT IN $A^{III}B^{VI}$ TYPE COMPOUNDS.

Eldar GOJAYEV

Prof. Dr., Azerbaijan Technical University, Department of Engineering Physics and Electronics, Baku

Sevinj OSMANOVA

Dos. Dr., Azerbaijan Technical University, Department of Engineering Physics and Electronics, Baku, Azerbaijan.

Naghi GASIMOV

Dos. Dr. Azerbaijan State Oil and Industry University, Department of Physics, Baku

Azerbaijan Technical University, Department of Engineering Physics and Electronics, Baku, Azerbaijan., ORCID NO: 0000-0001-9243-2297

Abstract

In the present work, the results of the study of the Raman scattering spectra in the binary compounds TlSe and InSe with a Ge impurity, in the ternary compounds $InGaTe_2$, $TlGaSe_2$ and the quaternary compound $Tl_2InGaSe_4$ in the frequency range 0-500 cm^{-1} are presented. The crystals were grown by Bridgman-Stockbarger methods. The excitation source was a Nd:YAG laser with an output wavelength of 532 nm and a maximum power of 10 MW. It was possible to change the laser power in the range of 0.001-10 MW, the beam diameter was several microns during focusing. Samples for studying the Raman spectra of crystals were prepared on high-quality crystals by simple chipping along the (0001) plane in the form of plane-parallel plates. The results of the Raman study of compounds involving elements of the IIIB subgroup showed that the spectral lines of the spectra of the studied ones differ significantly.

Key words: Raman scattering spectra, binary compounds, quaternary compound $Tl_2InGaSe_4$, Bridgman-Stockbarger

Introduction

As is known, most of the light propagating in a medium is absorbed and transmitted in accordance with the laws of reflection or absorption (these processes correspond to the real and imaginary parts of the permittivity, which is independent of the electric field in a linear approximation) [1-4]. A very small part of the light is scattered in all directions by the inhomogeneities of the medium. These inhomogeneities can be static, for example, dislocations in a crystal (and scatter light elastically, without changing its frequency), or they can be dynamic - fluctuations in the density of charge carriers. During elastic scattering of light, a quantum of incident light is absorbed and a quantum of scattered light is born, while the creation or annihilation of excitation quanta of the crystal occurs, in particular, elastic scattering of light can occur not only on lattice vibrations. Free and bound charge carriers, plasmons, polaritons, and magnons can also scatter light. If part of the energy of the incident light is spent on excitation of lattice vibrations, the frequency of the scattered light is less than the frequency of the supply (Stokes process), otherwise the energy is taken from vibrations of the crystal lattice (anti-Stokes process) and the frequency of the scattered light is greater than the frequency of the incident light [5-9]. The frequencies at which the spectra of scattered light are located are "combinations" of the frequency of the incident and the frequency of the natural phonon. Because of this, scattering is called “combination scattering” (or as usually Raman scattering). Thus, non-elastically scattered light carries information about the vibrational spectrum of the material under study for Raman scattering of light (RSL), which is characterized by a change in the frequency of the scattered radiation compared to the frequency of the exciting radiation. In contrast to photoluminescence, during Raman scattering the scattering system does not go into an excited state for short periods of time. In this case, the excited states are virtual. In the process of absorption of an incident photon, a virtual electronic transition occurs, corresponding to the creation of an electron-hole pair. Then, due to the creation or annihilation of a phonon, the electron passes into another virtual state corresponding to a new electron-hole pair. Finally, by emitting a scattered photon $\hbar\omega_2$, the electron returns to its original state. It

should be noted that, unlike infrared radiation, Raman spectra are due to the polarization of electron shells by external monochromatic electromagnetic radiation in the visible or UV range. Raman can be considered as a result of modulation of the induced dipole moment of nuclei. Since RS occurs with the participation of vibrations of the crystal lattice, it turned out to be possible to obtain important information about the dynamics of the motion of atoms and molecules of a crystal using this phenomenon [10–11]. One of the advantages of Raman, in comparison with other methods of radiation of vibrations in crystals, is the fact that the research tool is visible light. However, Raman observation in crystals is difficult due to the fact that the effective Raman cross section per unit cell is 10^{-27}-10^{-28} cm^2, and it turns out that the power of the scattered radiation reaching the receiver is 10^{-11}-10^{12} W.

Thus, powerful sources of monochromatic radiation and very sensitive receivers are required for Raman observation.

Experimental technique

Micro-Raman spectroscopy is a fairly effective method for determining internal stresses in crystals, since the frequency positions of the lines in the vibrational spectra make it possible to determine with great accuracy the magnitude of mechanical stresses that arise in crystals, and the use of micro-Raman scattering makes it possible to determine mechanical stresses in micron-sized regions. An important advantage is also the possibility of scanning the laser beam with a small step over the surface of the sample and determining the homogeneity of the crystal. The excitation source was a Nd:YAG laser with an output wavelength of 532 nm and a maximum power of 10 MW. It was possible to change the laser power in the range of 0.001–10 MW. Since the beam diameter was a few microns during focusing, a significant irradiation intensity could be achieved in this way.

Samples for studying the Raman spectra of bulk crystals were prepared on high-quality ingots by simple chipping along the (0001) plane in the form of plane-parallel plates. The laser beam is directed perpendicular to the plane of the layers. The reflected light through the spectrometer was incident on the receiver of the CCD camera.

Results and its discussion

Figure 1 shows the Raman spectra of the binary compound InSe doped with Ge at a temperature of 300 K and a laser power of 1 mW. A diffraction grating of 1800 lines per 1 mm was used, the exposure time was 1 minute. As follows from the figure, four spectral lines appear on the Raman spectrum at frequencies of 0, 40, 105, 180, and 230 cm^{-1}. The intensity of the first peak at a frequency of 0 cm^{-1} was 3200 a.u., the peak half-width was 4 cm^{-1}, the intensity of the second peak at a frequency of 40 cm^{-1} was 350 a.u., the peak half-width was 30 cm^{-1}, the intensity of the third maximum at a frequency of 115 cm^{-1} is 4800 a.u., the maximum half-width is 20 cm^{-1}. The intensity of the fourth weaker maximum at 180 cm^{-1} is 500 a.u., the peak half-width is 7.5 cm^{-1}. The intensity of the fifth maximum at a frequency of 230 cm^{-1} is 1500 a.u., the maximum half-width is 12 cm^{-1}.

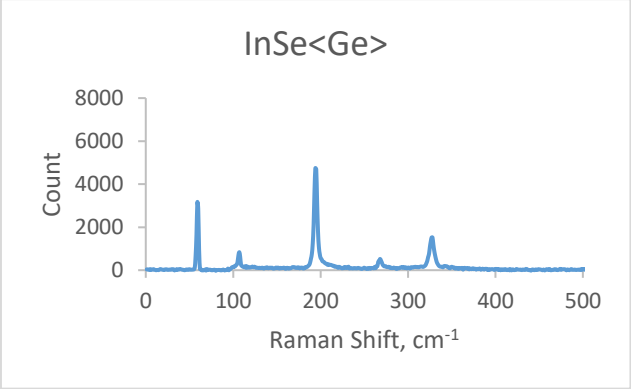


Fig.1 Raman spectra of the binary compound InSe with a Ge impurity.

Fig. 2 shows the Raman spectra of the binary compound TlSe doped with germanium. As follows from Fig. 2, three spectral lines are observed in the Raman spectrum of TlSe<Ge>. The first spectral line is observed at a frequency of 38 cm^{-1}, the intensity of the maximum is 1331 a.u., the peak half-width is 9 cm^{-1}, the intensity of the second maximum is at a frequency of 142 a.u. cm^{-1} was 763 a.u., the peak half-width was 23.5 cm^{-1}, the intensity of the maximum at a frequency of 159 cm^{-1} was 3750 a.u., the half-width was 35 cm^{-1}.

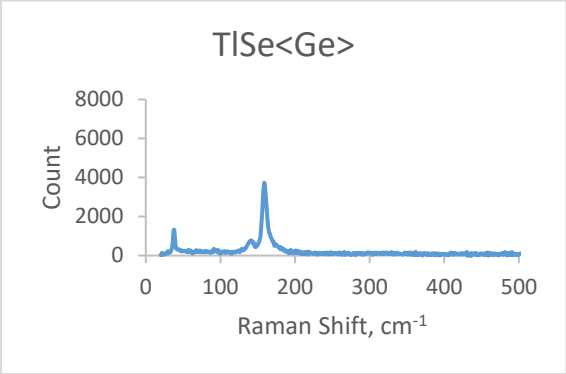


Fig. 2. Raman spectra of the binary compound TlSe doped with germanium.

In the Raman spectrum of InGaTe2, two spectral lines are observed, at a frequency of 123 cm^{-1} with an intensity of 7576 a.u., the peak half-width is 26.5 cm^{-1}, the second, weaker line is observed at a frequency of 142 cm^{-1} with an intensity of 3631 a.u., with a peak half-width of 24 cm^{-1} (Fig. 3.).

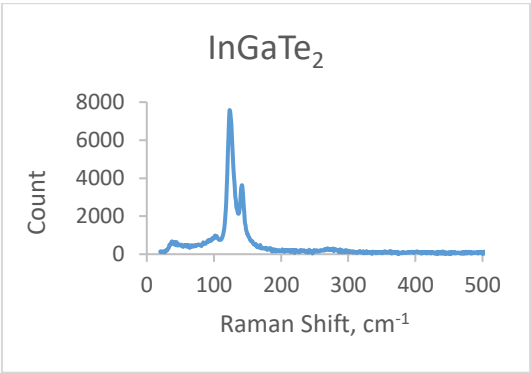


Fig. 3. Raman spectra of the ternary compound InGaTe2.

In the Raman spectrum of the ternary compound TlGaSe2 shown in Fig.4. four spectral lines are observed. At a frequency of 58 cm^{-1}, a peak with an intensity of 5428 a.u. is observed, the half-width of the peak is 4 cm^{-1}. At a frequency of 106 cm^{-1}, a double peak is observed with an intensity of 831 a.u., the peak half-width is 15 cm^{-1}.

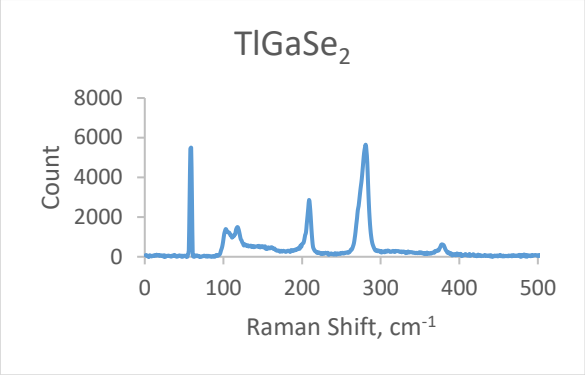


Fig. 4. Raman spectra of the ternary compound TlGaSe2.

The third spectral line is observed at a frequency of 210 cm^{-1}, the intensity of the peak is 2468 a.u., the half-width is 22.5 cm^{-1}, the fourth pronounced maximum appears at a frequency of 280 cm^{-1}, the intensity of the maximum is 5484 a.u., peak half-width 40 cm^{-1}, the fourth, weaker line appears at a frequency of 376 cm^{-1}, maximum intensity 494 a.u., peak half-width 15 cm^{-1}.

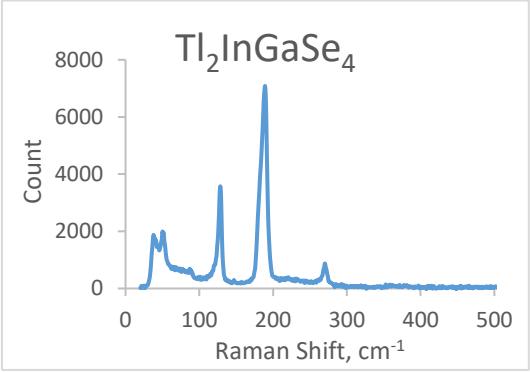


Fig. 5. Raman spectrum of the quaternary compound $Tl_2InGaSe_4$.

In the Raman spectrum of the quaternary compound $Tl_2InGaSe_4$ shown in Fig.5. four spectral lines are observed. At a frequency of 47 cm^{-1}, a peak with an intensity of 1639 a.u. is observed, the peak half-width is 20 cm^{-1}. At a frequency of 50 cm^{-1}, a peak is observed with an intensity of 1902 a.u., the peak half-width is 25 cm^{-1}, the third spectral line is observed at a frequency of 129 cm^{-1}, the peak intensity is 3574 a.u., the half-width is 19 cm^{-1}, the fourth pronounced maximum appears at a frequency of 201 cm^{-1}, the intensity of the maximum is 7086 a.u., the peak half-width is 17.5 cm^{-1}, the fifth maximum appears at a frequency of 297 cm^{-1}, the intensity of the maximum is 743 a.u., the half-width peak 25 cm^{-1}.

References

1. Jabarov S.H., Mammadov T.G., Mammadov A.I., Kichanov S.E., Alieva V.B., Lukin E.V., *J. Surf. Invest.*, 9 (2015), 35.
2. Ismayilova N.A., Jabarov S.H., *Optoelectron. Adv. Mater.-Rapid Commun.*, 11 (2017), 353.
3. Mikailov F.A., Basaran E., SEnturk E., Tumbek L., Mammadov T.G., aliev V.P., *Solid State Commun.*, 129 (2004), 761.
4. Panich A.M., *J. Phys.-Condens. Mat.*, 20 (2008), 293202.
5. Power CH., Molina I., Chacon L., Gonzalez J.,*Rev. Mex. Fis.*, 56 (2010), 118.

6. Borovoy N.A., Gololobov G.L., Gorb A.N.,Isayenko G.L., *Phys. Solid State*, 52 (2010), 1610.
7. Allakhverdiev K.R., Ahmedzade N.D., Mammadov T.Q., Mammadov T.S., Seyidov M.YU.,*Low Temp. Phys.*+, 26 (2000), 56.
8. Aliyev V.P., Babayev S.S., Mammadov T.G., Seyidov M.YU., Suleymanov R.A., Mikailov F.A., *T. Azerbaijan Natl. A. Sci. Phys. Astron.*, 24 (2004), 45.
9. Dubrovinskaia N.A., Dubrovinsky L.S., *Rev.Sci. Instrum.*, 74 (2003), 3433.
10. Yuksek N.S., Gasanli N.M., *Cryst. Res. Technol.*, 40 (2005), 264.
11. Perez F.V., Cadenas R., Power C., Gonzalez J., Chervin C.J., *J. Appl. Phys*, 101 (2007), 063534.

RELIABILITY ANALYSIS OF THE HOUSING-COVER CONNECTIONS OF GEAR REDUCERS

Iftikhar CHALABİ

Azerbaijan Technical University, Department of "Mechatronics and mashine design" Baku, Azerbaijan, H. Javidavenue 25, ORCID NO-0000-0003-2289-7931

ABSTRACT

Violation of the density between the housing and the cover of gear reducers can lead to gaps, noise and impacts from gear engagement, an increase in the load on the teeth, and in many cases, to their failure. Therefore, the presented report assessed the reliability of bolted connection connecting the housing and the gearbox cover according to various performance criteria. It was found that the probability of a violation of the density between the parts is many times higher than the probability of loss of bolt strength.

Keywords: Gear reducers, reliability, threaded connections, endurance, joint density

INTRODUCTION

Gear reducers are one of the main components of modern machines and equipment, and the correct assessment of their reliability, increasing their durability and maintainability are of great importance. Bolted or screw connections connecting the casing and the cover of gear reducers belong to the elements, the risk of failure of which is not too great. The failure of the elements of the connection with the loss of its strength is rare. But deformation of the connecting elements, spontaneous unscrewing of the nut and, as a result, a violation of the tightness between the casing and the cover can lead to disruption of the normal operation of the gearbox as a whole. A violation of the tightness between the casing and the gearbox cover can lead to errors, noise and shocks in the engagement of the wheels, an increase in the load on the gears, and in many cases, to their total failure.

In the presented work, as the main criteria for the functionality of the casing-cover connection of gear reducers, the tensile strength condition of the threaded part of the bolt, the condition of tightness between the casing and the cover and the condition of non-slip between the casing and the cover were taken as a basis.

DETERMINATION OF BOLT LOADS

To assess the reliability of the connection, it is necessary to determine the load on the most loaded bolt. Using the example of a single-stage cylindrical gearbox, we will consider the problem of determining the loads on the housing-cover connections. The reactions of the support F_n' and F_n'' arise in the bearing supports of the shaft from the action of the full normal force F_n arising in the cylindrical transmission (Fig. 1). These forces are transmitted directly to the bolts connecting the housing and the gearbox cover. We can also divide the force F_n acting on a more loaded bolt into two components. Firstly, the sliding force F_q is transmitted not only to the bolts, but also to the outer ring of the bearing. Therefore, this force does not significantly affect the reliability of the connection. Another component of the F_a is transmitted directly to the bolts and tries to detach the gearbox housing from the cover. The gaping force acting on the most loaded bolt, based on the figure, can be determined as follows:

$$F_b = F_{1a} = \frac{F_a(0{,}5a+e)}{a} = \frac{F_a(a+Dsin\alpha_w)}{2a}. \quad (1)$$

Where a - the distance between the bolts; D - outer diameter of the bearing; e - the distance between the axis of the shaft and the line of action of the force F_a; α_w - engagement angle.

For standard gears, $\alpha_w=20^0$ is accepted (Дунаев П.В., О.П.Леликов 2013). Taking $\mu_a=D/a$, we can write expression (1) as follows:

$$F_b = \frac{1}{2}F_a(1+\mu_a \cdot sin\alpha_w). \quad (2)$$

Structurally, it is possible to accept μ_a=0,65÷0,7 for existing gearboxes of cylindrical gears.

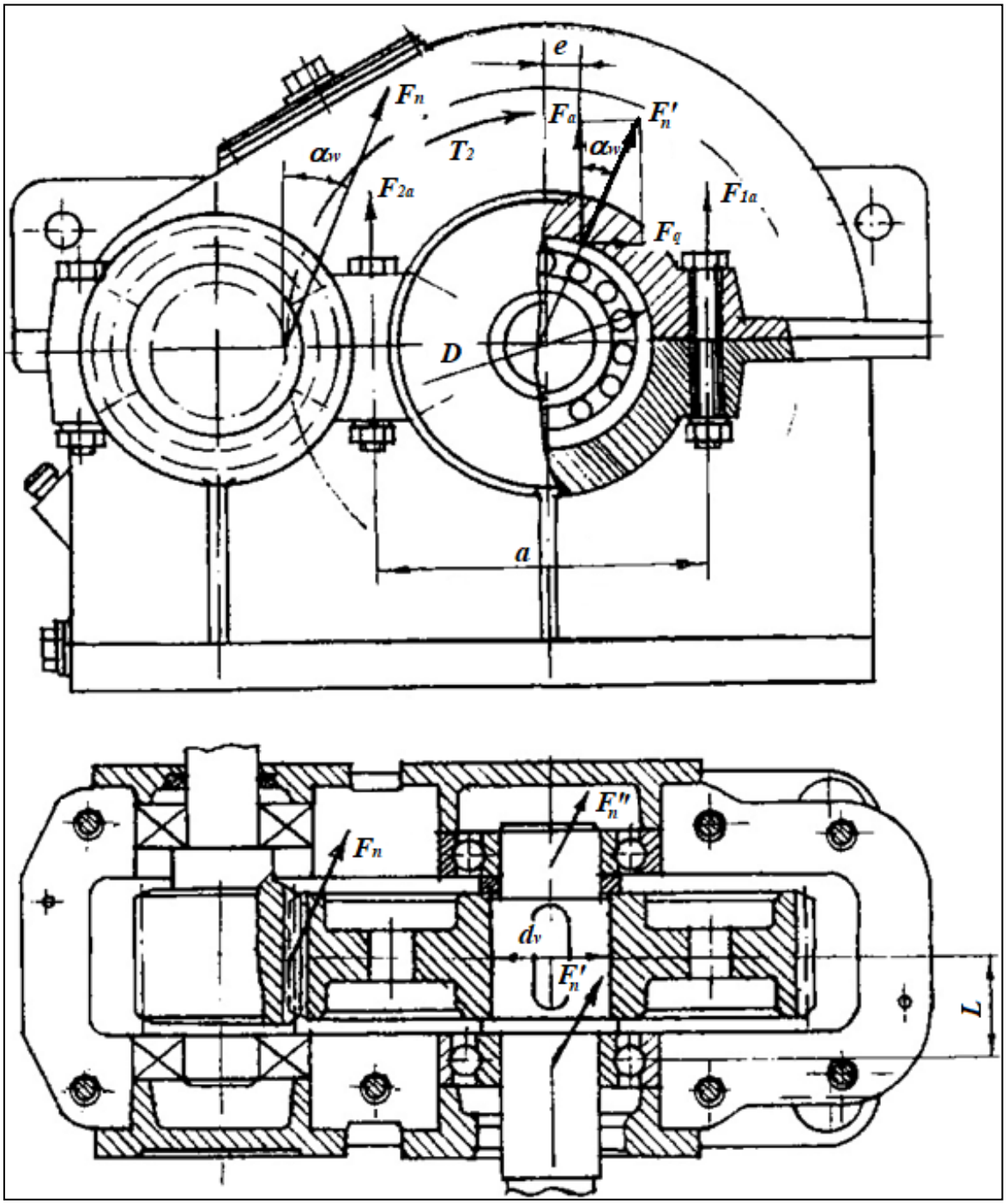


Fig. 1. Design scheme of the housing-cover connection of a cylindrical straight-tooth gearbox

Given the equal load on the supports (i.e. $F_n'=F_n''=0.5\ F_n$) in a single-stage cylindrical gearbox and the dependence of the normal force generated by the engagement on the torque transmitted by the driven shaft ($F_n=F_t/\cos\alpha_w=2T_2/d_2\cdot\cos\alpha_w$), (Abdullayev A.H., Güməyev M.H., Məmmədov H.S. (2014), we can determine the force F_a, which tries to break the connection of the housing and cover, as follows:

$$F_a = F_n' \cdot cos\alpha_w = \frac{1}{2} F_n \cdot cos\alpha_w = \frac{F_t}{2} = \frac{T_2}{d_2}.$$

Where F_t - circumferential force arising from cylindrical straight-tooth transmission; T_2 - torque on the driven shaft of the gearbox; d_2 - dividing diameter of the driven wheel.

Considering the last expression in the formula (2), we can write:

$$F_b = \frac{T_2}{2d_2}(1 + \mu_a \cdot sin\alpha_w). \quad (3)$$

As can be seen from the last expression, the external dividing force falling on the bolt directly depends on the torque on the driven shaft of the gearbox, inversely proportional to the diameter of the dividing circle of the driven wheel. First, let's consider the issue of assessing reliability by the condition of bolt strength. To ensure the density between the parts of the housing-cover connection of the gearbox, the bolt is tightened by a certain initial tension force F_0, and thus the force $F_и$ is not transferred to the bolt completely (Fig. 2, a). Part of the load is perceived by the deformed housing and the flanges of the cover. In this case, the calculated force acting on the bolt in the direction of its axis should be calculated according to the following formula (Иосилевич Г.Б., 1988):

$$F_h = F_0 + \chi F_b. \quad (4)$$

Where is F_0 - preliminary bolt tightening force; χ - external load factor.

The external load factor takes into account which part of the external force is perceived by the bolt. This coefficient becomes dependent on the geometric dimensions and elastic modulus of the materials of the connected parts and the bolt. Calculations show that when metal elements are connected, it receives values in the range χ=0.2÷0.4 (Иосилевич Г.Б., 1988).

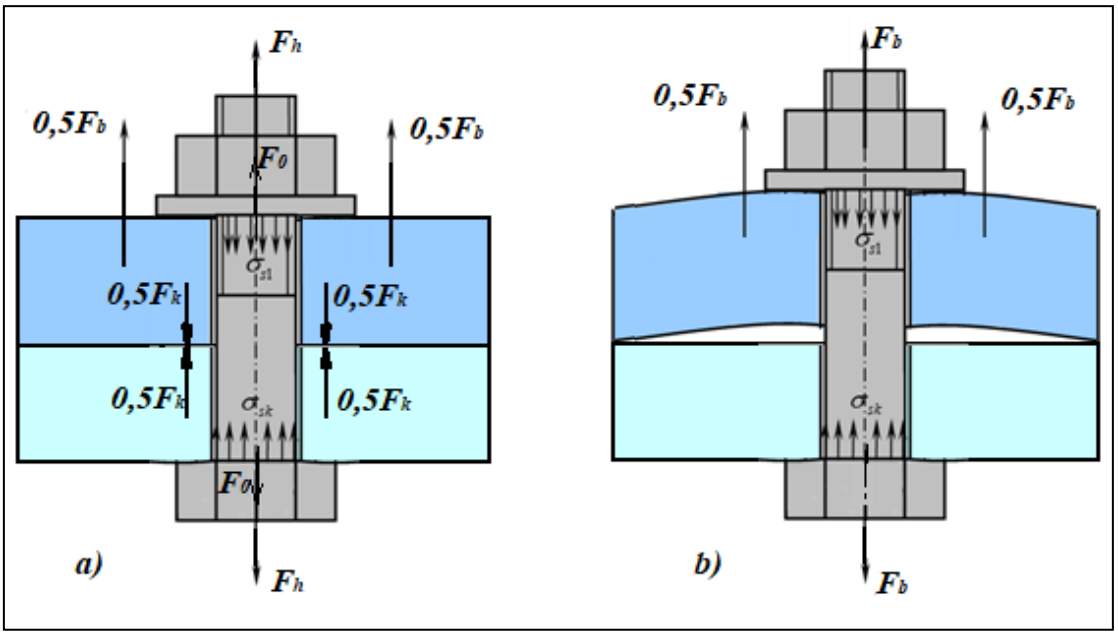


Fig.2. Design scheme of the bolted connection of the gearbox

In practical calculations, it can be assumed that the load and bearing capacity of the connection parts obey the normal distribution (Fig. 3). Then for the case under consideration, the survival probability of the connection according to the condition of bolt strength can be calculated by the following formula (Tschalabi I., Jäger P. 2005):

$$R_b^* = \Phi\left(\frac{\overline{W}_b - \overline{F}_h}{\sqrt{\sigma_{Wb}^2 + \sigma_{Fh}^2}}\right) \text{ or } R_b^* = \Phi\left(\frac{\overline{W}_b - \overline{F}_h}{\sqrt{\left(V_{Wb} \cdot \overline{W}_b\right)^2 + \left(V_{Fh} \cdot \overline{F}_h\right)^2}}\right). \quad (5)$$

Where $\overline{W}_b$ - Mathematical expectation of the bearing capacity of the bolt;

$\bar{F}_h$ - Mathematical expectation of the calculated load on the bolt;

σ_{Wb} - Standard deviation of the bearing capacity of the bolt

σ_{Fh} - Standard deviation of the calculated load on the bolt;

V_{Wb} - Coefficient of variation of the bearing capacity of the bolt;

V_{Fh} - Coefficient of variation of the calculated load on the bolt.

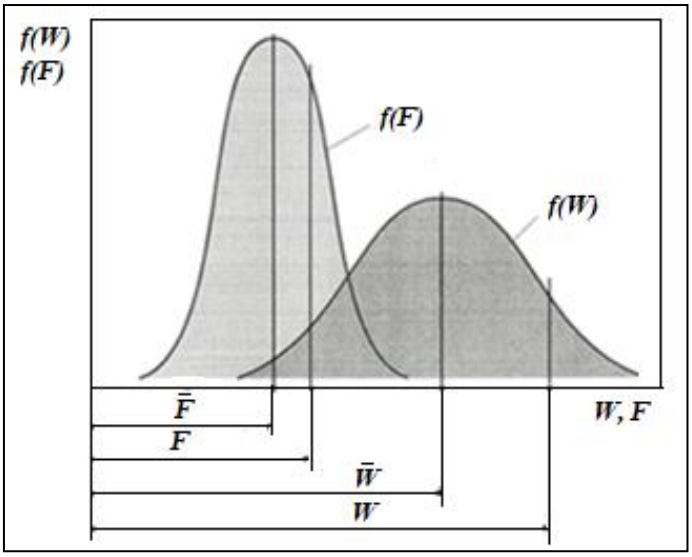


Fig. 3. Normal distribution of load values and load-bearing capacity of the elements of the housing-cover connection of gearbox

When the joint is opened for some reason in the housing-cover connection (for example, as a result of an increase in external force or self-unscrewing of the thread), F_0=0 and χ=1 occur, so that the bolt is only under the action of force F_b (Fig. 3, b). In this case, the probability of trouble-free operation of the housing-cover connection of the gearbox according to the condition of bolt strength can be calculated as follows:

$$R_b^{**} = \Phi\left(\frac{\overline{W}_b - \overline{F}_b}{\sqrt{\sigma_{Wb}^2 + \sigma_{Fb}^2}}\right) \quad \text{or} \quad R_b^{**} = \Phi\left(\frac{\overline{W}_b - \overline{F}_b}{\sqrt{\left(V_{Wb} \cdot \overline{W}_b\right)^2 + \left(V_{Fb} \cdot \overline{F}_b\right)^2}}\right). \qquad (6)$$

Where $\bar{F}_b$ - mathematical expectation of the force acting on the bolt when the density is violated;

σ_{Fb} - Standard deviation of the force acting on the bolt when the density is violated;

V_{Fb} - Coefficient of variation of the force acting on the bolt when the density is violated.

To ensure the condition of density in the housing-cover connection of the gearbox, the residual force arising at the contact of the connected parts must satisfy the condition $F_k=F_0-F_d>0$ (Иосилевич Г.Б., 1988). Where F_d is the part of the force acting on the connection perceived by the details, which can be defined by the following expression:

$$F_d = (1 - \chi)F_b. \qquad (7)$$

Thus, in the housing-cover connection, the density condition can be written as $F_0>F_d$, and the probability that the connection will work without failure in accordance with this condition can be determined by the following expression:

$$R_k = \Phi\left(\frac{\overline{F}_0 - \overline{F}_d}{\sqrt{\sigma_{F0}^2 + \sigma_{Fd}^2}}\right) \text{ or } R_k = \Phi\left(\frac{\overline{F}_0 - \overline{F}_d}{\sqrt{\left(V_{F0}\cdot\overline{F}_0\right)^2 + \left(V_{Fd}\cdot\overline{F}_d\right)^2}}\right). \quad (8)$$

Where $\bar{F}_0$ is the mathematical expectation of the preliminary tightening force;

$\bar{F}_d$ is the mathematical expectation of the force perceived by the connected parts;

σ_{F0} is the mean square deviation of the preliminary tightening force;

σ_{Fd} is the mean square deviation of the force perceived by the connected parts;

V_{F0} is the coefficient of variation of the preliminary tightening force;

V_{Fd} is the coefficient of variation of the force perceived by the connected parts.

Let's use the classical methods of probability theory to determine the ratio between reliability indexes according to various criteria for the survival probability of the housing-cover gearbox connection. Suppose that a test was carried out on the housing-cover connection with the number m, and after a certain period of operation, the bolt with the number n failed, losing strength. Of these, the bolt n_1 of the number failed, provided there is no breach of tightness, and the bolt n_2 of the number failed as a result of loss of tightness. Suppose that with the number of bolts m as a whole, there was no density violation on the number of bolts m_1, and with the number of bolts m_2, density violations occurred. The probabilities of uptime or failure according to various criteria can be described schematically in accordance with Fig. 4.

The survival probability of the bolt according to the strength condition can be determined by the following expression:

$$R_b = 1 - \frac{n}{m}. \quad (9)$$

Similarly, we can determine the survival probability by the density condition (R_k) and the probability of density violation (P_k) by the following formulas:

$$R_k = \frac{m_1}{m}; \qquad P_k = 1 - R_k = \frac{m_2}{m}. \quad (10)$$

The survival probabilities of the bolt according to the strength condition in cases of absence and presence of density, respectively, can be determined by the following expressions:

$$R_b^* = 1 - \frac{n_1}{m_1}; \qquad R_b^{**} = 1 - \frac{n_2}{m_2}. \quad (11)$$

By solving expressions (9-11) together, we can obtain the following expression to determine the probability that the bolt will work without failure due to the strength condition:

$$R_b = R_k(R_b^* - R_b^{**}) + R_b^{**}. \quad (12)$$

As already mentioned, a breach of tightness in the housing-cover connection of the gear reducer should also be considered as a transmission failure. Because the violation of tightness also leads to the fact that the gearbox loses its function. Given this, the probability that the housing-cover gearbox connection will work according to both criteria without failure can be determined as follows:

$$R = 1 - \frac{n_1+m_2}{m}. \quad (13)$$

Having made some simplifications in the last expression, given expressions (10) and (11), we can write the following expression:

$$R = R_k \cdot R_b^*. \quad (14)$$

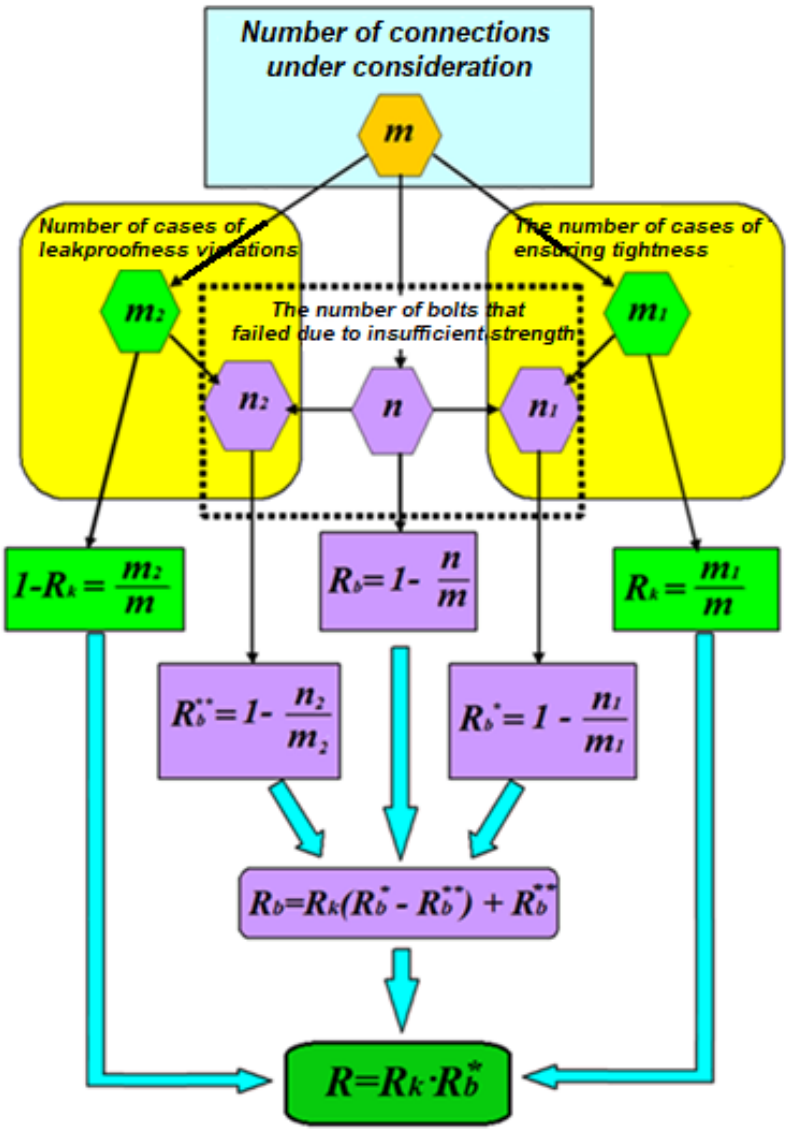


Fig. 4. Scheme for the reliability analysis of the connection between the casing and the cover of reducer

An assessment of the reliability of the casing-cover connection of a cylindrical gearbox with a gear ratio u=4, an axial distance a_w=224 mm, a diameter of the division of the bearing wheel d_2=360 mm at the location of the bearings is considered. Standard M12 bolts with a thread pitch of P=1,5 mm and an internal diameter of d_1=10,16 mm were selected for connecting the housing-cover gearbox. Since there were no special requirements for the design, the bolt material was selected steel 20, which corresponds to strength class 4.6. The yield strength of the bolt material was adopted as the bearing capacity. The yield strength of the selected material is assumed to be σ_y=240 N/mm2. Depending on the magnitude and fluctuation of the torque acting on the bearing shaft of the gearbox, as well as on the bearing capacity of the bolt material, the survival probability of the housing-cover connection was calculated.

Since the connection of the housing and the gear reducer cover is designed with a large margin factor according to all failure criteria, it is practically impossible for the connection to fail at rated load. The loss of operability of this connection occurs due to accidental overloads or shocks that occur during operation. Therefore, it is important to assess the reliability of the housing-cover connection depending on the load according to various performance criteria. To this end, on the basis of the methodology described above, an assessment of reliability indicators was carried out according to various criteria for the operability of the connection in question. In these calculations, the coefficient of variation of the bearing capacity V_{Wb}=0,05, the coefficients of variation

of the calculated and external forces acting on the bolt, $V_{Fh}=V_{Fb}=0,07$, the coefficients of variation of the initial tightening force and compression forces created on the part, $V_{F0}=V_{Fd}=0,1$ are adopted. The results are graphically shown in Fig. 5.

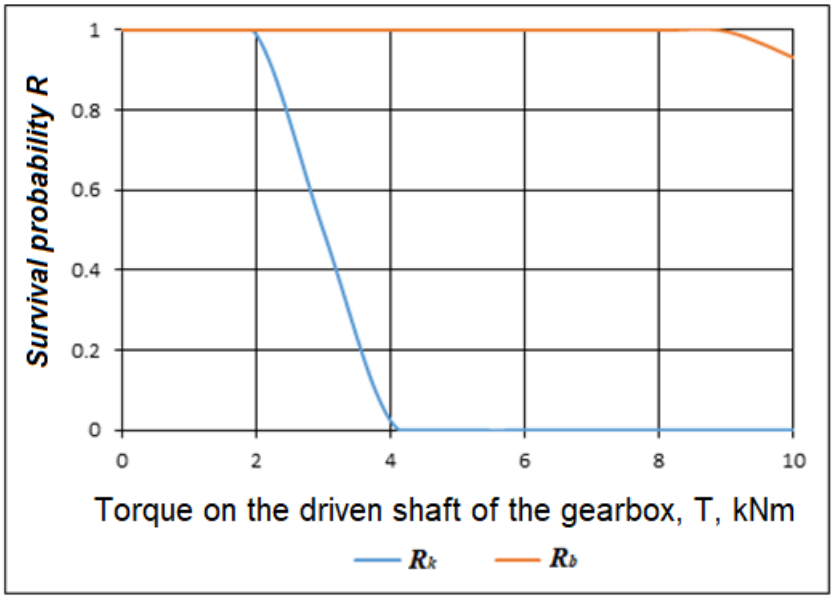


Fig. 5. Dependence of the reliability indicators of the housing-cover gearbox connection on the transmitted torque

CONCLUSIONS

As can be seen from the graph in Fig. 5, the reliability of the casing-cover connection of a cylindrical gear reducer is mainly determined by the condition of joint density. Since the bolts are designed with a large margin factor, even with a load many times higher than the nominal one, the indicator of their reliability gets the maximum value. And with a load exceeding the nominal by about two times, the probability of trouble-free operation drops sharply due to the tightness condition. And violation of the tightness condition can lead, as already mentioned above, to the occurrence of gaps in the engagement and shaft supports. This can eventually lead to the appearance of sound and vibration, as well as to increased impacts during engagement. Therefore, it is very important to control the initial tension force created on the bolts in order to increase the tightening in the housing-cover connection.

REFERENCES

1. Abdullayev A.H., Güməyev M.H., Məmmədov H.S. (2014) Tətbiqi mexanika. Dərs vəsaiti. – Bakı: “Təhsil” NPM.
2. Дунаев П.В., Леликов О.П. (2013) Детали машин. Курсовое проектирование. Учебное пособие. – Москва: «Машиностроение».
3. Иосилевич Г.Б. (1988) Детали машин. Учебник. – Москва: «Машиностроение».
4. Tschalabi I., Jäger P. (2005) Systematische Sicherheits- und Zuverlässigkeitsanalyse für Schraubenverbindungen//Konstruktion. Nr.1-2, S. 59-64.

FORTITUDE OF THE OPTIMUM HEIGHT OF THE MAIN BEAM OF A BRIDGE CRANE

Shahin Charkasov

Azerbaijan Technical University, Baku Azerbaijan

Summary

This article investigates the issue of optimal design of the wall of the double-walled girder of the bridge crane. A mathematical expression was proposed for determining the optimal height of the wall, taking into account the requirement to satisfy the stiffness condition of the main beam, and a numerical example was considered to visualize the result of the report.

Keywords: bridge crane, main beam, optimum height, moment of inertia, wall height

ABSTRACT

One of the basic indicators of the technology of the construction of the product is its metal capacity. Metal capacity should correspond to the optimal amount of metal used in the production of the product. The mass of the product is about 70% of its cost. A 1% reduction in mass leads to a 5% reduction in cost [1]. For structures with space metal construction, the concept of metal capacity is of greater importance. One of such constructions is the bridge crane construction. The metal capacity of the metal construction of this type of cranes is 80% of its total metal capacity. From this point of view, the optimization of the dimensions of individual elements of the bridge crane's metal structure remains one of the urgent issues in crane manufacturing.

PROBLEM STATEMENT

Construction of lifting machines is always accompanied by the search for optimal scientific solutions. Of these, the method of determining the optimal height of the main girder of a bridge crane is widespread (where the minimization of the weight of the main girder is considered as a condition). In all these or other solution methods, the search for the optimal solution is related to the search for one parameter, accompanied by several solution options. Recently, in connection with the wide application of computer technology, new mathematical methods have been developed in engineering reports, such as probability theory, variance analysis, linear programming, and other fields. With this, these methods have created a solid basis for the optimal design of lifting machines.

The task of optimal design of lifting machines is to choose an option from its constructive options that corresponds to the extreme value of the optimization criterion. As such criteria, productivity, cost, mass, longevity, etc. of the forklift. can be accepted. In some cases, the costs incurred can be chosen as the general criterion of optimization. This includes the sum of the annual costs of operating the machine and the initial capital costs.

In simple cases, the optimization problem is performed by mathematical operations that are not so complicated. But when the objective function depends on several variables, more complex methods must be applied. These methods are divided into two groups: classical method and mathematical programming. Classical methods include differential calculus, Lagrange's multiplication method, calculus of variations, and mathematical programming its linear, non-linear, and dynamic methods, Pontryagin's maximum principle, etc. is attributed.

The search for the optimal solution to the problem is performed in the following order:

- a mathematical model of the process or the constructed object is built.
- the optimization criterion is determined and its relationship with the main parameters characterizing the object is determined.
- a system of constructive, technological, operating and economic restrictions is defined;

- the problem of extreme design is solved by using one of the above methods

According to the analytical methods of optimization of cross-sectional dimensions of overhanging beams, the following principles should be expected in order to achieve a rational consumption of the beam material:

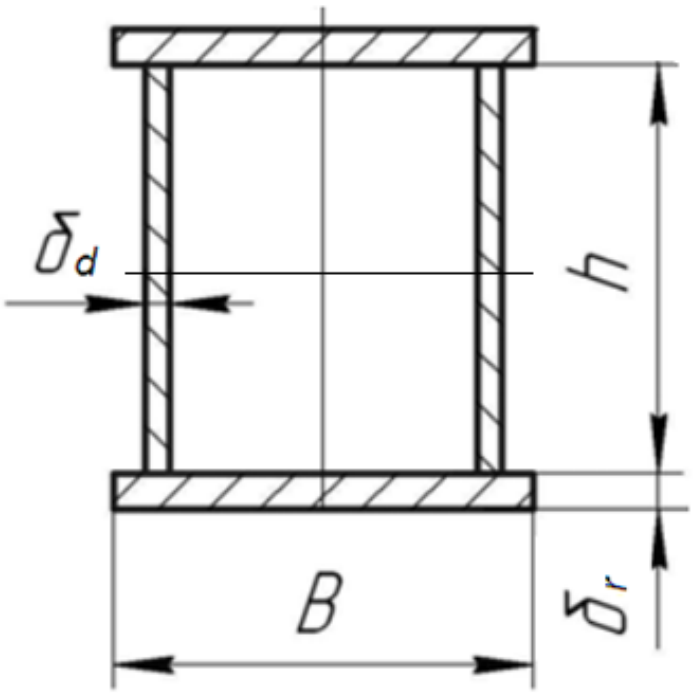
- a certain resistance moment Wx corresponding to the bending moment must be obtained (strengthening);
- a certain moment of inertia J x corresponding to the allowable deflection must be obtained (ensuring stiffness).

SOLUTION OF THE ISSUE

In crane construction, the height of the main girder of a bridge crane is structurally determined by the following expression:

h = (1/15...1/17)

Let's look at the issue of optimal design of the height of a double-walled beam (Figure 1) provided that the required rigidity is ensured.



When solving this issue, the following two conditions should be considered:

1. The maximum height of the beam hmax is limited by the condition of purchasing a beam with minimal mass;

2. The smallest height hmin of the beam is limited by the allowable value of the deflection of the beam caused by the positive load.

The weight per unit length of the main beam can be written as:

$$q = 2\gamma\left(B\delta_r + h\delta_d\right), \quad (1)$$

where - the specific gravity of the material;

- shelf width;

- shelf thickness;

h - height of the wall;

- is the wall thickness.

Deflection of the beam due to positive load in the vertical plane

$$f = \frac{QL^3}{48EJ_x} \le [f], \tag{2}$$

where Q is the weight of the payload located in the middle of the passage;

L – the length of the passage;

E = 2.1. 105 MPa - modulus of elasticity of steel;

Jx is the moment of inertia of the cross section of the beam with respect to the horizontal axis passing through its center of gravity, determined by the following formula:

$$J_x = 0{,}5B\delta_r\left(h+\delta_r\right)^2 + 0{,}5\delta_d h^3$$

[f] is the allowable deflection of the beam in the vertical plane caused by the positive load, defined as follows [2]:

$$[f] = L/700$$

Since h >> we can ignore the thickness of the shelf. In this case, expression (2) is written like this

$$f = \frac{A}{B\delta_r h^2 + \delta_d h^3} \le [f], \tag{3}$$

To solve the problem, let's use Lagrange's multiplication method [3]. In this method, the Lagrangian function is formulated, and the optimal value of the studied parameter is determined by checking the necessary extremum condition. Lagrangian function

$$L(B,h) = \varphi(B,h) + \lambda f(B,h), \tag{4}$$

Here $\varphi(B,h)$ is the objective function,

$\lambda f(B,h)$ - is the limiting function. Here λ - is the Lagrange constant.

The objective function

$$\varphi(B,h) = 2\gamma\left(B\delta_r + h\delta_d\right) \tag{5}$$

Limiting function

$$f(B,h) = \frac{A}{B\delta_r h^2 + \delta_d h^3} - [f] \ge 0 \tag{6}$$

Necessary extremum conditions

$$\frac{\partial L(B,h)}{\partial B} = \frac{\partial(\varphi(B,h) + \lambda f(B,h))}{\partial B} = 0 \quad (7)$$

$$\frac{\partial L(B,h)}{\partial h} = \frac{\partial(\varphi(B,h) + \lambda f(B,h))}{\partial h} = 0 \quad (8)$$

$$\frac{\partial L(B,h)}{\partial \lambda} = \frac{\partial(\varphi(B,h) + \lambda f(B,h))}{\partial \lambda} = 0 \quad (9)$$

From expressions (7) and (8) we can write

$$\frac{\partial L(B,h)}{\partial B} = 2\gamma\delta_r - \lambda A \frac{\delta_r}{h^2(B\delta_r + \delta_d h)^2} = 0 \quad (10)$$

And

$$\frac{\partial L(B,h)}{\partial h} = 2\gamma\delta_d - \lambda A \frac{2B\delta_r + 3\delta_d h}{h^3(B\delta_r + \delta_d h)^2} = 0 \quad (11)$$

Solving equations (9) and (10) together, we get such a ratio between the height of the wall and the thickness of the shelf

$$\frac{h}{B} = \frac{\delta_r}{\delta_d} \quad (12)$$

Therefore, the optimal ratio of the height of a double-walled beam to the width of its girdle is equal to the ratio of the thicknesses of the girder and the wall.

By determining the dependence of the width of the beam shelf on its height from expression (11), taking into consideration in expression (3), we get the following expression to determine the optimal height of the wall of the beam:

$$h \le \sqrt[3]{\frac{QL^3}{48E\delta_d[f]}} \quad (13)$$

Let's look at a specific numerical example to visualize the obtained result.

The load capacity of the overhead crane = 800 kN, the length of the bridge is L= 19 m, the height of the girder is h = 1590 mm, the thickness of the girder wall is = 8 mm [4]. Young's modulus E = 2.1.105 MPa for steel. Allowable deflection of the beam in the middle of the span [f] = L/700 = 19.103/700 = 27 mm.

Consider these data in expression (12).

$$h \le \sqrt[3]{\frac{800 \cdot 10^3 \cdot \left(19 \cdot 10^3\right)^3}{48 \cdot 2{,}1 \cdot 10^5 \cdot 8 \cdot 27}} = 1360mm$$

As can be seen, the value of the optimal height of the beam, (1590 -1360)100%/1560 = 14.4% is taken small. This allows to save metal.

CONCLUSION

1. A mathematical expression was obtained to determine the optimal height of the double-walled girder of the bridge crane, which ensures the stiffness condition.

2. The numerical example was solved, and it was determined that the value of the height of the beam calculated by the proposed expression is 14.4% less than the height in the real construction. This, in turn, means a reduction in the weight of the steel used to produce the metal structure of the double-girder bridge crane by approximately 1.1 t.

REFERENCES

1. В.Ю. Анцев, А.С. Толоконников, С.А. Потапов, П.Ю. Калабин. Совершенствование метода расчёта пролетных балок грузоподъемных машин мостового типа // Известия Тульского Государственного Университета . Технические науки. Тула: Изд-во ТулГУ. 2013
2. Справочник по кранам. В 2 т. Под общ. ред. М.М.Гохберга. – Л.: Машиностроение. Ленинградское отд.-ние, 1988
3. Гайдамака В. Ф. Грузоподъемные машины: Учебник. —К.: Выща шк. Головное изд-во, 1989
4. Курсовое проектирование грузоподъемных машин. / С.А.Казак и др.- М.:Высш. шк., 1989

KENTSEL DÖNÜŞÜM ÇALIŞMALARININ TEKNİK YÖNDEN DEĞERLENDİRİLMESİ ÜZERİNE BİR ÇALIŞMA

Ekrem TUŞAT[1], Tayfun ÇAY[2]

[1]*Prof. Dr., Konya Teknik Üniversitesi Mühendislik ve Doğa Bilimler Fakültesi Harita Mühendisliği Bölümü, Konya-TÜRKİYE, ORCID ID: https://orcid.org/0000-0003-4130-3764*

[2]*Prof. Dr., Konya Teknik Üniversitesi Mühendislik ve Doğa Bilimler Fakültesi Harita Mühendisliği Bölümü, Konya-TÜRKİYE, ORCID ID: https://orcid.org/0000-0000-0000-0000*

Özet

Köyden kente göç, ekonomik, sosyal ve toplumsal nedenlerle insan yaşamında kentlilik ve şehirleşme kavramları daha fazla yer almaya başlamıştır. Düzensiz göç ve beraberinde getirdiği plansız kentleşme, çarpık yapılaşma, inşaat kalitesi gibi ekonomik, sosyal, kültürel vb. nedenlerle özellikle kentsel yaşamın yeniden ele alınması, bozulmuş, çarpık alanlarda kentsel yenileme ve dönüşüm çalışmalarının yapılması bir zaruret halini almıştır. Bu çalışma kapsamında kentsel dönüşüm çalışmalarının yasal ve teknik yönden ele alınmış, konu ile ilgili mevcut durum incelenmiştir. Örnek bir çalışma olarak Konya İli Karatay İlçesi Aziziye Mahallesi Mevlana Müzesi batı kısmında yer alan K.743 ve K.749 nolu düzenleme sahası kapsamında yapılan kentsel dönüşüm çalışmaları teknik yönden değerlendirilmiştir.

Anahtar Kelimeler: Kentsel dönüşüm, planlama, yasal mevzuat, Konya Aziziye Mahallesi.

A STUDY ON THE TECHNICAL EVALUATION OF URBAN TRANSFORMATION PROJECTS

Abstract

The concepts of urbanity and urbanization have begun to occupy more place in human life due to economic, social and societal reasons as well as migration from the village to the city. Owing to economic, social and cultural reasons such as irregular migration, the unplanned urbanization it brings with it, unplanned housing and low construction quality. It has become especially necessary to reconsider urban life and to carry out urban renewal and transformation projects in degraded and unplanned areas. Within the scope of this study, the legal and technical aspects of urban transformation projects were discussed and the current situation on the subject was examined. As a case study, the urban transformation projects carried out within the scope of the land arrangement areas K.743 and K.749 located in the western section of the Mevlana Museum in the Aziziye Neighborhood of Karatay District in Konya Province were evaluated technically.

Keywords: Urban transformation, planning, legislation, Konya Aziziye Neighbourhood.

ENZİM REAKSİYONUNUN BAŞLANGIÇ HIZININ BELİRLENMESİ. TOPRAKTA KATALAZ ENZİMİNE UYGULANMASI

Fariz MİKAİLSOY

Iğdır Üniversitesi, Ziraat Fakültesi, Toprak Bilimi ve Bitki Besleme Bölümü, Iğdır, Türkiye. Toprak Bilimi, ORCID NO: 0000-0003-4543-5393

Erhan ERDEL

Iğdır Üniversitesi, Ziraat Fakültesi, Toprak Bilimi ve Bitki Besleme Bölümü, Iğdır, Türkiye. Toprak Bilimi, ORCID NO: 0000-0002-8011-9452

Fatih ER

Selçuk Üniversitesi Çumra Meslek Yüksekokulu, Konya, Türkiye, ORCID: 0000-0003-0549-4559

ÖZET

Çalışmada, toprağın katalaz enziminin kinetik parametrelerini (V_{max}, K_M, V_{max}/K_M, K_{SEE}, $[S]_{opt}$ ve $\upsilon_{0,max}$) hesaplamak için H_2O_2 substratının farklı konsantrasyonlarında (3, 6, 9, 12, 15, 18, 21, 24, 30 %) analizler yapılmıştır. Bu parametrelerin hesaplanması için analiz sonuçları kullanılarak önce hız (υ) değerleri hesaplanmıştır. Sonra ürün – substrat: [P]=f([S]) bağıntısını ifade eden farklı modeller belirlenmiştir. Daha sonra model seçim kriterlerine (R^2, R^2_{adj}, σ, A, D, UII, AIC) göre [P]=f([S]) bağıntısını yansıtan en uygun model belirlenmiştir. Belirlenen modele göre başlangıç hız: $\upsilon_0=d([P])/dt\,|_{t=0}$ formulü ile hesaplanmıştır. Çalışmadaki tüm hesaplamalar STATISTICA-10 paket programı ile yapılmıştır. Araştırma sonuçları; model seçim ölçütlerine göre uygun modelin Binom-1 olduğunu göstermiştir. Ayrıca, substrat konsantrasyonu arttıkça, katalaz enzim reaksiyonunun önemli bir inhibisyonunun olduğu tespit edilmiştir.

Anahtar Kelimeler: Toprak, enzim, katalaz, kinetik parametreler, başlangıç hız.

DETERMINING THE INITIAL RATE OF ENZYME REACTION. APPLICATION OF CATALASE ENZYME IN SOIL

ABSTRACT

In the study, to calculate the kinetic parameters of the soil catalase enzyme (V_{max}, K_M, V_{max}/K_M, K_{SEE}, $[S]_{opt}$ ve $\upsilon_{0,max}$) at different concentrations of the H_2O_2 substrate (3, 6, 9, 12, 15, 18, 21, 24, 30 %) In analyzes were made. To calculate these parameters, first the velocity (υ) values were calculated by using the analysis results. Then, different models expressing the relation product – substrate: [P]=f([S]) were determined. According to the model selection criteria (R^2, R^2_{adj}, σ, A, D, UII, AIC), the most suitable model reflecting the relation [P]=f([S]) was determined. Initial velocity was calculated with the formula $\upsilon_0=d([P])/dt\,|\,t=0$ according to the selected model. All calculations in the study were made with the STATISTICA-10 package program. Results showed that, the adequate model according to the model selection criteria was Binomial-1. It was also found that there was a significant inhibition of the catalase enzyme reaction as the substrate concentration increased.

Keywords: Soil, enzyme, catalase, kinetic parameters, initial rate.

GİRİŞ

Toprak kalite parametrelerinden biri olan toprak enzimleri, besin döngüsünden, organik maddenin parçalanmasından ve toprakta çok sayıda reaksiyonun katalizlenmesinden sorumludur. Toprak enzimleri genellikle mikrobiyal kökenli olmakla birlikte hayvansal ve bitki kökenlidir.

Topraktaki enzimlerin miktarı belirlenemediği için aktiviteleri belirlenir. Enzimler hakkında daha detaylı bilgi için enzimlerin etki mekanizmasının araştırılması önemlidir. Bu noktadan hareketle enzimlerin kinetik ve

termodinamiğinin belirlenmesi gerekmektedir (Edwards, 1970; Cornish-Bowden, 1976; Aliev ve ark., 1981; Khabirov ve Kuvatov 1990). Toprak enzimlerinin etkisinin kinetiği üzerine çok sayıda çalışma yapılmıştır. Toprak enzimlerinin incelenmesine yönelik kinetik yaklaşım, son yüzyılda ve özellikle 1950'lerden itibaren önemli ilerlemeler kaydetmiştir (Michaelis ve Menten, 1913; Tabatabai ve Bremner 1971; Khaziev ve Agafarova 1976; Aliev ve ark., 1981; Khabirov ve Kuvatov, 1990).

Toprak enzimlerinin, toprak parçacıklarının yüzeyinde hareketsiz kalan organizmaların enzimleri olarak kabul edilebileceği bilinmektedir. O zaman, durağan bir rejimde toprak enzimatik reaksiyonlarının kinetiğini incelemek daha uygundur. 'Hareketsiz enzimler' terimi 1971'de yasallaştırılmıştır ve uzayda protein moleküllerinin hareket özgürlüğünün herhangi bir kısıtlanması anlamına gelmektedir.

Durağan kinetik, enzimatik reaksiyonların incelenmesinde yaygın olarak kullanılmaktadır. Genellikle, enzimatik reaksiyon hızının substrat konsantrasyonuna bağımlılığını belirlemek için durağan kinetik çalışmalar yapılır. Kararlı durumda enzimatik reaksiyonların mekanizmasını incelerken, başlangıç hızını belirlemek gerekir (Hegyi ve ark., 2013).. Farklı substrat konsantrasyonlarında reaksiyon ürünlerinin oluşumunun başlangıç hızının (υ_0) ölçülmesine dayanır.

Genellikle, kinetik mekanizmaları açıklamak ve reaksiyonların kinetik parametrelerini belirlemek için, enzimler tarafından katalize edilen reaksiyonun başlangıç hızı hakkındaki verilerin kullanılması önerilir. Kinetik çalışmalarda kullanılan Michaelis-Menten modeli için enzimatik reaksiyonun başlangıç hızı (υ_0) bilinmelidir (Michaelis ve Menten, 1913; Aliev ve ark., 1981; Hegyi ve ark., 2013; Mikailsoy, 2022).

Bir substratlı enzimsel reaksiyonların şematik olarak klasik kinetiği aşağıdaki şekilde gösterilebilir (Michaelis ve Menten 1913);

$$\mathbf{E+S} \underset{\mathbf{k_{-1}}}{\overset{\mathbf{k_{+1}}}{\rightleftarrows}} \mathbf{ES} \xrightarrow{\mathbf{k_{+2}}} \mathbf{E+P} \tag{1}$$

Burada E-enzim; S-substrat; ES-enzim-substrat kompleksi (bazen buna Michaelis kompleksi denir); P-ürün (produkt); k_{+1}, k_{+2} ve k_{-1} – sırasıyla iki ileri ve bir ters reaksiyonun hız sabitleridir, S ve ES arasındaki çifte oklar enzim-substrat bağlanmasının tersinir olduğunu belirtir. Bu mekanizmada E enzimi, sadece reaksiyonu kolaylaştıran bir katalizördür.

Enzimatik reaksiyonun ilk (başlangıç) aşamasında substrat konsantrasyonunun azalması ihmal edilebilir. Böyleki, analizlerin yapıldığı ilk anda $[\mathbf{S}]_0 \gg [\mathbf{E}]_0$ olduğundan $[\mathbf{S}]_0 \gg [\mathbf{ES}]$ olur. Bu halde, $[\mathbf{S}] = [\mathbf{S}]_0 - [\mathbf{ES}]$ eşitliğinden aşağıdaki eşitlik $[\mathbf{S}] \approx [\mathbf{S}]_0$ bulunur. O zaman reaksiyonun başlangıç hız (υ_0) eşitliğini aşağıdaki biçimde yazabiliriz (Michaelis ve Menten, 1913; Edwards, 1970; Williams ve Williams, 1973; Cornish-Bowden, 1976; Panikov ve Ksenzenko, 1982).

$$v_0 = \frac{\mathrm{d}[\mathbf{P}]}{\mathrm{dt}} = k_{+2} \cdot [\mathbf{ES}] = \frac{k_{+2}[\mathbf{E}]_\mathbf{0}[\mathbf{S}]_0}{\mathbf{K_M} + [\mathbf{S}]_0} = \frac{\mathbf{V_{max}}[\mathbf{S}]_0}{\mathbf{K_M} + [\mathbf{S}]_0} \tag{2}$$

Aktif ES kompleksine ek olarak, inaktif bir ESS kompleksinin oluştuğu en basit enzimatik reaksiyonun substrat inhibisyonunun durağan kinetiğinin şeması aşağıdaki gibi olur;

$$\begin{aligned} &\mathbf{E+S} \underset{\mathbf{k_{-1}}}{\overset{\mathbf{k_{+1}}}{\rightleftarrows}} \mathbf{ES} \xrightarrow{\mathbf{k_{+2}}} \mathbf{E+P} \\ &\mathbf{ES+S} \underset{\mathbf{k_{-3}}}{\overset{\mathbf{k_{+3}}}{\rightleftarrows}} \mathbf{ESS}\left(\mathbf{ES_2}\right)\left(inactiv\right)\ \mathbf{K_{ESS}} \end{aligned} \tag{3}$$

Basit dönüşümler yoluyla, substratın fazlalığı ile inhibe edilen sabit (durağan, kararlı) reaksiyonun başlangıç hızı (υ_0) için bir ifade elde etmek mümkündür.

$$v_0 = \frac{\mathbf{V_{max}} \cdot [\mathbf{S}]_0}{\mathbf{K_M} + [\mathbf{S}]_0 + \frac{1}{\mathbf{K_{ESS}}}[\mathbf{S}]_0^2} = \frac{\mathbf{V_{max}} \cdot [\mathbf{S}]_0}{\mathbf{K_M} + \left(1 + \frac{[\mathbf{S}]_0}{\mathbf{K_{ESS}}}\right) \cdot [\mathbf{S}]_0} \tag{4}$$

(2) ve (4) nolu eşitliklerde , K_M – Michaelis sabitesi, K_{ESS} -enzimatik reaksiyonu inhibe eden (engelleyen) inaktif [ESS] kompleksinin oluşum hızını karakterize eden ayrışma katsayısıdır:

$$\mathbf{V_{max}} = k_{+2}\left[\mathbf{E}\right]_{\mathbf{0}}, \mathbf{K}_{\mathrm{M}} = \frac{\left[\mathbf{E}\right]\left[\mathbf{S}\right]}{\left[\mathbf{ES}\right]} = \frac{k_{-1}+k_{+2}}{k_{+1}}, \mathbf{K_{ESS}} = \frac{\left[\mathbf{ES}\right]\left[\mathbf{S}\right]}{\left[\mathbf{ESS}\right]} = \frac{k_{-3}}{k_{+3}} \quad (5)$$

İnhibitörlerin etkisinin incelenmesi, toprakta meydana gelen enzimatik kataliz mekanizması hakkında daha eksiksiz bilgi elde edilmesini sağlar. Topraklarda enzim reaksiyonlarının inhibisyonu üzerine birçok çalışma yapılmıştır (Panikov ve Ksenzenko, 1982; Tazdaït, 2013;Yano ve Suzuki, 2018; Yun ve Han, 2020)

Bilindiği gibi toprağın biyolojik özellikleri incelendiğinde en önemli enzimlerden biri katalazdır. Katalaz, toprak ortamı için toksik kimyasal madde olan hidrojen peroksiti parçalayan ve topraktaki mikroorganizmaların oksijen ihtiyacını karşılamada etkili olan enzimdir. Bu enzimin topraktaki işlevini belirlemek için kinetiğini araştırmak önemlidir.

Çalışmanın amacı killi-tınlı topraklarda katalaz enziminin başlangıç hızı ve kinetik parametrelerinin belirlenmesidir. Ayrıca bu çalışma, fazla substrat tarafından katalaz inhibisyonunun kinetik çalışmalarının sonuçlarını sunmaktadır.

MATERYAL VE METOD

Materyal

Örnekler Türkiye'nin Doğu Anadolu Bölgesi'nden (Iğdır) toplanmıştır. İncelenen bölge, mikroklima özelliğinden dolayı yazları sıcak, kışları ılımandır. Ovada en yüksek yağış Mayıs ayında, en düşük ise Ağustos ayında düşer. Iğdır ilinde yıllık ortalama yağış 254.2 mm, buharlaşma 1094.9 mm'dir. En soğuk ay Ocak, en sıcak ay Temmuz ayıdır (Anonim, 2018) ve bölgenin rakımı 850 m, ovanın merkez ilçesinde sulanan arazilerin eğimi düz ve düze yakın (% 0-2). Bazı toprak özellikleri Tablo 1'de belirtilmiştir.

Tablo 1. Toprak özellikleri.

Toprak özellikleri.	Sonuçlar
Tekstür	Killi tın
Organik madde, %	1.34
Kütle yoğunluğu, $g \cdot cm^{-3}$	1.16
pH (1:2,5)	8.22
Electriksel iletkenlik, $dS \cdot m^{-1}$	1.2
Toplam azot(%)	0.067
Kireç (%)	9.04

METOD

Toprak analizleri

Toprak fiziksel, kimyasal ve enzim analizleri için bozulmuş ve bozulmamış toprak örnekleri 0-30 cm derinlikten üç tekerrürlü olarak toplanmıştır.

Toprak tekstürü (Gee ve Bauder, 1986), toprak organik maddesi (Walkley ve Black, 1934), elektriksel iletkenlik (Rhoades, 1983), katalaz aktivitesi (Beck, 1971), kireç ve toprak pH'sı (Mclean, 1982), kütle yoğunluğu (Blake, 1965)' e göre belirlenmiştir. Toprak Reaksiyonu (pH): 1:2,5 oranındaki toprak: su karışımında cam elektrotlu pH metre ile belirlenmişir (McLean, 1982).

Kinetik parametrelerin hesaplanması

Çalışmada kinetik parametreleri **(υ_0, V_{max}, K_M, V_{max}/K_M ve K_{ESS})** hesaplamak için farklı substrat konsantrasyonlarında (3, 6, 9, 12, 15, 18, 21, 24, 30 %) katalaz enziminin aktivite analizleri yapılmıştır.

Katalaz enzim reaksiyonunun başlangıç hızını belirlemek için farklı modeller (Hiperbolik, Binom, Binom-parabolik, 5. derece polinom, 6. derece polinom, 5. derece psevdopolinom ve 6. derece psevdopolinom) kullanılmıştır (Tablo 2). Bu modellere göre her konsantrasyon için başlangıç hız hesaplamaları yapılmıştır.

Model seçim kriterlerine göre (Pearson's Korelasyon Katsayısı—R^2, Düzeltilmiş R-Kare—R^2_{adj}, Kök Ortalama Kare Hata—σ, Ortalama Mutlak Yüzde Hata—A, Uyum İndeksi—D, Theil's U İstatistik—UII , Akaike Bilgi Kriteri—AICc) en uygun model belirlenmiştir.

Tablo 2. Ürünün zamana göre değişimini ifade eden modeller.

№	Modeller	
1	Hyperbolik	$\left[\mathbf{P}(t)\right]=\frac{at}{b+t}$
2	Binom	$\left[\mathbf{P}(t)\right]=a_1 t^{a_2} e^{-a_3 t}$
3	Binom-parabolik	$\left[\mathbf{P}(t)\right]=a_1 t^{a_2} e^{-a_3 t \pm a_4 t^2}$
4	5. derece polinom	$\left[\mathbf{P}(t)\right]=a_0+a_1 t+a_2 t^2+\ldots+a_5 t^5=\sum_{k=0}^{5} a_k t^k$
5	6. derece polinom	$\left[\mathbf{P}(t)\right]=a_0+a_1 t+a_2 t^2+\ldots+a_6 t^6=\sum_{k=0}^{6} a_k t^k$
6	5. derece psevdopolinom	$\left[\mathbf{P}(t)\right]=a_1 t+a_2 t^2+\ldots+a_n t^n=\sum_{k=1}^{5} a_k t^k$
7	6. derece psevdopolinom	$\left[\mathbf{P}(t)\right]=a_1 t+a_2 t^2+\ldots+a_n t^6=\sum_{k=1}^{6} a_k t^k$

Substratın farklı konsantrasyonları $[S]_0$ için belirlenmiş başlangıç hız (υ_0) değerlerinin saptanmasından sonra, başlangıç hız (υ_0) ve substrat konsantrasyonları arasındaki kinetik parametrelerin (K_M, V_{max}, K_{ESS}) değerleri Brigs-Holdeyn'in hiperbolik modeli;

$$v_0=\frac{\mathbf{V_{max}}\cdot[\mathbf{S}]_0}{\mathbf{K}_\mathrm{M}+[\mathbf{S}]_0+\frac{1}{\mathbf{K_{ESS}}}[\mathbf{S}]_0^2}=\frac{\mathbf{V_{max}}\cdot[\mathbf{S}]_0}{\mathbf{K}_\mathrm{M}+\left(1+\frac{[\mathbf{S}]_0}{\mathbf{K_{ESS}}}\right)\cdot[\mathbf{S}]_0} \tag{6}$$

kullanılarak belirlenmiştir.

Düşük substrat konsantrasyonlarında, yani $[S]^2_0 \ll K_{ESS}$ olduğunda (6) nolu denklem klasik Michaelis-Menten (2) denklemine basitleştirilir:

$$[\mathbf{S}]_0^2 \ll \mathbf{K}_{ESS} \Rightarrow \frac{1}{\mathbf{K_{ESS}}}[\mathbf{S}]_0^2 \approx 0 \Rightarrow \quad v_0=\frac{\mathbf{V_{max}}[\mathbf{S}]_0}{\mathbf{K_M}+[\mathbf{S}]_0} \tag{7}$$

Yüksek substrat konsantrasyonlarında ise, yani $[S]^2_0 >> K_M$ olduğunda ise;

$$[\mathbf{S}]_0 \gg \mathbf{K}_\mathrm{M} \Rightarrow \frac{\mathbf{K}_\mathrm{M}}{[\mathbf{S}]_0} \approx 0 \Rightarrow v_0=\frac{\mathbf{K}_{ESS}\cdot\mathbf{V_{max}}}{\mathbf{K}_{ESS}+[\mathbf{S}]_0} \tag{8}$$

formulüne dönüştürülerek hesaplanır.

Kinetik parametreler (υ_0, V_{max}, K_M and K_{ESS}) model (7) ve (8) denklemleri ve yazılım programı (İSTATİKA-10) kullanılarak hesaplanmıştır.

BULGULAR VE TARTIŞMA

Katalaz enzim reaksiyon değerlerinin sonuçları Tablo 3'te gösterilmiştir. Tablo 3 incelendiğinde en yüksek ürünün %15 substrat konsantrasyonunda olduğu görülmektedir. Ayrıca, sonraki konsantrasyon artışlarıyla birlikte üründe bir azalma olduğu da gözlenmektedir.

Tablo 3 İncelenen topraktaki % H_2O_2 konsantrasyona göre **O_2** çıkış miktarı

	Zaman, t	**[S]=** % H_2O_2						
i	dak	3	6	9	15	21	27	30
1	**0.25**	1.15	1.78	1.92	2.21	1.45	0.85	0.42
2	**0.5**	1.68	2.51	2.94	3.15	2.68	1.42	0.74
3	**0.75**	2.05	3.10	3.72	4.12	3.44	1.78	0.97
4	**1.0**	2.52	3.73	4.12	4.75	4.12	2.07	1.25
5	**1.5**	3.00	4.67	4.97	6.24	4.59	2.60	1.61
6	**2.0**	3.45	5.42	6.05	6.87	4.91	3.03	1.99
7	**2.5**	3.85	5.93	6.55	7.43	5.22	3.45	2.31
8	**3.0**	4.08	6.37	7.28	8.30	5.79	3.78	2.63
9	**3.5**	4.42	6.88	7.86	9.17	6.15	4.12	2.88
10	**4.0**	4.67	7.12	8.17	9.95	6.75	4.56	3.09
11	**5.0**	5.00	7.65	9.15	11.25	7.23	4.82	3.32
12	**6.0**	5.35	8.25	10.25	12.30	7.85	5.25	3.51

Uygun Modelin Belırlenmesı

Uygun modelin seçimi istatistikel kriterler kullanılarak hesaplanmıştır. Örneğin, H_2O_2=3% konsantrasyonu için başlangıç hız değerinin farklı modellere göre seçilmesi Tablo 4'de verilmiştir.

Tablo 4. Farklı model ve istatistiklere göre H_2O_2 =3% konsantrasyonlarında toprağın başlangıç hızının hesaplanan değerleri.

İstatiksel parametreler	Model-1	Model-2	Model-3	Model-5	Model-6	Model-5	Model-6
	Hiperbol	Binom-1	Binom-2	Polin-5	Polin-6	PPolin-5	PPolin-6
	Başlangıç hız (v_0), ml O_2/ 1 dak 5 g toprak						
	3.9132	2.5580	2.6309	4.1058	4.6791	4.3961	4.9055
R^2	0.992819	0.999550	0.999594	0.998161	0.998714	0.997832	0.998612
R^2_{adj}	0.992166	0.999460	0.99945	0.996848	0.997428	0.996749	0.997621
σ	0.142990	0.037526	0.037589	0.090689	0.081943	0.092139	0.078820
D	0.998244	0.999887	0.999898	0.999539	0.999678	0.999463	0.999654
UII	0.037260	0.009323	0.008860	0.018851	0.015768	0.020472	0.016382
AICc	-3.6570	-6.1611	-5.9298	-3.4197	-2.9766	-3.8259	-3.7002
A, %	5.3079	0.7951	0.8079	2.2841	1.8323	2.7779	2.0077

Bilindiği gibi model seçimi, seçim kriterlerinden R^2 , R^2_{adj} ve D'nin en yüksek değerlerine ve σ, A, UII ve AICc'nin en küçük değerlerine göre yapılır (Tusat ve Mikailsoy, 2018).

Model seçim kriterlerine göre en uygun model Model-2'dir (Binom-1). Model-2'ye (Binom-1) göre başlangıç hız (υ_0) için [S]= [H_2O_2]=3 % hesaplanmış ve en uygun değer υ_0=2.5580 olarak bulunmuştur (Tablo 4).

Başlangiç Hizin Hesaplanmasi

Binom-1 modeline göre farklı H_2O_2 konsantrasyonlarındaki toprağın katalaz enzim reaksiyonunun başlangıç hız (υ_0) değerleri Tablo 5'te verilmiştir.

Tablo 5. Başlangıç hız (υ_0) değerleri.

№	[S], %	Başlangıç hız (υ_0),
1	3	2.5580
2	6	5.0248
3	9	7.6178
4	12	8.5678
5	15	8.6990
6	18	7.9453
7	21	6.7866
8	24	5.3866
9	27	3.6728
10	30	1.8557

Tablo 6. Düşük ve yüksek substrat konsantrasyonlarında toprağın katalaz enzim reaksiyonu için başlangıç hız (υ_0) değerleri.

№	[S],	υ_0	№	[S],	υ_0
	%	ml O_2/ 1 dak 5 g toprak		%	ml O_2/ 1 dak 5 g toprak
1	3	2.5580	1	18	7.9453
2	6	5.0248	2	21	6.7866
3	9	7.6178	3	24	5.3866
4	12	8.5678	4	27	3.6728
5	15	8.6990	5	30	1.8557

Kinetik Parametrelerin (V_{max}, K_M , K_{ESS}, V_{max}/K_M) Değerleri

Başlangıç hızın Tablo 6'daki düşük ve yüksek konsantrasyonlarındaki değerleri (7) ve (8) nolu eşitlikler kullanılarak hesaplanmıştır. Elde edilen verilerden kinetik parametrelerin (V_{max}, K_M, K_{ESS}, V_{max}/K_M) değerleri hesaplanmış ve sonuçlar Tablo 7'de verilmiştir.

Tablo 7. Toprakta H_2O_2 substratının düşük ve yüksek konsantrasyonlarda katalaz enzim reaksiyonunun kinetik parametrelerinin (V_{max}, K_M , K_{ESS}, V_{max}/K_M) değerleri.

	Kinetik Parametreler			İstatistiksel Parametreler			
Düşük Konsantrasyon	V_{max}	K_M	V_{max}/K_M	R^2 , %	A, %	σ	UII
	ml O_2/1dak 5g toprak	%		%			
	18.695	15.3317	1.2194	98.058	7.326	0.640	0.072
Yüksek Konsantrasyon	V_{max}	K_{ESS}		R^2 ,%	A, %	σ	UII
	ml O_2/1dak 5g toprak	%		%			
	18.695	9.8604	-	60.496	38.320	1.644	1.312

Enzimatik Reaksiyonun Ekstremum (Optimal Substrat ve Hız) Değerleri

Son olarak, enzimsel reaksiyonların mekanizmalarının daha ayrıntılı yorumlanmasında faydalı olan ekstremum (optimum supstrat, $[S]_{opt}$ ve hız $\upsilon_{0,max}$) değerlerin hesaplaması yapılmıştır.

Ekstremum değer, substratın optimum konsantrasyonunda enzimin spesifik aktivitesini belirlemek için önemlidir.

Enzimatik reaksiyonların mekanizmalarının daha fazla yorumlanması için yararlı olan ekstremum (optimum supstrat, $[S]_{opt}$ ve hız $\upsilon_{0,max}$) değerleri aşağıdaki formüller kullanılarak hesaplanmıştır (Yakovlev, 1965):

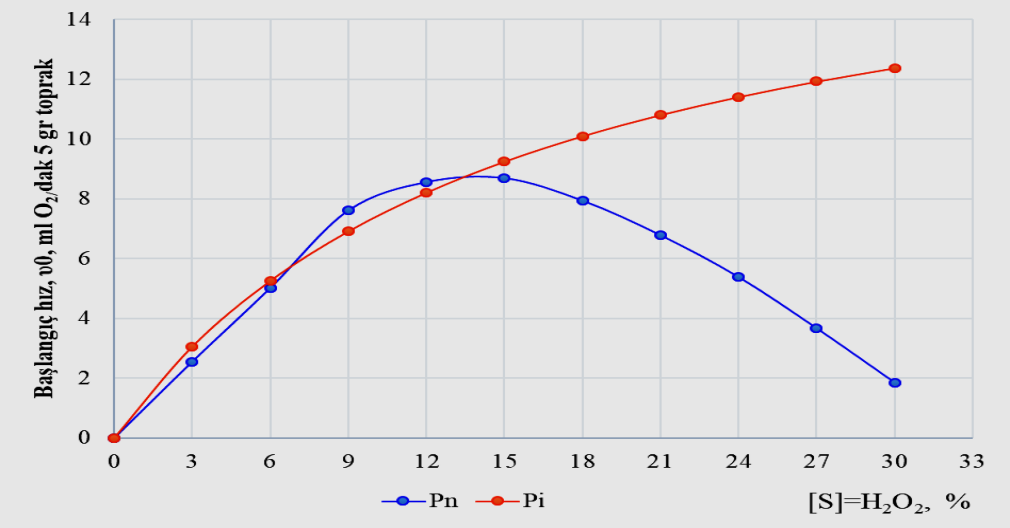
$$[\mathbf{S}]_{0,opt} = \sqrt{\mathbf{K}_M \cdot \mathbf{K}_{ESS}}, \quad \nu_{max} = f\left([\mathbf{S}]_{opt}\right) = \frac{\mathbf{V_{max}}}{\mathbf{1} + \mathbf{2}\sqrt{\mathbf{K}_M / \mathbf{K}_{ESS}}} \tag{9}$$

Bu değerler, Tablo 8'de verilmiştir.

Tablo 8. Deneme toprağının katalaz enzim reaksiyonunun ekstremum değerleri

Kinetik Parametreler						
V_{max}	K_M	V_{max}/K_M	K_{EES}	K_M/K_{EES}	$[S]_{opt}$	$\upsilon_{0,max}$
18.6950	15.3317	1.2194	9.8609	1.5548	12.2957	5.3508

Tablo 7'deki kinetik parametrelerin değerleri kullanılarak inhibisyon yokluğunda ve varlığında kinetik eğrilerin akışını gösteren grafik Şekil 1'de verilmiştir.



Şekil 1. Enzimatik reaksiyonun substrat inhibisyonu: **Pn**-inhibisyon yokluğunda beklenen hiperbolik eğri; **Pi**-substrat konsantrasyonlarının artmasıyla inhibisyonda bir artış gösteren deneysel veriler.

SONUÇLAR

Kinetik parametreler (V_{max}, K_M, V_{max}/K_M, K_{SEE}, $[S]_{opt}$ ve $\upsilon_{0,max}$), çalışılan toprağa ve uygulanan substrat konsantrasyonlarına bağlı olarak en uygun model olan binom-1 modeli kullanılarak belirlenmiştir.

Substrat konsantrasyonu arttıkça, katalaz enzim reaksiyonunun önemli bir inhibisyonu olduğu gözlenmiştir.

Enzimlerin kinetik ve inhibisyon çalışmalarında başlangıç hızın belirlenmesi oldukça önemlidir.

KAYNAKLAR

Aliev, S. A., Gadzhiyev, D. A., & Mikaylov, F. D., (1981). Kinetic indexes of catalase activity in the main soil groups of Azerbaijan. Soviet Soil Science, 13, 29-35.

Beck, T. H. (1971). Die messung der katalaseaktivitaet von Böden. Zeitschrift für Pflanzenernährung und Bodenkunde 130.1. 68-81 (in German).

Blake, G. R. (1965). Bulk density. In: Black, C.A. (ed.), Methods of Soil Analysis. Part II, American Society of Agronomy. Madison, Wisconsin, 374-390.

Cornish-Bowden, A. (1976). Principles of Enzyme Kinetics. Butterworths, London and Mir Publishing, Moscow, 190 p. (in Russian).

Edwards, V. H. (1970). The influence of high substrate concentration on microbial kinetics. Biotechnol Bioeng, 12, pp: 679–712. https://doi.org/10.1002/bit.260120504

Gee, G. W. & Bauder J. W. (1986). Particle-size analysis. Methods of Soil Analysis. Part 1. Physical and Minerological Methods. Second Edition. Agronomy, 9, 383-441.

Hegyi, G., Kardos, J., Kovács, M., Málnási-Csizmadia, A., Nyitray, L., Pál, G., Radnai, L., Rényi, A. & Venekei, I. (2013). Introduction to practical biochemistry. Eötvös Loránd University.

Khabirov, I. K., & Kuvatov, Yu. G. (1990). Kinetics and Thermodynamics of the Hydrolysis Reaction of 14c-Labelled Carbamide in the Pre-Urals Soils, Soviet Soil Science, 22(8), 83 – 94.

Khaziev, F. Kh., & Agafarova, Ya. M. (1976). Michaelis Constants of Soil Ferments, Soviet Soil Science, 8, 149 – 157.

Mclean, E. O. (1982). Soil ph and lime requirement. Methods of soil analysis part 2. Chemical and microbiological properties second edition. Agronamy, 9, 199-224. https://doi.org/10.2134/agronmonogr9.2.2ed.c12

Michaelis, L. & Menten, M. L. (1913). Die Kinetik der Invertinwirkung. Biochem. Z. 49 (352), 333–369.

Mikailsoy, F. D. (2022). Influence of high substrate concentrations on catalase reaction in loam soil (Igdir Province, Turkey). I. Theoretical foundations of the kinetics of enzymatic soil reactions. Soil science and agrochemistry, 3, 60-86. https://doi.org/10.51886/1999-740X_2022_3_60

Panikov, N. S., & Ksenzenko, S. M. (1982). Study of phosphohydrolase inhibition in sod-podzolic soil. Soviet Soil Science, 11, 43-49.

Rhoades J. D. (1983). Soluble salts. Methods of Soil Analysis: Part 2 Chemical and Microbiological Properties 9: 167-179.

https://doi.org/10.2134/agronmonogr9.2.2ed.c10

Tabatabai, M. A., & Bremner, J. M. (1971). Michaelis constants of soil enzymes. Soil Biol. Biochem., 3(4), 317-323. https://doi.org/10.1016/0038-0717(71)90041-1

Tazdaït, D., Abdi, N., Grib, H., Lounici, H., Pauss, A., & Mameri, N. (2013). Comparison of different models of substrate inhibition in aerobic batch biodegradation of malathion. Turk. J. Eng. Environ. Sci., 37, 221–230. https://doi.org/10.3906/muh-1211-7

Tusat, E., & Mikailsoy, F. (2018). An investigation of the criteria used to select the polynomial models employed in local GNSS/leveling geoid determination studies. Arab J Geosci 11, 801 https://doi.org/10.1007/s12517-018-4176-0

Walkley, A. & Black, L. A. (1934). An examination of the degtjareff method for determining soil organic matter, and a proposed modification of the chromic acid titration method. Soil Science, 37 (1), 29–38. doi: https://doi.org/10.1097/00010694-193401000-00003.

Williams, V. R., & Williams, H. B. (1973). Basic physical chemistry for the life sciences. Second Edition. Freeman and Company, San Francisco, 524 pp.

Yakovlev, V. A. (1965). Kinetika fermentativnogo kataliza. Moskva: Nauka, 248 s. (in Russian).

Yano, D., & Suzuki, T. (2018). Kinetic Analyses of the Substrate Inhibition of Paramecium Arginine Kinase. Protein J 37, 581–588. https://doi.org/10.1007/s10930-018-9798-2

Yun, K. İ., & Han, T. S. (2020). Relationship between enzyme concentration and Michaelis constant in enzyme assays, Biochimie, 176: 12–20.

https://doi.org/10.1016/j.biochi.2020.06.002

ОПРЕДЕЛЕНИЕ ТЕПЛОПРОВОДНОСТИ ПОЧВ НА ОСНОВЕ ЕЖЕДНЕВНЫХ ИЗМЕРЕНИЙ ТЕМПЕРАТУРЫ НА ПОВЕРХНОСТИ И НА РАЗНЫХ ГЛУБИНАХ ПОЧВЫ.

Droktora öğrencisi Reşat MİKAİL

Iğdır Üniversitesi, Fen Edebiyat Fakültesi, Matematik Bölümü, Iğdır, Türkiye, ORCID NO: 0000-0003-2918-7238

Prof. Dr. Elman HAZAR

Iğdır Üniversitesi, Fen Edebiyat Fakültesi, Matematik Bölümü, Iğdır, Türkiye, ORCID NO: 0000-0003-3895-2448

Prof. Dr. Fariz MİKAİLSOY

Iğdır Üniversitesi, Ziraat Fakültesi, Toprak Bilimi ve Bitki Besleme Bölümü, Iğdır, Türkiye, ORCID NO: 0000-0003-4543-5393

АННОТАЦИЯ

Управление тепловым режимом почв является важнейшим условием интенсивного сельскохозяйственного производства в условиях открытого и закрытого грунта. Современное управление основывается на прогнозных поливариантных расчетах теплового режима и выборе оптимального варианта воздействия на почвенный покров для улучшения теплового режима. Кроме того, при расчетах почвенных конструкций в теплицах, на стадионах. гольфовых полях и др. искусственных почвенных сооружениях целевого назначения, необходим предварительный конструкторский расчет мощности и состава слоев почвы, соответствующих целевому назначению конструкции. В основе такого рода расчетов лежит использование математических моделей переноса тепла в почве. Обязательным экспериментальным обеспечением физически обоснованных моделей является величина температуропроводности почвы, которая зависит от влажности почвы, а также определяется составом и свойствами почвенных горизонтов. Проблема состоит в разработке простых, точных, быстрых и научно-обоснованных методов получения этой важнейшей теплофизической характеристики. Цель данной работы заключалась обзор существующих а также предложенных методов для определения коэффициента температуропроводности почв.

Ключевые слова: почва, температуропроводность, аналитические решения.

DETERMINATION OF SOIL THERMAL DIFFUSIVITY BASED ON DAILY MEASUREMENTS OF TEMPERATURE THE SURFACE AND AT DIFFERENT DEPTHS OF THE SOIL

ABSTRACT

The management of the thermal regime of soils is the most important condition for intensive agricultural production in open and protected ground conditions. Modern management is based on predictive multivariate calculations of the thermal regime and the choice of the optimal option for influencing the soil cover to improve the thermal regime. In addition, when calculating soil structures in greenhouses, stadiums. golf courses and other artificial soil structures for the intended purpose, a preliminary design calculation of the thickness and composition of the soil layers corresponding to the intended purpose of the structure is required Such calculations are based on the use of mathematical models of heat transfer in the soil. Mandatory experimental support for physically based models is the value of soil thermal diffusivity, which depends on soil moisture, and is also determined by the composition and properties of soil horizons. The problem is to develop simple, accurate, fast and scientifically based methods for obtaining this most important thermophysical characteristic.

The purpose of this work was to review existing as well as proposed methods for determining the coefficient of thermal diffusivity of soils.

Key words: soil, thermal diffusivity, analytical solutions.

ВВЕДЕНИЕ

1. Постановка Задачи

Ученые разных дициплины все большее внимание уделяют экологии и энергетике почвооброзования. Несомненно, что солнечная энергия, приходящая на земную поверхност, а также атмосферные осадки играют основную роль в почвооброзовании. Эти же факторы и определяют тепловой и водный режимы уже сложившхся почв. Совместное изучение тепловых и водных режимов почвы явиться новым звеном в энергетике почвообразования (Герайзаде, 1982).

Температурным режимом почвы называют пространственное распределение температуры почвенного покрова и непрерывные изменения этого распределения во времени (Шеин и др. 2001, стр. 139-171). Температурный режим почвы играет значительную роль в процессах жизнедеятельности растений. От температуры существенно зависят скорости химический реакций, протекающих в почве и корнях, передвижение влаги в почве и в растении, газообмен в почве, растворимось минеральных солей и ряд других факторов (Неусыпина, 1979, стр. 53-62).

Для всестороннего знания тепловых и водных свойств почвы необходимо иметь также данные, с помощью которых можно было бы найти значения тепловых и водных характеристик для данного состава и состояния почвы. Появившиеся в последнее время подобные исследования показывает, что для каждого типа почвы требуется отдельное определение тепловых и водных свойств, желателно как в естественных, так и в лабораторных условиях. Основными тепловыми свойств почвы являются коэффициенты теплопроводности, температуропроводности, теплоемкости и теплоусвояемости. Знание вышеперечисленных характеристик почвы может приблизить разрешение такой острой проблемы современности как прогноз теплового и водного режимов почв и грунтов.

При обсуждении темпертурного режима почвы удобно польоваться температуропроводностью, т.к. именно этот параметр характеризует «распространение» измеряемой величины-температуры. Тем не менее для анализа механизмой проиходящих явлений приходится обращаться к понятиям теплопроводности и теплоемкости (Шеин и др. 2001, с. 139-171).

Следует отметить, что, несмотря на наличие множества исследований отдельно по тепловым и отдельно по водным с войстам почвы, работ, посвященных комплексному изучению одновременно и тепловых и влажностных параметров, относящихся к одним и тем же типам почвы, очень мало. В то же время процессы тепло- и влагообмена протекают в органическом, неразрывном единстве и количественное описание этих процессов возможно лищ на основе знания так называемых эффективных теплофизических характеристик, ослоожненных явлениями влагопереноса.

2. Выбор Модели Теплопереноса в Почве

Известно что, при моделирование почвенных процессов протекающих в системе «почва-растения-атмосфера» основными этапами являются **идентификация** (выбор уравнения описывающие эти процессы и краевых условий) и **реализация** (то есть решение прямой и обратной задачи) модели. Поэтому, при системном подходе анализа температурного режима почвы (в зависимости от исследовании его в лабораторных и или полевых условиях) иногда вынужденно прибегают к упрощению, как в уравнение теплопереноса, так и в постановке краевых условий.

Исходя из выше описанного соображения как правило, рассматривают модели эквивалентной теплопроводности, ограничиваясь только одним классическим одномерным уравнением (*Нерпин и Чудновский,* 1967; Чудновский, 1976; Шеин и Гончаров, 2006 и др.):

$$\frac{\partial}{\partial z}\left[\lambda\left(z,t\right)\frac{\partial \mathrm{T}}{\partial z}\right]=c_v\left(z,t\right)\frac{\partial \mathrm{T}}{\partial t}\quad ,\left\{0<z<L\ или\ \infty\ ;\ t>0\right\} \tag{2.1}$$

где $\mathrm{T}\left(z,t\right)-$температура почвы в точке x момент времени t, $\lambda\left(z,t\right)-$ коэффициент теплопроводности, $c_v\left(z,t\right)=\rho c_m\left(z,t\right)-$ объемная теплоемкость, $\rho-$плотность почвы, $c_m\left(z,t\right)-$

удельная теплоемкось, $\kappa = \lambda / c_v -$ эффективный коэффициент температуропроводности, зависящий от свойств, состояния почвы, профильное и временное изменение которых позволяет расшифровать для ряда конкретных агротехнических ситуаций функцию.

На основе многочисленных экспериментов А.Ф. Чудновским с учениками для большинство типичных почв становлены эмпирические зависимости $\lambda(w,\rho)$, $c_v(w,\rho)$ и $\kappa(w,\rho)$. Например, для коэффициентов теплопроводности и температуропроводности эти зависимости имеют вид (Чудновский, 1976, стр. 13; Сысуев, 1986, стр 85):

$$\lambda = \rho\left(c_m + 0.01w\right)\left[m_1\left(w - m_4\right)^2 + m_2\rho + m_3\right]10^{-3},\ \kappa = \left[m_1\left(w - m_4\right)^2 + m_2\rho + m_3\right]10^{-3}$$

где w –влажность почвы, ρ–плотность почвы, m_i–коэффициенты, зависящие от типа почвы, c_m– удельная теплоемкось сухой почвы.

Для ряда задач возможно существенное упрощение уравнения (2.1), если принимать постоянным коэффициент теплоемкости, а коэффициенты тепло- и температуропроводности – линейно изменяющимися в глубь почвы или постоянными.

Поствнока и решение различных задач теплоперноса в почвах с учетом растительного покрова, так и без него подробно описаны в работах (Чудновский, 1948, 154, 1976; 1979; de Vries, 1952; Карслоу и Егер, 1964; Тихонов и Самарский, 1966; Куртенер и Чудновский, 1979; Horton, 1982, 1983; Микайылов, 2009; Микайылов и Шеин, 2010; Шеин и Микайылов, 2011; Mikailsoy, 2017; Mikail etal., 2021 и др.)

3. Идентифткация Краевых Условий

3.1. Выбор начального условия

При периодической постановке задачи с целью теоретического описания задачи квазистационарного режима (например, суточного или годового хода температуры почвы) начальное условие отсутствует (так называемые «задачи без начального условия»). Возможность такой постановки задачи следует из экспериментального установленного факта о наличии строгой периодичности в суточных и годовых температурных ритмах и можно считать, что любой рассматриваемый момент удален от «начала» процесса на бесконечно длительный промежуток времени.

Естественно, что понятия «начало» и «бесконечная длительность» процесса достаточно условны и выражают обобщение опыта, утверждающего, что в естественных условиях температуры почвы выражается периодической функцией времени в форме гармоноческой кривой с конечным количеством гармоник, кратных основной (год или суток).

В зависимости от исходных данных решаемой задачи распределение температур в почве в начальной момент времени может быть самым произвольным (Чудновский, 1976 Куртенер и Чудновский, 1979). Поэтому в общем случае начальное условие записывается как

$$\mathrm{T}\left(z, t=0\right) = \psi(z) \quad , \quad 0 \le z \le L \ \textit{или}\ 0 \le z < \infty \tag{3.1}$$

где функция $\psi(z) -$ выражает изменения температуры на глубине [0, L] , аналитическое выражение которой необходимо определить заранее. Для удобства где a_n коэффициенты, получаемые в результате аппроксимации на промежутке [0, L] заданного распределения температур полиномом степени n.

Иногда функцию $\psi(x)$ аппроксимируют ступенчатом виде:

$$\mathrm{T}\left(z, t=0\right) = \begin{cases} \mathrm{T}_i \ , \ z_i < z \le z_{i+1} \ \left(i = 0,1,2,...,n\right) \\ \mathrm{T}_i = const \ , \ z_0 = 0 \ ; \ z_{n+1} = L \text{ или } \infty \end{cases} \tag{3.3}$$

Частным случаем (3.2) и (3.3) при $n = 0$ соответствует равномерному начальному условию

$$T(z, t = 0) = T_0 = const, \quad 0 \le z \le L \text{ или } 0 \le z < \infty \tag{3.4}$$

3.2. Выбор Граничных условий.

3.2.1. Выбор начального условия

Задача о распространении температурных волн в почве является одним из первых примеров приложения математической теории теплопроводности, развитой Фурье, к изучению явлений природы. Температура на поверхности Земли носит, как известно, ярко выраженную суточную и годовую периодичность (Тихонов и Самарский, 1966, с. 243, 238-247)

Наиболее удобной характеристикой, которая может фигурировать в качестве граничного условия 1 – го рода, является температура поверхности почвы. Оно может быть определена либо путем непосредственных измерений, либо расчетными методами. Но в обоих случаях приходится сталкиваться с затруднениями приципиального характера. Измерения температуры поверхности проводятся, во-первых, далеко не всегда и не везде, а во-вторых, отличаются невысокой точностью, так как фактически относятся не к поверхности, а к слою конечной толщины, где имеются наибольшие градиенты температуры; кроме того, в дневное время неизбежны ошибки за счет воздействия солнечной радиации. Ошибки при этом могут достигать нескольких градусов (Константинов, 1968). Более точные специальные измерения носят единичный характер и не могут служить базой для серийных расчетов. Используя данные градиентных наблюдений и сведения о структуре приземного слоя, можно рассчитать температуру подстилающей поверхности на основе достаточной разработанной теории приземного слоя (Монин и Яглом, 1965).

3.2.1. Граничного условия на поверхности 1 – го рода.

Условия 1 – го рода целесообразно использовать, когда нас интересуют только теплообменные процессы внутри почвенного массива, определяемые его структурными неоднородностями, а термическая ситуация вблизи поверхности почвы рассматривается как фон, на котором указанные процессы изучаются. К этой ситуации относится, например, анализ термических эффектов, связанных с рыхлением или уплотнением поверхностных слоев почвы, поверхностным пескованием торфянников, применением мульчи из сыпучих материалов.

Граничного условия на поверхности **1** – го рода записывается в обычном виде

$$T(z = 0, t) = \varphi(t) \ , \ 0 < t < \infty \tag{3.5}$$

где функция φ(t) выражает изменения температуры поверхности почвы от времени, аналитического выражению которого следует определить заранее.

Если в течении рассматриваемого интервале времени температура поверхности почвы не меняется, то условия 1 – го рода записывается в следующем виде

$$T(z = 0, t) = T_0 = \text{const}, \ 0 < t < \infty \tag{3.6}$$

Анализ результатов измерения суточного или годового хода температуры поверхности почвы позволяет выражать описать аналитическую вид функции φ(t) в следующем ступенчатом форме:

$$T(z = 0, t) = \begin{cases} T_i \ , \ t_i < t < t_{i+1} \ (i = 0, 1, 2, ..., n) \\ T_i = const; t_0 = 0 \ ; \ t_{n+1} = \infty \end{cases} \tag{3.6[1]}$$

Задчи о теплопроводности твердего тела с периодически изменяющейся температурой на поверхности представляют весьма большой практической интерес. Подобные задачи встречаются в следующих задачах (Карслоу и Егер, 1964, с. 62-95, 106-112):

- *При исследовании колебаний температуры коры Земли, периодически нагреваемой Солнцем,*
- *При работе различных экспериментальных установках для определения параметра температурапроводности,*
- *При вычислении периодически изменяющихся температур в стенках цилиндров паровых машин и двигателей внутренного сгорения и , наконец*
- *В теории автоматических систем регулировки температуры и т.д.*

Следует отметить, что для анализа и сравнительной оценки влияния различных факторов на распределение температуры в почве, на величины тепловых потоков и теплоаккумуляцию почвы лучше всего иметь дело с формулами простой стуктуры.

Наиболее простой вид эти формулы получают, когда задается временной ход температуры на поверхности. Поэтому граничным условиям 1 – го рода всегда следует отдавать предпочтение.

Если установлено, что изменения температуры на поверхности почвы является периодический характер, тогда для аналитического выражения функции φ(t) принимают:

$$\varphi(t) = \mathrm{T}_0 + \mathrm{T}_a \cdot \cos\left(\omega t + \varepsilon\right) \ \textit{или} \ \ \varphi(t) = \mathrm{T}_0 + \mathrm{T}_a \cdot \sin\left(\omega t + \varepsilon\right) \ \left(0 < t < \infty\right) \tag{3.7}$$

где, T_0 – средне суточное (или годовое) температура деятельной поверхности почвы, (^{0}C); T_a – амплитуда колебаний температуры деятельной поверхности почвы, (^{0}C); $\omega = 2\pi/\tau_0$ – круговая суточная (или годовая) частота; τ_0 – период (*длина*) температурной волны, выраженное в сутки или в годах, при τ_0=24 часа: ω=7,27221,10^{-5} (рад/с); t – время (часы); ε – сдвиг фазы, зависящей от начала отсчета времени.

Эти выражении для φ(t) изучалась еще Фурье и впервые была применена при определении температурных колебаний почвы. Если температура поверхности почвы является периодической функцией с периодом 2π/ω, то φ(t) разлагают в ряд Фурье:

$$\varphi(t) = \mathrm{T}_0 + \mathrm{T}_1 \cdot \cos\left(\omega t + \varepsilon_1\right) + \mathrm{T}_2 \cdot \cos\left(2\omega t + \varepsilon_2\right) + \ldots = \mathrm{T}_0 + \sum_{j=1}^{\infty} \mathrm{T}_j \cdot \cos\left(j\omega t + \varepsilon_j\right) \tag{3.8}$$

и следовательно граничное условие 1 – го рода на поверхности будет имет вид:

$$\mathrm{T}(0,t) = \mathrm{T}_0 + \sum_{j=1}^{m} \mathrm{T}_{aj} \cdot \cos\left(j\omega t + \varepsilon_j\right) = \mathrm{T}_0 + \varphi(t) \ , \ t \geq 0 \tag{3.9}$$

T_{aj} –амплитуда колебаний температуры деятельной поверхности почвы для j-й гармоники (С); j – индекс гармоники в ряду; ε_j – фазовый угол волны на уровне поверхности для j-й гармоники (радианы), m – номер гармоники. Уравнение (3.9) можно написать в виде:

$$\mathrm{T}\left(0,t\right) = \mathrm{T}_0 + \sum_{j=1}^{m}\left[A_j \cos\left(j\omega t\right) + B_j \sin\left(j\omega t\right)\right], \ t \geq 0 \tag{3.10}$$

Параметры (T_0, A_j и B_j) в уравнении (3.10) определяются по следующим формулам:

$$\mathrm{T}_0 = \frac{1}{\mathrm{N}}\sum_{i=1}^{\mathrm{N}} \mathrm{T}\left(0,t_i\right) \ , \ A_j = \frac{2}{\mathrm{N}}\sum_{i=1}^{\mathrm{N}} \mathrm{T}\left(0,t_i\right)\cos\left(j\omega t_i\right) , \ B_j = \frac{2}{\mathrm{N}}\sum_{i=1}^{\mathrm{N}} \mathrm{T}\left(0,t_i\right)\sin\left(j\omega t_i\right) \tag{3.11}$$

Сдвиги фазы (фазовый угол)-ε_j и амплитудные члены- T_{aj} уравнения (3.9) связаны с A_j и B_j соотношениями:

$$\mathrm{T}_{aj} = \sqrt{A_j^{\,2} + B_j^2} \ , \ \varepsilon_j = \begin{cases} \arctan\left(-B_j / A_j\right) & , \ A_j > 0 \\ \pi/2 & , \ A_j = 0 \\ \pi - \arctan\left(B_j / A_j\right) & , \ A_j < 0 \end{cases} \tag{3.12}$$

Для $m=1$ из (3.10)-(3.13) имеем:

$$\mathrm{T}(0,t)=\mathrm{T}_0+\mathrm{T}_a\cdot\cos\left(\omega t+\varepsilon\right)=\mathrm{T}_0+A\cdot\cos\left(\omega t\right)+B\cdot\sin\left(\omega t\right) \tag{3.13}$$

$$\mathrm{T}_0=\frac{1}{\mathrm{N}}\sum_{i=1}^{\mathrm{N}}\mathrm{T}\left(0,t_i\right)\ ,\ A=\frac{2}{\mathrm{N}}\sum_{i=1}^{\mathrm{N}}\mathrm{T}\left(0,t_i\right)\cos\left(\omega t_i\right),\ \ B=\frac{2}{\mathrm{N}}\sum_{i=1}^{\mathrm{N}}\mathrm{T}\left(0,t_i\right)\sin\left(\omega t_i\right)$$

$$\mathrm{T}_a=\sqrt{A^2+B^2}\ ,\ \varepsilon=\begin{cases}\arctan\left(-B/A\right) & ,\ A>0\\ \pi/2 & ,\ A=0\\ \pi-\arctan\left(B/A\right) & ,\ A<0\end{cases} \tag{3.14}$$

3.2.2. Граничного условия на поверхности 2 – го рода

В тех случаях, когда нас интересует влияние составляющих теплового баланса деятельно поверхности почвы на термический режим почвы, обычно применяют граничное условие 2-го рода (Чудновский, 1976, стр. 18-19; Куртенер и Чудновский, 1979, стр. 15):

$$-\lambda\frac{\partial\mathrm{T}(0,t)}{\partial\mathrm{z}}=\psi(t) \tag{3.15}$$

где $\psi(t)$ – алгебраическая сумма радиационного, турбулентного и транцпирационного потоков тепла; при расчетах эти величины задаются. Однако условия 2 – го рода не позволяет выявить роль и влияние на температурное поле в почве отдельных метеорологических параметров, так как в (3.15) в явном виде они не входят.

3.2.3. Граничного условия на поверхности 3 – го рода

Определенные преимущества дает применение гораничных условий 3 – го рода (Куртенер и Чудновский, 1979, стр. 16):

$$Q(0,t)=-\lambda\frac{\partial\mathrm{T}(0,t)}{\partial\mathrm{z}}=\alpha\left[\mathrm{T}_{воз}\left(\mathrm{t}\right)-\mathrm{T}_{\text{пов}}\left(0,\mathrm{t}\right)\right] \tag{3.16}$$

где $\mathrm{T}_{\text{воз}}$ (t) и $\mathrm{T}_{\text{пов}}$(0,t) – соответсвенно температура воздуха и поверхности почвы; α-коэффициент конвективного теплообмена.

Нетрудно заметить, что использовать условие 3 – го рода в таком виде можно только в том случае, когда скорость ветра велика и конвективный теплообмен существенно преобладает над остальными видами теплопередачи на границе почва – окружающая среда.

3.2.4. Граничного условия на поверхности 4 – го рода

По мимо перечисленных линейных краевых задач, ставятся также задачи с нелинейными граничными условиями, например вида (Тихонов и Самарский, 1966, стр. 184-190):

$$\lambda\frac{\partial\mathrm{T}(0,t)}{\partial\mathrm{z}}=\sigma\left[\mathrm{T}^4{}_{\text{пов}}(0,\mathrm{t})-\mathrm{T}^4{}_{\text{воз}}(\mathrm{t})\right] \tag{3.17}$$

Это граничное условия соответствует излкчению по закону Стефана – Болцмана с поверхности почвы в окружающую среду (воздуха) с температурой $\mathrm{T}_{\text{воз}}$(t).

3.3. Выбор граничного условия на глубине

3.3.1. Граничного условия на глубине 1 – го рода.

Почва обычно рассматривается как полуограниченный массив, и одно из граничных условий записывается как (Чудновский, 1976, стр. 18; Куртенер и Чудновский, 1979, стр. 15; Куртенер и Решетин, 1970, с. 38-45):

$$\lim_{z\to\infty} T\left(z,t\right) = const, \text{ или } \mathrm{T}\left(z\to\infty,t\right) = \mathrm{T}_0 \tag{3.18}$$

Однако при выполнении практических расчетов нет возможности в качестве исходных данных задать величины температуры почвы на бесконечности, так как они неизвестны. Поэтому обычно в таких случях вместо T(∞,t) задается температура на некоторой глубине z=L, начиная с которой при z > L величина T(z,t)=const. Таким образом, реальным условиям более соответствует не граничное условие (3.18), а условие

$$\mathrm{T}\left(z=L,t\right) = \mathrm{T}_0 = const \tag{3.19}$$

Укажем для примера, что если расчетный интервал времени не более суток, то в большинстве случаев L ≤ 0.5 м, для месячного и сезонных промежутков времени 1 ≤ L ≤ 2 м (Чудновский, 1976, стр. 18; Куртенер и Чудновский, 1979, стр. 15).

3.3.2. Граничного условия на глубине 2 – го рода

Так как температурные колебания с глубиной быстро затухают, и начиная с некоторой глубины z > L температура почвы на расчетном интервале времени практически не меняется. Следовательно при отсутсвии теплового потока на глубине следует ставить условии:

$$\frac{\partial \mathrm{T}(z=L,t)}{\partial z} = 0 \tag{3.20}$$

3.3.3. Граничного условия на глубине 3 – го рода.

На практике очень редко встречаются случаи, когда на определенной глубине почвы происходит вертикальный обмен температурами между подпочвой, температура которой составляет $T_{gr}(t)$, и и нижней поверхностью почвы. Это известно как граничное условие 3-го типа:

$$-\lambda \frac{\partial \mathrm{T}(L,t)}{\partial z} = h_{gr}\left[\mathrm{T(L,t)} - \mathrm{T_{gr}(t)}\right] \tag{3.21}$$

h_{gr} – коэффициент конвективного теплообмена.

3.4. Выбор граничного условия на контакте (*условия сопряжения*)

Граничные условия 4 – го рода возникают при рассмотрениипроцессов переноса в составных областях, представляющих собой соприкасающиеся части с различными свойствами и скоростями переноса и особенно важны при моделировании процессов с фазовыми переходами. Условия этого типа состоят в равенстве потенциалов и потоков переноса на разграничивающих поверхностях (Сысуев, 1986, стр. 66). Граничные условия 4 – го рода обычно применяются тогда, когда почва рассматриваются как многослойная система. Они формулируются в виде равенства температур и неразрывности тепловых потоков на границе слоев (Карслоу и Егер, 1964, с. 62-95, 106-112; Чудновский, 1976 стр. 22; Куртенер и Чудновский, 1979; стр 18):

$$\mathrm{T}\left(z,t\right)\Big|_{z=l_i-0} = \mathrm{T}\left(z,t\right)\Big|_{z=l_i+0} \tag{3.22}$$

$$\lambda_i \left.\frac{\partial \mathrm{T}(z,t)}{\partial z}\right|_{z=l_i-0} = \lambda_{i+1} \left.\frac{\partial \mathrm{T}(z,t)}{\partial z}\right|_{z=l_i+0} \tag{3.23}$$

где l_i – границы слоев $(i=1,2,3,...)$.

Если на границе происходит выделение (или поглощение) тепла, то (3.23) записывется как

$$\lambda_i \left.\frac{\partial \mathrm{T}(z,t)}{\partial z}\right|_{z=l_i-0} - \lambda_{i+1} \left.\frac{\partial \mathrm{T}(z,t)}{\partial z}\right|_{z=l_i+0} = q(t) \tag{3.24}$$

4. Постоновка и решение прямой задачи теплопереноса в почве

4.1. Решение без начальных условий при $\mathrm{T}(\infty,t)=\mathrm{T}_0$

Для определения коэффициента температуропроводностью по данным полевых или лабораторных экспериментов используют аналитического решения уравнения теплопроводности:

$$\frac{\partial \mathrm{T}}{\partial t} = \kappa \frac{\partial^2 \mathrm{T}}{\partial z^2} \quad , \quad \left(\kappa = \frac{\lambda}{\rho_b C_m} = \frac{\lambda}{C_v}\right) , \{0 < z < \infty \; ; \; t > 0\} \tag{4.1}$$

полученном при без начального и периодического граничнего условия на поверхности:

$$\mathrm{T}(z=0,t) = \mathrm{T}_0 + \sum_{j=1}^{m} \mathrm{T}_j \cdot \cos\left(j\omega t + \varepsilon_j\right) \tag{4.2}$$

а также при условии, что температура почвы на бесконечности постоянна, т.е.:

$$\mathrm{T}(z \to \infty, t) = \mathrm{T}_0 \tag{4.3}$$

который в безразмерном форме имеет вид (Карслоу и Егер, 1964, стр.70-73):

$$\begin{aligned} \mathrm{T}(y,\tau) = \mathrm{T}_0 + \sum_{j=1}^{m} \mathrm{T}_j \cdot e^{-b_j y} \cdot \cos\left(j\bar{\omega}\tau + \varepsilon_j - b_j\, y\right) - \\ - \sum_{j=1}^{m} \frac{2\mathrm{T}_j}{\sqrt{\pi}} \int_0^{y/2\sqrt{\tau}} \cos\left[j\bar{\omega}\left(\tau - \frac{y^2}{4v^2}\right) + \varepsilon_j\right] e^{-v^2} dv \end{aligned} \tag{4.4}$$

где $$0 \le y = \frac{z}{L} < \infty, \; \tau = \frac{\kappa}{L^2} t \; , \; \bar{\omega} = \omega \frac{L^2}{\kappa}, \; b_j = \sqrt{j\frac{\bar{\omega}}{2}} \tag{4.5}$$

Второй член в правой части (4.4) соответствует нестационарному возмущению, обусловленному начальном колебаний температуры поверхности почвы в момнт времени $t=0$; при достаточном большом t этот член исчезает, т.е. $t \to \infty \Rightarrow \frac{y}{2\sqrt{\tau}} = 0$. Оставшийся первый член соответствует установившимся колебанием температуры почвы с периодом $\tau_0 = 2\pi/\omega$.

Таким образом, решения уравнения (4.1) в исходных переменных запищутся в виде:

$$\mathrm{T}(z,t) = \mathrm{T}_0 + \sum_{j=1}^{m} \mathrm{T}_j \cdot e^{-z\sqrt{j\frac{\omega}{2\kappa}}} \cdot \cos\left(j\omega t + \varepsilon_j - z\sqrt{j\frac{\omega}{2\kappa}}\right) \tag{4.6}$$

При $m=1$ решение (4.6) в исходных переменных запищутся в виде:

$$\mathrm{T}(z,t) = \mathrm{T}_0 + \mathrm{T}_a \cdot e^{-z\sqrt{\omega/2\kappa}} \cdot \cos\left(\omega t + \varepsilon - z\sqrt{\omega/2\kappa}\right) \quad (4.7)$$

или $$\mathrm{T}(z,t) = \mathrm{T}_0 + \mathrm{T}(z) \cdot \cos\left(\omega t + \varepsilon - \frac{z}{d}\right) \quad (4.7^1)$$

где $$\mathrm{T}(z) = \mathrm{T}_a \cdot e^{-\frac{z}{d}}, \quad d = \sqrt{\frac{2\kappa}{\omega}} = \sqrt{\frac{\kappa\tau_0}{\pi}} \quad (4.8)$$

Здесь T(z) – амплитуда колебаний температуры почвы в глбине ***z***, d –глубина затухание температурных волн

Решение (4.7) в безразмерном форме имеет вид:

$$\mathrm{T}(y,\tau) = \mathrm{T}_0 + \Phi_a(b,y) \cdot \cos\left[\bar{\omega}\tau + \varepsilon - \psi(b,y)\right] \quad (4.9)$$

где $$\Phi_a(b,y) = \mathrm{T}_a \cdot e^{-by}, \ \psi(b,y) = by, \ b = \sqrt{\bar{\omega}/2} = \sqrt{\pi/\tau_0\kappa} \quad (4.10)$$

Эта задача изучалась еще Фурье и впервые была применена при определении температурных колебаний почвы (Карслоу и Егер, 1964, стр.70-71; Тихонов и Самарский, 1966, стр.-239).

На основе полученного решения (4.7) можно дать следующую характеристику процееса распространения температурной волны в почве. Если температура поверхности длительное время периодически меняется, то в почве устанавливается колебания температуры с тем же периодом, причем (Тихонов и Самарский, 1966, стр. 244).

1. Амплитуда колебаний экспоненциально убывает с глубиной *z*: т.е., если глубины растут в арифметической прогрессии, то амплитуды убывает в геометрической прогрессии (***1 закон Фурье***): в (4.8) это d –глубина затухание температурных волн или глубина, на которой амплитуда колебаний температуры почвы уменьшается в $e \approx 2.7$ раза по сравнению с амплитудой колебаний температуры деятельной поверхности.

Также следует отметить, что амплитуда колебаний падает тем быстрее, чем больше частота температурных волны, т.е. ω.

К определению коэффициента температуропроводности почвы, на основе использование решение (4.7) упрошенного уравнения теплопереноса (4.1), посвящено немало работ. Все эти методы, основаны на анализе хода температуры почвы на разных глубинах и во времени, причем все они предполагает либо наличие периодического хода температуры в определенный период, либо реалный ход температуры. Но эти методы дают усредненное значение коэффициента температуропроводности за рассматриваемый период времени, причем исходят они из постоянства величины κ, по всей глубине почвы.

Если $z = s = 2\pi d = 2\sqrt{\pi\tau_0\kappa}$, то есть на расстоянии одной длины волны амплитуда уменьшается в $e^{-2\pi} = 0,0019$ раз и, значит волны очень быстро затухают (Карслоу и Егер, 1964, стр-72]:

$$\mathrm{T}(z)_{z=s} = \left(\mathrm{T}_a \cdot e^{-z\sqrt{\omega/2\kappa}}\right)_{z=s} = \left(\mathrm{T}_a \cdot e^{-z\frac{2\pi}{s}}\right)_{z=s} = \mathrm{T}_a \cdot e^{-\frac{2\pi}{s}s} = \mathrm{T}_a \cdot e^{-2\pi} = 0,0019\mathrm{T}_a$$

2. Температурные колебания в почве происходят со сдвигом фазы. Сроки наступления (то есть время t_z запаздывания) максимумов и минимумов темпертуры на глубине ***z*** запаздывают по сравнению с соответствующими сроками для температуры поверхности в соответствии со ***вторым законом Фурье*** **(**Шеин и др. 2001, с. 139-140; *Тихонов и Самарский,* 1966, стр.244):

$$t_z = z\sqrt{\frac{1}{2\kappa\omega}} = \frac{z}{2}\sqrt{\frac{\tau_0}{\pi\kappa}}$$

Температурные колебания (например, положение максимума и минимума температуры) распространяются внутри почвы со скоростью (Карслоу и Егер, 1964, стр-72):

$$\left(2\kappa\omega\right)^{\frac{1}{2}} = \frac{z}{\tilde{t}}$$

Фаза температурной волны запаздывет по закону (Карслоу и Егер, 1964, стр-72):

$$\tilde{\varepsilon} = z\sqrt{\frac{\omega}{2\kappa}} = z\sqrt{\frac{\pi}{\kappa\tau_0}}$$

На самом деле из (4.7) имеем:

$$\omega t + \varepsilon - z\sqrt{\frac{\omega}{2\kappa}} = \omega\left(t - z\sqrt{\frac{1}{2\omega\kappa}}\right) + \varepsilon = \omega\left(t - \frac{z}{2}\sqrt{\frac{\tau_0}{\pi\kappa}}\right) + \varepsilon = \omega\left(t - t_z\right) + \varepsilon$$

т.е., что глубина проникновения годовых колебаний при одинаковой амплитуде на поверхности была бы в **19,1** раза больше глубины проникновения суточных колебаний.

3. Глубина проникновения тепла в почву зависит от периода колебаний температуры на поверхности. Относительное изменение температурой амплитуды равно:

$$\mathrm{T}\left(z\right)/\mathrm{T}_a = \cdot e^{-z\sqrt{\omega/2\kappa}} \tag{4.11}$$

т.е., чем меньше период, тем меньше глубина проникновения температуры. Для температурных колебаний с периодами T_1 и T_2 глубины $z=z_1$ и $z=z_2$ на которых происходит одинаковое относительное изменение температуры, связаны соотношением (***3 закон Фурье***)

$$z_2 = \sqrt{\frac{\mathrm{T}_2}{\mathrm{T}_1}}\, z_1 \tag{4.12}$$

Так, например, сравнение суточных и годовых колебаний, для которых $\mathrm{T}_2 = 365\mathrm{T}_1$ показывает, что

$$z_2 = \sqrt{\frac{\mathrm{T}_2}{\mathrm{T}_1}}\; z_1 = \sqrt{365}\; z_1 \approx 19{,}1 z_1 \tag{4.13}$$

т.е., что глубина проникновения годовых колебаний при одинаковой амплитуде на поверхности была бы в **19,1** раза больше глубины проникновения суточных колебаний.

4.2. Решение без начальных условий при $T(L,t)=T_0$

Для расчета температуры почвы T(z,t), а также определение парметров модели (4.1) теплопереноса в почве, обычно использую решение уравнения теплопроводности, полученные при условии, что температура на $z\to\infty$ постоянна, т. е. имеет место:

$$T(z\to\infty,t)=T_0 \tag{3.18}$$

Как было отмечено выще, реальным условиям более соответствует не граничное условие (3.18), а условие

$$\mathrm{T}\left(z = L, t\right) = \mathrm{T}_0 = const \tag{3.19}$$

Следовательно, следует рассмотрет следующую краевую задачу:

$$\frac{\partial \mathrm{T}}{\partial t}=\kappa\frac{\partial^2 \mathrm{T}}{\partial z^2}\ ,\ \left(\kappa=\frac{\lambda}{\rho_b C_m}=\frac{\lambda}{C_v}\right)\ ,\ \{0<z<L\ ;\ t>0\}$$

$$\mathrm{T}(0,t)=\mathrm{T}_0+\sum_{j=1}^{m}\mathrm{T}_j\cdot\cos\left(j\omega t+\varepsilon_j\right)\ ,\ t\geq 0 \qquad (4.14)$$

$$\mathrm{T}(L,t)=\mathrm{T}_0\ ,\ t\geq 0$$

Можно показать, что их решение также имеет вид (4.9), то есть

$$\mathrm{T}(y,\tau)=\mathrm{T}_0+\sum_{j=1}^{m}\left\{\Phi_j\left(b_j,y\right)\cdot\cos\left[\ j\bar{\omega}\tau+\varepsilon_j-\psi_j\left(y,b_j\right)\right]\right\} \qquad (4.6)$$

где функции $\Phi_j(y, b)$ и $\psi_j(y, b_j)$, определяются через (Микайылов, 2009):

$$\Phi_j\left(b_j,y\right)=\mathrm{T}_j\cdot\mathrm{K}^{-}\left(b_j,y\right),\ \psi_j=\mathbf{arctan}\left[\frac{\mathrm{P}_{2\mathrm{j}}^{-}\left(b_j,y\right)}{\mathrm{P}_{1\mathrm{j}}^{-}\left(b_j,y\right)}\right] \qquad (4.15)$$

Где

$$\mathrm{K}^{-}\left(b_j,y\right)=\mathrm{T}_j\cdot\sqrt{\frac{\mathbf{cosh}\left[2b_j\left(1-y\right)\right]-\cos\left[2b_j(1-y)\right]}{\mathbf{cosh}\left(2b_j\right)-\cos\left(2b_j\right)}}$$

$$\left.\begin{aligned}\mathrm{P}_{1\mathrm{j}}^{-}\left(b_j,y\right)&=\mathbf{cosh}\left(q\right)\cos\left(b_j y\right)-\mathbf{cosh}\left(b_j y\right)\cos\left(q\right)\\ \mathrm{P}_{2\mathrm{j}}^{-}\left(b_j,y\right)&=\mathbf{sinh}\left(q\right)\sin\left(b_j y\right)-\mathbf{sinh}\left(b_j y\right)\sin\left(q\right)\end{aligned}\right\} \qquad (4.16)$$

$q=b\left(2-y\right)$, $\mathbf{cosh}\left(\xi\right)=\frac{1}{2}\left(e^{\xi}+e^{-\xi}\right)$, $\mathbf{sinh}\left(\xi\right)=\frac{1}{2}\left(e^{\xi}-e^{-\xi}\right)$ – гиперболический косинус и синус соответственно.

4.3. Решение без начальных условий при $\partial T(L,t)/\partial z=0$.

С точки зрения почвоведение, намного реальным условиям на нижнем границе является условие (3.20), так как начиная с некоторой глубины z > L температура почвы на расчетном интервале времени практически не меняется, т.е. на глубине z > L тепловой потока отсутсвует. В этом случае, следует рассмотрет следующую краевую задачу:

$$\frac{\partial \mathrm{T}}{\partial t}=\kappa\frac{\partial^2 \mathrm{T}}{\partial z^2}\ ,\ \left(\kappa=\frac{\lambda}{\rho_b C_m}=\frac{\lambda}{C_v}\right)\ ,\ \{0<z<L\ ;\ t>0\}$$

$$\mathrm{T}(0,t)=\mathrm{T}_0+\sum_{j=1}^{m}\mathrm{T}_j\cdot\cos\left(j\omega t+\varepsilon_j\right)\ ,\ t\geq 0 \qquad (4.17)$$

$$\frac{\partial \mathrm{T}(L,t)}{\partial z}=0\ ,\ t\geq 0$$

И в этом случае можно показать, что их решение также имеет вид (4.6), где функции

где функции $\Phi_j(y, b)$ и $\psi_j(y, b_j)$, определяются через (Микайылов, 2009; 2010):

$$\Phi_j\left(b_j,y\right)=\mathrm{T}_j\cdot\mathrm{K}^{+}\left(b_j,y\right),\ \psi_j=\mathbf{arctan}\left[\frac{\mathrm{P}_{2\mathrm{j}}^{+}\left(b_j,y\right)}{\mathrm{P}_{1\mathrm{j}}^{+}\left(b_j,y\right)}\right] \qquad (4.18)$$

$$K^{+}\left(b_j, y\right) = T_j \cdot \sqrt{\frac{\mathbf{cosh}\left[2b_j\left(1-y\right)\right] + \cos\left[2b_j(1-y)\right]}{\mathbf{cosh}\left(2b_j\right) + \cos\left(2b_j\right)}}$$

где

$$\left.\begin{aligned} P_{1j}^{+}\left(b_j, y\right) &= \mathbf{cosh}\left(q\right)\cos\left(b_j y\right) + \mathbf{cosh}\left(b_j y\right)\cos\left(q\right) \\ P_{2j}^{-}\left(b_j, y\right) &= \mathbf{sinh}\left(q\right)\sin\left(b_j y\right) + \mathbf{sinh}\left(b_j y\right)\sin\left(q\right) \end{aligned}\right\} \qquad (4.19)$$

При $m = 1$ из (4.6) имеем

$$T(y,\tau) = T_0 + \Phi_a\left(b, y\right)\cdot\cos\left[\bar{\omega}\tau + \varepsilon - \psi\left(y, b\right)\right] \qquad (4.20)$$

Где

$$\Phi_a\left(b, y\right) = T_a \cdot \sqrt{\frac{\mathbf{cosh}\left[2b\left(1-y\right)\right] + \cos\left[2b(1-y)\right]}{\mathbf{cosh}\left(2b\right) + \cos\left(2b\right)}},$$

$$\psi\left(b, y\right) = \mathbf{arctan}\left[\frac{\mathbf{sinh}\left(q\right)\sin\left(by\right) + \mathbf{sinh}\left(by\right)\sin\left(q\right)}{\mathbf{cosh}\left(q\right)\cos\left(by\right) + \mathbf{cosh}\left(by\right)\cos\left(q\right)}\right] \qquad (4.21)$$

5. Решение обратной задачи теплопереноса в почве

5.1. Существующие расчетные методы определения коэффициента температуропроводности аналитическими методами

При решение многих воросов, связанных с тепловыми процессами в почве, приходится иметь дело с коэффициентом температуропроводности последней. По этому определению коэффициента температуропроводности почвы посвящено немало работ (Лайхман, 1947; Куртнер и Чудновский, 1948; Каганов и Чудновский, 1948; 1953; Колмогоров, 1950; Карслоу и Егер, 1964; 1979; Нерпин и Чудновский, 1967, 1975; Чудновский, 1948, 1954, 1976; Horton, 1982; Микайылов, 2009а, 2009б; Mikaiylov, F. D. and Shein, 2010).

Здесь мы рассмотрим только некоторые из них, которые представляют наибольщую ценность. Как показывает анализ имеющихся работ по вычеслению коэффициента температуропроводности, всегда для его определения необходимо иметь дело с решениями уравнения теплопроводности (4.1).

Для решения этого уравнения необходимо знать граничные условия. Это обычно достигается заданием на поверхности почвы или на некоторой ее глубине хода температуры во времени в виде периодического ряда за сутки или год.

При таких граничных условиях температура почвы на глубине x, т.е. решение уравнения теплопроводности для суточной температурной волны выражается решением (4.4)

Если температура почвы в течение суток может выражается ***одной гармоникой***, то есть $m = 1$ в (4.4), то коэффициент температуропроводности можно найти (Чудновский, 1948; Чичуа, 1964; Нерпин и Чудновский, 1975; Герайзаде, 1982):

- исходя из величины уменьшения суточной амплитуды температуры с глубиной или
- по запаздыванию фазы температурной волны на двух разных глубинах.

5.1.1. Метод – 1. (Формула который содержит логаритмы амплитуды)

Первый метод основан на использовании ***первого закона Фурье*** (4.8), описывающего затухание амплитуды колебиний температуры почвы с глбиной. Пусть на поверхности почвы установились гармонические колебания температуры с периодом τ_0 и амплитудой T_0. Тогда на глубинах $z=z_1$ и $z=z_2$

тоже наблюдаются колебания температуры почвы с тем же периодом τ_0 и амплитудами $T(z_1)$ и $T(z_2)$ соответственно:

$$T(z_1) = T_a \cdot e^{-\frac{z_1}{d}} \quad \text{и} \quad T(z_2) = T_a \cdot e^{-\frac{z_2}{d}}$$

Из отношения амплитуд колебаний температуры на двух глубинах $z=z_1$ и $z=z_2$ можно вывести формулы для рассчета температуропроводность κ :

$$\kappa = \frac{\pi (z_2 - z_1)^2}{\tau_0 \left[\ln T(z_1) - \ln T(z_2)\right]^2} = \frac{\pi (z_2 - z_1)^2}{\tau_0 \cdot \ln^2 \frac{T(z_1)}{T(z_2)}} = \frac{\omega}{2}\left\{\frac{z_2 - z_1}{\ln\left[T(z_1)/T(z_2)\right]}\right\}^2$$

Расчеты (Карслоу и Егер, 1964; Тихонов и Самарский, 1966; Шеин и др., 2001; Juri, 1991; Horton, 1982, 1983). По полевым данным о затухании волны с глубиной рассчитывают велечину коэффициента температуропроводности почвы при влажности, наблюдаемой во время измерений. Для врехней и нижней границ выделенного почвенного слоя определяют максимальное и минимальное значения температуры за время измерений: $T_{min}(z_1)$ и $T_{max}(z_1)$, $T_{min}(z_2)$ и $T_{max}(z_2)$. Рассчитывают амплитуды колебаний температуры на границах слоя:

$$T(z_1) = \frac{T_{max}(z_1) - T_{min}(z_1)}{2}\ ,\ T(z_2) = \frac{T_{max}(z_2) - T_{min}(z_2)}{2} \tag{5.1}$$

Зная глубины установки термометров в глубинах $z=z_i$ и $z=z_{i+1}$ и амплитуды колебания температуры почвы на этих глубинах $T(z_i)$ и $T(z_{i+1})$, по формуле (5.2) рассчитывают параметр температуропроводность κ, то есть:

$$\kappa_i = \frac{\pi (z_{i+1} - z_i)^2}{\tau_0 \ln^2 \left[\frac{T_{max}(z_i) - T_{min}(z_i)}{T_{max}(z_{i+1}) - T_{min}(z_{i+1})}\right]} \qquad (i = 1, 2, 3, ..) \tag{5.2}$$

Рассчитывают величину температуропроводности κ по формуле (5.2), подставляя длину периода $\tau_0 = 24$ час для суточных и 365 сут для годовых колебаний.

5.1.2. Метод – 2. (Формула который содержит арктангес амплитуды)

Этот вариант вычесления коэффициента температуропроводности предложен в работах (Каганов и Чудновский, 1948, 1953). Для этого необходимо знать распределение температуры по веремени на двух глубинах для ***четырех моментов времени***, промежуток между которими равнялся бы ***шести часам***, то есть одной четверти суток.

Для $t_1 = \tau_0 / 4$ из (4.7[1]) имеем:

$$T(z, t = t_1) = T_0 + T_a \cdot e^{-z/d} \cdot \cos\left(\frac{2\pi}{\tau_0} \cdot \frac{1}{4}\tau_0 + \varepsilon - z/d\right)\left(d = \sqrt{\frac{2\kappa}{\omega}}\right)$$

$$= T_0 + T_a \cdot e^{-z/d} \cdot \cos\left(\frac{\pi}{2} + \varepsilon - z/d\right) = T_0 - T_a \cdot e^{-z/d} \cdot \sin(\varepsilon - z/d)$$

Подобным образом, используя решения (4.7[1]) сначала для произволного глубины z и времени $t_1 = \frac{1}{4}\tau_0$, $t_2 = \frac{2}{4}\tau_0$, $t_3 = \frac{3}{4}\tau_0$, $t_4 = \frac{4}{4}\tau_0$ (например, если $\tau_0 = 24$ *ч*, то $t = 6, 12, 18$ и 24 *ч*) можно написать следующие четыре уравнения:

$$\left.\begin{aligned} \mathrm{T}_1(z,t_1) = \mathrm{T}_0 - \mathrm{T}_a \cdot e^{-z/d} \cdot \sin\left(\varepsilon - z/d\right),\ \mathrm{T}_2(z,t_2) = \mathrm{T}_0 - \mathrm{T}_a \cdot e^{-z/d} \cdot \cos\left(\varepsilon - z/d\right) \\ \mathrm{T}_3(z,t_3) = \mathrm{T}_0 + \mathrm{T}_a \cdot e^{-z/d} \cdot \sin\left(\varepsilon - z/d\right),\ \mathrm{T}_4(z,t_4) = \mathrm{T}_0 + \mathrm{T}_a \cdot e^{-z/d} \cdot \cos\left(\varepsilon - z/d\right) \end{aligned}\right\} \quad (5.3)$$

Вычитывая $\mathrm{T}_3(z,t_3)$ из $\mathrm{T}_1(z,t_1)$, $\mathrm{T}_4(z,t_4)$ из $\mathrm{T}_2(z,t_2)$ и разделив эти разности для глубины ***z*** получим:

$$\frac{\mathrm{T}_1(z,t_1) - \mathrm{T}_3(z,t_3)}{\mathrm{T}_2(z,t_2) - \mathrm{T}_4(z,t_4)} = \frac{-2\mathrm{T}_a \cdot e^{-z/dx} \cdot \sin\left(\varepsilon - z/d\ \right)}{-2\mathrm{T}_a \cdot e^{-z/dx} \cdot \cos\left(\varepsilon - z/d\ \right)} = \frac{\sin\left(\varepsilon - z/d\right)}{\cos\left(\varepsilon - z/d\right)} = \tan\left(\varepsilon - \frac{z}{d}\right)$$

откуда имеем $$\frac{z}{d} = \varepsilon - \arctan\left[\frac{\mathrm{T}_1(z,t_1) - \mathrm{T}_3(z,t_3)}{\mathrm{T}_2(z,t_2) - \mathrm{T}_4(z,t_4)}\right]$$

Для разных глубины $z=z_1$ и $z=z_2$ имеем:

$$\frac{z_1}{d} = \varepsilon - \arctan\left[\frac{\mathrm{T}_1(z_1,t_1) - \mathrm{T}_3(z_1,t_3)}{\mathrm{T}_2(z_1,t_2) - \mathrm{T}_4(z_1,t_4)}\right],\ \frac{z_2}{d} = \varepsilon - \arctan\left[\frac{\mathrm{T}_1(z_2,t_1) - \mathrm{T}_3(z_2,t_3)}{\mathrm{T}_2(z_2,t_2) - \mathrm{T}_4(z_2,t_4)}\right]$$

Вычитывая первого равенство со второго имеем:

$$d = \frac{z_2 - z_1}{\arctan\left[\frac{\mathrm{T}_1(z,t_1) - \mathrm{T}_3(z,t_3)}{\mathrm{T}_2(z,t_2) - \mathrm{T}_4(z,t_4)}\right] - \arctan\left[\frac{\mathrm{T}_1(z,t_1) - \mathrm{T}_3(z,t_3)}{\mathrm{T}_2(z,t_2) - \mathrm{T}_4(z,t_4)}\right]} \quad (5.4)$$

Так как $d = \sqrt{\frac{2\kappa}{\omega}} = \sqrt{\frac{\kappa\tau_0}{\pi}} \Rightarrow d^2 = \frac{\kappa\tau_0}{\pi}$ и $\kappa = \frac{\pi d^2}{\tau_0}$.

Далее, то после несложных преобразований для $z=z_i$ и $z=z_{i+1}$ окончательно имеем

$$\kappa_i = \frac{\pi}{\tau_0} \frac{\left(z_{i+1} - z_i\right)^2}{\arctan^2 \frac{\left[T_1(z_i) - T_3(z_i)\right]\left[T_2(z_{i+1}) - T_4(z_{i+1})\right] - \left[T_2(z_i) - T_4(z_i)\right]\left[T_1(z_{i+1}) - T_3(z_{i+1})\right]}{\left[T_1(z_i) - T_3(z_i)\right]\left[T_1(z_{i+1}) - T_3(z_{i+1})\right] + \left[T_2(z_i) - T_4(z_i)\right]\left[T_2(z_{i+1}) - T_4(z_{i+1})\right]}} \quad (5.5)$$

где; $\mathrm{T}_1(z)$, $\mathrm{T}_2(z)$, $\mathrm{T}_3(z)$ и $\mathrm{T}_4(z)$ – значения температуры на глубинах $z=z_i$ и $z=z_{i+1}$ почвы и в момент времени $t_i = i \cdot \tau_0 / 4$ (например, $\tau_0 = 24$ ч и $t_1=6$, $t_2=12$, $t_3=18$ и $t_4=24$ ч).

Как видно из формулы (5.5), измерив температуры почвы на двух глубинах $z=z_1$ и $z=z_2$ через каждые ***шесть часов в течение суток***, можно вычеслить величину коэффициента теплопроводности без применения специалных приборов. Началом времени отсчета можно выбрать один из четырехразовых сроков метеорологических наблюдений.

после несложных преобразований в этих уравнения окончательно имеем

5.1.3. Метод – 3. (Формула который содержит логаритмы амплитуды)

Используя принятие допущения в Методе – 2, (Колмогоров, 1950; Seeman, 1979; Horton, 1982) и используя систем уравнений (5.3), можно вывести формулу в следующем форме.

Вычитывая $\mathrm{T}_3(x,t_3)$ из $\mathrm{T}_1(x,t_1)$, $\mathrm{T}_4(x,t_4)$ из $\mathrm{T}_2(x,t_2)$ выраженные в (5.3)

$$\mathrm{T}_1(z,t_1) - \mathrm{T}_3(z,t_3) = -2\mathrm{T}_a \cdot e^{-z/d} \cdot \sin\left(\varepsilon - z/d\right)$$
$$\mathrm{T}_2(z,t_2) - \mathrm{T}_4(z,t_4) = -2\mathrm{T}_a \cdot e^{-z/d} \cdot \cos\left(\varepsilon - z/d\right)$$

и слагая их квадратов разности для произвольного глубины z имеем:

$$\left[T_1(z,t_1)-T_3(z,t_3)\right]^2+\left[T_2(z,t_2)-T_4(z,t_4)\right]^2=$$
$$=\left[-2T_a\cdot e^{-z/d}\cdot\sin\left(\varepsilon-z/d\right)\right]^2+\left[-2T_a\cdot e^{-z/d}\cdot\cos\left(\varepsilon-z/d\right)\right]^2=4T_a^2\cdot e^{-2z/d}$$

Для разных глубины z=z$_1$ и z=z$_2$ имеем:

$$\frac{\left[T_1(z_1,t_1)-T_3(z_1,t_3)\right]^2+\left[T_2(z_1,t_2)-T_4(z_1,t_4)\right]^2}{\left[T_1(z_2,t_1)-T_3(z_2,t_3)\right]^2+\left[T_2(z_2,t_2)-T_4(z_2,t_4)\right]^2}=\frac{4T_a^2\cdot e^{-2z_1/d}}{4T_a^2\cdot e^{-2z_2/d}}=e^{2(z_2-z_1)/d}$$

Логарифмируя левой и правой частей последного равенство и учитывая $\kappa=\pi d^2/\tau_0$, окончательно для произвольного периода τ_0 и глубины z=z$_1$ имеем:

$$\kappa_i=\frac{4\pi\left(z_{i+1}-z_i\right)^2}{\tau_0}\ln^{-2}\left\{\frac{\left[T_1(z_i)-T_3(z_i)\right]^2+\left[T_2(z_i)-T_4(z_i)\right]^2}{\left[T_1(z_{i+1})-T_3(z_{i+1})\right]^2+\left[T_2(z_{i+1})-T_4(z_{i+1})\right]^2}\right\}\quad(i=1,2,3,\ldots)\qquad(5.6)$$

где; T$_1$(z), T$_2$(z), T$_3$(z) и T$_4$(z) – значения температуры на глубинах z=z$_i$ и z=z$_{i+1}$ почвы и в момент времени $t_i=i\cdot\tau_0/4$ (например, τ_0 = 24 ч и t$_1$=6, t$_2$=12, t$_3$=18 и t$_4$=24 ч).

Как видно из формулы (5.5) и (5.6), измерив температуры почвы на двух глубинах z=z$_i$ и z=z$_{i+1}$ через каждые ***шесть часов в течение суток***, можно вычислить величину коэффициента теплопроводности без применения специалных приборов. Началом времени отсчета можно выбрать один из четырехразовых сроков метеорологических наблюдений. Следует отметить, что методs – 2 и 3 по сущности одиноково с методом-1, но их преимущество заключаются в том, что измеряемы значения почвенных температуры много $T_i\left(i=1,2,3,4\right)$, т.е. расчетные значения κ более достоверны.

5.1.4. Метод – 4. (Формула который содержит сдвиг фазы)

Основы метода по запаздыванию фазы температурной волны на двух разных глубинах состоит в следующем (Чудновский, 1966; Horton, 1982). Когда амплитуда температурных волн достигают максимальному значению в двух разных глубинах, определяют разницы времени $\Delta t=t_2-t_1$, когда достигается значения максимальных температуры почв на глубинах z=z$_i$ и z=z$_{i+1}$.

Далее используя решения (4.7) имеем:

$$\cos\left(\omega t_1+\varepsilon-\frac{z_1}{d}\right)=\cos\left(\omega t_2+\varepsilon-\frac{z_2}{d}\right)\text{ или же }\omega t_1+\varepsilon-\frac{z_1}{d}=\omega t_2+\varepsilon-\frac{z_2}{d}$$

откуда получим $$\kappa_i=\frac{1}{2\omega}\left(\frac{z_{i+1}-z_i}{\Delta t}\right)^2=\frac{\tau_0}{4\pi}\left(\frac{z_{i+1}-z_i}{\Delta t}\right)^2\qquad(5.7)$$

$$\kappa_i=\frac{1}{2\omega}\left(\frac{z_{i+1}-z_i}{\Delta t}\right)^2=\frac{\tau_0}{4\pi}\left(\frac{z_{i+1}-z_i}{\phi_2-\phi_1}\right)^2\left(i=1,2,3,..\right)\qquad(5.7^1)$$

При применение этого метода целосообразно вести наблюдение за ходом изменение температуры почвы, скажем через каждый час.

5.1.5. Метод –5. (Формула который использует численный метод)

Этот метод (Шеин и др., 2001; Шеин и Гончаров, 2006; и др.) основан в том, что основное уравнение теплопереноса (1.2)**,** переписываются в виде конечныч разностях:

$$\frac{T_i^{j+1}-T_i^j}{\Delta t}=\kappa\cdot\frac{\left(T_{i-1}^j-T_i^j\right)-\left(T_i^j-T_{i+1}^j\right)}{\left(\Delta z\right)^2}=\kappa\cdot\frac{T_{i-1}^j-2T_i^j+T_{i+1}^j}{\left(\Delta z\right)^2} \tag{5.8}$$

или $$T_i^{j+1}=T_i^j+\frac{\kappa\cdot\Delta t}{\left(\Delta z\right)^2}\left(T_{i-1}^j-2T_i^j+T_{i+1}^j\right) \tag{5.8^1}$$

Используя экспериментальные данные и формулы (5.8) можно вычислить коэффициента температуропроводности. Предполагая в (5.8^1) упрощение

$$\frac{\kappa\cdot\Delta t}{\left(\Delta z\right)^2}\approx\frac{1}{2} \tag{5.9}$$

разностное уравнения (5.8) примет вид:

$$T_i^{j+1}=\frac{1}{2}\left(T_{i-1}^j+T_{i+1}^j\right) \tag{5.10}$$

Используя экспериментальные данные и формулы (5.10) можно вычислить коэффициента температуропроводности

5.2. Другие Методы

Существуют и методы, учитывающие реальный ход температуры для определения коэффициента температуропроводности, не предполагающие, что поверхности почвы температура изменяется по синусоидальному закону, а меняется любым образом. Одной из первых таких формул является следующая (Лайхман, 1947; Каганов и Чудновский, 1953; Чураев, 1960; Чичуа, 1964; 1967; Герайзаде, 1982; Битюков, 2007):

$$\sqrt{\kappa}=\frac{\pi\int_0^{\infty}\left[T\left(z,t\right)-T\left(x,0\right)\right]dz}{\int_0^t\frac{\left[T\left(0,\tau\right)-T\left(0,0\right)\right]}{\sqrt{t-c}}d\tau} \tag{5.10}$$

При выводе этой формулы сделано предположение, что температура почвы в начальный момент времени распределена линейно.

В работе **(**Лайхман, 1947) приводятся еще две формулы, учитывающие реальный ход температуры. Здесь мы приводим одну из них.

При выводе формулы никаких органичивающих предположений о характере хода температуры почвы не сделано. Она выглядит следующим образом:

$$\kappa=\frac{\int_0^H\left[T\left(z,t\right)-T\left(z,0\right)\right]zdz+H\int_H^{\infty}\left[T\left(z,t\right)-T\left(z,0\right)\right]dz}{\int_0^t\left[T\left(0,t\right)-T\left(H,t\right)\right]dt} \tag{5.11}$$

где $h,H-$ некоторые определенные глубины в почве, **z**- координаты глубины почвы.

Следующая формула, которую мы здесь приводим (Чураев, 1960*)*, выводится при использовании экстремальных значений в распределении температуры почвы по глубине. Эта формула имеет следующий вид:

$$\kappa = \frac{\int_0^{H(0)} \left[T(z,t) - T(z,0)\right](z-h)\,dz + \int_{H(0)}^{H(t)} \left\{T(z,t) - T\left[z, t_m(z)\right]\right\}(z-h)\,dz}{\int_0^t \left\{T(h,t) - T\left[H(t); t\right]\right\} dt} \qquad (5.12)$$

где $t_m(z)$ – время, когда наблюдается экстремальное значение температуры на глубине ***z***; $T\left[z, t_m(z)\right]$ – экстремальное значение температуры.

Все эти формулы, предложенные для определения коэффициента температуро-проводности почвы, основаны на анализе хода температуры почвы на разных глубинах и во времени, причем все они предполагает либо наличие периодического хода температуры в определенный период, либо реальный ход температуры. Вычисление коэффициента температуропроводности по этим формулам требует знания значений только одной температуры почвы, что очень просто практически выполнить. Но эти формулы дают усредненное значение коэффициента температуропроводности за рассматриваемый период времени, причем исходят они из постоянства величины κ, по всей глубине почвы.

Анализ вышеприведенных методов вычисления тепловых характеристик или точнее коэффициента температуропроводности показывает, что для приближенных определений этих характеристик как в естественных, так и в лабораторных условиях можно воспользоваться одним из этих теоретических рассуждений.

5.3. Предлагаемый среднеинтегральный метод определения Коэффициента температуропроводности

5.3.1. Метод определения к на основе существуюших решений $T(\infty,t)=T_0$

Важным является также изучение средней температуры почвы, поскольку как и другие почвенные характеристики общее содержание температуры в профиле варьирует в меньшей степени, чем температуры на определенной глубине. Поэтому его удобнее использовать при определения коэффициента температуропроводности на основе экспериментов полевых и лабораторных условиях.

Определим среднюю в слое $0 \le y \le 1$ безразмерную температуры. Для этого проинтегрируем решение (4.7), от нулья до единице по переменной y:

$$T(y,\tau) = T_0 + \Phi_a(b,y)\cdot\cos\left[\bar{\omega}\tau + \varepsilon - \psi(b,y)\right] \qquad (4.9)$$

где $0 \le y = \frac{z}{L} < \infty,\ \tau = \frac{\kappa}{L^2}t,\ \bar{\omega} = \omega\frac{L^2}{\kappa},\ b = \sqrt{\frac{\bar{\omega}}{2}},\ \Phi_a(b,y) = T_a\cdot e^{-by},\ \psi(b,y) = by$ (4.10)

или

$$\frac{T(y,\tau) - T_0}{T_a} = \theta(y,\tau) = e^{-by}\cdot\cos\left(\bar{\omega}\tau + \varepsilon - by\right),\ \bar{\omega} = \omega\frac{L^2}{\kappa},\ b = \sqrt{\frac{\pi}{\tau_0\kappa}} \qquad (5.13)$$

После интегрировании (5.13) имеем:

$$\Theta(\tau,b) = \left\{\frac{1+e^{-b}\left[\sin(b) - \cos(b)\right]}{2b}\right\}\cdot\cos\alpha + \left\{\frac{1-e^{-b}\left[\sin(b) + \cos(b)\right]}{2b}\right\}\cdot\sin\alpha \qquad (5.14)$$

или упростив его получим:

$$\Theta(\tau,b) = \frac{\bar{T}(\tau) - T_0}{T_a} = \frac{1}{\sqrt{2}\,b}\left[\sin\left(\frac{\pi}{4} + \alpha\right) - e^{-b}\cdot\sin\left(\frac{\pi}{4} + \alpha - b\right)\right] \qquad (5.15)$$

где

$$\Theta(\tau)=\int_0^1\theta(y,\tau)dy=\int_0^1\left[\frac{\mathrm{T}(y,\tau)-\mathrm{T}_0}{\mathrm{T}_a}\right]dy=\frac{\bar{\mathrm{T}}(\tau)-\mathrm{T}_0}{\mathrm{T}_a},\ \alpha=\bar{\omega}\tau+\varepsilon,\ b=L\sqrt{\frac{\omega}{2k}} \qquad (5.16)$$

Важным является также изучение средней температуры почвы, поскольку как и другие почвенные характеристики общее содержание температуры в профиле варьирует в меньшей степени, чем температуры на определенной глубине. Поэтому его удобнее использовать при определения коэффициента температуропроводности на основе экспериментов полевых и лабораторных условиях.

Как видно из формулу (5.15), измерив осредненные безразмерные температуры $\Theta(\tau,b)$ почвенной колонки длиной L через каждые ***шесть часов в течение суток***, можно вычислить величину коэффициента ***температуропроводности*** **к** . На самом деле различных α из (5.15) имеем:

$$\alpha=\alpha_1=\frac{\pi}{2}+\varepsilon:\ \ \Theta_1=\frac{1}{\sqrt{2}\,b}\left[\cos\left(\frac{\pi}{4}+\varepsilon\right)-e^{-b}\cdot\cos\left(\frac{\pi}{4}+\varepsilon-b\right)\right]$$

$$\alpha_1=\frac{\pi}{2}+\varepsilon:\qquad \Theta_2=\frac{1}{\sqrt{2}\,b}\left[\cos\left(\frac{\pi}{4}+\varepsilon\right)-e^{-b}\cdot\cos\left(\frac{\pi}{4}+\varepsilon-b\right)\right]$$

$$\alpha_3=\frac{3\pi}{2}+\varepsilon:\qquad \Theta_3=\frac{1}{\sqrt{2}\,b}\left[-\cos\left(\frac{\pi}{4}+\varepsilon\right)+e^{-b}\cdot\cos\left(\frac{\pi}{4}+\varepsilon-b\right)\right]$$

$$\alpha_3=2\pi+\varepsilon:\qquad \Theta_4=\frac{1}{\sqrt{2}\,b}\left[\sin\left(\frac{\pi}{4}+\varepsilon\right)-e^{-b}\cdot\sin\left(\frac{\pi}{4}+\varepsilon-b\right)\right]$$

Вычитывая Θ_3 из Θ_1 и Θ_4 из Θ_2 получим разности:

$$\begin{aligned}\Theta_1-\Theta_3&=\frac{\sqrt{2}}{b}\left[\cos\left(\frac{\pi}{4}+\varepsilon\right)-e^{-b}\cdot\cos\left(\frac{\pi}{4}+\varepsilon-b\right)\right]\\ \Theta_4-\Theta_2&=\frac{\sqrt{2}}{b}\left[\sin\left(\frac{\pi}{4}+\varepsilon\right)-e^{-b}\cdot\sin\left(\frac{\pi}{4}+\varepsilon-b\right)\right]\end{aligned} \qquad (5.17)$$

Далее имеем:

$$\begin{aligned}&\left(\Theta_1-\Theta_3\right)^2+\left(\Theta_4-\Theta_2\right)^2=\\ &=\frac{2}{b^2}\left\langle\begin{array}{l}\left[\cos^2\left(\frac{\pi}{4}+\varepsilon\right)+\sin^2\left(\frac{\pi}{4}+\varepsilon\right)\right]+\left[e^{-2b}\cdot\cos^2\left(\frac{\pi}{4}+\varepsilon-b\right)+e^{-2b}\cdot\sin^2\left(\frac{\pi}{4}+\varepsilon-b\right)\right]-\\ -\left[2e^{-b}\cdot\cos\left(\frac{\pi}{4}+\varepsilon\right)\cos\left(\frac{\pi}{4}+\varepsilon-b\right)+2e^{-b}\cdot\sin\left(\frac{\pi}{4}+\varepsilon\right)\sin\left(\frac{\pi}{4}+\varepsilon-b\right)\right]\end{array}\right\rangle=\\ &=\frac{2}{b^2}\left\langle 1+e^{-2b}-2e^{-b}\left[\cos\left(\frac{\pi}{4}+\varepsilon\right)\cos\left(\frac{\pi}{4}+\varepsilon-b\right)+\sin\left(\frac{\pi}{4}+\varepsilon\right)\sin\left(\frac{\pi}{4}+\varepsilon-b\right)\right]\right\rangle=\\ &=\frac{2}{b^2}\left\langle 1+e^{-2b}-2e^{-b}\ \cos\left[\left(\frac{\pi}{4}+\varepsilon\right)-\left(\frac{\pi}{4}+\varepsilon-b\right)\right]\right\rangle=\frac{2}{b^2}\left[1+e^{-2b}-2e^{-b}\ \cos(b)\right]\end{aligned}$$

В результате имеем

$$\left(\Theta_1-\Theta_3\right)^2+\left(\Theta_4-\Theta_2\right)^2=2\left[\frac{1+e^{-2b}\ -2e^{-b}\cdot\cos(b)}{b^2}\right] \qquad (5.18)$$

Соотношение (5.18) можно записать в виде

$$\frac{1}{2}\psi(b)=\frac{1+e^{-2b}-2e^{-b}\cdot\cos(b)}{b^2} \tag{5.19}$$

где $$\psi(b)=(\Theta_1-\Theta_3)^2+(\Theta_4-\Theta_2)^2,\ \Theta_i(\tau)=\frac{\overline{T}_i(\tau)-T_0}{T_a}$$

Свойстава функции $\psi(b)$:

$$\lim_{b\to 0}\psi(b)=2\lim_{b\to 0}\left[\frac{1+e^{-2b}-2e^{-b}\cdot\cos(b)}{b^2}\right]=4,\ \lim_{b\to\infty}\psi(b)=2\lim_{b\to\infty}\left[\frac{1+e^{-2b}-2e^{-b}\cdot\cos(b)}{b^2}\right]=0$$

На рис. 5.1 приведен график зависимости функции $\psi(b)$ для величин $b=L\sqrt{\omega/2\kappa}$ равных от 0, 0.1, 0.2, ..., 5.0. Как видно из формулы (5.19) измерив осредненные безразмерные температуры почвенного слоя $[0\ ,\ L\ ]$ через каждые ***шесть часов в течение суток***, т.е., $\Theta_i(b),(i=1,\ 2,\ 3,\ 4)$, далее следует вычислит $\frac{1}{2}\psi(b)$ и используя график 5.1, можно вычислить величину параметра $b=b^*$, откуда находится значения коэффициента ***температуропроводности*** из формулы:

$$\kappa=\frac{\omega L^2}{2b^2}=\frac{2\pi}{\tau_0}\cdot\frac{L^2}{2b^2}=\frac{\pi}{\tau_0}\cdot\frac{L^2}{b^2}=\frac{\pi}{24}\cdot\frac{L^2}{b^2}=0,7854\cdot\frac{L^2}{b^2}\frac{см^2}{час} \tag{5.20}$$

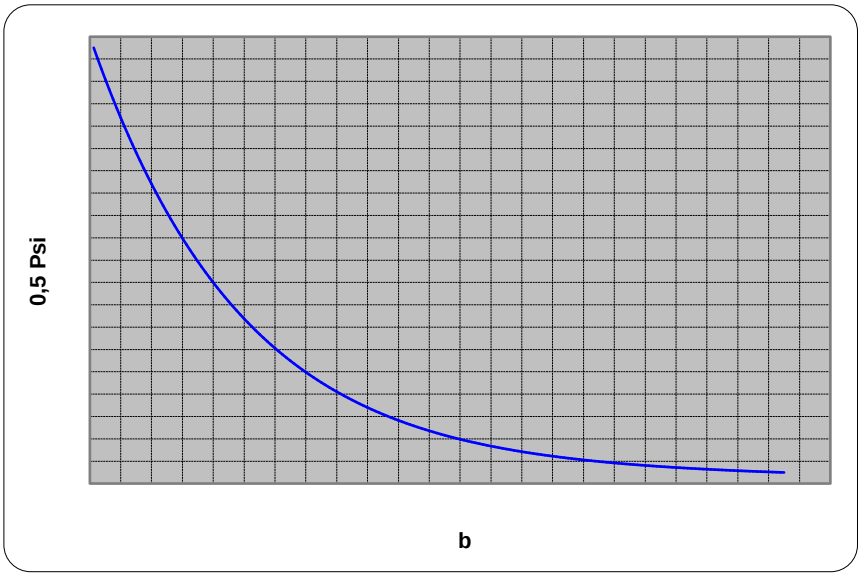


Рис. 5.1. График зависимости функции $\frac{1}{2}\psi(b)$ от параметра ***b***

Область применения.

Предложенный метод определения температуропроводности почвенных слоев является простым, надежным и удобным и дает возможность использовать его результаты в прогнозных математических моделях, используемых при оптимизации управления тепловым режимом естественных и искусственных почв в условиях открытого и закрытого грунта.

5. ЛИТЕРАТУРА

Герайзаде А.П. (1982). Термо – и влагоперенос в почвенных системах. Баку, Элм, 159 с.

Каганов М.А.,Чудновский А.Ф. (1948). Определениые коеффициента теплопроводности по данним срочных измерений температури. Изв. АН СССР, серия геофиз., 5, 1948.

Каганов М.А.,Чудновский А.Ф. (1953). Об определении коеффициента температуропро-водности почв. Изв. АН СССР, серия геофиз., 2

Карслоу Г., Егер Д. (1964).Теплопроводность твердых тел. М.: Наука, с.62-95, 106-112.

Колмогоров, А.Н. (1950). К вопросу об определении коэффициента температуропроводности почвы // Изв. АН СССР. Сер. гео. и геофиз. 14(2). 97—98.

Куртнер А.В. и Чудновский А.Ф. (1948). Отемпературном поле в почве как среде с переменными тепловыми характеристиками//Сб.тр.по агроном. физике, вып.4.

Куртенерв Д.А., Решетин О.Л. (1970). Об одном решении уравнения теплопроводности в связи с расчетом температуры почвы//В кн.: Теплообменв открытом и защищенном грунте. Л.: Гидрометеоиздат, с. 38-45.

Куртенерв Д.А., Чудновский А.Ф. (1979). Агрометеорологические основы тепловой мелиорации почв. Л.: Гидрометеоиздат, 231 с.

Лайхман Д.Л. О точном методе получения коэффициента температуропроводности почвы. Тр. ГГО, вып.2, 1947.

Микайылов Ф.Д. (2009а). Некоторые вопросы моделирования температурного режима почвы//Сб. трудов (CD) конференции «16 Зимняя школа по механике сплошных сред: Механика сплошных сред как основа современных технологий», 24–27 Февраля 2009 г, Пермь (Россия).

Микайылов Ф.Д. (2009б).Об одном решении уравнения теплопроводности в почве// Материалы конференции «Пятые научные чтения памяти Ю.П.Булашевича». 06 – 10 июля 2009 г. Екатеринбург (Россия).

Нерпин С.В. Чудновский А.Ф. Физика почв. М. 1967.

Неусыпина Т.А. (1979).Расчеты теплового режима почвы в модели формирования урожая. Сб. Трудов по агроном. физике «Теоретические основы и количественные методы программирование урожаев», Ленинград, с. 53-62.

Сеттон О.Г. (1958). Микрометеорология. Л.: Гидрометеоиздат, 1958, 356 с.

Сысуев В.В. Моделирование процессов в ландшафтно-геохимических системах. М.: Наука, 1986, с. 58-84.

Тихонов А.Н., Самарский А.А. (1966). Уравнение математической физики. - М.: Наука, с.238-247.

Чичуа Г.С. (1964). Теплофизические характеристики основных почвенных типов Грузинской ССР. Автореф. докт.диссертации, Тбилиси, 1964.

Чудновский А.Ф. (1948). Физика теплообмена в почве. Л.: Гостехиздат.

Чудновский А.Ф. (1954).Теплообмен в диспресных средах. Л.:, Гостехиздат, 1954.

Чудновский А.Ф. (1976). Теплофизика Почв. М.: Наука, 352 с.

Чураев Н.В. (1960). Применнение радиоактивных изотопов для исследовения процессов переноса влаги в торфе. Колл.журн, 23(5).

Шеин Е.В. и др. (2001).Полевые и лабораторные методы исследований фихических свойств и режимов почв. Изд-во Моск. ун-та., с. 139-171

Шеин Е.В., Гончаров В.М. (2006).Агрофизика. Ростов на Дону.: Феникс, 400 с.

Juri W.A., Gardner W.R., Gardner W.H. (1991). Soil Physics, New York, 328 p.

Horton, R.Jr. (1982). Determination and use of soil thermal properties near the soil surface. New Mexico Satate University, 151 p.

Kirham, D., Powers, W.L. (1972). Advanced Soil Physics, New York.

Marinova, T.K. (1993). On determining the conductivity coefficient of the basic soils in Bulgaria. Bulgarian Journal of Meteorology & Hydrology, 2, 65-69.

Mikailsoy, F. D. (2017). On the influence of boundary conditions in modeling heat transfer in soil. J. Eng. Phys. Thermophys. 90 (1), 67–79 (2017). https://doi.org/10.1007/s10891-017-1540-y .

Mikaiylov, F. D. and Shein, E. V. (2010). Theoretical foundations of experimental methods of determination of the thermal diffusivity of soils," Eurasian Soil Sci. 5, 597–605 (2010). https://doi.org/10.1134/S1064229310050091

Smith, W.O. 1939. Thermal conductivities in moist soils. Soil Science Society of America Proceedings, 4, 32–40.

ÇİRKAB SULARIN TƏMİZLƏNMƏSİNDƏ NANOTEXNOLOGİYANIN TƏTBİQİ İMKANLARI

g-m.e.n., dos. Natiq H.Paşa[1]

[1]*Azərbaycan Texniki Universiteti, Metallurgiya və materialşünaslıq fakultəsi, Kimya texnologiya, təkrar emal və ekologiya kafedrası, Bakı, Azərbaycan, ORCID ID: https://orcid.org/0000-0002-5666-6835*

Ləman Səfərova[2]

[2]*Azərbaycan Texniki Universiteti, Yüksək Təhsil İnstitutu, Ekologiya mühəndisliyi, Bakı, Azərbaycan, ORCID ID: https://orcid.org/0000-0002-5277-170X*

Özet

Hazırda dünyada aktual problemlərdən biri su çatışmazlığıdır. Hər keçən gün artan tələbala gələcəkdə daha çox su istehlakı və içməli su çatışmazlığı problemini həll etmək üçün tullantı sularının təkrar emalına böyük diqqət yetiriləcəkdir. Çirkab suların ənənəvi yolla təmizlənməsi dünyanın bir çox yerində onların tətbiqini çətinləşdirən mühəndislik təcrübəsi, aşağı səmərəlik, çox vaxt sərfi və böyük investisiyalar tələb etdiyi üçün əlçatanlığını çətinləşdirir. Buna görə də tullantı suların təmizlənməsinin təkmilləşdirilməsində yeni yanaşmalar davamlı aktuallığını qoruyur.

Nanotexnologiyanın çirkab suların təmizlənməsində tətbiq ediləbilirliyi potensialı yeni sahə olmaqla bərabər, bu problemləri aradan qaldırmaqda ümidvericidir. Nanotexnologiya optik, maqnit, mexaniki, keçirici xassələrə malik yeni strukturların yaradılması üçün maddənin atom və molekul səviyyəsində manipulyasiyası texnologiyasıdır. Nanotexnologiyada istifadə olunan nanomaterialların yüksək səth-həcm nisbəti, adsorbsiya qabiliyyəti, reaktivliyi və həssaslığı çirkab suların təmizlənməsində istifadəsini əlverişli edir.

Kiçik ölçüləri, geniş səth sahəsi və funksionallaşdırma rahatlığı sayəsində nanostrukturlar çirkab suların təmizlənməsi üçün daha əlverişli və sərfəli katalizator və redoks mühit yaratma imkanlarına malikdirlər.

Sənaye miqyasında nanofiber membranlar əsasən havanın təmizlənməsi üçün istifadə olunurlar. Aparılan sınaqların nəticələri onların suyun təmizlənməsində də perspektivliyinə inam yaradır. Nanofiber membranlar nəzərəçarpacaq çirklənmə olmadan yüksək effektivliklə mikrohissəcikləri sulu fazadan çıxara bilir. İstehsal zamanı nanoliflərin xassələrinə nəzarət etmək imkanı müxtəlif əlavələr tətbiq etməklə unikal imkanlara malik çoxfunksiyalı materiallar əldə etməyə imkan verir. Məsələn, təcrübələr keramika nanomaterialları və ya xüsusi adsorbentləri nanolifli çərçivəyə yerləşdirməklə filtrasiya zamanı ağır metalları və üzvi çirkləndiriciləri çıxarmaq üçün membranlar hazırlamağa imkan verir.

Keniya, Cənubi Afrika, Haiti kimi təmiz su çatışmazlığından əziyyət çəkən və bu səbəbdən ölüm nisbətinin yüksək olduğu ölkələrdə uğurla sınaqdan keçmiş, gümüş nanohissəcik tərkibli filtr vərəqlər 100 litrə qədər çirkab suyunu bakteriya və viruslardan təmizləməyə imkan verir.

ABŞ-da tullantı sularının təmizlənməsi üçün nanotexnologiyanın müxtəlif formaları hazırda pilot layihə səviyyəsində tədqiq edilir. Sıfır valentli dəmirin (nZVI) nanoölçülü hissəciklərini ehtiva edən bu layihələrdən biri artıq kommersiya səviyyəsinə və çirklənmiş ərazilərin təmizlənməsində praktiki tətbiqə çatmışdır.

Çirkab suların təmizlənməsində nanotexnologiyanın tətbiqinin hələ ki, bəzi məhdudiyyətləri də qalmaqdadır. Məsələn, karbon nanoborucuqlar suyun dezinfeksiyasını təmin etməsi üçün birbaşa virus, bakteriya və s. nanomembran ilə, reaktiv səthlə təmasda olmalıdır. Nanohissəciklər əhəmiyyətli dərəcədə faydalı edən ultra kiçik ölçüləri təəssüf ki, daha uzun davamlılıq və hissəciklərin daha yüksək reaktivliyi səbəbindən torpaq və su obyektlərində yeni növ çirklənmə yarada biləcəyini düşünürsək, ətraf mühit, heyvanlar, insanlar və bitkilər üçün bir çox təhlükələri ifadə edə bilən bir sıra mənfi təsirlər yarada bilər.

Hazırda suyun təmizlənməsi və dezinfeksiyası sahəsində nanotexnologiyalara əsaslanan proseslərin geniş tətbiqinin yaxın perspektivlərindən danışmaq mümkün deyil, çünki hələ çoxlu texniki problemlərin həlli tələb olunur. Ancaq inkişaf edən texnoloji üsullarla sulardan ağır metalların kənarlaşdırılması elektonspinnig və nanofiber membran metodları ilə mümkün olabiləcək kimi müşahidə edilməkdədir.

Bir çox elmi və texniki dövri nəşrlərdə çirkləndiricilərin və suyun dezinfeksiyasının əlavə məhsullarının mikro və nanokonsentrasiyalarının müxtəlifliyi və toksikliyi haqqında məlumatlarla bərabər, getdikcə daha çox tədqiqat işləri suyun təmizlənməsi və dezinfeksiyasının alternativ üsullarında nanotexnologiyanın mühüm rol oynadığına həsr olunmuşdur. Xüsusilə də mədən və emal zavodlarında, liman ballastını və sintinə sularını, neft tankerlərini yuduqdan sonra çirklənmiş suları təmizləyərkən istifadə edilən OreFilter texnologiyaları pilot tədqiqatlar səviyyəsində Yaxın Şərq, Kanada, ABŞ, Braziliya və Avstraliyadakı sənaye obyektlərində uğurla sınaqdan keçirilir.

Azərbaycanda çirkab suların təmizlənməsi üzrə nanotexnologiyadan istifadə sahəsində araşdırmalar hələ ki, kifayət qədər aparılmamışdır. Bu yeni sahənin imkanlarının tətbiqi, xüsusən Xəzərin neftlə çirklənən sularının təmizlənməsi istiqamətində araşdırmaların aparılması prespektivli ola bilər. Çirkab sularının təmizlənməsində nanotexnologiyanın tətbiqi ilə əlaqəli yuxarıda qeyd olunan problemlər əhəmiyyətli olmaqla yanaşı, onları müvəqqəti hesab etmək olar. Ümid etmək olar ki, qabaqcıl texnologiyaların tətbiq edilməsi ilə bu arzuolunmaz nəticələri aradan qaldırmaq mümkün olacaqdır.

Açar sözlər: nanotexnologiya, nanomaterial, nanofiltrasiya, nanomembran, çirkab sular.

APPLICATION POSSIBILITIES OF NANOTECHNOLOGY IN WASTEWATER TREATMENT

Abstract

The water scarcity is one of the major problems facing the world right now. In order to address the issue of increased water consumption and drinking water shortages, wastewater recycling will receive a lot more attention in the future due to the ever-increasing demand. The typical wastewater treatment process is expensive, time-consuming, labor-intensive, and needs specialized engineering knowledge in many parts of the world, which makes it difficult to implement. It also has low efficiency. Therefore, developing innovative methods to optimize wastewater treatment is still necessary.

Even though it is a relatively new field, the prospective application of nanotechnology in wastewater treatment holds potential for solving these issues. Nanotechnology refers to the technology of manipulating matter at the atomic and molecular level to produce new structures with optical, magnetic, mechanical, and conductive properties. Nanotechnology-derived nanoparticles are advantageous for treating wastewater because of their high surface-to-volume ratio, adsorption capacity, reactivity, and sensitivity.

Due to their small size, large surface area and ease of functionalization, nanostructures have the potential to create more convenient and cost-effective catalysts and redox media for wastewater treatment.

Nanofiber membranes are mostly utilized for air filtration on an industrial scale. The outcomes of the investigations undertaken support the viewpoints on purifying water held by nano fiber membranes. High-efficiency microparticle removal from the aqueous phase using nanofiber membranes is possible without much fouling. By using different additives, multifunctional materials with distinctive features may be created by manipulating the properties of nanofibers during manufacture. For instance, experiments enable the production of membranes to filter out heavy metals and organic pollutants by adding specific adsorbents or ceramic nanoparticles to a nanofiber framework.

Filter plates containing silver nanoparticles, which have been successfully tested in countries such as Kenya, South Africa and Haiti, where there is a shortage of clean water and therefore a high mortality rate, allow wastewater up to 100 liters to be cleaned of bacteria and viruses.

In the US, several types of nanotechnology are now being explored at the pilot project level for wastewater treatment. One of these initiatives, utilizing nanoscale zero valent iron (nZVI) particles to remediate polluted regions, has reached commercialization and practical implementation.

There are still certain restrictions on the use of nanotechnology in wastewater treatment. For instance, enabling Carbon nanotubes to provide water disinfection, nano membrane must come into direct contact with viruses, bacteria, etc. on reactive surface. Considering that the ultra-small size that makes nanoparticles so useful can unfortunately create a new type of pollution in soil and water bodies due to the longer persistence and higher

reactivity of the particles, several adverse effects could arise, which could pose many dangers to the environment, animals, humans, and plants.

Since numerous technical issues still need to be resolved, it is now difficult to discuss the near future of widespread application of procedures based on nanotechnology in the field of water treatment and disinfection. However, electrospinning and nanofiber membrane techniques have been found to be effective at removing heavy metals from water.

Numerous scientific and technical articles focus on the crucial role that nanotechnology plays in alternative water treatment techniques and ongoing research, as well as on the variety and toxicity of micro- and nano-concentrations of contaminants and the by-products of water disinfection. OreFilter technologies are being successfully tested in industrial facilities in the Middle East, Canada, the United States, Brazil, and Australia. They are particularly employed in mining and processing plants, port ballast and bilge water, and cleansing of dirty water after washing oil tankers.

The use of nanotechnology for wastewater treatment is still undergoing insufficient investigation in Azerbaijan. Applying this new field's potential, particularly through research aimed at purifying the Caspian Sea's oil-polluted waters, may be the approach to go. Despite their importance, the aforementioned issues with the use of nanotechnology in wastewater treatment might be regarded as temporary. It is believed that the use of innovative technology would make it feasible to completely avoid these negative effects.

Keywords: nanotechnology, nanomaterial, nanofiltration, nanomembrane, waste water.

THERMODYNAMICAL ANALYSIS of the GAS STREAM in the COMPRESSOR STATIONS

Valeh Bakhshali[1], Konul Huseynzade[2]

[1]*Corresponding author: Azerbaijan Technical University, Department of Mechanics, H. Javid ave., 25, AZ1073, Baku, Azerbaijan, ORCID ID: 0000-0001-9443-5440*

[2]*Ph.D. Student, Azerbaijan Technical University, H. Javid ave., 25, AZ1073, Baku, Azerbaijan*

Abstract

Results of a cycle of research to problems of the theory and practice of maintenance of reliable compressor stations and pipelines developed on the basis of the new strategy have been presented. The given strategy is developed by taking into account the modern positions of mechanics and ICT. It is connected by that absolutely new approach in questions of designing of the definition of parameters of appointment and economic substantiation of projects oil and gas pipelines now is necessary, namely working out and rationing of some characteristics of reliability which should be pawned in a package of initial technical requirements. Increasing the efficiency and durability of the compressor-pump stations, pipelines, etc. directly depends on the correct calculations and designing of the different elements and thermodynamics parameters. Using ANSYS software, simulation and thermodynamic analysis are performed on the basis of the 405GP15/70 and ARIEL heavy-duty balanced opposed piston compressors and pipelines used in the Caspian sea - Black sea Region. The article investigated the main causes of failures through the collection and analysis of data from different parts of the machines are used for transporting the oil and gas resources. An analysis of parameters due to the application of oil and gas transportation is presented and analyzed in this work. By observing the analysis results, we can decide whether our designed pipeline is safe or not under applied technical conditions. The durable and reliable work of compressor-pump stations and pipelines used in the oil and gas industry has great importance for practice. Investigation of complex problems with respect to mechanical and thermodynamically phenomena in the compressors and pumps gives the opportunity to solve the problems of increasing the durability of oil and gas transportation.

Keywords: Compressor, Pump, Thermodynamics, Pipeline, Dynamics.

1 Introduction

The energy security of the Black Sea - Caspian Sea Region depends on the technical conditions -reliability and durability of the machines and equipment used in oil and gas pipelines in Region. The overall goal of research is development of integrated model of the piston machine system that is than used to evaluate and improve current design and increase the environment conditions. Providing the technical security of oil and gas pipelines is one of the very important problems of exploitation and transport in oil and gas industry [1].

Pump-compressors stations today are essential in practically every industry field where any form of gas and oil is handled. Mechanically, aside from problems such as the type of stuffing box, selection of materials suitable for the gas to be handled, and regulation, there is little difference between an air compressor and a gas compressor. Therefore, a certain amount of standardization has been done on the basis of using available parts of standard air-compressing equipment when applying such machinery for handling gases other than air.

The reciprocating machines find the widest use, largely because of its ability to meet the needs of the greatest number of compressed-gas users. The most common of these is the horizontal machine although many vertical and V-type compressor units are built also. We considered the vertical compressor machine in previous works [2,3].

Compressor-pump stations are used on the oil and gas pipeline for the transport of this mineral resource. Current methods of reciprocating and centrifugal machinery design, see e.g. [2,3], are based on partial empirical relations and do not take into account many of the factors that are affecting the mechanical and thermodynamic processes in these machines. To date, no applied formulas are available for durability and reliability of the parts, for mechanical losses in the bearings, for energy losses in the kinematical couples of

machines used in the oil industry, nor has there been basic research of the impact phenomena in these kinematic couples. On the other hand, very detailed models leading to computer-intensive simulations have recently been developed for piston ring dynamics in the context of blow-by estimation [2], for lubrication conditions of the ring/liner contact, for dynamically loaded bearings, and for stress and failure analysis of assembly parts. However, until now, the insight gained with these models has not found its way into more detailed models for reciprocating machines such as reciprocating and centrifugal compressors. To this end, a modular system modeling approach as described below combined with model reduction is necessary in order to keep the computational efforts at reasonable magnitudes [4,5].

Duplex double-acting compressors are built in standard sizes for a wide range of pressures, with compressor cylinders arranged horizontally, vertically, or at an angle for a wide variety of special conditions. Compressors of this type may be driven by electric motors or internal-combustion engines. Only the actual capacity of a compressor and the energy or power it requires per unit of gas actually delivered should be considered, for they are the real standard of a compressor's efficiency [6,7,8].

One of the important problems of piston compressors is the problem of mechanical (friction, oscillation, and so on) losses in these machines. Investigations showed that the mechanical losses in piston compressors become about 70 % of total power losses [2].

2 Analysis of the compressor stations used in regional pipelines

The problem of maintenance of natural gas and products of its processing has got today a special urgency. Continuously increasing the requirement for natural gas for the supply of developing infrastructure of the most important industries, will demand input in a system of new compressor stations for the transportation of natural gas. The construction of high-efficiency high compressing compressor stations equipped with piston and centrifugal compressors with gas turbines by a drive most is. The stations of similar type have gained the greatest distribution in the world. Possessing big power consumption and productivity at small dimensions and weight, they applied, especially in the conditions of sea oil-gas fields.

The experience which has been saved up for the periods of installation, start-up-adjustment, and operation has allowed us to put and solve a number of the important problems of the theoretical and practical character connected with questions of calculation and maintenance of reliability of compressor stations [9,10,11].

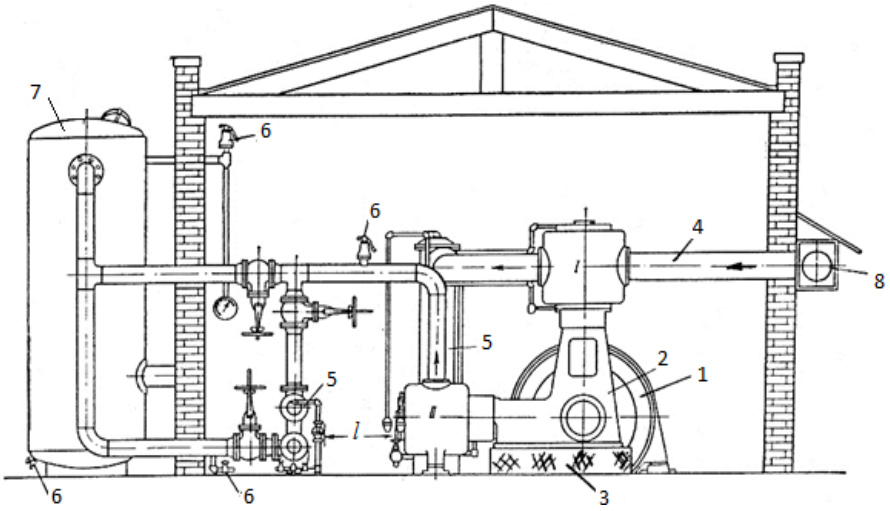


Fig. 1. The scheme of the compressor station. 1. A drive motor, 2. Piston compressor, 3. The foundation, 4. A gas pipeline, 5. An intermediate and end refrigerator, 6. The purge gate, 7. A receiver, 8. The absorb filter

The characteristics should provide the profitability of the project, efficiency, and safety of operation of compressor stations (Fig. 1). In these conditions, a new technical strategy is based on necessary, but sufficient requirements of offered projects by criteria of efficiency, profitability, and ecological compatibility [9,10,11].

3 Methods of the definition of parameters of the gas stream in the pipeline

In the modern period, it is necessary to compensate for the needs of humanity and the potential and energy in great measure. In the last two hundred years the quick development and industrialization of the countries connected with the direct consumption of energy. Kind of the energy sources and the rationality of the user from them of any country is the definition of the development level of the country. The potential requirement of the country is associated with the speed of social and economic development, growth of industrial production and natural atmosphere. The scientific, technological and geographical differences between the countries have influence on potential consumption. Having possessed the powerful industry and the highest level of national profit of any country attains parallelism with the growth of the potential consumption per head.

Definition of pressure loss at gas and oil movement on the cylindrical pipelines has great practical value in the calculation of regional pipelines. This question gets special importance in connection with the development of gas and oil pipelines. Therefore, the question of the definition of parameters of movement of a gas stream on the pipeline and its economic transportation has theoretical and practical value.

At first, we will consider the movement of compressed gas in the pipeline, therefore we will define losses of the pressure of gas depending on the length of the pipeline at the isothermal process of a current of air accepted for ideal gas. Let us consider the pipeline of diameter *D* and length *L* on which compressed gas moves is shown as length x. We will designate gas parameters in initial and final sections of the pipeline accordingly through P_0, T_0, and P_1, T_1, and gas parameters in sections, situated from the beginning of co-ordinates on distance x- through *P, T*. We noted that at the movement of compressed gas in a small initial site of the pipeline, its temperature will decrease in the course of heat exchange with walls of the pipeline cooled by an environment. Then the temperature field of a gas stream will be stabilized, owing to that the temperature of this stream practically remains constant.

Thus gas and oil temperature at its movement on the pipeline specified above we will consider as a constant. Besides, a task in view we will solve at a pressure of gas to 10 MPa taking into account the friction of a gas stream about pipeline walls at its isothermal current. Provided that, it is possible to use the equation of a condition of an ideal gas.

The considered movement of a gas and oil stream, as is known, is defined by three equations: conditions, continuity, and energy.

As on a condition of the decision of a task in view the temperature of gas *T* is constant, movement of a gas stream at its isothermal current is defined by following equations [13].

The equation of state:

$$\frac{P}{\rho} = RT \tag{1}$$

The continuity equation:

$$G = \rho w f \tag{2}$$

The equation motion in the differential form:

$$\frac{dP}{\rho} + wdw + dL_{fr} = 0 \tag{3}$$

Where *p* and *T* are pressure and gas temperature in the section of the pipeline with abscises *x*, *r* and *w* are density and speed of gas in the specified section, *R* is the gas constant of matter, G is the mass expense of matter in the unit of time, f is the area of the section of the pipeline through the passage, equal $f = \frac{\pi D^2}{4}$, *D* is internal diameter of the pipeline, dL_{fr} is the work of force of friction of gas particles about pipeline walls on an elementary site of length *dx* which is defined from the following expression:

$$dL_{fr} = \xi \frac{w^2}{2} \cdot \frac{dx}{D} \tag{4}$$

The factor of friction entering into this expression x in technically smooth pipes depends on the Reynolds Re number and can be defined under the formula:

$$\xi = 0{,}0032 + \frac{0{,}221}{\mathrm{Re}^{0{,}237}} \quad (5)$$

Where

$$\mathrm{Re} = \frac{\rho w D}{\mu} \quad (6)$$

Where *m* is the factor of viscosity of a gas, which depends on the gas temperature.

As gas and oil temperature in a considered problem is constant, the coefficient m will be constant. On the basis of equation (2) parameter *mw* also is a constant. Then, apparently from dependences (5) and (6), Reynolds's number *Re* and friction factor x at gas and oil movement remain constant.

From the equations (1), (2), (3) and (4) we find the velocity of the matter:

$$w = \frac{GRT}{Pf} \quad (7)$$

Differentiating this expression, we will receive:

$$dw = -\frac{GRT}{P^2 f} dp \quad (8)$$

Having substituted expressions (5), (6) and (7) in the differential equation (8), and after transformation we will have:

$$RTpdp - \frac{G^2R^2T^2}{f^2} \cdot \frac{dp}{p} + \xi \frac{G^2R^2T^2}{2Df^2} dx = 0 \quad (9)$$

Integrating the equation (9) taking into account the set boundary condition: at $x=0$, $p=p_0$, $T=T_0$, we will receive the following dependence:

$$\frac{RT}{2}(P^2 - P_0^2) - \frac{G^2R^2T^2}{f^2} \ln \frac{p}{p_0} + \xi \frac{G^2R^2T^2}{2f^2D} x = 0 \quad (10)$$

On this dependence, it is possible to define the pressure of the gas *p* in the given section of the pipeline. Setting various values of pressure of gas *p*, on the expression (10), it is possible to find corresponding lengths of sites of the pipeline at set parameters of pressure p_0 and volume productivity G_0.

On the basis of the given tables schedules of dependence of loss of pressure $\Delta p=p_0-p$ gas from the length of a site of pipeline *x*, при various values of the diameter of the pipeline are constructed.

We presented the dynamic analysis of the parameters of gas depending on the constructive parameters of the pipeline. In an attempt in this article, the pipeline is modeled by using Workbench software, and static analysis is done by using Workbench software. There is evaluated the pressure and constructive parameters of the pipeline. The Workbench focuses on attaching existing geometry, setting up the finite element model, solving, and reviewing results.

The novelty of the article is characterized by new theoretical methods for the determination of parameters of gas pressure in pipelines and cylinders of reciprocating machines taking into account the real working processes and the clearances in kinematic couples of crank-piston mechanisms. The reliability of the received scientific results is provided by the correctness of the statement of tasks and decisions on the basis of laws of mechanics and thermodynamics. The results of the investigation are generalized for any piston machines and pipelines used in the oil and gas industry.

The curve of dependence of loss of pressure of gas and oil Δp from the length of the pipeline *x* can be practically replaced by a straight line. With the increase in diameter of pipeline *D*, the loss of pressure of gas and oil on its given site sharply decreases. It is visible, that with the increase in pressure of air p_0 in the pipeline beginning, the pressure loss in the given site decreases at the set constant value of the expense of volume productivity G_0 proceeding on the pipeline. At an increase in the expense of gas and oil on the pipeline the pressure loss Δp on the given site increases at the set constant values of parameters of matter stream p_0, T_0, and diameter *D* of the

pipeline. The important practical conclusion is that for the reduction of loss of pressure of gas and oil, moving on the pipeline, it is necessary to increase the diameter of pipeline D at a present value of the expense of matter G_0 as from here follows. It in turn can lead to an increase in the expense of the metal necessary for the manufacturing of the gas and oil pipeline, that not always it can appear expedient.

4 Conclusions

From the discussion of the results of the research presented above, some conclusions can be drawn:

1. It is found the dependence to define the pressure of the gas P in the given sections of the pipeline.

2. An analysis of gas stress and damages due to the application of pressure is presented and analyzed in this work. By analyzing the results of obtaining a diagram for pressure loss in the pipeline is decided which dynamical and geometrical parameters are durable for the manufacturing of the pipeline.

The results of the investigation can be useful for the design and exploitation of compressor stations and pipelines used for the transportation of oil and gas resources.

References

Zhiltsov S.S, Zonn I.S., Andrey G. Kostianoy A.G. Oil and Gas Pipelines in the Black-Caspian Seas Region. Springer Cham (2016). DOI: https://doi.org/10.1115/1.1399378

Davitashvili N., Bakhshaliev V. Dynamics of Crank-Piston mechanisms. Springer Publisher (2016). DOI: https://doi.org/10.1007/978-981-10-0323-3

Bakhshali V.I., Mardanov N.T., Bekirova A.A., Ismayil I.A. (2022). Development of Methods for Processing Acoustic Emission Signals of Sensors for the Compressor-Pump Station's Control. In: 11th International Conference on Theory and Application of Soft Computing, Computing with Words and Perceptions and Artificial Intelligence - ICSCCW-2021. Lecture Notes in Networks and Systems, Springer, Cham, vol. 362, pp. 704-710. DOI: https://doi.org/10.1007/978-3-030-92127-9_93

Wittenburg J. Kinematics. Theory and Applications. Springer Verlag Berlin Heidelberg (2016). DOI: https://doi.org/10.1007/978-3-662-48487-6

Bakhshali Valeh I. (2020). Nanomechanics and its applications: mechanical properties of materials. Proc. of the International E-Conference on Advances in Engineering, Technology and Management - ICETM 2020. Institute of Research Engineers and Doctors, USA, pp. 77-81. DOI: https://doi.org/10.15224/978-1-63248-188-7-15

Burstein L, Ingman D.P. (2000). Pore Ensemble Statistics in Application to Lubrication Under Reciprocate Motion, Tribology Transactions; 43(2): 205-212. DOI: https://doi.org/10.1080/10402000008982330

Boyaci A., Hetzer H., Seemann W., Proppe C., Wauer J. (2009). Analytical Bifurcation Analysis of a Rotor Supported by Floating Ring Bearings. J. of Nonlinear Dynamics, 57(4), pp. 597-507. DOI: https://doi.org/10.1007/s11071-008-9403-x

Wannatong K., Chanchaona S., Sanitjai S. (2008). Simulation algorithm for piston ring dynamics. J. of Simulation Modelling Practice and Theory, 16 (1), 127-146. DOI: https://doi.org/10.1016/j.simpat.2007.11.004

Yang, W., Li, X., Tao, Y. et al. (2022). Causal analysis of natural gas station pipelines vibration and reduction measures. J. of Mechanical Science and Technology, **36**, 4409–4418. DOI:https://doi.org/10.1007/s12206-022-0805-3

Olson L. G., Jamison D. (1997). Application of a general purpose finite element method to elastic pipes conveying fluid, J. of Fluids and Structures, 11(2), 207–222. DOI:https://doi.org/10.1006/jfls.1996.0073

Liang Z., S. Li, J. Tian, L. Zhang, C. Feng and L. Zhang. (2015). Vibration cause analysis and elimination of reciprocating compressor inlet pipelines, J. of Engineering Failure Analysis, vol. 48, pp. 272–282. DOI: https://doi.org/10.1016/j.engfailanal.2014.11.003

YARI STATİK MESNETLENMİŞ BETONARME PLAKLARIN TEMAS PATLAMASI YÜKÜ ALTINDA DAVRANIŞININ İNCELENMESİ

Dursun BAKIR

Arş. Gör. Fırat Üniversitesi, Mühendislik Fakültesi, İnşaat Mühendisliği Bölümü, Merkez, Elazığ.,
ORCID NO: 0000-0001-6398-0497

Sedat SAVAŞ

Dr. Öğ. Üyesi. Fırat Üniversitesi, Mühendislik Fakültesi, İnşaat Mühendisliği Bölümü, Merkez, Elazığ.,
ORCID NO: 0000-0003-2466-3514

ÖZET

Dünyada son yüzyılda artan terör saldırılarında en çok kullanılan yöntem patlayıcı içerikli saldırılardır. Bu saldırılar araçlı, insan üzerine bağlanmış intihar tipi ve hedefe yerleştirilen bombalı saldırılardır. Saldırı tiplerine bakıldığında meydana gelen patlamalar; temas, yakın temas ve uzak patlamalar şeklindedir. Çalışmada 200×100×15 cm boyutlarında betonarme plaklara 1 kg TNT eşdeğeri olan patlayıcı temas halinde patlatılmıştır. Patlamalarda meydana gelen krater çukurları incelenmiştir.

Anahtar Kelimeler: Temas patlaması, TNT eşdeğerliği, Betonarme plak, Krater çukuru

INVESTIGATION OF THE BEHAVIOR OF SEMI-STATICALLY SUPPORTED REINFORCED CONCRETE SLABS UNDER CONTACT BLAST LOAD

ABSTRACT

The most widely used method in terrorist attacks that have increased in the last century in the world is attacks with explosive content. These attacks are vehicle, suicide type attached to people and bomb attacks placed on the target. Explosions that occur when looking at attack types; contact, close contact and distant explosions. In the study, an explosive equivalent to 1 kg TNT was detonated in contact with reinforced concrete slabs of 200×100×15 cm dimensions. Crater holes formed in the eruptions were investigated.

Keywords: Contact explosion, TNT equivalence, Reinforced concrete slab, Crater hole

GİRİŞ

Betonarme yapılarda döşemeler, sadece bina yapısının bir bileşeni olarak değil, aynı zamanda çeşitli terör saldırılarının ve askeri saldırıların birincil hedefidir. Bu nedenle, çeşitli ülkelerden araştırmacılar, beton levhalar gibi tipik bileşenlerin patlama direncinin nasıl arttırılması gerektiği üzerine çalışmalar yapmışlardır. Araştırmacılar, plaklar üzerinde yapılan deneyleri dört durum ile ifade etmişlerdir. Bunlar (i) patlama etkisi sonucu plağın deplasman yapmasına rağmen yüzeyde fazla hasar olmaması, (ii) plağın patlama yüküne maruz kalan yüzeyinde krater çukuru açılırken arka yüzeyde her hangi bir hasar olmaması, (iii) plak yüzeyinde derin krater çukuru açılırken arka yüzeyde parçalanmalar ve savrulma (şarapnel gibi), (iv) plağın delinmesidir. Bunlardan en yıkıcı olanı son iki durumdur. Aynı zamanda projelendirme açısından da son iki durum patlama yükü etkisinde istenmeyen plak davranışıdır. Bu davranışı incelemek için betonarme plak üzerine yapılan çalışmaları iki gruba ayırabiliriz. İlk grup, beton dayanımını arttırmak(Khan et al. 2020; Li et al. 2016; Li, Wu, and Hao 2015; Liao et al. 2022) donatı yerleşim şeklini değiştirmek, lifli beton dökmek bunlardan bazılarıdır (Maazoun et al. 2019; Yamaguchi et al. 2011). İkinci grupta ise plak geometrisi, plak kalınlığı, plağın ebatlarını artırarak patlama dalgası ile temas yüzeyini artırıp azaltarak geometrik bağlantı kurmak, plak ile patlayıcı arasındaki mesafeyi değiştirmektir(Morishita et al. 2004). Mesafe problemini ise üç kısma ayırabiliriz. Bunlar temas patlaması, yakın patlama ve uzak patlamadır. Temas ve yakın patlamada kullanılan patlayıcı miktarı, uzak patlamaya göre çok azdır. Bu yüzden maliyeti düşürmek için çoğunlukla temas ve yakın patlama deneyleri yapılmıştır.

Foglar vd.(2014) ekibinin yapmış oldukları çalışmalarında betonarme numunelerin saha testlerinin sonuçları sunulmuştur. Testler, değişen lif içeriği, lif tipi, lif mukavemeti ve beton mukavemet sınıfı ile gerçek ölçekli betonarme prekast plakalar (6 x 1.5 x 0.3 m) üzerinde yapılmıştır. Plaklar üzerine 25 kg TNT yükleri uygulanmıştır. Amaçları, patlama şoku dalgasının ilerlemesini, numunenin alt tarafındaki çatlakların ilerlemesini ve plakanın orta kısmının patlama yüklemesine maruz kalan son çöküşünün incelenmesidir(Şekil 1). Patlama dalgalarındaki yayılma oluşum süreci, hava şok dalgasının ve yayılma debris hızlarının tahmin edilmesini sağlamış, en üstteki çatlak ilerleme hızını ölçme girişimi başarılı olmamıştır. Bunun için yeni yapılacak deneylerde yeni tetikleme sistemi tasarlanması gerektiğini söylemişlerdir.



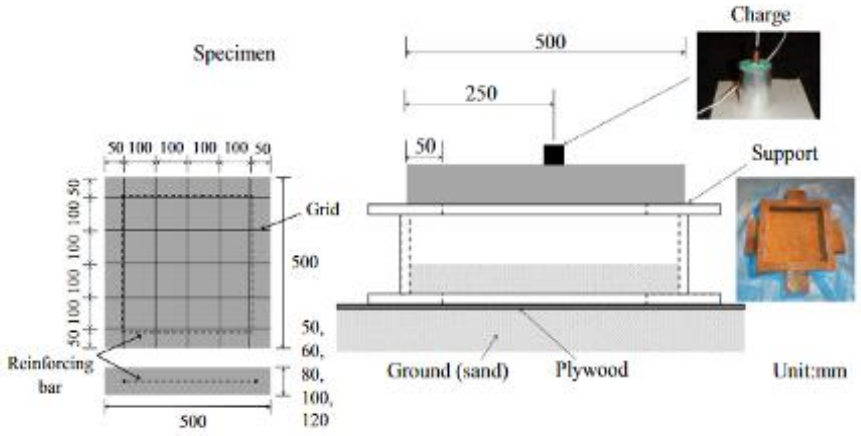
Şekil 1. Betonarme prekast plak düzeneği (Foglar et al. 2014)

Jun Li vd. (2016) tarafından yapılan deneysel çalışmada, mevcut tasarım ve araştırma uygulamaları temel olarak uzak alandaki veya yakınlardaki patlamaların altındaki yapısal tepkilere ve hasarlara odaklandığını ve temas patlamalarını içeren patlama senaryoları kapsamlı bir şekilde araştırılmadığını belirtmişlerdir. Temas patlamaları altında, şiddetli gerilme dalgası yayılımının yol açtığı yüksek derecede yerel hasar görülmesi ve bu hasar modu, yapısal elemanların genellikle eğilme veya kayma modunda tepki verdiği diğer dinamik yükleme türlerinden önemli ölçüde farklı olduğunu belirtmiştir. Çalışmalarında normal dayanımlı betondan ve çelik tel örgülü (1mm çapında ve 6 mm aralıklı tel kafes) betonarme döşemelerden yapılan performanslarının ölçümü yapılmıştır.



Şekil 2. Normal BA ile tel kafes takviyeli BA nın 1 kg TNT patlaması sonucunda plak ön ve arka görünüşleri(Li et al. 2016)

Ichino vd.(2020) yapmış oldukları çalışmada, iki aşamalı beton(tsc) modeli kullanarak temas patlatması uygulamışlardır. İki aşamalı beton modeli ile maksimum iri agrega çapı ve iri agrega tipinin etkileri, bu parametrelerin temas patlamasına maruz kalan bir TSC plakasının bölgesel kırılmasını nasıl etkilediğini belirlemek için deneysel olarak incelenmiştir. 50x50cm en ve boylarında 5 ila 12 cm arasında değişen kalınlığa sahip bir deney düzeneği kurulmuştur(şekil3). 1 kg Tnt temas edilerek patlatılmıştır. Basınç dayanımının 17,6 N/mm² olduğu durumda krater çapı ve krater derinliği, basınç dayanımındaki artışa rağmen kabaca değişim olmamıştır. 30,6 N/mm2 için krater çapları oldukça küçülmüştür.



Şekil 3.TSC deney düzeneği(Ichino, Beppu, and Williamson 2020)

Malzeme takviyesi olarak güçlendirilen betonun patlatılması çalışmasını yapan Wei Wang vd., 2021,yaşlanma direnci yüksek, asit ve alkali korozyona dayanıklı Poliizosiyanat-oksazodon (POZD) polimeri, güçlü tokluk, yüksek mukavemet ve yüksek uzama avantajlarına sahiptir. Beton plakaların temas patlaması etkisindeki hasar özelliklerinin etraflıca araştırılması için farklı yüklere sahip POZD beton plakaların temas patlaması testi yapılmıştır(Şekil4).



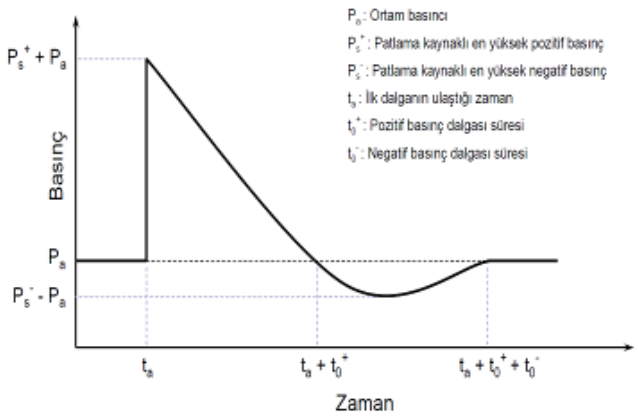
Şekil 4.POZD beton plakların temas patlaması(Wang et al. 2021)

Deneyde kullanılan betonarme taban plakasının boyutu 2000 mm × 2000 mm × 150 mm, aralarında HRB400Φ14200 × 200 çelik çubuk iki katman halinde düzenlenmiş, koruyucu katmanın kalınlığı 15 mm ve seçilen beton sınıfı C40'tır. Şok dalgasının etkisinin, plakanın patlamaya bakan yüzeyinde değişen derecelerde hasara neden olduğu şekil 5'ten görülebilir. Ancak, POZD kaplamanın plakanın arka patlama yüzeyindeki etkisi nedeniyle, betonun parçalanma derecesi etkin bir şekilde kontrol altına alınmış ve arka patlama yüzeyindeki POZD kaplama, betonun çökmesinde neden olmuştur. Bu şekilde, beton levhanın hasarı büyük ölçüde azaltılmıştır.



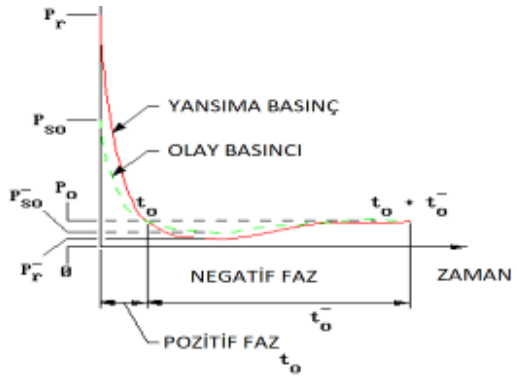
Şekil 5.POZD beton patlama sonrası hasar görüntüleri(Wang et al. 2021)

Patlamadaki en büyük problem, patlamanın ortasından hareket eden süpersonik bir patlama dalgası yaratmasıdır. Şekil 6 'da görüldüğü gibi patlama dalgası kaynağından uzaklaştıkça enerjisi azalır, artan basınç, yoğunluk ve hız tekrar orijinal ortam durumuna geri döner. Bununla birlikte, sıcaklık, patlama dalgasından artan entropi nedeniyle belirli bir artış elde eder. Artan basınca ve tekrar ortam basıncına geri dönme pozitif faz olarak adlandırılır ve bunu, ortam akışından daha düşük bir basınçla karakterize edilen negatif bir faz izler ve partikül akışının tersine çevrilmesine neden olur ve ortamda vakum oluşur(Chee, Krauthammer, and Astarlioglu 2008)



Şekil 6. Patlama Basınç-zaman grafiği

Genellikle yapının sönümlemesine ve patlama dalgasının yapıya gelme açısına göre değişen Pr Yansıma basıncı patlama ortamındaki Pso basıncından çok daha büyük olmaktadır(Şekil7).



Şekil 7. Açık hava patlaması için basınç zaman grafiği

Çalışmada, betonarme plak üzerine yerleştirilen patlayıcının TNT eşdeğerliği deneyleri yapılarak doğrulanmıştır. TNT eşdeğerliği belirlenen patlayıcının plağa temas halinde patlama deneyleri yapılarak oluşan kraterler incelenmiştir.

YÖNTEM

Numunelerin Hazırlanması

Uygulanacak patlama yüküne karşı davranışının belirlenmesi için karşılaştırmak için silindirik basınç dayanımı 30N/mm² olan 3 adet 200x100x15 cm plaklar imal edilmiştir. Deneysel çalışmada, patlayıcıya karşı dayanımını incelemek için güçlendirilmemiş hasır çelik ile güçlendirilmiş beton plaklar imal edilmiştir. Numuneler aynı beton dayanımı ve karşıma sahiptir(Tablo1).

Tablo1. Beton karışım oranları

Çimento	%16
Agrega (7-14 mm)	%35.40
Agrega (3-9 mm)	%4.40
Kum	%37.60
Su	%6.40
Kimyasal katkı	%0.20

Q131/131 (DINGRADE500A) çeliği(Tablo2) iki sıra alta iki sıra üste şaşırtmalı olarak 200x100x15cm boyutlarında kalıplara yerleştirilmiştir. Çelik hasır yerleştirildikten sonra hazırlanan beton karışımı titreşim tablasına yerleştirilerek titreşime maruz bırakılmıştır. Daha sonra kalıplardan sökülen beton numunelere 28 gün su kürü uygulanmıştır.

Tablo2.Q131/131 Çelik hasır

Donatı aralığı	150 mm
Donatı çapı	5.0 mm
Donatı kesit alanı	1.31 m²
Bidirectional donatı oranı	0.35%

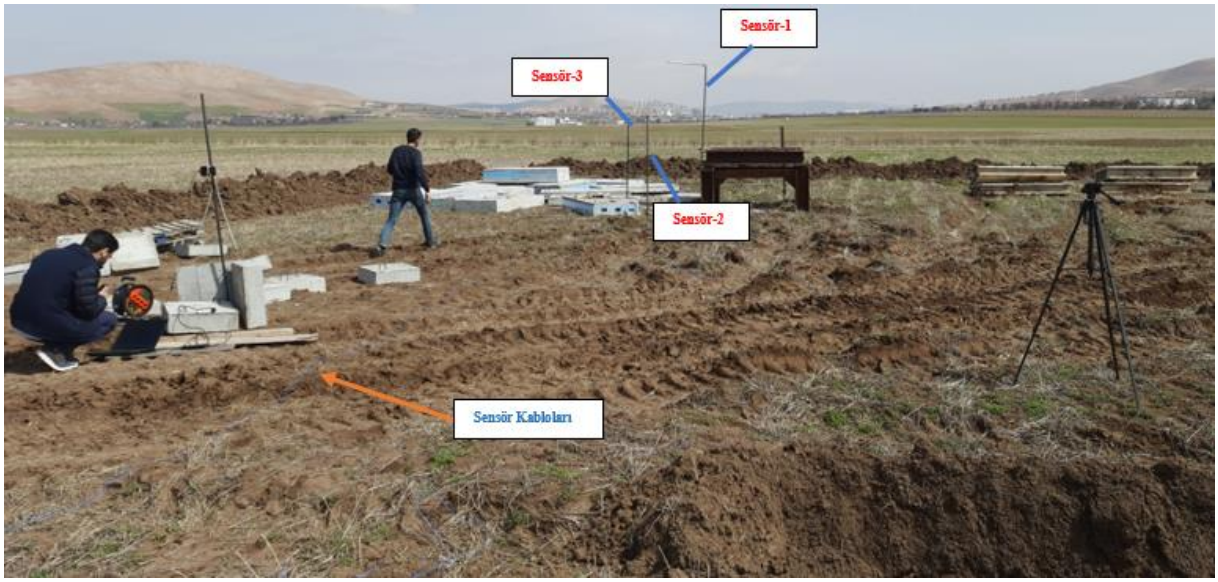
Beton karışım oranları(Tablo1) ve Donatı özellikleri(Tablo2) ile 200x100x15 cm kalıplara numuneler hazırlanmıştır(Şekil8). Bu numuneler yarı statik olarak patlatma sahasında mesnetlenmiştir.



Şekil8. Plak kalıplarının ölçüleri, donatı yerleşimi ve kalıpları

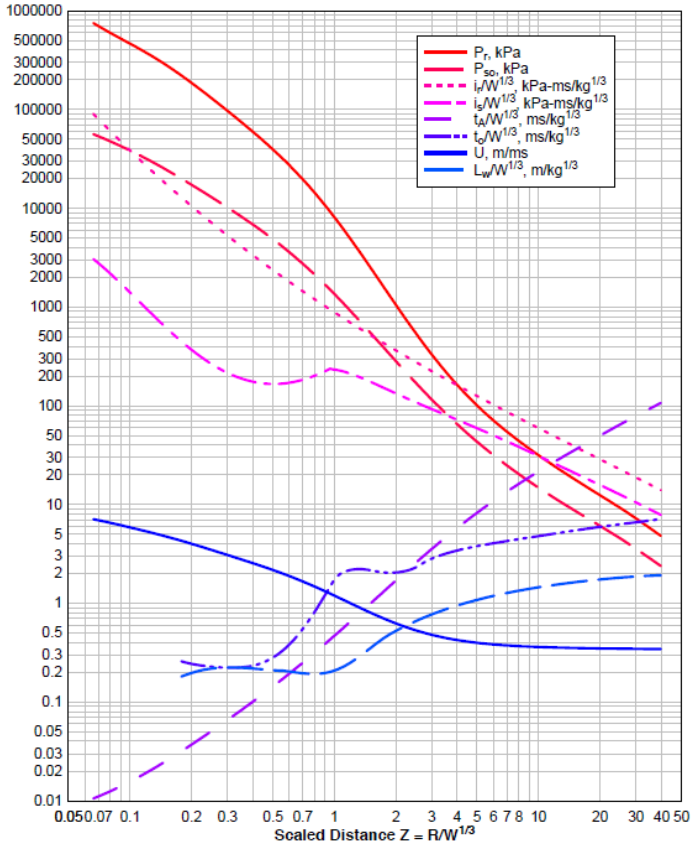
Patlayıcının Eş değerliğinin Belirlenmesi

TNT eşdeğerliğini kullandığımız mevcut patlayıcıya göre belirleyebilmemiz için saha deneyleri uygulanmıştır. Sahada patlama basınç sensörleri hazırlanan çelik çubuk elemanlara yerleştirilmiştir(Şekil9).



Şekil9. Deney Düzeneği

Eş değerlik hesabı UFC(Criteria(UFC) 2008) Serbest patlama ölçekleme faktörüne bağlı logaritmik grafiği(Şekil10) ile 0.91kg patlayıcı 3.2 m mesafede patlama testi yapıldı. Burada elde edilen ortam basıncı(Pso) ile 3.2 mesafede hesaplanan Z ölçeklenme faktörü kullanılarak eş değer TNT patlayıcı ağırlığı hesaplandı(denklem1-2).



Şekil10. Serbest patlama ölçeklenmiş logaritmik grafiği(Criteria(UFC) 2008)

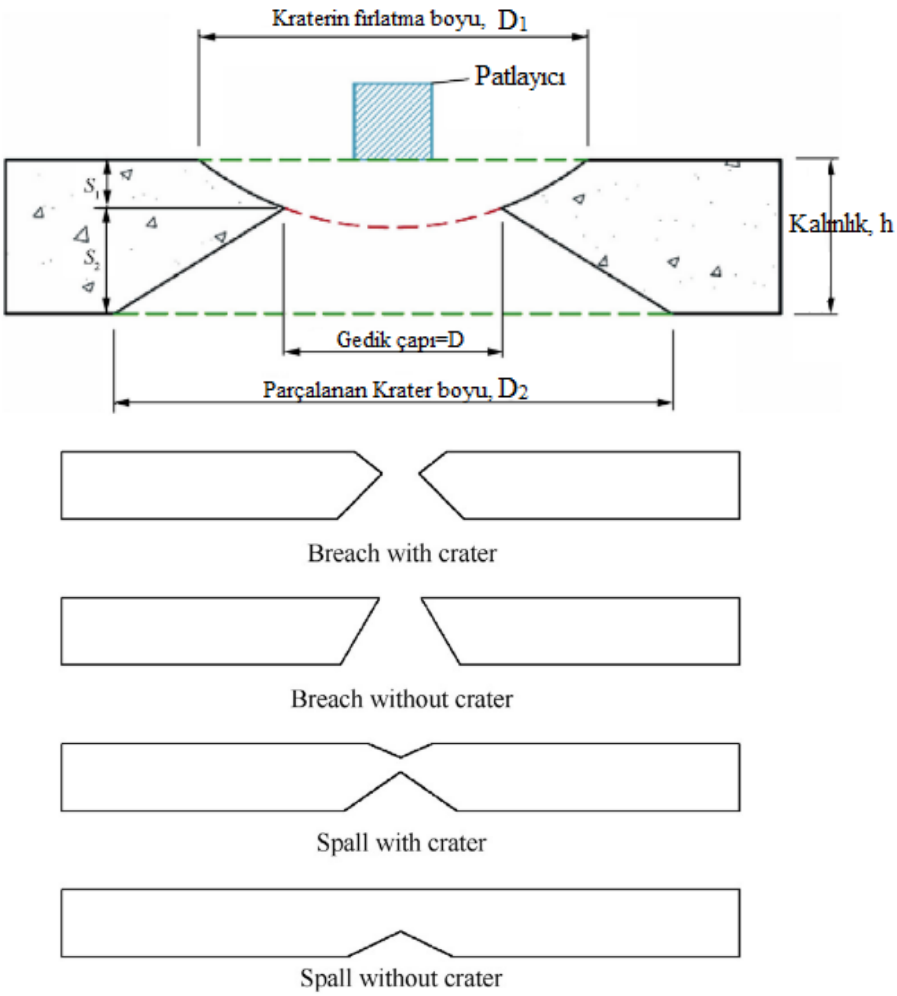
$$Z = \frac{R}{W^{\frac{1}{3}}} \qquad (1)$$

Tablo3. Sensor değerleri

SENSOR	Max Basınç		Min Basnç			
	Zaman	Basınç(N/m^2)	Zaman	Basınç(N/m^2)	Z (m/kg$^{(1/3)}$)	W (kg)
	8,590098	52924	8,594297	-11795,8	3,866359	0,570274

Krater Hesapları

Zemin seviyesinin üstünde bulunan bir patlayıcı yükü ile üretilen bir krater Şekil 11'de gösterilmiştir. D_2 kraterin Çapı ve H kraterin görünen derinliğidir. Bir patlamanın yarattığı kraterin derinliği genellikle çapının dörtte biri kadardır, ancak bu oran ilgili toprağın türüne bağlıdır. Bir patlama tarafından üretilen kraterin çapı, patlayıcı yükünün zemin seviyesine göre göreceli konumuna da bağlıdır.



Şekil11. Krater boyutlarının tanımları(Li et al. 2018)

Beton plakların krater çukuru hesapları için Mc Vay (McVay 1988) yakın temas ve temas patlamaları için amprik formüller üretmişlerdir(Li et al. 2018; Morishita et al. 2004).

Parçalanma Limiti,

$$\frac{T}{W^{1/3}} = 0.073\left(\frac{R}{W^{\frac{1}{3}}}\right)^{-0.58} \quad (2)$$

Yüzeyde Gedik Oluşma Limiti,

$$\frac{T}{W^{1/3}} = 0.073\left(\frac{R}{W^{\frac{1}{3}}}\right)^{-0.58} \quad (3)$$

Yüzeyde Gedik Oluşması, Krater Limiti olmadan, temas patlaması

$$\frac{T}{W^{1/3}} = 0.058\left(\frac{R}{W^{\frac{1}{3}}}\right)^{-0.38} \quad (4)$$

Burada $\frac{R}{W^{\frac{1}{3}}}$ değeri 0.15 m/kg$^{1/3}$ ile 0.5 m/kg$^{1/3}$ arasındadır.

Temas patlamasın da kırılma sınır değerleri,

$$\frac{T}{W^{1/3}} = 3.6 \quad (5)$$

Temas patlamasın da parçalanma sınır değerleri,

$$\frac{T}{W^{1/3}} = 2.0 \quad (6)$$

Olarak belirlenmektedir. Burada T plak kalınlığı, R patlayıcının uzunluğu, W patlayıcı ağırlığıdır.

SONUÇLAR

Patlama deneyi yapılan betonarme plaklara 1kg eşdeğerliği hesaplanan 0.62 kg patlayıcı temas ettirilerek patlatılmıştır(Şekil12). Patlama sonrası plakların 32x32 cm boyutlarında temas yüzeyinde lokal parçalanma(D_1) meydana gelmiştir. Plağın alt tabakasında herhangi bir hasar gözlemlenmemiş, yüzeyde ise kılcal çatlaklar gözlemlenmiştir. Kraterlerin ve parçalanma alanlarının bölgesinde donatı çubukları bulunmaktadır. Burada temas patlamasına maruz kalan bir betonarme plak, önerilen hasar büyüklüğü tahmin yöntemiyle ve ana hatları ile belirtilmiştir. Plakların dış ve iç kırılma parametreleri, fırlatma kraterinin, parçalanma kraterinin ve patlayıcı patlamasının oluşturduğu krater çukurunun çapı ölçülerek değerlendirildi. Yakın temas patlamasında oluşan ölçekleme faktörü olan Z değeri, krater boyutlarına göre temas patlamasındaki patlayıcının mesafesi olan standoff mesafesi belirlenebilmektedir. Burada;

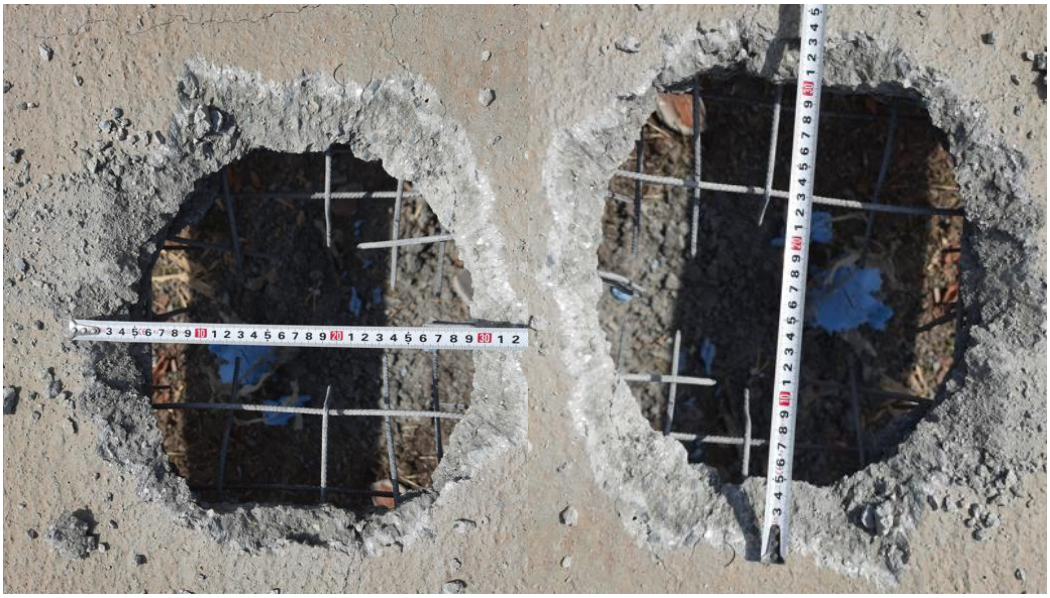
$$\frac{T}{W^{1/3}} = \frac{0.15}{0.62^{1/3}} = 0.20 \quad (7)$$

$$\frac{T}{W^{1/3}} = 0.20 < 2 < 3.6 \quad (8)$$

Patlama deneyleri değerlendirildiğinde denklem 7 ve 8 değerleri 5ve 6 denklemlerini doğrulamaktadır.



Şekil12. Plakların patlama görüntüleri



Şekil13. Krater Boyutları

TEŞEKKÜR

Bu çalışma TÜBİTAK 1001 desteğinin 219M392 no'lu projesinin desteği ile yapılmıştır.

KAYNAKLAR

Chee, KH, T. Krauthammer, and S. Astarlioglu. 2008. "Analysis of Shallow Buried Reinforced Concrete Box Structures Subjected to Airblast Loads." University of Florida.

Criteria(UFC), Unified Facilities. 2008. *Structures to Resist the Effects of the Accidental Explosions*.

Foglar, M., J. Pachman, V. Pelikan, R. Hájek, M. Künzel, and M. Kovar. 2014. "The Structural Response of a Reinforced Concrete Specimen Subjected to Adjacent Blast Loading." *WIT Transactions on the Built Environment* 141(September 2013):171–79. doi: 10.2495/SUSI140151.

Ichino, Hiroyoshi, Masuhiro Beppu, and Eric B. Williamson. 2020. "Blast-Resistant Performance of a Two-Stage Concrete Plate Subjected to Contact Explosions." *Construction and Building Materials* 259:119766. doi: 10.1016/j.conbuildmat.2020.119766.

Khan, Muhammad Umar, Shamsad Ahmad, Akhtar Abbas Naqvi, and Husain Jubran Al-Gahtani. 2020. "Shielding Performance of Heavy-Weight Ultra-High-Performance Concrete against Nuclear Radiation." *Progress in Nuclear Energy* 130(January):103550. doi: 10.1016/j.pnucene.2020.103550.

Li, Jun, Chengqing Wu, and Hong Hao. 2015. "Investigation of Ultra-High Performance Concrete Slab and Normal Strength Concrete Slab under Contact Explosion." *Engineering Structures* 102:395–408. doi: 10.1016/j.engstruct.2015.08.032.

Li, Jun, Chengqing Wu, Hong Hao, Zhongqi Wang, and Yu Su. 2016. "Experimental Investigation of Ultra-High Performance Concrete Slabs under Contact Explosions." *International Journal of Impact Engineering* 93:62–75. doi: 10.1016/j.ijimpeng.2016.02.007.

Li, Zhen, Yan Liu, Jun bo Yan, Wen li Yu, and Feng lei Huang. 2018. "Experimental Investigation of P-Section Concrete Beams under Contact Explosion and Close-in Explosion Conditions." *Defence Technology* 14(5):540–49. doi: 10.1016/j.dt.2018.07.025.

Liao, Qiao, Jiangtao Yu, Xingxing Xie, Junhong Ye, and Fangming Jiang. 2022. "Experimental Study of Reinforced UHDC-UHPC Panels under Close-in Blast Loading." *Journal of Building Engineering* 46(January 2021):103498. doi: 10.1016/j.jobe.2021.103498.

Maazoun, Azer, Stijn Matthys, Bachir Belkassem, David Lecompte, and John Vantomme. 2019. "Blast Response of Retrofitted Reinforced Concrete Hollow Core Slabs under a Close Distance Explosion." *Engineering Structures* 191(May):447–59. doi: 10.1016/j.engstruct.2019.04.068.

McVay, Mark K. 1988. "Spall Damage of Concrete Structures (Final Report)." *Technical Report SL-88-22* (Technical Report):431.

Morishita, Masahiro, Hideaki Tanaka, Tomohiro Ando, and Hiroyuki Hagiya. 2004. "Effects of Concrete Strength and Reinforcing Clear Distance on the Damage of Reinforced Concrete Slabs Subjected to Contact Detonations." *Concrete Research and Technology* 15(2):89–98. doi: 10.3151/crt1990.15.2_89.

Wang, Wei, Qing Huo, Jian-chao Yang, Jian-hui Wang, and Xing Wang. 2021. "Damage Analysis of POZD Coated Square Reinforced Concrete Slab under Contact Blast." *Defence Technology* (xxxx). doi: 10.1016/j.dt.2021.07.005.

Yamaguchi, Makoto, Kiyoshi Murakami, Koji Takeda, and Yoshiyuki Mitsui. 2011. "Scientific Paper: Blast Resistance of Polyethylene Fiber Reinforced Concrete to Contact Detonation." *Journal of Advanced Concrete Technology* 9(1):63–71. doi: 10.3151/jact.9.63.

BAZALT FİBER DONATI ÇUBUKLARININ BETON DAYANIMINA ETKİSİNİN İNCELENMESİ

Dursun BAKIR

Arş. Gör. Fırat Üniversitesi, Mühendislik Fakültesi, İnşaat Mühendisliği Bölümü, Merkez, Elazığ.,
ORCID NO: 0000-0001-6398-0497

Sedat SAVAŞ

Dr. Öğ. Üyesi. Fırat Üniversitesi, Mühendislik Fakültesi, İnşaat Mühendisliği Bölümü, Merkez, Elazığ.
ORCID NO: 0000-0003-2466-3514

ÖZET

Bazalt fiber, bazalt kayalarından elde edilerek çeşitli işlemlerden geçirilip epoksi reçine ile bağlayıcılığı sağlanarak elde edilmektedir. Bazalt fiberin nervürlü donatı çubuğu haline getirilip beton ile kullanılabilirliği araştırılmıştır. Beton ile aderans uyumu, çekme ve eğilmeye karşı davranışları incelenmiştir. Bazalt fiberin üretiminin ve epoksi reçinesinin özelliği farklı sonuçlar elde edilmesine neden olmuştur. Üretim sürecinin malzemenin kimyasal içeriğinden dolayı farklılığına sebebiyet vermiştir.

Anahtar Kelimeler: Bazalt fiber, Çelik donatı, Bazalt fiber donatı, betonarme**,**

INVESTIGATION OF THE EFFECT OF BASALT FIBER REINFORCEMENT BARS ON CONCRETE STRENGTH

ABSTRACT

Basalt fiber is obtained from basalt rocks, subjected to various processes and bonded with epoxy resin. The usability of basalt fiber with concrete was investigated by turning it into a deformed reinforcement. Adherence compatibility with concrete, behavior against tension and bending were investigated. The characteristics of basalt fiber production and epoxy resin have resulted in different results. The production process has caused differences due to the chemical content of the material.

Keywords: Basalt fiber, Steel reinforcement, Basalt fiber reinforcement, reinforced concrete,

GİRİŞ

Bazalt kayalarının 1300-1500 C sıcaklıklarında erimesi sonucu oluşan bazalt lifleri, çevre dostu ve yüksek dayanıma sahip olmaları tercih edilebilen malzeme olmuştur(Militký, Kovačič, and Rubnerová 2002; Ramakrishnan, Tolmare, and Brik 1998). Güçlendirme ihtiyacı olan betonarme yapılarda fiber takviyeli polimer (FRP),karbon fiber takviyeli polimer(CFRP), cam fiber takviyeli polimer (GFRP) ve aramid FRP gibi malzemeleri kullanılmaktadır. Bu malzemelerin maliyetlerinin yüksek olmasından dolayı alternatif malzeme arayışı araştırmacılar tarafından yapılmaktadır. Özellikle üretim ve şekillendirme işlemlerinde katkı maddesi olarak eklenen organik bir epoksi reçinesi yapısı itibariyle herhangi bir yangın durumunda insan sağlığını etkileyebilmesinden dolayı direncine sahip bir malzeme arayışına neden olabilmektedir(Sim, Park, and Moon 2005). Bazalt lifleri, kırılma gerilimine, patlama, darbe, yangın ve kimyasal bir olaylara karşı iyi bir dirence sahip olduğu bilinmektedir(Berozashvili 2001). Özellikle askeri ve sivil yapıların betonarme panelleri ve kubbelerde kullanıla bilinmektedir(Seydibeyoglu, K. Mohanty, and Misra 2017). Bazalt lifleri çoğunlukla patlamaya dayanıklı yapılarda tercih edilebilir, çünkü daha fazla sertliğe sahip lifi, daha az sapma ile hasara karşı daha fazla dirence ve kopmaya karşı daha yüksek dirence sahip olduğu belirlenmiştir. Basınç altında bazalt bileşimi yüksek mukavemet sağlayabilmektedir(Wilhelm and Curbach 2014).Çok sayıda araştırmacı, statik yükleme koşulları altında bazalt lifli betonun performansını incelemişlerdir. Bazalt fiberin temel mekanik özelliklerini belirleyebilmek için, basınç, çekme ve eğilme altında incelemişlerdir(Ayub, Shafiq, and Nuruddin 2014; Borhan 2013; Iyer, Kenno, and Das 2015; Kaijian and Deng 2010; Yang et al. 2021; Yang and Lian 2011; Zhou et al. 2020). Çekme, basınç ve üç nokta eğilme altındaki mekanik özellikleri

incelendiğinde, Bazalt lifleri, 3 kg/m3 miktarı ile basınç altında maksimum %7 mukavemet artışı göstermiştir. Yaklaşık 2 kg/m3'lük optimum lif içeriği çimento hamuru ile lifler arasındaki bağ kuvveti nedeniyle yarma çekme mukavemetine ve eğilme mukavemetinde başarılıdır. Liflerin birikmediği ancak iyi dağıldığı gözlemlenmiştir(Arslan 2016).

Bazalt fiberin daha iyi mukavemet göstermesi, diğer güçlendirme malzemelerinde kullanılan epoksinin kullanılmamasına alternatif olabileceği araştırılmıştır.

YÖNTEM

Bazalt fiberin nervürlü donatı çubuğu haline getirilmesi ile betonda çekme, eğilme ve donatı sıyırma testleri uygulanmıştır.

30N/mm² basınç dayanımına sahip beton(Tablo1), 10mm çapındaki bazalt fiber çubukları 150x150x150mm boyutlarındaki küp kalıplara yerleştirilmiştir(Şekil1).

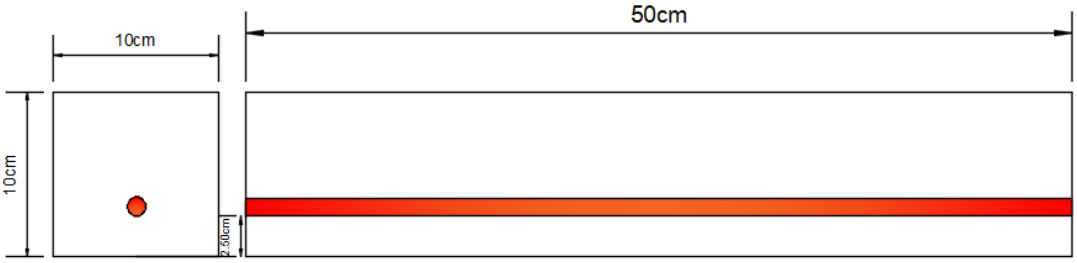


Şekil1. Bazalt Fiber yerleştirilmiş küp kalıplar

Üç noktalı eğilme deneyi için 10x10x50 cm boyutlarındaki kiriş kalıbına 10mm bazalt fiber donatı şekil2 deki gibi yerleştirilmiştir. Hazırlanan donatı planı ile kalıplar ölçüsünde hazırlanarak Şekil3 deki gibi beton dökümü yapılmıştır. Sıyırma testi düzeneğine Şekil1 deki kalıplarda hazırlanan küp numuneler yerleştirilmiş ve deneyi hazırlanmıştır(Şekil4).

Tablo1. Beton karışım oranları

Çimento	%16
Agrega (7-14 mm)	%35.40
Agrega (3-9 mm)	%4.40
Kum	%37.60
Su	%6.40
Kimyasal katkı	%0.20



Şekil2. Bazalt fiber donatı planı



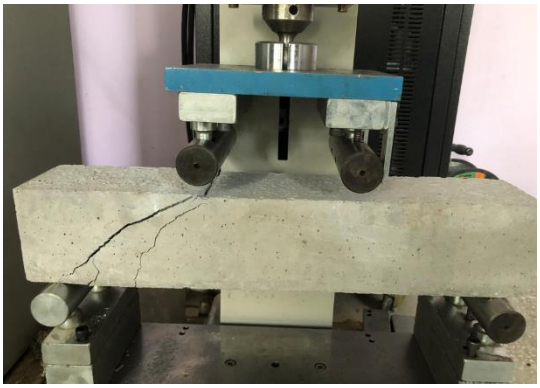
Şekil3. Eğilme deneyi için kiriş numunesinin hazırlanması



Şekil4. Sıyırma testi numune yerleşimi

SONUÇLAR

Çelik donatı ile bazalt fiber donatı çubuklarının dört noktalı eğilme ve sıyırma deneyleri yapılarak bazalt fiber donatı çubuklarının çelik donatı yerine kullanılabilirliği araştırılmıştır. Dört noktalı eğilme deneyinde numuneler yerleştirilmiş Tablo2 de ki sonuçlar elde edilmiştir. Çelik donatı ile Bazalt fiber arasında literatürde bahsedildiği gibi bazalt fiber lehine bir fark görülmemiştir. Çekme testinde ezilme meydana gelmiş, çelik donatı ile benzer davranışlar sergilemiştir. Sıyırma testinde ise 2cm sıyırma gerçekleşmiştir. Bunun sebebi ise üretimin yapıldığı fabrika ve kullanılan epoksi reçinenin kimyasal özelliklerinin olduğu kanaat getirilmiştir.



Şekil5.Dört noktalı eğilme deneyi

Tablo2. Dört noktalı eğilme sonuçları

Deney No	P(kN)	σ(MPa)	Malzeme
1	22.46	6.74	demir
2	21.44	6.43	bazalt
3	30.58	9.17	demir
4	21.67	6.5	bazalt
5	31.46	9.44	demir
6	23.41	7.02	bazalt

KAYNAKLAR

Arslan, Mehmet Emin. 2016. "Effects of Basalt and Glass Chopped Fibers Addition on Fracture Energy and Mechanical Properties of Ordinary Concrete: CMOD Measurement." *Construction and Building Materials* 114:383–91. doi: 10.1016/j.conbuildmat.2016.03.176.

Ayub, Tehmina, Nasir Shafiq, and M. Fadhil Nuruddin. 2014. "Mechanical Properties of High-Performance Concrete Reinforced with Basalt Fibers." *Procedia Engineering* 77:131–39. doi: 10.1016/j.proeng.2014.07.029.

Berozashvili, M. 2001. "Continuous Reinforcing Fibers Are Being Offered for Construction, Civil Engineering and Other Composites Applications." *Adv Mater Com News, Compos Worldwide* 6:5–6.

Borhan, Tumadhir M. 2013. "Thermal and Mechanical Properties of Basalt Fibre Reinforced Concrete." *Proceedings of World Academy of Science, Engineering and Technology* 313.

Iyer, Padmanabhan, Sara Y. Kenno, and Sreekanta Das. 2015. "Mechanical Properties of Fiber-Reinforced Concrete Made with Basalt Filament Fibers." *Journal of Materials in Civil Engineering* 27(11):1–8. doi: 10.1061/(asce)mt.1943-5533.0001272.

Kaijian, Huang, and Min Deng. 2010. "Stability of Basalt Fibers in Alkaline Solution and Its Effect on the Mechanical Property of Concrete." *Acta Materiae Compositae Sinica* 27(1):150–54.

Militký, Jiří, Vladimír Kovačič, and Jitka Rubnerová. 2002. "Influence of Thermal Treatment on Tensile Failure of Basalt Fibers." *Engineering Fracture Mechanics* 69(9):1025–33. doi: 10.1016/S0013-7944(01)00119-9.

Ramakrishnan, V., Neeraj S. Tolmare, and Vladimir B. Brik. 1998. "Performance Evaluation of 3-D Basalt Fiber Reinforced Concrete & Basalt Rod Reinforced Concrete." *Report* (November):97.

Seydibeyoglu, M. Ozgur, Amar K. Mohanty, and Manjusri Misra. 2017. *Fiber Technology for Fiber-Reinforced Composites*. Woodhead Publishing.

Sim, Jongsung, Cheolwoo Park, and Do Young Moon. 2005. "Characteristics of Basalt Fiber as a Strengthening Material for Concrete Structures." *Composites Part B: Engineering* 36(6–7):504–12. doi: 10.1016/j.compositesb.2005.02.002.

Wilhelm, Sebastian, and Manfred Curbach. 2014. "Review of Possible Mineral Materials and Production Techniques for a Building Material on the Moon." *Structural Concrete* 15(3):419–28. doi: 10.1002/suco.201300088.

Yang, Liyun, Huanzhen Xie, Shizheng Fang, Chen Huang, Aiyun Yang, and Yuh J. Chao. 2021. "Experimental Study on Mechanical Properties and Damage Mechanism of Basalt Fiber Reinforced Concrete under Uniaxial Compression." *Structures* 31(February):330–40. doi: 10.1016/j.istruc.2021.01.071.

Yang, Yong Xin, and Jie Lian. 2011. "Basalt Fiber Reinforced Concrete." *Advanced Materials Research* 194–196:1103–8. doi: 10.4028/www.scientific.net/AMR.194-196.1103.

Zhou, Hao, Bin Jia, Hui Huang, and Yanling Mou. 2020. "Experimental Study on Basic Mechanical Properties of Basalt Fiber Reinforced Concrete." *Materials* 13(6). doi: 10.3390/ma13061362.

DİKDÖRTGEN ÇEKİRDEKLİ BOŞLUKLU PLAKLARIN TEMAS PATLAMASI KARŞISINDA DAYANIMININ DENEYSEL VE SAYISAL İNCELENMESİ

Dursun BAKIR

Arş. Gör. Fırat Üniversitesi, Mühendislik Fakültesi, İnşaat Mühendisliği Bölümü, Merkez, Elazığ.
ORCID NO: 0000-0001-6398-0497

Hasan ÜSTÜNDAĞ

İnşaat Müh. Fırat Üniversitesi, Mühendislik Fakültesi, İnşaat Mühendisliği Bölümü, Merkez, Elazığ.
ORCID NO: 0000-0001-8346-182X

Sedat SAVAŞ

Dr. Öğr. Üyesi. Fırat Üniversitesi, Mühendislik Fakültesi, İnşaat Mühendisliği Bölümü, Merkez, Elazığ.
ORCID NO: 0000-0003-2466-3514

ÖZET

Patlama olayında can ve mal kayıplarını azaltmak için yapıların patlamaya karşı dayanımını arttırmak gerekmektedir. Yapıların dayanımını etkileyen en önemli faktörlerden birisi de yapı tasarımıdır. Çalışmada Patlama olayına karşı boşluklu sandviç plak tasarımı yapılmıştır. Genişliği 100 cm, uzunluğu 200 cm, üst ve alt plak kalınlıkları ise 5 cm olarak üç farklı dikdörtgen çekirdekli boşluklu plak hazırlanarak TNT eşdeğerliği 625 gr, 682gr ve 774 gr patlayıcılar temas halinde patlatılmıştır. Bu plakların sayısal analizlerinde ise ANSYS paket programı kullanılmış ve yüksek deformasyonlar etkisinde doğru sonuçlar verebilmesi, elemanlardaki hasar modellerini ve basınç dağılımlarını gerçeğe yakın bir şekilde çözümleyebilmesinden dolayı Düzgün Parçacık Hidrodinamiği yöntemi seçilmiştir.

Anahtar Kelimeler: Boşluklu plak, TNT eşdeğerliği, Düzgün Parçacık Hidrodinamiği, Temas patlaması

EXPERIMENTAL AND NUMERICAL INVESTIGATION OF THE RESISTANCE OF RECTANGULAR CORE HOLLOW PLATES AGAINST CONTACT EXPLOSION

ABSTRACT

In order to reduce the loss of life and property in the event of an explosion, it is necessary to increase the resistance of the structures against explosion. One of the most important factors affecting the strength of buildings is the design of the building. In the study, a hollow sandwich plate design was made against the explosion event. Three different rectangular-core hollow plates with a width of 100 cm, a length of 200 cm, and top and bottom plate thicknesses of 5 cm were prepared and explosives of 625 gr, 682 gr and 774 gr TNT equivalent were detonated on contact. In the numerical analysis of these plates, the ANSYS package program was used and the Smooth Particle Hydrodynamics method was chosen because it can give accurate results under the effect of high deformations and can analyze the damage models and pressure distributions in the elements in a realistic way.

Keywords: Hollow sandwich plate, TNT equivalence, Smooth Particle Hydrodynamics, Contact explosion

GİRİŞ

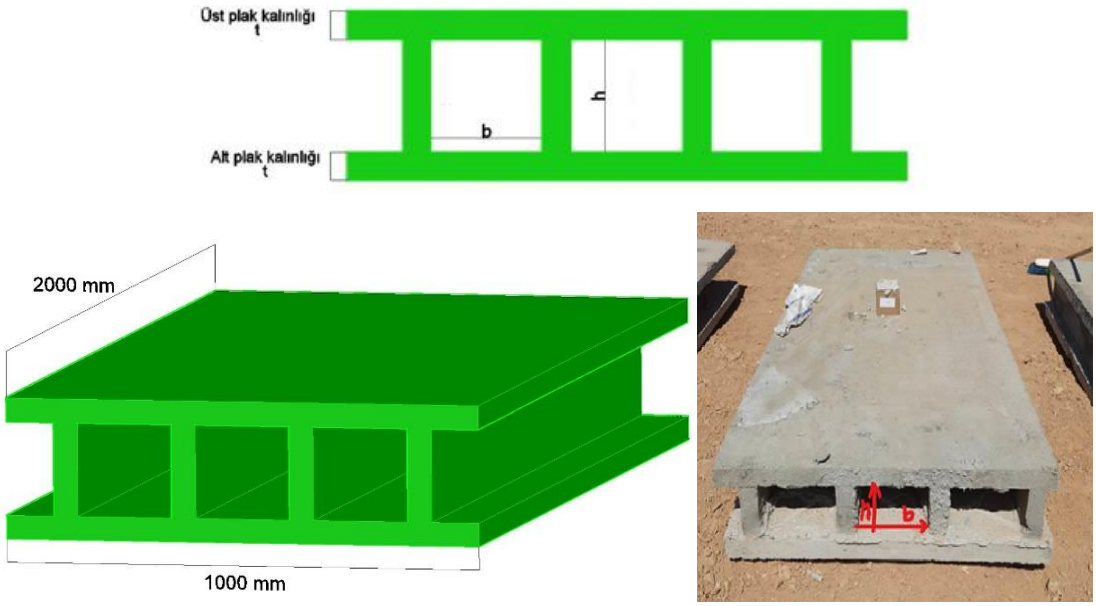
Günümüzde terör olaylarının artması ile çok sayıda can ve mal kaybı yaşanmaktadır. Terör saldırılarında kullanılan patlayıcı maddelerden kaynaklı patlamalarda maddi ve manevi büyük zararlar meydana gelmektedir. Patlamada oluşan negatif ve pozitif basınçlar dayanıklı yapı tasarımının önemini arttırmaktadır. Patlamaya karşı yapı stabilitesini arttırmak için çok sayıda çalışmalar yapılmıştır. Bu çalışmalardan bazılarında ultra erken dayanımlı çimento esaslı beton kullanılmış(Qi et al. 2022), fiber içeriğinde ultra yüksek performanslı fiber beton kullanılmış (Foglar et al. 2017; Li, Wu, Hao, et al. 2016; Magnusson and Hallgren

2004), bazılarında ise donatı planı veya donatı içeriği değiştirilmiştir(Li, Wu, and Hao 2016). Boşluklu tasarım yapılan çalışmalarda, güçlendirilmiş boşluk kesitli plaklara yakın temas patlaması uygulanmış, patlama karşısındaki davranışı incelenmiştir(Maazoun et al. 2019). Yapılan çalışmalarda boşluklu kesitli yapıların patlamaya karşı güçlendirilerek direncinin artırılması önerilmiştir(Buchan and Chen 2007).

Patlamaya karşı yapıların dayanımını sayısal olarak analiz etmek amacıyla çeşitli yöntemler kullanılmaktadır. Euler, Lagrange, ALE (Arbitrary Lagrange Euler), MM-ALE (Multi Material Arbitrary Lagrange Euler), Sonlu Elemanlar Metodu, Hibrit Yöntemler (iki farklı metodun kullanıldığı) ve Düzgün Parçacık Hidrodinamiği Yöntemi (SPH, Smooth Particle Hydrodynamics) yöntemleri en çok kullanılan yöntemlerdir. Düzgün Parçacık Hidrodinamiği Yöntemi darbe, patlama gibi dinamik yüklerin sayısal olarak modellenmesinde kullanılan sonlu eleman ağı kullanmayan bir parçacık yöntemidir. Euler, dinamik bir hareketteki büyük bozulmaları göreceli kolaylıkla yakalamaktadır. Ancak, bu yaklaşımla ilişkili büyük hesaplama yükü bulunmaktadır. Ayrıca, Euler tanımında serbest yüzeylerin, deforme olabilen sınırların ve hareketli arayüzlerin kesin konumunu belirlemek de oldukça zordur. Eleman tabanlı yöntemlerin bu sayısal zorlukları, büyük deformasyon içeren problemlere uygulanmalarına sürekli kısıtlama getirmektedir. Yapı patlama yüküne maruz kaldığında oluşacak çatlakların oluşumu, yayılması ve bunların etkileşimi kısmi veya tam hasara yol açar(Liu and Liu 2003). Düzgün Parçacık Hidrodinamiği Yöntemi, ciddi şekilde deforme olmuş bir yapıda malzeme noktası geçmişini sağlam bir şekilde hesaplama, Lagrange çerçevesinde yeniden ağ oluşturmayı ve Euler çerçevesinde hesaplama avantajına sahiptir. Yıllar içinde SPH'nin darbe ve patlama içeren birçok pratik uygulamada en etkili yöntem olduğu belirlenmiştir(Chakraborty and Shaw 2013; Shaw and Reid 2009; Shaw and Roy 2012). SPH yönteminde stabilite ve yoğunlukta sınırlamalar vardır(Karmakar and Shaw 2021). Elemanların aşırı deformasyona uğradığı durumlarda, ağ tabanlı olduklarından dolayı analizde kararsızlıklara sebep olurlar. Hesap alanı ve ağ (mesh) tabanlı teknikler komşu eleman sınırları boyunca hesap yaparak problemi çözerken, Düzgün Parçacık Hidrodinamiği Yöntemi en yakın komşu parçacıklar arasında interpolasyon yaparak aşırı deformasyon problemlerini kolayca çözebilmektedir(Vorobyev 2014). Bu durumlar incelendiğinde patlama altında yapısal tepkiyi modellemek için bu yöntem etkili olacaktır.

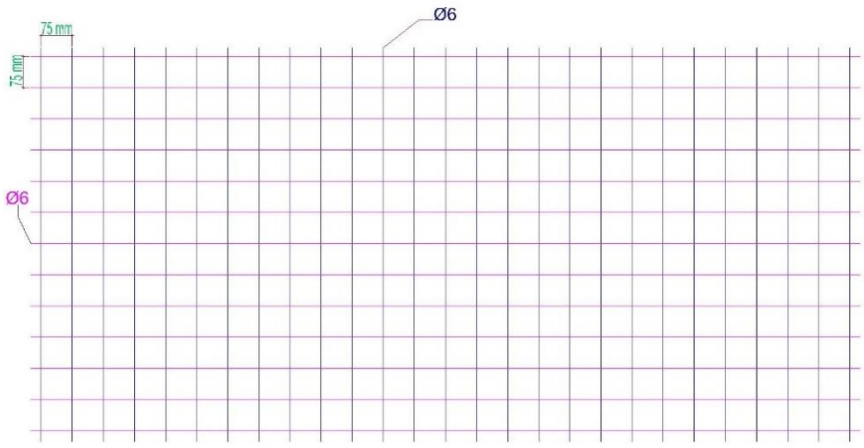
YÖNTEM

Boşluklu plakların genişliği 1000 mm, uzunluğu 2000 mm, üst ve alt plak kalınlıkları ise 50 mm'dir. Boşluk boyutları şekil1 de görüldüğü üzere genişlik, b, yükseklik ise h olarak tanımlanmıştır(Şekil1).



Şekil1. Boşluklu kesit tasarımı

Boşluklu plakların alt ve üst kısmına Şekil 2'de görülen 6 mm çapında donatıdan oluşan Q131 hasır çelik, 25 mm paspayı bırakılarak yerleştirilmiştir.



Şekil 2 Boşluklu plaklarda kullanılan hasır çelik özellikleri

Üç farklı kesite sahip dikdörtgen çekirdekli boşluklu plaklar, H yükseklik-genişlik olarak tanımlanmış ve imalatında 35 N/mm² basınç dayanımına sahip beton kullanılmıştır(Tablo1).

Tablo1. Deneyde kullanılan boşluklu plakların özellikleri

Numune adı	Boşluk yüksekliği / h (cm)	Boşluk genişliği / b (cm)	Beton sınıfı	TNT eşdeğeri patlayıcı ağırlığı (gr)
H15-15	15	15	C35	625
H15-17,5	15	17.5	C35	682
H15-20	15	20	C35	774

Düzgün Parçacık Hidrodinamiği Yöntemi

Düzgün Parçacık Hidrodinamiği Yöntemi 'nde sistem bir dizi parçacıkla temsil edilir ve parçacıklar, iç parçacık etkileşimlerine veya dış kuvvetlere göre serbestçe hareket edebilir. "Parçacık" kelimesi fiziksel bir kütle anlamına gelmez, bunun yerine uzayda bir bölgeyi ifade eder. Alan değişkenleri bu parçacıklarla ilişkilidir ve uzaydaki herhangi bir noktada düzleştirme yoluyla bulunur. Düzgün Parçacık Hidrodinamiği metodu, herhangi bir noktadaki fonksiyonun değerini, komşu noktalardaki değerleri kullanarak elde eden bir interpolasyon tekniğine dayanmaktadır((Du et al. 2016; S.M. Hosseini, Manzari, and Hannani 2007)). Düzgün Parçacık Hidrodinamiği Yöntemi 'nde problem bölgesindeki bir alan fonksiyonu f(x) şöyle yazılabilir:

$$\langle f(x)\rangle = \int_{\Omega} f(x')W(x-x',h)\,dx' \qquad (1)$$

Denklem 1'deki Ω değeri problem bölgesidir ve f üç boyutlu konum vektörü x ile alakalı bir alan fonksiyonudur. $W(x-x',h)$ düzleştirme çekirdeğinin fonksiyonudur. "h" ise düzleştirme çekirdeği fonksiyonunun etki alanını tanımlayan düzleştirme uzunluğudur. Düzleştirme çekirdeği fonksiyonu (W), bazı koşulları sağlayacak şekilde seçilmelidir ve bunlardan birincisi **Denklem 2'deki** normalizasyon şartıdır.

$$\int_{\Omega} W(x-x',h)dx' = 1 \qquad (2)$$

İkinci koşul ise **Denklem 3**'te verilen Dirac Delta fonksiyonu özelliğidir:

$$\lim_{h\to 0} W(x-x',h) = \delta(x-x') \qquad (3)$$

Son koşul ise **Denklem 4**'teki kompaktlık özelliğidir (Wang et al. 2015):

$$[\, W(x - x', h), \quad |x - x'| > (\mathrm{k} \times h)] \tag{4}$$

Yukarıda verilen k değeri, x noktasındaki düzleştirmeyle ilgili skaler bir faktörü temsil eder. Bu değer düzleştirme fonksiyonunun etki alanını tanımlar. Bu alana x noktasındaki destek alanı denir. Türevler için çarpım kuralına ve Gauss Yasası'na göre bu fonksiyonun türevi şu şekilde yazılabilir (Wang et al. 2015):

$$\langle \nabla . f(x) \rangle = \int_S f(x') W(x - x', h). \vec{n} dS - \int_\Omega f(x). \nabla W(x - x', h) dx' \tag{5}$$

Denklem 5'daki $\vec{n}$, S yüzeyine dik birim vektördür. Destek bölgesi problem alanı içindeyse, çekirdek fonksiyonunun kompaktlık durumuna göre, şunlar elde edilebilir:

$$[W(x - x', h) = 0] \tag{6}$$

$$[f(x')W(x - x', h) = 0] \tag{7}$$

Türevler **Denklem 6 ve Denklem 7'deki** şartlara göre düzenlenirse şu şekilde yazılabilir (Wang et al. 2015):

$$\langle \nabla . f(x) \rangle = -\int_\Omega f(x). \nabla W(x - x', h) dx' \tag{8}$$

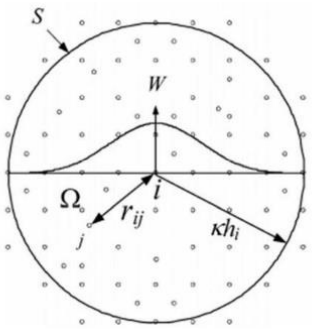
Daha sonra **Denklem 9 ve Denklem 10'de** gösterildiği gibi destek alanı içindeki tüm parçacıklar üzerinde bir toplama işlemi yapılır:

$$\langle f(x_i) \rangle = \sum_{j=1}^{N} \frac{m_j}{\rho_j} f(x_j) W_{ij} \tag{9}$$

$$\langle \nabla . f(x_i) \rangle = -\sum_{j=1}^{N} \frac{m_j}{\rho_j} f(x_j). \nabla W_{ij} \tag{10}$$

$$W_{ij} = W(x_i - x_j, h) \tag{11}$$

Şekil 3'te herhangi bir "i" parçacığı için tanımlanan destek alanı gösterilmiştir.

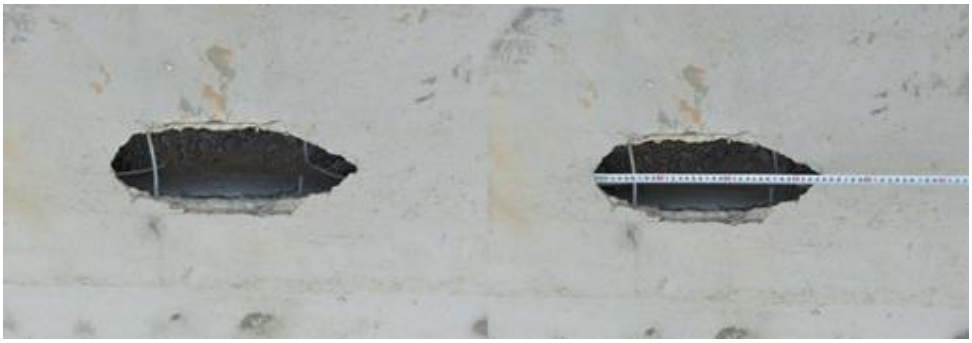


Şekil 3. "i" parçacığının destek alanı (Wang et al. 2015)

Yukarıdaki formülasyonlar, ilgilenilen problem tipi gereği değişik formüllerle birleştirilebilir ve yeniden yazılabilir. Literatürde bakıldığında Navier-Stokes denklemi veya Gradient yaklaşımlarının çekirdek fonksiyonu ile birlikte uygulandığı görülmektedir((Gharehdash et al. 2020; S. M. Hosseini, Manzari, and Hannani 2007; Wang et al. 2015; Zhang et al. 2017)).

SONUÇLAR

Boşluklu plaklar kullanılarak yapılan sayısal analizler sonucunda plak üst yüzeylerinde krater çukurları oluşmuş, üst plak tabakasındaki donatılar kırılmıştır. Ancak yapı bütünlüğü üç boşluklu plak tasarımında da korunmuştur(Şekil4,5,6).



Şekil. H15-15 Patlama sonrası görünümü

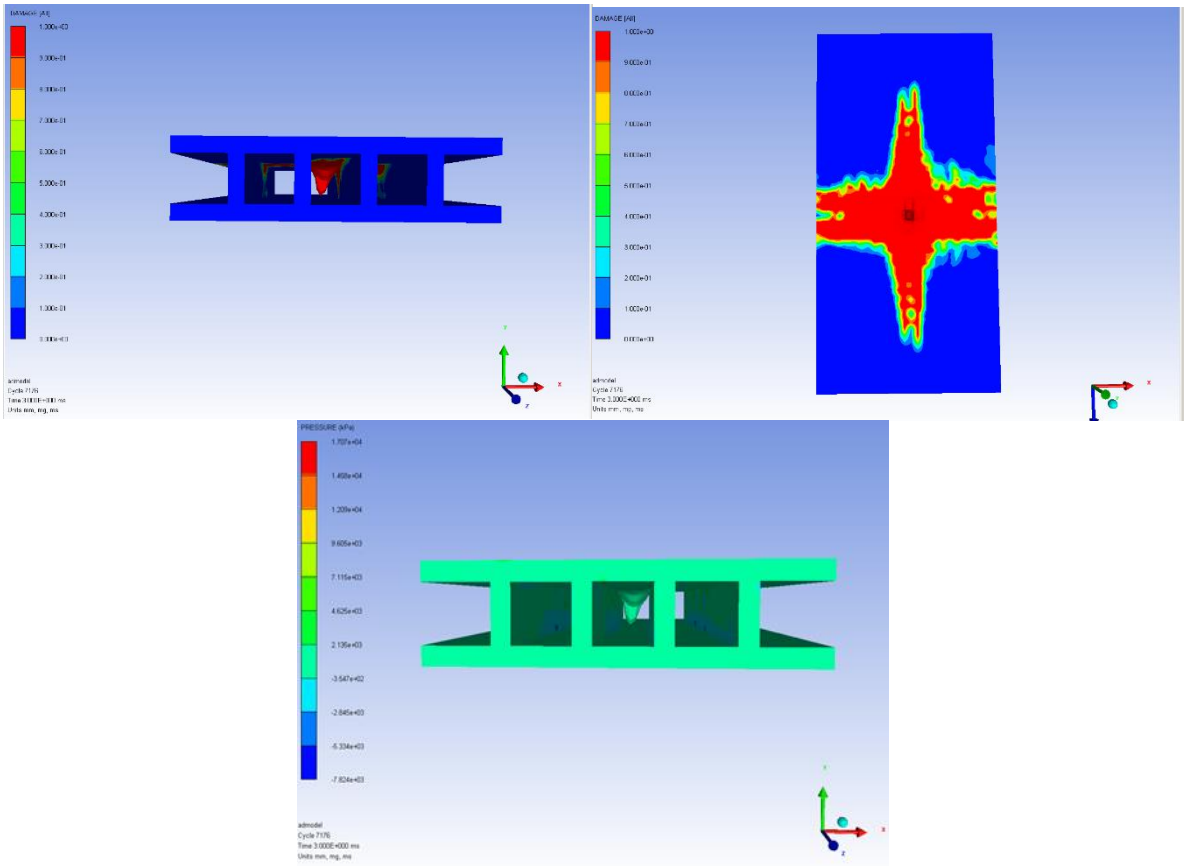


Şekil5. H15-17,5 Patlama sonrası görünümü



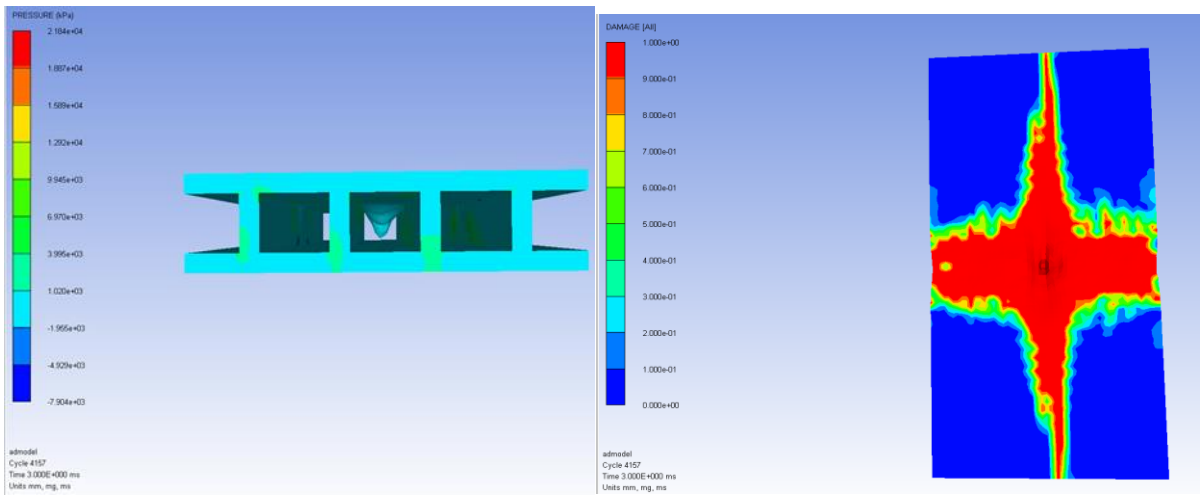
Şekil6.H15/20 Patlama sonrası görünümü

TNT eşdeğeri 625 gr patlayıcı kullanılan H15-15 numunesinde kullanılan ağ (mesh) için eleman boyutu 18 mm olarak seçilmiştir. Şekil 4'de H15-15 numunesinde sahada yapılan temas patlaması deneyi sonucu oluşan krater çukuru gösterilmiştir. Deneyde krater çukurunun eni 150 mm ve boyu 350 mm olarak ölçülmüştür. Yapılan sayısal analizde, krater çukuru boyutlarının deney verileriyle uyuştuğu görülmüştür.



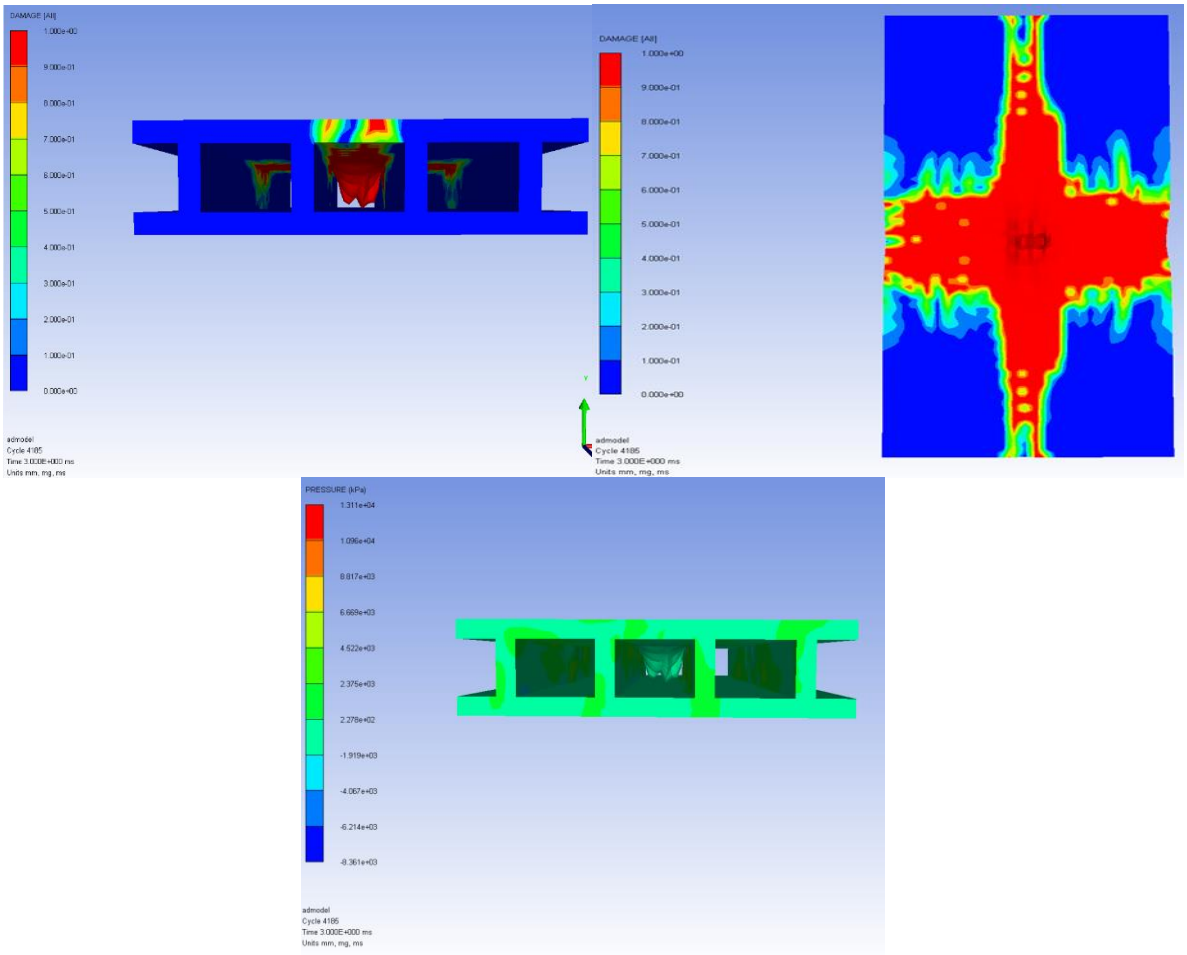
Şekil7.H15-15 Boşluklu plak basınç dağılımı

H15-17,5 numunesinde sahada yapılan temas patlaması deneyi sonucu oluşan krater çukuru gösterilmiştir(Şekil5). Deneyde krater çukurunun eni 180 mm ve boyu 340 mm olarak ölçülmüştür. Yapılan sayısal analizde, krater çukurunun eni 170 mm ve boyu 340 mm olarak belirlenmiştir(Şekil8).



Şekil8.H15-17,5 Boşluklu plak basınç dağılımı

H15-20 numunesinde sahada yapılan temas patlaması deneyi sonucu oluşan krater çukuru gösterilmiştir. Deneyde krater çukurunun eni 210 mm ve boyu 310 mm olarak ölçülmüştür(Şekil6). Yapılan sayısal analizde, krater çukurunun eni 200 mm ve boyu 300 mm olarak belirlenmiştir(Şekil9).



Şekil9.H15-20 Boşluklu plak basınç dağılımı

Yapılan çalışma incelendiğinde patlayıcı miktarlarına göre numunelerde oluşan krater çukurlarının yakın sonuçlar verdiği görülmüştür(Tablo2). Kullanılan SPH yöntemi bu deneyle doğrulanmıştır.

Tablo2. Deneysel ve Analiz sonuçların karşılaştırılması

Numune adı	TNT eşdeğeri patlayıcı ağırlığı (gr)	Deneydeki krater çukuru en/boy (mm)	Analizdeki krater çukuru en/boy (mm)
H15-15	625	150/350	150/350
H15-17,5	682	180/340	170/340
H15-20	774	210/310	200/300

TEŞEKKÜR

Bu çalışma TÜBİTAK 1001 desteğinin 219M392 no'lu projesinin desteği ile yapılmıştır.

KAYNAKLAR

Buchan, P. A., and J. F. Chen. 2007. "Blast Resistance of FRP Composites and Polymer Strengthened Concrete and Masonry Structures - A State-of-the-Art Review." *Composites Part B: Engineering* 38(5–6):509–22. doi: 10.1016/j.compositesb.2006.07.009.

Chakraborty, Sukanta, and Amit Shaw. 2013. "A Pseudo-Spring Based Fracture Model for SPH Simulation of

Impact Dynamics." *International Journal of Impact Engineering* 58:84–95. doi: 10.1016/j.ijimpeng.2013.03.006.

Du, Yang, Li Ma, Jinyang Zheng, Fan Zhang, and Anda Zhang. 2016. "Coupled Simulation of Explosion-Driven Fracture of Cylindrical Shell Using SPH-FEM Method." *International Journal of Pressure Vessels and Piping* 139–140:28–35. doi: 10.1016/j.ijpvp.2016.03.001.

Foglar, Marek, Radek Hajek, Josef Fladr, Jiri Pachman, and Jiri Stoller. 2017. "Full-Scale Experimental Testing of the Blast Resistance of HPFRC and UHPFRC Bridge Decks." *Construction and Building Materials* 145:588–601. doi: 10.1016/j.conbuildmat.2017.04.054.

Gharehdash, Saba, Milad Barzegar, Igor B. Palymskiy, and Pavel A. Fomin. 2020. "Blast Induced Fracture Modelling Using Smoothed Particle Hydrodynamics." *International Journal of Impact Engineering* 135(January 2019):103235. doi: 10.1016/j.ijimpeng.2019.02.001.

Hosseini, S. M., M. T. Manzari, and S. K. Hannani. 2007. "A Fully Explicit Three-Step SPH Algorithm for Simulation of Non-Newtonian Fluid Flow." *International Journal of Numerical Methods for Heat and Fluid Flow* 17(7):715–35. doi: 10.1108/09615530710777976.

Hosseini, S.M., M. T. Manzari, and S. K. Hannani. 2007. "A Fully Explicit Three-step SPH Algorithm for Simulation of Non-Newtonian Fluid Flow." *International Journal of Numerical Methods for Heat & Fluid Flow* 17(7):715–35. doi: 10.1108/09615530710777976.

Karmakar, Somnath, and Amit Shaw. 2021. "Response of R.C. Plates under Blast Loading Using FEM-SPH Coupled Method." *Engineering Failure Analysis* 125(September 2019):105409. doi: 10.1016/j.engfailanal.2021.105409.

Li, Jun, Chengqing Wu, and Hong Hao. 2016. "Spallation of Reinforced Concrete Slabs under Contact Explosion." *2016 2nd Asian Conference on Defence Technology, ACDT 2016* 42–45. doi: 10.1109/ACDT.2016.7437641.

Li, Jun, Chengqing Wu, Hong Hao, Zhongqi Wang, and Yu Su. 2016. "Experimental Investigation of Ultra-High Performance Concrete Slabs under Contact Explosions." *International Journal of Impact Engineering* 93:62–75. doi: 10.1016/j.ijimpeng.2016.02.007.

Liu, Gui-Rong, and M. B. Liu. 2003. *Smoothed Particle Hydrodynamics: A Meshfree Particle Method*. World Scientific Publishing.

Maazoun, Azer, Stijn Matthys, Bachir Belkassem, David Lecompte, and John Vantomme. 2019. "Blast Response of Retrofitted Reinforced Concrete Hollow Core Slabs under a Close Distance Explosion." *Engineering Structures* 191(April):447–59. doi: 10.1016/j.engstruct.2019.04.068.

Magnusson, J., and M. Hallgren. 2004. "Reinforced High Strength Concrete Beams Subjected to Air Blast Loading." *Structures and Materials* 15:53–62.

Qi, Shao bo, Guang yan Huang, Xu dong Zhi, and Feng Fan. 2022. "Sensitivity Analysis and Probability Modelling of the Structural Response of a Single-Layer Reticulated Dome Subjected to an External Blast Loading." *Defence Technology* (xxxx). doi: 10.1016/j.dt.2022.02.004.

Shaw, Amit, and S. R. Reid. 2009. "Heuristic Acceleration Correction Algorithm for Use in SPH Computations in Impact Mechanics." *Computer Methods in Applied Mechanics and Engineering* 198(49–52):3962–74. doi: 10.1016/j.cma.2009.09.006.

Shaw, Amit, and D. Roy. 2012. "Stabilized SPH-Based Simulations of Impact Dynamics Using Acceleration-Corrected Artificial Viscosity." *International Journal of Impact Engineering* 48:98–106. doi: 10.1016/j.ijimpeng.2011.08.008.

Vorobyev, Alexander. 2014. *A Smoothed Particle Hydrodynamics Method for the Simulation of Centralized Sloshing Experiments*. KIT Scientific Publishing.

Wang, Guangyu, Guirong Liu, Qing Peng, Suvranu De, Dianlei Feng, and Moubin Liu. 2015. "A 3D Smoothed Particle Hydrodynamics Method with Reactive Flow Model for the Simulation of ANFO." *Propellants, Explosives, Pyrotechnics* 40(4):566–75. doi: 10.1002/prep.201400244.

Zhang, A. man, Peng nan Sun, Fu ren Ming, and A. Colagrossi. 2017. “Smoothed Particle Hydrodynamics and Its Applications in Fluid-Structure Interactions.” *Journal of Hydrodynamics* 29(2):187–216. doi: 10.1016/S1001-6058(16)60730-8.

OPTIMUM DESIGN OF STEEL-CONCRETE COMPOSITE BOX GIRDER BRIDGES WITH HARMONY SEARCH ALGORITHM

Ozan İNCE

Firat University, Faculty of Engineering, Department of Civil Engineering, ORCID NO: 0000-0002-6319-1129

Prof. Dr. Mehmet ÜLKER

Firat University, Faculty of Engineering, Department of Civil Engineering, ORCID NO: 0000-0001-5427-7089

Abstract

In this study, a steel-reinforced concrete composite box-girder bridge was designed using classical methods. Then, it is aimed to determine the material savings to be achieved by making the optimum design of the box-section bridge. Metaheuristic algorithm methods are methods used in structure optimization and give successful results. In this study, Harmony Search algorithm is used for optimum design process. In the Harmony Search algorithm, random solutions are initially generated. Then, the randomly generated solution matrix is updated in cycles. The goal in each loop is to find a more optimal solution. In each loop, the newly created solution is created by utilizing existing solutions or randomly generated new solutions. The optimization algorithm was written in MATLAB program. In the optimum design problem, the geometric dimensions of the steel beams used in the bridge were taken into account as the design parameters. The amount of steel is taken into account as the objective function of the optimization problem. The optimum section area and optimum design variables were obtained as a result of the harmony search algorithm. In addition, the graph of the cross-sectional area and the number of iterations obtained during the optimization algorithm was presented.

Keywords: Composite box girder bridges, Optimum design, Harmony Search Algorithm

I. INTRODUCTION

In steel-reinforced concrete composite structures, the advantages of steel and concrete are used together. Steel elements have high tensile strength, but show weak strength due to the buckling effect under pressure. Concrete material, on the other hand, has a low tensile strength and non-ductile behavior despite its high compressive strength. It is aimed to combine the advantages of these materials in composite structures. The use of steel and concrete together provides an economic advantage. The amount of steel in composite structures is reduced 30-50% compared to steel structures [1].

The aim of the optimum design is to make the safe design of the structure in the most economical way. There are many optimization methods in the literature for the optimum design process. Metaheuristic algorithm methods perform well in the optimal design of structure problems [2-4]. Metaheuristic algorithm methods are generally practical methods that aim to reach the optimum result by converging in cycles. Due to the many variable parameters in the building design, there are many solution possibilities and many local minimum points. Among the local minimum points, the global minimum must be found. Metaheuristic algorithm methods are successful methods for finding the global minimum point within the local minimum points. In this study, the classical design methods were also used [5,6]. Then classical method and optimum design method were compared.

In this study, Harmony Search (HS) algorithm was used for optimum design of composite box-section bridges [7]. In the HS algorithm, solutions are generated randomly at the beginning and these solutions are recorded in a matrix. Then, depending on the parameters of the HS algorithm, new solutions are generated and the solution matrix is updated. Existing solution elements can be used to produce new solutions, or new solutions are randomly generated. In the algorithm, it is aimed to reach the best solution in loops.

In this study, a steel-reinforced concrete composite box-section bridge was designed using classical design methods. Then, the optimum design of this bridge with the HS algorithm was made and the steel material savings were determined. The maximum stress values were obtained by analyzing the composite bridge in the

CSiBridge program. The HS algorithm used in the optimization process is coded in the MATLAB programming language. As a result of the optimization process, the graph of the cross-sectional area of the steel profile and the number of iterations was obtained and the most optimum value was given.

MATERIAL AND METHOD

The Harmony Search algorithm aims to find the most suitable result among the randomly generated solutions. In the HS algorithm, a random harmony matrix is initially created. It is necessary to determine the value ranges that variable parameters can take in the matrix. Each row in the matrix represents a separate solution. In each cycle, new solutions are developed, compared with other solutions in the matrix, and the worst solution is removed from the matrix. The steps of the HS algorithm are summarized below.

1. Determining the parameters of the HS algorithm: At this stage, the matrix size to be used in the algorithm, HMCR, PAR and the termination criteria are determined.

2. Generation of HS matrix: HS matrix is generated randomly. In this matrix, each row represents a solution and each column represents the design parameter.

3. Creation of new solutions: In the HS algorithm, the parameters of the newly developed solutions are randomly generated or taken from the old solutions in the matrix.

4. Updating the HS matrix: At this stage, after the last solution included in the HS matrix, the worst solution is removed from the matrix.

5. Termination of the algorithm: In this last step, step 3 and step 4 are continued until the termination criterion is met.

II. NUMERICAL ANALYSIS

In this study, a three-span composite box-section bridge with span distances of 45-65-45 m was designed. Bridge length section is given in Figure 1. The bridge cross-section and design parameters (b_f, t_f, t_w, t_b, D_w) used in the optimum design process are given in Figure 2. In the bridge design, the design was made taking into account the AASHTO LRFD regulation. In Table 1, the bridge properties are given.

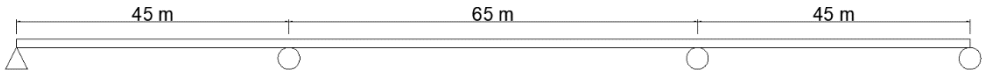


Fig. 1 Bridge length section

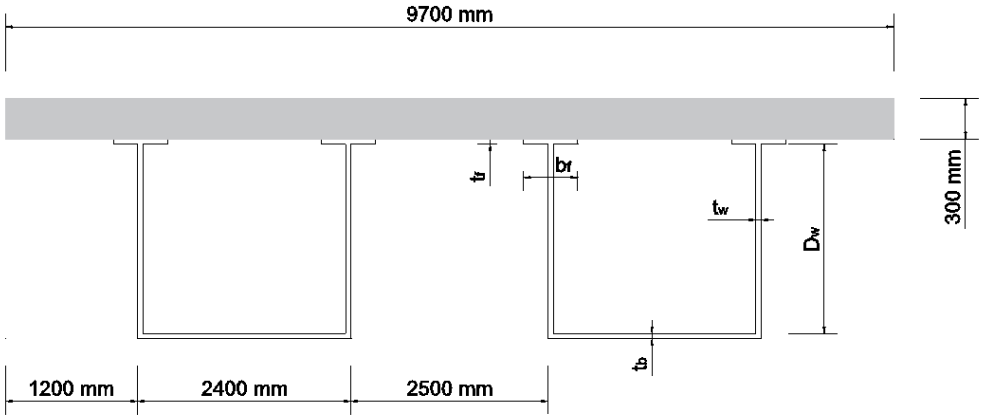


Fig. 1 Bridge cross-section and design parameters

Table 1. Properties of bridge

Parameter	
Concrete compressive strength	30 MPa
Steel profile yield strength	345 MPa
Reinforced concrete slab thickness	300 mm
Number of steel box profiles	2
Cross section width	9.7 m
Span distance	45-65-45 m

In the optimum design problem, the steel profile cross-sectional area is taken into account as the objective function. The objective function must satisfy the stress, deflection and geometric constraints of the design.

The cross-sectional area and iteration number graphs obtained in the optimum design algorithm of the composite box-section bridge are given in Figure 3. As a result of the analysis, it was determined that the optimum cross-sectional area of a box-section profile is 138520 mm^2. The design parameters and design variables obtained as a result of the optimum design of the bridge with the classical method and the HS algorithm are given in Table 2.

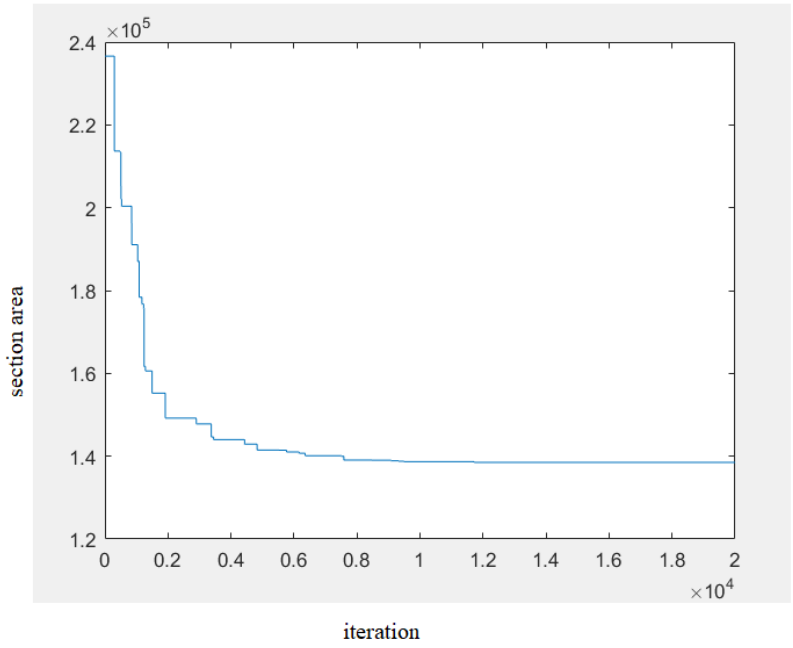


Fig. 3 Cross-sectional area (mm^2) and iteration number graph of the HS algorithm

Table 2. Results of the classical method and optimum design

	b_f (mm)	t_f (mm)	t_w (mm)	t_b (mm)	D_w (mm)	Section area (mm^2)
Classical method	765.0	32.0	17.5	10.0	2600.0	163960
HS	764.7	32.1	14.8	10.0	2214.0	138520

III. CONCLUSION

In this study, the design of steel-reinforced concrete composite box-section bridges was made using the classical method and metaheuristic algorithm. The HS algorithm was chosen as the metaheuristic algorithm

method. In the optimization problem, it is aimed to find the lowest cross-sectional area by taking the geometric dimensions of the steel profile cross-section as the design variable. The objective function must satisfy the stress, deflection and geometric constraints of the bridge. As a result of the analysis and optimum design, it was seen that around 15.5% of the steel material was saved compared to the classical methods. Thus, it is concluded that economical solutions can be obtained by applying modern optimization techniques to composite bridges.

IV. REFERENCES

[1] Thevendran, V., Shanmugam, N. E., Chen, S., & Liew, J. R.: Experimental study on steel-concrete composite beams curved in plan. Engineering Structures, 22(8), 877-889 (2000).

[2] Ali, Kaveh, and Mohammad Mahdi Motesadi Zarandi: "Optimal design of steel-concrete composite I-girder bridges using three meta-heuristic algorithms." Periodica Polytechnica. Civil Engineering 63.2: 317 (2019).

[3] Kaveh, A.: Optimum design of multi-span composite box girder bridges using Cuckoo Search algorithm. Steel and Composite Structures 2014;17(5):705-719 (2014).

[4] Degertekin, S. O.: Improved harmony search algorithms for sizing optimization of truss structures. Computers & Structures, 92, 229-241 (2012).

[5] Practical Steel Tub Girder Design (2005).

[6] Steel Bridge Design Handbook (2012). Design Example 4: Three-Span Continuous Straight Composite Steel Tub Girder Bridges.

[7] Geem, Z. W., Kim, J. H., & Loganathan, G. V. (2001). A new heuristic optimization algorithm: harmony search. *simulation*, *76*(2), 60-68.

[8] AASHTO-LRFD Bridge Design Specifications (2012). American Association of State Highway and Transportation Officials, Washington, DC.

DEĞİŞKEN BOŞLUK ORANINA SAHİP BETONARME KİRİŞLERİN NÜMERİK ANALİZİ

Faruk ERDEM

Gazi Üniversitesi, Teknoloji Fakültesi, İnşaat Mühendisliği Bölümü, Yenimahalle, Ankara, ORCID ID: 0000-0002-7117-9306

Alper BÜYÜKKARAGÖZ

Prof. Dr., Gazi Üniversitesi, Teknoloji Fakültesi, İnşaat Mühendisliği Bölümü, Yenimahalle, Ankara, ORCID ID:0000-0003-1074-7637

ÖZET

Betonarme yapılarda estetik nitelikleri ve yapı kullanım alanlarını korumak amacıyla elektrik, mekanik ve sıhhi tesisat gibi teknik sistemlerin kurulması için uygun ortamlara ihtiyaç duyulmaktadır. Bu ortamları tesis etmek adına kiriş gövdesine imalat öncesinde veya sonrasında donatılara zarar vermeden delme işlemiyle boşluklar oluşturulmaktadır. Önemli yapı taşıyıcı sistem elemanlarından biri olan kirişlerde gövde boşluğu varlığı kiriş taşıma gücünü ciddi oranda azaltmakta ve göçme tipini değiştirmektedir. Tasarım aşamasında öngörülmeyen bu boşlukların imalat sonrasında kiriş gövdesinde tatbik edilmesi kiriş davranışı ve yapı performansı üzerinde belirsizliklere yol açmaktadır. Bu nedenle gövde boşluklarının kirişin kapasitesi ve davranışı üzerindeki etkisinin belirlenmesi büyük önem taşımaktadır. Sonlu elemanlar yöntemi kullanılarak oluşturulan modellerin doğrusal olmayan analiz sonuçları ile gerçek eleman davranışı arasında gözlenen yakın uyum ve son zamanlarda yaşanan teknolojik gelişmeler mühendislik alanında sonlu elemanlar yöntemine dayalı paket programların kullanımını yaygınlaştırmıştır. Bu çalışma kapsamında gövde boşluklu kirişlerde boşluk oranının kiriş dayanımı ve davranışı üzerindeki etkisinin nümerik olarak araştırılması amaçlanmıştır. Bu doğrultuda Osman, Wu, Ji ve Abdulhameed (2017) tarafından boşluklu ve boşluksuz kirişlerin kesme davranışlarının incelendiği deneysel ve analitik çalışma verileri referans alınarak beton basınç dayanımı C30 olan bir adet boşluksuz referans kiriş ve değişken çaplı üç adet dairesel boşluklu kiriş sonlu eleman paket programı ANSYS ile simüle edilmiştir. Sonlu eleman yöntemine dayalı nümerik çalışma sonuçları ile referans çalışma deneysel test verileri karşılaştırılarak araştırmanın uygunluğu incelenmiştir. Elde edilen sonuçlara göre sonlu eleman analiz sonuçları ile deneysel veriler arasında büyük bir uyum olduğu tespit edilmiştir. Çalışma sonucunda değişken çaplara sahip dairesel boşluklu kirişlerin deplasman miktarları, yük taşıma kapasiteleri ve enerji tüketim kapasitelerindeki değişimler belirlenmiştir.

Anahtar kelimeler: Betonarme kiriş, Dairesel boşluklu kiriş, ANSYS, Sonlu elemanlar yöntemi.

NUMERICAL ANALYSIS OF REINFORCED CONCRETE BEAMS WITH VARIABLE OPENİNG RATIO

ABSTRACT

In reinforced concrete structures, suitable environments are needed for the establishment of technical systems such as electrical, mechanical and sanitary systems in order to preserve their aesthetic qualities and building usage areas. In order to establish these environments, openings are created in the beam body by drilling without damaging the reinforcements before or after manufacturing. The presence of web opening in the beams, which is one of the important structural elements, significantly reduces the beam carrying power and changes the type of collapse. The application of these openings, which are not foreseen at the design stage, on the beam body after manufacturing leads to uncertainties on the beam behavior and structure performance. Therefore, it is of great importance to determine the effect of web openings on the capacity and behavior of the beam. The close harmony observed between the nonlinear analysis results of the models created using the finite element method and the actual element behavior and the recent technological developments have made the use of package programs based on the finite element method widespread in the field of engineering. Within the scope of this study, it is aimed to numerically investigate the effect of opening ratio on beam strength and behavior in beams with web openings. In this direction, a reference beam with a concrete compressive strength of C30

and three circular hollow beams with variable diameters were simulated with the finite element package program ANSYS, based on the experimental and analytical study data in which the shear behavior of opening and without opening beams was examined by Osman, Wu, Ji ve Abdulhameed (2017). The suitability of the research was examined by comparing the results of the numerical study based on the finite element method with the experimental test data of the reference study. According to the results obtained, it has been determined that there is a great agreement between the finite element analysis results and the experimental data. As a result of the study, the displacement amounts, load carrying capacities and energy consumption capacities of circular hollow beams with variable diameters were determined.

Keywords: Reinforced concrete beam, Circular opening beam, ANSYS, Finite element analysis.

GİRİŞ

Betonarme yapılar servis ömrü boyunca kalıcı, hareketli, kar, rüzgar ve deprem yükleri gibi statik ve dinamik yüklerin etkisi altında kalmaktadır. Taşıyıcı sistem elemanları hizmet süresince yapıya etkiyen bu yükleri güvenli ve uygun şekilde taşımakta ve zemine aktarmaktadır. Mevcut yapılarda, taşıyıcı sistem elemanlarının davranışlarının tasarım aşamasında gerçekçi bir şekilde belirlenememesi halinde yapıya etki eden yüklerin altında ciddi hasarlar oluşmakta veya çökme meydana gelmektedir. Bu durumun önüne geçmek için betonarme yapıların performansının doğru değerlendirilmesi ve yapı güvenliğinin sağlanması son derece önemlidir. Teknoloji alanındaki hızlı gelişim, yapılarda insan ihtiyacına yönelik yaratıcı fikirlerin uygulanmasına imkan sağlayarak yapı tasarımında estetik nitelikleri ve işlevselliği ön plana çıkarmaktadır. Betonarme yapılarda mekanik, elektrik ve su tesisatı gibi teknik malzemelerin geçişi gerçekleştirilirken yapı kullanım alanını azaltmayacak estetik ve ekonomik bir çözüm amaçlanmaktadır. Bunu sağlamak için uygulamada yapım esnasında ya da sonradan kiriş gövdesinde farklı şekillerde ve boyutlarda boşluklar açılarak bu hizmetlerin iletimi sağlanmaktadır. Özellikle sonradan oluşturulan boşluk nedeniyle kiriş kesitinde meydana gelen ani rijitlik değişimi kiriş davranışını daha karmaşık bir hale getirmektedir. Yapıda oluşacak riskleri en aza indirgeyerek can ve mal kaybının önüne geçmek için betonarme kiriş gövdesinde farklı boyut ve konumlarda bırakılan boşlukların kiriş davranışı üzerindeki etkisinin bilinmesi oldukça önemlidir. Günümüzde bilgisayar teknolojisindeki hızlı gelişimle ile birlikte mühendislik alanında karmaşık mühendislik problemlerinin kolayca çözüme kavuşturulabilmesi için sonlu elemanlar yöntemi yaygın olarak kullanılmaya başlanmıştır. Betonarme elemanların sonlu elemanlar yöntemi ile modellenmesi ve gerçekleştirilen analizlerin sonuçları gerçek eleman davranışı ile iyi bir uyum içinde olması bu alanda yapılan çalışmaların sayısını arttırmıştır. Bu kapsamda literatürde gövde boşluklu kirişlerin sonlu eleman analiz sonuçlarının, kiriş davranışını tahmin etmede hassas ve doğru olup olmadığını göstermek için sonlu eleman analiz sonuçları ile deneysel çalışma sonuçlarının karşılaştırıldığı bazı araştırmalar yapılmıştır. Amiri ve Masoudnia (2011) tarafından betonarme kiriş gövdesinde değişken boşluk oranı ve boşluk tipi parametrelerinin kiriş davranışına etkisini incelemek için yürütülen bir çalışmada, sonlu eleman yazılımı olan ANSYS programı kullanılarak statik yükleme altında doğrusal olmayan analizler gerçekleştirilmiştir. Çalışma kapsamında yapılan analizlerden elde edilen bulgular ile mevcut deneysel çalışma sonuçları arasında gözlemlenen yakınlık ANSYS programında tasarlanan modellerin gerçek davranışı yansıttığını ispatlamıştır. Ayrıca kiriş gövdesinde boşluk tipi daire tercih edilmesinin kare boşluk tipine kıyasla daha yüksek taşıma kapasitesi sağladığı ve dairesel boşluk çapının kiriş derinliğinin %48'ini aştığı durumlarda kiriş taşıma kapasitesinde ciddi azalmalar olduğu gözlemlenmiştir. Saksena ve Patel (2013) tarafından boşluk geometrisi dairesel olan betonarme kirişlerde boşluk konumu ile boşluk çapı değişkenlerinin kiriş yük taşıma kapasitesi üzerindeki etkisinin araştırılması amacıyla yapılan bir diğer çalışmada ANSYS programı kullanılarak simülasyon gerçekleştirilmiş ve elde edilen analiz verilerinin deneysel çalışma test verileri ile büyük ölçekte uyum gösterdiği tespit edilmiştir. Kiriş derinliğinin %55'inden daha düşük boşluk çapı tercih edilmesinin ve kiriş eğilme bölgesinde boşluk teşkil edilmesinin kiriş taşıma kapasitesi üzerindeki etkisinin çok düşük olduğu belirlenmiş ve bu durumda kirişte boşluk bırakılması için en uygun yerin eğilme bölgesi olduğu belirlenmiştir. Literatürdeki mevcut çalışmaların aksine Aykac ve diğ. (2013)'nin yaptığı deneysel çalışmada, gövdesinde çok sayıda kare ve dairesel boşluk bulunan farklı donatı detayları ve donatı oranlarına sahip betonarme kirişlerin eğilme davranışı kapsamlı şekilde incelenmiştir. Çalışma kapsamında açıklığı boyunca bir boşluk ya da kesme bölgelerinde birer boşluk bırakılan kirişlerde boşluk etrafında meydana gelen gerilme birikmeleri sonucu ortaya çıkan gevrek kırılmanın önüne geçmek ve sünek davranışı sağlamak adına kiriş gövdesinde açıklık boyunca çok sayıda boşluk bırakılmıştır. Çalışma sonucunda dairesel boşluklu kirişlerde boşluk köşelerinde çapraz donatı kullanımının kare boşluklu kirişlere

kıyasla daha yüksek dayanım ve süneklik değerleri sağladığı tespit edilmiştir. Mohamed, Shoukry ve Saeed (2014)'in gövde boşluklu betonarme derin kirişlerde farklı donatı dağılımı ile boşluk konumu parametrelerinin kirişin taşıma kapasitesine etkisini inceledikleri bir diğer araştırmada, ABAQUS programıyla oluşturulan modellerin sonlu eleman analizleri gerçekleştirilmiş ve analiz sonuçları ile önceki deneysel çalışmalardan elde edilmiş olan sonuçlar arasında uyumlu değerler olduğu tespit edilmiştir. Betonarme derin kirişlerde gövde boşluğu bırakılması gereken durumlar için kiriş derinliğinin %20'sine karşılık gelen değerin altında bir boşluk büyüklüğü ve kiriş çekme donatısı dağılımının kiriş derinliğinin %10 ila %20'si arasında bulunması durumlarının kiriş taşıma gücünde çok az bir azalma oluşturmasından dolayı bu parametrelerin derin kirişlerde boşluk bırakılması durumunda en uygun tasarım tekniği olduğu tespitinde bulunulmuştur. Sayed (2019) tarafından kesme açıklığında dikey dairesel boşluk bulunan betonarme kirişlerde boşluk konumu, boşluk sayısı ve boşluk oranı değişkenlerinin kiriş kesme davranışına etkisinin incelendiği çalışma kapsamında ANYS programı ile sonlu eleman simülasyonu gerçekleştirilmiştir. Çalışma kapsamında elde edilen analiz sonuçlarına göre, oluşturulan modellerin doğruluğu kanıtlanırken dikey boşluk oranının kiriş rijitliği ve taşıma kapasitesi üzerindeki en kritik parametreler olduğu belirlenmiştir. Bu çalışma kapsamında ise betonarme kiriş gövdesinde dairesel boşluk oluşturulması durumunda kiriş davranışındaki değişimi gözlemlemek ve deneysel test verileri ile uyum içerisinde doğru sonlu elemanlar model tekniğini ortaya koymak amaçlanmıştır. Yürütülen bu çalışmada değişken boşluk oranlı kirişler ve boşluksuz referans kiriş üzerinde doğrusal olmayan sonlu eleman analizleri gerçekleştirilerek analitik bir çalışma yapılması hedeflenmiştir. Bu bağlamda ANSYS programı ile oluşturulan modellerin betonarme kirişlerin davranışını gerçekçi bir şekilde yansıttığını göstermek adına Osman, Wu, Ji ve Abdulhameed (2017) tarafından yürütülen çalışmanın deneysel test sonuçları ile sonlu eleman sonuçları karşılaştırılmıştır. Sonuçların iyi uyum içinde olması ANSYS'te oluşturulan modelleme tekniğinin betonarme kiriş davranışını doğru şekilde tahmin edilmesine imkan sağlamıştır. Bu doğrultuda bu çalışma kapsamında beton basınç dayanımı C30 olan değişken boşluk alanına sahip dairesel boşluklu betonarme kirişlerin deplasman miktarı, yük taşıma kapasiteleri ve enerji tüketim kapasitelerindeki değişim incelenmiştir.

MATERYAL VE YÖNTEM

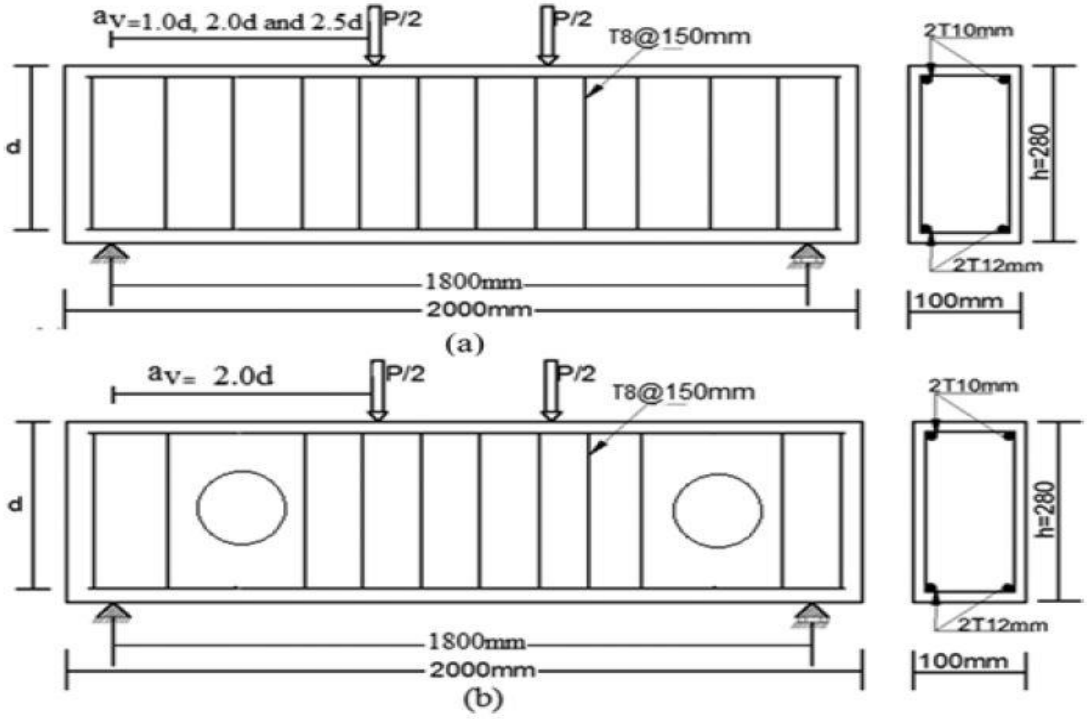
Yönteme Genel Bakış

Bu çalışma kapsamında betonarme kirişlerin gövdesinde boşluk bırakılması durumunda kiriş davranışında meydana gelen değişimi belirlemek ve oluşturulan sonlu eleman modellerinin gerçek kiriş davranışını ortaya koyabildiğini göstermek adına Osman, Wu, Ji ve Abdulhameed (2017) tarafından yapılan çalışma referans alınmıştır. Bu kapsamda Osman, Wu, Ji ve Abdulhameed (2017) tarafından deneysel çalışmada kullanılan kiriş numuneleri ile aynı boyut, donatı, beton sınıfı ve boşluk konumu kullanılmıştır. Çalışmada tüm kirişler dikdörtgen kesitli, 2 m uzunluğunda, 100 mm genişliğinde ve 280 mm yüksekliğindedir. Referans alınan iki adet deney elemanından biri boşluksuz diğeri ise her kesme açıklığında bir adet dairesel boşluk bulunan gövde boşluklu kiriştir. Ayrıca çalışma kapsamında sonlu eleman simülasyonu için kullanılacak olan iki adet dairesel boşluklu kiriş sırasıyla referans çalışmada kullanılan gövde boşluklu kiriş elemanında bırakılan boşluk alanından %50 daha fazla ve %50 daha az boşluk alanına sahiptir. Boşluklar kiriş yüksekliğinin ortasında konumlandırılmıştır. Tablo 1'de çalışma kapsamında yer alan kiriş elemanlarının özellikleri gösterilmiştir. Ayrıca sonlu eleman analizleri için kullanılacak olan modellerin donatı detayları ve kesitlerine ilişkin bilgiler Şekil 1 ve 2'de gösterilmiştir.

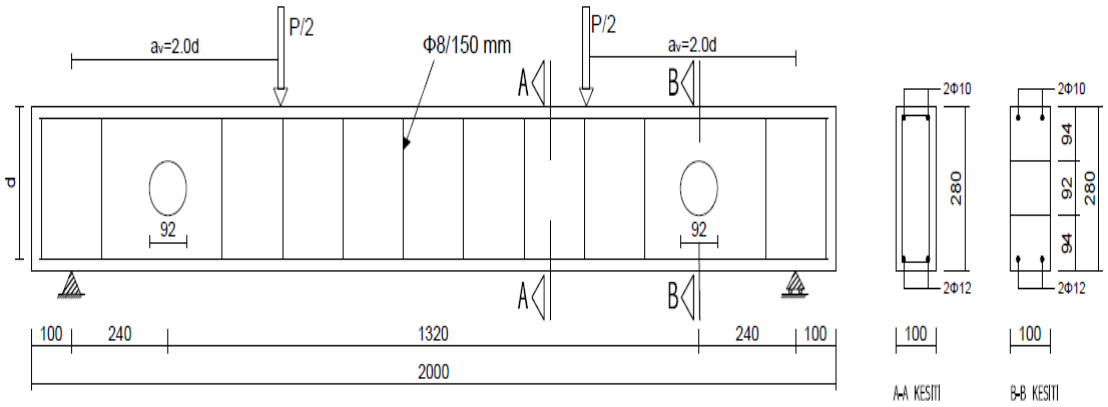
Tablo 1. Sonlu Elemanlar ile Modellenen Kirişler

Referans Alınan Çalışma	Kiriş Adı	Boşluk Tipi	Boşluk Boyutu (mm)	Çekme Donatısı	Basınç Donatısı	Etriye
Osman, Wu, Ji ve Abdulhameed (2017)	BS2	Boşluksuz	-	2φ12	2φ10	φ8/150
Osman, Wu, Ji ve Abdulhameed (2017)	BS20	Daire	130	2φ12	2φ10	φ8/150
Mevcut çalışma	BS20L	Daire	92	2φ12	2φ10	φ8/150
Mevcut çalışma	BS20H	Daire	159	2φ12	2φ10	φ8/150

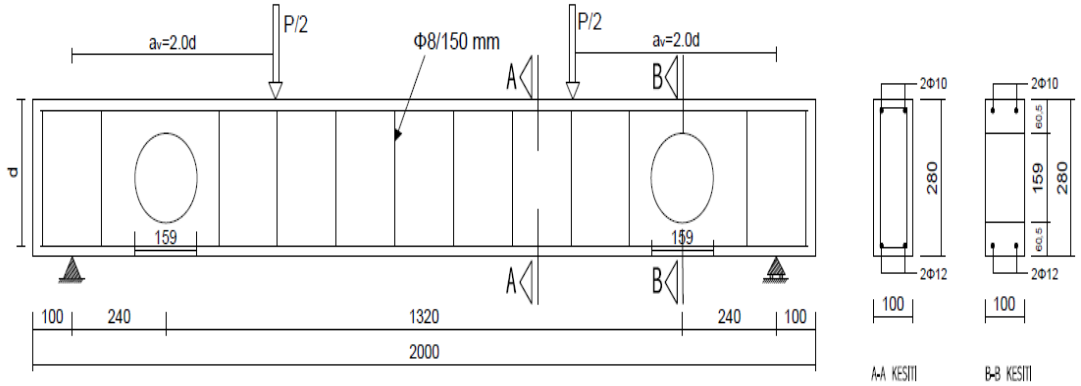
Osman, Wu, Ji ve Abdulhameed (2017) tarafından kesme yükleri altındaki kiriş numuneleri çift yükleme noktası altında test edilmiştir. Referans çalışmada kesme açıklığı-etkili derinlik oranı 2 olan deneysel test elemanları referans alınmıştır. BS2 kirişi referans çalışma kapsamında deneylerde test edilmek için üretilen boşluksuz ikinci seri kontrol kirişi temsil etmektedir. BS20 kirişi, BS2 kirişine karşılık gelen dairesel boşluklu referans kontrol kirişini sembolize etmektedir. BS20L kirişinin beşinci harfi olan "L" BS20 kirişinde bulunan boşluk alanının yarısı kadar boşluk alanına sahip kirişi ifade ederken, BS20H kirişinin beşinci harfi olan "H" ise bu alanın yarısı kadar arttırılmış alana sahip kirişi ifade etmektedir. Boşluklu kirişlerde boşluk oranının kiriş davranışına etkisini belirlemek amacıyla bütün kiriş elemanlarında boyuna ve enine donatılar aynı seçilmiştir. Boşluklar kiriş kesme bölgesinde mesnetten 240 mm mesafede konumlandırılmıştır. Bütün kirişler için etkili derinlik 260 mm alınmıştır.



Şekil 1. Referans Çalışma Boşluksuz ve Gövde Boşluklu Kiriş Detayları (Osman, Wu, Ji ve Abdulhameed (2017))



a)BS20L kirişi

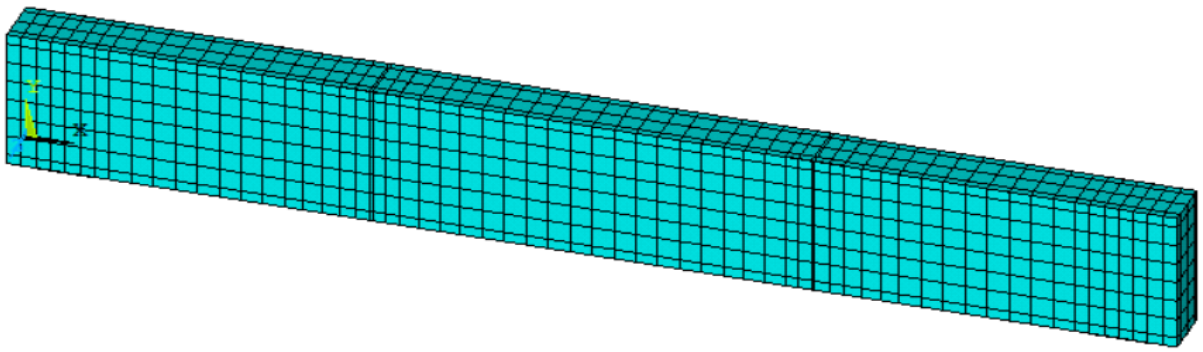


b)BS20H kirişi

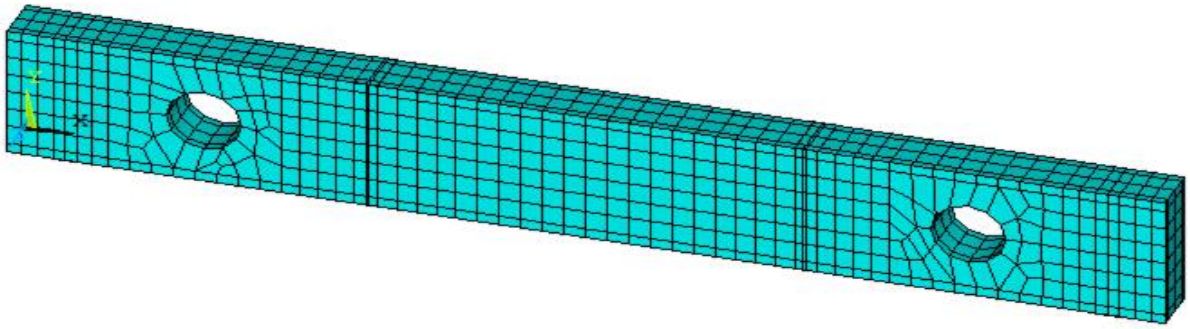
Şekil 2. Dairesel Gövde Boşluklu Kiriş Detayları

ANSYS Programı ile Sonlu Eleman Modellerinin Oluşturulması

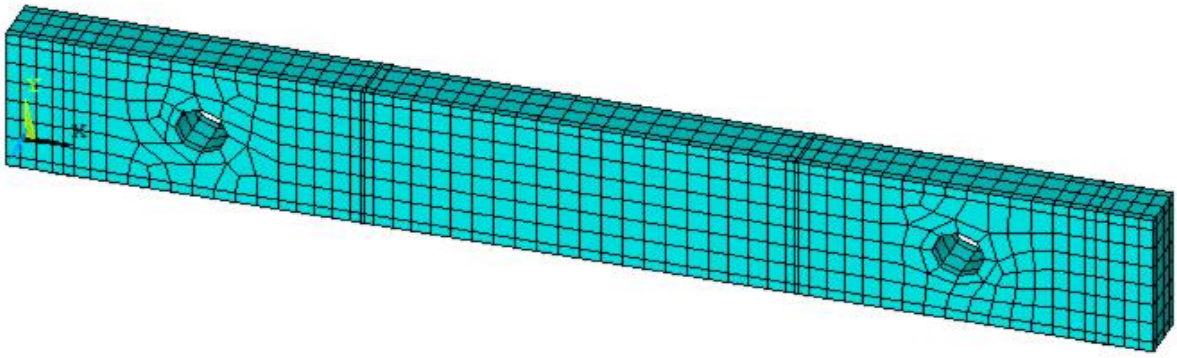
Nümerik çalışma doğrultusunda kiriş elemanlarının sonlu eleman analizlerini gerçekleştirmek için ANSYS Mechanical APDL 15.0 programı kullanılmıştır. ANSYS ile modellenen betonarme kirişler için beton karakteristik küp basınç dayanımı değeri için Osman, Wu, Ji ve Abdulhameed (2017) tarafından malzeme deneyleri sonucu elde edilen değerler referans alınmıştır. Bu bağlamda betonun 28 günlük ortalama karakteristik küp basınç dayanımı değeri 37 MPa olarak bulunmuştur. Betonun modellenmesi aşamasında plastik deformasyon, sünme, çekmede çatlama ve basınçta ezilme gibi betonun doğrusal olmayan davranışlarını ortaya koyma yeteneğine sahip Solid65 eleman tipi seçilmiştir. Boyuna donatılar ile çelik levhalar için akma dayanımı 420 MPa, etriyeler için ise 365 MPa alınarak referans çalışma ile aynı malzeme özellikleri kullanılmıştır. Donatı modellemesi için 3 boyutlu tek eksenli ve her düğüm noktasında üç serbestlik derecesi bulunan Link180 eleman tipi kullanılmıştır. Çelik yükleme levhaları için sekiz düğümlü ve her düğüm noktasında üç serbestlik derecesine sahip Solid185 eleman tipi kullanılarak modellemeler oluşturulmuştur. Bir adet boşluksuz ve üç adet dairesel boşluklu betonarme kiriş elemanının sonlu eleman modellerinde donatıların konumları da dikkate alınarak boyutu 40 mm olan mesh elemanlara bölünmüştür. Sonuç olarak BS2 kirişinde 2592 eleman ve 3059 düğüm noktası, BS20 kirişinde 2452 eleman ve 2962 düğüm noktası, BS20L kirişinde 2520 eleman ve 3027 düğüm noktası, BS20H kirişinde ise 2432 eleman ve 2957 düğüm noktası oluşturulmuştur. ANSYS programında oluşturulan sonlu eleman modelleri Şekil 3'de gösterilmiştir.



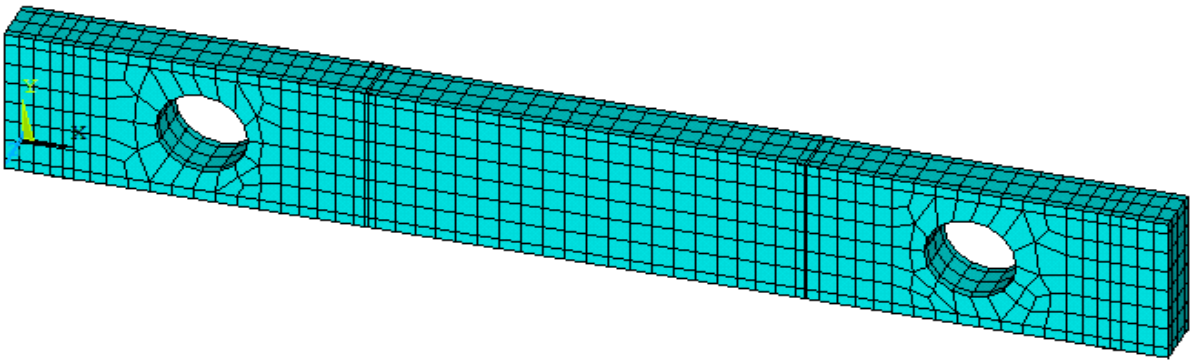
a)BS2 kirişi



b)BS20 kirişi



c)BS20L kirişi



d)BS20H kirişi

Şekil 3. ANSYS Programında Oluşturulan Sonlu Eleman Modelleri

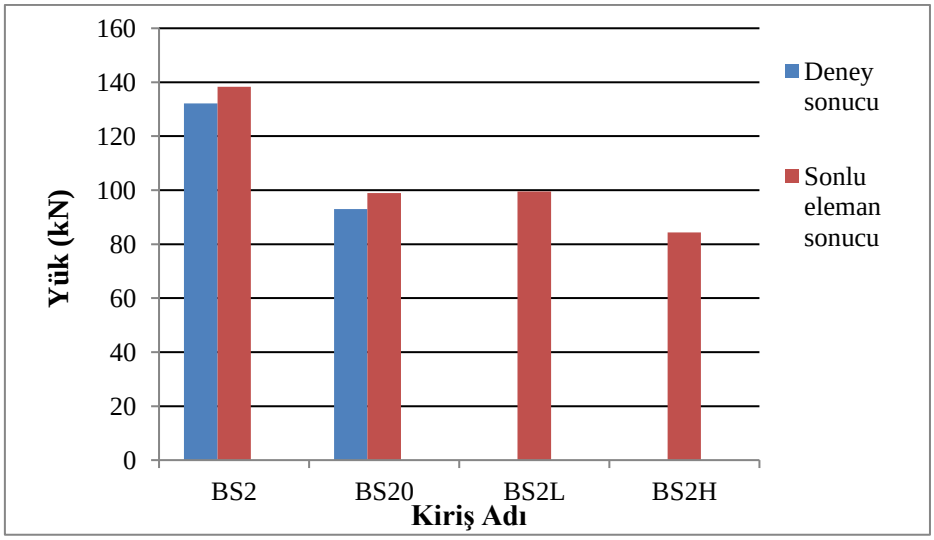
NÜMERİK ANALİZ DETAYLARI

Boşluklu ve boşluksuz kirişlerin sonlu elemanlar yöntemi ile oluşturulan kiriş modellerinin malzeme özellikleri ve yakınsama kriterlerinin doğru bir şekilde yansıtıldığından emin olmak için gerçekleştirilen doğrusal olmayan analiz sonuçları ile referans çalışma deneysel test verileri karşılaştırılarak modelleme tekniğinin uygunluğu incelenmiştir. Bu kapsamda Osman, Wu, Ji ve Abdulhameed (2017) tarafından yürütülen deneysel çalışma sonuçları ile elde edilen sonlu eleman sonuçları Tablo 2'de verilmiştir. Tablo 2'ye göre elde edilen sonuçlar nümerik çalışma ile deneysel çalışma sonuçları arasında iyi bir uyum olduğunu göstermektedir.

Tablo 2. Nümerik ve Deneysel Çalışma Sonuçlarının Karşılaştırılması

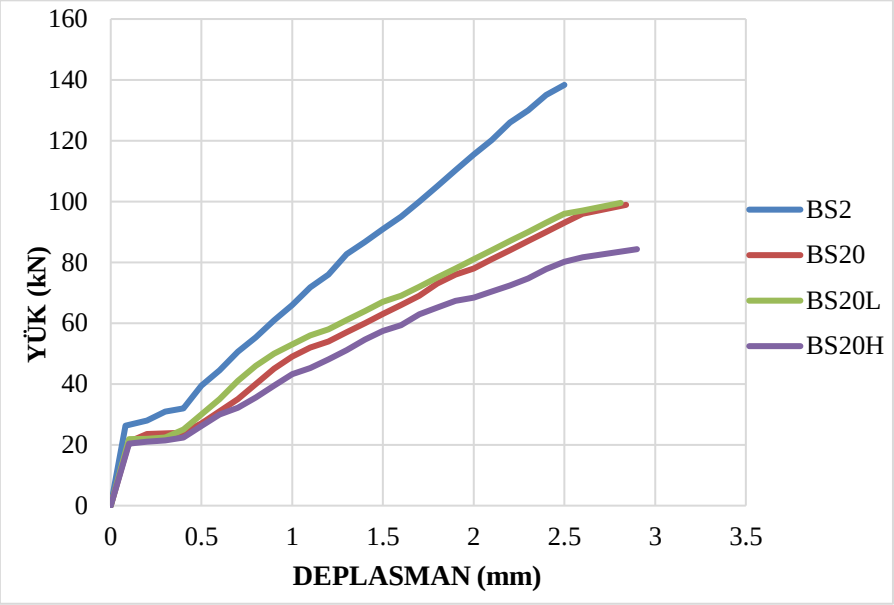
Kiriş	a_v/d	Çatlama Yükü (kN)		Göçme Yükü (kN)		Deney/Analiz	Maksimum Deplasman (mm)	
		Deney	Analiz	Deney	Analiz		Deney	Analiz
BS2	2	20.5	26.25	132.2	138.34	0.96	2.41	2.64
BS20		17	21.55	93	98.9	0.94	2.99	2.84
BS20L			21.86		99.54			2.81
BS20H			20.38		84.32			2.9
a_v: kesme açıklığı; d: etkili derinlik								

Sonlu eleman analizleri sonucunda kirişlerde kesme tipi göçme meydana geldiği belirlenmiştir. BS2 kirişinde ilk çatlak 26.25 kN yükteki mesnet noktasında oluşmuştur. Artan yüklemeler altında kiriş 138.34 kN'a ulaştığında ise göçmüştür. Sonlu elemanlar analiz sonucunda deneysel sonuçlara oranla %4.65 daha fazla göçme yükü elde edilmiştir. BS20 kirişinde ilk çatlağın 21.55 kN'da oluştuğu belirlenmiştir. Kiriş yaklaşık olarak 98.9 kN'da taşıma kapasitesine ulaşmıştır. Sonlu eleman analiz sonucunda elde edilen göçme yükü değerinin, deneysel test sonuçlarına kıyasla %6.34 daha büyük olduğu tespit edilmiştir. Kiriş gövdesindeki boşluk varlığı, taşıma kapasitesinde boşluksuz kirişe oranla %28.5 azalmaya yol açmıştır. BS20L, BS20H kirişlerinde sırasıyla ilk çatlaklar 21.86 kN ve 20.38 kN yükte oluşurken, taşıma kapasitelerine ise 99.54 kN ve 84.32 kN yük değerlerinde ulaşılmıştır. Ayrıca bu kirişlerde boşluksuz referans kirişe kıyasla %28.05 ve %39.04 gibi daha düşük yüklerde göçmenin oluştuğu tespit edilmiştir. Kiriş gövdesindeki mevcut büyük boşluk sebebiyle BS20H kirişinin, kiriş elemanları arasında en düşük göçme yüküne sahip olmasına karşın artan yüklemeler altında en yüksek deplasman miktarına ulaştığı görülmüştür.



Şekil 4. Karşılaştırmalı Nümerik ve Deneysel Nihai Yük Kapasitesi Değerleri

Şekil 4'deki sütun grafikte ise karşılaştırılmalı olarak BS2, BS20, BS2L ve BS2H kirişlerinin deney ve sonlu elemanlar analizine ait yük taşıma kapasitesi değerleri yer almaktadır.



Şekil 5. BS2, BS20, BS20L ve BS20H Kirişlerinin Sonlu Eleman Yük Deplasman Eğrileri

Şekil 5'de ANSYS ile iki noktalı yükleme altında basit mesnetli boşluksuz ve boşluklu betonarme kirişlerin doğrusal olmayan sonlu eleman analizleri ile elde edilen yük deplasman eğrileri gösterilmektedir. Buna göre genel olarak kiriş kesme bölgelerinde konumlandırılan boşlukların kiriş taşıma kapasitesinde önemli azalmalara yol açtığı ve deplasman miktarını arttırdığı tespit edilmiştir. Kiriş gövdesinde bulunan boşluk alanının arttırıldığında ise kiriş rijitliğinde ve göçme yükü değerlerinde ciddi azalmaların olmadığı gözlemlenmiştir.

Tablo 3. Nümerik Çalışma Sonucunda Kiriş Elemanlarının Enerji Tüketim Değerleri

Kiriş Adı	**Boşluk Tipi**	**Boşluk Boyutu (mm)**	**Enerji Tüketim Değeri (joule)**
BS2	Boşluksuz	-	215.23
BS20	Daire	130	168.52
BS20L	Daire	92	172.81
BS20H	Daire	159	153.60

Tablo 3'te görüldüğü üzere yapılan analizler sonucunda boşluksuz referans kirişte en yüksek enerji tüketim kapasitesine ulaşılmıştır. Gövde boşluk alanı en fazla olan BS20H kirişinde ise enerji tüketim kapasitesi en düşük değerde olduğu gözlemlenmiştir. Betonarme kiriş gövdesinde boşluk bırakılması durumunda enerji tüketim kapasitesinde yaklaşık olarak %22 ile %29 oranında azalmalar olduğu görülmüştür. Nümerik çalışma sonuçları göçme yükü, deplasman miktarı ve enerji tüketim kapasitesinin kirişte boşluk varlığından ve boşluk alanından açık bir şekilde etkilendiğini göstermiştir.

SONUÇLAR

Bu araştırmada betonarme kirişlerin gövdesinde boşluk bırakılması halinde kiriş davranışında meydana gelen belirsizlikleri ortaya koymak için sonlu elemanlar yöntemi kullanılarak oluşturulan modellerin, kirişlerin gerçek davranışını yansıtıp yansıtmadığını tespit edebilmek amacıyla Osman, Wu, Ji ve Abdulhameed (2017) tarafından yapılan deneysel çalışma referans alınarak bir doğrulama çalışması gerçekleştirilmiştir. Bu bağlamda ANSYS ile gerçekleştirilen sonlu eleman analiz sonuçları ile Osman, Wu, Ji ve Abdulhameed (2017) tarafından yürütülen çalışmanın deneysel test sonuçları karşılaştırılmıştır. Mevcut çalışma kapsamında gövdesinde değişken boşluk alanı bulunan dairesel boşluklu betonarme kirişlerin deplasman miktarı, yük taşıma kapasitesi ve enerji tüketim kapasiteleri ortaya konulmuştur. Analitik çalışmada elde edilen sonuçlar aşağıdaki gibidir:

1. Nümerik çalışma doğrultusunda ANSYS ile gerçekleştirilen sonlu eleman analiz sonuçlarının Osman, Wu, Ji ve Abdulhameed (2017) tarafından yapılan deneysel test sonuçları ile yakın uyum içerisinde olduğu ve dairesel boşluklu kirişlerin davranışını tahmin etmede sonlu elemanlar yöntemine dayalı sonuçların kabul edilebilir düzeyde olduğu görülmüştür.

2. Doğrulama çalışması sonucunda elde edilen bulgular betonarme kirişlerde göçme yükü, deplasman miktarı ve enerji tüketim kapasitesinin kiriş gövdesinde bırakılan boşluk varlığı ile değişen boşluk alanından büyük ölçüde etkilendiği net bir şekilde görülmüştür.

3. Betonarme kirişlerde boşluk varlığı ve boşluk alanındaki artış kirişlerin göçme yükü ve enerji tüketim kapasitelerinin önemli derecede azalmasına sebep olmakta ve deplasman miktarını arttırmaktadır.

4. Kiriş kesme bölgesine yerleştirilen boşluklar nihai yük taşıma kapasitesinde yaklaşık olarak %30 ila %40'a varan azalmalara neden olmakta dolayısıyla bu durumdan kaçınılması tavsiye edilmektedir.

5. Sınırlı sayıda kiriş elemanı üzerinde gerçekleştirilen araştırmalar sonucunda sonlu elemanlar yönteminin kullanılması tutarlı sonuçlar vermekle birlikte deney öncesi uygun tasarım tekniklerinin benimsenmesi açısından nümerik çalışmaların arttırılmasına fayda sağlayabilir.

KAYNAKLAR

Amiri, S., & Masoudnia, R. (2011). Investigation of the opening effects on the behavior of concrete beams without additional reinforcement in opening region using fem method. Australian Journal of Basic and Applied Sciences, 5(5), 617-627.

APDL, A. M. (2015). Version 15. ANSYS Inc, USA.

Aykac, B., Kalkan, I., Aykac, S., & Egriboz, Y. E. (2013). Flexural behavior of RC beams with regular square or circular web openings. Engineering Structures, 56, 2165-2174.

Mohamed, A. R., Shoukry, M. S., & Saeed, J. M. (2014). Prediction of the behavior of reinforced concrete deep beams with web openings using the finite element method. Alexandria Engineering Journal, 53(2), 329-339.

Osman, B. H., Wu, E., Ji, B., & Abdulhameed, S. S. (2017). Shear behavior of reinforced concrete (RC) beams with circular web openings without additional shear reinforcement. KSCE Journal of Civil Engineering, 21(1), 296-306.

Saksena, N. H., & Patel, P. G. (2013). Effects of the circular openings on the behavior of concrete beams without additional reinforcement in opening region using fem method. International Journal of Advanced Engineering Technology, 4(2).

Sayed, A. M. (2019). Numerical study using FE simulation on rectangular RC beams with vertical circular web openings in the shear zones. Engineering Structures, 198, 109471.

SONLU ELEMANLAR YÖNTEMİ İLE BETONARME KOLONLARIN ÇELİK LEVHALARLA KESMEYE KARŞI GÜÇLENDİRİLMESİ

Burak İTİŞKEN

Gazi Üniversitesi Teknoloji Fakültesi İnşaat Mühendisliği Bölümü, Yenimahalle, Ankara, Türkiye
ORCID ID: https://orcid.org/0000-0001-8774-3795

Alper BÜYÜKKARAGÖZ

Prof. Dr. Gazi Üniversitesi Teknoloji Fakültesi İnşaat Mühendisliği Bölümü, Yenimahalle, Ankara, Türkiye
ORCID ID: https://orcid.org/0000-0003-1074-7637

ÖZET

Bu çalışma kapsamında sonlu elemanlar metoduna göre analiz yapan Ansys programı ile mevcut betonarme bir kolonun, farklı boyut ve adetteki çelik levhalar ile güçlendirilmesi sonucunda kapasitelerinde nasıl bir değişim meydana geldiği incelenmiştir. Değişken olarak levha alanı ve beton dayanımı kullanılmış ve bu değişkenlerin kolonun kapasitesini nasıl etkilediği incelenmiştir. Çalışmada 200x200x1200 mm ebatlarında 6 adet kolonun analizleri yapılmıştır. Bu elemanlar için C20 ve C34 sınıfında beton kullanılmıştır. C20 sınıfı beton kullanılan elemanlar 2 mm kalınlığında ve 50 mm uzunluğundaki levhalar ile tüm yüzeylerinden 200 mm ve 100 mm aralıklarla kaplanmıştır. C34 sınıfı beton kullanılan kolon elemanlarda da aynı boyut ve aralıklarla çelik levha uygulanmıştır. Kolonların levhalar ile temas yüzeylerine yapışma etkisini yansıtmak için sürtünme katsayısı uygulanmıştır.

Tüm kolonlar aynı şekilde mesnetlenmiş ve eşit miktarda düşey yük uygulanmıştır. Ansys programı ile yapılan analizlerde yükler eşit parçalara bölünerek ayrı ayrı adımlarda kolon göçme yüküne ulaşıncaya kadar uygulanmıştır. Ayrıca kolonlarda meydana gelen ilk çatlak yükleri de belirlenmiştir. Analizlerde beton için gerilme – birim şekil değiştirme değerleri Hognestad beton modeline göre hesaplanmıştır. Modellenen elemanların her biri 25 mm'lik küçük boyutlu meshlere ayrılarak deneysel sonuçlara daha yakın sonuçlar elde edilmiştir. Toplamda kolon üst yüzeyinde bulunan 81 adet noktaya her adımda 2000 N 'luk yük verilerek analizler yapılmıştır.

Tüm analizler sonucunda yük – deplasman değerlerini veren grafikler elde edilmiştir. Deneysel sonuçlarla karşılaştırma amacı ile üretilmiş modellerin analizlerinden deney elemanlarına oldukça yakın sonuçlar elde edilmiştir. Deneyleri olmayan ve seçilen değişkenlere göre modellenen elemanlardan elde edilmiş yük-deplasman grafiklerine göre kolonların göçme yüklerinde bazı değişimler meydana gelmiştir. Elde edilen grafiklerden enerji tüketim değerleri ve süneklik değerleri elde edilmiş ve karşılaştırmalar yapılmıştır.

Anahtar Kelimeler: Kolon, Çelik levha, Sonlu Elemanlar Yöntemi, Ansys

STRENGTHENING OF REINFORCED CONCRETE COLUMNS AGAINST SHEAR WITH STEEL PLATES BY FINITE ELEMENT METHOD

ABSTRACT

The aim of this study is to investigate how an existing reinforced concrete column will change its capacity when it is covered with steel plates of different sizes and quantities by using ANSYS program, which analyzes the data accordingly to the finite element method. Plate area and concrete strength were used as variables and their effects on the capacity of the columns were examined. 6 columns of 200x200x1200 mm dimensions were analyzed in the scope of this thesis. C20 and C34 grade concretes are used for these columns. Columns with C20 grade concrete are covered with 2 mm thick and 50 mm long steel plates at 200 mm and 100 mm intervals from all surfaces. Columns using C34 grade concrete are also applied with the same steel plates of same dimensions and intervals. The friction coefficient was applied to reflect the adhesion effect of the columns to the contact surfaces of the steel plates.

All columns were supported in the same way, and all had an equal vertical load. In the analyzes made accordingly to the ANSYS finite element method, the loads were divided into equal parts and the columns were loaded in separate steps until they reached their respective failure loads. In addition to the failure loads, the first crack loads occurring in the respective concretes were studied. Stress - strain values for concretes were calculated according to the Hognestad concrete model in the analyzes. Each of the modeled elements was divided into small-sized meshes of 25 mm in order to obtain data which is closer to the experimental results. In total, 81 points on the upper surface of the column were given a load of 2000 N at each step and analyzed accordingly.

As a result of the analyses, graphs which represent load-displacement values were obtained. From the analysis of the models, which were created for the comparison purposes to the experimental results, results that are very close to the results of experimental elements were obtained. According to the load-displacement graphs observed from the elements that are without prior experimental results and, therefore, modeled according to the selected variables, changes in the failure loads were also observed. Energy consumption values and ductility values were obtained from the graphs and comparisons were made.

Keywords: Column, Steel plate, Finite Element Method, Ansys

GİRİŞ

Betonarme yapılarda eksenel yük kapasitesinin arttırılması için güçlendirme çalışmaları yapılmaktadır. Bunlar tamir harcıyla güçlendirme, epoksi reçinesi ile güçlendirme, polimerli beton ile güçlendirme, püskürtme beton ile güçlendirme, reçine betonları ile güçlendirme, lif takviyeli plastik levhalar ile güçlendirme, karbon lifli polimer ile güçlendirme, karbon takviyeli elyaf kumaş ile güçlendirme ve çelik plaka ile güçlendirme gibi yöntemler bulunmaktadır. Bu yöntemlerin hakkında daha belirgin bilgi sahibi olmak için birçok deneyler ve analizler yapılmaktadır.(Yavuz Emre Küçük, 2003)

Bu çalışma kapsamında ise sonlu elemanlar metoduna göre analiz yapan Ansys programı ile mevcut betonarme bir kolonun, farklı boyut ve adetteki çelik levhalar ile güçlendirilmesi sonucunda kapasitelerinde nasıl bir değişim meydana geldiği incelenmiştir. Günümüzde kullanılmakta olan birçok sonlu elemanlar ile analiz modeli bulunmaktadır. Bunlardan bazıları Ansys, Nastran ve Abaqus ‘dür. Ansys betonarme yapıların analizi için kullanılan en yaygın programlardan biridir. Bu tez kapsamında betonarme kısa kolonların etrafına sarılacak çelik takviyelerin, mevcut kolon kapasitesinde nasıl bir değişime neden olacağı incelenmiştir. Bu da ansys sonlu eleman metodu ile yapılacak analizler ile anlaşılmaya çalışılmıştır.

MATERYAL VE YÖNTEM

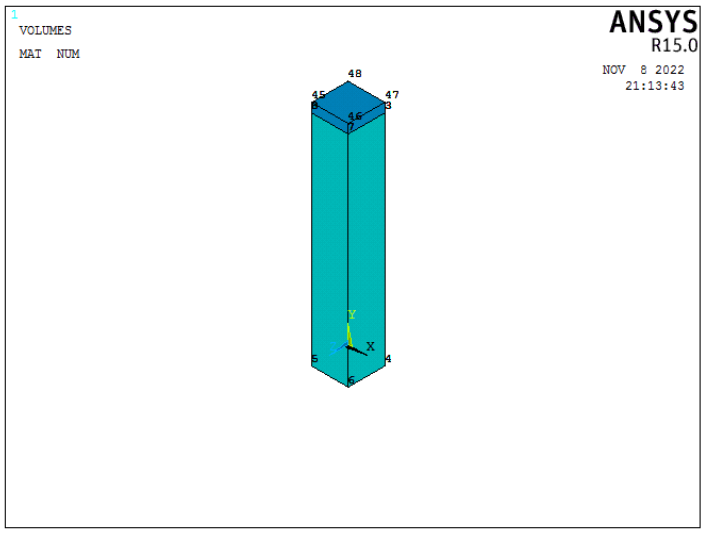
Sonlu elemanlar yöntemi ya da sonlu elemanlar metodu (FEM), mühendislik ve matematiksel modellerde sıklıkla kullanılan bir sayısal analiz yöntemidir. FEM, özellikle yapı statiği, ısı aktarımı, akışkanlar mekaniği, kütle aktarımı ve elektrik potansiyeli problemlerinde kullanılır; yöntem, özellikle iki veya üç boyutlu kısmi diferansiyel denklemleri ve sınır değer problemlerinin çözümünde uygulanır.(Vikipedi Özgür Ansiklopedi – Sonlu Elemanlar Metodu)

FEM, esasta geniş bir sistemi sonlu eleman adı verilen daha küçük bileşenlere ayırır: bu, denklemin çözüldüğü uzayın ayrıklaştırılarak küçük bölgelere bölünmesi ile gerçekleştirilir. Sınır değer probleminin bu formülasyonu sonucu bir cebirsel denklem sistemi elde edilir. Bu sistem daha sonra Rayleigh–Ritz veya Galerkin metodu gibi değişkenli metotlar ile çözülür. Bu metodlarda sonuçlar temel fonksiyonlar (basis function) cinsinden elde edilir, diğer bir deyişle bu fonksiyonlar kullanılarak asıl çözümün interpolasyonu yapılır.(Vikipedi Özgür Ansiklopedi – Sonlu Elemanlar Metodu)

Aslında sonlu elemanlar metodu bize daha karmaşık yapıların daha kolay çözülmesini sağlar. Bu çalışma kapsamında da sonlu elemanlar metodu kullanılarak da yapılan nonlineer analizler sonucunda çelik levhalar ile güçlendirilen kolonların kapasitelerinde nasıl bir değişim olduğu anlaşılmaya çalışılmıştır.

Burada analizleri yapılan tüm kolonların boyutları 200 x 200 x 1200 mm’dir. (Belal M. F., Mohamed H. M., Morad S. A., 2014). Fakat beton ezilmesini önlemek ve daha gerçekçi bir analiz yapabilmek için kolonların

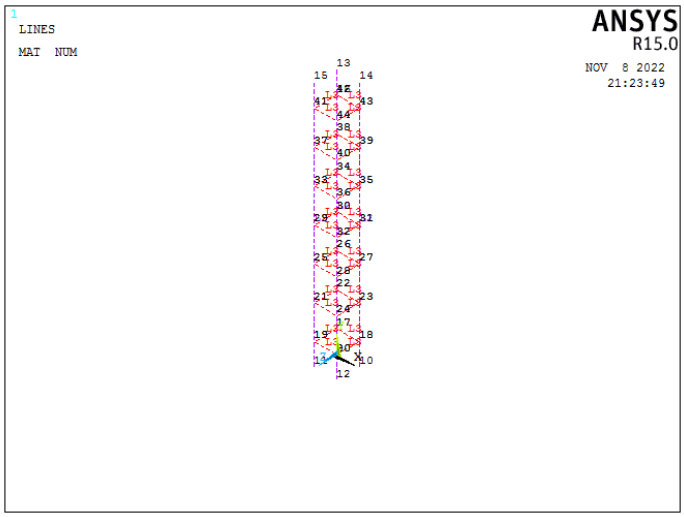
yüksekliği 1250 mm olarak modellenmiştir. Bunun için 50 mm'lik bir çelik levha kolonun üst yüzeyine konulmuştur. Modellenen eleman Şekil 1'de gösterilmiştir. (Şekil 1)



Şekil 1. Modellenen elemanın görünümü

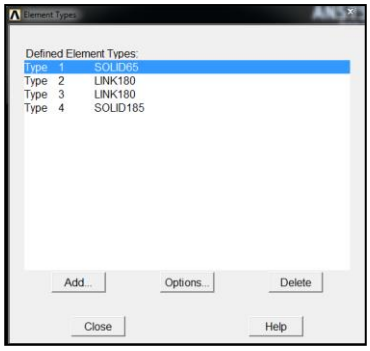
Kolonların hepsinde 4 adet Ø12 boyuna donatı ve 150 mm ara ile Ø8 etriye kullanılmıştır. Paspayı 50 mm olarak verilmiştir. (Belal M. F., Mohamed H. M., Morad S. A., 2014).

Kolon kesiti içerisindeki boyuna ve enine donatıların modellenmesi için öncelikle donatıların bulunduğu koordinatlarda düğüm noktaları tanımlamak gerekmektedir. Bu düğüm noktaları Ansys programında key pointlerdir. Bu key pointler, line komutu ile birleştirilerek donatılar modellenmiştir. Modellenen eleman şekil 2 de gösterilmiştir. (Uğur Yozgat, 2007).

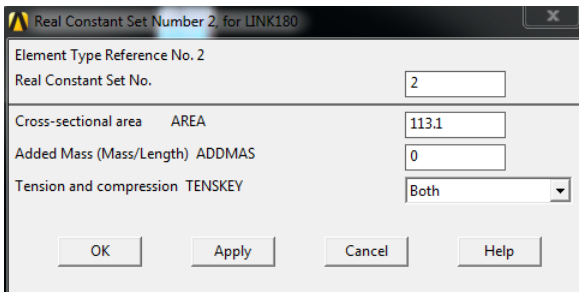


Şekil 2. Modellenen boyuna ve enine donatıların görünümü

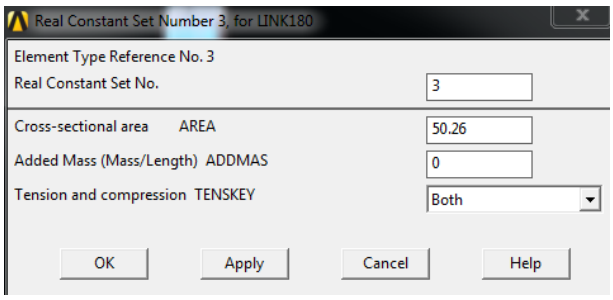
Ansys 'de betonlar için SOLID65, boyuna ve enine donatılar için LINK180, güçlendirme çelikleri için ise SOLID185 eleman tipi kullanılmıştır. Tanımlanan eleman tipleri aşağıdaki gibi programa girilmiştir. (Uğur Yozgat, 2007).



Analizleri yapılan bütün kolonlarda aynı donatı kullanılmıştır. Boyuna donatı kesit alanı ve enine donatı kesit alanı aşağıdaki gibi programa girilmiştir. (Belal M. F., Mohamed H. M., Morad S. A., 2014).

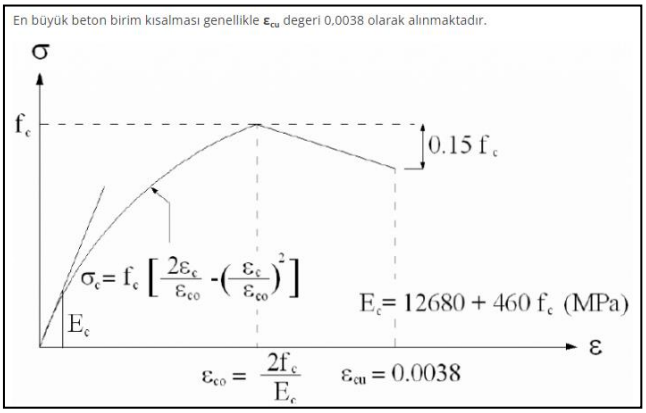


Boyuna donatı için



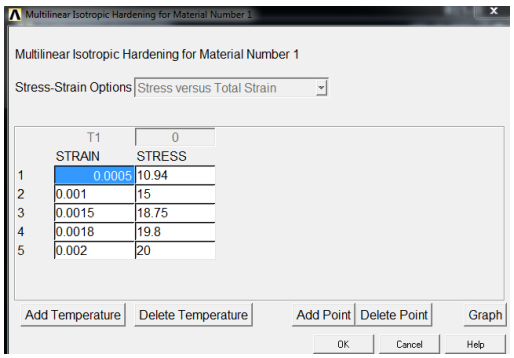
Enine donatı için

Her bir farklı malzeme teknik özelikleri de ayrı ayrı girilmiştir. İlk olarak betonun gerilme şekil değiştirme ilişkisi hognestad beton modeline göre girilmiştir. Hognestad beton modeli, sargısız betonların gerilme-şekil değiştirme davranışının Hognestad tarafından ortaya atılan modelidir. Bu model yalın betonu modellemek için kullanılmıştır. Hognestad beton modelinde gerilme-şekil değiştirme eğrisinin tepe noktasına kadar olan bölümü ikinci dereceden bir parabol, tepe noktasından sonra eğimi azalan bölüm ise, bir doğru olarak kabul edilmiştir. (Şekil 3) Hognestad modelinden elde edilen gerilme-şekil değiştirme eğrisi betonun doğrusallığının sınırını ve plastik davranışını belirlemekte kullanılacak olan Multilineer İzotropik Pekleşmeli Plastisite (VonMises) modelinde tanımlanmıştır. (Alper Büyükkaragöz ve Yağmur Kopraman , 2008).

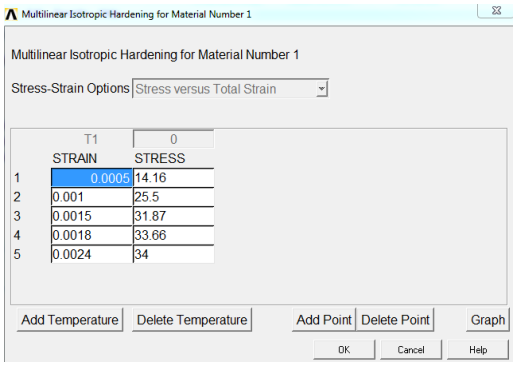


Şekil 3. Hognestad beton modeli

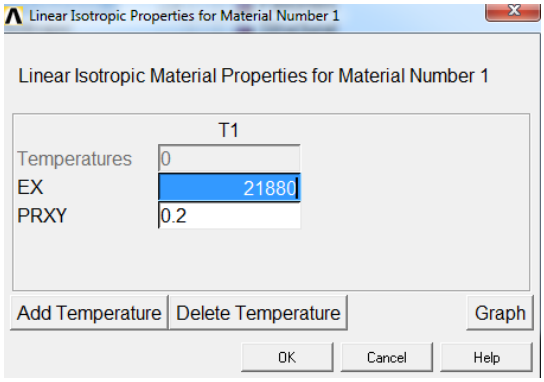
Aşağıda görülen gerilme – şekil değiştirme değerleri hognestad beton modeline göre hesaplanmıştır.



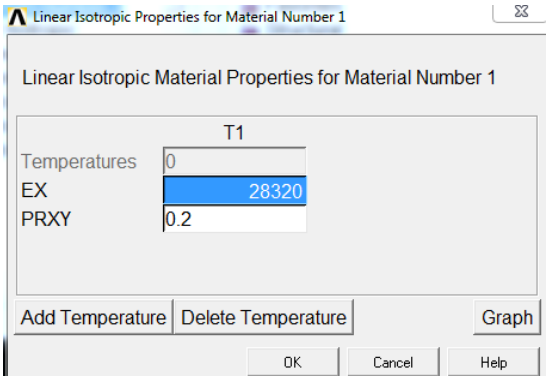
C20 Beton için



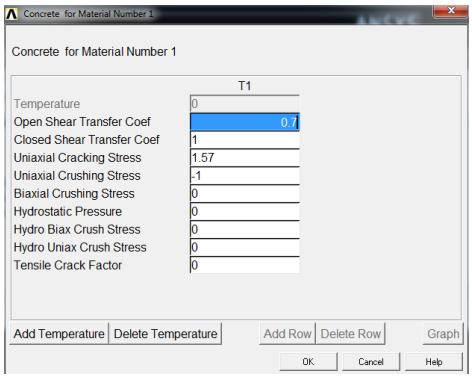
C34 Beton için



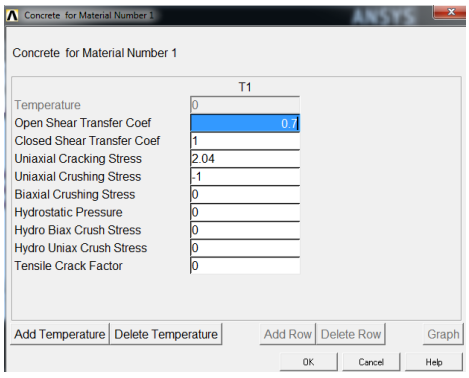
C20 Beton için



C34 Beton için

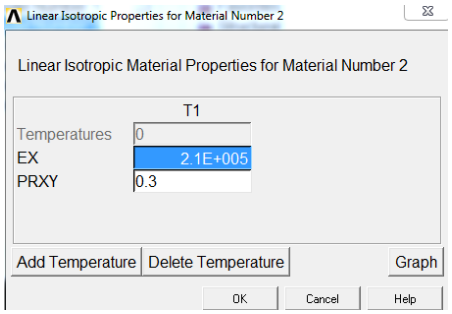


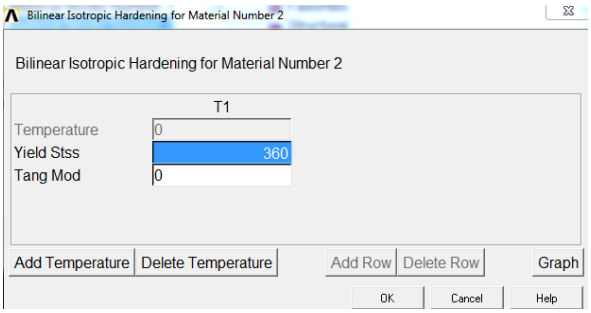
C20 Beton için



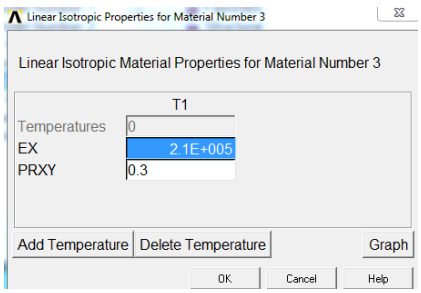
C34 Beton için

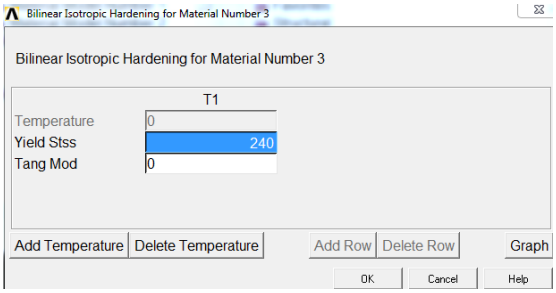
Boyuna donatı için girilen teknik değerler:



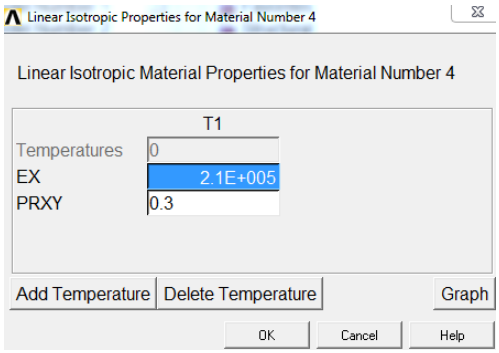


Enine donatı malzeme özellikleri için girilen teknik değerler:

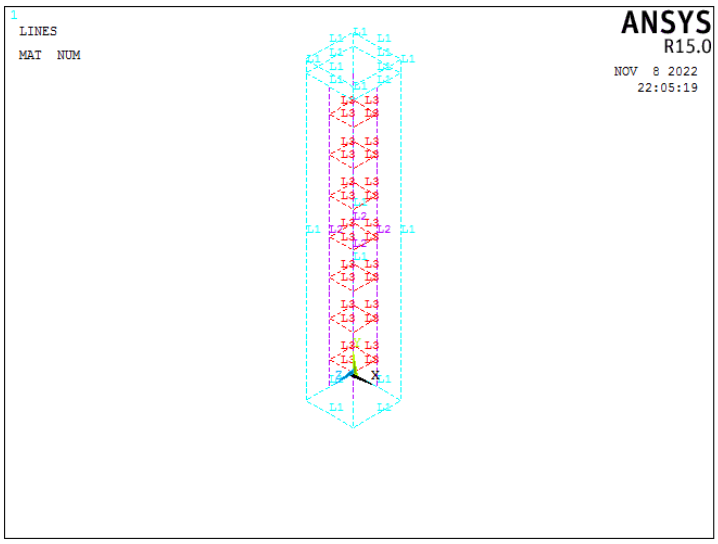




Çelik levha malzeme özellikleri için girilen değerler;

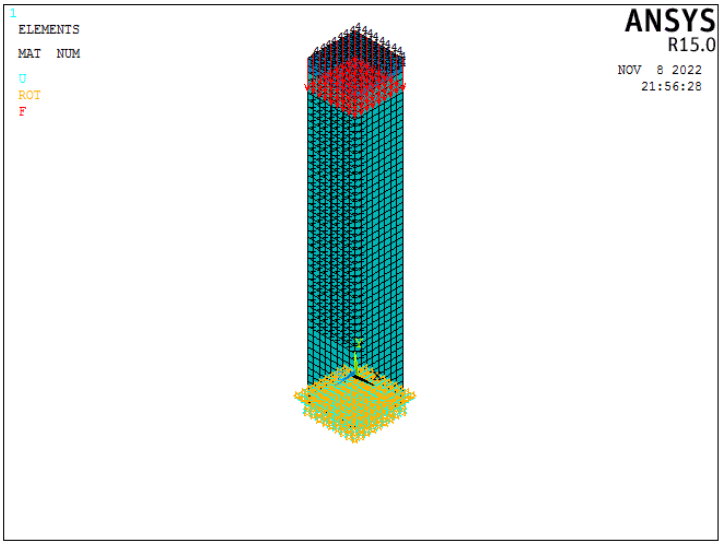


Malzeme özellikleri girildikten sonra eleman tipi malzeme ve kesit özelliklerinin atanması yapılmıştır. Eleman atamaları tamamlandığında ise meshlere ayırma işlemi yapılmıştır. Fakat mesh ayırma işleminde beton ve donatının arasında tam aderansın olduğu yani beton ve donatıya ait şekil değiştirme oranlarının aynı olduğu varsayılmaktadır. Bunu sağlamak içinde beton ve donatının düğüm noktalarının aynı yerlere denk gelmesi gerekmektedir. Bu sebeple beton, donatı ve levhalar 25 mm 'lik meshlere ayrılmıştır. Meshlere ayrılmış model şekil 4 de gösterilmiştir. (Ahmet Can Altunışık, Murat Günaydın, Ali Fuat Genç, Fatih Yesevi Okur, İnşaat Mühendisliğinde Ansys Uygulamaları Kitabı.)



Şekil 4. Meshlere bölünmüş model

Kolon alt yüzeyindeki 81 adet nokta Ux, Uy, Uz, Rotx, Roty ve Rotz olmak üzere 6 yönden tutularak mesnetlenmiştir. Ayrıca kolonun üstündeki 81 noktanın her birine -2000 N luk düşey yük verilerek toplamda 162000 N düşey yük verilmiştir. Analiz tamamlanana kadar her adımda aynı şekilde bu yükleme devam etmiştir. Tüm analizler sadece düşey yükler altında yapılmıştır.(Şekil 5)



Şekil 5. Düşey yükler uygulanmış ve mesnetlenmiş model

Çelik levha ile güçlendirilen kolonlarda aynı teknik özelikler girilerek modellenmiştir. Sadece kolonların levhalar ile temas yüzeylerine yapışma etkisini yansıtmak için sürtünme katsayısı uygulanmıştır.

BULGULAR VE TARTIŞMA

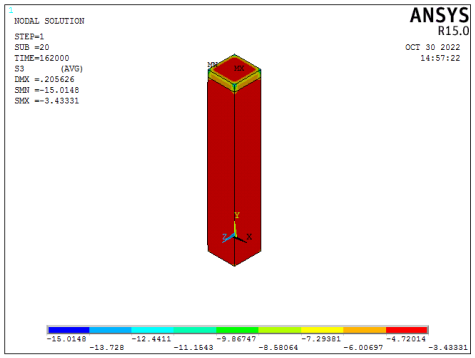
Çalışmada 200 x 200 x1200 mm ebatlarında 6 adet kolonun analizleri yapılmıştır. Bu elemanlar için C20 ve C34 sınıfında beton kullanılmıştır. C20 sınıfı beton kullanılan elemanlar 2 mm kalınlığında ve 50 mm uzunluğundaki levhalar ile tüm yüzeylerinden 200 mm ve 100 mm aralıklarla kaplanmıştır. C34 sınıfı beton kullanılan kolon elemanlarda da aynı boyut ve aralıklarla çelik levha uygulanmıştır. Kolonların levhalar ile temas yüzeylerine yapışma etkisini yansıtmak için sürtünme katsayısı uygulanmıştır.

Çalışmada kullanılan 6 tip kolon aşağıdaki gösterildiği gibi isimlendirilmiştir.

İSİM	AÇIKLAMA
C20-R	C20 beton dayanımlı referans kolon
A2H	C20 beton dayanımlı 200X50X2 mm levhalar 200 mm aralıklar ile yerleştirilen kolon
A2S	C20 beton dayanımlı 200X50X2 mm levhalar 100 mm aralıklar ile yerleştirilen kolon
C34-R	C34 beton dayanımlı referans kolon
B2H	C34 beton dayanımlı 200X50X2 mm levhalar 200 mm aralıklar ile yerleştirilen kolon
B2S	C34 beton dayanımlı 200X50X2 mm levhalar 100 mm aralıklar ile yerleştirilen kolon

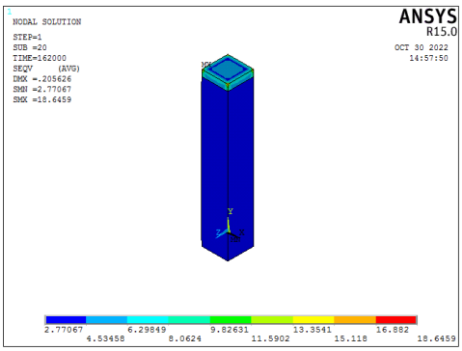
C20 referans beton ile yapılan analiz bulguları (C20-R):

C20 referans kolona her adım da yapılan düşey yüklemeler sonucunda betonda oluşan eksenel ve Von Mises gerilme değerleri aşağıda gösterilmektedir.



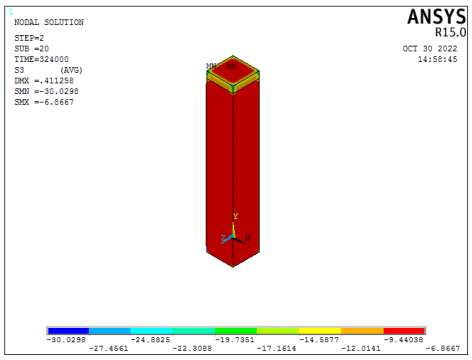
1.adım:C20-R Elemanı – Eksenel gerilme

(Şekil 6)



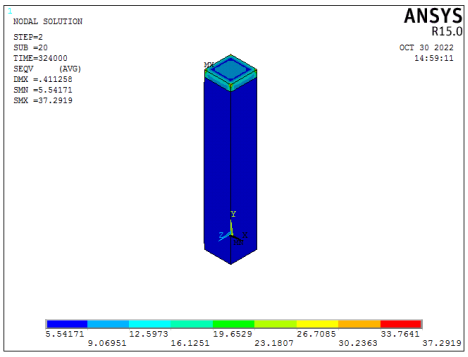
1.adım: C20-R Elemanı – Von mises gerilme

(Şekil 7)



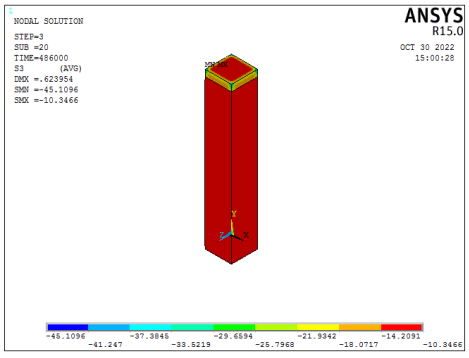
2.adım:C20-R Elemanı – Eksenel gerilme

(Şekil 8)



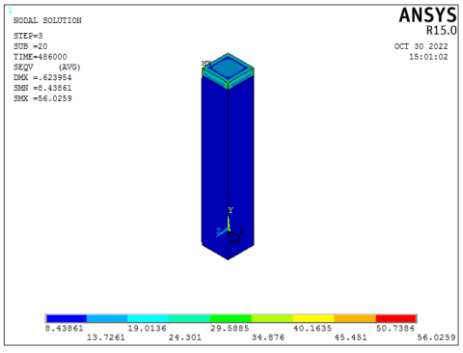
2.adım: C20-R Elemanı – Von mises gerilme

(Şekil 9)



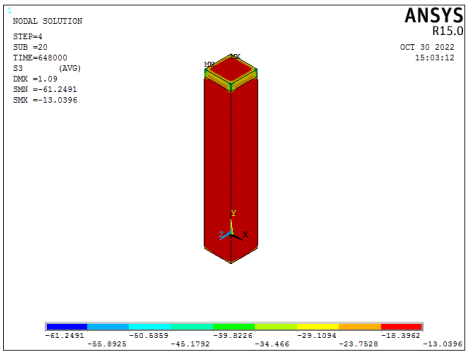
3.adım:C20-R Elemanı – Eksenel gerilme

(Şekil 10)



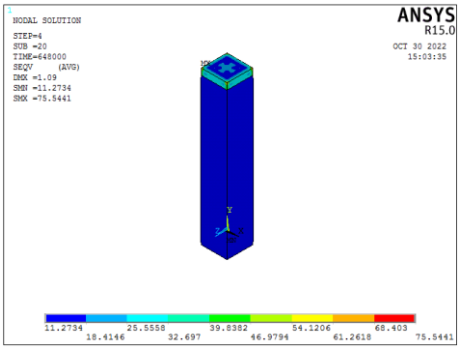
3.adım: C20-R Elemanı – Von mises gerilme

(Şekil 11)



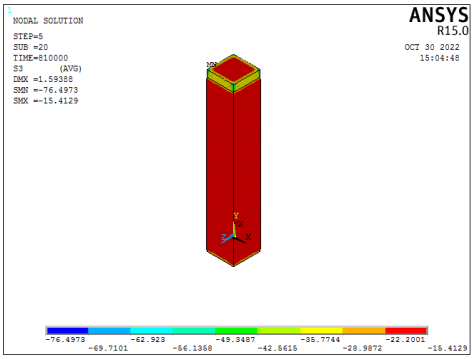
4.adım:C20-R Elemanı – Eksenel gerilme

(Şekil 12)



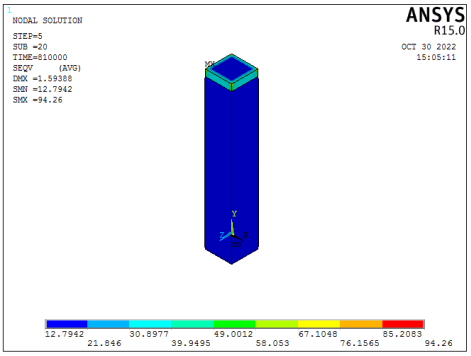
4.adım: C20-R Elemanı – Von mises gerilme

(Şekil 13)



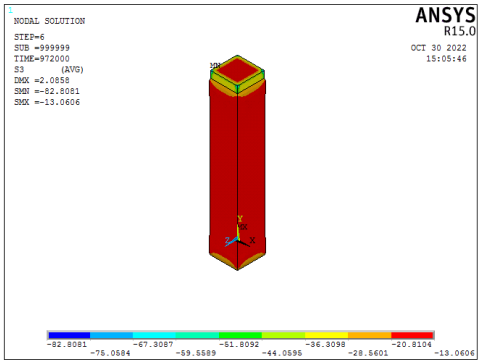
5.adım:C20-R Elemanı – Eksenel gerilme

(Şekil 14)



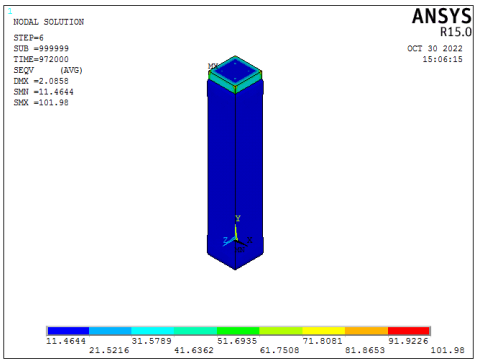
5.adım: C20-R Elemanı – Von mises gerilme

(Şekil 15)



6.adım:C20-R Elemanı – Eksenel gerilme

(Şekil 16)

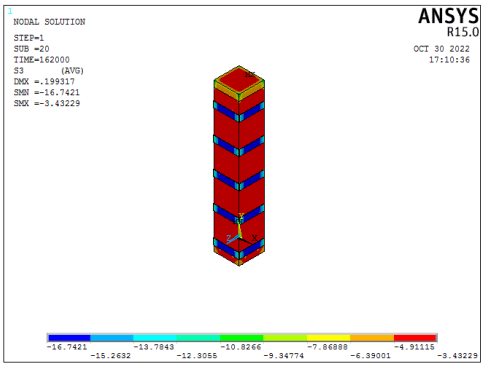


6.adım: C20-R Elemanı – Von mises gerilme

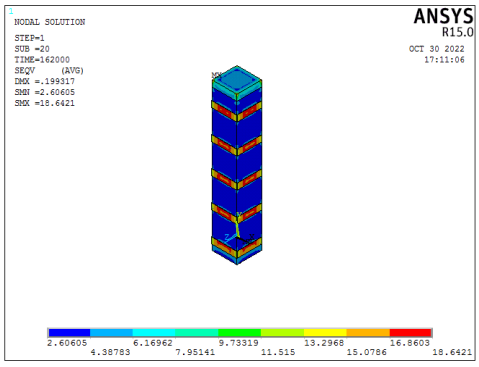
(Şekil 17)

C20 betonda 200 mm ara ile çelik levha kaplanmış kolonda yapılan analiz bulguları (A2H):

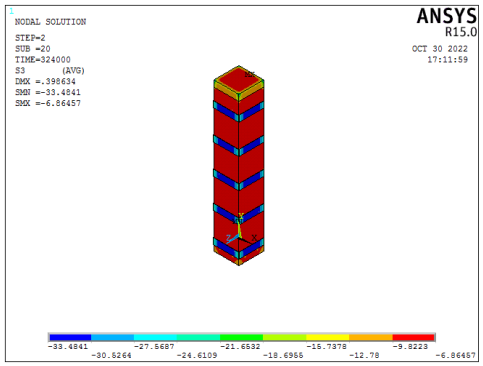
C20 betonda 2 mm kalınlığında ve 50 mm uzunluğunda çelik levhalar, 200 mm aralıklarla kolonun dört kenarına yerleştirilmiş ve bu modele göre analizler yapılmıştır. Yapılan analizler sonucunda elde edilen eksenel ve Von Mises gerilme değerleri aşağıda gösterilmektedir.



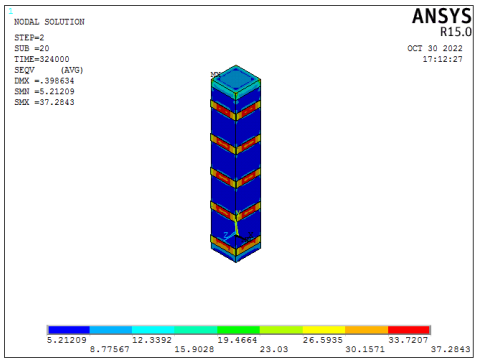
1.adım:A2H Elemanı – Eksenel gerilme (Şekil 18)



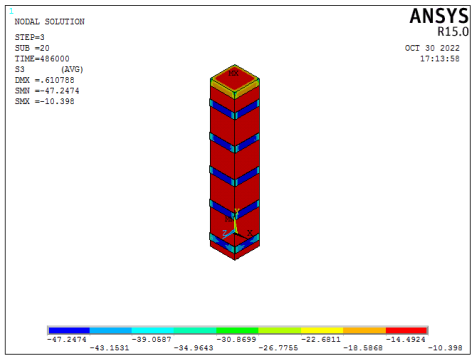
1.adım: A2H Elemanı – Von mises gerilme (Şekil 19)



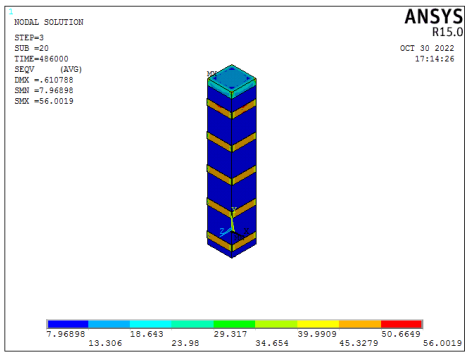
2.adım:A2H Elemanı – Eksenel gerilme (Şekil 20)



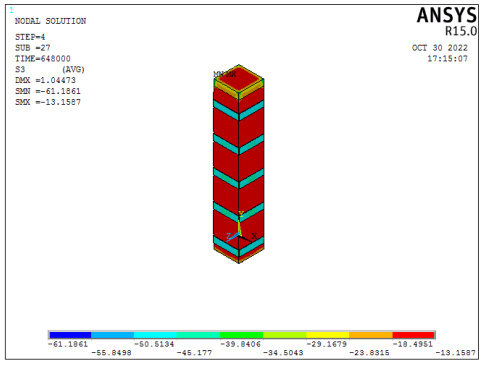
2.adım: A2H Elemanı – Von mises gerilme (Şekil 21)



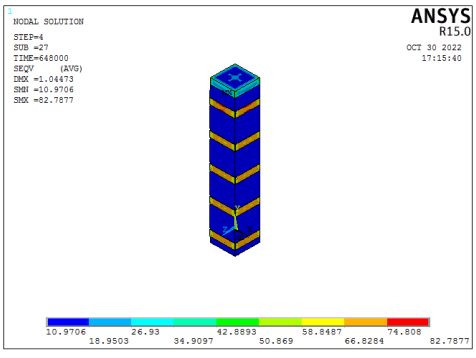
3.adım:A2H Elemanı – Eksenel gerilme (Şekil 22)



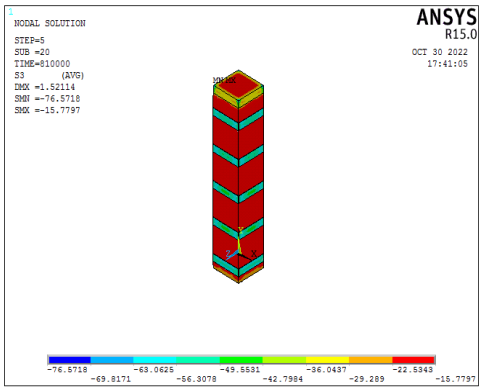
3.adım: A2H Elemanı – Von mises gerilme (Şekil 23)



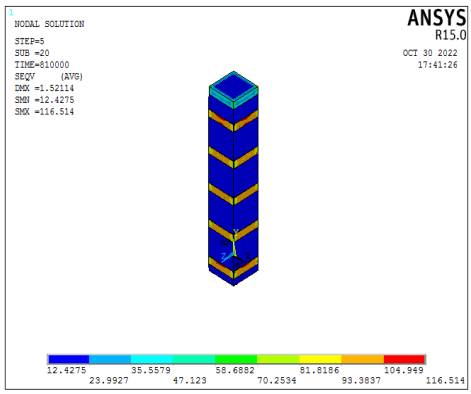
4.adım:A2H Elemanı – Eksenel gerilme (Şekil 24)



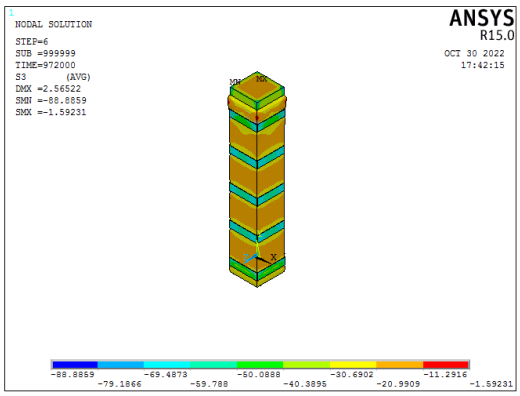
4.adım: A2H Elemanı – Von mises gerilme (Şekil 25)



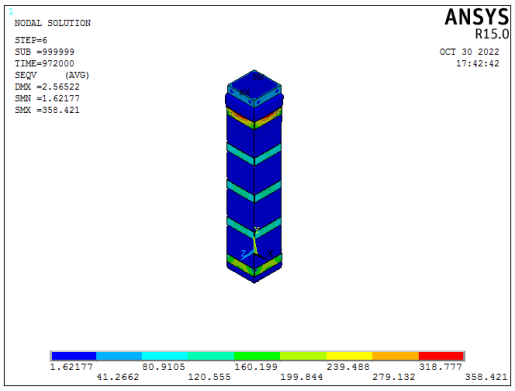
5.adım:A2H Elemanı – Eksenel gerilme
(Şekil 26)



5.adım: A2H Elemanı – Von mises gerilme
(Şekil 27)



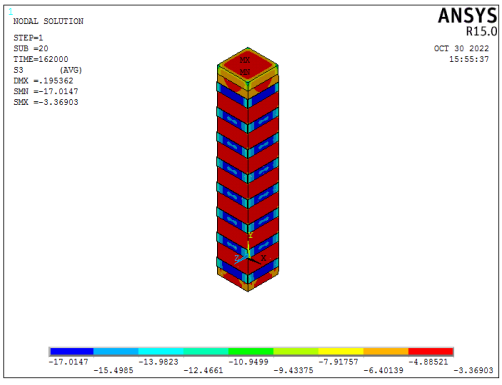
6.adım:A2H Elemanı – Eksenel gerilme
(Şekil 28)



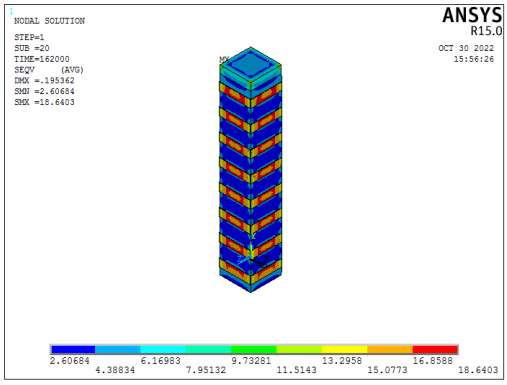
6.adım: A2H Elemanı – Von mises gerilme
(Şekil 29)

C20 betonda 100 mm ara ile çelik levha kaplanmış kolonda yapılan analiz bulguları (A2S):

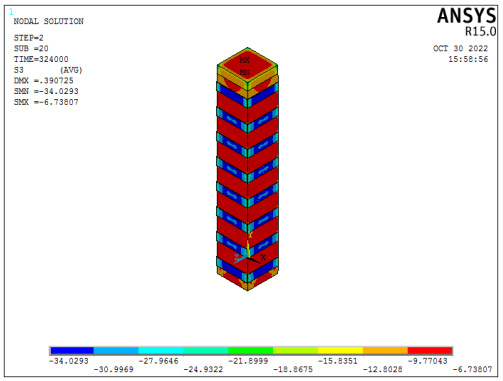
C20 betonda 2 mm kalınlığında ve 50 mm uzunluğunda çelik levhalar, 100 mm aralıklarla kolonun dört kenarına yerleştirilmiş ve bu modele göre analizler yapılmıştır. Yapılan analizler sonucunda elde edilen eksenel ve Von Mises gerilme değerleri aşağıda gösterilmektedir.



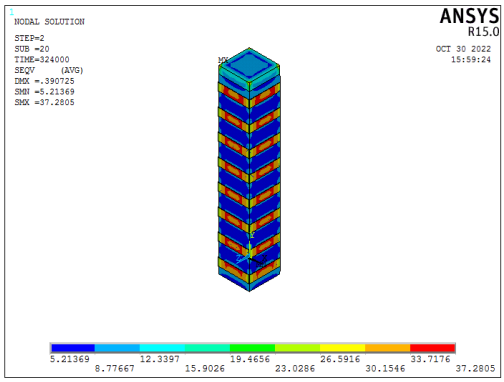
1.adım:A2S Elemanı – Eksenel gerilme
(Şekil 30)



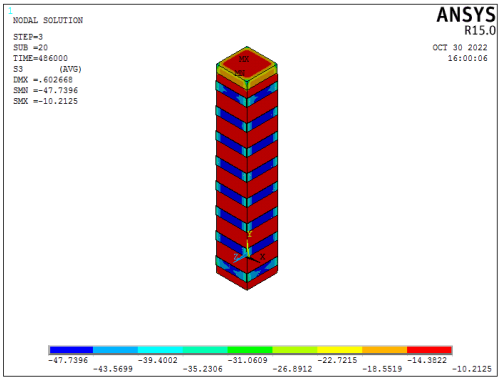
1.adım: A2S Elemanı – Von mises gerilme
(Şekil 31)



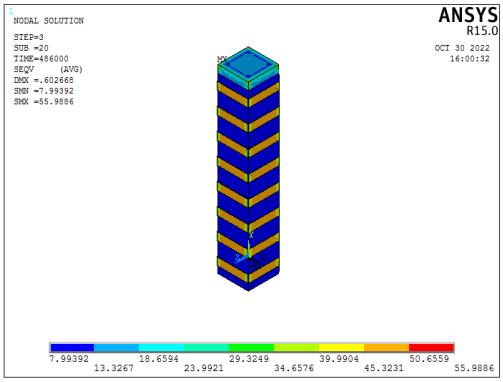
2.adım:A2S Elemanı – Eksenel gerilme
(Şekil 32)



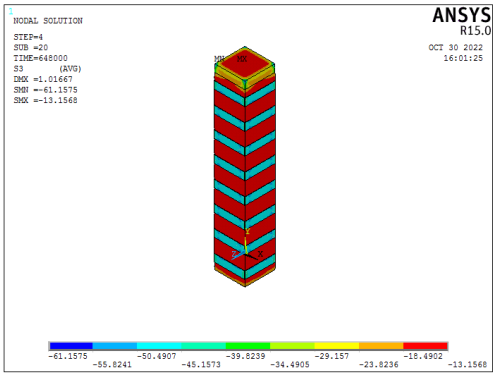
2.adım: A2S Elemanı – Von mises gerilme
(Şekil 33)



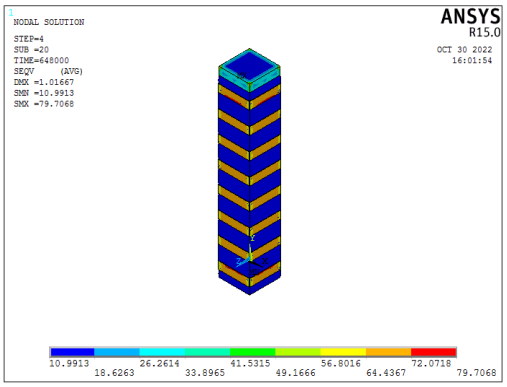
3.adım:A2S Elemanı – Eksenel gerilme
(Şekil 34)



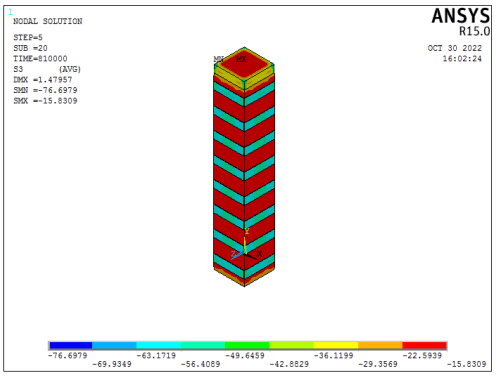
3.adım: A2S Elemanı – Von mises gerilme
(Şekil 35)



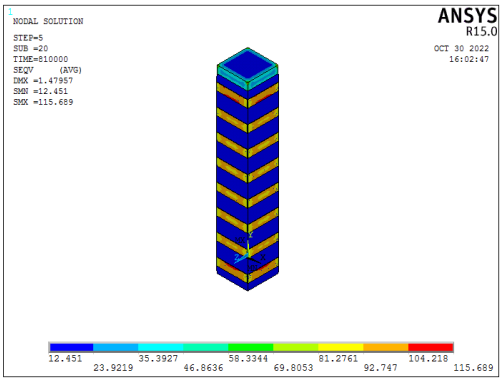
4.adım:A2S Elemanı – Eksenel gerilme
(Şekil 36)



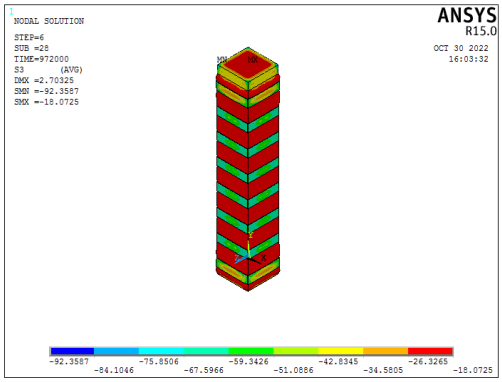
4.adım: A2S Elemanı – Von mises gerilme
(Şekil 37)



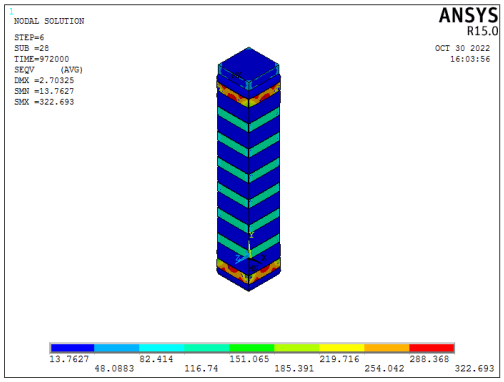
5.adım:A2S Elemanı – Eksenel gerilme
(Şekil 38)



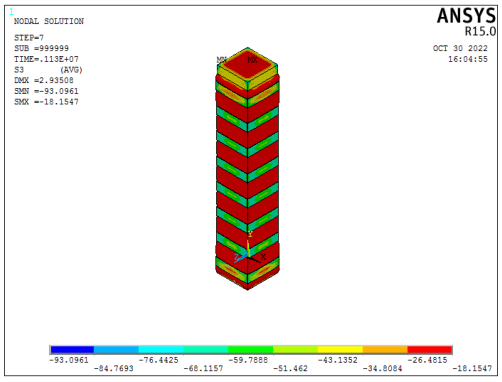
5.adım: A2S Elemanı – Von mises gerilme
(Şekil 39)



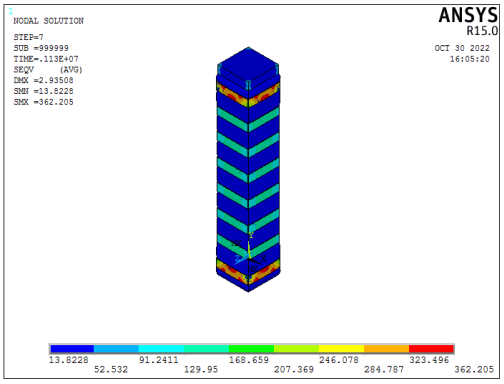
6.adım:A2S Elemanı – Eksenel gerilme
(Şekil 40)



6.adım: A2S Elemanı – Von mises gerilme
(Şekil 41)



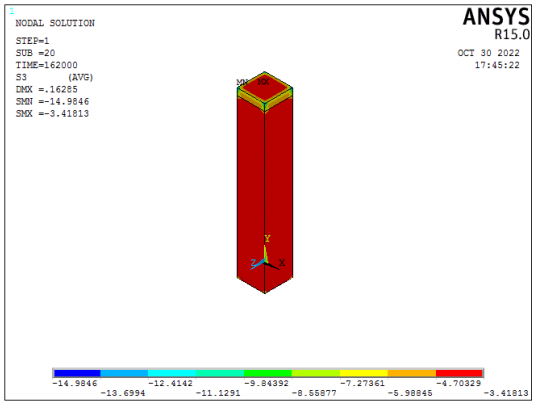
7.adım:A2S Elemanı – Eksenel gerilme
(Şekil 42)



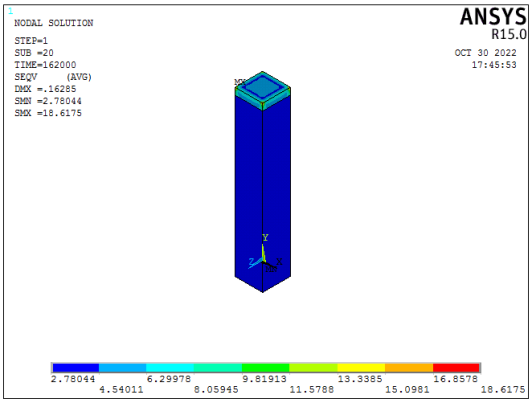
7.adım: A2S Elemanı – Von mises gerilme
(Şekil 43)

C34 referans beton ile yapılan analiz bulguları (C34-R):

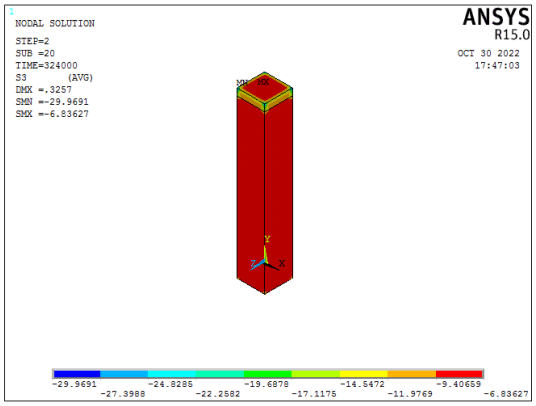
C34 referans kolona her adımda yapılan düşey yüklemeler sonucunda betonda oluşan eksenel ve Von Mises gerilme değerleri aşağıda gösterilmektedir.



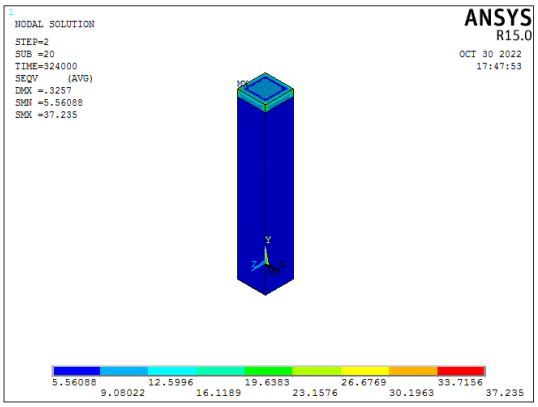
1.adım:C34-R Elemanı – Eksenel gerilme
(Şekil 44)



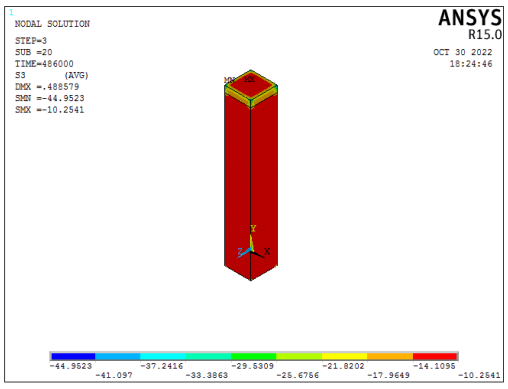
1.adım: 34-R Elemanı – Von mises gerilme
(Şekil 45)



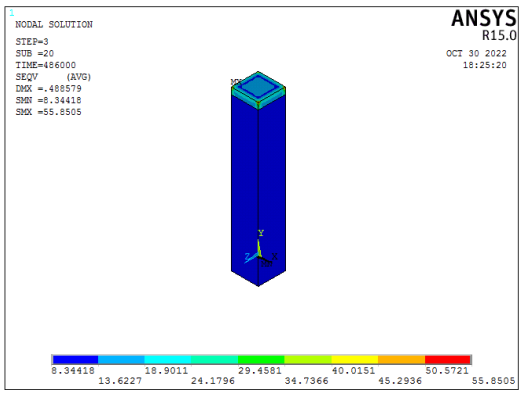
2.adım:C34-R Elemanı – Eksenel gerilme
(Şekil 46)



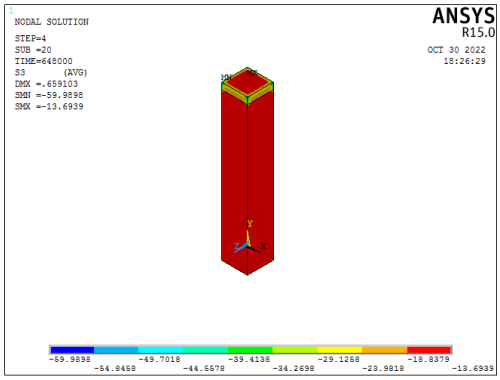
2.adım: 34-R Elemanı – Von mises gerilme
(Şekil 47)



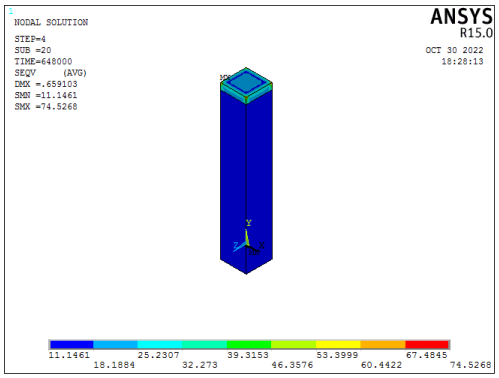
3.adım:C34-R Elemanı – Eksenel gerilme
(Şekil 48)



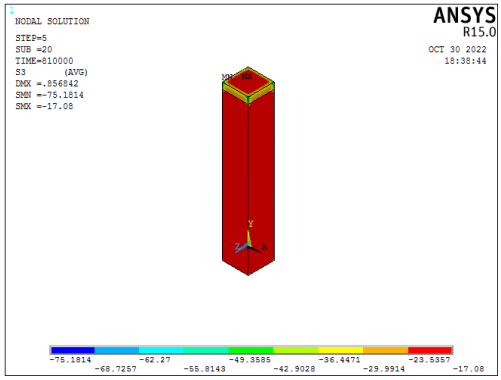
3.adım: 34-R Elemanı – Von mises gerilme
(Şekil 49)



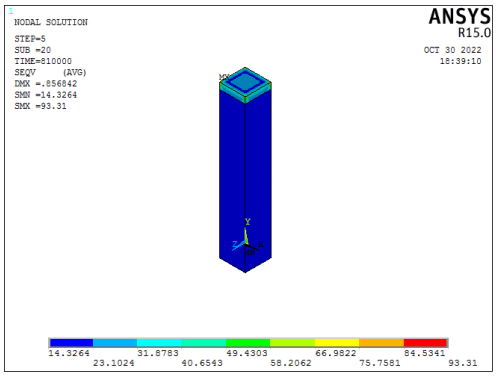
4.adım:C34-R Elemanı – Eksenel gerilme (Şekil 50)



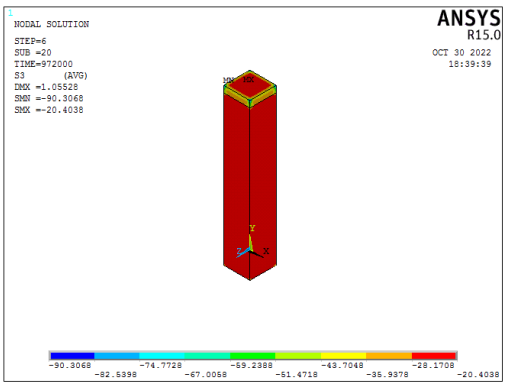
4.adım: 34-R Elemanı – Von mises gerilme (Şekil 51)



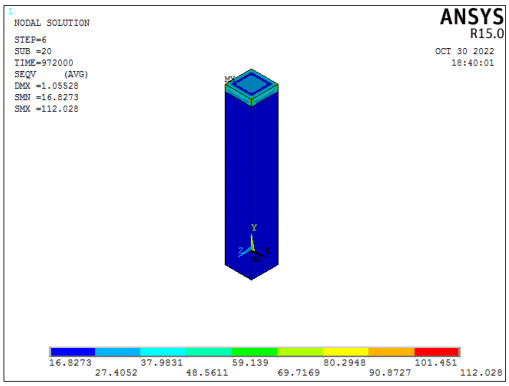
5.adım:C34-R Elemanı – Eksenel gerilme (Şekil 52)



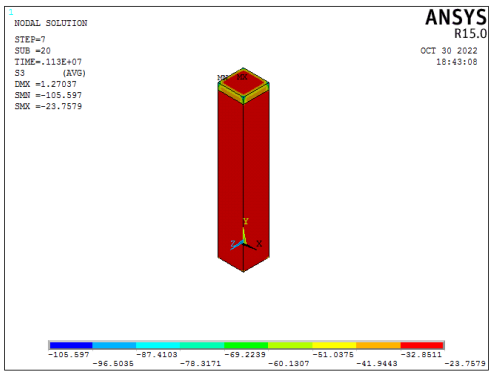
5.adım: 34-R Elemanı – Von mises gerilme (Şekil 53)



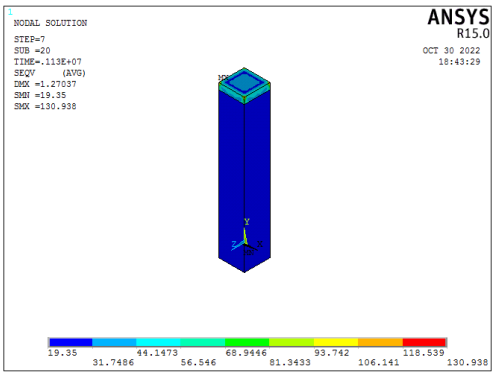
6.adım:C34-R Elemanı – Eksenel gerilme (Şekil 54)



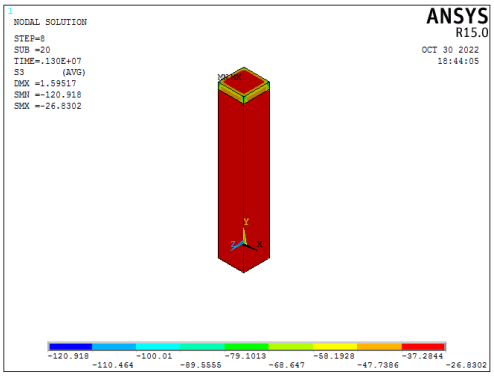
6.adım: 34-R Elemanı – Von mises gerilme (Şekil 55)



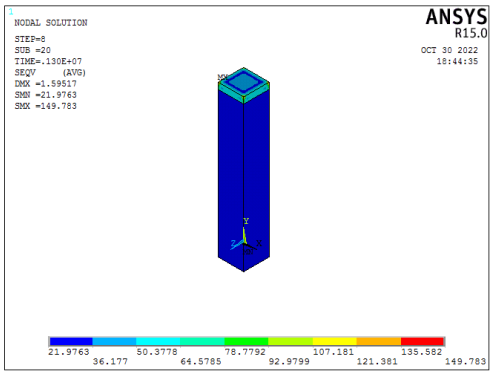
7.adım:C34-R Elemanı – Eksenel gerilme (Şekil 56)



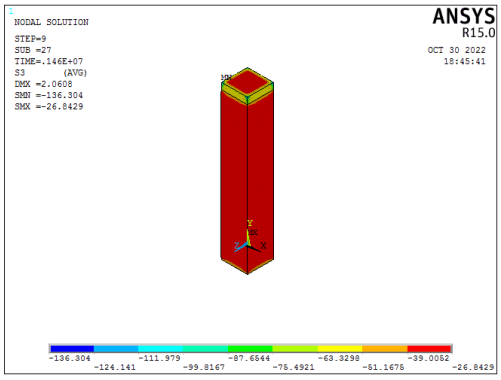
7.adım: 34-R Elemanı – Von mises gerilme (Şekil 57)



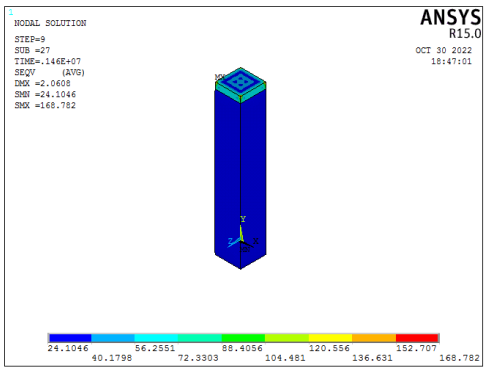
8.adım:C34-R Elemanı – Eksenel gerilme (Şekil 58)



8.adım: 34-R Elemanı – Von mises gerilme (Şekil 59)



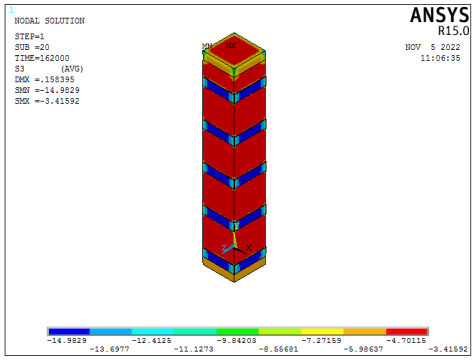
9.adım:C34-R Elemanı – Eksenel gerilme (Şekil 60)



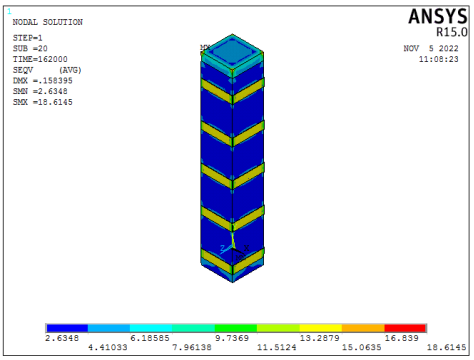
9.adım: 34-R Elemanı – Von mises gerilme (Şekil 61)

C34 betonda 200 mm ara ile çelik levha kaplanmış kolonda yapılan analiz bulguları (B2H) :

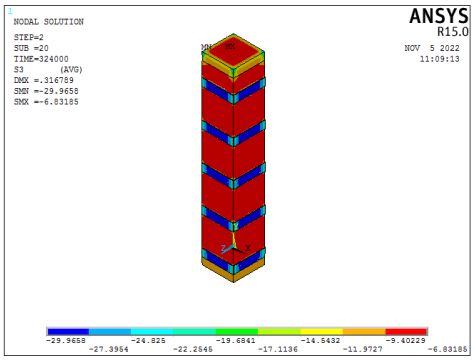
C34 betonda 2 mm kalınlığında ve 50 mm uzunluğunda çelik levhalar, 200 mm aralıklarla kolonun dört kenarına yerleştirilmiş ve bu modele göre analizler yapılmıştır. Yapılan analizler sonucunda elde edilen eksenel ve Von Mises gerilme değerleri aşağıda gösterilmektedir.



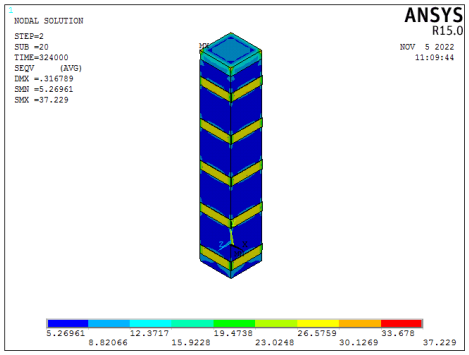
1.adım:B2H Elemanı – Eksenel gerilme (Şekil 62)



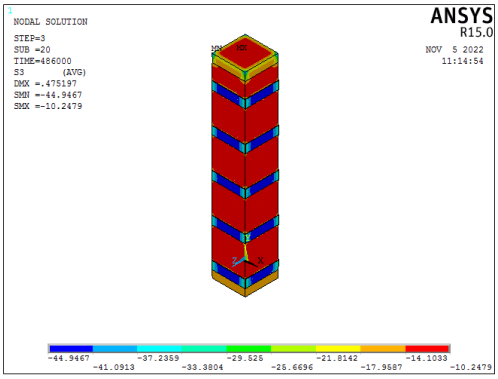
1.adım: B2H Elemanı – Von mises gerilme (Şekil 63)



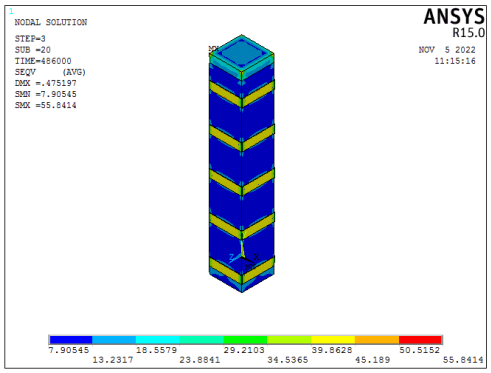
2.adım:B2H Elemanı – Eksenel gerilme (Şekil 64)



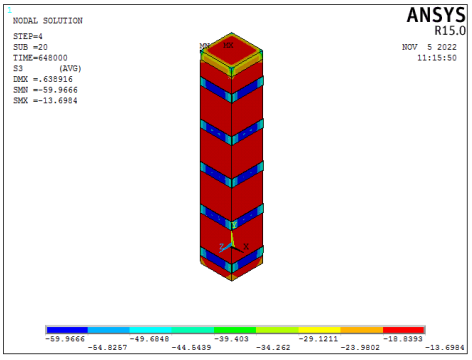
2.adım: B2H Elemanı – Von mises gerilme (Şekil 65)



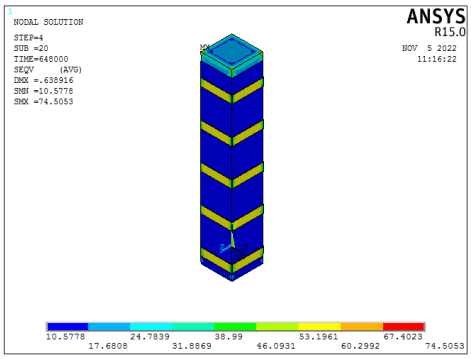
3.adım:B2H Elemanı – Eksenel gerilme (Şekil 66)



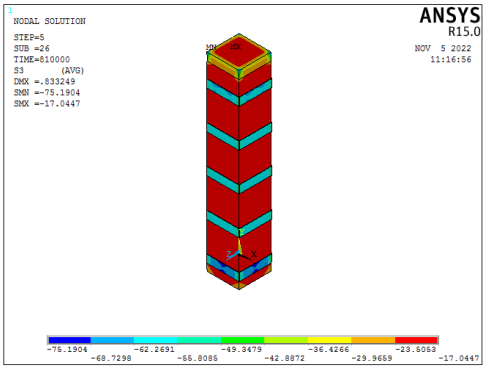
3.adım: B2H Elemanı – Von mises gerilme (Şekil 67)



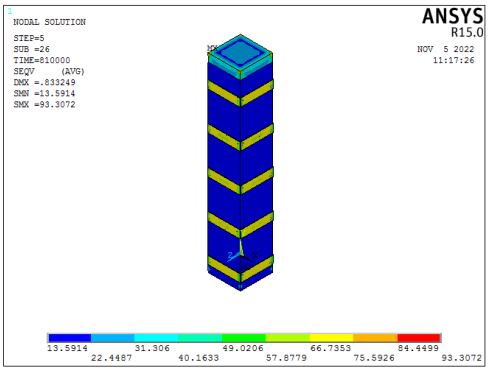
4.adım:B2H Elemanı – Eksenel gerilme (Şekil 68)



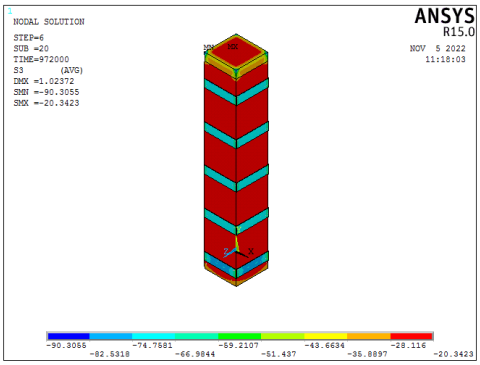
4.adım: B2H Elemanı – Von mises gerilme (Şekil 69)



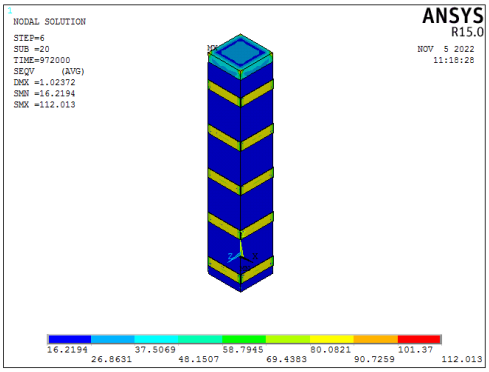
5.adım:B2H Elemanı – Eksenel gerilme (Şekil 70)



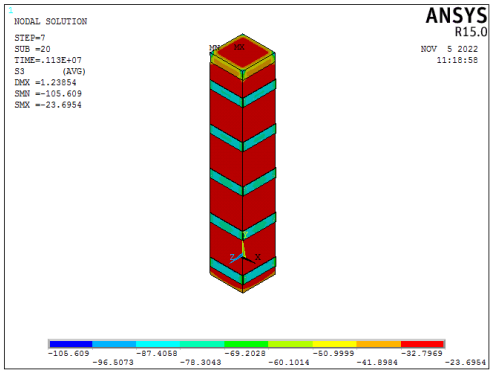
5.adım: B2H Elemanı – Von mises gerilme (Şekil 71)



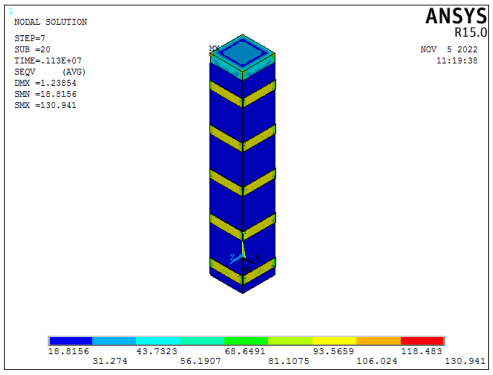
6.adım:B2H Elemanı – Eksenel gerilme (Şekil 72)



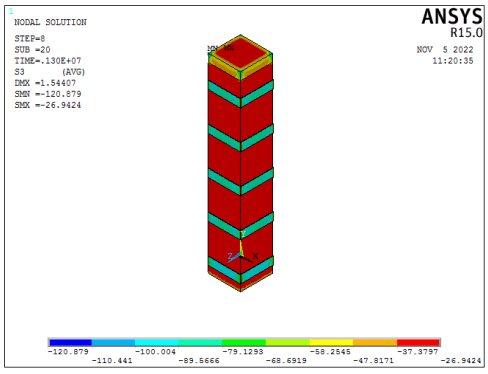
6.adım: B2H Elemanı – Von mises gerilme (Şekil 73)



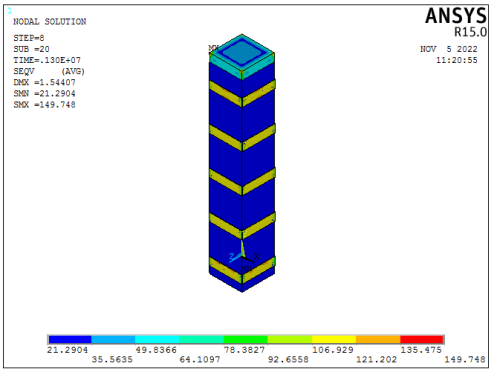
7.adım:B2H Elemanı – Eksenel gerilme (Şekil 74)



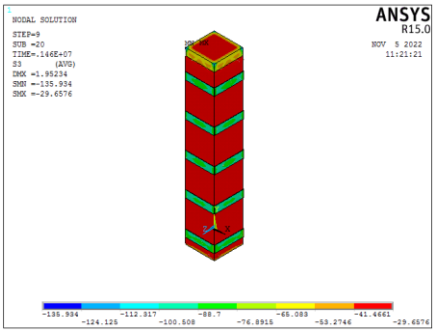
7.adım: B2H Elemanı – Von mises gerilme (Şekil 75)



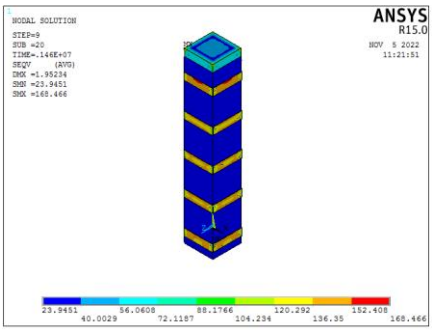
8.adım:B2H Elemanı – Eksenel gerilme (Şekil 76)



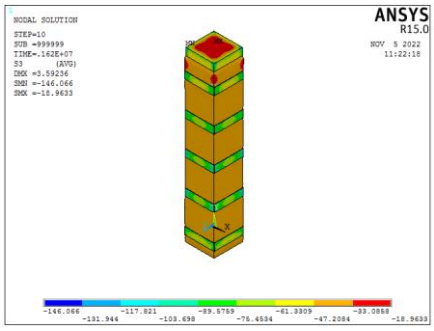
8.adım: B2H Elemanı – Von mises gerilme (Şekil 77)



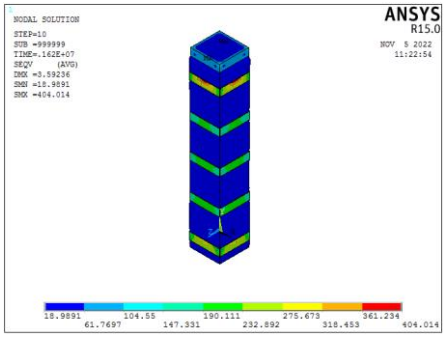
9.adım:B2H Elemanı – Eksenel gerilme
(Şekil 78)



9.adım: B2H Elemanı – Von mises gerilme
(Şekil 79)



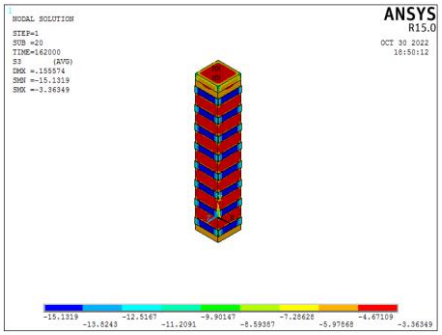
10.adım:B2H Elemanı – Eksenel gerilme
(Şekil 80)



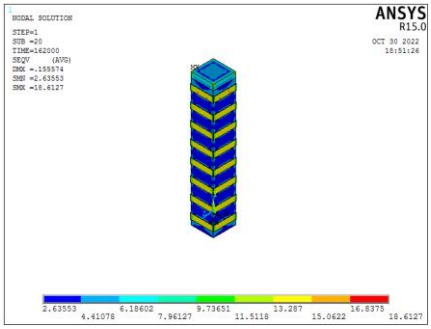
10.adım: B2H Elemanı – Von mises gerilme
(Şekil 81)

C34 betonda 100 mm ara ile çelik levha kaplanmış kolonda yapılan analiz bulguları (B2S) :

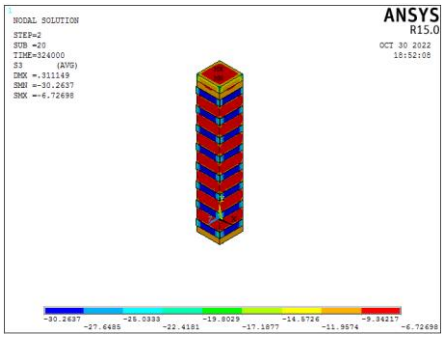
C34 betonda 2 mm kalınlığında ve 50 mm uzunluğunda çelik levhalar, 100 mm aralıklarla kolonun dört kenarına yerleştirilmiş ve bu modele göre analizler yapılmıştır. Yapılan analizler sonucunda elde edilen eksenel ve Von Mises gerilme değerleri aşağıda gösterilmektedir.



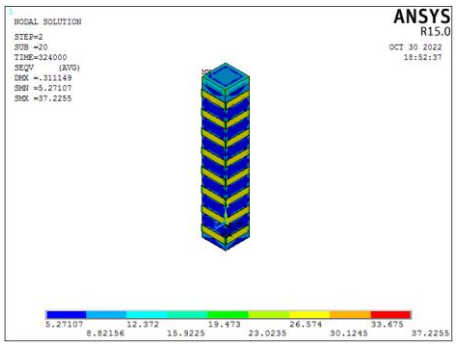
1.adım:B2S Elemanı – Eksenel gerilme
(Şekil 82)



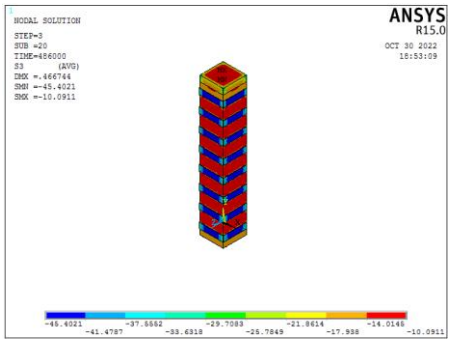
1.adım: B2S Elemanı – Von mises gerilme
(Şekil 83)



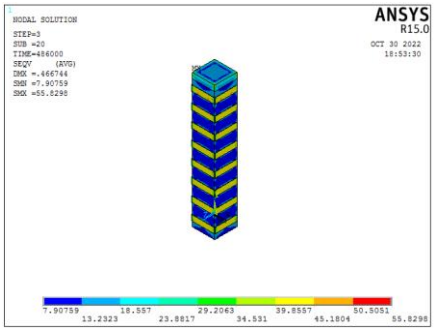
2.adım:B2S Elemanı – Eksenel gerilme (Şekil 84)



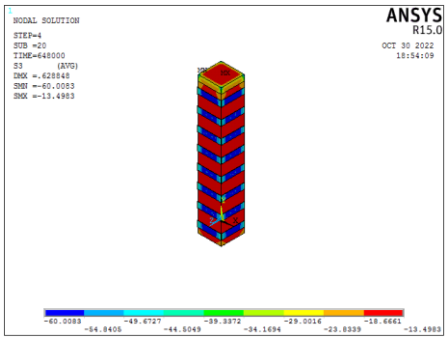
2.adım: B2S Elemanı – Von mises gerilme (Şekil 85)



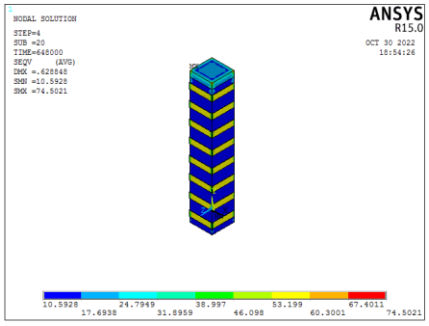
3.adım:B2S Elemanı – Eksenel gerilme (Şekil 86)



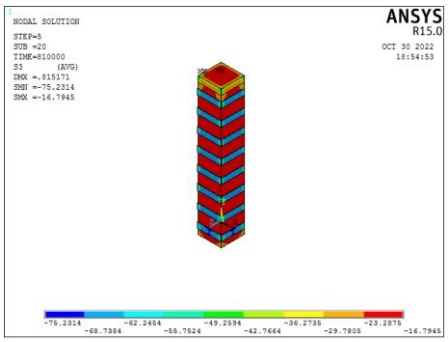
3.adım: B2S Elemanı – Von mises gerilme (Şekil 87)



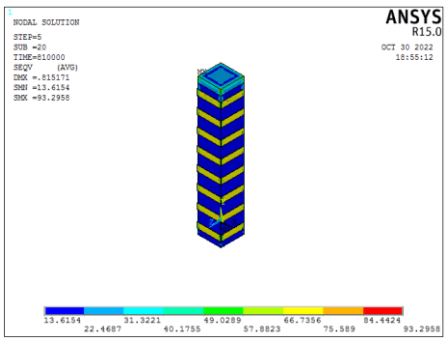
4.adım:B2S Elemanı – Eksenel gerilme (Şekil 88)



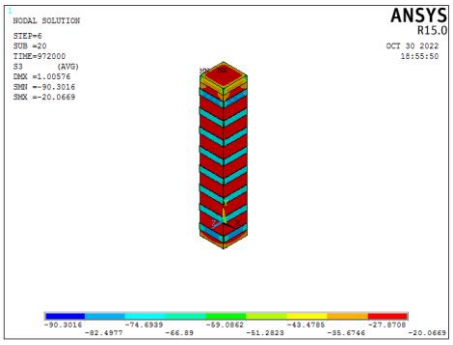
4.adım: B2S Elemanı – Von mises gerilme (Şekil 89)



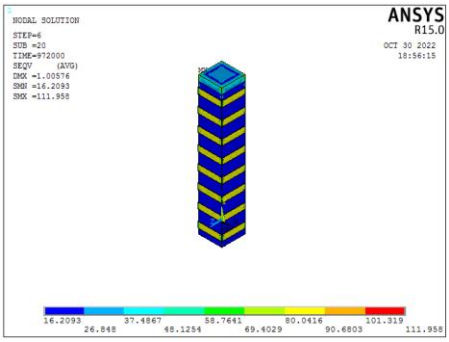
5.adım:B2S Elemanı – Eksenel gerilme (Şekil 90)



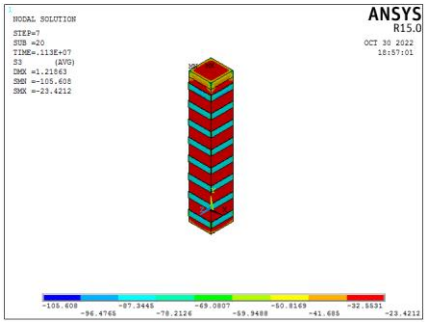
5.adım: B2S Elemanı – Von mises gerilme (Şekil 91)



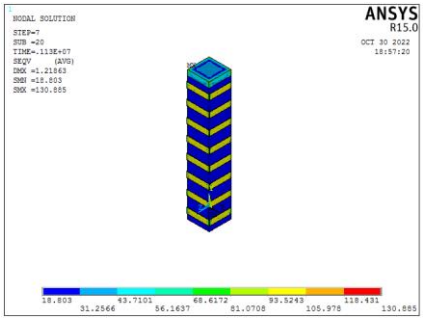
6.adım:B2S Elemanı – Eksenel gerilme (Şekil 92)



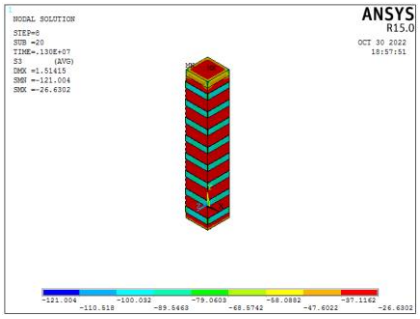
6.adım: B2S Elemanı – Von mises gerilme (Şekil 93)



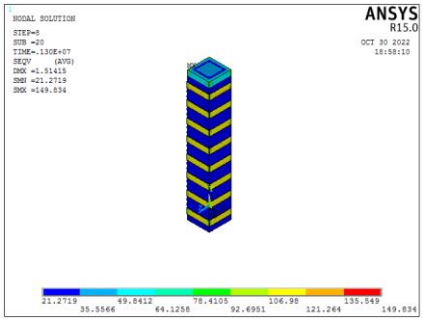
7.adım:B2S Elemanı – Eksenel gerilme (Şekil 94)



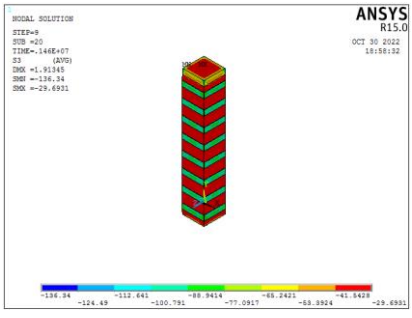
7.adım: B2S Elemanı – Von mises gerilme (Şekil 95)



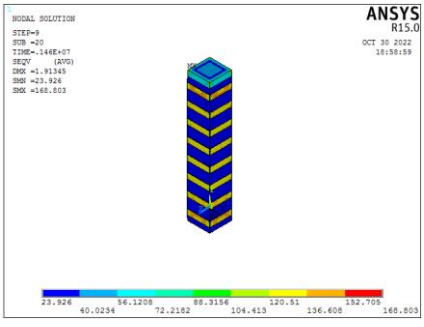
8.adım:B2S Elemanı – Eksenel gerilme (Şekil 96)



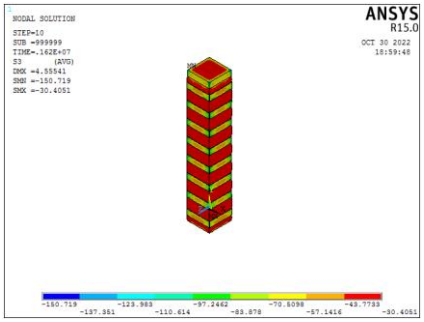
8.adım: B2S Elemanı – Von mises gerilme (Şekil 97)



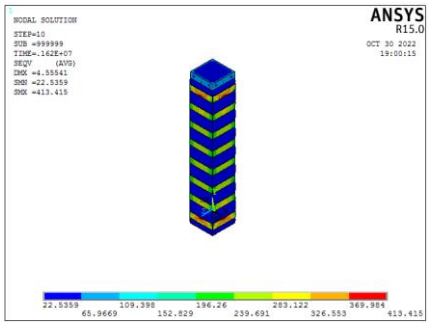
9.adım:B2S Elemanı – Eksenel gerilme (Şekil 98)



9.adım: B2S Elemanı – Von mises gerilme (Şekil 99)



10.adım:B2S Elemanı – Eksenel gerilme
(Şekil 100)



10.adım: B2S Elemanı – Von mises gerilme
(Şekil 101)

SONUÇ VE ÖNERİLER

Her adım için yapılan analizler sonucunda kolonlarda oluşan yük ve deplasman değerleri aşağıdaki çizilgelerde (Çizelge 1-2) gösterilmiştir.

Çizelge 1. C20 sınıfı elemanların yük ve deplasman değerleri

C20-R Elemanı		A2S Elemanı		A2H Elemanı	
YÜK (kN)	DEPLASMAN(mm)	YÜK (kN)	DEPLASMAN(mm)	YÜK (kN)	DEPLASMAN(mm)
0	0,000000	0	0,000000	0	0,000000
162	0,205626	162	0,195362	162	0,199317
324	0,411258	324	0,390725	324	0,398664
486	0,623954	486	0,602668	486	0,610788
648	1,090000	648	1,016670	648	1,044730
810	1,593880	810	1,479570	810	1,521140
875,205	2,085800	972	2,703250	936,6	2,565220
		979,29	2,935080		

Çizelge 2. C34 sınıfı elemanların yük ve deplasman değerleri

C34-R Elemanı		B2S Elemanı		B2H Elemanı	
YÜK (kN)	DEPLASMAN(mm)	YÜK (kN)	DEPLASMAN(mm)	YÜK (kN)	DEPLASMAN(mm)
0	0,000000	0	0,000000	0	0,000000
162	0,162850	162	0,155574	162	0,158395
324	0,325700	324	0,311149	324	0,316789
486	0,488579	486	0,466744	486	0,475197
648	0,659103	648	0,628848	648	0,638916
810	0,856842	810	0,815171	810	0,833249
972	1,055280	972	1,005760	972	1,023720
1134	1,270370	1134	1,218630	1134	1,238540
1296	1,595170	1296	1,514150	1296	1,544070
1458	2,060800	1458	1,913450	1458	1,952340
		1583,34	4,555410	1546,69	3,592360

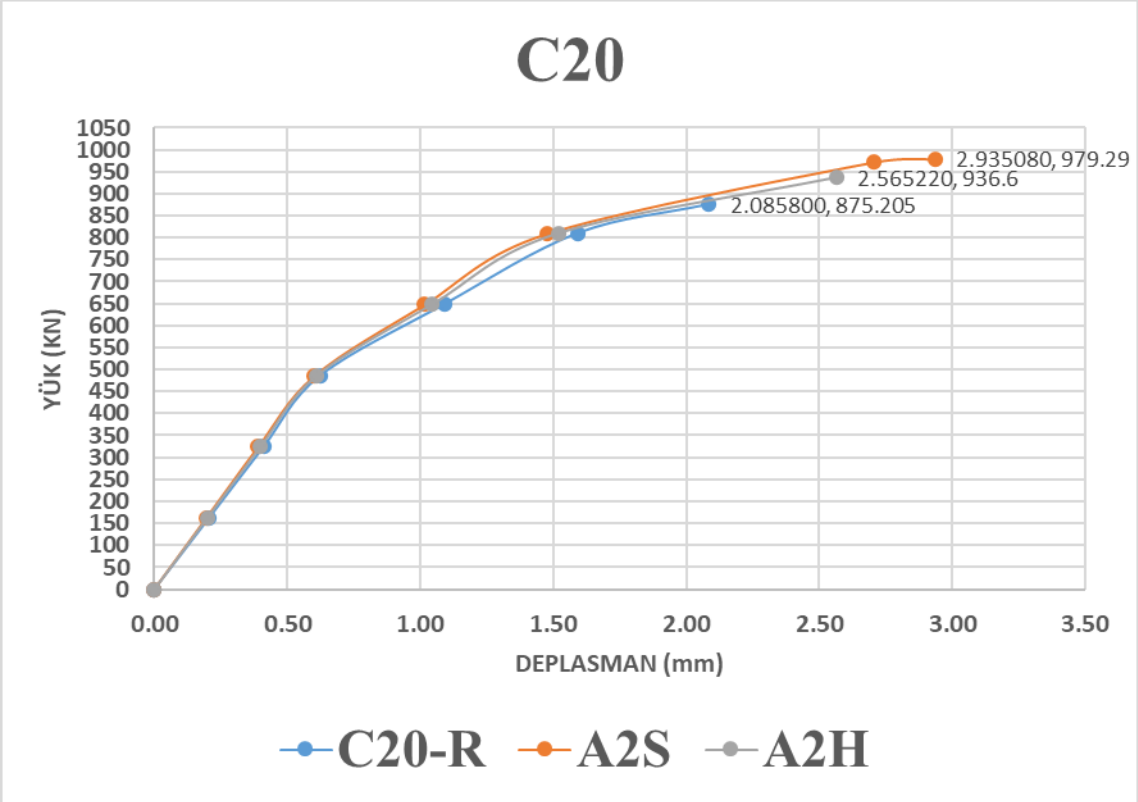
Yapılan analiz çalışmaları sonucunda deney elemanlarının ulaştığı maksimum yük kapasiteleri; C20-R elemanı için 875,205 kN, A2S elemanı için 979,29 kN, A2H elemanı için 936,6 kN, C34-R elemanı için 1458 kN, B2S elemanı için 1583,34 kN ve B2H elemanı için 1546,69 kN olarak elde edilmiştir. C20 sınıfı beton kullanılan

elemanlarda A2S elemanının göçme yükü en fazla çıkmıştır. C34 sınıfı beton kullanılan elemanlarda ise B2S kolonunun göçme yükü en fazla çıkmıştır.

A2S elemanının göçme anındaki değerinin referans elemanın göçme anındaki değerine oranı 1.12 kat daha fazla çıkmıştır. A2H elemanının göçme anındaki değeri referans elemanın göçme anındaki değerine oranı ise 1.07 kat daha fazla çıkmıştır. A2S elemanının göçme anındaki deplasman değeri referans elemanın göçme anındaki deplasman değerine oranı 1.4 kat daha fazla çıkmıştır. A2H elemanının göçme anındaki deplasman değeri referans elemanın göçme anındaki deplasman değerine oranı ise 1.23 kat daha fazla çıkmıştır. Buradan da anlaşılacağı üzere deplasman değeri en büyük çıkan A2S elemanı daha sünek davranmıştır.

B2S elemanının göçme anındaki değeri referans elemanın göçme anındaki değerine oranı 1.09 kat daha fazla çıkmıştır. B2H elemanının göçme anındaki değeri referans elemanın göçme anındaki değerine oranı ise 1.06 kat daha fazla çıkmıştır. B2S elemanının göçme anındaki deplasman değerini referans elemanın göçme anındaki deplasman değerine oranı 2.21 kat daha fazla çıkmıştır. B2H elemanının göçme anındaki deplasman değerini referans elemanın göçme anındaki deplasman değerine oranı ise 1.74 kat daha fazla çıkmıştır. Buradan da anlaşılacağı üzere deplasman değeri en büyük çıkan B2S elemanı daha sünek davranmıştır.

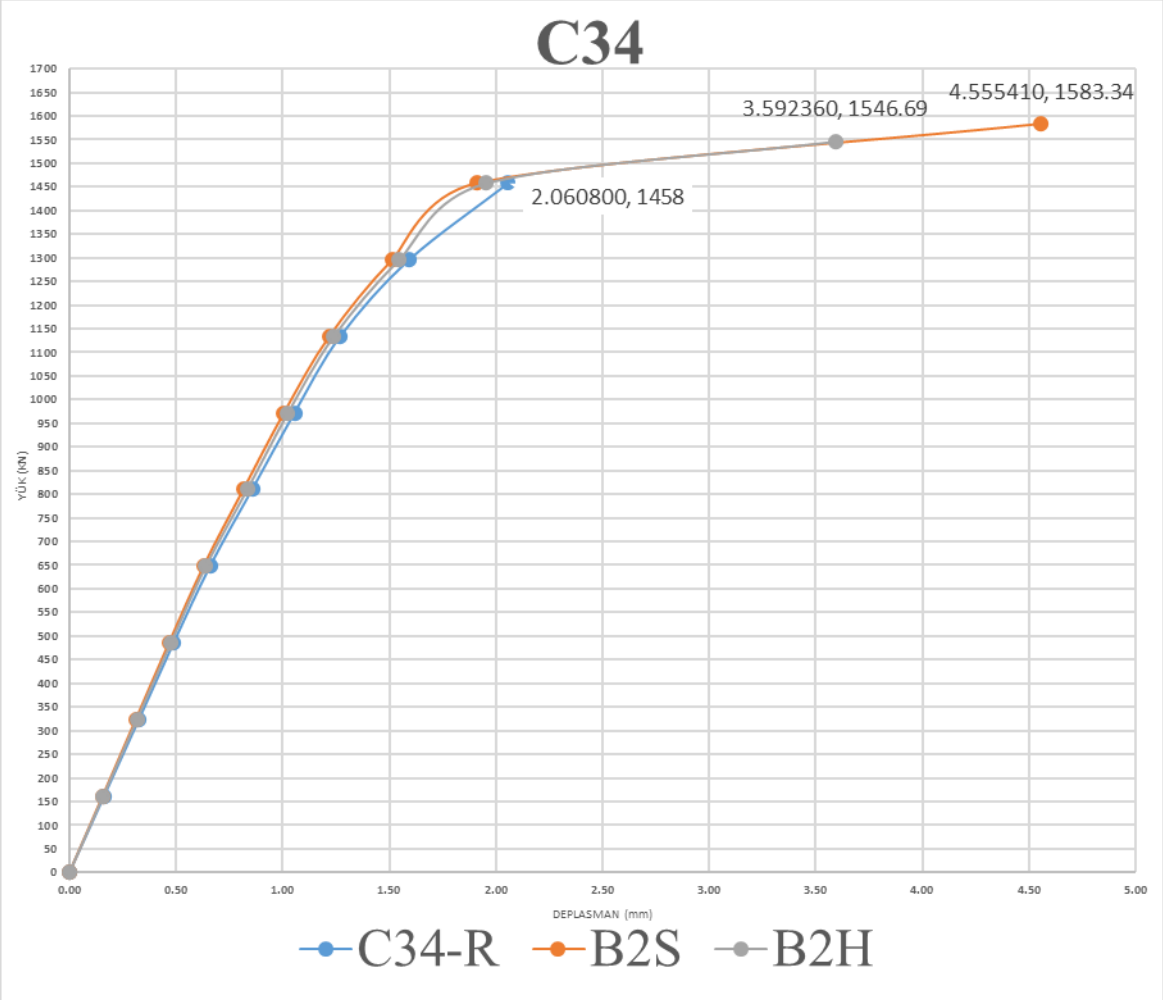
Yukarıdaki tablolardan anlaşılacağı üzere çelik levhalar ile kaplanan kolonlarda dayanımlar değişmiştir. Çelik levhaların aralıklarının azalması yani çelik levhaların sıklaşması sonucunda dayanımlarında bir miktar artış meydana gelmiştir. Ayrıca kolonların kapasitelerinde meydana gelen değişimlerin anlaşılması için bu yapılan analizlerin sonuçları grafikler halinde aşağıda verilmiştir.



C20 beton dayanımına sahip 3 adet kolon tipinin yük - deplasman grafikleri yukarıda verilmiştir. Grafikteki görüleceği üzere çelik levhalar ile güçlendirilen kolonların yük – deplasman grafiğindeki eğrilerinin tepe noktasında artış meydana gelmiştir. Tepe noktasında meydana gelen artış her bir elemanın kapasitelerinde meydana gelen artışı göstermektir. Ayrıca grafiklerdeki eğrilerin altına kalan alanın elemanların enerji tüketim kapasiteleri göstermektedir. Elemanların enerji tüketim kapasitesi sıralanışı ise A2S>A2H>C20-R şeklindedir.

Çizelge 3. C20 sınıfı elemanların yaklaşık olarak hesaplanan enerji tüketim kapasiteleri

ELEMAN İSMİ	ENERJİ TÜKETİM KAPASİTELERİ (j)
C20-R	1198,45
A2H	1655,64
A2S	2037,73



C34 beton dayanımına sahip 3 adet kolon tipinin yük - deplasman grafikleri yukarıda verilmiştir. Grafikteki görüleceği üzere çelik levhalar ile güçlendirilen kolonların yük – deplasman grafiğindeki eğrilerinin tepe noktasında artış meydana gelmiştir. Tepe noktasında meydana gelen artış aslında bize her bir elemanın kapasitelerinde meydana gelen artışı göstermektir. Ayrıca grafiklerdeki eğrilerin altına kalan alanın elemanların enerji tüketim kapasitelerini göstermektedir. Elemanların enerji tüketim kapasitelerinin sıralanışı ise B2S>B2H>C34-R şeklindedir.

Çizelge 4. C34 sınıfı elemanların yaklaşık olarak hesaplanan enerji tüketim kapasiteleri

ELEMAN İSMİ	ENERJİ TÜKETİM KAPASİTELERİ (j)
C34-R	1798,67
B2H	4143,17
B2S	5661,57

Elemanların göçme kapasitelerini kıyasladığımızda ;

- A2S kolonunun kapasitesinde C20-R referans kolon kapasitesine göre %11,89 oranında artış gözlenmiştir.
- A2H kolonunun kapasitesinde C20-R referans kolon kapasitesine göre %7.01 oranında artış gözlenmiştir.
- B2S kolonunun kapasitesinde C34-R referans kolon kapasitesine göre %8.60 oranında artış gözlenmiştir.
- B2H kolonunun kapasitesinde C34-R referans kolon kapasitesine göre %6.08 oranında artış gözlenmiştir.

Sonuç olarak elemanların dayanım, süneklik ve enerji tüketim kapasitelerine baktığımızda elde edilen sonuçlardan çelik levhalarla yapılan güçlendirme yönteminin etkili olduğu anlaşılmaktadır. Bu çalışma daha da genişletilerek dayanım, levha kalınlığı ve levha sıklığı arasında teorik formüller oluşturulması amaçlanmaktadır.

KAYNAKLAR

Yavuz Emre Küçük (2003) Betonarme yapıların çelik ile takviyesi. Yüksek l,isans Tezi,İstanbul Teknik Üniversitesi Fen Bilimleri Enstitüsü.

Vikipedi özgür Ansiklopedi – Sonlu Elemanlar Yöntemi.

Uğur Yozgat (2007) Eksenel Yüklü Kare Kesitli Betonarme Kolonların Sonlu Elemanlar Yöntemi İle Nonlineer Analizi, Yükseköğretim Kurulu Başkanlığı Tez Merkezi.

Ahmet Can Altunışık, Murat Günaydın, Ali Fuat Genç, Fatih Yesevi Okur, İnşaat Mühendisliğinde Ansys Uygulamaları Kitabı. Dynamıc Academy Yazılım İnşaat San. Tic. Ltd. Şti.

Belal M. F., Mohamed H. M., Morad S. A., (2014). "Behavior of Reinforced Concrete Columns Strengthened by Steel Jacket," Housing and Building National Research Center (HBNR) journal, http://dx.doi.org/ 10.1016/j.hbrcj.2014.05.002.

Alper Büyükkaragöz ve Yağmur Kopraman ,(2008) Eksenel Yük Etkisi Altındaki Kare Kesitli Mantolanmış Kolonun Sonlu Elemanlar Yöntemiyle Analizi, Gazi Üniversitesi Müh..Mim. Fak. Der.

RESEARCHING THE SYNERGY BETWEEN LEAN CONSTRUCTION AND BUILDING INFORMATION MODELING (BIM)

YALIN İNŞAAT VE YAPI BİLGİ MODELLEMESİ (YBM) ARASINDAKİ SİNERJİNİN ARAŞTIRILMASI

Furkan POLAT

Civil Engineer, Gebze Technical University, Civil Engineering Department, Gebze, Kocaeli.,
ORCID NO: 0000-0002-5199-5656

Sevilay DEMİRKESEN ÇAKIR

Associate Professor, Gebze Technical University, Civil Engineering Department, Gebze, Kocaeli.,
ORCID NO: 0000-0000-0000-0000

SUMMARY

This study investigates the synergy between Lean construction and BIM. In the literature, there is considerable evidence that Lean practices are associated with BIM applications. To enhance the performance of construction projects, it is essential to use both approaches in an effective way. In this respect, the study first presents what Lean is and how it is implemented in construction projects. Then, the study presents BIM and its implementation in the construction industry. In the last section, the study proposes the synergy between Lean and BIM and it presents how Lean and BIM are interrelated and what functions are common or what features can be enhanced when used simultaneously.

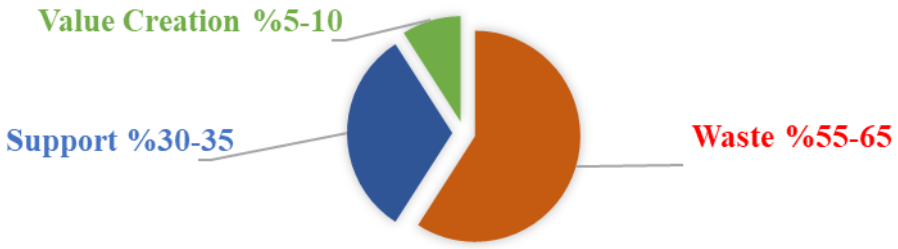
INTRODUCTION

The construction industry had always fallen behind from past to present according to labor productivity stats compared to all other sectors. According to Barbosa et al. (2017), construction workers work more inefficiently than other sector workers. The report shows that most construction workers do not add value to their work. As a result, many problems such as budget & time overruns, and poor-quality reveal in the construction industry due to low productivity.

According to Egan, (1998), studies in the United States (US), Scandinavia, and the UK have found that 30% of constructions are reworked. In addition, mistakes account for 3-6% of the total cost, and at least 10% of the materials were wasted. Love & Edwards, (2003) stated that the cost of rework in Australian construction projects reaches up to 35% of the total cost. It has been concluded that it contributes up to 50% of the total overrun costs of projects. As a result, one of the most important reasons for inefficiency and poor quality in the construction industry is reworking.

Khanh & Kim, (2014) stated that the most important wasting factors were the time of inspection of construction works, waiting for someone else's work to be done before continuing, accidents on the construction site, and time of transporting materials, equipment, and workers. In addition, it is mentioned that 9.36% of the total project cost consists of total waste cost. Mossman (2009), states that the construction process waste is approximately 55-65%. This is a very high ratio of waste/value. Lean construction tools are a significant opportunity to reduce waste in construction processes.

Figure 1. Waste and Value in Construction Process



According to Manyika et al. (2015), the digitalization and use of technology in the construction industry have lagged compared to other industries. Compared to other industries, the construction industry has lagged in terms of digitalization. All problems in the construction industry are an opportunity. Because there are many areas to develop the construction industry.

Today, different methods and implementations are developed to improve labor productivity in the construction industry. With the spread of methods such as Lean Construction & Agile project management, and implementations of technologies such as the Internet of Things (IoT) and Building Information Modelling (BIM), more efficient workflows are targeted in construction projects. Eldeep, Farag, & Abd El-Hafez, (2022) reported that significant increase in project efficiency by using BIM and Lean in the design phase. They stated that BIM and lean tools such as just-in-time reduced waiting time waste by almost 50% in the design process. These results show us that Lean and BIM have substantial potential. In this study, the potential of Lean and BIM will be examined by a literature review.

METHODS

There are many studies that analyze the interaction between BIM and Lean in literature. (Saieg, Sotelino, Nascimento, & Caiado, 2018) Both concepts have their own processes and methods. Lean construction and BIM have been developed to increase productivity, to improve quality and processes in the construction industry. With this aspect, they have many common points. It is seen that especially companies that implement Lean construction in the construction industry use BIM making it a Lean construction tool. Although there are a lot of common points between lean and BIM, there are still challenges when it comes to integrating these two concepts. There are many academic studies in the literature about the contribution of BIM to lean processes, but the contribution of Lean tools to BIM processes has not been studied much. (Pedo et al., 2021) In this study, a literature review about Lean construction tools and BIM was conducted through online science databases, paper congresses, and the International Group for Lean Construction (IGLC) conferences. While the literature is being searched, the articles in which especially Lean and BIM together were reviewed.

DISCUSSION

The concept of Lean Production was first coined by a member of the research team studying the international automobile industry in his book which is *The Machine That Changed the World*. “Lean” refers to a production system created to produce better products in less time and place by using fewer labor hours in contrast to the mass production system. (Ballard & Howell, 2003)

Lean focuses on value above all else. However, value creation is equated with cost reduction in some companies. This show that the concept of Lean is not fully understood. Therefore, Womack & Jones, (1996) explained what Lean thinking focuses on and what the principles are. Lean is not just eliminating waste and reducing costs, it is preparing the product or service according to the customer's requirements. Doing this, it is aimed to provide more value to the customer. (Hines, Holwe, & Rich, 2004)

Lean tools attempt to identify the underlying causes of problems. In Lean thinking, these problems can be defined as waste. Waste is the opposite of the concept of value. From the customer's perspective, value is something he or she is willing to pay for. In other words, a product or process that doesn't create value for the

customer is a waste. (LeMahieu, Nordstrum, & Greco, 2017) Waste in Lean thinking is considered under 8 main headings (Hartanti, Gunawan, Mulyana, & Herwinarso, 2022; Melton, 2005):

- Motion/Moving is defined as the spending of time and energy by employees to do a job. For example, if the distance between the office and the production area is too long, it will be an unnecessary waste of time and energy for the workers.
- Waiting is another waste in processes. It is the most important type of waste that causes delays in plans. For example, when an architect is designing a construction project when she/he needs to get ideas from engineers, she/he gets the answer after a long time due to insufficient communication between them.
- Overproduction is a waste type referring to a product or process that is not needed or produced earlier than planned. For example, preparing more rebar than necessary at the construction site. Excess stock represents the holding of goods or products that are not required for current needs. Stocking materials to be used months later in the construction site is defined as a type of waste.
- Defects are errors that can be seen in processes. Usually, this type of waste is easily distinguishable. For example, wrong manufacturing according to the project during the construction phase is defined as waste
- Extra transportation is defined as waste according to Lean thinking. Shorter routes should always be preferred for transport processes.
- Overprocessing is doing more work than necessary. Processes such as holding more meetings than required and excessive reporting are a waste. Increasing productivity by doing more work is a misconception.
- Non-utilized talent is also a waste. Every employee's skills need to be used. To ensure continuous improvement, this type of waste must be eliminated.

The idea of implementing the Lean philosophy refer as a new production philosophy in the construction industry is based on a study by Koskela (1992). The term "Lean Construction" was coined at the IGLC's first meeting in 1993 (Tezel et al., 2020). IGLC has led many studies on the implementation of the Lean philosophy in the construction industry. Developing tools such as planning, control, visualization, and continuous improvement, has changed the way of management is in the construction industry (Salem, Solomon, Genaidy, & Minkarah, 2006). (Egan (1998) mentioned that Lean Construction is a way to improve performance in the construction industry and some construction companies have achieved significant success in quality and efficiency by applying Lean techniques. In the early stages of Lean Construction, Lean tools such as 5S, Visualization, Just in Time (JIT), and Value Stream Mapping (VSM) were introduced by researchers to improve productivity and quality in the construction industry (Jiang et al., 2022). Since the construction and the manufacturing industry's work environment and way of doing work are not similar, tools had to be developed according to the construction projects. Aziz & Hafez (2013) mentions that managing construction processes according to Lean philosophy is different from ordinary practices. Because in the construction industry (1) net objectives are set for delivery processes (2) It is aimed at maximizing performance for the client at the project level (3) products and processes are designed simultaneously (4) production supervision is ensured throughout all projects. Planning and control stages are also very important in Lean Construction, as is practiced in the manufacturing industry.

Lean philosophy also has many benefits when compared to traditional project management. There is a certain amount of waste processes in every work organization. Lean allows us to eliminate these processes. It increases the concept of value created for the customer. It provides standardization by reducing variability. It reduces cycle times in production processes. It reduces and simplifies production steps. Increases transparency in processes. It creates a suitable environment for continuous improvement by using various tools. Because in Lean philosophy, the most perfect result is always aimed. (Koskela, 1992)

BIM is one of the most important developments in the architectural engineering and construction industry (AEC). The National Institute of Building Sciences (2007) has defined BIM as follows. "a digital representation of physical and functional characteristics of a facility. As such it serves as a shared knowledge resource for information about a facility forming a reliable basis for decisions during its life cycle from inception onward.". This technology contains solutions that can be a solution to many problems in the AEC industry. BIM creates one or more virtual models of a structure in its digital form. It provides better analysis

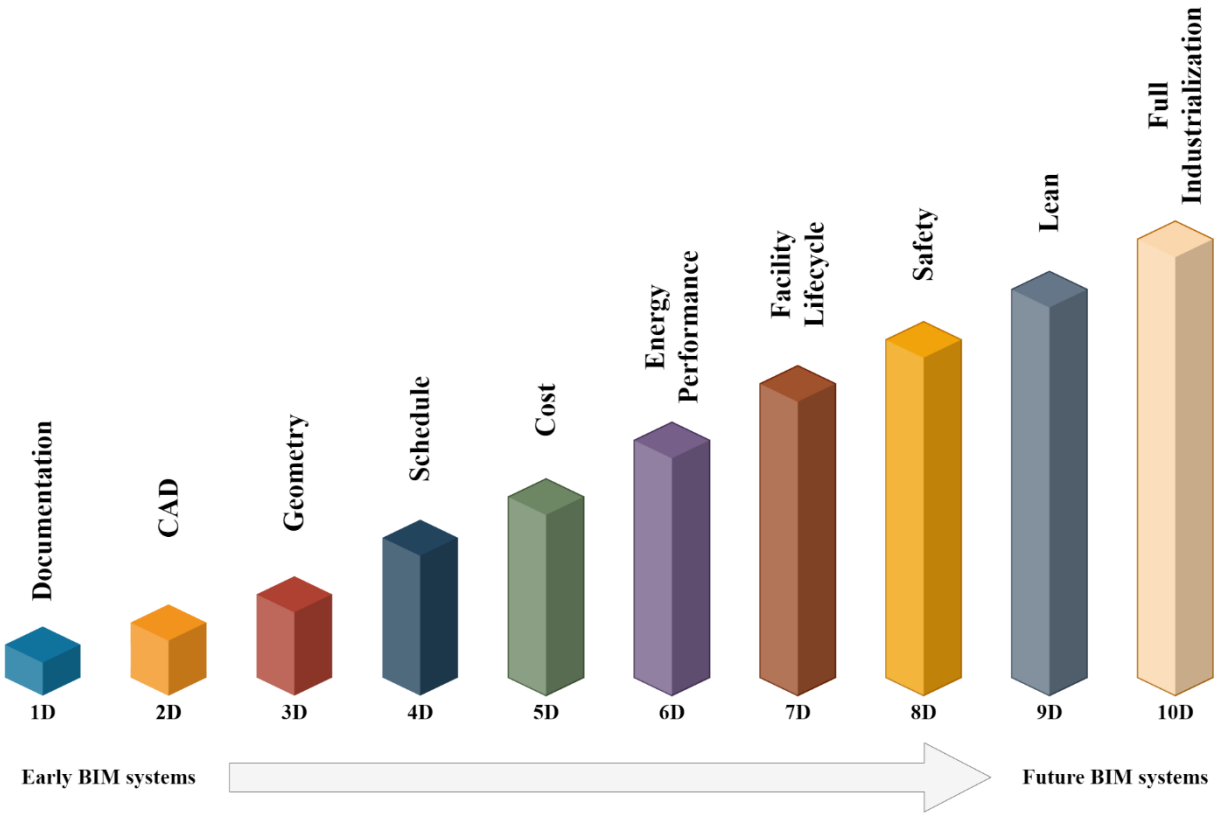
and control by improving the design phases. Computer-generated models generate a lot of data, supporting activities such as construction, manufacturing, and procurement. In addition, BIM contains many functions for modeling the lifecycle of a structure. A well-designed BIM Model makes it easy to build a higher quality building with lower cost and reduced project time. (Eastman, Teicholz, Sacks, & Liston, 2011)

According to Lee, Sacks, & Eastman (2006), BIM is the process of creating and managing building information in an interoperable and reusable way. One of the points to be considered here is that the entire lifecycle of the building should be considered and included in the processes. In addition, Lee et al., (2006) stated that a building consists of geometric components and geometric information is included in BIM design. BIM provides methods to facilitate the creation of building information and geometric shapes in a building model. It also preserves the validity of the information. Building designs can be maintained when an overhaul is required.

Documentation in a project built using traditional methods consists of a set of files transferred from the contractor along with a set of documents and boxes at the end of the project. However, a lot of information may be lost in this process, and editing documents according to the appropriate format can often cause problems. BIM is an excellent tool that can provide consistent information retrieval, more accessible document management, and better collaboration with various stakeholders.(Goedert & Meadati, 2008)

According to Smith (2014), BIM includes much more dimensions than 3D Modeling. The level of knowledge in the building model increases with each new dimension added. Each dimension has a purpose and consists of various information. Although there are various discussions between 6D and 7D, Smith (2014) has listed the BIM Dimensions as follows: 3D (shape), 4D (time), 5D (cost), 6D (facility management applications), and 7D (sustainability). In their study, (Ershadi, Davis, Jefferies, & Mojtahedi, 2021) revealed that the 10 dimensions of the BIM system characterize its full functionality. BIM dimensions are shown in Figure 2. Dimensions up to the 7th dimension have been used since the early 2000s through various software packages. However, 8D, 9D, and 10D still need improvement. While the simplest BIM provides technical documentation of a facility/building, an advanced BIM system includes aspects such as safety, lean construction, and full industrialization.

Figure 2. Dimensions of BIM



Recent studies have shown that BIM provides significant benefits in planning, conflict detection, design consistency, visualization, data management, cost estimation, lean construction practices, and team collaboration in the AEC industry. (Martínez-Aires, López-Alonso, & Martínez-Rojas, 2018)

Lean and BIM are two separate issues that are independent of each other. In other words, while lean construction applications can be applied without BIM, BIM applications can be used without Lean Construction. There are many studies in the literature examining both subjects separately. (Sacks, Koskela, Bhargav, Dave, & Owen, 2010) According to (Sepasgozar et al., 2021), the synergy between Lean and BIM has never been studied before 2009. However, recently, it is seen that the studies on the combination of lean, BIM, and other advanced digital technologies are increasing.

Sacks, Koskela, Bhargav, Dave, & Owen, (2010) has identified significant synergies with the matrix it developed to investigate the interaction between Lean and BIM. The authors identified 56 unique interaction points. The presence of many interaction points proves that there is an important synergy between BIM and Lean. In the case studies of Gerber, Becerik-Gerber, & Kunz (2010), it has been observed that the integration of Lean and BIM significantly reduces waste in time, material, and cost and increases the value in the perspectives of the customer. In addition, Yang (2019) argued that the collaborative use of Lean and BIM improves the level of project management and provides economic benefits.

Svalestuen, Lohne, & Laedre (2016) have argued that there are many interesting interactions between BIM and Lean. Interactions show that it reduces the number of non-value-adding activities. It also aimed to guide companies that want to apply Lean and BIM during the production phase of building projects by identifying 12 interactions.

According to Bhat, Trivedi, & Dave (2018), using Lean and BIM together can help solve some coordination issues. The authors suggest reducing the gap in the literature through further research.

Given this background, it is provided that construction projects can be more successfully executed by relying on the strong interaction between Lean and BIM. Performance improvements have already provided that several benefits can be achieved from this duo.

CONCLUSION

This study investigated the use of Lean methods and BIM in construction projects. To evaluate those, the background of Lean and BIM are presented accordingly. The study used an in-depth literature review to research the link between Lean and BIM. The strong evidence provided in the literature helped the authors to conclude that there is a positive and significant relationship between Lean applications and BIM implementation. The performance of BIM can either be enhanced through Lean principles or Lean methods can be more effectively implemented when integrated with BIM. The perceived benefits from this interaction are presented as part of the discussion section. This study may be a preliminary guide to research the Lean and BIM interaction over a structural model. The study can further create awareness regarding the use of both in construction projects to increase project success.

REFERENCES

Aziz, R. F., & Hafez, S. M. (2013). Applying lean thinking in construction and performance improvement. *Alexandria Engineering Journal*, *52*(4), 679–695. https://doi.org/10.1016/j.aej.2013.04.008

Ballard, G., & Howell, G. A. (2003). Lean project management. *Building Research and Information*, *31*(2), 119–133. https://doi.org/10.1080/09613210301997

Barbosa, F., Woetzel, J., Mischke, J., Ribeirinho, M. J., Sridhar, M., Parsons, M., … Brown, S. (2017). *Reinventing Construction: A Route To Higher Productivity*. Retrieved from https://www.mckinsey.com/~/media/mckinsey/business%20functions/operations/our%20insights/reinventing%20construction%20through%20a%20productivity%20revolution/mgi-reinventing-construction-a-route-to-higher-productivity-full-report.pdf

Bhat, V., Trivedi, J. S., & Dave, B. (2018). Improving design coordination with Lean and BIM, an Indian case study. *26th Annual Conference of the International Group for Lean Construction*, *2*, 1206–1216. The International Group for Lean Construction. https://doi.org/10.24928/2018/0479

Eastman, C. M., Teicholz, P., Sacks, R., & Liston, K. (2011). *BIM handbook : a guide to building information modeling for owners, managers, designers, engineers and contractors* (2nd Edition). Wiley.

Egan, J. (1998). *Rethinking Construction*. Retrieved from https://constructingexcellence.org.uk/wp-content/uploads/2014/10/rethinking_construction_report.pdf

Eldeep, A. M., Farag, M. A. M., & Abd El-hafez, L. M. (2022). Using BIM as a lean management tool in construction processes – A case study: Using BIM as a lean management tool. *Ain Shams Engineering Journal*, *13*(2). https://doi.org/10.1016/j.asej.2021.07.009

Ershadi, M., Davis, P., Jefferies, M., & Mojtahedi, M. (2021). Implementation of Building Information Modelling in infrastructure construction projects: a study of dimensions and strategies. *International Journal of Information Systems and Project Management*, *9*(4), 43–59. https://doi.org/10.12821/ijispm090403

Gerber, D. J., Becerik-Gerber, B., & Kunz, A. (2010). *Building information modeling and lean construction: technology, methodology and advances from practice*.

Goedert, J. D., & Meadati, P. (2008). Integrating Construction Process Documentation into Building Information Modeling. *JOURNAL OF CONSTRUCTION ENGINEERING AND MANAGEMENT*. https://doi.org/10.1061/ASCE0733-93642008134:7509

Hartanti, L. P. S., Gunawan, I., Mulyana, I. J., & Herwinarso, H. (2022). Identification of Waste Based on Lean Principles as the Way towards Sustainability of a Higher Education Institution: A Case Study from Indonesia. *Sustainability (Switzerland)*, *14*(7). https://doi.org/10.3390/su14074348

Hines, P., Holwe, M., & Rich, N. (2004). Learning to evolve: A review of contemporary lean thinking. *International Journal of Operations and Production Management*, Vol. 24, pp. 994–1011. https://doi.org/10.1108/01443570410558049

Jiang, L., Zhong, H., Chen, J., Cheng, J., Chen, S., Gong, Z., … Su, Z. (2022). Study on the construction workforce management based on lean construction in the context of COVID-19. *Engineering, Construction and Architectural Management*. https://doi.org/10.1108/ECAM-10-2021-0948

Khanh, H. D., & Kim, S. Y. (2014). Evaluating impact of waste factors on project performance cost in Vietnam. *KSCE Journal of Civil Engineering*, *18*(7), 1923–1933. https://doi.org/10.1007/s12205-014-1219-2

Koskela, L. (1992). *Application of the new production philosophy to construction*. Retrieved from https://leanconstruction.org/uploads/wp/media/docs/Koskela-TR72.pdf

Lee, G., Sacks, R., & Eastman, C. M. (2006). Specifying parametric building object behavior (BOB) for a building information modeling system. *Automation in Construction*, *15*(6), 758–776. https://doi.org/10.1016/j.autcon.2005.09.009

LeMahieu, P. G., Nordstrum, L. E., & Greco, P. (2017). Lean for education. *Quality Assurance in Education*, *25*(1), 74–90. https://doi.org/10.1108/QAE-12-2016-0081

Love, P. E. D., & Edwards, D. J. (2003). LEARNING TO REDUCE REWORK IN PROJECTS: ANALYSIS OF FIRM'S ORGANIZATIONAL LEARNING AND QUALITY PRACTICES. In *Project Management Journal* (Vol. 13).

Manyika, J., Ramaswamy, S., Khanna, S., Sarrazin, H., Pinkus, G., Sethupathy, G., & Yaffe, A. (2015). *Digital America: A Tale of the Haves and Have-Mores*. Retrieved from www.mckinsey.com/mgi.

Martínez-Aires, M. D., López-Alonso, M., & Martínez-Rojas, M. (2018, January 1). Building information modeling and safety management: A systematic review. *Safety Science*, Vol. 101, pp. 11–18. Elsevier B.V. https://doi.org/10.1016/j.ssci.2017.08.015

Melton, T. (2005). The benefits of lean manufacturing: What lean thinking has to offer the process industries. *Chemical Engineering Research and Design*, *83*(6 A), 662–673. https://doi.org/10.1205/cherd.04351

Mossman, A. (2009). Creating value: a sufficient way to eliminate waste in lean design and lean production. *Lean Construction Journal*. Retrieved from http://www.theclbm.com/faq.html

National Institute of Building Sciences. (2007). *US National Building Information Modeling Standard Version 1 - Part 1: Overview, Principles, and Methodologies*.

Pedo, B., Tezel, A., Koskela, L., Whitelock-Wainwright, A., Lenagan, D., & Nguyen, Q. A. (2021). Lean Contributions to BIM Processes: The Case of Clash Management in Highways Design. *Proc. 29th Annual Conference of the International Group for Lean Construction (IGLC)*, 116–125. International Group for Lean Construction. https://doi.org/10.24928/2021/0164

Sacks, R., Koskela, L., Bhargav, ;, Dave, A., & Owen, R. (2010). Interaction of Lean and Building Information Modeling in Construction. *Journal of ConstructionEngineering and Management*. https://doi.org/10.1061/ASCECO.1943-7862.0000203

Saieg, P., Sotelino, E. D., Nascimento, D., & Caiado, R. G. G. (2018). Interactions of Building Information Modeling, Lean and Sustainability on the Architectural, Engineering and Construction industry: A systematic review. *Journal of Cleaner Production*, *174*, 788–806. https://doi.org/10.1016/j.jclepro.2017.11.030

Salem, O., Solomon, ; J, Genaidy, ; A, & Minkarah, I. (2006). Lean Construction: From Theory to Implementation. *Journal of Management in Engineering*. https://doi.org/10.1061/ASCE0742-597X200622:4168

Sepasgozar, S. M. E., Hui, F. K. P., Shirowzhan, S., Foroozanfar, M., Yang, L., & Aye, L. (2021, January 1). Lean practices using building information modeling (BIM) and digital twinning for sustainable construction. *Sustainability (Switzerland)*, Vol. 13, pp. 1–22. MDPI AG. https://doi.org/10.3390/su13010161

Smith, P. (2014). BIM & the 5D Project Cost Manager. *Procedia - Social and Behavioral Sciences*, *119*, 475–484. https://doi.org/10.1016/j.sbspro.2014.03.053

Svalestuen, F., Lohne, J., & Laedre, O. (2016). BIM-stations: What it is and how it can be used to implement lean principles. *24th Annual Conference of the International Group for Lean Construction*. Retrieved from https://www.researchgate.net/publication/316204514

Tezel, A., Taggart, M., Koskela, L., Tzortzopoulos, P., Hanahoe, J., & Kelly, M. (2020). Lean construction and BIM in small and medium-sized enterprises (SMEs) in construction: A systematic literature review. *Canadian Journal of Civil Engineering*, *47*(2), 186–201. https://doi.org/10.1139/cjce-2018-0408

Womack, J. P., & Jones, D. T. (1996). *Lean Thinking: Banish Waste and Create Wealth for Your Corporation*. New York: Simon and Schuster.

Yang, S. (2019). Application of BIM during lean construction of high-rise buildings. *Stavební Obzor - Civil Engineering Journal*, *28*(3), 331–343. https://doi.org/10.14311/cej.2019.03.0027

OSMANLI DEVLETİ'NİN SON DÖNEMİNDEN CUMHURİYET'İN İLK YILLARINA TÜRKİYE'DE MÜHENDİSLİK EĞİTİMİ

Doç. Dr. Derya Çini Şimşek

Başkent Üniversitesi, İletişim Fakültesi Radyo, Televizyon ve Sinema Bölümü, ORCID: 0000-0002-0678-5801

ÖZET

Matematiksel düşünme becerisi ve düşünce sistematiğini temel alan mühendisliğin tarihi, ilkçağlara kadar dayanmaktadır. Toplum oluşumunun problemlerinin çözümü aşamasında var olan mühendisliğin ortaya çıkışıyla birlikte toplumsal gelişmişlik düzeyinde inanılmaz bir ivmelenme yaşanmıştır. Aydınlanma Çağı dediğimiz 18 yüzyıl Avrupa'nın, mühendislik de dahil her alanda büyük atılımlar yaptığı bir yüzyıl olmuş, Avrupa'da yaşanan gelişmeler Osmanlı Devleti'nde olmamıştır. Avrupa'da meydana gelen gelişmelerin farkına vararak devletin organizasyonel yapısında değişikliğe gidilmesi dair başlangıç adımları atan Osmanlı Devleti'nde mühendislik eğitimi, 1773 tarihinde kurulan Mühendishane-i Bahr-i Hümayun ile başlamış, ardından 1795 tarihinde açılan Mühendishane-i Berr-i Hümayun ile devam etmiştir. 1867 tarihine gelindiğinde Mülkiye Mühendisi ve Islah-i Sanayi Mektebi adıyla mühendis yetiştiren bir okul açılmıştır. Mektebin devamı sayılan Mühendis-i Mülkiye Mektebi sonradan eğitime başlamış ve okulun adı 1875 yılında Turuk-u ve Muabir Mühendis Mektebi olarak değiştirilmiştir. 1883 tarihinde eğitime başlayan Hendese-i Mülkiye Mektebi ile de sivil hizmetler için gerekli mühendis ihtiyacının karşılaması hedeflenmiştir. 1909 yılında Nafıa Nezaretine bağlı olarak Mühendis Mekteb-i Ali'si adını alan okul, eğitimine Yüksek Mühendis Mektebi açılıncaya kadar devam etmiştir. Cumhuriyetin ilanı sonrasında İstanbul Darülfununu Fen Fakültesine bağlı olarak kurulan Makina-Elektrik Enstitüsü'nde mühendislik eğitimi 1926 tarihinde başlamıştır. 1933'te gerçekleşen üniversite reformu sonucunda Darülfünun tüm kadro ve kurumları ile lağvedilince Maarif Vekaleti, İstanbul Üniversitesi adı ile bir yüksek öğretim okulu kurması konusunda yetkilendirilmiş, Yüksek Mühendis Mektebi de yeni kurulan üniversitenin çatısı altına alınmıştır. Fen Fakültesi'ne bağlı Makina ve Elektrik Enstitüsü de Elektro Mekanik Şubesi adıyla Yüksek Mühendis Mektebi'ne alındı. 1935 tarihine gelindiğinde Muhabere Şubesi açılarak Milli Eğitim Bakanlığına bağlanan mektep, 1944'de İstanbul Teknik Üniversitesi'ne dönüştürüldü ve ilerleyen dönemde Türkiye'de mühendislik eğitimi veren üniversite sayısında hızlı bir artış yaşandı.

Anahtar Kelimeler: Mühendislik, Türkiye, Eğitim, Tarih.

ENGINEERING EDUCATION IN TURKEY FROM THE LAST PERIOD OF THE OTTOMAN STATE TO THE FIRST YEARS OF THE REPUBLIC

ABSTRACT

The history of engineering, which is based on mathematical thinking skills and thought systematics, dates back to ancient times. With the emergence of engineering, which existed at the stage of solving the problems of society formation, an incredible acceleration has been experienced in the level of social development. The 18th century, which we call the Age of Enlightenment, was a century in which Europe made great breakthroughs in every field, including engineering, and the developments in Europe did not happen in the Ottoman Empire. Being aware of the developments in Europe and taking the initial steps to change the organizational structure of the state, engineering education in the Ottoman Empire started with Mühendishane-i Bahr-i Hümayun, which was founded in 1773, and continued with Mühendishane-i Berr-i Hümayun, which was opened in 1795. In 1867, a school to train engineers was opened under the name of Civil Engineer and Islah-i Sanayi Mektebi. Engineering School, which is considered to be the continuation of the school, started education later and the name of the school was changed to Turuk-u and Associate Engineer School in 1875. With the Hendese-i Mülkiye Mektebi, which started education in 1883, it was aimed to meet the need for engineers for civil services. The school, which was named the School of Engineers under the Ministry of Public Works in 1909, continued its education until the Graduate School of Engineering was opened. Engineering education started in 1926 at the Mechanical-Electric Institute, which was established under the Faculty of Science of Istanbul

Darülfünun after the proclamation of the Republic. As a result of the university reform that took place in 1933, when the Darülfünun was abolished with all its staff and institutions, the Ministry of Education was authorized to establish a higher education school under the name of Istanbul University, and the Graduate School of Engineering was brought under the roof of the newly established university. The Mechanical and Electricity Institute affiliated to the Faculty of Science was taken to the Graduate School of Engineering under the name of the Electromechanical Branch. In 1935, the School, which was connected to the Ministry of National Education with the opening of the Communication Branch, was transformed into Istanbul Technical University in 1944 and there was a rapid increase in the number of universities providing engineering education in Turkey in the following period.

Keywords: Engineering, Turkey, Education, History.

OSMANLI DÖNEMİNDE MEDRESEDEN MÜHENDİSHANEYE GEÇİŞİN TARİHİ

Doç. Dr. Derya ÇİNİ ŞİMŞEK

Başkent Üniversitesi, İletişim Fakültesi Radyo, Televizyon ve Sinema Bölümü, Ankara, Türkiye, ORCID: 0000-0002-0678-5801

:

Özet

Selçuklular dönemi bilinen ilk mühendislik eğitimi veren kurumu 11. yüzyılda kurulan Bağdat'taki Nizamiye Medresesi olmuş, onu Osmanlı Devletinde kurulan medreseler izlemiştir. İlk Osmanlı medreselerinde Nizamiye Medreseleri geleneğine dayalı bir eğitim yürütülmekte, nakli ilimler ağırlıklı olmakla birlikte akli ilimlere de yer verilmekteydi. Selçuklu Devleti dönemi başlayan, Osmanlı Devleti'nin kuruluşu ile gelişen medrese sistemi, Devletin dağılma sürecine girmesi ile diğer alanlarda olduğu gibi amacını aşmış ve bozulmalar başlamıştır. Osmanlılarda mühendislik eğitimi alanındaki gelişmeler de Avrupa'dan geri kalmaya başladığı bu dönemden sonra görülmeye başlamıştır. Osmanlı bu dönemde Avrupa'nın modern eğitim kurumlarından esinlenerek 1773 yılında bir kurs niteliğinde olan Tersane Hendesanesi açmış, kuruma 1781 yılından itibaren Mühendishâne denilmiştir. Topçu subayı yetiştirmek amacıyla 1734 yılında Üsküdar'da "Humbarahane ve Hendesehane" adı altında bir okul açılmış fakat yeniçerilerin ayaklanmalarından korkularak altı yıl sonra kapatılmıştır. Mühendishane-i Bahr-i Hümâyûn, 1776'da Kasımpaşa'da bahriyenin ihtiyaç duyduğu çağdaş mühendislik hizmetlerinin sağlanması amacıyla kurulmuştur. Yeniçeri Ocağı'nın II. Mahmud döneminde kaldırılması ile deniz ve kara eğitiminin birbirinden ayrılması gerekliliği öngörülerek Mühendishane-i Bahr-i Hümâyun ile Mühendishane-i Berr-i Hümâyûn'un ayrılarak müstakil birer okul haline getirilmesi düşünülmüştür. Bahr-i Hümâyun okulunun seyr-i sefain kısmı 1834 yılında Heybeliada'daki Kalyoncu Kışlası'na nakledilmiştir. Mekteb-i Bahriye bünyesine 1914 tarihinde alınan ilk deniz uçağı ile deniz tayyareciliği sınıfı oluşturulmuş ve ardından Yeşilköy'de Kara Tayyare Mektebi ve Deniz Tayyare Mektebi kurulmuştur. Cumhuriyet'in ilanı sonrasında 3 Mart 1924 tarihinde kabul edilen Tevhid-i Tedrisat Kanunu ile eğitim birliği sağlanarak bütün okullar Millî Eğitim Bakanlığı'na bağlanmıştır. Osmanlı Dönemi açılan mühendis okulları eğitim alanında Batı'ya açılan ilk kapı olarak değerlendirilmiş, bu okullar daha sonra açılan modern okulların da temelini oluşturmuştur.

Anahtar Kelimeler: Mühendislik, Medrese, Osmanlı Devleti, Eğitim.

THE HISTORY OF THE TRANSITION FROM MADRASA TO ENGINEERING IN THE OTTOMAN PERIOD

Abstract

The first institution of engineering education known during the Selcuk period was the Nizamiye Madrasa in Baghdad, which was established in the 11th century, followed by the madrasahs established in the Ottoman Empire. In the first Ottoman madrasahs, an education based on the tradition of Nizamiye Madrasahs was carried out, and mental sciences were also included, although transmission sciences were predominant. The madrasa system, which started in the Selcuk State period and developed with the establishment of the Ottoman State, exceeded its purpose and started to deteriorate with the disintegration of the State, as in other areas. The developments in the field of engineering education in the Ottomans began to be seen after this period, when it started to lag behind Europe. In this period, the Ottoman Empire, inspired by the modern educational institutions of Europe, opened the Tersane Hendesanesi, which was a course in the form of a course, in 1773, and the institution was called Muhendishane since 1781. A school named "Humbarahane and Hendesehane" was opened in Üsküdar in 1734 in order to train artillery officers, but it was closed six years later due to the fear of the janissaries' uprisings. Muhendishane-i Bahr-i Hümâyûn was established in Kasımpaşa in 1776 to provide modern engineering services needed by the navy. It was envisaged that the Janissary Furnace would be abolished during the reign of Mahmud II and that sea and land education should be separated from each other, and it was considered that Mühendishane-i Bahr-i Hümâyun and Mühendishane-i Berr-i Hümâyûn would be separated and turned into independent schools. The seyr-i sefain part of the Bahr-i Hümâyun school

was transferred to the Kalyoncu Barracks on Heybeliada in 1834. A naval aircraft class was established with the first seaplane purchased within the Mekteb-i Bahriye in 1914 and then the Kara Tayyare Mektebi and Deniz Tayyare Mektebi were established in Yeşilköy. With the Law on Tevhid-i Tedrisat, which was adopted on March 3, 1924 after the proclamation of the Republic, educational unity was ensured and all schools were connected to the Ministry of National Education. The engineer schools opened in the Ottoman Period were considered as the first gate opening to the West in the field of education, and these schools formed the basis of the modern schools opened later.

Keywords: Engineering, Madrasa, Ottoman State, Education.

SU İDARELERİNDE GELİR GETİRMEYEN SU BİLEŞENLERİNİN MALİYET ETKİLERİNİN PERFORMANS GÖSTERGELERİ İLE ANALİZİ

Cansu BOZKURT[1]

Ardahan Üniversitesi, Teknik Bilimler MYO, İnşaat Bölümü, Ardahan, Türkiye. ORCID ID: https://orcid.org/0000-0002-0987-1297

Mahmut FIRAT [2]

İnönü Üniversitesi, Mühendislik Fakültesi, İnşaat Mühendisliği Bölümü, Malatya, Türkiye
ORCID ID: https://orcid.org/0000-0002-8010-9289

Özet

Kentsel su yönetiminde kaliteli ve yeterli miktarda suyun abonelere zamanında iletilmesi gerekir. Ancak şebeke ana hatlarında ve servis bağlantılarında meydana gelen arızalar su kaybına neden olmaktadır. Arıza sayısının ve sızıntı miktarının artmasına bağlı olarak şebeke işletme koşulları bozulmakta ve hizmet kalitesi azalmaktadır. Dağıtım sistemlerinde kayıplar gelir getirmeyen su olarak tanımlanır. Gelir getirmeyen su temel olarak, dağıtım sisteminde sızıntılar, idari kayıplar ve yasal faturalandırılmamış tüketimlerden oluşmaktadır. Sızıntılar, dağıtım sistemlerinde doğrudan su kaybına neden olmaktadır. Sızıntıların fazla olmasına bağlı olarak su kaynağı verimsizliği ortaya çıkmakta ve işletme maliyetleri artmaktadır. Ayrıca sızıntı oranının artması işletme koşullarının bozulması, hizmet kalitesinin azalması ve abone şikayetlerinin artması üzerinde oldukça etkilidir. Diğer taraftan idari kayıplar tüketilen ancak ücreti ödenmeyen suyu içermektedir. Bu kayıplar idareler için doğrudan gelir kaybına neden olmaktadır. Diğer taraftan yasal faturalandırılmamış tüketimler (park, cami, peyzaj, itafiye vb.) tüketilen ancak ücreti alınamayan suyu içermektedir. Bu bileşen de idareler için doğrudan gelir kaybına neden olmaktadır. Dağıtım sistemlerinde finansal ve ekonomik olarak verimliliğin sağlanması için kayıp bileşenlerin düzenli izlenmesi gerekir. Bunun için uygun göstergelerin kullanılması gerekir. Bu çalışmada dağıtım sistemlerinde gelir getirmeyen su ve alt bileşenlerinin finansal ve ekonomik etkilerinin çeşitli performans göstergelerine göre analizi amaçlanmıştır. Bunun için gelir getirmeyen su ve alt bileşenlerini kapsayan çeşitli göstergeler tanımlanmıştır. Bu göstergeler pilot idarelerde test edilmiş ve sonuçlar yorumlanmıştır. Bu göstergelerin performans analizinde kullanılması ve doğru bir değerlendirme sunması için veri kalitesi oldukça önemlidir. Bunun için pilot idarelerde sadece verisi olan göstergeler analiz edilmiştir. Bu çalışmada kullanılan performans göstergelerinin su kayıp yönetimi ve kentsel su yönetiminde ekonomik verimliliğin izlenmesinde önemli katkı sunacağı düşünülmektedir.

Anahtar Kelimeler: İçme suyu dağıtım sistemi, gelir getirmeyen su, finansal etki, performans izleme

ANALYSIS OF COST EFFECTS FOR NON-REVENUE WATER COMPONENTS IN WATER UTILITIES WITH PERFORMANCE INDICATORS

Abstract

In urban water management, high quality and sufficient amount of water must be delivered to the customers in time. However, failures in main lines and service connections may cause water loss. Depending on the increase of faults and the amount of leakage can be cause operating conditions deteriorate and service quality decreases at the water network. Losses in distribution systems are defined as non-revenue water. Non-revenue water mainly consists of leakages in the distribution system, apparent losses and unbilled authorized consumption. Leaks cause direct loss of water in distribution systems. Due to the excess of leaks, water supply inefficiency occurs and operating costs increase. In addition, the increase in the leakage rate is very effective on the deterioration of operating conditions, the decrease in service quality and the increase in subscriber complaints. On the other hand, apparent losses include water that is unbilled metered consumption. These losses lead to a direct loss of income for administrations. On the other hand, unbilled unmetered consumption (park, mosque, landscape, fire department, etc.) means water that is consumed but cannot be charged. This component also causes direct income loss for the administrations. In order to ensure financial and economic

efficiency in distribution systems, regular monitoring of lost components is required. For this reason, appropriate indicators must be used. In this study, it is aimed to analyze the financial and economic effects of non-revenue water and its sub-components in distribution systems according to various performance indicators. Therefore, various indicators have been defined as non-revenue water and its sub-components. These indicators were tested at pilot administrations and the results were discussed. Data quality is very important for these indicators to be used in performance analysis and to provide an accurate assessment. For this purpose, only indicators with data were analyzed in pilot administrations. It is thought that the performance indicators used in this study will make an important contribution to the monitoring of economic efficiency in water loss management and urban water management.

Keywords: Water distribution system, non-revenue water, financial impact, performance monitoring

GİRİŞ

Kentsel su yönetiminde birim metreküp su satış bedeli üzerinde, su üretim maliyeti, şebeke arıza bakım ve onarım maliyeti, personel, ekipman maliyeti gibi çeşitli maliyetler etkilidir. Dağıtım sisteminde ayrıca şebekedeki arızalardan dolayı meydana gelen gelir getirmeyen su (GGS) ve alt bileşenlerinin de maliyetleri söz konusudur. Bu maliyetler fiziki kayıplar açısından, abonelere iletilemeyen (satışı yapılamayan) suyun maliyetinin yanı sıra sızıntıları önlemek için sahada yapılan çalışmaların oluşturduğu maliyetleri içermektedir (Deidda vd., 2014). Diğer taraftan sistemde kullanıcılar tarafından tüketildiği halde ücret alınamayan kayıpları içeren idari kayıplar idareler için doğrudan ekonomik kayıplara neden olmaktadır (Arregui vd., 2018). Görüldüğü GGS ve alt bileşenleri sadece su ve enerji kaynaklarının verimsiz kullanılmasına neden olmaz aynı zamanda birçok kalemde ekonomik kayıplar da oluşturmaktadır. Bu nedenle sürdürülebilir bir dağıtım sistemi işletme planı için GGS ve alt bileşenlerinin maliyet etkilerinin analiz edilmesi ve izlenmesi gerekir (Mukherjee vd., 2015).

GGS hacminin azaltılmasının ciddi bir ekonomik etkisi bulunmaktadır ve bu suyun sürdürülebilirliği için önemli bir adımdır (Farouk vd., 2021). (Zaini vd., 2017) faturalandırılmamış izinli tüketim, görünür ve gerçek kayıp hacimlerinden oluşan gelir getirmeyen suyun bileşenlerine göre gerçek hacmini ve maliyetini belirleyebilmek amacıyla çalışmada ekonomi ve verimlilik göstergeleri kullanılmıştır. Su dağıtım sisteminde ekonomik kayıp oranını belirlemek için iki farklı yöntem kullanılmış ve benzer sonuçlar elde edildiği görülmüştür. Çalışma geleceğe yönelik plan ve uygulamaların şekillenmesinde ve yöntemlerin bütçe analizinde faydalı olmuştur. (Farouk vd., 2021) GGS bileşenlerini azaltmaya yönelik stratejilerin incelendiği bu çalışmada su ölçüm sistemlerinin iyileştirilmesi, veri işleme ve sayaç hataları, yasadışı bağlantılardan kaynaklanan görünür kayıplar ile mücadele edildiğinde GGS oranı azaltılır ve gelir artırılır. Gerçek kayıp hacimlerinin azaltılması için ise su sızıntısı önleme, şebeke basıncını kontrol etme ve boruların iyileştirilmesi, rehabilitasyon gibi stratejiler uygulanmaktadır. Aynı zamanda yönetim süreçlerini geliştirmek, teknik personellere eğitim vermek, şebeke performansını izlemek gibi yöntemler de hem gerçek hemde görünür kayıp hacimlerini azaltmaktadır. (Tsitsifli vd., 2017) su dengesi bileşenleri ve performans göstergelerini tahmin ederek su dağıtım şebekelerinin performansını değerlendirmek ve GGS bileşenleri ile mücadele edebilmek için öncelikli bir önlem listesi sunan bir sistem geliştirilmiştir. Bu sistem biri Yunanistan ve biri de Kıbrıs olmak üzere iki su dağıtım şebekesine uygulanmıştır. Önerilen önlemlerden bazıları uygulandığında GGS hacminin ve enerji tüketiminin azaldığı ve para tasarrufu sağlandığı görülmüştür.

Bu çalışmada dağıtım sistemlerinde GGS bileşenlerinin maliyet etkilerinin analiz edilmesi ve değerlendirilmesi için çeşitli performans göstergeleri tanımlanmış ve uygulanmıştır. Göstergelerin sağladığı faydaların ve elde edilen sonuçların yorumlanması ve tartışılması hedeflenmiştir. Bu performans göstergeleri özellikle GGS bileşenlerinin azaltılması için uygulanan yöntemlerin oluşturduğu maliyetlerin izlenmesi açısından önemlidir.

ARAŞTIRMA VE BULGULAR

İçme suyu dağıtım sistemlerinde çeşitli faktörlere bağlı olarak kayıplar meydana gelmektedir. Bu kayıplar, şebeke ve elemanlarında meydana gelen sızıntılar (fiziki kayıplar) ve kaçak kullanımlar veya yasal abone sayaç hatalarından kaynaklanan kayıpları içeren idari kayıplar şeklinde gözlenmektedir (Farley vd., 2008). Ayrıca

dağıtım sistemine verilen ancak ücreti alınamayan ve yasal kullanıcılar tarafından tüketilen suyu içeren yasal faturalandırılmamış kullanımlar da söz konusudur (Pearson, 2019) (Tablo 1)

Tablo 1. Standart su dengesi (Pearson, 2019)

<table>
<tr><td rowspan="8">Sisteme giren hacim (m^3/yıl) (%100)</td><td rowspan="3">Yasal tüketim (m^3/yıl) (%...)</td><td rowspan="2">Faturalandırılmış yasal tüketim (m^3/yıl) (%...)</td><td>Faturandırılmış ölçülmüş kullanım (m^3/yıl) (%...)</td><td rowspan="2">Gelir getiren su (m^3/yıl) (%...)</td></tr>
<tr><td>Faturandırılmış ölçülmemiş kullanım (m^3/yıl) (%...)</td></tr>
<tr><td rowspan="2">Faturalandırılmamış yasal tüketim (m^3/yıl) (%...)</td><td>Faturalandırılmamış ölçülmüş kullanım (m^3/yıl) (%...)</td><td rowspan="7">Gelir getirmeyen su (m^3/yıl) (%...)</td></tr>
<tr><td>Faturalandırılmamış ölçülmemiş kullanım (m3/yıl) (%...)</td></tr>
<tr><td rowspan="5">Su kayıpları (m^3/yıl) (%...)</td><td rowspan="3">İdari kayıplar (m^3/yıl) (%...)</td><td>Yasadışı-kaçak kullanım (m^3/yıl) (%...)</td></tr>
<tr><td>Sayaç hatası (m^3/yıl) (%...)</td></tr>
<tr><td>Okuma hatası (m^3/yıl) (%...)</td></tr>
<tr><td rowspan="3">Fiziki kayıplar (m^3/yıl) (%...)</td><td>İletim hatlarında ve su dağıtım şebekelerindeki ana borulardaki kayıplar (m^3/yıl) (%...)</td></tr>
<tr><td>Depolardaki kaçak, depo giriş ve çıkışında meydana gelen kayıplar (m^3/yıl) (%...)</td></tr>
<tr><td>Servis bağlantıları ile sayaç arasındaki kayıplar (m^3/yıl) (%...)</td></tr>
</table>

Fiziki kayıplar, sisteme verilen suyun abonelere ulaşmadan zemine sızması şeklinde gözlenmektedir. Bu bileşenin yüksek oranlarda gözlenmesi su kaynağı verimsizliğine neden olmaktadır. Ayrıca terfili sistemlerde sızıntı oranının fazla olmasına bağlı olarak enerji maliyetleri de artmaktadır. Bu nedenle bu kayıpların azaltılması ile su üretim ve enerji maliyetlerinin daha etkin ve sürdürülebilir yönetimi mümkün olmaktadır (Ghoneim, 2006). Ayrıca idari kayıplar idareler için doğrudan gelir kaybına neden olmaktadır. Bu nedenle bu bileşenin önlenmesi ile idareler doğrudan gelir elde etmektedir (Canto Ríos vd., 2014). Benzer durum yasal faturalandırılmamış kullanımlar için de geçerlidir. Diğer taraftan GGS bileşenlerinin önlenmesi, azaltılması ve yönetilmesi için uygulanan yöntem veya süreçler çeşitli maliyetler oluşturmaktadır. Özellikle sızıntıların tespit edilmesi, yerinin belirlenmesi ve önlenmesi amacıyla sahada oldukça kapsamlı çalışmaların yapılması gerekmektedir. Bu çalışmalar, ekipman, işçilik, saha imalatları, veri ölçüm ve izleme sistemleri gibi birçok kalemde doğrudan maliyet içermektedir. Bu nedenle bu yöntemler uygulanmadan önce fayda ve maliyetler detaylı analiz edilmelidir. Ayrıca, yöntemler uygulandıktan sonra düzenli olarak verimlilik analizi yapılmalıdır. Bunun için uygun göstergelerin kullanılması oldukça önemlidir.

Bu çalışmada dağıtım sistemlerinde GGS bileşenlerinin maliyet etkilerinin analiz edilmesi ve değerlendirilmesi için çeşitli performans göstergeleri tanımlanmış ve uygulanmıştır (Tablo 2 ve Tablo 3). Bu performans göstergeleri özellikle GGS bileşenlerinin azaltılması için uygulanan yöntemlerin oluşturduğu maliyetlerin izlenmesi açısından önemlidir. Tanımlanan göstergeler pilot idarelerde test edilmiş ve elde edilen sonuçlar değerlendirilmiştir.

Tablo 2. GGS bileşenlerinin maliyet etkilerinin analizi için göstergeler (Bozkurt, 2022)

Kodu	Gösterge Adı	Birim	Gösterge Açıklama
EG-1	İdari Kayıpların Maliyeti (İşletme Gelirine göre)	%	Bu gösterge idari kayıpların maliyetinin toplam işletme gelirine oranını ifade eder. Bu gösterge için idari kayıp hacimleri saha verilerine göre belirlenmelidir. Bu gösterge yıllık olarak izlenmelidir.
EG-2	Fiziki Kayıpların Maliyeti (İşletme Gelirine göre)	%	Bu gösterge fiziki kayıpların maliyetinin toplam işletme gelirine oranını ifade eder. Bu gösterge için fiziki kayıp hacimleri saha verilerine göre belirlenmelidir.
EG-3	Faturalandırılmamış Yasal Kullanımların Maliyeti (İşletme Gelirine göre)	%	Bu gösterge faturalandırılmamış yasal kullanımların maliyetinin toplam işletme gelirine oranını ifade eder. Bu gösterge için faturalandırılmamış yasal kullanımların hacimleri saha verilerine göre belirlenmelidir. Bu gösterge yıllık olarak izlenmelidir.
EG-4	Sayaç Hatalarından Kaynaklı Kayıp Maliyeti (İşletme Gelirine göre)	%	Bu gösterge sayaç hatalarından kaynaklanan kayıpların maliyetinin toplam işletme gelirine oranını ifade eder. Bu gösterge için idari kayıp hacimleri saha verilerine göre belirlenmelidir.
EG-5	GGS Maliyet Oranı (İşletme Gelirine göre)	%	Bu gösterge gelir getirmeyen suyun maliyetinin toplam işletme maliyetine oranını ifade eder. Gelir getirmeyen su doğrudan gelir kaybına neden olduğu için bu kayıpların işletme maliyeti içinde yerinin analiz edilmesi ve gelir getirmeyen suyun azaltılması ile gelirde muhtemel artışın izlenmesi için kullanılabilir.
EG-6	Sızıntı Tespit Verimliliği	%	Bu gösterge sızıntı tespit verimliliğini ifade eder. Bunun için sızıntı tespiti uygulanarak elde edilen kazanımlar, ortaya çıkan maliyetler saha verilerine göre belirlenmelidir.
EG-7	Yasadışı-Kaçak Kullanımların Maliyeti (İşletme Gelirine göre)	%	Bu gösterge kaçak kullanımlardan kaynaklanan kayıpların maliyetinin toplam işletme gelirine oranını ifade eder. Bu gösterge için idari kayıp hacimleri saha verilerine göre belirlenmelidir.

Tablo 3. GGS bileşenlerinin maliyet etkilerinin analizi için göstergeler (Bozkurt, 2022)

Kodu	Performans Göstergesi	Birim	Gerekli Veriler
EG-1	(İdari Kayıpların Maliyeti / Toplam İşletme Geliri) *100/yıl	%	İdari Kayıpların Maliyeti (TL) Toplam İşletme Geliri (TL)
EG-2	(Fiziki Kayıpların Maliyeti / Toplam İşletme Geliri) *100/yıl	%	Fiziki Kayıpların Maliyeti (TL) Toplam İşletme Geliri (TL)
EG-3	(Faturalandırılmamış Yasal Kullanımların Maliyeti / Toplam İşletme Geliri) *100/yıl	%	Faturalandırılmamış Yasal Kullanımların Maliyeti (TL) Toplam İşletme Geliri (TL)
EG-4	(Sayaç Hatalarından Kaynaklı İdari Kayıp Maliyeti / Toplam İşletme Geliri) *100/yıl	%	Sayaç Hatalarından Kaynaklı İdari Kayıp Maliyeti (TL) Toplam İşletme Geliri (TL)
EG-5	Fİ 47: (GGS Maliyeti / Toplam İşletme Maliyeti) *100/yıl	%	GGS Maliyeti / Toplam İşletme Maliyeti (TL) Toplam İşletme Geliri (TL)
EG-6	(Sızıntı Tespit Ekipman-Tespit-İzleme Maliyeti / (Akustik Yöntem Kontrolü ile Tespit Edilen Onarilan Sızıntı Hacmi* Su Üretim Toplam Maliyeti)) *100/yıl	%	Sızıntı Tespit Ekipman-Tespit-İzleme Maliyeti (TL) Akustik Yöntem Kontrolü ile Tespit Edilen Onarilan Sızıntı Hacmi (M3) Su Üretim Toplam Maliyeti (TL)
EG-7	(Yasadışı-Kaçak Kullanımların Maliyeti / Toplam İşletme Geliri) *100/yıl	%	Yasadışı-Kaçak Kullanımların Maliyeti (TL) Toplam İşletme Geliri (TL)

Çalışma kapsamında tabloda verilen performans göstergeleri pilot idarelerden alınan veriler (Tablo 3) kullanılarak değerlendirilmiştir (Tablo 4).

Tablo 3. Performans gösterge hesabında kullanılan veriler

Gerekli Veriler	Birimi	Sistem-1	Sistem-2
İdari Kayıpların Maliyeti (TL)	TL	58863839	39133002
Toplam İşletme Geliri (TL)		552164267	478550000
Fiziki Kayıpların Maliyeti (TL)	TL	57451110	73192000
Faturalandırılmamış Yasal Kullanımların Maliyeti (TL)	TL	81957990	19898000
Sayaç Hatalarından Kaynaklı İdari Kayıp Maliyeti (TL)	TL	39242558	30000000
GGS Maliyeti	TL	194796790	133223002
Sızıntı Tespit Ekipman-Tespit-İzleme Maliyeti (TL)	TL	2440000	3450000
Akustik Yöntem Kontrolü ile Tespit Edilen Onarilan Sızıntı Hacmi (m3)	m3	14690000	8200000
Su Üretim Toplam Maliyeti (TL)		2.45	2.12
Yasadışı-Kaçak Kullanımların Maliyeti (TL)	TL	19621282	9133002

Tablo 4. Performans gösterge hesap sonuçları

Kodu	Gösterge Adı	Birim	Sistem-1	Sistem-2
EG-1	İdari Kayıpların Maliyeti (İşletme Gelirine göre)	%	10.67	8.17
EG-2	Fiziki Kayıpların Maliyeti (İşletme Gelirine göre)	%	10.40	15.30
EG-3	Faturalandırılmamış Yasal Kullanımların Maliyeti (İşletme Gelirine göre)	%	14.84	4.16
EG-4	Sayaç Hatalarından Kaynaklı Kayıp Maliyeti (İşletme Gelirine göre)	%	7.10	6.27
EG-5	GGS Maliyet Oranı (İşletme Gelirine göre)	%	3.55	27.84
EG-6	Sızıntı Tespit Verimliliği	%	6.77	19.84
EG-7	Yasadışı-Kaçak Kullanımların Maliyeti (İşletme Gelirine göre)	%	0.036	1.91

Tablo 3'te sunulan veriler kullanılarak gösterge hesapları yapılmış ve sonuçlar Tablo 4'te verilmiştir. Bu sonuçlar incelendiğinde Sistem 1'in idari kayıplarının maliyeti ve Sistem 2'nin fiziki kayıplarının maliyetinin yüksek olduğu görülmektedir. GGS maliyetinin düşürülebilmesi için öncelikle GGS'yu oluşturan bu bileşenlerin maliyetinin düşürülmesi gerekmektedir. Faturalandırılmamış yasal kullanımların maliyeti incelendiğinde Sistem 2'nin Sistem 1'e göre daha iyi durumda olduğu söylenebilir. Sayaç hatalarından kaynaklı kayıp maliyeti göstergesi incelendiğinde idari kayıpların maliyetinde de olduğu gibi Sistem 1, Sistem 2'ye göre daha yüksek değer almıştır ve bu maliyetler düşürülmelidir. GGS maliyet oranı sistem 1'de %3,55 değerini alırken Sistem 2'de %27,84 değerini almıştır. Toplam işletme gelirine göre hesaplanan bu oranın Sistem 2'de fazla olduğu görülmektedir. Tabloda EG-6 kodu ile ifade edilen sızıntı tespit verimliliği değerleri Sistem 1'de %6,77 iken Sistem 2'de 19,84 olarak hesaplanmıştır. Yüzeye çıkamayan sızıntıların tespit edilmesi ve erken müdahale GGS ile mücadelede oldukça büyük önem taşıdığı için bu değerlerin her iki sistem için de iyileştirilmesi gerekmektedir. Yasadışı-kaçak kullanımların toplam işletme gelirine oranı ile hesaplanan EG-7 kodlu gösterge değeri ise Sistem 2'de daha fazla çıkmıştır. Bu sonuç ta Sistem 2'nin kaçak kullanımlar ile mücadele etmede daha öncelikli davranması gerektiğini göstermektedir. Sonuç olarak tabloda sunulan performans gösterge değerleri GGS hacmini oluşturan faturalandırılmamış izinli tüketim, fiziki kayıplar ve idari kayıpların maliyet analizleri, kaçak kullanım oranları ve sızıntı tespit verimliliği açısından oldukça önemlidir. Bu göstergelerin izlenmesi GGS bileşenlerinin maliyet etkilerinin analizinde ve zayıf olan göstergelerin belirlenerek sistemin öncelikli olarak iyileştirilmesi gereken yönlerinin tespitinde katkı sağlayacağı düşünülmektedir.

SONUÇLAR

Su temin ve dağıtım sistemlerinde tüketiciye ulaştırılmak üzere kaynaktan alınıp şebekeye iletilen ancak ücreti alınamayan sular su kayıplarını oluşturmaktadır. Su kayıpları ise arıza bakım onarım maliyetlerini artırmakta, şebeke işletme koşullarını bozmakta ve kesintili su iletimi gibi teknik sorunlar açığa çıkmaktadır. Böylece

abone şikayetleri artmakta ve hizmet kalitesi düşmektedir. Sisteme verilen ve ücreti tahsil edilemeyen sular Su idarelerinin ortak sorunudur ve çözümü zaman alıcı ve maliyetli işlemleri içermektedir. Bu maliyetler bakım onarım maliyetleri, kayıplardan dolayı satılamayan su maliyeti, su üretim ve sistem işletme maliyetleri, sızıntı tespit ve önleme çalışmaları sırasında oluşan personel, ekipman ve işletme gibi önemli ekonomik etkiler meydana getirmektedir. GGS bileşenlerinin maliyet etkileri ve uygulanan yöntemlerin verimliliğin izlenebilmesi amacıyla bu çalışmada iki pilot sistemden elde edilen ölçülebilir saha verileri kullanılarak GGS bileşenlerinin maliyet analizleri performans göstergeleri yardımıyla hesaplanmış ve sonuçlar incelenmiştir.

Çalışmada GGS bileşenlerinin maliyet etkilerini içeren idari ve fiziki kayıpların maliyeti, faturalandırılmamış yasal kullanımların maliyeti, sayaç hatalarından kaynaklı kayıp maliyeti, GGS maliyet oranı, sızıntı tespit verimliliği ve yasadışı-kaçak kullanımların maliyeti olmak üzere 7 farklı gösterge 2 gerçek sistemden elde edilen veriler doğrultusunda hesaplanmıştır. Sonuçlar incelendiğinde Sistem 1'de idari kayıpların işletme gelirine göre maliyetini ifade eden EG-1 göstergesinin ve Sistem 2'de ise fiziki kayıplarının işletme gelirine göre maliyetini ifade eden EG-2 göstergesinin daha yüksek maliyet oluşturduğu görülmektedir. Ayrıca EG-3 faturalandırılmamış yasal kullanımların işletme gelirine göre hesaplanan maliyeti ise Sistem1'de yüksektir. GGS maliyetlerinin düşürülebilmesi için GGS bileşenlerini oluşturan bu maliyet oranlarının öncelikli olarak azaltılması gerektiği düşünülmektedir.

Sayaç hatalarından kaynaklı kayıp maliyeti göstergesi olan EG-4 göstergesinin Sistem 1 ve Sitem 2'de birbirine yakın sonuçlar verdiği görülmektedir. İdari kayıpların maliyetinin düşürülmesi için idari kayıp bileşeni olan bu göstergenin de iyileştirilmesi gerektiği görülmüştür. GGS'ların işletme gelirine göre maliyet oranını ifade eden EG-5 göstergesinin sırası ile Sistem 1 için %3.55 ve Sistem 2 için %27,84 oranını aldığı görülmüştür. Sistem 2 için bu değerin yüksek olduğu ve iyileştirilmesi gerektiği düşünülmektedir. EG-6 sızıntı tespit verimliliği göstergesi yüzeye çıkamayan suların tespit edilmesi ve arızalara erken müdahale ile su kayıp yönetimi ile mücadelede önemli rol oyanayan bir gösterge olduğu için Sistem 2'de yüksek olan bu oranın düşürülmesi gerekmektedir. Ayrıca yasadışı-kaçak kullanımlar ile mücadele için EG-7 göstergesinin Sistem 2'de iyileştirilmesi gerektiği görülmüştür. Bu çalışma kapsamında incelenen her iki sistem için de ekonomik göstergelerin sistematik bir şekilde izlenmesi gerektiği ve böylece performans göstergelerinin izlenmesi ile GGS bileşen hacimlerinin azaltılması ile su kayıp hacimlerinin ve bütçelerin korunabileceği düşünülmektedir.

TEŞEKKÜR

Bu çalışma TÜBİTAK (Proje No: 220M091) tarafından desteklenmiştir.

KAYNAKLAR

Arregui, F. J., Cobacho, R., Soriano, J., Jimenez-Redal, R. 2018. "Calculation proposal for the economic level of apparent losses (ELAL) in a water supply system". Water (Switzerland), *10*(12).

Cansu Bozkurt, Su kayıp yönetimi ve kontrolü için optimizasyon tabanlı en uygun strateji modelinin geliştirilmesi (Doktora Tezi, İnönü Üniversitesi, 2022;1-205.)

Canto Ríos, J., Santos-Tellez, R. U., Hansen Rodríguez, P., Antúnez Leyva, E., Nava Martínez, V. 2014. "Methodology for the identification of apparent losses in water distribution networks". Procedia Engineering, *70*, 238–247.

Deidda, D., Sechi, G. M., Zucca, R. 2014. "Finding economic optimality in leakage reduction: A cost-simulation approach for complex urban supply systems". Içinde *Procedia Engineering* (C. 70, ss. 477–486).

Farley, M., Wyeth, G., Ghazali, Z. B. M., Istandar, A., Singh, S. 2008. "*The Manager's Non-Revenue Water Handbook. A Guide to Understanding Water Losses*".

Farouk, A. M., Rahman, R. A., Romali, N. S. 2021. "Non-revenue water reduction strategies: a systematic review". Smart and Sustainable Built Environment.

Ghoneim, A. A. 2006. "Design optimization of photovoltaic powered water pumping systems". Energy Conversion and Management, *47*(11–12), 1449–1463.

Mukherjee, M., Chindarkar, N., Grönwall, J. 2015. "Non-revenue water and cost recovery in urban India: The case of Bangalore". Water Policy, *17*(3), 484–501.

Pearson, D. 2019. "*Standard Definitions for Water Losses*". *Standard Definitions for Water Losses*.

SU KAYIPLARININ SÜRDÜRÜLEBİLİR YÖNETİMİ İÇİN İZOLE BÖLGE PERFORMANSININ İZLENMESİ

Cansu BOZKURT

Ardahan Üniversitesi, Teknik Bilimler MYO, İnşaat Bölümü, Ardahan, Türkiye.
ORCID ID: https://orcid.org/0000-0002-0987-1297

Mahmut FIRAT

İnönü Üniversitesi, Mühendislik Fakültesi, İnşaat Mühendisliği Bölümü, Malatya, Türkiye.
ORCID ID: https://orcid.org/0000-0002-8010-9289

Özet

İçme suyu dağıtım sistemlerinde su kayıpları şebeke özelliklerine bağlı olarak çeşitli oranlarda gözlenmektedir. Bu kayıpların azaltılması ile su ve enerji verimliliğin sağlanması mümkün olmaktadır. Su kayıplarının daha etkin yönetilmesi için izole ölçüm bölgelerinin oluşturulması ve sahada uygulanması faaliyetleri önemli katkılar sunmaktadır. İzole ölçüm bölgeleri su kayıplarının azaltılması ve önlenmesi için uygulanan diğer yöntemlere de altlık oluşturmaktadır. Özellikle basınç kontrol yönetimi, aktif sızıntı kontrolü ile sızıntıların yönetimi ve minimum +gece debisi analizi gibi yöntemler için izole ölçüm bölgeleri oldukça önemlidir. Bu nedenle dağıtım sistemlerinde izole bölgelerin planlanması ve sahada aktif bir şekilde uygulanması gerekir. Ancak izole ölçüm bölge faaliyetleri çeşitli maliyetler oluşturmaktadır. Bu maliyetler genel olarak, şebeke verilerinin toplanması, izole bölge planlarının oluşturulması, izolasyon vana yerlerinin ve sayısının belirlenmesi, bölge giriş nokta sayısının ve yerinin belirlenmesi, giriş odası ve izolasyon vanası için saha imalatları ve işçilik maliyetleri şeklindedir. İzole bölgelerin su kayıpları ile mücadelede etkinliğinin test edilmesi ve verimliliğin izlenmesi gerekmektedir. Bunun için en uygun göstergelerin kullanılması önemlidir. Bu çalışmada dağıtım sistemlerinde su kayıplarının sürdürülebilir yönetimi için izole bölge faaliyetlerinin performansının izlenmesi amaçlanmıştır. Bunun için çeşitli göstergeler tanımlanmış ve pilot idareler için test edilmiştir. Tanımlanan göstergeler ile izole ölçüm bölge faaliyetleri ve su kayıp yönetimindeki verimliliğinin izlenmesi hedeflenmiştir. Bu göstergelerin performans analizinde kullanılması ve doğru bir değerlendirme sunması için veri kalitesi oldukça önemlidir. Bunun için pilot idarelerde sadece verisi olan göstergeler analiz edilmiştir. Bu çalışmada kullanılan performans göstergelerinin su kayıp yönetimi ve izole ölçüm bölge faaliyetlerinin performansının izlenmesinde önemli katkı sunacağı düşünülmektedir.

Anahtar Kelimeler: İçme suyu dağıtım sistemi, izole ölçüm bölgeleri, su kayıpları, performans izleme

MONITORING THE PERFORMANCE OF DISTRICT METERED AREA ACTIVITIES FOR SUSTANIABLE MANAGEMENT OF WATER LOSSES

Abstract

Water losses in water distribution systems are observed at various rates depending on the water network properties. By reducing these losses, it is possible to provide water and energy efficiency. In order to manage water losses more effectively, the establishment of district metered areas and their implementation in the field provide important contributions. Reducing and prevention of water losses with district metered areas could be form the basis for other methods. District metered areas are very important especially for methods such as pressure control management, active leak control and management of leaks and minimum night flow analysis. For this reason, district metered areas must be planned and actively applied in the field. However, applications of district metered area brings with various costs. These costs are generally in the form of collection of network data, creation of district metered area plans, determination of isolation valve locations and number, determination of zone entry point number and location, field manufacturing and labor costs for the inlet room and isolation valve. It is necessary to test the effectiveness of district metered areas for water losses and need to monitor the efficiency. For this, it is important to use the most appropriate indicators. In this study, it is

aimed to monitor the performance of district metered area activities for the sustainable management of water losses in distribution systems. Therefore, various indicators have been defined and tested for pilot administrations. With the defined indicators, it is aimed to monitoring of efficiency of the district metered area activities in water loss management. Data quality is very important for these indicators to be used in performance analysis and to provide an accurate assessment. For this purpose, existing data of performance indicators were analyzed in pilot administrations. Consequently, the performance indicators used in this study will make an important contribution to the monitoring of the performance of water loss management and isolated measurement zone activities.

Keywords: Water distribution system, district measurement areas, water losses, performance monitoring

GİRİŞ

İçme suyu dağıtım sistemleri kentsel su yönetiminde kritik öneme sahiptir. Vatandaşlara kaliteli suyun sürdürülebilir bir şekilde iletilmesi için sistemin işletme koşullarının ve performansının düzenli izlenmesi gerekir. Özellikle dağıtım sistemlerinde meydana gelen su kayıplarının önlenmesi ve yönetilmesi için uzun dönemli yöntemler tercih edilmelidir. Bu yöntemlerden en çok kullanılanı aktif kaçak kontrolü metodolojisi gösterilebilir (Moslehi vd., 2021). Aktif kaçak kontrolü temel olarak, izole ölçüm bölgelerinin planlanması (Savić ve Ferrari, 2014), minimum gece debisinin izlenmesi ve analizi (Serafeim vd., 2022) ve sızıntı yerinin tespiti ve onarımı (Steffelbauer vd., 2022) faaliyetlerini kapsamaktadır. Bu faaliyetler sızıntı yönetiminde uzun dönemli kentsel su yönetiminde önemli avantajlar sunmaktadır (Behzadian ve Kapelan, 2015). Ancak bu faaliyetlerin planlanması ve sahada uygulanması sırasında işçilik, boru malzemesi, saha imalatları ve veri izleme gibi çeşitli maliyetler ortaya çıkmaktadır (Farouk vd., 2021). Bu nedenle bu faaliyetlerin denetlenmesi, sağladığı faydaların ve verimliliklerinin izlenmesi oldukça önemlidir (Mutikanga ve Sharma, 2011), (Fantozzi vd., 2014).

İÖB tasarımında bağlantı sayısı, şebeke uzunluğu, performans göstergeleri, aktif kaçak kontrolü maliyetleri, boru çapı ve zemin yüksekliği gibi faktörler İÖB boyutunu etkileyebilmektedir (Gomes vd., 2015). Bu nedenle optimum tasarımı sağlamak önemlidir. (Alvisi ve Franchini, 2014) İÖB tasarımı için kullanılan grafik teorisi kullanılarak optimum çözümü tanımlamak için yeni bir metodoloji geliştirilmiş ve gerçek bir su dağıtım sistemine uygulanmıştır. Sonuçlar maksimum su talebi ve yangın hacimleri de dikkate alındığında esneklik ve minimum basınç şartları açısından en ideal çözümlerin tespit edildiğini göstermektedir. (Gomes vd., 2015) uygun İÖB sayısı ve boyutunu belirleyebilmek için Floyd-Warshall algoritması ve bazı kullanıcı esaslı kriterlere dayalı bir metodoloji geliştirmiştir. Geliştirilen metodoloji gerçek bir su dağıtım şebekesine farklı tasarım kriterleri için uygulanmıştır. Belirli bir su dağıtım sistemi için hidrolik davranış, şebekenin fiziksel özellikleri ve performans göstergelerine göre en uygun tasarım kriterleri belirlemiştir. (Charalambous, 2005) çalışmada İÖB'lerin yeniden boyutlandırılması ve ardından basınç yönetimi uygulaması ile Lemesos Su İdaresi'nde sızıntı seviyelerini düşürmeyi amaçlamıştır. Çalışmada basınç düşürme ve kontrolü ile dağıtım sistemindeki sızıntının ekonomik olarak kabul edilebilir seviyeye düşürülmesi ve etkin bir aktif kaçak yönetimi stratejisi ile bu seviyelerin korunması ile elde edilen kazanımlar sunulmuştur. Sonuçlar uygulanan yöntemlerin talep artışını dengeleme ve maliyet tasarrufunu sağlama konularında faydalı olacağını göstermektedir.

(Savić ve Ferrari, 2014) çalışmada bir su dağıtım şebekesinin davranışını etkileyen parametrelerle ilgili maliyet, güvenirlik ve su kalitesini ölçen performans göstergeleri dikkate alınmıştır. Çalışma için belirlenen göstergeler öncelikle İÖB tasarlanmadan önceki su şebekesine ve İÖB'ler kurulduktan sonraki su şebekesine uygulanmış ve böylece İÖB tasarımının PG'lerine etkisi araştırılmıştır. Hesaplanan performans göstergesi değerleri bir dizi olası çözüm için değerlendirilmiş ve gösterge hedeflerine göre en iyi çözümler belirlenmiştir. (Ferrari ve Savic, 2015) bir su dağıtım sistemi için grafik teorisi ile İÖB sayısı ve büyüklüğüne göre olası çözümler tanımlanmış, İÖB'lerin ekonomik performansı su sızıntısı azaltma, patlama frekansı azaltma ve basınca duyarlı su talebi azaltma gibi faydaları sağlayan performans göstergeleri ile değerlendirilmiş ve olası tüm çözümler için fayda maliyet analizi sunulmuştur. Analiz sonuçlarına göre İÖB'lerin sağlayacağı faydaların İÖB sayısı ve izolasyon vana sayısı ile de bağlantılı olduğu görülmüştür; buna göre İÖB ve izolasyon vana sayısı ne kadar fazla olursa, sızıntı ve basınca duyarlı talep azalması da o kadar az olmaktadır. Bu nedenle İÖB oluşturuken şebekedeki basıncı da azaltmak için basınç yönetimi uygulanmalıdır.

Bu çalışmada dağıtım sistemlerinde su kayıp yönetimi için uygulanan izole ölçüm bölgeleri yönteminin performansının analizi ve değerlendirilmesi için çeşitli performans göstergeleri tanımlanmış ve uygulanmuştur. Göstergelerin sağladığı faydaların ve elde edilen sonuçların yorumlanması ve tartışılması hedeflenmiştir.

ARAŞTIRMA VE BULGULAR

Gelir getirmeyen su (GGS), dağıtım sistemine verilen ancak ücreti alınmayan suyu ifade eder (Pearson, 2019). GGS oranının artması sistemi işletme verimliliğinin bozulmasına neden olmaktadır. Bu nedenle dağıtım sistemlerinde etkin ve sürdürülebilir bir strateji izlenmelidir.

Bu kapsamda izole ölçüm bölgelerinin planlanması ve uygulanması, minimum gece debisi analizi ve sızıntı yerinin tespiti faaliyetlerini kapsayan aktif kaçak kontrolü yaklaşımı sızıntı yönetiminde önemli faydalar sağlamaktadır (Ristovski, 2011).

İzole ölçüm bölgesi (İÖB), diğer şebekelerden ayrılmış (izole edilmiş), su giriş noktası bir veya iki olan ve şebeke bileşenleri kendi içinde değerlendirilen alt ölçüm bölgesi olarak ifade edilebilir (Spedaletti vd., 2022). İÖB yaklaşımının su kayıp yönetiminde beklenen faydayı sağlaması için sürekli izlenmesi ve su kayıp bileşenlerinin analiz edilmesi gerekir. İÖB yaklaşımı, planlama, saha çalışmaları, ekipman kurulum ve işletme maliyetleri önemli oranlara ulaşmaktadır. Bu nedenle İÖB'den en fazlayı faydayı elde etmek için su kayıp bileşenleri için önleme metodolojileri uygulanmalıdır.

İÖB yaklaşımında su, enerji, personel, arıza yönetim, GGS ve sızıntı kapsamında verimlilik değerlendirilmesi yapılması gerekir. Bunun için verisi ölçülebilir göstergelerin kullanılması doğru bir analiz için önemlidir. Literatürde su kayıp yönetimi kapsamında performans analizi için oldukça fazla sayıda gösterge önerilmiştir. Bu kapsamda uluslararası su birliği (IWA) tarafından Su ve Kanal İdarelerinin performansını değerlendirmek için toplam 170 göstergeden oluşan performans değerlendirme sistemi önermiştir (Alegre H., Hirnir W., Baptista J., 2006). Ülkemizde Türkiye Su Enstitüsü (SUEN) kıyaslamalı performans değerlendirme çalışması yapmakta ve idarelerin performansını değerlendirmektedir.

Literatürde önerilen performans göstergeleri ve değerlendirme sistemleri için verilerin kalitesi en önemli konu olarak ortaya çıkmaktadır. Birçok idarede sistem giriş debisinin ölçülmeldiği göz önüne alınırsa oldukça detay çalışma gerektiren verilerin düzenli bir şekilde ölçülmesi ve izlenmesi mümkün olmamaktadır. Bu nedenle performans analizinde verilerin düzenli ve doğru bir şekilde ölçülmesi oldukça önemlidir.

Bu çalışmada idarelerde su kayıp yönetimi kapsamında oluşturulan ve sahada uygulanan İÖB yaklaşımının performansının analizi ve değerlendirilmesi amaçlanmıştır. Bu kapsamda İÖB sızıntı izleme ve yönetimini kapsayan göstergeler tanımlanmıştır (Tablo 1 ve Tablo 2). Tanımlanan göstergeler pilot idarelerde test edilmiş ve elde edilen sonuçlar değerlendirilmiştir.

Tablo 1. Su kayıp yönetiminde İÖB performans analizi için göstergeler (Bozkurt, 2022)

Kodu	Gösterge Adı	Birim	Gösterge Açıklama
PD-1	İzole Bölge Yoğunluğu	%	Bu gösterge sistemde yapılan izole bölge şebeke oranını ifade eder. İzole bölge yöntemi su kayıplarının yönetilmesinde kullanılan en temel yaklaşımdır. Bunun için CBS şebeke veri tabanının güncel olması gerekir. Bu gösterge aylık ve yıllık izlenmelidir.
PD-2	Minimum Gece Debisi İzleme Oranı	%	Bu gösterge sistemde minimum gece debisi izlenen şebeke oranını ifade eder. İzole bölgelerde minimum gece debisi analizi su kayıplarının yönetilmesinde oldukça önemlidir. Bunun için giriş debisinin düzenli ölçülmesi ve CBS şebeke veri tabanının güncel olması gerekir. Bu gösterge aylık ve yıllık izlenmelidir.
PD-3	SCADA ile İzlenen İzole Bölge Oranı	%	Bu gösterge sistemde SCADA ile izlenen izole bölge oranını ifade eder. İzole bölgelerde minimum gece debisi analizi su kayıplarının yönetilmesinde oldukça önemlidir. Bunun için SCADA sisteminin olması ve CBS şebeke veri tabanının güncel olması gerekir. Bu gösterge aylık ve yıllık izlenmelidir.
PD-4	Minimum Gece Debisi Yapılan İzole Bölge Oranı	%	Bu gösterge sistemde minimum gece debisi yapılan izole bölge oranını ifade eder. İzole bölgelerde minimum gece debisi analizi su kayıplarının yönetilmesinde oldukça önemlidir. Bunun için giriş debisinin düzenli ölçülmesi ve CBS şebeke veri tabanının güncel olması gerekir. Bu gösterge aylık ve yıllık izlenmelidir.
PD-5	SCADA ile İzlenen Depo Oranı	%	Bu gösterge sistemde SCADA ile izlenen depo oranını ifade eder. İzole bölgelerde minimum gece debisi analizi su kayıplarının yönetilmesinde oldukça önemlidir. Bunun için SCADA sisteminin olması ve depo bilgilerinin güncel olması gerekir. Bu gösterge aylık ve yıllık izlenmelidir.
PD-6	İzole Bölge Yoğunluğu	%	Bu gösterge sistemde yapılan izole bölge oranını ifade eder. İzole bölge yöntemi su kayıplarının yönetilmesinde kullanılan en temel yaklaşımdır. Bunun için CBS şebeke veri tabanının güncel olması gerekir. Bu gösterge aylık ve yıllık izlenmelidir.
PD-7	Basınç Yönetimi Verimliliği	%	Bu gösterge sistemdeki basınç yönetimi uygulama oranını ifade eder. Bunun için öncelikli olarak sistemde debi-basınç analizine göre basınç yönetimi uygulanması gereken bölge sayısı belirlenmeli, SCADA sistemi ile bölgeler izlenmeli ve CBS şebeke veri tabanı güncel olmalıdır. Basınç yeni arıza oluşumunda ve sızıntılar üzerinde en etkili faktörlerden biri olduğu için yönetilmesi ve verimliliğin izlenmesi önemlidir. Bu gösterge yıllık izlenmelidir.
PD-8	Basınç Yönetimi Verimliliği	%	Bu gösterge sistemdeki basınç yönetimi uygulanan şebeke oranını ifade eder. Bunun için öncelikli olarak sistemde debi-basınç analizine göre basınç yönetimi uygulanması gereken bölge sayısı belirlenmeli, SCADA sistemi ile bölgeler izlenmeli ve CBS şebeke veri tabanı güncel olmalıdır. Basınç yeni arıza oluşumunda ve sızıntılar üzerinde en etkili faktörlerden biri olduğu için yönetilmesi ve verimliliğin izlenmesi önemlidir. Bu gösterge yıllık izlenmelidir.
PD-9	Hidrolik Modeli Yapılmış Bölge Oranı	%	Bu gösterge hidrolik model yapılmış ve kalibre edilmiş izole bölge oranını ifade eder. Bunun için güncel abone yönetim sistemi, CBS şebeke veri tabanı ve SCADA sistemi olmalıdır. Hidrolik model sistemin işletilmesi ve yönetilmesinde önemli avantajlar sunmaktadır. Bu gösterge yıllık olarak izlenmelidir.
PD-10	Hidrolik Modeli Yapılmış Şebeke Oranı	%	Bu gösterge kalibre edilmiş hidrolik model ile izlenen şebeke oranını ifade eder. Bunun için güncel abone yönetim sistemi, CBS şebeke veri tabanı ve SCADA sistemi olmalıdır. Hidrolik model sistemin işletilmesi ve yönetilmesinde önemli avantajlar sunmaktadır. Bu gösterge yıllık olarak izlenmelidir.

Tablo 1. Su kayıp yönetiminde İÖB performans analizi için göstergeler

Kodu	Gösterge Adı	Performans Göstergesi	Birim	Gerekli Veriler
PD-1	İzole Bölge Yoğunluğu	İzole Bölge Yoğunluğu: (İzole Bölge Yapılan Şebeke Uzunluğu (km) / Şebeke Uzunluğu (km)) *100/yıl	%	1-İzole Bölge Yapılan Şebeke Uzunluğu (km) 2-Şebeke Uzunluğu (km)
PD-2	Minimum Gece Debisi İzleme Oranı	Minimum Gece Debisi İzleme Oranı: (Minimum Gece Debisi İzlenen Şebeke Uzunluğu (km) / Şebeke Uzunluğu (km)) *100/yıl	%	1-Minimum Gece Debisi İzlenen şebeke uzunluğu (km) 2- Şebeke Uzunluğu (km)
PD-3	SCADA ile İzlenen İzole Bölge Oranı	(SCADA ile İzlenen İzole Bölge Sayısı / Toplam İzole Bölge Sayısı) *100/yıl	%	1-SCADA ile İzlenen İzole Bölge Sayısı 2-Toplam İzole Bölge Sayısı
PD-4	Minimum Gece Debisi Yapılan İzole Bölge Oranı	(Minimum Gece Debisi Analizi Yapılan İzole Bölge Sayısı/Toplam İzole Bölge Sayısı) *100/yıl	%	1-Minimum Gece Debisi Analizi Yapılan İzole Bölge Sayısı 2-Toplam İzole Bölge Sayısı
PD-5	SCADA ile İzlenen Depo Oranı	(SCADA ile izlenen Depo Sayısı / Toplam Depo Sayısı) *100/yıl	%	1-SCADA ile İzlenen Depo Sayısı 2-Toplam depo sayısı
PD-6	İzole Bölge Yoğunluğu	(Toplam İzole Bölge Sayısı / Yapılması Planlanan Toplam İzole Bölge Sayısı) *100/yıl	%	1-Toplam İzole Bölge Sayısı 2-Yapılması Planlanan Toplam İzole Bölge Sayısı
PD-7	Basınç Yönetimi Verimliliği	Basınç Yönetimi Verimliliği: (Basınç Yönetimi Uygulanan Bölge Sayısı / Basınç Yönetimi Uygulanması Gereken Toplam Bölge Sayısı) *100/yıl	%	1-Basınç Yönetimi Uygulanan Bölge Sayısı 2-Basınç Yönetimi Uygulanması Gereken Toplam Bölge Sayısı
PD-8	Basınç Yönetimi Verimliliği	Basınç Yönetimi Verimliliği: (Basınç Yönetimi Uygulanan Şebeke Uzunluğu/ Şebeke Uzunluğu) *100/yıl	%	1-Basınç Yönetimi Uygulanan Şebeke Uzunluğu (km) 2- Şebeke uzunluğu (km)
PD-9	Hidrolik Modeli Yapılmış Bölge Oranı	(Hidrolik Modeli Yapılmış-Kalibre Edilmiş İzole Bölge Sayısı / Toplam İzole Bölge Sayısı) *100/yıl	%	1-Hidrolik Modeli Yapılmış-Kalibre Edilmiş Şebeke Uzunluğu (km) 2- Şebeke Uzunluğu (km)
PD-10	Hidrolik Modeli Yapılmış Şebeke Oranı	(Hidrolik Model ile İzlenen Şebeke Uzunluğu (km) / Şebeke Uzunluğu (km)) *100/	%	1-Hidrolik Modeli Yapılmış-Kalibre Edilmiş İzole Bölge Sayısı 2-Toplam İzole Bölge Sayısı

Çalışma kapsamında tabloda verilen performans göstergeleri pilot idarelerden alınan veriler (Tablo 3) kullanılarak değerlendirilmiştir (Tablo 4).

Tablo 3. Performans gösterge hesabında kullanılan veriler

Gerekli Veriler	Birimi	Sistem-1	Sistem-2
İzole Bölge Yapılan Şebeke Uzunluğu	km	400	50
Şebeke Uzunluğu	km	4000	5300
Minimum Gece Debisi İzlenen Şebeke Uzunluğu	km	360	50
SCADA ile İzlenen İzole Bölge Sayısı	adet	36	4
Toplam İzole Bölge Sayısı	adet	40	40
Minimum Gece Debisi Analizi Yapılan İzole Bölge Sayısı	adet	30	4
SCADA ile İzlenen Depo Sayısı	adet	16	40
Toplam Depo Sayısı	adet	24	592
Yapılması Planlanan Toplam İzole Bölge Sayısı	adet	120	80
Basınç Yönetimi Uygulanan Bölge Sayısı	adet	8	4
Basınç Yönetimi Uygulanması Gereken Toplam Bölge Sayısı	adet	18	50
Basınç Yönetimi Uygulanan Şebeke Uzunluğu	km	50	50
Hidrolik Modeli Yapılmış-Kalibre Edilmiş Şebeke Uzunluğu	km	100	50
Hidrolik Modeli Yapılmış-Kalibre Edilmiş İzole Bölge Sayısı	adet	10	4

Tablo 4. Performans gösterge hesap sonuçları

Kodu	Gösterge Adı	Birim	Sistem-1	Sistem-2
PD-1	İzole Bölge Yoğunluğu	%	10.0	0.94
PD-2	Minimum Gece Debisi İzleme Oranı	%	9.0	0.94
PD-3	SCADA ile İzlenen İzole Bölge Oranı	%	90.0	10
PD-4	Minimum Gece Debisi Yapılan İzole Bölge Oranı	%	83.3	10
PD-5	SCADA ile İzlenen Depo Oranı	%	66.7	6.8
PD-6	İzole Bölge Yoğunluğu	%	33.3	50.0
PD-7	Basınç Yönetimi Verimliliği	%	44.4	8.0
PD-8	Basınç Yönetimi Verimliliği	%	12.5	0.94
PD-9	Hidrolik Modeli Yapılmış Bölge Oranı	%	25.0	10.0
PD-10	Hidrolik Modeli Yapılmış Şebeke Oranı	%	2.5	0.94

Tabloda verilen sonuçlar incelendiğinde, öncelikli olarak her iki sistemde izole bölge yoğunluğu analiz edilmiştir. Buna göre Sistem-1'de şebeke uzunluğunun %10'u izole ölçüm bölgesi iken Sistem-2'de bu oranı %0,94'dir. Buna göre her iki sistemde de sürdürülebilir su kayıp yönetimi faaliyetleri için bu oranlar iyileştirilmelidir. Benzer şekilde her iki sistemde PD-2 (minimum gece debisi izleme oranı) göstergesinin çok düşük seviyede olduğu tespit edilmiştir. Dağıtım sisteminde yüzeye çıkmayan sızıntıların farkına varılması ve önlenmesi için PD-2 göstergesinin iyileştirilmesi gerekir. Sistem-1'de PD-3 ve PD-4 göstergelerinin iyi düzeyde olduğu görülürken, Sistem -2'de bu göstergeler düşük seviyede kalmıştır.

Tabloda basınç verimliliği göstergeleri (PD-7 ve PD-8) incelendiğinde, her iki sistemde de bu göstergelerin iyileştirilmesi gerekmektedir. Basınç yönetimi, yeni arızaların oluşması ve mevcut arızalarda sızıntıların en aza indirilmesi için uygulanan en temel yaklaşımdır. Tabloda son olarak hidrolik model ile ilgili göstergeler (PD-9 ve PD-10) incelendiğinde, yine bu göstergelerin düşük seviyede kaldığı görülmektedir. Hidrolik model, sistem davranışının anlaşılması, işletme planının oluşturulması ve uygulanması ve sızıntıların anlaşılması

açısından önemli katkılar sunmaktadır. Sonuç olarak tabloda hesaplanan göstergeler, idarede aktif kaçak kontrolü bileşenleri için verimlilik değerlendirilmesi, sızıntı tespit ve önleme yöntemleri ile performans analizi için oldukça önemlidir. Bu göstergelerin sistematik olarak izlenmesi ve zayıf yönlerin tespit edilmesi sistem işletme verimliliğinin iyileştirilmesi açısından katkı sunacaktır.

SONUÇLAR

Su dağıtım sistemlerinde meydana gelen kaçakları hızlı bir şekilde tespit etmek ve erken müdahale ile onarımını sağlayarak, oluşabilecek kayıpları ve maliyetleri önlemek ve sistemleri daha kolay kontrol edebilmek amacıyla birbirinden bağımsız, küçük şebekelere bölme faaliyetleri oldukça önemlidir. Bu çalışmada su dağıtım sistemlerinde meydana gelen kayıpları azaltmak ve etkin bir şekilde su kayıp yönetimini sağlamak amacıyla oluşturulan İÖB'ler ve performansları analiz edilmiştir. Bunun için şebeke fiziksel özellikleri, su kaçaklarının tespiti uygulamaları, basınç verileri, su tüketimleri ve minimum gece debileri gibi İÖB oluşturulması ve yönetiminde önemli rol oynayan 10 performans göstergesi belirlenmiştir. Belirlenen performans göstergelerinin analizinde gerekli olan veriler iki pilot idarenin su dağıtım sistemlerinden elde edilmiş ve idarelerin performansları değerlendirilmiştir. Sonuçlar her iki sistem için de sürdürülebilir kayıp yönetiminin sağlanması için izole bölge yoğunluğu, yüzeye çıkamayan sızıntıların tespiti için minimum gece debisi faaliyetlerinin iyileştirilmesi gerektiğini göstermektedir. Ayrıca sistem 1 için iyi düzeyde olan SCADA ile izlenen ve minimum gece debisi yapılan izole bölge oranını temsil eden PD-3 ve PD-4 göstergelerinin sistem 2 için de iyileştirilmesi gerektiğini göstermiştir. Son olarak basınç verimliliği (PD-7 ve PD-8) ve hidrolik model göstergeleri (PD-9 ve PD-10) göstergelerinin her iki sistem için de yetersiz düzeyde olduğu ve sızıntı analizinin etkin bir şekilde sağlanması için iyileştirilmesi gerektiği görülmektedir. Çalışmada iki gerçek sistem için tasarlanan İÖB'lerinin performans analizi yapılmış ve sonuçlar sunulmuştur. Bu çalışmanın İÖB'lerin etkin bir şekilde izlenmesi ve sürdürülebilir su kayıp yönetiminin sağlanması amacıyla sistem performanslarının analiz edilmesi ve öncelikli olarak iyileştirilmesi gereken göstergelerin belirlenmesinde katkı sağlayacağı düşünülmektedir.

TEŞEKKÜR

Bu çalışma TÜBİTAK (Proje No: 220M091) tarafından desteklenmiştir.

KAYNAKLAR

Alegre H., Hirnir W., Baptista J., P. R. 2006. "*Performance Indicators for Water Supply Services*". Tarihinde adresinden erişildi https://books.google.com/books?id=nfSZiheXeRsC&pgis=1

Alvisi, S., Franchini, M. 2014. "A procedure for the design of district metered areas in water distribution systems". Procedia Engineering, *70*, 41–50.

Behzadian, K., Kapelan, Z. 2015. "Advantages of integrated and sustainability based assessment for metabolism based strategic planning of urban water systems". Science of the Total Environment, *527–528*, 220–231.

Cansu Bozkurt, Su kayıp yönetimi ve kontrolü için optimizasyon tabanlı en uygun strateji modelinin geliştirilmesi (Doktora Tezi, İnönü Üniversitesi, 2022;1-205.)

Charalambous, B. 2005. "Experiences in DMA redesign at the Water Board of Lemesos, Cyprus". Leakage 2005, 1–11.

Fantozzi, M., Popescu, I., Farnham, T., Archetti, F., Mogre, P., Tsouchnika, E., … Bimpas, M. 2014. "ICT for efficient water resources management: The ICeWater energy management and control approach". Procedia Engineering, *70*, 633–640.

Farouk, A. M., Rahman, R. A., Romali, N. S. 2021. "Economic analysis of rehabilitation approaches for water distribution networks: comparative study between Egypt and Malaysia". Journal of Engineering, Design and Technology.

Ferrari, G., Savic, D. 2015. "Economic performance of DMAs in water distribution systems". Procedia Engineering, *119*(1), 189–195.

Gomes, R., Sousa, J., Muranho, J., Marques, A. S. 2015. "Different design criteria for district metered areas in water distribution networks". Procedia Engineering, *119*(1), 1221–1230.

Moslehi, I., Jalili-Ghazizadeh, M., Yousefi-Khoshqalb, E. 2021. "Developing a framework for leakage target setting in water distribution networks from an economic perspective". Structure and Infrastructure Engineering, *17*(6), 821–837.

Mutikanga, H. E., Sharma, S. K. 2011. "Multi-criteria Decision Analysis : A Strategic Planning Tool for Water Loss Management", *101*, 3947–3969.

Pearson, D. 2019. "*Standard Definitions for Water Losses*". *Standard Definitions for Water Losses*.

Ristovski, B. 2011. "Pressure management and active leakage control in particular DMA (Lisiche) in the city of Skopje , FYROM". Water Utility Journal 2, (Figure 1), 45–49.

Savić, D., Ferrari, G. 2014. "Design and performance of district metering areas in water distribution systems". Procedia Engineering, *89*, 1136–1143.

Serafeim, A. V., Kokosalakis, G., Deidda, R., Karathanasi, I., Langousis, A. 2022. "Probabilistic estimation of minimum night flow in water distribution networks: large-scale application to the city of Patras in western Greece". Stochastic Environmental Research and Risk Assessment, *36*(2), 643–660.

Spedaletti, S., Rossi, M., Comodi, G., Cioccolanti, L., Salvi, D., Lorenzetti, M. 2022. "Improvement of the energy efficiency in water systems through water losses reduction using the district metered area (DMA) approach". Sustainable Cities and Society, *77*(October 2021).

Steffelbauer, D. B., Deuerlein, J., Gilbert, D., Abraham, E., Piller, O. 2022. "Pressure-Leak Duality for Leak Detection and Localization in Water Distribution Systems". Journal of Water Resources Planning and Management, *148*(3), 1–13.

STRUCTURAL PERFORMANCE ASSESSMENT OF THE HISTORICAL TOMB OF EMİR SALTUK

Bora AKSAR

Dr., Isik University, Faculty of Engineering and Natural Sciences, Department of Civil Engineering, Istanbul, Turkey., ORCID NO: 0000-0002-9972-5516

Ali Ikbal TUTAR

Research Assistant, Gebze Technical University, Faculty of Engineering, Department of Civil Engineering, Kocaeli, Turkey., ORCID NO: 0000-0003-2577-075X

Vesile Hatun AKANSEL

Dr., Mugla Sitki Kocman University, Faculty of Engineering, Department of Civil Engineering, Mugla, Turkey., ORCID NO: 0000-0003-3152-1215

Ferit CAKIR

Prof. Dr., Gebze Technical University, Faculty of Engineering, Department of Civil Engineering, Kocaeli, Turkey., ORCID NO: 0000-0002-9641-2004

ABSTRACT

Throughout history, people have respected the dead of their loved ones and built various tombs and monumental works for them. Monumental tombs, which were designed as mausoleums and cupolas in the Islamic era, have great importance in Islamic art. In many regions of Anatolia, there are many cupolas with different designs built for different people. Emir Saltuk Tomb or Mausoleum of Emir Saltuk, which is among the most beautiful examples of monumental tombs in Anatolia, is one of the most important structures of the Saltuks period in Erzurum, Turkey. The tomb, which is estimated to have been built in the second half of the 12th century, has an octagonal body, and a high pulley and is covered with a dome and a conical cone. Although the roof was replaced in 1956, the building has been well preserved. However, it is still necessary to examine the structural performance and seismic behavior of this historical monument and to strengthen the damaged parts, if any, with appropriate techniques. It is very important to safely transfer historical artifacts, which are the common heritage of humanity, to future generations. This study focused on the structural performance of the historical tomb. For this purpose, a three-dimensional finite element model of the structure was prepared and the performance of the structure was examined by conducting static and dynamic analyzes.

Keywords: Masonry Structures, Emir Saltuk Tomb, Masonry Tomb, Structural Performance, Finite Element Method, Static Analysis, Modal Analysis, Response Spectrum Analysis

INTRODUCTION

From the beginning of civilization different kinds of structures have been used for venerating the dead and honing their memories. Tombs are often used as funerary structures in Anatolia throughout history. This tradition goes back to central Asia. According to the Chinese source, Gokturks mummified the dead and kept bodies in a funerary tent before burying them (Kapusuzoğlıu, 2015). In Islamic geography, such monumental structures are also known by names such as cupola, maqam, buk'a, darih, or dome, apart from the tomb. These concepts can be used interchangeably, or they can be named according to the rank and position of the people buried in these buildings, their social, political, or religious position, or the architectural features of the building. The earliest tomb that still exists is the Kubbetü's-Suleybiye (892-902) built for Muntasir Billah by his mother nearby Samerra (Tokuz, 2019). The structure has a cuboid shape built of brick. Four small ovoid domes are placed on top of each rounded corner. Following the construction of this building, some monumental structures were constructed in the Islamic communities such as Sâmânoğlu İsmail Tomb in Bukhara, Uzbekistan (907-914), Künbet-i Kabus Tomb in Gurgan, Iran (1006-1007) ve Sultan Sencer Tomb in Merv, Turkmenistan (1157) (Tokuz, 2019). If some examples are given to some tombs in Turkey, the best examples can be listed as: Emir Saltuk Tomb in Erzurum, Mama Hatun Tomb in Tercan, Ebu 'l Kasım Tomb in Tokat,

Melik Gazi Tomb in Kırşehir, Gömeç Hatun Tomb in Konya, Boyalıköy and Saya Baba Tombs located in Afyon, Turumtay Tomb in Amasya. Döner Tomb in Kayseri and Yeşil Tomb in Bursa (Fig.1).

In the Qarakhanid Dynasty (Karahanlılar), tombs containing brick materials and rich ornamental elements were constructed under regional conditions; these decorative elements also influenced tombs built during the Great Seljuk period. These tombs are usually square and dome-shaped with square planning (Tokuz, 2019). In the Anatolian Seljuk, the tombs have two main groups. The first group consists of a square, polygonal or circular upper chamber covered by a tetrahedral, polyhedral, or conical dome. In the second group, the general shape of tombs are rectangular and have eyvan-shaped prayer rooms. The second group consists of rectangular tombs whose prayer rooms take the form of an eyvan. Northeastern Turkey host most of the earliest Anatolian tombs. Melik Gazi and Hacı Çıkrık located in Niksar are examples of two earliest Anatolian tombs from the twelfth century. Melik Gazi is a brick-rubble structure. On the other hand, Hacı Çıkrık is a cut stone- rubble structure. They both have a tetrahedral dome with a square chamber.

Historical tombs have been studied from many perspectives, including theology, architecture, ornamental arts, and sociology. However, it is not well known how these structures perform structurally or how they behave during earthquakes.

Therefore, this study focuses on the structural performance of the masonry tombs. The main purpose of this study is to examine the structural performance of the Emir Saltuk Tomb located in the south of the city center of Erzurum.

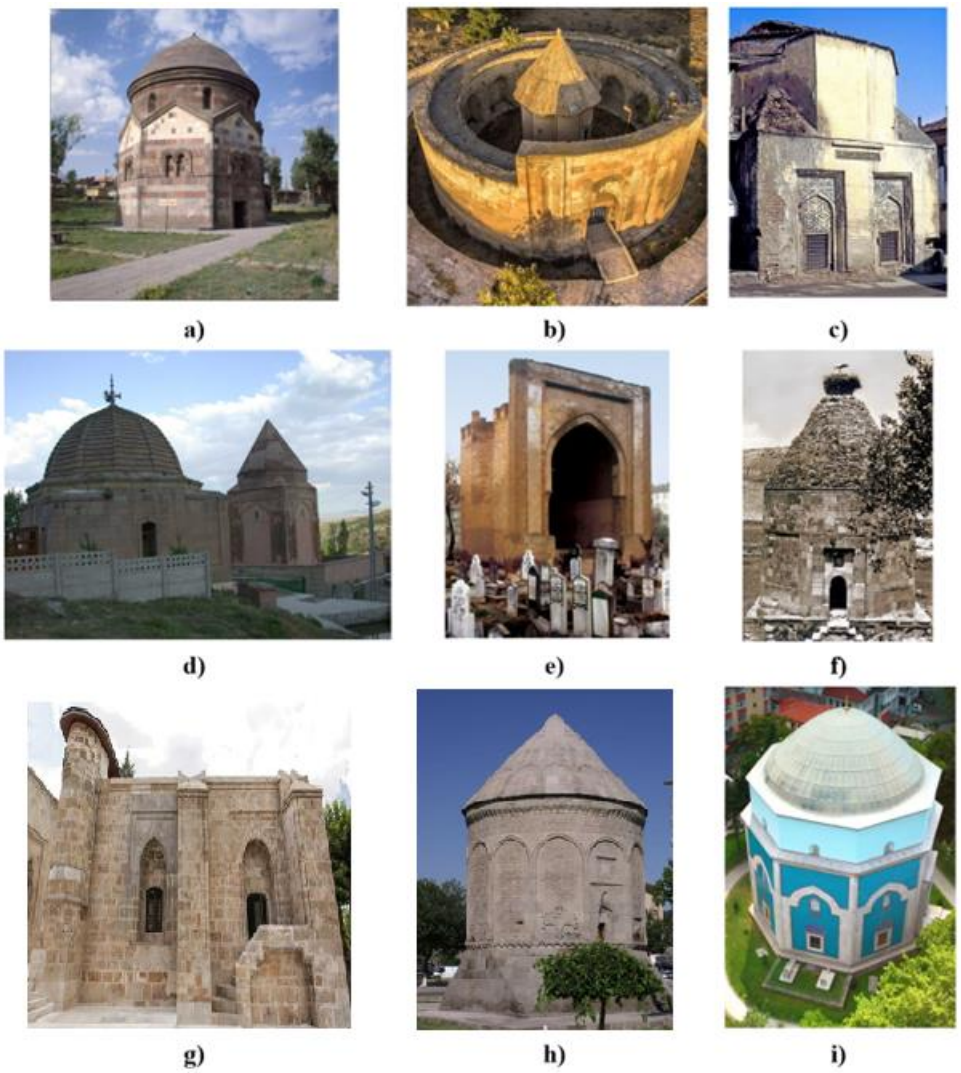


Fig. 1. a) Kümbet of Emir Saltuk, Erzurum (https://archives.saltresearch.org/handle/123456789/6807)

b) Türbe of Mama Hatun, Tercan (https://galeri.uludagsozluk.com/r/mama-hatun-k%C3%BClliyesi-2124520)
c) Türbe of Ebu'l Kasım, Tokat (http://islam-portal.com/ansiklopedi/dia/ayrmetin.php-idno=100335.htm)
d) Türbe of Melik Gazi, Kırşehir (https://www.kulturportali.gov.tr/turkiye/kayseri/gezilecekyer/melikgazi-turbesi)
e) Türbe of Gömeç Hatun, Konya (https://islamansiklopedisi.org.tr/gomec-hatun-turbesi)
f) Türbe of Boyalıköy, Afyon (https://islamansiklopedisi.org.tr/boyalikoy-kulliyesi)
g) Türbe of Turumtay, Amasya (https://www.kulturportali.gov.tr/turkiye/amasya/gezilecekyer/torumtay-turbes)
h) Döner Kümbet, Kayseri (https://www.kulturportali.gov.tr/turkiye/kayseri/gezilecekyer/doner-kumbet)
i) Yeşil Tomb, Bursa (https://www.bursa.com.tr/tr/mekan/yesil-turbe-42/)

HISTORICAL EMIR SALTUK TOMB

Erzurum is among the major historical centers in eastern Anatolia, Turkey. Due to its natural, historical, and archeological assets, it is considered a valuable ancient city not only in Turkey but around the world. Throughout its history, the city has been conquered by many ancient civilizations along the historical Silk Road. Historically, it has been an important center for the Roman Empire, the Byzantine Empire, Persia, Armenia, and Turkish civilizations (Cakir and Uysal, 2014). There has been a history and culture in Erzurum for almost 7000 years. In the ancient city, different architectural styles and cultural effects have been imposed over the centuries. As a result, it has a very rich cultural and historical heritage. Among these historical structures in the city is Emir Saltuk Tomb. Emir Saltuk (or Saltuk Bey) was the founder of the Saltuklu Principality, one of the first Turkish principalities established in Anatolia. It is thought that the tomb was built after Emir Saltuk's death and this is where Emir Saltuk's mausoleum is located (Gedik, 2022).

Based on its architectural style, Emir Saltuk Tomb is dated to the twelfth century. Although the dome section of the structure was restored in 1956, it has been well preserved through centuries. Türbe of Emir Saltuk is an octagonal structure. Façade of the türbe covered by alternating squares of light-colored and red stones. Darker colored stones are used on all façades except four sides. The tomb is a two-story structure. The upper chamber can be reached by the door on the northern wall, while access to the lower chamber is from inside. The lower chamber has a 5.4-meter by 4.26-meter rectangular room covered by an arch of stone blocks and no windows or openings aside from the entrance (Fig. 2).

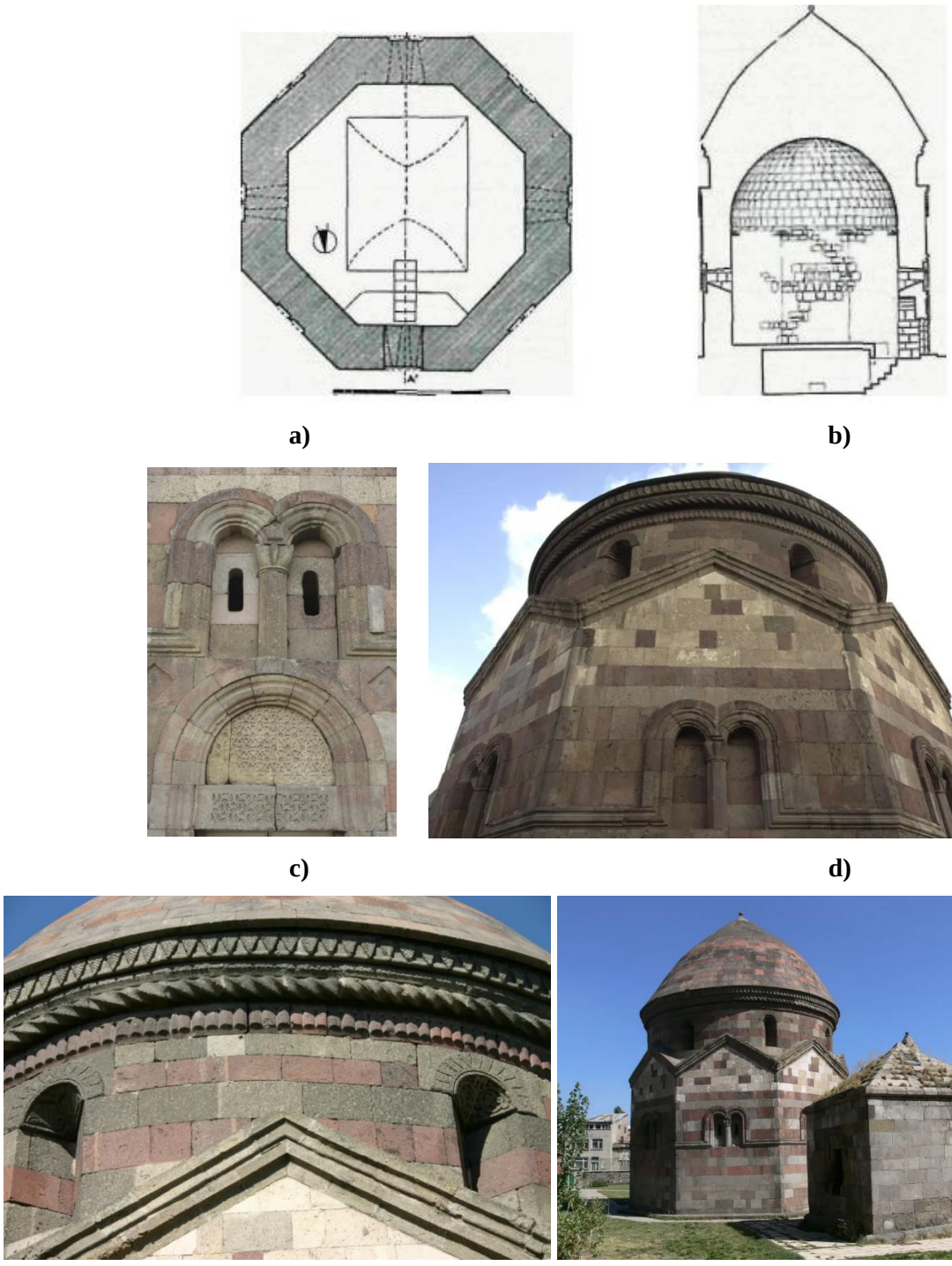


Fig. 2. Details from Emir Saltuk Tomb (https://www.sanatinyolculugu.com/anadolunun-ilk-turbesi-emir-saltuk/)

NUMERICAL MODEL AND STRUCTURAL ANALYSES

The three-dimensional and numerical models were prepared using ANSYS Workbench Software. SOLID 65 elements with eight nodes and three degrees of freedom per node were selected for the modeling process. A numerical model consisting of 165110 nodes and 96533 solid elements is shown in Fig. 3. In this study, Static, Modal, and Response Spectrum Analyses were performed on the numerical model. In order to present the results of the analysis, contour pictures, bars, and scale tables were used. Furthermore, the foundation sections were designed with fixed boundary conditions. Table 1 lists the mechanical properties used in the numerical analyses.

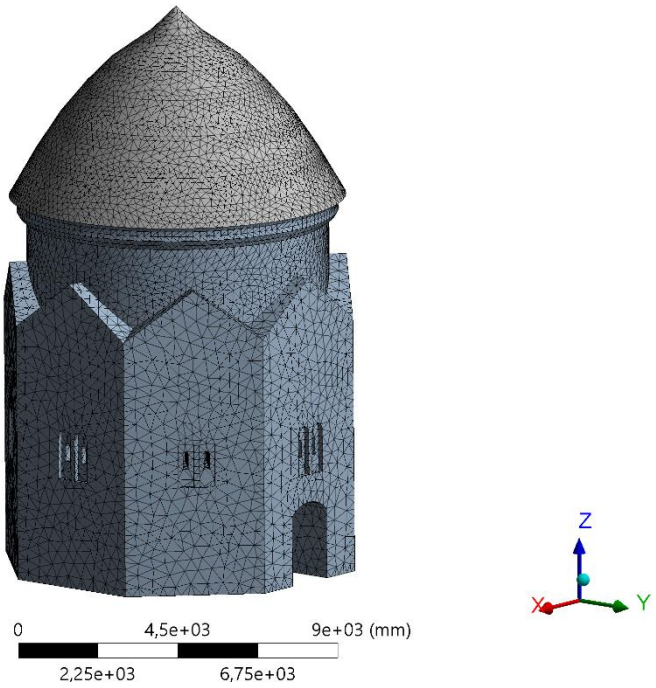


Fig. 3. Finite Element Model of Emir Saltuk Tomb

Table 1. Mechanical properties of the materials

Specimen	Density (kg/m^3)	Poisson's Ratio	Modulus of Elasticity (MPa)	Bulk Modulus (MPa)	Shear Modulus (MPa)
Masonry Walls	2300	0,234	34006,5	21300	13780
Roof	1400	0,33	10636,4	10400	4000

In the modeling and analyzing phase, the following parameters were used:

1. In the modal analysis, 30 modes were considered, and the first 30 modes were emphasized to account for more effective total mass participation in three orthogonal directions.
2. Response spectrum analysis was used in the dynamic analyses, and earthquake data were obtained from Turkish Earthquake Hazard Maps (https://tadas.afad.gov.tr) according to the actual location of the tomb.
3. The DD-2 earthquake (standard design earthquake) is considered the ground motion level. (DD-2 Earthquake: A ground motion level with a recurrence period of 475 years and a 10% probability of exceedance in 50 years.) ZB class was chosen as the soil class (ZB soil class: less weathered, moderately strong rocks)

STATIC ANALYSIS

Firstly, static analysis was performed considering only the own weight of the structure. According to the analysis results, the maximum displacement is obtained as 0.075 mm in the top section of the tomb (Fig. 4). The maximum principal stresses obtained as 0,31 MPa, and the minimum principal stresses obtained as -0,81 MPa (Fig. 5). When it was looking at the places where the principal stresses occur, it was seen that the stresses generally occur around the triangular transition elements located under the dome.

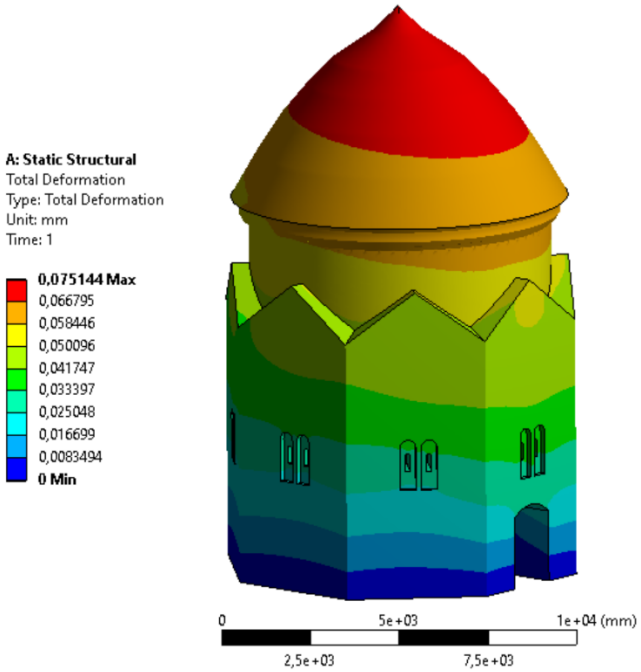


Fig. 4. Maximum displacements observed in structure (mm)

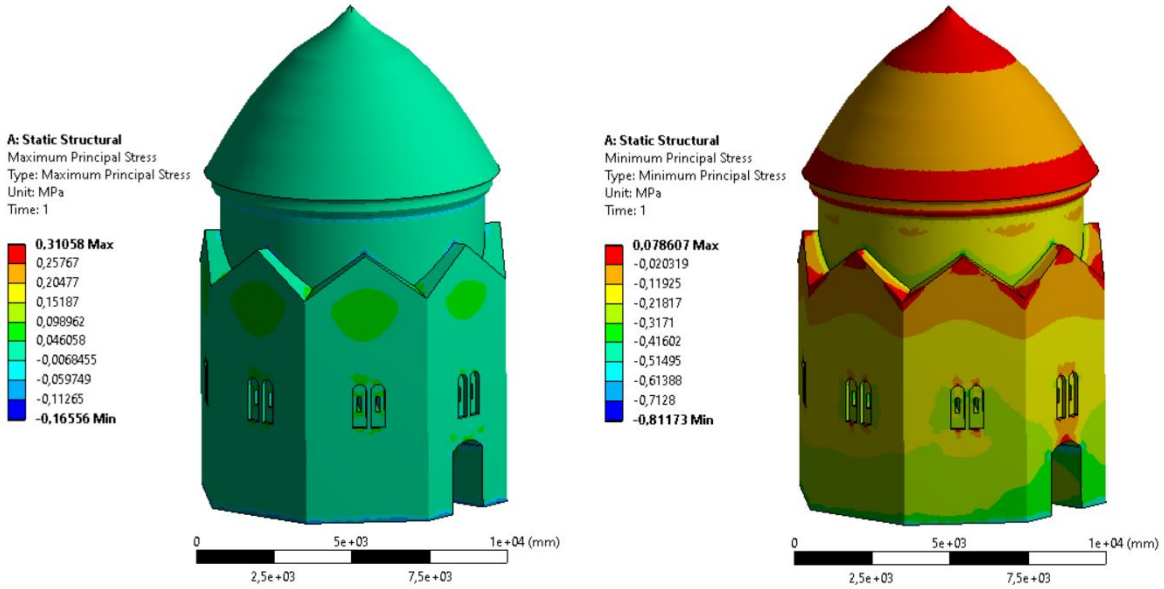


Fig. 5. Maximum and minimum principal stresses observed in structure (MPa)

MODAL ANALYSIS

During the dynamic analysis phase, modal analysis was performed to determine the free vibration modes. In order to understand the dynamic characteristics of a structure, frequency values, and mode shapes are very important. To achieve more effective total mass participation in three orthogonal directions, solutions were made in 30 modes. Table 2-4 shows the frequency values for the first three dominant mode shapes and the mass participation ratios calculated taking into account all mode shapes. Moreover, the first six mode shapes are given in Fig. 6.

Table 2. The frequency values and mass participation ratios (X direction)

MODE	FREQUENCY	PERIOD	PARTIC.FACTOR	RATIO	EFFECTIVE MASS	CUMULATIVE MASS	RATIO EFF.MASS TO TOTAL MASS
1	24.1648	0.41382E-01	-0.29072	0.010614	0.845192E-01	0.817448E-04	0.688269E-04
2	24.2670	0.41208E-01	27.391	1.000000	750.294	0.725747	0.610990
3	52.6593	0.18990E-01	-0.60212	0.021982	0.362543	0.726097	0.295231E-03
4	67.2637	0.14867E-01	0.71805E-02	0.000262	0.515591E-04	0.726098	0.419864E-07
5	75.1646	0.13304E-01	-12.749	0.465451	162.547	0.883309	0.132368
6	77.1392	0.12964E-01	0.33231E-01	0.001213	0.110429E-02	0.883310	0.899265E-06
7	79.3937	0.12595E-01	-0.63803E-01	0.002329	0.407088E-02	0.883314	0.331506E-05
8	79.4650	0.12584E-01	4.0777	0.148868	16.6277	0.899396	0.135405E-01
9	117.469	0.85129E-02	6.1153	0.223255	37.3966	0.935565	0.304533E-01
10	118.006	0.84741E-02	0.15106E-01	0.000551	0.228202E-03	0.935565	0.185833E-06
11	125.694	0.79559E-02	0.72673	0.026531	0.528134	0.936076	0.430078E-03
12	125.744	0.79527E-02	-0.42411E-01	0.001548	0.179872E-02	0.936078	0.146476E-05
13	130.495	0.76631E-02	-0.51774	0.018902	0.268058	0.936337	0.218289E-03
14	132.255	0.75611E-02	0.61161E-03	0.000022	0.374071E-06	0.936337	0.304619E-09
15	133.162	0.75096E-02	-0.44612E-02	0.000163	0.199027E-04	0.936337	0.162074E-07
16	145.997	0.68495E-02	0.60010E-02	0.000219	0.360117E-04	0.936337	0.293256E-07
17	147.624	0.67740E-02	5.7121	0.208535	32.6278	0.967894	0.265699E-01
18	148.149	0.67500E-02	-0.71991E-02	0.000263	0.518266E-04	0.967894	0.422042E-07
19	161.121	0.62065E-02	0.70431E-03	0.000026	0.496050E-06	0.967894	0.403951E-09
20	169.293	0.59069E-02	0.22064E-02	0.000081	0.486840E-05	0.967894	0.396451E-08
21	171.534	0.58298E-02	-0.14027E-01	0.000512	0.196760E-03	0.967894	0.160228E-06
22	171.995	0.58141E-02	-5.6879	0.207653	32.3525	0.999185	0.263458E-01
23	177.017	0.56492E-02	0.38730E-02	0.000141	0.150002E-04	0.999185	0.122152E-07
24	177.238	0.56421E-02	-0.55822	0.020379	0.311615	0.999486	0.253759E-03
25	186.797	0.53534E-02	-0.71372	0.026056	0.509400	0.999979	0.414822E-03
26	187.248	0.53405E-02	-0.14823E-01	0.000541	0.219734E-03	0.999979	0.178937E-06
27	190.298	0.52549E-02	-0.27981E-02	0.000102	0.782910E-05	0.999979	0.637551E-08
28	192.270	0.52010E-02	0.14307	0.005223	0.204690E-01	0.999999	0.166686E-04
29	195.976	0.51027E-02	0.34703E-01	0.001267	0.120427E-02	1.00000	0.980680E-06
30	197.639	0.50597E-02	-0.80293E-03	0.000029	0.644703E-06	1.00000	0.525004E-09

Table 3. The frequency values and mass participation ratios (Y direction)

MODE	FREQUENCY	PERIOD	PARTIC.FACTOR	RATIO	EFFECTIVE MASS	CUMULATIVE MASS	RATIO EFF.MASS TO TOTAL MASS
1	24.1648	0.41382E-01	27.083	1.000000	733.488	0.715169	0.597305
2	24.2670	0.41208E-01	0.28744	0.010613	0.826216E-01	0.715250	0.672816E-04
3	52.6593	0.18990E-01	-0.43542E-02	0.000161	0.189591E-04	0.715250	0.154391E-07
4	67.2637	0.14867E-01	0.73801	0.027250	0.544656	0.715781	0.443532E-03
5	75.1646	0.13304E-01	-0.31648E-01	0.001169	0.100159E-02	0.715782	0.815628E-06
6	77.1392	0.12964E-01	-13.281	0.490389	176.390	0.887767	0.143641
7	79.3937	0.12595E-01	2.3293	0.086008	5.42583	0.893057	0.441844E-02
8	79.4650	0.12584E-01	0.42977E-01	0.001587	0.184701E-02	0.893059	0.150409E-05
9	117.469	0.85129E-02	-0.13849E-01	0.000511	0.191800E-03	0.893059	0.156189E-06
10	118.006	0.84741E-02	6.2315	0.230089	38.8316	0.930921	0.316219E-01
11	125.694	0.79559E-02	-0.31415E-01	0.001160	0.986896E-03	0.930922	0.803664E-06
12	125.744	0.79527E-02	-0.50195	0.018534	0.251957	0.931168	0.205178E-03
13	130.495	0.76631E-02	0.12083E-02	0.000045	0.145988E-05	0.931168	0.118883E-08
14	132.255	0.75611E-02	0.80108E-01	0.002958	0.641730E-02	0.931174	0.522583E-05
15	133.162	0.75096E-02	0.30785E-03	0.000011	0.947725E-07	0.931174	0.771766E-10
16	145.997	0.68495E-02	2.9872	0.110297	8.92319	0.939874	0.726647E-02
17	147.624	0.67740E-02	0.81657E-04	0.000003	0.666783E-08	0.939874	0.542984E-11
18	148.149	0.67500E-02	5.2072	0.192269	27.1151	0.966312	0.220808E-01
19	161.121	0.62065E-02	-0.11921	0.004402	0.142121E-01	0.966326	0.115734E-04
20	169.293	0.59069E-02	0.76329E-01	0.002818	0.582608E-02	0.966332	0.474438E-05
21	171.534	0.58298E-02	-5.7633	0.212800	33.2151	0.998717	0.270482E-01
22	171.995	0.58141E-02	0.10462E-01	0.000386	0.109462E-03	0.998717	0.891390E-07
23	177.017	0.56492E-02	-0.98991	0.036551	0.979921	0.999673	0.797983E-03
24	177.238	0.56421E-02	-0.40028E-02	0.000148	0.160223E-04	0.999673	0.130475E-07
25	186.797	0.53534E-02	0.14746E-01	0.000544	0.217442E-03	0.999673	0.177070E-06
26	187.248	0.53405E-02	-0.55879	0.020632	0.312241	0.999978	0.254269E-03
27	190.298	0.52549E-02	0.14193	0.005241	0.201451E-01	0.999997	0.164049E-04
28	192.270	0.52010E-02	0.90638E-02	0.000335	0.821523E-04	0.999997	0.668995E-07
29	195.976	0.51027E-02	0.41515E-03	0.000015	0.172350E-06	0.999997	0.140351E-09
30	197.639	0.50597E-02	0.52952E-01	0.001955	0.280397E-02	1.00000	0.228337E-05

Table 4. The frequency values and mass participation ratios (Z direction)

MODE	FREQUENCY	PERIOD	PARTIC.FACTOR	RATIO	EFFECTIVE MASS	CUMULATIVE MASS	RATIO EFF.MASS TO TOTAL MASS
1	24.1648	0.41382E-01	-0.35542	0.012525	0.126322	0.134254E-03	0.102869E-03
2	24.2670	0.41208E-01	-0.23955E-02	0.000084	0.573846E-05	0.134260E-03	0.467302E-08
3	52.6593	0.18990E-01	-0.97329E-02	0.000343	0.947298E-04	0.134360E-03	0.771417E-07
4	67.2637	0.14867E-01	28.376	1.000000	805.189	0.855879	0.655693
5	75.1646	0.13304E-01	0.21018E-01	0.000741	0.441745E-03	0.855880	0.359728E-06
6	77.1392	0.12964E-01	0.71598	0.025232	0.512632	0.856425	0.417454E-03
7	79.3937	0.12595E-01	-0.40754	0.014362	0.166090	0.856601	0.135253E-03
8	79.4650	0.12584E-01	-0.53182E-02	0.000187	0.282829E-04	0.856601	0.230317E-07
9	117.469	0.85129E-02	-0.48723E-03	0.000017	0.237392E-06	0.856601	0.193317E-09
10	118.006	0.84741E-02	0.67590E-01	0.002382	0.456843E-02	0.856606	0.372023E-05
11	125.694	0.79559E-02	-0.24103E-02	0.000085	0.580950E-05	0.856606	0.473088E-08
12	125.744	0.79527E-02	-0.33382E-01	0.001176	0.111434E-02	0.856607	0.907447E-06
13	130.495	0.76631E-02	-0.85411E-03	0.000030	0.729508E-06	0.856607	0.594064E-09
14	132.255	0.75611E-02	-0.81954E-01	0.002888	0.671650E-02	0.856614	0.546948E-05
15	133.162	0.75096E-02	0.99777E-03	0.000035	0.995550E-06	0.856614	0.810711E-09
16	145.997	0.68495E-02	8.5030	0.299658	72.3018	0.933456	0.588778E-01
17	147.624	0.67740E-02	-0.18487E-01	0.000652	0.341771E-03	0.933456	0.278316E-06
18	148.149	0.67500E-02	-4.6365	0.163397	21.4975	0.956303	0.175061E-01
19	161.121	0.62065E-02	4.1307	0.145570	17.0624	0.974437	0.138945E-01
20	169.293	0.59069E-02	4.6701	0.164579	21.8096	0.997616	0.177603E-01
21	171.534	0.58298E-02	0.68329E-01	0.002408	0.466883E-02	0.997621	0.380199E-05
22	171.995	0.58141E-02	0.10622E-02	0.000037	0.112830E-05	0.997621	0.918816E-09
23	177.017	0.56492E-02	0.32910	0.011598	0.108305	0.997736	0.881967E-04
24	177.238	0.56421E-02	0.13333E-02	0.000047	0.177759E-05	0.997736	0.144755E-08
25	186.797	0.53534E-02	-0.55526E-02	0.000196	0.308315E-04	0.997736	0.251072E-07
26	187.248	0.53405E-02	0.17959	0.006329	0.322515E-01	0.997770	0.262635E-04
27	190.298	0.52549E-02	-0.66394E-01	0.002340	0.440816E-02	0.997775	0.358972E-05
28	192.270	0.52010E-02	-0.46831E-02	0.000165	0.219313E-04	0.997775	0.178594E-07
29	195.976	0.51027E-02	0.42156E-03	0.000015	0.177710E-06	0.997775	0.144716E-09
30	197.639	0.50597E-02	-1.4469	0.050990	2.09346	1.00000	0.170478E-02

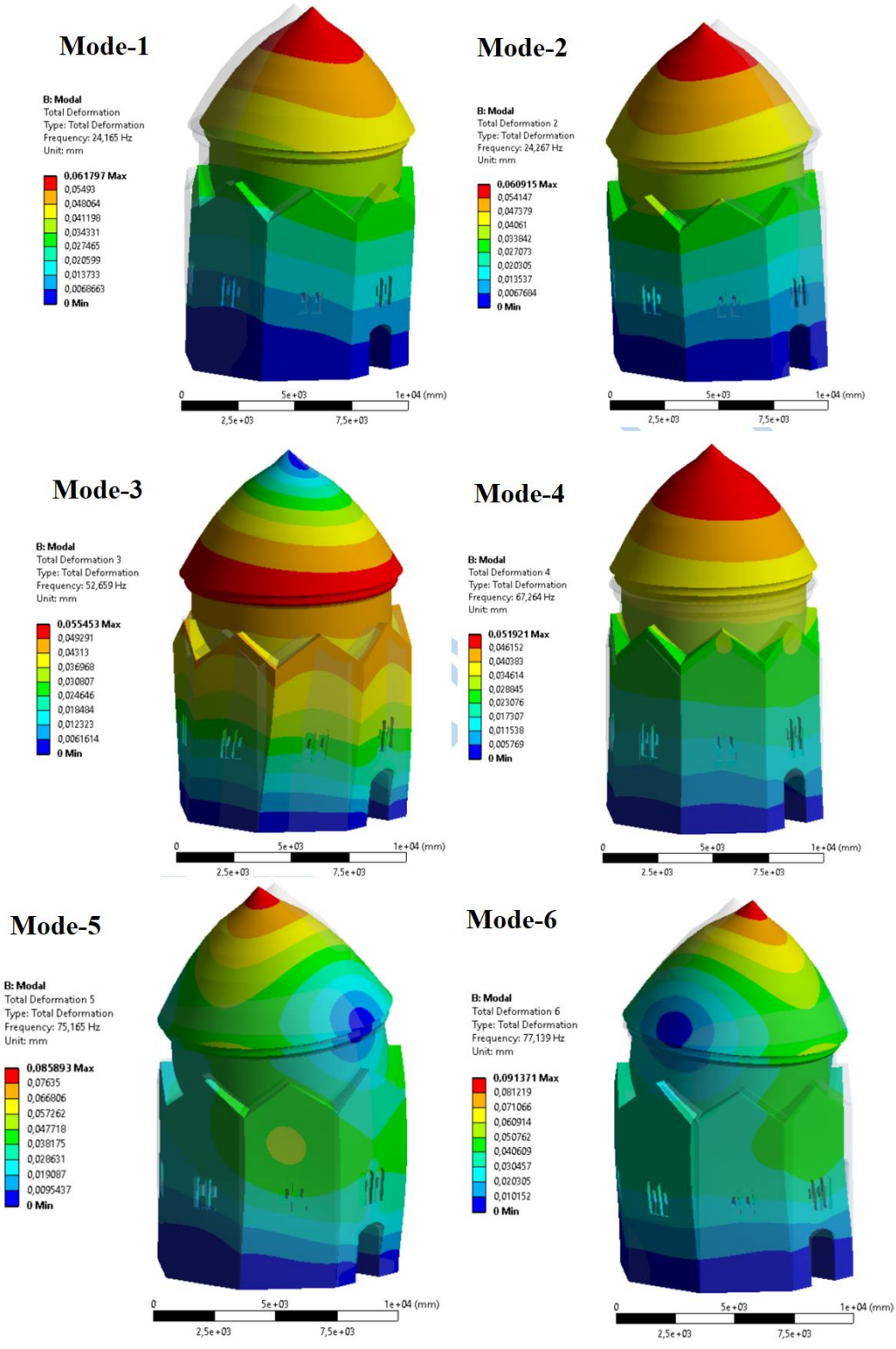
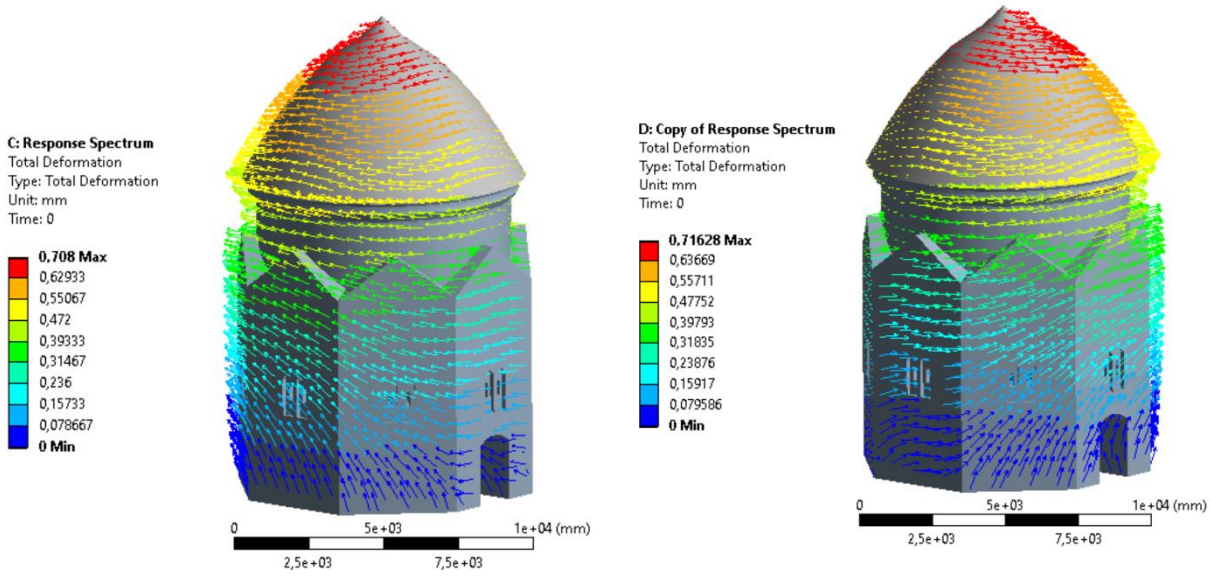


Fig. 6. The first six mode shapes

RESPONSE SPECTRUM ANALYSES

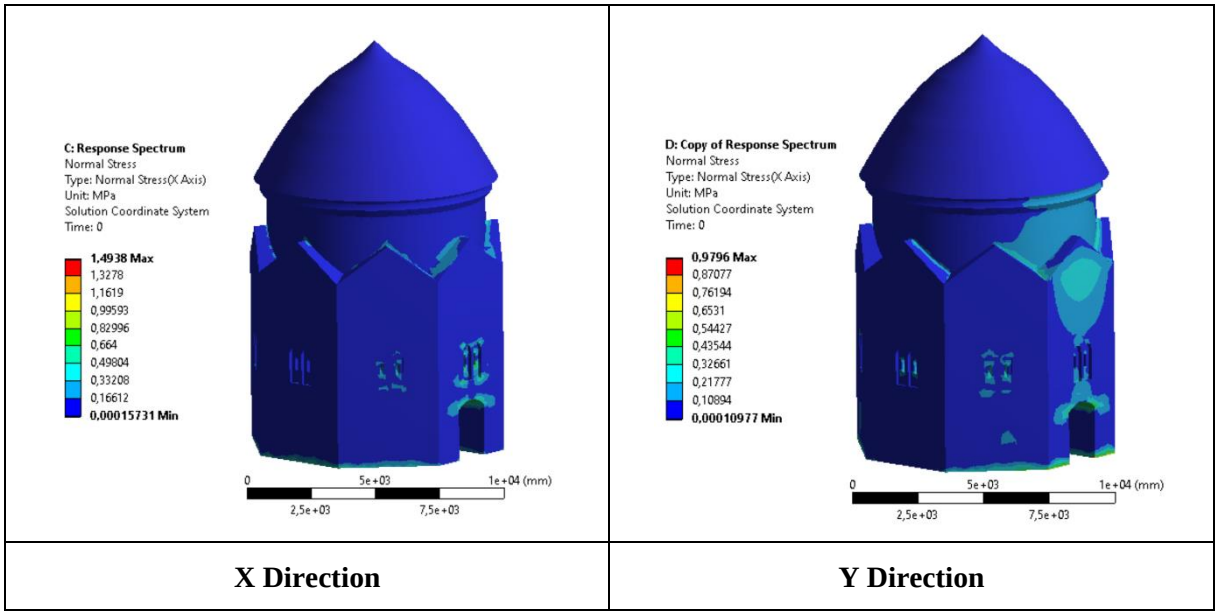
For the dynamic analysis, response spectrum analysis was used, and earthquake data were gathered from https://tadas.afad.gov.tr/ based on the location of the tomb. As far as ground motion levels are concerned, DD-2 earthquake (standard design earthquakes) was considered based on the ZB soil class. Due to the symmetrical shape of the structure and the first two modes being coupled modes, response spectrum analysis was applied separately in each horizontal direction (X and Y direction). The horizontal displacements obtained as a result of the analyzes are given in Fig. 7.



X Direction **Y Direction**

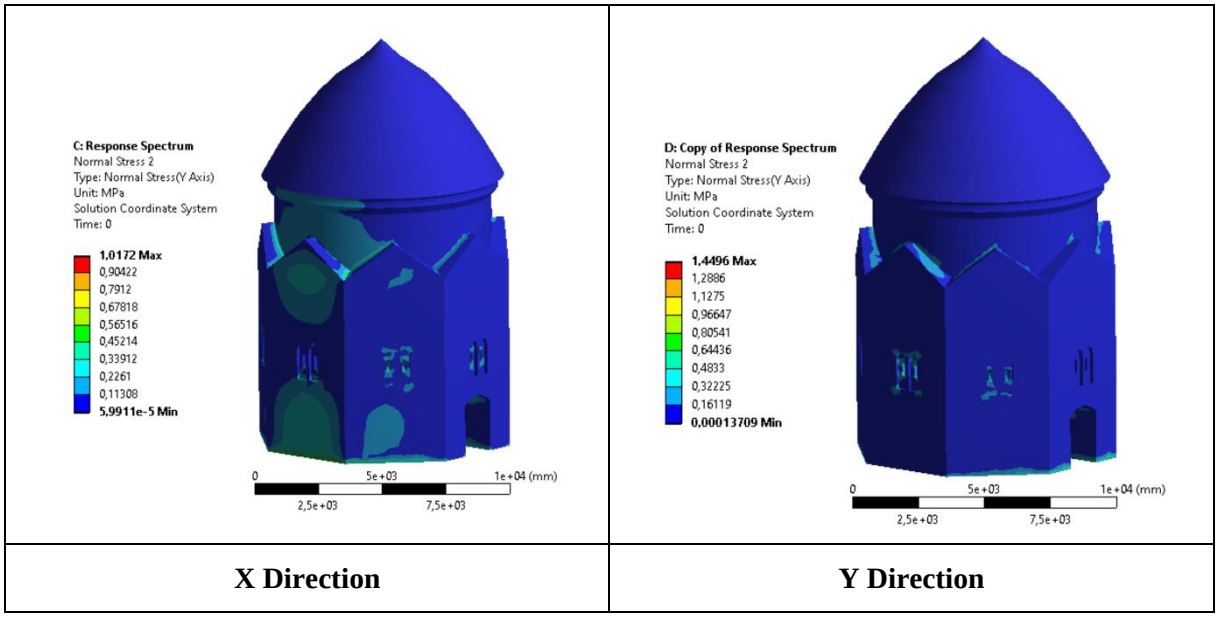
Fig. 7. Total displacements in the X and Y direction (mm)

When the normal stresses obtained after response spectrum analyzes were examined, it was seen that the normal stress values obtained in the X direction were concentrated on the door edges and triangular transition elements of the structure. It was seen that the normal stress values obtained in the Y direction were concentrated around the door and in the connection sections where the dome and the masonry walls (Fig. 8 and Fig. 9).



X Direction	Y Direction

Fig. 8. Normal stresses (X axis) (MPa)



X Direction	Y Direction

Fig. 9. Normal stresses (Y axis) (MPa)

CONCLUSION

Although the tombs are the subject of many studies in terms of architecture and art history, the structural performance of these structures or their earthquake behavior has not been studied much. The purpose of this study is to examine the structural performance of masonry tombs. This study aims to determine the structural performance of the Emir Saltuk Tomb located in the city center of Erzurum. The numerical model was analyzed using Static, Modal, and Response Spectrum Analyses. The results of the analysis were presented using contour pictures, bars, and scale tables. According to the results of the analyses, the structure generally has good condition because it is geometrically symmetrical and small, and the resulting stresses are generally small.

REFERENCES

AFAD, Turkish Accelerometric Database, and Analysis System, https://tadas.afad.gov.tr/

ANSYS Workbench, Finite Element Software, USA. www.ansys.com

Cakir, F., Uysal, H. (2014). "Seismic performance of historical masonry clock tower with adjacent walls", Earthquakes and Structures, 7(2), 217-231.

Kapusuzoğlu, G. (2015). "Marriage And Funeral Traditions In Turkic Cultural Environment According To Chinese Sources", TAD, C. 34/ S. 58, 2015, s.507-522.

Tokuz, H. (2019). "Ottoman Tomb Architecture In Bosnia And Herzegovina", M.Sc. Thesis, Marmara University, Turkey.

Gedik, Y. (2022). "Dynamic identification study of Emir Saltuk cupola", M.Sc. Thesis, Erzurum Technical University, Turkey.

TRAFİK KAZA KARA NOKTALARINDAKİ TRAFİK GÜVENLİK SİSTEMİNİN ÖNEMİ 'GÖKÇEBEY KAVŞAĞI ÖRNEĞİ''

Dr. Öğr. Üyesi Adem AHISKALI

Kastamonu Üniversitesi, Müh. Mim. Fak., İnşaat Mühendisliği Bölümü, Kastamonu, Türkiye., ORCID ID: 0000-0002-1265-7312

Yüksek İnşaat Mühendisi Aydın ARSLAN

Kastamonu Üniversitesi, Müh. Mim. Fak., İnşaat Mühendisliği Bölümü, Kastamonu, Türkiye., [2]ORCID ID: 0000-0002-6713-0585

Özet

Dünyadaki değişimler ve teknolojinin hızlı bir şekilde gelişmesi, insanlığı daha konforlu, güvenilir ve hızlı ulaşım imkânlarına zorlamıştır. Bu gelişmeler sonucunda, karayollarının da içinde bulunduğu ulaştırma ağlarının yapımı sırasında, güvenlik sistemlerinin önemi daha fazla dikkate alınmaktadır. Ulaştırma Mühendisliği'nin en önemli konularından biri olan Güvenlik Sistemleri, en fazla çözüm aranan konular arasında olduğunu söyleyebiliriz. Ülkemizde alternatifler içerisinde en fazla tercih edilen ulaştırma şekli kara yoludur. Bu nedenledir ki artan nüfus sayısı ile birlikte, teknolojide yaşanan gelişmeler ve taşıt sayısının artması, doğrudan trafik yoğunluğunda hızlı bir artışa neden olmaktadır. Gözlemlenen bu artış, trafikte olumsuzlukların yaşanmasına sebep olmaktadır. Dolayısıyla, söz konusu insan güvenliği olan ve bu amaçla can güvenliğini sağlamak için üstünde durulması gereken konu "Karayolları Güvenlik Sistemlerinin Trafik Kazalarına Etkisi" konusudur. Bahsi geçen konuda çözüm odaklı çalışmaların ve araştırmaların, yapılması gerektiğine inanmaktayız. Bu nedenledir ki;

Sunulan çalışmada, Kastamonu Karayolları Bölge Müdürlüğü sorumluluğunda bulunan Zonguldak - Bolu il sınırı arasındaki yollar incelenmiş olup, trafik kazalarının yoğun olarak yaşandığı alanlar tespit edilerek ihtiyaç duyulan noktalara Karayolu Güvenlik sistemlerinin etkisi araştırılmıştır. Kara nokta tespit yöntemleri kullanarak, "Trafik Kaza Kara Noktaları" olarak belirlenmiş olan Gökçebey Kavşağı incelenmeye alınmış ve güvenlik sistemleri açısından bir eksiklik olup olmadığı ortaya konulmuştur. Trafik kaza kara noktaları ile ilgili çözüm önerileri sunularak, ileri dönemlerde oluşabilecek trafik kazalarının önüne geçilmesi planlanmıştır. Karayolu güvenlik sistemlerinden aktif ve pasif güvenlik sistemlerinin tanınması, ayırt edilmesi ve ihtiyaç duyulan kesimlere doğru şekilde uygulanması amaçlanmıştır. Aktif ve pasif güvenlik sistemleri, ekonomik külfetinden daha çok olumlu sonuç veren, düşük maliyetli sistemlerdir. Bu nedenle, eksik güvenlik sistemi tamamlandığında verimli sonuçlar alınacağından, bu çalışmanın önemli olduğunu düşünmekteyiz.

Anahtar Kelimeler: Trafik Kazası, Kaza Sebepleri, Karayolu Güvenlik sistemleri

TRAFFIC ACCIDENTS AT LAND POINTS IMPORTANCE OF TRAFFIC SAFETY SYSTEM 'GÖKÇEBEY INTERCHANGE EXAMPLE''

Abstract

The changes in the world and the rapid development of technology have forced humanity to more comfortable, reliable and fast transportation opportunities. As a result of these developments, the importance of security systems is taken into consideration more during the construction of transportation networks, including highways. We can say that Security Systems, one of the most important subjects of Transportation Engineering, is among the most sought-after solutions. The most preferred mode of transportation among the alternatives in our country is the land route. For this reason, together with the increasing number of population, the developments in technology and the increase in the number of vehicles directly cause a rapid increase in traffic density. This observed increase causes negativities in traffic. Therefore, the subject, which is human safety and which should be emphasized in order to ensure life safety for this purpose, is the subject of "The Effect of Highway Safety Systems on Traffic Accidents". We believe that solution-oriented studies and researches should be done on the subject. This is why;

In the presented study, the roads between Zonguldak - Bolu provincial border, which is under the responsibility of Kastamonu Regional Directorate of Highways, were examined and the effects of Highway Safety systems on the needed points were investigated by determining the areas where traffic accidents were experienced intensely. Using black spot detection methods, Gökçebey Junction, which has been designated as "Traffic Accident Black Spots", has been examined and it has been revealed whether there is a deficiency in terms of security systems. It is planned to prevent traffic accidents that may occur in the future by presenting solutions for traffic accident black spots. It is aimed to recognize, distinguish between active and passive safety systems from road safety systems and to apply them correctly to the needed sections. Active and passive safety systems are low-cost systems that give more positive results than their economic burden. For this reason, we think that this study is important as efficient results will be obtained when the missing security system is completed.

Keywords: Traffic accident, Causes of Accident, Road Safety systems

A COMPARATIVE ANALYSIS OF TRAVEL TIME, SPEED AND DELAY OF DIFFERENT VEHICLES IN MINNA, NIGER STATE, NIGERIA

Shehu, M.[1], Ogaji, A. N.[2], Abdulrahman H. S.[4], Haruna, A. M.[5], Adamu, H. N.[5], Mahmud, M. B.[6]

[1,2,3,4,5,6]*Department of Civil Engineering, Federal University of Technology, Minna, Niger State, Nigeria*

Abstract

The speed, travel time and delays are major indicators of the performance of a traffic facility. A comparative analysis of travel time, speed and delay for different vehicles was carried out on the Kpakungu-Gidan-Kwano road stretch using the average car method and the license plate matching technique combined. Boarding and alighting of passengers was not significant enough to cause a large increase in travel time. Increase in travel time was mainly due to the presence of road defects on pavement surface, non-uniformity in cross section width of pavement and increase in volume of traffic at peak hours. Travel time and speeds of these vehicle categories did not vary significantly, mainly because of congestion experienced for better parts of the journey. Typical range of travel time for private cars falls between 15minutes to 20minutes, while tricycle and buses falls between 20minutes to 28 minutes and 25minutes to 35minutes respectively. Speeds of vehicles decrease as they approach distressed sections of pavement surface. Tricycles move with journey speeds of 19km/hr to 28km/hr and running speeds of 24km/hr to 30km/hr, private cars move with running speeds of 25km/hr to 40km/hr and journey speeds of 27km/hr to 40km/hr while buses move with journey and running speeds of 20km/hr to 30km/hr and 15km-33km/hr. Delay and travel time can be reduced to significantly improve traffic flow by expansion of the road stretch, routine and in-depth maintenance to repair pavement defects and allocation of fixed locations for boarding and alighting of passengers.

INVESTIGATION OF THE EFFECTS OF ROTOR SLOTS STRUCTURE ON MOTOR PARAMETERS IN INDUCTION MOTORS

Yildirim Özüpak

Dicle University, Silvan Vocational School, 0000-0001-8461-8702

Mehmet Çinar

Bitlis Eren University, Tatvan Vocational School, ORCID:0000-0002-1542-9120

ABSTRACT

Asynchronous machines basically consist of two parts, the stator and the rotor. Asynchronous machines, in the industrial field; It has a high usage rate due to its advantageous aspects such as low costs, ease of use, no maintenance, and ease of production. In parallel with the advancing technology, the quality of productivity in asynchronous machines continues to increase. These motors are; They are in many application areas because they work efficiently, do not require much maintenance and have a strong structure. Today, the use of asynchronous motors is preferred in the branches of the industry that require high finances. Therefore; The efficiency and low cost of induction motors has managed to attract the attention of researchers, and this issue has attracted the attention of researchers. In this study, the rotor slot structures, which seriously affect the efficiency of asynchronous motors, are emphasized. The design and analysis were made using the ANSYS-Rmxprt-Maxwell program, which performs a solution based on the finite element method (FEM). In the study, first a model was created and it was investigated how the parameters were affected by the experiment-observation method. Optimal values have been tried to be eliminated depending on the rotor slot type of the motor.

Keywords: Motor, Slot type, Parameter, FEM.

INTRODUCTION

Asynchronous machines basically consist of two parts, the stator and the rotor. The task of the stator, which is the stationary part, creates the magnetic field, and the rotor, which is the moving part, creates the rotational motion. When a three-phase alternating voltage is applied to the stator windings of induction motors, a rotating magnetic field is created in the stator windings. A voltage is induced on the rotor by cutting the short-circuit bars standing in this magnetic field Lee at all., 2017). The short-circuit currents created by this induced voltage create the magnetic field on the rotor. As a result of the interaction of the rotor magnetic field and the stator magnetic field, a torque is generated. With this moment, the rotor starts to rotate in the direction of the rotating field (Barbour A.; Thomson W.T. 1997).

Since the invention of asynchronous machines, many studies have focused on maximum efficiency. Studies on the rotor slot geometry of induction motors also constitute an important part of these studies.

When the other studies available in the literature are examined; It is seen that optimizing the rotor slot geometry makes significant contributions to the motor performance. A few of the rotor slot geometry studies on different models are given below.

The ratios corresponding to the optimal torque and current values were found. These results were interpreted separately for each rotor slot shape. According to the results; When using a rectangular bar, if the ratio between bar height and bar thickness increases without changing the cross-sectional area, the starting torque will increase and the starting current will decrease. Higher starting torque values were obtained when step-shaped bars were used. In deep rectangular bars, on the other hand, a decrease in the breaking torque was observed as the height of the bar increased (Özüpak Y., 2022).

The optimization of the stator and rotor slots has been carried out, aiming to increase the performance of the asynchronous motor. For this, parameters such as the width and depth of the slot structures were optimized by

the iteration method in the program they used. Thanks to the new optimal slot shape they obtained, they reduced the total losses and increased the efficiency.

In recent years, especially as a result of rapid developments in the automation sector, the performance of different types of motors used has continued to gain importance rapidly. The criteria in the performance of these motors can be evaluated as failure rates, maintenance-repair costs, electricity usage costs, motor-equipment costs and motor efficiency. It can be said that the efficiency of the motors used in applications where precision operations and accuracy rates must be at a very high level can come to the fore as the most important parameter. As mentioned above, it is seen that there are both academic and industrial studies to increase motor efficiency. Academic researchers generally examine in detail the faults that motors encounter in different situations and continue to work on eliminating them. Researchers examine different scenarios (load amounts, torque effect, current-voltage fluctuations, number of slots, slot openings, etc.) and investigate their effects on motor efficiency with experimental or simulation applications (Özüpak Y., 2022).

MATERIAL AND METHOD

In the study, special software in the finite element method package program was used and firstly, a 2-D model of the induction motor was created with Rmxprt. While creating this motor model, the motor parameters were treated exactly.

In this model, the rotor slots models given in Figure 1 were used to work on. The analyzes made with these rotor slot models are compared. In the study, the experiment-observation method was applied on the rotor slot structures. These two slots structures are intended to be the most compatible values.

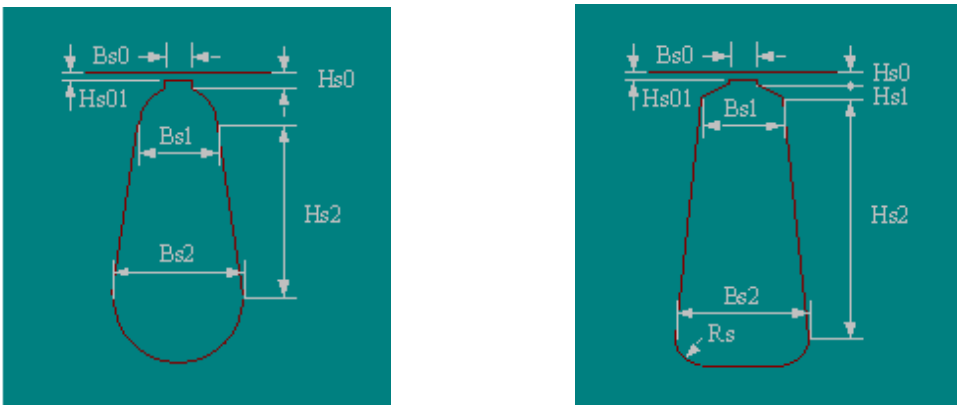


Figure 1. Rotor slots types

The analyzes were started by keeping the slot value constant and an optimal structure was tried to be obtained. These three optimal triple combinations obtained as a result were compared with each other and with the baseline data.

Designed Motor Model

The motor model prepared to work on it is presented in Figure 2. The motor was transferred to the Maxwell environment for the magnetic field analysis of this motor. Then, different scenarios on the stator and rotor slot numbers were tried with appropriate slot geometries and the most suitable slot numbers were determined in order to obtain an acceptable efficiency value for the motor. After the number of stator slots was determined, performance improvement was made by making corrections on the stator slot geometry. In this way, good yields were obtained. The stator parameters are given in Table 1.

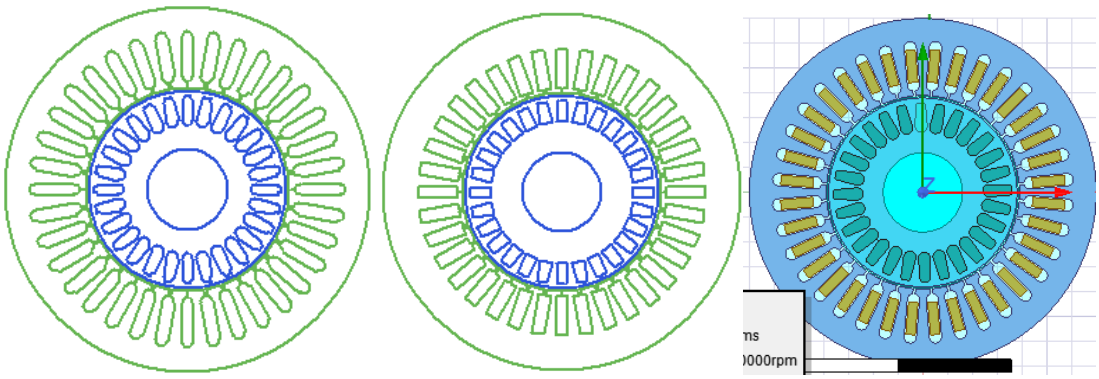


Figure 2. Structures of motor

Table 1. Stator Core Parameters.

Name	Value
"Outer Diameter"	140mm
"Inner Diameter"	78mm
Length	250mm
"Stacking Factor"	0.95
"Steel Type"	D21_50
"Number of Slots"	36

The values of the parameters specified in Figure 1 are given in Table 2.

Table 2. Stator Slots Parameters.

Name	Value
"Auto Design"	Auto design Hs2, Bs1 and Bs2"
"Parallel Tooth"	"Design Bs1 and Bs2 based on Tooth Width"
Hs0	2mm
Hs2	15mm
Bs0	1mm
Bs1	5mm
Bs2	5mm

A gap was left between the stator outer diameter and the rotor outer diameter, and the most suitable rotor inner diameter was determined for the rotor outer diameter. It indicates that an angular rotor geometry is used here, unlike the view in Figure 1. The appearance of the stator slots obtained with the values in the table is given in Figure 3.

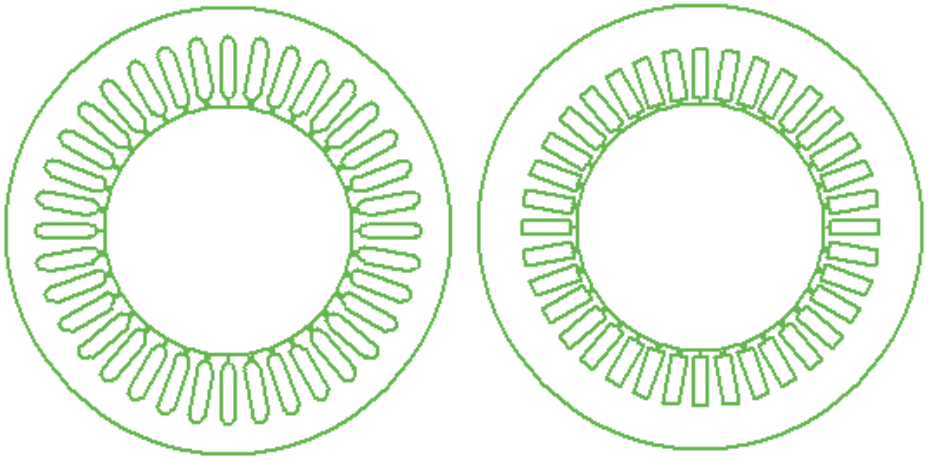


Figure 3. View of the stator slots.

The rotor parameters are given in Table 3.

Table 3. Rotor Core Parameters.

Name	Value
"Stacking Factor"	0.95
"Number of Slots"	28
"Outer Diameter"	76mm
"Inner Diameter"	32mm
Length	250mm
"Steel Type"	D21_50

The selected rotor slots type are given in Figure 4.

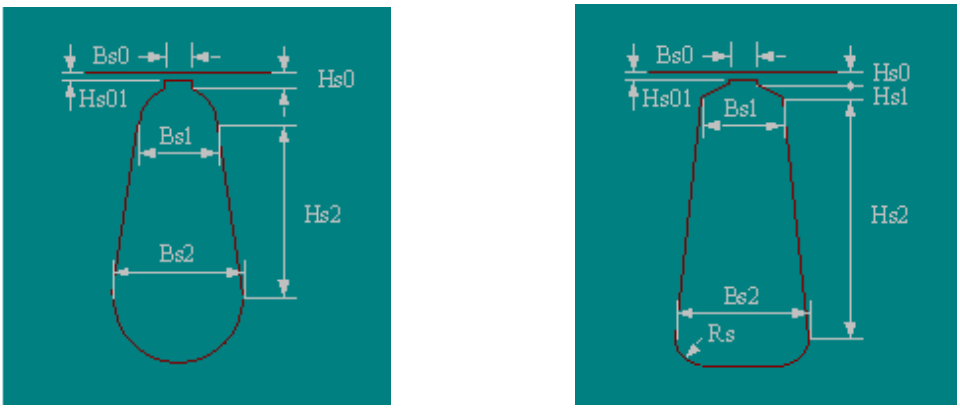


Figure 4. Selected rotor slots geometry.

The values of the parameters indicated in the figure are given in Table 4.

Table 4. Rotor Slot Parameters.

Name	Value
Hs0	2mm
Hs01	2mm
Hs2	8mm
Bs0	3mm
Bs1	4mm
Bs2	5mm

The appearance of the rotor slots obtained with the values in the table is given in Figure 5.

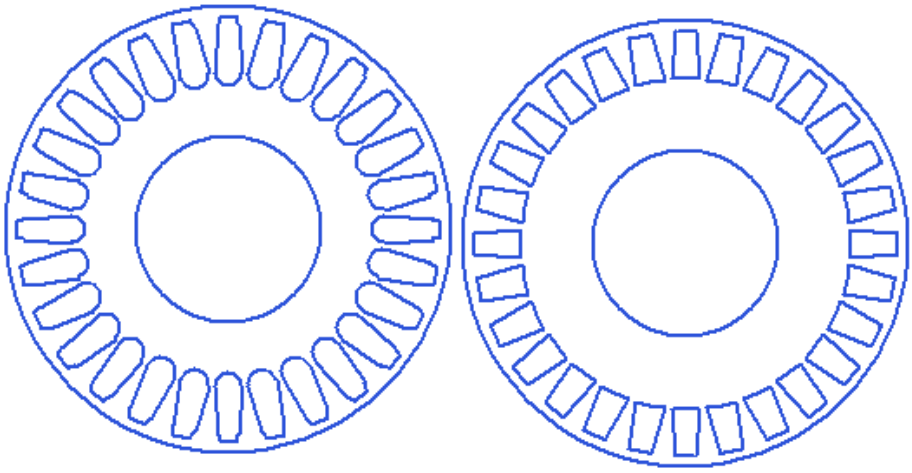


Figure 5. View of rotor slots.

RESULTS AND DISCUSSION

At the beginning of the study, analyzes were made by changing the structure of the rotor slot of the motor model. Analyzes were made with two different rotor slot structures selected and the results were compared. In this part of the study, these two situations will be analyzed and the results will be presented.

Case 1

Parametric and magnetic field analysis results obtained depending on the selected slot structure are presented below.

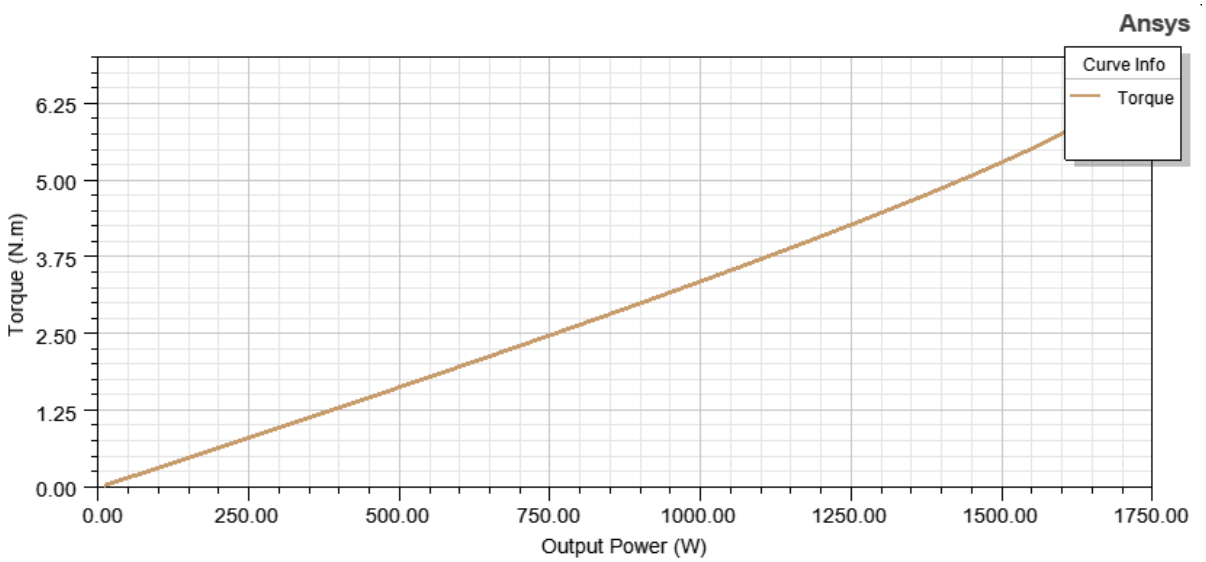


Figure 6. Torque-output power curve

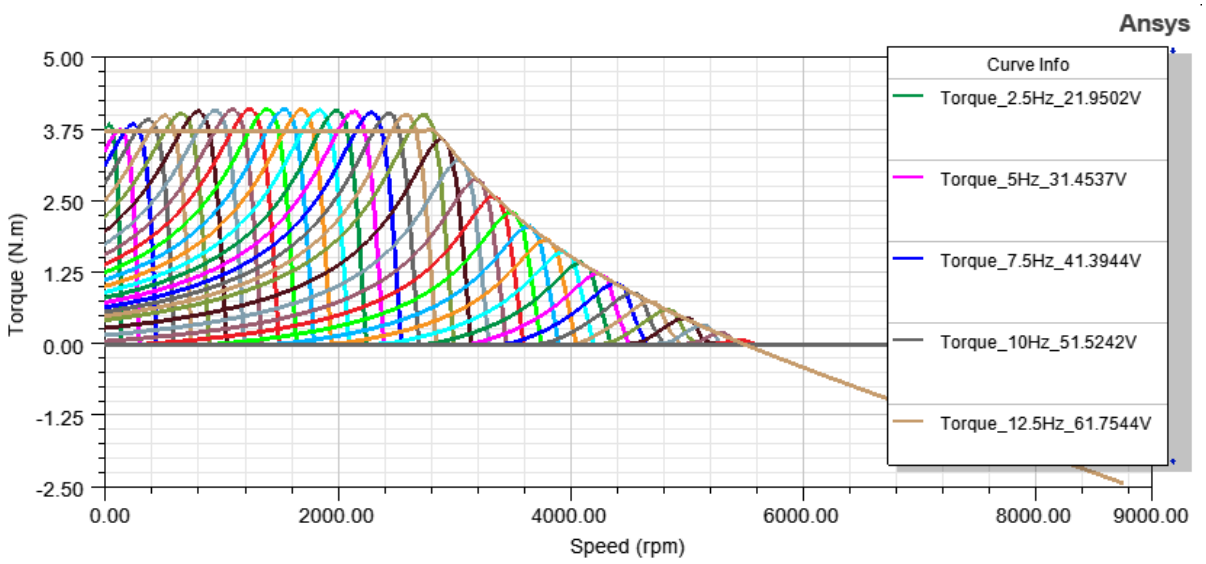


Figure 7. Speed-torque graph

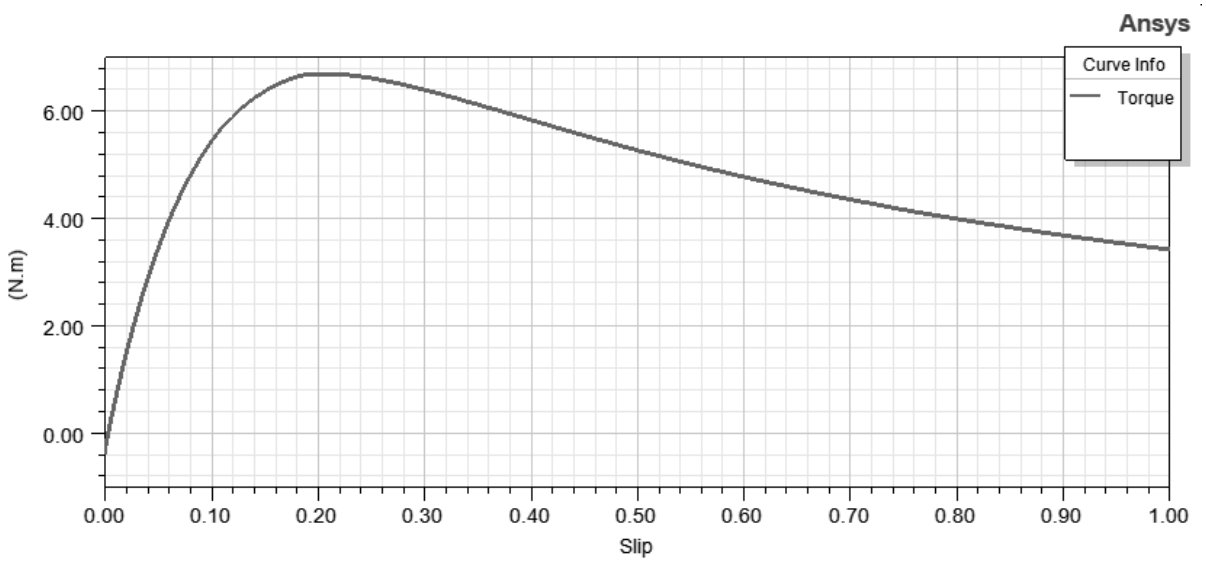


Figure 8. Slip-Torque curve

Case 2

Parametric and magnetic field analysis results obtained depending on the selected slot structure are presented below.

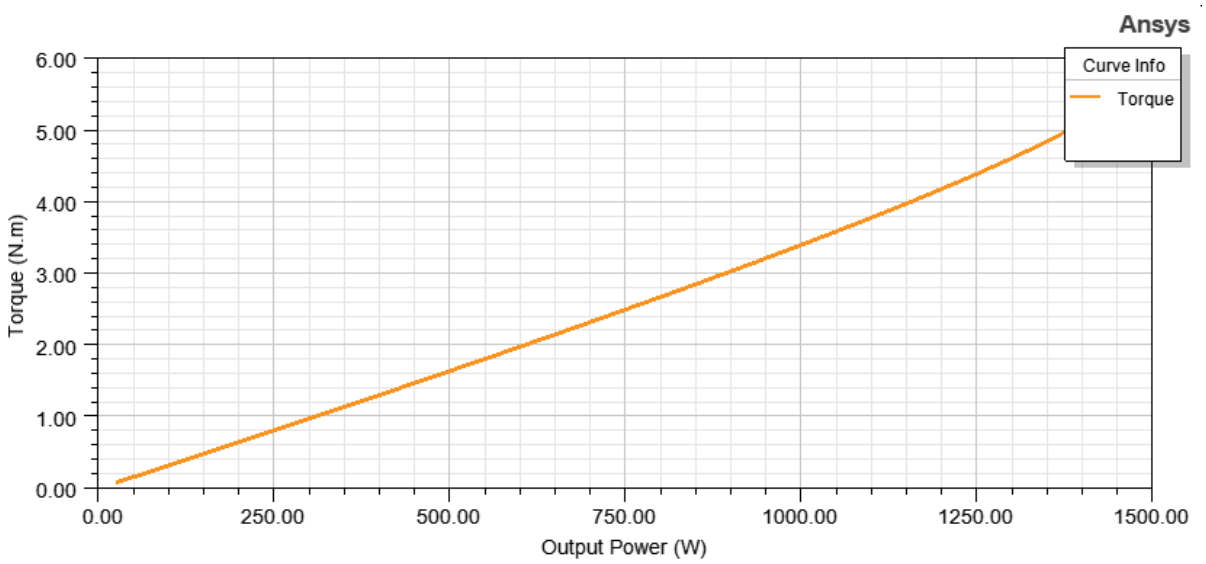


Figure 9. Case 2 torque-power curve

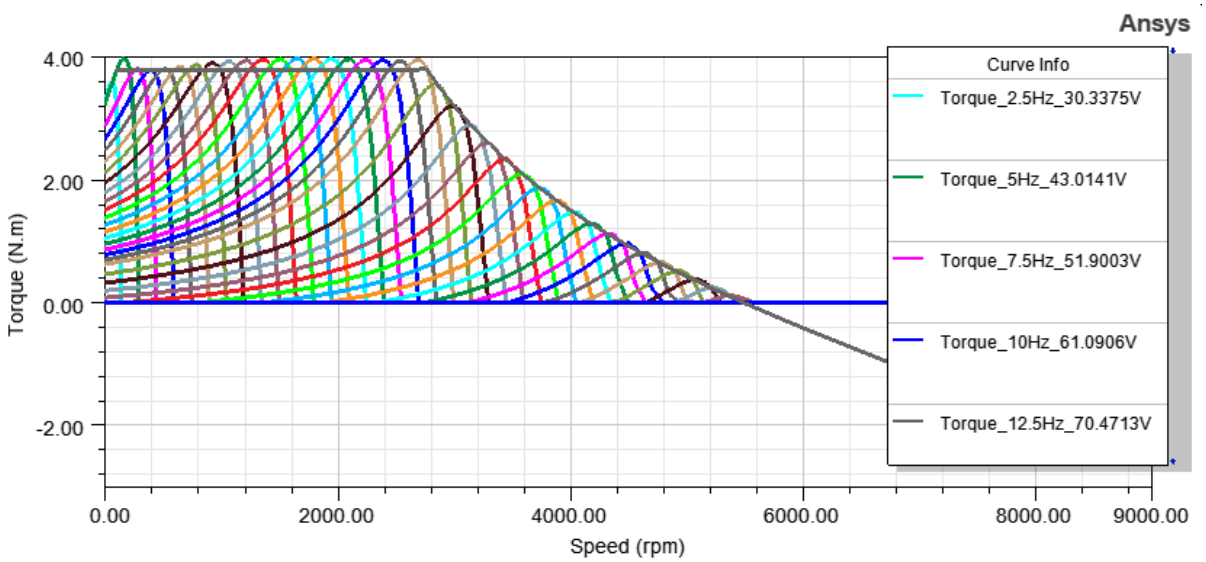


Figure 10. Case 2 speed-torque curve

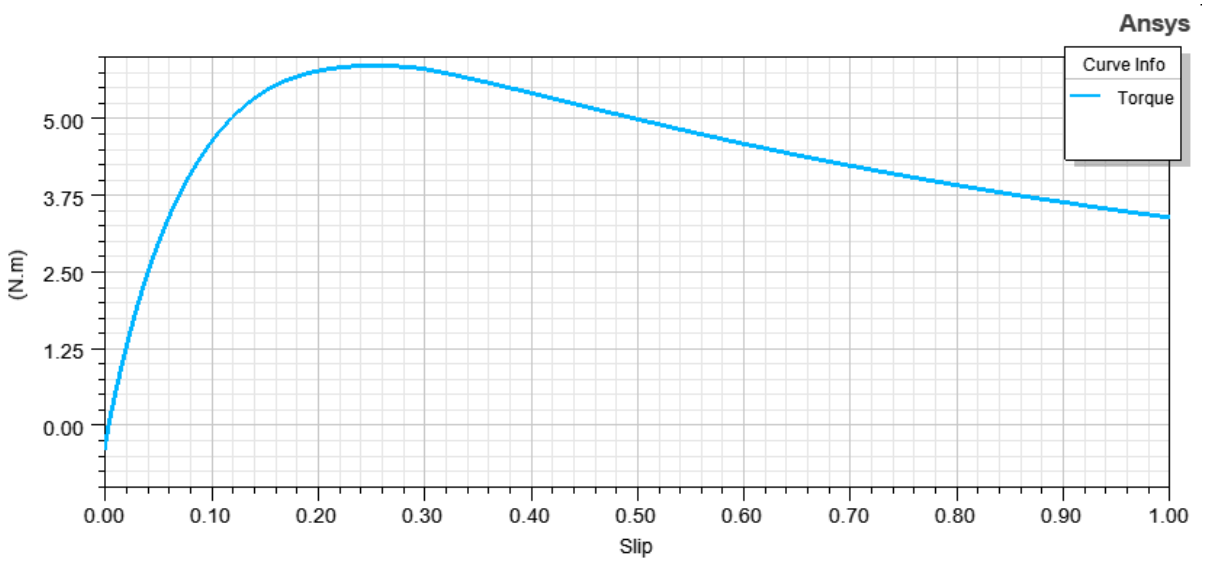


Figure 11. Case 2 torque-slip curve

CONCLUSION

In this study, unlike other publications available in the literature, the width parameters in the rotor slot geometry were kept constant and the analysis was made only with the structure of the rotor slots. Here, values such as stator slot length and width, stator and rotor slot numbers, motor inner and outer diameter, number of windings, core length were also kept constant. The study focused on and interpreted the relations of rotor slot structures with each other. Therefore, another feature of the study that is different from other similar studies; The reason is that it does not focus on a single result, but proposes many rotor slot structures that provide approximately the same optimal efficiency values. In this way, the common aspects of these optimal values, which have negligibly low efficiency differences between each other, and the structure of the rotor slot can be evaluated as optimal features. By using this study, the slot parameters can be determined separately by applying the test observation method for the determined slot structure of the asynchronous motors that are intended to be designed. In this study, analyzes were made with the Finite Element Method (FEM) by making use of the special software in the finite element package program. As a result, two different optimal rotor structures were tried to be determined.

REFERENCES

Barbour A.; Thomson W.T., Finite element study of rotor slot designs with respect to current monitoring for detecting static airgap eccentricity in squirrel - cage induction motors. Conf. Rec. - IAS Annu. Meet. (IEEE Ind. Appl. Soc., vol. 1, 1997, p. 112–9. doi:10.1109/ias.1997.643016.

Lee, Ha Jeong, Sang Hyeon Im, and Gwan Soo Park. "Shape Design of a Rotor Bar for Improving Starting Torque and Running Efficiency in Squirrel Cage Induction Motor." 21st International Conference on the Computation of Electromagnetic Fields (Compumag 2017). Vol. 1. 2017.

Özüpak Y. Efficiency Analysis of BLDC for variable magnetic field. 2022. MANAS Journal of Motorering, Volume 10 (Issue 1) © 2022

Özüpak, Y., Investigation of the Effect of Design Parameters of Small Brushless DC Motors on Motor Performance by Finite Element Method, Brilliant Motorering, 3(2022), 4658. https://doi.org/10.36937/ben.2022. 4658.

Özüpak, Y. (2022). Re-Analysis of Internal Permanent Magnet Brushless DC Motor With Increased Magnet Dimensions. Ejons International Journal, 6(22), 353–365. Retrieved from https://ejons.org/index.php/ejons/article/view/294

ANALYSIS OF A MOTOR USED IN ELECTRIC VEHICLES USING FEM BASED ANSYS-RMXPRT-MAXWELL

Yildirim Özüpak

Dicle University, Silvan Vocational School, 0000-0001-8461-8702

Mehmet Çinar

Bitlis Eren University, Tatvan Vocational School, ORCID:0000-0002-1542-9120

ABSTRACT

In recent years, it is seen that electric vehicles take place in R&D investments and important projects for the future in the automotive industry in our country and in the international market. Electric vehicles find a wide place in automobile fairs and attract attention. Predictions that fossil fuels are not renewable in the future lead the manufacturers in this direction. It is expected that electric vehicles will save fuel, reduce city noise and reduce carbon emissions. Electric motors are preferred in electric vehicles because they provide instant torque, create strong and balanced acceleration, and have less carbon dioxide emissions compared to fossil fuels. For this reason, the design and analysis of high efficiency electric motors has become the focus of attention of researchers. In the design of electric motors, computer aided analyzes are used to calculate the electromagnetic analysis of the motor, losses, efficiency and torque value. In this study, it is aimed to perform electromagnetic analysis of the brushless direct current motor used in the propulsion system of the electric vehicle and to present the results. For this purpose, electromagnetic analyzes of an electric motor, which was pre-designed using ANSYS-Rmxprt software, which performs a solution based on Finite Element Method (FEM), were carried out with ANSYS-Maxwell software and other performance values of the motor were obtained.

Keywords: Motor, Efficiency, ANSYS-Maxwell

INTRODUCTION

In recent years, it is seen that electric vehicles take place in R&D investments and important projects for the future in the automotive industry in our country and in the international market. Electric vehicles find a wide place in automobile fairs and attract attention. Predictions that fossil fuels are not renewable in the future lead the manufacturers in this direction. It is expected that electric vehicles will save fuel, reduce city noise and reduce carbon emissions. The degree of reduction in carbon dioxide emissions depends on electricity generation, and a serious reduction is aimed in the use case (Bouscayrol A. At all., 2016, Zhu S. At all., 2018). Published academic studies, commercial targets announced by automotive manufacturers and the interest in electric vehicles at fairs indicate that this technology will be widely used in the future. An electric car is a car that drives using one or more electric motors, using electricity stored in batteries and/or other energy storage devices. Electric motors give instant torque, providing powerful and balanced acceleration. Today, in parallel with the rapid development of computer technology, computer-aided analysis software helps motor manufacturers in process steps. This software provides important inputs in the design of electric motors and are used as a virtual laboratory. After the motor designs are improved in the simulation environment, they are converted into prototypes, thus saving time and reducing costs. Integrated operation of simulations in multi-physics applications is seen as an important advantage. The subject of this paper is the electromagnetic analysis of the brushless direct current motor used in the drive system of the electric vehicle and the presentation of the results. The specifications of the motor were determined by taking into account the vehicle hood space limits and the vehicle's torque and speed requirements. Brushless direct current motors are a useful type of motor with high efficiency, high torque and less heating because friction loss is not inside the motor. ANSYS-Workbench software, which has become an industrial standard and is widely used, has been used in computer aided analysis. In electromagnetic analysis, the design of the electric vehicle motor was made and its performance was analyzed. ANSYS-Workbench product is an application that integrates structural, thermal, low frequency and high frequency electromagnetic applications. Computer aided analysis, which is very useful in electric vehicle motor design, can also be used to examine the effect of thermal effects on structural form.

MATERIAL AND METHOD

Rmxprt is a software that is used in the first step of Electric Motor - Generator designs, guides the designer and provides detailed analytical solutions of the motor that is formed as a result of the design. Due to its full compatibility with Maxwell software, the design made with this software can be transferred directly to the Maxwell environment and model creation for finite element analysis can be done easily. In this study, the motor was first designed in the Rmxprt environment. In the study, the motor design was carried out to be suitable for both hybrid and full electric vehicle use for a general sedan vehicle. The motor was designed considering the electric motor powers of Toyota and Mitsubishi, the market leader in hybrid vehicles, in the fully electric vehicle prototype. In addition, considering the gearboxes of the vehicles, the nominal speed of the motor can be considered to be in the range of approximately 4500-6500 rpm. It is assumed that the designed motor will be used instead of the internal combustion motor or the internal combustion motor will be downsized and placed next to the motor. Input information was taken into consideration as a design criterion in electric motor design and analytical solution was created with Rmxprt software. Another important point in the design is the choice of material. Stainless steel was chosen as the rotor material, and NdFe35 type magnet, which has high magnetic density and is difficult to demagnetize, was chosen as the magnet material. Magnet properties are given in Table-1.

Table 1. Properties of NdFe35

Grade	Remanence (BR) mT (KGS)	Coercive Force (Hcb) kA/m (kOe)	Intrinisc Coercive Force (Hcj) kA/m (kOe)	Max. Energy Product (BH)max	Max. Operating Temp TW
N35	1170-1220 (11.7- 2.2)	868 (10.9)	955 12	263-287 (33-36)	80

M19-24G type of e-silica sheet type was used for the stator. The B-H curves of the sheet used are given in Figure1.

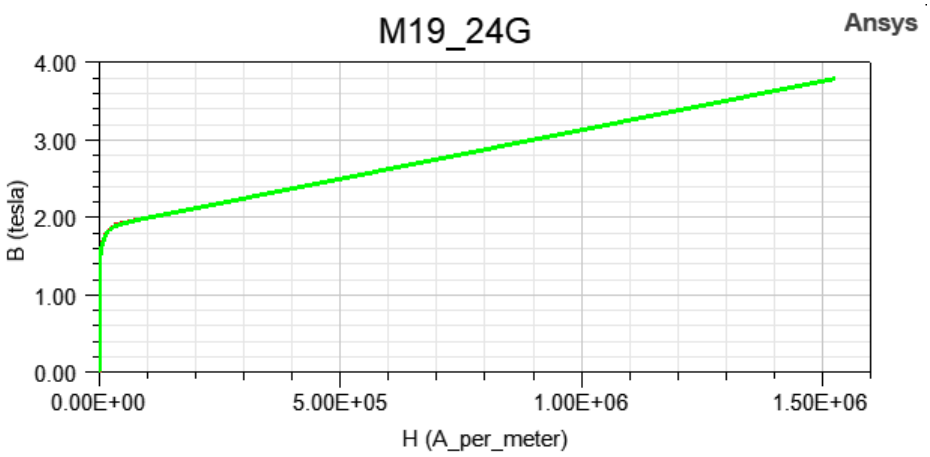


Figure 1. B-H curve for M19-24G type sheet

The winding diagram of the motor is shown in Figure-2.

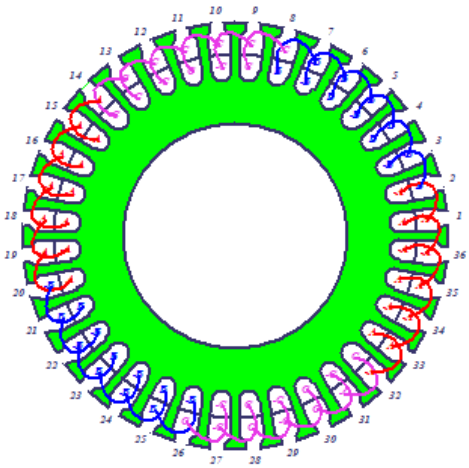


Figure 2. Motor winding diagram

The motor efficiency-speed curve obtained as a result of the analyzes is shown in Figure-3.

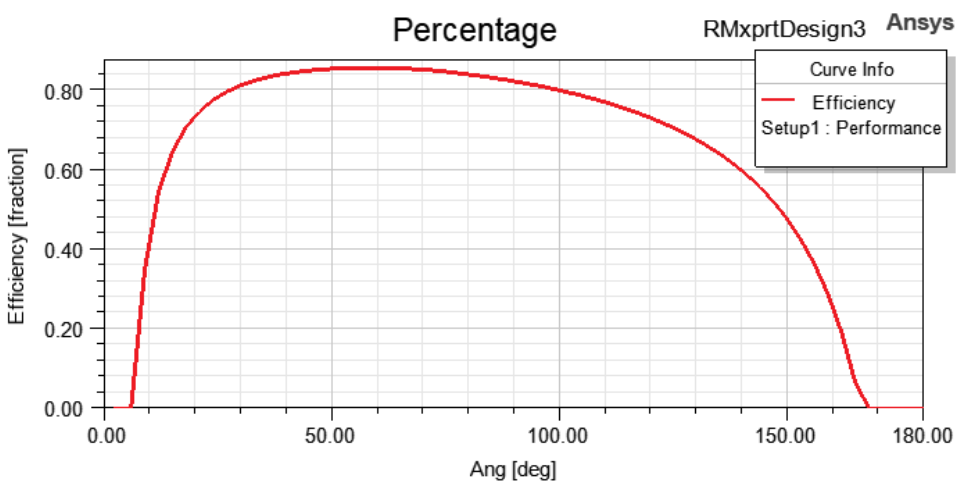


Figure 3. Motor efficiency – speed curve obtained as a result of the analysis

As a result of the motor simulation, it is seen that the efficiency of the motor is high between wide speed values. This indicates that the motor will be efficient at different speeds, in other words, at low or high speeds of the vehicle.

RESULT AND DISCUSSION

In order to perform electromagnetic analysis of the motor, whose design and analytical results are obtained in Rmxprt, the model created by the finite element method (FEM) must be transferred to Maxwell software. Maxwell is a software package that performs finite element analysis for low frequency electromagnetic field simulation (Arnold A., 2018). It can be used in the design and analysis of motors, accumulators, transformers and other electromagnetic structures. In order for the electromagnetic analyzes to be completed quickly, 2 Dimensional (2-D) analyzes were carried out, taking into account the symmetrical structure of the motor. Since thickness information and symmetry factor can be added as software parameters in electromagnetic analysis, working on the smallest symmetry of the geometry saves both time and computer power (Özüpak Y., 2022). For this reason, in this study, the smallest symmetry of the motor, that is, the 2-dimensional state, is used. The finite element mesh of the motor, which was designed and first analyzed in Rmxprt, was transferred to

Maxwell-2D software as seen in Figure 4. Rmxprt transfers the settings and inputs Maxwell needs in the most optimal way.

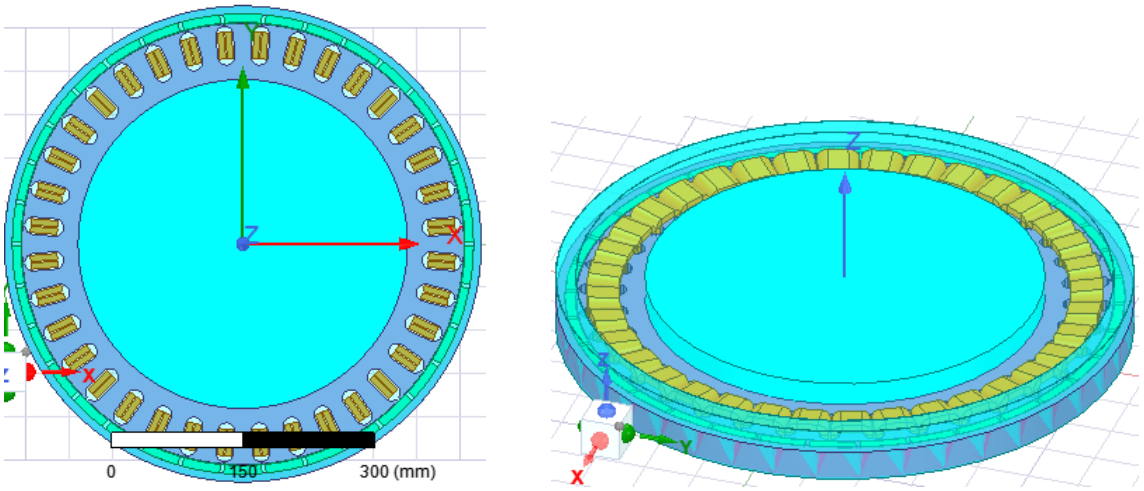


Figure 4. Motor 2D/3D FEM model

In this paper, the number of mesh elements has been chosen according to the size of the motor, and the number of mesh elements has been tightened in the regions where the magnetic flux shows the greatest variation, so that the solution is realistic. The obtained FEM image is given in Figure 5.

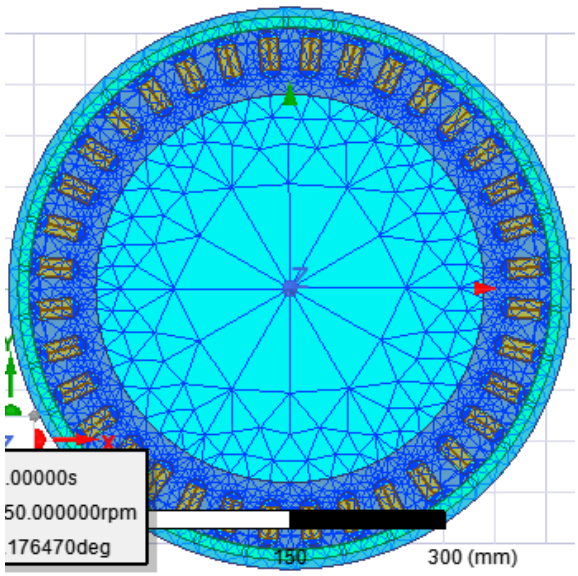


Figure 5. Mesh structure of the motor

In the FEM model of the motor, 15,000 finite elements were created and the analyzes were completed. Electromagnetic analyzes were performed at full load and the obtained motor torque-time curve is shown in Figure 6, the induced voltage-time curve in Figure 7 and the current-time curve in the windings in Figure 8.

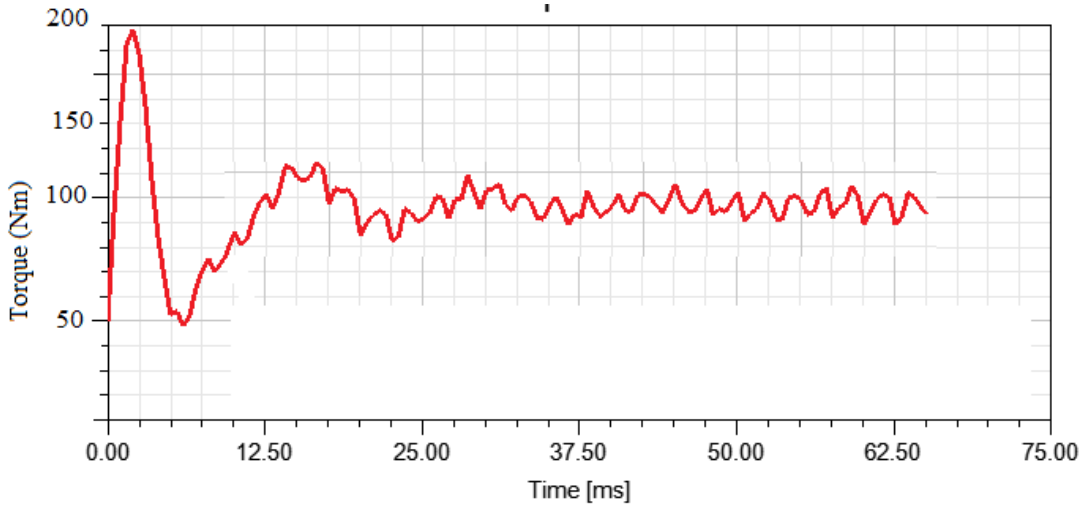


Figure 6. Torque-time graph

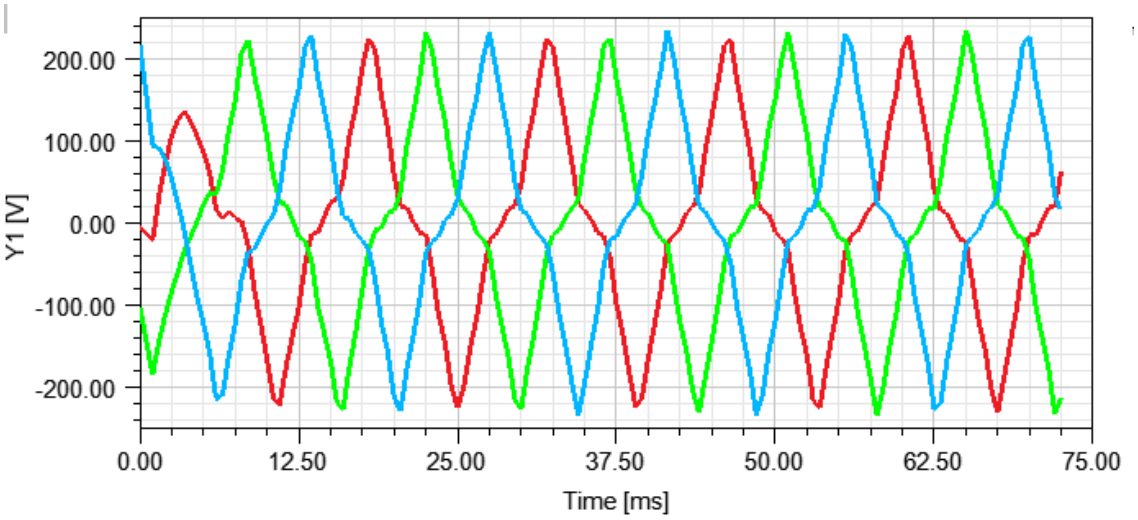


Figure 7. Induced voltage-time

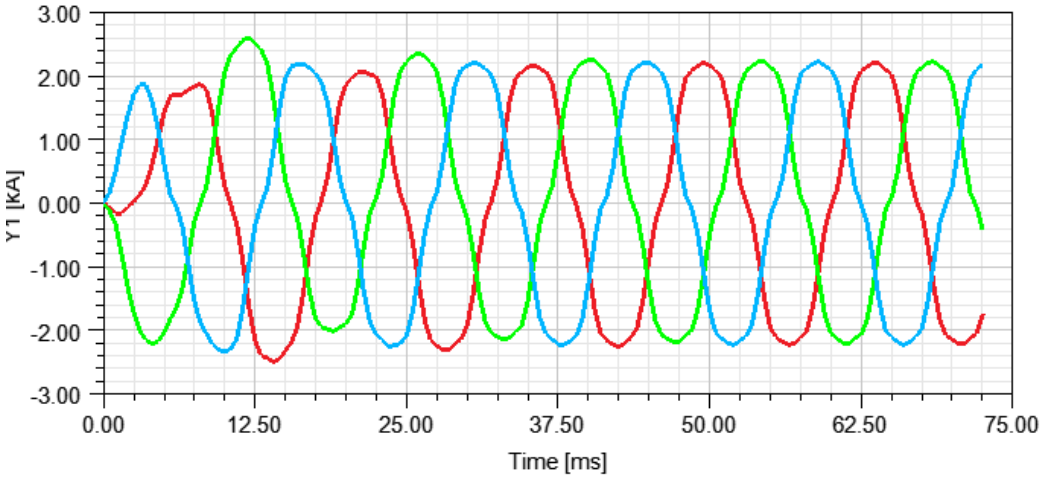


Figure 8. Current-time graph

The magnetic flux lines on the motor are shown in Figure 9 and the magnetic flux density plots are shown in Figure 10. As can be seen from the curves above, the motor outputs are consistent with the results found in the literature [5]. This shows that the motor design is suitable.

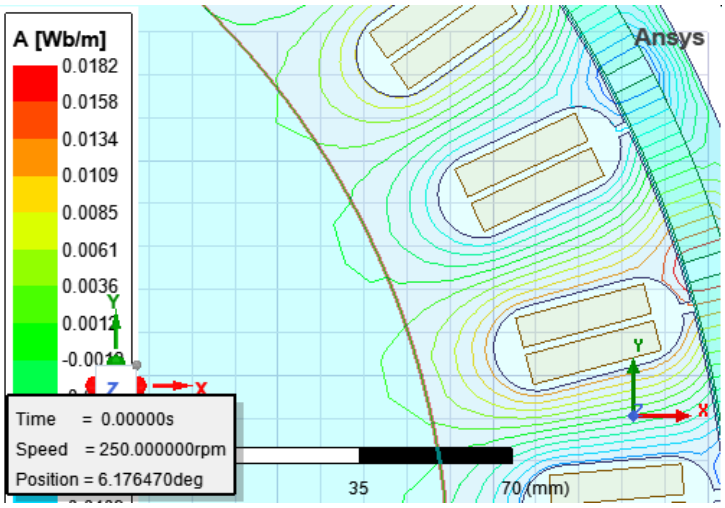


Figure 9. Graph of magnetic flux lines

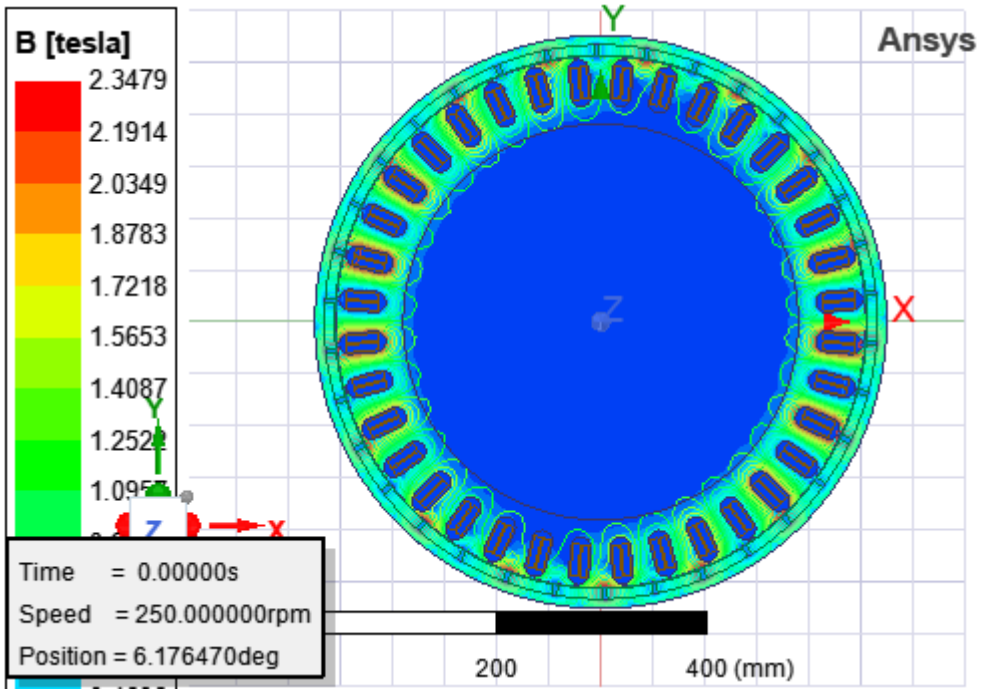


Figure 10. Magnetic field intensity graph

Figure 9 shows the graph of magnetic flux lines and Figure 10 shows the magnetic field formed as a result of excitations in the windings. The magnetic field intensity increases as the motor is loaded, and since it is simulated at full load, partial saturation can be seen in the motor sheet. After this study, it was seen that the operation of the motor was compatible with the literature and references [6].

CONCLUSION

In motor design, multi-physics based analysis software is used to perform electromagnetic analysis of the motor and to calculate the temperature changes caused by the calculated electromagnetic losses. In this study, the electric motor used in electric vehicles was designed using ANSYS Rmxprt and Maxwell software, and losses and magnetic flux densities were obtained as a result of the analysis. The results from electromagnetic analysis with the finite element method and the calculated losses were consistent. In addition, values such as motor torque, efficiency and speed were obtained as a result of simulation. The results also reveal the accuracy of the method used.

REFERENCES

Bouscayrol A., Boulon L., Hofman T., Chan C.C., (2016) Special Section on Advanced Powertrains for More Electric Vehicles, IEEE Transactions on Vehicular Technology, 6 (3), 995 – 997.

Zhu S., Hu Y., Liu C., Wang K., (2018) Iron Loss and Efficiency Analysis of Interior PM Machines for Electric Vehicle Applications, IEEE Transactions on Industrial Electronics, 65 (1), 114-124.

Arnold A., (2018) Magnetic Technologies. Sintered Neodymium- Iron-Boron Magnets. http://www.arnoldmagnetics. Com /products/neodymium-iron-boron-magnets.

Özüpak Y. (2022) Efficiency Analysis of BLDC for variable magnetic field. 2022. MANAS Journal of Motorering, Volume 10 (Issue 1)

Özüpak, Y., (2022) Investigation of the Effect of Design Parameters of Small Brushless DC Motors on Motor Performance by Finite Element Method, Brilliant Motorering, 3, 4658. https://doi.org/10.36937/ben.2022. 4658.

Özüpak, Y. (2022). Re-Analysis of Internal Permanent Magnet Brushless DC Motor With Increased Magnet Dimensions. Ejons International Journal, 6(22), 353–365. Retrieved from https://ejons.org/index.php/ejons/article/view/294

AMBULANS KABİNİ HAVASININ ISITILMA SÜRECİNİN İNCELENMESİ

INVESTIGATION OF THE HEATING PROCESS OF THE AMBULANCE CABIN AIR

Muhsin KILIÇ

Prof. Dr., Bursa Uludağ Üniversitesi, Mühendislik Fakültesi, Makine Mühendisliği Bölümü, Nilüfer, Bursa, Türkiye, ORCID NO: 0000-0003-2113-4510

Candaş YURDAKUL

Bursa Uludağ Üniversitesi, Mühendislik Fakültesi, Makine Mühendisliği Bölümü, Nilüfer, Bursa, Türkiye, ORCID NO: 0000-0003-2855-0701

ÖZET

Günümüzde, yaşam alanının bulunduğu bir çok yerde ambulans hizmeti mevcuttur. Ambulanslar hastaya ilk müdahale ve en yakın sağlık kuruluşuna taşınması yönünden hayati öneme sahiptir. Ambulansın hastaya servis verme sürecinde kabin içindeki termal koşullar ve hava kalitesi büyük önem arzetmektedir. Soğuk iklim şartlarına sahip bölgelerde aracın ısıtma sistemlerinin çalışması bazen yeterli olmamaktır. Ayrıca kabinin hızlı ısıtılması sürecinde de aracın ısıtma sistemi yeterli olmamaktadır. Bu sebeple kabin içerisine aracın ısıtma sistemine ek olarak ısıtıcı ilave edilmektedir. Böylelikle saatlerce soğuk havaya maruz kalmış araç kabini daha çabuk ısıtılmakta ve istenen termal koşullara ulaşma süresi önemli ölçüde kısaltılmaktadır. Bu çalışmada, ambulans kabini içerisine ilave edilen ısıtıcıyla havanın ısıtılması süreci deneysel ve sayısal olarak HAD yöntemiyle incelenerek elde edilen sonuçlar karşılaştırılmıştır. Farklı koşullar altında zamana bağlı çözümler ve kabin içindeki havanın rejime girme süresi değerlendirilmiştir. Ayrıca kabin içindeki hava hızı ve sıcaklık dağılımı termal konfor koşulları açısından incelenerek sonuçlar yorumlanmıştır.

Anahtar Kelimeler: Ambulans, Deneysel, HAD, Isıtma, Sıcaklık, Termal

ABSTRACT

Today, ambulance service is available in many places where living space is located. Ambulances are of vital importance in terms of first aid and transporting the patient to the nearest health institution. The thermal conditions and air quality in the cabin are of great importance in the ambulance service process. In regions with cold climate conditions, the operation of the vehicle's heating systems is sometimes not sufficient. In addition, the heating system of the vehicle is not sufficient during the rapid heating of the cabin. For this reason, a heater is added to the cabin in addition to the vehicle's heating system. Thus, the vehicle cabin, which has been exposed to cold air for hours, is heated more quickly and the time to reach the desired thermal conditions is significantly shortened. In this study, the process of heating the air with the heater added to the ambulance cabin was examined experimentally and numerically by the CFD method, and the results obtained were compared. Transient solutions under different operating conditions and the time interval to enter the steady-state regime of the air in the cabin were evaluated. In addition, the air velocity and temperature distribution in the cabin were examined in terms of thermal comfort conditions, and the results were interpreted

Keywords: Ambulance, CFD, Experimental, Heating, Temperature, Thermal

GİRİŞ

Araç içi ısıl konfor çalışmaları, diğer ısıl konfor çalışmalarına göre oldukça azdır. Araç kabin geometrisindeki ve havalandırma sistemindeki karmaşıklık, bu durumun başlıca sebeplerinden birisidir. Araç kabininin iklimlendirilmesinde termal geçişler hakimdir. Bu durum, aracın bulunduğu dış ortam sıcaklığı, menfezlerden gelen şartlandırılmış hava, güneş ışınım etkileri, nem seviyesi, hava hızları, termal kaçaklar, insan sayısı vb. gibi etmenlerin birbiri içerisinde yapmış olduğu ısı transfer modeli şeklidir. Yapılan deneysel ve sayısal çalışmalar, bir sonraki yapılan çalışmalar için önem arzetmektedir (Kılıç ve Akyol, 2012). Özellikle HAD analizi ile yapılan çalışmalarda sınır şartlarının belirlenmesi ve termal geçişlerin daha iyi bir şekilde simüle

edilmesi, doğru sonuca ulaşılması yönünden zaman kazandırmaktadır (Kılıç ve Sevilgen, 2009). Günümüz teknolojisinin gelişmesiyle, araç içi ısıl konfor çalışmaları önem kazanarak daha optimize sistemlerin oluşmasına olanak sağlamaktadır (Kılıç ve Akyol, 2009).

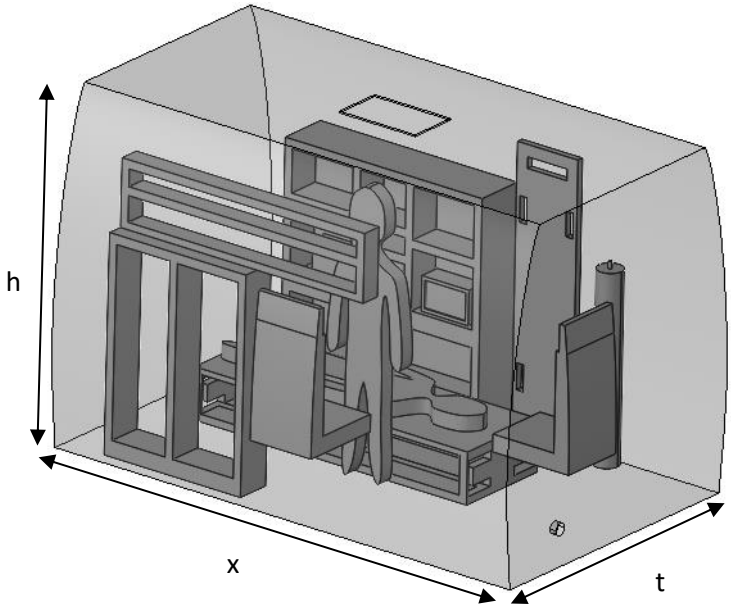
HAD analiziyle yapılan termal konfor çalışmalarında referans alınan parametre insan sağlığıdır. Örneğin bir otobüs kabininde, kış aylarında menfezlerden gelen sıcak havanın direkt insan üzerine gelmesi ya da az gelmesi insan sağlığını olumsuz yönde etkilemektedir (Korukçu ve Kılıç, 2011). Bu durumda termal konfor şartlarında yolcuların ve menfezlerin konumu, homojen sıcaklık dağılımına göre optimize edilmelidir (Kılıç ve Korukçu, 2012).

Korukçu vd. (2013) bir araç kabini içerisindeki ısınma sürecini, menfezden gelen farklı hava hızlarına göre HAD yöntemini kullaranak analiz edip sonuçları doğrulamış ve yorumlamışlardır. Yine benzer bir çalışmada ise Sevilgen ve Kılıç (2010) araç içerisindeki hava hızı ve sıcaklık etkilerini geçici rejimde HAD analizi yöntemi kullanarak belirleyip sıcaklık dağılımına olan etkilerini incelemişlerdir. Han vd. (2001) ise ısıl konfor etkilerinin öneminden ve araç dizayn başlangıcında göz önüne alınması gereken ısıl konfor etmenlerinden bahsetmişlerdir. Mhetre ve arkadaşları (2019), araç kabininin maruz kaldığı güneş radyasyon yükünü araştırmış ve sonuçları sayısal olarak incelemişlerdir. Sevilgen ve Kılıç (2012), araç kabini içerisindeki sıcaklık dağılımını üç eksende inceleyerek ısıl konforun araç yakıtına olan etkisine değinip, soğutucu gazın çevreye olan zararlarından bahsetmişlerdir.

Ambulans kabinin termal konfor şartlarının sağlanmasında başlıca parametreler vardır. Soğuk iklim şartlarının olduğu bölgelerde, hasta olmadığında dışarıda bekleyen bir ambulansın kabini, ortam sıcaklığı ile hemen hemen aynı değere gelmektedir. Anlık bir hasta hizmeti gelişmesi durumunda ambulans kabininin kısa bir sürede ısıtılması ve hastaya ulaşması gerekmektedir. Bu durumda kabinin ısınması süresi ve kabin içi sıcaklık dağılımının homojen olması termal konfor yönünden oldukça öneme sahiptir. Bu çalışmada ambulans kabininin ısıtılma süreci deneysel ve sayısal olarak incelenmiştir. Deneysel çalışma sürecinde kabin için uygun ortam şartları sağlanarak ısıtılma süreci başlatılmış ve sedye üzerindeki hava sıcaklık değerleri kaydedilmiştir. Sayısal olarak HAD analizi yöntemiyle bir inceleme yapılmış ve zamana bağlı olarak belirli periyotlarla değerler kaydedilmiştir. Bu durum sonucunda ısınma süreci ve sistemin rejime girme süresi, termal konfor açısından değerlendirilmiştir.

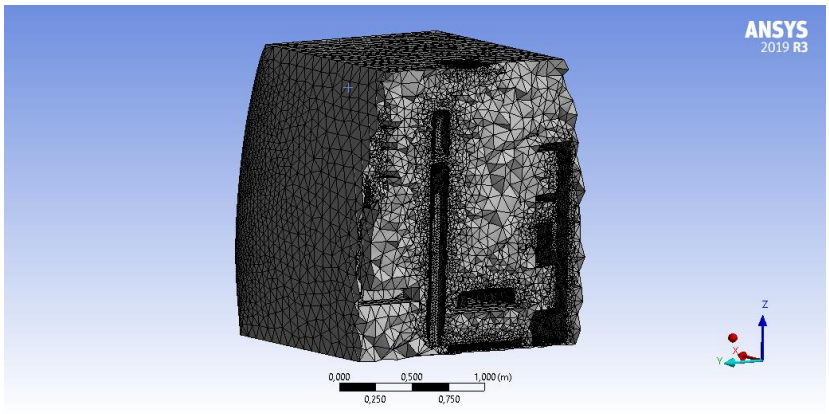
MATERYAL VE YÖNTEM

Çalışmaya konu olan araç modeli kabini, Mercedes 417 Sprinter modeline aittir. HAD analizi için üç boyutlu modellemede, kabinin iç hacim ölçüleri baz alınarak dış sınırlar belirlenmiştir. İç detayının modellenmesinde Sedye, iki adet insan, iki adet koltuk, iki adet dolap, oksijen tüpü, ısıtıcı sıcak hava giriş menfezi, havalandırma menfezi ve yedek taşıma sedyesi modellenmiştir. Üç boyutlu modelleme Solidworks ticari yazılımında yapılmıştır. Oluşan görüntü Şekil 1'de verilmiştir.



Şekil 1. Modellenen üç boyutlu kabin geometrisi

HAD analizi, Ansys Fluent ticari yazılımı kullanılarak yapılmıştır. Mesh modellemesinde esas alınan kriter element sayısının yeterliliği ve mesh modelinin geometrik sınırlar ile uyumluluğudur. Bu durumda gerçekleştirilen mesh işlemi sonucunda oluşan mesh görüntüsü Şekil 2'de verilmiştir.



Şekil 2. Mesh kesit görüntüsü

Geometri ve mesh işlemi için uygulanan parametreler Tablo 2'de gösterilmiştir.

Tablo 2. Geometri ve mesh işlemi parametreleri

Parametre	**Değer**
Inflatıon katman sayısı	7
Eleman boyutu	0,02 m
Eleman sayısı	524520
Skewness mesh kalite aralığı	0 – 0,25
x	3000 mm
t	1800 mm
h	2000 mm

HAD analizinin çözümlenmesi geçici rejimde analiz edilmiştir. Çözüm için belirlenen termal sınır şartlar, HAD analizi ve deneysel çalışma için aynıdır. Kabin içi, kabin kapısı kapalı olacak şekilde ısıtılmıştır. Isıtılma süreci boyunca kabinin bulunduğu ortam sıcaklığı sabit olarak 278 K değerindedir. Isıtıcı test süreci boyunca 370 K değerindedir. Kabin içerisinde bir yatan hasta ve bir hemşire bulunmaktadır. Tüm bu durumlar ışığında HAD analizi için sınır şartları belirlenmiştir. Analiz çözümü için belirlenen sınır şartları Tablo 3'te verilmiştir. Çözüm metodu olarak belirlenen yöntemler Tablo 4'te verilmiştir.

Tablo 3. HAD analizi sınır şartları

Parametre	**Kriter**
Türbülans Modeli	Spalart - Allmaras
Kabin duvarları sıcaklığı	278 K
Isıtıcı havası hız ve sıcaklığı	5 m/s ve 370 K
Hemşire ve hasta insan modeli sıcaklığı	309 K
Kabin içi havası başlangıç sıcaklığı	278 K

Tablo 4. Çözüm metodu

Parametre	**Metot**
Pressure – Velocity Coupling	Simple
Gradient	Least Squares Cell Based
Pressure	Second Order
Momentum	Second Order Upwind
Modified Turbulent Viscosity	First Order Upwind
Energy	Second Order Upwind
Transient Formulation	First Order Implicit

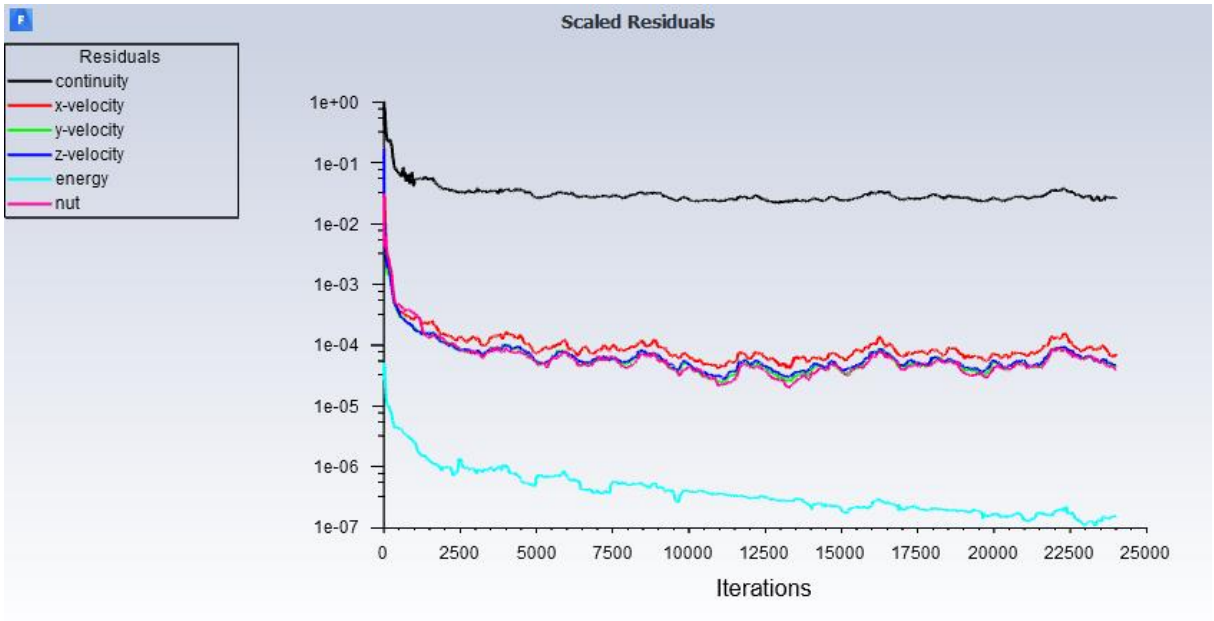
Çözüm için belirlenen başlangıç kriterleri Tablo 5'te verilmiştir. Burada yirmi dakikalık bir ısınma süresi için zaman adımı ve periyot kriterleri belirlenmiştir. Belirlenen değer ve kriterler Tablo 5'te verimiştir.

Tablo 5. Çözüm başlangıç kriterleri

Parametre	**Kriter**
Type	Fixed
Method	User - specified
Number of Time Steps	12 000
Time Step Size (s)	0,1
Max Iterations / Time Step	2
Reporting Interval	4
Profile Update Interval	1

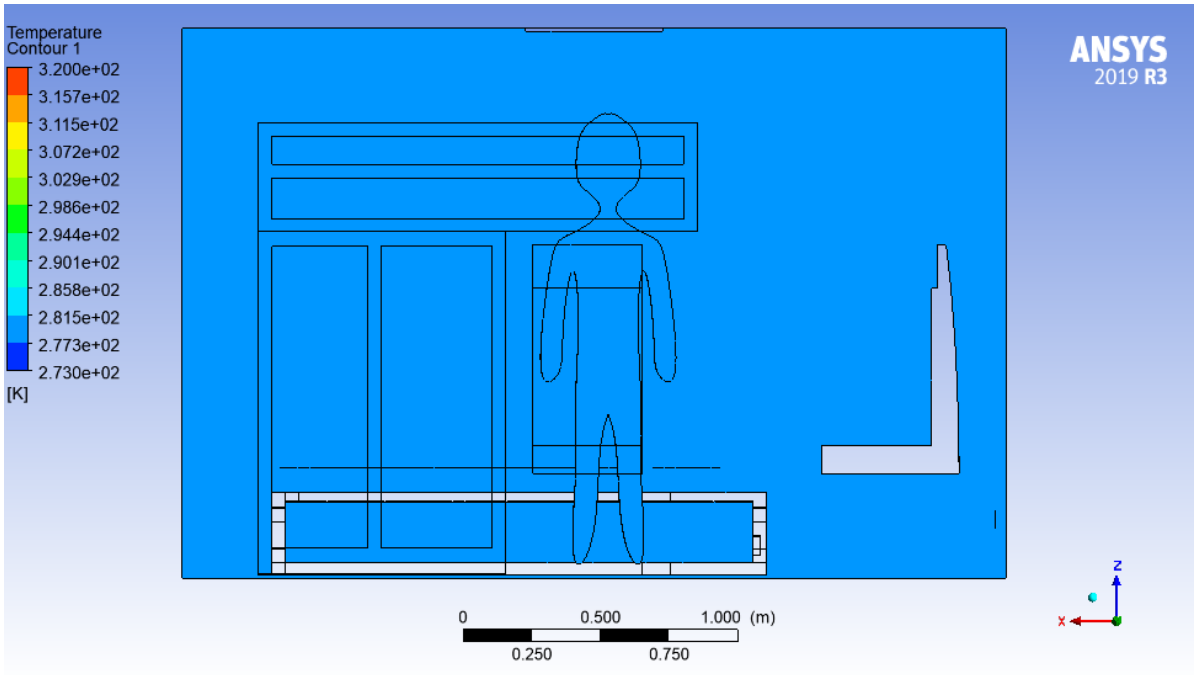
BULGULAR VE TARTIŞMA

Çözüm sonrası elde edilen yakınsama grafiği Şekil 3'te gösterilmiştir. Grafiğe bakıldığında değerlerin normal bir şekilde çözümlendiği gözlemlenmiştir.

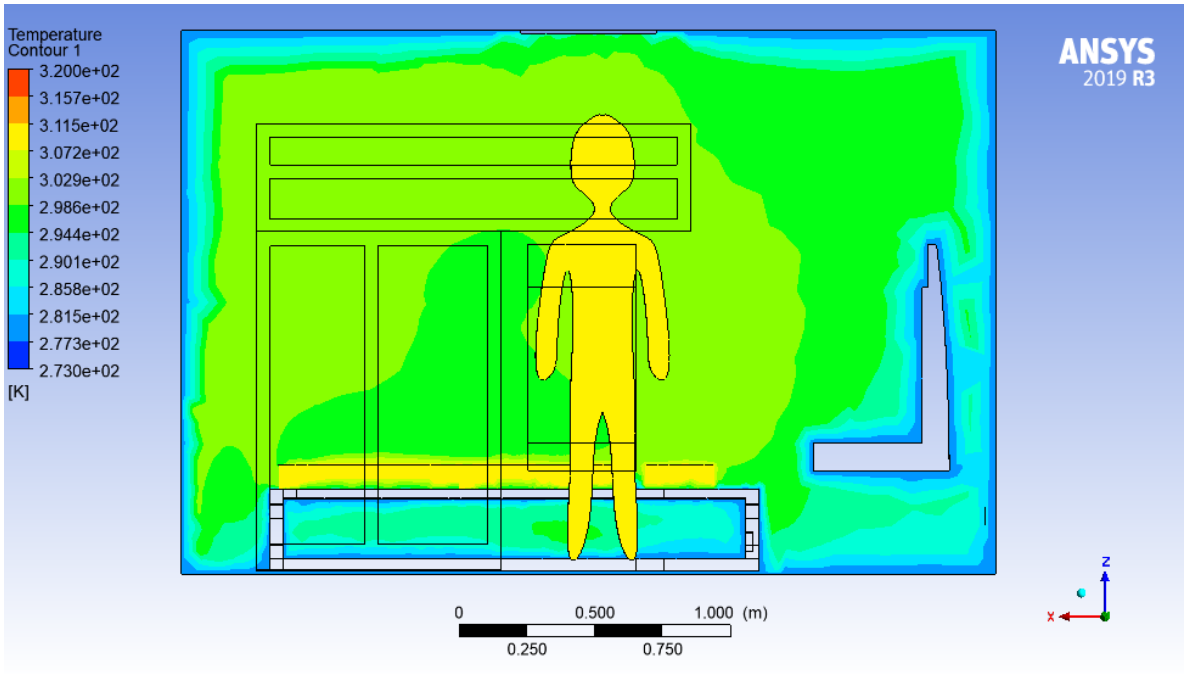


Şekil 3. HAD analizi yakınsama grafiği

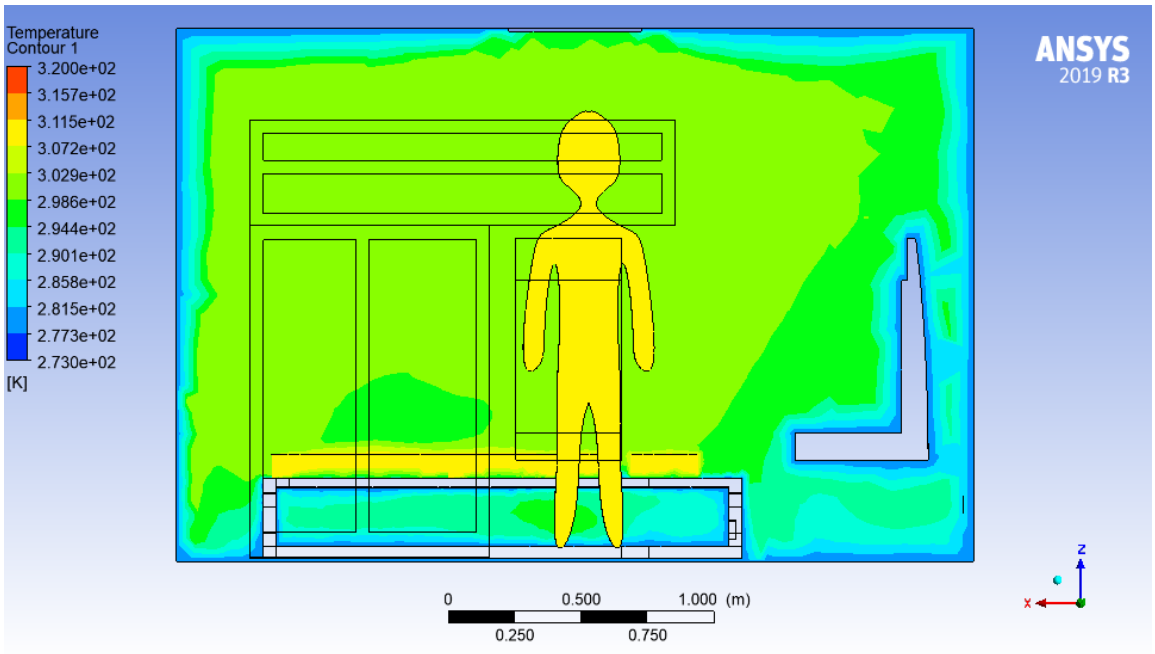
HAD analizi çözümlemesi sonucunda elde edilen 0, 5, 10, 15 ve 20 dakika periyotlarında kaydedilen kabin içi sıcaklık dağılımı görüntüleri Şekil 4 - Şekil 8 aralığında gösterilmiştir. Başlangıçta 278 K değerindeki ortam havası, yirmi dakika ısınma süresi sonrasında 295 – 300 K aralığında bir dağılım göstermektedir.



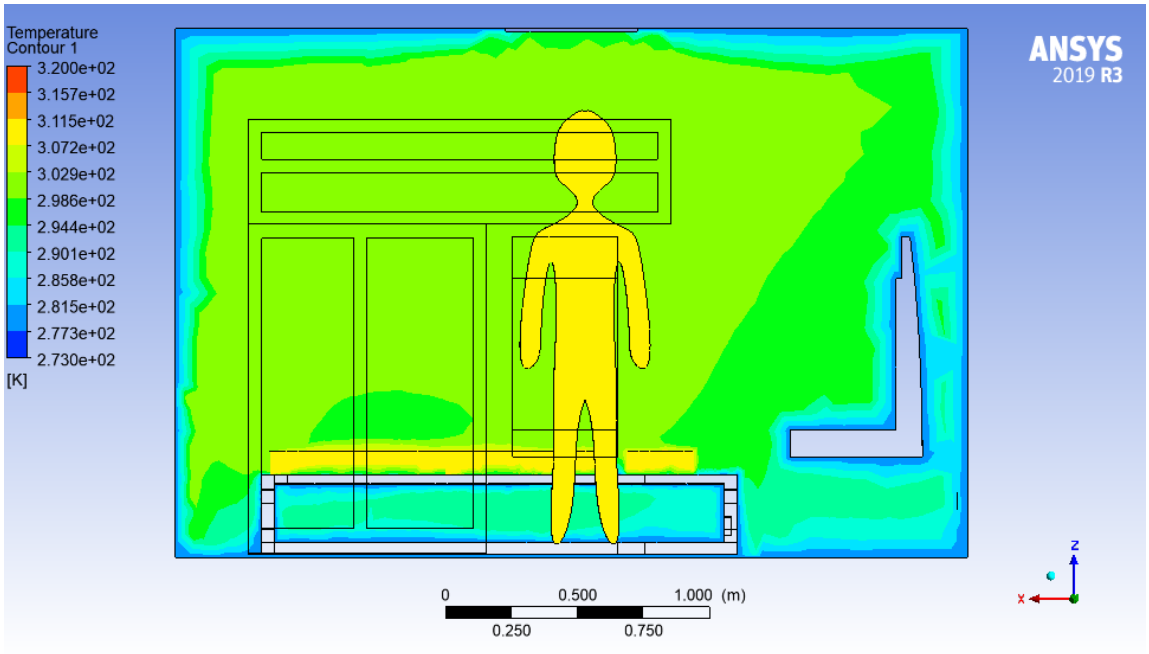
Şekil 4. 0. dk (başlangıç zamanı) sıcaklık dağılımı görüntüsü



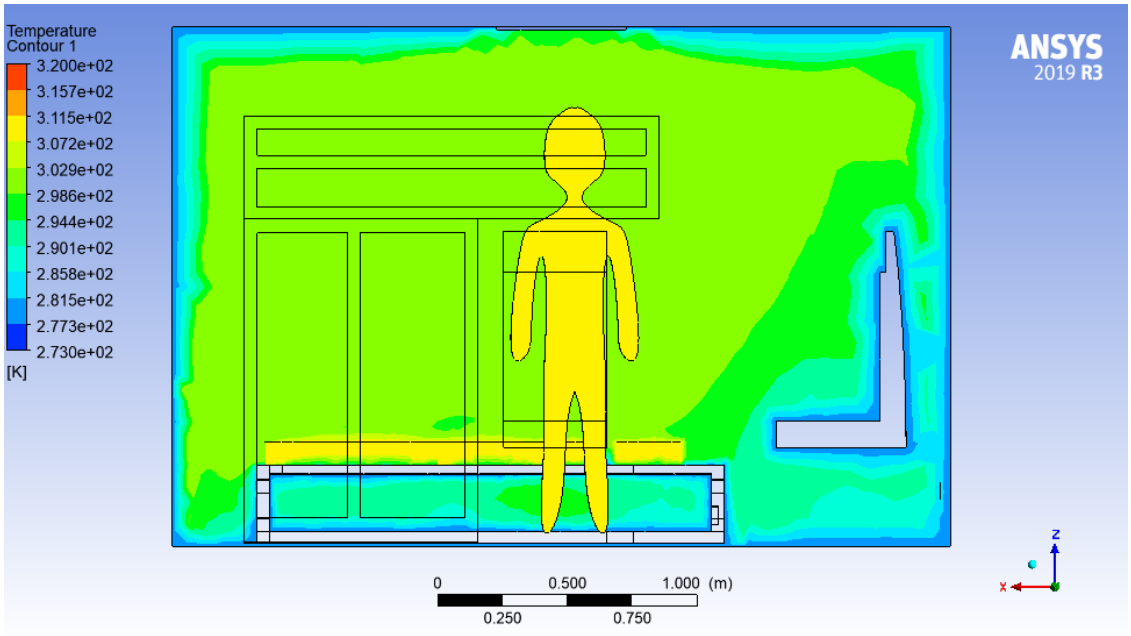
Şekil 5. 5. dk sıcaklık dağılımı görüntüsü



Şekil 6. 10. dk sıcaklık dağılımı görüntüsü

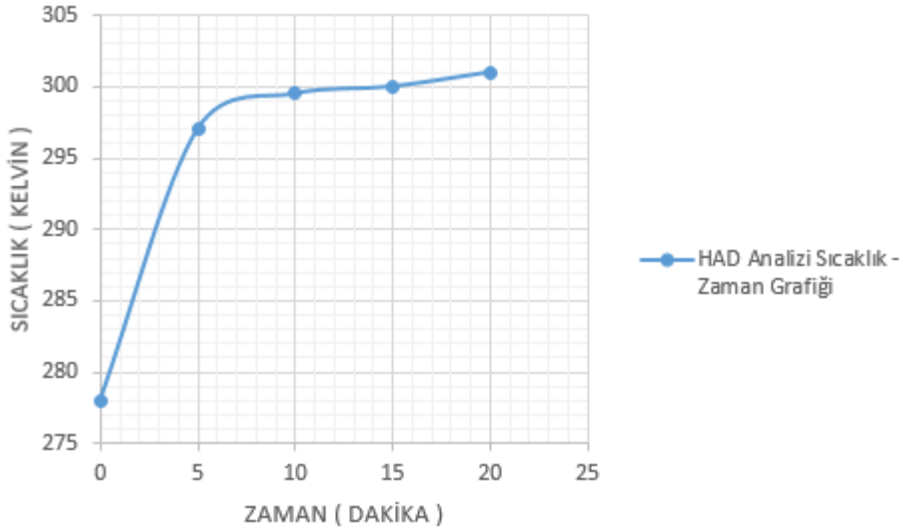


Şekil 7. 15. dk sıcaklık dağılımı görüntüsü



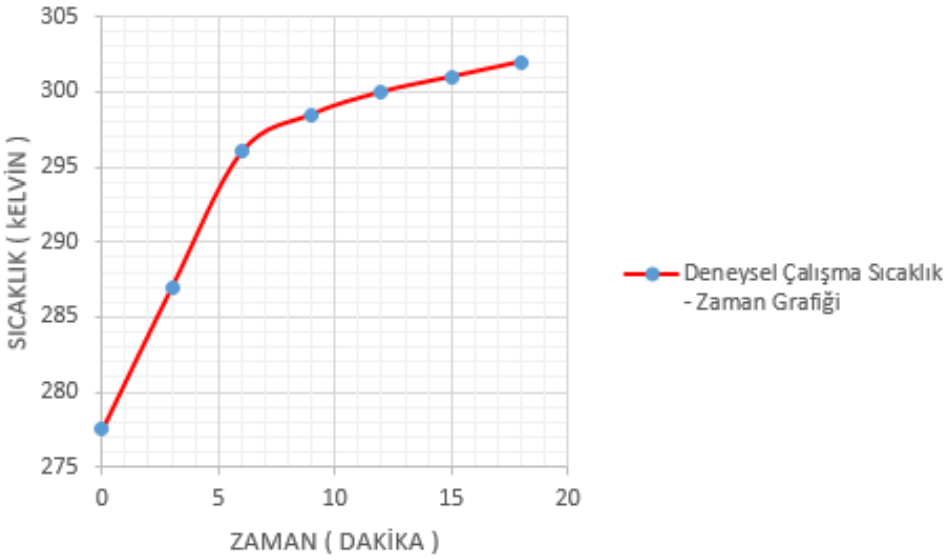
Şekil 8. 20. dk sıcaklık dağılımı görüntüsü

Elde edilen görüntülerde sıcaklık dağılımının koltuk ve sedye altlarında homojen dağılmadığı gözlemlenmiştir. Isıtıcının menfez konumu kabin geometrisine tam olarak simetrik bir bölümde kalmamaktadır ve yan kapı tarafına daha yakındır. Bu sebeple sıcak havanın dağılımı homojen değildir. Sedye üzeri hava sıcaklığı elde edilen sıcaklık – zaman grafiği Şekil 9'da gösterilmiştir. Sedye üzeri hava sıcaklığı değerleri incelendiğinde kabin 10. dk sonrasında yaklaşık 300 K sıcaklığında rejime girmeye başlamaktadır.



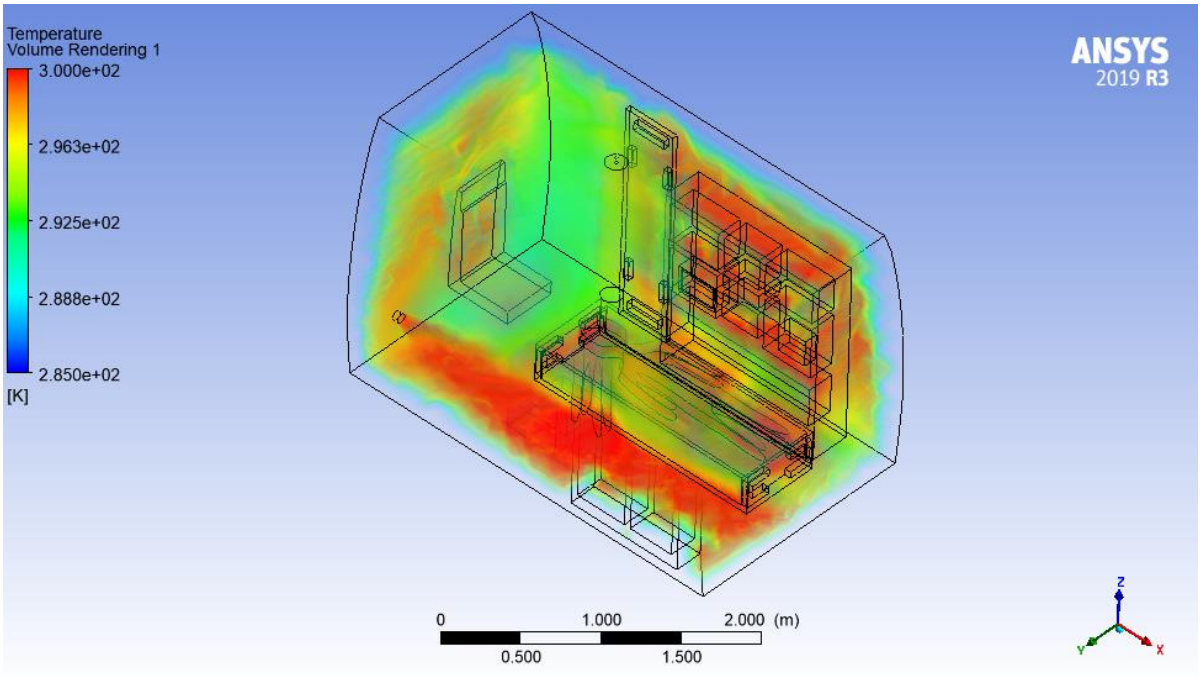
Şekil 9. HAD analizi sıcaklık – zaman grafiği

Deneysel olarak ölçüm sağlandığında sedye üzeri hava sıcaklığından elde edilen veriler Şekil 10'da gösterilmiştir.



Şekil 9. Deneysel çalışma sıcaklık – zaman grafiği

Elde edilen deneysel veriye göre sedye üzeri hava sıcaklığı incelendiğinde kabin içi 9. dk sonrasında rejime girmeye başlamaktadır. Bu bilgiler değerlendirildiğinde, ambulans kabininin belirli bölgelerine sıcak hava menfezlerinin konumlandırılması önerilmektedir. Kabin içi hacimsel sıcaklık dağılımı Şekil 10'da gösterilmiştir. Bu bölümler belirlenirken sıcaklığın homojen olmadığı ve düşük olduğu sedyenin sağ alt bölümleri, kabinin sağ dolap bölümü ve oksijen tüpünün olduğu bölümler olarak düşünülebilir.



Şekil 10. Kabin içi sıcaklık dağılımının hacimsel gösterimi (20. dk)

SONUÇ VE ÖNERİLER

Bu çalışmada ambulans kabininin ısıtılma süreci deneysel ve sayısal olarak incelenmiştir. Ambulans kabini üç boyutlu olarak modellenerek hesaplamalı akışkanlar dinamiği analizleri gerçekleştirilmiş ve gerçek ambulans üzerinde yapılan ölçümlerle analizler doğrulanmıştır. Kabin içindeki sıcaklık dağılımın zamana bağlı olarak değişimi ve rejime girme süresi elde edilmiştir. Kabin içindeki sıcaklık dağılımının homojen olmadığı gözlemlenmiş ve problemli bölgeler belirlenirken bu bölgeler için ilave sıcak hava menfezlerinin konumlandırılması önerilmiştir. Yapılan çalışma HAD analizlerinin tasarım aşamasındaki problemleri belirlemede etkin bir yöntem olduğunu göstermektedir.

KAYNAKÇA

Currle J. ve Maue J. 2000.”Numerical Study of Influence of Air Vent Area and Air Mass Fluxon the Thermal Confort of Car Occupants”, SAE Technical Paper Series, 2000(01):0980

Doğan, B., 2011. Bir taşıt içindeki havalandırma/ısıtma (ısıl dağılım) probleminin sayısal olarak incelenmesi. Tez (Yüksek Lisans) - Yıldız Teknik Üniversitesi, Fen Bilimleri Enstitüsü, İstanbul, Türkiye.

Han T., Huang L., Kelly S., Huizenga C. ve Hui Z. 2001. “Virtual Thermal Comfort Engineering”, SAE Technical Paper Series, 2001(01):0588

Kataoka T., 2001. “Prediction of Occupant’s Thermal Sensation Under the Transient Environment in a Vehicle Compartment”, SAE Technical Paper Series, 2001(01):0586

Kaynaklı, Ö., Kılıç, M., 2005. An investigation of thermal comfort inside an automobile during the heating period. Applied ergonomics, 36(3): 301-312.

Kılıç M., Akyol Ş. M. 2009. “Otomobil Kabinlerinin Isıtılmasında Farklı Hava Yönlendiricileri Kullanımının Isıl Konfora Etkisi”, Isı Bilimi ve Tekniği Dergisi, 29(1):25-36.

Kılıç M., Akyol Ş. M. 2012. “Experimental investigation of thermal comfort and air quality in an automobile cabin during the cooling period”, Heat and Mass Transfer 48 (8), 1375-

1384.

Kılıç, M., Korukçu, M.Ö. 2012. "Otomobillerde ısıtma sürecinde farklı menfez kullanımının ısıl konfora etkisi", Dokuz Eylül Üniversitesi Mühendislik Fakültesi Fen ve Mühendislik Dergisi, 14(3), 1-13.

Kılıç M., Sevilgen G. 2009." Evaluation of heat transfer characteristics in an automobile cabin with a virtual manikin during heating period", Numerical Heat Transfer, Part A: Applications 56 (6), 515-539.

Korukçu, M.Ö., Kılıç, M. 2011. "Otomobil Kabini içerisindeki Hava Hızının Isıl Konfora Etkisinin İncelenmesi", Sakarya University Journal of Science 15 (1), 60-67.

Korukçu, M.Ö., Kılıç, M. 2012. "Transient effects of different heating modes on temperature and humidity inside the automobile cabin during heating period", Journal of Thermal Science and Technology 32 (1), 101-107.

Mhetre, N., 2019. Prediction of HAVC Cool-Down Performance inside a Minibus Passenger Cabin Using CFD and Its Experimental Validation. SAMRIDDHI: A Journal of Physical Sciences, Engineering and Technology, 2019, 11.01: 47-56.

Mhetre, N., Sathyanarayan, S., Diwan, M., Kumar, S., Hulwan, D. 2019. Prediction of HAVC Cool-Down Performance inside a Minibus Passenger Cabin Using CFD and Its Experimental Validation. SAMRIDDHI: A Journal of Physical Sciences, Engineering and Technology, 11(01), 47-56.

Pirouz, Behrouz., 2021 CFD Investigation of Vehicle's Ventilation Systems and Analysis of ACH in Typical Airplanes, Cars, and Buses. Sustainability, 2021, 13.12: 6799.

Reggio M., Kudriavtsev V. ve Alexandrov A., 2001. "Analysis of Flow Patterns amd Heat Transfer in Generic Passenger Car Mini-Environment", 9th Annual Conferance of the CFD Society of Canada, 27-29 May, Kitchener/Ontario

Roy D., El Khoury K., Clodic D. ve Petitjean C. 2001. "Modelling of In-Vehicle Heat Transfers Using Zonal Approach", SAE Technical Paper Series, 2001(01):1333

Sevilgen, G., Kılıç, M. 2010. Transient numerical analysis of airflow and heat transfer in a vehicle cabin during heating period. International Journal of Vehicle Design 52 (1/2/3/4), 144-159

Sevilgen, G., Kilic, M. 2012. Three dimensional numerical analysis of temperature distribution in an automobile cabin. Thermal science, 16(1), 321-326.

BAZ YAĞ TİPİNİN GRES AKIŞ BASINCI DAVRANIŞI ÜZERİNE ETKİSİ

Kübranur AĞTOPRAK

Belgin Oil R&D Center, Kocaeli, Turkey., ORCID NO: 0000-0002-9125-5644

Dr. Uğur KARAASLAN

Belgin Oil R&D Center, Kocaeli, Turkey., ORCID NO: 0000-0003-2972-4224

ÖZET

Gres baz yağ, kalınlaştırıcı ve çeşitli katıklardan oluşan yarı sıvı bir yağlayıcıdır. Bu özelliğinden dolayı çok çeşitli sektör ve ekipmanlarda kullanılmaktadır. Oda sıcaklığında yarı sıvı özelliğinden ve belli bir sıcaklığa kadar bu özelliğini yitirmemelerinden kaynaklı olarak uygulandıkları yüzeylerde akmadan kalabilirler ve bu nedenle sıvı yağlayıcılara göre avantaj sağlarlar. Diğer bir yandan ise yüksek sıcaklıklarda sıvı forma geçerken düşük sıcaklıklarda kıvamları artarak katı forma geçebilmektedirler. Bu nedenle düşük sıcaklıklarda uygulandığı ekipmanlarda (örneğin rulmanlar) katılaşıp sistemi durdurmamaları için özel baz yağlar ve kalınlaştırıcı tipleri seçilmelidir. Ayrıca gresler bir pompa vasıtası ile uygulanacak ekipmanlara iletilmektedir. Bu çalışmada greslerin düşük sıcaklıklarda pompalanabilme kabiliyetlerine gresi oluşturan baz yağların etkisi araştırılmıştır. Ölçümler MiniTest FFK Gres Analizörü cihazıyla yapılmıştır. Parafinik, naftanik ve sentetik (PAO ve PAG) baz yağlar kullanılarak NLGI 2 sınıfı lityum gresi oluşturulmuş ve düşük sıcaklıklarda (-20 °C ve -30 °C) akış basınçları ölçülmüştür. Sonuç olarak kullanılan baz yağ tipinin yağlama greslerinin akış basıncını doğrudan etkilediği tespit edilmiştir. Akış basıncını en düşükten başlayarak sırasıyla sentetik, naftanik ve parafinik baz yağlarının verdiği tespit edilmiştir. Çalışmada akma noktaları birbirinden farklı aynı viskozitede baz yağlar kullanılmıştır. Yağların gresin akış basıncı değerlerine etkisi akma noktası değerleri ile paralellik göstermektedir. Bu nedenle parafinik baz yağın akma noktası değeri çeşitli oranlarda akma noktası düşürücü (PPD) katık kullanılıp düşürülerek lityum gresinin akış basınçları tekrar ölçülmüştür. Yapılan ölçüm sonunda beklenenin aksine baz yağın akma noktası değerleri düşmesine rağmen akış basıncı değerleri yükselmiştir. PPD katığı olan PAMA (Polimetilmetakrilat) tipi polimerin düşük sıcaklıklarda büzüşerek sıvıların aksine kalınlaştırıcı ile beraber gresi daha kıvamlı hale getirdiği ve akmaya karşı direnç oluşturduğu düşünülmektedir. Ayrıca, farklı polimer tiplerinin gres akış basıncına etkisi incelenmiştir. Akış basıncını negatif yönde etkilediği bulunmuştur. Bu çalışma göstermiştir ki yağlayıcı gres formülasyonu oluşturulurken düşük sıcaklık performansı isteniyor ise sentetik baz yağ kullanımı gerekmektedir. İlave edilen polimerler, gresin düşük sıcaklıkta pomplanabilirliğini olumsuz etkilemektedir.

Anahtar Kelimeler: Yağlayıcı gres, baz yağ, akma noktası, akış basıncı, pompalanabilirlik.

EFFECT OF BASE OIL TYPE ON GREASE FLOW PRESSURE BEHAVIOR

ABSTRACT

Grease is a semi-liquid lubricant composed of thickener, base oil and additives. Due to this property, they are used in so many sectors and equipment. Although grease is semi-liquid at room temperature, it is liquid at high temperatures and solid at low temperatures. Thanks to this feature, it can stay on the applied surfaces without flowing. With this feature, it provides superiority over liquid lubricants. Special base oils and thickener types should be selected so that they don't stop the system in equipment (bearings etc.) where it's applied by means of a pump at low temperatures. In this study, the effect of the base oils that compose the grease on the pumpability of greases at low temperatures was investigated. Measurements were made via MiniTest FFK Grease Analyzer. NLGI 2 class lithium grease was obtained using paraffinic, naphthenic and synthetic (PAO and PAG) base oils and flow pressures were measured at -20°C and -30°C. Consequently, it was determined that the type of base oil used directly effects the flow pressure of the greases. Flow pressures were measured from lowest to high value by using synthetic, naphthenic and paraffinic base oils, respectively. The effect of oils on the flow pressure values of the grease shows parallelism with the pour point of base oils. To understand

the pour point effect on grease flow pressure, the pour point of the paraffinic base oil was reduced by pour point depressant (PPD) additive at various rates and then flow pressures of the grease were measured again. It was observed that although the pour point values of the base oil decreased, the flow pressure values increased. It's thought that PAMA (Polymethylmethacrylate), which is a PPD additive, shrinks at low temperatures, making the grease more viscous and resisting flowing with the thickener, unlike liquids. In addition, the effect of different polymer types on the grease flow pressure was investigated. It was found that it effects the flow pressure negatively. This study showed that synthetic base oil should be used if low temperature performance is desired while formulating a lubricating grease formulation. Polymer additive prevented the mobility of the grease and decreased the pumpability behavior at low temperatures.

Keywords: Lubricating greases, base oil, pour point, flow pressure, pumpability.

INTRODUCTION

Grease is a semi-liquid lubricant composed of thickener, base oil and additives. Due to this property, they are used in so many sectors and equipment. Recently, lubricating greases are used to extend the service life and increase efficiency of all moving equipment. Therefore, it is extremely important for a wide variety of industry applications and daily lubrication challenges.

Grease is widely used in Rolling-contact bearings, and is the principal component which directly influences the lubrication performance. Grease lubrication depends on grease components including base oils, their viscosity, thickeners and their concentration, which are chosen to meet lubricating performances required (Yokouchi et al., 2011). Although grease is semi-liquid at room temperature, it is liquid at high temperatures and solid at low temperatures. Thanks to this feature, it can stay on the applied surfaces without flowing. With this feature, it provides superiority over liquid lubricants. Special base oils and thickener types should be selected so that they don't stop the system in equipment (bearings etc.) where it's applied by means of a pump at low temperatures. The flow pressure of the greases that lubricate through the pump from the central system is important. The base oils used in this study are as follows; The lubricating properties of paraffinics are good. Naphtanics have a solvent effect and have good low temperature performance. PAG and PAO are known for their low temperature performance. Parafinic base oils in group I. PAO in Group IV. Naphthanics and PAG in group V.

Peskoe said, lubricants flow more slowly at lower temperatures as the kinetic energy of their molecules is reduced (Peskoe., 2020). Kumar et al., reported low-temperature flowability is an important property of greases that effects performance in low temperature environments. Also, they said this property becomes more desirable in centralized lubrication systems. Subsuquently, they explained the low-temperature behavior of a grease depends on its composition such as base oil, type and length of thickener fibers, and polymers (Kumar et al., 2020). Base oil greatly influences the flow properties of a grease, has been explained by Kumar. All else being equal, for example, synthetic oil-based grease is expected to flow better than a grease formulated with mineral base oil, Kumar explained. Also reported base oil viscosity and polymer present in the grease also might influence the flow characteristics of a grease at low temperatures (Peskoe., 2020). In the study of Salomonsson et al., the flow pressures of lithium greases containing paraffinic and naphtanic base oil were measured. According to their results, the pumpability of naphthenic greases was clearly superior to the pumpability of paraffinic greases at temperatures between -20°C and -40°C (Salomonsson et al., 2007). Casserly et al reported that the solubility of the base oil is an important parameter for the processing of grease. In their experimental results, they emphasized that there is a significant relationship between base oil solvency and thickener efficiency. They reported that the selection of base oils is important for the mobility of the grease. They also emphasized the importance of high solvent and low PAH content of modern naphtanic base oils for special applications such as grease (Casserly et al., 2018).

Polymers, in general, are known to deteriorate the low temperature flowability properties of greases (Kumar et al., 2020). The polymers used in this study (PAMA, OCP and PIB) are also known as viscosity index improvers (VII). As VII increases, the viscosity of the oil is less effected by temperature change. In the book published by Braun, these molecules are defined as chain-like molecules whose solubility depends on chain length, structure, and chemical composition. The absolute increase in viscosity and the VI depends on the type, the molecular weight and the concentration of viscosity modifiers in the formulation (Braun., 2017).

Çınar and Karaaslan investigated the effect of pour point additive on the low temperature (-20°C) pumpability performance of greases. For this purpose, 0.5%, 1%, 2% and 3% pour point depressant (PPD) was added directly to lithium greases. As a result of their study, they determined that pour point additive negatively effects low temperature flow pressures (pumpability) of greases (Çınar and Karaaslan., 2021). PPD is one of the alternatives to improve the low temperature performance of a lubricants. Soldi et al. studied the effect of PPD additive on paraffinic base oil. As a result, they reported that PPD improved the pour point of paraffinic base oil (Soldi et al., 2007).

MATERIALS AND METHOD

Materials

In this study several types base oils (Paraffinic, naphthanic, synthetic (PAG (Polyalkylene Glycol), PAO (Polyalphaolefin)) and polymers (PAMA (Poly alkyl methacrylates), OCP (Olefin copolymers), PIB (Poly isobutilene)) commercialy available were used. Also, NLGI number 2 lithium hydroxy stearate grease was used.

Methods

Kinematic viscosity, pour point and penetration number were measured according to ASTM D445, D97 and D217 standards with Kinematic Viscometer, Pour Point Tester and Penetrometer, respectively. In addition, flow pressure measurements of the lubricating greases were made in accordance with the DIN 51805 (Kesternich Technique) method with using MINITEST-FFK equipment.

Experiment

The viscosity of the base oils was adjusted to 150 cSt. NLGI 2 class lithium grease was obtained using paraffinic, naphthenic and synthetic (PAO and PAG) base oils as a blend. A mixture of base oils and PAMA (as a pour point depressant) were prepared and lithium grease was obtained. Likewise, greases were obtained separately with OCP and PIB polymers in base oils. Flow pressures were measured at -20°C and -30°C with an increasing pressure of 30 mbar every 30 seconds.

FINDINGS AND DISCUSSION

In this study, the effect of the base oils that compose the grease on the pumpability of greases at low temperatures was investigated. NLGI 2 class lithium grease was obtained using paraffinic, naphthenic and synthetic (PAO and PAG) base oils and flow pressures were measured at -20°C and -30°C.

Experimental results of grease samples obtained by using different type base oils are shown in Table 1. Pour points of the base oils are shown in Figure 1. The lowest pour point was found as -42°C with PAO base oils. Subsequently, PAG, naphthanic and paraffinic base oils were detected as -39°C, -18°C and -9°C, respectively. Flow pressure of different base oil in grease are shown in Figure 2. According to Fig. 2, base oils with low pour points have been found to improve flow pressure. It has been determineted that synthetic base oils have low pour points, giving them the property to provide advantages mobility at low temperatures.

Table 1. Experimental results of grease data with different base oil type

Grease Base Oil Content	Thickener Type	NLGI #	Worked Penetration (25°C, 60 strokes)	Base Oil Viscosity (@40°C, cSt)	Base Oil Pour Point (°C)	Flow Pressure (-20°C, mbar)	Flow Pressure (-30°C, mbar)
Paraffinic	Lithium	2	276	150	-9	360	630
Naphthanic	Lithium	2	279	150	-18	240	450
PAG	Lithium	2	279	150	-39	240	420
PAO	Lithium	2	287	150	-42	150	270

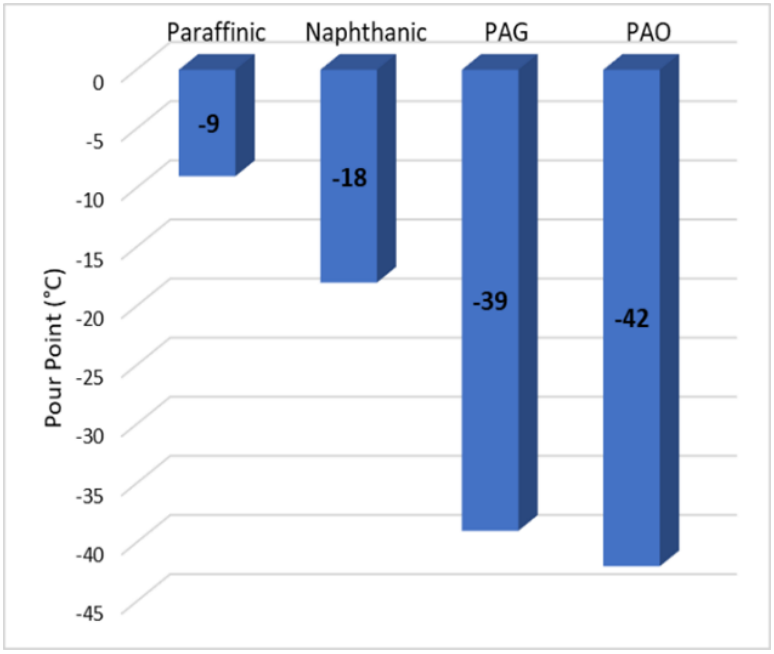


Fig. 1. Pour point of base oils

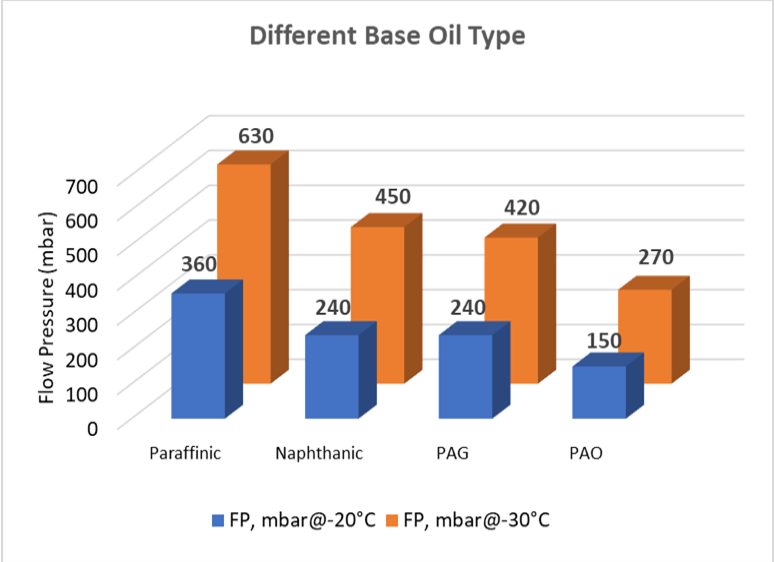


Fig. 2. Grease flow pressure behavior of different base oil types

Experimental results of grease samples obtained by using different type base oils with PAMA as a PPD are shown in Table 2. Pour points of the paraffinic is shown in Figure 3. Effect of paraffinic base oil with PAMA (as a PPD additive) to grease sample's flow pressure is shown in Figure 4. Despite the addition of pour point additive, flow pressure showed reverse trend in paraffinics. There is even an increase. It's stable after a certain rate. Effect of naphthanic base oil with PAMA additive to grease sample's flow pressure is shown in Figure 5. Pour point additive was also added to the naphtanic base oil, but no change up to 1% was observed at -20°C. Subsequently, it increased at 2%. An increase in flow pressure was observed with PAMA concentration at -30°C. Flow pressure is more effective at -30°C. Conversely, this was lower than the increase rate of paraffinic base oil. Effect of PAO base oil with PAMA additive to grease sample's flow pressure is shown in Figure 6. The same things were detected for synthetic (PAO) base oil. In addition, since naphtanic and synthetic base oils have so low pour points, the negative effect of polymer additives was lower than paraffinic oil.

Table 2. Grease data include different base oil type with PAMA as a PPD

Grease Base Oil Content	Thickener Type	Base Oil Viscosity (@40°C, cSt)	NLGI #	Worked Penetration (25°C, 60 strokes)	Base Oil Pour Point (°C)	Flow Pressure (-20°C, mbar)	Flow Pressure (-30°C, mbar)
Paraffinic	Lithium	150	2	276	-9	360	630
Paraffinic + 0.3% PAMA	Lithium	150	2	276	-19	390	1050
Paraffinic + 0.5% PAMA	Lithium	150	2	276	-21	480	1230
Paraffinic + 1% PAMA	Lithium	150	2	276	-24	480	1230
Paraffinic + 2% PAMA	Lithium	150	2	276	-27	480	1230
Naphthanic	Lithium	150	2	279	-18	240	450
Naphthanic + 0.3% PAMA	Lithium	150	2	279	-18	240	450
Naphthanic + 0.5% PAMA	Lithium	150	2	279	-21	240	480
Naphthanic + 1% PAMA	Lithium	150	2	279	-21	240	510
Naphthanic + 2% PAMA	Lithium	150	2	279	-21	270	540
PAO	Lithium	150	2	287	< -42	150	270
PAO + 0.3% PAMA	Lithium	150	2	287	< -42	150	270
PAO + 0.5% PAMA	Lithium	150	2	287	< -42	150	270
PAO + 1% PAMA	Lithium	150	2	287	< -42	150	300
PAO + 2% PAMA	Lithium	150	2	287	< -42	180	330

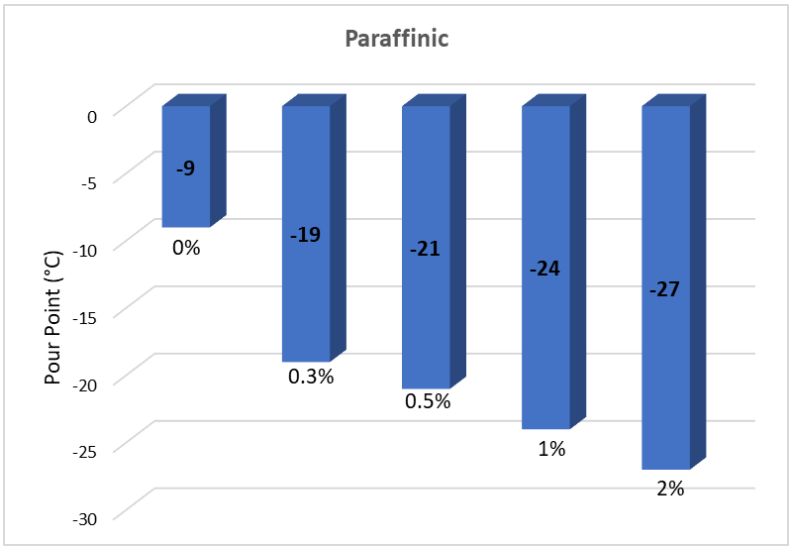


Fig. 3. Effect of PAMA base PPD additive to paraffinic base oil pour point

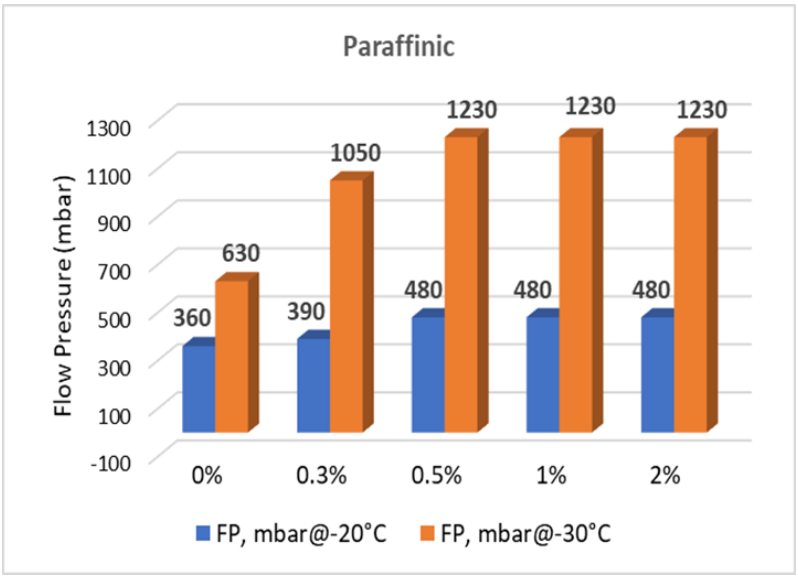


Fig. 4. Effect of PAMA on flow pressure of grease containing paraffinic base oil at -20°C and -30°C

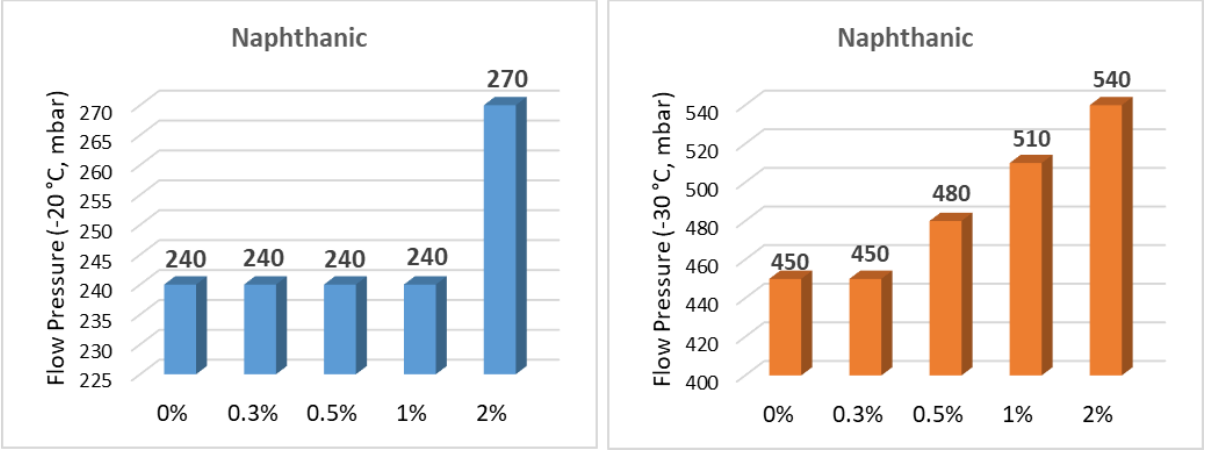


Fig. 5. Effect of PAMA on flow pressure of grease containing naphtanic base oil at -20°C and -30°C

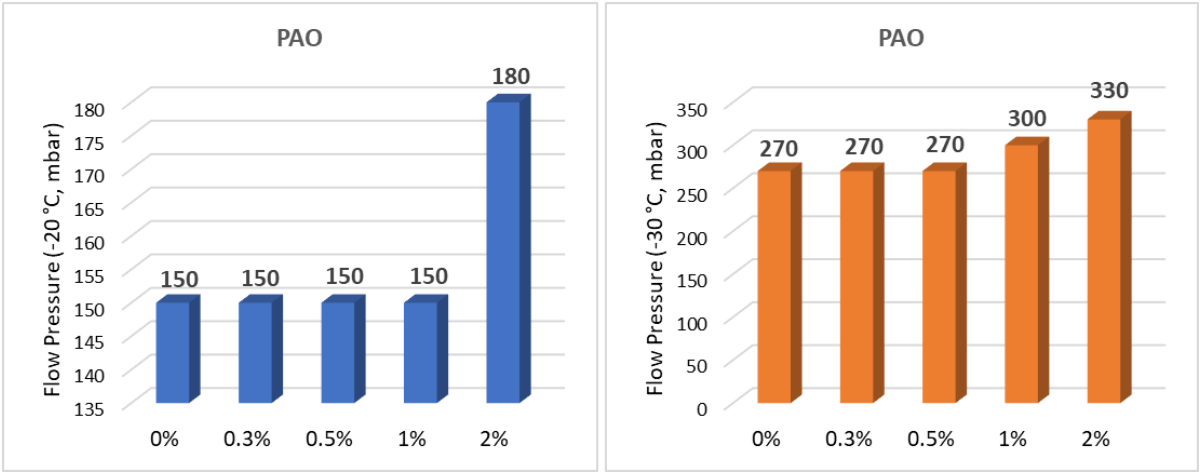


Fig. 6. Effect of PAMA on flow pressure of grease containing PAO base oil at -20°C and -30°C

In addition, ready-to-use PIB and OCP-based polymers were dissolved in different base oil and mixtures were add into the grease. Subsequently, grease flow pressures were measured to see the effect on flow pressure in other types of polymers. Experimental results of grease sample obtained by using different base oil with PAMA, OCP & PIB are shown in Table 3. Grease flow pressures measured by adding different polymers into paraffinic, naphtanic and PAO base oils are shown in Figure 9. Figure 10 and Figure 11, respectively. According to Fig. 9, Fig. 10 and Fig. 11, the polymer increased the flow pressure in all oils, again more in paraffinics. This is explained as follows; viscosity index polymers shrink at low temperatures and expand at high temperatures. Here too, it has a negative effect on the flow pressure as it shrinks with the grease at low temperatures.

Table 3. Experimental results of grease data by using different base oil with PAMA, OCP & PIB

Grease Base Oil Content	Thickener Type	Base Oil Viscosity (@40°C, cSt)	NLGI #	Worked Penetration (25°C, 60 strokes)	Base Oil Pour Point (°C)	Flow Pressure (-20°C, mbar)	Flow Pressure (-30°C, mbar)
Paraffinic	Lithium	150	2	276	-9	360	630
Paraffinic + 2% PAMA	Lithium	150	2	276	-27	480	1230
Paraffinic + 2% OCP	Lithium	150	2	276	-9	450	1230
Paraffinic + 2% PIB	Lithium	150	2	276	-9	480	1230
Naphthanic	Lithium	150	2	279	-18	240	450
Naphthanic + 2% PAMA	Lithium	150	2	279	-21	270	540
Naphthanic + 2% OCP	Lithium	150	2	279	-18	240	540
Naphthanic + 2% PIB	Lithium	150	2	279	-18	330	690
PAO	Lithium	150	2	287	-42	150	270
PAO + 2% PAMA	Lithium	150	2	287	< -42	180	330
PAO + 2% OCP	Lithium	150	2	287	-42	150	270
PAO + 2% PIB	Lithium	150	2	287	-42	210	390

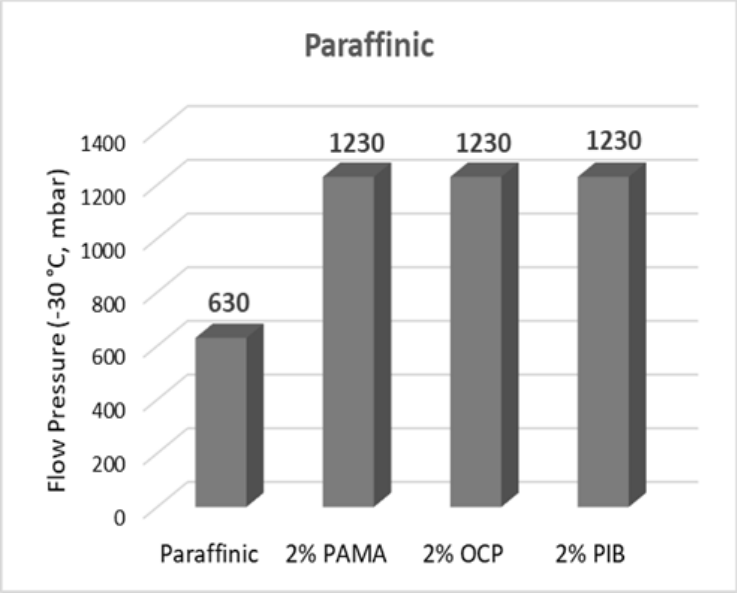


Fig. 9. Effect of different polymers on flow pressure of grease containing paraffinic base oil at -30°C

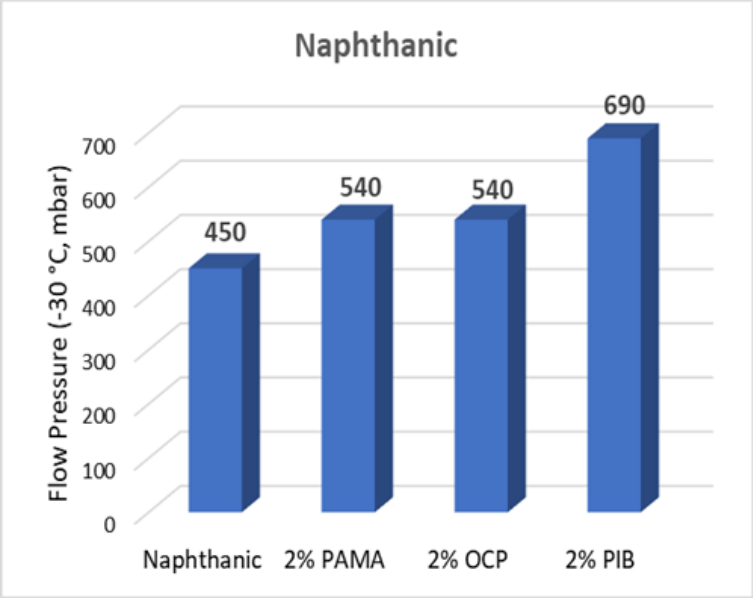


Fig. 10. Effect of different polymers on flow pressure of grease containing naphthanic base oil at -30°C

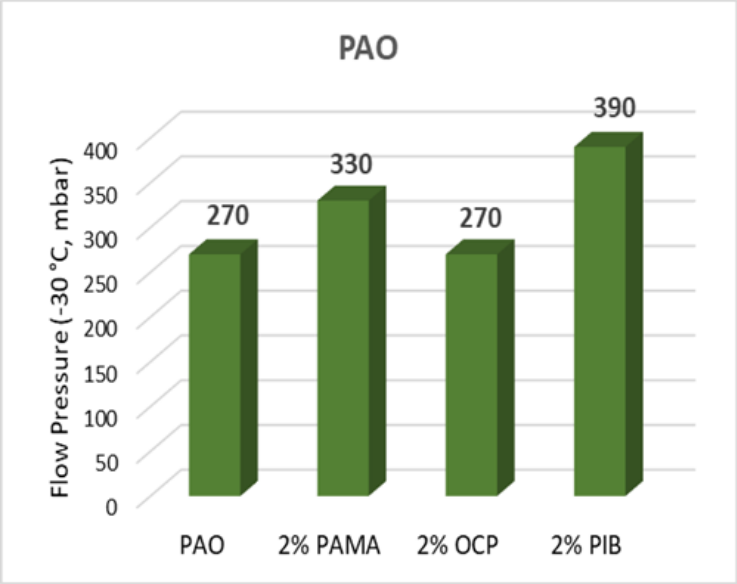


Fig. 11. Effect of different polymers on flow pressure of grease containing PAO base oil at -30°C

CONCLUSION

This study shows that base oil type used to compose a grease directly effectes the flow pressure of the greases. According to the grease flow pressure results containing different base oil types, PAO base oils showed the lowest flow pressure. Naphtanic base oils followed. Paraffinic base oils showed the highest flow pressure properties. The effect of oils on the flow pressure of the grease showed parallelism with the pour point of base oils. In addition, it was found that polymer additives increase the grease flow pressure. Despite the addition of PPD (PAMA) to base oils, flow pressures increased though decreased the pour point fo base oil used in grease. Besides OCP and PIB polymers added to the base oil negatively effected the grease flow pressure. It is thought that the polymers shrink with the grease at low temperatures and negatively effected the mobility of the grease so it increases the flow pressure. Therefore, if the grease is to be used in very low temperature conditions, it should be produced with synthetic type base oil and the use of polymeric type additives should be avoided.

REFERENCES

Braun, J. (2017). Additives. *Lubricants and lubrication*, 117-152.

Casserly, E., Langlais, T., Springer, S. P., Kumar, A., & Mallory, B. J. L. M. (2018). The effect of base oils on thickening and physical properties of lubricating greases. *Lube Magazine*, (144), 32-37.

Çınar, N. & Karaaslan, U. (2021). Low temperature fluidity properties of lubricating greases and the effect of pour point additive on grease fluidity. *Ispec international congress on multidisciplinary studies*, Nov. 11-12, 219-236.

Dandan, M. A., Yahaya, A., & Syahrullail, S. (2019). The Effect of the Different Percentage of Pour Point Depressant (PPD) On the Tribological Properties of Palm Kernel Oil. *Tribology in Industry*, *41*(3).

Kumar A., Shah R., & Miller C. (2020). Comparative and correlative studies of water resistance, tackiness and low-temperature properties in a wide range of greases. *NLGI Spokesman*, 84(6), 40-52.

Peskoe-Yang, L. (2020). Grease flow. *Tribology & Lubrication Technology*, *76*(12), 22-24.

Salomonsson, L., Stang, G., & Zhmud, B. (2007). Oil/thickener interactions and rheology of lubricating greases. *Tribology Transactions*, *50*(3), 302-309.

Soldi, R. A., Oliveira, A. R., Barbosa, R. V., & César-Oliveira, M. A. (2007). Polymethacrylates: Pour point depressants in diesel oil. *European Polymer Journal*, *43*(8), 3671-3678.

Yokouchi, A., Hokao, M., & Sugimura, J. (2011). Effects of soap fiber structure on boundary lubrication of lithium soap greases. *Tribology Online*, *6*(4), 219-225.

INVESTIGATION OF HIGH TEMPERATURE PERFORMANCE OF DIFFERENT TYPES OF VISCOSITY INDEX IMPROVER POLYMERS WITH HTHS AND TGA

Meryem BOSTANCI

Belgin Madeni Yağlar Ar-Ge Merkezi, Kocaeli, Türkiye., ORCID NO: 0000-0001-8143-4289

Dr. Uğur KARAASLAN

Belgin Madeni Yağlar Ar-Ge Merkezi, Kocaeli, Türkiye., ORCID NO: 0000-0003-2972-4224

ÖZET

Bu çalışma, ticari olarak temin edilebilen farklı tip VII polimerleri ile hazırlanan SAE 5W-30 motor yağlarınıntermogravimetrik bozunmasını kapsamaktadır. Bu amaçla farklı tipte seçilen VII polimerleri (PAMA, HSD ve OCP) ve bu polimerlerin Grup I, Grup II, Grup III, Grup IV ve Grup V baz yağlarda %5 oranında hazırlanan karışımlarının TGA analizleri gerçekleştirilmiştir. Baz yağların, polimerlerin bozunma sıcaklığına etkisini incelemek için numunelerin bozunma sıcaklıkları TGA cihazı ile ölçülmüştür. TGA taramaları, nitrojen atmosferi altında 50-900°C arasında ve 10°C/dk tarama hızında gerçekleştirilmiştir. Bu çalışmanın sonunda sırasıyla en yüksek bozunma sıcaklığını PAMA, OCP ve HSD'nin verdiği görülmüştür. Ayrıca sentetik baz yağların VII polimerlerinin bozunma sıcaklığını daha yüksek bir sıcaklığa kaydırdığı tespit edilmiştir. Bu çalışma, ticari olarak temin edilen farklı tipteki kullanıma hazır VII katıklarının HTHS ile yüksek sıcaklık performanslarının tespit edilmesi ve bu katıklarla hazırlanan SAE 5W-30 motor yağlarının termogravimetrik bozunması üzerine etkisini kapsamaktadır. Bu amaçla OCP, PAMA ve HSD tip VII polimerlerinin %5, %10 ve %15'lik karışımları 150°C'de hazırlanarak HTHS ölçümleri yapılmıştır. Ayrıca bu VII katkı maddeleri, aynı baz yağ ve katık paketi ile SAE 5W-30 viskozite sınıfına sahip motor yağı formülasyonları hazırlanmış ve TGA analizleri yapılmıştır. Polimer konsantrasyonlarının bozunma sıcaklığına etkisini incelemek için Grup I ve III'deki OCP tip VII polimerin %5, %10 ve %15'lik karışımları hazırlanmış ve TGA analizleri yapılmıştır. TGA taramaları, 50 - 700°C arasında, azot atmosferi altında ve 10°C/dk'lık bir tarama hızında gerçekleştirilmiştir. Bu çalışmanın sonunda PAMA tip VII katkı maddesinin en yüksek, HSD tipinin ise en düşük HTHS viskozitesine sahip olduğu görülmüştür. Ayrıca farklı konsantrasyonlarda hazırlanan OCP tip VII'nin termogravimetrik bozunma sıcaklığına konsantrasyonun önemli bir etkisinin olmadığı tespit edilmiştir. Sonuç olarak OCP ve HSD tip VII'lerin düşük HTHS viskozite değerine sahip olduğundan viskozite indeksi geliştirici katkı maddesi olarak motor yağında kullanımının uygun olduğu tespit edilmiştir.

Anahtar Kelimeler: TGA, HTHS, viskozite indeks geliştiriciler, PAMA, HSD, OCP, baz yağlar.

FARKLI VİSKOZİTE İNDEKS GELİŞTİRİCİ POLİMERLERİN HTHS VE TGA İLE YÜKSEK SICAKLIK PERFORMANSININ İNCELENMESİ

ABSTRACT

Viscosity index improvers (VII) are high molecular weight and long chain polymers used to reduce the effect of temperature on the viscosity of lubricants and to keep the oil viscosity at the desired level at different temperatures. Since they are polymeric in nature, they are temperature sensitive, so they swell at high temperatures and shrink at low temperatures. Thanks to these properties, it reduces the variation of viscosity in engine oils, gear oils and hydraulic oils with temperature. Various VII polymers are commercially available in the market, such as polymethacrylates (PAMA), olefin copolymers (OCP), and hydrogenated styrene-diene copolymers (HSD). This study covers the determination of high temperature performances of commercially available different types of ready-to-use VII additives with HTHS and their effect on the thermogravimetric degradation of SAE 5W-30 engine oils prepared with these additives. For this purpose, HTHS measurements were carried out by preparing 5, 10 and 15% mixtures of OCP, PAMA and HSD type VII polymers at 150°C. In addition, engine oil formulations with SAE 5W-30 viscosity class were prepared with these VII additives,

the same base oil and additive package, and TGA analyzes were carried out. In order to examine the effect of polymer concentrations on the degradation temperature, mixtures of 5, 10 and 15% of OCP type VII polymer in Groups I and III were prepared and TGA analyzes were performed. TGA scans were performed under a nitrogen atmosphere between 50-700°C and at a scan rate of 10°C/min. At the end of this study, it was observed that PAMA type VII additive has the highest and the HSD type has the lowest HTHS viscosity. In addition, it was determined that the concentration didn't have significant effect on the thermogravimetric degradation temperature of the OCP type VII polymer prepared at different concentrations. As a result, it was determined that OCP and HSD type VII's are suitable for use in engine oil as VII additives, since they have low HTHS viscosity values.

Keywords: TGA, HTHS, viscosity index improvers, PAMA, HSD, OCP, base oils.

INTRODUCTION

Lubricating oils consist of largely base oils and small-amount of chemical additives (Mang and Lingg, 2007). They are blendstocks used to formulate a variety of lubricating oils for use in engines and other machinery. There are two main sources of base oils: (a) mineral base oils and (b) synthetic base oils.

- **Mineral Base:** Mineral oils are refined petroleum-based hydrocarbons.
  - Paraffinic
  - Naphthenic
  - Aromatic
- **Synthetic Base:** Synthetic base stocks are produced from carefully chosen and well defined chemical raw materials and by specific chemical (PAO, Esters, PAG) (Wu at al., 2017).

Also, base oils are divided into 5 groups by American Petroleum Institute (API) varying degrees of quality and performance characteristics. The first three groups are refined from petroleum crude oil. Group IV base oils are full synthetic (polyalphaolefin) oils. Group V are base oils not included in groups I to IV (Prinz, 2018).

Table 1: API Base Oil Classification (Prinz, 2018).

	API BASE OIL CATEGORIES				
	Base Oil Category	Sulfur (%)		Saturates (%)	Viscosity Index
Mineral	Group I (solvent refined)	>0.03	and/or	<90	80 to 120
Mineral	Group II (hydrotreated)	<0.03	and	>90	80 to 120
Mineral	Group III (hydrocracked)	<0.03	and	>90	>120
Synthetic	Group IV	PAO Synthetic Lubricants			
Synthetic	Group V	All other base oils not included in Groups I, II, III or IV			

Lubricant additives are used to improve the existing properties in the base oil, to impart desired properties and to increase the specific properties required where they are used. To meet these required performances, a wide variety of additives such as antiwear (AW), viscosity index improver (VII), pour point depressant (PPD), extreme pressure (EP), detergent and dispersant, antioxidant, antifoam, rust inhibitor, bearing corrosion inhibitors, etc. are added to engine oils (Müjdeci and Kaleli, 2010).

Lubrication at high temperatures has been improved with the advent of viscosity index improvers (Stanciu, 2017). VI improvers are polymeric materials prepared by the polymerization of the appropriate monomers.

There are three types of VII polymers such as olefin copolymers (OCPs), polyalkyl methacrylates (PAMAs) and hydrogenated styrene-diene (HSD) (Canter, 2011).

VI improvers act through swelling of the polymer chain as the temperature rises to offset the decrease in base oil viscosity. Thus, they contribute more to viscosity at high temperatures and less at low temperatures.

1- Polymethacrylates (PAMA)

Polymethacrylates (PAMAs) are highly branched copolymers of short (C1 – C5), medium (C6 – C11), and long (>C12) methacrylate esters with 250000 to 750000 g/mol molecular weight (Rudnick, 2009). Uniquely, PAMA includes the polar ester functional group and synthesized through free radical polymerization. Their physical and chemical properties depend on the block or star shaped forms of monomers and their chain lenght. For example, solubility, thickening effect and viscosity index change with chain length. Short chain (<C7) have poor solubility, long chain (> C7) have better solubility in oil (Bostancı et al., 2021). The advantage is very high VI improvement and excellent low temperature properties by pour point depression. The disadvantage is cost and moderate thickening efficiency (Willett et al, 2018).

2- Olefin Copolymers (OCP)

Olefin copolymer (OCP) is a copolymer of ethylene and one of more olefins including propylene, butylene, or octene and having molecular weight from 50000 to 200000 g/mol. They are synthesized via Ziegler-Natta vanadium-based or metallocene catalysis (Willett et al, 2018). The ratio of ethylene propylene monomers effects the properties of the polymer such as thickening efficiency and low temperature solublity. Generally, the mass content of ethylene in OCP is 40-60 % m/m (Rubin and Sen, 1990). The advantages are high thickening efficiency and low cost. The disadvantages are poor shear stability and some OCPs can behave like wax if ethylene content is too high (>50%) (Willett et al, 2018).

3- Hydrogenated Styrene-Diene Copolymers (HSD)

HSD based viscosity index improvers are synthesized through anionic solution polymerization of styrene-diene polymers to form random, block, or star-shaped viscosity modifiers polymerization (Jukic et al, 2009). Their molecular weights changes between 50000 and 100000 g/mol and their properties are depending on styrene and diene blocks. Diene blocks effect the solubility of the polymer with positive side. On the other hand, while styrene monomers improve the thermal, oxidative, and shear stability of the polymer, the styrene blocks are oil insoluble over most temperatures. Because of having good high temperature and low temperature properties of styrene-isoprene copolymers, they are widely used in engine oils and transmission fluids (Goldmints and Oberoi, 2017).

TGA (Thermo Gravimetric Analysis) is a method of thermal analysis in which the mass of a sample is measured over time as the temperature changes. This measurement provides information about physical phenomena, such as phase transitions, absorption, adsorption and desorption; as well as chemical phenomena including chemisorptions, solid-gas reactions and thermal decomposition. The plot of mass or mass percent versus time is called a thermogram or thermal decay curve. It is especially useful for the study of polymeric materials, including thermoplastics, thermosets, elastomers, composites, films, fibers, coatings and paints (Ng et al, 2018).

The technique is particularly useful for the following types of measurements:

• Thermal cracking point of base fluids or formulations contained within the substance

• Decomposition temperature

• Changes in mass due to decomposition, oxidation, evaporation, or combustion

• Study a kinetic of dehydration of a hydrate/solvate at different temperatures and under different conditions.

• Thermal and oxidative stabilities

• Absorbed moisture content of organic and inorganic materials

• Volatilization rate of materials: residual water or/and solvents

• Estimation of product lifetimes

• Effects of reactive atmospheres on materials

• Filler content of polymers resign

• Residual solvent and carbon black content

There are three types of thermogravimetry:

- **Isothermal or Static Thermogravimetry**: In this technique, the sample weight is recorded as a function of time at constant temperature.
- **Quasistatic Thermogravimetry**: In this technique, the sample temperature is raised in sequential steps separated by isothermal intervals, during which the sample mass reaches stability before the start of the next temperature ramp.
- **Dynamic Thermogravimetry**: In this technique the sample is heated in an environment whose temperature is changed in a linear manner.

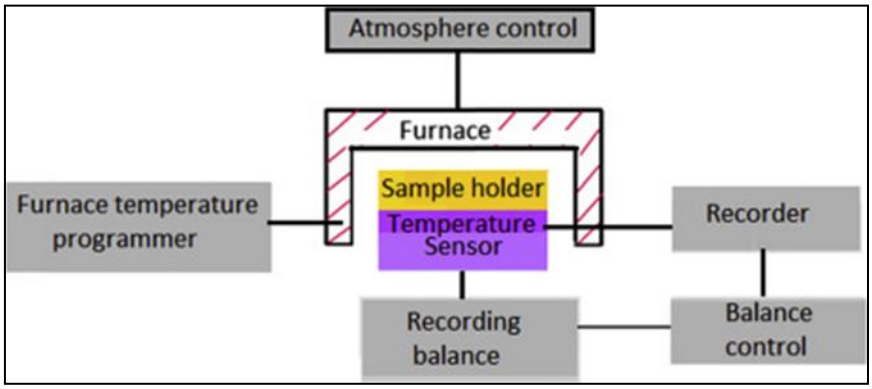


Figure 1: Schematic illustration of atypical TGA system (Loganathan et al, 2017)

HTHS (High Temperature High Shear) measures the viscosity (resistance to flow) of an engine lubricant at elevated temperatures (150°C) under constant shear, simulating the narrow tolerances and high speeds between moving parts in a hot engine. The lower the measured torque, the lower the HTHS viscosity of the oil, resulting in a higher fuel efficiency (Mesmaeker, 2016).

METHOD

Within the scope of this study, thermogravimetric degradation temperatures of Group I, II, III, IV and V base oils and different ready to use VII additives were measured. PAO (Polyalphaolefin) was used for Group IV and TMPO (Trimethylolpropane Trioleate) was used for Group V base oil. These ready to use PAMA, OCP and HSD based VII additives were selected for each group and provided by commercially.

5%, 10% and 15% mixtures of selected PAMA, HSD and OCP type VII polymers were prepared in Group I and Group III base oil. Polymeric additeve effects on HTHS results was studied just only with Group III base oil. Kinematic viscosity and High Temperature High Shear (HTHS) viscosities of these mixtures were measured.

SAE 5W-30 grade engine oils were prepared with these selected PAMA, OCP and HSD type VII additives and same additive package. The kinematic viscosities of these engine oils are kept at the same level. Then, their TGA and HTHS measurements were performed.

To mesure the effect of polymer concentration on thermogravimetric degradation temperature, 5%, 10% and 15% mixtures of OCP type raw VII polymer were prepared in Group I and Group III.

Properties of base oils used to prepare VII mixtures in this study were given in Table 1.

Table1: Base Oil Properties.

Technical Properties	Group I	Group II	Group III	Group IV	Group V
Kinematic Viscosity at 40°C, mm^2/s	30,74	29,31	32,10	30,48	47,8
Kinematic Viscosity at 100°C, mm^2/s	5,23	5,33	6,02	5,79	9,72
Viscosity Index	100	116	135	134	194
Flash Point, °C	218	226	240	237	311
Pour Point, °C	-9	-15	-15	-66	-54

HERZOG branded kinematic viscosity instrument was used to measure the kinematic viscosity of base oils and SAE 5W-30 grade engine oils at 40°C and 100°C. Viscosity Index (VI) values were calculated automatically by the instrument according to ASTM D 2270 method.

PERKIN ELMER branded thermogravimetric analyser instrument with TGA 4000 model was used to measure thermogravimetric degradation of base oils, ready to use VII additives, base oil-VII polymer mixtures and SAE 5W-30 grade engine oils which were prepared with different VIIs.

For high temperature performance properties, CANNON branded HTHS instrument was used to determine viscosity at high temperature and high shear conditions. Tests were carried out at 150°C and under pressure.

RESULTS AND DISCUSSION

The base oil and ready to use VII polymer studies were carried out by scanning the samples in TGA device, under N_2 atmosphere between 50-900°C and 10°C/min. The decomposition temperature values were obtained by taking the derivative (DTG) of the thermogravimetric decomposition curve.

As it seen in Figure 2 and 3, when the TG and DTG curves of Group I, II, III, IV and V base oils were examined, it was determined that the Group V base oil has highest degradation temperature curve.

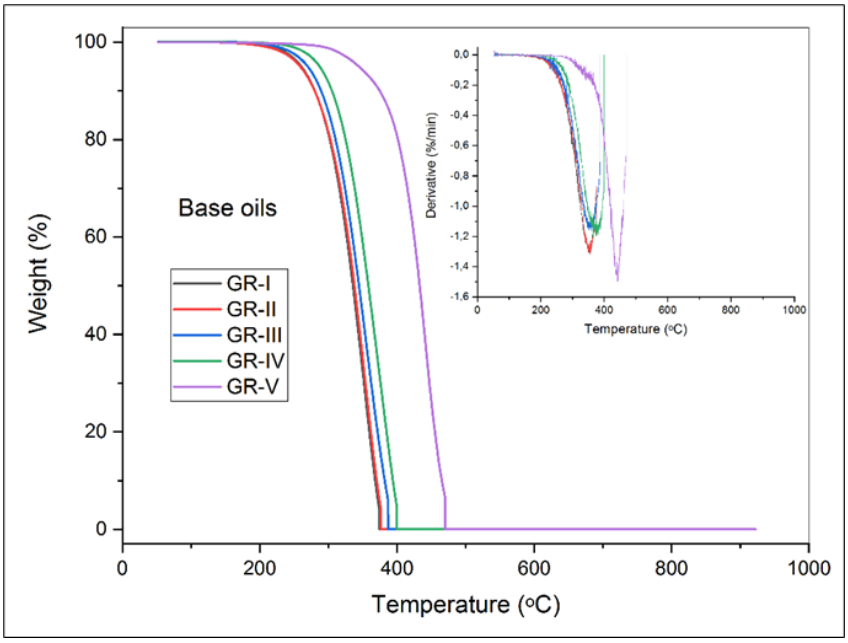


Figure 2: TG and DTG Curves of Group I, II, III, IV and V Base Oils

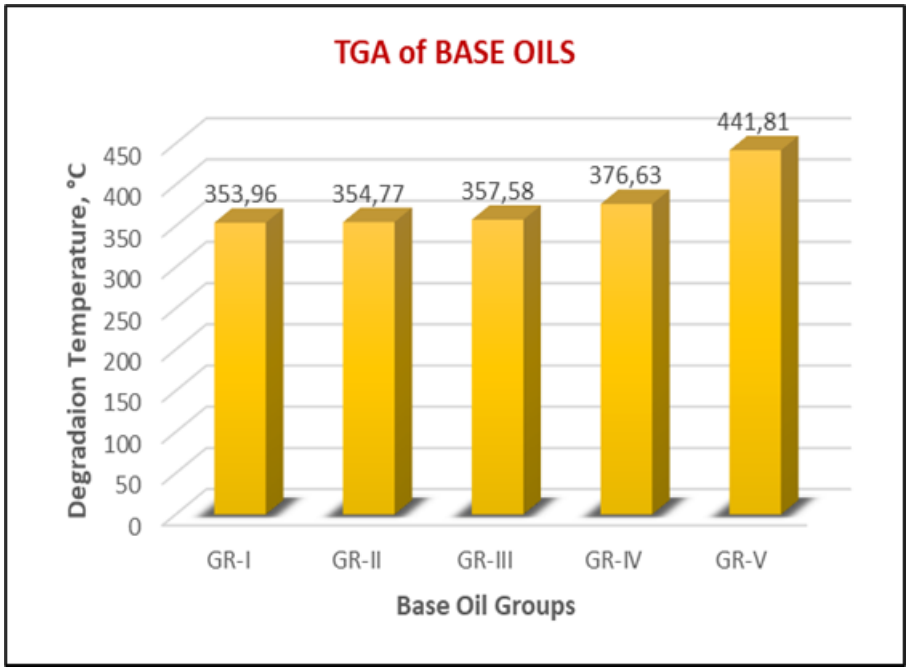


Figure 3: Degradation Temperatures of Different Base Oil Groups Measured by TGA

TGA curves of different PAMA, OCP and HSD based ready to use VII polymers are given in Figure 4, 5 and 6. For this purpose, 4 different VII samples procured from the market for each group and analysed. As it seen on Figure 7, degradation temperatures of OCP and HSD-based ready to use polymers were determined close to each other and lower than PAMA based ready to use VII polymers.

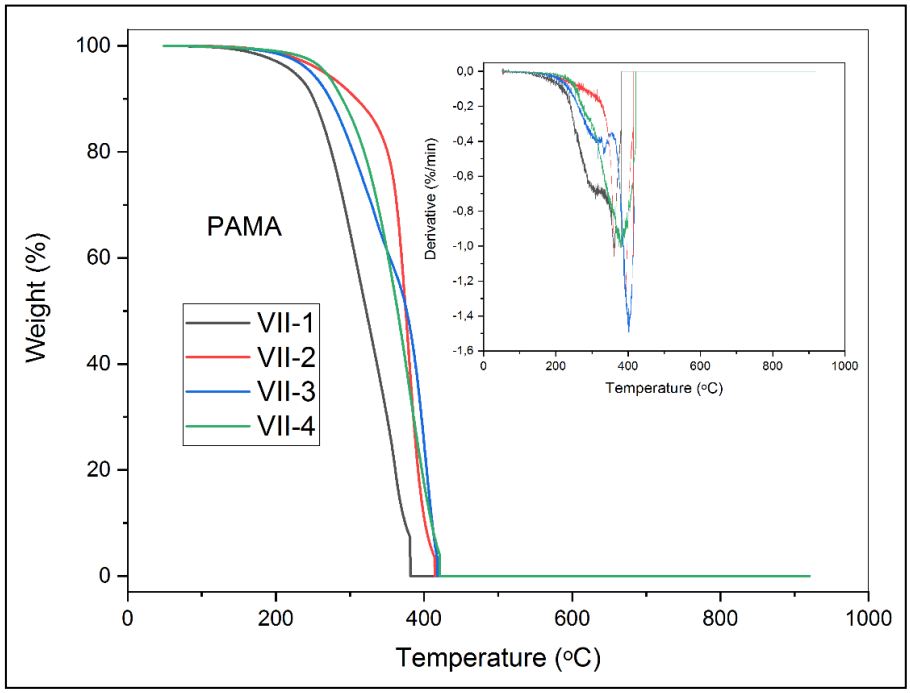


Figure 4: TG and DTG Curves of Different PAMA Based Ready to Use VII Polymers.

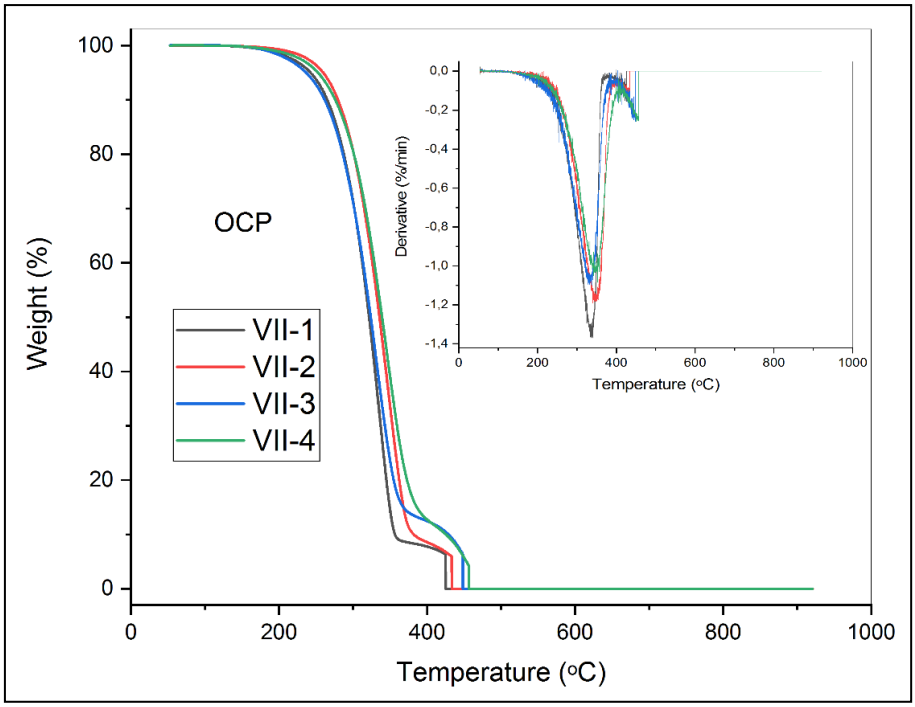


Figure 5: TG and DTG Curves of Different OCP Based Ready to Use VII Polymers.

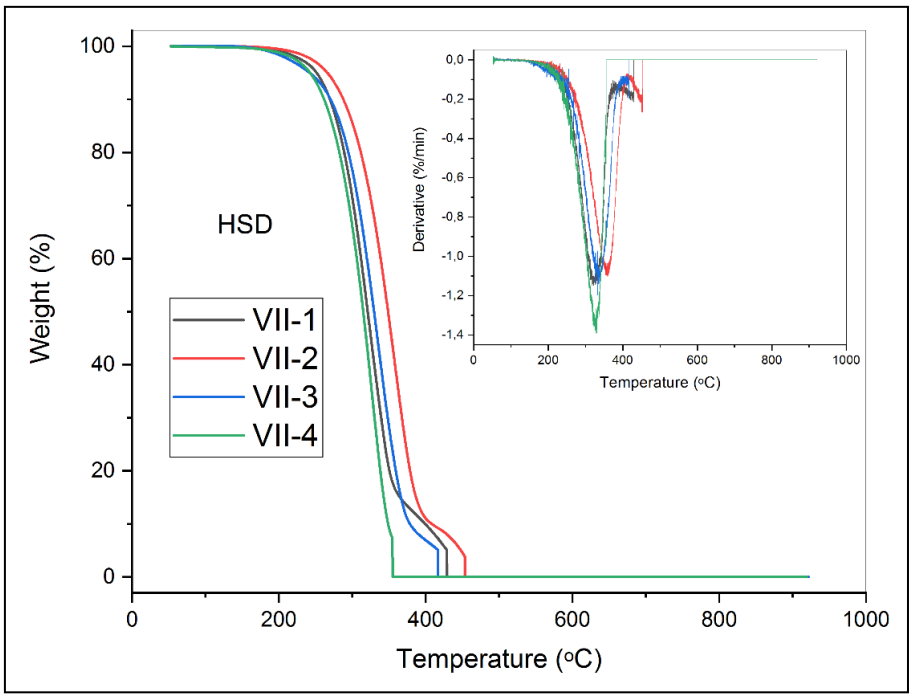


Figure 6: TG and DTG Curves of Different HSD Based Ready to Use VII Polymers.

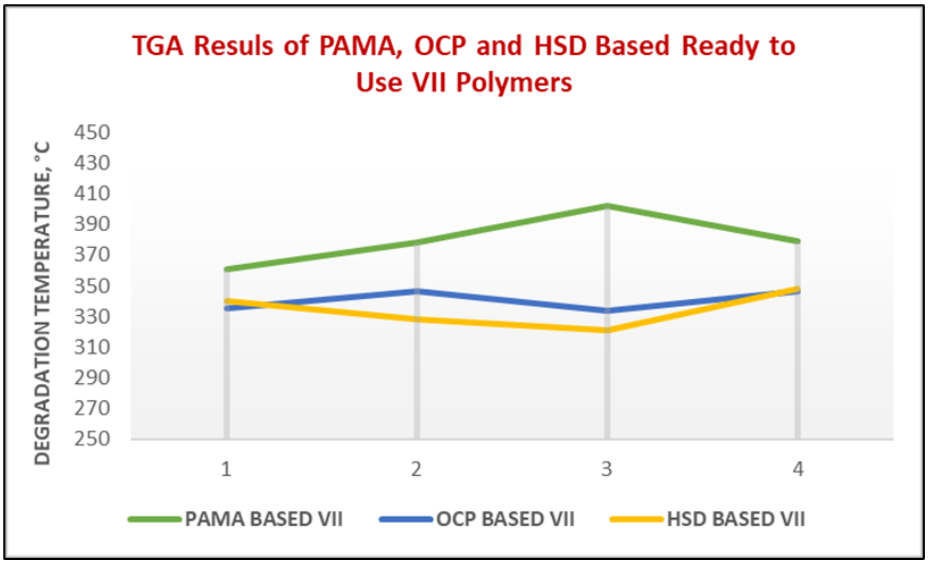


Figure 7: TGA Results of PAMA, OCP and HSD Based Ready to Use VII Polymers

To examine the effect of raw VII polymer concentration on thermogravimetric degradation temperature, OCP type raw VII polymer was provided. The mixtures of this OCP polymer were prepared in GR-I and GR-III base oil at 5%, 10% and 15% concentration. In figure 8, it was determined that the degradation temperature of OCP-Based VII polymer increased with increasing concentration. Also, the concentration effect was observed better in GR-III base oil.

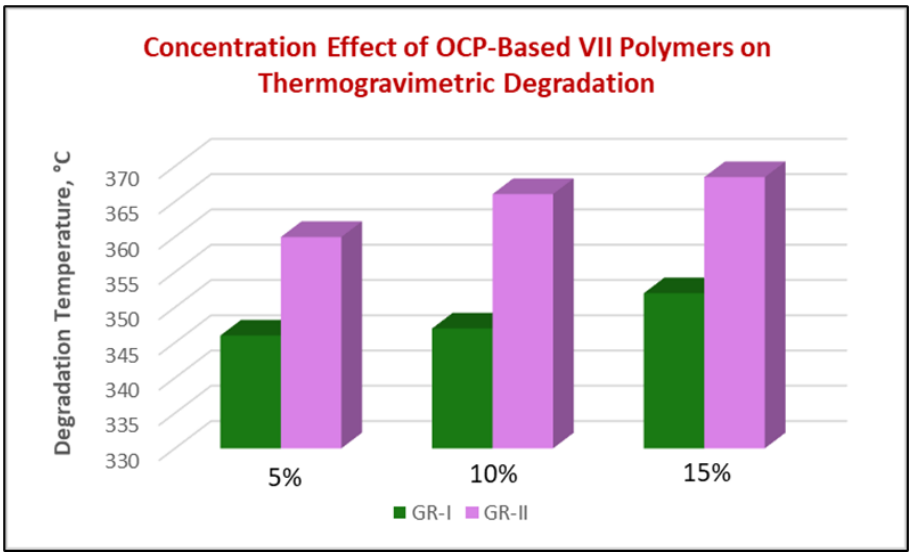


Figure 8: TGA Results of OCP-Based VII Polymer Mixture in GR-I and GR-III at Different Concentration

Figure 9 presents the effect of polymer concentrations on HTHS viscosity of the polymer mixtures. It was observed that, for each VII polymers, HTHS viscosity increased with increasing concentration. Furthermore, While the PAMA based VII polymer mixtures have the highest HTHS viscosity, HSD based VII polymer mixtures has the lowest HTHS viscosity among all three polymer mixtures.

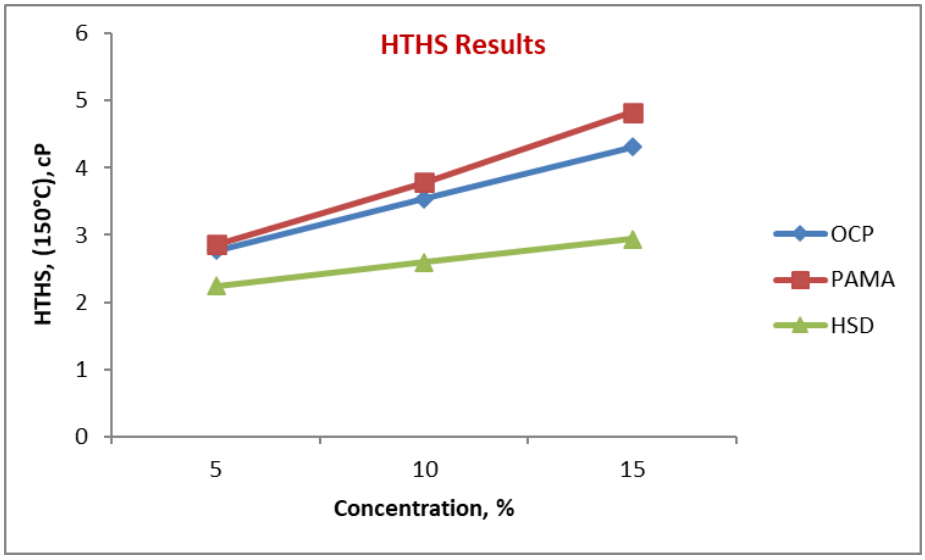


Figure 9: Effect of Polymer Concentration on HTHS Viscosity

To see the effect of different VII additives on thermogravimetric degradation temperature and HTHS performance of finished product, SAE 5W-30 grade engine oil was prepared with these selected VIIs. Same base oil, same additve package but different VII additive (PAMA, OCP and HSD-based) were used and kinematic viscosity at 100°C values were kept at the same level.

As you see in figure 10, although the degradation temperatures of PAMA, OCP and HSD based VII polymers are different, the degradation temperatures of SAE 5W-30 engine oils with the same viscosity value prepared with these polymers were found close to each other. Engine oil prepared with PAMA based VII polymer found slightly higher than the others.

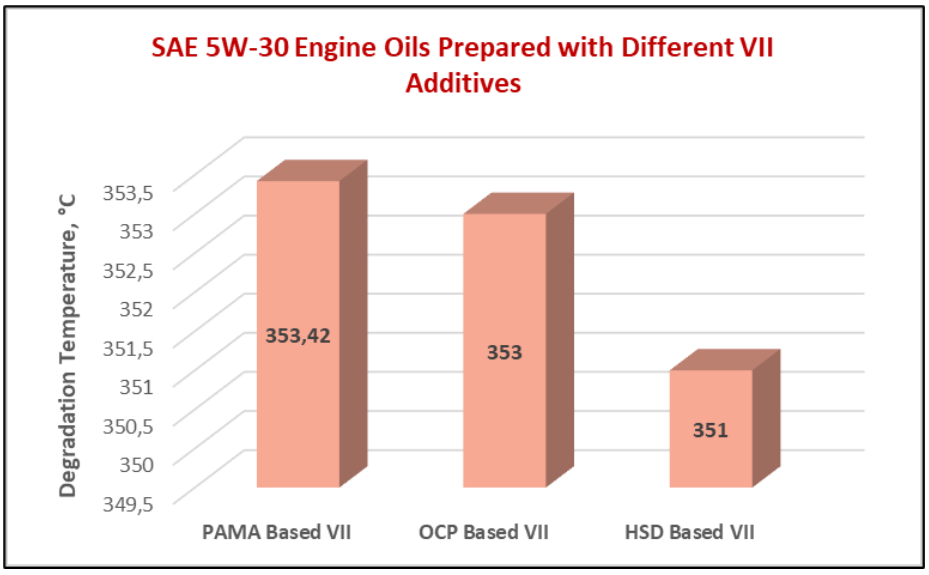


Figure 10: TGA Results of SAE 5W-30 Engine Prepared with PAMA, OCP and HSD-Based VII Additives

In figure 11, it was detected that engine oil prepared with PAMA-Based VII has the highest HTHS viscosity value than OCP and HSD-based. These results were found to be compatible with the thermogravimetric decomposition temperatures of engine oils prepared with these polymers.

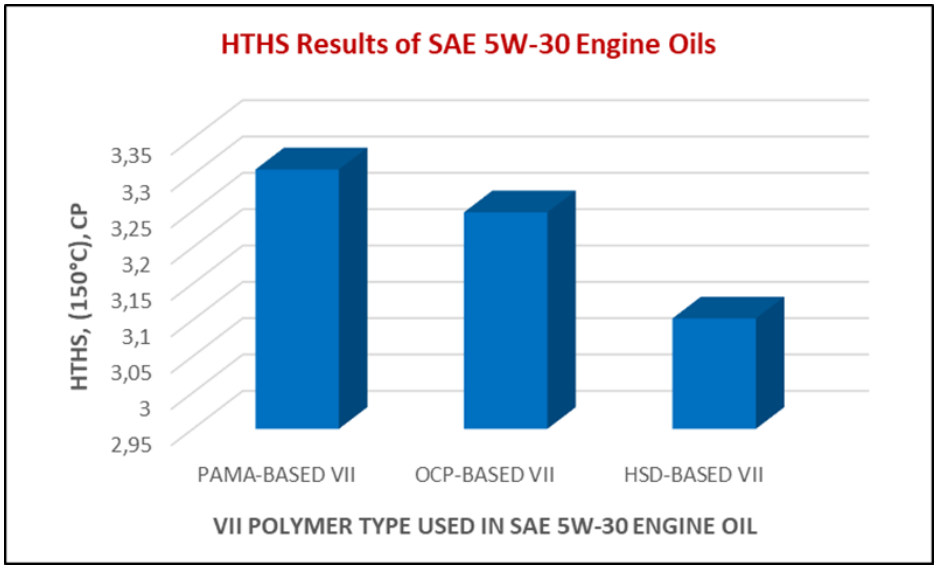


Figure 11: HTHS Results of SAE 5W-30 Engine Prepared with PAMA, OCP and HSD-Based VII Additives

CONCLUSION

To summarize all the studies, it was determined that the degradation temperature of the TMPO ester selected for Group V base oil was highest than the others due to its molecular structure and heat resistance feature.

Also, compared with synthetic type base oils (PAO (Group IV) and TMPO (Group V)) it was observed that mineral base oils (Group I, II and III) have lowest degradation temperatures. But though Group III base oil is also mineral based its degradation temperature is slightly higher from Group I and II due to its high quality. So, it is concluded that base oil type and quality have directly affect on degradation temperature of end products.

Degradation temperatures of OCP and HSD-based ready to use polymers were determined close to each other and lower than PAMA based ready to use VII polymers. The reason why PAMA type VII polymers have the highest degradation temperature is thought to be about their high molecular weight and ester type molecular structure.

It was determined that the degradation temperature of OCP-Based VII polymer slightly increased with increasing concentration in GR-I and GR-III. The concentration effect was observed better in GR-III base oil.

Although the degradation temperatures of PAMA are higher than OCP and HSD based VII polymers, the reason why TGA results of SAE 5W-30 engine oils with these polymers are close to each other is due to the effect of base oil. The decomposition temperature of Group III base oil showed a more dominant effect than VIIs.

The analysis results show that HTHS performance of OCP and HSD type VII polymers are better than PAMA. Engines work under high temperature and high shear conditions. Therefore, low HTHS values of OCP and HSD type VII additive, makes them suitable for using in engine oil as viscosity index improver additive. The lowest HTHS results were obtained from HSD type VII, show that the HSD type viscosity index improvers are the best VII for new generation engine oils where fuel economy is important.

Similar HTHS results were obtained from SAE 5W-30 engine oils prepared with these selected VII additives. HTHS result of HSD type VII-based SAE 5W-30 engine oil was found lowest, PAMA type VII based engine oil was found highest. These results again show that HSD type VII is the best polymer for engine oil formulations.

As a result, high temperature properties of lubricants are mostlt depended on base oil and VII polymer type and concentration.

REFERENCES

Bostancı, M.& Karaaslan U. (2021). Comparison of Low and High Temperature Performance Properties of Different Types of Viscosity Index Improver (VII) Polymers. 6th International Mediterranean Science and Engineering Congress (IMSEC 2021) October 25-27.

Canter, N. (2011). Viscosity Index Improvers. Tribology & Lubricant Technology.

Cosimbescu, L., Tarasevich, B., Bhattacharya, P., Robinson, J., Krueger, S., Ramasamy, U.S., & Martini, A. (2016). Viscosity Modifiers: A Fundamental Study. Applied Synthetic Chemistry Group Energy Processes and Materials.

Goldmints, I. & Oberoi, S. (2017). Hydrogenated Styrene-diene Co-polymer Viscosity Modifiers", Lubricant Additives: Chemistry and Applications. Third Edition. CRC Press, Boca Raton, FL.

Jukic, A., Ragosic, M, Franjic, I. & Soljic, I. (2009). Molecular interaction in some polymeric additive solutions containing styrene-hydrogenated butadiene copolymer. European Polymer Journal, No. 45, pp. 2594–2599.

Loganathan, S., Valapa, R.B., Mishra R., Pugazhnthi, G., & Thomas, S. (2017). Thermogravimetry Analysis for Characterization of Nanomaterials.

Mang, T., & Lingg, G. (2007). Base Oil. Lubricants and Lubrication, 34-62.

Mesmaeker, D., (2018). Low HTHS Oils: The Art of Balancing Fuel Efficiency and Engine Protection. https://www.q8oils.com/automo-tive/ low-hths-oils.

Müjdeci, S., & Kaleli, H. (2010). Engıne Oil Additives, Theır Propertıes and Interactıon. Journal of Engineering and Natural Sciences, 138-149.

Prinz, F. (2018). Understanding the Differences in Base Oil Groups.

Rubin, I.D., & Sen, A. (1990). Solution Viscosities of Ethylene-Propylene Copolymers in Oils. Journal of Applied Polymer Science, Vol. 40, 523-530.

Rudnik, L.R, (). (1947). Lubricant Additives. Chemistry and Applications, 2nd ed., USA.

Stanciu, I. (2017). Viscosity index improvers for multi-grade oil of copolymers polyethylenepropylene and hydrogenated poly(isoprene-co-styrene). Journal of Science and Arts, No. 4(41), pp. 771-778.

Willet, E., Vore, A.D., & Vargo, D. (2018). Viscometric and Low Temperature Behavior of Lubricants with Blended VI Improvers. Functional Products Inc.

Wu, M.M., Ho, S.C., & Luo, S. (2017). Synthetic Lubricant Basestocks. Springer Handbook of Petroleum Technology, 1043-1061.

EXPERIMENTAL STUDY OF THE EVOLUTION OF THE BREACH AND THE DİSCHARGE THROUGH THE BREACH RESULTING FROM PIPING DUE TO SEEPAGE AT THE EARTH-FILL DAM WITH CLAY CORE

Mehmet Sukru GUNEY

Izmir University of Economics, Civil Engineering, Izmir, Turkey, ORCID ID: https://orcid.org/0000-0003-1441-4784

Emre DUMLU

Izmir Institute of Technology, Civil Engineering, Izmir, Turkey, ORCID ID: https://orcid.org/0000-0003-4311-3040

Merve OKAN

Izmir University of Economics, Civil Engineering, Izmir, Turkey, ORCID ID: https://orcid.org/0000-0001-6095-2992

Birol KAYA

Dokuz Eylul University, Civil Engineering, Izmir, Turkey, ORCID ID: https://orcid.org/0000-0002-7655-526X

ABSTRACT

Internal erosion, also known as piping, is one of the most important causes of earth-fill dam failures. Many researchers dealing with numerical analyses in this area make some simplified assumptions about the shape of the breach and the discharge of water flowing through the breach. This study was conducted in the scope of the project supported financially by the Scientific and Technological Research Council of Turkey and it consists of an experimental study that aims to provide data needed to perform numerical analyses with more realistic approaches. A dam with a height of 0.65 m, a bottom width of 2 m, and a crest width of 0.05 m was built in a flume 0.80 m wide, 0.75 m high, and 18.60 m long. Before the construction of the dam, some common soil mechanics tests were carried out. The dam body was constructed of clay and sand mixture with a clay core 15 cm wide at the bottom and 1 cm wide at the crest. The weak layer with a cross-section of 5x5 cm^2 along the centerline consisted of rock salt. The temporal evolution of the breach resulting from the piping was recorded by means of the high-precision cameras. The flow rate through the breach was measured by a triangular weir located at the channel downstream. Gauss' area formula was applied to determine the time-varied total and wetted areas of the breach at downstream side. The changes in water depth in the channel were also recorded. The so-obtained experimental findings are presented. The experimental findings continue to be compared with the numerical results obtained from the software PLAXIS 3D.

Keywords: Earth-fill dam; Clay core; Piping; Breach geometry; Breach development; Discharge; triangular weir.

INTRODUCTION

Piping is one of the main causes of earth-fill dam failures. Soil erosion in earth structures, particularly in earth dams and levees, might occur through the embankment, foundation, or from the embankment to the foundation. This kind of erosion has the following phases: a) initiation and continuation of erosion, b) progression to form a pipe and c) formation of a breach (Fell et al., 2003). The evolution of breach resulting from piping is an important issue in an experimental and numerical investigation concerning embankment dam failure. The European FP5 IMPACT (Investigation of Extreme Flood Process and Uncertainty) project, which was conducted from 2001 to 2004, focused on assessing and lowering the risks of extreme flooding driven by weather-related disasters or the failure of dams and other flood-defense systems (Y. Zech et. al.,2007). Physical modeling in the lab, field data gathering, field testing, theoretical investigations, and computer simulations have all been utilized in such researches. There has been a lot of research about dam failures, particularly because of overtopping, in the literature, but there have not been many studies about dam failure due to piping because it's so challenging to observe erosion and perform controlled tests. (Greco et al. 2008;Chen et al. 2019; Sharif et al. 2015). Greco et al. (2008) simulated the evolution of a breach in an earth-fill dam by using a two-dimensional depth-averaged (2DH) numerical model. Chen et al. (2019) indicated that between 1954 and 2018,

3541 dam breach accidents occurred and more than 30% of them were due to piping. Sharif et al. (2015) constructed a dam in a laboratory flume by using a mixture of sand, silt, and clay with different compaction rates and examined the changes in the depth, area, and volume of erosion during the piping evaluation by utilizing an image processing technique. The majority of researchers that perform numerical studies make some simplistic assumptions regarding the characteristics of a breach and the flow of water through it. Zewdu (2019) investigated slope stability analysis in the case of failure and measured seepage discharges by using a triangular weir. Morris et al. (2008) revealed that instead of simplified approaches, more realistic approaches are required about the breach mechanism as well as the breach geometry and flow through the breach.

The aim of this study is to realize experiments to study the evolution of dam failure resulting from piping at the bottom of an earth-fill dam with clay core.

EXPERIMENTAL PROCEDURE

The dam was constructed in a rectangular flume with a width of 0.80 m, a height of 0.75 m, and a length of 18.60 m (Figure 1). The dam having 0.65 m height, 2 m bottom width and 0.05 m crest width was constructed with side slopes of 1:1.5. The dam body was constructed by clay and sand mixture with clay core 15 cm wide at bottom and 1 cm wide at crest. A pump was used in order to provide water circulation in the closed system.



Figure 1. Experimental set-up

Some soil mechanics experiments were carried out before building the dam. The soil mixture used in the construction of the dam was prepared by using 85 % fine sand and 15 % clay. The grain- size distribution of the mixture obtained from the wet sieve and hydrometer analyses is shown in Figure 2.

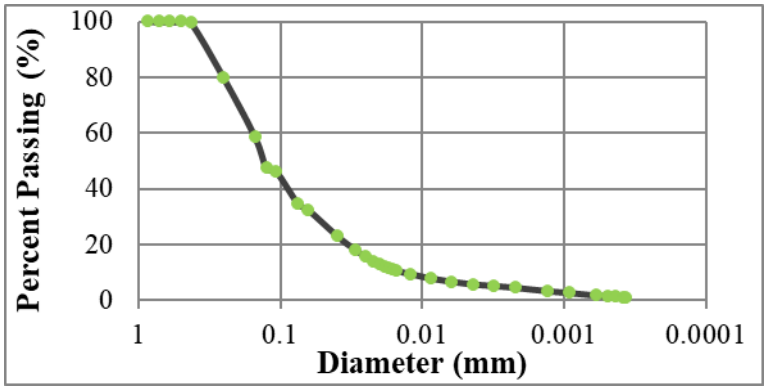


Figure 2. Grain size distribution

From Figure 2, some characteristic diameters were obtained as D_{10}= 0.014 mm, D_{30}= 0.056 mm, D_{50}= 0.13 mm, and D_{60}= 0.15 mm. The uniformity coefficient C_u was 10.7 and the curvature coefficient C_c was equal to 1.49.

The specific weight of the mixture was found as G_s = 2.67, from the test ASTM D854 – 14.

The permeability values for the mixture and clay core, obtained from the falling head permeability test, were found as k= $1.18 \cdot 10^{-3}$ cm/s and $8.6 \cdot 10^{-5}$ cm/s, respectively.

In addition, the direct shear test was performed. The cohesions of the mixture and of the clay core were found to be as 11.68 kN/m^2 and 3.1 kN/m^2, respectively. The internal friction angles of the mixture and clay core were found as 39.84° and 33.6°, respectively.

The standard proctor tests (ASTM-698) were performed by applying 13 drops (50% reduced energy) to increase the probability of the piping (Figure 3). The maximum dry density and optimum water content were obtained as ρ_{drymax}= 1.653 g/cm^3 and w_{opt} = 15.4 % from the test.

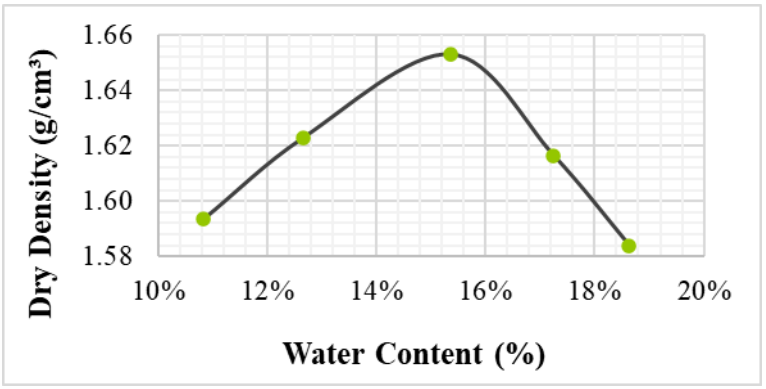


Figure 3. Standard proctor test with 13 blows

The dam was constructed in 6 layers of 10 cm and an upper layer of 5 cm. During the compaction, the mixture was distributed homogenous and compacted by using a plate and proctor hammer. At the end of the construction, the square-shaped molds were removed and the excessive soil materials were carefully trimmed by means of a trowel.

Some pictures taken during the dam construction are given in Figure 4.



Figure 4. Some pictures taken during the dam construction

The flow rate through the breach was measured by a 90° triangular weir (Figure 5) located at the channel downstream. The calibration curve of the triangular weir is given in Figure 6.

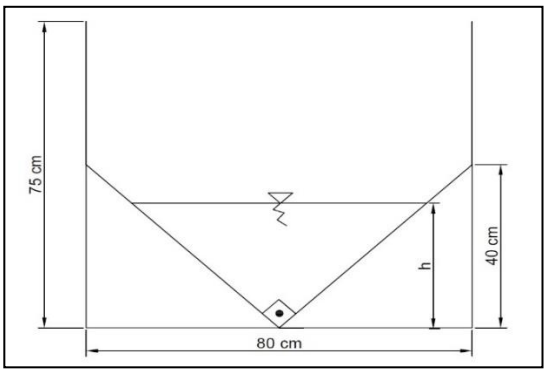


Figure 5. the 90° triangular weir used to measure the flow rate

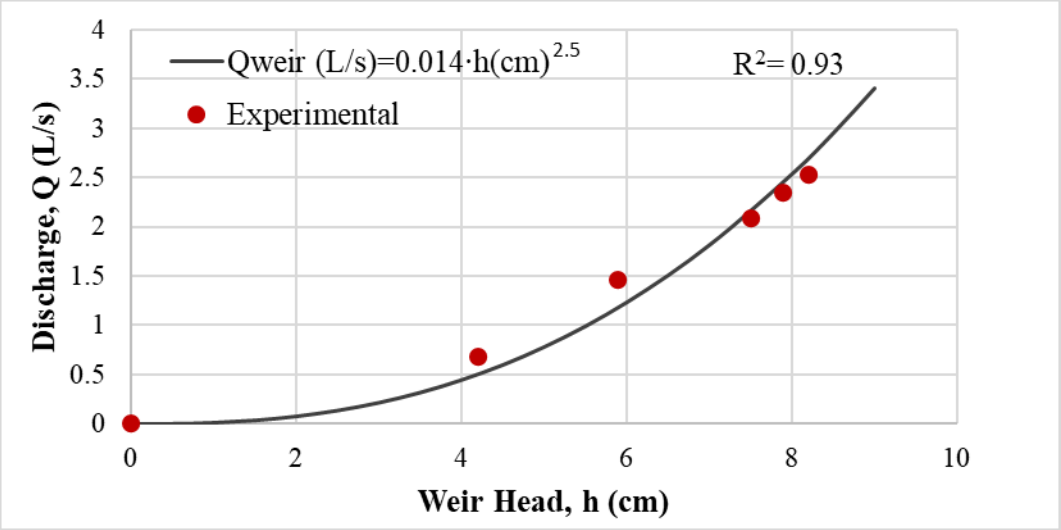


Figure 6. Calibration curve of the 90° triangular weir

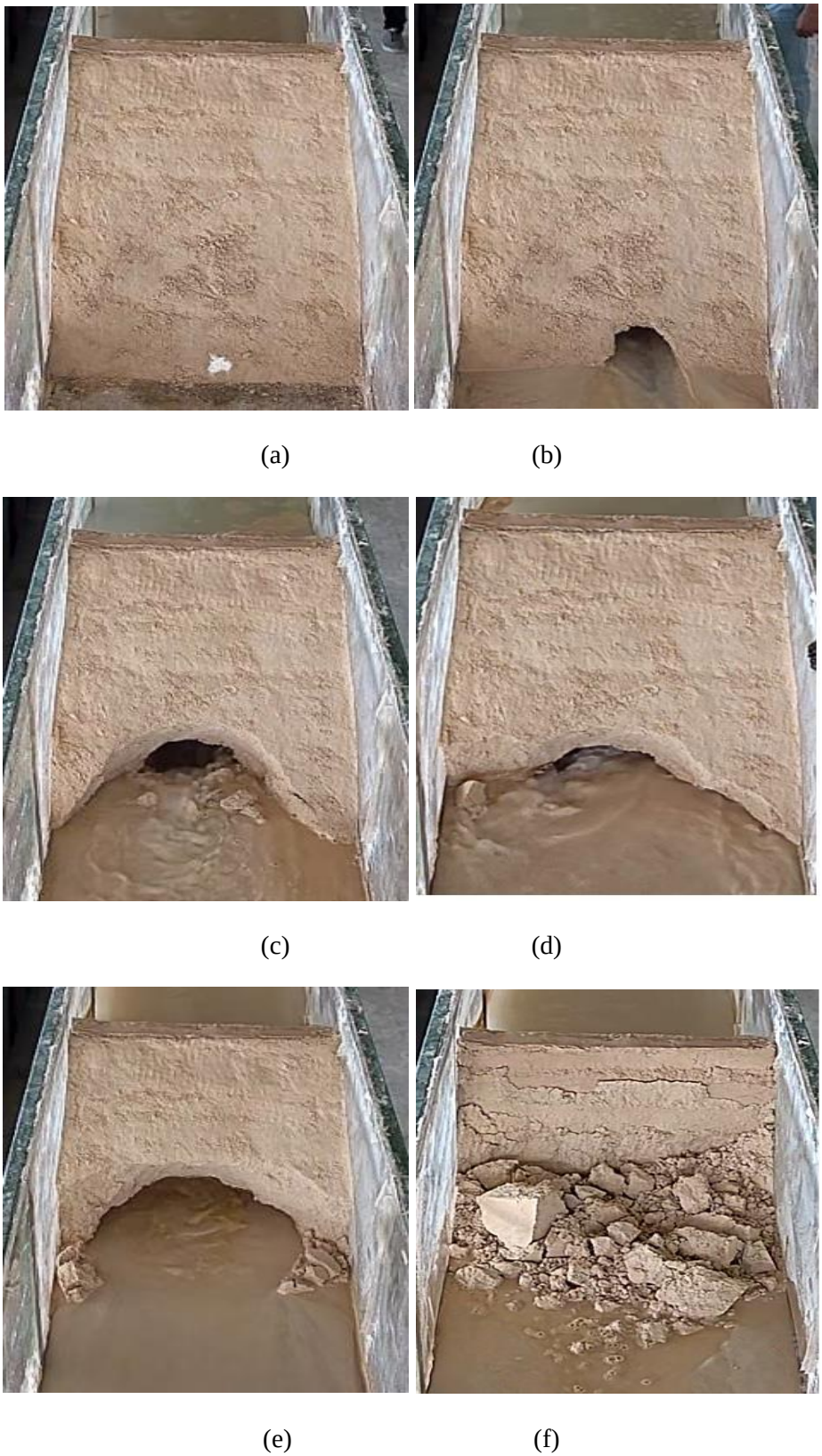
The following empirical equation was obtained from the regression analysis:

$$Q_{weir}(L/s) = 0.014 \cdot h(cm)^{2.5} \quad (1)$$

High-precision cameras located at different locations recorded the evolution of the dam failure. In order to regulate the water level, an electromagnetic sensor was used which starts and stops the pump when the water depth in the channel was 61 cm and 59.5 cm, respectively. During the experiments, the piping occurred before the water depth reached these specified values.

EXPERIMENTAL FINDINGS

The temporal evolution of the breach recorded by the cameras located at the downstream and over the dam are given in Figure 7 and Figure 8, respectively. The time t=0 corresponds to the starting of the seepage.

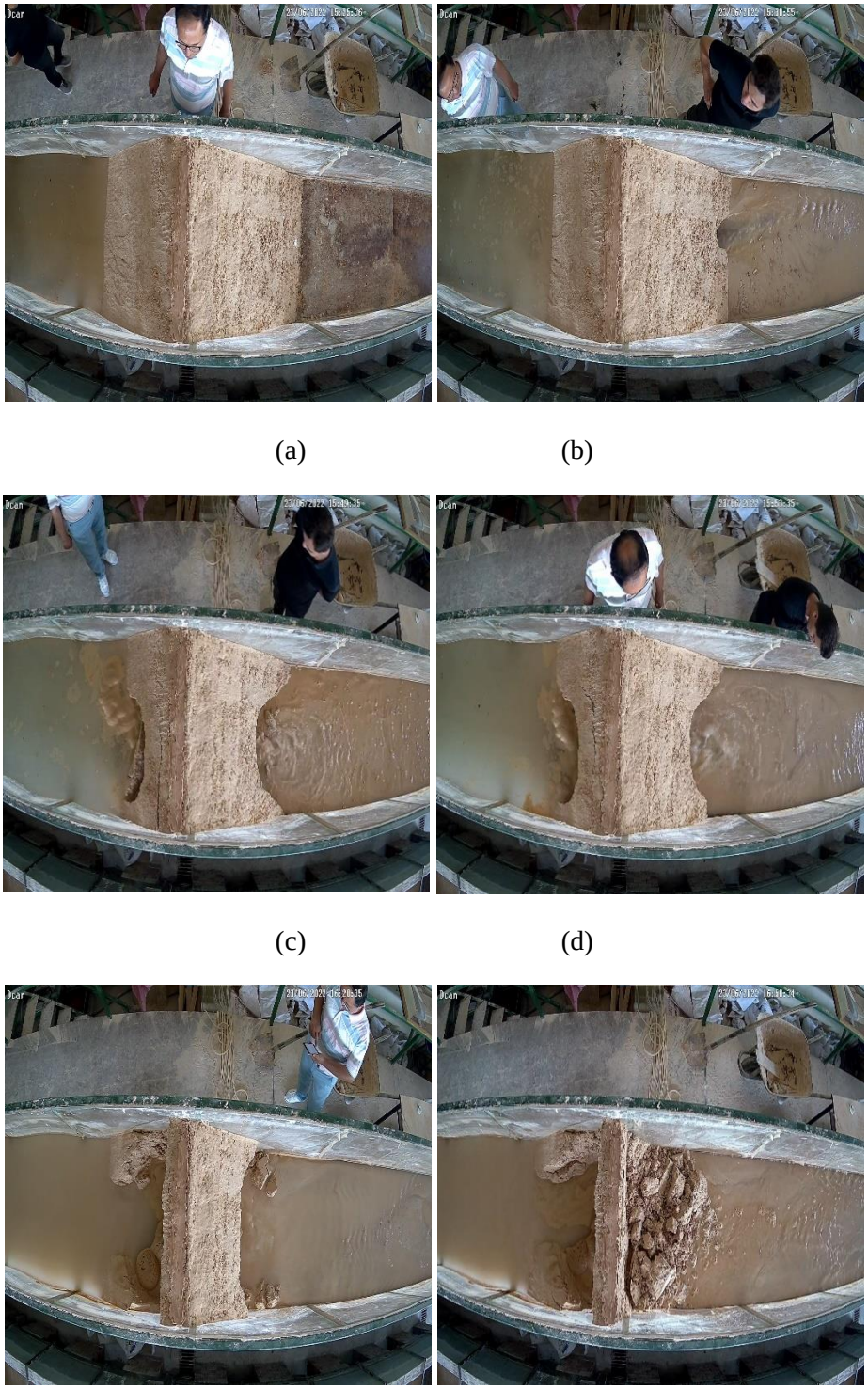


(a) (b)

(c) (d)

(e) (f)

Figure 7. The temporal development of the breach at downstream a) t=0 s, b) t=320 s, c) t=1440 s, d) t=1800 s, e) t=3600 sec, f) t=5620 s



(a) (b)

(c) (d)

(e) (f)

Figure 8. The temporal development of the breach at top view a) t=0 s, b) t=320 s, c) t=1440 s, d) t=1800 s, e) t=3600 sec, f) t=5620 s

The water depths in the channel were determined from the camera recordings. In order to investigate the shape of the breach and the changes in its geometry, the downstream camera images were used. The downstream camera recording were flattened and edited by means of the Hit-film-Express version 2021.1, so that the

boundary conditions were accurately scaled. Moreover, extra-sensitive solutions were implemented to ensure that the images are completely flat. The images taken from the records corresponding to a certain time were scaled and the boundary coordinates of the breach at the downstream side were specified at Get-data Graph Digitizer 2.26 software. In addition, the so-specified coordinates were evaluated by the Gauss Area functions.

The temporal water depths in the channel and the flow rates calculated by using Eq. (1) are given in Figure 9 and Figure 10, respectively.

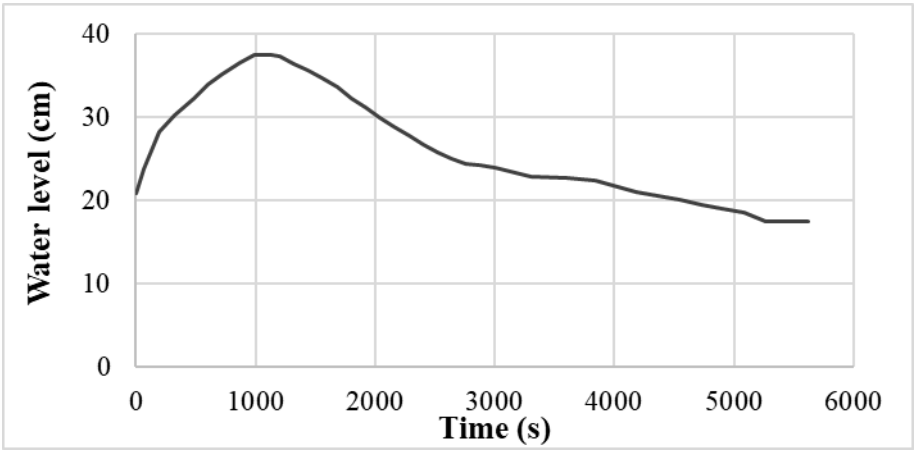


Figure 9. Time-varied water depths in channel

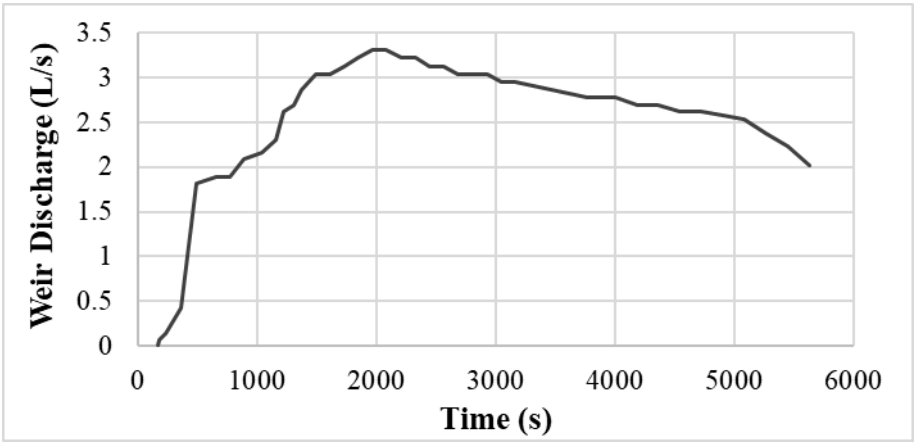


Figure 10. Time-varied discharges through the breach

The temporal variations of the breach area at downstream are given in the Figure 11.

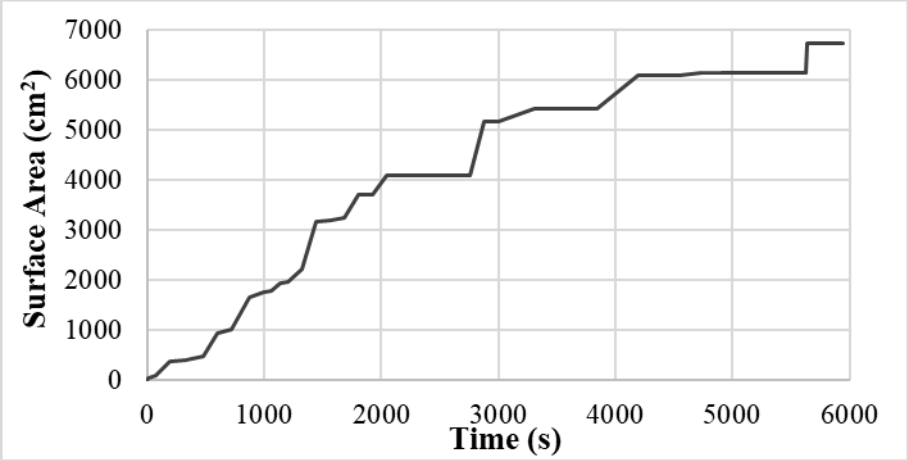


Figure 11. Temporal variations of the breach area at downstream

The time-dependent wetted areas at downstream are presented in Figure 12.

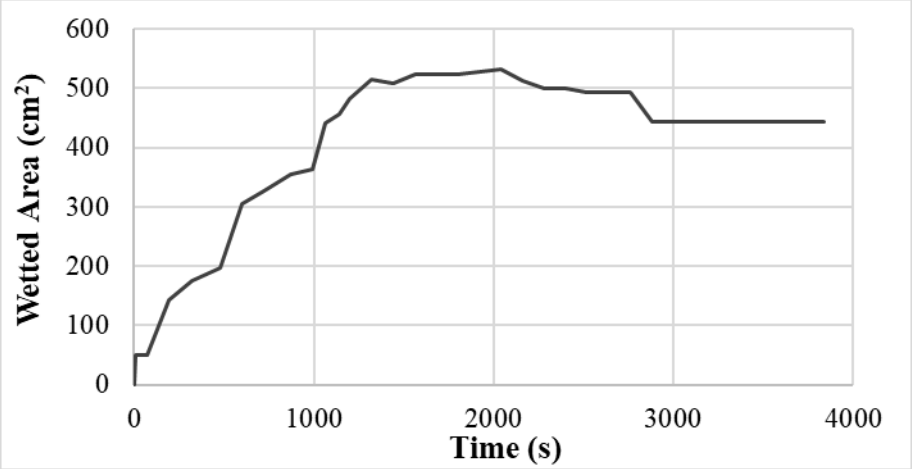


Figure 12. The time varied wetted areas at downstream

RESULTS AND CONCLUSIONS

In this study, the time-varied evolution of breach resulting from piping at the bottom of earth-fill dam with clay core was investigated experimentally. The discharge through the breach was measured by a 90° triangular weir. The boundary coordinates of the downstram breach surface areas and wetted areas were obtained by using the Get-Data Graph Digitizer, and so-obtained coordinates were evaluated by applying the Gauss-area function. During the experiment, it was observed that the breach started on the downstream side and then developed towards to upstream side. The maximum breach surface area was recorded as A_{down}= 6743.4 cm^2 at t=5920 s. The recorded maximum wetted area was found to be $A_{wetted\text{-}downs}$=532.6 cm^2 at t=2040 s. After the collapse of the downstream part, the experiment was terminated. The experimental findings continue to be compared with the numerical results obtained from the software PLAXIS 3D.

ACKNOWLEDGEMENTS

The authors thank the Scientific and Technological Research Council of Turkey (TUBITAK) for supporting financially this study through the project 119M609.

REFERENCES

Amanuel Zewdu. (2019). Seepage and Slope Stability Analysis of Earthen Dam: A Case Study of Koga Dam, Ethiopia. World News of Natural Sciences, 26, 191–217.

Greco, M., Pontillo, M., Iervolino, M., and Leopardi, A. (2008). 2DH numerical simulation of breach evolution in an earth dam. Riverflow2008, Vol. 1, M. S. Altinakar, M. A. Kökpınar, I. Aydın, S. Çokgör, and S. Kırkgöz, eds., Kubaba, Ankara, Turkey, 661–667.

M. W. Morris, M. Hassan, A. Kortenhaus, P. Geisenhainer, and P. Visser, Y. Zhu. (2008). Modeling breach initiation and growth. Floodrisk, Oxford, United Kingdom.

R. Fell, C. H. Wan and M. Foster. (2003). Progress report on methods for estimating the probability of failure of embankment dams by internal erosion and piping. University of New South Wales, Sydney, Australia.

S. shui Chen, Q. ming Zhong, and G. ze Shen. (2019). Numerical modeling of earthen dam breach due to piping failure. Water Sci. Eng., vol. 12, no. 3, pp. 169–178.

Y. A. Sharif, M. Elkholy, M. Hanif Chaudhry, and J. Imran. (2015). Experimental Study on the Piping Erosion Process in Earthen Embankments," J. Hydraul. Eng., vol. 141, no. 7, p.

04015012.

Y. Zech & S. Soares-Frazão. (2007). Dam-break flow experiments and real-case data. A database from the European IMPACT research, Journal of Hydraulic Research, 45:sup1, 5-7, DOI: 10.1080/00221686.2007.9521827.

TYPE 1 ENERGY AUDIT APPLIED TO A SCHOOL LIGHTING SYSTEM BASED ON THE ISO 50002 STANDARD

Prof. Diego Penagos-Vásquez

Faculty of Engineering, Department of Mechatronics and Electromechanics, Instituto Tecnológico Metropolitano, Robledo Campus, Calle 73 No. 76A-354, Vía al Volador, Medellín, Colombia. Industrial Energy Management., ORCID NO: 0000-0002-1340-0914

Prof. Diana Ivonne González-Arango

Faculty of Engineering, Department of Mechatronics and Electromechanics, Instituto Tecnológico Metropolitano, Robledo Campus, Calle 73 No. 76A-354, Vía al Volador, Medellín, Colombia. Industrial Energy Management., ORCID NO: 0000-0001-8862-0316

Prof. Oscar Darío Monsalve-Cifuentes

Faculty of Engineering, Department of Mechatronics and Electromechanics, Instituto Tecnológico Metropolitano, Robledo Campus, Calle 73 No. 76A-354, Vía al Volador, Medellín, Colombia. Industrial Energy Management., ORCID NO: 0000-0002-7268-9535

Abstract

Currently, the consumption and production of electrical energy worldwide depend on the use of the natural environment and resources in a way that continues to have destructive effects on the planet. Therefore, it is essential to ensure sustainable consumption and production patterns, as indicated in the United Nations Sustainable Development Goal 12th, which aims to decouple economic growth from environmental degradation, increase resource efficiency and promote sustainable lifestyles. Sustainable consumption and production patterns can be achieved through energy audits in different public facilities. The school is the place where an inconsistency in the control and independence of the lighting system of one of the blocks is identified, thus requiring an assessment of energy use activities and their appropriate use for the creation of cost reduction plans. In this work, it was necessary to perform a preliminary inspection type 1 energy audit on the lighting system, applying the ISO 500002:2014 standard [1] that specifies the process requirements for conducting an energy audit concerning energy performance. The institution has a luminaire distribution board where there is no proper order in the management of the thermomagnetic switches. Therefore, a measurement plan was carried out to determine the potential energy savings, to make a proposal to improve the system, considering the implementation of the technical regulations for lighting and public lighting [2]. By simulating a lighting system for one of the classrooms in the block, it became evident that by distributing the lamps with LED lights instead of fluorescent tubes, it was possible to achieve a saving of 41.4% in electrical energy in one classroom alone.

Keywords: Energy Savings, Lighting System, Improvement Opportunity.

References

[1] International Organization for Standardization (2014). Energy audits - Requirements with guidance for use (ISO 50002).

[2] Technical regulation of lighting and public lighting (2010), General appendix, Ministry of mines and energy.

EXPERIMENTAL STUDY ON BRICKS USING PAPERWASTE

B.Rohini[1]

G Pulla Reddy Engineering College(Autonomous),Assistant Professor, Department of Civil Engineering, Kurnool, India., ORCID ID: https://orcid.org/0000-0002-4921-0426

R. Bala Murali Krishna

University College of Engineering, JNTU GV, Assistant Professor, Department of Civil Engineering, Vizianagaram, India, ORCID ID: https://orcid.org/0000-0000-0003-1944

Abstract

Commonly used material for construction purpose in India are Bricks. Conventional bricks are manufactured by firing of clay in high temperature kilns. Utilization of industry and agricultural waste products in the industry has been the focus of research in order to reduce the use of conventional material. More waste paper is ending up in landfill or dump sites rather than being recycled. So, the present study focuses on use of paperwaste as replacement in sand. The purpose of this research is to determine the compressive strength, water absorption capacity, efflorescence and even the structure of papercrete brick is assessed ,which determines their aptness for use as a building material.

Keywords: compressive strength, water absorption capacity, efflorescence, papercrete bric**k.**

.

I. Introduction

Bricks are commonly used building material all over the world for constructing walls , pavement and other elements in masonry construction. Conventional bricks are manufactured by firing of clay in high temperature kilns. The present study is aimed at utilization of waste products in brick manufacturing. Waste product considered here is paper waste.Urbanization lead to a vast generation of paper waste and discharge of these waste materials became a major problem . Dumping and landfilling of solid waste leads to environmental degradation.Some of the papers referred during the execution of experimental study have been discussed below.

Yash Liladia, Shivam Malviya, Arbaz Baig (2020) studied the utilization of paper to produce bricks and concluded that the free weight of papercrete brick was 1/3 to 2/5 lesser than the customary clay brick. Due to lighter weight and more flexibility, these bricks are potentially idealistic material for earthquake prone regions. Brij Bhushan, Varinder S Kanwar, Siby John (2019) studied the utilization of sludge for the brick manufacturing and concluded that the paper sludge can be utilized as an additive in the form of powder in the production of bricks up to 20% of replacement of soil. Addition of sludge in bricks leads to well sounded bricks provided a limited amount of sludge is added.Veenu Rani, Er. Vikram, Er. Sunil Kumar (2018) studied development of ecofriendly lightweight brick using waste paper and concluded that addition of more paper in mix proportion due to which weight loss is also higher. Papercrete bricks are light in weight which can handled by any person. Annoy Kumar Ghosh (2018) studied about a sustainable building material and concluded that the study recognized papercrete as a sustainable building material and emphasized on more research towards its performance parameters. The weight of this bricks is $1/3^{rd}$ to $2/5^{th}$ lesser than conventional clay bricks.K. Anandaraju, B. Jose Ravindra Raj, R. Vijaya Sarathy (2015) studied about the experimental Investigation of Papercrete Bricks and concluded that the bricks are not suitable for water logging and external walls. It can be used in inner partition walls. Since, the waste materials are used, it will reduce the landfills and pollutionRohit Kumar Arya, Rajeev Kansal (2015) studied utilization of waste paper to produce ecofriendly bricks and concluded that papercrete has high fire resistance, good sound absorbent, good thermal resistance with an R value between 2-3 per inch. In walls 12-16 inches thick, the long energy saving of papercrete will be a great advantage for the house owner and environment.YD Shermale, MB Varma (2015) studied about an efficient use of waste paper and concluded papercrete is far lighter a material than concrete or wood and has good water absorption and insulation capacity, less shrinkage and is environment friendly, has high strength to weight ratio.Maneesh Kumar CS, Ashik Moulana, Venkateshan (2015) studied about an experimental study on use of

recycle paper mill waste in light weight brick and the recycle paper mill waste holds the moisture in these pores and fibrous envelopes providing obstacle for moisture to move towards surface. This fibrous nature gives very high energy absorbing ability and hence the high compressive strength. Neha Thakur, Sandeep Salhotra (2005) studied about an experimental investigation of papercrete bricks and concluded that Papercrete bricks were having less compressive strength, but strength was increased with partial replacement of sand by coconut fibre and bricks were named as C0-Fi bricks. From the literature survey conducted, the main objective of study is to include paper as replacement for sand. The tests conducted are compression test, water absorption test, sound test, structure observation and efflorescence test as per IS.

II. MATERIALS USED

1.CEMENT:

Cement is one of the binding materials in this research. 53 grade Ordinary Portland Cement (OPC) confirming to IS: 8112-1989 cement used.



Figure 1 : Cement

2.SAND:

Sand particles consist of small grains of silica (SiO_2). According to the size of grains, the sand is classified as fine, coarse and gravel. The properties were analyzed as per BIS standard as shown in Table 1. Locally availabe sand is collected for the experimental work.



Figure 2: Sand

Table 1: Sieve analysis-Sand

IS Sieve Size	Weight Retained on Sieve(gm)	Percentage of weight Retained	Percentage of weight Passed	Cumulative percentage of weight Retained
4.75mm	6	0.6	99.4	0.6
2.36mm	22	2.2	97.2	2.8
1.18mm	179	17.9	79.3	20.7
600micron	309	30.9	48.4	51.6
300micron	338	33.8	14.6	81.4
150micron	146	14.6	0	100
TOTAL	1000			261.1

Fineness Modulus=261.1/100=2.611

Fine aggregate which satisfies the requirement of experimental work and conforming to zone-2, as per IS 383:1970.

3.PAPER:

For the experimental work, different type of papers like newspaper, magazines, old invitation cards, paper tickets etc are collected from different sources for making papercrete. The papers, which were collected, cannot be used directly. It should be made into paper pulp before mixing with other ingredients.

PULP GENERATION:

The papers, which were collected, cannot be utilized immediately. It should be made into a paper pulp before mixing with other ingredients. The papers were kept in the tank for 3 to 4 days, otherwise until the papers degrade into a paste-like form.



Figure 3: Paper Pulp

After soaking for 3-4 days then the pulp is removed from water and kept aside so that excess water present in it will be drained out and it can be used effectively without any problem.If excess quantity of is present then it will be difficult to make a uniform mixture and it will take more time to dry.

III. PROCEDURE

1. Materials were collected from different sources.
2. Waste papers like newspapers, from books and record papers. The collected papers cannot be used directly these are kept in water tub with full of water for 3-4 days until the paper becomes soft and it can be made into paste.
3. Then the total paper pulp is taken out and kept aside so that the excess water can be removed from the pulp because if excess water is present then it cannot make good bonding with cement sand and the setting time also changes due to excess water.
4. Cement and sand were taken in required proportions and they are mixed thoroughly to get a uniformity in the mixture. Then small quantity of water is added to it and mixed again.
5. Into the cement sand mixture, the paper pulp is added in small quantities with continuous mixing. Because adding total paper pulp at a time can make mixing difficult and cannot make the mix uniform lumps can be formed if paper pulp is added at a time.
6. Then sufficient water is added to the mixture and again thoroughly such that the mixture is uniform.
7. The mould of size 190×90×90mm are taken and the mixture is filled into the mould with trowel make sure that it should spread to corners. After filling remove excess material present with the help of trowel and make the surface smooth.
8. Keep the mould aside without disturbing and let it dry. Remove the brick from the mould and keep it for air drying.
9. Then the test is performed on the bricks and results are noted down.

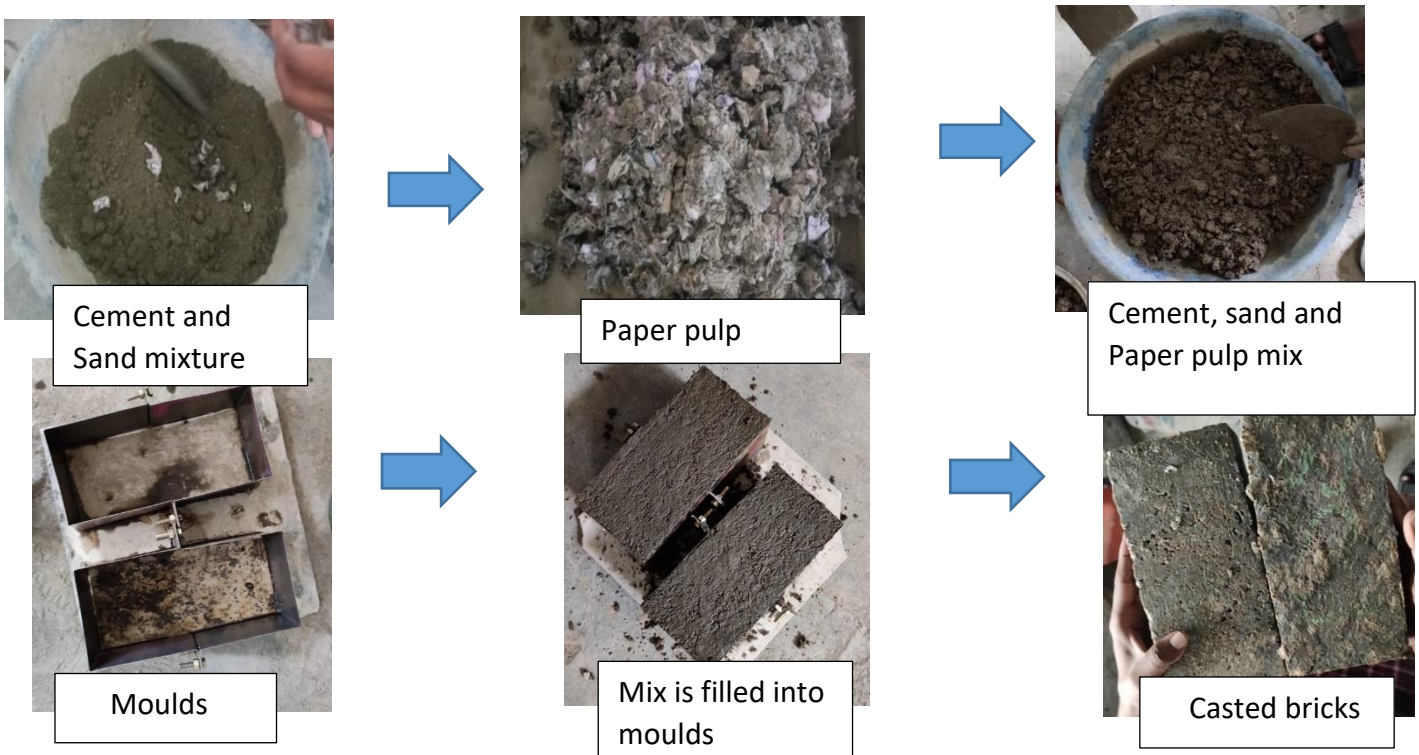


Figure 4 : Casting Procedure

IV. TESTS CONDUCTED

1.COMPRESSION TEST:

This test was held out by Compression Testing Machine after the 7th day from the date of casting papercrete brick. Papercrete bricks never fail catastrophically, it just compressed like squeezing rubber. Therefore, great care must be considered while testing the papercrete brick because in papercrete load should be applied up to half compression only. The papercrete bricks are having elastic behavior and less brittleness, due to this the structure was not fully collapsed, when the papercrete brick fails at higher load. Only the outer faces cracked and peeled out.

1. First the irregularities in the surface were removed.
2. The brick was placed centrally on the bottom plate of the universal testing machine.
3. Then the upper plate of the universal testing machine was lowered down up to the brick was hold tightly without any movement.
4. Then load is applied on the brick axially at a rate, when cracks are appeared on the outer side of brick then loading stops. The brick is removed from the machine and the compressive strength obtained is noted down.





Figure 5 : Papercrete placed in UTM

2.WATER ABSORPTION TEST:

Water absorption test is required to check whether the bricks are suitable for water logged areas or not. As per standards the bricks should not absorb water more than 20% of its original weight. The water absorption of bricks is not related directly to the porosity owing to the nature of pores themselves. Some of Pores may be through pores which permit air to escape in absorption tests and allow free passage of water in absorption tests, but other are completely seated and inaccessible to water under ordinary conditions. Immerse completely dried specimen in clean water at a temperature of 27+2°C for 24 hours. Remove the specimen and swipe out any traces of water with damp cloth and weigh the specimen after it has been removed from water.

3.SOUNDNESS TEST:

In this test two bricks were taken over and they were struck on each other. When the bricks were strong enough and not broken and a clear ringing sound was produced. Then the bricks are risk-free to use.



Figure 6 : Soundness Test

4.EFFLORESCENCE:

The soluble salts, if presents in bricks will cause efflorescence on the surface of bricks. For finding out the presence of soluble salts in a brick, this test was carried out. According to IS: 3495 part-3 , ends of bricks are kept in 25mm depth water till entire water is absorbed or evaporated , when there is no perceptible deposit , efflorescence is Nil , but there is slight efflorescence when 10% of exposed area has thin deposit of salts.



Figure 7 : Bricks placed in tray with water for efflorescence test

5.STRUCTURE:

Bricks are taken and are broken into half to check the uniformity of mixture and to check the voids present in the brick. The paper pulp used in making the brick should be present uniformly throughout the brick and there

should be less voids in the brick. If the paper pulp settles in only part of brick then it is not good to use and if the voids are more then it is not used for construction purpose.



Figure 8 : Papercrete broken into two halves

V. RESULTS

1.COMPRESSION TEST:

The test results of compressive strength of the bricks obtained are tabulated in Table 2.

Table 2 : Compressive strength(N/mm^2)

	Compressive Strength(N/mm^2)	
Compositions	**7 Days**	**14 Days**
1	**5.92**	**6.39**
2	**5.64**	**5.88**
3	**3.96**	**4.48**

The variation in strength of bricks on increasing the paper pulp content is shown in Figure 9 for three composition taken.

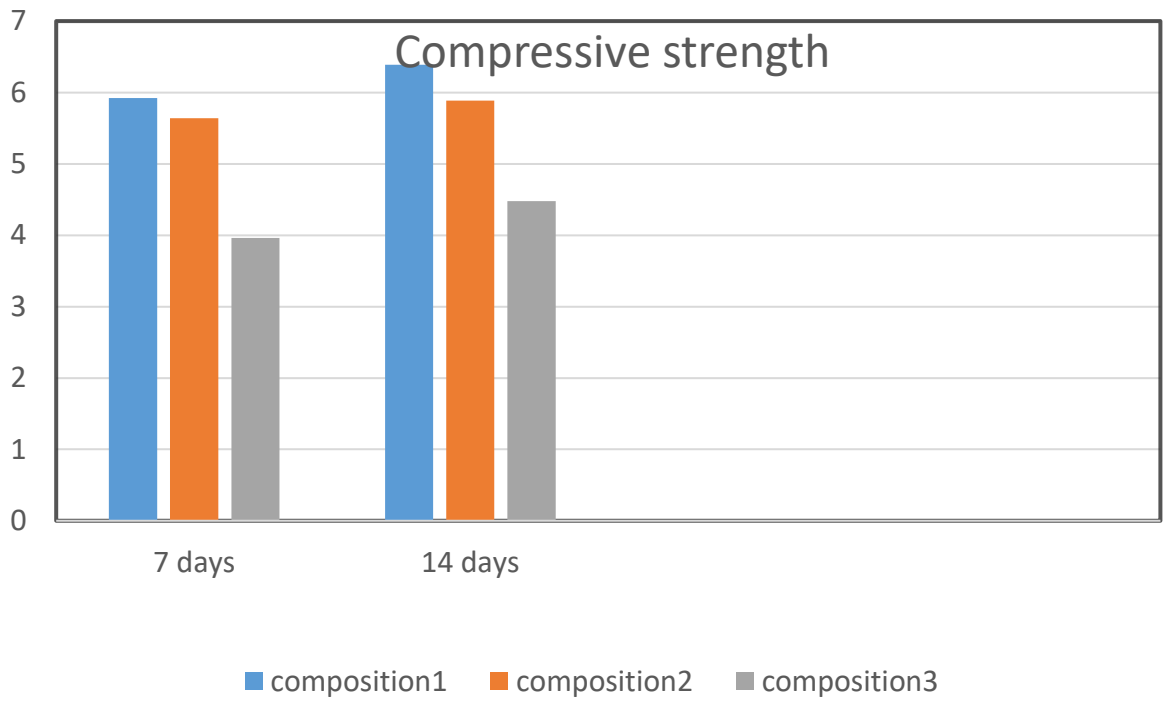


Figure 9 : Variation of compressive strength of brick for 7 days and 14 days.

From the Figure 9, it can be observed that the compression values of the brick here are changing with the variation in percentage of paper pulp that is used in making the brick.When 15% of paper pulp is added, the compressive of the brick can be observed higher and if the paper pulp is added in higher quantities then the compression strength starts decreasing.

According to Bureau of Indian Standards (BIS):1077-1957, the minimum compressive strength of bricks is 3.50 N/mm^2. But the obtained values of compressive strength are in the range of 3-7 N/mm^2 which is greater than the minimum value.

2.WATER ABSORPTION:

The test results obtained after soaking 24 hours in water are tabulated in Table 3. Figure 10 represents the water absorption variation for the three compositions.

Table 3: Water absorption

Composition	Initial Weight(gm)	Weight after 24 hours of soaking(gm)	Difference in weight in percentage (%)
1	2734	3074	12.43
2	2658	3096	16.67
3	2132	2598	21.85

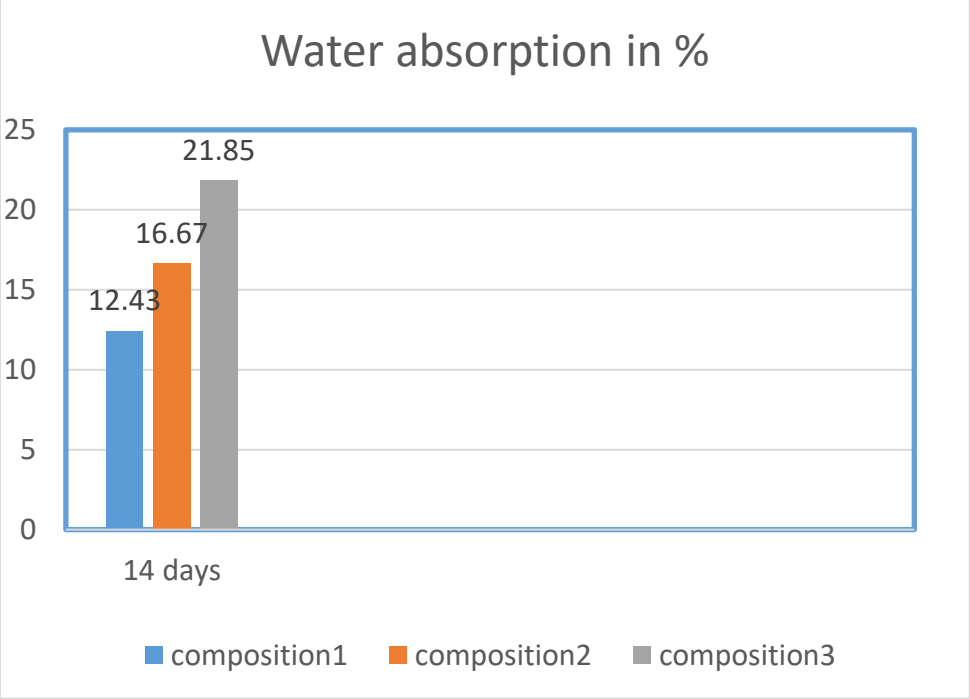


Figure 10 : Variation of water absorption for three different compositions

The actual water absorption capacity of the brick according standards should be less than 20% of actual weight of the brick. The test results obtained from Figure 10 shows that when the percentage of paper pulp in the brick varies then the water absorption capacity is also varying. For the brick with less paper pulp content i.e.,15% and 25% the water absorption capacity is less and within the limits, but for paper pulp content of 35% the water absorption is more and exceeding the limits i.e., Greater than 20% of its actual weight.

3.SOUNDNESS TEST:

The soundness of the brick is varying with the variation in paper pulp percentage present in it. The bricks in which the paper pulp content is 15% and 25%, when two bricks struck each other then they produced a good metallic sound and they were not broken or damaged, But the bricks which contain 35% of paper pulp content when struck were giving a dull sound and the bricks were not broken.

4.EFFLORESCENCE:

After keeping the brick vertically in water of 25mm depth in a tray, let the water evaporate. After complete evaporation of water let the bricks dry in shade . The deposition of salt on the bricks indicate the presence of efflorescence.Here it was observed that there are no salt deposits on surface of bricks. So, the efflorescence for the bricks is Nil.

5.STRUCTURE OF BRICK:

The brick was taken and broken into two halves, then the two parts of the bricks are examined clearly. Here the paper pulp that is added is spread uniformly throughout the brick and there are no lumps of the cement or papercrete. Then they are checked for pores if any, there are very less pores present and there are no large pores which can affect the working of brick. As the bricks are satisfying the conditions these bricks are acceptable as construction material.

VI. CONCLUSIONS

From the test results obtained, these conclusions were made:

1. According to Bureau of Indian Standards (BIS):1077-1992, the minimum compressive strength of bricks is 3.50 N/mm^2.Considering the obtained results the maximum compressive strength is 6.39 N/mm^2 which is 54.77% greater than the minimum compressive strength.
2. As per the research the bricks should not absorb water more than 20%. The water absorption capacity of papercrete bricks is changing with the percentage of papercrete incorporated in the bricks. Bricks with 15% and 25% of papercrete has shown the test results within the limits (i.e., less than 20%), which is acceptable and when the percentage of papercrete increased the water absorption capacity has exceeded more than 20% which makes it not suitable.
3. Addition of papercrete up to 25% in bricks leads to well sounded bricks, further increase in percentage of papercrete doesn`t give metallic sound when struck.
4. Addition of papercrete in bricks gives nill efflorescence value which is acceptable.
5. Since, papercrete brick mainly consists of waste material, it will reduce the landfill and pollution. Hence, the overall cost can be reduced as compared to conventional brick.

REFERENCES

1. Neha Thakur, Sandeep Salhotra (2020) “An experimental investigation of papercrete bricks” volume 29, No.10S,2020.
2. 1. Yash Liladia, Shivam Malviya, Arbaz Baig (2020), “The utilization of paper to produce bricks” volume:07, Issue:02, Feb 2020.
3. Brij Bhushan, Varinder S Kanwar, Siby John (2019) “The utilization of sludge for the brick manufacturing” volume-9, Issue-2, December 2019.
4. Veenu Rani, Er. Vikram, Er. Sunil Kumar (2018) “Development of ecofriendly lightweight brick using waste paper” volume 5, Issue 10, June 2018.
5. Annoy Kumar Ghosh (2018) “A sustainable building material” volume 05, Issue 10, October 2018.
6. K. Anandaraju, B. Jose Ravindra Raj, R. Vijaya Sarathy (2015) “The experimental Investigation of Papercrete Bricks” volume 2, Issue 2, June 2015.
7. Rohit Kumar Arya, Rajeev Kansal (2015) “utilization of waste paper to produce ecofriendly bricks” volume 5, Issue 8, August 2016.
8. YD Shermale, MB Varma (2015) “An efficient use of waste paper” volume 5, Issue 3, 2015.
9. Maneesh Kumar CS, Ashik Moulana, Venkateshan (2015) “An experimental study on use of recycle paper mill waste in light weight brick” volume 01, Issue 02, May 2015.

QUANTUM DOTS SYNTHESIS AND APPLICATION IN SOLAR CELLS

Babak Emdadi

Khazar University, Physics and Electronics Department, Baku, Azerbaijan., ORCID NO: 0000-0002-1001-6239

Ahmed Asimov

Khazar University, Physics and Electronics Department, Baku, Azerbaijan., ORCID NO: 0000-0001-7289-4216

ABSTRACT

Nanostructures have confirmed to be a very appealing choice for sensor application due to their physical and chemical attributes. In last years, carbon quantum dots (CQDs) as a novel part of carbon nanostructures has been broadly utilized in the field of sensors. CQDs have powerful fluorescence resilience, which signifies that actually after a prolonged period of continued excitation, the fluorescence emission intensity is able to remain stable. Pyrolysis is able to be used to combine carbon quantum dots (CQDs) by warming carbon origins to response temperatures increase to 1200 °C. Pyrolysis permits one to synthesize carbon quantum dots within various hours, but with many changeable yields varying from 0.01% to 51%, relating to the carbon source and behavior condition. The X-ray diffraction template disclosed the amorphous nature of prepared carbon quantum dots. In this work, the gathered product was characterized by X-ray diffraction (XRD) examination. The reality of a wide zenith at $2\theta = 17°$ determines the carbon quantum dots of graphene and graphite since the graphene and graphite exhibit more tipped mounts in the XRD pattern. The outcomes disclosed that the prepared carbon quantum dots deliver excitation-dependent fluorescence emission. The acquired conclusions from photoluminescence spectroscopy demonstrate that as-prepared carbon quantum dots were able to be applied as a fluorescent search for the identification of ascorbic acid.

Keywords: Quantum dot, CQDs, X-ray diffraction, Pyrolysis, toxicity, solar cell

INTRODUCTION

At the present time, the biomedical field concentrates on progressing novel race nanomaterials like Quantum dots for multitasking targets such as medical diagnostics, drug delivery, gene therapy, etc. Furthermore, 'Quantum dots' famed as semiconductor Nano crystals are with high speed becoming a crucial device for diverse biomedical applications owing to their outstanding photophysical attributes. In the previous decades, a novel group of fluorescent bits appeared as a good applicant for single molecule and single particle tracking (SPT) in living cells and organisms, the semiconductor quantum dots (Pierobon & Cappello, 2012). Quantum dots (QDs), frequently defined as 'artificial atoms,' show distinct energy statuses, and their bandgap can be exactly modulated by changing the measure (Klimov, 2007). QD span is generally among 2 and 10 nm in diameter. The structure of the QDs contains a semiconductor core, over-coated by a shell, and a cap enabling progressed solubility in aqueous buffers (Ghasemi, Peymani, & Afifi, 2009).

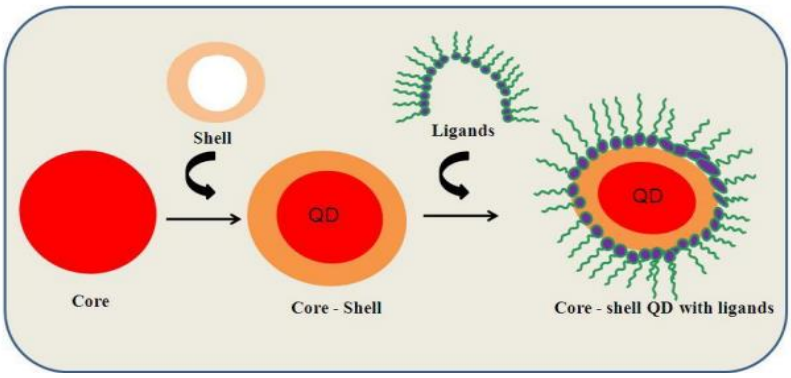


Fig. 1. Schematic image of the fundamental structure of Quantum dots (QDs)

QDs are nanometer-measure semiconductor crystals compound of groups II to VI or III to V elements and are specified as particles with physical proportions more diminutive in comparison to the exciton Bohr radius (Chan, Maxwell, Gao, Bailey, Han, & Nie, 2002). QDs show special luminescence characteristics and electronic attributes such as broad and ongoing attraction spectra, thin transpiration spectra, and increased light consistency (Bruchez Jr, Moronne, Gin, Weiss, & Alivisatos, 1998). They attract white light and then reemit a particular hue for a few nanoseconds subsequently relating to the band gap of the material (Valizadeh, Mikaeili, Samiei, Farkhani, Zarghami, Akbarzadeh, & Davaran, 2014, Bakalova, Ohba, Zhelev, Ishikawa, & Baba, 2004).

Unlike quantum wells, in position the movement of carriers is limited to a disc via the being the crystal process of slim epitaxial substrates (Herman, 1983), the production of quantum wires or dots, which limit the carriers to a place with at least two of three dimensions confined to the span of the de Broglie wavelength, needs far more developed tech. The first procedure of getting quantum dots was performed by Reed and his colleagues (1986), who etched them in a system including two-dimensional electron gas.

The stages of this procedure are displayed in figure. 2: The level of an example including one or more quantum wells is hidden with a polymer mask, and afterward somewhat revealed (figure. 2. a). The displayed template corresponds to the form of the constructed nanostructure. Inasmuch as the needed strong resolution, the mask is not revealed to seeable light, but to the electron or ion beam (electron/ion beam lithography). At the exposed places the mask is removed (figure. 2. b). Then, the total level is covered with a slim metal layer (figure. 2. c).

By utilizing a specific solution, the polymer film and the protective metal level are terminated, and a clear surface of the sample is got, except for the formerly exposed areas, where the metal layer stays (figure. 2. d). Subsequently, by chemically etching the spaces not shielded by the metal mask (figure. 2. e), the slim pillars are created, including the cut-out fragments of quantum wells (figure. 2. f).

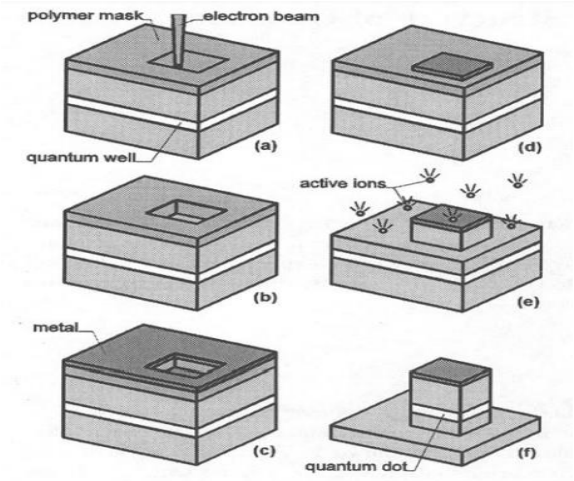


Fig. 2. Procedure of quantum dot etching

Hence, the movement of electrons, which is originally limited to the surface of the quantum well, is better limited to a tiny pillar with a diameter on the order of 10-100 nm.

The procedure of extending a slim electrode over the surface of a quantum well can generate both single quantum dots (Ashoori, Stormer, Weiner, Pfeiffer, Pearton, Baldwin & West, 1992, Ashoori, Stormer, Weiner, Pfeiffer, Baldwin & West, 1993) and large arrays (matrices) of dots (Hansen, Smith, Lee, Brum, Knoedler, Hong & Kern, 1989, Lorke, Kotthaus & Ploog, 1990, Meurer, Heitmann& Ploog, 1992, Sikorski & Merkt, 1989). A very valuable characteristic of quantum dots whose electrons are limited by the electric field built by a set of electrodes is their flat lateral restriction, presenting no edge effects. The probability of maintaining specific numerical values is also very significant.

MATERIALS AND METHODS

Nanometer-size carbon dots which are the counterparts of silicon nanoparticles at present light up. They are non-venomous, plentiful, permanent, and bio-consistent. Albeit, the regular photoluminescence quantum output of carbon dots is not high yet, they are non-blinking and have considerable two-photon attraction cross-sections which are desirable for one-photon or two-photon bio-imaging.

Diverse ways have been utilized to synthesize QDs (Bera, Qian, Tseng & Holloway, 2010) but, usually, strategies for QD synthesis employed top-down processing strategies and bottom-up techniques (figure. 3).

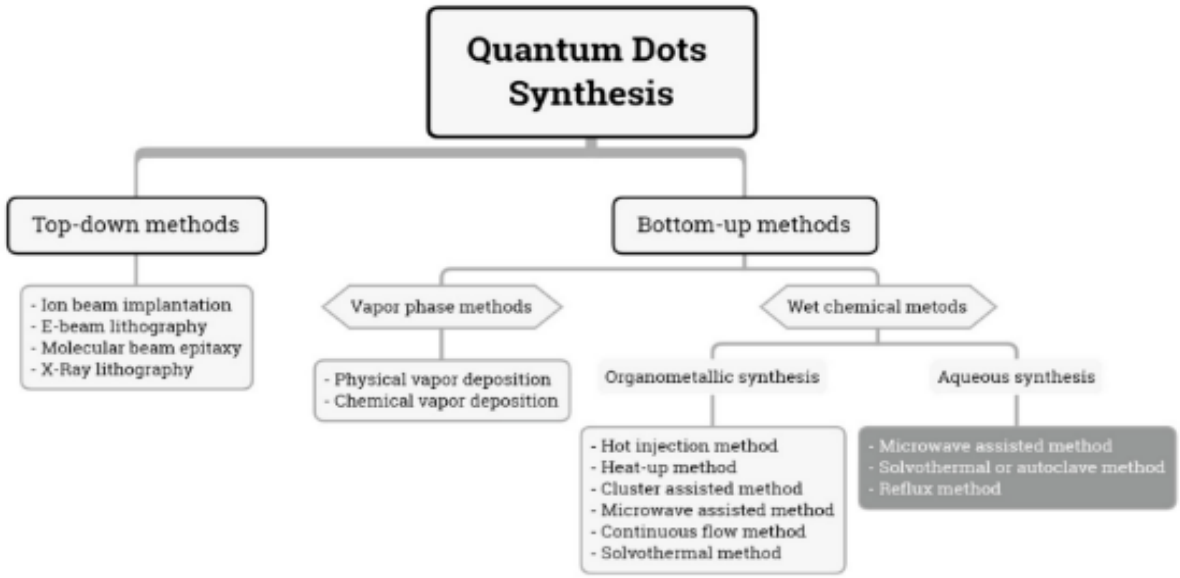


Fig. 3. Synthesis methods of QDs

Top-down processing techniques contain molecular beam epitaxy (MBE), ion insemination, e-beam lithography, and X-ray lithography. Utilizing the further bottom-up technique, colloidal QDs are organized by self-assembly in the solution following a chemical decrease (Mattoussi, Palui & Na, 2012, Birudavolu, Nuntawong, Balakrishnan, Xin, Huang, Lee & Huffaker, 2004, Nakata, Mukai, Sugawara, Ohtsubo, Ishikawa, & Yokoyama, 2000, Bertino, Gadipalli, Martin, Rich, Yamilov, Heckman & Mancini, 2007).

There are diverse self-assembly strategies (bottom-up), which have been employed to combine the QDs, and they may be extensively classified into wet-chemical and vapor-phase strategies (Bera, Qian, Tseng & Holloway, 2010): (a) wet-chemical techniques mostly follow the customary precipitation ways with accurate managing parameters for a single solution or mixture of solutions. The mechanical factors of the organization of CDs stay vague. There are fewer studies have tried to specify and examine how CDs polymerize/carbonize following the construction of a medium molecule; however, in-depth analyses are needed to explain the chemical nature of the shaped intermediate types and the chemical procedures that are happening.

The characterization of QDs is divided into four techniques, which are spectroscopy, scattering, electrical, and microscopy techniques (figure. 4).

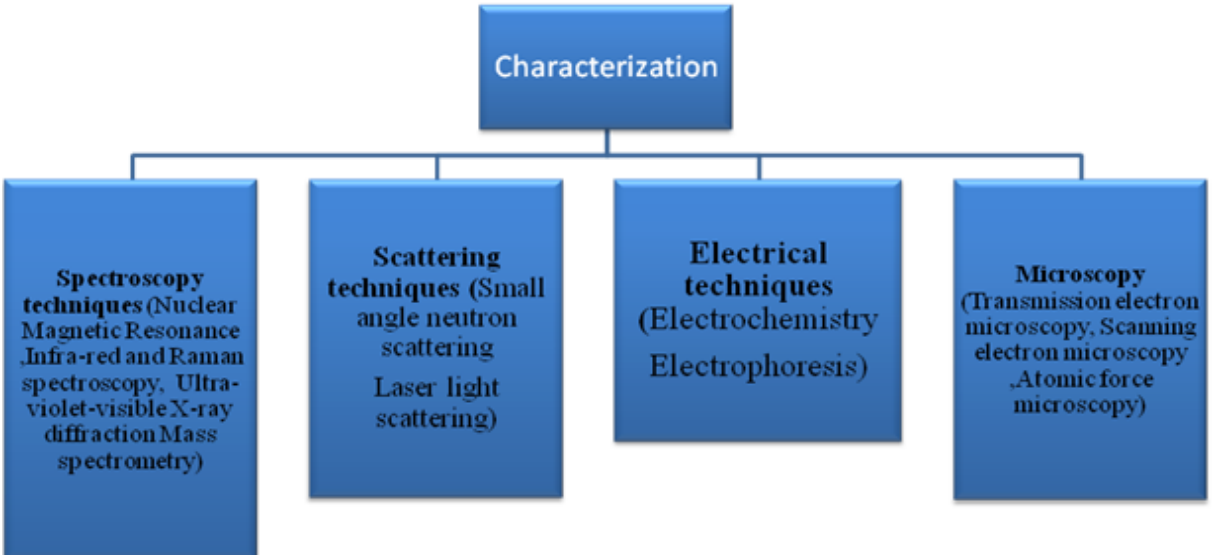


Fig. 4. Characterization methods of QDs

Optical characterization of QDs is usually provided by UV-VIS and photoluminescence spectroscopy, which offer fast, non-destructive and contactless options.

The precipitation procedure consistently includes both nucleation and confined development of nanoparticles. Nucleation may be classified as analogous, diverse in content, or secondary nucleation (Burda, Chen, Narayanan & El-Sayed, 2005). Similar nucleation happens when solute atoms or molecules mix and attain an important measure in the absence of the help of a pre-existing solid interface. Humid-chemic ways are usually microemulsion, sol-gel (Bang, Yang & Holloway, 2006, Spanhel, & Anderson, 1991, Bera, Qian, Sabui, Santra & Holloway, 2008), competitive reaction chemistry, hot-solution decomposition (Qu & Peng, 2002, Murray, Norris, & Bawendi, 1993, Qu, Peng & Peng, 2001), sonic waves or microwaves (Li, Qian, & Ren, 2005), and electrochemistry. (b) steam-phase ways for generating QDs start with techniques in which substrates are developed in an atom-by-atom method. Afterward, the self-assembly of QDs happens on a layer in the absence of any planning (Xin, Wang, Yin, Kim, Dobrowolska, Merz & Furdyna, 1996, Leonardi, Selke, Heinke, Ohkawa, Hommel, Gindele & Woggon, 1998, Kurtz, Shen, Schmidt, Grün, Hong, Litvinov & Klingshirn, 2000, Swihart, 2003). Self-assembly of nanostructures in material developed by MBE, sputtering, liquid metal ion sources, or accumulation of gaseous monomers are usually classified under vapor-phase ways (Bera, Qian, Tseng & Holloway, 2010). MBE has been mostly utilized to self-assemble QDs from III-V semiconductors and II-VI semiconductors utilizing the big lattice mismatch. For instance, InAs on GaAs has a 7% inconformity and lead to SK growth (Xin, Wang, Yin, Kim, Dobrowolska, Merz & Furdyna, 1996).

Quantum dot-sensitized solar cells (QDSSCs) have engrossed much consideration as third-race photovoltaic cells due to their profitable vigor transformation performance, low price, and simple cell construction (Nozik, Beard, Luther, Law, Ellingson & Johnson, 2010). QDSSCs borrow the analogous working rule of dye-sensitized solar cells (DSSCs) with the displacement of dye by semiconductor quantum dots (QDs) (O'regan, & Grätzel, 1991). In previous years, much strive had concentrated on the revision of photoelectrodes, containing the optimization of TiO_2 films and the construction of a fresh diversity of QD sensitizers to enhance the implementation of QDSSCs (Yang, Zhu, Sun, Huang, Luo, Li & Meng, 2012). Separated from the layout of photoelectrodes, the sensible election of a counter electrode (CE), as well as an electrolyte, is also thought crucial to ameliorate the implementation of QDSSCs (Liang, Chen, Dai, Wu, Zhang, Li & Qian, 2015).

We have to pay consideration to this prominent point that majority of conventional QDs generally include toxic materials such as cadmium, mercury, and lead that are detrimental to biological systems and ultimately will eventuate in drastic environmental troubles and concerns.

One of the important QDs application is carbon quantum dots (CQDs). The amazing attributes of carbonic nanomaterials such as nanodiamonds, fullerenes, carbon nanotubes, graphene sheets, and fluorescent carbon nanoparticles or carbon quantum dots (CQDs) have motivated vast analyses on them due to their excellent

possibility for a broad diversity of technical usages. Between the electronic and physicochemical attributes of CQDs, their optical characteristics and their fluorescence publications specifically have motivated increasing attraction in recent decades. For multiple years, semiconductor quantum dots have been considerably studied for their powerful and harmonic fluorescence transpiration attributes, which capable their applications in biosensing and bioimaging.

According to the previous researches, there are clear and substantial arguments and reasons to creation of CQDs to replace semiconductor quantum dots. Low toxicity, biocompatibility, low cost, and chemical inertness in addition to having similar fluorescence properties can be significant advantages of CQDs in comparison to semiconductor quantum dots. In the figure. 5, we can see the chemical structure of CQDs.

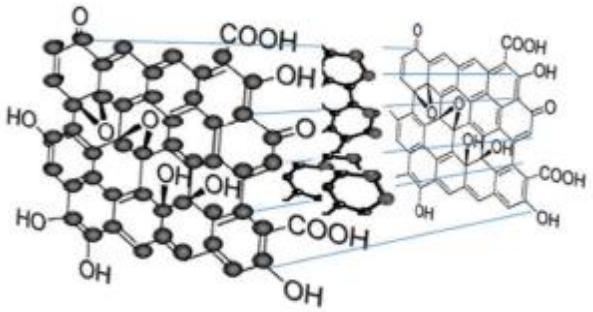


Fig. 5. Chemical structure of CQDs

Lately, nanomaterials with layered organizations have obtained consideration because of their special attributes and are one of the most skillful immobilized molecules. These covered nanomaterials can be mixed with other nanomaterials or polymers to significantly progress the sensibility, activity of immobilized molecules, and consistency of the consequent sensors. Fluorescent semiconductor quantum dots have developed wide promising applications containing biological labeling and solid-state lighting.

Pyrolysis has found a more comprehensive description in clarifying each chemical conversion conveyed about by the app of warmth, even with air or other additives. Pyrolysis is able to be used to combine carbon quantum dots (CQDs) by warming carbon origins to response temperatures increase to 1200 °C. Pyrolysis permits one to synthesize carbon quantum dots within various hours, but with many changeable yields varying from 0.01% (Jian, Wu, Lin, Li, Lin, Harroun & Huang, 2017) to 51% (Li, Harroun, Su, Huang, Unnikrishnan, Lin, & Huang, 2016), relating to the carbon source and behavior condition. Pyrolysis is able to generally utilize broadly further and diverse carbon sources, varying from silicon carbide (Lee, Lee, Lim, Yoo & Cho, 2020), flour (Teng, Ma, Ge, Yan, Yang, Zhang & Bi, 2014), etc. In pyrolysis, carbon quantum dots (CQDs) outcome from intermolecular dehydration, carbonization, and condensation, and the consequent carbon skeleton is preserved jointly by chemic classes such as $–SO_2$, $–HSO_3$, and $–H_2PO_4$ (Tang, Zhang, Zhang, Xiao, Shi, Chen & Xu, 2019).



Fig. 6. Photoluminescence (PL) emission spectra

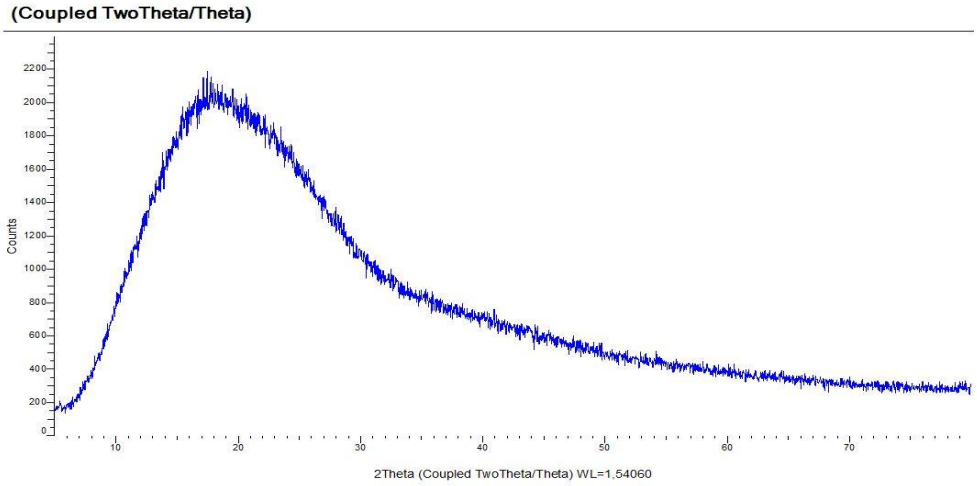


Fig. 7. Xrd rentgen pattern of prepared CQD

Moreover, in this work the prepared carbon quantum dots were characterized by X-ray diffraction design. The X-ray diffraction template disclosed the amorphous nature of prepared carbon quantum dots.

FINDINGS AND DISCUSSION

The PL publication is able to changeable according to the conversions in the measure of the bandgap and chemical functionalization. QDs display more increased photoluminescence as contrasted with other carbon-based substances. Substantially, QDs have demonstrated PL due to the conversion in diverse parameters of the combinations like concentration, size, pH, and excitation wavelength as shown in figure. 6 where the dependency of PL has been confirmed specifically to quantum confinement, edge effect, composition, structure, and shape. According to our Pl diagram as shown in figure. 6, the peak of diagram is shifted from 670 to 730 nm. Typically, shifting excitation wavelength is related to the publication wavelength and the altitude of the band is characteristically seen in photoluminescence (PL) spectra. By large the shifting excitation wavelength also shifts towards the more heightened wavelength of the publication wavelength.

For prepared carbon quantum dots, the XRD design in figure. 7 shows broad ridges at $2\theta = 17°$ which is corresponding to the amorphous nature and disordered carbons in carbon quantum dots. The reality of a wide zenith at $2\theta = 17°$ determines the carbon quantum dots of graphene and graphite since the graphene and graphite exhibit more tipped mounts in the XRD pattern. XRD is able to be utilized to specify the purity of carbon quantum dots generated by soy flour. One of the prominent points of this pattern (figure. 7) is that there is no extra pinnacle in the XRD pattern which points to the great purity of prepared carbon quantum dots.

CONCLUSION

Carbon quantum dots (CQDs) have powerful fluorescence resilience, which signifies that actually after a prolonged period of continued excitation, the fluorescence emission intensity is able to remain stable. These outstanding attributes make carbon quantum dots an excellent choice in sensor applications. For analysis of the phase structure and the crystallinity of the acquired carbon quantum dots, X-ray diffraction was used. The outcomes disclosed that the prepared carbon quantum dots deliver excitation-dependent fluorescence emission. The acquired conclusions from photoluminescence spectroscopy demonstrate that as-prepared carbon quantum dots were able to be applied as a fluorescent search for the identification of ascorbic acid. The PL of carbon quantum dots (CQDs) is able to be considerably quenched by Cr (VI), which pursues a dynamic quenching system.

The photoluminescence investigations containing spectra, quantum yield and lifetime disclose the light-emitting procedure of carbon dots. They are significant to extra our understanding of the carbon dots and to make available the knowledge for their future applications. The fluorescence spectra of carbon dots display usually two various kinds of photoluminescence: the excitation-independent part in the succinct wavelength, and the excitation-dependent part in the more extended wavelength.

REFERENCES

Herman, M. A. (1983). Semiconductor heterojunction superlattices. Polish, Postepy Fizyki, 34, 431.

Reed, M. A., Bate, R. T., Bradshaw, K., Duncan, W. M., Frensley, W. R., Lee, J. W., & Shih, H. D. (1986). Spatial quantization in GaAs–AlGaAs multiple quantum dots. Journal of Vacuum Science & Technology B: Microelectronics Processing and Phenomena, 4(1), 358-360.

Ashoori, R. C., Stormer, H. L., Weiner, J. S., Pfeiffer, L. N., Pearton, S. J., Baldwin, K. W., & West, K. W. (1992). Single-electron capacitance spectroscopy of discrete quantum levels. Physical review letters, 68(20), 3088.

Ashoori, R. C., Stormer, H. L., Weiner, J. S., Pfeiffer, L. N., Baldwin, K. W., & West, K. W. (1993). N-electron ground state energies of a quantum dot in magnetic field. Physical review letters, 71(4), 613.

Hansen, W., Smith III, T. P., Lee, K. Y., Brum, J. A., Knoedler, C. M., Hong, J. M., & Kern, D. P. (1989). Zeeman bifurcation of quantum-dot spectra. Physical review letters, 62(18), 2168.

Lorke, A., Kotthaus, J. P., & Ploog, K. (1990). Coupling of quantum dots on GaAs. Physical review letters, 64(21), 2559.

Meurer, B., Heitmann, D., & Ploog, K. (1992). Single-electron charging of quantum-dot atoms. Physical review letters, 68(9), 1371.

Sikorski, C., & Merkt, U. (1989). Spectroscopy of electronic states in InSb quantum dots. Physical review letters, 62(18), 2164.

Pierobon, P., & Cappello, G. (2012). Quantum dots to tail single bio-molecules inside living cells. Advanced drug delivery reviews, 64(2), 167-178.

Klimov, V. I. (2007). Spectral and dynamical properties of multiexcitons in semiconductor nanocrystals. Annu. Rev. Phys. Chem., 58, 635-673.

Chan, W. C., Maxwell, D. J., Gao, X., Bailey, R. E., Han, M., & Nie, S. (2002). Luminescent quantum dots for multiplexed biological detection and imaging. Current opinion in biotechnology, 13(1), 40-46.

Bruchez Jr, M., Moronne, M., Gin, P., Weiss, S., & Alivisatos, A. P. (1998). Semiconductor nanocrystals as fluorescent biological labels. science, 281(5385), 2013-2016.

Valizadeh, A., Mikaeili, H., Samiei, M., Farkhani, S. M., Zarghami, N., Akbarzadeh, A., & Davaran, S. (2012). Quantum dots: synthesis, bioapplications, and toxicity. Nanoscale research letters, 7(1), 1-14.

Bakalova, R., Ohba, H., Zhelev, Z., Ishikawa, M., & Baba, Y. (2004). Quantum dots as photosensitizers?. Nature biotechnology, 22(11), 1360-1361.

Bera, D., Qian, L., Tseng, T. K., & Holloway, P. H. (2010). Quantum dots and their multimodal applications: a review. Materials, 3(4), 2260-2345.

Mattoussi, H., Palui, G., & Na, H. B. (2012). Luminescent quantum dots as platforms for probing in vitro and in vivo biological processes. Advanced drug delivery reviews, 64(2), 138-166.

Birudavolu, S., Nuntawong, N., Balakrishnan, G., Xin, Y. C., Huang, S., Lee, S. C., ... & Huffaker, D. L. (2004). Selective area growth of InAs quantum dots formed on a patterned GaAs substrate. Applied physics letters, 85(12), 2337-2339.

Nakata, Y., Mukai, K., Sugawara, M., Ohtsubo, K., Ishikawa, H., & Yokoyama, N. (2000). Molecular beam epitaxial growth of InAs self-assembled quantum dots with light-emission at 1.3 μm. Journal of Crystal Growth, 208(1-4), 93-99.

Bertino, M. F., Gadipalli, R. R., Martin, L. A., Rich, L. E., Yamilov, A., Heckman, B. R., ... & Mancini, D. C. (2007). Quantum dots by ultraviolet and x-ray lithography. Nanotechnology, 18(31), 315603.

Burda, C., Chen, X., Narayanan, R., & El-Sayed, M. A. (2005). Chemistry and properties of nanocrystals of different shapes. Chemical reviews, 105(4), 1025-1102.

Bang, J., Yang, H., & Holloway, P. H. (2006). Enhanced and stable green emission of ZnO nanoparticles by surface segregation of Mg. Nanotechnology, 17(4), 973.

Spanhel, L., & Anderson, M. A. (1991). Semiconductor clusters in the sol-gel process: quantized aggregation, gelation, and crystal growth in concentrated zinc oxide colloids. Journal of the American Chemical Society, 113(8), 2826-2833.

Bera, D., Qian, L., Sabui, S., Santra, S., & Holloway, P. H. (2008). Photoluminescence of ZnO quantum dots produced by a sol–gel process. Optical Materials, 30(8), 1233-1239.

Qu, L., & Peng, X. (2002). Control of photoluminescence properties of CdSe nanocrystals in growth. Journal of the American Chemical Society, 124(9), 2049-2055.

Murray, C., Norris, D. J., & Bawendi, M. G. (1993). Synthesis and characterization of nearly monodisperse CdE (E= sulfur, selenium, tellurium) semiconductor nanocrystallites. Journal of the American Chemical Society, 115(19), 8706-8715.

Qu, L., Peng, Z. A., & Peng, X. (2001). Alternative routes toward high quality CdSe nanocrystals. Nano letters, 1(6), 333-337.

Li, L., Qian, H., & Ren, J. (2005). Rapid synthesis of highly luminescent CdTe nanocrystals in the aqueous phase by microwave irradiation with controllable temperature. Chemical Communications, (4), 528-530.

Xin, S. H., Wang, P. D., Yin, A., Kim, C., Dobrowolska, M., Merz, J. L., & Furdyna, J. K. (1996). Formation of self-assembling CdSe quantum dots on ZnSe by molecular beam epitaxy. Applied physics letters, 69(25), 3884-3886.

Leonardi, K., Selke, H., Heinke, H., Ohkawa, K., Hommel, D., Gindele, F., & Woggon, U. (1998). Formation of self-assembling II–VI semiconductor nanostructures during migration enhanced epitaxy. Journal of crystal growth, 184, 259-263.

Kurtz, E., Shen, J., Schmidt, M., Grün, M., Hong, S. K., Litvinov, D., ... & Klingshirn, C. (2000). Formation and properties of self-organized II–VI quantum islands. Thin Solid Films, 367(1-2), 68-74.

Swihart, M. T. (2003). Vapor-phase synthesis of nanoparticles. Current opinion in colloid & interface science, 8(1), 127-133.

Ghasemi, Y., Peymani, P., & Afifi, S. (2009). Quantum dot: magic nanoparticle for imaging, detection and targeting. Acta Biomed, 80(2), 156-165.

Nozik, A. J., Beard, M. C., Luther, J. M., Law, M., Ellingson, R. J., & Johnson, J. C. (2010). Semiconductor quantum dots and quantum dot arrays and applications of multiple exciton generation to third-generation photovoltaic solar cells. Chemical reviews, 110(11), 6873-6890.

O'regan, B., & Grätzel, M. (1991). A low-cost, high-efficiency solar cell based on dye-sensitized colloidal TiO2 films. nature, 353(6346), 737-740.

Yang, Y., Zhu, L., Sun, H., Huang, X., Luo, Y., Li, D., & Meng, Q. (2012). Composite counter electrode based on nanoparticulate PbS and carbon black: towards quantum dot-sensitized solar cells with both high efficiency and stability. ACS applied materials & interfaces, 4(11), 6162-6168.

Liang, N., Chen, W., Dai, F., Wu, X., Zhang, W., Li, Z., ... & Qian, X. (2015). Homogenously hexagonal prismatic AgBiS 2 nanocrystals: controlled synthesis and application in quantum dot-sensitized solar cells. CrystEngComm, 17(9), 1902-1905.

Jian, H. J., Wu, R. S., Lin, T. Y., Li, Y. J., Lin, H. J., Harroun, S. G., ... & Huang, C. C. (2017). Super-cationic carbon quantum dots synthesized from spermidine as an eye drop formulation for topical treatment of bacterial keratitis. ACS nano, 11(7), 6703-6716.

Li, Y. J., Harroun, S. G., Su, Y. C., Huang, C. F., Unnikrishnan, B., Lin, H. J., ... & Huang, C. C. (2016). Synthesis of self-assembled spermidine-carbon quantum dots effective against multidrug-resistant bacteria. Advanced Healthcare Materials, 5(19), 2545-2554.

Lee, N. E., Lee, S. Y., Lim, H. S., Yoo, S. H., & Cho, S. O. (2020). A novel route to high-quality graphene quantum dots by hydrogen-assisted pyrolysis of silicon carbide. Nanomaterials, 10(2), 277.

Teng, X., Ma, C., Ge, C., Yan, M., Yang, J., Zhang, Y., ... & Bi, H. (2014). Green synthesis of nitrogen-doped carbon dots from konjac flour with “off–on” fluorescence by Fe 3+ and L-lysine for bioimaging. Journal of Materials Chemistry B, 2(29), 4631-4639.

Tang, J., Zhang, J., Zhang, Y., Xiao, Y., Shi, Y., Chen, Y., ... & Xu, W. (2019). Influence of group modification at the edges of carbon quantum dots on fluorescent emission. Nanoscale Research Letters, 14(1), 1-10.

THE EFFICACY OF IOT (INTERNET OF THINGS) AND DIGITAL RESOURCES AMONG STUDENTS: IMPLICATION ON EDUCATIONAL MANAGEMENT

Moses Adeolu AGOI

Lagos State University of Education, Lagos Nigeria, ORCID ID: 0000-0002-8910-2876

Oluwakemi Racheal OSHINOWO

Lagos State University of Education, Lagos Nigeria., ORCID ID: 0000-0003-0568-6446

Abstract

The advent and incorporation of digital technology into school curriculum are characteristic features of the 21st century education system. Today, smart devices are equipped with sensors and can be manipulated from anyway and at any time. The interconnectivity of these smart devices or systems via the internet to leverage data collected by embedded sensors is referred to as the Internet of Things (IoT). However, the applications of the IoT in education are limitless but in general, IoT enhances quick and convenient access to digital resources among students. This paper is a content survey of the Internet of Things and digital resources. The paper enumerates the drifting of students from traditional methods of learning to digitalized technology which is equipped with interactive applications and simulations along side with space and time liberty. Further discussions were made on other aspect of IoT and how it benefits both students and the teachers. In order to collect relevant information for the paper discussion, online Google form questionnaire instrument was used to retrieve data from respondents. The responses retrieved were subjected to reliability analysis. Conclusively, recommendations were made.

Keyword: Internet of Things, Digital Resources, Students, Educational Management.

INTRODUCTION

The modern day education system is becoming more digitalized, thanks to the advent of cyber technologies. Today, so many devices are embedded with sensors that can help communicate with one another through wireless connectivity from anyway in the world. The interconnection of identifiable devices or object is known as Internet of Things. IoT has the potential that can help improve the quality of learning process by providing students with an engaging and content creating environment. Digital resources and the use of the IoT as tools are exponentially changing the traditional ways in which students learn.

RELATED LITERATURE

Oxford Dictionary defines IoT as the interconnectivity of physical objects or devices embedded with sensors thereby enabling them to send and receive data using the Internet. Sundmaeker & Guillemin (2010), refers to the term Internet of Things as the virtual representations of special identifiable objects in an internet-like structure. Bejamin et al. (2015), opine that there is a very high possibility that IoT objects will become more mobile and smarter over time. Yunguang Chen & Xue Dong (2017), denote that IoT equipments are increasingly making digital resources accessible to students, teachers and educational administrators. IoT devices are also helpful in record keeping and providing students, teachers and the educational administrators with comfortable environment. According to Gallagher et al. (2019), the increase in the availability of online educational resources and the need to use them during the pandemic led teachers to make decisions on what digital instructional materials to use to teach their students. The early digital learning resources were basically electronic versions of paper-based teaching materials (Li, 2021). Mayer (2019) state that digital learning resources are designed to elicit engagement from students. Boetcher & Conrad (2016) explain that engaging students with digital materials are essentially important in situations where in-person learning contact is reduced or

eliminated.

Digital resources, students and Educators

Digital instructional resources can go a very long way to help enhance students' learning while teachers share digital material with the entire class. Below are some strategies to ensure effectively online resources management among students. Viz:-

1. Personalize learning:

The use of IoT device to tailor instruction so as to meet students' needs and abilities is one of the best ways of enhancing deeper learning experience. Educators can use digital resources to differentiate and individualize instruction to reach each student

2. Gather data and feedback:

Collection of data and feedback is an important measure to help understand which digital resources best suit a particular learner. The use of online assessments helps educators to collect data quickly and identify where learners are excelling or struggling.

3. Empower learners:

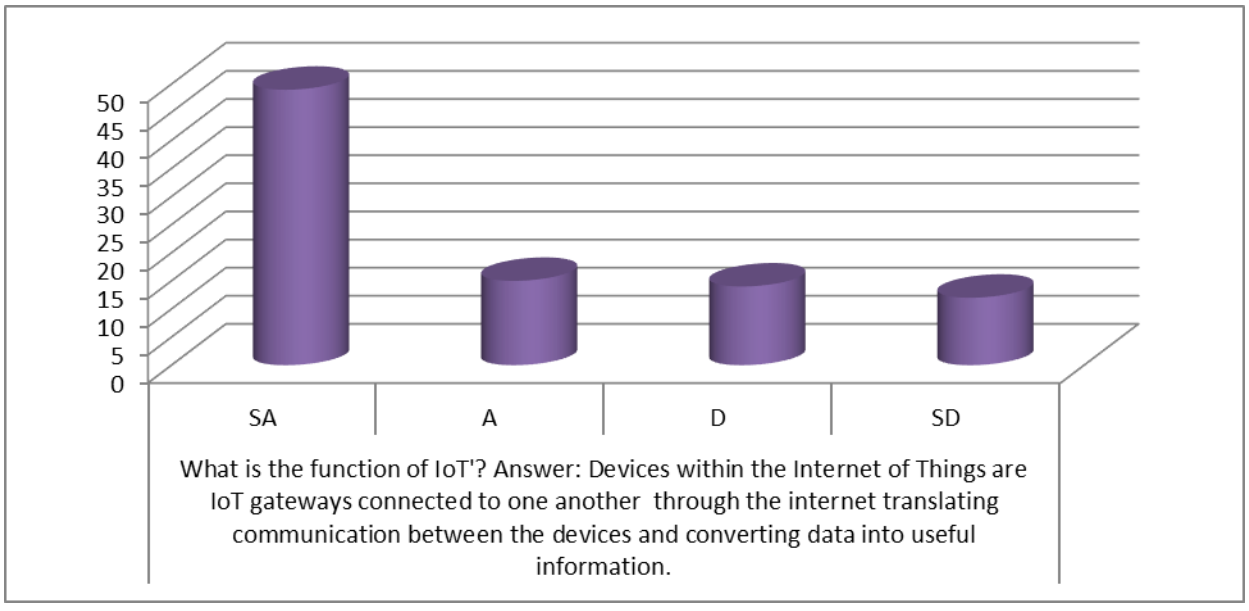
The use of digital resources to personalize students' learning is another to empower students. The use of digital resources is helpful to students as self-directed learning at the learners' pace makes education more meaningful.

MATERIALS AND METHODS

This paper adopted a content survey of internet of things and digital resources. For the purpose of this paper discussion, online Google form questionnaire instrument was used to collect relevant data from respondents. The responses gathered were collated and subjected to Cronbach's alpha reliability analysis by experts. The result of 0.87 gave a good reliability index of the instrument. The entire exercise took place within the duration of 4 weeks before completion.

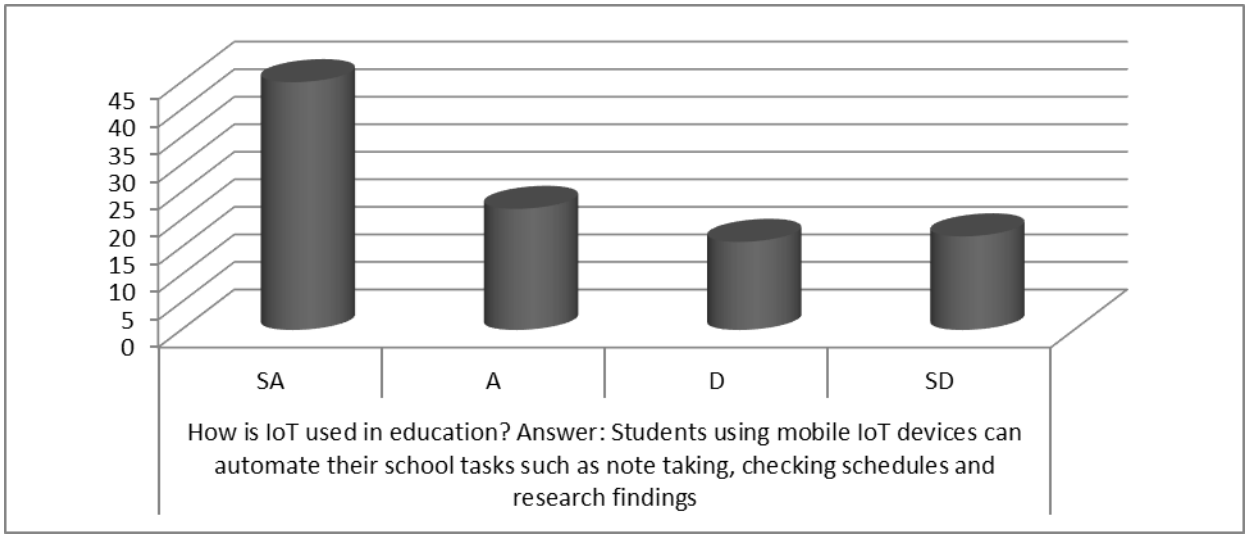
RESULTS AND DISCUSSION

Fig.1: Chat Analysis



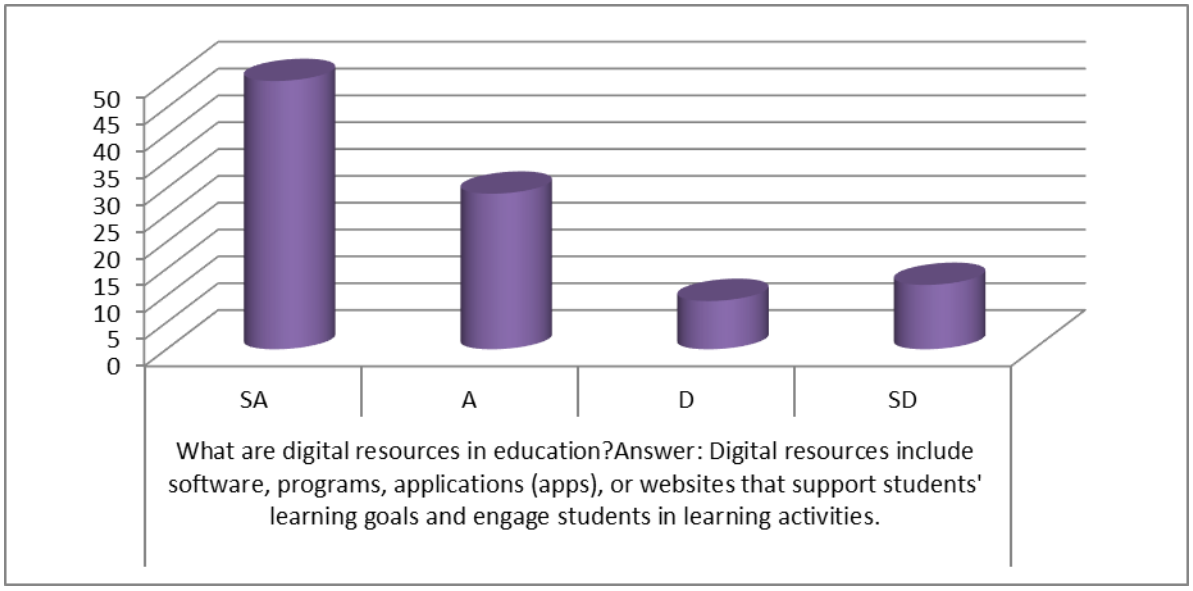
The chart analysis in fig.1 depicts that a greater number of the respondents agree with the statement that the function of Internet of Things technology is to basically convert data into useful information between physically communicating objects usually referred to as 'Things'.

Fig.2: Chat Analysis



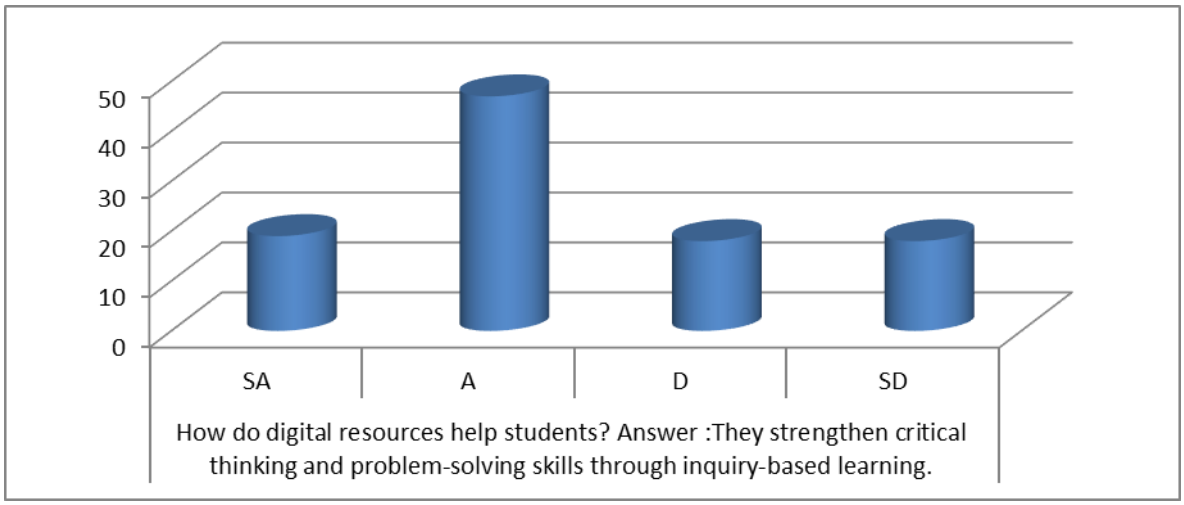
The result of the graph in the chart analysis as shown in fig. 2 depicts that majority of the respondents are in support with the statement that IoT technology is very useful in education system. According to the respondents, students use mobile IoT devices to automate their school tasks while school's greatest benefits include reduced operating costs and increased energy efficiency.

Fig.3: Chat Analysis



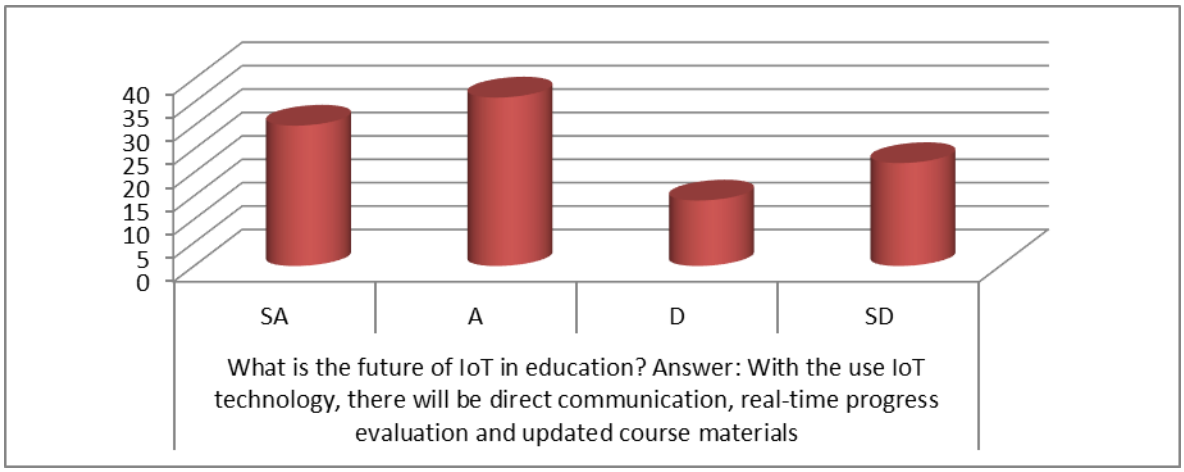
A higher amount of the respondents in fig.3, concur that digital resources are sampled as Software, Programs, Application or Website that students utilize as enhancements for better learning experiences.

Fig.4: Chat Analysis



The analysis graph in fig. 4 depicts that a significant amount of the respondents supported that digital resources has the potentials that strengthen critical thinking and problem-solving skills through inquiry-based learning. The respondents otherwise referred to digital contents as augments for primary instructional materials for students' learning.

Fig.5: Chat Analysis



A greater number of the respondents as shown in fig.5 support that the adoption and incorporation of IoT technology into education curriculum will ensure direct communication, real-time progress evaluation and course materials' update. The respondents submitted that teachers can still engage students in an effective and innovative way while they are in far distance away from their students.

CONCLUSION

The technology of Internet of Things has geometrically increased access to digital learning resource. With this influx, the usage of digital resources significantly influenced the quality of learning students receive. In fulfillment of future-proof education, educational managers and institutions need to fully integrate the usage of IoT into school curriculum to help develop digital and innovative skills.

RECOMMENDATION

The following recommendations were made based on the paper findings:

1. Government and stake holders in education should help equip schools at various levels with adequate computing gadgets and internet facilities.
2. School Managers should ensure the adoption and incorporation of IoT Technology into school curriculum.
3. School heads or managers should periodically organize in-service training for teachers on trending educational technologies.

REFERENCE LIST

1. Aldridge, IoT in the Classroom: How Traditional Education is Changing, downloaded from http://aldridge.com/future-iot-in- the-classroom-education/ on August 14, 2017
2. Jeanette Cajide (2017). The Connected School. How IoT Could Impact Education.
3. Samer Barakat (2016). Education and the Internet of Everything, International Business Management. Vol. 10 (18). Pp. 4301-4303.
4. Yogita Pundir; Nancy Sharma &Dr. Yaduvir Singh (2016). Internet of Things (IoT): Challenges and Future Directions. International Journal of Advanced Research in Computer and Communication Engineering. Vol. 5. Issue 3.
5. Yunguang Chen & Xue Dong (2017). The Development and Prospect of New Technology in Modern distance education.

ANTIMICROBIAL ACTIVITY OF CERTAIN CYANOBACTERIA ON PATHOGENIC BACTERIA

HARIKRISHNA JIVVAJI AND B.S. ANURADHA*

Dean faculty of science sand Board of studies, Department of Microbiology, Sree Chaitanya deemed to be University Warangal, Telangana

ABSTRACT

Cyanobacteria are found everywhere in fresh water, where thy are exposed to antibiotics and resistant organisms, but their role on water pathogenic and non-pathogen bacteria was never identified concerning the effects of antibiotics on cyanobacteria,

In this study we aimed to evaluate the susceptibility of four cyanobacterial isolates from different genera.

The paper deals with the antimicrobial sensitivity of some cyanobacteria with selected disease causing pathogenic bacteria, experiments were conducted with the source of selected cyanobacteria strips are made and conducted antibiotic sensitivity test to find the effect of cyanobacteria showing effect on the bacterial strains.

THREE DC/DC CONVERTERS WITH CONTINUOUS INPUT AND OUTPUT CURRENT FOR LED APPLICATIONS

Felix A. Himmelstoss

Prof. Dr, University of Applied Sciences Technikum Wien, Faculty of Electronic Engineering and Entrepreneurship, Power Electronics Section, Vienna, Austria., ORCID ID: https://orcid.org/0000-0001-8482-2295

ABSTRACT

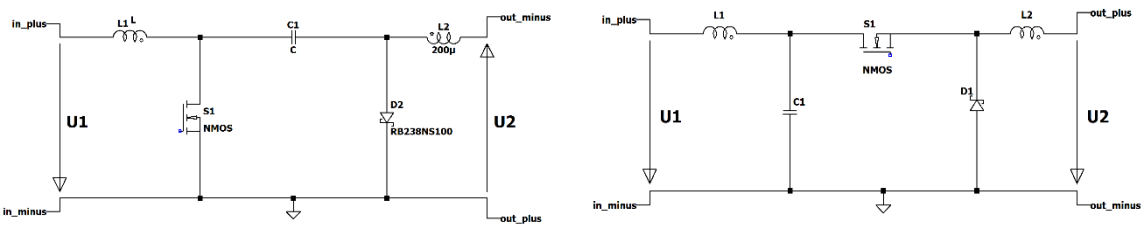
Light emitting diodes (LEDs) are efficient devices for producing light for street lighting, lighting in buildings, and also for smaller applications such as torchlights or in emergency lighting. Furthermore, infrared LEDs can be used for medical thermal treatment and ultra-violet diodes are used in disinfection devices for water, air or surfaces. All these applications need converters with continuous output current for supplying the LEDs. Three converters derived from the Buck, Boost and Cuk converter with continuous input and output current are presented. With these converters one can adapt the input voltage to the necessary voltage across the load which can be lower, higher or as well both lower and higher. The function of the converters is explained. The input voltage can change and also the load changes with the temperature. With a current controller the current through the load can be stabilized to the desired value and so to the desired light stream. Models for designing a linear controller are derived. A special concept of a nonlinear control which is especially fitting for these converters is explained and applied to the treated converter topologies. This leads to a very robust control. The described converters can be expanded by an additional switch to pulse the light stream. This is especially useful for disinfection, but it can also be used to modulate the light stream with some information which can be received by photo diodes or transistors and demodulated. All considerations are supported by simulations.

Keywords: DC/DC converters, current control, efficiency, lighting.

INTRODUCTION

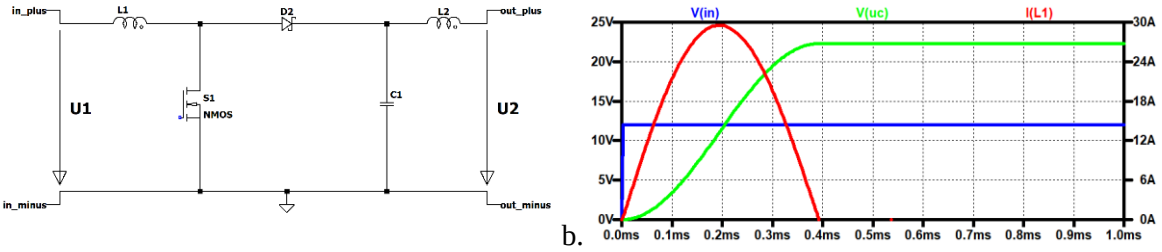
In this paper three converters which are qualified to drive LEDs with a continuous current and additionally have also a continuous input current are treated. The continuous input current is especially interesting when fuel cells, solar generators and batteries are supplying the system.

Figure 1 and Figure 2. show the three here treated converters. The input voltage source is connected at the left side, marked with connector designators, in_plus and in_minus, and the load is connected to the right side between the connectors out_plus and out _minus. It should be mentioned here that other loads which need a current supply other than LEDs can be driven with such converters. The converter will normally work in the continuous inductor current mode. This means that the current in the steady-state mode does not reach zero within a switching period. During start-up and when the load changes considerably the discontinuous mode can happen. When the electronic switch S1 is turned on, a positive voltage lies across both inductors and the current through them increases. When the active switch S1 turns off, the diode D2 turns on and a negative voltage lies across the inductors and the current decreases. This happens for all three converters.



a. b.

Figure 1. Continuous input and output current converters: a. Cuk derived, b. Buck derived with input filter



a. b.

Figure 2. Boost derived continuous input and output current converter: a. circuit diagram, b. inrush current (red), capacitor voltage (green), input voltage (blue)

Figure 1.a shows a Cuk converter without the output capacitor. Therefore, the converter has current output and no voltage output. The output current has to be controlled to avoid an overload of the LEDs. One can see that the voltage at the output is inverted, that means in this case only that the polarity of the LEDs must also be inverse compared to the two other topologies. Figure1.b shows a Buck converter with omitted output capacitor. An input LC filter is connected to the Buck structure. Therefore, the input current is continuous compared to the pulsating input current of the normal Buck. Figure 2.a shows a Boost converter with an additional output inductor. The parent circuits for the here used converters are described in detail in the text books e.g. Mohan et al. (2003), Rozanov et al. (2015), Zach (2022). In these books comprehensive material for studying Power Electronics are given.

LEDs can be used for lighting purposes, but can also be used for disinfection devices (Himmelstoss & Edelmoser, 2022 and the cited literature there), and also in medical thermal treatment (Himmelstoss & Edelmoser, 2016). In all these applications high efficiency is necessary to save energy and not to forget reduce the cooling expenditure which reduces weight, space and cost. LEDs can also be used as combined light source and by modulation of the light stream to send informations, cf. Edelmoser & Himmelstoss (2016).

OUTPUT CURRENT BOOST CONVERTER

The circuit diagram is depicted in Figure 2.a. With ideal devices one can write for the charge balance of the capacitor with the mean-values of the inductor currents and with the duty cycle d (this is the on-time of the active switch referred to the switching period)

$$\left|-\bar{I}_{L2}\right| d = \left(\bar{I}_{L1} - \bar{I}_{L2}\right)(1-d) \ . \tag{1}$$

The current through L1 depends on the load current, which is equal to the current through L2

$$\bar{I}_{L1} = \bar{I}_{L2} \frac{1}{1-d} \ . \tag{2}$$

The connection between the input voltage and the voltage across the capacitor can be found by the voltage-time balance across L1 and leads to the well-known voltage transformation ratio of the Boost converter according to

$$U_{C1} = U_1 \frac{1}{1-d} = U_2 \ , \tag{3}$$

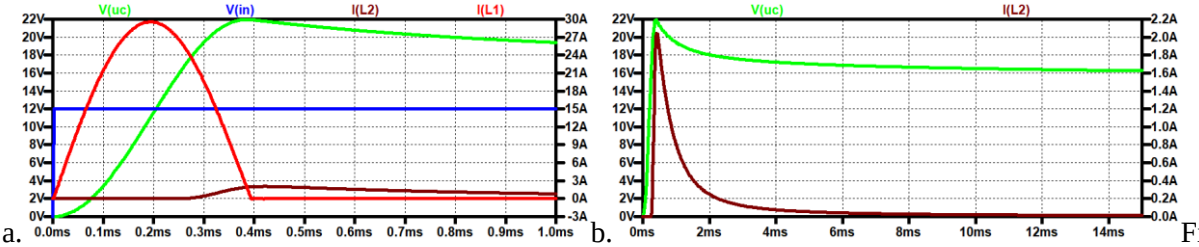
which is equal to the output voltage. We will need this connection for generating the control law of the converter.

What happens when the voltage supply is connected to the system?

When the voltage source is applied to the converter, the impedance of the input source influences the inrush current. When we look at the circuit diagram (Figure 2.a), we can see that the inductor L1 and the capacitor C1 form a resonance circuit. With no or a very small source resistor (e.g. when using a car battery) and a load which needs a voltage of more than double the input voltage before the current starts to flow, the voltage across

the capacitor will rise up to nearly the double of the input voltage. Figure 2.b shows the inrush current and the voltage across the capacitor. Idealized (without parasitic resistors of the source, the diode, the coil and the capacitor) the current would reach the maximum value of

$$I_{IN;\max} = U_1 \sqrt{\frac{C_1}{L_1}} \quad . \tag{4}$$



a. b. Figure 3. Inrush current with load: inrush current (red), capacitor voltage (green), input voltage (blue), current through L2 (load current, black)

In our example (Figure 3) the load begins to draw current when the voltage reaches about 16 V. Figure 3.a shows the inrush current with attached load through L1, the voltage across the capacitor, the input voltage and the current through L2. As predicted this current start when the voltage at the capacitor reaches 16 V. The current discharges the capacitor to 16 V at 15 ms (Figure 3.b). Now one can start with the switching of the transistor.

It should be mentioned here that in reality it would not look so nice, because the input inductor saturates and therefore gets a smaller value. The capacitor will therefore be charged faster. When the current reaches zero, the diode D1 turns off (in practice a little bit later because of the reverse recovery effect).

When one starts immediately with the necessary duty cycle (hard-start), again a large current starts to flow. Again a large current occurs at the input, and the input inductor saturates, it is designed for the maximum working point stress, leading to an even higher current (Figure 4).

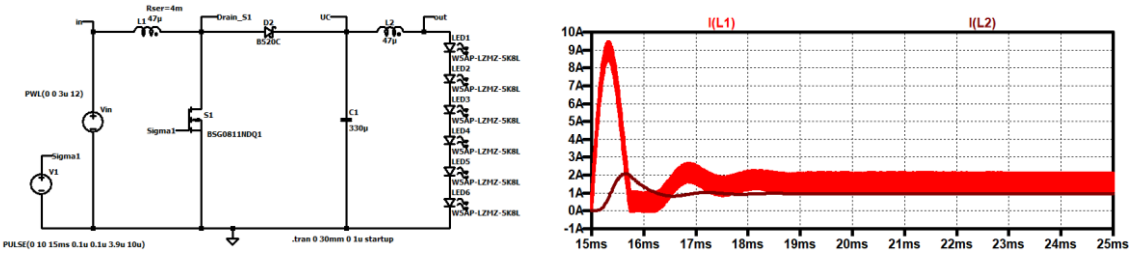


Figure 4. Hard-start of the converter: a. simulation circuit, b. currents through the coils L1 (red) and L2(black)

To reduce this overcurrent a soft start is implemented. The duty cycle is increased up to the desired value within the soft-start-time. Figure 5 shows the implementation of the pwm-modulation with the comparator U1. The desired duty cycle signal has to be gained to control the MOSFET (the comparator is supplied by plus/minus 5 V). Therefore, the voltage controlled voltage-source E1 is used. Now the current overshot is small and the current in the load reaches the desired value only with a little overshot (which is no danger for the diodes) and a small ringing.

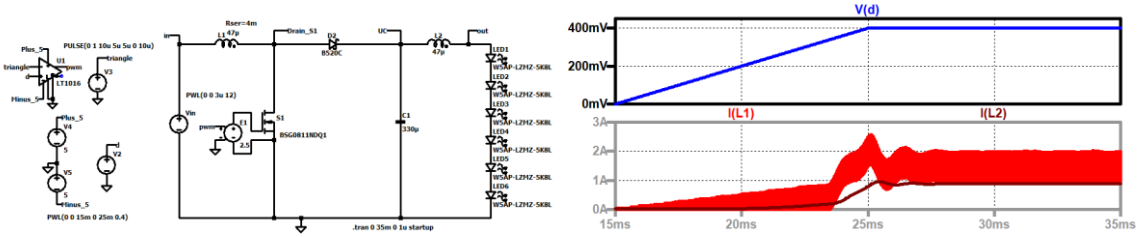


Figure 5. Soft-start: a. simulation circuit, b. duty cycle (blue, voltage value is equal to the duty cycle value); current through the coils L1 (red), L2 (black)

Converter with control law

Besides linear controllers this converter can be controlled with a nonlinear controller which is described now. In the steady state the current in the load has the connection with the input current according to (2). Including (3) leads to the control law

$$I_{L1,ref} = I_{L2,ref} \frac{U_{C1}}{U_1} \ . \tag{5}$$

Figure 6 shows the implementation of this nonlinear control concept. Figure 7 shows the simulation again starting after the turn-on transient at 15 ms. The desired current value is first increased from zero to 1 A within 5 ms. Then at 25 ms the value is reduced within 0.1 ms to 0.6 A and at 30 ms the desired value goes up to 1 A again. At 35 ms the input voltage goes down to 8 V and the current controller reacts immedeately and the output current shows only a very low transient. This proves the high effectiveness of this control concept. When the controller is implemented by a microcontroller, this can be easily realized. The simulations are depicted in Figure 7 and show the efficient control of the system. The reactions of the currents through the coils during soft start, reference value step-down, reference value step-up, input voltage step-down are depicted.

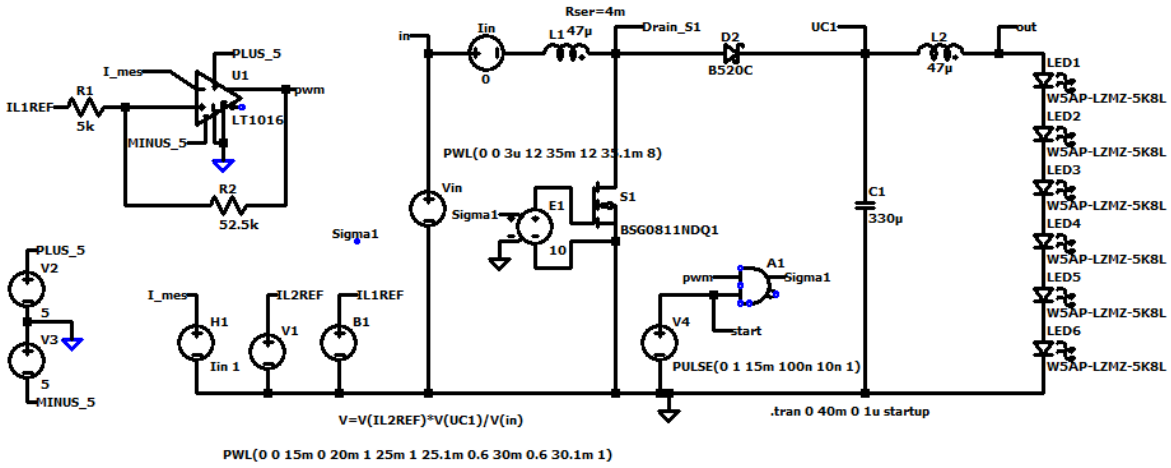


Figure 6. Simulation circuit of the nonlinear control

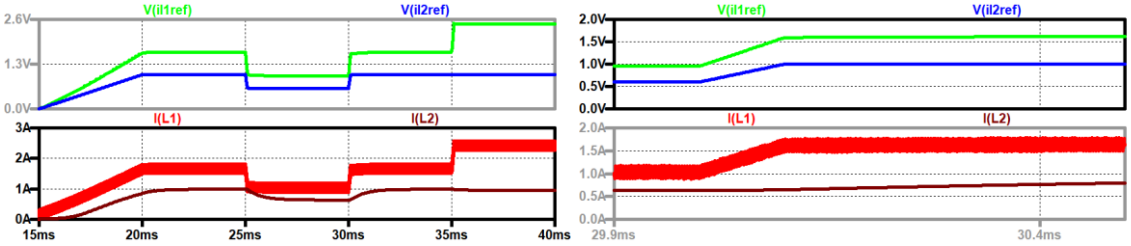


Figure 7. Nonlinear control: a. soft start, reference value step-down, reference value step-up, input voltage step-down; b. detail of the reference step-up, calculated reference value for L1 (green), reference value of L2 (blue), current through L1 (red), current through L2 (black)

Idealized model of the converter

In the continuous inductor current mode the converter has two modes. In mode M1 the active switch S1 is on and the passive switch (diode) D2 is off, and in mode M2 the active switch S1 is off and the diode D2 is on. The simplest model of the converter is an idealized one, when all parasitics are omitted; that means no resistors in the coils, the capacitor, the transistor, and the diode. The load is simulated by a voltage source VLED and a resistor RLED. The state variables of the converter are the current through the coil and the voltage across the capacitor. The input variable is the input voltage. This simple model is efficient, especially when the voltages are much higher than the forward voltage of the diode.

For M1 one gets

$$\frac{di_{L1}}{dt}=\frac{u_1}{L_1} \qquad \frac{di_{L2}}{dt}=\frac{u_{C1}-V_{LED}-R_{LED}i_{L2}}{L_2} \qquad \frac{du_{C1}}{dt}=-\frac{i_{L2}}{C_1} \tag{6}$$

and written in the state-space description form according to

$$\frac{d}{dt}\begin{pmatrix} i_{L1} \\ i_{L2} \\ u_{C1} \end{pmatrix}=\begin{bmatrix} 0 & 0 & 0 \\ 0 & -\frac{R_{LED}}{L_2} & \frac{1}{L_2} \\ 0 & -\frac{1}{C_1} & 0 \end{bmatrix}\cdot\begin{pmatrix} i_{L1} \\ i_{L2} \\ u_{C1} \end{pmatrix}+\begin{bmatrix} \frac{1}{L_1} \\ 0 \\ 0 \end{bmatrix}\cdot(u_1)+\begin{pmatrix} 0 \\ -\frac{V_{LED}}{L_2} \\ 0 \end{pmatrix}. \tag{7}$$

The state equations for mode M2 are

$$\frac{di_{L1}}{dt}=\frac{u_1-u_{C1}}{L_1}, \quad \frac{di_{L2}}{dt}=\frac{u_{C1}-V_{LED}-R_{LED}i_{L2}}{L_2}, \qquad \frac{du_{C1}}{dt}=\frac{i_{L1}-i_{L2}}{C_1} \tag{8}$$

resulting in

$$\frac{d}{dt}\begin{pmatrix} i_{L1} \\ i_{L2} \\ u_{C1} \end{pmatrix}=\begin{bmatrix} 0 & 0 & -\frac{1}{L_1} \\ 0 & -\frac{R_{LED}}{L_2} & \frac{1}{L_2} \\ \frac{1}{C_1} & -\frac{1}{C_1} & 0 \end{bmatrix}\cdot\begin{pmatrix} i_{L1} \\ i_{L2} \\ u_{C1} \end{pmatrix}+\begin{bmatrix} \frac{1}{L_1} \\ 0 \\ 0 \end{bmatrix}\cdot(u_1)+\begin{pmatrix} 0 \\ -\frac{V_{LED}}{L_2} \\ 0 \end{pmatrix}. \tag{9}$$

Combining these two matrixes with the state-space averaging method, the idealized large signal model is achieved according to

$$\frac{d}{dt}\begin{pmatrix} i_{L1} \\ i_{L2} \\ u_{C1} \end{pmatrix} = \begin{bmatrix} 0 & 0 & \frac{d-1}{L_1} \\ 0 & -\frac{R_{LED}}{L_2} & \frac{1}{L_2} \\ \frac{1-d}{C_1} & -\frac{1}{C_1} & 0 \end{bmatrix} \cdot \begin{pmatrix} i_{L1} \\ i_{L2} \\ u_{C1} \end{pmatrix} + \begin{bmatrix} \frac{1}{L_1} \\ 0 \\ 0 \end{bmatrix} \cdot (u_1) + \begin{pmatrix} 0 \\ -\frac{V_{LED}}{L_2} \\ 0 \end{pmatrix} . \tag{10}$$

With the perturbation concept around the working point (the working point values are written with capital letters and a zero in the index, the perturbations are written with small letters and a roof on top) the small signal model is achieved. Now the perturbation of the duty cycle is a second input variable. One gets for the idealized small signal model

$$\frac{d}{dt}\begin{pmatrix} \hat{i}_{L1} \\ \hat{i}_{L2} \\ \hat{u}_{C1} \end{pmatrix} = \begin{bmatrix} 0 & 0 & \frac{D_0-1}{L_1} \\ 0 & -\frac{R_{LED}}{L_2} & \frac{1}{L_2} \\ \frac{1-D_0}{C_1} & -\frac{1}{C_1} & 0 \end{bmatrix} \cdot \begin{pmatrix} \hat{i}_{L1} \\ \hat{i}_{L2} \\ \hat{u}_{C1} \end{pmatrix} + \begin{bmatrix} \frac{1}{L_1} & \frac{U_{C10}}{L_1} \\ 0 & 0 \\ 0 & -\frac{I_{L10}}{C_1} \end{bmatrix} \cdot \begin{pmatrix} \hat{u}_1 \\ \hat{d} \end{pmatrix} . \tag{11}$$

To get a transfer function, the linearized model has to be Laplace-transformed. The abbreviations A_{ij} and B_{ij} are used for the matrix elements of the state matrix and the input matrix, respectively:

$$\begin{bmatrix} s & 0 & -A_{13} \\ 0 & s-A_{22} & -A_{23} \\ -A_{31} & -A_{32} & s \end{bmatrix} \cdot \begin{pmatrix} I_{L1}(s) \\ I_{L2}(s) \\ U_{C1}(s) \end{pmatrix} = \begin{bmatrix} B_{11} & B_{12} \\ 0 & 0 \\ 0 & B_{32} \end{bmatrix} \cdot \begin{pmatrix} U_1(s) \\ D(s) \end{pmatrix} . \tag{12}$$

To calculate the denominator one has to solve the determinant

$$DEN = \begin{vmatrix} s & 0 & -A_{13} \\ 0 & s-A_{22} & -A_{23} \\ -A_{31} & -A_{32} & s \end{vmatrix} = s^3 - A_{22}s^2 - (A_{13}A_{31} + A_{23}A_{32})s + A_{13}A_{22}A_{31} \tag{13}$$

and for getting the numerator for IL2 referred to the duty cycle

$$NUM_IL2 = \begin{vmatrix} s & B_{12} & -A_{13} \\ 0 & 0 & -A_{23} \\ -A_{31} & B_{32} & s \end{vmatrix} = A_{23}B_{32}s + A_{23}A_{31}B_{12} . \tag{14}$$

The transfer function between the current I_{L2} and the duty cycle results in

$$G_{IL2D}(s) = \frac{I_{L2}(s)}{D(s)} = \frac{A_{23}B_{32}s + A_{23}A_{31}B_{12}}{s^3 - A_{22}s^2 - (A_{13}A_{31} + A_{23}A_{32})s + A_{13}A_{22}A_{31}} \tag{15}$$

Inserting the matrix values again leads to

$$G_{IL2D}(s) = \frac{I_{L2}(s)}{D(s)} = \frac{-\frac{I_{L10}}{C_1L_2}s + \frac{(1-D_0)U_{C10}}{C_1L_1L_2}}{s^3 + \frac{R_{LED}}{L_2}s^2 + \left(\frac{(1-D_0)^2}{C_1L_1} + \frac{1}{C_1L_2}\right)s + \frac{(1-D_0)^2R_{LED}}{C_1L_1L_2}} . \tag{16}$$

With this transfer function a linear control can be designed e.g. again with the help of LTSpice (cf. Himmelstoss 2022,1).

For the working point one gets

$$(D_0 - 1)U_{C10} + U_{10} = 0 \qquad -R_{LED}I_{L20} + U_{C10} - V_{LED} = 0 \qquad (1-D_0)I_{L10} - I_{L20} = 0 . \tag{17}$$

This leads to the working point values according to

$$U_{C10}=\frac{U_{10}}{1-D_0} \qquad I_{L20}=\frac{U_{C10}-V_{LED}}{R_{LED}} \qquad I_{L10}=\frac{I_{L20}}{1-D_0}\ . \tag{18}$$

OUTPUT CURRENT BUCK CONVERTER WITH INPUT FILTER

The circuit diagram of the continuous output current Buck converter is shown in Figure 1.b.

Stationary case

In the idealized steady-state the voltage across the capacitor is equal to the input voltage, and the voltage across the load must be, caused by the voltage-time balance across L2 as in the normal Buck converter, the input voltage multiplied by the duty cycle. For an output current converter the connection between the input and output currents is of importance. The charge balance across the capacitor can be written according to

$$\left|\bar{I}_{L1}-\bar{I}_{L2}\right|d=\bar{I}_{L1}(1-d). \tag{19}$$

The current term on the left side is negative. Therefore, the absolute value has to be taken to obtain the charge. This charge must be equal to the one on the right side.

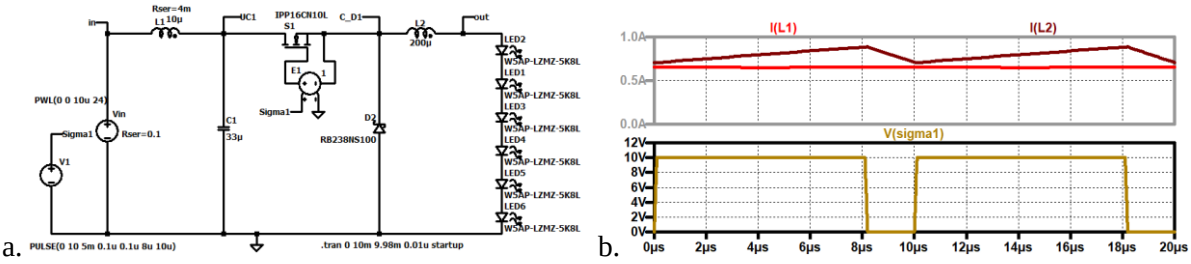


Figure 8. Continuous output current Buck converter with input filter: a. simulation circuit, b. current through the coils L2 (black) and L1 (red), control signal (brown)

Turning on the input voltage

The input filter is a resonant circuit and causes an inrush current and a damped ringing. The maximum current depends on the input inductor L1, the input capacitor C1 and the step of the input voltage U1 according to (4). The smaller the input capacitor and the larger the input inductor the lower the inrush current. The parasitic resistors damp the inrush current. Fig 9 shows the influence on the inrush current. A larger resistor damps more and the maximum current is lower.

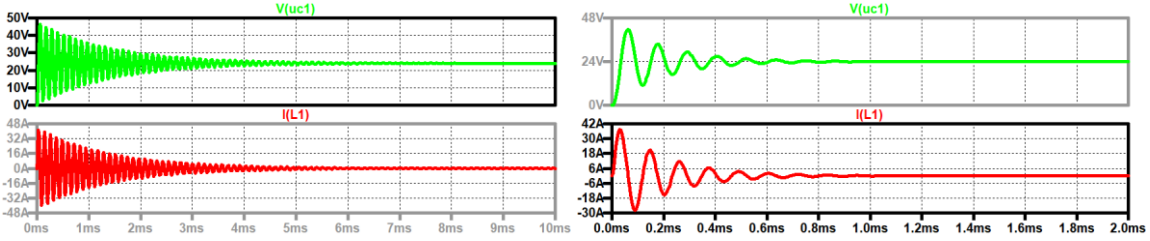


Figure 9 Continuous output current Buck converter with input filter, transient of the inrush current, capacitor voltage (green), input current (red), values according the simulation circuit Figure 8: a. parasitic resistors 14 mΩ, b. parasitic resistors 104 mΩ

Hard-start

A hard-start after the transient, caused by the connection of the supply voltage, is shown in Figure 10.a

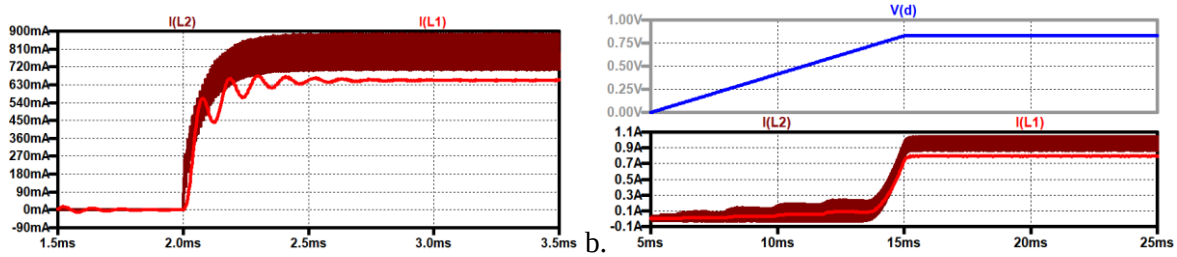


Figure 10.a. Buck converter with input filter a. hard-start, b. soft-start: current through the coils L2 (black) and L1 (red), duty cycle (blue)

In this case no dangerous overshot occurs. However, it is always better to make a soft-start as shown in Figure 10.b.

Two-point controller

The easiest way to control this circuit is by a two-point controller, realized by a comparator. The clocking of the active switch starts after the input transient.

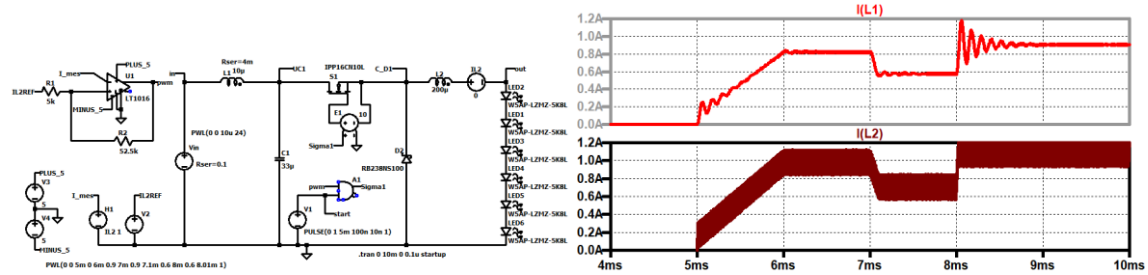


Figure 11. Buck converter with input filter current controlled with a two-point controller: a. simulation circuit, b. current through the coils L1 (red) and L2 (black)

Figure 11 shows an increase of the reference value from zero to 0.9 A in the time interval between 5 and 6 ms, which leads to a damped ringing of the input filter. At 7 ms the reference value decreases within 100 µs to 0.6 A causing only a small ringing at the input filter. A more pronounced ringing occurs, when the reference value makes a step within 10 µs to 1 A at 8 ms.

Quasi-idealized model of the Buck converter with input filter

In this model we omit the resistors of the inductors, of the capacitor and the active switch, and model the diode with the forward voltage V_D at the working point and model the LEDs by the knee-voltage V_{LED} and the differential resistor R_{LED}.

The state equations are in mode M1

$$\frac{di_{L1}}{dt}=\frac{u_1-u_{C1}}{L_1},\quad \frac{di_{L2}}{dt}=\frac{u_{C1}-V_{LED}-R_{LED}i_{L2}}{L_2},\quad \frac{du_{C1}}{dt}=\frac{i_{L1}-i_{L2}}{C_1}, \tag{20}$$

$$\frac{d}{dt}\begin{pmatrix} i_{L1}\\ i_{L2}\\ u_{C1}\end{pmatrix}=\begin{bmatrix} 0 & 0 & -\frac{1}{L_1}\\ 0 & -\frac{R_{LED}}{L_2} & \frac{1}{L_2}\\ \frac{1}{C_1} & -\frac{1}{C_1} & 0\end{bmatrix}\cdot\begin{pmatrix} i_{L1}\\ i_{L2}\\ u_{C1}\end{pmatrix}+\begin{bmatrix}\frac{1}{L_1}\\ 0\\ 0\end{bmatrix}\cdot(u_1)+\begin{pmatrix} 0\\ -\frac{V_{LED}}{L_2}\\ 0\end{pmatrix} \tag{21}$$

and in mode M2

$$\frac{di_{L1}}{dt}=\frac{u_1-u_{C1}}{L_1},\quad \frac{di_{L2}}{dt}=\frac{-V_D-V_{LED}-R_{LED}i_{L2}}{L_2},\qquad \frac{du_{C1}}{dt}=\frac{i_{L1}}{C_1}, \tag{22}$$

$$\frac{d}{dt}\begin{pmatrix} i_{L1}\\ i_{L2}\\ u_{C1}\end{pmatrix}=\begin{bmatrix} 0 & 0 & -\frac{1}{L_1}\\ 0 & -\frac{R_{LED}}{L_2} & 0\\ \frac{1}{C_1} & 0 & 0\end{bmatrix}\cdot\begin{pmatrix} i_{L1}\\ i_{L2}\\ u_{C1}\end{pmatrix}+\begin{bmatrix}\frac{1}{L_1}\\ 0\\ 0\end{bmatrix}\cdot(u_1)+\begin{pmatrix} 0\\ -\frac{V_{LED}+V_D(1-d)}{L_2}\\ 0\end{pmatrix}. \tag{23}$$

With the state space averaging method one gets the quasi-idealized large signal model according to

$$\frac{d}{dt}\begin{pmatrix} i_{L1}\\ i_{L2}\\ u_{C1}\end{pmatrix}=\begin{bmatrix} 0 & 0 & -\frac{1}{L_1}\\ 0 & -\frac{R_{LED}}{L_2} & \frac{d}{L_2}\\ \frac{1}{C_1} & -\frac{d}{C_1} & 0\end{bmatrix}\cdot\begin{pmatrix} i_{L1}\\ i_{L2}\\ u_{C1}\end{pmatrix}+\begin{bmatrix}\frac{1}{L_1}\\ 0\\ 0\end{bmatrix}\cdot(u_1)+\begin{pmatrix} 0\\ -\frac{V_{LED}+V_D(1-d)}{L_2}\\ 0\end{pmatrix}. \tag{24}$$

Using again the perturbation concept, the quasi-idealized small signal model around the working point is obtained according to

$$\frac{d}{dt}\begin{pmatrix} \hat{i}_{L1}\\ \hat{i}_{L2}\\ \hat{u}_{C1}\end{pmatrix}=\begin{bmatrix} 0 & 0 & -\frac{1}{L_1}\\ 0 & -\frac{R_{LED}}{L_2} & \frac{D_0}{L_2}\\ \frac{1}{C_1} & -\frac{D_0}{C_1} & 0\end{bmatrix}\cdot\begin{pmatrix} \hat{i}_{L1}\\ \hat{i}_{L2}\\ \hat{u}_{C1}\end{pmatrix}+\begin{bmatrix} \frac{1}{L_1} & 0\\ 0 & \frac{U_{C10}+V_D}{L_2}\\ 0 & -\frac{I_{L20}}{C_1}\end{bmatrix}\cdot\begin{pmatrix}\hat{u}_1\\ \hat{d}\end{pmatrix}. \tag{25}$$

Using abbreviations for the matrix elements and transforming (25) into the Laplace domain leads to

$$\begin{bmatrix} s & 0 & -A_{13}\\ 0 & s-A_{22} & -A_{23}\\ -A_{31} & -A_{32} & s\end{bmatrix}\cdot\begin{pmatrix} I_{L1}(s)\\ I_{L2}(s)\\ U_{C1}(s)\end{pmatrix}=\begin{bmatrix} B_{11} & 0\\ 0 & B_{22}\\ 0 & B_{32}\end{bmatrix}\cdot\begin{pmatrix} U_1(s)\\ D(s)\end{pmatrix}. \tag{26}$$

Calculation of the denominator gives

$$DEN=\begin{vmatrix} s & 0 & -A_{13}\\ 0 & s-A_{22} & -A_{23}\\ -A_{31} & -A_{32} & s\end{vmatrix}=s^3-A_{22}s^2-(A_{13}A_{31}+A_{23}A_{32})s+A_{13}A_{22}A_{31}. \tag{27}$$

Calculation of the numerator for IL2 results in

$$NUM_IL2=\begin{vmatrix} s & 0 & -A_{13}\\ 0 & B_{22} & -A_{23}\\ -A_{31} & B_{32} & s\end{vmatrix}=B_{22}s^2+A_{23}B_{32}s-A_{13}A_{31}B_{22}. \tag{28}$$

The transfer function between the output current and the duty cycle is therefore

$$G_{IL2D}(s)=\frac{I_{L2}(s)}{D(s)}=\frac{B_{22}s^2+A_{23}B_{32}s-A_{13}A_{31}B_{22}}{s^3-A_{22}s^2-(A_{13}A_{31}+A_{23}A_{32})s+A_{13}A_{22}A_{31}} \tag{29}$$

$$G_{IL2D}(s)=\frac{\frac{U_{C10}+V_D}{L_2}s^2-\frac{D_0I_{L20}}{C_1L_2}s+\frac{U_{C10}+V_D}{L_1L_2C_1}}{s^3+\frac{R_{LED}}{L_2}s^2+\left(\frac{L_2+L_1D_0^2}{C_1L_1L_2}\right)s+\frac{R_{LED}}{C_1L_1L_2}}. \tag{30}$$

For the stationary working point connections one gets

$$-U_{C10}+U_{10}=0\,,\ -R_{LED}I_{L20}+D_0U_{C10}+(-V_{LED}-D_0V_D)=0\,,\quad I_{L10}-D_0I_{L20}=0\ . \tag{31}$$

These result in the working point connections

$$U_{C10}=U_{10}\,,\qquad I_{L20}=\frac{D_0U_{C10}-V_{LED}-D_0V_D}{R_{LED}}\,,\qquad I_{L10}=D_0I_{L20}\ . \tag{32}$$

OUTPUT CURRENT CUK CONVERTER

The circuit diagram of the Cuk derived current converter is shown in Figure 1.a. The simulation circuit, the currents through the coils, and the control signal in the steady-state mode are shown in Figure 12.

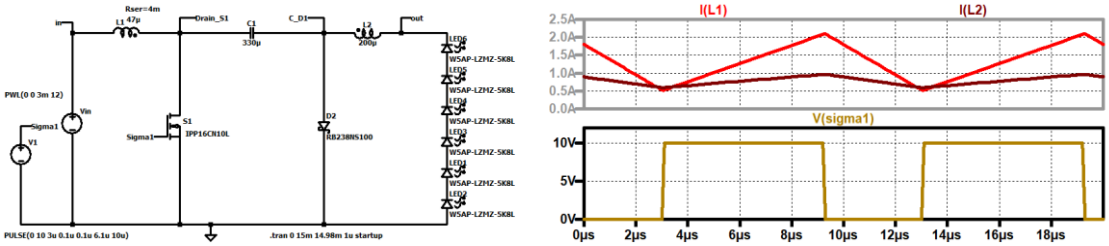


Figure 12. Cuk derived LED driver in steady-state: a. simulation circuit, b. currents through the coils L1 (red), L2 (black); control signal (brown)

With the charge balance

$$\bar{I}_{L20}\,d=\bar{I}_{L10}(1-d) \tag{33}$$

and the voltage-time balance across L1

$$U_1 d=\left|U_1-U_{C1}\right|(1-d) \tag{34}$$

one gets

$$\bar{I}_{L20}=\bar{I}_{L10}\frac{1-d}{d}\qquad\qquad U_{C1}=U_1\frac{1}{1-d}\ . \tag{35}$$

Figure 13 shows the voltage turn-on and a hard-start of the converter at 5 ms.

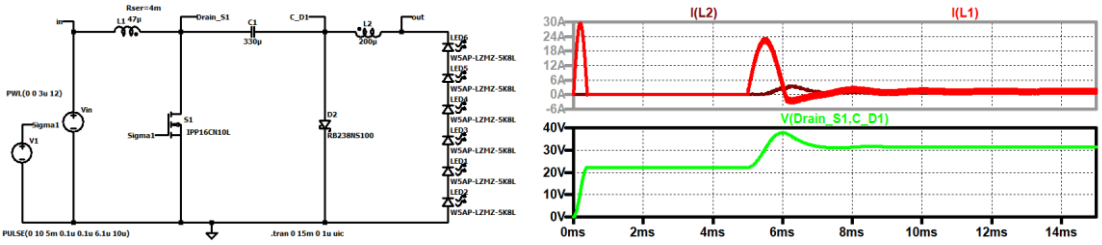


Figure 13. Cuk derived LED driver voltage turn-on and hard-start: a. simulation circuit, b. currents through the coils L1 (red), L2 (black); voltage across the capacitor (green)

When the voltage is applied to the converter, an inrush current occurs and charges the capacitor. When the current reaches zero again, the diode turns off and the capacitor stays charged. There is only one inrush pulse and no ringing. When the switch is turned on directly with the necessary duty cycle for the desired load current, again a large transient occurs. Therefore, a soft-start is advisable to reduce this overshot.

In Figure 14 two soft-starts are shown with a ramp (the duty cycle is increased linearly) of 15 ms (a) and (b) with a ramp lasting 85 ms.

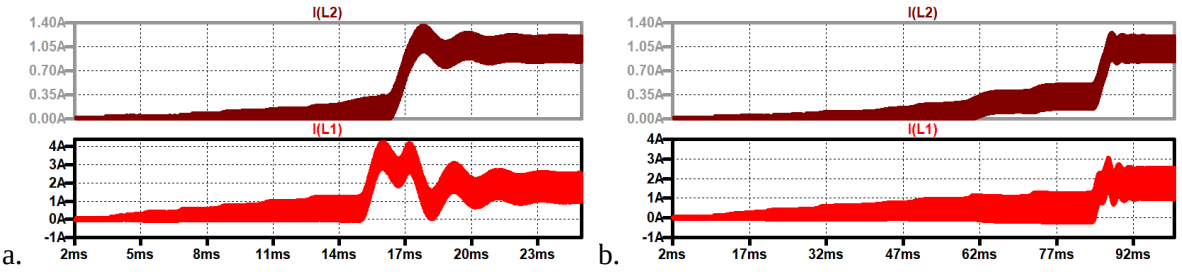


Figure 14. Cuk derived LED driver voltage soft-start: current through the coils L1 (red), L2 (black) with ramp duration of a. 15 ms, b. 85 ms

Control law

From the charge balance of the capacitor (33) and the voltage-time balance across L1 (34), the control law for generating the reference value of the input current can now be calculated with the desired output current $I_{L2,ref}$, the input voltage U_1, and the voltage across C1 according to

$$I_{L1,ref} = I_{L2,ref} \frac{U_{C1} - U_1}{U_1} \ . \tag{36}$$

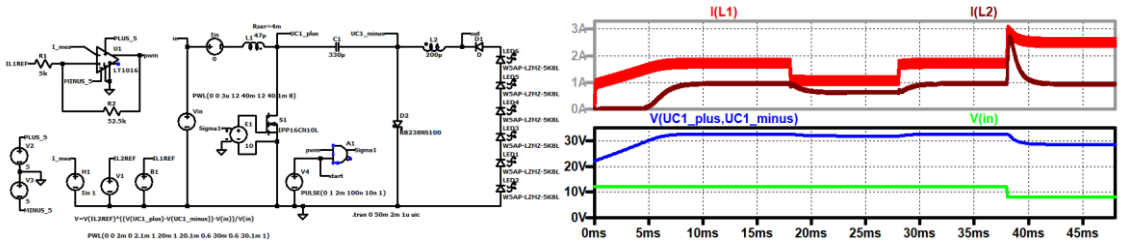


Figure 15. Cuk derived LED driver with control law: a. simulation circuit, b. currents through the coils L1 (red), L2 (black); voltage across the capacitor (blue), input voltage (green)

The control law works efficiently for changes of the desired value, but fast changes of the input voltage lead to an overshot of the output current.

More refined model by including the diode

Mode M1 is equal to mode M1 of the Boost converter (6, 7). Mode M2 differs from the Boost converter. The state equations are

$$\frac{di_{L1}}{dt} = \frac{u_1 - V_D - R_D(i_{L1} + i_{L2}) - u_{C1}}{L_1}, \qquad \frac{di_{L2}}{dt} = \frac{-V_{LED} - R_{LED} i_{L2} - R_D(i_{L1} + i_{L2}) - V_D}{L_2}, \quad \frac{du_{C1}}{dt} = \frac{i_{L1}}{C_1} \tag{37}$$

leading to the state space description

$$\frac{d}{dt}\begin{pmatrix} i_{L1} \\ i_{L2} \\ u_{C1} \end{pmatrix} = \begin{bmatrix} -\frac{R_D}{L_1} & -\frac{R_D}{L_1} & -\frac{1}{L_1} \\ -\frac{R_D}{L_2} & -\frac{R_D + R_{LED}}{L_2} & 0 \\ \frac{1}{C_1} & 0 & 0 \end{bmatrix} \cdot \begin{pmatrix} i_{L1} \\ i_{L2} \\ u_{C1} \end{pmatrix} + \begin{bmatrix} \frac{1}{L_1} \\ 0 \\ 0 \end{bmatrix} \cdot (u_1) + \begin{pmatrix} -\frac{V_D}{L_1} \\ -\frac{V_{LED} + V_D}{L_2} \\ 0 \end{pmatrix} . \tag{38}$$

Combining (7) and (38) leads to the refined large signal model

$$\frac{d}{dt}\begin{pmatrix} i_{L1} \\ i_{L2} \\ u_{C1} \end{pmatrix} = \begin{bmatrix} \frac{R_D(d-1)}{L_1} & \frac{R_D(d-1)}{L_1} & \frac{d-1}{L_1} \\ \frac{R_D(d-1)}{L_2} & -\frac{R_{LED}+R_D(1-d)}{L_2} & \frac{d}{L_2} \\ \frac{1-d}{C_1} & -\frac{d}{C_1} & 0 \end{bmatrix} \cdot \begin{pmatrix} i_{L1} \\ i_{L2} \\ u_{C1} \end{pmatrix} + \begin{bmatrix} \frac{1}{L_1} \\ 0 \\ 0 \end{bmatrix} \cdot (u_1) + \begin{pmatrix} \frac{V_D(d-1)}{L_1} \\ -\frac{V_D(1-d)+V_{LED}}{L_2} \\ 0 \end{pmatrix}. \quad (39)$$

Linearizing results in the refined small signal model

$$\frac{d}{dt}\begin{pmatrix} \hat{i}_{L1} \\ \hat{i}_{L2} \\ \hat{u}_{C1} \end{pmatrix} = \begin{bmatrix} \frac{R_D(D_0-1)}{L_1} & \frac{R_D(D_0-1)}{L_1} & \frac{D_0-1}{L_1} \\ \frac{R_D(D_0-1)}{L_2} & -\frac{R_{LED}+R_D(1-D_0)}{L_2} & \frac{D_0}{L_2} \\ \frac{1-D_0}{C_1} & -\frac{D_0}{C_1} & 0 \end{bmatrix} \cdot \begin{pmatrix} \hat{i}_{L1} \\ \hat{i}_{L2} \\ \hat{u}_{C1} \end{pmatrix} + \begin{bmatrix} \frac{1}{L_1} & \frac{R_D I_{L10}+R_D I_{L20}+U_{C10}+V_D}{L_1} \\ 0 & \frac{R_D I_{L10}+R_D I_{L20}+U_{C10}+V_D}{L_1} \\ 0 & -\frac{I_{L10}+I_{L20}}{C_1} \end{bmatrix} \cdot \begin{pmatrix} \hat{u}_1 \\ \hat{d} \end{pmatrix}. \quad (40)$$

Using again abbreviations for the matrix elements and Laplace transformation results in

$$\begin{bmatrix} s-A_{11} & -A_{12} & -A_{13} \\ -A_{21} & s-A_{22} & -A_{23} \\ -A_{31} & -A_{32} & s \end{bmatrix} \cdot \begin{pmatrix} I_{L1}(s) \\ I_{L2}(s) \\ U_{C1}(s) \end{pmatrix} = \begin{bmatrix} B_{11} & B_{12} \\ 0 & B_{22} \\ 0 & B_{32} \end{bmatrix} \cdot \begin{pmatrix} U_1(s) \\ D(s) \end{pmatrix}. \quad (41)$$

Calculation of the denominator leads to

$$DEN = \begin{vmatrix} s-A_{11} & -A_{12} & -A_{13} \\ -A_{21} & s-A_{22} & -A_{23} \\ -A_{31} & -A_{32} & s \end{vmatrix} = s^3 - (A_{11}+A_{22})s^2 - (A_{11}A_{22}+A_{12}A_{21}+A_{13}A_{31}+A_{23}A_{32})s - A_{12}A_{23}A_{31} - A_{13}A_{21}A_{32} + A_{13}A_{22}A_{31} + A_{11}A_{23}A_{32}. \quad (42)$$

Calculation of the numerator for IL2 gives

$$NUM_IL2 = \begin{vmatrix} s-A_{11} & B_{12} & -A_{13} \\ -A_{21} & B_{22} & -A_{23} \\ -A_{31} & B_{32} & s \end{vmatrix} = B_{22}s^2 + (-A_{11}B_{22} + A_{23}A_{31}B_{12} - A_{23}B_{32} + A_{21}B_{12})s + A_{13}A_{21}B_{32} + A_{23}A_{31}B_{12} - A_{11}A_{23}B_{32} - A_{13}A_{31}B_{22}. \quad (43)$$

The transfer function between the output current and the duty cycle is now relatively complex

$$G_{IL2D}(s) = \frac{B_{22}s^2 + (-A_{11}B_{22} + A_{23}A_{31}B_{12} - A_{23}B_{32} + A_{21}B_{12})s + (A_{13}A_{21}B_{32} + A_{23}A_{31}B_{12} - A_{11}A_{23}B_{32} - A_{13}A_{31}B_{22})}{s^3 - (A_{11}+A_{22})s^2 - (A_{11}A_{22}+A_{12}A_{21}+A_{13}A_{31}+A_{23}A_{32})s + (A_{13}A_{22}A_{31} + A_{11}A_{23}A_{32} - A_{12}A_{23}A_{31} - A_{13}A_{21}A_{32})}. \quad (44)$$

CONCLUSIONS

To supply LEDs, converters with continuous output current are necessary to get a stable light stream and to avoid overcurrent, which can destroy the LEDs. Perusing the literature most drivers concerned have a capacitor in parallel to the load and not a current output, cf. the comprehensive overview written by Bento and Cardoso (2021). In this paper three converters are treated which have not only a continuous output current but also a continuous input current. Therefore, no input capacitor is necessary, even when the supply source is in a far distance. The control of the converter can be done with a linear controller. For all three topologies the state space description and the transfer function between the output current and the duty cycle are derived and can be used as starting point for designing a linear controller. For the Buck converter with input filter a simple two-point controller for controlling the output current is sufficient. For the two other topologies a new concept is demonstrated. From the steady-state connections a control law for the necessary input current is derived. This desired input current is used for the two-point controller as reference value. The control law can also be

found by using the stationary connections between the working point values which result from the linearization process. It should be menioned that using the steady-state working point values – when the parasitic resistors are included – leads to a more precise feedforward control. The here described converters can easily be modified by connecting a further active switch between the output connectors (c.f. Himmelstoss 2022,2). With this modification the load current can be switched on and off immediately. This is especially interesting when the load are UVC-LEDs used in disinfection devices and for modulating information on the light stream (Edelmoser).

REFERENCES

F. Bento, F. & Cardoso, A. J. M. (2021). Comprehensive survey and critical evaluation of the performance of state-of-the-art LED drivers for lighting systems. Chinese Journal of Electrical Engineering, vol. 7, no. 2, pp. 21-36.

Edelmoser, K. H., & Himmelstoss, F. A. (2016). High Dynamic Current Source for LED Light and Data Transmission Applications. Power Conversion and Intelligent Motion PCIM Europe 2016, 1741-1748.

Himmelstoss, F. A., & Edelmoser, K. H. (2016) Thermo-Puncture Devices – Mechanical and Electrical Concepts. Proceedings Power Electronics and Motion Control PEMC 2016, 221-226.

Himmelstoss, F. A. (2022, 1): Controller design of a Buck converter with the help of LTSpice, INTERNATIONAL ASIAN CONGRESS ON CONTEMPORARY SCIENCES-VI, 195-202.

Himmelstoss, F. A. (2022, 2). Liquid and surface disinfection with pulsed UVC LEDs. 2. Ahi Evran International Conference on Scientific Research. Kirshehir, Turkey, 21.-23. October 2022

Mohan, N., Undeland, T. & Robbins, W. (2003). Power Electronics: Converters, Applications and Design. New York: W. P. John Wiley & Sons.

Rozanov, Y., S. Ryvkin, S. Chaplygin, E. & Voronin, P. (2015). Power Electronics Basics. Boca Raton: CRC Press.

Zach, Franz. (2022). Leistungselektronik. Frankfurt: Springer, 6th edition.

ATMOSPHERIC OXYGEN ANALYSER

Sowmiya N

Bannari Amman Institute of Technology, Biomedical Engineering, Sathyamangalam, Erode, India

Brindha M

Saranathan college of engineering, Computer Science and Business System, Panjappur, Tiruchirappalli, India

Vigneswar R

Bannari Amman Institute of Technology, Biomedical Engineering, Sathyamangalam, Erode, India

Abstract

In day-to-day life, Oxygen plays an important role in our Human body. Humans breathe through their mouth and nose into their lungs to obtain the oxygen they require. Our cells can break down food to produce the energy we need to survive, thanks to oxygen. Other creatures may breathe through various organs, but all animals breathe in order to deliver oxygen to their bodies. In this project, the design and implementation of a low-cost, portable oxygen monitoring system is presented. Due to the low penetration of health technology, especially in under-developed countries, low-cost oxygen measurement devices have been of interest in this field . IoT based low-cost remote blood oxygen monitoring has also received attention for telemedicine.We have used STM32 Microcontroller and OLED to display the oxygen level in the atmosphere. Here,we are using the galvanic type of oxygen sensor. At the point when oxygen levels are low (below 21%) , these sensors are functioned to sound an alert. Buzzer-based alarm while high pollution is detected. Oxygen monitoring is an important metric for checking patients affected with respiratory diseases. It can be implemented as a small device, and therefore, has been used widely in various applications.

Keywords: Oxygen, stm-32,respiratory diseases, low cost, Oxygen sensor

ELECTRIC TRANSFORMER: PRINCIPLE OF OPERATION THROUGH ELECTROMAGNETISM

Giselle Francine BRITO MUNIZ

Federal Institute of Education, Science and Technology of Bahia, Electrical Engineering, Vitória da Conquista, Bahia, Brazil., ORCID NO: 0000-0003-0029-2130

Kenedy Marconi GERALDO DOS SANTOS

Prof. Dr., Federal Institute of Education, Science and Technology of Bahia, Electrical Engineering, Vitória da Conquista, Bahia, Brazil., ORCID NO: 0000-0002-4980-7011

ABSTRACT

The use of clarity, depth and intentionality in teaching such essential theories of science is still a challenge for the learning community worldwide. In this sense, electrical engineering still lacks a greater attention to the learning process and the setting of knowledge. An example that can be mentioned is the electronic devices, such as the electrical transformer, considering its importance for the learning of electric machines and its other applications in electrical engineering and electronics. In this way, the main objective of this work is to provide a better and more objective understanding of the theoretical foundation of the device called electric transformer, through the equations of the theoreticians Maxwell, Faraday and Lenz, foundations of the electromagnetism, besides reproducing a practical implementation of the equipment. The methodology used was the application of integrative literature review, from educational publications of books about the segment, being an inclusion criterion in the content of the interconnections of the subject that relate the equations of the theorists mentioned above, and also provide the explanation of each variable in the mathematical models involved. Besides, it was accomplished in the laboratory, the demonstration of the voltage modification of a prototype of shielded core transformer, through the recycling of an electronic waste. It was observed that the use of Maxwell's equations in the construction of knowledge about transformers must precede the conceptualization of the device itself, due to its capacity to allow the expansion of the basic concepts of its operation. Moreover, the practical application was relevant for the conclusion of the construction process of scientific knowledge in engineering, which cannot receive only mathematical incentive but also needs visualization and applicability.

Keywords: Electromagnetism; Single-Phase Transformer; Impedance.; Experiment; Active learning.

I. INTRODUCTION

In ancient times, certain materials, when subjected to friction with materials of a different nature, transferred "virtues", and these properties were associated in a supposed mutual transference. The mathematical development of electricity and magnetism impacted the history and sequence of scientific discoveries relevant to the technical progress of all mankind.

The first considerations of electrical phenomena are said to have been made by the philosopher Thales of Miletus 1 in the 5th century B.C., by providing friction between amber and sheepskin. Tales noticed after performing the experiment, that amber attracts small pieces of straw and feathers, but did not consider the relevance of the phenomenon, attributing to it the same characteristics of magnetite (CAVALCANTE, 2012).

According to OLIVEIRA et al (2019), from the mathematical development of Maxwell, it was possible to create new devices and scientific discoveries in the areas of engineering, with the further study on conductors, improvements in devices such as antennas in the process of energy production with Faraday's law, and in the process of transporting electrical energy with the study of conductance.

James Clerk Maxwell, xx Scotsman, synthesized all the equations that described Electricity and Magnetism, developed until then. First published in the paper called "The Dynamic Theory of the Electromagnetic Field" in 1884 in a set of 20 equations that Maxwell wrote through his components, and were synthesized by Oliver Heaviside with the help of Willard Gibbs.

Understanding the laws of electromagnetism contributes to the development of its applications, which have since advanced and impacted various sectors of society. One such application is the electric transformer. The transformer is a static "machine" (with no moving parts), whose purpose is to transmit, by means of a magnetic field, electrical energy from one circuit to another without direct connection, with a desired voltage level without altering the frequency.

The transformer is an electromagnetic device consisting of at least two coils coupled through a magnetic core of high magnetic permeability. The principle of operation of the transformer is based on the phenomenon of electromagnetic induction, and in particular the mutual electromagnetic induction between coils.

Without the developments and syntheses made by theoreticians such as Maxwell, Faraday, and Gauss, devices such as the electric transformer could not be mathematically supported, and thus offer a scientific and creative solution for the change of electric voltage and current.

Thus, the main objective of this work is to provide a better and more objective understanding of the theoretical basis of the device called the electric transformer, through the equations of the theoreticians Maxwell, Faraday and Lenz, foundations of electromagnetism, and to reproduce a practical application of the equipment.

II. MATERIALS AND METHODS

Regarding the methodological procedures, the research has a descriptive and experimental nature, which presents remarkable characteristics described by Marconi and Lakatos (2017), who state that experimental research: "describes what will be" - when there is control over certain factors; the importance lies in the cause and effect relationships. Based on this assumption, it was sought, through the practical application of the fundamental theories of electromagnetism, the verification of the working principle of electric transformers.

The practical application of transformer prototypes, which sought the execution of a closed test, was performed from the deconstruction of an unused transformer scrap, which had a "U" type laminated core. From this deconstruction on, the organization of the plates made of the silicon steel alloy was organized, in addition to the choice and handling of the primary and secondary coils, and their new core format.

Thus, the four corner bolts that held the plates and the transformer covers in place were removed. Before all the plates were separated, their arrangement was observed. Gradually, the plates were removed, noting relative difficulty when removing the initial plates, given the presence of the coils. The entire length of the coil wire was unwound, in order to assist in the construction processes.

Through this reuse, it became possible to use its materials to build new transformers, with modifications in all their structures. The 8.6 x 5.7 cm sheets can be seen in Figure 1. The wire material used for winding the coils consists of enameled copper, with AWG 21 numbering.

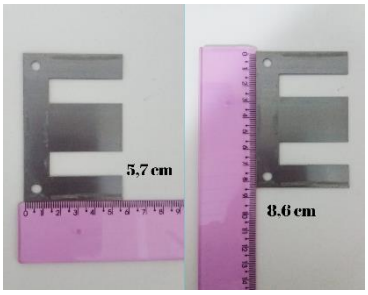


Figure 1. Measuring the sheet dimensions

The prototype was made so that the test was closed, i.e., with stacking and fixing of 21 sheets in "E" format, being interleaved in their positions, so that there would be two paths for the magnetic flux to travel, in this way, the new laminated core is of the "shielded" type, as seen in Figure 2.

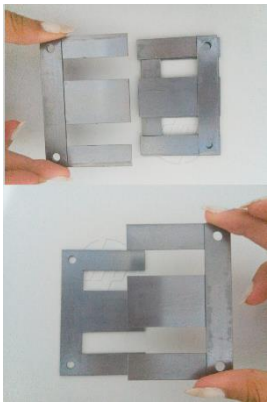


Figure 2.Arrangement and mounting of the plates

For purposes of theoretical experimentation, a small direct voltage was applied to the primary coil, followed by an analysis of its frequency and waveform generated in the secondary, by means of the oscilloscope. Subsequently, small values of alternating voltage were applied to the primary coil in the closed test, as shown in Figure 3, and from such applications, it became possible to understand in a laboratory environment, with the help of an oscilloscope, the behavior of the transformed voltages in the secondary coils, their existing dependence with the number of turns, and the impacts caused by the resistance and impedance relations with the coils, which can be seen in Figure 3.

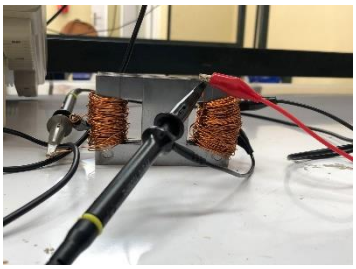


Figure 3. Stress application

Initially, the resistances of the transformer coils were measured using a digital multimeter, with scales in 200mΩ. Furthermore, the resistances of the cables used were measured to minimize errors in the measurements.

For the purpose of theoretical experimentation, a direct voltage of 2V was applied to the primary coil, followed by an analysis of its frequency and waveform generated in the secondary, by means of the oscilloscope.

Subsequently, the runs of alternating voltage on the primary in the closed test were small and from such applications, it became possible to understand in a laboratory environment, with the help of an oscilloscope, the behavior of the transformed voltages in the secondary coils, their existing dependencies with the number of turns, and the impacts caused by the resistance and impedance relationships with the coils.

III. FINDINGS and DISCUSSION

The main axis of discussion of this paper is not based on the simple exposition of the electromagnetic theory, and Maxwell's equations, but with clarity, demonstrate how the progress and electromagnetic understanding, makes almost any explanation of the working principle of an electric transformer. Thus, for more effective learning regarding the electronic device, the journey of knowledge of the theoretical foundations of electromagnetism are not only necessary, as well as boost effective learning.

The first equation named by Maxwell is about the relationship between electric flux and electric charge. He appropriated the discoveries and publications of Gauss, who claimed that electric fields are generated by the simple presence of electric charges, or through the variation in time of magnetic fields. However, magnetic fields can be produced by currents, that is, the flow of moving charges, or through the temporal variation of the electric field. Such a relationship can be seen in the equality of equations (1) and (2) according to Hayt in their integral and point forms, respectively:

$$\oint_S E\,dS : \frac{Qint}{Eo} \tag{1}$$

$$\nabla . E : \frac{\rho}{Eo} \tag{2}$$

where S is a closed surface; dS is a vector perpendicular to S; Qint is the electric charge inside S; E is the electric field measured in N/C; Eo is the electric permittivity in vacuum (8.85×10^-12 C^2/Nm^2); ρ is the electric charge density (q: RρdV).

So that the electric flux through a surface is always equal to the density of electric charges present on the surface in question, having only its contribution to the total flux.

Known as Maxwell's second equation, or Gauss's law for magnetism, this fundamental relationship states that the magnetic flux through any closed surface is always zero, since the amount of magnetic field lines entering the surface is always equal to the amount leaving it. These equations formalize the non-existence of magnetic monopoles (magnetic charges). This theory can be visualized in its integral and punctual forms, respectively, in equations (3) and (4), which, according to Hayt, are

$$\oint_S B\,dS : 0 \tag{3}$$

$$\nabla . B : 0 \tag{4}$$

where S is a closed surface; dS is a vector perpendicular to S; B is the magnetic field measured in Tesla.

Also known as Faraday-Lenz's Law, this relevant fundamental theory addresses a pillar of the study performed at work. From the statement that a time-varying magnetic field generates an electric field, many other understandings can be made. The union of the studies of these physicists conclude that the rate of change of the magnetic field flux across the surface bounded by a circuit is equal to the electromotive force (fem) induced in this circuit. This means that if no such flux variation occurs, there will not be enough force to generate this magnetomotive force. These relationships are seen in integral and pointwise forms, respectively, in equations (5) and (6), which are also presented by Hayt:

$$\oint_C E\,dl : -\frac{d(\Phi)}{dt} \tag{5}$$

$$\nabla . E : -\frac{\partial B}{\partial t} \tag{6}$$

where C is a closed curve; dl is a vector parallel (tangential) to C; E is the electric field; Φ is the magnetic flux on the open surface resting on C.

More commonly referred to as Ampere-Maxwell's Law, the conclusion of this set of theories discovered, studied, and put together, cooperates with Faraday's Law, since in the same way that the variation of the

magnetic flux generates an electric field, it can also be stated that with the variation of the electric flux there is a magnetic field.

The circulation of the magnetic field along a closed line (called amperian) that surrounds the current i is equal to the product of this current by the constant μo. Equations (7) and (8), repeated by Hayt, show that:

$$\oint_C B\,dl : \mu o(\varepsilon o.\frac{d\phi}{dt} + i) \tag{7}$$

$$\nabla.B : \mu o.J + \mu\varepsilon o.\frac{\partial E}{\partial t} \tag{8}$$

where dl is a vector parallel tangential to C; B is the magnetic field measured in Tesla; μo is the magnetic permeability in vacuum (4π×10^-7 T.m/A); i is the electric current flowing through C. dq/ dt; j is the electric current density (i: ∫ j.dS); Eo is the electric permittivity in vacuum (8.85 × 10^-12 C^2/Nm^2; Φ is the electric flux on the open surface supported on C.

It can be seen, therefore, that magnetic fields are produced by electric currents and by electric fields that vary in time. Alternating current, also called AC voltage or current (alternating current), consists of alternating polarity of charge flow in time variation. Thus, we have equation (9) described by Faraday and presented by Hayt:

$$v(t) : -N.\frac{d\phi}{dt} \tag{9}$$

where v(t) is the measured induced voltage in V; N is the number of turns; dΦ/dt is the measured electromagnetic flux variation in Wb/s.

A sinusoidal function is easily obtained for electric power generation, through alternating current (Rêgo, 2015). Thus, a coil subjected to this induction produces at its terminals the electric voltage of equation (5). The waveform generated is a graph of a magnitude as a function of a variable, such as time or position, etc.

The amplitude of a waveform at any instant of time is its value within the observed instant. The maximum value of a function measured from zero, which is also called the peak value. The difference of the peak values, whether negative or positive, i.e., peak-to-peak, is the simple sum of the amplitudes. The frequency (f) is calculated by the number of repetitions occurring in a time t, and is measured in Hertz (Hz), which is one cycle per second. In turn, the period (T) is the inverse of the frequency, that is, the time between consecutive repetitions. These units can be seen in Figure 4.

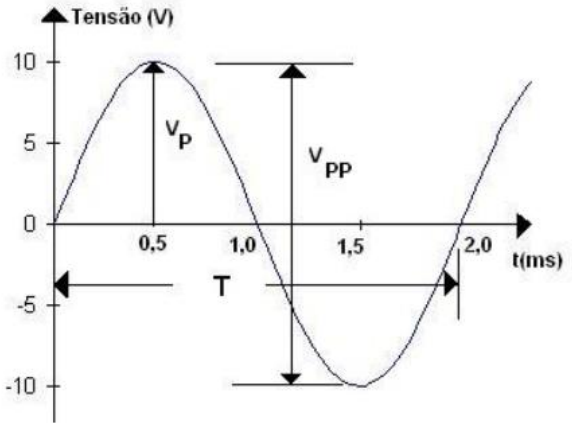


Figure 4. Sine waveform

The alternating current makes it possible to use and build electric generators, motors, and various electronic elements, predominating in practices and applications that require this form of energy.

One of the most relevant initial terms is magnetic permeability, which is the facility that the material has to magnetize itself; it can be expressed mathematically in equation (10), presented by Hayt, as:

$$\mu : \frac{B}{H} \tag{10}$$

where B is the magnetic field measured in Tesla; H is the induced field measured in Ampere-spire/meter.

The magnetic permeability of a material depends on the inductor field strength.The higher the inductor field, the lower the permeability, i.e. the harder it is to magnetize the material. This behavior is exhibited by all magnetic materials.Non-magnetic materials have a permeability that is approximately constant and much lower than the permeability of magnetic materials. For calculation purposes, the permeability of non-magnetic materials is taken to be the following magnetic constant: 4π.10 ^(- 7) H/m. Thus, non-magnetic media such as air, aluminum and wood, among others, have a μo of 4π.10^(- 7) H/m. In relation to this μo, many values are determined. Thus, relative permeability is defined as the ratio between the permeability of the material and the magnetic constant:

$$\mu r : \frac{\mu}{\mu o} \tag{11}$$

The relative permeability (μr) is a number (without unit) that indicates how many times the permeability of the material (μ) is greater than the permeability of non-magnetic materials (μo). For non-magnetic materials the relative permeability is approximately equal to unity (μr : 1) and for magnetic materials it is much larger than unity (μr > > 1).

Furthermore, inductance is the ability of an inductor to store energy and provide it in the magnetic field that is created by the flow of electric current (BUENO; ASSIS, 2015). Energy is needed to set up the magnetic field and this energy needs to be released when the field drops. As a result of the magnetic field associated with the current flow, inductors generate an opposite voltage proportional to the rate of change of current in a circuit. Inductance is caused by the magnetic field generated by electric currents flowing within an electric circuit. Usually, coils of wire are used because a coil increases the coupling of the magnetic field and increases the effect.

When indicating an inductor in a circuit diagram or within an equation, the symbol "L" is usually used. In circuit diagrams, inductors are usually numbered, L1, L2, etc. The SI unit of inductance is Henry, H, which can be defined in terms of the rate of change of current and voltage. Since inductors behave in alternating circuits, they will also have different conductance than direct current circuits. Thus, the inductance will always have permanent conditions.

When an inductor is applied in a direct current circuit, its inductance will only occur in the moments in which there is a variation of flux, that is, in the alternating polarity of the circuit. In AC circuits, as the voltage and current coefficients are constantly changing, that is, as variation occurs, inductance will occur at all times. It is valid the statement that coils, inductors, will also obtain ohmic resistance, which depends on the material, its length, its cross-sectional area, according to Ohm's Second Law.

According to (MARKUS, 2001) if there were a perfect, or ideal, inductor, this resistance value would be zero, but this is not possible, because all conductor material, usually composed of metallic elements, will always obtain some value, even if low, of resistance.

Reactance, in turn, consists precisely in the permanent opposition in relation to the current that varies in time. The inductive reactance is understood through the mathematical relationship seen in equation (12), also exposed by Hayt, as:

$$XL : 2.\Pi.f.L \tag{12}$$

where XL is the inductive reactance measured in Ohms (Ω); f is the frequency of the alternating current measured in Herzt (Hz);L is the inductance of the inductor measured in Henrys (H).

The inductive reactance is directly proportional to the rate of change of the current flowing through the inductor, that is, directly proportional to the frequency. Thus, it can be seen that the higher the frequency of oscillation of the circuit's power supply, the greater the opposition to the time-varying current.

Impedance represents the set of oppositions that a circuit offers to the flow of sinusoidal current. Although it is the ratio between two phasors, it is not a phasor, because it does not correspond to a quantity that varies as a sinusoid (SADIKU,2013). In this sense, impedance is found through:

$$Z : R + jX \tag{13}$$

where Z is impedance in ohms; R is resistance in ohms; j is an imaginary component; X is reactance in ohms.

For there to be inductive impedance, therefore, there needs to be reactance, i.e., natural opposition of inductors to the variation of electric current in alternating current circuits. Considering equation (12) and (13), also exposed by the Hayt theorist, then the inductive impedance is given by:

$$ZL : j\omega L \tag{14}$$

where ZL is the inductive impedance in Ohms; j is an imaginary component; and L is the inductance in Henrys.

Transformers are electromagnetic devices used to transform electrical energy between voltage levels. In general, these equipments consist of a ferromagnetic core surrounded by conductive windings, and their functionality is based on coupled electric and magnetic fields (MERRITT, 2003).

In transformers considered ideal, the coil that represents the primary containing Np turns, if subjected to a certain voltage Vp, will have an alternating current circulating in its conductor. Based on this assumption, and grounded on Ampère's Law seen in equations (5) and (6), where the electric current over variation, i.e., traveling through a core, will generate a magnetic field, it can be understood that the flow will traverse the Ns turns of the coil corresponding to the secondary, providing the alternating current is and voltage Vs of the same winding. Thus, the voltage and current of the primary winding are found by:

$$Vp : Np.\frac{d\phi}{dt} \tag{15}$$

While in the secondary winding:

$$Vs : Ns.\frac{d\phi}{dt} \tag{16}$$

Thus, if the quotient between the number of turns of the primary Np and the number of turns of the secondary Ns is greater than 1, the primary voltage will be higher than the secondary, configuring itself as a voltage-lowering transformer. If this same quotient is less than 1, the secondary voltage will be higher than that of the primary, which is a voltage-raising transformer. Therefore, an ideal transformer transforms currents in the inverse ratio of the turns of its windings.

Understanding the relationships that exist between the components of an ideal transformer requires more concepts and connections. Among them is the concept of flux density, which is equivalent to the number of field lines passing through the surface subjected to induction; furthermore, in magnetic circuits, the opposition to the magnetic flux is analogous to the electrical resistance in electrical circuits, and is called reluctance (ℜ).

In this sense, Ampère's Law allows the statement that in a toroidal magnetic core, the magnetic field strength (H), measured in Tesla (T)[N/A.m] is obtained by:

$$H : \frac{Ni}{2\pi r} \quad (17)$$

where N is the number of turns; i is the current measured in A; r is the average radius.

The flux density (B) is the area that the flux lines traverse, and this, obtained and in conjunction with equation (17) assures us that:

$$B : \mu.H \quad (18)$$

$$B : \frac{\mu Ni}{2\pi r} \quad (19)$$

where B is the magnetic flux density measured in Wb/m^2; μ is magnetic permeability of the material; H is the magnetic field strength (T).

Finally, the primary objective, the magnetic flux (φ) measured in Weber (W), since 1W: [V.s], found by:

$$\phi : BA \quad (20)$$

$$\phi : \frac{\mu NiA}{2\pi r} \quad (21)$$

where A is the cross-sectional area.

Considering that there is no dependence relationship of magnetic reluctance with current or number of turns, it can be considered that ℜ measured in Ampere turns per Weber (Ae/Wb), can be obtained by:

$$\Re : \frac{l}{\mu A} \quad (22)$$

where l is conductor length; μ is magnetic permeability of the material; A is the cross-sectional area of the material.

In addition to the conclusions made possible by Ampère's Law, it is feasible to add to the existing relationships, the concepts of magnetomotive force (fmm) and reluctance (ℜ). Understanding the magnetomotive force (fmm) as the cause of the appearance of a magnetic field, being necessary to conduct the magnetic flux in the magnetic circuit. It can be seen that it can be considered the cause, and the magnetic flux (φ) the effect generated. The physical support for there to be the path for φ to travel, is given by the reluctance (ℜ) and permeance or permeability of the material (μ) This relationship of cause and consequence, is permeated by Rowland's Law, which states that the magnetic flux is the product between the reluctance of the material and the applied magnetomotive force, then analogously, it is correct to state that:

$$fmm : \Re\psi \quad (23)$$

Considering that the toroidal core has a compliance l and can be replaced by 2π, then the flux (φ) can also be considered as:

$$Ni : \Re\phi \quad (24)$$

where ℜ is the magnetic reluctance, measured in [Ae/Wb].

Enabling the generalization of fmm as:

$$fmm : Ni \quad (25)$$

here N is the number of turns; i is the measured current in A.

It is remarkable the similarity of equation (25) with Ohm's first Law, and also of equation (22) with Ohm's Second Law.

Thus, it can be seen that the main purpose of a transformer is to convert an alternating electrical power, which is at one voltage and frequency level, into a power of the same frequency at another voltage level, i.e., transform one voltage into another (CHAPMAN, 2013). Thus, seeing the electromagnetic laws, as well as each of the variables involved in the mathematical formulations, plays a relevant role in learning that involves electrical transformers, as well as other electronic devices.

The intention for the completion of the educational progress, is the realization of a simple prototype transformer, with the sole purpose of visualizing voltage transformation, even in undesirable situations of scale operation, or even the complete and compound machine. For this, the methodology already described was applied, and it was first visualized that when the primary coil was induced with a direct voltage of two volts, the frequency analyzed in the oscilloscope is 0Hz, that is, there is no variation of magnetic flux, and with this, there is no magnetic induction effect, so that the secondary coil has 0 volt (Figure 5).

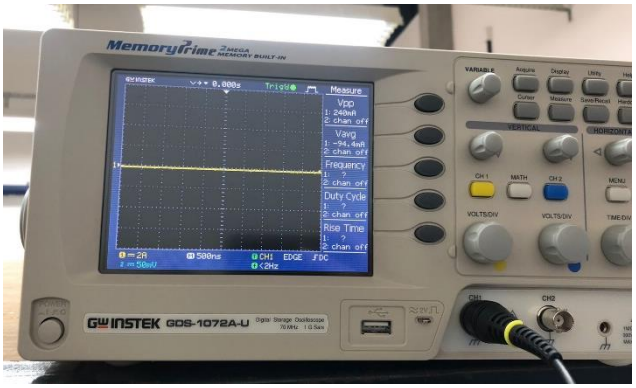


Figure 5. Oscilloscope with zero frequency.

This phenomenon verifies Maxwell's laws, so that a transformer can only act in alternating current, that is, in AC circuits.

Small alternating voltages were applied to the primary of the transformer, enabling the measurement in the secondaries, as shown in Figure 06. With the number of turns of the coils, it was expected that the measurements would be half the applied voltage, given the existing relationship between the number of turns chosen. However, instead of 50%, only 28% and 24% were found, respectively.

In this way, although the expected proportions did not occur, a considerable voltage drop was noted in the secondary coil of the prototype. The reluctance of the circuit was high, due to a lower magnetic permeability. Furthermore, the impedance also had its value reduced, since the frequency of the flux variation was not high.

Furthermore, it can be seen that since the number of turns in the coils was not considerably high, the magnetomotive force (fmm) was compromised, also causing the flux (φ) to decrease. As a consequence of this, the induction did not make it possible for the secondary voltage to be half the primary voltage, having a very low coupling.

Thus, regardless of the practical results not being perfectly as expected, the visualization of the transformer in a laboratory environment provides a process of acquisition of technical knowledge, especially for higher education students.

IV. CONCLUSION and RECOMMENDATIONS

In view of the presentations made, it became apparent the fundamental role of the electromagnetic theory in the performance and progress of the understanding of electric transformers. Thus, it is advocated the study of the Maxwell, Faraday and Lenz equations, in a detailed and step-by-step manner, prior to the direct study of the operation of the transformer machine. This is because a clear understanding of the various parameters, units and variables of the equations of electromagnetism endorse, explain and demonstrate the reasons and ways in which an electrical transformer can be created.

Furthermore, prototyping and incentives for practical application after receiving and learning the theoretical program content about transformers are also advocated. The visualization in a laboratory environment can influence, facilitate and instigate the acquired knowledge.

REFERENCES

Alexandre, C. K.; Sadiku, M. N. O. (2013). Fundamentos de Circuitos Elétricos. Porto Alegre: AMGH.

Bueno, M.; Assis, A.K.T. (2015). Cálculo de Indutância e de Força em Circuitos Elétricos. Apeiron Montreal.

Cavalcante, M. A. (2012). Uso do espelho de Lloyd como método de ensino de óptica no Ensino Medio. BRA. Revista Brasileira de Ensino de Fisica.

Chapman, S. J. (2013). Fundamentos de Máquinas Elétricas.

Hayt, W. H.; Buck, J. A. (2003). Eletromagnetismo. Rio de Janeiro, BRA: LTC Editora S.A.

Lakatos, E. M. & Marconi, M. A. (1991) Metodologia Científica. Editora Atlas, BRA.

Markus, O.(2001). Circuitos Elétricos: Corrente Contínua e Corrente Alternada. Èrica.

Merritt, S. Y.; Chaitkin, S. D. (2003). Efficiency standards for low voltage substation transformers," Conference Record of the 2003 Annual Pulp and Paper Industry Technical Conference.

Oliveira, M. C.,Oliveira, A. M., Gomes, A. K.F. & Aranha, E. R. (2019) Aplicações das Equações De Maxwell na Engenharia Elétrica. Revista Acadêmica Ensino De Ciências e Tecnologias, BRA.

Rêgo, A.K.; Rodrigues, C.L.C. (2015). Eletricidade em CA. Ouro Preto, BRA: CEAD.

EFFECT OF DIETARY ZINC ON THE GROWTH OF JUVENILES COMMON CARP *(CYPRINUS CARPIO)*[1]

Shokri Omar Mustafa MUSTAFA

Fisheries Faculty, Firat University, 23119 Elazığ, TURKEY, 0000-0003-3290-1092

Muzaffer Mustafa HARLIOĞLU

Fisheries Faculty, Firat University, 23119 Elazığ, TURKEY, 0000-0001-8288-0571

Mehmet Nuri ÇAKMAK

Fisheries Faculty, Firat University, 23119 Elazığ, TURKEY, 0000-0002-3241-1491

Abstract

The common carp (*Cyprinus carpio*) is an important and high value food, and carp species are from the family of freshwater fish, widely cultivated around the world. Carp food represents the highest proportion of the total cost of the fish farm. Therefore, appropriate mineral supplementation in early developmental stages and at an early age is very important to support carp. The current research was organized to study the effectiveness of supplemented diet of different Zn level on the weight gain, proportional growth in weight, specific growth rate, and feed conversion rate and condition factor in the common carp juveniles. Four iso-nitrogenous (35% crude protein) practical diets were produced with graded levels of dietary zinc sulphate was included as the dietary zinc source to the basal diet supplemented with increasing zinc levels (T1, control, 85 mg Zn kg^{-1}; T2, 105 mg Zn kg^{-1}; T3, 125 mg Zn kg^{-1} and T4, 145 mg Zn kg^{-1}). The results showed that dietary zinc supplementation had a positive effect on the specific growth weight, fish body weight, weight gain, feed conversion rate, proportional growth in weight and condition factor of juvenile carp. For all parameters studied, the best results were found in the juveniles fed T2, but the significantly lowest growth ($P < 0.05$) was obtained in juveniles fed the basal diet containing 85 mg Zn/kg^{-1}. The findings showed that 105 and 125 mg Zn/kg-1 diet caused significantly higher FCR, SGR and ADG in comparison to those fed with diets containing 85 and 145 mg Zn/kg^{-1}. In addition, feed intake was raised with increasing dietary zinc amounts up to 105 mg/kg^{-1} diet. In conclusion, this study confirms the positive effects of the use of 105 mg of zinc sources in diet to enhance growth performance of carp juveniles. The findings of the present study will help scientists, fish feed producers and fish farmers.

Key words: condition factor, feed conversion rate, mineral, nutrition, proportional growth, weight gain

1. Introduction

The common carp (*Cyprinus carpio*) distributes naturally in warm waters around the world and has also been cultivated (Saoud et al., 2007; Barakat et al., 2011; Abou-Daoud et al. 2014). Roumieh et al. (2013) stated that the negative effects of the carp farm on the environment are less than other species and it can be economically well-organized since it does not require a high level of protein compared to other species such as trout. In addition, carp has satisfactory growth (Bariche, 2005; Borgwardt et al. 2020) with low dissolved oxygen requirement and can tolerant high water temperature, and has potential to breed in intensive farms (Saoud et al., 2007, 2008). Accordingly, there have been increases in the number of carp farms in recent years in the world (i.e., in the Middle East and Indo-Pacific region) (FAO, 2019; FAO. 2020).

Recently, worldwide aquaculture production has been gradually increasing as a facility and key to improving world fish production (FAO, 2012; FAO, 2014; FAO, 2019; FAO. 2020). However, the biggest obstacle to fish production is the need to strike a balance between high fish growth and optimum use of the feed provided (Ajani et al., 2011). For example, in fish nutrition, minerals are essential for growth performance and immunity, especially essential elements such as Fe, Zn, Cu, Mn, Sr, Se are the most crucial supplements, but

[1] Note: This study was carried out as a part of PhD studies of Shokri Omar Mustafa MUSTAFA

require small amounts. Otherwise, increasing the amount of elements in the formula may cause toxicity in fish (Jiang et al., 2016).

Zinc is recognized as a fundamental trace element for the normal development and growth of fish. They absorb zinc from both water and dietary sources, moreover, dietary Zn is more efficiently benefited (Lall, 2002; Lim and Webster, 2001; Feng et al., 2011). Fish receive minerals from the water they live in through their skin, gill and lateral lines. Zinc is an element of moderate bioavailability. 25-75% of zinc in the diet can be utilized. Dietary phosphorus, calcium, protein source, phytic acid levels and zinc form influence the digestibility of dietary zinc. Phytate acts a complex with movement cations such as manganese, iron and zinc, in the intestinal system and averts their absorption. . In addition, the complexing of zinc to phytates is promoted by calcium.(Lim et al., 2001). Moreover, a study shows that zinc uptake is significantly increased in different tissues after adding methionine in the formulation ratio (Kaur et al., 2019).

The dietary zinc requirement of carp under normal conditions in terms of purified diets containing different amounts of zinc were found to affect not only the appetite, growth rate and mortality, but also the levels of zinc, iron, and copper in the tissues, it has suggested that the approved level of zinc is 15 to 30 mg of the dry diet (Ogino & Yang, 1978). However, the insufficiency symptoms of zinc were found to be slow growth, cataract, fin and skin erosion, and high mortality in the feeds containing 1 mg/kg Zn. Zinc deficiency also affects protein and carbohydrate digestion by reason of reductions in carboxypeptidase activities (Ogino & Yang, 1978; Watanabe et al., 1997). Therefore, fish feed producers should be very careful when including the exact amount of elements to their diets (Balachandran, 2001; Akram et al., 2019).

Currently, zinc oxide (ZnO, 72% Zn) and zinc sulfate monohydrate ($ZnSO_4 \bullet H_2O$, 35% Zn) are the most commonly used zinc sources in the feed production industry. Mostly, 80-90 % ZnO is used are zinc chloride ($ZnCl_2$, 48% Zn), zinc carbonate ($ZnCO_3$, 52% Zn), and zinc sulfate heptahydrate ($ZnSO_4$. $7H_2O$, 22% Zn) (Jeng and Sun., 1980). The common carp is considered to be a very important aquaculture species in many Asian and some European countries. It is an importance aspect to increase the growth rate of carp juveniles by feeding (Khan et al., 2016; FAO, 2019).

The purpose of present study was to determine weight gain, proportional growth in weight, specific growth rate, feed conversion rate and condition factor in juvenile *C. carpio* fed practical diets containing different levels of zinc (T1, control, 85 mg Zn kg^{-1}; T2, 105 mg Zn kg^{-1}; T3, 125 mg Zn kg^{-1} and T4, 145 mg Zn kg^{-1}).

2. Materials and methods

Experimental procedures were performed following the approved guidelines of the Firat University Ethical Committee.

In this study, a basal diet containing 35 ± 0.02 % crude protein, 6 % crude fat and 4,300 kcal/kg gross energy was used (Table 1). Nutritional requirements was prepared by considering the requirements of the common carp fish juvenile (NRC, 1993). Then, diets containing zinc sulfate monohydrate ($ZnSO_4 \bullet H_2O$, 35% Zn) in different amounts (T1, control, 85 mg Zn kg^{-1}; T2, 105 mg Zn kg^{-1}; T3, 125 mg Zn kg^{-1} and T4, 145 mg Zn kg^{-1}) were formed. The percentage of dry matter, crude protein, crude fat, gross energy (kcal/kg), crude ash, crude cellulose, lysin, methionine, calcium and phosphorus of experimental diets and control were given in Table 1. In addition, the percentage content of fish meal, soybean meal, yellow corn, wheat flour, oil, vitamin mix and mineral mix of control diet used in the present study were given in Table 2.

Table 1. The proximate composition of the basal diet, (% as is).

Diet Items	%
Dry Matter	92.4
Crude protein	35
Crude Fat	6
Gross Energy (kcal/kg)	4,300
Raw Ash	7
Raw Cellulose	3.5
Lysine	1.9
Methionine	0.7
Calcium	1.5
Phosphorus	1.2

Table 2. Composition of the basal diet, %.

Items	%
Fish Meal	20.0
Soybean Meal	35.0
Yellow Corn	21.5
Wheat flour	20
Fish oil	2.0
Vitamin Mix	1.0
Mineral Mix	0.5
Total	100

Vitamin Mix: Vitamin A 3.22 (I.U/100 g fillet), Vitamin D 208.40 (I.U/100 g fillet), Vitamin E 0.16 (I.U/100 g fillet), Vitamin K 0.16 (I.U/100 g fillet), and Vitamin C 1200 mg/kg.
Minerla Mix mg/g: Fe 50, Cu 3, Co 0.01, Mn 20, I 0.1 and Se 0.1

In this study, a total of 240 carp juvenile (11.7 ±0.4 g in weight and 9 ±0.3 cm in length) were used. Carp juveniles were provided from the Government Water Management Affairs of IX. Area Directory, Keban, Elazığ, TURKEY. This study was carried out with three replicates. 20 carp juveniles were placed in each aquarium (143 cm X 37 cm X 30 cm). Fish were acclimated to conditions of the experiment for two weeks. Fish were fed commercial feed during acclimation period. The experiment was designed in 158 L water containing 12 aquariums with replicate per treatment, each aquarium supplied with well-aerated and dechlorinated tap water for 7 weeks. Two hundred and forty juveniles (11.8 ± 0.1 g) were randomly distributed into 4 treatment groups with each replicates.

The water temperature was maintained at 27 ± 1°C, pH= 7–8, dissolved oxygen (DO) > 6 mg/L, total ammonia < 0.6 mg/L and water Zn < 2.2 mg/L. Each aquarium continuously aerated and experiment performed under the natural photoperiod. The daily feed amount to be given to the juveniles was calculated according to following formula. It was given in two meals a day at equal intervals for 60 days.

The daily Feed Amount= Feeding Coefficient x Total Fish Weight / 100 with considering water temperature (Song-bo et al., 2012)

The basal diet was provided from a commercial juvenile carp feed producer (GÜRDAL YEM, Kahramanmaraş, http://www.gurdalyem.com.tr/). The content analysis of the experimental pellets was carried out by "Kahramanmaraş Sütçü İmam Üniversitesi Üniversite-Sanayi-Kamu İşbirliği Geliştirme Uygulama ve Araştırma Merkezi (ÜSKİM) Laboratuvarları".

The ration element was mixed until they become a completely homogeneous mixture and they were dough together with the water added to the mixture in a ratio of 1/1. The pulp material was pelleted by passing through the mincing machine. The prepared pellets were placed in trays and dried in a feed oven at 60 ºC for 24 hours.

Pellet size was prepared taking into consideration the weight of the fish. The rations were stored in plastic containers for use at 4 ºC.

The following growth performance parameters were investigated in the present study:

2.1. Weight Gain

Following method specified by NRC (1993) was used to determine the weight gain of the fish.

Weight Gain (WG, g) = Final weight (g) – intial weight (g)

Average daily weight gain (ADG) was also determined as below (Panase and Mengumphan 2015):

Average daily weight gain (ADG) = (final weight – intial weight)/ Days

2.2. Live weight gain

Live weight gain (LWG); was obtained by subtracting the average weight at the beginning of the period from the average absolute weight of the fish at the end of the period. The average live weight was found by dividing the total weight by individual number.

LWG = Wt-Wt-1 Wt: Average absolute weight at the end of the period (g) Wt-1: Average absolute weight per period (g) (NRC 2011):

OB = [(Wt-Wt-1) / Wt-1] x 100 (Skalski et al., 2005)

OB = Proportional Growth

Wt: Average weight at the end of the period (g).

Wt-1: Average weight per period (g).

2.3. Specific Growth Rate

The specific growth rate (SGR) refers to what percentage of the fish's own weight grows in one day. The specific growth rate (SGR) was found in the following equation:

G = [(In W2 – In W1) / (t2 – t1)] X 100

Where W1 and W2 are body weight at the start and end of the growth period respectively, and t2 – t1 is the length of the period in days (Jobling, 1994).

2.4. Feed Conversion Rate

The feed conversion ratio (FCR) is used to determine how much feed is consumed for one unit body weight gain. The total amount of feed consumed during the trial and the total LWG provided by the fish in each period was determined.

The feed conversion ratio was worked out according to the following formula (Jhingran, 1991):

Feed conversion ratio = quantity of feed taken (g) /weight increased (g)

2.5. Condition Factor

The Condition Factor (CF) was found by the following equation (Skalski et al., 2005):

$CF = (W / L^3) \times 100$

CF = Condition factor

W: Total weight of the fish (g).

L: Total length of the fish (cm).

2.6. Statistical Analysis

Using SPSS program to analyses the data. One-way variance analysis was employed to test effects of the diets on growth and feed utilization parameter. Duncan's Multiple Range Test (Duncan, 2007) was applied to compare the significance of the various parameters among the tested treatments.

3. Results

Supplementation of zinc sulfate monohydrate in the diet of juvenile common carps improved weight gain, proportional growth in weight, specific growth rate, food conversion rate, and condition factor. The best result was obtained from the fish fed with T2. In addition, the final length and weight of juveniles fed all Zn-supplemented diets increased significantly compared to the control. No mortality was observed in any treatments.

It was found that the juveniles of the common carp fed with T2 (105 mg/kg^{-1}) exhibited the highest growth performance in terms of final weight, weight gain, final length, feed utilization efficiency, FCR, SGR and ADG parameters (Table 3). On the other hand, the lowest growth was obtained when the juveniles fed with basal diet containing 85 mg Zn/kg^{-1}. This difference was statistically significant ($P<0.05$).

It was also found that the feed conversion efficiency as regars FCR, SGR and ADG was higher in fish fed with feeds containing different Zn levels, in fish fed with 105 and 125 mg Zn/kg-1 diet, compared to those fed with diets having 85 and 145 mg Zn/kg-1 (Table 3). It was also determined that feed intake was increased with increasing dietary zinc concentrations up to 105 mg/kg^{-1}diet.

The findings also showed that feed utilization efficiency was closely related to growth performance. In the present study, FCR, SGR and ADG improved with increasing dietary zinc levels (Table 3).

Table 3. Number of fish, mean initial and final weight, mean initial and final length, LWG, feed intake, FCR, SGR and ADG of the juveniles

Parameters	T1 (Control)	T2	T3	T4
Number of fish	60	60	60	60
Mean initial weight (g)	11.7 ± 0.4	11.7 ± 0.4	11.7 ± 0.4	11.7 ± 0.4
Mean final weight (g)	28,44 ± 0,09^{c}	40,89 ± 0,17^{a}	29,49 ± 0,15^{b}	28,82 ± 0,25^{c}
Mean initial length (cm)	9 ± 0.3	9 ± 0.3	9 ± 0.3	9 ± 0.3
Mean final length (cm)	11.4 ± 0,4	15 ± 0,27	12.7 ± 0,54	11.5 ± 0,45
LWG (g)	16.74	29.19	17.79	17.12
Feed intake	58.53^{a} ± 0.05	58.53^{a} ± 0.05	58.53^{a} ± 0.05	58.53^{a} ± 0.05
FCR	3.3 ^{abc} ± 0.13	1.5 ^{a} ± 0.05	2.5 ^{b} ± 0.10	2.9 ^{b} ± 0.11
SGR	26.7 ^{abc} ± 1.00	57.7 ^{a} ± 0.05	34.4 ^{a} ± 0.08	30.2 ^{b} ± 0.09
ADG	0.26 ^{abc} ± 0.04	0.57 ^{a} ± 0.01	0.34 ^{a} ± 0.02	0.30 ^{b} ± 0.03

^{a,b,c} Means with superscripts in the same row are significantly different at $P<0.05$.

4. Discussion

In aquaculture farms fish are subjected to various conditions such as intensive stocking, inappropriate, handling, and forced feeding with unnatural feeding regime (Kumar et al., 2014, 2016; Kumar et al., 2017a). Supplying artificial diets with vital elements is a crucial aquaculture activity for sustaining average development performance, appropriate physiological conditions, and maximize fish immunity versus abiotic and biotic factors (Kumar et al., 2017a; Khalil et al.,2019; Kumar et al., 2020ab). Zinc is known as the second microelements in the animal body and is involved in various enzymatic activities of fish metabolism (Zalewski et al., 2005; Rajan et al., 2016; Tawfik et al., 2017; Uniyala et al., 2017). On the other hand, zinc cannot be accumulated in the fish, so regular dietary Zn intake, thus, is an obligatory (Case and Carlson, 2002; Zalewski et al., 2005). Therefore, fish get trace elements from feed and water. It also illustrates that decreased gill sodium points in copper exposed fish and oedema of the principal epithelium, which characteristically existed in both levels of zinc disclosure (Kumar et al., 2020ab).

The effect of dietary tricalcium phosphate on zinc convenience to the juveniles of common carp (2-3 g on average) and rainbow trout were investigated by Satoh et al. (1992). They found that tricalcium phosphate was reduced zinc retention in carp vertebrate, on the other hand, the grow rate of carp fish was much weaker than rainbow trout. Therefore, Satoh et al. (1992) suggested that this may be due to the absence of the stomach in carp which cannot dissolved tricalcium phosphate. Moreover, Sallam et al. (2020) found that the improving growth performance of rabbitfish (*Siganus rivulatus*) by adding Zn-Met and ZnO-NPs was superior to ZnO in diet and innate immune response.

Rahman et al. (2018) indicated that the adequate level of zinc supplementation (10 mg/kg) into the dietary feed of *Labeo rohita* fish affected positively the growth rate of this species. Furthermore, according to Zenhom (2020) the requirements of zinc for common carp fry with an average 1.0 ± 0.01g is 15-30 mg Zn/kg^{-1} dry ration in order to improve feed utilization efficiency, growth performance, minerals contents in fish muscle, and body composition (Zenhom, 2020). On the other hand, (Zenhom,2020) did not investigate the effect of dietary zinc more than 35 mg Zn/kg^{-1} on carp juveniles. Similarly, the present study also clearly indicated that the juvenile common carp (with an average 9 ±0.3g) requires 105-125 mg Zn/kg^{-1} dry diet to improve growth parameters and feed utilization efficiency. These findings showed that the dietary Zn demand of the common carp juveniles was lower than some other fish species such as trout (Satoh et al., 1992).

Positive effects of dietary zinc have also been observed for fish and crustaceans in some other studies. For example, the growth rate, survival and immunity of freshwater prawn *Macrobrachium rosenbergii* was improved at ZnO-NPs (30 mg kg−1) by (Muralisankar et al., 2014). In addition, the development and haematological parameters of the grass carp were increased with 30 mg kg−1 ZnO-NPs dietary addition by (Faiz et al., 2015). Dietary zinc also improved the growth rate, bone mineralization and stress response in the early age of gilthead seabream under feed enhancement (Izquierdo et al., 2016). Similarly, the positive effects of dietary zinc have also been observed for the common carp juveniles in the present study. The results showed that zinc supplementation resulted in significantly better fish live body weight, weight gain, feed conversion rate, proportional growth in weight, condition factor, specific growth weight.

Sarker and Satoh (2008), showed that WG and SGR in the fingerlings of rainbow trout did not illustrate any significant difference among treatments of Zn throughout the culture period. However, the zinc levels of 55 and 103 µg/g have influenced bone mineralization in the fingerlings of rainbow trout (Sarker and Satoh, 2008). On the other hand, in the present study, FCR, SGR and ADG parameters had enhanced with increasing nutritional zinc amounts up to a certain point (105 mg Zn kg^{-1}). A similar trend was found in tilapia fish by Tawfik et al. (2017). This discrepancy can be clarified by the fact that the fish Zn demand changes with age, development period, season and physiological status (i.e., ripening period and health). However, different supplemental Zn provenances can also control its demand for regular development; wound healing and further immune parameters of the common carp juveniles (Zalewski et al., 2005).

Sallam et al. (2020), recently investigated the effect of addition from various Zn resources (organic, inorganic, and nano-particle Zn) on development performance in *S. rivulatus*. They found that the development performance and ration use of *S. rivulatus* consumed Zn-included diets exceeded the control fish, and Zn-Met and ZnO-NPs are better development stimulators than ZnO in mass form. Furthermore, Kumar et al., (2020ab) found that, high amounts of ZnO-NPs indicated that a sensitive toxicity in fish. For example, more than 200 mg ZnO-NPs k-1 caused destructive modifications on the cellular and metabolic actions in carp and trout. In

a different study, García- Gómez et al. (2020), stated that high amount of ZnO-NPs can also exposed fish cells line that showed casing occupation commotion and unstable molecules that cause damage to DNA in the cells of rabbitfish (*Siganus rivulatus*).

5. Conclusion

The key successful of aquaculture production sector is that related to improve the nutrition because it is a major footstep beginning for succeeds the enterprise of the common carp, as nutrition corresponds to the highest outfitted cost between 65-70% in the aquaculture management (Ghanawi et al., 2011). Especially in aquaculture conditions, diet supplemented with different levels of zinc can improve overall physiological condition, growth performance and economic income in common carp farm (Sallam et al., 2020; Fayed et al., 2019; Khalil et al., 2019).

Based on the results of the present research, it is possible to significantly improve growth rate, LWG, FCR, SGR, and condition factor by using convenient level of zinc in carp fish juvenile diet (105 mg/kg). On the other hand, basal diet containing 85 mg Zn/kg^{-1} causes the lowest growth. Further researches are required to investigate the zinc demands of different juvenile size of carps. In addition, the differences in dietary Zn demands among fish species can be due to the adaptive mechanism of metal absorption and utilization in their habitats when the results obtained in this study are compared with the results of other studies in the literature. Therefore, the features and structures of developmental adaption to mineral demand of fish need more research in advance. Therefore, further research is needed on the characteristics and structures of the developmental adaptation of fish to mineral demand.

References

Abou-Daoud, Y., Ghanawi, J., Farran, M., Davis,D., Saoud, I. (2014). Effect of dietary protein level on growth performance and blood parameters of marbled spinefoot, *Siganus rivulatus*. *Journal of Applied Aquaculture* 26, 103–118

Ajani, F., Dawodu, M.O., Bello-Olusoji, O.A. (2011). Effects of feed forms and feeding frequency on growth performance and nutrient utilization of *Claria sgariepinus* fingerlings. *African Journal of Agricultural Research*, 6 (2), 318- 322.

Akram, H., Fatima, M., Sha S.Z.H, Afzal, M., Hussain, S.M., Hussain, M., Iqbal Khan, Z., Akram, K.H. (2019). Dietary zinc requirement of *Labeo rohita* juveniles fed practical diets. *Journal of Applied Animal Research*, 47 (1).

Balachandran, K.K. (2001). Post-Harvest Technology of Fish and Products, Daya Publishing House, Delhi, 77.

Barakat, A., Roumieh, R., Abdel Meguid, N., Ghanawi, J., Saoud, I.P. (2011). Feedregimen affects growth, condition index, proximate analysis and myocyte ultrastructure of juvenile spinefoot rabbitfish, *Siganus rivulatus*. *Aquaculture Nutrition*, 17, 773–780.

Borgwardt, F., Unfer, G., Auer, S., Waldner, K., El-Matbouli, M., Bechter T (2020)..Direct and Indirect Climate Change Impacts on Brown Trout in Central Europe: How Thermal Regimes Reinforce Physiological Stress and Support the Emergence of Diseases. *Frontiers in Environmental Science* 8, (59) doi: 10.3389/fenvs.2020.00059

Case, C., Carlson, M. (2002). Effect of feeding organic and inorganic sources of additional zinc on growth performance and zinc balance in nursery pigs. *Journal of Animal Science* 80:, 1917–1924.

Chupan, L., Zusková, E., Niksirat, H., Panáček, A., Lünsmann, V. Haange, S.B., Bergen, M.V., Jehmlich, N. (2017). Effects of chronic dietaryexposure of zinc oxide nanoparticles on the serum protein profile of juvenile common carp (*Cyprinus carpio* L.). *Science of The Total Environment*, 579 (1), 1504-1511.

Faiz, H., Zuberi, A., Nazir, S., Rauf, M., Younus, N. (2015). Zinc oxide, zinc sulphate and zinc oxide nanoparticles as source of dietary zinc comparative effect ongrowth and hematological indices of

juvenile Grass Carp (*Ctenopharyngodon Idella*) *International Journal of Agriculture and Biology* (17), 568-574

FAO. (2012). The State of World Fisheries and Aquaculture 2012 – Meeting the sustainable development goals. Rome.Licence: CC BY-NC-SA 3.0 IGO.

FAO. (2014). The State of World Fisheries and Aquaculture 2017 – Meeting the sustainable development goals. Rome.Licence: CC BY-NC-SA 3.0 IGO.

FAO. (2019). The State of World Fisheries and Aquaculture 2019 – Meeting the Sustainable development goals. Rome. Licence: CC BY-NC-SA 3.0 IGO.

FAO. (2020). The State of World Fisheries and Aquaculture 2020 – Meeting the Sustainable development goals. Rome. Licence: CC BY-NC-SA 3.0 IGO.

Fayed, W.M.A., Khalil, R.H., Sallam, G.R., Mansour, A.T., El-khayata, B.K. Omar, E.A., (2019). Estimating the effective level of Yucca schidigera extract for improvement of the survival, haematological parameters, immunological responses and Water quality of European seabass juveniles (*Dicentrarchus labrax*). *Aquaculture Reports* (15), 100208.

Feng, L., Tan, L.N., Liu, Y., Jiamg, W.D., Hu, K. Li, S.H. and Zhou, X.Q., (2011). Influence of dietary zinc on lipid peroxidation, protein oxidation and antioxidant defence of juvenile Jian Carp (*Cyprinus Carpio Var Jian*). *Aquaculture Nutrition Journal*. (17), 875-882

García-Gómez, C., García, S., Obrador, A., Almendros, P., González, D. Fernández, M.D., (2020). Effect of ageing of bare and coated nanoparticles of zinc oxide applied to soil on the Zn behaviour and toxicity to fish cells due to transfer from soil to water bodies. *Science of The Total Environment* 706, 135713.

Ghanawi, J., Roy L., Davis, D.A., Saoud, I.P. (2011). Effects of dietary lipid levels on growth performance of marbled spinefoot rabbitfish *Siganus rivulatus*. *Aquaculture* 310, 395-400

Jeng, S.S,, Sun, L.T. (1980). Effects of dietary zinc levels on zinc concentrations in tissues of common carp. *National Taiwan Ocean University*. 134-140.

Jhingran, V.G. (1991). Fish and Fisheries of India, *3rd ed. Hindustan Publishing Corporation, Delhi, India* 727

Jiang, H., Qin, D., Mou, Z.H., Zhao, J., Tang, S. Wu, S., & Gao, L. (2016). Trace elements in farmed fish (*Cyprinus carpio, Ctenopharyngodonidella and Oncorhynchus mykiss*) from Beijing: implication from feed, Food Additives and Contaminants: Part B, 9 (2), 132-141, doi: 10.1080/19393210.2016.1152597.

Jobling, M. (1994). Fish Bionergetics book, *First edition, Edmundsbury Press St. Edmunds. Suffolk.* ISBN 0421 58090 X.

Kaur, J., Singh, A., Datta, S.N. (2019). Methionine Modulated Bioavailability of Inorganic Zinc (ZnSO4. 7H2O) in Common Carp (*Cyprinus carpio L*) Through Diets Containing Tricalcium Phosphate. *International Journal of Environment, Agriculture and Biotechnology* 4(4),

Khalil, H.S., Mansour, A.T., Godaa, A.M.A., Omar, E.A. (2019). Effect of selenium yeast supplementation on growth performance, feed utilization, lipid profile, liver and intestine histological changes, and economic benefit in meagre, *Argyrosomus regius*, fingerlings. *Aquaculture* 501, 135–143.

Khan, M.N., Shahzad, K., Chatta, A., Sohail, M., Piria. M. Treer, T. (2016). A review of introduction of common carp *Cyprinus carpio* in Pakistan: origin, purpose, impact and management. *Croatian Journal of Fisheries*, 71-80.DOI: 10.1515/cjF-2016-0016.

Kumar, N., Ambasankar, K., Krishnani, K., Bhushan, S., Minhas, P. (2016). Dietary pyridoxine protects against stress and maintains immune-hematological status in *Chanos hanos* exposed to endosulfan. *Basic and Clinical Pharmacology and Toxicology* 119, 297-308

Kumar, N., Krishnani, K., Kumar, P., Singh, N.P. (2016a). Zinc nanoparticles potentiate thermal tolerance and cellular stress protection of *Pangasius hypophthalmus* reared under multiple stressors. *Journal of Thermal Biology* 70, 61-68

Kumar, N., Krishnani, K., Kumar, P., Jha, A.K., Gupta, S.K. Singh, N., (2 017a). Dietary zinc promotes immuno-biochemical plasticity and protects fish against multiple stresses. Fish Shellfish Immunol. 62, 184-194

Kumar, N., Krishnani, K.K., Singh,N.P. (2020ab). Effect of zinc on growth performance and cellular metabolic stress of fish exposed to multiple stresses. Fish Physiology and Biochemistry 46, 315-329

Lall, S.P. (2002). The minerals. In: Fish Nutrition, 3rd edn (Halver, J.E. & Hardy, R.W.eds). *Academic Press, San Diego*, CA. 259–308

Lim, C., Klesius., P.H.,Webster, C.D. (2001). The role of dietary phosphorus, zinc, and selenium in fish health in: Nutrition and Fish Health, (Lim C, and Webster CD eds.), *Food Products Press*, 201-212

Izquierdo, M.S., Ghrab, W., Roo, J., Hamre, K., Hernández-Cruz, C.M. Bernardini, G., Terova, G., Saleh, R., (2016). Organic, inorganic and nanoparticles of Se, Zn and Mn in early weaning diets for gilthead seabream (*Sparus aurata;* Linnaeus, 1758). *Aquaculture research Journal* 48(6), 2852-2867

Muralisankar, T., Bhavan, P.S., Radhakrishnan, S., Seenivasan, C., Manickam, N., Srinivasan, V., (2014). Dietary supplementation of zinc nanoparticles and its influence on biology, physiology and immune responses of the freshwater prawn, *Macrobrachium rosenbergii*. *Biological Trace Element Research* (160), 56–66

National Research Council (NRC). (1993). Nutrient Requirements of Fish, Washington, D.C, USA, *National Acedemic Press*, 114

NRC. (2011). Nutrient Requirements of Fish and Shrimp. *National Academy Press*, Washington, DC, 392.

Ogino, C., Yang, G.Y. (1978) Requirement of rainbow trout for dietary zinc. *Bulletin of the Japanese Society for the Science of Fish* (44), 1015-1018

Panase, P., Mengumphan, K. (2015). Growth Performance, Length Weight Relationship and Condition Factor of Backcross and Reciprocal Hybrid Catfish Reared in Net Cages. *International Journal of Zoological Research* 57, 64 doi: 10.3923/ijzr

Rahman, M.M., Rahman, R., Chowdhury, M.M. (2018). Evaluation of the Effects of Dietary Vitamin C, E and Zinc Supplementation on Growth Performances and Survival Rate of Rohu, *Labeo Rohita* (Hamilton, 1822). IOSR *Journal of Agriculture and Veterinary Science* (IOSR-JAVS) 11(2), 68-74

Rajan, T.S., De Nicola, G.R., Iori, R., Rollin, P., Bramanti, P. Mazzon, E., (2016). Anticancer activity of glucomoringin isothiocyanate in human malignant astrocytoma cells. *Fitoterapia* 110, 1-7

Roumieh, R., Barakat, A., Abdelmeguid, N.E., Ghanawi, J., Saoud, I.P. (2013). Acute and chronic effects of aqueous ammonia on marbled spinefoot rabbitfish, *Siganus rivulatus* (Forsskål 1775). *Aquaculture Research* 44, 1777-1790

Sallam, A.E., Mansour, A.T., Alsaquf, A.S., Salem, M.E. El-Feky, M.M.M. (2020). Growth performance, anti-oxidative status, innate immunity, and ammonia stress resistance of *Siganus rivulatus* fed diet supplemented with zinc and zinc nanoparticles. *Aquaculture Report*. 18. 100410.

Saoud, I.P., Kreydiyyeh, S., Chalfoun, A., Fakih, M. (2007). Influence of salinity onsurvival, growth, plasma osmolality and gill Na–K–ATPase activity inthe rabbitfish (*Siganus rivulatus*). *Journal of Experimental Marine Biology and Ecology* 348, 183-190

Saoud, I.P., Mohanna, C., Ghanawi, J. (2008) Effects of temperature on survival andgrowth of juvenile spinefoot rabbitfish (*Siganus rivulatus*). *Aquaculture Research* (39), 491-497

Sarker, M.S.A., Satoh, S. (2008) Effects of dietary phosphorus and zinc levels on growth artd bone mineralization in fingerlings of rainbow trout, *Oncorhynchus mykiss*. *Bangladesh Fisheries Research* 12(1), 01- 09

Satoh, S., Izume, K., Takeuchi, T., Watanabe, T. (1992). Mineral Nutrition in Fish-XXV.Effect of Supplemental Tricalcium Phosphate on Zinc and Manganese Availability to Common Carp. *Nippon Suisan Gakkaishi* 58(3), 539-545

Skalski, G.T., Picha, M.E., Gilliam, J.F., Borski, R.J. (2005). Variable Intake, Compensatory Growth, and Increased Growth Efficiency in Fish: Models and Mechanisms. Ecology 86(6), 1452–1462. http://www.jstor.org/stable/3450771

Song-bo, C.H., Wei-xing, C.H., Zhao-ting, F. (2012). Effect of Water Temperature on Feeding Rhythm in Common Carp (*Cyprinus carpio)* haematopterus Temminck et Schlegel). *Journal of Northeast Agricultural University* 19(1), 57-61

Tawfik, M., Moustafa, M., Abumourad, I., El-Meliegy, E., Refai, M. (2017).Evaluation of nano zinc oxide feed additive on tilapia growth and immunity. In: *15th International Conference on Environmental Science and Technology. Rhodes, Greece.*

Uniyala, S., Garga, A.K., Jadhava, S.E., Chaturvedib, V.K., Mohantaa, R.K. (2017). Comparative efficacy of zinc supplementation from different sources on nutrient digestibility,hemato-biochemistry and anti-oxidant activity in guinea pigs. *Livestock Science Journal* (204), 59–64.

Watanabe, T., Kiron, V., Satoh, S. (1997). Trace minerals in fish nutrition, *Aquaculture* 151, 185-207

Zalewski, P.D., Truong-Tran, A.Q., Grosser, D., Jayaram, L., Murgia, C., Ruffin, R.E.,. (2005). Zinc metabolism in airway epithelium and airway inflammation:basic mechanisms and clinical targets. A review. *Pharmacology and Therapeutics Journal* 105, 127-149

Zenhom, M.M., (2020). Dietary Zinc Requirement of common carp (*Cyprinus carpio*) Fry. *Abbassa International Journal for Aquaculture* 13(1), 177-190

FACTORIAL ANALYSIS OF QUICKLIME PRODUCTION FROM EGGSHELL

Salisu Nuhu

Department of Polymer Technology, College of Science and Technology, Hussaini Adamu Federal Polytechnic Kazaure, Jigawa State

Abstract:

This study developed empirical response surface models for optimizing the quicklime characteristics. The calcination process parameters evaluated were calcination temperature, calcination time, and eggshell particle size. Two process models were successfully developed and validated for RSM models. The modeling validation runs were within the 95% prediction interval of the developed models and their residual errors compared to the predicted values were less than 5%. Results from this study shows that the significant parameters that influenced the quicklime yield and reactivity are calcination temperature, calcination time and eggshell particle size. The RSM approach shows that a compromised setting of calcination temperature of 945.91^{o}C and calcination time of 180.82 min will produce quicklime of optimal yield of 99.6608 % and optimum level of calcination time of 210 min and calcination temperature of 895.03^{o}C produced optimum quicklime reactivity of 0.467835^{o}C/s. The RSM models developed in this study can be used in the quicklime production industries to find the settings of the calcination process that will maximize quicklime quantity and quality. This will reduce the downtime encountered by industries having problems caused by variation in the quality of purchased quicklime.

Key: Eggshell, 0ptimization, Calcination, Respones, Surface Methodology RSM

NEW APPROACH STUDY FOR THE EVALUATION OF EPDM RUBBER WASTE

Melisa Temiz

Konya Technical University, Faculty of Engineering and Natural Sciences, Chemical Engineering Department, Konya, Turkey., ORCID ID: https://orcid.org/0000-0002-4049-8179

Nimet Ozmeral

Konya Technical University, Faculty of Engineering and Natural Sciences, Chemical Engineering Department, Konya, Turkey., ORCID ID: https://orcid.org/0000-0003-3463-8697

Suheyla Kocaman

Konya Technical University, Faculty of Engineering and Natural Sciences, Chemical Engineering Department, Konya, Turkey., ORCID ID: https://orcid.org/0000-0001-5199-8577

Alaaddin Cerit

Necmettin Erbakan University, Konya Eregli Kemal Akman Vocational School, Textıle Clothıng and Leather Shoes Department, Konya, Turkey., ORCID ID: https://orcid.org/0000-0003-2414-2313

Gulnare Ahmetli

Konya Technical University, Faculty of Engineering and Natural Sciences, Chemical Engineering Department, Konya, Turkey., ORCID ID: https://orcid.org/0000-0002-9381-4139

Abstract

Ethylene propylene diene monomer rubber (EPDM) finds applications in several industrial branches due to its properties. EPDM (ethylene propylene diene monomer) is an important synthetic rubber and is used in many different sectors. In parallel with the increase in the amount of use, EPDM waste occurs. EPDM wastes are not likely to be remelted and reprocessed due to their cross-linking and are a significant loss for the plastics industry and are often consumed as fuel. Another method of evaluating EPDM residues is to reduce them to small sizes and use them as fillers in different polymers. In this study, new epoxy composites were created using EPDM waste filler. EPDM waste was used in bisphenol-A type epoxy resin at a ratio of 5-10-15-20-30 wt%, either alone or as a hybrid filler with nano-carbon black (CB). The EPDM:CB ratio was selected as 1:1, 1:3, and 3:1 by weight. The composites were prepared according to ASTM D 638 standards using the casting technique. Composites'morphology was characterized by Scanning Electron Microscopy (SEM). Effect of EPDM:CB ratio, filler amount, water sorption, and low temperature on the mechanical properties of the composites were investigated. In order to determine the effect of water sorption and low temperature, the samples were tested for 3-21 days. A decrease was observed also in the mechanical properties (tensile strength, e-modulus, and hardness) of 30 wt% filler composites formed with both EPDM and hybrid filler, considering the effect of low temperature (freezing) and water sorption. Moreover, the mechanical properties of composites decreased as the test time increased.

Keywords: epoxy resin, EPDM, composite

COMPARATIVE STUDY ON EPOXY-BASED NANOCOMPOSITES

Murat Işık

Konya Technical University, Faculty of Engineering and Natural Sciences, Chemical Engineering Department, Konya, Turkey., ORCID ID: https://orcid.org/0000-0003-0576-1071

Gulnare Ahmetli

Konya Technical University, Faculty of Engineering and Natural Sciences, Chemical Engineering Department, Konya, Turkey., ORCID ID: https://orcid.org/0000-0002-9381-4139

Abstract

Epoxies are usually reinforced using inorganic and organic nanofillers such as graphene, carbon nanotubes (CNT), nano silica, nanoclay (NC), polyimide, cellulose nanofibers, etc. CNTs are considered to be critical nanomaterials in various fields of nano-electronic components, chemical sensors, composite reinforcement materials, and film materials. The superiority of CNT especially is that the addition of even a small amount of CNTs into the composites can enhance their electrical conductivity, thermal, and mechanical properties. Nanoclays have become widely used reinforcing agents for epoxy and other polymer composites among various nanoparticles. This is because of their better mechanical performance, and montmorillonite is the most widely used in materials applications. The flame-retardant, antimicrobial, anti-corrosion and self-healing properties of polymer-clay nanocomposites are known, in addition, they are biocompatible and harmless to the environment. In this study, bisphenol A-type epoxy resin was modified with bio-based acrylated epoxidized soybean oil (AESO) in 90:10 and 85:15 ratios by weight. Hydroxyl functionalized *CNT* (CNT-OH) and montmorillonite-type NC were used as reinforcement in the epoxy matrix. The composites were prepared according to ASTM D 638 standards using the casting technique. Four point probe technique was used for electrical conductivity measurement. For thermal properties, Thermogravimetric analysis (TGA) was applied. The effect of AESO amount, filler type, and filler ratio on mechanical properties (such as tensile strength, e-modulus, and hardness), electrical conductivity, and thermal stability was investigated. Higher mechanical properties were achieved with NC. Increasing the AESO amount in epoxy resin caused a decrease in mechanical properties.

Keywords: epoxy resin, modification, CNT, nanoclay, composite

EVALUATION OF RUBBER WASTES IN COMPOSITES

Nimet Ozmeral

Konya Technical University, Faculty of Engineering and Natural Sciences, Chemical Engineering Department, Konya, Turkey., ORCID ID: https://orcid.org/0000-0003-3463-8697

Merve Turkben

Selcuk University, Faculty of Engineering, Chemical Engineering Department, Konya, Turkey., ORCID ID: https://orcid.org/0000-0002-5587-9126

Suheyla Kocaman

Konya Technical University, Faculty of Engineering and Natural Sciences, Chemical Engineering Department, Konya, Turkey., ORCID ID: https://orcid.org/0000-0001-5199-8577

Ulku Soydal

Selcuk University, Faculty of Sciences, Biotechnology Department, Konya, Turkey. ORCID ID: https://orcid.org/0000-0001-8894-3940

Gulnare Ahmetli

Konya Technical University, Faculty of Engineering and Natural Sciences, Chemical Engineering Department, Konya, Turkey., ORCID ID: https://orcid.org/0000-0002-9381-4139

Abstract

The composition of solid waste is divided into several types, including rubber waste. About 17,000,000 tons of scrap tires are generated in the world every year, and this amount is around 180,000-300,000 tons per year in Turkey. Most of the rubber waste produced comes from automobile, truck, and motorcycle tires. Only 40% of rubber waste is recyclable, excluding energy recovery and landfill applications. In 2018, the amount of rubber waste burned for energy recovery and disposed of in landfills was 7.2% and 3.4%, respectively. Reliable industrial technology and processes are needed to reuse and recycle these wastes. Processed waste can be transformed into cheaper and more sustainable materials. The cycle of producing new tires from used, worn rubber waste increases sustainability. The use of worn tires and scrap tire granules in new products is significantly. It helps reduce the carbon footprint by one-third compared to products made without recycled materials. Using waste tires as filler material to create new composites seems to be one of the most important methods of sustainable management. In this way, it can contribute to the reduction of the waste tire rubber amount after consumption. In this study, two-type of rubber wastes: ground tire rubber (GTR) and ethylene-propylene-diene monomer rubber (EPDM) was used as reinforcement in an epoxy matrix. Bisphenol A-type epoxy resin and its blend with polyurethane-modified epoxy in a 1:1 ratio were used as matrices. The effect of rubber and epoxy matrix type on composites' mechanical properties was investigated. Also, the effect of water sorption and low temperature on mechanical properties was studied.

Keywords: epoxy resin, tire waste, EPDM, composite

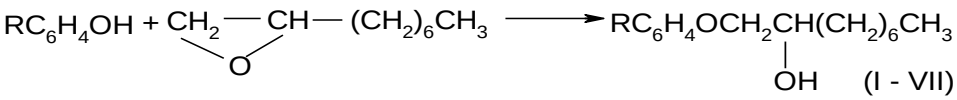
1,2- NONANDİOLUN FENOKSİ EFİRLƏRİNİN SİNTEZİ

Ədilə Mahmudova

Azərbaycan Dövlət Pedaqoji Universiteti, Analitik və üzvi kimya kafedrası, Baku , Azərbaycan, ORCID: https://orcid.org/ 0000-0003-2326-1994

Özet

Üzvi kimyanın ən aktual və perspektiv tədqiqat sahəsi arzu olunan xassələrər malik yeni bioloji aktiv birləşmələrin sintez və tədqiq edilməsidir. Bu baxımdan, tərkibində fenoksi qrupları olan poliefirlərin xassələrinin öyrənilməsi mühüm əhəmiyyət kəsb edir. Halogenhidrinlərin müxtəlif üzvi birləşmələrlə, xüsusən də əvəz edilmiş fenollarla kondensləşmə məhsulları dərman preparatlarının və sürtkü yağları üçün çoxfunksiyalı aşqarların sintezində qiymətli sintonlardır. Ariloksialkanolların bir çox törəmələri bioloji aktiv dərmanlardır və xalq təsərrüfatının müxtəlif sahələrində geniş istifadə olunur. 1,2-Nonandiolun yeni 1-aril efirlərinin sintezi və bəzi çevrilmələri həyata keçirilmişdir. Birləşmələr (I-VII) əsasi mühitdə 1-bromo-2-nonanol və heptiloksiran ilə əvəz edilmiş fenollardan 65-70% çıxımla sintez edilmişdir:



Iki fərqli metodla sintez edilən birləşmələrin (I–VII) fiziki-kimyəvi xassələri eyni idi. Spirtlər (I, III, IV) kristal maddələr, (II, V - VII) isə efir qoxusu olan şəffaf mayelərdir. Təmizlik dərəcəsi 99,0-99,6% təşkil edən birləşmələr (II, V-VII) QMX metodu ilə müəyyən edilmişdir. Birləşmələrin İQ spektrlərində (I – VII) OH qrupunun geniş udma zolaqları 3390 – 3440 sm-1 intervalında müşahidə olunur.

Açar sözlər: poliefirlər, fenoksi efirləri, ariloksialkanollar, antimikrob aşqarlar

SYNTHESIS OF 1,2-NONANEDIOL PHENOXY ETHERS

Abstract

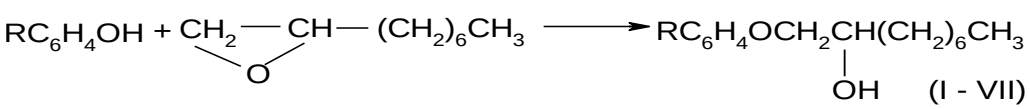
The most relevant and promising area of research in organic chemistry is the creation of new bioactive compounds with desired properties. In this regard, it is very important to study the properties of polyesters containing phenoxy groups.

The condensation products of halohydrins with various organic compounds, in particular with substituted phenols, are valuable intermediates in the synthesis of drugs and multifunctional additives for lubricating oils.

Many derivatives of aryloxyalkanols are biologically active drugs and are widely used in various sectors of the national economy.

The synthesis and some transformations of 1-aryl esters of 1,2-nonanediol, which have not yet been studied, have been carried out.

Compounds (I–VII) were synthesized in 65–70% yield from 1-bromo-2-nonanol and substituted phenols with heptyloxirane in basic medium:



The physicochemical parameters of compounds (I–VII) synthesized by two independent routes were identical.

Alcohols (I, III, IV) are crystalline substances, and (II, V - VII) are transparent liquids with an ethereal smell. The degree of purity of compounds (II, V–VII), which is 99.0–99.6%, was determined by GLC.

In the IR spectra of compounds (I – VII), broad absorption bands of the OH group are observed in the region of 3390 – 3440 cm^{-1}.

Keywords: polyethers, phenoxy ethers, aryloxyalkanols, antimicrobial additives

MOLTEN CAUSTIC SALT ELECTROLYSIS OF FERROUS Ti/Mn WASTE BY MICROWAVE RADIATED BATH

Y. I. TOSUN

Şırnak University, Engineering Faculty,Mining Engineering Department, Şırnak, Orcid.org/0000-0003-2515-6637

ABSTRACT

The molten salt electrolysis of ilmenite, pyrolusite, manganite waste sludges contained low level Ti, Mn metal content as ferrous waste ore in Mining of Zn and Lead ores in Hakkari and Siirt Province. The molten caustic salt electro winning of low metal contents become a great advantageous recovery for ferroalloy production. However the necessity of calcium and carbon for reduction of high ferrous Mn and Ti alloys are provided by Şırnak asphaltite slime and the Zn and lead bearing ore waste. Even molten electrolysis of waste effluent acidic liquors and the metal containing sludge were neutralized by lime oxidizing as alkaline washing prior to electrolysis. Molten salt electrolysis at 600 ºC provided high iron ferrotitanium production at suitable yields rates as reduced metal alloys content of batch tests. The batch tests with the waste lead-zinc ore at 600 ºC by use 3/1 coal waste slime and 10/1 lime salt per waste weight improved metal recoveries over 54% feTi and 67% feMn.

Keywords: Salt elektrolysis, Recovery of heavy metals, microwave melted salt, biochar, elctrolysis waste granules, hazardous industrial waste, Asphaltite sludge, ferrotitanium, ilmenite sludge waste, ferrous metal waste

DEMİRLİ ÇİNKO/TİTANYUM/ MANGANEZLİ CEVHER ATIKLARININ MİKRODALGADA ERİMİŞ KOSTİK İÇERSİNDE ELEKTROLİZ KULLANILARAK DEĞERLENDİRİLMESİ

ÖZET

Hakkari ve Siirt İli Kurşun çinko cevherleri madenciliğinde demirli atık cevherler olarak ilmenit, piroluzit, manganit atık çamurları üretilmektedir. Bunların erimiş tuz elektrolizi düşük seviyedeki Ti, Mn metal içeriğini değerlendirebilmektedir. Düşük metal içeriklerinin erimiş kostik tuzu elektrolizi ile geri kazanımı, ferro alaşım üretimi için büyük bir avantaj sağlamaktadır. Ancak yüksek demir içerikli Mn ve Ti alaşımlarının indirgenmesi için kalsiyum ve karbon ihtiyacı olmaktadır. Bunlar Şırnak asfaltit toz atıkları ile Zn ve kurşun içeren cevher atıkları tarafından sağlanmaktadır. katı atık karışımın ve asidik likörlerin erimiş tuz elektrolizden önce alkali yıkama olarak kireç ile oksitlenerek nötrleştirilmektedir. 600 ºC'de erimiş tuz elektrolizi testlerinde indirgenmiş metal alaşım içeriği uygun verim oranlarında elde edlmiş ve yüksek demir içereren ferrotitanyum üretimi sağlanmıştır. Atık ağırlığı başına 3/1 kömür atığı balçık ve 10/1 kireç tuzu kullanılarak 600 ºC'de atık kurşun-çinko cevheri üzerinde yapılan toplu testlerde, metal geri kazanımları %54 feTi ve %67 feMn üzerinde gerçekleşmiştir.

Anahtar Kelimeler: Tuz elektolizi, Ağır metallerin kazanılması, mikrodalga eritilmiş tuz, biochar, atık granül elektrolizi, tehlikeli endüstriyel atık, Asfaltit çamur, ferrotitanyum, ilmenite çamur atığı, demirli metal atıkları

MICRO JET GRINDING OF WASTE SLAG, SOOT CARBON OF WASTE TYRE, WASTE SOOT OF COAL BOILERS BY MICROWAVE RADIATION

Y. I. TOSUN

Şırnak University, Engineering Faculty,Mining Engineering Department, Şırnak, orcid.org/0000-0003-2515-6637

ABSTRACT

The waste tire slag soot as waste sludge contained high black carbon content as carbon source required micronized grinding in micro jet mill. The pressurized nitrogen flow grinding of in spiral jet mill was tested for grinding for soot waste in Şırnak Province. The ground contents become a great advantageous recovery for black carbon production. However the necessity of spiral jet mill for reduction of high slag size soot of waste tire over 100 micron provided by coal boiler soot. Microwave radiated cycling zone, spiral jet zone length, rotor blade designs in the glove chamber isolators of spiral jet mill were different for the laboratory test jet mill, cage blade mill, pin mills. The two powered co-micronized grinding process are integrated. The micronized grinding under high size reduction rates reduces the feed size of 74 micron waste slag soot to below 5 micron.

Keywords: Micro Jet Grinding,Waste Slag, Soot Carbon, Waste Tyre, Coal Boiler Soot, Microwave Radiation

ATIK LASTİK KURUM KARBONUNUN VE KÖMÜR KAZANLARININ UÇUCU ATIK KURUMUNUN MİKRODALGA RADYASYONU İLE MİKRO JET ÖĞÜTMESİ

ÖZET

Atık kazan is çamurlarının karbon kaynağı olarak yüksek siyah karbon içeriği içerdiğinden ve atık lastik cürufu kurumunun mikro jet değirmende mikronize öğütülmesi gerekmektedir. Şırnak ilinde kazan kurum atığının öğütülmesi için spiral jet değirmeninde basınçlı azot akışıyla kurumun mikronize jet öğütülmesi test edilmiştir. Atık lastik kurumunun karbon içeriği, siyah karbon üretimi için büyük bir avantajla geri kazanılabilmektedir. Ancak kömür kazanı kurumunun ve atık lastik kurumunun oluştuğu 100 mikronun üzerindeki topak boyut büyük cüruf boyutlu kurumların mikronize jet değirmende öğütülerek değerlendirebilecektir. Laboratuvar testlerinde spiral jet değirmeni tasarımı da irdelenmiştir. Kafes kanatlı değirmen, pimli değirmen için spiral jet değirmenin öğütme odası izolatörleri, mikrodalga döngü bölgesi, spiral jet bölge uzunluğu, rotor kanat tasarımları farklı olmaktadır. iki güç iletimli mikronizasyon süreci entegre edilmiştir. Yüksek boyut küçültme oranları altında mikronizasyon ile atık cüruf kurumunun 74 mikronluk besleme boyutunu 5 mikronun altına düşürülebilmiştir.

Anahtar Kelimeler: Mikro Jet Öğütme, Atık Cüruf, Kurum Karbon, Atık Lastik, Kömür Kazanı Kurum, Mikrodalga Radyasyonu

ECO-FRIENDLY SULFONYLHYDRAZONE SYNTHESIS WITH POTENTIAL BIOACTIVITIES AND THEORETİCAL CALCULATIONS

Leman MESİYAVA

Azerbaijan Technical University, Chemical technology, Recycling and ecology, Department, Baku, Azerbaijan, ORCID NO: 0000-0002-9908-7294

Ümmühan ÖZDEMİR ÖZMEN

Gazi University, Science Faculty, Department of Chemistry, Ankara, ORCID NO: 0000-0001-9161-9367

Ayla BALABAN GÜNDÜZALP

Gazi University, Science Faculty, Department of Chemistry, Ankara, ORCID NO: 0000-0002-5740-3674

Ebru AKTAN

Gazi University, Science Faculty, Department of Chemistry, Ankara, ORCID NO: 0000-0001-9412-9160

ABSTRACT

Pollution caused by chemicals is an important problem in the world and therefore environmentally friendly chemicals and materials are needed. Sulfonic acid derivatives were used to prepare environment-friendly chemicals and materials such as pesticides, scale, and corrosion inhibitor compounds and polymer nanofibers. In addition, sulfonylhydrazones derived from sulfonic acid hydrazide have distinctive biological and pharmaceutical properties such as antibacterial, diuretic, antitumor, antiviral, antineoplastic activity, carbonic anhydrase, and choline esterase enzyme inhibition.

Since the excess hydrazine used in the synthesis of sulfonylhydrazones is both an expensive reagent and highly toxic, it must be isolated and purified from the product. Therefore, in the recent synthesis methods, sulfonylhydrazones have been obtained using a reduced amount of hydrazine with green solvent and mild reaction conditions and an environmentally friendly approach.

In our study, 2-OH-4-metoxy-acetophenonethanesulfonylhydrazone (4MeO-afesh) was synthesized by one-pot reaction method in this approach. The structure of the compound was characterized by elemental analysis and spectroscopic (FT-IR, ^{1}H-NMR) methods, respectively. Quantum chemical calculation is also an effective way to study the molecular structure and structural properties of inorganic and organic compounds besides experimental methods. In continuation of this work, the molecular structure of 4MeO-afesh was determined by computational studies. The structure of the newly synthesized 4MeO-afesh molecule, which is a sulfonamide derivative, was optimized with DFT/B3LYP method and 6-31+G (d,p) basis set. After determining the stable structure of the synthesized molecule, HOMO and LUMO energies, chemical reactivity descriptors and molecular electrostatic potential (MEP) map were examined with the same basis set. All calculations were performed using Gaussian 09 package program. As a result, this study will be useful to a scientist who wants to investigate the details of the molecule.

K**eywords**: Sulfonyl hydrazone, One-pot reaction, Green Chemistry, Computational studies

INTRODUCTION

It is well-known that hydrazones exhibit a broad spectrum of biological activities such as antimicrobial, antitumor , antidepressant-like activities. Forexample; The reaserchers evaluated the antiviral activity of hydrazone derivatives against hepatitis A virus. 4-Fluorobenzoic acid ([5-bromothiophen-2-yl] methylene) hydrazide exhibited highest inhibitory activity against *Candida albican).*Nitroheterocyclic based 1,2,4-benzothiadizines was synthesized. The activity of this compound is tested successfully against virulent tubercle bacilli (H37Rv strain).

In organic synthetic chemistry, sulfonyl hydrazone compounds are important research compounds and have been widely used in the synthesis of various natural products and biologically active molecules in recent years

(1-7). In fact, some compounds containing the sulfonyl hydrazone structural unit are anti-carbonicanhydrase (8), anti-Alzhemier (9), anti-tumor (10,11) antifungal (12), anti-microbial(13), anti-tubercular (14), anti-depressant, (15) anti-arrhythmic, (16) anti-asthmatic (17) and other potential medicinal products value (Figure 1). In addition, some sulfonyl hydrazones with special structures can also be used as sensors (18,19). Therefore, it is very important to develop a mild, green and efficient method for the synthesis of sulfonyl hydrazone derivatives (20,21).

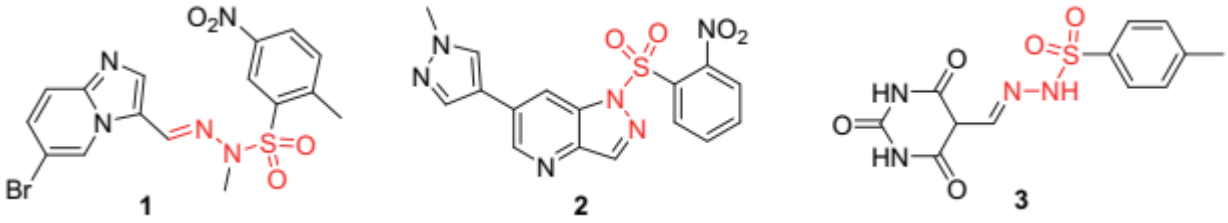


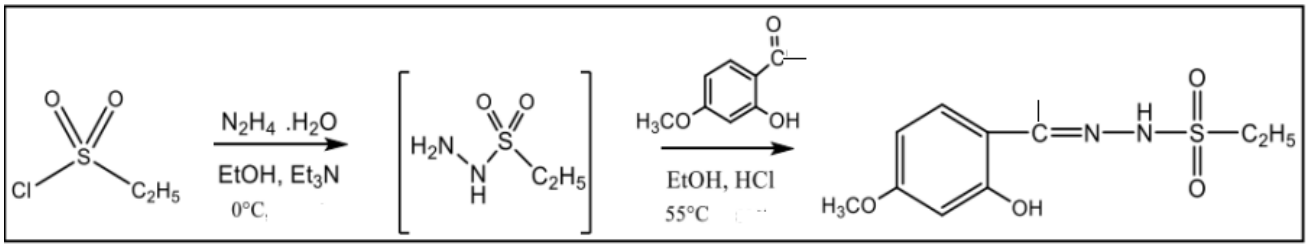
Fig.1. Some biologically active molecules bearing sulfonyl hydrazone moiety

Our research group conducts research on the synthesis and biological activity of aromatic/heteroaromatic alkyl sulfonyl hydrazone (22-27). Here, based on previous research, using sulfonyl hydrazides, 2 hydroxy4-methoxy-acetophenone as raw material, aromatic ethane sulfonyl hydrazone compound is efficiently synthesized by one crucible reaction at room temperature (Scheme 1). This synthetic method has the advantages of mild conditions, wide substrate application range and good selectivity, which is in line with the development trend of synthetic chemistry.

In our study, 2OH-4MeO-acetophenonethanesulfonylhydrazone (4MeO-afesh) was synthesized by one-pot reaction method in this approach. The structure of the compound was characterized by elemental analysis and spectroscopic (FT-IR, ^{1}H-NMR) methods, respectively.

MATERIAL AND METHOD

Since the excess hydrazine used in the synthesis of sulfonylhydrazones is both an expensive reagent and highly toxic, it must be isolated and purified from the product. Therefore, in the recent synthesis methods, sulfonylhydrazones have been obtained using a reduced amount of hydrazine with green solvent and mild reaction conditions and an environmentally friendly approach. In this work; 2OH-4MeO-Acetophenonethane sulfonylhydrazones were synthesized.



etan sulfonyl chloride ethansulfonyl hydrazide ethansulfonyl hydrazones

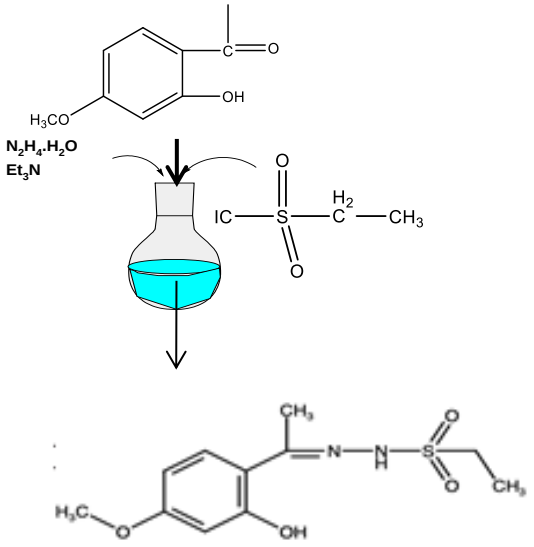
Fig. 2. Preparation of sulfonylhydrazone (One-pot condition: ethan sulfonyl chloride (1 mmol), hydrazinehydrate (1.2mmol), Acetophenon Compound (1.2 mmol).

One pot reaction

Environmentally friendly one pot reaction is chosen to be performed.

A solution of hydrazine hydrate (1.2 mmol) in ethanol (5 mL) was added dropwise to a stirring cold solution of the ethane sulfonyl chloride (1 mmol) in ethanol (5 mL), at 0 °C. After, triethylamine (1.0 mmol) was added dropwise. The mixture was stirred at room temperature for 1 h. The reaction was monitored by TLC using hexane/ethyl acetate (1:1) as eluent. After complete consumption of sulfonyl hydrazide, solution of 2OH-4MeO-Acetophenon (1.44 mmol) in ethanol (5 mL) was added dropwise . The reaction is allowed to continue for about 2 hours at 60 °C. The solution is taken to the vacum evaporator to remove the solvent ethanol. After this15 ml pure water is added and followed by acidification of the medium with HCl until pH reached 4.0. This process was monitored by pH-indicator strips. The stirring solution was kept at 60 °C for 2 to 3 h to afford the desired sulfonyl hyrazone.

2OH-4MeO-Acetophenon



Scheme 1 Synthesis of sulfonyl hydrazone derivatives by one-pot reaction

RESULT and DISCUSSION

The synthesis of the targeted compound was carried out in one pot and in two steps (Fig. 2 and **Scheme 1.** The synthesized Sulfonylhydrazone compound is 2OH-4MeO-Acetophenonethane sulfonylhydrazone. The elemental analysis (C, H, N, S) results were in good agreement with those calculated for the suggested formula. The sharp melting points obtained indicate the purity of the synthesized compound.

Characterization of compound

IR spectra

Selected vibration frequencies of sulfonyl hydrazones are given in Table 1. Bands in the region of 3165 cm^{-1} may be due to υ (NH) stretching vibration for 2OH-4MeO-Acetophenonethane sulfonylhydrazone. The strong bands at 1632 cm^{-1} is assigned to υ (C=N) stretching mode of the imine group for compound. Ligand also display bands at 1232cm^{-1} which are assigned to υ (C–O) stretching vibrations. υas(SO_2) and υs(SO_2) stretching vibrations are observed between 1321cm^{-1} and 1100cm^{-1}forcompound.

Table1. IR Spectrum data of synthesized 4MeOAfesh

Selected group	N-H	C-H Ar)	CH_3 (as)	C=N	SO_2 (as)	C-O	SO_2(s)
cm^{-1}(wave number)	3165	2974	2941	1632	1321	1232	1110

^{1}H NMR spectra

The ^{1}H NMR spectra of the compound was recorded in DMSO.^{1}H NMR data of DMSO-d6 solutions of the sulfonylhydrazone is exhibited in Table 2 and Fig. 3. In this study, 4MeO-Acetophenonethane sulfonylhydrazone show signals at 2.47 ppm which are attributed to the imines CH3 protons (–N=CC**H3** –). Signals at 1.42 ppm , 3.35 ppm and 3.68 ppm are assigned to the CH_2-C**H$_3$**, SO2-C**H2, H3**CO-Ar protons, respectively for compound. In general, the multiples observed at 6.30–7.80 ppm are assigned to compound ring protons;. Signals at 13.75 ppm and 11.70 ppm are assigned to the N**H** and O**H** protons, respectively for 4MeO-Acetophenonethanesulfonylhydrazone. The high field shift of NH protons may be due to the involvement of this group with a hydrogen bond in DMSO-d6, which is well known for its interaction with an amide proton.

Table2.^{1}H NMR Spectroscopic Data of 4MeOAfesh

Marking	CH_2-CH_3	SO2-CH2	CH_3C=N	H3CO-Ar	CH(Ar)	OH	NH
4MeOAfesh	1.42 (s,3H)	3.35 (2H)	2.47 (s,1H)	3.68 (3H)	6.30-7.80 (m, 3H)	11.70 (s,1H)	13.75 (s,1H)

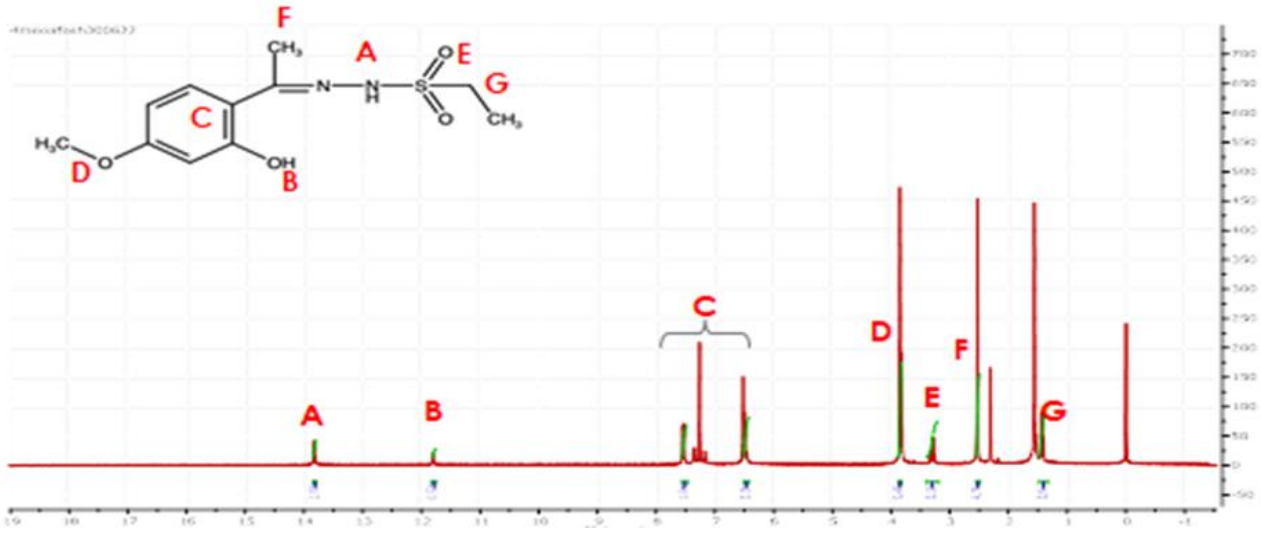


Fig.3.^{1}H NMR Spectrum of 4MeO-Afesh

The elemental analysis results of the compounds:

The elemental analysis results of the compounds are given in Table3.

Anal. Calcd for Compound $C_{11}H_{15}N_2O_4S$ (4MeO-afesh) ; C, 39.66; H, 4.58; N, 11.57; S, 13.21; Found: C, 38.85; H, 4.01; N, 10.33; S, 11.09.

Table3.Elemental Analysis Data Of Synthesized Compound

Compound	Molecular Formula (MA,g/mol)	color	%C	%H	%N	%S
4MeO-Afesh	$C_{11}H_{15}N_2O_4S$ (257.04)	Light yellow	38.85(39.66)	4.01(4.58)	10.33 (11.57)	11.09 (13.21)

* Theoretical values are given in parentheses

The structure of 4MeO-afesh is confirmed by FTIR, 1H NMR spectroscopic method and elemental analyses . Afterwards, theoretical studies were started.

Theoretical Calculation

Quantum chemical calculation is also an effective way to study the molecular structure and structural properties of inorganic and organic compounds besides experimental methods. In continuation of this work, the molecular structure of 4MeO-afesh was determined by computational studies. The structure of the newly synthesized 4MeO-afesh molecule, which is a sulfonamide derivative, was optimized with DFT/B3LYP method and 6-31+G (d,p) basis set. After determining the stable structure of the synthesized molecule, HOMO and LUMO energies, chemical reactivity descriptors and molecular electrostatic potential (MEP) map were examined with the same basis set. All calculations were performed using Gaussian 09 package program. As a result, this study will be useful to a scientist who wants to investigate the details of the molecule.

Molecular Structure Analysis

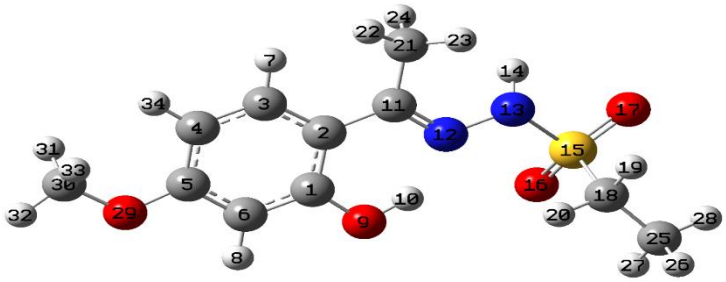


Fig 4. The optimized structure of 4MeO-afesh

In theoretical calculations, the scanning was performed in the range of 0-360º with 10º changes around the relevant dihedral angles, N12-N13-S15-C18 and C4-C5-O28-C30. After potential energy surface (PES) calculations, the obtained minimum energy conformers were re-optimized with DFT calculations using the B3LYP method and the 6-31+G(d,p) basis set.

The optimized geometry of the compound enabled us to obtain information about its structure since its crystal structures could not be obtained. Atomic numbers of optimized geometries are given in the figure.

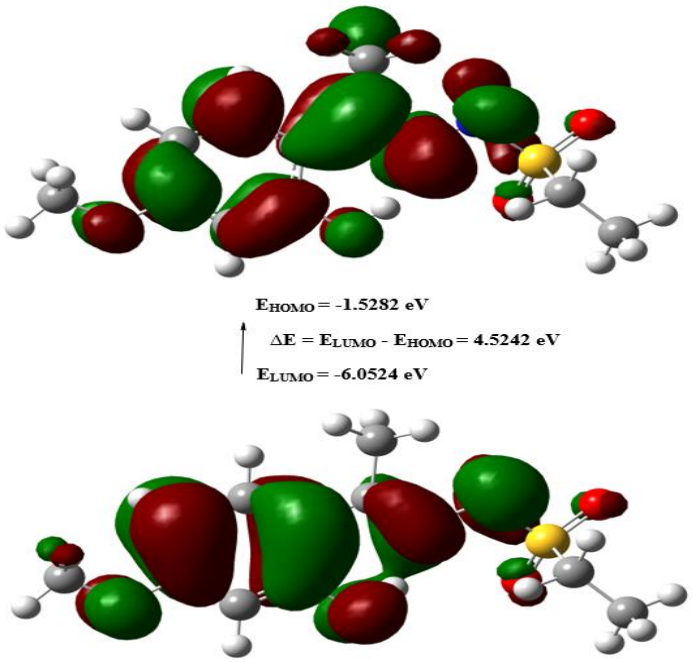


Fig.5. The Frontier Molecule Orbitals of 4MeO-afesh

It is well known that the electron donating ability of a molecule is explained by HOMO and the ability to accept electrons is explained by LUMO. The energy gap between HOMO and LUMO gives information about the chemical stability of a molecule. The frontier molecular orbital's of 4MeO-afesh. obtained using B3LYP/6-31+G (d,p) were given in the Figure5.

HOMO was localized on the whole molecule except ethyl group and methyl groups, while LUMO was localized on the whole molecule except the ethyl group and methyl group of methoxy group. The energy band gap ($\Delta E=E_{LUMO}-E_{HOMO}$) of dye 1 and dye 2 were 4.5242 eV.

Global reactivity descriptors

Global reactivity descriptors; energy band gap (ELUMO-EHOMO), electronegativity (χ),

chemical potential (μ), global hardness (η), global electrophilicity index (ω) and global softness (S) of 4MeO-afesh molecule have been listed in the Table 4.

Table 4. Global reactivity descriptors of 4MeO-afesh molecule

$I= -E_{HOMO}$	-1.5282 eV		$\mu = -\chi$	-2.2621 eV
$A= -E_{LUMO}$	-6.0524 eV		$\eta =(I-A)/2$	-3.7903 eV
$\Delta E= E_{LUMO}-E_{HOMO}$	-4.5242 eV		$S= 1/2\eta$	-0.2638 eV
$\chi= (I+A) /2$	2.2621 eV		$\omega = \mu^2 /2\eta$	-0.6750 eV

Molecular electrostatic potential (MEP) map

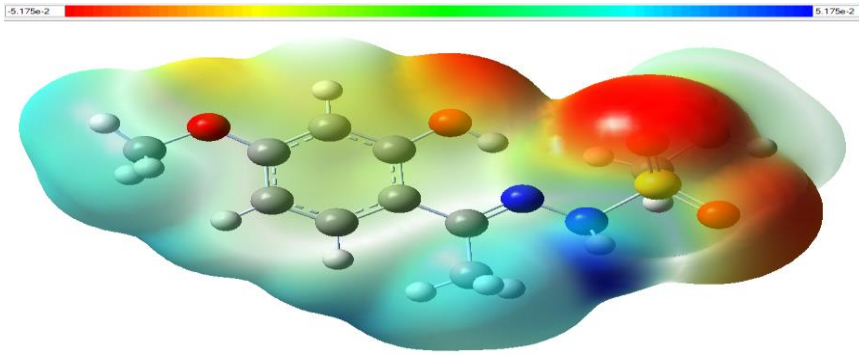


Fig.6. Nucleophilic or electrophilic region, the electrostatic potential surface maps of 4MeO-afesh

In order to obtain information about the nucleophilic or electrophilic region, the electrostatic potential surface maps of 4MeO-afesh were obtained at the B3LYP / 6-31+G(d,p) level as seen in the Figure 6.

Electrostatic potentials increase from red to blue color region, that is, red colored regions exhibit nucleophilic regions and blue colored regions exhibit electrophilic regions.

In the MEP map of 4MeO-afesh, it is seen that the positive potential region is on the hydrogene atom of NH group, and the negative potential regions are around the oxygen atoms.

According to the data obtained from the elemental, ^{1}H NMR and IR spectrum analysis it can be seen that the desired sulfony hydrazones were successfully obtained.

CONCLUSION

In this work; A new compound that is both environmentally friendly and a potential drug candidate has been synthesized and characterized by IR and ^{1}H NMR spectroscopic method and elemental analyses. In addition, these compounds was investigated theoretical calculation. As a result, this study will be useful to a scientist who wants to investigate the details of the molecule.

REFERENCE

1. Li, X.-W.; Liu, X.-H.; Chen, H.-J.; Wu, W.-Q.; Qi, C.-R.; Jiang, H.F. Angew. Copper-Catalyzed Aerobic Oxidative Transformation of Ketone-Derived *N*-Tosyl Hydrazones: An Entry to Alkynes, Chem., Int. Ed. 2014, 53, 14485.

2. Xia, Y.; Wang, J.-B. N-Tosylhydrazones: versatile synthons in the construction of cyclic compounds, Chem. Soc. Rev. 2017, 46, 2306.

3. Zhu, J.; Mao, M.; Ji, H.-J.; Xu, J.-Y.; Wu, L.. Palladium-Catalyzed Cleavage of α-Allenylic Aryl Ether toward Pyrazolemethylene-Substituted Phosphinyl Allenes and Their Transformations via Alkenyl C–P(O) Cleavage, Org. Lett. 2017, 19,1946.

4. Ishikawa, T.; Kimura, M.; Kumoi, T.; Iida, H. Coupled Flavin-Iodine Redox Organocatalysts: Aerobic Oxidative Transformation from *N*-Tosylhydrazones to 1,2,3-Thiadiazoles, ACS Catal. 2017, 7,4986.

5. Liu, Z.-Q.; Wu, P.; He, Y.; Yang, T.; Yu, Z.-K. [4+1] Cycloaddition of Enaminothiones and Aldehyde *N*-Tosylhydrazones Toward 3-Aminothiophenes, Adv. Synth. Catal.2018, 360, 4381.

6. Ishitobi, K.; Muto, K.; Yamaguchi, Pd-Catalyzed Alkenyl Thioether Synthesis from Thioesters and *N*-Tosylhydrazones, J. ACS Catal. 2019, 9, 11685.

7. Xia, Y.; Wang, J.-B. Transition-Metal-Catalyzed Cross-Coupling with Ketones or Aldehydes via *N*-Tosylhydrazones, J. Am. Chem. Soc. 2020, 142, 10592.

8. Ü.Ö. Özmen, A. Altuntaş, A.B. Gündüzalp, Fatma Arslan F. Hamurcu, New aromatic/heteroaromatic propanesulfonylhydrazone compounds:Synthesis, physical properties and inhibition studies against carbonic anhydrase II (CAII) enzyme, Spect. Chim. Acta: Part A 128 (2014) 452-460.

9. Bilen, E., Ozmen, UO., Cete, S., Alyar, S., Yasar, A. Bioactive sulfonyl hydrazones with alkyl derivative: Characterization, ADME properties, molecular docking studies and investigation of inhibition on choline esterase enzymes for the diagnosis of Alzheimer's disease, Chemico-biological interactions,360, (2022) 109956.

10 . Kendall, J. D.; Rewcastle, G. W.; Frederick, R.; Mawson, C.; Denny, W. A.; Marshall, E. S.; Baguley, B. C.; Chaussade, C.; Jackson,S. P.; Shepherd, P. R. Synthesis, biological evaluation and molecular modelling of sulfonohydrazides as selective PI3K p110α inhibitors, Bioorg. Med. Chem. 2007, 15, 7677.

11. Ma, Y.; Sun, G., Chen, D.; Peng, X.; Chen, Y. -L.; Su, Y.; Ji, Y.;Liang, J.; Wang, X.; Chen, L.; Ding, J.; Xiong, B.; Ai, J.; Geng,M.-Y.; Shen, Design and Optimization of a Series of 1-Sulfonylpyrazolo[4,3-*b*]pyridines as Selective c-Met Inhibitors, J. J. Med. Chem. 2015, 58, 2513.

12. Neumann, D. M.; Cammarata, A.; Backes, G.; Palmer, G. E.; Jursic,B. S. Synthesis and antifungal activity of substituted 2, 4, 6-pyrimidinetrione carbaldehyde hydrazones, Bioorg. Med. Chem. 2014, 22, 813.

13. Gunduzalp, A. B.; Ozmen, U. O.; Cevrimli, B. S.; Mamas, S.; Cete, S. Synthesis, characterization, electrochemical behavior, and antimicrobial activities of aromatic/heteroaromatic sulfonylhydrazone derivatives, Med. Chem. Res. 2014, 23, 3255.

14. James, J. P.; Bhat, K. I.; More, U. A.; Joshi, S. D. Design, synthesis, molecular modeling, and ADMET studies of some pyrazoline derivatives as shikimate kinase inhibitors,Med. Chem. Res. 2018, 27, 546.

15. Tripathi, A. C.; Upadhyay, S.; Paliwal, S.; Saraf, S. K. Derivatives of 4, 5-dihydro (1H) pyrazoles as possible MAO-A inhibitors in depression and anxiety disorders: synthesis, biological evaluation and molecular, Med. Chem.Res. 2018, 27, 1485.

16. Guo, X. K.; Yang, Q.; Xu, J.; Zhang, L.; Chu, H. X.; Yu, P.; Zhu, Y.Y.; Wei, J. L.; Chen, W. L.; Zhang, Y. Z.; Zhang, X. J.; Sun, H. P.;Tang, Y. Q.; You, Q. D. Design and bio-evaluation of indole derivatives as potent Kv1. 5 inhibitors, Bioorg. Med. Chem. 2013, 21, 6466.

17. Nunes, I. K. D.; de Souza, E. T.; Martins, I. R. R.; Barbosa, G.; deMoraes, M. O.; Medeiros, M. D.; Silva, S. W. D.; Balliano, T. L.; da Silva, B. A.; Silva, P. M. R.; Carvalho, V. D.; Martins, M. A.; Lima,L. M. Discovery of sulfonyl hydrazone derivative as a new selective PDE4A and PDE4D inhibitor by lead-optimization approach on the prototype LASSBio-448: *In vitro* and in vivo preclinical studies**,** Eur. J. Med. Chem. 2020, 204, 112492.

18. Arshad, M. N.; Sheikh, T. A.; Rahman, M. M.; Asiri, A. M.; Marwani, H. M.; Awual, M. R. J. Fabrication of cadmium ionic sensor based on (*E*)-4-Methyl-*N*′-(1-(pyridin-2-yl)ethylidene)benzenesulfonohydrazide (MPEBSH) by electrochemical approach, Organomet. Chem. 2017, 827, 49.

19. Asiri, A. M.; Hussain, M. M.; Arshad, M. N.; Rahman, M. M. A Ce 2+ sensor based on napthalen-1-yl-methylene-benzenesulfonohydrazide (NMBSH) molecules: ecological sample analysis, New J. Chem. 2018, 42, 4465.

20. H. Saeidian, H. Sadighian, M. Abdoli, M. Sahandi, 73-78. Versatile and green synthesis, spectroscopic characterizations, crystal structure and DFT calculations of 1, 2, 3–triazole–based sulfonamides, Journal of Molecular Structure 1131 (2017)

21. I. Grib, A. Bouzina, N. Aouf, M. Berredjem, 1086-1091. A practical and green approach towards synthesis of new *N*-sulfonylimines under ultrasound irradiation, Phosphorus, Sulfur, and Silicon, 191(8) (2016)

22. U. O. Ozdemir, F. Ilbiz, A.B. Gunduzalp, N. Ozbek, Z.K. Genc, F. Hamurcu, S. Tekin, Alkyl sulfonic acide hydrazides: Synthesis, characterization, computational studies and anticancer, antibacterial, anticarbonic anhydrase II (hCA II) activities

Journal of Molecular Structure, 1100, 464-474 (2015).

23. U.O. Ozdemir, N. Ozbek, Z.K. Genc, F. Ilbiz, A.B. Gunduzalp, New bioactive silver (I) complexes: Synthesis, characterization, anticancer, antibacterial and anticarbonic anhydrase II activities, Journal of Molecular Structure, 1138, 55-63 (2017).

24. U.O. Ozmen, E. Aktan, , F. Ilbiz, A.B. Gunduzalp, N. Ozbek, M. Sari, , O. Celik, S Saydam, Characterization, antibacterial, anticarbonic anhydrase II isoenzyme, anticancer, electrochemical and computational studies of sulfonic acid hydrazide derivative and its Cu(II) complex Inorganica Chimica Acta 423, 194-203 (2014).

25. F. Hamurcu, S. Mamas, U.O. Ozdemir, A.B. Gunduzalp, O.S. Senturk, New series of aromatic/ five-membered heteroaromatic butanesulfonyl hydrazones as potent biological agents: Synthesis, physicochemical and electronic properties, Journal of Molecular Structure, 1118, 18-27 (2016).

26. Neslihan Ozbek, Ümmühan Ozmen Ozdemir , Ahmet Fazıl Altun , Ertan Sahin , Sulfonamide-derived hydrazone compounds and their Pd(II) complexes: Synthesis, spectroscopic characterization, X-ray structure determination, invitro antibacterial activity and computational studies Journal of Molecular Structure 1196 (2019) 707-719.

27. S. Alyar, Ü.Ö. Özmen, Ş. Adem, H. Alyar, E. Bilen, K. Kaya, Synthesis, spectroscopic characterizations, carbonic anhydrase II inhibitory activity, anticancer activity and docking studies of new Schiff bases of sulfa drugs, Journal of Molecular Structure, 1223, 128911 (2021).

THE SOLUTION OF THE PROBLEM OF CYCLE LOADING OF HEREDITARY ELASTICO-PLASTIC BALL AT PULSATING INTERNAL PRESSURE

Mehriban MAMMADOVA

Institute of Mathematics and Mechanics of NAS of Azerbaijan, "Mechanics of deformable solids" department, B.Vahabzade str.9, AZ 1141, Baku, Azerbaijan, ORCID: 0000-0002-6762-4059

Abstract

We'll suppose that the material of ball is mechanically incompressible and its hereditary - elastico-plastic properties are described by the known relations of V.V. Moskvitin. At supposition that the hereditary elastico-plastic properties of ball material at initial loading are mathematically described by the relations of physically nonlinear hereditary elasticity.

The hereditary elastico-plastic properties of ball material at initial loading are mathematically described by the relations of physically nonlinear hereditary elasticity. Following from this we used the following nonlinear relation of V.V. Moskvitin for physically nonlinear hereditary elasticity:

$$\frac{S_{ij}^{(1)}}{2G_0} = \varphi^{(1)}\left(\varepsilon_{+}^{(1)}\right)e_{ij}^{(1)} - \int_0^t R(t-\tau)\varphi^{(1)}\left(\varepsilon_{+}^{(1)}(\tau)\right)e_{ij}^{(1)}(\tau)d\tau ,$$

where $S_{ij}^{(1)} = \sigma_{ij}^{(1)} - \sigma^{(1)}\delta_{ij}$, $e_{ij}^{(1)} = \varepsilon_{ij}^{(1)} - \varepsilon^{(1)}\delta_{ij}$ are deviations of tensors of the stresses $\sigma_{ij}^{(1)}$ and the deformations $\varepsilon_{ij}^{(1)}, \sigma^{(1)} = \sigma_{ij}^{(1)}\ \delta_{ij}/3,\ \varepsilon^{(1)} = \varepsilon_{ij}^{(1)}\delta_{ij}/3$ respectively, δ_{ij} are Kronecker symbol; $\varepsilon_{+}^{(1)} = \left(\frac{2}{3}e_{ij}^{(1)}e_{ij}^{(1)}\right)^{1/2}$ are intensity of deformations, G_0 is a instant shear modulus; $R(t)$ is a function of heredity (relaxation); $\varphi^{(1)}$ is a function characterizing the physical nonlinearly of material. As we see, the intensity of the deformations $\varepsilon_{+}^{(1)}$ in our case has the form:

$$\varepsilon_{+}^{(1)} = \frac{2}{3}\left(\varepsilon_{\varphi}^{(1)} - \varepsilon_{r}^{(1)}\right).$$

The process of loading and unloading alternate in every cycle till the destruction time.

At condition of mechanical incompressibility and at the power approximation of the function of the nonlinearity we'll get exact solution of the problem of determination of stress-strain state of ball at initial loading in general case of an arbitrary kernel of heredity.

Since the balls material is hereditary elastico-plastic, then at noted unloading the ball will have the remainder stresses, deformations and permutations.

Thus, the solution of problem on determination of stress-deformed state of thick-walled hereditary elastico-plastic ball is constructed at action of internal pressure of changing by the pulsating cycles principle, with using solution of similar problem at the first loading.

Keywords: internal pressure, elastico-plastic ball, stress, deformation, failure, creeping

Problem statement.

The thick-walled hollow ball made of hereditary elastico-plastic material of the internal radius a *, the external radius* b *is cyclically deformed by the internal pressure* $P_n(t)$ *where* $n = 1,2,\ldots$ *is the number of cycles, depending on time in the following form*

$$P_n(t)=\begin{cases}P(t), & for\ \ t_{n-1}\le t\le t_{n-1}+t_a\\ 0, & for\ \ t_{n-1}+t_a<t\le t_n=t_{n-1}+t_a+t_b\end{cases}$$

Here $n=1,2,...\ (t_0=0)$.

As we see the duration of each cycle of loading is t_a+t_b. At this the loading of the ball of the internal pressure $P(t)$ occurs in every n-th cycle. t_a is a duration of loading in one cycle. Then instant relief of pressure occurs at the time $t=t_{n-1}+t_a$. At this at the points of ball holds the process of unloading, with duration of the time t_b. Thus, the process of loading and unloading alternate in every cycle till the destruction time.

We'll suppose that the material of ball is mechanically incompressible and its hereditary- elastico-plastic properties are described by the known relations of V.V. Moskvitin [1].

Problem solution.

1. The stress-strain state of a ball at the first initial loading. Initial loading of ball occurs it the time interval $t\in[0,t_a]$. Let at this the components of stress occurring in the ball will be $\sigma_r^{(1)}(r,t),\ \sigma_\varphi^{(1)}(r,t)=\sigma_\theta^{(1)}(r,t)$, the deformations $\varepsilon_r^{(1)}(r,t),\varepsilon_\varphi^{(1)}(r,t)=\varepsilon_\theta^{(1)}(r,t)$ and the permutations $u^{(1)}(r,t)$. For their determination we've the following statement of the problem:

$$\frac{\sigma_\varphi^{(1)}-\sigma_r^{(1)}}{2G_0}=\varphi\left[\frac{2}{3}\left(\varepsilon_\varphi^{(1)}-\varepsilon_r^{(1)}\right)\right]\left(\varepsilon_\varphi^{(1)}-\varepsilon_r^{(1)}\right)-$$

$$-\int_0^t R(t-\tau)\varphi\left[\frac{2}{3}\left(\varepsilon_\varphi^{(1)}-\varepsilon_r^{(1)}\right)\right]\left(\varepsilon_\varphi^{(1)}-\varepsilon_r^{(1)}\right)d\tau\,. \tag{1.1}$$

$$\varepsilon_r^{(1)}+2\varepsilon_\varphi^{(1)}=0\,, \tag{1.2}$$

$$\frac{\partial\sigma_r^{(1)}}{\partial r}=\frac{2\left(\sigma_\varphi^{(1)}-\sigma_r^{(1)}\right)}{r}, \tag{1.3}$$

$$\sigma_r^{(1)}\Big|_{r=a}=-p(t),\ \sigma_r^{(1)}\Big|_{r=b}=0, \tag{1.4}$$

$$\varepsilon_r^{(1)}=\frac{\partial u^{(1)}}{\partial r},\ \varepsilon_\varphi^{(1)}=\frac{u^{(1)}}{r}\,. \tag{1.5}$$

The equation (1.1) together with (1.2) are determining relations. The equation (1.1) was written at supposition that the hereditary elastico-plastic properties of ball material at initial loading are mathematically described by the relations of physically nonlinear hereditary elasticity. Following from this at (1.1) we used the following nonlinear relation of V.V. Moskvitin for physically nonlinear hereditary elasticity:

$$\frac{S_{ij}^{(1)}}{2G_0}=\varphi^{(1)}\left(\varepsilon_+^{(1)}\right)e_{ij}^{(1)}-\int_0^t R(t-\tau)\varphi^{(1)}\left(\varepsilon_+^{(1)}(\tau)\right)e_{ij}^{(1)}(\tau)d\tau\,,$$

where $S_{ij}^{(1)}=\sigma_{ij}^{(1)}-\sigma^{(1)}\delta_{ij},\ e_{ij}^{(1)}=\varepsilon_{ij}^{(1)}-\varepsilon^{(1)}\delta_{ij}$ are deviations of tensors of the stresses $\sigma_{ij}^{(1)}$ and the

deformations $\varepsilon_{ij}^{(1)}, \sigma^{(1)} = \sigma_{ij}^{(1)}\ \delta_{ij}/3,\ \varepsilon^{(1)} = \varepsilon_{ij}^{(1)}\delta_{ij}/3$ respectively, δ_{ij} are Kronecker symbol; $\varepsilon_{+}^{(1)} = \left(\frac{2}{3}e_{ij}^{(1)}e_{ij}^{(1)}\right)^{1/2}$ are intensity of deformations, G_0 is a instant shear modulus; $R(t)$ is a function of heredity (relaxation); $\varphi^{(1)}$ is a function characterizing the physical nonlinearly of material. As we see, the intensity of the deformations $\varepsilon_{+}^{(1)}$ in our case has the form:

$$\varepsilon_{+}^{(1)} = \frac{2}{3}\left(\varepsilon_{\varphi}^{(1)} - \varepsilon_{r}^{(1)}\right).$$

The relations (1.2)-(1.5) are the conditions of mechanical incompressibility, equilibrium equation, boundary, conditions and the Cauchy geometrical relations, respectively.

From (1.2) subject to (1.5) follows

$$u^{(1)} = \frac{c(t)}{r^2},\ \varepsilon_{r}^{(1)} = -\frac{2c(t)}{r^3},\ \varepsilon_{\varphi}^{(1)} = \varepsilon_{\theta}^{(1)} = \frac{c(t)}{r^3}. \tag{1.6}$$

Here $c(t)$ is the unknown function subjected to the definition.

Approximates the function $\varphi^{(1)}\left(\varepsilon_{+}^{(1)}\right)$ by the following form: $\varphi^{(1)}\left(\varepsilon_{+}^{(1)}\right) = B_1\left(\varepsilon_{+}^{(1)}\right)^{\beta_1}$ where $B_1 > 0,\ \beta_1 < 0$ are experimentally determined constants of material. At this the equation (1.1) subject to (1.6) takes the form

$$\sigma_{\varphi}^{(1)} - \sigma_{r}^{(1)} = 3G_0B_1\frac{2^{1+\beta_1}}{r^{3(1+\beta_1)}}\left[c^{1+\beta_1}(t) - \int_0^t R(t-\tau)c^{1+\beta_1}(\tau)d\tau\right]. \tag{1.7}$$

From the equation of the equilibrium (1.3) using (1.7) and the first from the boundary conditions (1.4), we'll get

$$\sigma_{r}^{(1)} = -p(t) + \frac{G_0B_1 2^{\beta_1+2}\left(r^{3(1+\beta_1)} - a^{3(1+\beta_1)}\right)}{(1+\beta)(ar)^{3(1+\beta_1)}}\left[c^{1+\beta_1}(t) - \int_0^t R(t-\tau)c^{1+\beta_1}(\tau)d\tau\right]. \tag{1.8}$$

Satisfying the second boundary condition (1.4) we find

$$c^{1+\beta_1}(t) - \int_0^t R(t-\tau)c^{1+\beta_1}(\tau)d\tau = \frac{(1+\beta_1)(ab)^{3(1+\beta_1)}p(t)}{G_0B_1 2^{2+\beta_1}\left(b^{3(1+\beta_1)} - a^{3(1+\beta_1)}\right)}.$$

The received equation is Volterra integral equation of the second order. It is a linear equation relative to $c^{1+\beta_1}(t)$. Solving it, let's determine the unknown function $c(t)$

$$c(t) = \left(\frac{1+\beta_1}{B_1G_0 2^{\beta_1+2}}\right)^{1/(1+\beta_1)}\frac{a^3b^3}{\left(b^{3(1+\beta_1)} - a^{3(1+\beta_1)}\right)^{1/(1+\beta_1)}}\left[p(t) + \int_0^t \Gamma(t-\tau)p(\tau)d\tau\right]^{1/(1+\beta_1)}.$$

After the determination $c(t)$ the permutation $u^{(1)}(r,t)$ is determined by the first formula (1.6) the deformations $\varepsilon_{r}^{(1)},\ \varepsilon_{\varphi}^{(1)} = \varepsilon_{\theta}^{(1)}$ by the second and the third formula (1.6), the tresses $\sigma_{r}^{(1)}$ by (1.8), $\sigma_{\varphi}^{(1)} = \sigma_{\theta}^{(1)}$ by (1.7):

$$u^{(1)} = \left(\frac{1+\beta_1}{B_1G_0 2^{\beta_1+2}}\right)^{1/(1+\beta_1)}\frac{a^3b^3}{r^2\left(b^{3(1+\beta_1)} - a^{3(1+\beta_1)}\right)^{1/(1+\beta_1)}} \times$$

$$\times\left[p(t)+\int_0^t \Gamma(t-\tau)p(\tau)d\tau\right]^{1/(1+\beta_1)}, \tag{1.9}$$

$$\sigma_r^{(1)}=\frac{\left(\frac{b}{r}\right)^{3(1+\beta_1)}-1}{\left(\frac{b}{a}\right)^{3(1+b_1)}-1}p(t), \tag{1.10}$$

$$\sigma_\varphi^{(1)}=\sigma_\theta^{(1)}=\frac{\frac{1}{2}(1+3\beta_1)\left(\frac{b}{r}\right)^{3(1+\beta_1)}+1}{\left(\frac{b}{a}\right)^{3(1+b_1)}-1}p(t). \tag{1.11}$$

Consequently, at condition of mechanical incompressibility and at the power approximation of the function of the nonlinearity $\varphi^{(1)}\left(\varepsilon^{(1)}\right)$ we'll get exact solution of the problem of determination of stress-strain state of ball at initial loading in general case of an arbitrary kernel of heredity.

2. The inverse creeping thick-walled ball. Let at the time $t=t_1=t_a$. The pressure in the ball is instantly removed. In this case at the point of sphere occurs unloading. Since the balls material is hereditary elastico-plastic, then at noted unloading the ball will have the remainder stresses, deformations and permutations.

For the determination of components of remainder values of the stresses $\sigma_r^{(0)}$, $\sigma_\varphi^{(0)}$, the deformations $\varepsilon_r^{(0)},\varepsilon_\varphi^{(0)}=\varepsilon_0^{(0)}$, the permutations $u^{(0)}$ following V.V. Moskvitin [1] we introduce the differences:

$$\begin{aligned}&\sigma_r^*=\sigma_r^{(1)}-\sigma_r^{(0)},\ \sigma_\varphi^*=\sigma_\varphi^{(1)}-\sigma_\varphi^{(0)},\sigma_\theta^*=\sigma_0^{(1)}-\sigma_\theta^{(0)},t>t_1,\\&\varepsilon_r^*=\varepsilon_r^{(1)}-\varepsilon_r^{(0)},\ \varepsilon_\varphi^*=\varepsilon_\varphi^{(1)}-\varepsilon_\varphi^{(0)},\varepsilon_\theta^*=\varepsilon_\theta^{(1)}-\varepsilon_\theta^{(0)},\ u^*=u^{(1)}-u^{(0)}.\end{aligned} \tag{2.1}$$

Supposing that the process of unloading is also described by the nonlinear equations of V.V. Moskvitin [1] we'll write:

$$\begin{aligned}\frac{\sigma_\varphi^*-\sigma_r^*}{2G_0}&=\varphi^{(0)}\left[\frac{2}{3}\left(\varepsilon_\varphi^*-\varepsilon_r^*\right)\right]\left(\varepsilon_\varphi^*-\varepsilon_r^*\right)-\\&-\int_0^{t_*}R(t_*-\tau)\varphi^{(0)}\left[\frac{2}{3}\left(\varepsilon_\varphi^*-\varepsilon_r^*\right)\right]\left(\varepsilon_\varphi^*-\varepsilon_r^*\right)d\tau,\end{aligned} \tag{2.2}$$

$$\varepsilon_r^*+2\varepsilon_\varphi^*=0. \tag{2.3}$$

To (2.2) and (2.3) we add the deficient equations:

$$\frac{\partial\sigma_r^*}{\partial r}=\frac{2\left(\sigma_\varphi^*-\sigma_r^*\right)}{r}, \tag{2.4}$$

$$\sigma_r^*\big|_{r=a}=-p(t),\ \sigma_r^*\big|_{r=b}=0, \tag{2.5}$$

$$\varepsilon_r^*=\frac{\partial u^*}{\partial r},\ \varepsilon_\varphi^*=\frac{u^*}{r}, \tag{2.6}$$

where $t_* = t - t_a \left(t \geq t_a\right)$.

Let's take into account the one case. In differences (2.1) the values with the upper indices (1.1) are taken at the point $t > t_1$ but not at the point t_1.

These values corresponds to the pressure $p(t)$ monotonically changing on $0 \leq t \leq t_1$ and reminding invariable and equal $p(t_1)$ at $t > t_1$.

Now if the function $\varphi^{(0)}$ is approximate in the form $\varphi^{(0)}\left(\varepsilon_+^*\right) = B_0 \varepsilon_+^{\beta_0}$ after which we compare the relations (2.2)-(2.6) with the corresponding relations (1.1)-(1.5), then we'll come to the conclusion

$$u^* = \left(\frac{1+\beta_0}{G_0 B_0 2^{\beta_0+2}}\right)^{1/(1+\beta_0)} \frac{a^3 b^3}{r^2\left(b^{3(1+\beta_0)} - a^{3(1+\beta_1)}\right)^{1/(1+\beta_0)}} \times$$

$$\times \left[p(t_a)\left(1 + \int_0^{t_*} \Gamma(t_* - \tau) p(\tau) d\tau\right)\right]^{1/(1+\beta_0)}, \tag{2.7}$$

$$\sigma_r^* = \frac{\left(\frac{b}{r}\right)^{3(1+\beta_0)} - 1}{\left(\frac{b}{a}\right)^{3(1+\beta_0)} - 1} p(t_a), \tag{2.8}$$

$$\sigma_\varphi^* = \sigma_\theta^* = \frac{\frac{1}{2}(1+3\beta_0)\left(\frac{b}{r}\right)^{3(1+\beta_0)} + 1}{\left(\frac{b}{a}\right)^{3(1+\beta_0)} - 1} p(t_a). \tag{2.9}$$

Allowing for (2.7)-(2.9) in relations (2.1) we'll get the expression of initial values

$$u^{(0)} = \left[\left(\frac{1+\beta_1}{G_0 B_1 2^{2+\beta_1}} \frac{p(t_a)\left(1 + \int_0^t \Gamma(\xi) d\xi\right)}{b^{3(1+\beta_1)} - a^{3(1+\beta_1)}}\right)^{1/1+\beta_1} -\right.$$

$$\left. - \left(\frac{1+\beta_0}{G_0 B_0 2^{2+\beta_0}} \frac{p(t_a)\left(1 + \int_{t_a}^t \Gamma(t-\tau) d\tau\right)}{b^{3(1+\beta_0)} - a^{3(1+\beta_0)}}\right)^{1/1+\beta_0}\right] \frac{a^3 b^3}{r^2}, \tag{2.10}$$

$$\sigma_r^{(0)} = \left[\frac{\left(\frac{b}{r}\right)^{3(1+\beta_1)} - 1}{\left(\frac{b}{a}\right)^{3(1+\beta_1)} - 1} - \frac{\left(\frac{b}{r}\right)^{3(1+\beta_0)} - 1}{\left(\frac{b}{a}\right)^{3(1+\beta_0)} - 1}\right] p(t_a), \tag{2.11}$$

$$\sigma_{\varphi}^{(0)}=\sigma_{\theta}^{(0)}\left[\frac{\left(1+3\beta_1\right)\left(\frac{b}{r}\right)^{3(1+\beta_1)}+1}{\left(\frac{b}{a}\right)^{3(1+\beta_1)}-1}-\frac{\left(1+3\beta_0\right)\left(\frac{b}{r}\right)^{3(1+\beta_0)}+1}{\left(\frac{b}{a}\right)^{3(1+\beta_0)}-1}\right]\frac{p(t_a)}{2}. \qquad (2.12)$$

The loading process is continued, during the time t_b or till the time $t_1=t_a+t_b$ beginning from $t=t_a$. Therefore at the end of unloading processes the remainder permutations will be determined by the formula (2.10) at $t=t_a+t_b$. The remainder stresses are expressed in the form (2.11), (2.12).

If the process of unloading occurs by the linear visco-elastic principle, then in received relations we must accept: $B_0=1,\ \beta_0=0$

3. Stress-strain state of a ball at pulsating internal pressure. Let the amplitude of internal pressure stay constant at the all process of cyclic pulsating pressure and it will be equal to $p(t_a)=p_*$. We are interested in the cyclic process of loading after the full unloading. For determination of stress component and deformations at any cycle of loading, following to V.V. Moskvitin [1] consider the differences:

$$\sigma_{r_*}^{(n)}=(-1)^n\left(\sigma_r^{(n-1)}-\sigma_r^{(n)}\right);\ \sigma_{\varphi_*}^{(n)}=(-1)^n\left(\sigma_{\varphi}^{(n-1)}-\sigma_{\varphi}^{(n)}\right);$$

$$\varepsilon_{r_*}^{(n)}=(-1)^n\left(\varepsilon_r^{(n-1)}-\varepsilon_r^{(n)}\right);\ \varepsilon_{\varphi_*}^{(n)}=(-1)^n\left(\varepsilon_{\varphi}^{(n-1)}-\varepsilon_{\varphi}^{(n)}\right);$$

$$\sigma_{\theta_*}^{(n)}=\sigma_{\varphi_*}^{(n)};\ \varepsilon_{\theta_*}^{(n)}=\varepsilon_{\theta_*}^{(n)},$$

where $n\geq 2,\ t>t_1$.

Here the values with the upper indices $(n-1)$ are stresses and deformations, respectively, which appear in the ball with the internal pressure $p(t)$, monotonically changing on the segment $t_{n-1}\leq t\leq t_{n-1}+t_a$ and staying invariable and equal to $p(t_{n-1}+t_\alpha)=p_*$ at $t>t_{n-1}+t_a$.

The values with the upper indices (n) are unknown stresses and reformating respectively, appear during the loading of internal pressure in the n-th cycle.

As in the above, for determination of the component's $\sigma_{r_*}^{(n)},\ \sigma_{\varphi_*}^{(n)},\ \varepsilon_{r_*}^{(n)},\ \varepsilon_{\varphi_*}^{(n)}$ let's use the construction of the problem of V.V. Moskvitin:

$$\frac{\sigma_{\varphi_*}^{(n)}-\sigma_{r_*}^{(n)}}{2G_0}=\varphi^{(n)}\left[\frac{2}{3}\left(\varepsilon_{\varphi_*}^{(n)}-\varepsilon_{r_*}^{(n)}\right)\right]\left(\varepsilon_{\varphi_*}^{(n)}-\varepsilon_{r_*}^{(n)}\right)-$$

$$-\int_0^{t_n^*}R\left(t_n^*-\tau\right)\varphi^{(n)}\left[\frac{2}{3}\left(\varepsilon_{\varphi_*}^{(n)}-\varepsilon_{r_*}^{(n)}\right)\right]\left(\varepsilon_{\varphi_*}^{(n)}-\varepsilon_{r_*}^{(n)}\right)d\tau, \qquad (3.2)$$

$$\varepsilon_{r_*}^{(n)}+2\varepsilon_{\varphi_*}^{(n)}=0, \qquad (3.3)$$

$$\frac{\partial\sigma_{r_*}^{(n)}}{\partial r}=\frac{2\left(\sigma_{\varphi_*}^{(n)}-\sigma_{r_*}^{(n)}\right)}{r}, \qquad (3.4)$$

$$\sigma_{r_*}^{(n)}\Big|_{r=a} = -p_*,\ \sigma_{r_*}^{(n)}\Big|_{r=b} = 0, \tag{3.5}$$

$$\varepsilon_{r_*}^{(n)} = \frac{\partial u_*^{(n)}}{\partial r},\ \varepsilon_{\varphi_*}^{(n)} = \frac{u_*^{(n)}}{r}\ , \tag{3.6}$$

Here $t_n^* = t - \left(t_{n-1} + t_a\right),\ t_{n-1} + t_a$ is a time of beginning of unloading and the following loading in n-th cycle.

Representation the function $\varphi^{(n)}\left(\varepsilon_{+*}^{(n)}\right)$ in the form $\varphi^{(n)}\left(\varepsilon_{+*}^{(n)}\right) = B_n\left(\varepsilon_{+*}^{(n)}\right)^{\beta_n}$ where β_n, β_n are experimentally determined constants of material, let's compare the relations (3.2)-(3.6) with the corresponding relations (l.l)-(l.5) of initial loading. At this, we can make the following conclusions, according to V.V. Moskvitin's theorem on variable loading.

Here

$$\begin{aligned}\sigma_i^{(1)} &= \sigma_i^{(1)}\left(r, t, B_1, \beta_1, a, b, p(t)\right),\\ \varepsilon_i^{(1)} &= \varepsilon_i^{(1)}\left(r, t, B_1, \beta_1, a, b, p(t)\right),\end{aligned} \tag{3.7}$$

where

$$\begin{aligned}\sigma_{i*}^{(1)} &= \sigma_i^{(1)}\left(r, t_n^*, B_n, \beta_n, a, b, p_*(t)\right),\\ \varepsilon_{i*}^{(1)} &= \varepsilon_i^{(1)}\left(r, t_n^*, B_n, \beta_n, a, b, p_*(t)\right).\end{aligned} \tag{3.8}$$

Here $i = r, \varphi, \theta$.

As a result by using (3.1), (3.7) and (3.8) we'll get the expression for the unknown values of stress and deformation:

$$\sigma_i^{(n)} = \sigma_i^{(1)} - \sum_{k=2}^{n}(-1)^k \sigma_{i*}^{(k)}$$

$$\varepsilon_i^{(n)} = \varepsilon_i^{(1)} - \sum_{k=2}^{n}(-1)^k \varepsilon_{i*}^{(k)},\ \left(i = r, \varphi, \theta\right).$$

Conclusion.

Thus, the solution of problem on determination of stress-deformed state of thick-walled hereditary elastico-plastic ball is constructed at action of internal pressure of changing by the pulsating cycles principle, with using solution of similar problem at the first loading.

Reference

1. Moskvitin V. V. (1981). *The cyclic loading of structural elements.* Moscow: Nauka.

BİTKİSEL BAZLI SÜTLER VE SÜT ENDÜSTRİSİNDE KULLANIMI

Nuray GÜZELER

Çukurova Üniversitesi, Mühendislik Fakültesi, Gıda Mühendisliği Bölümü, Adana, Türkiye., ORCID ID: https://orcid.org/0000-0001-5246-2491

Dilek SAY

Çukurova Üniversitesi, Pozantı Meslek Yüksekokulu, Adana, Türkiye., ORCID ID: https://orcid.org/0000-0003-3932-6414

İrem Döndü BAKIR

Çukurova Üniversitesi, Mühendislik Fakültesi, Gıda Mühendisliği Bölümü, Adana, Türkiye., ORCID ID: https://orcid.org/0000-0002-8393-011X

ÖZET

Günümüzde sağlıklı beslenme konusunda bilinç artmıştır. Tüketicilerin sağlıklı yaşam için besinin önemini anlaması onları beslenmedeki alternatiflere yönlendirmektedir. Özellikle Tip II diyabet, kardiyovasküler hastalıklar, sindirim sistemi hastalıkları gibi beslenmeye bağlı hastalıkların artması yanında hayvansal gıda alımını reddetme gibi etik yönelimler de söz konusu olmuştur. Bu nedenle hayvansal gıdalara olan ilgi azalmıştır. Sağlıklı beslenme kadar artık vegan ve vejeteryan beslenme de ön plana çıkmıştır. Son yıllarda süt endüstrisi, tüketici eğilimlerinde değişiklikler ve sürdürülebilir üretim çabalarından dolayı sektörde yenilik yapmaya ve pazara yeni ürünler getirme yoluna gitmektedir. Hayvan sütüne benzetilerek formüle edilen ve "süt" olarak piyasaya sunulan bitki bazlı süt/benzeri içecekler, bitki bazlı süt içeceği/sebze sütleri veya süt alternatifli içecekler, alternatif sütlü içecekler segmentleri ortaya çıkmıştır. Gelişen teknoloji ile birlikte baklagiller (soya fasulyesi), yağlı tohumlar (ayçiçek, susam, keten, kenevir), sert kabuklu meyveler (badem, fındık, hindistan cevizi, ceviz), tahıllar (yulaf, pirinç, susam) bitkisel bazlı süt üretiminde kullanılmaya başlanmıştır. Süt endüstrisinde, soya sütü, hindistan cevizi sütü, badem sütü, pirinç sütü ve yulaf sütü gibi bitkisel bazlı sütler, yüksek fonksiyonel özellikleri nedeniyle tüketicilerden artan talep görmektedir. Tahıl ve tahıl sütleri, kolesterol veya laktoz içermediklerinden vejeteryan, özel diyet yapan ve laktoz intoleransı olan kişiler tarafından tercih edilmektedir. Bu çalışmada, bitkisel kaynaklı sütler ve bu sütlerin kullanımlarına yer verilmiştir.

Anahtar Kelimeler: Bitkisel bazlı süt, süt endüstrisi, vegan beslenme

PLANT BASED MILKS AND THEIR USE IN THE DAIRY INDUSTRY

ABSTRACT

Today, awareness of healthy nutrition has increased. Consumers understanding of the importance of food for a healthy life directs them to alternatives in nutrition. In addition to the increase in nutrition-related diseases such as Type II diabetes, cardiovascular diseases, and digestive system diseases, there have also been ethical tendencies such as refusing to take animal food. For this reason, interest in animal foods has decreased. Vegan and vegetarian nutrition has come to the fore as well as healthy nutrition. In recent years, the dairy industry has been trying to innovate in the sector and bring new products to the market due to changes in consumer trends and sustainable production efforts. Segments of plant-based milk/similar beverages, plant-based milk drinks/vegetable milks or milk alternative beverages, alternative milk beverages, which are formulated by analogy with animal milk and presented to the market as "milk", have emerged. With the developing of technology; Legumes (soybean), oil seeds (sunflower, sesame, flax, hemp), hard-shelled fruits (almond, hazelnut, coconut, walnut), cereals (oat, rice, sesame) have begun to be used in plant-based milk production. In the dairy industry, plant-based milks such as soy milk, coconut milk, almond milk, rice milk and oat milk are in increasing demand from consumers due to their high functional properties. Cereal and cereal milks are preferred by vegetarians, people on special diets and those with lactose intolerance, as they do not contain cholesterol or lactose. In this study, plant-based milks and their uses are included.

Keywords: Plant-based milk, dairy industry, vegan nutrition

GİRİŞ

İnsanların beslenmesinde hayvansal sütler önemli bir enerji, protein, yağ ve kalsiyum kaynağıdır (Muehlhoff, Bennett ve McMahon, 2013). Bugün, süt ve süt bazlı gıdaların beslenmedeki rolü, FAO ve birçok ülkenin hükümetleri ve akademik grupları tarafından belirlenmiştir. Bununla birlikte, piyasada çok fazla bitkisel bazlı süt benzeri içeceğin olması ve bu içecekler için süt teriminin kullanılmasından dolayı sütün tanımı son yıllarda incelemeye alınmıştır (Wijesinha, Bettoni, Burlingame, 2013).

Bitkisel süt "baklagiller, yağlı tohumlar veya tahılların inek sütünün görünümüne benzeyen su özütleri" olarak tanımlanmaktadır (Jeske, Zannini, Arendt, 2018). Bitkisel kaynaklı süt alternatifleri, bitki materyalinin suda ekstrakte edilmesi, parçalanarak boyutlarının küçültülmesi ve homojen hale getirilmesiyle elde edilmektedir (Sethi, Tyagi, Anurag, 2016). Gelişen teknoloji ile beraber soya fasulyesi gibi baklagiller, ayçiçek, susam, keten, kenevir gibi yağlı tohumlar, badem, fındık, hindistan cevizi, ceviz gibi sert kabuklu meyveler, yulaf, pirinç, susam gibi tahıllar bitkisel süt üretiminde kullanılmaktadır (Sethi, Tyagi, Anurag, 2016: Röös, Garnett, Watz, Sjörs, 2018). Son yıllarda, tahıllar ve bunlardan elde edilen ürünler protein, mineral, vitamin ve antioksidanlar gibi sağlığa yararlı biyoaktif bileşenler bakımından zengin oldukları için de fonksiyonel gıdalar ve nutrasötikler olarak kabul edilmektedir (Das, Chaudhuri, Chakraborty, 2012). Bitkisel sütler, hayvansal sütlerin aksine önemli miktarda fenolik asitler, flavonoidler, stilbenler, lignanlar, hidrolizlenebilir tanenler, kondanse tanenler, proantosiyanidinler, karotenoidler, alkoloidler, fitatlar, terpenler, fitoöstrojenler gibi fitokimyasallar ve diyet lifi içerirler ayrıca düşük glisemik indekse sahiptirler (Chalupa-Krebzdak, Long, Bohrer, 2018: Röös, Garnett, Watz, Sjörs, 2018). Tüm bitkisel kaynaklı sütler, laktoz intoleransı olan veya süt proteinlerine alerjisi olan tüketiciler tarafından laktozsuz, kolesterolsüz ve düşük kalorili olmaları gibi ortak faydaları nedeniyle inek sütüne tercih edilir (Cruz, Capellas, Hernández, Trujillo, Guamis, Ferragut, 2007). Soya sütü inek sütüne en iyi alternatif olarak bilinmekte ve kullanılmaktadır. Ancak soyadan ileri gelen fasulyemsi tat ve bazı besin öğelerinin eksikliği nedeniyle soya sütü yerine badem, pirinç, yulaf ve hindistan cevizi sütü kullanımı artmıştır (Bernat, Cháfer, Chiralt, González-Martínez, 2014: Vanga ve Raghavan, 2018).

Tüketicilerin beslenme konusunda farkındalık düzeylerinin artması ile birlikte vejeteryan ve vegan beslenme tiplerinin ortaya çıkması, hayvansal gıdaların üretiminin neden olduğu çevre kirlilikleri üzerine birçok olumsuz araştırmaların ortaya çıkması, hayvan haklarına olan duyarlılığın artması, laktoz intoleransı gibi hayvansal gıdalarda bulunan alerjik reaksiyonların bitkisel türevlerinde bulunmaması, kolesterol içermemesi ve yağ oranlarının daha düşük olması ve gıda trendinin bu yöne çekilmesi gibi nedenlerle hayvansal süt ve süt ürünlerine alternatif olarak bitkisel bazlı süt ve süt ürünlerinin öneminin arttığı görülmektedir (Erk, Seven, Akpınar, 2019: Yiğit, 2019). Bitkisel sütler direk olarak tüketilebildiği gibi yoğurt, kefir, peynir, dondurma gibi süt ürünlerinde de kullanılmaya başlanmıştır.

Bu çalışmada, bitkisel gıdalara talebin artmasından dolayı tüketimi artan bitkisel bazlı sütler ve bu sütlerin endüstrideki kullanımlarına yer verilmiştir.

BİTKİSEL BAZLI SÜTLER

Soya Sütü

Soya fasulyesi karbonhidratlar, proteinler ve lipitler açısından zengindir. Linoleik (18:2) ve linolenik (18:3) asitler gibi önemli miktarda çoklu doymamış yağ asitleri içerir, kolesterol içermez ve önemli miktarda vitamin ve mineral içeriğine sahiptir (Liu, 2012). Soya ürünleri fitokimyasallar açısından zengindir, başlıcaları izoflavonlar, saponinler, fitik asit, tripsin inhibitörleri, fitosteroller, fenolik asitler ve lektinlerdir, kolesterol seviyelerini düşürürler, bazı kanserler, osteoporoz ve diğer kronik bulaşıcı olmayan dejeneratif hastalık riskini azaltırlar (Sethi, Tyagi, Anurag, 2016). Soya fasulyesinden elde edilen soya sütü bitkisel fonksiyonel içeceklerden en popüler olanıdır (Wang, Swain, Kwolek, Fehr, 1983).

Badem Sütü

Bademlerin ana bileşenleri proteinler, lipitler, çözünür şekerler, mineraller ve liflerdir (Roncero, Álvarez-Ortí, Pardo-Giménez, Gómez, Rabadán, Pardo, 2016). Bademlerin çoğu, %35 ile 52 arasında lipit, ardından %22-25 ile proteinlerdir. Lipitler çoğunlukla doymamış yağ asitleridir ve proteinler çoğunlukla esansiyel amino

asitlerdir. Kalsiyum, magnezyum, selenyum, potasyum, çinko, fosfor ve bakır gibi besinler açısından zengindirler ve arabinoz varlığı nedeniyle prebiyotik özelliklere sahiptirler (Sethi, Tyagi, Anurag, 2016). Bademler, zengin besin bileşimlerine dayanarak, bitki bazlı süt ikamelerinin üretimi için kullanılır. Badem sütü antioksidanlar (flavonoidler, E vitamini ve poliaminler), lifler ve fitosteroller gibi faydalı biyoaktif bileşiklere sahiptir (Ferragut, Valencia-Flores, Pérez-González, Gallardo, Hernández-Herrero, 2015).

Pirinç Sütü

Kahverengi pirincin suda ıslatılmasıyla elde edilen pirinç sütü, karbonhidrat açısından zengin bir kaynak olduğu için şeker oranı inek sütüne göre daha yüksektir. Soya ve bademin aksine alerjen etkisinin olmaması başlıca avantajıdır. Pirinç sütü diğer bitkisel kaynaklara göre daha sulu kıvamdadır. İnek sütüne benzer. Protein içeriği badem sütü gibi düşüktür ancak daha tatlıdır. Protein oranı oldukça düşük olmasına rağmen kompleks karbonhidratlara sahiptirler ve oldukça zengin lif içeriğine sahiptirler. Kalsiyum, doğal fosfor, B, D ve E vitamini içeren pirinç sütü hem doğrudan içilebilir hem de çeşitli ürünlerin üretiminde kullanılır (Yiğit, 2019).

Yulaf Sütü

Yulaf içerdiği vitaminler, fenolik asitler, flavonoidler, steroller ve fitik asit gibi antioksidan aktivite gösteren birçok bileşiğin iyi bir kaynağıdır (David, 2000). Yulaf aynı zamanda sindirim sistemi için faydalı olan ve kolonorektal kansere karşı koruyucu olan betaglukan gibi lif bileşikleri için de iyi bir kaynaktır, yüksek lif içeriği sayesinde ideal kilonun korunmasına yardımcı olur, kolesterol ve lipit düşürücü etkiler gösterir (Wood, 1991). Yulaf tüketiminin insanda Lactobacillus plantarum gibi laktik asit bakterilerinin probiyotik düzeylere ulaşmasını desteklediği bildirilmiştir (Kedia, Vazquez, Pandiella, 2008). Yulaf sütü yüksek oranda lif, A, D, E ve B1 vitaminleri ve mineraller (kalsiyum, potasyum, sodyum, magnezyum ve demir) içerir. Yulaf sütü içecek olarak tüketilmesinin yanı sıra, shake, yemek pişirme ve fırınlama, sos ve çorba, kek yapımında kullanılmaktadır.

Hindistan Cevizi Sütü

Hindistan cevizi meyvesi genel olarak %51.7 çekirdek, %9.8 su ve %38.5 kabuktan oluşur. Hindistan cevizi sütü genellikle rendelenmiş hindistan cevizi etinden üretilir. Temel olarak hindistan cevizi sütü, sulu fazda bulunan bazı proteinler tarafından stabilize edilen bir su içinde yağ emülsiyonudur. Hindistan cevizi sütü, Asya mutfağında yaygın kullanılmaktadır Hindistan cevizi sütü kullanan popüler Tay yemekleri arasında köriler ve tatlılar bulunur (Tansakul ve Chaisawang, 2006). Hindistan cevizi sütü demir, kalsiyum, potasyum, magnezyum ve çinko gibi minerallerden zengin olup önemli miktarda E ve C vitamini de içermektedir (Sethi, Tyagi, Anurag, 2016)

Fındık Sütü

Fındık, içerdiği karbonhidrat, protein, lipid, vitamin, lif, fenolik bileşikler, mineraller, tokoferoller, fitosteroller ve skualen nedeniyle insan sağlığı ve beslenmesinde önemli bir rol oynamaktadır (Ermiş, Güneş, Zent, Çağlar, Yılmaz, 2018). Fındığın sağlığa faydalarının yanı sıra amino asitler ve organik asitler gibi aktif tat bileşikleri vardır ve bu bileşikler onu yaygın olarak tüketilen ve kabul gören bir gıda haline getirir (Tey, Brown, Chisholm, Delahunty, Gray, Williams, 2011). Fındık sütü üretiminde doğal fındığın kullanılması, belirli aroma ve tadın algılanmasını sağlarken, farklı lezzet elde etmek için kavrulmuş fındıklar da kullanılabilir (Öztürk, Seyhan, Borçaklı, 2019).

Yer Fıstığı Sütü

Yerfıstığı, oleik ve linoleik asitler için iyi bir kaynaktır, tipik bir yer fıstığının %50 sini yağ oluşturur, bunun yaklaşık %80'i doymamış ve bu doymamış yağ asitlerinin çoğu oleik ve linoleik asitlerdir (Baker, 2002). Yer fıstığı ayrıca polifenoller, antioksidanlar, fitosteroller, vitaminler, mineraller ve flavonoidler, resveratrol, fenolik asitler gibi bazı önemli bileşikleri içerir. Yer fıstığının Co enzim Q10 ile birlikte en yüksek miktarda

arginin olmak üzere 20 amino asidin tamamını içerdiği ve bu biyoaktif bileşiklerin hastalıklar üzerinde önleyici etkisinin olduğu ve uzun ömürlülüğü teşvik ettiği düşünülmektedir (Duncan, Gorbet ve Talcott 2006).

BİTKİSEL SÜTLERDEN ELDE EDİLEN ÜRÜNLER

Yoğurt

Soya sütünden yoğurt üretiminde iki farklı (*S .thermophilus, L. delbrueckii* subsp. *bulgaricus*) sıvı kültür kullanılarak yapılan bir çalışmada, yoğurtların duyusal özelliklerinin % 20 kültür içeren örneklerde daha yüksek puanlar aldığı bildirilmiştir (Ashaye, Taiwo, Fasoyiro, Akinnagbe, 2001).

İnek sütüne %25, 50 ve 75 oranlarında pirinç sütü eklenerek üretilen probiyotik yoğurtlarda, yoğurtların viskozite değerlerinin arttığı, tekstür ve serum ayrılması değerlerinin azaldığı, kimyasal ve mikrobiyolojik değerlerinde azalma olduğu bildirilmiştir. Pirinç sütü oranının artmasıyla birlikte duyusal açıdan yoğurtların beğenisinde azalma meydana geldiği belirtilmiştir (Uzuner, 2012).

Yılmaz, Ersan ve Topçuğlu (2019), badem sütünün probiyotik yoğurt üretiminde kullanılabilirliğini belirlemek, tüketiciye yeni ve fonksiyonel bir süt ürünü sunmak için badem sütü-rekonstitüe süt kompozisyonları ile farklı konsantrasyonlarda (%0, %25, %50, %75 ve %100) probiyotik yoğurtları üretmişler ve 21 gün süre ile 4°C'de depolamışlardır. Depolama süresince probiyotik yoğurtların mikrobiyolojik ve bazı fizikokimyasal özelliklerini incelemişlerdir. %100 badem sütü ile üretilen yoğurtta, depolama süresince probiyotik bakteri sayılarının arttığını ve badem sütünün bu bakterilerin gelişimini stimüle ettiğini saptamışlardır. Yine yoğurtların depolanması sırasında tüm bakteri sayısının 10^6>kob/g üzerinde olmasından dolayı fonksiyonel özellikleri arttırıcı etkisinin olduğunu bulmuşlardır. Badem sütü ilavesinin probiyotik yoğurdun fizikokimyasl özellikleri üzerine herhangi bir olumsuz etki oluşturmadığı da belirlemişlerdir.

Termal (T) ve UVC (sarmal tüp tipi) destekli termal (UV – C-T) işlemlerle pastörize edilmiş yulaf sütünden set tipi yoğurt üretimi yapılan bir çalışmada, UV-C-T ile muamele edilmiş yulaf sütünün kullanımının yoğurdun özelliklerini iyileştirme potansiyeline sahip olduğunu bulunmuştur (Demir, Simsek, Yıldırım, 2021).

Kefir

Kefir, inek, koyun, keçi, manda, deve sütü gibi her türlü hayvan sütünden yapılabileceği gibi ceviz sütü, kakao küspesi içeceği, pirinç sütü, hindistan cevizi sütü, soya sütü ve yer fıstığı sütü gibi bitkisel sütlerden de üretilebilir (Nielsen, Gürakan ve Ünlü 2014). Kefirin kimyasal, dokusal ve duyusal özellikleri için hangi sütten yapıldığı önemlidir.

Dinkçi, Kesenkaş, Korel ve Kınık (2015), inek ve yulaf sütünü karıştırarak kefir üretim potansiyelini değerlendirmişlerdir. Bu amaçla %20, %40 ve %60 oranında yulaf sütü içeren kefir örneklerinin fizikokimyasal, reolojik, mikrobiyolojik ve duyusal özelliklerini depolama boyunca incelenmişlerdir. Yulaf sütü konsantrasyonu artışının örneklerin viskozite ve pH'sının düşmesine neden olduğunu bildirmişlerdir. Laktik asit bakterilerinin sayısının en yüksek oranda yulaf içeren kefirlerde göründüğünü belirlemişlerdir. %20 yulaf sütü içeren kefir koku, tat ve kıvam açısından panelistler tarafından tercih edilmiştir. Yulaf sütü kullanımının benzer piyasa ürünlerine alternatif olarak kefir üretimde kullanılabileceğini belirlemişlerdir.

Sulistyaningtyas, Lunggani, ve Kusdiyantini (2016), %3, %9 ve %15 konsantrasyonlarda *Lactobacillus bulgaricus* ve *Candida* kefir mikroorganizmalarının karışımını kullanarak fermente edilen kırmızı pirinç sütü kefirinin besin içeriğini belirlemişlerdir. Tüm kefir örneklerinde yağ, su ve kül içeriğinin standart kefir özelliğini karşıladığını, karbonhidrat ve protein içeriğinin ise karşılamadığını bulmuşlardır. %9 konsantrasyonunda karışık kültür içeren kırmızı pirinç kefir örneğinin, kefirin standart kalitesini karşılayan besin içeriğine sahip olduğunu bildirmişlerdir.

Atik, Gürbüz, Bölük ve Palabıyık (2021), *Spirulina platensis* ilave edilmiş vegan kefirin üretilmesinde badem ve soya sütünü kullanmışlardır. Kefir örneklerinin depolanması sürecinde laktobasil ve laktokok sayıları ile toplam fenolik içeriklerinin arttığını belirlemişlerdir.

Erol (2020), laktoz intoleransı olan, kalp ve damar hastalığı ve diyabet hastalığı olanlar ile vejetaryenlere alternatif bir ürün olarak badem sütünden bal ve muz içeren kefir üretmiş ve kefir yapımında bademden elde edilen bitkisel sütün alternatif olarak kullanılabileceği bildirmiştir.

Goçer ve Koptagel (2023) fındık sütü, kaju sütü, yer fıstığı sütü, ceviz sütü ve badem sütü kullanarak kefir üretmişlerdir. Fındık sütünün, yüksek yağ ve düşük karbonhidrat içeriği nedeniyle fermantasyon sürecinin uzun olduğunu, fındık kefirinin metabolik konsantrasyonun daha düşük ve pH değerinin yüksek olduğunu saptamışlardır. Ceviz sütünün karbonhidrat içeriğinin düşük olması nedeniyle ceviz kefirinin pH değerinin istenilen seviyeye düşmediğini ve yüksek olduğunu belirlemişlerdir. Fındık sütü ve fındık kefirinin doymamış yağ asitleri oranını yüksek, doymuş yağ asitleri oranını düşük bulmuşlardır. Kaju kefirinin ise en yüksek toplam organik asit içeriğine sahip olduğunu belirlemişlerdir.

Peynir

Bitki bazlı peynir yapımında bitkisel proteinlerin özellikleri önemlidir. Öncelikle bitki materyalinden bitkisel bazlı süt elde edilir. Bu süt kolloidal özellikte olup, raf ömrü uzun ve stabil homojen ürün elde etmesi zordur. Bu nedenle de katı ve çözünmeyen parçacıklarının birikmesinden dolayı kumlu, granül bir yapı oluşmaktadır (Fu ve Yano, 2020). Baklagillerin proteinleri iyi teknolojik özelliklere sahip olmasının yanı sıra ucuzdur. Bu nedenle bitki bazlı peynir benzeri ürünlerde kullanılması uygun olmakla birlikte formülasyon geliştirmede az sayıda baklagil proteini araştırılmıştır (Mefleh, Pasqualone, Caponio, Faccia, 2022). Bakliyat bazlı peynir alternatifleri fermantasyonlu veya fermantasyonsuz olarak üretilebilir. Fasulye aroması enzimatik hidroliz yoluyla hafifletilir ve tohumların endojen fitazı ve eklenen maya ve diğer faydalı mikroorganizmalar sayesinde fitat içeriği azalırken protein sindirilebilirliği iyileştirilir (Dey, Prasad, Kaur, Singh, Luwang, 2017)

Tofu bilinen ve endüstriyel üretimi olan bitkisel kaynaklı bir peynirdir. Tofu üretiminde; soya fasulyesi suda ıslatılır ve öğütülür. Sonrasında soya sütü süzülür, kaynatılır, pıhtılaştırılır. Fasulye pıhtıları kalıplanır ve preslenir. Tofu, kremsi beyaz renkli, pürüzsüz dokulu ve yumuşak tattadır (Wang, Swain, Kwolek, Fehr, 1983).

Dondurma

Dondurma; sevilerek tüketilen, proteince zengin, besleyici bir süt ürünüdür. Dondurmanın fonksiyonelliğini arttırmak amacıyla çeşitli bitkisel sütlerden yararlanılması için çalışmalar yapılmaktadır.

Ahanian, Pourahmad, Mırahmadı, (2014), susamlı dondurma üretiminde yağsız süt yerine soya sütü kullanarak ürettikleri dondurmaların fiziksel, kimyasal ve duyusal özelliklerini belirlemişlerdir. İkame ürün olarak kullanılan soya sütünün oranın artmasıyla birlikte pH, toplam kurumadde, protein, yağ, hacim artışı ve viskozite değerlerinin arttığını, asitlik ve yağsız kurumadde değerlerinin ise azaldığını belirlemişlerdir. Ayrıca %50 oranına kadar soya sütü ilavesinin dondurmanın duyusal özelliklerini önemli derecede etkilemediğini saptamışlardır.

Matias, Padılha, Bedanı ve Saad (2016), soya sütünü peynir altı suyu protein izolatı (WPI) yerine kullanarak sinbiyotik dondurma üretmişlerdir. Dondurmadaki pH değerinin artmasının soya proteinlerinden kaynaklandığını ifade etmişlerdir. *L. acidophilus* LA-5 ile *Bifidobacterium* BB-12'nin depolama süresince 7.5 log CFU/g'nin üzerinde olduğunu belirlemişlerdir. Buna ilaveten, soya sütü ve/veya WPI + inülin içeren dondurmaların laktoz intoleransı olan veya laktoz duyarlılığına sahip bireyler için sinbiyotik bir ürün olarak değerlendirilebileceğini bildirmişlerdir.

Góral, Kozłowicz, Pankiewicz, Kluza ve Wójtowicz (2018), stabilizör olarak inülin ile keçiboynuzu sakızının dondurma üzerindeki etkilerini ve hindistan cevizi sütünün ise dondurmanın fizikokimyasal özellikleri üzerine etkilerini araştırdıkları çalışmalarında yüksek miktarda protein içeriğine sahip hindistan cevizi sütünden yüksek yağ içeriğine sahip dondurma üretilebildiğini belirlemişlerdir. Hindistan cevizi sütü ile geleneksel dondurma üretimine benzer bir üretim gerçekleştirilebileceğini sonucuna varmışlardır.

Rıeskorn, Peters, Little ve Terry (2016), yağ içeriği azaltılarak pancar küspesi ilavesi ile besin değeri arttırılmış dondurma üretimi yapmışlardır. Bir dondurma grubunda ise krem şanti yerine hindistan cevizi sütü kullanmışlardır. Üretimi yapılan ahududu/pancar dondurmasının hindistan cevizi sütü ilave edilmiş dondurmaya göre düşük yağlı, asitlik değerinin düşük, viskozite ve sertliğinin daha az olduğunu bulmuşlardır.

Diğer

Muhallebi yapımında belirli oranlarda fındık ve inek sütü karışımı kullanıldığında fındık sütünün en fazla %50 kullanım oranıyla sütlü tatlılarda kullanılabileceğini belirtmiştir (Ersöz, 2019).

SONUÇ VE ÖNERİLER

Tüketicilerin son zamanlarda sağlıklı ve sürdürülebilir olan beslenme alışkanlıklarını benimsemeleri, yaşam tarzı olarak hayvansal kaynaklı gıdalar yerine bitkisel kaynaklı gıdaları tercih etmeleri gibi nedenlerle bitkisel bazlı süt ve süt ürünlerinin öneminin arttığı görülmektedir. Bitkisel sütler laktozsuz olması, kolesterol içermemesi ve düşük kalorili olmaları nedeniyle tercih edilebilmektedir. Aynı zamanda bitkisel sütler zengin mineral, vitamin, diyet lifi ve antioksidan içerikleri ile fonksiyonel gıdalar sınıfına girmektedir. Bu özellikleri ile bitkisel bazlı sütlerin kullanım alanı artmıştır. Bitkisel sütler ve bunların uygun formülasyonlarının oluşturulması ve geliştirilmesi ile elde edilecek süt ürünlerinin sürdürülebilir bir alternatif olarak değerlendirilmesi mümkündür. Bu konuda daha fazla çalışmanın yapılması yararlı olacaktır.

KAYNAKÇA

Ahanian, B., Pourahmad, R., Mırahmadı, F., 2014. Effect of substituting soy mılk ınstead of skım mılk on physıcochemıcal and sensory propertıes of sesame ıce cream. Indian journal of scientific research, 7(1): 1134-1143.

Ashaye, O. A., Taiwo, L. B., Fasoyiro, S. B., & Akinnagbe, C. A. (2001). Compositional and shelf-life properties of soy-yogurt using two starter cultures. *Nutrition & Food Science*.

Atik, D. S., Gürbüz, B., Bölük, E., & Palabıyık, İ. (2021). Development of vegan kefir fortified with Spirulina platensis. *Food Bioscience*, *42*, 101050.

Baker, G. L., Sims, C. A., Gorbet, D. A., Sanders, T. H., & O'keefe, S. F. (2002). Storage water activity effect on oxidation and sensory properties of high-oleic peanuts. *Journal of food science*, *67*(5), 1600-1603.

Bernat, N., Cháfer, M., Chiralt, A., & González-Martínez, C. (2014). Vegetable milks and their fermented derivative products. *International Journal of Food Studies*, *3*(1).

Chalupa-Krebzdak, S., Long, C. J., & Bohrer, B. M. (2018). Nutrient density and nutritional value of milk and plant-based milk alternatives. *International dairy journal*, *87*, 84-92.

Cruz, N., Capellas, M., Hernández, M., Trujillo, A. J., Guamis, B., & Ferragut, V. (2007). Ultra high pressure homogenization of soymilk: Microbiological, physicochemical and microstructural characteristics. *Food research international*, *40*(6), 725-732.

Das, A., Raychaudhuri, U., & Chakraborty, R. (2012). Cereal based functional food of Indian subcontinent: a review. *Journal of food science and technology*, *49*(6), 665-672.

Peterson, D. M. (2001). Oat antioxidants. *Journal of cereal science*, *33*(2), 115-129.

Demir, H., Simsek, M., & Yıldırım, G. (2021). Effect of oat milk pasteurization type on the characteristics of yogurt. *LWT*, *135*, 110271.

Dey, A., Prasad, R., Kaur, S., Singh, J., & Luwang, M. D. (2017). Tofu: technological and nutritional potential. *Indian Food Industry Magazine*, *36*(3), 8-24.

Dinkçi, N., Kesenkaş, H., Korel, F., & Kınık, Ö. (2015). An innovative approach: cow/oat milk based kefir. *Mljekarstvo: časopis za unaprjeđenje proizvodnje i prerade mlijeka*, *65*(3), 177-186.

Duncan, C. E., Gorbet, D. W., & Talcott, S. T. (2006). Phytochemical content and antioxidant capacity of water-soluble isolates from peanuts (Arachis hypogaea L.). *Food research international*, *39*(8), 898-904.

Durand, A., Franks, G. V., & Hosken, R. W. (2003). Particle sizes and stability of UHT bovine, cereal and grain milks. *Food Hydrocolloids*, *17*(5), 671-678.

Erk, G., Seven, A., Akpınar, A. (2019). Vegan ve vejetaryan beslenmede probiyotik bitkisel bazlı sütü ürünlerinin yeri. Gıda, 44(3):453-462.

Ermiş, E., Güneş, R., İnci, Z. E. N. T., Çağlar, M. Y., & YILMAZ, M. T. (2018). Characterization of hazelnut milk fermented by Lactobacillus delbrueckii subsp. bulgaricus and Streptococcus thermophilus. *Gıda*, *43*(4), 677-686.

Erol, H. (2020). *Badem sütünden ballı ve muzlu kefir üretimi* (Master's thesis, Namık Kemal Üniversitesi).

Ersöz, D. *Fındık sütünden muhallebi üretimi ve bazı özelliklerinin araştırılması* (Master's thesis, Fen Bilimleri Enstitüsü)

Ferragut, V., Valencia-Flores, D. C., Pérez-González, M., Gallardo, J., & Hernández-Herrero, M. (2015). Quality characteristics and shelf-life of ultra-high pressure homogenized (UHPH) almond beverage. *Foods*, *4*(2), 159-172.

Fu, W., & Yano, H. (2020). Development of "new" bread and cheese. *Processes*, *8*(12), 1541.

Góral, M., Kozłowicz, K., Pankiewicz, U., Góral, D., Kluza, F. And Wójtowicz, A., 2018.Impact of stabilizers on the freezing process, and physicochemical and organolepticproperties of coconut milk-based ice cream. Lwt - food science and technology, 92; 516 522.

Gocer, E. M. C., & Koptagel, E. (2023). Production of milks and kefir beverages from nuts and certain physicochemical analysis. *Food Chemistry*, *402*, 134252.

Jeske, S., Zannini, E. and Arendt, E.K. 2018. Past, present and future: The strength of plant-based dairy substitutes based on gluten-free raw materials. *Food Research International*, 110:42–51.

Kedia, G., Vazquez, J. A., & Pandiella, S. S. 2008. Fermentability of Whole Oat Flour, PeriTec Flour and Bran by Lactobacillus Plantarum. Journal of Food Engineering, (89), 246 249.

Liu, K. (2012). *Soybeans: chemistry, technology, and utilization*. Springer.

Matias, N. S., Padilha, M., Bedani, R., & Saad, S. M. I. (2016). In vitro gastrointestinal resistance of Lactobacillus acidophilus La-5 and Bifidobacterium animalis Bb-12 in soy and/or milk-based synbiotic apple ice creams. *International Journal of Food Microbiology*, *234*, 83-93.

Mefleh, M., Pasqualone, A., Caponio, F., & Faccia, M. (2022). Legumes as basic ingredients in the production of dairy-free cheese alternatives: a review. *Journal of the Science of Food and Agriculture*, *102*(1), 8-18.

Muehlhoff, E., Bennett, A., & McMahon, D. (2013). *Milk and dairy products in humannutrition*. Food and Agriculture Organization of the United Nations (FAO).

Öztürk, T., Öztürk, B., Seyhan, F., & Borcakli, M. (2019). *U.S. Patent ApplicationNo.16/087,151*.

Roncero, J. M., Álvarez-Ortí, M., Pardo-Giménez, A., Gómez, R., Rabadán, A., & Pardo, J. E. (2016). Virgin almond oil: Extraction methods and composition. *Grasas y aceites*, *67*(3), e143-e143.

Röös, E., Garnett, T., Watz, V. and Sjörs, C. 2018. The role of dairy and plant based dairy alternatives in sustainable diets. SLU Future Food Reports 3, London.

Rıeskorn, C., Peters, K., Little, R., Terry, P., 2016. The effects of coconut milk and beet pureeon the nutritional, physical and sensory characteristics of raspberry ıce cream. Postersession: food/nutrition science; education; management; food services/culinary;research. Journal of the academy of nutrıtıon and dıetetıcs. Samford university. September 2016 suppl 1-abstracts, (9): 116.

Sethi, S., Tyagi, S. K., & Anurag, R. K. (2016). Plant-based milk alternatives an emerging segment of functional beverages: a review. *Journal of food science and technology*, *53*(9), 3408-3423.

Sulistyaningtyas, A. R., Lunggani, A. T., & Kusdiyantini, E. (2019, June). Kefir produced from red rice milk by Lactobacillus bulgaricus and candida kefir starter. In *IOP Conference Series: Earth and Environmental Science* (Vol. 292, No. 1, p. 012038). IOP Publishing.

Tansakul, A., & Chaisawang, P. (2006). Thermophysical properties of coconut milk. *Journal of Food Engineering*, *73*(3), 276-280.

Tey, S. L., Brown, R. C., Chisholm, A. W., Delahunty, C. M., Gray, A. R., & Williams, S. M.(2011). Effects of different forms of hazelnuts on blood lipids and α-tocopherolconcentrations in mildly hypercholesterolemic individuals. *European journal of clinical nutrition*, *65*(1), 117-124.

Uzuner, A. E. (2012). Probiyotik Yoğurt Üretiminde Pirinç Sütü Kullanımı. Ege Üniversitesi. *Fen Bilimleri Enstitüsü, Yüksek Lisans Tezi, İzmir, 75s*.

Vanga, S. K., & Raghavan, V. (2018). How well do plant based alternatives fare nutritionally compared to cow's milk?. *Journal of food science and technology*, *55*(1), 10-20.

Yiğit, A. A. (2020). Animal and plant-based milk and their antioxidant properties. *Veterinary Journal of Mehmet Akif Ersoy University*, *4*(2), 113-122.

Wang, H. L., Swain, E. W., Kwolek, W. F., & Fehr, W. R. (1983). Effect of soybean varieties on the yield and quality of tofu.

Wijesinha-Bettoni, R., & Burlingame, B. (2013). Milk and dairy product composition. *Milk and dairy products in human nutrition*, 41-102.

Wood, P. J. (1991). Oat β-glucan-physicochemical properties and physiological effects. *Trends in Food Science & Technology*, *2*, 311-314.

SUDA ÇÖZÜNÜR CdTe KUANTUM NOKTALARININ SENTEZİ ve KARAKTERİZASYONU

Melda PATAN ALPER

Dr. Öğr. Üyesi, Yeditepe Üniversitesi, Fen Edebiyat Fakültesi, Fizik Bölümü, Ataşehir, İstanbul., ORCID NO: 0000-0002-2314-6032

ÖZET

Geniş ve çeşitli potansiyel uygulamaları olan kuantum noktalarına günümüzde bilimsel araştırmalarda sıklıkla rastlanmaktadır. Kuantum fiziği, fizik lisans öğrencileri ve birçok disiplinlerarası öğrenci için büyüleyici bir konudur. Kuantum fiziğinin teorik derslerini deneysel çalışmalarla birleştirmek, konuyu öğrenciler için daha anlaşılır ve ilgi çekici hale getirebilir. Bu çalışmanın amacı, lisans öğrencileri için bir deney tasarlamaktır. Deney, sulu ortamda yarı iletken CdTe kuantum noktaların sentezini ve optik karakterizasyonunu kapsar. Çalışma iki bölümden oluşmaktadır, ilk bölüm CdTe kuantum noktaları analitik bir teknik kullanılarak sentezi ve büyütülmesi ve ikinci bölüm ise farklı boyutlardaki bu nanoparçacıkların optik karakterizasyonudur. Bu deneyin temel bilimsel ve eğitsel amaçları, diğerlerine göre daha az tehlikeli ve pratik bir yöntemle konunun anlaşılmasını kolaylaştırmak ve öğrencileri nanobilim ve nanoteknoloji araştırmalarına teşvik etmektir.

Anahtar Kelimeler: Kuantum Noktaları, Kuantum Nokta Sentezi, Nanopartiküller, UV spektroskopisi

SYNTHESIS AND CHARACTERIZATION of WATER SOLUBLE of CdTe QUANTUM DOTS

ABSTRACT

Quantum dots (QDs), which have wide and diverse potential applications, are frequently encountered in scientific research today. Quantum physics is a fascinating subject for physics undergraduates and many interdisciplinary students. Combining the theoretical lessons of quantum physics with experimental studies can make the subject more understandable and interesting for students. The aim of this study is to design an experiment for undergraduate students. The experiment covers the synthesis and optical characterization of semiconductor CdTe QDs in aqueous medium. The study consists of two parts, the first part is the synthesis and growth of CdTe QDs using an analytical technique and the second part is the optical characterization of these nanoparticles of different sizes. The main scientific and educational aims of this experiment are to facilitate the understanding of the subject with a less dangerous and practical method compared to others and to encourage students to research nanoscience and nanotechnology.

Keywords: Quantum Dots, Synthesis QDs, Nanoparticles, UV spectroscopy

INTRODUCTION

The development of semiconductors and the production of quantum dots contributed to many technological developments [1,2]. The use of faster, cheaper novel methods alongside traditional semiconductor manufacturing processes has played an important role in device development and equipment development for the application. The chemical properties of quantum dots allow the electro-optical properties to be adjusted depending on the size, thus providing application-oriented quantum dot production, that is, the design of new generation electronic devices, such as solar panels, transistors, light emitting diodes, photovoltaics, data storage devices, fluorescent labels, DNA nanosensors, etc [3].

Quantum dots are a visually interesting way of demonstrating quantum effects in physics. In quantum mechanics lessons, students learn theoretically the particles in finite and infinite wells, and they have the opportunity to empirically reinforce the concepts they see in the course with such experiments. In this experimental work, too, the transition energies can be explained as a "particle" in a box, here is a displaced electron particle and a nanocrystal box [4-6].

Students acquire the infrastructure to carry out this experiment with the general chemistry, modern physics, and introductory optics courses they took before the quantum mechanics course, which is the 3rd year course in the physics department. With this study, students bring together several important topics; inorganic chemistry concepts, materials science, quantum mechanics and the latest trends in nanotechnology.

Since nanocrystals have size dependent electrical, optical, physical, and chemical, properties, thus it is important to seek out processes that control the physical dimensions of nanoparticles. Efforts in the literature have concentrated on controlling nanocrystal physical dimensions via a range of chemical parameters such as annealing temperatures and times, PH of solution, and reagents types. There are many state-of-the-art methods for synthesizing QDs such as sol-gel, colloidal, electro deposition, solution phase reduction methods. Synthesis of NPs in solution colloidal method was chosen due to easy to produce ease of implementation and cost effective for this undergraduate student experiment. Colloidal QDs have been widely studied in both basic and practical research, and significant advances have been made in their synthesis. This chosen method enables quantum dots to be used in light-emitting diodes (LEDs), gas, pressure and temperature sensing detectors, two- or three-dimensional imaging and solar cells, as well as in biotechnology and medicine.

METHOD

Materials

Production and testing of CdTe quantum dots requires many chemicals and equipment. The chemicals were obtained from Sigma-Aldrich; Tellurium powder (purity 99,999 % size: about 200 mesh), Sodium Borohydride (purity ≥96%), Cadmium Chloride (−10 mesh, 99.999%), Sodium Hydroxide, Mercaptopropionic acid (puriss., ≥99.0% (HPLC)

Glass and plastic standart lab. equipment (beaker, pipette, cuvettes, volumetric flask, tubes etc.), centrifuge, HPLC water machine, PH meter, Mass balance, Uv-Vis Spectrum System

The chemicals used in the experiment are given in the table.

Hazard

In this experiment, water soluble quantum dots were synthesized. It is crucial because the students will not need to work with more hazardous substances. Since it is a chemical synthesis and some materials have dangers, a preliminary study was conducted with the students before the experiment. Some precautions were taken to avoid exposure to chemicals throughout the experiment. Assessment for Control of Substances Hazardous to Health Regulations (COSHH) form was prepared, it includes titles such as name of supervisor, aim, substances, quantities used and stored, hazard identified, preautions, emergency procedure, fire, first aid for affected personnel (contact) etc. The hazards of the chemicals used and how to be protected from them were explained in this form. Some of examples for precautions: An approved respirator or equivalent, breathing apparatus, googles, gloves, lab. coat. The refrigerator and the fume chamber was used to store the chemicals and the prepared samples shown in Figure 1.



Figure 1. The chemicals stored in the refrigerator and the fume chamber

Synthesis of QDs

Since most published scientific studies involve complex processes and in-depth theoretical knowledge, the colloidal synthesis of aqueous CdTe, a simple, fast and relatively safe method, was preferred for undergraduate students [7-9]. The aim was to synthesize different sizes of cadmium telluride (CdTe) quantum dots and to characterize their optical properties. CdTe contains heavy metal and some hazadous chemicals, for this reason, risk assessment of all chemicals used in synthesis was performed before the experiment, allowing the necessary precautions to be taken. It is very important to wear gloves, protective clothing, and goggles throughout the experiment. All the preparations and syntheses should be executed in a well-ventilated fume chamber. Additionally, the laboratory experiment should be conducted under the supervision of trained (lecturer) and qualified staff (lab technician). however, before the experiment, the precautions taken for the experiment were discussed with a technician from a chemistry department

CdTe QDs were synthesized in an aqueous system by mixing tellurium and cadmium precursors in the presence of a thiolate capping agent mercaptopropionic acid (MPA) under vacuum.

This process takes place in two steps: Synthesis of NaHTe Precursor Solution and Cadmium Ion Solution. For the NaHTe precursor solution, 0.4 g Te powder and 1.6 g $NaBH_4$ were combined in a glass vial and this mixture dissolved in 5 ml HPLC water. After a short time, the mixture takes on a bright light and purple color shown in Figure 2. Then, 1.0 mmol cadmium chloride is dissolved in 150 ml HPLC water in a three necked flask.



Figure 2. The NaHTe precursor solution

The synthesis temperature is approximately 100 °C, and the synthesis pH is taken between 7-8. 0.2 ml of MPA was added to form the mixture and 3 ml of Te precursor solution was injected into the mixture. The first color obtained was red and the mixture quickly turned yellow, this process took place in about 10 minutes. The solution is usually lightened in the first 10 or 15 minutes of growth, starting with golden yellow and becoming orange. The sample taken between the first 10-15 minutes during the growth stage is yellow in color and represents the particles with the smallest radius obtained, as shown in Figure 3.

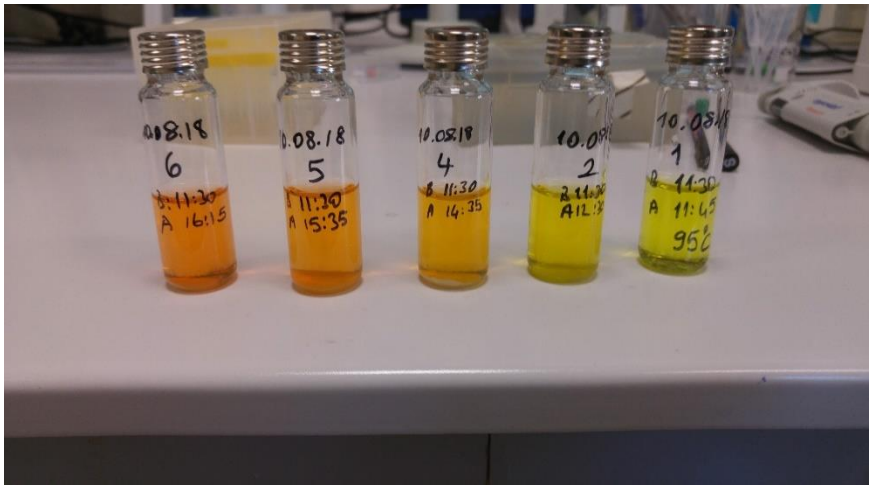


Figure 3 CdTe QDs in aqueous solution with different sizes

Characterization of the Samples

In the second week of the experiment, the technique of UV-Visible spectroscopy was used to characterize the optical properties of semiconductor nanoparticles. Longer synthesis times allows the formation of larger quantum dots. In the early stages of the synthesis, extracted samples were quantum dots of smaller size. At the same time, the colors of the quantum dots started changing from yellow to red.

The QDs or NPs band gap energy increase with particle size, which changes the optical properties, such as the absorption spectra of QDs. The absorption spectra is one of the methods used to find E_g. Data from this method

can be obtained from information about the UV-Visible spectroscopy, bad gap energy that particles have and the radii of particles. The optical absorption measurement measurements were recorded on Perkin Elmer Lambda 25 UV/Visible absorption spectrophotometer between 300-700 nm.

RESULTS AND DISCUSSION

For each sample, the absorption wavelength graph of the data from the absorption spectrometer measurements was drawn. These absorption peaks are given in Figure 4. From this graph , students can clearly see that exciton absorption peaks shift red with heat treatment time.

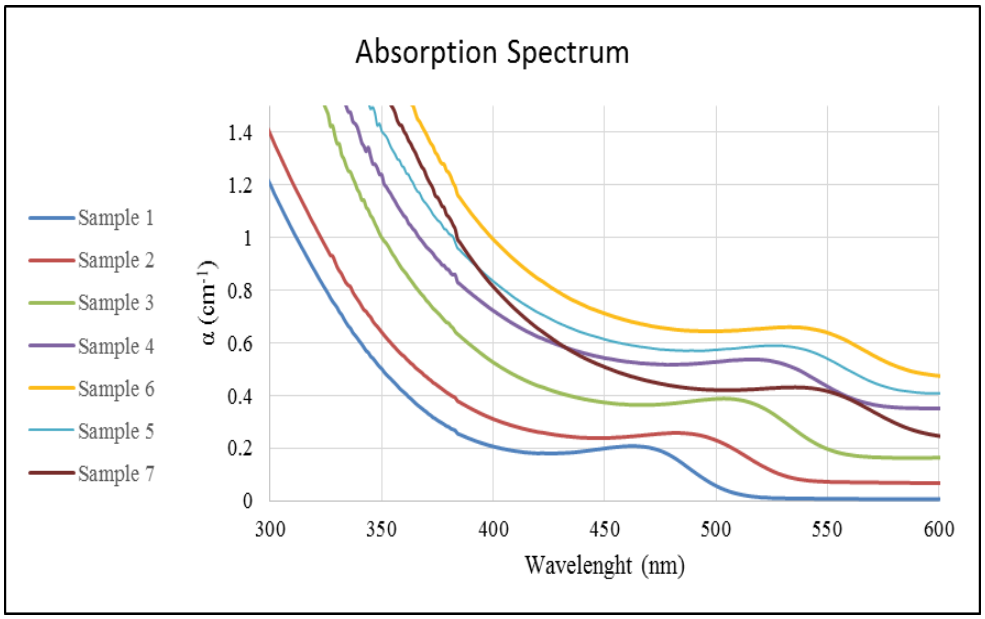


Figure 4 Absorption peaks of the CdTe QDs

During the synthesis, 7 samples were obtained at 7 different times. The time-dependent color change in these samples was observed by the students and when the color change was visible, the main sample was withdrawn. Samples and time data are given in Table 1.

The absorption coefficient (α) waveform plot was used by the students using data from UV-VIS spectroscopy. Band gaps were calculated using the Tauc plot method. The Brus equation (effective mass approximation) was used to determine the size of the particles. Particle radii obtained according to band gaps and effective mass model are given in Table 2.

Table 1. UV/Visible absorption peak wavelength and treatment time for the samples

Solution Sample	Absorption Peak wavelength (nm)	Treatment Time
1	463	15 min
2	483	60 min
3	502	120 min
4	514	180 min
5	526	240 min
6	534	300 min
7	536	375 min

Table 2. Quantum dot sample absorption peak wavelengths, band gaps and radii for all samples

Sample	Eg (eV)	Radius (nm)
1	2.543	1.93
2	2.439	2.02
3	2.401	2.06
4	2.300	2.17
5	2.270	2.21
6	2.241	2.24

CONCLUSION

This experimental study allowed students to learn about multiple subjects such as nanoparticle synthesis methods, quantum mechanics, spectroscopic techniques and nanotechnology. First, students successfully gained quantum dot synthesis skills and observed the unique properties of quantum dots in the synthesis process, allowing them to compare observations with quantum mechanics theory of finite square/potential wells. The temperature was kept constant throughout the synthesis and time dependent size variation was observed. As the time increased, the band energy decreased and increased in size.

This is evidence that infers from Brus equation the size of the particle becomes smaller. Thus optimal heat treatment time and temperatures of the synthesis may allow the particle radius to be tunable.

Students learned that particle size was well controlled by heat treatment time and different characterization methods could be used to calculate the sizes of these particles.

Among these methods, measurements were made by UV-VİS spectroscopy.

It is seen that the change in the dimensions of the quantum dots is not much, one of the reasons for this is that the experiment takes place in a limited time. These results were reached in the experimental period of about 3 hours. It is thought that as the experiment time increases, the quantum dots will get larger. Since the dimensions are very small, the band energy calculations were compared by taking values from different parts of the graph in order to minimize the error, and it was seen that the values did not affect the size calculation.

Results indicate that the size dependence of absorption spectra at various QD dimensions provides evidence for the quantum confinement effect. Furthermore, bandwidth expansion is compatible with theoretical radius calculation based on the effective mass model.

REFERENCES

[1] Koole R., Groeneveld E., Vanmaekelbergh D., Meijerink A. ve Donega C. M. (2014). Size Effects on Semiconductor Nanoparticles. *Nanoparticles*, Springer, pp. 13-51.

[2] Giancoli D. C. (2009) Physics for Scientists & Engineers. New Jersey: Pearson.

[3] Reid P. J., Fujimoto B., Gamelin D. R. (2014). A Simple ZnO Nanocrystal Synthesis Illustrating Three-Dimensional Quantum Confinement. J. Chem. Educ., 91, 280–282

[4] Ekimov A., Onushchenko A. (1981). Quantum Size Effect in Three Dimensional Microscopic Semiconductor Crystals. Journal of Experimental and Theoretical Physics Letters, 34:345.

[5] Rossetti R., Nakahara S., Brus L. (1983). Quantum Size Effects in The Redox Potentials Resonance Raman Spectra. and Electronic Spectra of CdS Crystallites in Aqueous Solution. Journal of Chemical Physics, 79:1086.

[6] Brus. L. (1984). Electron-electron and electron-hole interactions in small semiconductor crystallites: the size dependence of the lowest excited electronic state. Journal of Chemical Physics, 80:4403.

[7] Feng L., Kuang H., Yuan X., Huang H., Yi S., Wang T., Deng K., Tang C. and Zeng Y. (2014). A novel method for aqueous synthesis of CdTe duantum dots. Spectrochimica Acta Part A: Molecular and Biomolecular Spectroscopy, 123:298-302.

[8] Yong K. T., Law W. C., Roy I., Jing Z., Huang H., Swihart M. T. and Prasad P. N. (2011) Aqueous phase synthesis of CdTe quantum dots for biophotonics. Journal of Biophotonics, 4:1-2, 9-20.

[9] Choi S. Y., Shim J. P., Kim D. S., Kim T. Y. and Suh K. S.(2012). Aqueous Synthesis of CdTe Quantum Dot Using Dithiol-Functionalized Ionic Liquid. Journal of Nanomaterials, 2012, 1-6.

ANALYSIS OF THERMAL AND CORROSION BEHAVIOR OF Ti-44Ni-6Cd SHAPE MEMORY ALLOY

Ti-44Ni-6Cd ŞEKİL HATIRLAMALI ALAŞIMIN TERMAL VE KOROZYON DAVRANIŞININ ANALİZİ

Esra BALCİ

Dr., Fırat University, Science, Physics, Elazıg, TURKEY, ORCID NO: 0000-0003-0127-7602

Cengiz TATAR

Prof. Dr., Fırat University, Science, Physics, Elazıg, TURKEY, ORCID NO: 0000-0002-0876-9071

Fethi DAĞDELEN

Assoc. Prof. Dr., Fırat University, Science, Physics, Elazıg, TURKEY, ORCID NO: 0000-0001-9849-590X

ABSTRACT

In this study, TiNiCd shape memory alloys was investigated some physical and chemical properties. The alloy was prepared by the arc-melting production method, and the chemical ratio was chosen as $Ti_{50}Ni_{44}Cd_6$ (% at.). Some thermodynamic parameters of the prepared alloy were investigated by DSC analysis, then, structural properties were investigated by SEM-EDX and XRD. Afterwards, mechanical properties were investigated by Vickers microhardness method, and corrosion related parameters were observed by electrochemical corrosion. The thermal activation energy of the alloy was calculated using the Kissinger and Ozawa method. The average thermal activation energy calculated according to Kissinger and Ozawa method was 132.14 kJ/mol. Considering the XRD and SEM-EDX analyzes, it was determined that the Ti element was the dominant component in the precipitation phases of the alloy. The microhardness of Ti44Ni6Cd alloy was calculated to be approximately 355 $HV_{0.3}$. Additionally, the corrosion resistance (R_p) value of the $Ni_{44}Ti_{50}Cd_6$alloy was calculated as 1.253 ($M\Omega\ cm^{-2}$).

Keywords: Shape Memory Alloys, TiNiCd, Microhardness, Corrosion.

INTRODUCTION

Materials on which the desired reactions can be obtained with external effects (such as magnetic and electric field, pressure, temperature) are called "smart materials" (Cao, Cudney, & Waser, 1999). The contribution of smart materials is quite high among the basic elements that play a role in the advancement and introduction of modern technology (Mohammed et al., 2022). There are many groups of smart materials, but; SMAs are a preferential smart materials (Balci, Karaderi, Kahraman, & Dağdelen, 2022). These smart alloys were first described by eg Arne Ölendar in 1932 (Balcı & Dagdelen, 2022). In the materials science, materials that have the ability to return to their original shape or size whenever heated or cooled by a certain thermal process are called shape memory alloys. These alloys are functional materials that are sensitive to thermal changes. Shape memory alloys for their unique shape memory effect (SME) and high flexibility; they are application in many different fields such as space and aviation, automotive, robotics, biomedical (Buchler, 1963; Jani, Leary, Subic, & Gibson, 2014; Kauffman & Mayo, 1997; Ölander, 1932; Song, Ma, & Li, 2006; Vernon & Vernon, 1941).

TiNi SMAs group included in the smart alloy system, due to their high elasticity, high thermal stability, high corrosion resistance and biocompatibility, they have become the most used and preferred alloys for long years (E Balci, Dagdelen, Mohammed, & Ercan, 2022; Degeratu & Bizdoaca, 2003; Dolce & Cardone, 2001; Kaczmarek, 2007; Maleki-Ghaleh, Khalili, Khalil-Allafi, & Javidi, 2012; Nemat-Nasser, Yong Choi, Guo, Isaacs, & Taya, 2005). The increasing Ni element in the matrix is defined as one of the most important parameters governing the strength and transformation temperatures of some NiTi shape memory alloys (Frenzel et al., 2010). Compared with the coatomic NiTi of NiTi alloys dominated by the nickel element; It has higher strength and lower conversion temperatures (Padula et al., 2012). Some physical properties (thermodynamic parameters:TP, phase transformation temperatures:PTTs, structural and mechanical

properties) and biocompatibility of the new alloy formed with elements added to NiTi-based shape memory alloys can be improved (Balci et al., 2022). Nitinol alloys can generally be added with elements that provide improving properties such as Ta, Cu, Nb, V, Hf, Zr, Cd, Pd (Duerig & Melton, 1989; Es-Souni, Es-Souni, & Fischer-Brandies, 2005; Mousavi, Karimzadeh, & Abbasi, 2008; Ying, Hai-Chang, Li-Jian, Li, & Xin-Qing, 2011). There are no studies investigating the physical and chemical properties of the Cd added NiTi alloy. The element cadmium is a metal located between Zn and Hg in the periodic table, and its chemical behavior is parallel to zinc (Bernhoft, 2013). It is known that elements such as Ti, V, Ta do not have biological side effects (Dagdelen et al., 2020); but Cd, which is abundant in nature, has high toxicity for animals and plants (Feng, Wei, Tu, Ding, & Song, 2013). Cadmium is used in electroplating to better the corrosion resistance behavior of alloys (Cancer, 1993; Genchi, Sinicropi, Lauria, Carocci, & Catalano, 2020; Organization, 2019).

In this study, phase transformation temperatures, electrochemical corrosion behavior, structural properties of triple TiNiCd shape memory alloy were investigated in detail.

MATERIALS and METHOD

Initially, high purity (99.9%) Ti, Ni and Cd powders were mixed with a mechanical mixer at the desired rates (Table 1). The mixed elemental powders were pressed to form disc-like pellets. Then, it was alloyed by arc-melting method in the appropriately selected medium. DSC (Differential Scanning Calorimetry), XRD (X-ray diffraction), SEM-EDX (scanning electron microscope-energy dispersive X-ray spectrometer) and electrochemical characterization analyzes were taked to examine the physical and chemical parameters of alloy. In the sample, the transition between austenite and martensite phases was measured by DSC. Moreover, in order to determine the TPs of the alloy, heat flux measurements at different heating-cooling ratio were made in an Argon gas atmosphere. The XRD measurements was performed. λ-$Cu_{K\alpha}$ beam of wavelength 1.5418A was used at room temperature. The microstructure analysis measurements of the alloy were made with a scanning electron microscope-energy dispersive X-ray spectrometer (SEM-EDX) device. The Vickers microhardness technique was used for mechanical properties. For this procedure, the average of seven different results was calculated. Electrochemical corrosion analysis of the sample was performed by Gamry, Interface 1000B Potentiostat/Galvanostat/ZRA employing Potentiodynamic corrosion technique in 3.5% sodium chloride solution at room temperature (RT). Ag/AgCl electrode was used as the reference electrode, which is frequently used in electrochemical methods.

Table 1. Atomic and weight percent ratios of the designed alloy

Concentration (% at.)			Concentration (% wt.)		
Ti	**Ni**	**Cd**	**Ti**	**Ni**	**Cd**
50	44	6	42.4	45.7	11.9

FINDING and DISCUSSION

Phase transitions and phase transformations that occur in solid structures occur with many interesting changes depending on the material properties. Figure 1 displays the DSC curve of alloy obtained in different heating and cooling ratio. Each measurement was made in a completed thermal cycle. The main phases in SMAs are austenite (main phase) phase, martensite (product phase) phase. Austenite; it has a high temperature or cubic crystal structure known as the main phase. The martensite phase, on the other hand, is the low temperature phase, exhibiting a tetragonal or monoclinic crystal structure (Otsuka & Wayman, 1999; Patoor, Lagoudas, Entchev, Brinson, & Gao, 2006). These two phase are clearly observed in Figure 1. The characteristic PTT for shape memory alloys, including austenite start (A_s), austenite finish (A_f), martensite start (M_s), and martensite finish (M_f) temperatures were achieved by the tangent technique. The PTT resulting from thermal cycles completed under different heating-cooling rates of SMA are given in Table 2. NiTi-based SMAs can be used up to 100°C, since they generally have low transformation temperatures (Firstov, Van Humbeeck, & Koval, 2006). According to Dagdelen et al. show that A_s=12 °C and A_f=20 °C of the austenite PTTs of NiTi-3V alloy (Dağdelen, Balci, & Ercan). In another study available in the literature, Dagdelen F. et al. found the phase transformation temperature of the TiNiNbTa alloy to be A_s = 44 °C and A_f = 88 °C (Dagdelen, Balci, Qader,

Aydogdu, & Saydam, 2021). The austenite phase transformation temperatures of the NiTi alloy in this study was found to be A_s =72 ℃ and A_f =111,3 ℃. It can be said that the transformation temperatures of the ternary alloy formed by adding the NiTi base alloy with the Cd element have increased. In addition, when the examined Figure 1 and Table 2, A_s and A_f were changed depend on heating rate. It depends on the amount of heat flux to which the sample is exposed. Other physical quantities obtained with the help of DSC analysis measurements, which determine the thermal characteristics of the alloy, were calculated. One of these parameters is enthalpy (ΔH). The amount of energy taken or given for phase changes of materials is the phase transformation enthalpies. The enthalpy (ΔH) values measured depending on the changing temperature values during the phase transformations of the sample were determined. The area under the endothermic DSC peaks was calculated and found to be 21.6 J/g.

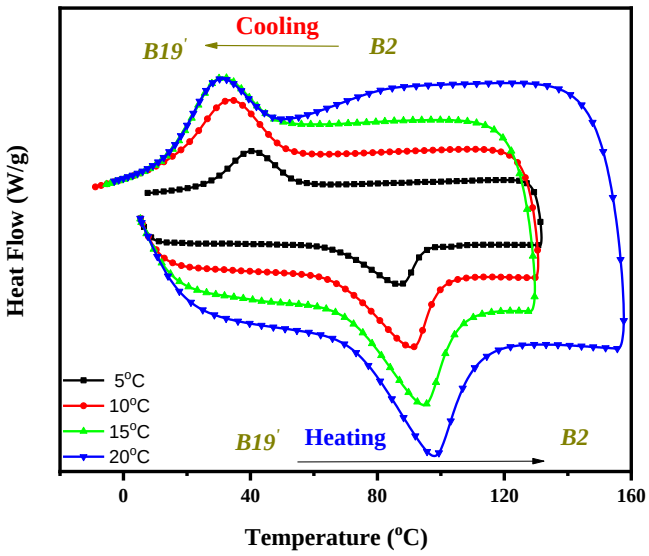


Figure 1. Differential scanning calorimetry curves of TiNiCd SMA

Table 2. Some thermal parameters of TiNiCd alloy

Heating-colling rate	A_s (℃)	A_f (℃)	A_p (℃)	M_s (℃)	M_f (℃)	ΔH_{M-A} J/g	ΔH_{A-M} J/g
5 ℃	66.9	95.1	86.9	55.0	27.0	21.1	-19.1
10 ℃	67.6	99.9	90.8	50.6	16.3	21.6	-21.0
15 ℃	71.3	105.9	94.6	48.5	14.5	21.1	-17.4
20 ℃	72.0	111.3	97.9	46.2	14.0	21.1	-15.3

The energy required for the phase transformation of materials is defined as the activation energy (Ea) (Kaya, Özdemir, Kaya, & Keskin, 2020). The activation energy was determined by taking the different heating-cooling ratios of the thermal cycles (5,10,15 and 20℃). DSC peaks and conversion temperatures were used to calculate the activation energy that occurs in the completed thermal cycle. The value of Ea, which can be calculated by many different methods, is mostly found by using the Ozawa and Kissinger methods. The phase transformation peaks obtained using different heating rates are evaluated. The Kissinger (Kissinger, 1957) and Ozawa method (Ozawa, 1970) can be found with the following equations, respectively:

$$\frac{d(\ln(\beta/A_p^2))}{d(\ln(1/A_p))} = -\frac{E_a}{R} \qquad 1$$

$$\Delta E \cong -2.19R\frac{d\log\beta}{d(1/A_p)} \qquad 2$$

where R (R = 8.314 J mol-1) is the universal gas constant, β is heating rate, and Amax is the maximum peak temperature during the phase transformations. From these two methods, thermal activation energy can be obtained with graphs that will provide the relationship between Kissinger method $\ln(\beta/A_p^2)$ and $(1000/A_p$)), but between $\log\beta$ and $1000\ /\ A_p$ in Ozawa method. The *Ea*'s obtained by using the linear graph slopes in Figure 3.a and Figure 3.b by Kissinger and Ozawa methods were calculated. Calculated activation energy values and averages are given in Table 3. According to the calculations obtained, the average activation energy of the alloy was found to be 132,14 kJ/mol. In a study by E.Ercan et al., the average activation energy of the $Ni_{30}Ti_{50}Cu_{20}$ shape memory alloy was calculated as 63.208 kJ/mol (Ercan, Dağdelen, Mediha, & Balcı, 2019). In another study by E.Balcı et al., the average activation energy of the NiTiNbTa(Balcı & Dagdelen, 2022) and TiNiTa(E Balci et al., 2022).shape memory alloys were calculated as 56.35 kJ/mol and 64.14 kJ/mol, respectively. In this study, the activation energy of the TiNiCd alloy produced by the same method was higher when compared to the studies listed above.

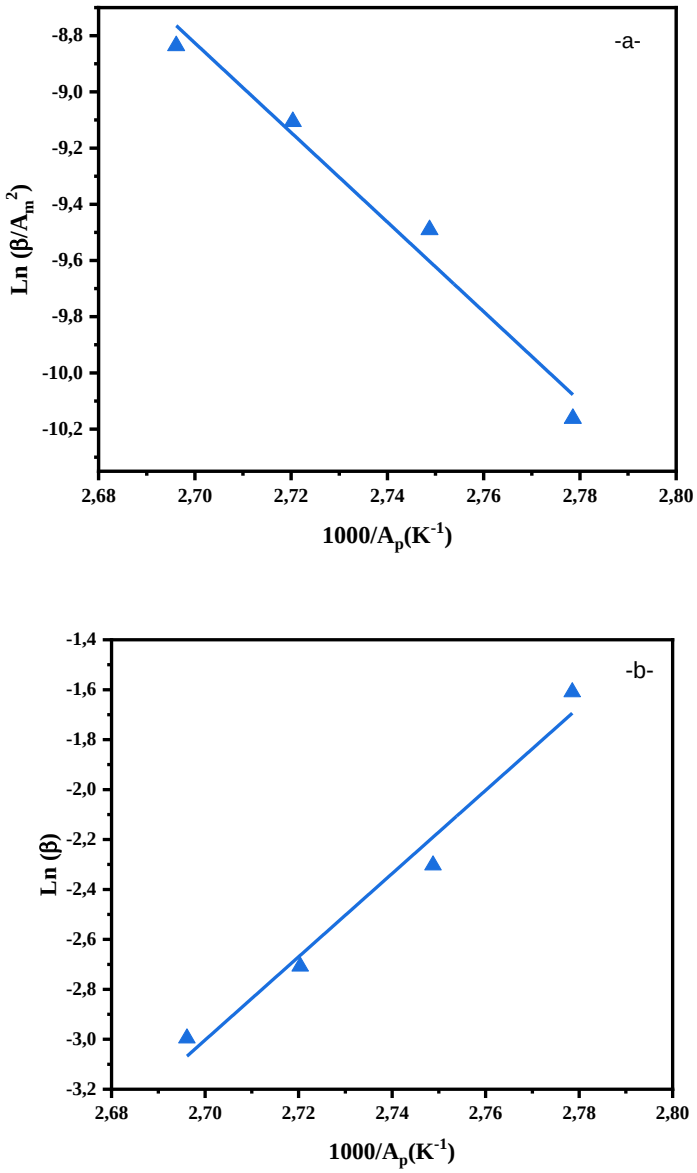


Figure 3. Graphs for the calculation of thermal activation energies a) Kissinger method, b) Ozawa method

Table 3. Activation energies and average values of alloys according to Kissinger and Ozawa method

$Ea_{Kissinger}$ (kJ/mol)	Ea_{Ozawa} (kJ/mol)	$Ea_{avarege}$ (kJ/mol)
132,5	131,79	132,14

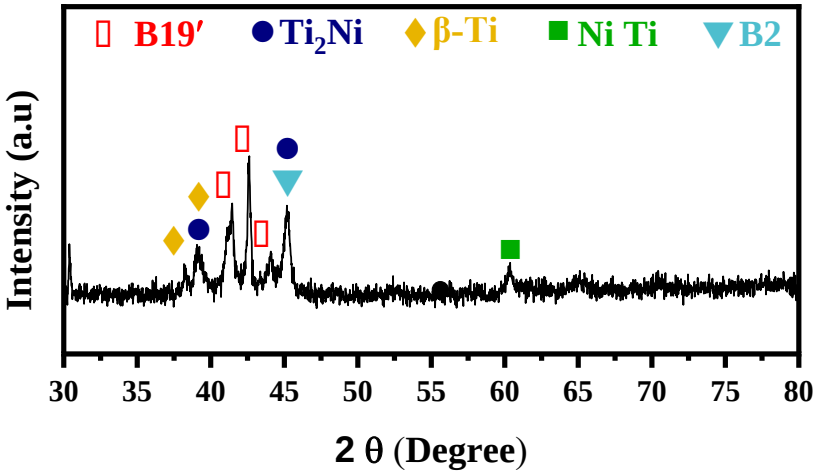


Figure 4. XRD pattern of TiNiCd alloy

Figure 4 displays the XRD patterns found for alloy at RT. The peaks were indexed by the literature (Esra Balci & Dagdelen, 2022; Balcı & Dagdelen, 2022; E Balci et al., 2022; Esra Balci, Dagdelen, Qader, & Kok, 2021; Dagdelen et al., 2021; Li, Rong, & Li, 1999; Tillmann & Momeni, 2015). There are basically characteristic diffraction peaks of different phases in all the XRD patterns of the sample: B19', B2, NiTi, Ti_2Ni. Generally, both B19' (martensite) and B2 (austenite) phases are defined in NiTi-based SMAs. In addition to generally characteristic phases, β-Ti (titanium-rich phase) peaks were found in the quaternary alloy formed by adding Cd element.

Vickers microhardness technique was used to investigate the effect of Cd on the microhardness of NiTi-based alloys. The microhardness test was performed seven times for the alloy, and the average value was calculated as 355 $HV_{0.1}$. In a study by I. N. Qader et al., it was found that the microhardness of the NiTiSn alloy, which was doped with Sn at different rates, changed in the range of approximately 180-455 HV (Qader, Kok, & Cirak, 2021). In an another article by C. Tatar et al., the microhardness analysis result of NiTiCu SMA was found to be approximately 200-500 HV (Tatar, Acar, & Qader, 2020).

The microstructure and chemical element components of the alloy were investigated by SEM-EDX analysis. EDX results from certain marked regions shown in Figure 5 are given in Table 5. The areas marked with SEM image illuminate that generally, the alloy is present in a homogeneous structure; but in some regions, this precipitate structure is found. It was determined that titanium element was the dominant element in the precipitate structures of the alloy. As a result, the precipitate phases are rich in titanium element. The surface analysis (SEM) results agree well with the chemical composition (EDX) analysis of alloy. The data obtained by both analyzes support each other when compared with the XRD results. The result of EDX analysis of the entire surface of the alloy shows that Ti is the dominant element, while the component incorporation ratio also varies for different microstructures. On the basis of the variability, many external factors may be responsible for the physical properties of SMA (such as thermal cycles, different heat flux, chemical etching processes).

SEM images **EDX Analysis**

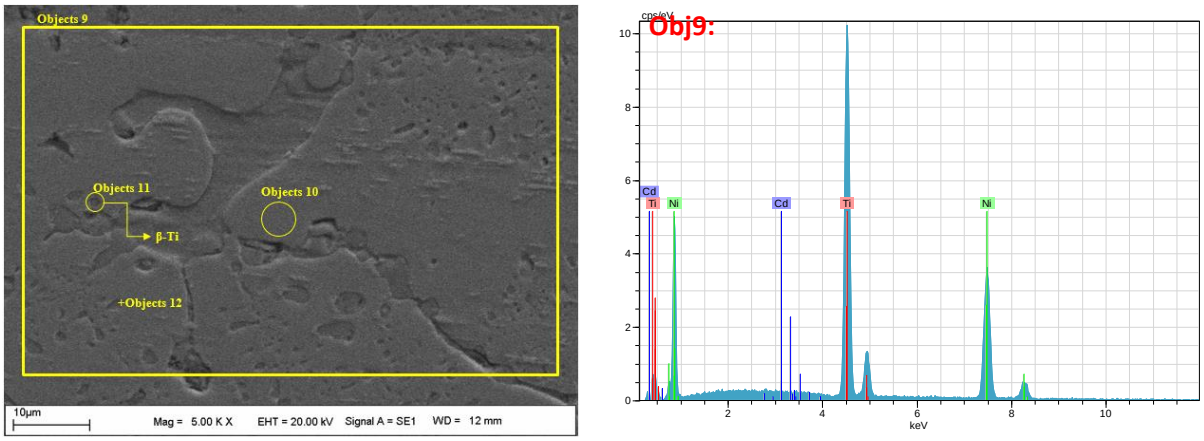


Figure 5. SEM-EDX analysis for alloy.

Table 5. EDX outcomes on the SEM image of alloy.

Objects	Ni (at. %)	Ti (at. %)	Cd (at. %)
9	46.89±1.5	52.70±1.4	0.41±0.1
10	49.22±1.5	50.45±1.3	0.33±0.1
11	48.37±1.6	51.23±1.4	0.40±0.1
12	49.33±1.5	50.36±1.3	0.31±0.1

The loss of metallic properties of the alloy as a result of chemical reactions with its environment as a result of electrochemical events in general is called "corrosion". Materials must be tested for corrosion in response to their intended use. Although there are many methods in corrosion behavior analysis, the potentiodynamic method was used in this study. Corrosion analysis of the alloy and the parameters related to it were found. First of all, Taffel slopes were obtained by tangential method by taking the anodic (βa) and cathodic (βc) polarization lines. In addition, the corrosion potential (E_{corr}) and current (I_{corr}) were found by extrapolating from these polarizations (βa and βc). The corrosion rate (C_R) of the alloy was calculated with this equation, with the deterioration of the alloy for approximately one year (Rahmani, Sadooghi, & Hashemi, 2020):

$$C_R = \gamma \times i_{corr} \times EW / \rho_{alloy} \quad (3)$$

According to Eq. (3), the corrosion rate is proportional to the metric conversion factor ($\gamma = 3.27 \times 10^{-3}$), i_{corr}, and equivalent weight (EW); also C_R reversibly proportion with the density of the alloys (ρ_{alloy}). The EW value found using equation (4) (Baboian, 2005):

$$EW = \frac{1}{\sum \frac{n_i \times f_i}{W_i}} . \quad (4)$$

here f_i and W_i are mass friction and atomic weight of the i^{th} element; n_i is the number of valance electrons of the i^{th} element in the alloy. Also, the value of ρ_{alloy} depends on the density of each participation elements and their amount in the alloy(Najib, Abdullah, Saad, Samsudin, & Ani, 2017):

$$\frac{1}{\rho_{alloy}} = \sum \frac{f_i}{\rho_i} \ . \qquad (5)$$

Stern–Geary equation was used to calculate corrosion resistance (Rp)(Hwang, Cho, Lee, Yoo, & Shin, 2008):

$$Rp = \frac{(\beta_a x \beta_c)}{2{,}303 \ x \ I_{corr} \ x \ (\beta_a + \beta_c)} \qquad (6)$$

The corrosion resistance of alloy evaluated in in 3.5% sodium chloride solution at room temperature and the Taffel curve drawn accordingly are shown in Figure 6. The obtained values are listed in Table 6. The corrosion resistance was calculated with the help of Eq. 6.

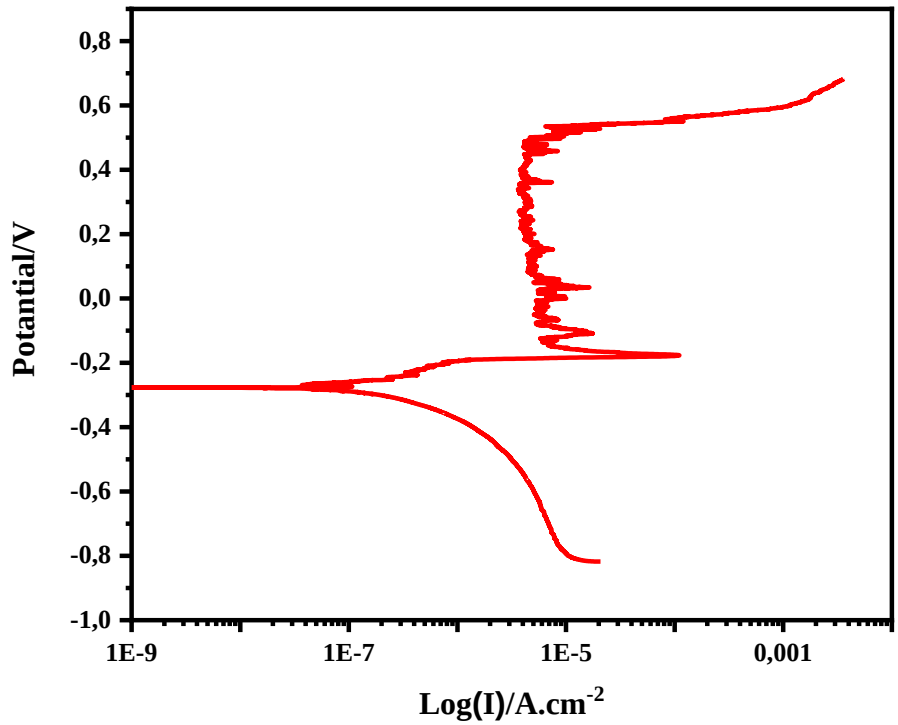


Figure 6. Taffel plots of Cd6 SMA in the SBF solution at the room temperature

Table 6. Electrochemical analysis parameters of the SMA

b_a/V	b_c/V	E_{corr}/V	I_{corr}/mA.cm^{-2}	Corrosion Rate /mmpy	Corrosion Resistance (R_p)/ MΩ cm^{-2}
0.791	0.256	-0.276 V	0.462 x10^{-6}	0.264	1.253

According to the equation used and the calculations obtained, Rp was found 1.253 MΩ cm^2. In a study by E.Balci et al., the corrosion behavior of $Ti_{50}Ni_{30}Ta_{20}$ alloy was analyzed as a result of Potentiodynamic methods and its corrosion resistance (Rp) was found to be 0.071 MΩ cm^2 (E Balci et al., 2022). E.Balci et al. analyzed the corrosion behavior of Ti27Ni19Nb4Ta and Ti27Ni19Nb4 (at %) V alloys as a result of Potentiodynamic methods, and the corrosion resistance was found as 0.979 and 0.327, respectively (Esra Balci & Dagdelen, 2022). Standard resistance classes are given in Table 7 (Mareci et al., 2014; Popoola, Olorunniwo, & Ige,

2014). The corrosion rate value of the alloy was found to be 0.264 mmpy. $Ni_{44}Ti_{50}Cd_6$ SMA is in very stable corrosion class.

CONCLUSIONS and RECOMMENDATIONS

Shape memory properties, some mechanical properties (such as microhardness, microstructural properties), chemical, thermal and corrosion behavior of $Ti_{50}Ni_{44}Cd_6$ SMA were investigated in this study. Some evaluations of the alloy in line with these researches and investigations can be given as follows.

- As a result of DSC analysis of $Ti_{50}Ni_{44}Cd_6$ alloy, it can be said that it exhibits shape-memory alloy properties and the addition of Cd increases the workability of this alloy in areas above 100°C.
- With the addition of Cd, both the transformation phase transformation enthalpies and thermal activation energy increased.
- Titanium-rich (β-Ti) phase was found in microstructure evaluations.
- The Cd element added to the NiTi alloy improved the corrosion results of the alloy. Since Cd is known to have a biological side effect, it is recommended to be used as a building and building material instead of medical applications.

REFERANCES

Baboian, R. (2005). *Corrosion tests and standards: application and interpretation* (Vol. 20): ASTM international.

Balci, E., & Dagdelen, F. (2022). The comparison of TiNiNbTa and TiNiNbV SMAs in terms of corrosion behavior, microhardness, thermal and structural properties. *Journal of Thermal Analysis and Calorimetry*, 1-7.

Balcı, E., & Dagdelen, F. (2022). Thermal, Structural Properties and Potential Dynamic Corrosion Study of Ti-27Ni-21Nb-2Ta SMA. *Iranian Journal of Science and Technology, Transactions A: Science, 46*(1), 353-359.

Balci, E., Dagdelen, F., Mohammed, S., & Ercan, E. (2022). Corrosion behavior and thermal cycle stability of TiNiTa shape memory alloy. *Journal of Thermal Analysis and Calorimetry*, 1-8.

Balci, E., Dagdelen, F., Qader, I. N., & Kok, M. (2021). Effects of substituting Nb with V on thermal analysis and biocompatibility assessment of quaternary NiTiNbV SMA. *The European Physical Journal Plus, 136*(2), 145.

Balci, E., Karaderi, C. C., Kahraman, H., & Dağdelen, F. (2022). NiTiNbX (X= Ta ve V) Biyouyumlu Şekil Hatırlamalı Alaşımların Yapay Vücut Sıvısı İçerisinde Hücre Kültür Testi ve Bakteri Üreme Değerlendirilmesi. *International Journal of Innovative Engineering Applications, 6*(1), 59-64.

Bernhoft, R. A. (2013). Cadmium toxicity and treatment. *The Scientific World Journal, 2013*.

Buchler, W. J. (1963). Effect of low-temperature phase changs on the mechanical properties of alloys near composition TiNi. *Journal of Apply Physics., 34*, 1475-1477.

Cancer, I. A. f. R. o. (1993). Beryllium, cadmium, mercury, and exposures in the glass. *Apresentado em: IARC Working Group on the Evaluation of Carcinogenic Risks to Humans: Beryllium, Lyon*.

Cao, W., Cudney, H. H., & Waser, R. (1999). Smart materials and structures. *Proceedings of the National Academy of Sciences, 96*(15), 8330-8331.

Dagdelen, F., Balci, E., Qader, I., Aydogdu, Y., & Saydam, S. (2021). Effects of Substituting Nb with Ta on Microstructure and Thermal Properties of Novel Biocompatible TiNiNbTa Shape Memory Alloys. *Physics of Metals and Metallography, 122*(14), 1572-1580.

Dagdelen, F., Balci, E., Qader, I., Ozen, E., Kok, M., Kanca, M., . . . Mohammed, S. (2020). Influence of the Nb content on the microstructure and phase transformation properties of NiTiNb shape memory alloys. *JOM Journal of the Minerals Metals and Materials Society, 72*(4), 1664-1672.

Dğdelen, F., Balci, E., & Ercan, E. Ti-27Ni-20Nb-3V Alaşımın Faz Dönüşüm Sıcaklıkları, Korozyon Direnci ve Yapısal Özelliklerinin İncelenmesi. *Bitlis Eren Üniversitesi Fen Bilimleri Dergisi, 10*(3), 796-802.

Degeratu, S., & Bizdoaca, N. (2003). Shape memory alloys: fundamentals, design and applications: Universitaria Press, Craiova, Romania.

Dolce, M., & Cardone, D. (2001). Mechanical behaviour of shape memory alloys for seismic applications 2. Austenite NiTi wires subjected to tension. *International journal of mechanical sciences, 43*(11), 2657-2677.

Duerig, T., & Melton, K. (1989). *Wide hysteresis NiTiNb alloys.* Paper presented at the European symposium on martensitic transformations.

Ercan, E., Dağdelen, F., Mediha, K., & Balcı, E. (2019). Investigation of Thermodynamic Properties of Ni30Ti20Cu20 Shape Memory Alloy. *Bitlis Eren Üniversitesi Fen Bilimleri Dergisi, 8*(4), 1194-1202.

Es-Souni, M., Es-Souni, M., & Fischer-Brandies, H. (2005). Assessing the biocompatibility of NiTi shape memory alloys used for medical applications. *Analytical and bioanalytical chemistry, 381*(3), 557-567.

Feng, R., Wei, C., Tu, S., Ding, Y., & Song, Z. (2013). A dual role of Se on Cd toxicity: evidences from the uptake of Cd and some essential elements and the growth responses in paddy rice. *Biological Trace Element Research, 151*(1), 113-121.

Firstov, G., Van Humbeeck, J., & Koval, Y. N. (2006). High temperature shape memory alloys problems and prospects. *Journal of Intelligent Material Systems and Structures, 17*(12), 1041-1047.

Frenzel, J., George, E. P., Dlouhy, A., Somsen, C., Wagner, M.-X., & Eggeler, G. (2010). Influence of Ni on martensitic phase transformations in NiTi shape memory alloys. *Acta Materialia, 58*(9), 3444-3458.

Genchi, G., Sinicropi, M. S., Lauria, G., Carocci, A., & Catalano, A. (2020). The effects of cadmium toxicity. *International journal of environmental research and public health, 17*(11), 3782.

Hwang, D. Y., Cho, J. Y., Lee, D. H., Yoo, B. Y., & Shin, D. H. (2008). Plasma electrolytic oxidation of AZ91 Mg alloy in the sodium stannate electrolyte. *Materials transactions*, 0806020436-0806020436.

Jani, J. M., Leary, M., Subic, A., & Gibson, M. A. (2014). A review of shape memory alloy research, applications and opportunities. *Materials & Design (1980-2015), 56*, 1078-1113.

Kaczmarek, M. (2007). Corrosion resistance of NiTi alloy in simulated body fluids. *Archives of Materials Science and Engineering, 28*(5), 269-272.

Kauffman, G. B., & Mayo, I. (1997). The story of nitinol: the serendipitous discovery of the memory metal and its applications. *The chemical educator, 2*(2), 1-21.

Kaya, I., Özdemir, Y., Kaya, E., & Keskin, M. E. (2020). The heating–cooling rate effect on thermal properties of high nickel-rich NiTi shape memory alloy. *Journal of Thermal Analysis and Calorimetry, 139*(2), 817-822.

Kissinger, H. E. (1957). Reaction kinetics in differential thermal analysis. *Analytical chemistry, 29*(11), 1702-1706.

Li, B., Rong, L., & Li, Y. (1999). Microstructure and superelasticity of porous NiTi alloy. *Science in China Series E: Technological Sciences, 42*(1), 94-99.

Maleki-Ghaleh, H., Khalili, V., Khalil-Allafi, J., & Javidi, M. (2012). Hydroxyapatite coating on NiTi shape memory alloy by electrophoretic deposition process. *Surface and Coatings Technology, 208*, 57-63.

Mareci, D., Bolat, G., Cailean, A., Santana, J., Izquierdo, J., & Souto, R. (2014). Effect of acidic fluoride solution on the corrosion resistance of ZrTi alloys for dental implant application. *Corrosion Science, 87*, 334-343.

Mohammed, S. S., Balci, E., Qadir, H. A., Qader, I. N., Saydam, S., & Dagdelen, F. (2022). The exploring microstructural, caloric, and corrosion behavior of NiTiNb shape-memory alloys. *Journal of Thermal Analysis and Calorimetry, 147*(21), 11705-11713.

Mousavi, T., Karimzadeh, F., & Abbasi, M. (2008). Synthesis and characterization of nanocrystalline NiTi intermetallic by mechanical alloying. *Materials Science and Engineering: A, 487*(1-2), 46-51.

Najib, A., Abdullah, M. Z., Saad, A., Samsudin, Z., & Ani, F. C. (2017). Numerical simulation of self-alignment of chip resistor components for different silver content during reflow soldering. *Microelectronics Reliability, 79*, 69-78.

Nemat-Nasser, S., Yong Choi, J., Guo, W.-G., Isaacs, J. B., & Taya, M. (2005). High strain-rate, small strain response of a NiTi shape-memory alloy. *Journal of Engineering Materials and Technology, 127*(1), 83-89.

Organization, W. H. (2019). Preventing disease through healthy environments: exposure to cadmium: a major public health concern: World Health Organization.

Otsuka, K., & Wayman, C. M. (1999). *Shape memory materials*: Cambridge university press.

Ozawa, T. (1970). Kinetic analysis of derivative curves in thermal analysis. *Journal of thermal analysis, 2*(3), 301-324.

Ölander, A. (1932). An electrochemical investigation of solid cadmium-gold alloys. *Journal of the American Chemical Society, 54*(10), 3819-3833.

Padula, S., Qiu, S., Gaydosh, D., Noebe, R., Bigelow, G., Garg, A., & Vaidyanathan, R. (2012). Effect of upper-cycle temperature on the load-biased, strain-temperature response of NiTi. *Metallurgical and Materials Transactions A, 43*(12), 4610-4621.

Patoor, E., Lagoudas, D. C., Entchev, P. B., Brinson, L. C., & Gao, X. (2006). Shape memory alloys, Part I: General properties and modeling of single crystals. *Mechanics of Materials, 38*(5-6), 391-429.

Popoola, A., Olorunniwo, O., & Ige, O. (2014). Corrosion resistance through the application of anti-corrosion coatings. *Developments in corrosion protection, 13*(4), 241-270.

Qader, I. N., Kok, M., & Cirak, Z. D. (2021). The effects of substituting Sn for Ni on the thermal and some other characteristics of NiTiSn shape memory alloys. *Journal of Thermal Analysis and Calorimetry, 145*(2), 279-288.

Rahmani, K., Sadooghi, A., & Hashemi, S. (2020). The effect of Al2O3 content on tribology and corrosion properties of Mg-Al2O3 nanocomposites produced by single and double-action press. *Materials Chemistry and Physics, 250*, 123058.

Song, G., Ma, N., & Li, H.-N. (2006). Applications of shape memory alloys in civil structures. *Engineering structures, 28*(9), 1266-1274.

Tatar, C., Acar, R., & Qader, I. N. (2020). Investigation of thermodynamic and microstructural characteristics of NiTiCu shape memory alloys produced by arc-melting method. *The European Physical Journal Plus, 135*(3), 1-11.

Tillmann, W., & Momeni, S. (2015). In-situ annealing of NiTi thin films at different temperatures. *Sensors and Actuators A: Physical, 221*, 9-14.

Vernon, L. B., & Vernon, H. M. (1941). Process of manufacturing articles of thermoplastic synthetic resins: Google Patents.

Ying, C., Hai-Chang, J., Li-Jian, R., Li, X., & Xin-Qing, Z. (2011). Mechanical behavior in NiTiNb shape memory alloys with low Nb content. *Intermetallics, 19*(2), 217-220.

CHALLENGES AND OPPORTUNITIES OF BLOCKCHAIN IN ELECTRIC VEHICLES

İsa AVCI

Karabuk University, Engineering Faculty, Computer Department, Karabuk, Türkiye., ORCID ID: https://orcid.org/ 0000-0001-7032-8018

Bahadır Furkan KINACI

Kara*buk University, Engineering Faculty, Railway System Department, Karabuk, Türkiye., ORCID ID: https://orcid.org/ 0000-0001-6872-2630*

ABSTRACT

Depending on the development of technologies, it has been seen frequently in recent years that electric vehicles have been widely produced. Especially due to the increase in vehicle fuel costs, electric vehicles are preferred by users. For these reasons, we observe that the electric vehicle industry is spreading quickly. This means a significant increase in the exchange of data and energy between these vehicles. The current centralized system is less secure in terms of security and more prone to data modification and deletion by attackers. Therefore, looking for alternatives that provide excellent protection for this huge amount of data and energy became necessary. This article will explain the use of blockchain in this field and how it can address the trading of transmitted and received energy between electric vehicles. The advantages of using blockchain with electric cars and how it can secure energy trading transactions will also be demonstrated. A group of researchers in this field and the challenges this technology faces in energy trading will also be discussed. The studies will be examined, and suggestions will be made in terms of investment and security. Also, the future points of these the blockchain technologies in the future will be discussed.

Keywords: Electric vehicles, Energy trading, Blockchain, Blockchain

ELEKTRİKLİ ARAÇLARDA BLOCKCHAIN'İN ZORLUKLARI VE FIRSATLARI

ÖZET

Bu Teknolojilerin gelişmesine bağlı olarak son yıllarda elektrikli araçların yaygın olarak üretildiği sıklıkla görülmektedir. Özellikle araç yakıt maliyetlerinin artması nedeniyle elektrikli araçlar kullanıcılar tarafından tercih edilmektedir. Bu nedenlerle elektrikli araç sektörünün hızla yayıldı gözlemlenmektedir. Bu, bu araçlar arasındaki veri ve enerji alışverişinde önemli bir artış anlamına gelmektedir. Mevcut merkezi sistem, güvenlik açısından daha az güvenlidir ve saldırganlar tarafından verilerin değiştirilmesine ve silinmesine daha yatkındır. Bu nedenle, bu büyük miktarda veri ve enerji için mükemmel koruma sağlayan alternatifler aramak gerekli hale gelmiştir. Bu makale, bu alanda blok zincirinin kullanımını ve elektrikli araçlar arasında iletilen ve alınan enerjinin ticaretini nasıl ele alabileceğini açıklanacaktır. Elektrikli arabalarla blok zinciri kullanmanın avantajları ve enerji ticareti işlemlerini nasıl güvence altına alabileceği de gösterilecektir. Ayrıca, bu alan yaşanan teknolojinin enerji ticaretinde karşılaştığı zorluklar da tartışılacaktır. Yapılan çalışmalar incelenecek, yatırım ve güvenlik açısından önerilerde bulunulacaktır. Ayrıca, bu çalışmada blockchain teknolojilerinin geleceği tartışılacaktır.

Anahtar Kelimeler: Elektrikli araçlar, Enerji ticareti, Blockchain, Blockchain güvenliği

INTRODUCTION

For regular vehicles, traffic is in charge of up to 70% of CO2 gas release (WEC, 2021; WEO, 2021). Conversely, in electric cars, you can find a clean environment, less noise due to its silent engine, no crowded-on fuel station, lower costs, maintenance savings, and convenience. However, most information and communications technology systems are centralized, which means non-transparency, disintegration, insecurity, and less trust (Lacity an Van Hoek, 2021). Thus, this led to the search for other sources of the available and appropriate solutions with Blockchain technology. Blockchain is a decentralized technology; it

can solve the trading energy between the electric vehicle parties and be summed by the power grid stations, charging stations, and the electric vehicles. And to directly perform business operations, this technology makes the owners of electric cars communicate due to its peer-to-peer network (Swan, 2015). Another thing blockchain uses the immutable technology, which means the data and the transactions have stored on it in complex ways. So dishonest or cheating drivers in this system cannot change the records because the Blockchain network data are visible to all with high clarity to the parties who trade energy on the network (Zhong et al., 2016). The ledger is open with the Blockchain that stores electric vehicles' energy trading data in time order. Trading the energy between the participants in the electric vehicle system using Blockchain makes this trading more traceable, transparent, and trusted (Lombardi et al., 2018). The following shape will explain how the blockchain system generally works with electric vehicles.

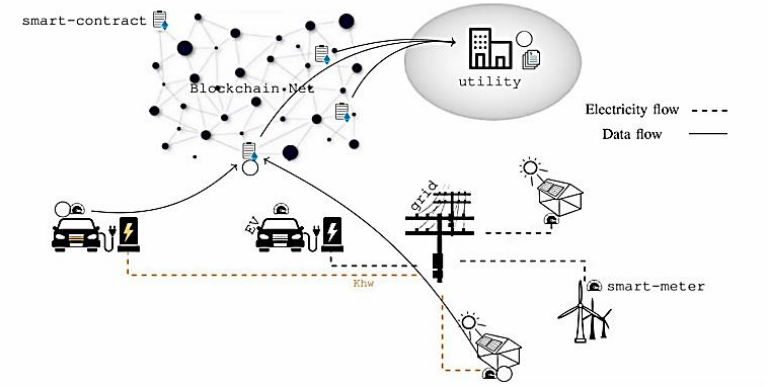


Figure 1. General picture for Blockchain and EVS

The three leading players are utility companies or power grids, electric vehicles, and charging stations (Figure 1). And there are data and electricity exchanged between those three elements. Blockchain will connect all these things. Initially, the utility or the grid will register every electric vehicle and charging station as a new user on the smart contract. It is also responsible for adding wallet balances. Battery swapping and charging services offered by the power grid stations to offer some benefits to the electric vehicles, the drivers need to recognize the trusted and reliable power grid stations. So complete information about power grid stations should be publicly available to help them choose the good one from the existing charging and swapping stations (Amasova et al., 2018). Blockchain can handle all these transactions compared between it to the centralized registry. Most of the essential things that can cover our daily needs in the system of the electric vehicle, and the Blockchain can handle them, such as: Calculate battery discharge rate (Alahmed et al., 2016; Hakak et al., 2020], identifying good reputable charging stations, what is the energy request at the peak off hours, find the closest route between the start point and the endpoint of charging station (Yao et al., 2015), selling the excess energy to benefited from it or power grid stations (vehicle to grid and the grid to vehicle) (Zhou et al., 2019; Zhou et al., 2018), and what is the energy need during the peak hours (Alahmed et al., 2016; Rehman et al., 2018).

BLOCKCHAIN CONDITIONS IN ELECTRIC VEHICLES

The centralized system for the energy trading in the electric vehicle does not have enough ability to deal with the development and many electric vehicles (Bunger et al., 2016). And the use of blockchain technology in this field will give this system excellent protection, data against external attacks, the possibility of tracking, and arguably more transparency. The following points must be available in the blockchain system to be applied to electric vehicles.

Accuracy

In this point, the required applications for energy trading have to be correct, visible, and trusted. So Blockchain can make sure the operations of individuals for the duration of electric vehicle electricity trading, an example of decreasing data accuracy is "using inappropriate platforms to store and process data related to energy trading" (Lu et al., 2014).

Fast Processing

For fast processing of transection, electric-powered vehicles are growing each day. In the last two years, hundreds of electricity charging stations spread worldwide to cover the electricity demands, So Blockchain is needed to technique several thousand transactions each second (Hakak et al., 2020). Also, the developers of smart contracts should have enough experience in writing smart contracts and not using a bug; the bugs inside the smart contracts can change the goal of intelligent contracts to a damaging cause (Amasova et al., 2018).

Privacy Protection

As it is known that any breaking of data privacy or identity stealing will degrade the user's trust within the device and the reputation of the electricity companies, centralized data storage can enable the machine individuals to get entry to the information of the strength trading events (Knirsch et al., 2018). So, the solution will be with the Blockchain as the records are continual to be had with no chance of hacking, changing, or security breaking. Moreover, Blockchain is an immutable era secured by using cryptographically hashed values of facts (Abdella and Shuaib, 2018). Another essential thing is Blockchain uses cryptographic keys to recognize users; also, it hides the recognition of the users (Elhaddad, 2020).

Security

For security, the solution with the Blockchain, you know the contributors of the electric vehicles power trading require fully secure and reliable information for sharing and processing. Blockchain technology affords a public and allotted machine that could successfully shop, manipulate, proportion, and replace electricity buying and selling statistics at the ledger; the catalog is sent to some of the miners who go on with display and affirm the statistics up-dates to assure records integrity (Sing and Kim, 2017; Hassija et al., 2020).

The Legal Issues

For legal issues, most of the blockchain systems do now not offer a way to confirm the identification of the members. The conventional centralized systems can discover customers through 3rd party; in a blockchain-based answer, cryptocurrencies may be transferred online, which can help money laundering or maybe finance terrorist tasks (Amasova et al., 2018).

Communication Between Platform

In platform use, the members of energy buying and selling systems for electric cars can use special blockchain systems. Blockchain platforms ought to have complete help to alternate correctly and manner information in an on-hand, efficient, and rapid manner amongst those unique platforms (Rueegger and MacHado, 2020; Miraz and Donald, 2019). Blockchain generation is an excellent preference in this region as it has a united records code to observe (Singh et al., 2020).

Storage

The size of data generated by electric motors will increase for storage problems. And present electric powered cars can create thousands of gigabytes of information each second; thus, the increased fee of the ledger may

be affected without delay; ledger size grows depending on the type of the Blackchin and the used applications (Wang et al., 2019; Esmaeilian et al., 2019).

OPPORTUNITIES OF BLOCKCHAIN IN ENERGY TRADING

The opportunities in electric vehicles can be energy traceability, improving market efficiency, Stakeholders' reputation, billing and payments, energy auctioning, and vehicle-to-grid energy trading. It will be explained one after the other; the following points show the opportunities of Blockchain technology.

Traceability

Managing the assets: Blockchain traceability feature method coping with the belongings record all through asset processing, and the Blockchain's smart contracts can report the alternate transactions. At the same time, energy is transferred from the battery to some other customer (Jake, 2021). The reputation of the plant supplying: through the usage of Blockchain, the electric automobile proprietors can also affirm the type and popularity of the plant supplying electricity to the grid stations (Orecchini et al., 2015). The actual time gets right of entry to the smart grid: this will keep away from the crowding resulting from electric automobiles at a smart grid, especially at some stage in top hours, via information traceability and immutable transaction file.

Market Efficiency

This can be done by lowering energy buying and selling prices, maximizing contributors' earnings, and satisfying the community restrictions. Blockchain generation can play multiple positions inside the energy trading market. The proprietors of electrical chargers can be provided a reward to carry their chargers online for public use; it assists the operators of power grid stations in higher management. More excellent energy chargers inside the community allow electric vehicle owners to buy energy from people who provide reasonably-priced costs (Hou et al., 2020; Esmaeilin et al., 2019).

Stakeholders' Reputation

It is the opportunity that the electric vehicle drivers maybe offer at the wrong time to restrict statistics to the clever grid. And this will motivate unfair power allocation to electric-powered automobiles. A smart contract can put penalties on dishonest or selfish drivers.

Payments

Electric car owners prefer a quick, relied-on, and verifiable charge machine to decrease billing and price dishonesty. Many digital currencies consisting of Bitcoin are primarily based totally on a public decentralized blockchain ledger; Bitcoin and Ethereum platforms support micropayment transactions like Satoshi. Blockchain technology allows micro-payments with no need for a third-party (Ahmad et al., 2021).

Auctioning of the Energy Trading

All through height hours and non-pinnacle hours, auctioning is one of the techniques that may be followed via electric-powered motors. Blockchain guarantees an excessive level of acceptance as true with amongst actors concerned in auctioning energy; wise contracts automate the bidding technique to rush up the manner of strength auctioning. While the auctioning manner has been completed, the technique considers numerous parameters for declaring a winner, a player's provided bid fee, and the gap between customers and dealers (Ahmad et al., 2021). Using the electric-powered automobile can promote extra power to the neighboring vehicles at a charge that suits each (PankiRaj etal., 2019; Leong et al.,2019).

Car-to-Grid Energy Trading

The existing car-to-grid power buying and selling platforms are to reduce the mismatch between demand and supply of electricity during peak hours. Via purchasing power from electric automobiles can encourage automobile proprietors to participate in the automobile-to-grid electricity trading technique (Zhou et al., 2019). The blockchain era can assist in automating and securing car-to-grid power buying and selling. Smart contracts with digital signatures and consensus algorithms, it can emphasize that cryptocurrency rewards are transferred to the pockets of the electric automobile owner who sells strength to the smart grid. Blockchain creates healthful competition among smart grid owners to shop for electricity from electric-powered motors to attain man or woman demands for the duration of peak hours (Zhou et al., 2018).

RELATED COMPANIES

Vandebron & TenneT companies are examples of these companies. Vandebron is located in Amsterdam, founded in 2013, and supplies inexperienced electricity to communities (Vandbron, 2021). However, this business enterprise no longer generates any electricity. TenneT is a power transmission operator in the Netherlands and Germany and materials power to greater than forty-one million users. In both organizations, the energy trading transactions between the stakeholders have finished using a Hyper ledger blockchain platform that's advanced via IBM and hosted the use of the Linux basis (IBM, 2021). The aim of this partnership between the two businesses is to stabilize the grid's call for with its transport thru the assessment of depended on statistics stored on the Blockchain.

MotionWerk is a German corporation startup that makes a specialist of personal and public strength charging stations accountable to exchange energy between electric automobiles. The implementation of the blockchain era right here is the use of the percentage & Charge (Carrie Hampel, 2021). Percentage & charge is software that gives a P2P issuer that lets electric powered-powered vehicles and charging station proprietors change power in a relaxed and dependable without a third-party carrier (Motionwerk, 2021). Percentage & fee also proposes a decentralized protocol for electrical motors' power charging statistics system.

Power Ledger, this company has developed the usage in Australia and permits P2P solar power buying and selling between electric vehicles (V2G, G2V, POWR token, and ATM) [38]. Presents a platform that permits tracking, buying, and selling strength using Blockchain generation. It also enables car-to-Grid and Grid-to-automobile electricity buying and selling. Moreover, it offers flexibility to the users to sell surplus energy using shifting the cryptocurrency as bills to the pockets of the power producers. The business enterprise also created a software token known as the strength Ledger coin (POWR) that allows the participants to invest in the device. And in the latest years, they've turned out to be more interested in electric car electricity by turning electric automobiles into cellphones ATMs (Jemma Green, 2021; Power Ledger, 2021). Lightency, based in 2018, and affords software program-based answers to power businesses. Presents a decentralized power market to connect individuals, which include (customers, grid operators, and prosumers) (Lightency, 2021). Lightency lets customers come to be prosumers and will enable them to promote the surplus strength for coins benefits. The Difference between a consumer & prosumer a consumer is a person who buys a product and uses it; a prosumer is a person who buys a product, uses it, and spreads the word about it.

CHALLENGES

Scalability Blockchain may be tormented by the scalability of current blockchain systems. The current country of blockchain technology can't host billions of electric vehicles with actual-time information processing (Liu et al., 2018; Salah et al., 2020). But personal structures are greater scalable than public blockchain plat-paperwork, however, most do no longer observe a decentralized shape for storing and processing facts and transactions. The most famous blockchain coins, Bitcoin and Ethereum, can execute up to twenty transactions / Sec most effectively (Kim et al., 2018; Carlo, 2021). Researchers have proposed solutions along with hashing to address the scalability problems of current blockchain structures.

The Inevitably in the Blockchain, records are immutable methods that the facts saved in the ledger can't be (modified, deleted, or hacked); therefore, irreversibility is a top-notch characteristic of Blockchain and guarantees information protection (Huang and Thürer, 2019). For Privacy Public blockchain platforms

consisting of Ethereum and Bitcoin provide immutable information and hide identification over the device. Then again, non-public blockchain platforms are extra involved approximately gadget performance than hiding identity. Consistent with the (GDPR) which is fashionable data safety law in abbreviation any virtual entity inclusive of (encrypted or hashed digital identifiers or private records) ought to be inaccessible to unauthorized users (Gyongyosi and Imre, 2019). The researchers have applied unique techniques to ensure that facts saved on the Blockchain comply with GDPR standards (Mengiste and Kazemi, 2021). Last for security Attackers may utilize the weak spot of smart contracts to transfer cryptocurrency tokens from a consumer's wallet (Ahmad et al., 2021).

CONCLUSION

The development of technology in recent years has been accelerating in the field of blockchain. The most important feature of these developments should be the prioritization of security. Commercial energy trade has become the most important concept in many countries in recent years. It will be inevitable to use blockchain technology in secure trade between countries. In particular, the establishment of a safe trade will increase the orientations in this field.

Fewer skills in blockchain theory can much affect the energy trading inside the EVS companies. One of the things that cause great concern in breaching information security is the frightening phase that occurs in quantum computer systems. The blockchain structures can affect transaction execution and velocity and also can affect the strength of buying and selling operations. One of the demands for the winning public blockchain is the privacy of the facts because facts and transactions are open and easy to anyone. In the future, commercial activities in this area will allow it to be used in other areas.

REFERENCES

Abdella, J., & Shuaib, K. (2018). Peer to peer distributed energy trading in smart grids: A survey. Energies, 11(6), 1560.

Ahmad, R. W., Salah, K., Jayaraman, R., Yaqoob, I., Ellahham, S., & Omar, M. (2021). The role of blockchain technology in telehealth and telemedicine. International journal of medical informatics, 148, 104399.

Alahmad, A., Al Juheshi, F., Sharif, H., Alahmad, M., Shuaib, K., Abdul-Hafez, M., & Aljuhaishi, N. (2016, November). Overview of ICT in the advancement of electric vehicle penetration: Overview of vehicle grid communication system and charging infrastructure and a case study of economic and environmental benefits of electric vehicles in Nebraska. In 2016 12th International Conference on Innovations in Information Technology (IIT) (pp. 1-6). IEEE.

Amosova, N., Kosobutskaya, A. Y., & Rudakova, O. (2018, December). Risks of unregulated use of blockchain technology in the financial markets. In 4th International Conference on Economics, Management, Law and Education (EMLE 2018) (pp. 9-13). Atlantis Press.

Burger, C., Kuhlmann, A., Richard, P., & Weinmann, J. (2016). Blockchain in the energy transition. A survey among decision-makers in the German energy industry. DENA German Energy Agency, 60, 1-44.

Carlo R.W. De Meijer, "Remaining challenges of blockchain adoption and possible solutions," online, accessed 5/11/2021, February 2020, https://www.finextra.com/blogposting/18496/remaining-challenges-ofblockchain adoption-and-possible-solutions.

Carrie Hampel, "Share&Charge launches Open Charging Network," online, accessed 02/08/2021, March 2020, https://www.electrive.com/2020/03/03/sharecharge-launches-opencharging- network/.

Elhadad, A. (2020). Data sharing using proxy re-encryption based on DNA computing. Soft Computing, 24(3), 2101-2108.

Esmaeilian, B., Sarkis, J., Lewis, K., & Behdad, S. (2020). Blockchain for the future of sustainable supply chain management in Industry 4.0. Resources, Conservation and Recycling, 163, 105064.

Gyongyosi, L., & Imre, S. (2019). A survey on quantum computing technology. Computer Science Review, 31, 51-71.

Hakak, S., Khan, W. Z., Gilkar, G. A., Haider, N., Imran, M., & Alkatheiri, M. S. (2020). Industrial wastewater management using blockchain technology: architecture, requirements, and future directions. IEEE Internet of Things Magazine, 3(2), 38-43.

Hassija, V., Chamola, V., Garg, S., Krishna, D. N. G., Kaddoum, G., & Jayakody, D. N. K. (2020). A blockchain-based framework for lightweight data sharing and energy trading in V2G network. IEEE Transactions on Vehicular Technology, 69(6), 5799-5812.

Hou, J., Wang, C., & Luo, S. (2020). How to improve the competiveness of distributed energy resources in China with blockchain technology. Technological Forecasting and Social Change, 151, 119744.

Huang, J., Li, S., & Thürer, M. (2019). On the use of blockchain in industrial product service systems: A critical review and analysis. Procedia CIRP, 83, 552-556.

IBM, "IBM blockchain - enterprise blockchain solutions and services," online, accessed 02/08/2021, June 2016, https://www.ibm.com/blockchain.

Jake Frankenfield, "Accelerating Energy Transition with Blockchain Technology," online, accessed 09/06/2021, January 2020, https://www.ifpenergiesnouvelles.com/article/accelerating-energytransition blockchain-technology.

Jemma Green, "Power ledger," online, accessed 04/08/2021, April 2019, https://www.powerledger.io/.

Lacity, M., & Van Hoek, R. (2021). What we've learned so far about blockchain for business. MIT Sloan Management Review, 62(3), 48-54.

Leong, C. H., Gu, C., & Li, F. (2019). Auction mechanism for P2P local energy trading considering physical constraints. Energy Procedia, 158, 6613-6618.

Lightency, "Lightency: The bright side of energy," online, accessed 04/09/2021, July 2017, https://lightency.io.

Liu, H., Zhang, Y., & Yang, T. (2018). Blockchain-enabled security in electric vehicles cloud and edge computing. IEEE Network, 32(3), 78-83.

Lombardi, F., Aniello, L., De Angelis, S., Margheri, A., & Sassone, V. (2018). A blockchain-based infrastructure for reliable and cost-effective IoT-aided smart grids.

Lu, C., Rong, K., You, J., & Shi, Y. (2014). Business ecosystem and stakeholders' role transformation: Evidence from Chinese emerging electric vehicle industry. Expert Systems with applications, 41(10), 4579-4595.

Kim, S., Kwon, Y., & Cho, S. (2018, October). A survey of scalability solutions on blockchain. In 2018 International Conference on Information and Communication Technology Convergence (ICTC) (pp. 1204-1207). IEEE.

Knirsch, F., Unterweger, A., & Engel, D. (2018). Privacy-preserving blockchain-based electric vehicle charging with dynamic tariff decisions. Computer Science-Research and Development, 33(1), 71-79.

Mengiste, S. A., & Kazemi, G. (2021). Conceptualization of A GDPR-Mining Blockchain-Based Auditor: A Systematic Review.

Miraz, M. H., & Donald, D. C. (2019). Atomic cross-chain swaps: development, trajectory and potential of non-monetary digital token swap facilities. arXiv preprint arXiv:1902.04471.

Motionwerk, "Experience the seamless and sustainable future of mobility based on blockchain technology," online, accessed 02/08/2021, September 2018, https://motionwerk.com/.

Orecchini, F., Santiangeli, A., Zuccari, F., & Dell'Era, A. (2015). The concept of energy traceability: application to EV electricity charging by Res. Energy Procedia, 82, 637-644.

PankiRaj, J. S., Yassine, A., & Choudhury, S. (2019). An auction mechanism for profit maximization of peer-to-peer energy trading in smart grids. Procedia Computer Science, 151, 361-368.

Power Ledger, "Power ledger and Silicon Valley power trial to turn electric vehicles into mobile atms," online, accessed 04/08/2021, May 2019, https://medium.com/power-ledger/successful-power-ledger-andsilicon- valley-power-trial-to-turn-electric-vehicles-into-mobile-atms- 67816c80bdf9.

Rehman, A., Mazhar Rathore, M., Paul, A., Saeed, F., & Ahmad, R. W. (2018). Vehicular traffic optimisation and even distribution using ant colony in smart city environment. IET Intelligent Transport Systems, 12(7), 594-601.

Rueegger, J., & MacHado, G. S. (2020, May). Rational exchange: Incentives in atomic cross chain swaps. In 2020 IEEE International Conference on Blockchain and Cryptocurrency (ICBC) (pp. 1-3). IEEE.

Salah, K., Alfalasi, A., Alfalasi, M., Alharmoudi, M., Alzaabi, M., Alzyeodi, A., & Ahmad, R. W. (2020, January). IoT-enabled shipping container with environmental monitoring and location tracking. In 2020 IEEE 17th Annual Consumer Communications & Networking Conference (CCNC) (pp. 1-6). IEEE.

Singh, M., & Kim, S. (2017). Blockchain based intelligent vehicle data sharing framework. arXiv preprint arXiv:1708.09721.

Singh, R., Tanwar, S., & Sharma, T. P. (2020). Utilization of blockchain for mitigating the distributed denial of service attacks. Security and Privacy, 3(3), e96.

Swan, M. (2015). Blockchain: Blueprint for a new economy. " O'Reilly Media, Inc.".

Vandebron, "Duurzame Energie van nederlandse bodem," online, accessed 02/08/2021, May 2018, https://vandebron.nl/.

Wang, G., Shi, Z., Nixon, M., & Han, S. (2019, July). Chainsplitter: Towards blockchain-based industrial iot architecture for supporting hierarchical storage. In 2019 IEEE International Conference on Blockchain (Blockchain) (pp. 166-175). IEEE.

WEO-2017 Special Report: World Energy Investment Outlook – Analysis, online, accessed 5/22/2021, June 2014, https://www.iea.org/reports/world-energy-investment-outlook.

World Energy Council, "World Energy Trilemma Index," online, accessed 5/30/2021, March 2021, https://www.worldenergy.org/transition-toolkit/world-energy-trilemma-index.

Yao, L., Chen, Y. Q., & Lim, W. H. (2015, December). Internet of things for electric vehicle: An improved decentralized charging scheme. In 2015 IEEE international conference on data science and data intensive systems (pp. 651-658). IEEE.

Zhong, W., Yu, R., Xie, S., Zhang, Y., & Tsang, D. H. (2016). Software defined networking for flexible and green energy internet. IEEE Communications Magazine, 54(12), 68-75.

Zhou, Z., Wang, B., Dong, M., & Ota, K. (2019). Secure and efficient vehicle-to-grid energy trading in cyber physical systems: Integration of blockchain and edge computing. IEEE Transactions on Systems, Man, and Cybernetics: Systems, 50(1), 43-57.

Zhou, Z., Tan, L., & Xu, G. (2018, October). Blockchain and edge computing based vehicle-to-grid energy trading in energy internet. In 2018 2nd IEEE conference on energy internet and energy system integration (EI2) (pp. 1-5). IEEE.

INVESTIGATION OF E-SECURITY STANDARDS USED IN INTELLIGENT TRANSPORTATION SYSTEMS

İsa AVCI

Karabuk University, Engineering Faculty, Computer Department, Karabuk, Türkiye. ORCID NO: 0000-0001-7032-8018

Bahadır Furkan KINACI

Karabuk University, Engineering Faculty, Railway System Department, Karabuk, Türkiye. ORCID NO: 0000-0001-6872-2630

Abstract

With the developments in technology, digitalization and digital infrastructure systems have started to develop. These emerging developments have led to the development of IOT (Internet of Things) technology and have found use in every subsystem suitable for digitalization. Intelligent transportation systems (ITS) structure, which has emerged in recent years and has an important place in the development of transportation systems, has started to form and has become a global field of study. Intelligent transportation systems have enabled vehicles, infrastructures, and all kinds of IOT-based devices to exchange data with each other. This emerging communication structure allows the formation of a safe, efficient, fast, environmentally friendly and low-cost transportation structure. In addition to its efficient structure, the IOT technology used in intelligent transportation systems may reveal various security and control risks, as it uses a certain communication infrastructure. In order to eliminate these risks and take various precautions, many institutions have published various regulations, standards, and studies. In this study, the E-Security standards used in intelligent transportation systems around the world will be examined and the current situation regarding the E-Security structure will be analyzed.

Keywords: Intelligent Transportation Systems, Security, E-Security Standards

AKILLI ULAŞIM SİSTEMLERİNDE KULLANILAN E- GÜVENLİK STANDARTLARININ İNCELENMESİ

Özet

Teknolojide yaşanan gelişmeler ile birlikte dijitalleşme ve dijital alt yapı sistemleri gelişim göstermeye başlamıştır. Ortaya çıkan bu gelişmeler IOT (Nesnelerin İnterneti) teknolojisinin gelişmesini sağlamış ve dijitalleşmeye uygun her alt sistemde kullanım alanı bulmuştur. Son yıllarda ortaya çıkan ve ulaşım sistemlerinin gelişimi için önemli bir yer tutan Akıllı ulaşım sistemleri (AUS) yapısı oluşmaya başlamış ve küresel bir çalışma alanı haline dönüşmüştür. Akıllı ulaşım sistemleri araçların, alt yapıların ve her türlü IOT tabanlı cihazın birbirleri arasında veri alışverişi yapmalarına olanak sağlamıştır. Ortaya çıkan bu haberleşme yapısı güvenli, verimli, hızlı, çevreci ve düşük maliyetli ulaşım yapısının oluşmasına olanak sağlamaktadır. Akıllı ulaşım sistemlerinde kullanılan IOT teknolojisi ortaya koymuş olduğu verimli yapısına ek olarak belirli bir haberleşme alt yapısı kullanıyor olması çeşitli güvenlik ve kontrol risklerini ortaya çıkarabilmektedir. İlgili bu riskleri ortadan kaldırmak ve çeşitli önlemler almak için birçok kurum çeşitli düzenlemeler, standartlar ve çalışmalar yayınlamıştır. Bu çalışmada dünya üzerinde akıllı ulaşım sistemlerinde kullanılan E-Güvenlik standartları incelenerek E-Güvenlik yapısı ile ilgili mevcut durum analiz edilecektir.

Anahtar Kelimeler: Akıllı Ulaşım Sistemleri, Güvenlik, E-Güvenlik Standartları

INTRODUCTION

With the developing technology, ITS emerges as a subject of great importance for countries. When the application areas of ITS systems are examined, it has been determined that there are applications in all areas of road, air, sea, and rail transport. It is expected that all systems and subsystems needed while performing ITS

applications will be efficient, operable, cost-effective, and compatible with interoperability. The efficient structures needed for ITS applications are shaped within the framework of regulations, reports, and standards put forward by organizations with expertise in the relevant field. The standards that emerged because of the studies carried out by expert organizations contribute to the studies as they describe the most appropriate way needed to do a job (U.S. Department of Transportation), (Tufan, H).

Although the standard studies carried out are based on interest, during the emergence of the standard, due to similar reasons such as the expectations of the standard-setting institution, application areas, existing systems, and the requirements of these systems, it may not be able to create a fully sufficient reference for each system to be established. The expectations and capabilities of the systems to be implemented regarding reference to the relevant standards will reveal the holistic or departmental applicability of the standard (Society of Automotive Engineers of Japan, 2020).

INTELLIGENT TRANSPORTATION SYSTEM (ITS)

Intelligent Transportation System is a system that enables the collection, storage/processing of real-time data and the application of the results obtained by applying advanced electronic, information, and communication technologies to roads, vehicles, and sub-systems to maximize efficiency in the transportation sector and to ensure safe and comfortable transportation. ITS aims to reduce travel times in smart cities, increase traffic safety, use existing road capacities efficiently, increase mobility, use energy efficiently and reduce damage to the environment. In line with these purposes, vehicles, equipment, infrastructure, and superstructure systems are developed. In the ITS structure, it becomes easier to receive and send data with versatile data transmission and redundant communication systems between the center and the field. ITS are information communication-based systems that include data exchange and monitoring, measurement, analysis, and control mechanisms (T.C. UAB, 2022).

When the sub-application components of ITS are examined; intelligent infrastructure, intelligent vehicle, intelligent traffic management (intelligent intersection management, electronic supervision, etc.), intelligent transportation management (intelligent stop, intelligent public transportation, etc.), and electronic payment systems and applications are discussed. From the perspective of transportation management, ITS can be grouped into four main groups. These groups are:

- ATIS- Advanced Traffic Information System
- ATMS- Advanced Traffic Management System
- APTS- Advanced Public Transport System
- EMS- Emergency Management System

ITS provides significant access to cleaner, safer, and more efficient transport systems. Due to their superiority, ITS systems have found application in all areas of road, air, maritime, and railway transportation and have been integrated into all systems and subsystems used. In Figure 1, examples of the application areas of ITS systems are shown.

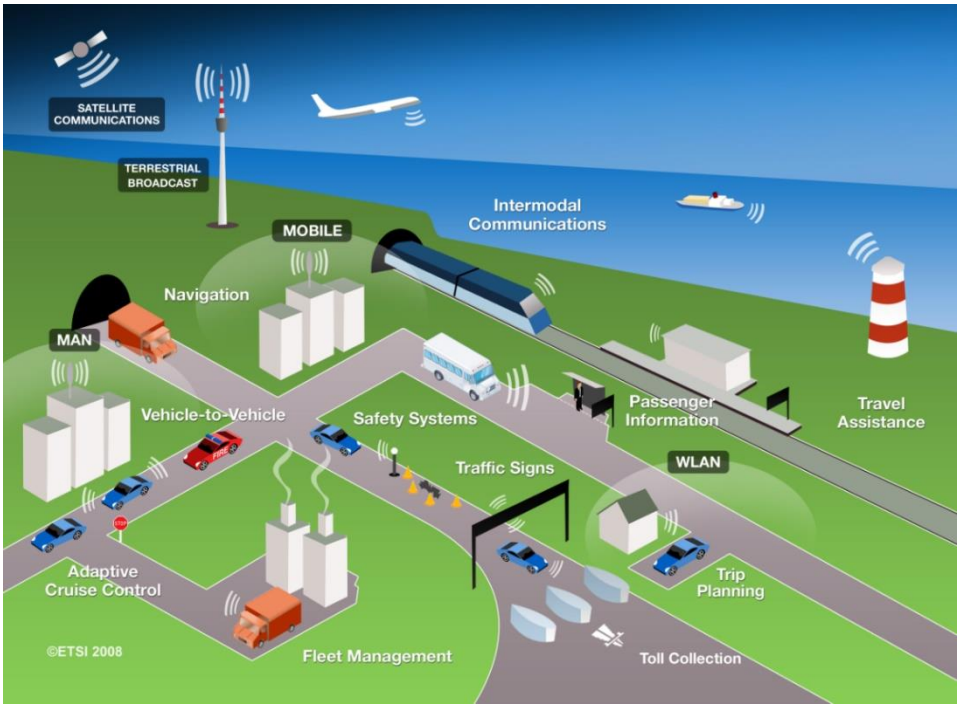


Figure 1. ITS Application Areas (European Telecommunications Standards Institute, ETSI Kooperatif AUS Sistemleri , 2022)

ITS has become the focal point of various policies and action plans around the world. When the foundations of ITS studies are examined, it first started with Comprehensive Automobile Traffic Control Systems (CACS) in Japan in the late 1960s and early 1970s, and Electronic Route Guidance Systems (ERGS) in the USA and Germany. After these years, ITS applications started to become widespread in the mid-1980s, and applications such as electronic toll collection systems, smart intersection control systems, passenger and driver information systems, and traffic control centers were implemented in the 90s. With these applications, joint projects started to be developed by starting cooperation between the state and the private sector.

Cooperative Intelligent Transport System

Cooperative Intelligent Transport System (C-ITS) is one of the technologies that aim to increase the safety, efficiency, and environmental performance of transportation as an innovative technology and enables vehicles to interact with each other and their environment. A safe and comfortable journey is ensured by informing the drivers about all the events that occur during the journey through communication devices placed inside the vehicle and on the roadside, and vehicle-vehicle and vehicle-infrastructure communication. C-ITS is a work on the agenda with the creation of test corridors and the development of driverless/connected vehicle applications, especially in European Union countries.

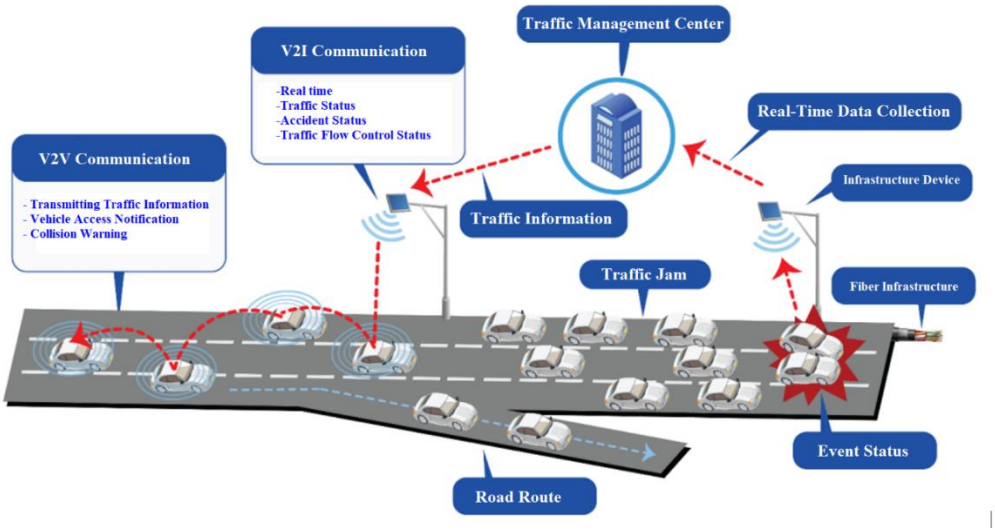


Figure 2. Cooperative Intelligent Transportation Systems (T.C. UAB, 2022)

E-SECURITY

Communication between devices and systems forms the basis of ITS systems. ITS systems cause security problems because of the infrastructure they use. In order to minimize these problems, E-Security studies and standards related to these studies are used.

E-SECURITY STANDARDS

Along with the standard reviews, it has been determined that most of the studies in the field of ITS consist of USA and EU studies. E-Security standards and the basic details of these standards will be determined in this section. The determined standards are given in Table 1.

Table 1. E-Security Standards

Sıra	Standard	Description
1	ETSI 102 731 Securtiy Svcs & Arch	Security Services and Architecture (European Telecommunications Standards Institute, ETSI 102 731 Security Svcs & Arch, 2010)
2	ETSI 102 940 Communication Security Belt and Management	ITS communication security architecture and security management (European Telecommunications Standards Institute , ETSI 102 940 Comms Security Arch & Mgmt, 2016)
3	ETSI 102 941 Trust and Privacy Management	Security and Privacy Management
4	ETSI 103 097 Security Header and Certificate Formats	Security header and certificate formats (European Telecommunications Standards Institute, ETSI 103 097 Security Header & Cert Formats, 2015)
5	ETSI 103 601 ITS Security Security management messages	Security management messages communication requirements and distribution protocols (European Telecommunications Standards Institute, ETSI 103 601 ITS Security Security management messages, 2020)
6	IEEE 1609.2 WAVE - Security	IEEE Standard for Wireless Access in Vehicle Environments - Security Services for Applications and Management Messages
7	IEEE 1609.2 WAVE - Security Change 1	IEEE 1609.2a-2017 - IEEE Standard for Wireless Access in Vehicle Environments--Security Services for Applications and Management Messages - Amendment 1 (Institute of Electrical and

		Electronics Engineers, IEEE 1609.2 WAVE - Security Amendment 1, 2017)
8	IEEE 1609.2 WAVE - Security Change 2	IEEE Standard for Wireless Access in Vehicle Environments--Security Services for Applications and Management Messages - Amendment 2--PDU Functional Types and Encryption Key Management (Institute of Electrical and Electronics Engineers, IEEE 1609.2 WAVE - Security Amendment 2, 2017)
9	ISO 21177 SVI Security	Secure tool interface – ITS station security services for secure session creation and authentication
10	NEMA TS 8 Cyber and Physical Security	Cyber and Physical Security for ITS (National Electrical Manufacturers Association)
11	ITS Forum Security Guide	Safety guide for the driver assistance system
12	SAE J2945/1 V2V Basic Security	Embedded System Requirements for V2V Security Communications
13	SAE J2945/2 V2V	Security Awareness V2V DSRC Requirements for Security Awareness
14	FIPS 140-2	Security Requirements for Cryptographic Modules (National Institute of Standards and Technology, 2022)
15	ASTM Archiving Traffic Data	Standard Specification for Archiving ITS - Generated Traffic Monitoring Data
16	ASTM E2259-03a	Standard Guide for Archiving and Retrieval of ITS Generated Data
17	ASTM Metadata to support ADMS	Standard Practice for Metadata Supporting Archived Data Management Systems
18	DDS	Data Distribution Service
19	DDS-RPC	Remote Procedure Call over DDS (DDS-RPC)
20	DDS-Security	DDS security
21	ISO EFC - Security Profile Guidelines	Electronic Toll Collection - Guidelines for security protection profiles
22	ISO 16787:2017	ITS - Assisted Parking System (APS) - Performance Requirements and Test Procedures
23	SAE J2945/4	Road Safety Applications
24	SAE J2945/9	Performance Requirements for Safety Communication to Sensitive Road Users
25	SAE J3161 C-V2X BSM Performance	Embedded System Requirements for LTE V2X V2V Security Communications
26	ITU-T ITS Secure Software Update	ITU-T ITS Secure Software Update

CONCLUSION

ITS applications have entered a continuous development process. It will also continue to increase in importance. ITS applications are an important issue in terms of revealing a fast, efficient and safe transportation structure. While installing ITS systems, potential security problems may arise in the systems. In this respect, one of the important issues of ITS applications is E-Security systems.

In this study, E-Security standards in ITS applications were examined. Among the examined standards, it was determined that ISO, ETSI, IEEE and SAE standards predominate. It has been determined that the existing standard structures are not sufficient and should continue to be developed.

REFERENCES

European Telecommunications Standards Institute . (n.d.). *ETSI 102 940 Comms Security Arch & Mgmt, 2016.*

European Telecommunications Standards Institute. (2022, 06 05). *ETSI Kooperatif AUS Sistemleri* . Retrieved from https://www.etsi.org/newsroom/news/753-2014-02-joint-news-cen-and-etsi-deliver-first-set-of-standards-for-cooperative-intelligent-transport-systems-c-its

European Telecommunications Standards Institute. (n.d.). *ETSI 102 731 Security Svcs & Arch, 2010.*

European Telecommunications Standards Institute. (n.d.). *ETSI 103 097 Security Header & Cert Formats, 2015.*

European Telecommunications Standards Institute. (n.d.). *ETSI 103 601 ITS Security Security management messages, 2020.*

Institute of Electrical and Electronics Engineers. (n.d.). *IEEE 1609.2 WAVE - Security Amendment 1, 2017.*

Institute of Electrical and Electronics Engineers. (n.d.). *IEEE 1609.2 WAVE - Security Amendment 2, 2017.*

National Electrical Manufacturers Association. (n.d.). *NEMA TS 8 Cyber and Physical Security, 2018.*

National Institute of Standards and Technology. (2022). *(NIST) FIPS 140-2.*

Society of Automotive Engineers of Japan. (2020). *ITS Standardization Activities of ISO/TC 204.*

T.C. UAB. (2022, 04 19). *Akıllı Ulaşım Sistemleri (AUS)*. Retrieved from T.C. Ulaştırma ve Alt Yapı Bakanlığı: https://hgm.uab.gov.tr/akilli-ulasim-sistemler-aus

Tufan, H. (n.d.). *Akıllı Ulaşım Sistemleri Uygulamaları ve Türkiye İçin Bir AUS Mimarisi Önerisi, Ulaştırma ve Haberleşme Uzmanlığı Tezi, 2014, Ankara.*

U.S. Department of Transportation. (n.d.). *Intelligent Transportation Systems Benefits, Costs, and Lessons Learned, Update Report, 2018.*

A LIGHTWEIGHT DEEP LEARNING MODEL FOR THE CLASSIFICATION OF A LIMITED LUNG SOUND DATASET

Ahamadi Abdallah IDRISSE

Gazi University, Institute of Informatics, Department of Computer Science, Ankara, Türkiye, ORCID NO: 0000-0002-1258-9196

Oktay YILDIZ

Doç. Dr., Gazi University, Faculty of Engineering, Department of Computer Engineering, Ankara, Türkiye, ORCID NO: 0000-0001-9155-7426

Ugur BAYSAL

Prof., Hacettepe University, Department of Electrical and Electronics Engineering, Ankara, Türkiye, ORCID NO: 0000-0002-2846-6780

Abstract

Determining whether the status of a lung sound is healthy or unhealthy is a critical task as the health of a patient could be in danger if an incorrect diagnosis is made. When doctors use stethoscopes to examine the status of a patient's lungs by listening to their sounds, the accuracy of the results depends primarily on the experience of the doctor. In this research, we proposed an Automatic Recognition System (ARS) that automates the classification of a given lung sound by training a lightweight deep learning model named MobileNet on a limited lung sound dataset that was collected at a public hospital in Turkey. The trained model learns low-level sound features (Mel-Frequency Cepstrum Coefficients) and accurately classifies lung sound into three different categories, namely: Normal, Rhal and Rhoncus. Because the lung sound dataset in our possession was small, during the training phase, audio data augmentation methods were employed to generate more samples which contributed positively to the performance of the model. Indeed, we were able to reach a 97% classification accuracy, and the proposed deep learning model has fewer parameters. This model achieved promising results, and therefore, its implementation on mobile devices could be a debut of an interesting future research endeavor.

Keywords: Lung sound classification, MobileNet, MFCC

I. INTRODUCTION

Lung sounds are generated when air flows through the respiratory system. These sounds reveal important details regarding the pulmonary status of patients. Doctors generally use a stethoscope to listen to lung sounds in order to diagnose patients with pulmonary conditions. Determining whether the status of a lung sound is healthy or unhealthy is a crucial task due to the fact that a patient's health might be at risk if an erroneous diagnosis is made. Given that lung sounds include nonlinear and nonstationary structural characteristics, the doctor or physician in charge of this task must possess the necessary training. Automatic recognition systems (ARS) may provide a solution to the challenge of lung sound classification for healthcare professionals (Bardou et al., 2018). The mechanized respiratory sound examination has recently gained popularity as a more reliable alternative to traditional auscultation methods for diagnosing lung sounds because it overcomes the drawbacks of traditional auscultation techniques and gives clinicians a trustworthy tool for more accurate diagnosis. This is due to the combination of electronic stethoscopes with pattern recognition and artificial intelligence (Zulfiqar et al., 2021).

Normal and adventitious breathing sounds are the two main types of lung noises. Normal breathing sounds occur when there are no respiratory difficulties, but adventitious breathing noises arise when various pulmonary illnesses are present. A healthy breathing sound is identified in the windpipe with higher frequency components that are audible throughout both the intake and exhalation phases. While on the chest wall, it is characterized by a low noise on inhaling and a barely detectable noise on exhaling. Adventitious breathing sounds occur when healthy breathing sounds are followed by additional sounds. Abnormal breathing sounds

might be continuous like wheezing, discontinuous like crackles, or possess both of the aforementioned features like squawks. The presence of this type of sound indicates a lung condition (Reichert et al., 2008).

Three different lung sounds—normal, rhonchus, and crackle—are used in this research. Rhonchus is a continuous low-pitched sound that may be heard during breathing. Rhonchus sounds are known to be present in patients suffering from illnesses such as asthma and bronchitis. Crackles are discontinuous and explosive adventitious sounds that are more common during the breathing phase. The presence of a crackle in lung sounds typically indicates a condition in the airways or pulmonary tissue (Nguyen and Pernkopf, 2021).

Deep learning techniques such as convolutional neural networks (CNN) are regarded as the most advanced method for classifying data and detecting large-scale objects (Bardou et al., 2018). These methods have demonstrated excellent performance in a variety of audio classification applications. For instance, Bardou et al. conducted a study that aimed to classify a lung sound dataset and, among different approaches used as classifiers, their proposed CNN algorithm registered the highest classification accuracy with a value of 95.56% (Bardou et al., 2018). Traditional machine learning techniques (SVM, KNN, etc.) have been proven to also produce better outcomes in the recognition of abnormal breathing sounds. Güler et al. deployed machine learning techniques to distinguish a dataset of lung sounds recorded from 60 patients. The Naive Bayes algorithm reached the highest classification accuracy at 95% with 10-cross validation (Güler et al., 2020).

In this study, an upgraded version of the dataset used in (Güler et al., 2020) was selected as the targeted dataset. Because we noticed that none of the acknowledged state-of-the-art algorithms for lung sound classification have used deep learning techniques on this dataset. That is why we intend to use a pre-trained model for the classification of that dataset. We chose the MobileNet specifically because this model has the benefit of having few parameters, which makes it much simpler to integrate on embedded and mobile platforms. MFCC (Mel-Frequency Cepstrum Coefficients) features will be extracted from the lung sounds and then be used as inputs to feed the deep learning model. Given that our dataset has fewer samples and that deep learning models train best on huge volumes of data, we opted to use data augmentation techniques to generate extra training examples. Hence, the utilization of data augmentation techniques has contributed to a better model performance. The acquired findings are unquestionably encouraging given that deep learning networks require a lot of data to provide better outcomes. Additionally, the suggested model has fewer parameters that make it easier for it to operate on mobile platforms.

II. MATERIALS AND METHODS

Figure 1 depicts a flowchart of the processes involved in addressing the lung sound categorization task. First, lung sounds are recorded from different patients using an electronic stethoscope. This phase results in the creation of audio wave files. The small size of these lung sounds necessitates the use of data augmentation techniques to produce additional samples. The MFCC characteristics are then derived from the audio lung sounds and inputted to the MobileNet to complete the classification task and determine whether the patient's lungs are healthy or unhealthy.

Dataset

A more recent version of the dataset used by Güler et al. is the dataset that was used in this study. Lung sounds were recorded from 60 patients at a governmental hospital in Turkey during their study. The same data preparation processes were used to prepare the new 117 lung audio files. So, the entirety of the dataset we have consists of 177 audio recordings that are divided into 3 classes.

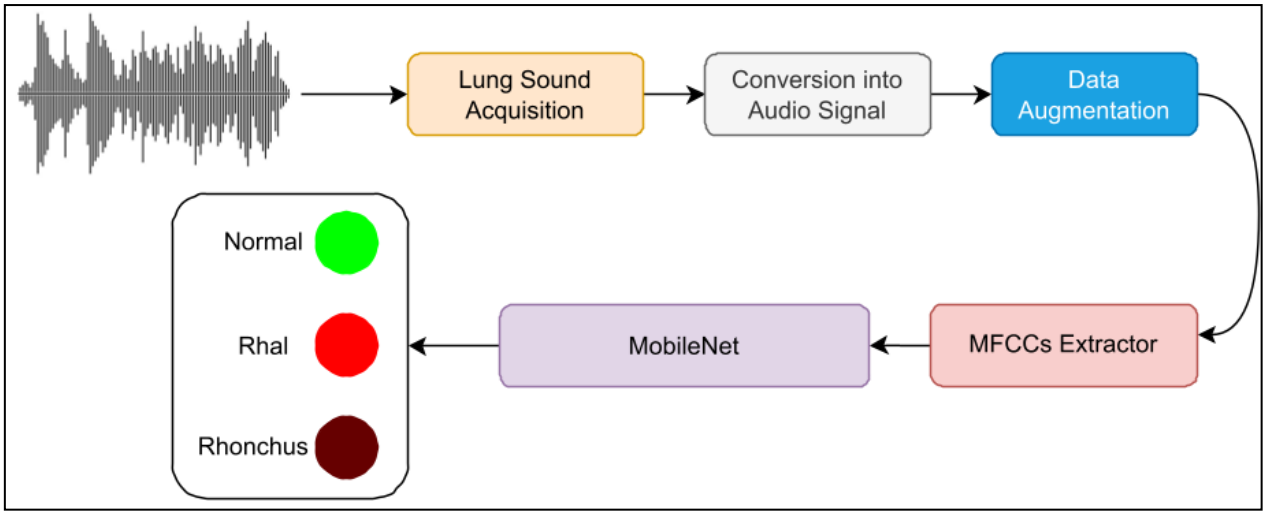


Figure 1 Diagnostic System Diagram.

Methodology

Convolutional neural networks

A CNN is a deep learning subclass with at least one convolutional layer that uses a backpropagation approach to learn the spatial hierarchy of features automatically and adaptively. It is made up of a variety of different building elements including convolution layers, pooling layers, and fully connected layers (Albawi et al., 2017). Convolution may be mathematically explained by equation (1), where I is the original picture, K denotes the filter matrix, and S denotes the converted image.

$$S(i,j) = (I \times J)(i,j) = \sum_m \sum_n I(m,n)\, K(i-m, j-n) \quad (1)$$

MobileNet

MobileNet is a lightweight deep neural network that uses depth-separable convolutions. The MobileNet technique splits a regular convolution into two depth-dependent and point-wise convolutions. The depthwise convolution employs a single kernel for each input channel, and the outputs of the depthwise convolution are fused together using a 1x1 convolution. This split results in the development of a lighter network by lowering computation and the size of the MobileNet model. Howard et al. developed MobileNet in 2017 to work on mobile and embedded vision systems (Howard et al., 2017). The fact that the MobileNet algorithm can easily be implemented on mobile devices is one of the reasons that pushed us to choose this model.

Data augmentation

Deformation techniques, commonly referred to as data augmentation techniques, are frequently employed to create new samples from an existing sample. Data augmentation techniques are frequently utilized when dealing with a limited dataset (Salamon and Bello, 2017).

Feature extraction

MFCC features are generated according to the cepstral representation of an audio signal. MFCCs are used to represent the short-time power spectrum of audio clips. They are based on the discrete cosine transform of the log power spectrum on a non-linear Mel scale. The frequency band of MFCCs are evenly spaced on the Mel scale, which closely replicates the human hearing system. As a result, MFCCs are an important component in many audio signal processing applications (Sharma et al., 2020).

III. EXPERIMENTAL STUDY AND RESULTS

Google Colab is an easy-to-use platform with predefined compute and hardware specs that allows deep learning models to be executed rapidly and flexibly. For these reasons, the experiments for this work were carried out on this platform. We started by employing some preprocessing methods, such as dividing each lung sound into five segments. Then, we extract the MFCC features of each segment and their corresponding labels, so we will be able to store them as a JSON (JavaScript Object Notation) file. As a result, the JSON file is used as a dataset for our model. A training set, a validation set, and a testing set had to be created from the dataset. To complete that, the dataset was randomly split between 80% training set and 20% testing set, with 20% of the training set being used as validation set. After that, the inputs are fed to the algorithm and the functioning of the model is evaluated using evaluation metrics such as confusion matrix, accuracy, and F1-Score.

During the experiment, the MobileNet was retrained for 1000 epochs, and the performance of the model can be seen in Figure 2 below. The training accuracy curve of the model appears to be stable during the whole training period, having been on top at the earliest stage of the training. The accuracy validation curve on the other hand, exhibits minor variations throughout the epochs and a clear fall in the middle, but quickly resumes its trajectory. The training loss evaluation of the model evolves similarly to the training accuracy curve, a clear projection since the early stages with tiny variations during the training. The validation loss eval is the one with significant irregularities, ups and downs, in the training session.

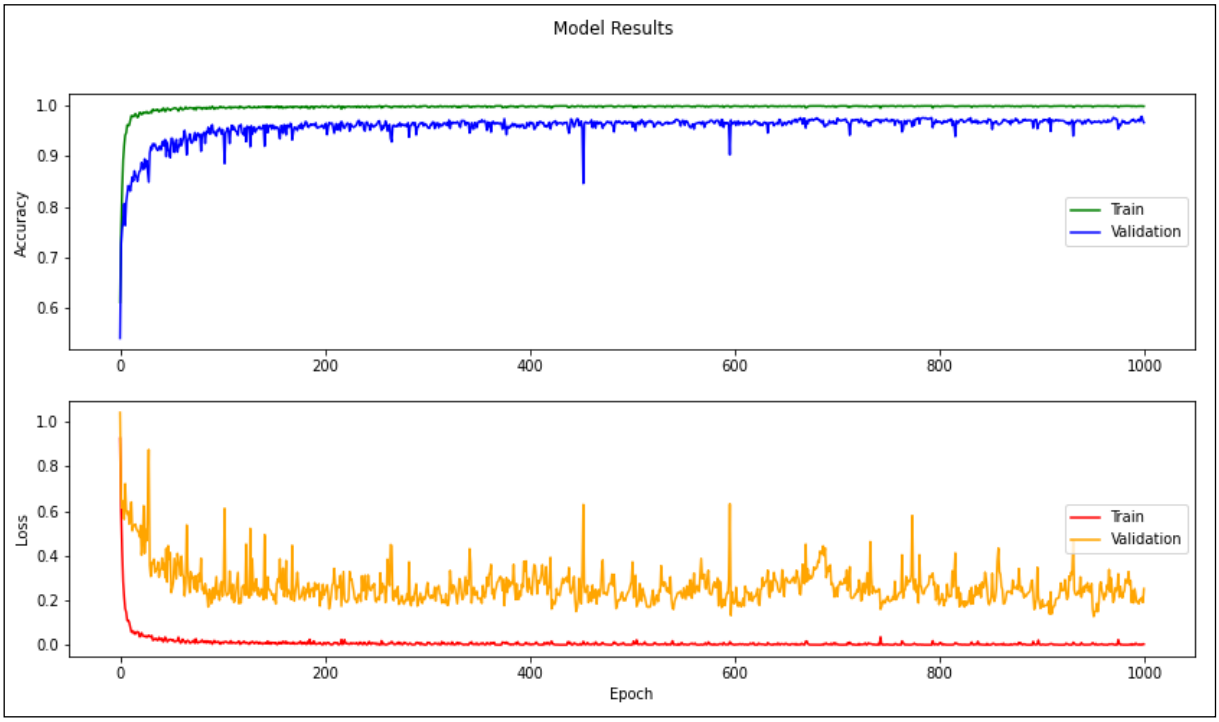


Figure 2 Graph of the model's accuracy and loss.

Figure 2 above shows that the model performed with satisfactory results. In addition, Table 1 below supports the previous statement in numbers. The values of the different metrics are depicted in Table 1. According to these values, in terms of precision, the Rhonchus class obtained the highest precision value of 0.99 while the minimum value was achieved for the Normal class at 0.96. On the other hand, in the recall metric, it is the normal class that is leading with a recall value of 0.98, whereas the other classes are sharing the same recall value of 0.97. In the F1-score metric, the Rhonchus class is again in front with an F1-score value of 0.98, while the other classes (Normal and Ral) reached the same F1-score value of 0.97. The confusion matrix of the model is also provided in Figure 3 below in order to show how the model classified the different classes during the experiment. The confusion matrix showed that the normal class was classified much better compared to the

pathological classes. In the non-healthy classes, the model was able to recognize the Rhonchus class more than the Ral class.

Table 1. Values of the model's Precision, Recall, and F1-Score outcomes.

	Precision	**Recall**	**F1-Score**
Normal	0.96	0.98	0.97
Ral	0.97	0.97	0.97
Rhonchus	0.99	0.97	0.98
Average	0.97	0.97	0.97

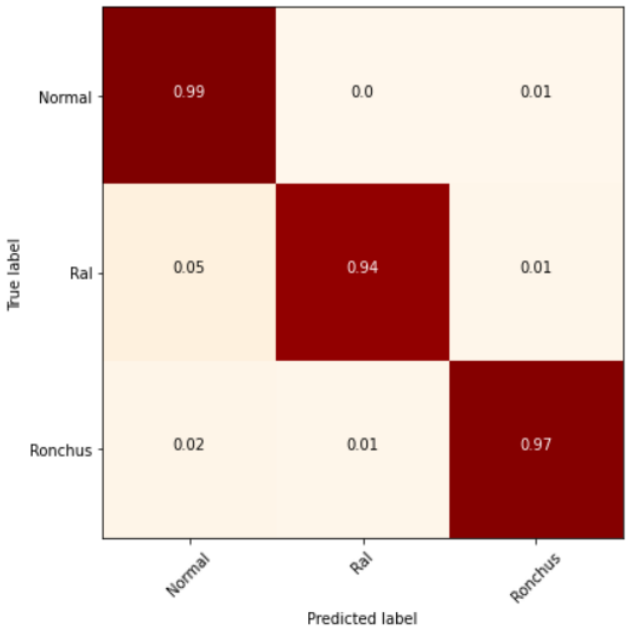


Figure 3 Confusion matrix of the Model.

IV. DISCUSSION AND CONCLUSION

In this paper, the MobileNet model was proposed for the classification of a lung sound dataset that was collected from different patients at a public hospital in Turkey. The differentiation of lung sounds is a complicated task for health professionals due to lung sounds possessing characteristics that require highly competent skills to make the right diagnosis. Automatic Recognition Systems are used to facilitate this issue for doctors. In this work, MFCCs are the features extracted from the lung sounds. Due to the small size nature of the dataset, before extracting the MFCCs, offline audio data augmentations were applied to the dataset. In the study conducted by Güler et al., they achieved a classification accuracy of 95%, which is less than what the proposed model of this research reached at 97%, considering the fact that deep learning models require a huge loads of data to perform better. MobileNet was introduced for mobile and embedded applications, and its implementation in this research promisingly leads us to future research fronts, such as integrating this algorithm into an embedding device to allow doctors perform the classification of lung sounds automatically.

V. ACKNOWLEDGMENT

The Hacettepe University Non-Interventional Clinical Researches Ethics Board granted approval for clinical trials with the 2021/13-79 decision number and the date of June 29, 2021. Thank you to all the patients who consented to the use of their data and to Prof. Dr. Ethem GELIR, Head of the Department of Physiology Faculty of Medicine at Hacettepe University, for organizing the clinical investigations.

VI. REFERENCES

Albawi, S., Mohammed, T. A., & Al-Zawi, S. (2017). Understanding of a convolutional neural network. International conference on engineering and technology (ICET) (pp. 1-6). Ieee.

Bardou, D., Zhang, K., & Ahmad, S. M. (2018). Lung sounds classification using convolutional neural networks. Artificial intelligence in medicine, 88, 58-69.

Güler H. C., Yildiz O., Baysal U., Cinyol F. B., Koksal D., Babaoglu E., and Ulasli S. S (2020) Classification of abnormal respiratory sounds using machine learning techniques. Medical Technologies Congress (TIPTEKNO), Antalya, Turkey, pp. 1-4.

Howard, A. G., Zhu, M., Chen, B., Kalenichenko, D., Wang, W., Weyand, T., ... & Adam, H. (2017). Mobilenets: Efficient convolutional neural networks for mobile vision applications. arXiv preprint arXiv:1704.04861.

Nguyen, T., & Pernkopf, F. (2021). Crackle Detection In Lung Sounds Using Transfer Learning And Multi-Input Convolutional Neural Networks. 43rd Annual International Conference of the IEEE Engineering in Medicine & Biology Society (EMBC) (pp. 80-83). IEEE.

Reichert, S., Gass, R., Brandt, C., & Andrès, E. (2008). Analysis of respiratory sounds: state of the art. Clinical medicine. Circulatory, respiratory and pulmonary medicine, 2, CCRPM-S530.

Salamon, J., & Bello, J. P. (2017). Deep convolutional neural networks and data augmentation for environmental sound classification. IEEE Signal processing letters, 24(3), 279-283.

Sharma, G., Umapathy, K., & Krishnan, S. (2020). Trends in audio signal feature extraction methods. Applied Acoustics, 158, 107020.

Zulfiqar, R., Majeed, F., Irfan, R., Rauf, H. T., Benkhelifa, E., & Belkacem, A. N. (2021). Abnormal respiratory sounds classification using deep CNN through artificial noise addition. Frontiers in Medicine, 8.

ADVANCEMENT OF CHAT BOT TECHNOLOGY IN CUSTOMER SERVICE

Leyla ZEYNALLI-HUSEYNZADE

Baku Engineering University, Engineering, Computer and Information Technologies, Baku, Azerbaijan., ORCID ID: https://orcid.org/0000-0003-1916-4761

Abstract

The rapidly developing world suddenly stopped with the outbreak of the COVID-19 pandemic. Something positive that this crisis has caused is that people's attitudes towards technology have changed and become more relaxed. Even people of the older generations who do not have technological knowledge easily master technological advances and, to some extent, have begun to incorporate them into their lives. Modern customers include Generation Y and Generation Z, representing 2 billion (27%) and 1.8 billion (24%) of the population, respectively. They pay special attention to self-service portals and prefer the prompt resolution of the request. Chat bots with integrated work flows can instantly offer the solution accordingly. The rise in the use of artificial intelligence chat bot helps to replace the need for people to interact with customers. Chat bots have come a long way since they were first introduced, and over time they are being used more and more in e-commerce and e-services, as their application is to create promising opportunities to achieve excellence in customer services. This article first presents an overview of its features and functionality, which highlights the relevance of chat bots for customer service. Then, from the point of view of functionality, two main categories of the purpose of chat bots are presented, namely "improving service performance" and "meeting customer expectations". Chat bot categories will be discussed in detail. The positive impact of the categories on the quality of service, which constitutes the functional purpose of chat bots, as well as the insignificant role of chat bots in customer service is a very important issue. The development of chat bots promises that the business side will automate simple payments and allow users to pay directly through live chat or some messenger applications. This process may be instant and simple, but it makes the customer happy and increases customer satisfaction.

Introduction

Chat bots are artificial intelligence programs designed to simulate communication with customers. Customers can communicate with chat bots using various methods. Two types of chat bots are widely used nowadays, the Flow chat bots and the AI chat bots. Flow chat bots are tree-based models, that is, whatever direction the programmer prompts from the beginning, the user acts from that direction. Artificial intelligence chat bots simulate human-like conversations using the processing of natural language (A, S., & John, D. (2015)). In addition to programmed commands, artificial intelligence chat bots can understand other languages and make decisions based on available information. Chat bots provide a fast and flexible customer experience along with problem solving services and a personal assistant role. Communicating with a chat bot is more convenient for customers and takes less time. As mentioned earlier, the bot uses artificial intelligence to instantly search for large amounts of information and is able to accurately select the most suitable and correct answer for the client (Brandtzaeg, P., & Følstad, A. (2017)). This fast way used to manage incoming requests by customers helps businesses develop customer engagement along with support service anytime.

The foundations of a complex chat bot

Currently, most businesses take advantage of the chat bot service with the purpose of automating the user experience and operational features. Chat bots are known as advanced virtual assistants that collect data to provide effective customization, including simple programs, and can learn and improve data as they process it. Chat bots are seamlessly integrated into many parts of our daily lives. Recently, the rapid development of digital transformation has led to an increase in the use of chat bots. Advanced technologies force enterprises to use digital communication channels to interact with their customers and conduct transactions. Chat bots are among the best forms of artificial intelligence applied in enterprises (Hill, J., Randolph Ford, W., & Farreras,

I. G. (2015)). There is no doubt that businesses benefit from chat bots because they refine performance and provide convenience to customers at the same time, they also provide additional services to internal employees, customers and partners. In the digital age, by using chat bot, companies can expand, customize, and make experiences accessible. The foundation of artificial intelligence chat bots are subgroups of NLP (Natural Language Processing) and NLU (Natural Language Understanding), an important technology used to improve the ability to recognize sentence structure, understand-interpret information, and answer questions (T.Lalwani, S.Bhalotia, A.Pal, S.Bisen, V.Rathod May 2018). Instead of relying on a pre-programmed response, artificial intelligence chat bots first identify a request from a client or user and then clarify what the user is looking for, at the next stage the chat bot returns the answer it believes to be correct based on the information obtained. With this rule, the machine analyzes both right and wrong answers and over time learns what the "correct" answer is. As chat bots became more advanced, they began to be used in NLP and NLU functionality, which makes it possible to accurately revert to many variants of human input, as well as to present different types of responses. There are two main steps in the foundation of chat bots, one of which is the design of the connection, and the other is the construction of the bot itself. It is possible to use various tools to map this interaction in the setting of the design, and to use platforms or frames in the construction of the bot. The use of chat bots, organized with decision-making based on artificial intelligence, plays an effective role in properly understanding customers and context (Abdul-Kader, S. A., and Woods, J. 2015). These features provided by artificial intelligence-based chat bots are used in electronic commerce and large-scale businesses.

Developing customer service

Customer service is important for the vast majority of businesses. Firstly, it is more difficult to attract a new customer than to retain an existing customer, because regular customers spend more money on new customers. Also, happy customers bring 2.6 times more income to your business than a dissatisfied customer, which at the same time makes your business stand out even more. One of the few features that distinguish brands in modern markets with high competition is customer service, which is considered a phenomenon. This not only increases customer engagement, but also allows customers to share their brand and, as a result, gain new customers. Customers are always waiting for help, which creates difficulties for the customer service teams (Q.Chena, Y.Gongb, Y.Luc, Ji.Tangd, June 2022). The need for a lot of resources, including staff, time and money, arises in order to promptly provide the help that customers want. In such cases, the possibility of using the functionality of chat bots helps to offer the client the desired help. There are many benefits of using artificial intelligence-based chat bots for clients:

- Leads to an increase in sales
- Offers customers help in different languages.
- Finds out what they want before redirecting customers
- Provides quick solutions to complaints and makes a comeback to more requests
- Helps reduce customer service cost
- Helps to get a large return on investment with minimal effort

The introduction of artificial intelligence chat bot in customer service has helped greatly improve the customer experience in more than one way.

1. Reduces customer waiting time. Chat bots reduce the time spent waiting in line. Instead of waiting for answers to frequently asked questions-by mail, phone call, or other methods, instant answers are provided.

2. Saving - Artificial Intelligence Chat bots save work time and resources, as well as support customer service. Artificial intelligence chat bots have the ability to easily handle a large number of customer requests without increasing the number of employees. Artificial intelligence chat bots do not fall out of motivation, do not get tired and are able to work continuously without interruptions. It helps businesses improve their efficiency and productivity.

3. Data Collection - Artificial intelligence chat bots constantly collect relevant information about customer behavior, needs and interests, and this collected information begins to be used more and more over time. The

data to perfect customer service, also helps to identify the target market. The data collection feature of artificial intelligence chat bots is considered more convenient because it uses more natural methods of data collection and is able to collect data from a larger number of people in a limited time. By analyzing customer data, they are offered better service, product and etc.

4. Self-service - Another advantage of artificial intelligence chat bots is that they allow businesses to provide their customers with a self-service tool. It also reduces customer service costs while helping improve the customer experience. According to a report from Microsoft in 2019, more than 90% of users are on the side of organizing a business as a kind of self-service portal.

5. Employee satisfaction - Artificial intelligence chat bots are used significantly over time in customer service, their ability to solve frequently asked questions quickly and efficiently is widely used. The feature allows employees to develop their skills and devote more time to solving more important and complex tasks for both customers and the organization. With so many advantages, there is no doubt that artificial intelligence chat bots are becoming more common in the field of customer service and the vast majority of companies take advantage of this service (K.Sidaoui, M.Jaakkola, J.Burton, July 2020).

Application of artificial intelligence chat bots in industry

As a result of the development of technology and the success of the digitalization process, virtual space lags behind natural space. Chat bots become famous actors in interaction with users. Chat bots act as virtual assistants to customers to find information in a short time, to easily remember everything they need (Villegas, W., Arias-Navarrete, A., & Palacios, X. (2020)). According to the research by Forrester, messaging is the most preferred customer service method by customers in the United States, Korea, India and Singapore. So it's no surprise that customers like to interact with chat bots more. This great technology is applied to all areas and has become an integral part of companies. Almost every large company has its own chat bots that answer specific questions and offer customer service. Chat bots are used in many industries and they have proven to be very useful in saving time, money and resources.

1. AI chat bots in education

Chat bots have evolved in many industries and education field is one of them. Chat bots increased communication, productivity, and minimized uncertainty. Chat bots simplify the necessary administrative documentation processes for students, inform them about the rules of the university, provide technical support and assistance.

2. Artificial intelligence chat bots in healthcare

The lockdown caused by the COVID-19 pandemic has also put the healthcare industry under pressure, creating a shortage of human resources and funding. Chat bots used in this area reduced waiting time, provided medical advice, scheduled appointment times, and collected feedback related to patients.

3. AI Chat bots in finance field

AI chat bots offer numerous advantages in the financial field. Chat bots communicate with customers, learn about their problems, provide them with relevant information, accept payments from users and offer other services. Currently, in banks, as in other areas, they integrate technology into their business flows. The vast majority of companies operating in the financial sector use chat bots.

We can say that chat bots are not only used in the above-mentioned sectors, but also the vast majority of companies increase the effectiveness of customer service by using chat bots. Its wide application leads to the improvement of artificial intelligence cat bots in the field of customer service and increasing service functionality over time.

Conclusion

According to the studies conducted, it turns out that about 40 percent of incoming requests to chat bots are not informative, but emotional. Artificial intelligence can support customer engagement strategies in a variety of ways.

- Data-based estimates: Artificial intelligence tools use a data-based approach, which means it makes strategic decisions based on data collection, analysis, and interpretation.
- Simplified work flows: Chat bots supported by artificial intelligence could be the first line of support for potential problems. Meeting the basic needs of customers and ensuring that the current work flow is not blocked gives teams more time to focus on more complex tasks.
- Predictive behaviour: Artificial intelligence tools should be able to analyse all the details of customer behaviour so that they can predict what they can do next. This allows companies to offer products or services according to the needs and interests of customers.

The introduction of artificial intelligence tools like chat bots can help boost business sales and grow. Based on the research, the improvement of chat bots increased the sales and customer satisfaction. Every day people take advantage of the functionality of artificial intelligence. Asking Siri for help, asking Netflix for advice on movies, and other services require artificial intelligence. Artificial intelligence is important for business because it can allow you to perform previously manual work quickly and reliably on a large scale. Chat bots change the way they work by reducing errors, reducing costs and people interaction. Artificial intelligence makes an invaluable contribution to the efficiency of the service, as the implementation of chat bots is ambitious, effective and fast, and operates smoothly with agility, practicality and accessibility. They respond to relatively simple and standardized requests and aim to serve as many users as possible. It acts as the highest level of service, fast and with high objectiveness and stable interaction. The artificial intelligence chat bot service has reduced queues at other customer service centers and contact centers and allows employees to solve difficult questions, contributing to the efficiency of the service. Chat bots are useful in many ways, and chat bots are improving every day in artificial intelligence technology, and this shows that they are a new revolution in customer service.

References

A, S., & John, D. (2015). Survey on chatbot design techniques in speech conversation systems. International Journal of Advanced Computer Science and Applications

Brandtzaeg, P., & Følstad, A. (2017). Why people use chatbots. In I. Kompatsiaris, & et al. (Eds.), Internet science: Vol. 10673. Cham: Springer

Hill, J., Randolph Ford, W., & Farreras, I. G. (2015). Real conversations with artificial intelligence: A comparison between human–human online conversations and human–chatbot conversations. Computers in Human Behavior, 49, 245–250

T.Lalwani, S.Bhalotia, A.Pal, S.Bisen, V.Rathod May 2018, Implementation of a Chatbot System using AI and NLP International Journal of Innovative Research in Computer Science & Technology (IJIRCST) ISSN: 2347-5552, Volume-6, Issue-3

Abdul-Kader, S. A., and Woods, J. 2015. “Survey on Chatbot Design Techniques in Speech Conversation Systems,” IJACSA) International Journal of Advanced Computer Science and Applications

Q.Chena, Y.Gongb, Y.Luc, Ji.Tangd, June 2022, Classifying and measuring the service quality of AI chatbot in frontline service, Journal of Business Research Volume 145, Pages 552-568

K.Sidaoui, M.Jaakkola, J.Burton, July 2020, AI feel you: customer experience assessment via chatbot interviews Journal of Service Management ISSN: 1757-581

Villegas, W., Arias-Navarrete, A., & Palacios, X. (2020). Proposal of an architecture for the integration of a chatbot with artificial intelligence in a smart campus for the improvement of learning. Sustainability, 12(1500)

DIGITAL TRANSFORMATION METRICS

Leyla ZEYNALLI-HUSEYNZADE

Baku Engineering University, Engineering, Computer and Information technologies, Baku, Azerbaijan., ORCID ID: https://orcid.org/0000-0003-1916-4761

Abstract

There have been many studies on performance measurement and management processes in general, and many studies have reviewed the complexity of transformative factors. When it comes to managing the performance of digital transformation projects, the most important thing is: do we know how to measure the value proposition targeted by transformation and can organizations manage what they can measure? Physical capital (production of products or services and distribution) or human capital (supply of products or services) are the main purpose for many businesses. Inventory, utility, productivity and other traditional basic activity criteria are kept under control by these organizations. Today, the main performance criteria measured by businesses are not always influenced by digital change. Literally, the main purpose of digital transformation is to increase the sales, continuity and consumer satisfaction, as well as, networking and value change. According to studies, Digital Performance İndicators will be used to find out how far the organization has progressed in its Digital Strategy and how it has optimized its digital market results. Once the transformation is complete and the digital business becomes a traditional performance experience, some indicators will "transition" while others will become permanent benchmarks for business success. Some organizations have a formal mechanism to control the development of measurement structures. It highlighted the importance of moving from performance analysis to performance management, as well as to a more dynamic performance measurement system than a static performance measurement system. The design of a performance measurement system can help businesses move from a cost model that encourages radical innovation rather than cost-effectiveness as an opportunity to develop new capabilities. Digitally represented internal and external communications and business structures, including technical advances in information technology such as applications, computing power, telephones and sensors are part of digital transformation. Thanks to these changes, new opportunities emerge in assessing performance. Managers should use indicators to help implement digital transformation.

Keywords: Digital transformation metrics, key performance indicators, digitization, transformation process

Introduction

Digital transformation has been an integral part of the success of businesses over the past few decades. As new technologies became the mainstream for businesses and customers, businesses had to accept and adapt to this. Digital transformation involves much more than the digitization of products, work flows and business models (Kırmızı, M. and Kocaoglu (2022)). Customer experience is a global concept that affects all aspects of business, such as products, the market and the new economy. Digital transformation is a continuous process that goes far beyond the definition of digitalization.

Digitization, although integral, is only one aspect of digital transformation. But as digital expectations are constantly changing, the signs indicating the status of transformational initiatives are also changing (Chen, Y., Visnjic, I., Parida, V. and Zhang, Z. (2021)). Relevant key performance indicators vary according to market conditions and the needs of businesses; therefore, key performance indicators that your team used to measure success last year may not tell you much about the state of your digital transformation journey today. Knowing the right performance indicators and measurements to follow is critical to determining whether a digital journey is on the right track (De la Boutetière, H., Montagner, A. and Reich, A. (2018),). Let's take a look at some of the most important indicators to measure and how you can determine which performance indicators are suitable for the team and journey. Companies need pre-defined indicators to measure whether best practices are implemented and whether the digital transformation process generates the intended value.

The best performance indices that can make it easier to measure digital transformation success are listed below.

1. Cost-benefit analysis of digital adoption

Digital adoption means making full use of digital technologies for the intended purpose. For example, the use of chat bots to make customer service operational and even better, etc (Nasiri, M., Saunila, M. and Ukko, J. (2022)). What are the results/benefits obtained with digital technology like this? For example, how many percent of consumer accessibility is solved using a chat bot? How does this software impact customer satisfaction? How much do businesses save by automating customer service? Businesses should also consider the costs of digital transformation, such as the cost of developing and deploying chat bots.

2. Investment refund in digital transformation

Not every investment in digital transformation can produce the desired results for the organization, and not every positive result is equally effective. The benefits of the technologies used in organization should outweigh the costs of using such a resource as time spent and investment. It is also recommended to define investment and value measurements and set a time frame for achieving predetermined goals (Matt, C., Hess, T. and Benlian,A (2015)).

3. User interaction methods

User interaction refers to how many customers interact with a product or service. The high level of interaction means whether customers are accepting the technology (Kane, G.C., Palmer, D., Nguyen-Phillips, A., Kiron, D. and Buckley, N. (2017)). There are three commonly used criteria to measure the number of users interacting with a service or product:

- Daily active users: measures the total number of people who visit and interact with a particular product or program on a given day.
- Weekly active users: shows the number of people who have interacted with the app or platform for a week.
- Monthly active users: refers to the number of people who visit or interact with a product within a month.
- Monthly customer compliance count: if the company shows less compliance without a decrease in the number of monthly active users, it means an increase in customer satisfaction.

4. Digital opportunities

IT infrastructure and employee skill levels of businesses are the most important factors impacting digital transformation processes. The success of integrating new technologies into businesses is directly proportional to the level of digital development of organizations (Berman, S.J. (2012)). The technologies and digital skills currently used (the skill level of the employees who will use the new tools) are the factors that influence the digital development level of the organization.

5. Evaluation of the reliability of digital transformation

In order to understand potential reliability problems, it is necessary to evaluate the suitability of organizations (the ability of customers to access products or services when they need them), security (the belief of customers that their data will be safely managed by the organization) and system performance (Kane, G.C., Palmer, D., Phillips, A.N., Kiron, D. and Buckley, N. (2015)). Some of the most common criteria that require focusing to evaluate performance are shown below:

- Mean failure time or mean time until the first failure of the system: is a statistical parameter that indicates the reliability of the system. It is used for system failures that are impossible to repair, after the failure occurs, the relevant component of the system must be replaced.
- Mean solution time: it is the criterion that measures the average time it takes to identify and eliminate the cause of a failure after its occurrence.

- Mean time before failure or mean time between two failures: if a failure occurs, the component can be repaired.

6. Employee productivity

It is inevitable that after a successful digital transformation, work volume performed by employees will increase. By monitoring employee productivity (improving the time it takes for an employee to complete their work), it is possible to measure the efficiency of the digital transformation process. For example, when more basic tasks are automated, such as automating document collection, employees can focus on more productive tasks.

Over time, more and more companies are adopting digital transformation and using technology to improve every aspect of their business (Khin, S. and Ho, T.C. (2019)). When the company begins to implement and develop these technological solutions, IT leaders should be able to demonstrate the results of these changes and control the impact of these technologies.

Conclusion

Performance indicators or key performance indicators play an important role in determining whether a new integrated digital process yields good results. Many large companies and organizations invest significant funds in digital tools, practices, and transformation initiatives to maximize investment returns. Therefore, key performance indicators are crucial in identifying areas that need to be improved while determining which strategies are best practices for success (Gökalp, E. and Martinez, V. (2021)). More importantly, digital transformation is an ongoing process therefore, having clear performance indicators for the different stages of the process can help you focus and demonstrate value (Hess, T., Matt, C., Benlian, A. and Wiesböck, F. (2016)). This article touched on many issues and indicators for measuring digitalization, but the truth is that the correct set of performance indicators depends on many factors, including the stage of digital maturity of the organization, its budget, goals, etc. The metrics that matters are those that help you understand if the conversion really brings value to your customers and provide opportunities for the organization to be more efficient and adapt to market changes.

References

Kırmızı, M. and Kocaoglu (2022), "Digital transformation maturity model development framework based on design science: case studies in manufacturing industry", Journal of Manufacturing Technology Management, Vol. 33 No. 7, pp. 1319-1346.

Nasiri, M., Saunila, M. and Ukko, J. (2022), "Digital orientation, digital maturity, and digital intensity: determinants of financial success in digital transformation settings", International Journal of Operations & Production Management, Vol. 42 No. 13, pp. 274-298.

Berman, S.J. (2012), "Digital transformation: opportunities to create new business models", Strategy and Leadership, Vol. 40 No. 2, pp. 16-24.

De la Boutetière, H., Montagner, A. and Reich, A. (2018), Unlocking Success in Digital Transformations, McKinsey & Company, pp. 1-14.

Matt, C., Hess, T. and Benlian, A. (2015), "Digital transformation strategies", Business and Information Systems Engineering, Vol. 57 No. 5, pp. 339-343.

Kane, G.C., Palmer, D., Nguyen-Phillips, A., Kiron, D. and Buckley, N. (2017)."Achieving digital maturity", MIT Sloan Management Review, Vol. 59 No. 1, pp. 1-29.

Kane, G.C., Palmer, D., Phillips, A.N., Kiron, D. and Buckley, N. (2015), "Strategy, not technology, drives digital transformation", MIT Sloan Management Review and Deloitte University Press, Vol. 14, pp. 1-25.

Khin, S. and Ho, T.C. (2019), "Digital technology, digital capability and organizational performance", International Journal of Innovation Science, Vol. 11 No. 2, pp. 177-195.

Gökalp, E. and Martinez, V. (2021), "Digital transformation capability maturity model enabling the assessment of industrial manufacturers", Computers in Industry, Vol. 132, 103522.

Chen, Y., Visnjic, I., Parida, V. and Zhang, Z. (2021), "On the road to digital servitization – the (dis)continuous interplay between business model and digital technology", International Journal of Operations and Production Management, Vol. 41 No. 5, pp. 694-722.

Hess, T., Matt, C., Benlian, A. and Wiesböck, F. (2016), "Options for formulating a digital transformation strategy", MIS Quarterly Executive, Vol. 15 No. 2, pp. 123-139.

REDUCING TICKET RESOLUTION TIME THROUGH SUGGESTION IN THE HELP DESK SYSTEM

Buğra Kaan TÜRKMENOĞLU

Gazi University, Engineering Faculty, Computer Engineering Department, Ankara, Turkey, ORCID NO: 0000-0003-3001-2005

Oktay YILDIZ

Gazi University, Engineering Faculty, Computer Engineering Department, Ankara, Turkey, ORCID NO: 0000-0001-9155-7426

ABSTRACT

Communication between users and customer service representatives is provided through the help desk system. Users report their problems and requests to customer service representatives using the help desk system. The necessity to have knowledge on many subjects, the difficulty of transferring information, reopened tickets, lack of IT resources, and employee dependency cause an increase in the number of open tickets for the customer service representative. The purpose of this study is to design a recommender system that will detect tickets that have the same meaning as the tickets closed by the customer service representatives. To the best our knowledge, we conducted the first research study, which purposed at reducing ticket resolution time by recommending similar open tickets to customer service representatives. The dataset has 48206 ticket pairs, which were paired as cartesian and manually tagged to determine the similarity of each ticket pair. Data preprocessing steps were applied to ticket descriptions. Document embeddings were obtained by using Word2vec and Doc2vec. The similarity of help desk ticket descriptions was calculated by measuring the cosine, manhattan and euclidean distances of document embeddings. To evaluate the performance of vectorization models, MSE, RMSE and MAE were calculated. Cosine distance showed a lower error rate than other distance types. The Doc2vec model performed the best with 0.2717 MSE, 0.5212 RMSE, and 0.4903 MAE using the cosine distance. The results show that the tickets that similar to the tickets closed, could be closed as soon as possible, the recommender system can give representatives a long time to solve problems, and a Doc2vec model can overcome the Turkish ticket similarity difficulty.

Keywords: Help Desk, Recommendation system, Ticket Recommendation, Semantic Similarity, Word2vec, Doc2vec

INTRODUCTION

The help desk system is the main communication tool used for reporting problems and requests. Therefore, the help desk is used by the majority of staff in companies. The satisfaction provided by this system is of great importance to companies. Thus, the help desk system is the subject of many studies (Lekshmy, Anusree, & Varunika, 2018).

The help desk includes processes that customer service representatives need to master (Wang, Li, Zhu, & Gong, 2011). Therefore, these systems become dependent on customer service representatives (Apriyanto, Rahmawati, Setiawan, Budi, & Haryono, 2019). However, due to the complexity of the processes included in this system, it is very difficult to master the processes (Wang, Li, Zhu, & Gong, 2011). In addition, disruption of processes occurs because of insufficient resources (Apriyanto, Rahmawati, Setiawan, Budi, & Haryono, 2019). For this reason, the number of tickets for customer service representatives increases, and the tickets take longer to resolve. If the processes are not automated, users will be dissatisfied because it takes a long time to resolve tickets (Samarakoon, Kumarawadu, & Pulasinghe, 2011). In some help desk systems, when users open a new ticket, solutions for tickets similar to that ticket are shown as suggestions (Wang, Li, Zhu, & Gong, 2011). Similarly, when customer service representatives close a ticket, they can receive tickets that are similar to that ticket as suggestions. Thus, because they have a good grasp of the subject, they can close tickets similar to that ticket in a short time.

Companies use an automated help desk system to achieve customer satisfaction (Wang, Li, Zhu, & Gong, 2011). Increasing the quality of customer service also increases the success of companies (Lekshmy, Anusree,

& Varunika, 2018). Therefore, the use of automated help desk systems increases day by day (Samarakoon, Kumarawadu, & Pulasinghe, 2011). It is critical that systems with many options include a recommendation mechanism. Users are freed from drowning among many options with the recommendation mechanism (Ghasemi & Momtazi, 2021).

Various efforts have been made to automate the help desk along with the calculation of ticket similarity. Lekshmy, Anusree, and Varunika (2018) proposed an automated help desk system for better customer satisfaction. It was aimed to detect closed tickets that are semantically similar to the new ticket. The Wordnet method was used to calculate similarity between sentences, which were tagged using the POS tagger. The similarity range is between 0 and 1. Tickets were ordered by similarity value. A genetic algorithm was chosen to cluster the most similar tickets. The most similar ticket in each cluster was determined. Apriyanto, Rahmawati, Setiawan, Budi, and Haryono (2019) introduced a help desk system that will improve customer service quality. It was aimed to provide solutions to problems quickly. The Nearest Neighbor Retrieval algorithm was used to detect similar tickets. The similarity of the tickets according to the attributes was calculated. Samarakoon, Kumarawadu, and Pulasinghe (2011) introduced an automated help desk system. The proposed system calculates the similarity by considering the context of the text and the word order. A genetic algorithm was preferred to update the parameters. The mean reciprocal rank was used as a performance metric. Liu et al. (2019) aimed to calculate the similarity between critical information about maintenance equipment and historical scenes. Document representations were extracted using TF-IDF. With the cosine similarity, the similarity of the documents was calculated. Wang, Li, Zhu, and Gong (2011) introduced an intelligent help desk system. Past tickets with a similar meaning to the new request were sorted according to their degree of similarity. Relevant tickets clustered into different clusters using a mixture language model and symmetric matrix factorization. iHelp conducted a request based case summarization by taking a recommendation from each ticket set.

The purpose of this study is to obtain models that will advise tickets, which have same meaning with the ticket that closed by customer service representatives, to customer service representatives. Unlike other studies, instead of suggesting solutions to users, it aims to recommend tickets to customer service representatives that can be closed in a short time. Another difference is that it focuses on the semantic similarity of Turkish help desk tickets.

The main contributions of this research work are as follows:

- Ensuring that open tickets, which have the same meaning as tickets closed by customer service representatives, are closed quickly by recommending customer service representatives.
- Allowing customer service representatives to spend more time on difficult problems by speeding up ticket closing time (Samarakoon, Kumarawadu, & Pulasinghe, 2011).
- Increasing the efficiency of the help desk system by closing tickets in a short time.

THEORETICAL BACKGROUND

Data preprocessing, vectorization, similarity measures and performance evaluation metrics applied to calculate ticket similarity were explained.

Data Preprocessing

Helpdesk ticket descriptions contain natural language. Ticket descriptions can also contain HTML expressions. Therefore, data preprocessing steps must be applied in order for the ticket descriptions to be processed by the models such as machine learning algorithms, vectorization methods and neural networks. Implementation of data preprocessing steps can many benefits, such as increasing performance, reducing dimension, and increasing success.

Vectorization

Word2vec

According to word embedding, words in similar contexts are semantically similar (Qurashi, Holmes, & Johnson, 2020). Therefore, Word2vec can extract the meanings of words (Zhang & Zhou, 2019). Word2vec has two methods, which are Skip gram and Continuous Bag of Words. In the Skip Gram, the target word is the input, and context words are the output. Unlike Skip Gram, Continuous Word Bag takes context words as input, outputting the target word. The number of unique words in the dataset determines the number of input and output neurons of the Word2vec model. Except for the input and output neurons, other neurons become passive with a value of zero. The number of hidden layer neurons specifies the dimension of the word embeddings.

Doc2vec

Document representation are generally obtained by averaging the word representations. However, this approach ignores the order of the words. The order of the words in the text contributes to the meaning. Doc2vec shows better performance than Word2vec at catching the semantics of texts (Zhang & Zhou, 2019). In contrast to the word embedding of Word2vec, Doc2vec supplies document embeddings. Doc2vec has two methods: Distributed Memory Paragraph Vector (DMPV) and Distributed Bag of Words (DBOW) (Ghasemi & Momtazi, 2021). In the DM, the context words and document id are input, and the target word is the output. Unlike DM, DBOW takes document id as input, outputting words from the document by regarding window size. Document id and words have different vector spaces.

Similarity Measures

The similarity between ticket descriptions was measured by using cosine, manhattan, and euclidean distances. Cosine distance calculates the cosine of the angle between vectors as seen in Eq. (1) (Thyagarajan & Mueller, 2016). Cosine distance has a common usage for high-dimensional data (Zahrotun, 2016). The cosine similarity is one minus the cosine distance as seen in Eq. (2).

$$\text{Cosine Distance}(S1, S2) = \frac{(S1 * S2)}{||S1||||S2||} = \frac{\sum_{i=1}^{n} S1iS2i}{\sqrt{\sum_{i=1}^{n}(S1i)^2}\sqrt{\sum_{i=1}^{n}(S2i)^2}} \quad (1)$$

$$\text{Cosine Similarity}(S1, S2) = 1 - \text{Cosine Distance}(S1, S2) \quad (2)$$

The Manhattan distance is sum of the absolute differences between the two vectors, as seen in Eq. (3).

$$\text{Manhattan Distance}(S1, S2) = \sum_{i=1}^{d} |S1_i - S2_i| \quad (3)$$

The euclidean distance is the distance of the line between two points, as seen in Eq. (4).

$$\text{Euclidean Distance}(S1, S2) = \sqrt{\sum_{i=1}^{d} (S1_i - S2_i)^2} \quad (4)$$

Performance Evaluation Metrics

Mean squared error (MSE), root mean squared error (RMSE) and mean absolute error (MAE) were calculated for ticket similarity. Each metric was calculated by averaging the 5-fold cross-validation results. MSE defines the mean of the squares of the errors as seen in Eq. (5). RMSE is the square root of the MSE as seen in Eq. (6). MAE is the arithmetic average of the absolute errors as seen in Eq. (7).

$$MSE = \left(\frac{1}{n}\right)\sum_{i=1}^{n}(Y_i - Y'_i)^2 \quad (5)$$

$$RMSE = \sqrt{\left(\frac{1}{n}\right)\sum_{i=1}^{n}(Y_i - Y'_i)^2} \quad (6)$$

$$MAE = \left(\frac{1}{n}\right)\sum_{i=1}^{n}(Y_i - Y'_i) \quad (7)$$

EXPERIMENTAL STUDY

267 Turkish ticket descriptions were collected from a help desk system. The dataset was created by pairing tickets as cartesian, and manually labeling ticket pairs. The dataset contained 48206 pairs of tickets. The dataset was divided into two parts: train, and test at a rate of 80 and 20 percent. Since the ticket descriptions have natural language and HTML expressions, data preprocessing steps were applied. HTML expressions were removed, URL expressions were removed, text was tokenized, punctuations were removed, words containing non-alphabetic characters were removed, words consisting of single-characters were removed, and stop words were removed. Word2vec and Doc2vec methods were used to obtain document embeddings. The CBOW and the DMPV were chosen as the training algorithms for the Word2vec and the Doc2vec methods, respectively. The Word2vec model was trained to obtain word embeddings. The word embedding dimension was set to 300. Document embeddings were obtained by averaging word embeddings by using Word2vec. The Doc2vec model was trained to obtain document embeddings in contrast to the word embeddings of Word2vec. The document embedding dimension was set to 300. The similarity of document embeddings was measured.

EXPERIMENTAL RESULTS

Word2vec

In ticket similarity performance performed using the Word2vec method, cosine distance outperformed manhattan and euclidean distances. By using the cosine distance and the Word2vec method, 0.2841 and 0.2843 MSE, 0.533 and 0.5332 RMSE, 0.4963 and 0.4964 MAE were obtained for the train and test dataset, respectively. Figure 1 depicts the performance of ticket similarity for the test dataset.

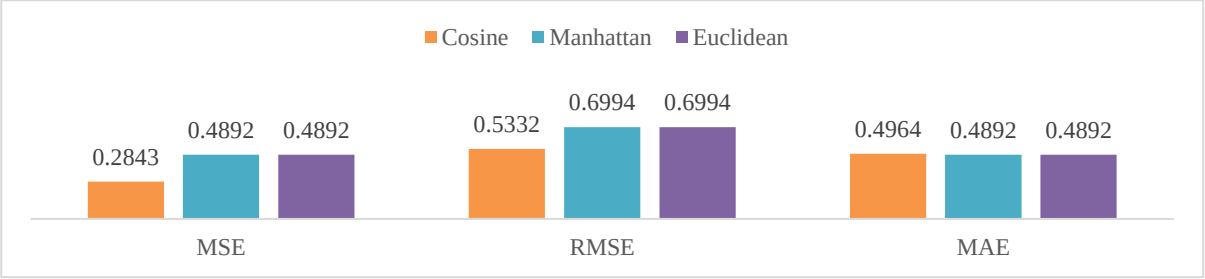


Figure 1. Ticket Similarity Performance of Word2vec for the Test Dataset

Doc2vec

In ticket similarity performance performed using the Doc2vec method, cosine distance outperformed manhattan and euclidean distances. By using the cosine distance and the Doc2vec method, 0.2717 and 0.2717 MSE, 0.5212 and 0.5212 RMSE, 0.4903 and 0.4903 MAE were obtained for the train and test dataset, respectively. Figure 2 depicts the performance of ticket similarity for the test dataset.

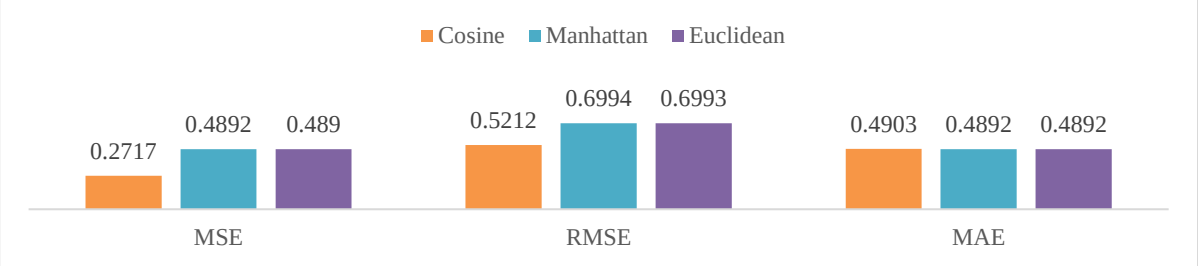


Figure 2. Ticket Similarity Performance of Doc2vec for the Test Dataset

DISCUSSION AND CONCLUSION

Users use the help desk system to report their problems and requests. The necessity to have knowledge of many modules, the difficulty of transfer of experience, recurring tickets, lack of IT resources, and dependency on the administrator cause many tickets to accumulate on the customer service representative. This study proposes a recommendation system that will detect tickets that have the same meaning as the tickets closed by the customer service representatives. The dataset has 48206 pairs of tickets. The dataset was created by pairing tickets as cartesian and manually labeling ticket pairs. Data preprocessing steps were applied to ticket descriptions. Document representations were obtained using Word2vec and Doc2vec. The similarity of help desk ticket descriptions was measured using cosine, manhattan, and euclidean distances. The performance of models was measured using MSE, RMSE, and MAE. The Doc2vec method performed better than the Word2vec method. Cosine distance showed a lower error rate than other distance types. The Doc2vec model performed the best with 0.2717 MSE, 0.5212 RMSE, and 0.4903 MAE using the cosine distance.

FUTURE WORKS

The amount of data labeled effects the model performance. In this study, we manually labeled 48206 ticket pairs. We aim to increase the amount of labeled data in our future work. In this study, we purposed to overcome the difficulty of the ticket description similarity with Word2vec and Doc2vec methods using data preprocessing steps that are specific to help desk ticket descriptions. We aim to use the Siamese networks to maximize performance in our future work.

REFERENCES

Apriyanto, R., Rahmawati, I. I., Setiawan, H., Budi, & Haryono. (2019). Application of Case-Based Reasoning in Helpdesk Systems. 2019 Fourth International Conference on Informatics and Computing (ICIC) (pp. 1-7). IEEE. doi:https://doi.org/10.1109/ICIC47613.2019.8985881

Ghasemi, N., & Momtazi, S. (2021). Neural text similarity of user reviews for improving collaborative filtering recommender systems. Electronic Commerce Research and Applications, 45. doi:https://doi.org/10.1016/j.elerap.2020.101019

Lekshmy, V. G., Anusree, P. K., & Varunika, V. S. (2018). An Implementation of Genetic Algorithm for Clustering Help Desk Data for Service Automation. 2018 International Conference on Advances in Computing, Communications and Informatics (ICACCI) (pp. 952-956). IEEE. doi:https://doi.org/10.1109/ICACCI.2018.8554532

Liu, T., Li, S., Gu, X., Wang, T., Lu, P., Cao, X., . . . Feng, C. (2019). Historical Similar Ticket Matching and Extraction used for Power Grid Maintenance Work Ticket Decision Making. 2019 3rd International Conference on Data Science and Business Analytics (ICDSBA) (pp. 302-307). IEEE. doi:https://doi.org/10.1109/ICDSBA48748.2019.00070

Qurashi, A. W., Holmes, V., & Johnson, A. P. (2020). Document Processing: Methods for Semantic Text Similarity Analysis. 2020 International Conference on INnovations in Intelligent SysTems and Applications (INISTA) (pp. 1-6). IEEE. doi:https://doi.org/10.1109/INISTA49547.2020.9194665

Samarakoon, L., Kumarawadu, S., & Pulasinghe, K. (2011). Automated Question Answering for Customer Helpdesk Applications. 2011 6th International Conference on Industrial and Information Systems (pp. 328-333). IEEE. doi:https://doi.org/10.1109/ICIINFS.2011.6038089

Thyagarajan, A., & Mueller, J. (2016). Siamese Recurrent Architectures for Learning Sentence Similarity. Proceedings of the Thirtieth AAAI Conference on Artificial Intelligence (AAAI-16), (pp. 2786-2792).

Wang, D., Li, T., Zhu, S., & Gong, Y. (2011). iHelp: An Intelligent Online Helpdesk System. IEEE transactions on systems, man, and cybernetics. Part B, Cybernetics: a publication of the IEEE Systems, Man, and Cybernetics Society, 41(1). doi:https://doi.org/10.1109/TSMCB.2010.2049352

Zahrotun, L. (2016). Comparison Jaccard similarity, Cosine Similarity and Combined Bothof theData ClusteringWith Shared Nearest Neighbor Method. Computer Engineering and Applications, 5(1).

Zhang, H., & Zhou, L. (2019). Similarity Judgment of Civil Aviation Regulations Based on Doc2Vec Deep Learning Algorithm. 2019 12th International Congress on Image and Signal Processing, BioMedical Engineering and Informatics (CISP-BMEI) (pp. 1-8). IEEE. doi:https://doi.org/10.1109/CISP-BMEI48845.2019.8965709

DURUM UZAYI ORTALAMASI METODUYLA BİR GERİ DÖNÜŞLÜ DÖNÜŞTÜRÜCÜ İÇİN KÜÇÜK SİNYAL ANALİZİNİN YAPILMASI

Metin SALİHMUHSİN

Dr. Öğr. Üyesi, Kahramanmaraş Sütçü İmam Üniversitesi, Mühendislik Mimarlık Fakültesi, Elektrik-Elektronik Mühendisliği Bölümü, Kahramanmaraş, Türkiye., ORCID NO: 0000-0003-2069-9376

ÖZET

Bu çalışmada izolasyonlu bir geri dönüşlü dönüştürücünün durum uzayı ortalaması metodu ile durum uzayı denklemleri elde edilmiştir. Sonrasında ise Matlab programı kullanılarak dönüştürücünün simulasyonu yapılmıştır. Dönüştürücü girişine 35 V'luk bir dc kaynak bağlanmış, çıkışı ise 311 V'a sabitlenmiştir. Oluşturulan durum uzayı denklemleri kullanılarak dönüştürücünün önce kararlı durum analizi yapılmış ve bulunan değerlerin bir önceki çalışmamızda aynı parametreler için grafiksel olarak elde edilen değerler ile örtüştükleri gösterilmiştir. Sonrasında ise dönüştürücü için küçük sinyal analizinde kullanılmak üzere pals genişliğinden–çıkış voltajına transfer fonksiyonu çıkarılmış ve sistemin frekans tepkisi bulunarak Bode genlik ve faz eğrileri şeklinde gösterilmiştir.

Anahtar Kelimeler: Geri Dönüşlü Döniştürücü, Durum Uzayı Ortalaması Metodu, Küçük Sinyal Analizi

SMALL SIGNAL ANALYSIS OF A FLYBACK CONVERTER USING STATE SPACE AVERAGING METHOD

ABSTRACT

In this study, State Space Averaging method is utilized to obtain a state space model of a flyback convertor. After that Matlab program is used to simulate the operation of the converter. A 35 V dc input is applied as a source to the convertor where as the output is set to 311 V. By using the developed state space model, steady state analysis of the convertor is performed in prior and shown that the results are similar to those obtained in one of our previous study where the circuit with the same parameters was simulated and the results were displayed graphically. After that, the transfer function from duty cycle to output voltage is obtained in order to be used in the small signal analysis of the convertor. The frequency response of the system is found by means of the Bode plots and displayed graphically.

Keywords: Flyback Convertors, State Space Averaging Method, Small Signal Analysis

1. GİRİŞ

Geri dönüşlü dönüştürücü (Flyback convertor) endüktanslı ve elektriksel izolasyonu olan da-da tipi bir dönüştürücü türüdür. Giriş ve çıkış arasındaki elektriksel izolasyon bu işlem için tasarlanmış bir trafo veya aralarında manyetik bağlantı bulunan iki endüktans ile sağlanır. Kullanılan trafonun aynı zamanda da-da dönüştürücülerde kullanılan endüktansında işlevini yerine getirmesi sebebi ve tek transformatör içeren basit yapısı nedeni ile düşükten orta güç aralığına kadarki dönüştürücüler içerisinde çok kullanılan bir dönüştürücü çeşididir. Genellikle 100 W'a kadar olan endüstriyel uygulamalarda kullanılsalarda özel trafo tasarımları sayesinde birkaç kW'a kadar kullanıldıkları uygulamalarda bulunmaktadır. Basit topolojileri, düşük maliyetleri ve tek trafoda çıkışa eklenen birden fazla sargı ile çoklu çıkışa sahip olabilme gibi özellikleri sayesinde pek çok endüstriyel uygulamada kullanım alanı bulmaktadır [1-3].

Literatürde geri dönüşlü dönüştürücüler konusunda pek çok çalışma bulunmaktadır. Bunlardan konumuzla alakalı 2 tanesi aşağıda özetlenmiştir. Spiazzi et al [4] bu dönüştürücü çeşidinin kritik çalışma modunda çalıştırılması üzerine bir çalışma yapmışlardır. Bu çalışma modunda dönüştürücü, sürekli iletim modu ile kesikli iletim modunun sınır şartlaarında çalışmaya zorlanmıştır. Literatürde dönüştürücünün bu modda çalıştırılması durumunda anahtar için sıfır voltaj komütasyonuna olanak sağladığı, EMI'yı azalttığı ve devre

elemanları üzerindeki stresi düşürdüğü rapor edilmiştir. Yayınlarında dönüştürücünün teorik analizi yapıldıktan sonra hem açık hemde kapalı çevrimdeki çalışması incelenmiştir. Simulasyonlar kullanılarak farklı anahtarlama düzeneği içeren 3 farklı yaklaşımın karşılaştırılması yapılmış ve ayrıca hesaplamalarda yapılan yuvarlama hatalarının etkilerinin gözlemlenmesi gerçekleştirilmiştir. Çalışmanın deneysel kısmı ise ST Microelectronics New Smart Power IC VIPower M3 entegresi kullanılarak yapılmıştır. Bu entegre kullanılarak çok çıkışlı bir geri dönüşlü dönüştürücü prototipi yapılmış ve simulasyonlarla benzetiminin yapıldığı şekilde çalıştığı gösterilmiştir.

Bu çalışmanın bir ön çalışması niteliğinde olan makalemizde [5] bir geri dönüşlü dönüştürücü için simulasyon ortamında tasarım çalışması yapılmış ve istenen bazı parametre değerleri grafiksel olarak gösterilmiştir. Simulasyonlar Matlab/Simulink kullanılarak yapılmıştır. Tasarımı yapılan dönüştürücü girişine 35 V dc uygulanmış, çıkış voltajı ise 311 V'a sabitlenmiştir. Tasarlanan dönüştürücünün başarılı bir şekilde çalıştığı ve devre içerisinde istenilen değişkenlerin değerlerini grafiksel olarak doğru bir şekilde gösterdiği rapor edilmiştir.

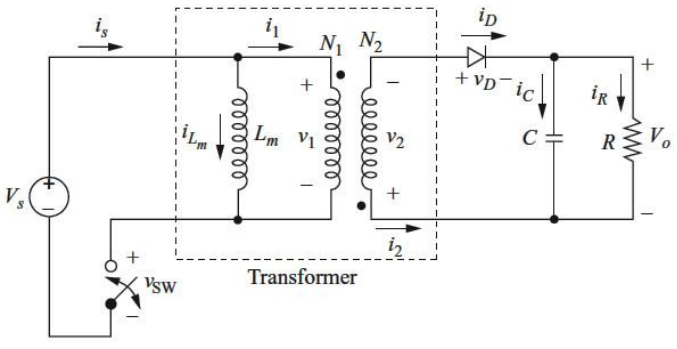
Bu çalışma [5]'de belirtilen bir önceki çalışmamızın bir devamı niteliğindedir. Çalışmanın amacı durum uzayı ortalaması metodu kullanılarak bir geri dönüşlü dönüştürücünün durum uzayi matrislerinin elde edilmesidir. Sonrasında elde edilen durum uzayı modeli kullanılarak dönüştürücü için ortalama çalışma koşulları değerlerinin bulunması ve küçük sinyal analizi yapılmıştır. Dönüştürücünün girişine 35 V'luk bir dc kaynak bağlanmış çıkışı ise 311 V'a ayarlanmıştır. Çalışma simulasyon ortamında Matlab kullanılarak yapılmış ve elde edilen bulgular grafiksel olarak gösterilmiştir.

2. GERİ DÖNÜŞLÜ DÖNÜŞTÜRÜCÜLERİN TEORİK ANALİZİ

Geri dönüşlü döniştürücüler bir transformatör ve bir anahtar kullanılarak girişlerine uygulanan bir dc volyajı seviyesini çıkışlarında bir diğer voltaj seviyesine döniştürmek için kullanılırlar. Kullanılan transformatörün giriş (primer) tarafındaki sargısı yüksek frekanslı bir anahtar kullanılarak bir dc kaynağa bağlanmaktadır. Anahtar bir ***T*** periyodu ile açılıp kapatılır. Transformatörün çıkış tarafındaki sargısı ise bir diyot ve kapasitör yardımı ile çıkıştaki yüke bağlanır. Anahtarın bir periyotluk zaman içerisinde ***DT*** süresince kapalı (**on**) ve ***(1-D)T*** süresince açık (**off**) olduğu kabul edilir. Burada ***D: 0 < D < 1*** aralığında bir gerçel sayıya karşılık geldiği kabul edilir ve pals genişliği (duty cycle) olarak adlandırılır.

Bir geri dönüşlü dönüştürücünün analizi ve durum uzayı denklemlerinin bulunması genellikle 2 aşamada yapılır. Bunlar bir ***T*** periyodu içerisinde anahtarın kapalı olduğu süre ve buna karşılık gelen durum uzayı denklemleri ve periyot içerisinde anahtarın açık olduğu süre ve buna karşılık gelen durum uzayı denklemleridir. Her iki durum için denklemler elde edildikten sonra durum uzayı ortalaması metodu (state space averaging) kullanılarak sistemin toplam durum uzayı modeli elde edilir.

Bir geri dönüşlü dönüştürücünün devre şeması Şekil 1'de verilmiştir. Bu çalışmada yapılan analizlerde transformatör dışındaki devre elemanlarının ideal olduğu, devrenin kararlı durumda çalıştığı ve çıkıştaki kapasitörün yeterince büyük olduğu kabul edilecektir. Devredeki transformatör ideal bir transformatöre mıknatıslanma endüktansını gösteren bir Lm endüktansı eklenerek temsil edilmiş ve diğer kayıplar ihmal edilmiştir.

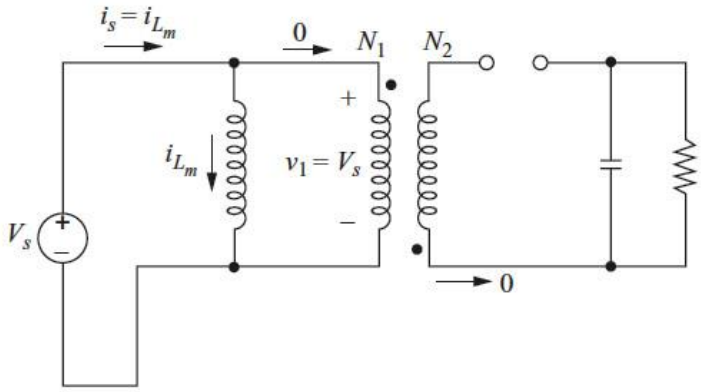


Şekil 1. Bir geri dönüşlü dönüştürücünün devre şeması.

Bu dönüştürücü çeşidinin diğer izolasyonlu dönüştürücü çeşitlerinden farklılığı trafoda kullanılan nokta notasyonundan kaynaklanmaktadır. Bir geri dönüşlü dönüştürücünün doğru bir şekilde çalışabilmesi için sargılardaki voltaj polaritelerini gösteren nokta gösteriminin anahtar kapalı durumda olduğunda çıkıştaki diyodu ters yönde polarlayacak şekilde seçilmesi gerekmektedir. Bu açıklamalar ışığında bir geri dönüşlü dönüştürücü için anahtarın kapalı ve açık olduğu durumlara karşılık gelen devre denklemleri şu şekilde olmaktadır.

2.1. Anahtarın Kapalı Olması Durumu

Geri dönüşlü dönüştürücünün bu duruma karşılık gelen eşdeğer devre şeması Şekil 2'de verilmiştir.



Şekil 2. Anahtarın **kapalı** durumu için geri dönüşlü dönüştürücünün devre şeması.

Anahtar kapalı durumda iken ***Vs*** kaynağından gelen enerşji transformatörün giriş sargısının ***Lm*** endüktansında depolanmaktadır. Trafoda kullanılan nokta notasyonunun doğru şekilde ayarlanması sebebi ile trafonun çıkış sargısında bu süre içerisinde bir akım akmaz. Çıkıştaki yük ise bu süre zarfında kapasitör tarafından beslenir. Bu durumu temsil eden devre denklemleri aşağıda verilmiştir ($\frac{N_1}{N_2} = \frac{1}{N}$ olarak alınmıştır).

$$\frac{di_{Lm}}{dt} = \frac{V_s}{L_m} \tag{1}$$

$$\frac{dv_c}{dt} = \frac{-v_c}{RC} \tag{2}$$

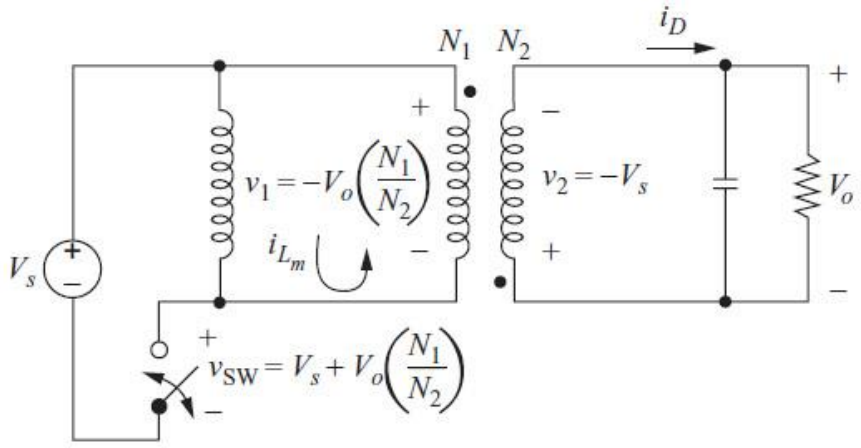
Bu denklemlere karşılık gelen durum uzayı matrislerinin $\dot{x} = A_1 x + B_1 u \quad ve \quad y = C_1 x$ şeklinde olduğu kabul edilirse, devrenin durum uzayı modeli aşağıda verildiği gibi olmaktadır.

$$\begin{bmatrix} \frac{di_{Lm}}{dt} \\ \frac{dv_c}{dt} \end{bmatrix} = \begin{bmatrix} 0 & 0 \\ 0 & \frac{-1}{RC} \end{bmatrix} \begin{bmatrix} i_{Lm} \\ v_c \end{bmatrix} + \begin{bmatrix} \frac{V_s}{L_m} \\ 0 \end{bmatrix} \tag{3}$$

$$y = [0 \quad 1] \begin{bmatrix} i_{Lm} \\ v_c \end{bmatrix}$$

2.2 Anahtarın Açık Olması Durumu

Anahtarın açık olması duruma karşılık gelen eşdeğer devre şeması Şekil 3'te verilmiştir.



Şekil 3. Anahtarın **açık** durumu için geri dönüşlü dönüştürücünün devre şeması.

Anahtar açık durumda olduğunda çıkıştaki diyot iletime geçmektedir. Bu sebeple anahtar kapalı iken primer sargısının ***Lm*** endüktansına depolanan enerji trafonun çıkış sargısı tarafından çıkıştaki yüke aktarılır. Bu süre zarfında çıkışa aktarılan enerji hem yükü beslemekte hemde kapasitörü şarj etmektedir.Yük üzerindeki voltajın sabit kaldığı kabul edilirse bu duruma karşılık gelen devre denklemleri aşağıda verildiği gibi olmaktadır.

$$\frac{di_{Lm}}{dt} = \frac{-v_c}{L_m N} \tag{4}$$

$$\frac{dv_c}{dt} = \frac{i_{Lm}}{CN} - \frac{v_c}{RC} \tag{5}$$

Bu denklemlere karşılık gelen durum uzayı matrislerinin $\dot{x} = A_2 x + B_2 u \quad ve \quad y = C_2 x$ şeklinde olduğu kabul edilirse bu durumda dönüştürücünün durum uzayı matrisi aşağıda verildiği gibi olmaktadır.

$$\begin{bmatrix} \frac{di_{Lm}}{dt} \\ \frac{dv_c}{dt} \end{bmatrix} = \begin{bmatrix} 0 & \frac{-1}{L_m N} \\ \frac{1}{CN} & \frac{-1}{RC} \end{bmatrix} \begin{bmatrix} i_{Lm} \\ v_c \end{bmatrix} + \begin{bmatrix} 0 \\ 0 \end{bmatrix} \tag{6}$$

$$y = [0 \quad 1] \begin{bmatrix} i_{Lm} \\ v_c \end{bmatrix}$$

2.3. Durum Uzayı Ortalaması Metodu

Durum uzayı ortalaması metodu anahtarlamalı dönüştürücü devrelerinin analizinde sıkça kullanılan bir metottur. Bu yöntem kullanılırken önce eldeki devre için gerekli durum değişkenleri belirlenir. Anahtarın kapalı ve açık olduğu durumlar için devre denklemleri oluşturulur. Sonrasında ise denklemlerin bir periyot boyunca ortalamarı alınarak istenilen durum uzayı denklemleri elde edilir. Geri dönüşlü dönüştürücü için anahtarın kapalı ve açık olduğu durumlara karşılık gelen devre denklemleri bir önceki kısımda bulunmuştu. Bu durumda devrenin bir ***T*** periyodu boyunca ortalamasının alındığı ve devrenin kararlı durumdaki çalışma koşullarına karşılık gelen durum uzayı devre denklemleri

$$\dot{x} = Ax + Bu \qquad ve \qquad y = Cx$$

olarak gösterilmekte ve bu denklemlerde

$$A = A_1 D + A_2(1 - D)$$
$$B = B_1 D + B_2(1 - D) \quad (7)$$
$$C = C_1 D + C_2(1 - D)$$

olmaktadır. Böyle bir devre için kararlı durum ve küçük sinyal analizleri yapılırken önce devrede istenilen değişkenlere, çıkış değişkenine ve anahtarın pals genişliği ***D*** değişkenine bir çalışma noktası etrafında küçük salınımlar uygulandığı kabul edilir. Sonrasında ise yukarıdaki denklemler tekrar düzenlenir. Bu durumda

$$x = X + \tilde{x}$$

$$y = Y + \tilde{y}$$

$$d = D + \tilde{d}$$

olmaktadır. Burada ***X***, ***Y*** ve ***D*** değişkenlerin kararlı durumdaki değerlerini ve $\tilde{x}$, $\tilde{y}$ ve $\tilde{d}$ ise bu değişkenlere uygulanan küçük salınımları temsil etmektedir (girişin sabit kaldığı kabul edilmektedir). Devre kararlı durumda çalışırken

$$\dot{x} = 0$$

olacağından:

$$X = -A^{-1}BU \quad (8)$$

$$Y = -CA^{-1}BU \quad (9)$$

olmaktadır. Bu ise devrenin kararlı durumdaki çalışma koşullarına karşılık gelmektedir.

Devrenin küçük sinyal analizi yapılırken ise

$$\dot{x} = (X \dot{+} \tilde{x}) = (\dot{\tilde{x}})$$

olduğu kabul edilerek bu denklemlerdeki yerine yazılmakta ve denklemler tekrar düzenlenmektedir. Düzenlenen denklemlerde kararlı durumlara karşılık gelen değişkenlerin türevlerinin ve küçük sinyallerin çarpımlarına karşılık gelen terimlerin ihmal edilmesi ile devrenin küçük sinyal analizinin yapılmasına olanak sağlayan durum denklemleri elde edilmektedir.

VII. 3. SİMULASYONLAR

Yukarıda teorik analizi verilen geri dönüşlü dönüştürücü için, yükseltici çeşidi bir dönüştütücü işlevini yerin getiren bir simulasyon çalışması yapılmıştır. Simulasyonlar yapılırken bir önceki kısımda elde edilen durum uzayı ortalaması dönüştürücü modeli kullanılmıştır. Programlar Matlab yazılımı kullanılarak yazılmıştır. Simulasyonu yapılan geri dönüşlü dönüştürücünün özellikleri Tablo 1'de verişmiştir.

Tablo 1. Simulasyonu yapılan geri dönüşlü dönüştürücünün özellikleri

DC Giriş Voltajı	(V)	35
DC Çıkış Voltajı	(V)	311
Anahtarlama Frekansı	(Hz)	62500
Lm	(µH)	11
C	(µF)	3
N		15
R	(Ω)	387
Pals Genişliği (D)		0.372
Çıkış Voltajı Dalg	(%)	1

Mıknatıslanma endüktansı ve çıkış kapasitörü değerleri sürekli iletim çalışma modu (CCM) ve daha az çıkış voltaj dalgalanması elde etme amacıyla hesaplanananın iki katı olarak alınmıştır. Simulasyonlar yapılırken önce Matlab kullanılarak denklem (8) ve (9)'da belirtilen devrenin kararlı durum çalışma koşulları elde edilmiştir. Simulasyonu yapılan devre için bu değerler $i_{Lm} = 19.2\ A$ ve $v_c = 311\ V$ olarak elde edilmiştir. Bu değerlerin daha önceki bir çalışmamızda yaptığımız [5] ve bu geri dönüşlü dönüştürücünün durum değişkenleri ve çıkışındaki değişimleri grafiksel olarak göstermek için yapılan simulasyonlardaki değerlerle örtüştükleri görülmektedir.

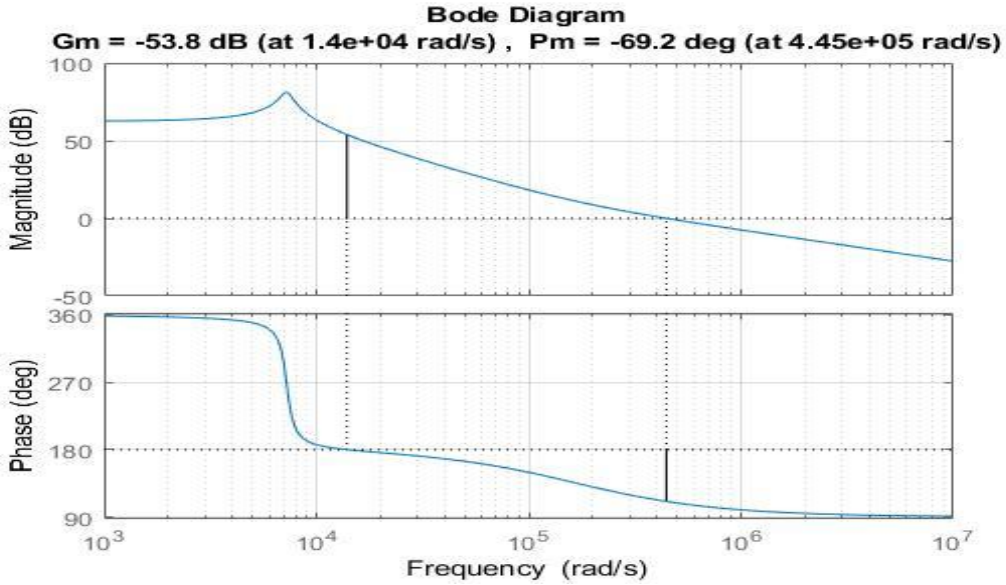
Bu simulasyondan sonra eldeki dönüştürücünün küçük sinyal analizi yapılmıştır. Analiz yapılırken bir önceki kısımda verilen durum uzayı ortalaması yöntemi kullanılmıştır. Bu yöntem kullanılarak eldeki dönüştürücü için puls genişliğinden–çıkış voltajına transfer fonksiyonu şu şekilde elde edilmiştir.

$$\frac{v_c(s)}{d(s)} = \frac{-4.16 * 10^5 s + 6.989 * 10^{10}}{s^2 + 840s + 5.25 * 10^7} \tag{10}$$

Görüldüğü gibi açık çevrim transfer fonksiyonunun sağ yarı düzlemde bir sıfırı bulunmaktadır. Ancak kutuplarına bakıldığında her iki kutbununda

$$s_{1,2} = -420 \pm j7233.5$$

olacak şekilde sol yarı düzlemde olduğu görülmektedir. Bu sebeplede açık çevrim sistemimiz kararlı bir sistemdir. Bu transfer fonksiyonu için Bode genlik ve faz eğrileri Şekil 4'te verilmiştir.



Şekil 4. Transfer fonksiyonu için Bode genlik ve faz eğrileri.

Şekil 4'te görüldüğü gibi sistemin kazanç marjini ***f = 14 kHz*** frekansında ***-53.8 dB*** olmakta ve faz marjini ise ***f = 445 kHz*** frekansında ***-69.2º*** olmaktadır.

VIII. 4. SONUÇ

Bu çalışmada izolasyonlu bir geri dönüşlü dönüştürücünün durum uzayı ortalaması metodu ile durum uzayı modeli elde edilmiştir. Elde edilen durum denklemleri kullanılarak dönüştürücünün önce kararlı durumdaki çalışma koşulları analizi yapılmış ve bulunan değerlerin bir önceki çalışmamızda aynı parametreler için grafiksel olarak elde edilen değerler ile örtüştükleri gösterilmiştir. Daha sonra ise dönüştürücünün küçük sinyal analizinin yapılabilmesi için pals genişliğinden–çıkış voltajına transfer fonksiyonu çıkarılmıştır. Bu transfer fonksiyonu kullanılarak sistemin frekans tepkisi Bode genlik ve faz eğrileri şeklinde grafiksel olarak gösterilmiştir.

KAYNAKLAR

[1] Hart, D.W. 2011. Power Electronics, 2nd Edt., McGraw Hill Publication, New York, USA

[2] Mohan, N., Undeland, T.M., Robbins, W.P. 2003. Power Electronics, Converters, Applications and Design, 3rd Edt, John Willey & Sons Publication, New Jersey, USA

[3] Rashid, M.H. 2004. Power Electronics, Circuits, Devices and Applications, Third Edition, Pearson Education Publication, New Jersey, USA

[4] Spiazzi G, Tagliavia D, Spampinato S. 2000. DC-DC Flyback Convertors in the Critical Conduction Mode: a Re-examination; IEEE Industry Applications Conference; 8-12 Oct. 2000; Rome, Italy. 2426-2432.

[5] Salihmuhsin, M. 2022. Simulation of a Flyback Convertor Operating in an Open Loop , 2. International Mediterraneans Scientific Research and Innovation Congress, pp 1072-1078, KKTC-Girne.

RADYO FREKANSI (RF) MAGNETRON KOPARTMA YÖNTEMİYLE BOR OKSİT (B_2O_3) KATKILI TUNGSTEN OKSİT (WO_3) İNCE FİLMLERİN ELDE EDİLMESİ VE YAPISAL ÖZELLİKLERİNİN İNCELENMESİ

Bahdişen Gezer

Uşak Üniversitesi, Mühendislik Fakültesi, Elektrik-elektronik Mühendisliği, Uşak, Türkiye., ORCID ID: https://orcid.org/0000-0002-2096-7185

Mustafa Atalan

Uşak Üniversitesi, Eşme Meslek Yüksekokulu, Eczacılık Hizmetleri, Uşak, Türkiye., ORCID ID: https://orcid.org/0000-0001-8543-6951

Can Gezer

Sofya Teknik Üniversitesi, Uçak Mühendisliği, Sofia, Bulgaria., ORCID ID: https://orcid.org/0000-0001-5725-7681

Rahşen gezer

Sofya Tıp Fakültesi, Samakov Hastanesi, Sofia, Bulgaria., ORCID ID: https://orcid.org/0000-0001-6147-059X

Özet

Metal borürler, gösterdikleri üstün kimyasal, fiziksel, korozyon, aşınma ve yüksek sıcaklık dayanımları nedeniyle günümüz sanayisinde en çok ilgi çeken malzemeler arasında yer almaktadır. Tungstenin oluşturduğu borür bileşikleri bu özelliklere sahip malzemelerin başında gelmektedir. Tungsten borürler özellikle gösterdikleri yüksek aşınma ve korozyon direnci, yüksek sıcaklık dayanımı, yüksek sertlik, kimyasallara karşı dayanım gibi özellikleriyle filaman/elektrot malzemesi ve aşınmaya dirençli ince film kaplama olarak kullanılmaktadır. Metal oksit malzemeler sahip oldukları görünür bölgedeki optik geçirgenlikleri, geniş bant aralıkları ve yüksek yük konsantrasyonundan dolayı güneş pillerinde, elektrokromik cam uygulamalarında, transistörlerde ve enerji depolama sistemlerinde yaygın olarak kullanılmaktadır. Son yıllarda en sık kullanılan metal oksit malzemeler arasında WO3 ve B2O3 bulunmaktadır.

Bu çalışmada, bakır oksit ve tungsten oksit ince filmler radyo frekans magnetron kopartma yöntemi ile sentezlenerek farklı büyütme şartlarında ve cam alttaşlar üzerinde farklı tabakadan 800nm ye kadar büyütüldü. Kaplama elektroliti; tungsten oksit (WO3), hidrojen peroksit (H2O2), sülfürik asit (H2SO4) ve bor oksit (B2O3)'den oluşmaktadır. Büyütülen ince filmler üzerine, RF gücü, alttaş sıcaklığı, kalınlık ve alttaşların türü gibi büyütme şartlarının etkisi X-ışını difraksiyonu (XRD), X-ışını fotoelektron spektroskopisi (XPS), Atomik kuvvet mikroskobu (AFM) ve optik absorpsiyon ölçümleri yapılarak yapısal özellikleri belirlenmiştir. B2O3 ve ince filmler RF magnetron kopartma tekniği ile cam alttaşlar üzerinde büyütülmüştür. Büyütülen B2O3WO3 ince filmlerin; XRD sonucunda filmlerde (002) düzlemine ait pikler daha baskın, (10l) ve (11l) düzlemlerine ait pikler de gözlenmiştir. Taramalı elektron mikroskobu (SEM) analizlerinde ise ortalama partikül boyutu yaklaşık 3 µm olarak gözlenen ve küresel morfolojiye sahip olduğu belirlenmiştir. Ayrıca farklı kalınlıklarda elde edilen filmlerde elektrokromik ve optik özelliklerine, kısmi oksijen basıncına, plazma gücüne ve alttaş sıcaklığının etkileride incelenmiştir.

Anahtar Kelimeler: B2O3, WO3, RF magnetron kopartma, İnce film.

OBTAINING BORON OXIDE (B_2O_3) DOCUMENTED TUNGSTEN OXIDE (WO_3) THIN FILM BY RADIO FREQUENCY (RF) MAGNETRON BREAKING METHOD AND INVESTIGATION OF THEIR STRUCTURAL PROPERTIES

Abstract

Metal borides are among the most attractive materials in today's industry due to their superior chemical, physical, corrosion, abrasion and high temperature resistance. Boride compounds formed by tungsten are

among the materials with these properties. Tungsten borides are used as filament/electrode material and wear-resistant thin film coating, especially with their high wear and corrosion resistance, high temperature resistance, high hardness, resistance to chemicals. Metal oxide materials are widely used in solar cells, electrochromic glass applications, transistors and energy storage systems due to their optical transmittance in the visible region, wide band gaps and high charge concentration. WO_3 and B_2O_3 are among the most commonly used metal oxide materials in recent years.

In this study, copper oxide and tungsten oxide thin films were synthesized by radio frequency magnetron plucking method and grown up to 800 nm from different layers on glass substrates under different magnification conditions. Coating electrolyte; It consists of tungsten oxide (WO_3), hydrogen peroxide (H_2O_2), sulfuric acid (H_2SO_4) and boron oxide (B_2O_3). The effects of growth conditions such as RF power, substrate temperature, thickness and type of substrate on the grown thin films were determined by X-ray diffraction (XRD), X-ray photoelectron spectroscopy (XPS), Atomic force microscopy (AFM) and optical absorption measurements. B_2O_3 and thin films were grown on glass substrates by RF magnetron detachment technique. Grown $B_2O_3WO_3$ thin films; As a result of XRD, peaks belonging to the (002) plane were more dominant in the films, and peaks belonging to the (10l) and (11l) planes were also observed. In scanning electron microscopy (SEM) analyzes, it was determined that it had a spherical morphology with an average particle size of approximately 3 μm. In addition, the effects of electrochromic and optical properties, partial oxygen pressure, plasma power and substrate temperature on films obtained in different thicknesses were also investigated.

Keywords: B2O3, WO3, RF magnetron plucking, Thin film

HYDROLOGICAL MODELLING OF GURARA WATERSHED UNDER THE IMPACT OF LAND-USE AND CLIMATE

Abdullahi Yahaya Ibrahim

Ahmadu Bello University Zaria, Nigeria, ORCID NO: 000-0001-8194-0376

Dr. Al'amin Danladi Bello

Ahmadu Bello University Zaria, Nigeria, ORCID NO: 000-0001-5864-3576

ABSTRACT

Land-use and climate change are major anthropogenic factors that changes the hydrological response of a watershed. Whence the Gurara watershed was evaluated due to its significance for power generation, water supply and enormous irrigation activities it provided for the residence in Abuja and environs. An integrated approach of multi temporal Geographical Information Systems (GIS) based hydrological modeling known as Hydrological Simulation Program FORTRAN (HSPF) Model was used in this study. The model was calibrated and validated with correlation coefficient value of 0.98 (both calibration and validation) and Nash Sutcliffe efficiency of 0.91 for the calibration and 0.90 for the validation. Five land use scenarios (1991-2030) were generated using remote sensing data and Land Change Modeller (LCM). The generated land-use scenarios were combined with 30 years climatic data (1991-2020) in order to evaluate the hydrological changes due to impact of land-use and climate change. The baseline scenario (1991) is characterized by large extents of forest areas (17.5%) and bare-land areas (54.02%) and an insignificant extent of urban areas (0.15%) and produced low surface runoff (85.4 x $10^5 m^3$) after simulation, compared to other scenarios. However the final scenario (2030), was characterized by an increased percentage of built up areas (22.6%) and agricultural areas (55.6%) leading to an increase in surface runoff (126.1 x $10^5 m^3$). Trend Analysis was used to assess the variability in the streamflow's of the watershed. The analysis of the results shows that surface runoff accounts for 93.15% of the rainfall influx, an indication that a large percentage of the rainfall is converted to overland flow.

The results of this study provide useful information on the changes on the hydrology of the sub-tropical watershed under the impact of land use dynamics and climate change for effective management of water resources of the area.

Keywords: climate change, hydrology, land-use, Gurara watershed

1.0 INTRODUCTION

Among other natural resources, water resources occupy a special place in environmental constancy, growth and sustainable economic development. To boost healthy living, increase food security and to prevent stress on the available water resources, which can give birth to serious consequences like drought and flooding, sustainable planning and proper management of the available water resources through the most economical means should be the top priority for any society.

There has been unprecedented inflow of people and unplanned land use changes in many countries in the preceding decades which has led to substantial climatic and hydrological changes and to a large extent biased the availability and distribution of water resources in most regions of the world (Lambin et al., 2001), the Gurara watershed not being exempted. The Gurara catchment houses the Gurara dam, which is an eight hundred and eighty million cubic meters multipurpose dam built to serve three major purposes which are; conveyance of raw water to augment inflow from Usuma river into Usuma dam for water treatment and distribution, transfer of water to a thirty megawatt hydro power station for the generation and transmission of electricity to Kukenda substation and modern irrigation of a six thousand hectare land area at Azare.

Musa Dalil et al. (2013) utilized remote sensing to study the impact of Gurara dam on the land cover of upper Gurara watershed and discovered that the construction of the dam led to a consecutive increase in the activity level within the watershed and as a result, tremendous and unplanned changes were recorded between the years 2000 and 2013 with increase in built up area recording one of the highest percentage increases.

In recent studies, Oseni and Bloodless (2017) carried out the hydrological characterization of the Gurara watershed for streamflow prediction coupling GIS and the Muskingum River Routing method and taking into the consideration the current land use of the watershed. He successfully produced discharge hydrographs for all ungauged sub-watershed utilizing the available data for one of the watersheds and the available data on the physical make-up of the watershed.

Also, Oluwaseye and Onemayin (2013) modeled the flooding of the upper Gurara watershed using remote sensing data and a geospatial streamflow model GeoSFM. Discovered that the most sensitive parameters of the model were; fraction of flow lost within the rivers reach, fraction of hydrologically active soil layer, SCS runoff curve number and potential Evapotranspiration. He however concluded on the note that the model was found inadequate in estimating the total flow and using a higher resolution of remotely sensed data would improve the flow estimation accuracy.

A number of methodologies have been utilized to achieve the evaluation of the impact of changes in land use and land cover on the hydrology and climate in sub watershed, watershed, sub-regional and regional scales. Among them are the mathematical or statistical methods (Yi, Jinxi, Yiyi, Xiang, & Yan, 2019) and the paired watershed method (Brown, Zhang, McMahon, Western, & Vertessy, 2005). However, a method that combines Geographical Information Science (GIS) technology and boundary conditions to simulate the hydrological processes of the watershed, has proven to not only be economical but accurate in producing a comprehensive evaluation of the watershed processes (Bello, Haniffah, Hashim, & Anuar, 2018).

Watershed models simulate the natural processes that occur in a watershed such as flow of water, sediments, chemicals, nutrients and microbial organisms within watersheds, and evaluate quantitatively and qualitatively, the impact of anthropogenic activities and changing land systems on these processes (V. P. SINGH, 2006). Watershed models operate in a holistic way contrary to other models which focus on individual or multiple processes at a small scale without an exhaustive consideration of the entire watershed extent (Edsel et al., 2011). Watershed models are essential and effective tools for investigating the complex nature of processes that affect the surface and subsurface hydrology, they also help in assessing the impacts of land use changes and aid decisions on best management practices.

In this study the Hydrological simulation Program Fortran (HSPF) was deployed for the watershed modeling. HSPF is a comprehensive, continuous, semi-distributed simulation watershed scale model supported by the United States Environmental Protection Agency (USEPA), used for simulation of hydrological, Environmental and water quality related processes of different extents and complexities (OGUTVEREN, 2004). HSPF simulates the land, sub-land and hydrological sections of a watershed. Hydrological simulation in HSPF consists of five storage classes (interception, upper-zone, lower zone, base flow and deep percolation) each describing different forms of outflow (Diaz, McAnally, & Martin, 2011).

The aim of this study is to multi-temporal data using watershed modeling to estimate the impact of LULC and climate change on the hydrology of the watershed while the objectives are to 1. Develop a hydrological model of the Gurara watershed 2. To evaluate the impact of land use and climate change on the water shed 3. To determine which of them i.e. land use or climate has more influence on the watershed 4. To determine future impacts of land-use and climate change in the watershed and finally 5. To design Best management practices for flood control.

2.0 MATERIALS AND METHODS

2.1Study Area

The Gurara Watershed is located in the northern part of Nigeria, between lat 8°15 and 10°05'N and long 6°30' and 8°30E and has a total catchment area of 16,650km^2 at Izom. The basin is tailored in the north east-south west direction with its headwaters starting from the western side of the Jos plateau. The watershed is centered in-between the semi-arid north and the sub-humid climate in the south and its climate is characterized by dry northern winters and wet northern summers (Ibrahim & Isiguzo, 2009). There are two major seasons experienced in the watershed which are the wet and dry seasons. The dry season lasts between November and march while the wet season begins in May and lasts till October(Oluwaseye & Onemayin, 2013). The vegetation is the savannah grassland with a sparse distribution of tropical forest (Ibrahim & Isiguzo, 2009).

The terrain is undulating and dissected with ca clay loam soil and red laterite /alluvial soil being the prevalent soil types (O. D. Jimoh & Sule, 1992). The mean annual rainfall at the location counts 1400mm and the mean monthly maximum and minimum temperature in the catchment are 37.3 °c and 19.7 °c respectively (Jimoh & Ayodeji, 2003). There are five hydrological stations located within the watershed namely Gantan, Izom, Jere, Kachia and Kurmin Musa.

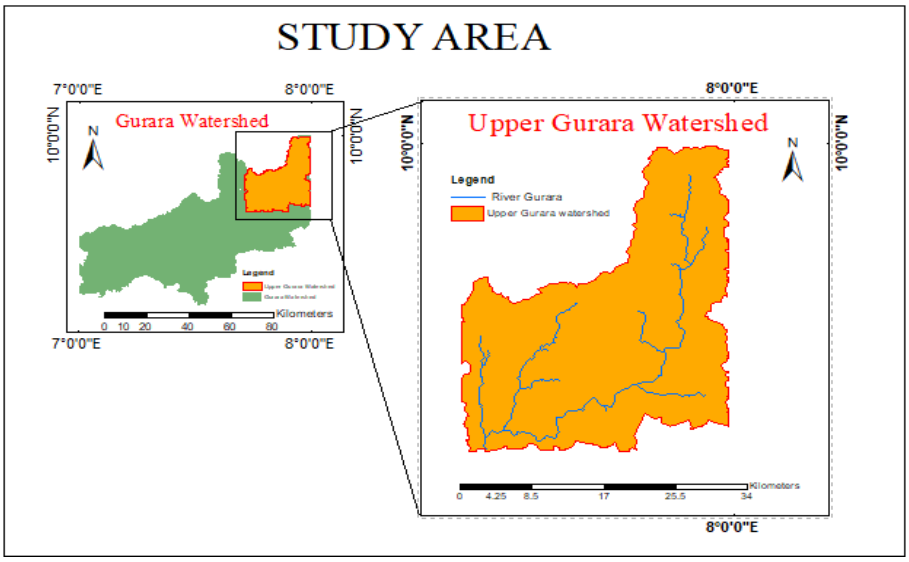


Figure 1: Location and Characteristic of Gurara watershed

2.2 Data Collection

Remotely sensed images for a period of 5 years was from Landsat 4-5 thematic mapper (TM), Landsat 7 Enhanced thematic mapper (ETM+) and Landsat 8 operational land manager (OLI/TIRS) satellites which was downloaded from the earthexplorer.usgs.gov website. The data for discharge for the gauging station at kachia was obtained from Kaduna state water board while metrological data was gotten from Nigerian Metrological Agency (NIMET). The soil Map of the study area was gotten from the Ministry of Agriculture. The DEM was downloaded from USGS website.

2.3 DEM Delineation

The digital elevation model of pixel size 30m by 30m for the study area was downloaded from the United States Geological Survey website. The downloaded raster data usually comes in Geographic coordinates which is in three dimensions. For proper spatial location of the raster data in the GIS working space the raster data is required to be re-projected to an equivalent two-dimensional coordinate system known as the Universal transverse Mercator (UTM).

The digital elevation model was imported to the BASINS 4.5 ArcMap software for terrain processing. The automatic delineation tool was used to carry out watershed characterization wherein all sub-catchments, flow direction, slope, elevations, flow outlets and other physical characteristics of the catchment was defined.

Table 1: Data and Information used for the Study

Data Type	Data Name/Unit	Period covered	Time Step	Source
Metrological	Rainfall (mm), temperature (°C), wind speed (m/s), cloud cover (Okta), solar radiation (MJm-2) and evaporation (mm)	1980 – 2010	Daily	Nigerian Metrological Agency, NOAA Data Online
Hydrological	stream flow	1971 - 1989 2001 – 2010	Monthly/Daily	Ministry of water Resources, Kaduna State Water Board, Gurara Water development Authority.
Spatial	DEM	2014	30m x 30m	Earthexplorer.usgs.gov
	Remote sensed Imagery	1987 – 2013	30m x 30m	Earthexplorer.usgs.gov
	Soil			Ministry of Agriculture
	Land use	1987 – 2013	30m x 30m	Generated Using Remote Sensing

2.4 Image Classification and Accuracy Assessment

Remotely sensed maps of 1991 to 2020 were downloaded from earth-explorer and processed in ArcMap 10.7 software. The images were re-projected before classification. The supervised classification method was used to carry out the land use categorization. This process involved sectioning the study area, sample collection, composite band generation, classification and assessment of classification accuracy (Anad, 2017). For the supervised classification, the maximum likelihood classification method was used due to its acceptability amongst researchers (Bello et al., 2018). For sectioning of the study area for acquiring of the ground-truth samples the stratified random sampling method was used because its tendencies to give a more representative sample of the watershed land use categories (Congaltol, 1988).

Table 2: Accuracy assessment of classified maps using error matrix and kappa analysis

Land Cover Class	1991		2001		2013		2020	
	Producers Accuracy (%)	Users Accuracy (%)	Producers Accuracy (%)	Users Accuracy (%)	Producers Accuracy (%)	Users Accuracy (%)	Producers Accuracy (%)	Users Accuracy (%)
Built-up	100	75	100	75	100	62.5	100	67
Bareland	83	67	53.3	61.5	66.6	100	50	67
Agricultural	80	75	83.3	62.5	100	87.5	75	75
Forest	80	100	55.5	83.3	100	100	100	100
Waterbodies	100	67	100	100	100	100	100	67
Outcrop	75	100	100	75	100	100	67	100
Overall	80.4		60		88.7		73.5	
Kappa Overall	83.9		72.7		90.7		78.1	

2.5 Hydrological Modeling

The Hydrological Simulation Program Fortran popularly called HSPF is a comprehensive, semi distributed watershed model supported by the United States environmental protection agency USEPA, used for simulation of hydrological, environmental and water quality related processes of different sizes and complexities (J. Singh, Knapp, Arnold, & Demissie, 2005).

The model has three main modules, PERLAND, IMPLAND and RCHRES which are used in simulating pervious land segments, impervious land segments and free flow reaches or mixed reservoirs respectively (J.

Singh et al., 2005). The model routes water from one reach to another using the storage routing technique and hydrological behavior using the kinematic wave technique (J. Singh et al., 2005).

The hydraulic characteristics of reaches are defined in the function tables provided by the model and the effects of vegetation type, density, root growth, stage development and soil moisture are all lumped into the LZETP module.

The module is embedded in the Better Assessment Integrating Point and Non point Sources GIS software popularly called BASINS which fosters the delineation and sectioning of the watershed. The mathematical representation of the watershed is done by an embedded plug-in in the software known as the Watershed Data Management Program which facilitates the preparation of the input metrological and hydrological datasets. The dataset required by the model for proper simulation are the land use land cover information, Digital elevation model and other data like air temperature, dew point temperature, precipitation, stream discharge, open evaporation and solar radiation, wind speed.

For calibration and validation of the model, HSPF expert system software (HSPEXP++) was used. The calibration and validation process was done by parameter adjustment according to the guidelines of United States environmental protection board (USEPA) technical note 6. The calibration and validation of the hydrological model was done using the observed stream flow. The calibration was done using the data set of 2002 to 2005 while the validation was done using the dataset of 2006 to 2009.

For the evaluation of simulation results, a number of standard numerical and statistical criterion are employed I comparing the observed and simulated data.

The R^2 coefficient of determination, which is the square of pearson's product moment correlation coefficient. It represents the fraction of variability on one variable that can be explained by the variability in the second variable (Diaz et al., 2011). It is given by;

$$R^2 = \left\{ \frac{\sum_{j=1}^{n}(c_j - \bar{o})(s_j - \bar{o})}{\left[\sum_{j=1}^{n}(c_j - \bar{o})^2\right]^{0.5}\left[\sum_{j=1}^{n}(s_j - \bar{s})^2\right]^{0.5}} \right\} \quad 1$$

Oj represents the observed stream flow

O represents the average observed stream flow

Sj represents model-simulated stream flow

S represents the average simulated stream flow

Also, The Nash-Sutcliffe coefficient, which represents the fraction of the variance in the measured data explained by the model (Diaz et al., 2011). The value of the coefficient ranges from zero to one and a value of one represents a perfect fit. The coefficient id determined by the formula;

$$NS = 1 - \frac{\sum_{j=1}^{n}(c_j - s_j)^2}{\sum_{j=1}^{n}(c_j - \bar{c}_j)^2} \quad 2$$

Oj represents the observed stream flow

Sj represents model-simulated stream flow

Finally, Mean relative error, which is expressed as the difference between the simulated data and the observed data divided by the corresponding observed data

$$MRE(\%) = \frac{\sum_{j=1}^{n} \frac{(s_j - c_j)}{c_j}}{n} \times 100 \quad 3$$

Oj represents the observed stream flow

Sj represents model-simulated stream flow

2.6 Estimation of Hydrological Parameters

The HSPF model requires a representative land use classification in combination with the topographical characteristics and the observed metrological data and observed stream-flow to create the user control input file required for calibration and validation of the model. The land use classified map of 2013 was used to carry out the model generation because of data availability as the only DEM available for the study area was captured 2014 and therefore in order to get a representative model the two datasets were thus used. Following the generation of the un-calibrated model, the observed streamflow of years 2001 to 2010 were used to calibrate and validate the model. Furthermore, the calibrated model parameters were transferred to the newly generated land use scenarios (1991 - 2010) for simulation and determination of hydrological variation by observation of the relative change in water balance parameters across the simulated years. In addition, in order to determine which of the two concepts of study have a stronger influence on the watershed a scenario combination technique used by Chen et al. (2019) was adopted. The technique involved generation of historical climate scenarios and combining with the existing historical land use scenarios such that a land use scenario is kept constant and combined with varying climate scenarios and vice versa. An evaluation of such exercise would give detailed evidence as to which of the phenomena (climate change and land use change) has more influence on the watershed hydrology as well as the watershed parameters that are most sensitive to climate and land use changes.

2.7 Mann and Kendall Trend Analysis

Mann and Kendall test is a non-parametric statistical test used for trend analysis of climatologic and Hydrologic time series (Karmeshu, 2012). It detects trends in the time series by comparing the relative magnitude of the sample data rather than the data values of the time series. It has the advantages of analyzing datasets that are not normally distributed and it has low sensitivity to abrupt breaks due to heterogeneity in the time series (Karmeshu, 2012). The values in the time series are evaluated in a sequential order such that each data value is compared with subsequent data values. If the value from a preceding period is greater than a value from an earlier time period the Mann and Kendall statistic S is increased by 1. However, if the contrary is the case, the statistic is decreased by the same unit. The outcome of the statistical operation produces a number of test statistics used to evaluate the result.

The Mann and Kendall test statistic S, computed using the relationship below:

$$S = \sum_{i=1}^{n-1} \sum_{j=i+1}^{n} sign(T_j - T_i) \quad 4$$

Where S is the test statistic, T_j and T_i are the annual values in years i and j

Secondly, the Z_S statistic measures the significance of the trend and tests the null hypothesis.

$$Z_s = \begin{cases} \frac{s-1}{\sigma} \; for \; S > 0 \\ 0 \; for \; s = 0 \\ \frac{s+1}{\sigma} \; for \; s < 0 \end{cases}$$

Where S is the Mann and kendall test statistic and σ represents the variance of the time series.

If Z_S is greater than $Z_{ά/2}$ where ά represents the significance level, a trend is said to exist and the null hypothesis rejected and if the contrary is the case, then the null hypothesis if no trend is accepted.

2.8 Future Land Use Modelling

The land change Modeler (LCM) in the IDRISI SELVA 7.0 software was used to carry out this exercise.

The land change modeler is a vertical module embedded in IDRISI 7.0 software used in studying and addressing environmental problems such as land use change / conversion and biodiversity conservation taking into consideration the static conditions, dynamic transitions and planned development (Eastman, 2012). The modeler uses two machine learning algorithms Markov and Cellular Automata Markov algorithms to carry out future land use projections from historical land use maps. The model involves a series of stages to prepare which are the change analysis where the various changes that have transpired in a catchment between two time periods are identified. In this stage, significant transition potentials are identified, as well as the transition drivers. The initial maps which the succeeding analysis was based on are provided. The provided maps was used to understand the type and degree of changes that occurred, gains and losses in each category, establish the basis of the model and finally produce the change maps.

Secondly, generation of transition potentials which involves identification by the model, the potential of transition from one land use category to another. It is identified and modeled and maps of suitability, also known as transition maps are produced. Subsequently, the change prediction is done by using trained data produced from the transition potential stage to predict the land use changes for future years. The two modules offered by IDRISI 7.0 to carry out this task are the hard and soft prediction modules. However the hard prediction module, specifically the MARKOV module, which is based on a single scenario that produces a land cover map, displaying changes in the land categories that were input at the beginning of the modeling process was used. Finally, the amount of change is recalculated and allocated evenly across all the various years to which the land use change is to be predicted and also specifies the frequency at which the dynamic change occurs.

2.9 Modeling of Best Management Practices

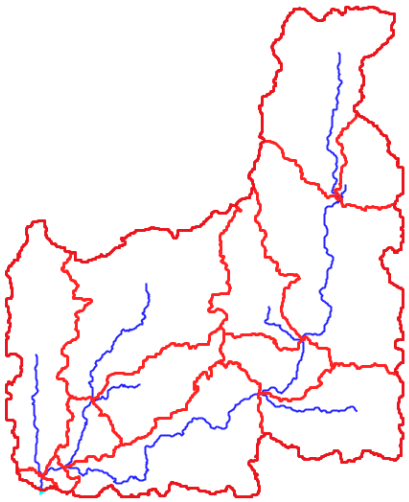
In HSPF Storm water BMP's are in two major categories which are the Low impact development (LID) BMP's and the Sewer and open channel BMP's. The LID BMP's are majorly used to develop BMP's within the confines of an urbanized area while the sewer and open channel BMP tool is used for designing BMP'S for watershed areas. They are modeled as channels (circular, rectangular, triangular, trapezoidal etc.) represented by their depth- area- volume relationship in a table known as the hydraulic function table (FTABLE). We modeled the channel by specifying the channel dimensions and manning's roughness and control devices attached to the exit of the channel.

After the aforementioned modeling steps are completed, the model automatically generated the modified characteristics of the flow in the specified sub-watershed reach based on the percentage of the sub-watershed area the channel is to be installed.

3.0 RESULTS AND DISCUSSION

3.1 Terrain Analysis and Basin Characterization

The DEM for the study area was obtained from USGS EROS data center and was accessed through USGS Global Visualization viewer (GLOVIS). The only DEM available for the area was captured by the satellite at early 2014. After downloading the DEM in raster format, it was imported into Arcmap 10.7 for reprojection. The raster DEM was assigned Geographical coordinates as the default coordinates, however in order to facilitate its recognition and easy utilization in the GIS environment it was re-projected to its corresponding Universal Transverse Mercator (UTM) coordinates for which the study area falls within the WGS 1984 zone 32 Northern hemisphere coordinates. After reprojection the DEM was exported from the GIS environment and imported into the BASINS 4.5 ArcView environment for Delineation, terrain analysis and Generation of Hydrologic response units. The automatic delineation tool in the BASINS software was employed to carry out the catchment delineation. A total number of 10 sub catchments and 11 reaches were delineated using a threshold value of 5000. The gauging station was located on the delineated catchment at Latitude 9º40'N and Longitude 7º58'E corresponding to reach 11 in the delineated catchment. A total catchment area of 300.84km2 and a total drainage area of 450km2 with a max slope and elevation of 12.01m and 685m respectively were delineated as the boundary parameters for the study area.



:teristics

Polygon ID	Stream Link	Stream Length (m)	Area (m^2)	Average Slope
0	1	27936	100.63	4.37
2	3	2617	18.03	4.40
1	2	12137	48.31	8.69
3	4	10314	32.73	12.01
4	5	407	17.23	5.24
7	8	7433	11.81	4.03
8	9	25538	36.17	5.10
5	6	6542	25.57	3.70
6	7	6771	6.81	9.19
9	10	2264	1.57	4.62
10	11	1911	1.98	4.12

3.2 Land Use Classification

For the upper Gurara watershed six land use classes were adopted for classification of its land use which are; Agricultural areas, Forest areas, built up areas or urban areas, water bodies/wetlands, bare lands and outcrop. Remotely sensed raster data was downloaded from USGS EROS data center to carry out the land use classification. Landsat 4.5 TM class 1 level 1, Landsat 7 ETM class1 level 1 and Landsat 8 OLI/TIRS class 1 level 1 data of pixel resolution 30m by 30m, 7.5 minute, one arc interval and 0 cloud percentage was used to classify 1991, 2001, 2013 and 2020 respectively. The supervised maximum likelihood classification procedure was adopted for the classification because it is considered the most accepted and most used classification method all over the world. The first four bands of the downloaded remotely sensed images was imported into the Arcmap environment and the image composition tool in Arcmap was used to superimpose all four image bands to produce the composite image to be used for the classification. After composition of the image bands, the delineated shape-file of the study area was imported and was used to clip out the study area from the composite image. After the clipping, the training samples manager was initialized to begin the collection of training samples from the composite image. The Stratified Random Sampling scheme was used for collecting training samples. The study area was sectioned into three parts and five samples for each land use class was taken from each section making a total of ninety samples that was taken for the whole study area. After the training samples were taken, the maximum likelihood classification tool in Arcmap was used to carry out the

classification. The table below shows the percentage of land use change extracted from the classified land use maps.

Table 3: Percentage of land-use change in upper Gurara watershed

.

Land Use Year	Land Use Category (km^2)					
	Water bodies	Forest	Agricultural	Built-up	Outcrop	Bare land
1991	3	60	171	1	58	527
2001	2	285	218	3	58	254
2013	68	91	381	55	33	192
2020	59	94	425	71	22	148

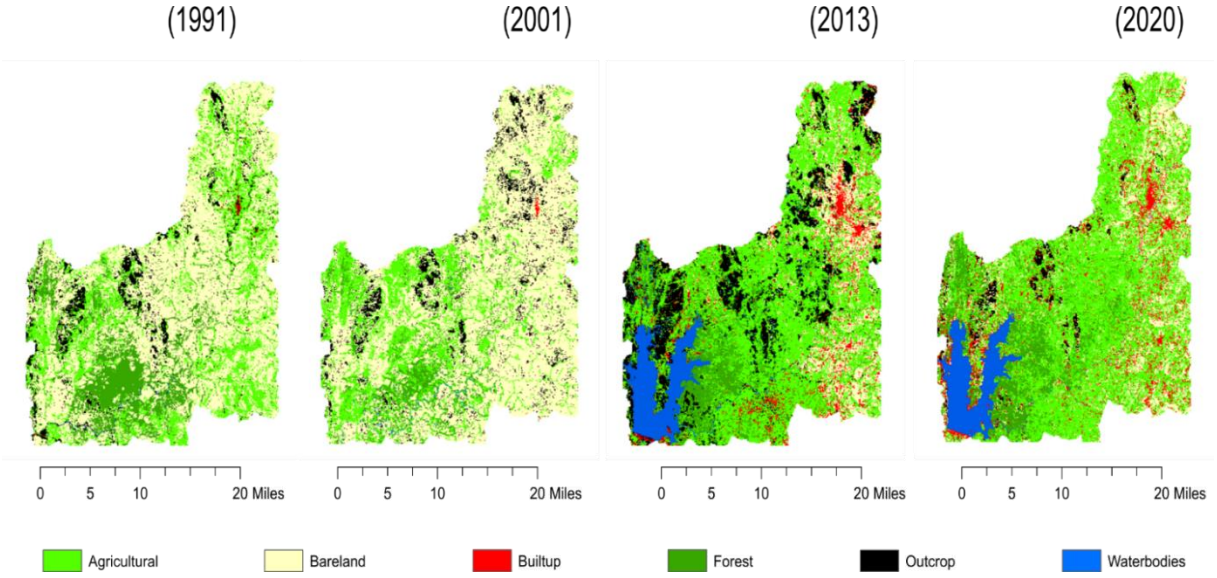


Figure 3: Classified historical Land use Scenarios for upper Gurara watershed (1991-2020)

3.3 Accuracy Assessment of Classified Maps

For the accuracy assessment of the classified maps two methods were used to test for the classification accuracy which are the error matrix popularly called confusion matrix and the kappa coefficient methods. Before proceeding with the accuracy analysis ground-truthing samples were taken from two points for each land use class from each cell to serve as observed samples. After the ground truthing exercise, the accuracy analysis was performed using the methods mentioned above. We recorded an overall accuracy of 83.9%, 72.7%, 90.7% and 78.1% for 1991, 2001, 2013 and 2020 respectively and overall kappa coefficient of 0.80, 0.60, 0.88 and 0.73 for 1991, 2001, 2013 and 2020 respectively. The table 2 above shows a summary of the accuracy computations.

3.4 Calibration and Validation

Calibration of the model was done by manual parameter adjustment and was further facilitated by the HSPFEXP+ program and BASINS HSPF technical note 6 which contains detailed explanation on how to adjust parameters to achieve a good simulation. The HSPFEXP program gives multiple outputs that enable analysis of model performance. These outputs include; Normal plots of simulated and observed stream flow for the amount of years simulated, cumulative flow, percentage of daily flow exceeded, yield duration curve and Evapotranspiration histogram. Also, the program generates statistical reports of the performance evaluation for the simulation runs. The observed hydrological time series used for the calibration extends from 2002 to 2009. The dataset was sectioned into two parts and the first part used for the calibration was for a period of

four years from first January 2002 to 31st December, 2005 and that for the validation was for a similar period from first January, 2006 to 31st December 2009. The accuracy analysis of the model simulation showed good performance as the results showed a coefficient of determination value of (R^2) 0.97/0.96, percentage bias (PBIAS) of -2.18% which indicated that the prediction accuracy had a 2.18 percent underestimation, Nash Sutcliffe efficiency (NS) of 0.94 and a root mean square error of 0.25 for the calibration period and R^2 of 0.96, PBIAS of 0.046 percent, NS value of 0.91 and a RMSE of 0.25 for the validation period.

Table 4: Summary of HSPF model accuracy assessment for stream flow prediction

Efficiency Criteria	**Calibration**	**Validation**
Correlation coefficient	0.98	0.98
Coefficient of Determination	0.97	0.96
Mean Error	-2.85	0.05
PBIAS (%)	-2.18	0.046
RMSE-Observations ratio	0.253	0.254
Nash-Sutcliffe Efficiency	0.90	0.91

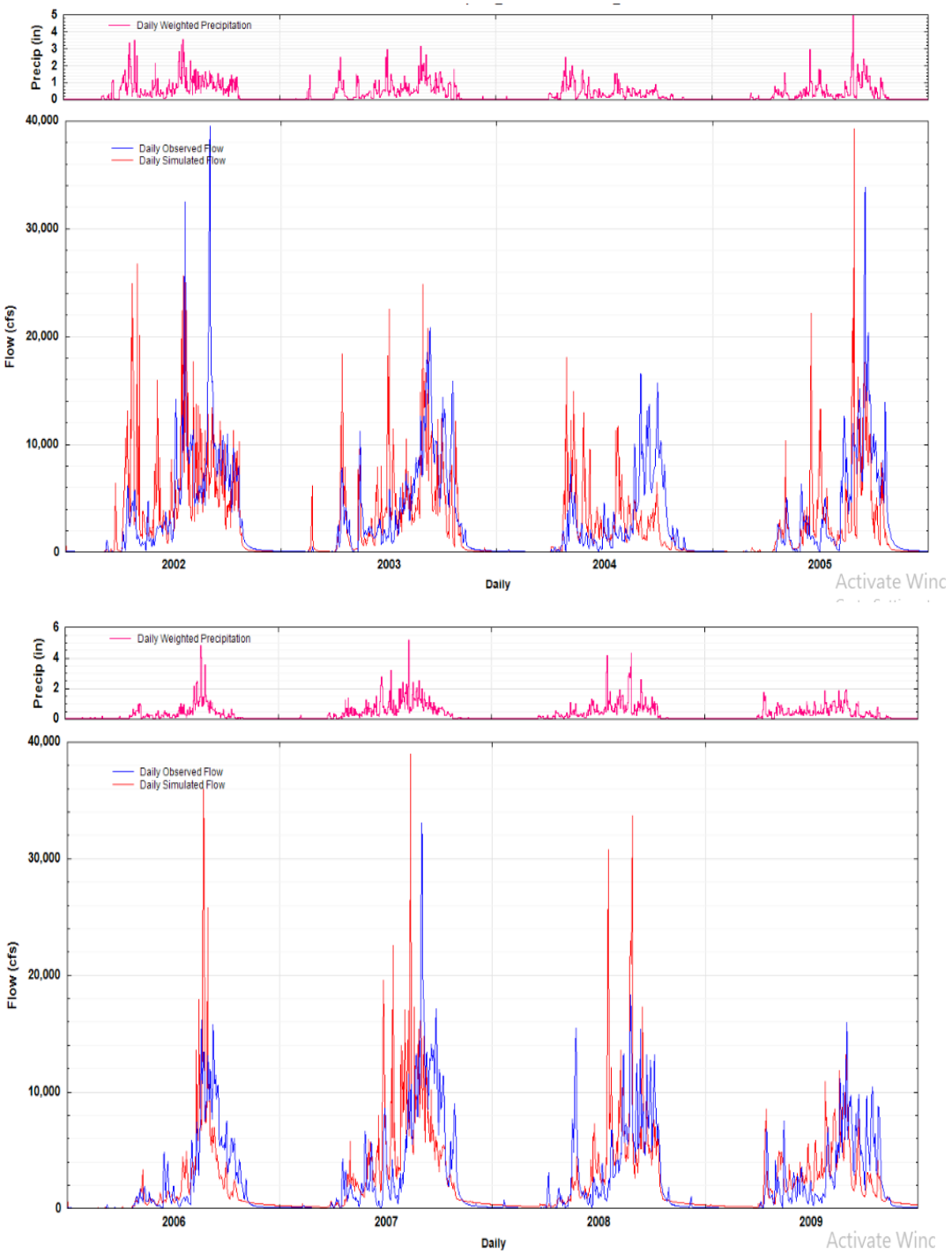


Figure 4: simulated and observed stream flow Graphs for the calibration and validation period

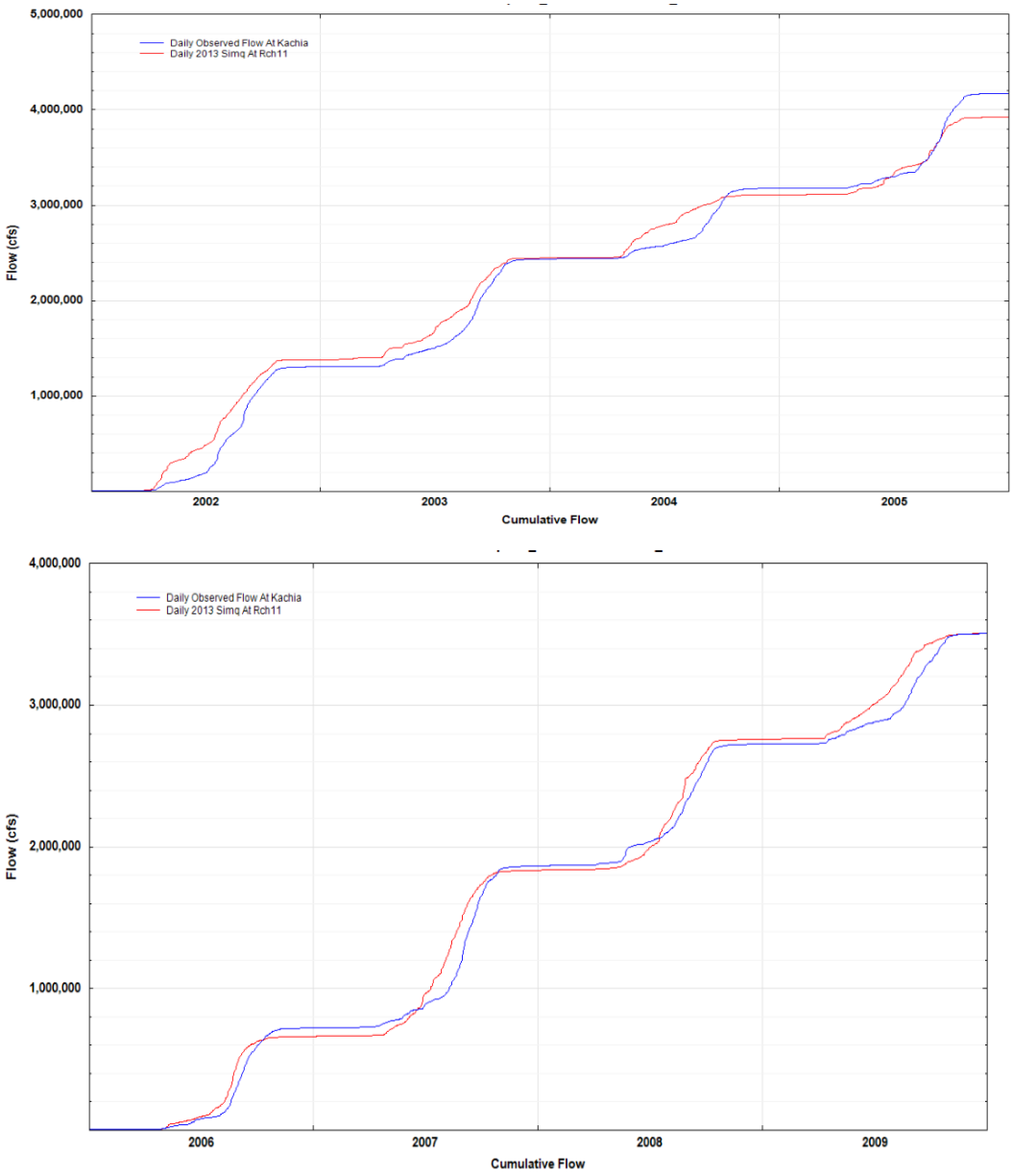


Figure 5: simulated and observed Cumulative flow Graphs for calibration period

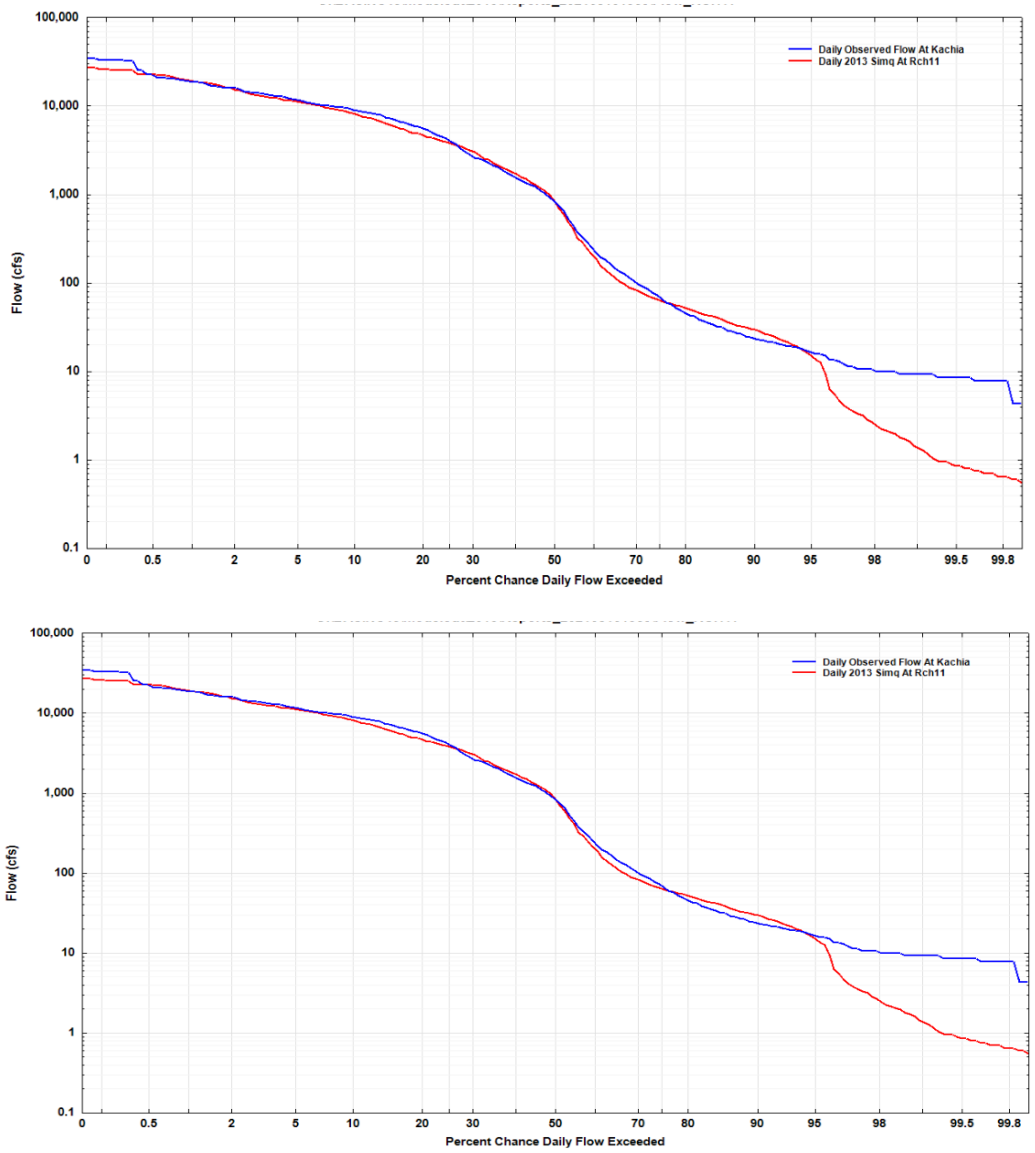


Figure 6: simulated and observed Graphs for percentage chance daily flow exceeded for calibration and validation period

The peak stream flow for the calibration period was 40,533cfs (1147.77m^3/s) while for the validation period it was 57,391cfs (1625.13 m^3/s) and the minimum stream flow for the calibration period was 0.329cfs (0.005 m^3/s) while for the validation period 1.052cfs (0.029 m^3/s) was recorded as the minimum value giving an indication of seasonal hydrological extremes in the watershed. The model results show that the model was able to accurately mimic the watershed hydrology in view of the contrast between the mean calibrated and validated values for streamflow which shows a 10.28 percent difference which is far less than the maximum standard set by the developers of the model of 43 percent.

3.5 Calibrated Parameters Assessment

The calibrated parameters show the hydrological characteristics of the watershed. Table 4.7 gives a summary of the calibrated parameters according to the land use classes. In HSPF, three major parameters affect the general water balance of the watershed. They are LZSN, LZETP and DEEPFR representing Lower Zone Nominal Soil Moisture Storage, Lower Zone Evapotranspiration and fraction of ground water inflow to deep recharge. LZSN is a conceptual parameter that requires calibration to reach its acceptable value, however no

guidelines are presented in literature. The calibrated LZSN values for each land use in the watershed were in the minimum end of the range specified by HSPF developers. LZETP is a coefficient that defines the actual Evapotranspiration probability from the lower zone (root zone of the soil profile) of the watershed; it is a function of vegetation type. The calibrated values all fell in the range suggested by HSPF developers. The calibrated values for LZETP decreased in the following order Wetland/water bodies with a value of 0.52, Forest areas with a value of 0.49, Agricultural areas, built up areas and bare land with values of 0.48, 0.2 and 0.1 respectively. The final parameter that had a great influence on the general water balance to be calibrated was the fraction of infiltrated water inflow into deep recharge DEEPFR. The calibrated values for DEEPFR for all land use types were very low with Built up areas recording the lowest values of 0.001 due to its impervious nature. The low values indicate the poorly drained nature of the soil present in some areas of the watershed that prevent all the infiltrated water from reaching the aquifers (Diaz Ramirez, McAnally, & Martin, 2011).

The next set of parameters to be calibrated was parameters that related to storm flow volume and rate. HSPF calculates and assigns infiltration rates using the HSG soil classification (USEPA, 2000). A large percentage of the soils in the upper Gurara watershed were classified in the group C of the HSG soil classification translating to a soil type of clay loam. For the upper Gurara catchment, the infiltration rate was calibrated to a value of 0.02 $mmh^{-1}$for all green areas and 0.01 mmh^{-1} for built up areas and bare land. All the low values recorded for the infiltration are due to the growing percentage of built-up areas and the high clay percentage of the soils in the watershed which also gives an indication of a high runoff potential in the watershed.

The next calibration stage was to optimize parameters that affect storm runoff volume. These parameters which are slope (SLSUR), length (LSUR) and manning's coefficient of runoff (NSUR), of the watershed were extracted from the 30m by 30m resolution digital elevation model used in the watershed delineation. The DEM showed that the watershed is characterized with a sloping topography of value 0.06, which falls on the extreme end of the characterization specified by HSPF. The manning's coefficient of runoff was calibrated following the land use type with water bodies and forest areas having the highest values of 0.4, agricultural having 0.2, bare land having 0.25 and built-up areas with the lowest of 0.1.

HSPF ascertains direct runoff as amount of surface runoff and interflow. The interflow in the watershed is represented by the parameter INTFW. The parameter calculates the amount of water that finds its way into the soil profile, the greater the INTFW parameter the more reduced the surface runoff is and vice versa (USEPA, 2000). The INTFW parameter was calibrated to a value of 2 throughout the watershed translates to a high runoff potential in the watershed as the larger percentage of water received in the watershed remains as surface runoff. Following the previous parameter, the interflow recession parameter (IRC) parameter which determines the behavior of the water present in the interflow section of the watershed was calibrated to a high value of 0.8 which describes the high rate at which the water from interflow is discharged and the slow recession of storm events in the watershed.

Following the aforementioned stages of calibration, the parameters affecting the distribution of flow in the watershed into high and low events was calibrated. The parameters that affect this distribution in HSPF are INFILT, the base ground water recession (AGWRC) and the fraction of remaining Evapotranspiration from base flow parameter (BASETP). The AGWRC parameter depends of the physiographic and climatic characteristics of the watershed. It is the ratio of current groundwater release to the groundwater release 24 hours earlier (Diaz et al., 2011). Its calibrated value was within the range specified by the HSPF developers. The BASETP parameter affects the Evapotranspiration from areas close to the water bodies. It is the portion of potential evaporation that is fulfilled only as discharge from the groundwater into the streambed exists (USEPA, 2000).

The values for this parameter were calibrated as 0.05 for water bodies and 0.01 for all other land use types.

Finally, the calibration was done on parameters that affected the seasonal balance in climate and hydrology of the watershed. These parameters include; the percentage of intermediaries capable of intercepting rainfall CEPSC and the upper zone nominal storage parameter (UZSN). The CESPC parameter decreased in a sequence with forest and built-up areas recording the highest values of 0.46 and 0.45 respectively while agricultural areas, water bodies and bare lands were calibrated to values of 0.44, 0.40 and 0.1 respectively. This parameter estimates the amount of rainfall retained by vegetation or any intermediary between the atmosphere and the ground, and finally evaporates back to the atmosphere. Built up areas and forest areas

recorded the highest values because of the barrier created by rooftops and thick vegetation that prevents rainfall from reaching the ground. The upper zone nominal storage is related to the surface characteristics and topography of the watershed (USEPA, 2000). A decrease in the value of UZSN increases the surface runoff and vice versa. The parameter was calibrated to a value of 0.5 for the whole watershed. This is due to the uniformly distributed nature of the clay-loam soil all over the study area which is a soil that supports high surface retention of water suggesting a high potential for runoff generation. Details of calibration is shown in table 8 in appendix A.After calibration and validation, the calibrated values of the model were maintained and the land use swapped. Each land use scenario for the years considered for the study was used to generate a UCI file and simulation was done. The HSPFEXP+ program was then used to generate the water budget for each simulated year.

In order to properly represent the water balance of the watershed the model calculated the potential and actual Evapotranspiration. The model generates the potential Evapotranspiration using the Hamon method (Diaz et al., 2011). After the potential evaporation is generated, the model calculates the actual Evapotranspiration as a function of five layers of moisture storage, after meeting the Evapotranspiration demand. These layers are the interception storage, upper and lower zone storages, base flow and active groundwater storage.

3.6 Analysis of Water Balance

From the results of the water balance for the watershed estimated by the model (Table 6) it was seen that firstly, streamflow discharge accounted for an average of 93.15% of the total water losses in the watershed for the years 1991 to 2020 respectively giving an indication that a large percentage of water influx from rainfall ends up as overland flow. Secondly, it was seen that the ratio of interflow and base flow to overland flow was calculated to an average of 0.27 and 0.038 for the years 1991 to 2020 respectively, meaning that overland flow is the main mechanism of direct runoff in the watershed. This was attributed to the high slope and undulating nature of the terrain in the area and the nature of the soil in the watershed which had the value for infiltration capacity as an average of 0.1mm/hr.

Also, on the average only 5.8% of the total precipitation returned back to the atmosphere through Evapotranspiration. The larger portion of the water influx is returned back to the stream due to the climatic and vegetative peculiarities of the study area, coupled with the sloping terrain.

Furthermore, after the classification of the land use scenarios, corresponding reductions in the total percentage of water bodies was noticed, before and after the construction of the dam. This can be attributed to the large increase in agricultural activities in the watershed, which has led to constant withdrawals of the surface water for irrigation purposes.

Generally, increases in percentage of water balance components was observed in rainfall influx, stream discharge and slightly in actual Evapotranspiration with values of 37.4%, 40% and 16.4% respectively. On the other hand, non-significant changes were observed in deep water losses through the aquifer (0.1% of total rainfall) and storage within the watershed (0.85% of total rainfall)

Table 5: values for calibrated parameters for upper Gurara watershed

Parameter Description(unit)	DEFINITION OF TERMS	WATER BODIES	BARE LAND	FORE ST	AGRICULTU RAL	BUILT-UP
AGWRC	Base ground water recession	0.96	0.96	0.991	0.99	0.96
AGWETP	Fraction of remaining ET from Ground water	0.05	0.038	0.038	0.038	0.038
BASETP	Fraction of remaining ET from Base flow	0.05	0.01	0.01	0.01	0.01
CEPSC(mm)	Interception storage capacity	0.4	0.1	0.46	0.44	0.45
DEEPER	Fraction of Groundwater inflow from deep recharge	0.029	0.01	0.034	0.033	0.01
INFILT (mm/hr)	Index of infiltration	0.02	0.01	0.02	0.02	0.01
INTFW	Interflow inflow parameter	2	2	2	2	2
IRC	Interflow recession parameter	0.8	0.8	0.8	0.8	0.8
KVARY	Variable groundwater recession	0	0	0	0	0
LZETP	Lower zone Evapotranspiration parameter	0.52	0.1	0.49	0.48	0.2
LZSN	Lower zone nominal moisture storage	1.8	1.8	1.9	1.9	1.8
NSUR	Manning's roughness for overland flow	0.4	0.25	0.4	0.2	0.1
UZSN	Upper zone nominal moisture storage	0.5	0.5	0.5	0.5	0.5

Table 6: Average annual Water balance for upper Gurara watershed (Simulation period 1st January 2002 to 31st December 2009)

Element	CONSTITUENT(MM^{-year} X 10^5)				
		1991	**2001**	**2013**	**2020**
Rainfall		124	84	151	171
Runoff		115.5	76.1	143.3	161.7
	Overland	85.4	55.9	112.4	126.1
	Interflow	26.6	17.5	27.6	31.6
	Base flow	3.6	2.7	3.4	3.9
EvapoTRANSPIRATION LOSSES	Interception	3.5	3.6	4.2	4.6
	Upper Zone	1.4	1.4	1.2	1.6
	Lower Zone	1.79	1.73	1.67	1.54
	Ground Water	0.037	0.052	0.12	0.068
	Base flow	0.12	0.13	0.15	0.16
ACTUAL EVAPOTRANSPIRATION		6.8	6.9	7.4	7.9
Deep Groundwater		0.13	0.098	0.12	0.15
STORAGE		1.84	5.50	0.90	1.07

3.7 Mann and Kendall Analysis of Climatic Trends:

The climatic parameters selected for analysis were the Annual maximum, minimum and average temperatures, the total annual precipitation and the average monthly trends for temperature and precipitation. The Mann and Kendall Statistical test was used to analyze the thirty years trend in the selected variables.

The result (table 7) showed increasing trend annually for all tested parameters. The average, maximum and minimum temperatures for the study period were recorded as 24.51ºc, 39.99ºc and 23.14ºc respectively with p

values of 0.00069, 0.0056 and 0.0091. The precipitation in the study area also showed an annual significant increasing trend during the study period with p value of 0.0027.

Table 7: Results for Mann and Kendall test for Annual trend of climatic Variables

Variable	S	Variance(s)	P-Value	Z-value	Significance level	Hypothesis
Taverage	191	3141	0.00069	3.39	0.05	Ho rejected
Tmax	156	3140	0.0056	2.76	0.05	Ho rejected
Tmin	147	3139	0.0091	2.60	0.05	Ho rejected
Ptotal	169	3141	0.0027	2.99	0.05	Ho rejected

Where S= Mann Kendall statistics value

3.8 LULC vs. Climate Changes:

After completing all hydrological simulations, the results showed that the two subjects, Land us and Climate change, have gone a long way in shaping the watershed hydrology to what it is presently. However, in order to ascertain which of the two has a stronger influence on the watershed hydrology, seven scenarios were created combining the land use and climate scenarios, simulating and analyzing the hydrological parameters of each simulation. The scenarios created are shown in the Table 8 below.

Table 8: Scenario Combinations for climate and land use changes

Scenarios	**Climate data**	**Land use data**
S1	1991-2001	LULC1991
S2	2001-2013	LULC1991
S3	2013-2020	LULC1991
S4	1991-2001	LULC1991
S5	1991-2001	LULC2001
S6	1991-2001	LULC2013
S7	1991-2001	LULC2020

The baseline land use scenario was kept constant and combined with three climate scenarios, representing the past, recent and current study periods.

Seven hydrological parameters of the watershed were studied for each simulation to determine the changes that occurred in the watershed between the outlined study periods. The parameters studied were; surface runoff, interflow, base flow, groundwater, potential and actual Evapotranspiration and total volume of water in the outflow reach.

All analyzed parameters showed an increasing trend throughout the three study periods which corresponds to the increasing trend of rainfall and temperature as confirmed by the Mann and Kendall test discussed above. Although the deep and active ground water experienced slight reduction in the second scenario (2001-2013), they recorded high values in the final scenario (2013-2020).

As for the impact of land use change in the watershed, the same scenario combination technique was used. The baseline climate scenario of 1991 – 2001 was kept constant and simulated with varying land use scenarios, ranging from 2001 to 2020. Following the simulations, all studied parameters experienced minute changes excluding the total volume of water at the outflow reaches, which showed constant increases between 1991 and 2013 and slightly dropped by 21.81% in 2020.

In view of the above analysis, it can be seen that although the change in land use over the years resulted in some degree of alteration in the volume of water in the watershed, the variations in climatic elements had a more pronounced effect of the hydrological components of the watershed.

Table 9: Hydrology of Gurara watershed under varied climate scenarios

Element	1991-2001	2001-2013	2013-2020
Rainfall	436.6	443.52	624.82
Surface	216.809	223.905	373.917
Interflow	148.713	146.797	174.334
Baseflow	24.371	24.164	26.687
Total	389.893	395.094	574.93
deep groundwater	0.757	0.751	0.836
active groundwater	25.8843	25.798	28.58
potential evaporatranspiration	54.46	57.708	57.724
Actual evapotranspiration	46.23	37.766	49.061
total ouutflow	1595400	1617100	2342400

Table 10: Hydrology of Gurara watershed under varied LULC scenarios

Element	1991	2001	2013	2020
Rainfall	436.6	436.6	436.6	436.6
Surface	216.809	216.995	285.756	285.944
Interflow	148.713	148.7	86.12	81.21
Base-flow	24.371	24.371	21.737	24.372
Total	389.893	389.966	393.606	393.622
deep groundwater	0.757	0.752	0.67	0.61
active groundwater	25.884	25.881	23.359	23.347
potential evapotranspiration	54.46	54.46	54.46	54.46
interception	25.257	27.2	29.638	33.197
Upper-zone evaporation	9.406	9.406	5.649	9.406
Lower-zone evaporation	10.289	10.31	10.338	10.342
groundwater evaporation	0.47	0.49	0.634	0.635
baseflow evaporation	0.807	0.807	0.813	0.807

3.9 Projected Land Use Scenario

Following the analysis done on the trend of land use change and its possible influence on the watershed hydrology, a future land use scenario was generated to further visualize the possible future changes and investigate the extent to which it alters the hydrological cycle.

Generation if the future land use scenario was facilitated by the Terraset IDRISI software utilizing the Cellular Automata Markov and Markov machine learning algorithms, which uses two historical land use scenarios to generate a future scenario. Historical scenarios of 2013 and 2020 were used to generate a land use scenario for 2030 and various transitions in all land use categories were observed.

On comparing the baseline and predicted land use scenarios it was observed that large increases in agricultural activities and built up areas are expected. These two categories recorded increases from a total area of 434 km2 to 456 km2 and 68 km2 to 183 km2 respectively for a period of ten years. Increases in these categories have significant implications on the watershed and its inhabitants because an increase in agricultural activities translates to an increase in water demand while an increase in built up areas, coupled with the soil type and sloping nature of the watershed translates to reduction in the total amount of infiltrating water, increase in surface runoff and consequently increase in the amount of flood occurrences if measures are not taken to properly attenuate and drain off the amount of surface runoff. Forest, bare land and outcrop land use categories were predicted to decrease from 146 km^2 to 71 km^2, 91 km^2 to 67 km^2 and 22 km^2 to 17 km^2 respectively. Reductions in these land use categories are as a result of consequent expansions in built up areas and agricultural areas.

Table 11: Predicted Land Use Scenario

LAND USE CATEGORY	2020 OBSERVED (km^2)	2020 PREDICTED (km^2)	2030 PREDICTED (km^2)
AGRICULTURAL	434	435	456
FOREST	91	66	67
BUILT UP	68	66	183
OUTCROP	22	25	17
WATER/WETLANDS	59	44	26
BARE LANDS	146	184	71

3.10 Impact of Projected Land Use Scenario

Following the prediction of the land use losses and gains, four scenarios were created and simulated to determine the impact of predicted land use on the watershed.Seven hydrological parameters were studied and compared to determine the degree to which the predicted land use change would affect the watershed. The parameters studied were surface runoff, interflow, base flow, groundwater, potential Evapotranspiration and total flow at the outlet of the watershed.

After all simulations were completed, the two scenario combinations were compared significant changes were noticed in the watershed hydrology. Increases were observed in surface runoff, base flow, deep and active groundwater and total outflow of 8.05%, 9.75%, 13.53%, 7.29% and 3.92% respectively while decreases occurred in interflow and Evapotranspiration by 32.13% and 0.44% respectively.

The table below shows a summary of the percentage of changes that occurred between the baseline scenario and the predicted scenario.

Table 12: Average hydrological changes between 2020 and 2030 in the upper Gurara Watershed

Hydrologic parameter	2020	2030	percentage change
Surface	126.1	136.2	8.05
Interflow	31.6	21.4	-32.13
Base flow	3.99	4.39	9.75
Deep Groundwater	0.15	0.17	13.53
Active Groundwater	4.8	5.15	7.29
Actual Evapotranspiration	7.93	7.89	-0.5
Total Outflow	2634800	2,738,7.8000	3.92

On comparing the two scenarios, it can be deduced that the major increase expected would occur in the amount of water on the surface and at the watershed outlets. The major reason attributable to the increase in surface flow is the increase in urban areas. This is because an expansion in urban areas automatically translates to an increase in impervious areas, rise in population and thereby an increase in bush felling/ burning and increase in agricultural activities etc. all of which constitute alteration of the natural make-up of the environment.

3.11 Simulation of Best Management Practices

Considering the catchment characteristics in terms of soil, slope and its flooding susceptibility, based on findings made in the previous sections, best management practices in form of detention channels were designed and simulated in HSPF. This was done to help attenuate the volume and intensity of possible floods that would occur in the watershed. This was done by generating three scenarios wherein trapezoidal storage channels were designed and placed in two major tributaries leading to the catchment outlet. The watershed consists of eleven reaches with reaches seven and nine being the major reaches carrying water to the catchment outlet located at reach 11.

The best suited channel was selected and used in simulation following a calibration process that involved iterating values for the channel geometry. The properties of the channel iterated were the channel length, manning's roughness value, Longitudinal slope, height increment, maximum depth, top width and channel slope. Table (4.15) shows the properties of the channel used in both scenarios for flood attenuation.

Table 13: Channel Properties

S/N	Channel properties	Value(m)
1	Length	855
2	Manning's Roughness coefficient	0.025
3	Longitudinal slope	0.00771
4	Height increment	0.5
5	Maximum depth	4
	Top width	75
6	Side slope	0.04236
7	Weir crest length	0.1
8	Weir Invert height above channel bottom	2
9	Weir discharge coefficient	0.6

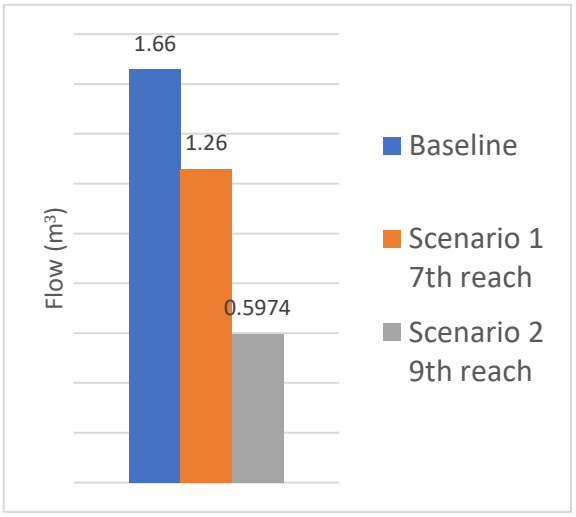


Table 13: BMP simulation

For the first scenario, the channel was placed in the seventh reach which is one of the main reaches which water passes through to the outlet. After simulation, the total runoff at the watershed outlet was reduced from 1.66MCM to 1.26MCM amounting to a total reduction of 23.95%. As for the second scenario, the channel was placed on reach nine which is another major contributing tributary to the watershed outlet. Following the simulation, the runoff at the outlet reduced from 1.66MCM to 599,740 m^3 amounting to a total reduction of 64.08% of the total runoff. In the final scenario, the channel was placed on both reaches seven and nine which gave the highest percentage reduction of 90.79%, attenuating the total runoff at the outlet reach from 1.66MCM to 153,850 m^3.

4.0 CONCLUSION AND RECOMMENDATION

The hydrology of the Gurara watershed was modeled using the HSPF model and used to analyze the impact of land use and climate change on the watershed. To achieve this objective, various processes were undergone build a standard model structure capable of running simulations and making tangible inferences. Four land use scenarios were created using the supervised classification. The classified land use scenarios were combined with the already delineated and characterized watershed to generate our base model for subsequent scenarios. The model was calibrated and validated and sensitivity analysis was done to know the most important parameters that affect the hydrology of the watershed.

From the results of the modeling it can be deduced that:

Increase in Agricultural and built-up areas are the main contributors to hydrological alteration from the Land use changes perspective, while temperature is the main driver of hydrological change from the climate perspective. However, the climate change had a stronger influence in shaping the hydrology of the watershed. This fact was also proven from the combined scenario analysis carried out in section 4.9 with climate change resulting in 72.46% increase between 1992 and 2020 while the change in land use resulted in a slight increase in surface runoff of 31.80% in 2013 with similar observations made in other hydrological parameters. There is great potential for flooding in the future from observation of the 2030 scenario, if proper measures on better urban development planning and watershed management are not taken. The major watershed parameters that

need to be constantly monitored are the index of infiltration, lower zone evapotranspiration, interception, fraction of groundwater flow from deep storage and base groundwater recession as they exhibited highest sensitivity from the sensitivity analysis.[DA1]

Finally the results further prove that utilizing hydrological modeling in watershed planning and management would go a long way in ensuring efficient and effective watershed operations as well as promoting safety and sustainability of the watershed

The following are recommended:

More efforts should be channeled towards constant watershed planning and management, incorporation of remote sensing and watershed modelling in planning activities and constant updating of land use maps to monitor the progression of change.

Measures should be taken to eliminate un-controlled and indiscriminate deforestation while encouraging afforestation programs in order to preserve the state of the watershed and its resources.

Unplanned erection of building and impervious structures should be checked by design and implementation of urban expansion plans such that channels of water flow won't be obstructed or wrongly channeled.

Flood management practices like construction of detention ponds at strategic locations should be implemented to reduce the impact of sudden flash floods

REFRENCES

Anad, A. (2017). Image classification.

Bello, A.-A. D., Haniffah, M. R. M., Hashim, N. B., & Anuar, K. M. (2018). Estimation of Hydrological Changes in a Tropical Watershed Using Multi-Temporal Land-Use and Dynamic Modelling. *Jurnal Teknologi*, *80*(3). doi:10.11113/jt.v80.11179

Brown, A. E., Zhang, L., McMahon, T. A., Western, A. W., & Vertessy, R. A. (2005). A review of paired catchment studies for determining changes in water yield resultingfrom alterations in vegetation. *Journal of Hydrology,, Journal of Hydrology,* (1-4), 28-61.

Chen, Q., Chen, H., Wang, J., Zhao, Y., Chen, J., & Xu, C. (2019). impacts of Climate Change and Land-Use Change on Hydrological Extremes in the Jinsha River Basin. *Water, 11*, 1398. doi:10.3390/w11071398

Congaltol, R. (1988). A Comparison of Sampling Schemes Used in Generating Error Matrices for Assessing the Accuracy of Maps Generated from Remotely Sensed Data. *PHOTOGRAMMETRIC ENGINEERING AND REMOTE SENSING, 54*(5), 593.

Diaz Ramirez, McAnally, & Martin. (2011). ANALYSIS OF HYDROLOGICAL PROCESSES APPLYING THE HSPF MODEL IN SELECTED WATERSHEDS IN ALABAMA, MISSISSIPPI, AND PUERTO RICO. *American Society of Agricultural and Biological Engineers, 27*(6), 937-955.

Diaz, R. J. N., McAnally, W. H., & Martin, J. L. (2011). ANALYSIS OF HYDROLOGICAL PROCESSES APPLYING THE HSPF MODEL IN SELECTED WATERSHEDS IN ALABAMA, MISSISSIPPI, AND PUERTO RICO. *American Society of Agricultural and Biological Engineers, 27*(6), 937-955.

Eastman, J. R. (2012). *Idrise Selva MAnual*. clarks university: carks lab.

Edsel, B. D., Janey, V. C., Eugene, J. L., Jessica, R. P., James, P. D. a., & Mark, D. A. (2011). Watershed Modeling and its Applications: A State-of-the-Art Review. *The Open Hydrology Journal,, 5*, 26.

Ibrahim, H. M., & Isiguzo, E. A. (2009). Flood frequency analysis of Gurara River catchment at Jere, Kaduna State, Nigeria. *Scientific Research and Essay, 4*(6), 10.

Jimoh, & Ayodeji, O. S. (2003). Impact of the Gurara River (Nigeria) interbasin water transfer scheme on the Kaduna River at the Shiroro Dam. *Water Resources Systems, Hydrological Risk Management and Development*.

Jimoh, O. D., & Sule, B. (1992). *Hydrological analysis of waterbalance in the Gurara riverbasin catchment*. Paper presented at the international Confrence on Hydraulic Engineering software Hydrosoft 92, Universidad politencia, Valencia.

Karmeshu, N. (2012). Trend Detection in Annual Temperature & Precipitation using the Mann Kendall Test – A Case Study to Assess Climate Change on Select States in the Northeastern United States. *Master of Environmental Studies Capstone Projects, 8*(2012).

Lambin, E. F., Turner, B. L., Geist, H. J., Agbola, S. B., Angelsen, A., Bruce, J. W., . . . Folke, C. (2001). The causes of land-use and land-cover change: moving beyond the myths. *Global environmental change, 11*, 261-269.

Musa Dalil, Audu Philemon Mairabo, Abdul Husaini, Usman Muhammad Babangida, Abubakar, A., & (2013). Impact of Gurara Dam on Land Cover in the Surrounding Communities of Kaduna State, Nigeria. *A Journal Of Environment and Earth Science, 5*(16).

OGUTVEREN, U. B. (2004). Hydrological modeling of Seydi Suyu watershed (Turkey) with HSPF. J Hydrol. *ResearchGate*. doi:10.1016/j.jhydrol.2003.09.002

Oluwaseye, A., & Onemayin, J. (2013). Flood modelling of upper Gurara watershed using remote sensing data and the geospatial streamflow model. *WIT Transactions on Ecology and The Environment, 172*. doi:doi:10.2495/RBM130041

Oseni, T. A., & Bloodless, D. (2017). Hydrological Characterization of a Watershed for Streamflow Prediction. *International Journal of Environmental and Ecological Engineering, 11*(5), 2017.

Singh, J., Knapp, H. V., Arnold, J. G., & Demissie, M. (2005). HYDROLOGICAL MODELING OF THE IROQUOIS RIVER WATERSHED USING HSPF AND SWAT1. *JOURNAL OF THE AMERICAN WATER RESOURCES ASSOCIATION*, 343-361.

SINGH, V. P. (2006). *WATERSHED MODELS*. 6000 Broken Sound Parkway NW, Suite 300: Taylor & Francis Group.

USEPA. (2000). *Estimating Hydrology and Hydraulic Parameters for HSPF*

Yi, H., Jinxi, S., Yiyi, H., Xiang, T., & Yan, Z. (2019). Impacts of different weather conditions and landuse change on runoff variations in the Beiluo River Watershed, China. *Sustainable Cities and Society, 50*(101674). doi:https://doi.org/10.1016/j.scs.2019.101674

EXPERIMENTAL ANALYSIS OF CIRCULAR, SQUARE AND RECTANGULAR NOTCHES ON THE TENSILE STRENGTH OF COMPOSITE MATERIALS

Saeed Nawaz

Department of design and manufacturing engineering, National University of Sciences and Technology (NUST) Islamabad, Pakistan

Naveed Ahmad Khan

Department of mechanical engineering, HITEC University, Taxila Rawalpindi Pakistan

Muhammad Yasir Khan

Department of mechanical technology, Government College of technology, Taxila Pakistan

ABSTRACT

Fibre Reinforced Polymer (FRP) Composite Laminates are being preferred in present products due to their high strength-to-weight ratio. Further, due to the functional requirements and additional weight reduction, notches and/or holes are made in the FRP composite laminates. These notches cause the strength reduction of FRP composite laminates commonly known as the "Hole Size Effect". In this study, an experimental investigation of the Notch Size Effect (i.e. the Hole Size Effect) for the case of carbon/epoxy FRP composite laminates is presented. Specimens with different notch shapes and sizes are tested in tension under quasi-static loading and the strength reduction for the dissimilar shapes and sizes is determined for specimens stacked with changed ply orientations. Solvent impregnation method is used for fabrication of the specimens using sports grade composite prepregs. Experimental results obtained from Universal Testing Machine are found in close agreement with the past literature.

Keywords: Fibre Reinforced Polymer (FRP), Hole Size Effect, Composites, UTM

INTRODUCTION

A composite material is made up of two or more distinct materials that have dissimilar physical and chemical properties than those possessed by the individual constituent materials. The engineered man-made composite materials include plywood, which is made up of wooden sticks glued together at different angles. Similarly, in FRP composite laminates, the wooden sticks are replaced with the fibers and matrix arrangement with the glue. One of the most dominant properties of FRP composite materials is its high strength-to-weight ratio which allows it to be used in high-end applications [1]. The isotropic materials like metals, ceramics, and polymers offer identical properties in all directions, whereas the FRP composite laminate materials exhibit anisotropic behavior. This means that the FRP composite laminate materials have directional properties which depend on the way it has been fabricated/manufactured. Consequently, the properties of the composite materials are highly in the hands of the design engineers, hence, composite presents one of the emerging fields of today because of its versatility.

A composite material consists of minimum with two constituent materials; a fiber as the reinforcement which determines the strength and stiffness of the material joined together by the matrix or resin which binds this fiber together and helps in distributing the load among the neighboring fibers. An imaginary overview of these constituent materials within the composite material is graphically presented in Figure 1.

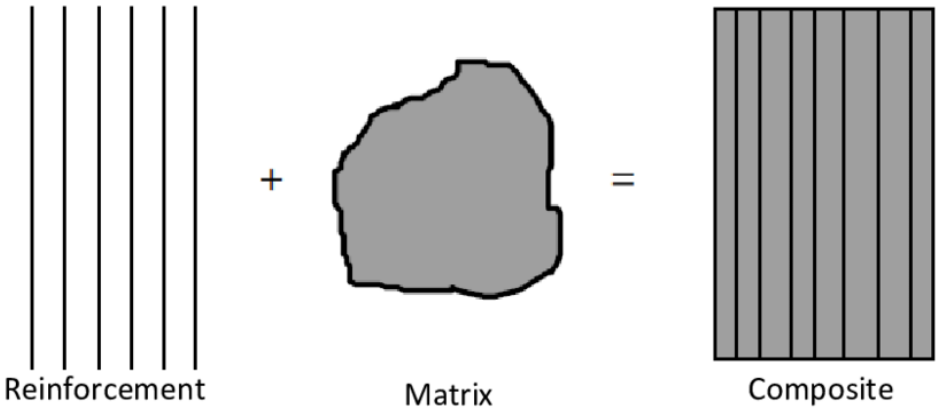


Figure 1. Reinforcement and Matrix make up the composite material

Practical applications often require notches in structural members likewise these notches are also needed structural members made of FRP composite laminates. The presence of these notches shown in Figure 2 may be attributed to a number of reasons:

a. Mechanical joining of parts like riveting.

b. Laying of cables.

c. For access to view like windows in aircraft [2].

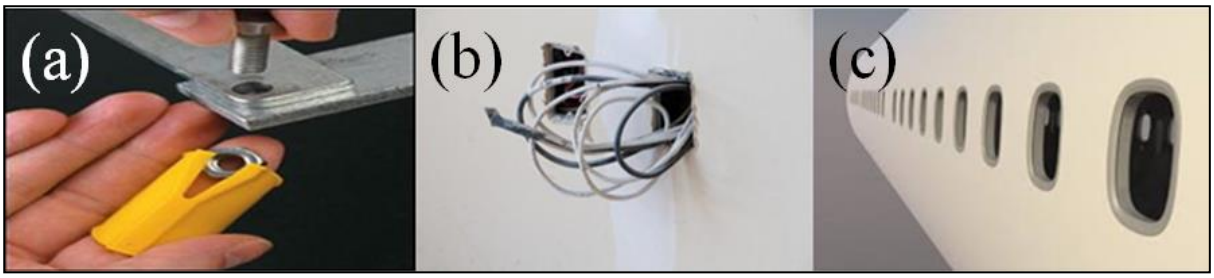


Figure 2. (a) Circular notch for riveting, (b) Square notch for laying of cables (c) Rectangular notch for access to view

The structural members embedded with notches significant drop of strength in comparison with the structural members without notches. In conventional materials like metals, the estimation of decrease in strength caused by the notch is very easy which is generally associated with the geometry and loading parameter of the structural member. However, for the case of FRP composite materials besides geometry and loading parameter, the strength is further influenced by ply orientation and the laminate stacking sequence (LSS). Therefore, the estimation of strength reduction caused by the notches presents a very complex behavior in FRP composite laminates. This study presents the Notch Size Effect (NSE) using various shapes of notches such as circular shape, square shape, and rectangular shape for the case of Carbon Fibre Reinforced Polymer (CFRP).

History of size effects dates back to the 1500s to the era of Leonardo Di Vinci. The size effect is, when by increasing the volume or size of test samples its ability to withstand force or pressure is affected under similar conditions. When considering failures in material size effects are very important. From a practical point of view when organizing strength values, the size of the test specimens is considerably small. If they show a significant change in its strength when increasing its size then serious failure could occur if size effect is not taken into consideration [3]. Therefore it is very important for a designer to study the effect of hole size from all aspects. Especially in fields like aerospace where any small damage can lead to high payoffs and loss of human life and that is why 27% of an average aircraft cost is exhausted on its safety [4].

There is a wide range of application of carbon fiber reinforced polymer especially in aerospace as mentioned earlier. In aircraft, it is an essential part of the main body, a tail assembly which provides stabilization and wing box. Seemingly interlaminar strength is highly required in places which are likable to impact damage. One way to improve interlaminar strength is by using textile yarn to wrap fibers before the curing process. As a result of experimentation transverse stitches revealed a considerable decrease in tensile strength [5]. Conventionally strength decreases with the increase in notch size but why it so? To explain this behavior various efforts have been made. It is believed that when fiber breaks, it transmits its stress to its neighboring fibers. This condition is called local load sharing condition (LLS). As the size of the composite material increases, the probability area where the initial fiber initiates to break under load also increases. This initial break affects the nearby intact fibers and in the end, result in ultimate failure [6].

Xiaodong Xu and Michael R. Wisnom compared sharp center-notched tensile tests with open hole tests. They used carbon/epoxy quasi-isotropic laminates to study size effects in notched [45/90/_45/0]4s at different dimensions. Both portrayed a similar trend in strength reduction for small sizes; however center-notched specimens had higher tensile strength than the open-hole specimens [7]. The Notch Size Effect, hence, should be brought into consideration while designing structures containing notches as they define the limitation of the stress which it can support during its utilization. Therefore, it becomes necessary to design and perform tensile tests on notched composite laminates so that the designer can define the appropriate limiting stresses while designing the components and provide a secure and productive design for structures [8].

The tensile strength of quasi-isotropic composite laminates was subjected to experimentation and testing only with changing hole size, laminate thickness and ply thickness, with respect to the open hole [9]. In addition to this, there are many minor factors which need to be considered when combined can lead to a critical defect. These defects usually arise at the microscopic level. These may include resin rich cluster, fibers not properly embedded with resin or misaligned fibers. A considerable decrease is observed in the strength because of change in the volume between the gauges. Also at the free edges of the composite high interlaminar stresses may appear which can also lead to premature failure [3].

Therefore it is very important to compare the results obtained via testing and experimentation to be compared with results obtained by numerical an analytical means [10]. Further, even though a few studies with nonconventional notches have been reported but test data for notched specimens with nonconventional geometries is severely limited.

MATERIALS AND METHODS

Engineering Analysis Approach

Generally, the engineering solutions for the investigation may be obtained by using analytical, experimental or numerical approach. In this study, the experimental approach has been used for the investigation of Notch Size Effect. Experimental analysis has been performed on newly developed CFRP composite laminates using three different laminate stacking sequences as depicted in Table 1.

Table 1 Laminate stacking sequence

Sr. No	Laminate Configuration	Stacking Sequence
1	Unidirectional (UD)	$[0/0/0/0]_{2s}$
2	Cross-ply (CP)	$[0/90/0/90]_{2s}$
3	Angle-ply (AP)	$[45/-45/45/-45]_{2s}$

Each laminate configuration is evaluated by using four shapes of the notches as shown in Figure 3.

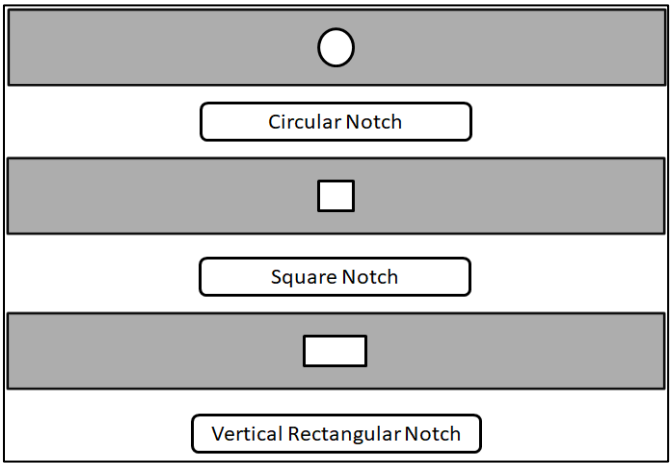
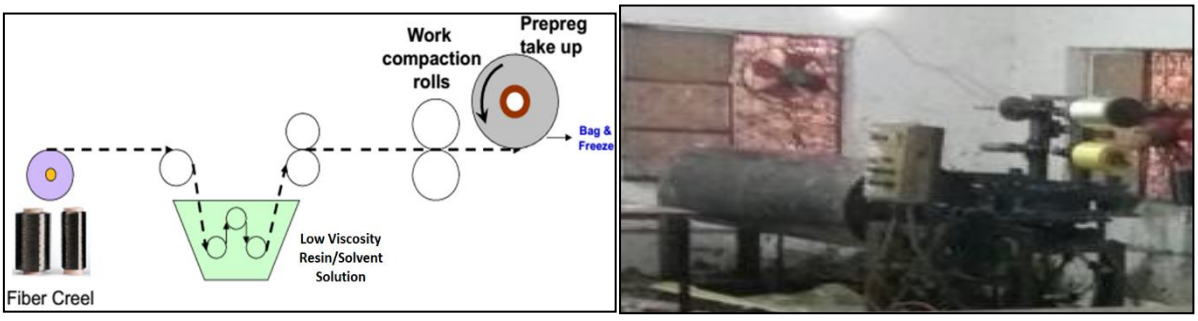


Figure 3. Laminate stacking configurations

Prepreg Manufacturing

Composite laminates are developed for the experimental investigation by originally manufacturing of prepregs (preimpregnated) in a semi-cured form using two types of fibers such as carbon fibers and glass fibers as the reinforcement materials. Subsequently, the composite laminates are fabricated by stacking the newly manufactured prepregs as per the required laminate configurations for the study.

In this study, the manufacturing of prepregs are done by using solvent impregnation method [11]. In solvent impregnation method, the long (continuous) fibers are thoroughly dipped into the resin container to ensure that the fibers are completely saturated by the resin as demonstrated in the pictorial view in Figure 4 (a) pictorial view and (b) equipment of the solvent impregnation method. The carbon fibers and glass fibers as reinforcements for the prepregs manufacturing as constituent materials are (TC 36S – 12K of Tairyfil) [12] with the Epoxy as Matrix (ESP – 135 A / B of EPORITE) [13].



a. Pictorial view b. Equipment

Figure 4. Solvent impregnation method

The long fibers are appropriately directed on to the take-up spool usually termed as prepreg drum (take-up spool). Thereafter, the newly manufactured prepregs are kept in the freezer in -18^0C temperature till the fabrication of fabrication of composite laminates.

Laminate Fabrication

Composite laminates are fabricated by laying the prepregs one top of each other as per the laminate stacking configuration is given in Figure 5 in the preceding para the stacking of prepregs is manually carried out. The same epoxy resin is used between the adjacent plies as in the prepregs manufacturing to ensure compatible bonding of the composite laminate. The curing of the composite laminate is carried out by using specially developed platent molds in an oven. The composite laminates are made with the dimensions 310 mm, 120 mm and 1 mm in length, width and thickness respectively. The curing cycle is performed by maintaining the oven temperature of 150^0 C for a period of 30 minutes.

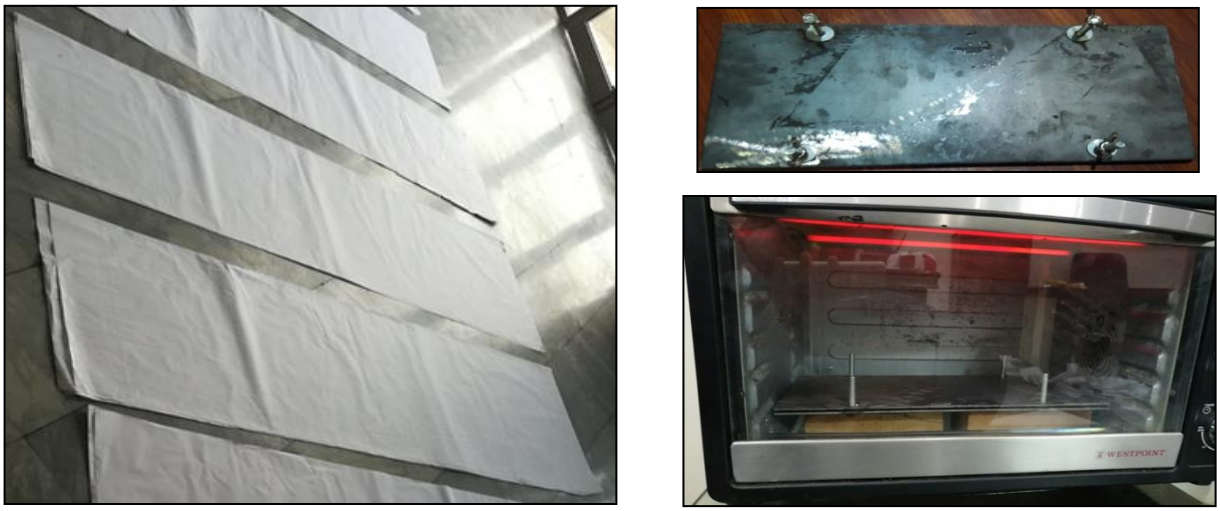


Figure 5. Staking and curing of composite laminate

Specimen Preparation

The tensile specimens are prepared by using previously fabricated composite laminates. Slitting method is carried out using Universal Milling Machine 2.5 mm slitting saw. The dimensions of the tensile specimens have strictly been followed as per ASTM Standard (Standard Test Method for Open-hole Tensile Strength of Polymer Matrix Composite Laminates) [14]. The tensile specimens dimensions are 300 mm in length (including gauge length of 200), 36 mm in width with a thickness of 1 mm having a notch at central of the specimen as shown in Figure 6. The notches are prepared initially by using computerized numerically controlled (CNC) milling machine by carbide drill bits and then by using the hand file.

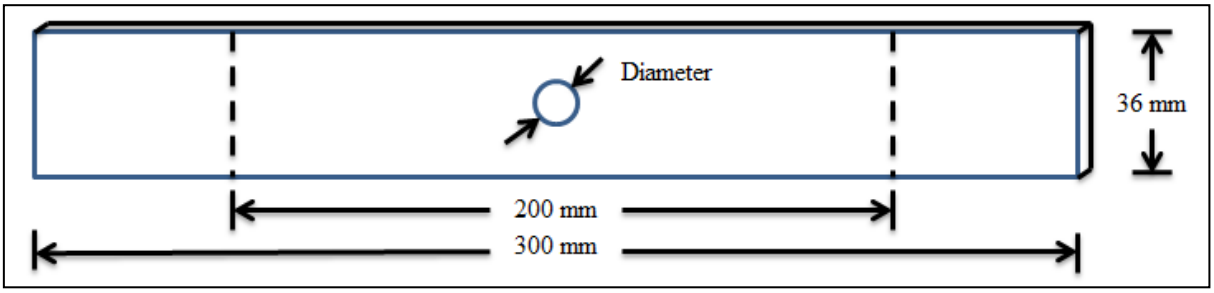


Figure 6. Tensile specimen

The tensile testing is carried out as per the ASTM D3039 Standard (standard test method for tensile properties of polymer matrix composite materials) [15] on the Universal Testing Machine (WDW 100E). The loading of the tensile specimens has been done with a displacement rate of 2 mm/min.

RESULTS AND DISCUSSION

This section deals with the experimental results of CFRP composite materials containing notches subjected to the tensile loading. The results show the Notch Size Effect of CFRP composite laminate stacked in various laminate configurations i.e. UD, CP and AP configurations. Three different shapes of notches have been used for the investigation of Notch Size Effect i.e. circular shape, square shape and vertical rectangular shape for all the laminate configurations.

Unidirectional (UI) Configuration

a. Circular notch

Results of the dissimilar notch sizes (circular shape) are presented for the investigation of the notch size effect in this section. The summary of the experimental results of three dissimilar notches is tabulated in Table 2, where CN denotes the circular notch. The Notch Size Effect for the case of circular notches is also graphically presented in Figure 7.

Table 2 Experimental results for circular shape notches

Specimen Ref	Hole diameter (mm)	Specimen width	d/w ratio	Strength (MPa)
UD-CN1	3	36	0.083	497.5
UD-CN2	6	36	0.167	414.1
UD-CN3	9	36	0.250	325.4

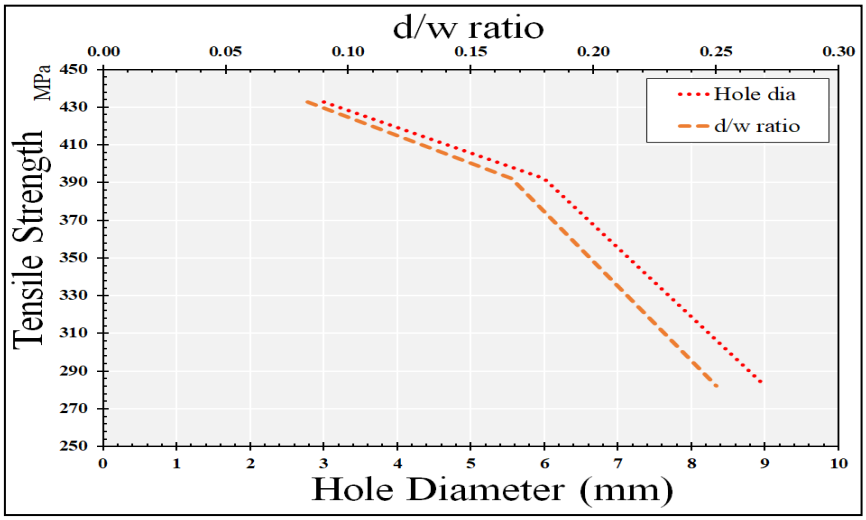


Figure 7. Strength reduction for circular shape notches

It can be observed from the results that with the increase of notch size (circular hole) or diameter to width ration (d/w ratio), the tensile strength of the CFRP composite laminate of UD configuration decreases. Further, by an increase in notch size of 3mm to its preceding dimension, the overall reduction in tensile strength occurs of 23.7 percent.

b. Square notch

Results of dissimilar notch sizes (square shape) made up of CFRP composites of UD configuration are presented and analyzed in this section. The summary of the experimental results is tabulated in Table 3, where SN denotes the square notch.

Table 3 Experimental results for square shape notches				
Specimen Ref	Side length (mm)	Specimen width	l/w ratio	Strength (MPa)
UD-SN1	3	36	0.083	442.66
UD-SN2	6	36	0.167	410.71
UD-SN3	9	36	0.250	313.10

It can be observed from the results that the tensile strength of the CFRP composite laminate decreases with the increase of notch size (square shape) or length to width ratio (l/w ratio). Additionally, by an increase in notch size of 3mm to its preceding value, the overall reduction in tensile strength occurs of 28 percent.

c. Vertical rectangular notch

Results for the case of dissimilar notch sizes (vertical rectangular shape) made up of CFRP composites of UD configuration are presented for the examination in this section. Vertical rectangular shape notch means the size of the notch with respect to the length of the specimen kept constant and change in dimension of the notch is done along the specimen width. The summary of the experimental results is tabulated in Table 4, where VRN denotes the vertical rectangular notch.

Table 4 Experimental results for vertical rectangular shape notches				
Specimen Ref	Vertical length (mm)	Specimen width	l/w ratio	Strength (MPa)
UD-VRN1	3	36	0.083	420.4
UD-VRN2	6	36	0.167	380.2
UD-VRN3	9	36	0.250	272.6

It can be observed from the results that the tensile strength of the CFRP composite laminate decreases with the increase of notch size (vertical rectangular shape) or l/w ratio. Additionally, by an increase in notch size of 3mm to its preceding dimension, the overall reduction in tensile strength is about 50 percent.

Cross Ply (CP) Configuration

a. Circular notch

Results of dissimilar notch different sizes (circular shape) made on CFRP composites of CP configuration are presented and analyzed in this section. The summary of the experimental results are tabulated in Table 5.

Table 5 Experimental results for circular shape notches				
Specimen Ref	Hole diameter (mm)	Specimen width	d/w ratio	Strength (MPa)
CP-CN1	3	36	0.083	258.7
CP-CN2	6	36	0.167	240.7
CP-CN3	9	36	0.250	220.2

It can be observed from the results that with the increase of notch size (circular hole) or d/w ratio the tensile strength of the CFRP composite laminate of CP configuration decreases. Further, by an increase in notch size of 3mm to its preceding dimension, the overall reduction in tensile strength occurs about 17 percent.

b. Square notch

Results of the dissimilar notch (square shape) size made on CFRP composites of CP configuration are presented and analyzed in this section. The summary of the experimental results is tabulated in Table 6.

Table 6 Experimental results for square shape notches				
Specimen Ref	Side length (mm)	Specimen width	l/w ratio	Strength (MPa)
CP-SN1	3	36	0.083	244.4
CP-SN2	6	36	0.167	227.4
CP-SN3	9	36	0.250	190.5

It can be observed from the results that the tensile strength of the CFRP composite laminate of CP configuration decreases with the increase of notch size (square shape) or l/w ratio. Additionally, by an increase in notch size of 3mm to its preceding dimension, the overall reduction in tensile strength occurs of 27 percent.

c. Vertical rectangular notch

Results of the dissimilar notch sizes (vertical rectangular shape) made up of CFRP composites of CP configuration are presented and examined in this section. Vertical rectangular notch means the size of the notch with respect to the specimen length is kept constant and increase in notch size done with respect to the specimen width. The summary of the experimental results are tabulated in Table 7.

Table 7 Experimental results for vertical rectangular shape notches				
Specimen Ref	Vertical length (mm)	Specimen width	l/w ratio	Strength (MPa)
CP-VRN1	3	36	0.083	420.4
CP-VRN2	6	36	0.167	380.2
CP-VRN3	9	36	0.250	272.6

It can be observed from the results that the tensile strength of the CFRP composite laminate of CP configuration decreases with the increase of notch size (vertical rectangular shape) or l/w ratio. Additionally, by an increase in notch size of 3mm to its preceding dimension, the overall reduction in tensile strength is about 30 percent.

Angle Ply (AP) Configuration

a. Circular notch

Results of dissimilar notch different sizes (circular shape) made on CFRP composites of AP configuration are presented and analyzed in this section. The summary of the experimental results are tabulated in Table 8.

Table 8 Experimental results for circular shape notches				
Specimen Ref	Hole diameter (mm)	Specimen width	d/w ratio	Strength (MPa)
AP-CN1	3	36	0.083	251.3
AP-CN2	6	36	0.167	187.0
AP-CN3	9	36	0.250	162.2

It can be observed from the results that with the increase of notch size (circular hole) or d/w ratio the tensile strength of the CFRP composite laminate of AP configuration decreases. Further, by an increase in notch size of 3mm to its preceding dimension, the overall reduction in tensile strength occurs about 49 percent.

b. Square notch

Results of the dissimilar size (square shape) notch made on CFRP composites of AP configuration are presented and analyzed in this section. The summary of the experimental results is tabulated in Table 9.

Table 9 Experimental results for square shape notches				
Specimen Ref	Side length (mm)	Specimen width	l/w ratio	Strength (MPa)
AP-SN1	3	36	0.083	223.2
AP-SN2	6	36	0.167	183.1
AP-SN3	9	36	0.250	156.7

It can be observed from the results that the tensile strength of the CFRP composite laminate of AP configuration decreases with the increase of notch size (square shape) or l/w ratio. Additionally, by an increase in notch size of 3mm to its preceding dimension, the overall reduction in tensile strength occurs of 39 percent.

c. Vertical rectangular notch

Results of the dissimilar notch sizes (vertical rectangular shape) made up of CFRP composites of AP configuration are presented and examined in this section. Vertical rectangular notch means the size of the notch with respect to the specimen length is kept constant and increase in notch size done with respect to the specimen width. The summary of the experimental results are tabulated in Table 10.

Table 10 Experimental results for vertical rectangular shape notches				
Specimen Ref	Vertical length (mm)	Specimen width	l/w ratio	Strength (MPa)
AP-VRN1	3	36	0.083	196.0
AP-VRN2	6	36	0.167	142.3
AP-VRN3	9	36	0.250	131.2

It can be observed from the results that the tensile strength of the CFRP composite laminate of AP configuration decreases with the increase of notch size (vertical rectangular shape) or l/w ratio. Additionally, by an increase in notch size of 3mm to its preceding dimension, the overall reduction in tensile strength is about 46 percent.

CONCLUSION

This research deals with the investigation of Notch Size Effect in FRP composite laminates under tensile loading generally known as the Hole Size Effect. In this study three different shapes of notches (circular, square and rectangular) has been considered for the analysis of Notch Size Effect. Further, the FRP composite laminate materials i.e. CFRP have been used. The outcome of the study are as below:

a. Plots presents the similar leaning behavior with the increase of size circular, square and rectangular notch for CFRP composite laminates under tensile loading.

b. For UD configuration, the CFRP composite laminate exhibit approximately 40 percent more tensile strength in comparison with square and rectangular notches

c. The FRP composite laminates with UD configuration possess significantly high strength with respect to the other laminate configurations like CP and AP.

d. The minimum tensile strength achieved for the case of AP laminate configuration.

e. The minimum tensile strength achieved for the case of vertical rectangular notches.

REFERENCES

[1] S. W. GAY, Daniel; HOA, S. V.; TSAI, *Composite Materials: Design and Applications. 1 ed. United States of America: CRC Press. 2002. 523 p*. 2002.

[2] A. A. Bouzgou, A. Tati, and A. Khechai, *Applied Mechanics, Behavior of Materials, and Engineering Systems*. 2017.

[3] M. R. Wisnom, "Size effects in the testing of fibre-composite materials," *Compos. Sci. Technol.*, 1999.

[4] S. S. Kessler, S. M. Spearing, M. J. Atalla, C. E. S. Cesnik, and C. Soutis, "Damage detection in composite materials using frequency response methods," *Compos. Part BEngineering*, vol. 33, no. 1, pp. 87–95, 2002.

[5] A. Yudhanto *et al.*, "Effect of stitching on plain and open-hole strength of CFRP laminates," *Compos. Part A Appl. Sci. Manuf.*, vol. 68, no. 3, pp. 2770–2778, 2013.

[6] T. Okabe and N. Takeda, "Size effect on tensile strength of unidirectional CFRP composites experiment and simulation," *Compos. Sci. Technol.*, vol. 62, no. 15, pp. 2053–2064, 2002.

[7] X. Xu, M. R. Wisnom, Y. Mahadik, and S. R. Hallett, "An experimental investigation into size effects in quasi-isotropic carbon/epoxy laminates with sharp and blunt notches," *Compos. Sci. Technol.*, vol. 100, pp. 220–227, 2014.

[8] G. H. Erçin, P. P. Camanho, J. Xavier, G. Catalanotti, S. Mahdi, and P. Linde, "Size effects on the tensile and compressive failure of notched composite laminates," *Compos. Struct.*, vol. 96, pp. 736–744, 2013.

[9] B. G. Green, M. R. Wisnom, and S. R. Hallett, "An experimental investigation into the tensile strength scaling of notched composites," *Compos. Part A Appl. Sci. Manuf.*, 2007.

[10] B. Y. Chen, T. E. Tay, P. M. Baiz, and S. T. Pinho, "Numerical analysis of size effects on open-hole tensile composite laminates," *Compos. Part A Appl. Sci. Manuf.*, 2013.

[11] "Summary y of Methods used to Manufacture PMCs Preliminary Manufacturing Considerations."

[12] Formosa Plastics Corporation, "Carbon fiber-TAIRYFIL Catalog." 2015.

[13] "EPORITE ESP-135 A / B," no. 11, p. 4529318.

[14] ASTM, "Standard Test Method for Open Hole Tensile Strength of Polymer Matrix Composite Laminates ," *ASTM Stand. D5766/D5766M-02*, 2002.

[15] S. T. Method, "Standard Test Method for Tensile Properties of Polymer Matrix Composite Materials 1," vol. 3.

PHYSICAL-CHEMICAL AND MECHANICAL PROPERTIES OF AMPELODESMOS MAURITANICUS NATURAL FIBERES

Mr. Abdessamed ATOUI

Laboratoire de Mécanique Appliquée des Nouveaux Matériaux (LMANM), 8 Mai 1945 Guelma University, Algeria., https://orcid.org/0000-0003-3516-565X

Prof. Dr. Abderrezak BEZAZI

Laboratoire de Mécanique Appliquée des Nouveaux Matériaux (LMANM), 8 Mai 1945 Guelma University, Algeria., https://orcid.org/0000-0002-4461-6689

Prof. Dr. Salah GUENFOUD

Laboratoire de Mécanique Appliquée des Nouveaux Matériaux (LMANM), 8 Mai 1945 Guelma University, Algeria., http://orcid.org/0000-0002-3856-4624

Prof. Dr. Abilo SILVA

Department of Eletromechanical Engineering, University of Beira Interior, 6201-001 Covilhã, Portugal., http://orcid.org/0000-0002-3856-4624

Prof. Dr. P.N.B. REIS

University of Coimbra, CEMMPRE, Department of Mechanical Engineering, Coimbra, Portugal., https://orcid.org/0000-0002-2100-7223

Prof. Dr. Fabrizio SCARPA

Bristol Composites Institute, University of Bristol, Bristol, UK., https://orcid.org/0000-0002-5470-4834

ABSTRACT

One of the surest ways to preserve our planet is to eliminate or reduce the use of fossil materials and develop new ones eco- friendly. Among these materials are bio-composites which have been constantly developing over the last decade, where researchers and industrials are permanently trying to find various fibrous plants that contain cellulose and can be used as reinforcement for bio-composites. These lignocellulosic fibres from plants have many advantages, such as biodegradability, low density, quite good mechanical properties and relatively low-cost price, which makes them competitive with synthetic fibres, especially glass ones. In this study, the plant of *Ampelodesmos mauritanicus* was considered, because it can be widely found in the regions of North Africa and also in the Mediterranean basin. The study of the chemical and mechanical properties of the fibres extracted from the plant is the subject of this work. The physical-chemical properties were studied using Fourier transform infrared spectroscopy (FTIR), and thermogravimetric analysis (TGA). In addition, the tensile mechanical properties of the extracted fibres were determined and in view of the significant dispersion in the results, a statistical study was carried out.

Keywords: Ampelodesmos Mauritanicus cellulose, FTIR, TGA, DSC.

IMAGE-TO-IMAGE TRANSLATION BASED FACE PHOTO DE-MESHING USING WASSERSTEIN GANs

Abdul Jabbar

College of Computer Science and Technology, Zhejiang University, Hangzhou 310027, China

Abstract

Most of the existing face photo de-meshing methods have accomplished promising results; there are certain quality problems with these methods like the inpainted regions would appear blurry and unpleasant boundaries become visible. Such artifacts cause generated face photos unreal. Therefore, we propose an effective image-to-image translation framework called Face De-meshing Using Wasserstein Generative Adversarial Networks (De-mesh WGANs). The De-mesh WGANs is a two-stage model: (i) binary mask generating module, is a three convolution layers-based encoder-decoder network architecture that automatically generates a binary mask for the meshed region, and (ii) face photo de-meshing module, is a GANs-based network that removes the mesh mask and synthesizes the meshed area. A combination of careful losses (pixel loss, perceptual loss, smooth loss, and adversarial loss) is used to reassure the better quality of the de-mesh face photos. To facilitate the training of the proposed model, we have designed a dataset of clean/corrupted photo pairs using the CelebA dataset. Qualitative and quantitative evaluations of the De-mesh WGANs on real-world corrupted face photo images show the better performance than the previously proposed face photo de-meshing models. Furthermore, we also offer the ablation study for performance assessment of the additional network *i.e.*, perceptual network.

Keywords: image recovery, autoencoder, wasserstein generative adversarial networks

PHYSICO-CHEMICAL AND THERMAL ANALYSIS OF WASHINGTONIA PALM LEAFLET FIBERS

Dr. Nasser BOUHEMAME

Kasdi Merbah Ouargla Unversity, ORCID. https://orcid.org/0000-0003-4483-0666

Prof. Dr. Abderrezak BEZAZI

Laboratoire de Mécanique Appliquée des Nouveaux Matériaux (LMANM), 8 Mai 1945 Guelma University, ORCID. https://orcid.org/0000-0002-4461-6689

Dr. Hocine KHELIFA

Larbi Tebessi Tebassa University

Prof. Dr. Kamal Eddinne AIADI

Kasdi Merbah Ouargla Unversity

Prof. Dr. Gilberto García DEL PINO

Department of Mechanical Engineering, State University of Amazonas-UEA, Manaus, Brazil

Prof. Dr. P.N.B. REIS

University of Coimbra, CEMMPRE, Department of Mechanical Engineering, Coimbra, Portugal, ORCID. https://orcid.org/0000-0001-5203-3670

Prof. Dr. Fabrizio SCARPA

Bristol Composites Institute, University of Bristol, Bristol, UK., ORCID. https://orcid.org/0000-0002-5470-4834

ABSTRACT

For ecological reasons, the attention of researchers and industrials is drawn to natural fibers for their distinctive characteristics such as biodegradability, lightness and their abundant availability in fibrous form at very competitive prices compared to synthetic fibers. For these reasons, modern industries are increasingly integrating natural fibers as reinforcement in composite materials in various applications. The aim of this work is to study the possibility of using washingtonia palm leaflet fibers as reinforcement in bio-composite materials. For this reason, it is necessary to determine the physico-chemical and thermal properties of these lignocellulosic fibers. Molecular and structural components were identified using the FTIR technique. Physicochemical properties were determined by thermogravimetric (TGA) and differential scanning calorimetry (DSC). The results obtained were compared with those of other fibers available in the literature. Leaflet fibers can occupy an important place in the field of bio-composite structures and can substitute glass fibers.

Key words: Palm washingtonia leaflet, physico-chemical properties, FTIR, TGA and DSC.

CITRIC ACID IS A CRUCIAL COMPOUND PLAYING AN ALLEVIATION ROLE OF SALT-INDUCEDOXIDATIVE STRESS IN MORINGA OLEIFERA

Nasraoui Hajaji Afefand Ammari youssef

Forest Ecology Laboratory, National Research Institute in Rural Engineering, Waterand Forestry, University of Carthage, Tunisia

Abstract

Our study was conducted in order to investigate the effects of citric acid as a component of response to abiotic stress on plant growth and oxidative stress state.For these reasons, germinated Moringa oleiferaseeds were transferred on sandy and vermicular (1/2 w/w) soiland watered by Hoaglandsolution. After two weeks, seedling were irrigated by Hoagland solution in absence of salt(Control), in presence of 10g/l or 10g/l NaCl +10mM Citric acid. Moringa oleifera growth is significantly affected by salinity(10g/l).

In fact, irrigation by saltwater causes diminution of shoot fresh weight and leaves morphological parameters, photosynthetic pigments and total soluble proteins contents. In another way, saltstress induced accumulation of totalfree amino acids,soluble sugar and proline tenors.When citric acidissuppliedinirrigation solution,a significant enhancementofleaves morphological parameters, shootgrowth, photosynthetic pigmentsandtotal soluble proteinscontents. The important content ofcitric acid in leaves tissues wasaccompanied by diminution of total free amino acids, soluble sugar and proline tenors. More that, undersalinity stresscondition, MDA (Malondialdehyde) and Hydrogen peroxide; H2O2 accumulationwas detected/reflectingthe imbalance situationinleaves tissuesand membrane damage causedby induced-oxydatif stress. Antioxidativeenzymes stimulation wasshowed through activation of superoxidase dismutase (SOD)and catalase (CAT). A dramaticdrop ofMDAand H2O2contents accompanied by notably loss of SOD and CAT activities wereshowed when citric acid is suppliedsimultaneously with salt in irrigation solution.

Based on our data, we can suggest that citric acid can play a crucial role in the improvement of Moringa oleiferaplants ability toresistagainstsalinity stress.

Keywords: citric acid, Oxidativestress, salinity, Moringa oleifera

INFLUENCE OF $BiSb_3Te_6$ SEMICONDUCTOR COMPOUND MECHANICAL AND ELECTRICAL STRENGTH OF LOW-DENSITY POLYETHYLENE

Alasgarova Durdana

Sumgayit State University, Physics of solids and semiconductors, Azerbaijan, Sumgayıt, 0000-0002-1905-8902

Eldar Gojayev

Azerbaijan Technical University, Enginiering Physics and electronica, Baki, Azerbaijan

Kamal Gulmammadov

Azerbaijan Technical University, Enginiering Physics and electronica, Baki, Azerbaijan, 0000-0003-0066-4088

Gafarova Dilara

Azerbaijan University of Architecture and Construction, Baku Azerbaijan, 0000-0002-8927-2592

Abstract

The paper presents the results of a study of the mechanical and electrical strengths of composites based on low-density polyethylene modified with a semiconductor compound BiSe3Te6. It was found that at low filler contents, the strengths of the composites increase. Polymer composites LDPE + BiSe3Te6 were obtained by hot pressing at the melting temperature of the polymer matrix under a pressure of 15 MPa for 10 minutes. The samples were made in the form of a film; the electrical and mechanical strengths of the studied compositions were investigated at room temperature. The electrical conductivity is observed by the residual current, which is established after 1-2 hours after the appearance of a voltage of 100 V on the composite. Measurements of the resistance of the samples were made using an E6-13A teraohmmeter in the range of 20-150^{0}C with linear heating at a rate of 3 deg/min. Samples for testing the force dependence of mechanical strength were cut out of the film with a special knife in the form of a double blade, the working part was 10 mm long and 3 mm wide. The decrease in mechanical and electrical strength is observed for all studied composites at high contents of semiconductor filler. This decrease can be explained by the fact that the polymer matrix plays a binding role, and the electrical and mechanical strengths of the polymer + semiconductor composition are determined mainly by the strength of the polymer soldering between conductor particles. Therefore, a decrease in the electrical and mechanical strength of the compositions with an increase in the volume content of the semiconductor is associated with a decrease in the proportion of the polymer layer between the semiconductor particles and the degree of interaction between the phases of the components of the compositions.

Key words: mechanical and electrical strengths, electrical conductivity, LDPE, $BiSe_3Te_6$

Introduction

The study of changes in the mechanical and electrical strengths of compositions based on low-density polyethylene under the action of mechanical and electrical stresses is of great scientific and practical interest, since during the operation of various devices with elements of polymer compositions, they are exposed to external factors [1-3]. The strength properties of polymer compositions depend on the volume content of individual components, their structure, interfacial interactions of the bulk filler, and also on the amount of charges accumulated in the compositions during various electrical impacts [5].

Therefore, when developing electret and piezoelectric composites, certain requirements are imposed on them, namely: easy processing, high plasticity, mechanical and electrical strength, increased dielectric constant, and a certain conductivity. An analysis of the physical and mechanical properties of polymers and composites based on them shows that the above requirements are most complete form corresponds composites with semiconductor fillers $BiSb_3Te_6$.

This paper presents the results of experimental data on the study of preliminary electrical treatment for the strength of a composition based on polyethylene and a semiconductor compound Bi Se_3Te_6.

EXPERIMENTAL TECHNIQUE

Polymer composites LDPE + BiSb3Te6 were obtained by hot pressing at the melting temperature of the polymer matrix under a pressure of 15 MPa for 10 minutes. The samples were made in the form of a film; the electrical and mechanical strengths of the studied compositions were investigated at room temperature.

The electrical conductivity is observed by the residual current, which is established after 1-2 hours after the appearance of a voltage of 100 V on the composite. Measurements of the resistance of the samples were made using an E6-13A teraohmmeter in the range of 20-150^{0}C with linear heating at a rate of 3 deg/min, using a setup that is similar to the setup for studying dielectric parameters. Samples for testing the force dependence of mechanical strength were cut out of the film with a special knife in the form of a double blade, the working part was 10 mm long and 3 mm wide.

To compensate for the stress during the test, the load P is not suspended directly from the sample, but by means of a figured lever, the arm of which automatically decreases as the length of the sample increases. Assuming that the cross section of the sample decreases in proportion to the relative elongation, that is, the volume remains unchanged, and the arm of which automatically changes as the length of the sample increases, then for σ=const the arm should decrease with increasing transformation according to the formula

$$R = R_0\left(\frac{1}{1+\varepsilon}\right),$$

where: ε - relative elongation, R_0 and R - projections of the radius vector on the horizontal axis in the initial and immersed positions. The thickness of the samples before testing was measured using an ИЗВ -2 instrument with an accuracy of 1 μm.

The electrical strength of the composition was studied according to the method described in [6].

Experimental results and their discussion.

The results of experimental studies of the electrical and mechanical strengths of composites modified with $BiSb_3Te_6$ semiconductor fillers are shown in Figure.

As follows from Figure, the introduction of a small amount of additives into the composition of the polymer, from semiconductor compounds $BiSb_3Te_6$ leads to a significant increase in its electrical and mechanical strengths.

However, as follows from the experimental data, in all cases, with an increase in the volume content of the filler, the strengths from the beginning strongly increase to a maximum. This means that by studying the change in the strength of composites depending on the volume content of fillers, it is possible to determine the optimal conditions for modifying the electrophysical properties of LDPE.

Our studies have shown that the change in the electrical and mechanical strengths of polymer films after the using of the optimal additive also has a significant effect the nature of the polymer.

The established increase in the electrical characteristics of the optimal modified LDPE films can be explained by a change in the physical structure of the polymers at using of the semiconductor additive $BiSb_3Te_6$

It is known that the using of an additive into polymers leads to the formation of a supramolecular organization in the form of coarse and fine spherulitic polymer structures.

It is shown that the highest strength of a non-oriented polymer is provided by the formation of a fine spherulite structure in it, obtained by introducing structure formers into the melt. Violation of an unoriented sample mainly occurs along the boundaries of structural formations.

The strength of these regions depends on the number of passing molecules simultaneously participating in the crystallization of two adjacent segments. The nature of such molecules depends both on the composition and on the amount of modifying additives.

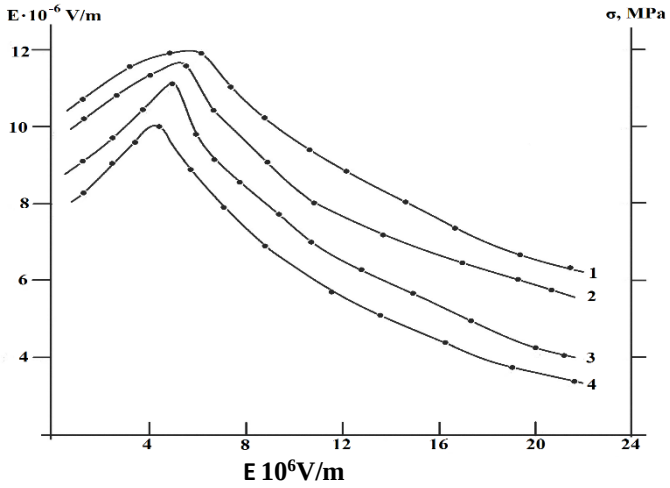


Fig. Dependences of electrical and mechanical strength on the voltage of electrical processing

Based on the foregoing, it follows that the increase in the electrical and mechanical strengths of the LDPE+xvol% $BiSb_3Te_6$ composites with the optimal modification of the composite film can be explained by the formation of a supramolecular organization in the form of a fine spherulite structure.

It is likely that the introduction of semiconductor additives into the polymer in the optimal amount to form a homogeneous, time-stable fine spherulite structure, and creates additional centers of structure formation, while the electrical properties deteriorate significantly. It also follows from the experimental data that the introduction of an optimal semiconductor additive into LDPE significantly reduces the rate of decrease in the electrical and mechanical strengths of the modified film during electrical aging. It is known that the rate of decrease in the electrical characteristics of polymer dielectrics during its electrical aging is mainly due to oxidative degradation.

In this case, the rate of decrease in the electrical strength of the studied composites during its aging, with the introduction of the optimal amount of additives, once again indicates the formation of densely packed structures that prevent oxygen diffusion and the development of ionization processes during electrical destruction. It should be noted that the formation of the structure of the modified polymer, which differs from the structure of the original LDPE, is mainly determined by a change in the crystallization conditions. It has been established that the packing density of structural elements in the matrix decreases significantly from the center to the interface.

The introduction of semiconductor modifiers, which play the role of artificial nuclei of structure formation, into a crystallizing polymer leads to a significant increase in the packing density of supramolecular formations, which is due to more favorable conditions for the crystallization of modified polymers. Low-dispersed particles and large aggregates of modifiers, which do not initiate polymer crystallization, promote the formation of a defective structural zone around itself with a reduced packing density of structural elements.

Modifiers affect the degree of crystallinity and size of semiconductor crystallites, increasing these characteristics with small additions and reducing them to values lower than those of the original polymers with a significant content. As a rule, small additions increase the ordering of the polymer and at the same time reduce the packing density of the micromolecule in the boundary layers.

On the other hand, the strength characteristics of the filled polymer depend on the size, shape of the particles, and the volume content of the filler. With an increase in the content of fillers, the strength characteristics of the composition improve to a certain limit. With a further increase in the filler content, the strength characteristics deteriorate, which is caused by an increase in the rigidity of the polymer chains and the occurrence of large internal stresses and dangerous defects in the material.

Thus, an increase in the particle size causes an increase in the stress concentration in the matrix. Other things being equal, the use of smaller particles leads to a higher strength value of materials, which is confirmed by temperature data.

It should be noted that a decrease in mechanical and electrical strength is observed for all studied composites at high contents of semiconductor filler.

This decrease can be explained by the fact that the polymer matrix plays a binding role, and the electrical and mechanical strengths of the polymer + semiconductor composition are determined mainly by the strength of the polymer soldering between conductor particles. Therefore, a decrease in the electrical and mechanical strength of the compositions with an increase in the volume content of the semiconductor is associated with a decrease in the proportion of the polymer layer between the semiconductor particles and the degree of interaction between the phases of the components of the compositions.

REFERENCES

1. Turik A.B., Garmashov S.I. Dielectric losses in statistical mixtures. // FTT, 2011, 53(6), pp. 1129 - 1132.

2. Aleksandrov E.L., Lebedov E.A., Konstantinova N.N., Aleshin A.N. Switching effect in composite films based on conjugated semifluorene polymer and ZnO nanoparticles. // FTT, 2010, 52(2), pp. 393-396.

3. Chmotin I.A., Ryfkina N.G., Solovieva A.B. Features of electrical properties of composites with shungite filler. // Navy. A. 2004, 46(6) pp. 1061-1070.

4. Kalinin Yu.E., Remizov A.N., Sitnikov A.V. Electrical properties of amorphous nanocomposites (Co_{45}, Fe_{45}, Zr_{10})x$(Al_2O_3)_{1-x}$. // FTT, 2004, 46(11), pp. 2076-2082.

5. Lusheikin G.A. New polymer-containing piezoelectric materials. // FTT, 2006, 48(6), pp. 960-964.

6. Godzhaev E.M., Akhmedova Kh.R., Gamzaeva A.Yu., Osmanova S.S., Mekhtieva Sh.M. Obtaining and researching the properties of new composite materials with semiconductor filler. Proceedings of the VIII International Symposium on Fundamental and Applied Sciences, section "Physical Sciences", Moscow 2013, volume 1, pp. 112 -123.

7. Ershova O.V., Ivanichi S.K., Chuprova L.V., Bakhaeva A.N. Modern composite materials based on a polymer matrix. // International Journal of Applied and Fundamental Research. Moscow, 2015, No. 4, pp. 14 -18.

8. Astafurov S.V., Shilko E.V., Ovcharenko V.E., Psakhie S.G. Investigation of the influence of the properties of interfacial boundaries on the mechanical characteristics of metal-ceramic composites. // Physical Mechanics, 2014, 17(3), pp.53-63.

9. Fatykhov M.A., Enikeev T.I., Akimov I.A. Mechanical properties of composite materials depending on the temperature regime of their manufacture. // Bulletin of OSU, Natural and technical sciences. 2006, No. 2, volume 2, pp. 87-92.

KINEMATIC ANALYSIS OF THE MECHANISM OF THE PLANING MACHINE

Savalan KARIMOV

Dosent, Azerbaijan Technical University, Faculty of Mechanical Engineering and Robotics, Department of Mechatronics and Machine Design, ORCID NO: 0000-0001-7711-6683

Samaya BAGIROVA

Head teacher, Azerbaijan Technical University, Faculty of Mechanical Engineering and Robotics, Department of Mechatronics and Machine Design, ORCID NO: 0000-0003-3273-9937

İlaha RAHIMOVA

Head laborant, Azerbaijan Technical University, Faculty of Mechanical Engineering and Robotics, Department of Mechatronics and Machine Design, ORCID NO: 0000-0002-4176-5515

ABSTRACT

The article considers the kinematic analysis of a six-stage rocker mechanism of the third class of flat feet. The graph-analytical method with the help of a special point (Assur point) builds plans for the velocities and accelerations of the mechanism, taking into account the inertia force of the links, using the Assur points, unknown forces are determined.

Key words: planer, link motion, coriolis, point Assur, crank.

RESEARCH METHOD

In mechanical engineering, a planing machine is generaly used for the processing of plane surfaces. It uses a six-stage mechanism with a plane link, the degree of freedom of which is equal to one.

In the planer, for the movement of the cutter head, a third-class flat-lever mechanism is used, a kinematic diagram, which is shown in Fig. 1.

In complex dam motion, the absolute velocity is equal to the sum of the velocities of its relative motion with the velocity of displacement. In the mechanism under consideration, the wings 2 and 4 perform a complex movement. The joint movement of the rocker with 3 rocker point is a moving action. The forward movements of 2 and 4 rocker stones behind the rocker of 3 are relative movements.

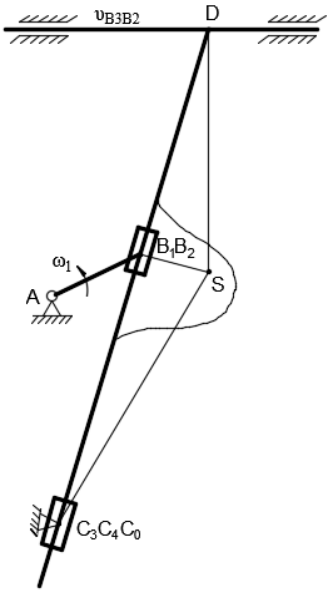


figure 1. Crank - scotch mechanism of the third class

1 – crank; 2 - slide; 3 - coulisse; 4 – slide; 5 - cutting head; 6 - stand.

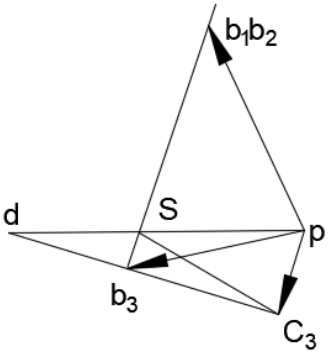


figure 2. The plan of velocities of the mechanism.

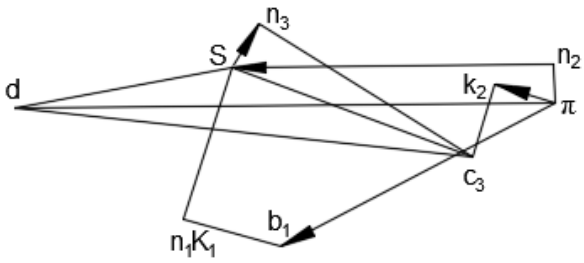


figure 3. Mechanism acceleration plan.

Structural analysis shows that this mechanism is a third-class mechanism.

$$\omega_1 \ , \ l_{AB} \ , \ l_{AC} \ , \ l_{CD} \ , \ l_{BS_3} \ , \ l_{DS_5} \ , \ y \ ,$$

To carry out a kinematic analysis of the mechanism, it is necessary to give its kinematic scheme (the dimensions of the lengths of its elements) and the angular velocity of the input element – the knee AB. Suppose that the input sentence AB moves with a constant ω, angular velocity.

Kinematic analysis is carried out by graphic-analytical methods [1].

To build a plan for the position of the mechanism, we select the scale μ_l

To build a velocity plan, we compose a vector equation for plane-parallel motion. Assume the angular velocity of the input link AB. $V_{B1} = \omega_1 . l_{AB}$

This is the velocity in the direction perpendicular to the link AB, $\overrightarrow{V_{B1}} \perp AB$. The velocity of point B_2 attributable to rocker 2 will be, $\vec{V}_{B_2} = \overrightarrow{V_{B\,1}}$, since points B_1 and B_2 move together. The velocity of point B_3 related to the link of the stage is determined from the vector equation of the complex movement [2].

$\vec{V}_{B_1} = \vec{V}_{B_3} + \vec{V}_{B_1B_3}$

Here: $\vec{V}_{B_3}$ velocity portable, $\vec{V}_{B_1B_3}$ relative velocity.

From here:

$$\vec{V}_{B_3} = \vec{V}_{B_1} + \vec{V}_{B_3B_1} \quad (1)$$

In (1) the equations, $\vec{V}_{B_1}$ – unknown, $\vec{V}_{B_3B_1}$ - known by direction

$\vec{V}_{B_3B_1}$ // CD, magnitude unknown, $\vec{V}_{B_3}$ - unknown in magnitude and direction. Because of this, the vector equation (1) cannot be solved graphically and analytically. Since we consider the mechanism a class III mechanism, in the kinematic analysis of these mechanisms we will use the method of singular points or Assur points. As the point of Assur, we select the points of intersection perpendicular to the line of velocity $\vec{V}_D$ and $\overrightarrow{V}_{B_3B_1}$. This is a special point to designate S [3]. We assume that this point refers to link 3. From the beginning, we determine the velocities $\vec{V}_S$ from the following vector equations.

$$\vec{V}_S = \vec{V}_{B_3} + \vec{V}_{SB_3} \quad and \quad \vec{V}_s = \vec{V}_D + \vec{V}_{SD}$$

From here:

$$\vec{V}_{B_3} + \vec{V}_{SB_3} = \vec{V}_D + \vec{V}_{SD}$$

Taking into account equation (1)

$$\vec{V}_{B_1} + \vec{V}_{B_3B_1} + \vec{V}_{SB_3} = \vec{V}_D + \vec{V}_{SD} \quad (2)$$

From (2) it can be seen that $\vec{V}_{B_3B_1}$ and $\vec{V}_{SB_3}$, as well as the vector $\vec{V}_D + \vec{V}_{SD}$. Collenary vector equations (2) allow you to determine the velocity $\vec{V}_S$ т.е. $\vec{V}_S$ points of Assur [4]. After determining the velocity of point S, we proceed to determine the velocity of C_3 referring to the link motion (coulisse) 3.

$\vec{V}_{C_3} = \vec{V}_S + \vec{V}_{C_3S}$

$\vec{V}_{C_3} = \vec{V}_{C_0}^{\,0} + \vec{V}_{C_3C_0}$

From here:

$$\vec{V}_S + \vec{V}_{C_3S} = \vec{V}_{C_3C_0} \quad (3)$$

Here: $\vec{V}_{C_3S} \perp$ CS и $\vec{V}_{C_3C_0} \parallel$ CD

Solving the vector equation (3) determines the velocity $\vec{V}_{C_3}$. The velocity of point D (Fig.2) is determined by constructing from the triangle similarity condition $\triangle\ CSD \sim \triangle\ C_3SD$ [5].

In complex motion, if the moving motion is a curve, the absolute accelerations is equal to the sum of the transfer, relative and karyolysis accelerations. Since the rockers 2 and 4 perform complex motion in the mechanism under consideration, the accelerations of points B_3 and C_3 related to these points are found from the vector equations of complex motion. After constructing the accelerations plan of the mechanism, the angular moments of the linear positions of the points of these mechanisms are found. To find linear accelerations, it is necessary to equel the line section reflecting the acceleration of the point from the accelerations plan by the scale of the accelerations plan. To find the angular momentum of the dam, it is necessary to divide the tangent moment of an arbitrary point related to the dam by the length of the dam.

The problem of accelerations is solved similarly to the problem of velocities. Here, as well as to determine the velocities, we use the singular point S on link 3. From the beginning, the acceleration of point B_1 is determined [6]. For $\omega_1 = const$

$$\vec{a}_{B_1} = \vec{a}^{n}_{B_1} = \omega_1^2 . l_{AB} \ , \ \vec{a}^{n}_{B_1} \ // \ BA \, .$$

Acceleration point B_3 is determined from the vector equation of complex motion.

$$\vec{a}_{B_3} = \vec{a}_{B_2} + \vec{a}^{k}_{B_3B_2} + \vec{a}^{r}_{B_3B_2} \quad (4)$$

Here: $\vec{a}^{k}_{B_3B_2}$ - coriolis acceleration, $\vec{a}^{r}_{B_3B_2}$ - relative (relative) acceleration [7]. The direction of the Coriolis acceleration is determined by rotating the relative velocities by 90°. $\vec{V}_{B_3B_2}$ in the direction of the angular velocity of the portable motion - ω_3

The magnitude of this acceleration according to the formula:

$$\vec{a}^{k}_{B_3B_2} = 2\omega_3 \cdot \vec{V}_{B_3B_2} \quad (5)$$

Relative accelerations $\vec{a}^{r}_{B_3B_2}$ directed perpendicular to the coriolis acceleration, i.e. parallel to $\vec{V}_{C_3C_2}$

Equation (4) is not solved separately. Therefore, we consider the acceleration of point S [8].

$$\vec{a}_S = \vec{a}_{B_3} + \vec{a}^{n}_{SB_3} + \vec{a}^{\tau}_{SB_3} \qquad \vec{a}_S = \vec{a}_D + \vec{a}^{n}_{SD} + \vec{a}^{\tau}_{SD}$$

From here:

$$\vec{a}_{B_3} + \vec{a}^{n}_{SB_3} + \vec{a}^{\tau}_{SB_3} = \vec{a}_D + \vec{a}^{n}_{SD} + \vec{a}^{\tau}_{SD}$$

Taking into account (5), we have.

$$\vec{a}_{B_2} + \vec{a}^{k}_{B_3B_2} + \vec{a}^{r}_{B_3B_2} + \vec{a}^{n}_{SB_3} + \vec{a}^{\tau}_{SB_3} = \vec{a}_D + \vec{a}^{n}_{SD} + \vec{a}^{\tau}_{SD} \quad (6)$$

The solution of equation (6) determines the acceleration $\vec{a}_S$.

After that, we proceed to the definitions of the acceleration of the point C_3 [9].

Let's write the accelerations C_3 relative to the point S and C_o:

$$\vec{a}_{C_3} = \vec{a}_S + \vec{a}^{n}_{C_3S} + \vec{a}^{\tau}_{C_3S} ; \quad \vec{a}_{C_3} = \vec{a}^{0}_{C_0} + \vec{a}^{k}_{C_3C_0} + \vec{a}^{r}_{C_3C_0} ; \ \vec{a}^{0}_{C_0} = 0$$

From here:

$$\vec{a}_S + \vec{a}^{n}_{C_3S} + \vec{a}^{\tau}_{C_3S} = \vec{a}^{k}_{C_3C_0} + \vec{a}^{r}_{C_3C_0} \quad (7)$$

The solution of the vector equation (7) determines the acceleration of the point C_3

After that, from similar $\Delta\, CDS$ and $\Delta\, C_3dS$, the point acceleration is determined $D - \vec{a}_D$ (Fig.3).

RESULT

The article solves the problem of the velocity of a third-class flat rocker mechanism that moves the cutting head of the machine. The velocities of the points of the mechanism and the angular velocities of its points are found.

In the second part of the article, a plan of the acceleration of this mechanism is drawn up, the linear acceleration of its points are searched, then the angular acceleration of the points of the mechanism, price and direction.

LITERATURE

1. Kəngərli A.M. Maşın və mexanizmlər nəzəriyyəsi, Dərslik, Bakı, 2004.
2. Kərimov S.X. və b. Maşın və mexanizmlər nəzəriyyəsi kursu. Dərs vəsaiti, Bakı, NPM "Təhsil", 2012, 350s.
3. Xəlilov Ə.M. Tətbiqi mexanika. Bakı, Dərslik, "Təhsil", 2008.527s.
4. Н. И. Левитский. Теория механизмов и машин, М, «Наука», 1990.
5. Əliyev Ş.N., Məmmədov F.H., Kəngərli L.A. Maşın və mexanizmlər nəzəriyyəsi. Layihələndirmə. Dərs vəsaiti. Bakı, "Təhsil" NPM, 2010, 286 s.
6. Kəngərli A.M., Əliyev Ş.N., Kərimov S.X. Maşın və mexanizmlər nəzəriyyəsi kurs layihəsi. Dərslik. Bakı, "Təhsil" NPM, 2005, 428 s.
7. Məmmədov F.H., Xəlilov İ.Ə. Kərimov S. Tətbiqi mexanika. Bakı, Turxan NPB, 2015 il.
8. Артоболевский И.И. Теория механизмов и машин. Москва, 1985
9. Кореняко А.С. Теория механизмов и машин. Москва, 1976

RED ROBİN PHOTİNİA YAPRAKLARINDAN ELDE EDİLEN DOĞAL BOYA İLE BOYANMIŞ FARKLI KUMAŞ YAPILARINDAKİ YÜNLÜ KUMAŞLARIN BOYANMA ÖZELLİKLERİ VE RENK AÇISINDAN GÖRSEL DEĞERLERİNİN İNCELENMESİ

Habip DAYİOĞLU [1]

[1]*İstanbul Ticaret Üniversitesi, Mimarlık ve Tasarım Fakültesi, Tekstil ve Moda Tasarımı Bölümü, İstanbul, Türkiye, ORCID ID: https://orcid.org/0000-0002-2069-4412*

Nigar MERDAN [2]

[2]*İstanbul Ticaret Üniversitesi, Mimarlık ve Tasarım Fakültesi, Tekstil ve Moda Tasarımı Bölümü, İstanbul, Türkiye, ORCID ID: https://orcid.org/0000-0001-7246-4849*

Irmak BAYBURTLU [3]

[2]*İstanbul Ticaret Üniversitesi, Mimarlık ve Tasarım Fakültesi, Tekstil ve Moda Tasarımı Bölümü, İstanbul, Türkiye, ORCID ID: https://orcid.org/0000-0002-2493-2967*

Sema Hatun TÜRKER [4]

[1]*İstanbul Ticaret Üniversitesi, Mimarlık ve Tasarım Fakültesi, Tekstil ve Moda Tasarımı Bölümü, İstanbul, Türkiye, ORCID ID: https://orcid.org/0000-0002-1559-9373*

Abstract

Especially in recent years, dyeing textiles with environmentally friendly natural dyes is gaining more and more importance in terms of chemicals harmful to the environment in the waste water formed after conventional dyeing of textile products. In this study, wool fabric in different textures was dyed at different pH values with the natural dye obtained from the leaves of the Red Robin Photinia (Photinia x fraseri/alev calisi) plant. The colour appearances obtained were evaluated visually according to the different textures of the woven fabric.

The aim of this study is to investigate the colour properties of dyed wool fabric by use of these plant leaves. The natural dye was extracted from the leaves of Red Robin Photinia plant. In this study, 100% wool woven fabric samples in plain, twill and satin weave with the same yarn count were used. Citric acid, ferrous sulfate and tin chloride were used as mordant material. These mordant materials were applied to the undyed wool fabric samples according to the pre-mordanting method. The CIELab values, colour strengths (K/S) and the colour fastness of rubbing, washing and light were investigated. In addition, the colour changes of the natural dye solution obtained from Red Robin Photinia at pH 3.0, 5.0, 7.0, 9.0 and 11.0 in acidic, neutral and basic pH values were determined and the indicator properties of this natural dye were determined. As a result, the artistic value of these dyed samples were investigated in terms of natural dye.

The natural dye, which was analyzed technically, was applied to the three basic weaving reports in weaving and the colour /texture structure report relationship was evaluated visually. With this evaluation, it is aimed to present a mini colour chart created with the colour tones obtained from the plant in question to the weaving designers who make natural dye applications. It is thought that this study will set an example for making a new colour chart for dyes and fabric / texture structure report combinations to be obtained with other suitable plants. With this colour chart, it is aimed to contribute to the design processes of companies in their collections using natural dyes in industrial production.

Keywords: Natural Dye, Environmentally Friendly, Weaving Structures, Design.

Introduction

Environmental pollution and excessive use of synthetic dyestuffs cause serious health hazards and disruptions in the eco-balance of nature (Karadag, 2007).

The used natural dyes are less toxic and less allergenic compared to synthetic dyes. Due to these advantages, these dyes have found application again in recent years in the fields of food, pharmaceuticals, cosmetics and textiles (Shabbir et al., 2016).

In the evaluation of ecological and economic resources, interest in the production of eco textiles based on natural dyes is increasing and dyes obtained from various dye plants are used for dyeing natural fibers such as wool, silk and cotton (Samantaa and Agarwal, 2009; Shahid et al., 2013).

Natural dyestuffs derived from plants, animals or minerals without chemical treatment show better compatibility with the environment due to their non-toxic nature (Goodarzian and Ekrami, 2010) and potential for renewability (Das and Sinha, 2012).

Synthetic dyes are commercially more advantageous than natural dyes in terms of low cost, wide color range and high color fastness. Being able to cope with these superior properties of synthetic dyestuffs have been the focus of attention of researchers in recent years. Both non-environmentally burdened mordanting agents and methods and more environmentally friendly dyeing methods have been the subject of research (Shahid et al., 2013).

Most of the natural colorants are commonly obtained from the flower parts of plants (Saha and Datta, 2008).

There are natural chromogens such as indigo, anthraquinone, naphthoquinone, phenalon, tannin, anthocyanin, carotenoid, flavonoid and chlorophyll in dye plants (Karadag and Deveoglu, 2011).

Today, scientists working in the field of natural colorant technology have focused on improving the extraction of colorants from the plant and their application to the modified surface. Different techniques such as UV, microwave or ultrasonic treatment in dyestuff extraction, and gamma radiation treatment, bio-polishing, cationization and mercerization processes are emphasized for surface modification of the fibre (Sinha et al., 2013). The discovery of natural colorant sources has been the subject of many studies over the past few decades. Despite all efforts, scientists have investigated very few of the hundreds of thousands of species found on earth (Siva, 2007).

Germination and flowering of annual and biennial plants often occurs only once a year. For this reason, some problems are encountered in using the flowers of the plant as a natural dye source. For example, all perennials begin to bloom after a few years. Reasons such as not being easily available / scarcity of flowers increase the cost of dyestuffs obtained from these plants. Therefore, there is a need to investigate the coloring potential of the non-flowering parts of commonly grown and less expensive plants. This research includes the dyeability properties of the leaves of the flame bush (Photinia x Fraseri 'Red Robin') as a natural dye source in wool dyeing. There are some studies in the literature on the color and fastness properties of natural dye obtained from various plant leaves applied to wool and silk materials.

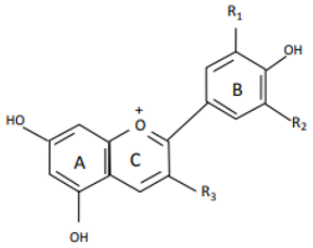
Examination of the dyeing properties of cotton and wool with the dye obtained from Prunus persica leaves (Önal et al., 2021), dyeing of silk and wool with the dye extracted from eucalyptus leaves by the foulard method (Mongkholrattanasit et al., 2010) are the researched subjects. Gong et al. investigated the UV protection properties of pigments obtained from the leaves of the camphor tree (Cinnamomum Camphora) on silk and wool (Gong et al., 2019). In another study, in which camphor tree (Cinnamomum Camphora) wastes and fallen leaves were examined as a dye source, the color properties of merino wool were investigated (Rather et al., 2020). Singh and Srivastava examined whether various plant leaves could be an alternative natural dye source (Singh and Srivastava, 2017), Banna et al. examined different mordant applications of the dye obtained from mango leaves on silk, cotton and polyester (2019). Juglans regia L. leaves (Önal et al., 2021), Illicium Griffithii leaves (Vankar and Dixit, 2011), Lemon leaves (Sangeetha et al., 2015), Henna leaves (Alam et al., 2007), Mimusops Elengi Linn leaves (Hossain et al., 2021), Vitis vinifera L. leaves (Mansour et al., 2016), apple tree leaves (Eser et al., 2016), Junipers leaves (Özdemir, 2017), grape leaves (Haji et al., 2016) and hamelia leaves (Paul et al., 2005) are researched studies in the dyeing of protein fibers as a natural dye source.

Flame bush (Photinia x Fraseri 'Red Robin'), used as a natural dye source in this research, is a plant belonging to the Rosaceae family, with a height of 4-6 m and a maximum width of 2-4 m. (Figure 1). The forms of this hybrid are quite durable. It is the ideal choice for hedge applications with its flame red leaves. These shrubs generally have two leaf colors (red-young and green-adult) in the same growth period in spring (Cetiner and Zencirkiran, 2020; Wang et al., 2017).

The chromophore group in the natural dye obtained from the leaves of the flame bush is in the anthocyanin structure (Figure 2) (Oren-Shamir and Nissim-Levi, 1999).



Figure 1. Red Robin Photinia



$R_1 = H, R_2 = H$	pelargonidin
$R_1 = OH, R_2 = H$	cyanidin
$R_1 = OH, R_2 = OH$	delphinidin
$R_1 = OCH_3, R_2 = H$	peonidin
$R_1 = OCH_3, R_2 = OH$	petunidin
$R_1 = OCH_3, R_2 = OCH_3$	malvidin
$R_3 = OH$	3-hydroxyanthocyanidin

Figure 2. Basic structure of anthocyanins (Keles, 2015)

The aim of this study is to use Red Robin Photinia leaves as a natural dye source to obtain a cheap and easily available natural colorant for the textile industry and to examine the color strength, color fastness of the wool fabric and the visual values of the obtained dyeing in terms of color.

2. Material and Method

2.1. Material

In this study, 100% wool yarn with a yarn count of 66/2 Nm was used to produce a fabric with three different structures as 1/1 plain, 2/2 twill Z and 4/1 satin. The weft density is 24 yarn/cm, the warp 24 yarn/cm. The weight of the fabrics were approximately 165g/m2. Three different mordants were used in this study such as citric acid, ferrous sulfate and tin chloride.

Mordanting and dyeing processes were carried out in the laboratory at atmospheric dyeing machine (Thermal). Color measurements of the dyed samples were measured by using Macbeth 2180 UV color measuring device. Washing fastness tests were carried out on Gyrowash Washer Tester. Rubbing fastness tests were performed in Crockmeter (James Heal) tester and light fastnesses were performed in James Heal light fastness tester.

Natural dye obtained from Robin Photinia leaves by citric acid + water extraction method was used for dyeing.

2.2. Method

Dyestuff Extraction

In the applications, citric acid + water extraction method was used. For extraction, 100 g of Red Robin Photinia leaves were boiled in 1000 ml of water and 0.5 g/l citric acid (pH 4) for 1 hour and the obtained natural dyestuff was filtered and left to cool.

Mordanting

Pre-mordanting was applied to fabric samples in three different textures with plain, twill and satin weaves. Three different mordant substances, citric acid, ferrous sulfate and tin chloride, were applied to 2 g of wool fabric in a liquor at 1/40 liquor ratio for one hour at boiling temperature. At the end of the mordanting process, the excess liquor in the fabric was removed and no rinsing was performed.

Dyeing Process

The dyestuff extract obtained from Red Robin Photinia leaves was used in undiluted form. Before dyeing the pH values of the dye liquors were adjusted to 4.5, 5.5, 6.5, 7.5 and 8.5. Mordanted wool fabric samples were prepared in these liquors, after dyeing in a 1:40 liquor ratio for 1 hour at boiling temperature, by overflow washing was done with 500 ml cold water. Afterwards, the samples were washed with 250 ml of hot water at 60 °C, followed by 250 ml of boiling soaping(5 g/1000ml water), and finally, after rinsing with 500 ml of cold water. Then the samples were squeezed and left to drying. Figure 3 shows the temperature-time diagram of the dyeings.

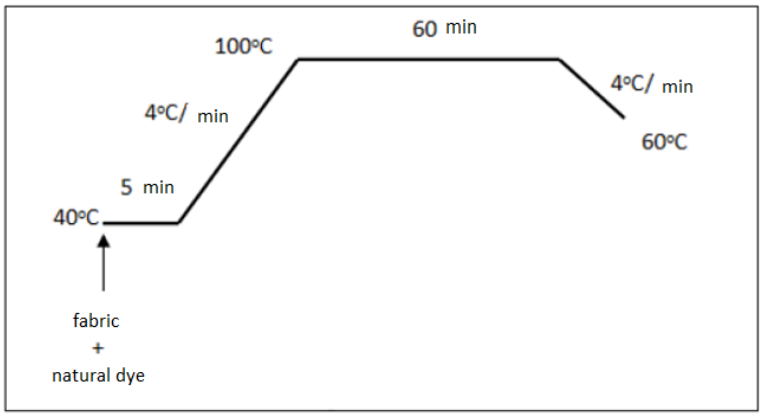


Figure 3. Diagramme of tempereture-time.

Colorimetric Measurements

L *(brightness), a*(red-green), b*(yellow-blue) and chroma values of the samples dyed in this study were determined by Macbeth 2180 UV Color Measurement Device, Datamaster computer program and CIELab system, under the D65 illuminat at 10° standard observer. carried out using Color yield is given by the K/S value, which is the Kubelka-Munk equation (Xin: 2006).

Color Fastness Tests

In this study, the color resistance of the samples dyed against washing was tested according to the ISO 105-C06: 2010 standard (ISO 105-C06: 2010, Test for Color Fastness of Textiles-Colour Fastness to Washing). The color change in the samples and the degree of staining of the accompanying fabric were determined by gray scales.

Determination of color fastness to dry and wet rubbing was carried out on the basis of ISO 105-X12:2016 standard, and color bleeding on accompanying standard cloths was evaluated with A03 gray scale in a standard light cabinet (ISO 105-X12:2016, Tests for Color Fastness -Part X12: Color Fastness). to Rubbing).

The color fastness of dyeing to light was determined based on the EN ISO 105-B02 standard (EN ISO 105-B02, Textiles - Tests for Color Fastness, to Artificial Light) and evaluated with a blue scale.

Visual Assessment in Terms Of Color and Hue Method

Real dyed fabric samples were determined by comparing with the original fashion and home pantone color chart.

2.3. Measurement results

CIELab Values

Table 1 shows the colorimetric properties of plain, twill and satin knit fabrics without mordant dyeing according to CIELab color coordinates.

Table 1. CIELab Values of dyeing with no mordant.

Without mordant - CIELab Values - D65 - 10°										
	L*	**a***	**b***	**C***	**h°**	**X**	**Y**	**Z**	**x**	**y**
Plain	61,92	4,88	21,56	22,11	77,23	30,00	30,30	19,24	0,38	0,38
Twill	62,18	4,67	21,71	22,20	77,87	30,25	30,62	19,40	0,38	0,38
Satin	62,29	4,69	22,12	22,61	78,02	30,38	30,74	19,28	0,38	0,38

Colorimetric properties of citric acid mordant dyeing of plain, twill and satin weave fabrics according to CIELab color coordinates are given in Table 2. In fabrics with three different textures, dyeing at pH 6.5 is darker than dyeing without mordant. In the samples with plain, twill and satin weave on the red-green axis, the red nuance is more at pH 8.5. For three different fabrics on the yellow-blue axis, the yellow nuance is higher at pH 6.5 and the blue nuance is higher at pH 4.5. The most saturated color was obtained in satin knitted fabric at pH 5.5 (Table 2).

Table 2. CIELab values of dyeing mordanted by citric acid.

	pH	Citric acid - CIELab Values - D65 - 10°									
		L*	a*	b*	C*	h°	X	Y	Z	x	y
Plain	4.5	61,94	4,23	23,59	23,97	79,84	29,86	30,34	18,24	0,38	0,39
	5.5	63,02	3,96	24,74	25,06	80,90	31,03	31,61	18,59	0,38	0,39
	6.5	59,53	2,22	45,45	45,50	87,20	26,71	27,61	8,17	0,43	0,44
	7.5	63,49	3,62	35,37	35,56	84,16	31,48	32,18	14,10	0,40	0,41
	8.5	63,41	4,59	33,34	33,65	82,15	31,65	32,08	14,90	0,40	0,41
Twill	4.5	62,88	3,54	24,09	24,35	81,63	30,75	31,44	18,79	0,38	0,39
	5.5	63,64	3,23	25,49	25,70	82,79	31,56	32,36	18,75	0,38	0,39
	6.5	61,53	3,08	46,76	46,86	86,23	29,09	29,85	8,80	0,43	0,44
	7.5	64,93	3,78	35,32	35,52	83,89	33,26	33,96	15,18	0,40	0,41
	8.5	63,91	4,75	34,51	34,84	82,17	32,30	32,70	14,77	0,40	0,41
Satin	4.5	62,39	3,59	24,82	25,08	81,78	30,21	30,87	18,02	0,38	0,39
	5.5	63,28	2,96	26,05	26,22	83,52	31,06	31,93	18,17	0,38	0,39
	6.5	61,42	3,35	47,03	47,15	85,92	29,05	29,73	8,67	0,43	0,44
	7.5	65,52	3,72	35,32	35,52	83,99	33,96	34,71	15,63	0,40	0,41
	8.5	64,62	5,12	34,61	34,98	81,58	33,26	33,57	15,26	0,41	0,41

In dyeing with iron sulfate mordant; In all three fabrics with plain, twill and satin weaves, all dyeing is darker than dyeing without mordant. On the red-green axis, there is more green nuance at pH 4.5, and more red nuance at pH 4.5. On the yellow-blue axis, there is more blue nuance at pH 5.5 and more yellow nuance at pH 6.5. The most saturated color was obtained in plain knitted fabric at pH 6.5 (Table 3).

Table 3. CIELab values of samples dyed after ferric sulphate mordanting

	pH	Ferric sulphate - CIELab Values - D65 - 10°									
		L*	a*	b*	C*	h°	X	Y	Z	x	y
Plain	4.5	48,61	2,45	18,37	18,54	82,40	16,82	17,28	10,80	0,37	0,38
	5.5	36,57	7,17	17,01	18,46	67,13	9,69	9,31	5,35	0,40	0,38
	6.5	41,04	7,02	20,69	21,84	71,26	12,26	11,89	6,28	0,40	0,39
	7.5	39,46	6,63	18,81	19,94	70,59	11,25	10,93	6,08	0,40	0,39
	8.5	43,07	5,89	17,09	18,07	70,98	13,41	13,21	8,17	0,39	0,38
Twill	4.5	50,11	2,61	18,74	18,92	82,06	18,04	18,51	11,59	0,37	0,38
	5.5	38,03	7,28	17,55	19,00	67,49	10,51	10,11	5,80	0,40	0,38
	6.5	40,77	7,02	19,74	20,95	70,43	12,10	11,72	6,40	0,40	0,39
	7.5	40,94	6,35	17,88	18,98	70,46	12,11	11,83	6,94	0,39	0,38
	8.5	43,98	6,47	17,82	18,96	70,05	14,11	13,82	8,41	0,39	0,38
Satin	4.5	48,57	2,46	18,86	19,02	82,56	16,79	17,24	10,60	0,38	0,39
	5.5	36,55	7,58	17,85	19,39	66,99	9,73	9,30	5,17	0,40	0,38
	6.5	40,31	7,39	20,38	21,68	70,07	11,86	11,44	6,05	0,40	0,39
	7.5	38,99	7,47	19,09	20,50	68,64	11,08	10,65	5,82	0,40	0,39
	8.5	43,61	6,52	17,86	19,01	69,94	13,87	13,57	8,21	0,39	0,38

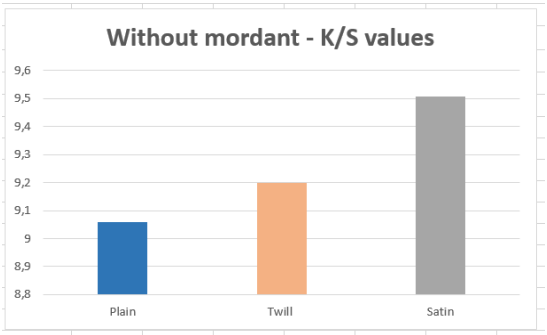
In dyeing with tin chloride mordant; In three fabrics with plain, twill and satin weave, dyeing is generally darker than dyeing without mordant. On the red-green axis, red nuance is higher at pH 5.5 and green nuance is higher at pH 6.5. On the yellow-blue axis, there is more yellow nuance at pH 4.5, and more blue nuance at pH 5.5. The most saturated color was obtained in satin knitted fabric at pH 4.5 (Table 4).

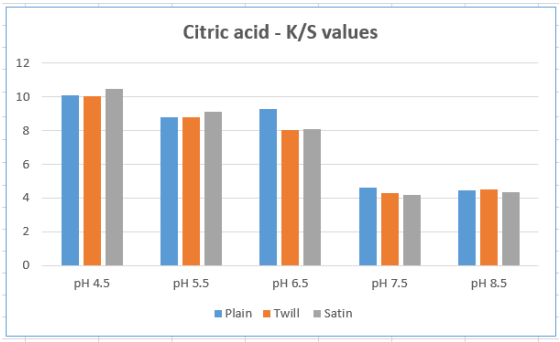
Table 4. CIELab valuesw of samples dyed after tin chloride mordanting.

	pH	Tin chloride - CIELab Values - D65 - 10°									
		L*	a*	b*	C*	h°	X	Y	Z	x	y
Plain	4.5	57,87	1,48	44,51	44,53	88,10	24,82	25,82	7,63	0,43	0,44
	5.5	48,81	0,04	29,40	29,40	89,92	16,54	17,44	7,49	0,40	0,42
	6.5	63,04	4,60	32,24	32,56	81,88	31,23	31,64	15,11	0,40	0,41
	7.5	61,46	1,75	41,78	41,81	87,60	28,68	29,78	10,37	0,42	0,43
	8.5	60,92	2,76	43,42	43,50	86,36	28,34	29,16	9,52	0,42	0,44
Twill	4.5	58,56	2,00	44,55	44,59	87,43	25,64	26,55	7,95	0,43	0,44
	5.5	48,14	-1,00	30,68	30,70	91,87	15,86	16,91	6,84	0,40	0,43
	6.5	60,57	4,10	32,92	33,17	82,91	28,30	28,76	13,06	0,40	0,41
	7.5	62,08	1,76	40,84	40,87	87,53	29,37	30,50	11,07	0,41	0,43
	8.5	58,88	3,50	44,36	44,50	85,49	26,34	26,90	8,16	0,43	0,44
Satin	4.5	59,15	2,01	44,80	44,84	87,43	26,26	27,19	8,17	0,43	0,44
	5.5	46,85	-0,49	29,67	29,67	90,96	15,00	15,91	6,54	0,40	0,42
	6.5	59,91	4,35	32,14	32,43	82,30	27,65	28,03	12,91	0,40	0,41
	7.5	62,44	2,39	40,22	40,29	86,60	29,94	30,92	11,51	0,41	0,43
	8.5	60,52	3,28	44,25	44,37	85,76	28,03	28,70	9,04	0,43	0,44

K/S values

In Figures 4 and 5, the K/S values at the maximum absorption wavelength (400 nm) of the samples that were not mordanted and dyed with natural dyestuff obtained from Red Robin Photinia leaves after mordanting with citric acid are given.





Plain	9,0600
Twill	9,1975
Satin	9,5060

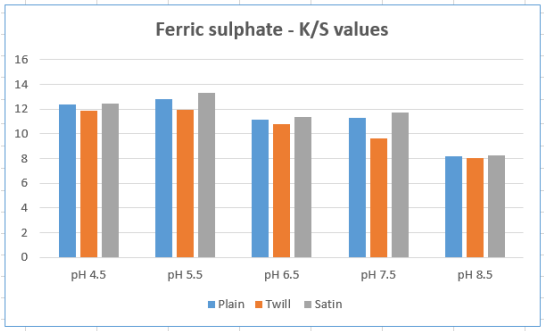
	pH 4.5	pH 5.5	pH 6.5	pH 7.5	pH 8.5
Plain	10,0784	8,7675	9,2598	4,5944	4,4662
Twill	10,0602	8,7770	8,0570	4,3052	4,4911
Satin	10,4897	9,1258	8,0897	4,2031	4,3355

Figure 4. K/S Values of samples with no mordanting.

Figure 5. K/S values of citric acid mordanted dyed samples.

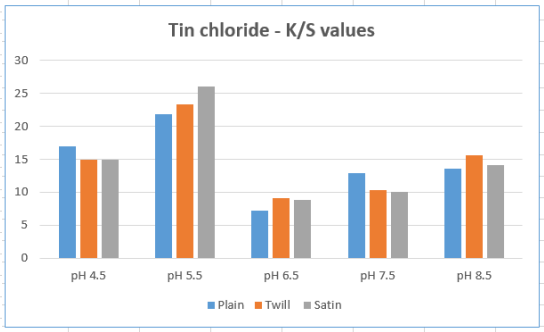
In dyeing with citric acid mordant; compared to other pH applications, the highest color yield (K/S) values were obtained in dyeing at pH 4.5 on fabrics with three different textures. The highest K/S value was obtained in satin fabric (pH:4.5 –K/S: 10.4897) (Figure 4).

In dyeing with iron sulfate mordant; The K/S values for the three fabrics are generally higher than for dyeing without mordant. The highest K/S value was obtained in plain fabric (pH: 5.5 –K/S: 13.3441) (Figure 6).



	pH 4.5	pH 5.5	pH 6.5	pH 7.5	pH 8.5
Plain	12,3966	12,8017	11,1492	11,3054	8,1932
Twill	11,8647	11,9143	10,7791	9,6224	8,0287
Satin	12,4145	13,3441	11,3964	11,7423	8,2820

Figure 6. K/S values of dyed samples by ferric sulphate mordanting.



	pH 4.5	pH 5.5	pH 6.5	pH 7.5	pH 8.5
Plain	16,9834	21,8420	7,2039	12,8398	13,6263
Twill	14,8762	23,2821	9,1309	10,3535	15,6401
Satin	14,9774	26,0363	8,8583	10,0784	14,1109

Figure 7. K/S values of dyed samples mordanted by tin chloride.

In dyeing with tin chloride mordant; K/S values for three fabrics with plain, twill and satin weave are generally higher than dyeing without mordant. The highest K/S value was obtained in satin fabric (pH: 5.5 –K/S: 26.0363) (Figure 7).

RGB color values obtained with CIELab values

The RGB color codes of the samples obtained by using the CIELab values determined by the spectroscopic measurements of the dyes in the easyrgb program are shown in Figure 8 (https://www.easyrgb.com/en/convert.php#inputFORM).

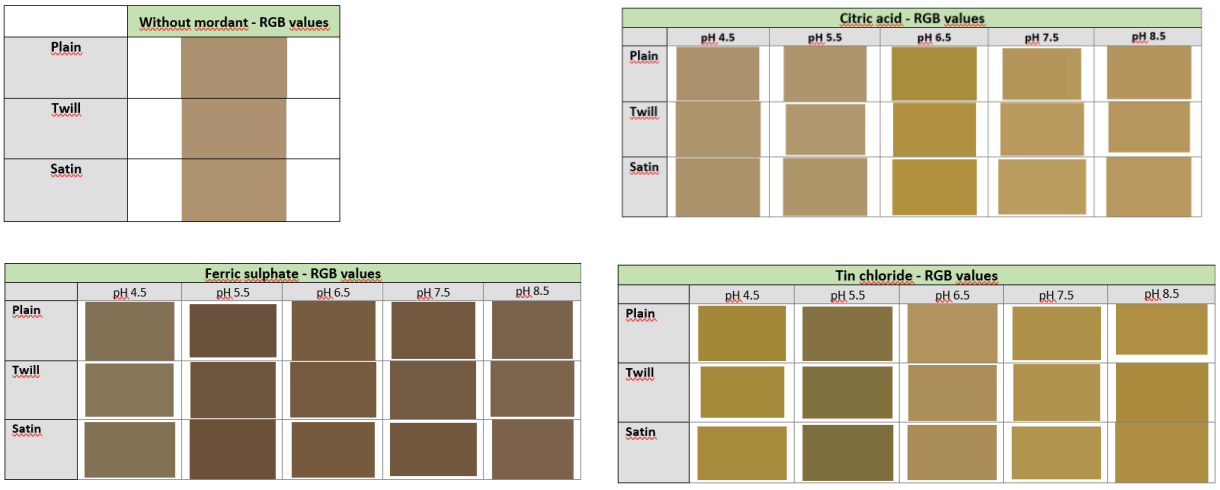


Figure 8. RGB colour values obtained from CIELab values.

Washing, rubbing and light fastness of dyeing

In Table 5, the washing, rubbing and light fastness values of the samples dyed without mordanting are given. Here, the washing staining fastness values and dry rubbing fastness values are among the values accepted by the industry (Table 5).

Table 5. Washing, rubbing and light fasness values of the samples dyed without mordanting.

	Washing							Rubbing		Light
	Color change	Staining								
		CA	CO	PA	PET	PAN	WO	dry	wet	
WITHOUT MORDANT										
Plain	3	5	5	5	5	5	5	4	3/4	2/3
Twill	3	5	5	5	5	5	5	4	3/4	2/3
Satin	3	5	5	5	5	5	5	3/4	3/4	2/3

It is seen from Table 6, that the washing, crocking and light fastness values of samples dyed after mordanting with citric acid . After citric acid mordanting,the staining washing fastness and dry crocking fastness values was found industrially acceptabla. (Table 6).

Table 6. The washing, crocking and light fastness values of samples dyed after citric acid mordanting.

		Washing							Rubbing		Light
		Color change	Staining								
			CA	CO	PA	PET	PAN	WO	dry	wet	
	pH	Mordant: CITRIC ACID									
Plain	4,5	2/3	5	5	5	5	5	5	5	4/5	2/3
	5,5	3	5	5	5	5	5	5	5	4/5	2/3
	6,5	4	5	5	5	5	5	5	4	3/4	2/3
	7,5	4	5	5	5	5	5	5	4	3/4	2/3
	8,5	4/5	5	5	5	5	5	5	4	3/4	2/3
Twill	4,5	2/3	5	5	5	5	5	5	5	4/5	2/3
	5,5	3	5	5	5	5	5	5	5	4/5	2/3
	6,5	4	5	5	5	5	5	5	4	3/4	2/3
	7,5	4	5	5	5	5	5	5	4	3/4	2/3
	8,5	4/5	5	5	5	5	5	5	4	3/4	2/3
Satin	4,5	2/3	5	5	5	5	5	5	5	4/5	2/3
	5,5	3	5	5	5	5	5	5	5	4/5	2/3
	6,5	4	5	5	5	5	5	5	4	3/4	2/3
	7,5	4	5	5	5	5	5	5	4	3/4	2/3
	8,5	4/5	5	5	5	5	5	5	4	3/4	2/3

In Table 7, the washing, rubbing and light fastness values of the dyed samples after mordanting with iron sulfate are given. Wash-staining fastness values and dry-rubbing fastness values in iron sulfate mordant are among the values accepted by the industry (Table 7).

Table 8 shows the washing, rubbing and light fastness values of the dyed samples after mordanting with stannous chloride are given. Wash-staining fastness values and dry-rubbing fastness values in tin chloride mordant are among the values accepted by the industry (Table 8).

Table 7. The washing, crocking and light fastness values of samples dyed after ferric sulphate mordanting.

		Washing							Rubbing		Light
		Color change	Staining								
			CA	CO	PA	PET	PAN	WO	dry	wet	
	pH	Mordant: FERRIC SULPHATE									
Plain	4,5	2/3	5	5	5	5	5	5	5	3/4	3/4
	5,5	4	5	5	5	5	5	5	3	3/4	3/4
	6,5	4	5	5	5	5	5	5	3	3/4	3/4
	7,5	3/4	5	5	5	5	5	5	3	3/4	3/4
	8,5	4/5	5	5	5	5	5	5	3	3/4	3/4
Twill	4,5	2/3	5	5	5	5	5	5	5	3/4	3/4
	5,5	4	5	5	5	5	5	5	3	3/4	3/4
	6,5	4	5	5	5	5	5	5	3	3/4	3/4
	7,5	3/4	5	5	5	5	5	5	3	3/4	3/4
	8,5	4/5	5	5	5	5	5	5	3	3/4	3/4
Satin	4,5	2/3	5	5	5	5	5	5	5	3/4	3/4
	5,5	4	5	5	5	5	5	5	3	3/4	3/4
	6,5	4	5	5	5	5	5	5	3	3/4	3/4
	7,5	3/4	5	5	5	5	5	5	3	3/4	3/4
	8,5	4/5	5	5	5	5	5	5	3	3/4	3/4

Table 8. The washing, crocking and light fastness values of samples dyed after tin chloride mordanting

		Washing							Rubbing		Light
		Color change	Staining								
			CA	CO	PA	PET	PAN	WO	dry	wet	
	pH	Mordant: TIN CHLORIDE									
Plain	4,5	4	5	5	5	5	5	5	4	3/4	3-4
	5,5	3	5	5	5	5	5	5	4/5	3/4	3-4
	6,5	3/4	5	5	5	5	5	5	5	4/5	3-4
	7,5	4	5	5	5	5	5	5	4	3/4	3-4
	8,5	4/5	5	5	5	5	5	5	4/5	3/4	3-4
Twill	4,5	4	5	5	5	5	5	5	4/5	3/4	3-4
	5,5	3	5	5	5	5	5	5	4	3/4	3-4
	6,5	3/4	5	5	5	5	5	5	5	4/5	3-4
	7,5	4	5	5	5	5	5	5	4	3/4	3-4
	8,5	4/5	5	5	5	5	5	5	4/5	3/4	3-4
Satin	4,5	3/4	5	5	5	5	5	5	4/5	3/4	3-4
	5,5	3	5	5	5	5	5	5	4	3/4	3-4
	6,5	3/4	5	5	5	5	5	5	5	4/5	3-4
	7,5	4	5	5	5	5	5	5	4	3/4	3-4
	8,5	4/5	5	5	5	5	5	5	4/5	3/4	3-4

3. Visual Assessment in Terms Of Color and Hue

The original sample images do not fully reflect the actual color tone for photographic reasons. The true color tone values of the samples included in the research should be determined from the pantone color chart.

Within the scope of the study, using plain, twill and satin weave reports, which are the three basic weaves of the weaving, the visual evaluations of the fine woolen fabric with the natural dyestuff obtained from the Red Robin Photinia plant without mordant, citric acid, iron sulfate, and tin chloride mordanted with these pattern reports were examined as follows.

Pattern types are represented by the following letters in the color chart consisting of the samples examined. The corresponding color codes and names in the Pantone catalog of the samples using citric acid are as follows.

Plain – P

Twill- T

Satin – S

Without Mordant Samples





P **T** **S**

Figure 9. Without mordant patterns and Pantone color response.

Without mordant, Pantone: 15-1220 TPX.

Citric Acid Mordanted Samples



P T S

Figure 10. Mordanted patterns with citric acid, pH 4.5 and Pantone color response. Citric Acid pH 4.5, Pantone: 15-1225 TPX.



P T S

Figure 11. Mordanted patterns with citric acid, pH 5.5 and Pantone color response. Citric Acid pH 5.5, Pantone; 15-0942 TPX.



P **T** **S**

Figure 12. Mordanted patterns with citric acid, pH 6.5 and Pantone color response.

Citric Acid Ph 6.5, Pantone; 16-0742 TPX.



P **T** **S**

Figure 13. Mordanted patterns with citric acid, pH 7.5 and Pantone color response.

Citric Acid pH 7.5, Pantone; 15-0628 TPX.





P T S

Figure 14. Mordanted patterns with citric acid, pH 8.5 and Pantone color response.

Citric Acid pH 8.5, Pantone; 16-0945 TPX.

Ferrous Sulfate Mordanted Samples





P T S

Figure 15. Mordanted patterns with ferrous sulfate, pH 4.5 and Pantone color response.

Ferrous Sulfate pH 4.5, Pantone; 18-0830 TPX.



P **T** **S**

Figure 16. Mordanted patterns with ferrous sulfate, pH 5.5 and Pantone color response. Ferrous Sulfate pH 5.5, Pantone; 18-0930 TPX.



P **T** **S**

Figure 17. Mordanted patterns with ferrous sulfate, pH 6.5 and Pantone color response. Ferrous Sulfate pH 6.5, Pantone; 18-0937 TPX.



P **T** **S**

Figure 18. Mordanted patterns with ferrous sulfate, pH 7.5 and Pantone color response.
Ferrous Sulfate pH 7.5, Pantone; 19-1034 TPX.



P **T** **S**

Figure 19. Mordanted patterns with ferrous sulfate, pH 8.5 and Pantone color response.
Ferrous Sulfate pH 8.5, Pantone; 17-1036 TPX

Tin Chloride Mordanted Samples





P **T** **S**

Figure 20. Mordanted patterns with tin chloride, pH 4.5 and Pantone color response.

Tin Chloride pH 4.5, Pantone; 16-0742 TPX.





P **T** **S**

Figure 21. Mordanted patterns with tin chloride, pH 5.5 and Pantone color response.

Tin Chloride pH 5.5: Pantone; 17-0840 TPX.





P **T** **S**

Figure 22. Mordanted patterns with tin chloride, pH 6.5 and Pantone color response.

Tin Chloride pH 6.5, Pantone; 16-0946 TPX.





P **T** **S**

Figure 23. Mordanted patterns with tin chloride, pH 7.5 and Pantone color response.

Tin Chloride pH 7.5, Pantone; 15-0942 TPX.



P **T** **S**

Figure 24. Mordanted patterns with tin chloride, pH 8.5 and Pantone color response.

Tin Chloride pH 8.5, Pantone; 16-0946 TPX

4. Results and Evaluation

CIELab values:

• In dyeing with citric acid mordant; in fabrics with three different textures, dyeing at pH 6.5 is darker than dyeing without mordant. In the samples with plain, twill and satin weave on the red-green axis, the red nuance is more at pH 8.5. For three different fabrics on the yellow-blue axis, the yellow nuance is higher at pH 6.5 and the blue nuance is higher at pH 4.5. The most saturated color was obtained in satin knitted fabric at pH 5.5.

• In dyeing with iron sulfate mordant; in all three fabrics with plain, twill and satin weaves, all dyeing is darker than dyeing without mordant. On the red-green axis, there is more green nuance at pH 4.5, and more red nuance at pH 4.5. On the yellow-blue axis, there is more blue nuance at pH 5.5 and more yellow nuance at pH 6.5. The most saturated color was obtained in plain knitted fabric at pH 6.5.

• In dyeing with tin chloride mordant; in three fabrics with plain, twill and satin weave, dyeing is generally darker than dyeing without mordant. On the red-green axis, red nuance is higher at pH 5.5 and green nuance is higher at pH 6.5. On the yellow-blue axis, there is more yellow nuance at pH 4.5, and more blue nuance at pH 5.5. The most saturated color was obtained in satin knitted fabric at pH 4.5.

K/S values:

• In dyeing with citric acid mordant; compared to other pH applications, the highest color yield (K/S) values were obtained in dyeing at pH 4.5 on fabrics with three different textures. The highest K/S value was obtained in satin fabric (pH:4.5 –K/S: 10.4897).

• In dyeings with iron sulfate mordant; the K/S values for the three fabrics are generally higher than for dyeing without mordant. The highest K/S value was obtained in plain fabric (pH: 5.5 –K/S: 13.3441).

• In dyeing with tin chloride mordant; K/S values for three fabrics with plain, twill and satin weave are generally higher than dyeing without mordant. The highest K/S value was obtained in satin fabric (pH: 5.5 – K/S: 26.0363).

Washing, rubbing and light fastnesses:

• Washing staining fastness values and dry and wet rubbing fastness values of all dyeings in the research, except light fastness, are among the values accepted by the industry.

• The washing color change values of the dyeings were lower than the staining values. Generally, dry rubbing fastnesses are higher than wet rubbing fastnesses.

• Promising results were obtained with the natural dyestuff obtained from Red Robin Photinia plant leaves used in this study, as an alternative to synthetic dyestuffs.

Visual assessment in terms of color

In the color chart that find out as a result of the research, it was observed that there was no tonal difference according to the 3 main weaving patterns. However, it has been observed that pH values create color and hue differences.

Likewise, in the samples without mordant, there were changes in color tones according to pH values, except for the different image created by three different weave patterns, and it was observed that the weave patterns did not affect the light value perceptibly on the color hue.

In the samples using citric acid, no tonal difference was observed, in which three different weaving patterns were decisive. However, there were differences in hue and color at different pH values.

In the samples using ferrous sulfate, no tonal difference was observed, in which three different weaving patterns were decisive. There were differences in hue at different pH values. However, unlike the samples mordanted with citric acid, color differences were not observed.

In the samples using tin chloride, no tonal difference was observed, in which three different weaving patterns were decisive. However, like citric acid there were differences in hue and color at different pH values.

References

Alam, M.M., Rahman, M. L., Haque, M.Z. (2007). Extraction of Henna Leaf Dye and its Dyeing Effects on Textile Fibre. Bangladesh J. Sci. Ind. Res. 42(2), 217-222

Banna, B.U. at al. (2019). Effectiveness of dyeing with dye extracted from mango leaves on different fabrics by using various mordants. North 2(10):123-143

Cetiner, S. ve Zencirkiran, M. (2020). Alev Calisi (Photinia x fraseri Dress. 'Red Robin')'nın Farkli Saksi ve Yetiştirme Ortamlarinda Fidan Büyüme Ozelliklerinin Belirlenmesi. Bartın Orman Fakültesi Dergisi, 22(2): 294-306

Das, P. ve Sinha, K. (2012) .Natural dye from bixa seeds as a potential alternative to synthetic dyes for use in textile industry. Desalination and Water Treatment, 40(1-3), 298-301

Eser, F. at al. (2016).Dyeing of Wool and Cotton Fabrics with Leaves of Apple (Malus Domestica) Tree. Journal of Natural Fibers, Vol. 13, NO. 3, 289–298

Gong, A. at al. (2019). Natural pigment during flora leaf senescence and its application in dyeing and UV protection finish of silk and wool – a case study of Cinnamomum Camphora, Dyes and Pigments, Volume 166, July 2019, Pages 114-121

Goodarzian, H. ve Ekrami, E. (2010). Wool dyeing with extracted dye from pomegranate (Punica Granatum) Peel. World Applied Sciences Journal, 8 (11),1387-1389

Haji,A., Qavamnia, S.S., Bizhaem, F.K. (2016). Optimization of oxygen plasma treatment to improve the dyeing of wool with grape leaves. Industria Textila, vol. 67, 4, 244-249

Hossain, S. at al. (2021). A natural dye extracted from the leaves of Mimusops Elengi Linn and its dyeing properties on cotton and silk fabrics. The Journal of The Textile Institute, Vol. 112, NO. 3, 455–461

ISO 105-C06: 2010, Test for Colour Fastness of Textiles-Colour Fastness to Washing.

ISO 105-X12:2016, Tests for Colour Fastness -Part X12: Colour Fastness to Rubbing.

EN ISO 105-B02, Textiles - Tests for Colour Fastness, to Artificial Light.

Karadag, R. (2007). Dogal Boyamacilik. T.C. Kultur ve Turizm Bakanligi, Geleneksel El Sanatları Döner Sermaye İsletmesi Merkez Mudurlugu, Ankara

Karadag, R. Deveoglu, O. (2011). Genel Bir Bakış Doğal Boyarmaddeler. M.Ü. Fen Bilimler Dergisi. 23. 1, 21-32

Keles, Y. (2015). Antosiyanin Pigmentlerin Biyokimyasi ve Analizi. Turk Bilimsel Derlemeler Dergisi, 8 (1), 19-25

Mansour, R., Mighri, Z., Mhenni, F. (2016). Exploring the Potential Uses of Vitis vinifera L. Leaves as Raw Material for Textile Dyeing without Metal Mordants. Fibers and Polymers. Vol.17, No.10, 1621-1626

Mongkholrattanasit, R., Kryštufek, J., Wiener, Y. (2010). Dyeing and Fastness Properties of Natural Dyes Extracted from Eucalyptus Leaves Using Padding Techniques. Fibers and Polymers 2010, Vol.11, No.3, 346-350

Onal, A. at al. (2021). Investigation of the dyeing properties of cotton fabrics and wool yarns using Prunus persica leaf extract. Journal of the Indian Chemical Society, Volume 98, Issue 7, 1-5

Oren-Shamir, M. ve Nissim-Levi, A. (1999). Temperature and gibberellin effects on growth and anthocyanin pigmentation in Photinia leaves, Journal of Horticultural Science & Biotechnology, 74 (3), 355-360

Onal, A. at al. (2021). Investigation of the dyeing properties of the colorant extracted from Juglans regia L. leaves on cellulosic and protein fabrics. JOTCSA. 2021; 8(2): 453-460

Ozdemir, H. (2017). Dyeing Properties of Natural Dyes Extracted from the Junipers Leaves (J. excelsa Bieb. and J. oxycedrus L.). Journal of Natural Fibers, 2017, Vol. 14, No. 1, 134–142

Paul,S., Grover, E., Sharma, A.(2005). Natural Dyeing of Silk with Hamelıa Leaves.J, Dailying, Foods & H.S, 24 (l) : 36 - 41

Rather, L.J. at al. (2020). Instrumental characterization of merino wool fibers dyed with Cinnamomum camphora waste/fallen leaves extract: An efficient waste management alternative. Journal of Cleaner Production, Volume 273, 10, 123021, 1-15

Saha, P. Datta, S.(2008). Dyeing of textile fibre using Marigold flower as floral dye. Colourage 55(5), 52-56

Samantaa, A. K. Agarwal, P. (2009). Application of natural dyes on textiles, Indian J. Fibre Text. Res. , 34, 384-399

Sangeetha, K., Gomathi, R., Bhuvaneshwari, M. (2015). Dyeing of Silk Fabric using Lemon Leaves Extract with the Effect of Different Mordants. International Journal of Innovative Research in Science, Engineering and Technology, Vol. 4, Issue 6, 4694-4697

Shabbir, M. at al. (2016) . Application of Terminalia chebula natural dye on wool fiber-evaluation of color and fastness properties. Textiles and Clothing Sustainability 2:1-8

Shahid, M., Islam, S., Mohammad, F. (2013). Recent advancements in natural dye applications: A review. Journal of Cleaner Production 53:310 – 331

Singh; R., Srivastava, S. (2017). A critical review on extraction of natural dyes from leaves International Journal of Home Science 2017; 3(2): 100-103

Sinha, K., Chowdhury, S., Saha, P.D., Datta, S. (2013). Modeling of microwave-assisted extraction of natural dye from seeds of Bixa orellana (Annatto) using response surface methodology (RSM) and artificial neural network (ANN). Ind Crop Prod., 41,165-171

Siva, R. (2007). Status of natural dyes and dye yielding plants in India. Curr Sci., 92(7) 916-925

Xin, H.J, ed. (2006), Total Colour Management in Textiles, Woodhead Publishing Limited.

Wang, C., Xiao, H., Liu, J. Zhou, J. (2017). Differences in leaf functional traits between red and green leaves of two evergreen shrubs Photinia 3 fraseri and Osmanthus fragrans.J. For. Res., 28(3),473–479

Vankar, P.S., Dixit, S. (2011). Natural Dyeing of Cotton, Wool and Silk with the Stem and Leaves Extract of Illicium Griffithii. RJTA Vol. 15 No 2, 77-83

Pantone For Fashion and Home, Pantone Inc., 2003

Internet references

https://www.easyrgb.com/en/convert.php#inputFORM (Erişim tarihi: Kasım 2022)

https://www.pantone.com